YEDOMA PERMAFROST LANDSCAPES AS PAST ARCHIVES, PRESENT AND FUTURE CHANGE AREAS

EDITED BY: Lutz Schirrmeister, Alexander N. Fedorov, Duane Froese, Go Iwahana, Ko Van Huissteden and Alexandra Veremeeva

PUBLISHED IN: Frontiers in Earth Science

frontiers Research Topics

ISSN 1664-8714
ISBN 978-2-88976-466-2
DOI 10.3389/978-2-88976-466-2

About Frontiers

Frontiers is more than just an open-access publisher of scholarly articles: it is a pioneering approach to the world of academia, radically improving the way scholarly research is managed. The grand vision of Frontiers is a world where all people have an equal opportunity to seek, share and generate knowledge. Frontiers provides immediate and permanent online open access to all its publications, but this alone is not enough to realize our grand goals.

Frontiers Journal Series

The Frontiers Journal Series is a multi-tier and interdisciplinary set of open-access, online journals, promising a paradigm shift from the current review, selection and dissemination processes in academic publishing. All Frontiers journals are driven by researchers for researchers; therefore, they constitute a service to the scholarly community. At the same time, the Frontiers Journal Series operates on a revolutionary invention, the tiered publishing system, initially addressing specific communities of scholars, and gradually climbing up to broader public understanding, thus serving the interests of the lay society, too.

Dedication to Quality

Each Frontiers article is a landmark of the highest quality, thanks to genuinely collaborative interactions between authors and review editors, who include some of the world's best academicians. Research must be certified by peers before entering a stream of knowledge that may eventually reach the public - and shape society; therefore, Frontiers only applies the most rigorous and unbiased reviews.
Frontiers revolutionizes research publishing by freely delivering the most outstanding research, evaluated with no bias from both the academic and social point of view.
By applying the most advanced information technologies, Frontiers is catapulting scholarly publishing into a new generation.

What are Frontiers Research Topics?

Frontiers Research Topics are very popular trademarks of the Frontiers Journals Series: they are collections of at least ten articles, all centered on a particular subject. With their unique mix of varied contributions from Original Research to Review Articles, Frontiers Research Topics unify the most influential researchers, the latest key findings and historical advances in a hot research area! Find out more on how to host your own Frontiers Research Topic or contribute to one as an author by contacting the Frontiers Editorial Office: frontiersin.org/about/contact

YEDOMA PERMAFROST LANDSCAPES AS PAST ARCHIVES, PRESENT AND FUTURE CHANGE AREAS

Topic Editors:
Lutz Schirrmeister, Alfred Wegener Institute Helmholtz Centre for Polar and Marine Research (AWI), Germany
Alexander N. Fedorov, Melnikov Permafrost Institute, Siberian Branch of the Russian Academy of Sciences (RAS), Russia
Duane Froese, University of Alberta, Canada
Go Iwahana, University of Alaska Fairbanks, United States
Ko Van Huissteden, VU Amsterdam, Netherlands
Alexandra Veremeeva, Institute of Physical-Chemical and Biological Problems in Soil Science (RAS), Russia

Citation: Schirrmeister, L., Fedorov, A. N., Froese, D., Iwahana, G., Van Huissteden, K., Veremeeva, A., eds. (2022). Yedoma Permafrost Landscapes as Past Archives, Present and Future Change Areas. Lausanne: Frontiers Media SA. doi: 10.3389/978-2-88976-466-2

Table of Contents

frontiers | Frontiers in Earth Science

EDITORIAL
published: 07 June 2022
doi: 10.3389/feart.2022.929873

Editorial: Yedoma Permafrost Landscapes as past Archives, Present and Future Change Areas

Lutz Schirrmeister[1], Alexander N. Fedorov[2], Duane Froese[3], Go Iwahana[4], Ko van Huissteden[5] and Alexandra Veremeeva[6]*

[1]Alfred Wegener Institute Helmholtz Centre for Polar and Marine Research (AWI), Permafrost Research Section, Potsdam, Germany, [2]Melnikov Permafrost Institute, Siberian Branch of the Russian Academy of Sciences (RAS), Yakutsk, Russia, [3]Department of Earth and Atmospheric Sciences, University of Alberta, Edmonton, AB, Canada, [4]International Arctic Research Center, University of Alaska Fairbanks, Fairbanks, AK, United States, [5]Faculty of Science, Earth and Climate, Vrje Universiteit Amsterdam, Amsterdam, Netherlands, [6]Institute of Physical-Chemical and Biological Problems in Soil Science (RAS), Pushchino, Russia

Keywords: Yedoma Ice Complex, circum Arctic, nonglaciated Beringia, environmental changes, late Pleistocene to Holocene

Editorial on the Research Topic

Yedoma permafrost landscapes as past archives, present and future change areas

Edited and reviewed by:
Michael Lehning, Swiss Federal Institute of Technology Lausanne, Switzerland

****Correspondence:***
Lutz Schirrmeister
Lutz.Schirrmeister@awi.de

Specialty section:
This article was submitted to Cryospheric Sciences, a section of the journal Frontiers in Earth Science

Received: *27 April 2022*
Accepted: *11 May 2022*
Published: *07 June 2022*

Citation:
Schirrmeister L, Fedorov AN, Froese D, Iwahana G, van Huissteden K and Veremeeva A (2022) Editorial: Yedoma Permafrost Landscapes as past Archives, Present and Future Change Areas. Front. Earth Sci. 10:929873. doi: 10.3389/feart.2022.929873

INTRODUCTION

Yedoma Ice Complex (IC) ice-rich fine-grained permafrost deposits formed during the Marine Isotope Stages 4 to 2 covered several million km^2 of the Arctic mainland. The Yedoma domain spanns from the Taymyr Peninsula in the west to the Yukon of Northwest Canada, and from Central Yakutia in the south to the Arctic shelves in the north. Today about 2.6 million km^2 in Siberia, Alaska and Northwest Canada are considered to contain remnants of the Yedoma IC deposits (Strauss et al.) and thus belong to the Yedoma domain. The cold and dry (continental) climate conditions that were common across these areas define common depositional features such as prevalence of widespread fine-grained sediments, large syngenetic polygonal ice wedges and other specific ground ice types. These occur along with large quantities of buried, well-preserved organic matter, and fossil remains of the mammoth megafauna and other tundra-steppe faunal and floral fossils. The once extensive periglacial landscapes of the Yedoma domain are synonymous with Ice Age Beringia, and developed over tens of millennia in unglaciated regions where late Pleistocene syngenetic permafrost aggraded and later underwent widespread degradation during the Lateglacial and early-Holocene warming. This last period of rapid thaw transformed the Yedoma domain from tundra-steppe polygonal tundra into a lake-rich thermokarst landscape across the poorly drained lowlands. At the same time, vast shares of the continental Arctic shelf were flooded by the postglacial transgression of Arctic seas. Ice-rich Yedoma deposits were and still are vulnerable to climate warming, leading to diverse landscape responses such as deepening of the active layer, surface subsidence, thermokarst, thermo-erosion, as well as remobilization of increasingly vulnerable long-buried organic matter and the subsequent release of greenhouse gases.

In the present Research Topic on Yedoma permafrost landscape, the study regions comprise areas at the Kara Sea coast, coasts of the Laptev and East Siberian seas and in their hinterland in the Yana-Indigirka and Kolyma lowlands, in Central Yakutia, as well as at the Alaskan Chukchi Sea coast, in the Brooks Range foothills, and in Central Alaska (**Figure 1**). The entire study region in this Research

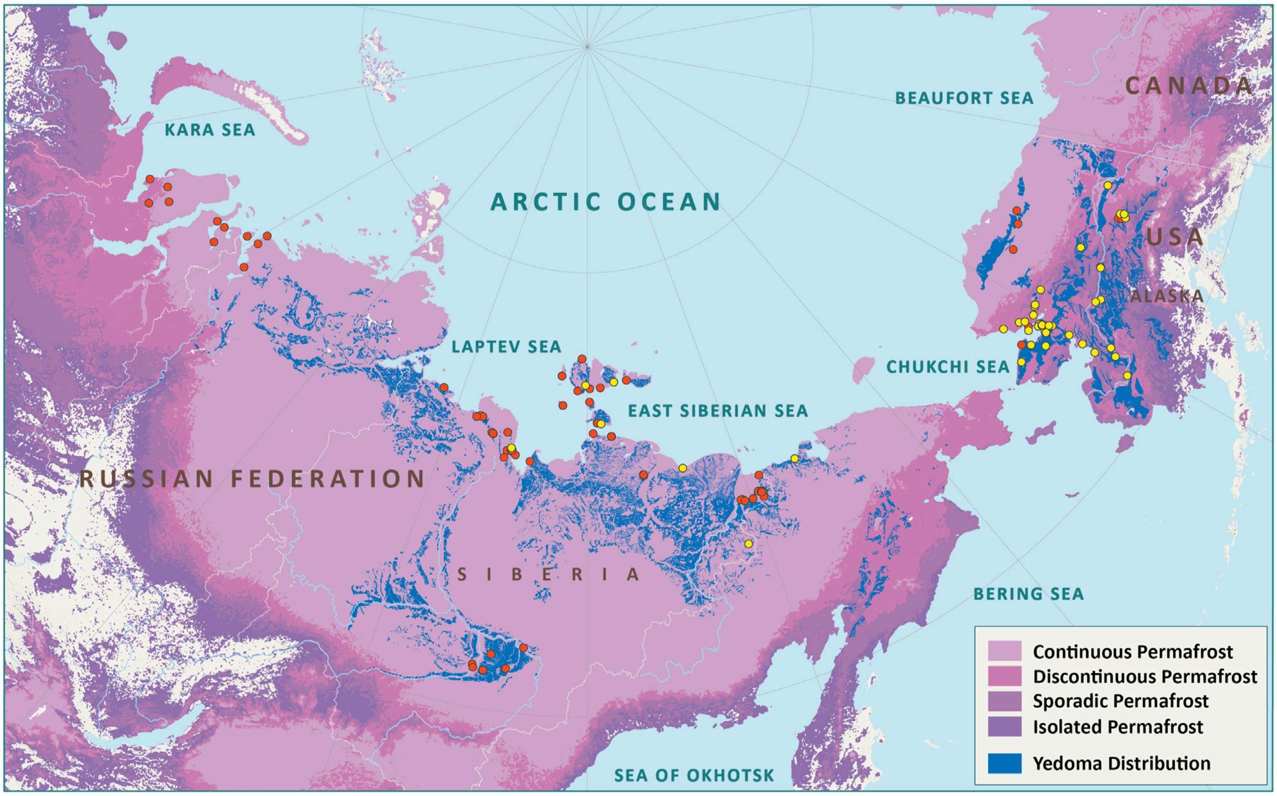

FIGURE 1 | Distribution of Yedoma Research Topic study sites. Red circles—single sites that are subject of the various papers in the Research Topic; Yellow circles—locations of the historical observations according to Shur et al. (Map by Sebastian Laboor, AWI).

Topic covers a wide area between 66.8°E (Marre Sale Polar Station, Yamal Peninsula) and -147.7°E (Vault Creek Tunnel, Fairbanks) and between 61.76°N (Tabaga, Central Yakutia) and 76.17°N (Cape Anisii, Kotelny Island).

OVERVIEW INFORMATION

The topics of the present article collection cover a wide range of scientific approaches and research interest.

Yedoma Research History and Distribution

The history of Yedoma research from its beginning in the early 19th century to the mid-20th century is presented by a review paper of Shur et al. A detailed digital map of the pan-Arctic Yedoma domain is presented by Strauss et al. This domain covers 2,587,000 km^2 of the Arctic and sub-Arctic and Yedoma deposits are found within 480,000 km^2 of this region.

Paleo-Ecological, Geochronological, Cryolithological, and Archaeological Studies

A large number of site-specific results are presented on paleo-ecological, geochronological, and cryolithological characteristics of Yedoma deposits and also include some archaeological findings. From Western Siberia, Streletskaya et al. conclude, that the formation of ice-rich permafrost on the Kara Sea coast occurred in two stages, i.e., as marine stage with characteristic marine and coastal conditions (Marine Isotope Stage (MIS) 5—MIS 3) and as continental stage (MIS 3—MIS 2).

From the Sobo-Sise Island in the Lena River Delta, Wetterich et al. present paleoecological results of pollen, chironomid, diatom, and mammal bone studies. The records confirm the existence of tundra-steppe environments during MIS 3 with partly warmer-than-today summers and wetter conditions allowing for stagnant water (i.e., polygon ponds). During MIS 2, summers were colder and drier but shallow polygonal ponds were suitable for maintaining chironomid fauna.

Almost 2000 fossil bones of the Mammoth fauna were studied by Kuznetsova et al. at the southern coast of the Dmitry Laptev Strait. The collection consists of 13 mammal species with prevalent woolly mammoth (40.5%), bison (19%), horse (18.8%), reindeer (15.8%), and rare findings of woolly rhinoceros, saiga antelope, elk, moose, cave lion and wolf (each <1%). Tumskoy and Kuznetsova conclude that the cryostratigraphical subdivisions identified on both sides of the Dmitry Laptev Strait are identical and allow for reconstructing the regional geological development from the end of the middle Pleistocene to the present.

Extensive geological observations and site descriptions of the Yana Rhinoceros Horn Site (Yana RHS) in the course of archaeological excavations are presented by Pitulko and Pavlova from the lower Yana River. The culture-bearing horizon reflects that several human habitation episodes took place here during the late MIS3.

Results of cryogenic weathering from exposures at the lower Kolyma River by Shmelev et al. emphasize that polygenetic Yedoma deposits were affected by post-depositional processes, mainly by cryogenic weathering. Holocene warming caused thawing of the upper part of the Yedoma deposits and re-deposition, but also intensified cryogenesis due to more frequent freeze-thaw cycles.

The plant macrofossil assemblage from an exposure near Cherskiy (Kienast and Davydov) reveals the predominance of grassland vegetation composed of tundra steppes, meadow steppes and saline meadows in this area during the late early to early middle Pleistocene (Early Olyorian).

From Central Yakutia north of Yakutsk, Hughes-Allan et al. present a high-resolution record of a sediment core which spans the Pleistocene-Holocene transition and encompasses the continuous Holocene time series. There was considerable variation in biogeochemical proxies both between and within three stratigraphic units.

From Alaska, Kanevskiy et al. present new cryostratigraphical data of the recently excavated sections of the CRREL Permafrost Tunnel near Fairbanks. They provide new opportunities to study the structure, properties and biogeochemical characteristics of Yedoma deposits to deduce the deposition history. The study shows differences from earlier permafrost tunnel investigations in that an earlier thaw unconformity was not prominent. The study underscores the complexity in correlating between Yedoma deposits, even over short distances, but also the need to replicate observations of Yedoma formation across regions and through detailed cryostratigraphy and dating.

Mineralogical, Geochemical and Organic Matter Studies Including the Greenhouse Gas Potential

A new method combination (portable X-ray fluorescence (pXRF) with a bootstrapping technique) is introduced by Monhoval et al. 1) in a method paper that generated the first mineral element inventory of permafrost deposits from the ice-rich Yedoma region. In the resulting Yedoma domain Mineral Concentrations Assessment (YMCA) dataset, the total concentrations of 10 mineral elements (Si, Al, Fe, Ca, K, Ti, Mn, Zn, Sr, and Zr) in Yedoma domain deposits have been quantified in 75 different profiles. In a second paper (Monhoval et al. 2), the iron redistribution upon thermokarst processes in the Yedoma domain is considered. A key conclusion is that changes from frozen to unfrozen state leads to modifications of multiple environmental conditions (fluctuating redox conditions, subsidence, leaching, and drainage) with indirect impact on Fe-oxides distribution and hence on a portion of mineral-protected organic carbon pools.

In Central Yakutia, Ulrich et al. explores geochemistry and weathering indices of Yedoma and Alas deposits beneath thermokarst lakes. The geochemical and sedimentological properties of Yedoma IC deposits are traceable in talik and frozen deposits below thermokarst lakes as they differ from lacustrine thermokarst deposits.

A first deep mercury inventory of late Pleistocene permafrost deposits down to 36 m depth below surface compares two sites in Central Yakutia and on Bykovsky Peninsula (Laptev Sea) in a study by Rutkowki et al. Increasing thermokarst processes and coastal erosion in Arctic permafrost regions will liberate the available Hg and very likely enable the increase of highly toxic CH_3Hg^+ in the terrestrial ecosystem, the Arctic Ocean, and the food chains of both realms.

Types and micromorphology of authigenic carbonates in Yedoma IC deposits at the lower Kolyma were studied by Rogov et al. These deposits contain authigenic carbonates of several generations: polymorphic (calcite and aragonite) and isomorphic (manganocalcite, rhodochrosite, and siderite) calcium carbonates and complex Fe-Al compounds.

An aerobic long-term incubation experiment was conducted over a course of 1.5 years (Melchert et al.) to study sources of CO_2 produced in freshly thawed Yedoma deposits from the Lena River Delta. Dual carbon isotopic source assessment revealed that large proportions of up to 80% ancient organic and about 18% inorganic carbon were likely released from these deposits. The pool of young organic matter was preferentially respired in microbial consumption. The contribution of ancient carbon sources, both organic and inorganic, to the CO_2 may further increase (by about 6–7%) upon longer thaw as indicated at the end of the aerobic incubation at 4°C after 1.5 years.

Heavy and light mineral associations from 18 permafrost sites in the northern Siberian Arctic were studied by Schirrmeister et al. The records suggest mostly local sediment sources and highlight the role of sediment reworking under periglacial regimes through time, including for example the formation of Holocene thermokarst and thermo-erosional deposits sourced by remobilized Yedoma IC deposits.

Studies of dissolved organic carbon (DOC) from permafrost deposits are a fairly new permafrost research topic. Stolpmann et al. analyze in the Lena River Delta the influence of lakes and ponds, interposed in a stream catchment, on DOC concentrations and export. They found decreasing DOC concentration from a thermokarst lake via a stream to a river channel. The data also indicate that old Yedoma and Holocene carbon might be mobilized into thermokarst lake systems. Under future climate, degrading Yedoma permafrost will cause changes in groundwater and subsurface flow in Arctic watersheds and may increase DOC export. Lakes and ponds may act as DOC filters by diluting incoming waters of higher DOC concentrations and modifying DOC to CO_2 and CH_4.

Biogeochemical Inventories and Microbiology

Biogeochemical inventories and trajectories in permafrost soils are considered by Desyatkin et al. who studied the degradation of arable soils in Central Yakutia and the negative consequences of global warming for Yedoma landscapes. The abandonment of croplands under the conditions of the recent continuous warming of the climate does not result in the restoration of the initial landscape but strengthens negative impacts on soils. As a result of thermokarst, the development of microtopography, and downward shift of the permafrost table, the morphology of soils is reconstructed with a change in their classification position. The cryosols are transformed into Solonets and eroded Cambisol types, and the large spatial contrast in soil properties, such as pH, bulk density, and organic carbon content, appears in the soil profiles.

One paper in our collection deals with microbiological studies of permafrost deposits in Central Yakutia. Cherbunina et al. suggest that two Ice Complex horizons differ in water origin of wedge ice and in their cryogenic evolution, evidenced by differences in chemistry, water isotopic signatures, and microbial community compositions. Microbial community similarity between ground ice and host deposits is shown to be a proxy for syngenetic deposition and freezing. They show a high degree of community similarity consistent with syngenetic formation of ice wedges and host deposits. As well, they found a correspondence between the origin of the water and degree of evaporative transformation in ice wedges with the microbial community composition.

Under the topic studies of modern and future environmental changes Park et al. investigate the impacts of excess ice on permafrost, soil water dynamics, and CO_2 and CH_4 fluxes in a Siberian tundra site under the strong future emission scenarios. The model results indicate that the warming air temperature and higher snow depth were major factors driving active layer thickness increases and permafrost degradation. In contrast, the presence of a moss layer and large excess ice content stabilize permafrost.

Remote Sensing and Geophysical Studies of Landscape Changes

Geophysical investigation of permafrost underground using 3D ground penetrating radar observations was performed by Schennen et al. at the same study area on Bol'shoy Lyakhovsky Island (New Siberian Archipelago) to point out advantages and disadvantages for deducing subsurface permafrost properties under completely frozen (springtime) and superficially thawed (summertime) conditions. When comparing selected reflections recorded in summer and spring, the spring data show a higher dynamic range in amplitudes and a higher vertical resolution, resulting in a generally sharper image of subsurface structures. In contrast, summer images provide a lower dynamic range and lower vertical resolution resulting in a smoother image of subsurface structures. This might ease reflector tracing and picking, but hinders a detailed imaging and interpretation as using the spring data.

Yedoma IC remnants usually are presented by positive relief forms - Yedoma uplands. Due to the high ice content up to 90% they are susceptible to vertical surface displacements by thaw and refreeze of ground ice in the upper permafrost layer and permafrost degradation due to thermokarst, thermoerosion, and thermodenudation. Huissteden et al. explore the relation between a data set from 2017 to 2019 of InSAR measurements of vertical surface displacements during the thaw season, and geomorphological features at a site in the Yana-Indigirka Lowland. Distinct spatial clusters of displacement trajectories can be discerned, which relate to geomorphological processes and ground ice conditions. Strong subsidence occurred in particular in 2019. In the wet year of 2017, marked heave occurred at Yedoma plateau surfaces, likely by ice accumulation at the top of the permafrost driven by excess precipitation.

Teshebaeva et al. investigate permafrost dynamics and degradation on the Yamal Peninsula from satellite radar observations. Surface relief dynamic analysis shows about 2 m net loss of surface topography over 14 years (2000–2014) associated with active discharge of water and sediments. In addition, InSAR time-series analysis shows active subsidence for the time period from 2017 to 2018 in three distinct spatial locations. The observed three locations show rates from 60 up to 120 mm/yr of seasonal surface changes.

Iijima et al. evaluated the distribution of topographic subsidence caused by thermokarst development in Central Yakutia. The results of InSAR stacking analysis show that the interannual trend of surface subsidence by thawing permafrost of Yedoma IC mainly occurred in deforested areas and agricultural fields. The thermokarst development in Central Yakutia has progressed since the 2000s. InSAR analysis using the ALOS series of satellites can detect topographic changes over the years. By comparing with digital surface models and high-resolution images from unmanned aerial systems, which have a resolution of the order of less than 10 cm, we can effectively examine the development of thermokarst in the area where the InSAR displacement appeared.

CONCLUSION

Papers written in this Yedoma Research Topic represent a broad view on the current state of knowledge in permafrost research with respect to unique Yedoma domain landscapes in the past, present, and future. Research in this field has been conducted for many decades, and still remains active and important. The main topics are understanding the formation and transformation of Yedoma IC deposits based on paleo-environment records, present Yedoma landscape dynamics, and their future response to climate change. The Yedoma domain once covered vast areas of the terrestrial Arctic and still stores large amounts of buried carbon some of which likely will be mobilized under ongoing and future warming. Understanding the formation and storage of organic matter preserved in Yedoma deposits requires paleoenvironmental research to estimate the extrinsic (climate) and intrinsic (periglacial processes) controls on permafrost aggradation and degradation. The 26 studies in this Research Topic originate from an international group of authors highlight the common interest in this particularly important type of permafrost and the potential of Yedoma research as a scientific bridge between different disciplines and various national scientific communities.

This paper collection is the final activity of the International Permafrost Association (IPA) action group "The Yedoma

Region: A Synthesis of Circum-Arctic Distribution and Thickness".

AUTHOR CONTRIBUTIONS

LS has drafted the text and all other authors have contributed with their own suggestions.

Conflict of Interest: The authors declare that the research was conducted in the absence of any commercial or financial relationships that could be construed as a potential conflict of interest.

Publisher's Note: All claims expressed in this article are solely those of the authors and do not necessarily represent those of their affiliated organizations, or those of the publisher, the editors and the reviewers. Any product that may be evaluated in this article, or claim that may be made by its manufacturer, is not guaranteed or endorsed by the publisher.

frontiers in Earth Science

ORIGINAL RESEARCH
published: 18 June 2021
doi: 10.3389/feart.2021.681511

Paleo-Ecology of the Yedoma Ice Complex on Sobo-Sise Island (EasternLena Delta, Siberian Arctic)

S. Wetterich[1]*, N. Rudaya[2,3], L. Nazarova[1,4,5], L. Syrykh[6], M. Pavlova[7], O. Palagushkina[5], A. Kizyakov[8], J. Wolter[1,9], T. Kuznetsova[10,5], A. Aksenov[11,12], K. R. Stoof-Leichsenring[1], L. Schirrmeister[1] and M. Fritz[1]

[1]Alfred Wegener Institute Helmholtz Centre for Polar and Marine Research, Potsdam, Germany, [2]PaleoData Lab, Institute of Archaeology and Ethnography SB RAS, Novosibirsk, Russia, [3]Biological Institute, Tomsk State University, Tomsk, Russia, [4]Institute of Geosciences, University of Potsdam, Potsdam, Germany, [5]Research Laboratory of Palaeoclimatology, Palaeoecology, Palaeomagnetism, Kazan (Volga Region) Federal University, Kazan, Russia, [6]Faculty of Geography, Herzen State Pedagogical University of Russia, St. Petersburg, Russia, [7]Melnikov Permafrost Institute Siberian Branch of the Russian Academy of Science, Yakutsk, Russia, [8]Department of Cryolithology and Glaciology, Faculty of Geography, Lomonosov Moscow State University, Moscow, Russia, [9]Institute of Biochemistry and Biology, University of Potsdam, Potsdam, Germany, [10]Department of Paleontology, Faculty of Geology, Lomonosov Moscow State University, Moscow, Russia, [11]Department of Polar Geography, Arctic and Antarctic Research Institute, St. Petersburg, Russia, [12]Institute of Earth Sciences, Petersburg State University, St. Petersburg, Russia

OPEN ACCESS

Edited by:
Davide Tiranti,
Agenzia Regionale per la Protezione Ambientale (ARPA), Italy

Reviewed by:
Nadia Solovieva,
University College London, United Kingdom
Xiaozhong Huang,
Lanzhou University, China

***Correspondence:**
S. Wetterich
sebastian.wetterich@awi.de

Specialty section:
This article was submitted to Quaternary Science, Geomorphology and Paleoenvironment, a section of the journal Frontiers in Earth Science

Received: 16 March 2021
Accepted: 03 June 2021
Published: 18 June 2021

Citation:
Wetterich S, Rudaya N, Nazarova L, Syrykh L, Pavlova M, Palagushkina O, Kizyakov A, Wolter J, Kuznetsova T, Aksenov A, Stoof-Leichsenring KR, Schirrmeister L and Fritz M (2021) Paleo-Ecology of the Yedoma Ice Complex on Sobo-Sise Island (EasternLena Delta, Siberian Arctic). Front. Earth Sci. 9:681511. doi: 10.3389/feart.2021.681511

Late Pleistocene permafrost of the Yedoma type constitutes a valuable paleo-environmental archive due to the presence of numerous and well-preserved floral and faunal fossils. The study of the fossil Yedoma inventory allows for qualitative and quantitative reconstructions of past ecosystem and climate conditions and variations over time. Here, we present the results of combined paleo-proxy studies including pollen, chironomid, diatom and mammal fossil analyses from a prominent Yedoma cliff on Sobo-Sise Island in the eastern Lena Delta, NE Siberia to complement previous and ongoing paleo-ecological research in western Beringia. The Yedoma Ice Complex (IC) cliff on Sobo-Sise Island (up to 28 m high, 1.7 km long) was continuously sampled at 0.5 m resolution. The entire sequence covers the last about 52 cal kyr BP, but is not continuous as it shows substantial hiatuses at 36–29 cal kyr BP, at 20–17 cal kyr BP and at 15–7 cal kyr BP. The Marine Isotope Stage (MIS) 3 Yedoma IC (52–28 cal kyr BP) pollen spectra show typical features of tundra–steppe vegetation. Green algae remains indicate freshwater conditions. The chironomid assemblages vary considerably in abundance and diversity. Chironomid-based T_{July} reconstructions during MIS 3 reveal warmer-than-today T_{July} at about 51 cal kyr BP, 46-44 and 41 cal kyr BP. The MIS 2 Yedoma IC (28–15 cal kyr BP) pollen spectra represent tundra-steppe vegetation as during MIS 3, but higher abundance of *Artemisia* and lower abundances of algae remains indicate drier summer conditions. The chironomid records are poor. The MIS 1 (7–0 cal kyr BP) pollen spectra indicate shrub-tundra vegetation. The chironomid fauna is sparse and not diverse. The chironomid-based T_{July} reconstruction supports similar-as-today temperatures at 6.4–4.4 cal kyr BP. Diatoms were recorded only after about 6.4 cal kyr BP. The Sobo-Sise Yedoma record preserves traces of the West Beringian tundra-steppe that maintained the Mammoth fauna including rare evidence for woolly rhinoceros' presence. Chironomid-based T_{July} reconstructions complement previous plant-macrofossil based T_{July} of regional MIS 3 records. Our study from the eastern Lena Delta fits into and extends previous paleo-ecological Yedoma studies to characterize Beringian paleo-environments in the Laptev Sea coastal region.

Keywords: permafrost, Yedoma, paleo-ecology, pollen, chironomids, Mammoth fauna, late Pleistocene, Beringia

INTRODUCTION

Late Pleistocene permafrost of the Yedoma type is a prominent and widespread permafrost feature that formed during sea-level lowstands on vast areas of the unglaciated Beringian lowlands and on the nowadays flooded East Siberian shelf between the Laurentide to the east and the Scandinavian ice sheets to the west during marine isotope stages (MIS) 4 to 2 (Hopkins, 1959). Ice Complex (IC) permafrost aggradation took place by evolving ice-wedge polygons forming the so-called Yedoma IC (Katasonov, 1954/2009) of up to 50 m thick sequences. In West Beringia, the main area of potential Yedoma IC distribution includes the now submerged East Siberian shelf and Arctic coastal lowlands from Taymyr Peninsula to Chukotka (Grosse et al., 2013), although it is also described from interior regions of Central Yakutia (Soloviev, 1959) and the Yana Upland (Kunitsky et al., 2013; Opel et al., 2019). In East Beringia, muck deposits comparable in genesis to those of Siberian Yedoma IC occur at the Arctic Foothills, on Seward Peninsula, in interior Alaska and in the Yukon Territory (Péwé, 1955; Kanevskiy et al., 2011; Schirrmeister et al., 2016).

Large syngenetic ice wedges, ice-oversaturated fine-grained deposits and a considerable organic content characterize Yedoma IC deposits (Schirrmeister et al., 2013). The organic component of Yedoma IC preserves floral and faunal fossils, and thus evidence of late Pleistocene environmental and climatic conditions of Beringia and their variations over time (e.g., Sher et al., 2005). The Yedoma permafrost archive has been widely used to infer rather qualitative than quantitative paleo-environmental reconstructions by applying numerous fossil records such as those from Mammoth fauna bones (e.g., Kuznetsova et al., 2019), insect remains (e.g., Sher et al., 2005), plant macro-remains (e.g., Kienast et al., 2005), pollen (e.g., Andreev et al., 2011), testate amoebae (e.g., Bobrov et al., 2004) or ostracods (Wetterich et al., 2005). Generally, the combination of several fossil proxy records from a certain permafrost sequence largely enhances its significance for paleo-ecological interpretations (e.g., Kienast et al., 2011; Wetterich et al., 2018). In this context, the present study combines a pollen-based paleo-vegetation reconstruction with lacustrine chironomid and diatom analyses. While pollen analysis provides detailed insights into vegetation dynamics over time with high comparability to other regional pollen records (Andreev et al., 2011), lacustrine fossil proxies highlight on-site freshwater conditions by habitat preferences of certain species, and species diversity (Palagushkina et al., 2012; Hoff et al., 2015; Palagushkina et al., 2017; Biskaborn et al., 2019). If specimen counts per sample are sufficiently high, numerical reconstructions of certain ecological parameters are deducible such as mean air temperature of the warmest month (T_{July}), water depth, ion content and pH (Nazarova et al., 2013; Nazarova et al., 2017a; Pestryakova et al., 2018).

The study area on Sobo-Sise Island in the eastern Lena Delta fits into and extends previous paleo-ecological Yedoma studies in the Laptev Sea coastal region including the Lena Delta and Bykovsky Peninsula (Schirrmeister et al., 2002a; Schirrmeister et al., 2003; Bobrov et al., 2004; Kienast et al., 2005; Sher et al., 2005; Wetterich et al., 2005; Wetterich et al., 2008a; Wetterich et al., 2011; Schirrmeister et al., 2011a; Schirrmeister et al., 2011b; Wetterich et al., 2014; Schirrmeister et al., 2017; Khazin et al., 2019; Kuznetsova et al., 2019; Wetterich et al., 2019a), which examined floral and faunal fossils. These studies characterized the West Beringian environments generally as tundra-steppe covering a considerable patchiness of different habitats that created a landscape mosaic of dry uplands and slopes, wetlands, floodplains and shallow waters of low-center polygon tundra as especially well seen in insect and plant macrofossil data (Kienast et al., 2005; Sher et al., 2005; Wetterich et al., 2008a). However, aquatic conditions in West Beringia during MIS 3-2 are rather poorly constrained yet and are mainly based on findings of: 1) green algae *Botryococcus* and *Pediastrum* remains in palynological samples, 2) submerged and water plant macro-fossils, and 3) ostracod valves in Yedoma IC deposits. Other aquatic fossils such as from branchiopods, cladocerans and chironomids have only little been studied yet in Yedoma IC deposits (Neretina et al., 2020; Rogers et al., 2021). Numerical reconstructions of paleo-climate parameters such as summer air temperature and annual precipitation in West Beringia are scarce (Andreev et al., 2011) or poorly developed in case of ice-wedge stable water isotopic composition reflecting winter climate (Opel et al., 2018; Wetterich et al., 2021). Pitulko et al. (2017) present T_{July} and precipitation reconstructions from 34 to 10 kyr BP for the western part of the Yana-Indigirka Lowland (east of our study region), while from the Bykovsky Yedoma archive only two points in time, at around 48 and 35 kyr BP, provide estimated T_{July} values based on plant macrofossils (Kienast et al., 2005). Further quantitative paleo-proxy reconstruction data are lacking for the Laptev Sea coastal region. Thus, additional information is mandatory to better constrain the West Beringian climate and environment through stadial-interstadial as well as glacial-interglacial transitions.

In addition to a recent study of the cryostratigraphic inventory of the Sobo-Sise Yedoma cliff (Wetterich et al., 2020) and to previous paleo-environmental Yedoma research in the Laptev Sea coastal region, the present study aims

1) To provide detailed pollen-based reconstructions of paleo-vegetation in combination with occasional bone findings of the Mammoth fauna;

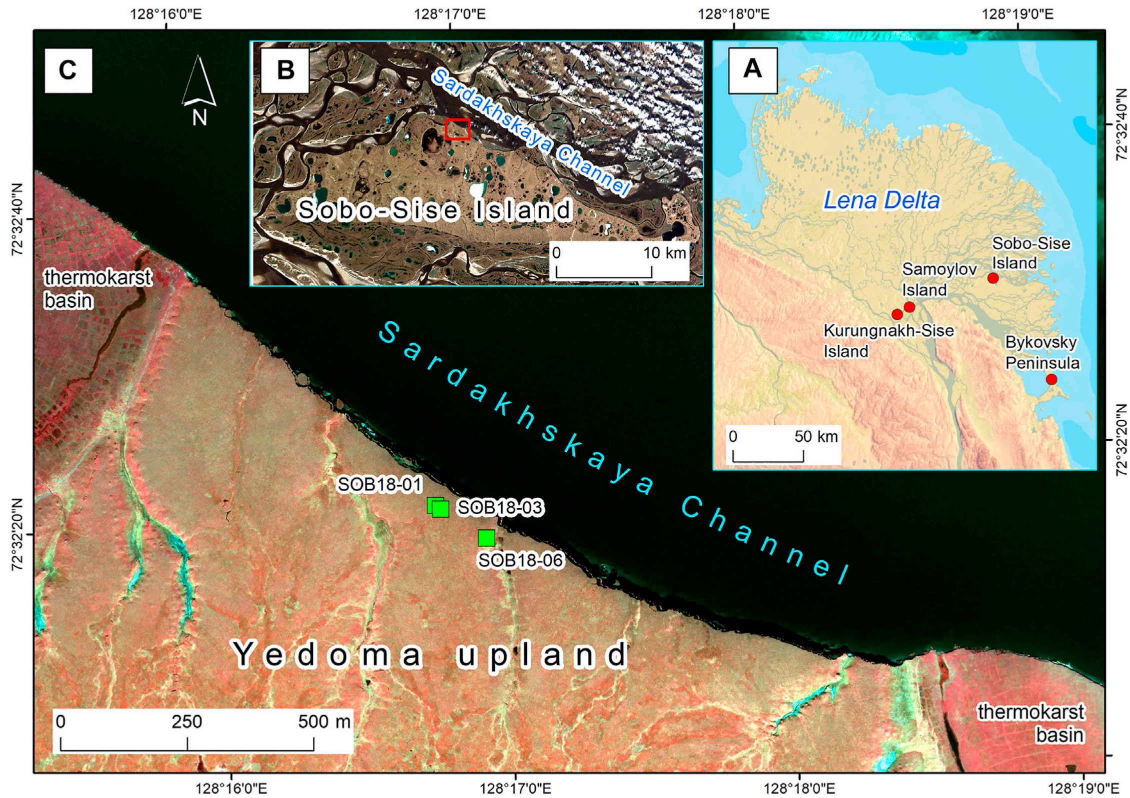

FIGURE 1 | Study area in north-eastern Siberia showing **(A)** the Lena Delta with key locations, **(B)** Sobo-Sise Island (image based on Sentinel-2A scene, June 27, 2018) and **(C)** the Sobo-Sise Yedoma cliff facing the Sardakhskaya Channel (image based on GeoEye-1 scene, July 08, 2014) with positions of the sampled sediment profiles SOB18-01, SOB18-03 and SOB18-06. Panel **(A)** is based on the semitransparent layer of the ESRI ArcGIS Living Atlas of the World (World Topo Base, 2021) with underlying bathymetry of (IBCAO grid, 2021).

2) To reconstruct past freshwater lacustrine conditions such as water depth, salinity, pH, and T_{July} air temperatures based on chironomid and diatom fossils;
3) To disentangle regional paleo-environmental dynamics in West Beringia by combining the present record with previous research results and interpretations.

STUDY SITE AND PREVIOUS RESEARCH

Sobo-Sise Island in the Eastern Lena Delta

The Lena Delta is the largest delta in the Arctic and occupies about 32,000 km^2 (Are and Reimnitz, 2000). It is divided by six major channels (Fedorova et al., 2015) of which the Sardakhskaya Channel drains the eastern part of the delta (**Figure 1**). Here, on Sobo-Sise Island at the Sardakhskaya Channel Yedoma uplands occupy about 19% of the land surface while most of the island is characterized by permafrost degradation features such thermokarst basins and thermo-erosional valleys of Holocene age (Fuchs et al., 2018). A prominent Yedoma IC remnant at the north-eastern shore of Sobo-Sise Island builds an up to about 28 m high almost vertical cliff (72°32′ N, 128°17′ E) stretching about 1,700 m along the shore (**Figure 1**).

The modern meteorological conditions in the Lena Delta are monitored on Samoylov Island where a mean annual air temperature of −12.3°C, mean July air temperature of 9.5°C and mean February air temperature of −32.7°C are recorded for the last two decades (1998–2017; Boike et al., 2019), while the mean annual rainfall amounts to 169 mm and the mean annual winter snow cover to 0.3 m (2002–2017; Boike et al., 2019).

On Sobo-Sise Island, dwarf shrub-moss-tussock tundra plant communities inhabit the structured land surface of Yedoma uplands, pingos, floodplains, and thermokarst basins. Species of the *Salix*, *Dryas*, *Saxifraga*, *Polygonum*, *Carex*, *Poa*, *Trisetum*, *Equisetum*, and *Luzula* genera, and unspecified mosses and lichens are common (Raschke and Savelieva, 2017).

Evolution of the Sobo-Sise Yedoma Sequence

The Sobo-Sise Yedoma cliff attracts scientific attention due to both, the exceptionally high and vertically exposed permafrost archive spanning MIS 3-1 (Wetterich et al., 2020) and the ongoing rapid thermo-erosion releasing substantial amounts of organic matter into the Lena River (Fuchs et al., 2020).

The geochronological record of the Sobo-Sise Yedoma spans the last 52 cal kyr BP based on radiocarbon dating and age-height modeling (**Figure 2**; Wetterich et al., 2020). The permafrost sequence differentiates into three cryostratigraphic units that

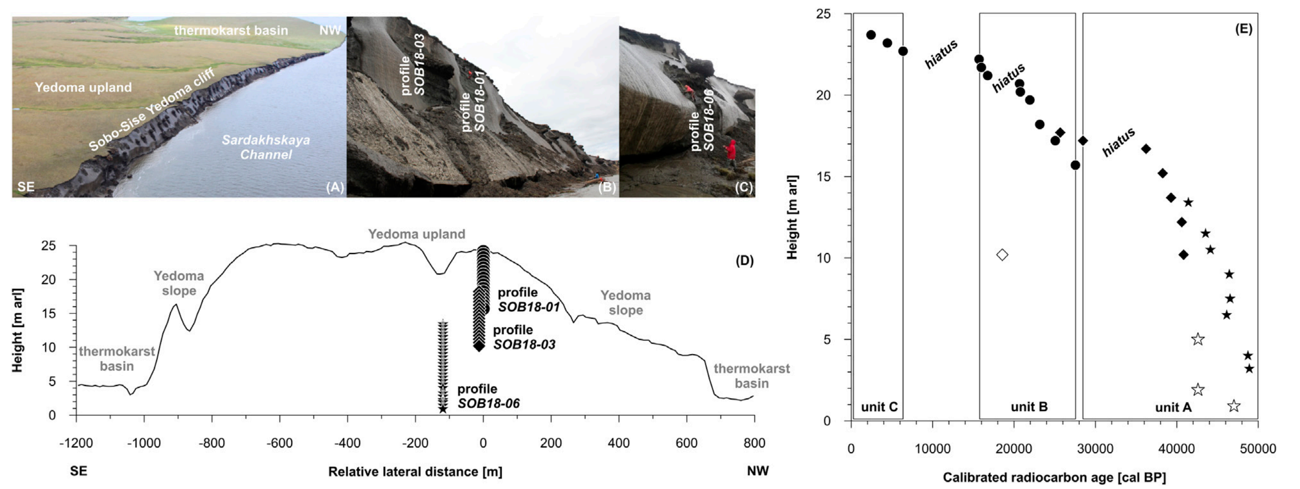

FIGURE 2 | Overview of the sampled profiles at Sobo-Sise showing **(A)** the Yedoma cliff, **(B)** profiles SOB18-01 and SOB18-03, **(C)** profile SOB18-06, **(D)** sampling scheme across the Yedoma cliff and **(E)** age-height relation of the exposure in meter above river level (m arl) and calibrated radiocarbon ages (redrawn from Wetterich et al., 2020). Note the sampling overlap of the profiles SOB18-01 (circles), SOB18-03 (diamonds) and SOB18-06 (stars) and their alignment to cryostratigraphic units A, B and C. The hollow symbols indicate ages of re-deposited material or infinite radiocarbon ages.

are MIS 3 Yedoma IC (unit A; 52–28 cal kyr BP), MIS 2 Yedoma IC (unit B; 28–15 cal kyr BP) and MIS 1 Holocene cover (unit C; 7–0 cal kyr BP). The cryostratigraphic sequence of the Sobo-Sise Yedoma cliff is not continuous, but has chronological gaps (hiatuses) at 36–29 cal kyr BP, at 20–17 cal kyr BP and at 15–7 cal kyr BP (**Figure 2**).

The chronological gaps provide evidence of past changes in climatic conditions as well as in sediment deposition and erosion regimes. Similar observations have been made on adjacent Yedoma IC sites on Bykovsky Peninsula and Kurungnakh-Sise Island (Wetterich et al., 2020). The two older gaps during MIS 3 and MIS 2 are likely related to repeated changes in the regional hydrological systems due to outburst floods of glacial Lake Vitim along the Lena Valley into the Arctic Ocean as proposed by Margold et al. (2018), while the MIS 2-1 gap corresponds to deglacial permafrost thaw (thermokarst) that took place Arctic-wide at the late Pleistocene-Holocene transition.

The Sobo-Sise Yedoma cliff rapidly erodes with a mean annual shoreline retreat rate of up to 9.1 m yr^{-1} over the last decades (1965–2018; Fuchs et al., 2020). Surface elevation changes due to thaw subsidence on Yedoma uplands range between −2 cm yr^{-1} (based on Sentinel-1 InSAR, 2017, for the entire Sobo-Sise Island; Chen et al., 2018) and −3.4 cm yr^{-1} (based on on-site rLiDAR at the studied Yedoma cliff, Günther et al., 2018). Thus, the Sobo-Sise Yedoma IC remnant of today is characterized by substantial and rapid permafrost degradation (Fuchs et al., 2020).

METHODS

Fieldwork and Dating

Three vertical sediment profiles were sampled on rope at accessible positions of the Yedoma cliff to cover the entire exposed permafrost inventory (Wetterich et al., 2019b; **Figure 2**). The frozen samples were obtained using a hammer and axe at 0.5-m resolution. Vertical overlaps of the three profiles guaranteed complete coverage of the exposure (**Figure 2D**).

The sampling resulted in a total of 61 sediment samples. Upon return to the labs, samples were freeze-dried (Zirbus Subliminator 3–4–5) and split into subsamples for several analyses. Accelerator mass spectrometry (AMS) radiocarbon dating was applied to identified organic macro-remains in 31 sediment samples totaling in 32 radiocarbon dates (Wetterich et al., 2020), which were calibrated using the IntCal13 calibration dataset (Reimer et al., 2013). Ages are given as calibrated years before present (cal yr BP) or calibrated thousand years before present (cal kyr BP). Paleo-ecological analyses were conducted on a sample set of 33 samples from the profiles SOB18-01 (n = 14), SOB18-03 (n = 7) and SOB18-06 (n = 12) covering the entire sequences at resolution of less than 1 m.

Pollen Analysis

The pollen samples (2–6 g of dry sediment) were prepared using standard procedures including treatment with 10% HCl and 10% KOH, sieving (250 mm), treatment with 45% HF, acetolysis, and mounting in glycerin (cf. Fægri and Iversen, 1989). One *Lycopodium* spore tablet was added to each sample to calculate total pollen and spore concentrations (cf. Stockmarr, 1971). Pollen and spore residues mounted in water-free glycerin were analyzed under a Zeiss AxioImager D2 light microscope at 400 magnification. The identification of pollen and spores was performed using a reference pollen collection and pollen atlases (e.g., Beug, 2004). Non-pollen palynomorphs (NPPs) were identified using descriptions, sketches, and photographs published by van Geel (2001). The percentages of all taxa were calculated based on setting the total of all pollen and spore taxa equal to 100%. The results of pollen analysis are displayed in the pollen diagram produced with the Tilia/TiliaGraph software. The

TABLE 1 | List of bone findings of the late Pleistocene Mammoth fauna on Sobo-Sise Island in the eastern Lena Delta.

Order	Family	Species	Total	ZIN RAS St. Petersburg (1927)	Expedition Lena Delta (1998)	Lena Delta Reserve Tiksi (1990, 2000)	Lena Delta Reserve Tiksi (2018)
Proboscidea	Elephantidae	*Mammuthus primigenius* (BLUMENBACH, 1799)	30	11	5	8	6
Artiodactyla	Bovidae	*Bison priscus* (BOJANUS, 1827)	7	6			1
	Cervidae	*Rangifer tarandus* L., 1758	3				3
Perissodactyla	Equidae	*Equus* ex eg. *caballus* L., 1758	4	1	1	2	
	Rhino-cerotidae	*Coelodonta antiquitatis* (BLUMENBACH, 1799)	1				1
		Total	**45**	**18**	**6**	**10**	**11**

TABLE 2 | Radiocarbon ages of *Mammuthus primigenius* bone fragments from Sobo-Sise Island (Eastern Lena Delta) calibrated using CALIB REV8.2 (Reimer et al., 2020). Results are rounded to the nearest 10 yr for samples with standard deviation in the radiocarbon age greater than 50 yr.

Sample ID	Lab ID	^{14}C date (yr BP)	Calibrated age range 2σ (cal yr BP)	Calibrated median age (cal yr BP)	Skeleton element	Locality	Year of sampling	References
SOB18-bone-02	AWI2749.1.2	13,668 ± 57	16,310–16,750	16,520	Tusk, fragment	Shore	2018	Wetterich et al. (2020)
GIN-4115	GIN-4115	14,340 ± 120	17,100–17,860	17,490	Tusk, fragment	"Bone horizon" at 13–15 m arl	1984	Grigoriev (1988)
LDR- O299	KIA-32839	17,070 ± 70	20,460–20,830	20,630	Forearm		1990	This paper
MKh-O621	GIN-10235	19,200 ± 220	22,650–23,760	23,180	Rib, fragment	Shore	1998	Sher et al. (2005)
IM-835	IM-835	24,400 ± 650	27,410–29,950	28,620	Bone			This paper
MKh-O624	GIN-13929 (GrA-46013)	>45,000	Not calibrated	Not calibrated	Vertebra, fragment	Shore	1998	This paper

visual definition of the pollen record is supported by cluster analysis in CONISS (Grimm, 2004).

Mammal Bone Analysis

Mammal bone findings in fresh slump debris at the cliff foot were collected in 2018 during fieldwork (**Table 1**), later on identified, and are currently stored at the Lena Delta Reserve (LDR), Tiksi, Russia. Archive data of late Pleistocene mammal bones from Sobo-Sise Island (**Table 1**) are available from sampling in 1927 (Zoological Institute Russian Academy of Science - ZIN RAS, Sankt-Petersburg, Russia), in 1990 and 2000 (LDR, Tiksi, Russia) and in 1998 (Collection of the Russian-German "Lena Delta" Expedition, Moscow, Russia), Radiocarbon dates are available for five specimens of these archive collections (**Table 2**).

Chironomid Analysis

The treatment of sediment samples for chironomid analysis followed standard techniques described in Brooks et al. (2007). Subsamples of wet sediments were deflocculated in 10% KOH, heated to 70°C for 10 min by adding boiling water and left for another 20 min. The sediment was then passed through stacked 225 and 90 µm sieves. Chironomid larval head capsules (HC) were picked out of a grooved Bogorov sorting tray under a stereomicroscope at 25–40x magnification and were mounted in Hydromatrix two at a time, ventral side up, under a 6 mm diameter cover slip. Chironomids were identified to the highest possible taxonomic resolution following Wiederholm (1983) and Brooks et al. (2007). Information on ecological preferences of identified chironomid taxa was taken from Brooks et al. (2007), Moller Pillot (2009), Moller Pillot (2013) and Nazarova et al. (2008); Nazarova et al. (2011); Nazarova et al. (2015); Nazarova et al. (2017b).

Mean July air temperatures (T_{July}) were inferred by using a North Russian (NR) chironomid-based temperature inference model (WA-PLS, 2 component; r^2 boot = 0.81; RMSEP boot = 1.43°C) (Nazarova et al., 2015) based on a modern calibration data set of 193 lakes and 162 taxa from East and West Siberia (61–75°N, 50–140°E, T_{July} range 1.8–18.8°C) (Nazarova et al., 2008; Nazarova et al., 2011; Nazarova et al., 2015). T_{July} for the lakes from the calibration data set was derived from New et al. (2002). The T_{July} model previously applied for paleo-climatic inferences in East Siberia and Russian and European Arctic demonstrates high reliability of the reconstructed parameters (Syrykh et al., 2017; Nazarova et al., 2017c; Plikk et al., 2019; Nazarova et al., 2020). Chironomid-based reconstruction was performed in C2 version 1.7.7 (Juggins, 2007). The data were square-rooted to stabilize species variance.

In order to capture the diversity of the chironomid communities that is necessary for a reliable temperature reconstruction we aimed at extracting at least 50 chironomid larval head capsules (HC) from each sample (Heiri and Lotter, 2001; Larocque, 2001), though as low as 30 head capsules can be enough for assessing dominant environmental trends (Quinlan and Smol, 2001). The profiles SOB18-06 and SOB18-01 contained mostly sufficient numbers of HC, apart from the samples SOB18-06-18, SOB18-01-02 and SOB18-01-01, where chironomids were not found. The profile SOB18-03 contained very low concentration of chironomid samples (2–14 HC). Therefore, chironomids from this profile were used for qualitative ecological reconstruction while quantitative air temperature reconstruction should be considered with caution. The reliability of the chironomid-inferred temperature reconstruction was assessed by two methods. First, the percentages of the fossil chironomid taxa that are absent or rare in the modern calibration dataset were calculated. A taxon is considered to be rare in the dataset when it has a Hill's N2 below 5 (Hill, 1973). The environmental optima of taxa that are rare in the modern dataset are likely to be poorly estimated (Brooks and Birks, 2000). Second, to determine whether the modern calibration models had adequate analogues for the fossil assemblages, the modern analogue technique (MAT) was performed using C2 version 1.7.7 (Juggins, 2007), with squared chord distance as the dissimilarity coefficient (DC) (Overpeck et al., 1985). Confidence intervals were based on minimum DC distance within the calibration sets (Laing et al., 1999). Fossil assemblages above the 95% confidence interval were considered to have no analogues in the calibration set; while assemblages with the confidence interval between 75 and 95% were considered to have fair analogues (Francis et al., 2006; Solovieva et al., 2015; Palagushkina et al., 2017).

Diatom Analysis

Diatom samples were prepared in a water bath following Battarbee (1986). High-refractive Naphrax resin was used for the production of permanent slides. The diatom species identification followed international and Russian literature (Zabelina et al., 1951; Krammer and Lange-Bertalot, 1986; Krammer and Lange-Bertalot, 1988; Krammer and Lange-Bertalot, 1991a; Krammer and Lange-Bertalot, 1991b). Specimen counts followed parallel transects across the slide under light microscope Zeiss Axioplan and immersion oil. However, specimen counts remained generally low and far below 300 individuals per sample that are commonly used for quantitative interpretations and the potential application of transfer functions. Instead, the ecological characteristics of single species findings are described in relation to habitat preference, salinity, pH of the host water, geographical distribution, and water velocity (Barinova et al., 2006) and T_{July} (Pestryakova et al., 2018), but should not be overinterpreted due to the limited dataset.

RESULTS

Paleo-Vegetation

The cluster analysis of the Sobo-Sise Yedoma pollen record results in three units, which correspond to the cryolithological units A-C that were previously defined by Wetterich et al. (2020) of MIS 3, MIS 2 and MIS 1 age, respectively (**Figure 3**).

Pollen spectra of MIS 3 (Unit A, 52-28 cal kyr BP) are characterized by high percentages of herbaceous pollen with the prevalence of sedge (up to 70%) and grass (up to 53%). Deciduous trees and shrubs were represented by *Salix* whose abundance increased after 39.3 cal kyr BP. *Betula* sect. *Apterocaryon* (dwarf birches) and *Alnus* subg. *Alnobetula* (shrubby alder species), however, remain in low abundance. *Rubus chamaemorus* appeared at 44.1 cal kyr BP and became an abundant taxon after 39.3 cal kyr BP and until the Holocene. To estimate the presence of conifers in the past vegetation we have used not only percentages but also estimated the pollen concentrations. These are independent of the total percentage indicator. Only for conifers, the concentration numbers showed a different picture compared to percentages throughout the entire record. While the percentages of *Pinus sylvestris* in Unit A are similar to its respective concentrations, suggesting its real low abundance in the vegetation, the concentrations of *Larix* are more representative than the *Larix* pollen percentages because *Larix* pollen tends to accumulate directly on the site. The entire record of Unit A reveals both relatively high percentages and concentrations of *Picea*. Another characteristic feature of Unit A is the constant presence of green algae *Botryococcus* and *Pediastrum* remnants; an indicator of freshwater ponds close to the site.

The MIS 2 (Unit B, 28–15 cal kyr BP) pollen spectra are similar to those of Unit A, but differ by lower pollen concentrations, lower abundances of sedge and grass and increased *Artemisia* pollen. The concentration of *Larix* decreased. All these features are characteristic for more arid conditions than in Unit A. MIS 2 landscapes in the eastern Lena Delta were dominated by steppe-like communities.

The MIS 1 (Unit C, 7–0 cal kyr BP) pollen composition differs sharply from those of units A and B by increased total pollen concentrations, and high percentages and concentrations of arboreal pollen. The main feature is the dominance of dwarf birch (*Betula* sect. *Apterocaryon*) as well as the significant amount of alder (*Alnus* subg. *Alnobetula*), and Ericaceae pollen. The percentages of Poaceae, Cyperaceae and *Artemisia* significantly decreased, while the concentrations of all conifers sharply increased. Green algae are absent in Unit C.

Mammoth Fauna

Bone findings of the Mammoth fauna are commonly rare on Sobo-Sise Island and mostly found below the Yedoma cliff. Only Grigoriev (1988) mentions a "bone horizon" at about 13–15 m arl. In 2018, during fieldwork bones of Mammoth fauna species were found in fresh slump debris well above the beach level are thought to originate from the cliff. According to Kuznetsova et al. (2019) such bones findings are classified as group C bone fossils whose original position can be related to the outcrop above. The preservation of vivianite (bluish crystals and accretions of hydrated iron phosphate that might form under anoxic conditions on bone material; Guthrie, 1990; Rothe et al., 2016) on some bones supports our assumption that the bones originated from the Sobo-Sise Yedoma cliff. In total, 11 bone

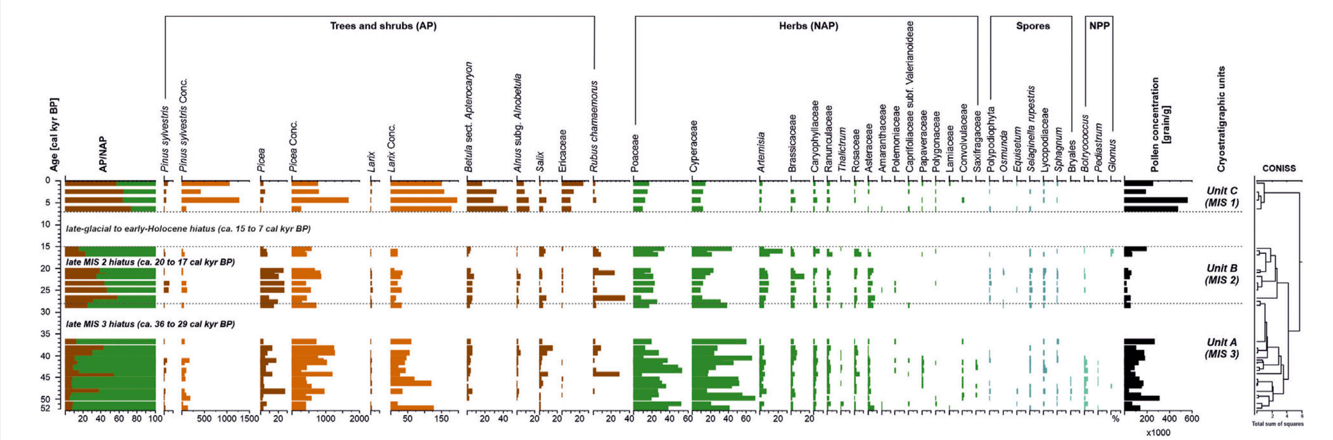

FIGURE 3 | Pollen diagram of the Sobo-Sise Yedoma record. For several taxa the concentrations (Conc.) are given (grain/g x1,000). AP - arboreal pollen, NAP - non-arboreal pollen, NPP - non-pollen palynomorphs.

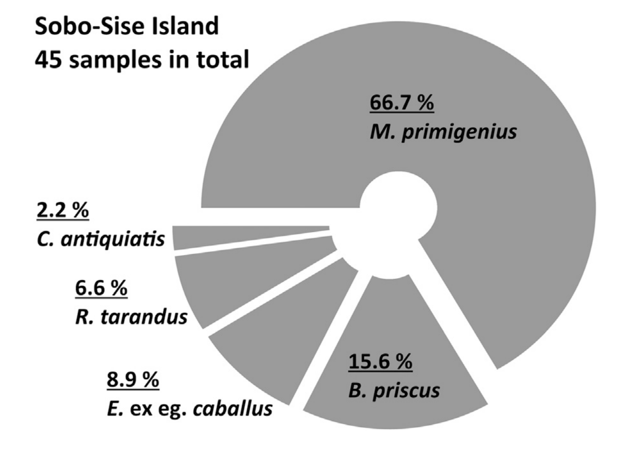

FIGURE 4 | Percentage of bone findings on Sobo-Sise Island comprising archive and new data. Percentages are given above species names.

fragments were obtained (**Table 1**; **Supplementary Table S1**) and are currently stored at the Lena Delta Reserve Tiksi (Russia). Six bones belong to *Mammuthus primigenius* (BLUMENBACH, 1799), three to *Rangifer tarandus* L., 1758 and one to *Bison priscus* (BOJANUS, 1827) and *Coelodonta antiquitatis* (BLUMENBACH, 1799) each. One tusk fragment (SOB18-bone-02; *M. primigenius*) was radiocarbon dated to 13,668 ± 57 yr BP (16,520 cal yr BP; **Table 2**; Wetterich et al., 2020).

It should be noted that bones of *R. tarandus* might belong to modern representatives of this species. Despite the low number of bone findings from the present study, main features of such bone collections of the West Beringian Mammoth fauna (Sher et al., 2005; Kuznetsova et al., 2019) are represented. Those are the prevalence of mammoth bones and the presence of other large grazers such as horse and bison. The finding of woolly rhinoceros remains is somewhat remarkable as it has not been found in the Lena Delta records so far (Wetterich et al., 2008a; Kuznetsova et al., 2019). In addition to the recent bone collection we consider further unpublished data of mammal bones from Sobo-Sise Island stored in several collections in Russia. First bone findings on extinct Mammoth fauna species on Sobo-Sise Island were obtained in July 19–20, 1927 by the Hunting and Fishing Team of the Yakut Expedition (A. Romanov). In total 18 bone samples from Sobo-Sise were transferred in 1928 to the Zoological Institute of the Russian Academy of Sciences (ZIN RAS) in St. Petersburg (Russia). This collection comprises three species that are *M. primigenius*, *B. priscus* and *Equus* ex eg. *caballus*. Mammoth is represented by 11 bones of which most probably eight belong to the same skeleton (cervical vertebrae, left heel bone and fragments of the lower jaw, tusk, left branch of pelvis, left femur, left humerus) because those were collected at one location - the thawing slope of a conical thermokarst mound (baidzherakh) at a lake shore. Six bison bones (two cervical vertebrae and four skull fragments) and one horse bone (third phalanx) complement this collection (**Table 1**).

In 1988, the first radiocarbon date on bone material from Sobo-Sise was published where a tusk fragment found *in situ* at about 13–15 m arl revealed an age of 14,340 ± 120 yr BP (17,490 cal yr BP; GIN-4115) (Grigoriev, 1988). Another mammoth bone found on Sobo-Sise was dated to 24,400 ± 650 yr BP (28,620 cal yr BP; IM-835) although no further information is available (**Table 2**). Six bones were found on Sobo-Sise in 1998 in course of the Russian-German Expedition "Lena Delta," of which five belong to mammoth (one skull fragment, two rib fragments and two vertebral fragments) and one to horse (humerus fragment). One mammoth rib fragment (MKh-O621) was radiocarbon-dated to 19,200 ± 220 yr BP (23,180 cal yr BP; GIN-10235) and one mammoth vertebral fragment (MKh-O624) to >45,000 yr BP (GIN-13929, GrA 46013) (**Table 2**).

The bone collection of the Lena Delta Reserve Tiksi (Russia) contains eight mammoth bones collected on Sobo-Sise in 1990 and identified in 2005 by T.V. Kuznetsova (MSU, Russia) as forearm bones (radius and ulna), two fragments of tibia and fragments of cervical vertebra, vertebra, right branch of pelvis,

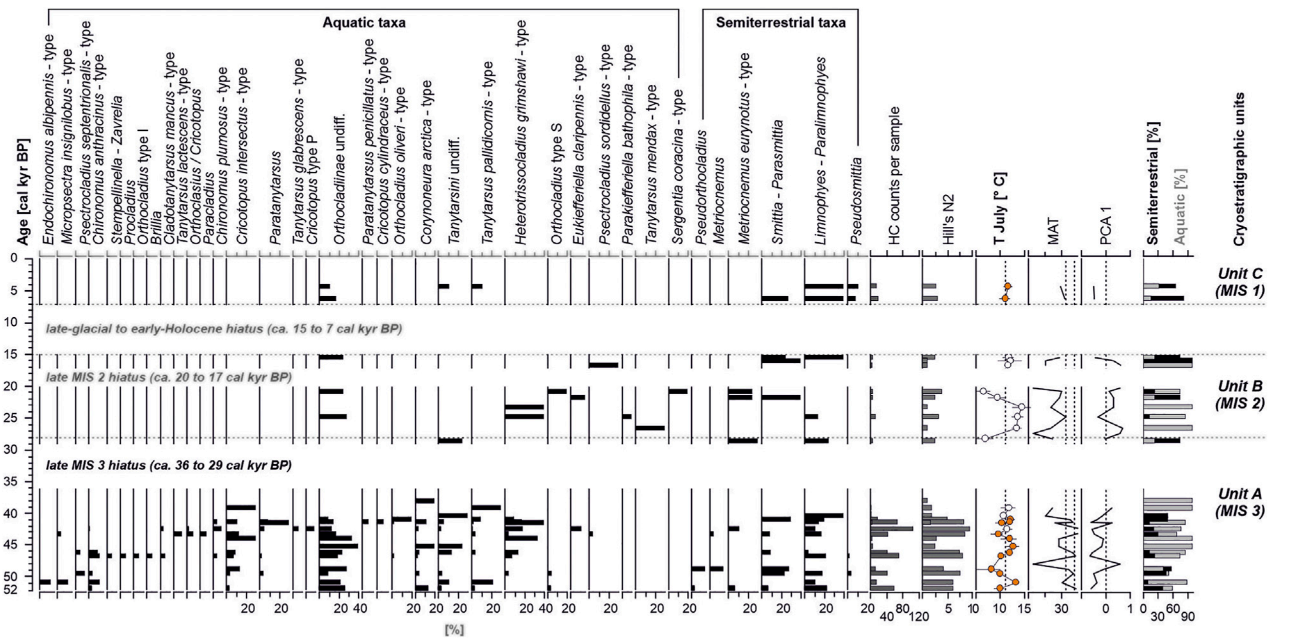

FIGURE 5 | Chironomid diagram of the Sobo-Sise Yedoma record. HC - head capsule, MAT - Modern Analogue Technique, PCA 1 - first axis of the principal component analysis. The dotted line in the reconstruction T_{July} reconstruction indicates the modern value of 11°C. The dotted lines in the MAT indicate the 75% (30.40) and 95% (34.97) confidence intervals. Note that hollow symbols of the reconstructed T_{July} are based on low HC concentrations and should therefore be considered with caution.

heel bone. Two more horse bones were found in 2000 and identified as the damaged shoulder blade and the right branch of pelvis. A sample of a mammoth forearm (LDR-O299) from this collection was radiocarbon-dated to 17,070 ± 70 yr BP (20,630 cal yr BP; KIA-32839). The overall collection of Mammoth fauna bones from Sobo-Sise in various years comprises 45 specimens (**Figure 4**): *M. primigenius* – 66.7% (30 specimens), *B. priscus* – 15.6% (7 specimens), *E.* ex gr. *caballus* – 8.9% (4 specimens), *R. tarandus* – 6.6% (3 specimens) and *C. antiquitatis* – 2.2% (1 specimen) (**Figure 4**). The sparse available radiocarbon dates of *M. primigenius* comprise five finite and one infinite ages. Two ages fall into the MIS 3 interstadial period and four into the MIS 2 stadial (**Table 2**).

Paleo-Limnology

The chironomid record of the Sobo-Sise Yedoma record exhibits three zones, which delineate the cryolithological stratification into three units A-C covering MIS 3 to MIS 1 (**Figure 5**). The chironomid fauna of the record comprises 39 taxa. The number of chironomid HC per sample varies considerably with highest concentration found in Unit A, while units B and C show relatively low concentrations. All fossil chironomid taxa were represented in the modern training sets. Only three taxa that had only single occurrence in the investigated profiles have Hill's N2 <5 in the training set and therefore were defined as not well-represented in the NR training sets and model: *Orthocladius/Cricotopus* (N2 = 1.9 in the SOB samples and 0 in the NR training set), *Pseudorthocladius* (N2 = 1.8 in the SOB samples and 4.0 in the NR training set), *Tanytarsus lactescens*-type (N2 = 1 in the SOB samples and 1 in the NR training set). The low representation of these taxa in the SOB profiles does not hamper the quality of the reconstruction. MAT for T_{July} reconstruction revealed that the samples from the interval 43.3–42.5 cal kyr BP had no analogues in the calibration set (MAT above 95%; **Figure 5**). The remaining profile samples have good or fair analogue in the NR training set. The high representation of the taxa in the training set, together with the predominantly good MAT statistics results, indicated that the temperature reconstruction from the investigated profiles is mainly reliable. Samples with poor MAT tests should be interpreted with caution.

The MIS 3 chironomid fauna of Unit A (52-28 cal kyr BP) is composed of 36 taxa, while their diversity (N2) varies considerably. Several periods within Unit A exhibit rich chironomid fauna: 52 to 49 cal kyr BP, 48 to 46 cal kyr BP and 43 to 40 cal kyr BP (median N2 = 8.9; **Figure 5**). The representation of typical aquatic taxa vs. semiterrestrial taxa varies within unit A. Between 52 and 49 cal kyr BP the communities are dominated by taxa characteristic for moderate climatic conditions: *Endochironomus albipennis*-type, *Micropsectra insignilobus*-type, *Chironomus anthracinus*-type, *Tanytarsus pallidicornis*-type and *Cricotopus interectus*-type. The reconstructed T_{July} varies around modern level (11°C) with one excursion of about 1.5°C above modern T_{July} at 50.8 cal kyr BP. The decline of semiterrestrial taxa at the same time might indicate higher water level under relatively warm conditions. Later on, until about 49 cal kyr BP the share of semiterrestrial taxa reaches up to 57% and the reconstructed T_{July} declines to about 1°C below modern. Such cooling might have induced shallowing of the water level by reducing the seasonally thawed uppermost ground below the ponds. Between 48 and 38 cal kyr BP, the chironomid fauna is dominated by typical aquatic taxa although chironomid counts and diversity decrease considerably between 46 and 44 cal kyr BP when the reconstructed T_{July} rises up to 1.5°C above modern. The period between 44 and 41.5 cal kyr BP is characterized by the highest diversity and concentration of chironomids. The communities are dominated by the *Heterotrissocladius grimschawi*-type that occurs in oligotrophic lakes and is indicative of moderate conditions with temperature optima of 11–12°C. Reconstructed T_{July} slightly varies around modern with warmer-than-today T_{July} around 41 cal kyr BP. After 41.5 cal kyr BP, a strong decline of chironomid communities is observed and also reflected in the PCA 1 sample scores. Between 40.4 and 38 cal kyr BP only few chironomid remains have been found. Semiterrestrial taxa disappear around 39 cal kyr BP probably indicating another episode of a higher water level. At 36.7 cal kyr BP no chironomids have been found in the sediments, which probably suggest another dry out. Above the hiatus, the uppermost sample from Unit A (SOB18-03-03) is dated to 28.4 cal kyr BP. Here, the chironomid fauna is poor and is represented mainly by semiterrestrial (*Limnophies-Paralimnophies*, *Metriocnemus eurinotus*-type) or phytophilic taxa (Tanytarsini). The reconstructed T_{July} is of about 8°C, which is about 3°C below modern T_{July}.

The abundance and diversity of chironomids are generally low during MIS 2 (Unit B, 28 – 15 cal kyr BP). Between 27.7 and 23.3 cal kyr BP, the chironomid fauna is dominated by aquatic taxa (*Tanytarus mendax*-type, *Heterotrissocladius grimschawi*-type). After 21.8 cal kyr BP the proportion of semiterrestrial taxa rise and taxa characteristic for littoral zone of lakes (*Eukiefferiella claripennis*-type) and for cold environments (*Orthocladius* type S, *Sergentia coracina*-type) appear. In the sediment layer dated to 20.4 cal kyr BP no chironomid remains have been found. The samples between 16.7 and 15.4 cal kyr BP are represented either by littoral phytophilic and acidophilic *Psectrocladius sordidellus*-type or by the typical semiterrestrial *Smittia-Parasmittia*, *Limnophies-Paralimnophies*-types that are both indicative for unstable water levels and erosion processes.

In MIS 1 (Unit C, 7 – 0 cal kyr BP) chironomid remains were found only between 6.4 and 4.4 cal kyr BP. The chironomid fauna is poor (median N2 = 2.9) and dominated by semiterrestrial taxa such as *Smittia-Parasmittia*, and *Limnophies-Paralimnophies* in presence of the phytophilic Tanytarsini taxa. The reconstructed T_{July} at 6.4 cal kyt BP is at modern level (11.1°C) with a slight increase toward 4.4 cal kyr BP (11.7°C). After 4.4 cal kyr BP chironomids are absent from the record. Diatom fossil valves were only found in three samples of the uppermost unit C after 6.4 cal kyr BP. Highest counts were found in the uppermost sample SOB18-01 with 185 specimens, while sample SOB18-01-02 contained only five specimens. The diatom flora of the Sobo-Sise Yedoma record is represented by 25 taxa, belonging to 17 genera (**Supplementary Table S2**) and dominated by benthic species (**Supplementary Table S3**) while benthic–planktonic species occur much less and planktonic species are absent from the record. Most of the diatom species are indifferent to salinity. Alkaliphilic and alkalibiontic species dominate the record and most of the diatom species are cosmopolitans while boreal species are present with *Hannaea arcus* and *Pinnularia alpina*, and arctic-alpine species with *Pinnularia gibba* and *Navicula vulpina*. Flow-velocity preferences are known for 19 species of the 25 species identified in the Sobo-Sise record. Nine of them are indifferent, six species indicate flowing water and three standing water. Overall, the diatom flora of Unit C indicates the presence of shallow water with low salinity and neutral pH. The low representation of diatoms in the record might point to low silica availability in the host water or generally aquatic conditions not suitable to maintain stable diatom communities. For the normal development of diatoms, a rather significant concentration of silica is required, which is used for building of their frustules (Wasser et al., 1989). In the absence or lack of silica, the diatom frustules become thinner, and when the concentration of silicon in water falls below 0.3 mg L^{-1}, the growth of diatoms completely stops (Proshkina-Lavrenko, 1974; Martin-Jézéquell, Lopez, 2003).

DISCUSSION

Paleo-Ecology of the Sobo-Sise Yedoma Cliff in Regional Context

Detailed paleo-ecological information has been obtained from Yedoma IC deposits and its Holocene cover from two nearby locations on Bykovsky Peninsula (outcrop Mamontova Khayata) and Kurungnakh-Sise Island in the central Lena Delta (**Figure 1**). The Bykovsky Yedoma archive has been intensively studied for pollen, plant macrofossils, testate amoebae, freshwater ostracods, fossil insect remains and mammal bones of the late Pleistocene Mammoth fauna (Schirrmeister et al., 2002a; Bobrov et al., 2004; Kienast et al., 2005; Sher et al., 2005; Wetterich et al., 2005; Andreev et al., 2011; Kuznetsova et al., 2019) based on well-described cryolithological properties of the frozen deposits with well-established radiocarbon-based chronology (Schirrmeister et al., 2002b). The Yedoma IC and its stratigraphic context of fluvial sands underneath and Holocene cover on top exposed at the shore of Kurungnakh-Sise Island has been studied in terms of paleo-ecology of pollen, plant macrofossils, testate amoebae, ostracods, insect fossil remains and fossil mammal bones in detail by Schirrmeister et al. (2003) and Wetterich et al. (2008a). Main paleo-ecological results from both locations are discussed in comparison to those from the present study on Sobo-Sise Island below for the MIS 3 interstadial, the MIS 2 stadial and the MIS 1 interglacial periods.

Interstadial MIS 3 Environments

The new pollen record from Sobo-Sise Island matches those from Bykovsky Peninsula (Andreev et al., 2002; Schirrmeister et al., 2002a) and Kurungnakh-Sise Island (Schirrmeister et al., 2003; Wetterich et al., 2008a) and is further supported and enhanced by plant macrofossil studies from Bykovsky Peninsula (Kienast et al., 2005) and Kurungnakh-Sise Island (Wetterich et al., 2008a). The regional vegetation during MIS 3 as reconstructed from pollen and plant macrofossils of Yedoma IC deposits is characterized tundra-steppe vegetation with dominance of Cyperaceae and Poaceae pollen and some amounts of *Artemisia* and *Salix* between 53 and 43 cal kyr BP. High abundance of these taxa and presence of Caryophyllaceae as well as generally higher pollen concentrations are noted between 40 and 36 cal kyr BP. The permanent presence of *Salix* pollen points to the occurrence of willow shrubs in more protected and wet places. Low percentages and low concentrations of *Pinus sylvestris* point to low abundance in the past vegetation. In contrast, *Larix* shows a distinct difference with low percentages but high concentrations. Assuming that *Larix* tends to accumulate directly on the site, we deduce that *Larix* pollen concentrations are more representative than the *Larix* pollen percentages. We therefore suggest that *Larix* was a member of plant communities associated with Unit A and *Pinus sylvestris* pollen were rather derived from long-distance transport. The entire record of Unit A reveals relatively high percentages and concentrations of *Picea*. Since it is difficult to assume suitable conditions for spruce in the late Pleistocene of the Lena Delta region, we have to conclude that this is redeposition driven by wind or river transport. The redeposition *in situ* is also possible, however, age-height modeling did not reveal any inversions within Unit A (Wetterich et al., 2020). Stagnant water is indicated by the presence of green algae *Botryococcus* and *Pediastrum* remains. The Bykovsky and Kurungnakh-Sise records both show that remains of typical steppe and meadow plants of the *Festuca*, *Kobresia*, *Linum*, *Silene,* and *Potentilla* genera (Kienast et al., 2005) as well as wetland plants such as *Carex* sect. *Phacocystis*, *Saxifraga hirculus*, and *Eriophorum angustifolium* are common in the fossil record. At about 51 cal kyr BP and 40 cal kyr BP in the Bykovsky record, the occurrence of the temperate aquatic plant *Callitriche hermaphroditica* provides evidence of mean T_{July} of 12°C or more, while the finding of the steppe taxon *Thesium* dated to 51 cal kyr suggests T_{July} of 15°C or more. The chironomid-based T_{July} reconstruction for MIS 3 from the Sobo-Sise Yedoma record shows some variation (**Figure 5**) and points to warmer-than-today (>11°C) temperatures at about 51 cal kyr BP, 46-44 and 41 cal kyr BP showing a general agreement with the plant macrofossil-based T_{July} estimates from the Bykovsky Yedoma record (Kienast et al., 2005). Interstadial climate variability during MIS 3 has been previously deduced from proxy records across West Beringia (Anderson and Lozhkin, 2001) although with regional differences in the onset and duration of climatic optimum conditions (Wetterich et al., 2014). Those were recorded on Kurungnakh-Sise Island between 43 and 36 cal kyr BP and on Bykovsky Peninsula 45-38 cal kyr BP (Wetterich et al., 2014 and references therein). Thus, the Sobo-Sise chironomid record supports warmer-than-today summers as recorded in the Bykovsky and Kurungnakh-Sise Yedoma archives given dating uncertainties and different proxies. T_{July} reconstructions from the western part of the Yana-Indigirka lowland (east of the study area) reveal similar-to or warmer-than-today temperatures (by up to 4–4.5°C) and higher-than-today annual precipitation (by up to 50–100 mm) between about 39 and 31 cal kyr BP (Pitulko et al., 2017), although older deposits are not captured in this record starting at 39.2 cal kyr BP. The early MIS 3 warmer-than-today conditions are represented by the Bykovsky and Sobo-Sise data, while late MIS 3 deposits are missing in these records and the Yana-Indigirka Lowland data misses the early MIS 3 deposits but represent the late MIS 3 phase of warmer (and moister)-than-today summer conditions in western Beringia.

The regional MIS 3 interstadial environments and vegetation as reconstructed from pollen data provided favorable conditions to maintain the Mammoth fauna as seen in the Bykovsky records (Schirrmeister et al., 2002a; Sher et al., 2005; Kuznetsova et al., 2019), but also supported by Sobo-Sise record with one radiocarbon-dated mammoth bone of 28,620 cal yr BP (**Table 2**).

The aquatic conditions during MIS 3 are reflected by the chironomid data from the Sobo-Sise Yedoma. Varying dominance of aquatic and semiterrestrial taxa over time represent the transition from higher to shallower water levels (Nazarova et al., 2017a). However, the supposed main freshwater type of the Beringian tundra-steppe environments are ice-wedge low-center polygon ponds which rarely exceed 1 m water depth in modern tundra landscapes (Wetterich et al., 2008b). The onset of ice-wedge polygon development with shallow ponds is represented by prevailing semiterrestrial chironomid taxa between 52 and 48 cal kyr BP. Evolving low-center polygons during MIS 3 climatic optimum with warmer-than-today T_{July} likely induced deeper thaw and thus higher water level in the ponds that explains the higher share of aquatic chironomid taxa from 48 to 36 cal kyr BP. Freshwater ostracod fossil findings with highest abundance and diversity recorded at about 44 cal kyr BP on Kurungnakh-Sise Island (Wetterich et al., 2008a) support the existence of permanent water bodies. The Bykovsky ostracod record is more diverse and its best representation spans from about 48 to 41 cal kyr BP (Wetterich et al., 2005). Later on the ostracod fauna in the Bykovsky Yedoma record vanishes toward the MIS 3-2 transition, and in the Sobo-Sise chironomid record the uppermost sample at 28 cal kyr BP after the hiatus at 36–29 cal kyr BP exhibits a poor representation of only semiterrestrial taxa. Both dynamics reflect deterioration of the aquatic habitats in polygon ponds, probably induced by cooling at the MIS 3-2 transition leading to shallowing or dry-out of the water bodies.

Stadial MIS 2 Environments

The pollen-based paleo-vegetation records from Sobo-Sise Island and from Bykovsky Peninsula both highlight open tundra-steppe with prevailing Poaceae with present Cyperaceae, *Artemisia*, Brassicaceae and Caryophyllaceae pollen (Schirrmeister et al., 2002a; Andreev et al., 2002; Andreev et al., 2011) while MIS 2 deposits are largely missing in the Kurungnakh-Sise sequence (Schirrmeister et al., 2003; Wetterich et al., 2008a). MIS 2 pollen concentrations are generally lower than during MIS 3. *Selaginella rupestris* spores indicate very dry habitats, while larger amounts of reworked Pinaceae pollen and *Glomus* spores indicate disturbed soils due to the presence of large grazers of the Mammoth fauna. Such pollen composition reflects rather cold and dry summer climate conditions if compared to MIS 3. The *Larix* concentrations are low suggesting colder summers than during MIS 3. Still present green algae *Botryococcus* and *Pediastrum* remains point to the occasional presence of low-centred polygons while the absence of aquatic plant macro-fossils in deposits dated to 26.3 cal kyr BP (Kienast et al., 2005) suggests unstable aquatic environments during MIS 2. Dominating arctic pioneer species and decreased floristic diversity of the plant macro-fossil record point to harsh summer climate.

Evidence for subsistence of the Mammoth fauna during the MIS 2 stadial is found in four mammoth radiocarbon dates from Sobo-Sise Island ranging from 23,180 to 16,520 cal yr BP (**Table 2**) and corresponding to comparable data from Bykovky Peninsula in regional context (Schirrmeister et al., 2002a; Sher et al., 2005; Kuznetsova et al., 2019). Interestingly, one age of 17,490 cal yr BP falls into the MIS 2 sedimentary hiatus (20 - 17 cal yr BP) as estimated in the Sobo-Sise record sampled in 2018 (Wetterich et al., 2020) although a lack of deposits in a sequence due to hampered deposition or post-depositional erosion does not necessarily indicate a lack of past wildlife.

Cold and dry summer climate with unstable aquatic conditions is further seen in the chironomid record of Sobo-Sise with very low concentrations and diversity during the entire MIS 2 unit. Aquatic taxa are found from 28 to 23 cal kyr BP, afterward semiterrestrial taxa prevail. The period from 17 to 15 cal kyr BP is characterized by littoral phytophilic and acidophilic taxa as well as by typical semiterrestrial taxa. The ostracod record from the Bykovsky Yedoma lacks findings in the MIS 3-2 transition period from 32 to 25 cal kyr BP (zone III in Wetterich et al., 2005) and was interpreted as extremely unfavorable conditions for aquatic life due to dry-out of polygon ponds. Starting from about 25 cal kyr BP until about 21 cal kyr BP the ostracod record from Bykovsky is poor in abundance and diversity and no ostracods were found after 21 cal kyr BP. Improved aquatic conditions and present ostracod fossils are seen in a sample dated to 16.9 cal kyr BP. MIS 2 aquatic conditions as seen in chironomids from Sobo-Sise and ostracods from Bykovsky point to shallow polygon ponds or just wet polygon centers due to low summer precipitation feeding the water bodies and cold summer temperatures causing shallow thaw depth and inhibited ground ice melt. Due to the unfavorable aquatic conditions and the resulting poor chironomid record, the chironomid-based T_{July} reconstruction for MIS 2 relies on very low concentration of chironomids in sediments (**Figure 5**) and its reliability is therefore limited. Therefore, warmer-than-today T_{July} as seen in the chironomid record between 27 and 23 cal kyr BP seems unlikely to represent MIS 2 conditions. However, the coldest T_{July} up to about 4°C below modern is found at about 20 cal kyr BP (**Figure 5**). This reconstructed low T_{July} is caused by a high representation of indicative for colder conditions chironomid taxa like *Orthocladius* type *S* (T optimum in the NR model 9.5°C) and *Metriocnemus eurinotus*-type (T optimum in the NR model 9.2°C) (Nazarova et al., 2015).

Interglacial MIS 1 Holocene

In the Sobo-Sise record, the Holocene pollen spectra of Unit C differ noticeably from those of the late Pleistocene Yedoma IC units A and B, and are characterized by dominating *Betula* sect. *Apterocaryon* and the significant amounts of *Alnus* subg. *Alnobetula* and Ericaceae pollen, all together indicating humid shrub-tundra vegetation after about 7 cal kyr BP with isolated *Larix* stands. The increased concentration of *Pinus sylvestris* and *Picea* can be a result of long-distance transport of Holocene coniferous forests located south of the Lena Delta (Müller et al., 2009). The pollen records of the Holocene cover deposits of the Bykovsky Yedoma and the Kurungnakh-Sise Yedoma span from about 9.2 cal kyr BP to modern and from about 9.1 to 2.9 cal kyr BP, respectively. These records differentiate into early to middle Holocene and late Holocene pollen zones (Schirrmeister et al., 2002b; Wetterich et al., 2008a). The early Holocene pollen spectra indicate shrub-tundra (or forest tundra) vegetation dominated by *Alnus* subg. *Alnobetula*, *Betula* sect. *Apterocaryon* and *Salix* as well as by Ericales with some Cyperaceae and Poaceae until about 8.4 cal kyr BP (Andreev et al., 2011). After 8.4 cal kyr BP the shrub-tundra gradually disappears and is replaced by modern high Arctic and Arctic tundra vegetation. The plant macrofossil record from Bykovsky comprises two records dated to about 8.6 and 3 cal kyr BP. Warmer summers are reflected by the early Holocene plant species composition while the late Holocene record points to increased humidity and decreased summer temperatures by a smaller share of cryoxerophilous pioneer vegetation and tundra-steppe vegetation and a larger share of tundra bog species. Such Holocene climatic deterioration is seen in prevalence of tundra bog plants, while the occurrence of nival meadow plants such as *Saxifraga nivalis* and *Ranunculus nivalis* suggests a short growing season due to a thick snow cover and predominating cool and moist conditions (Schirrmeister et al., 2002b). The absence of true water plant species in the late Holocene and the reduced share of plants inhabiting marshy sites at shallow water lake shores point to impoverishment of aquatic conditions. The plant macrofossil record from Kurungnakh-Sise differentiates into data from the early Holocene dated to about 9.1 cal kyr BP and the mid to late Holocene dated to about 6.7 to 2.9 cal kyr BP (Wetterich et al., 2008a). The early Holocene plant composition comprises tundra-steppe species such as *Kobresia myosuroides* and *Potentilla* cf. *stipularis* while the number of wetland and tundra bog plants is low. Thus, the temperature increase toward the early Holocene is not reflected in these data although a single Betulaceae fruit was found. The pollen data from Kurungnakh-Sise, however, show a clear increase in *Betula* sect. *Apterocaryon*, *Alnus* subg. *Alnobetula*, *Betula* sect. *Betula*, and Ericales pollen as mentioned above. The mid to late Holocene plant species composition from Kurungnakh-Sise reflects wet tundra with wetland sedges such as *Carex* sect. *Phacocystis* and dominating willow shrubs. The presence of *Betula* cf. *fruticosa* and *Ledum palustre* suggests subarctic temperature conditions (Wetterich et al., 2008a).

The Holocene chironomid from Unit C of the Sobo-Sise Yedoma record is sparse. Semiterrestrial and phytophilic taxa dominated till ca 4.4 cal kyr BP and disappeared thereafter. The composition of chironomid communities indicates the presence of a very shallow overgrown waterbody that dried out after 4.4 cal kyr BP. Rare diatom fossils were only found within the uppermost samples of the Holocene cover after about 6.4 cal kyr BP. The dominating ecological preferences of the diatom species are characterized as cosmopolitan, benthic, alkaliphilic, indifferent to salinity. If compared to modern Yakutian diatom reference data with statistically quantified optimum ecological rages of certain conditions (Pestryakova et al., 2018) three species are found in the Holocene Sobo-Sise diatom record. Those are *Diploneis elliptica* (optimum T_{July} of 11.9°C) and *Stauroneis anceps* (optimum T_{July} of 11.2°C) from Unit C deposits dated from 6.4 to 2.5 cal kyr BP.

Compared to the Holocene chironomid-based T_{July} reconstruction of ca 11.5°C at 6.4 to 4.4 cal kyr BP it seems obvious that the chironomid-based and diatom-based T_{July} reconstructions do not contradict each other. The finding of the diatom species *Epithemia adnata* (T_{July} >15°C) in the uppermost sample of Unit C points to warmer conditions than today, while the indication of optimum ion content (expressed as electrical conductivity of 586 µs cm^{-1}) of *E. adnata* would support such warm summer temperatures with increased evaporation. Modern electrical conductivity values in polygon ponds in the Lena Delta are more than two-fold lower and range from 27 to 254 µs cm^{-1} (Wetterich et al., 2008b). However, the Sobo-Sise fossil diatom record is very limited and its environmental indication should be interpreted with caution. Ostracod fossils have not been found in the Holocene cover deposits on the Yedoma IC on Bykovsky Peninsula (Wetterich et al., 2005) and Kurungnakh-Sise Island (Wetterich et al., 2008a), but are found on Bykovsky in late Holocene deposits dated to about 3 cal kyr BP that accumulated in thermokarst basins here and elsewhere in the region (Wetterich et al., 2009; Morgenstern et al., 2013). Such observation might be explained by landscape reorganization due to massive permafrost thaw starting in the lateglacial period when climate warming toward the Holocene increased thermokarst processes and thus the rates of northern lake formation starting ~14 cal kyr BP and peaking around 10.4 cal kyr BP (Brosius et al., 2021). Although lake formation slowed down around 10–8 cal kyr BP, the major occurrence of Holocene aquatic habitats in West Beringian Yedoma landscapes is found in thermokarst basins evolving since the deglacial rather than on degrading Yedoma uplands.

CONCLUSION

The regional Yedoma records in the Lena Delta and on Bykovsky Peninsula confirm the existence of late Pleistocene tundra-steppe environments in West Beringia during MIS 3 with partly warmer-than-today summers and wetter conditions allowing for stagnant water (i.e., polygon ponds). During MIS 2, summers were probably colder than during MIS 3 and drier with unstable aquatic conditions in the polygonal landscape. However, the aquatic conditions in shallow ponds of low-center polygons during MIS 3 and MIS 2 were suitable for maintaining chironomid faunae although highly dynamic and prone to episodically dry-out or drainage causing low abundance and diversity of chironomids in the records. Diatom frustules occurred in the sediment record only after 6.4 cal kyr BP, probably due to post-depositional dissolution processes or to the lack of silica in the earlier period of pond development.

In addition to previous plant macrofossil-based T_{July} reconstructions from the Bykovsky Yedoma record available for only two periods around 51 and 40 cal kyr BP, the present chironomid-based T_{July} estimates fills the period in between with data from about 52 to 41 cal kyr BP. The record reveals warmer-than-today T_{July} at about 51 cal kyr BP, 46-44 and 41 cal kyr BP highlighting early MIS 3 climate optimum conditions.

The Sobo-Sise pollen record suggests that *Larix* was a member of the regional MIS 3 tundra-steppe communities. The Holocene vegetation differentiates into early Holocene shrub-tundra replaced by mid- and late Holocene modern wet tundra.

The finding of a bone from woolly rhinoceros (*Coelodonta antiquitatis*) most likely originating from the Sobo-Sise Yedoma cliff is somewhat remarkable since the species has not been reported yet from the Lena Delta region or Bykovsky Peninsula, and is generally rare in collections of fossil bones of the late Pleistocene Mammoth fauna in northern part of West Beringia.

DATA AVAILABILITY STATEMENT

The original contributions presented in the study are included in the article/**Supplementary Material**, further inquiries can be directed to the corresponding author.

AUTHOR CONTRIBUTIONS

SW, NR and LN designed the study and wrote the original draft of the manuscript. SW, AK, LN and NR acquired funding. AK, AA, SW, LSc and MF participated in the field investigation and collected sample material. KS supervised pollen preparation. NR and MP performed pollen analysis and interpretation. LN and LSy performed chironomid analysis and interpretation. OP performed diatom analysis and interpretation. TK performed mammal bone analysis and interpretation. JW and MF supported overall proxy data interpretation. All authors contributed in writing and editing the manuscript.

FUNDING

This work has been supported by the by the Russian Foundation of Basic Research (RFBR grant No. 18-05-60221 to AK) and the Deutsche Forschungsgemeinschaft (DFG grants No. WE4390/7-1 to SW and NA760/8-1 to LN). NR worked in the frame of project NIR IAET SB RAS No. 0264-2019-0010. MF was supported by the NUNATARYUK project that has received funding from the European Union's Horizon 2020 research and innovation program under grant agreement No. 773421.

ACKNOWLEDGMENTS

We thank our colleagues from the Hydrobaza Tiksi for help with fieldwork in 2018 that was conducted in the framework of the joint Russian-German expeditions *LENA 2018* supported by the Samoylov Research Station. Sarah Olischläger (AWI Potsdam) is acknowledged for pollen preparation.

SUPPLEMENTARY MATERIAL

The Supplementary Material for this article can be found online at: https://www.frontiersin.org/articles/10.3389/feart.2021.681511/full#supplementary-material

REFERENCES

Anderson, P. M., and V. Lozhkin, A. (2001). The Stage 3 Interstadial Complex (Karginskii/middle Wisconsinan Interval) of Beringia: Variations in Paleoenvironments and Implications for Paleoclimatic Interpretations. *Quat. Sci. Rev.* 20, 93–125. doi:10.1016/S0277-3791(00)00129-3

Andreev, A. A., Schirrmeister, L., Siegert, Ch., Bobrov, A. A., Demske, D., Seiffert, M., et al. (2002). Paleoenvironmental changes in northeastern Siberia during the Upper Quaternary e evidence from pollen records of the Bykovsky Peninsula. *Polarforschung* 70, 13–25. doi:10.2312/polarforschung.70.13

Andreev, A. A., Schirrmeister, L., Tarasov, P. E., Ganopolski, A., Brovkin, V., Siegert, C., et al. (2011). Vegetation and Climate History in the Laptev Sea Region (Arctic Siberia) during Late Quaternary Inferred from Pollen Records. *Quat. Sci. Rev.* 30, 2182–2199. doi:10.1016/j.quascirev.2010.12.026

Are, F., and Reimnitz, E. (2000). An Overview of the Lena River Delta Setting: Geology, Tectonics, Geomorphology, and Hydrology. *J. Coastal Res.* 16 (4), 1083–1093. doi:10.2307/4300125

Barinova, S. S., Medvedeva, L. A., and Anisimova, O. V. (2006). *Bioraznoobrazie Vodoroslei—Indikatorov Okruzhayushchei Sredy (Biological Diversity of Algae—Environmental Indicators)*. Pilies Studio: Tel Aviv.

Battarbee, R. W. (1986). "Diatom Analysis," in *Handbook of Holocene Paleoecology and Palaeohydrology*. Editor B. E. Berglund (New York: Wiley), 527–570.

Beug, H.-J. (2004). *Leitfaden der Pollenbestimmung für Mitteleuropa und angrenzende Gebiete*. München: Verlag Friedrich Pfeil.

Biskaborn, B. K., Nazarova, L., Pestryakova, L. A., Syrykh, L., Funck, K., Meyer, H., et al. (2019). Spatial Distribution of Environmental Indicators in Surface Sediments of Lake Bolshoe Toko, Yakutia, Russia. *Biogeosciences* 16, 4023–4049. doi:10.5194/bg-2019-14610.5194/bg-16-4023-2019

Bobrov, A. A., Andreev, A. A., Schirrmeister, L., and Siegert, C. (2004). Testate Amoebae (Protozoa: Testacealobosea and Testaceafilosea) as Bioindicators in the Late Quaternary Deposits of the Bykovsky Peninsula, Laptev Sea, Russia. *Palaeogeogr. Palaeoclimatol. Palaeoecol.* 209, 165–181. doi:10.1016/j.palaeo.2004.02.012

Boike, J., Nitzbon, J., Anders, K., Grigoriev, M., Bolshiyanov, D., Langer, M., et al. (2019). A 16-year Record (2002-2017) of Permafrost, Active-Layer, and Meteorological Conditions at the Samoylov Island Arctic Permafrost Research Site, Lena River delta, Northern Siberia: an Opportunity to Validate Remote-Sensing Data and Land Surface, Snow, and Permafrost Models. *Earth Syst. Sci. Data* 11 (1), 261–299. doi:10.5194/essd-11-261-2019

Brooks, S. J., and Birks, H. J. B. (2000). Chironomid-inferred Late-Glacial and Early-Holocene Mean July Air Temperatures for Kråkenes Lake, Western Norway. *J. Paleolimnology* 23, 77–89. doi:10.1023/A:1008044211484

Brooks, S. J., Langdon, P. G., and Heiri, O. (2007). *Using and Identifying Chironomid Larvae in palaeoecologyQRA Technical Guide No. 10*. London, UK: Quaternary Research Association.

Brosius, L. S., Anthony, K. M. W., Treat, C. C., Lenz, J., Jones, M. C., Bret-Harte, M. S., et al. (2021). Spatiotemporal Patterns of Northern lake Formation since the Last Glacial Maximum. *Quat. Sci. Rev.* 253, 106773. doi:10.1016/j.quascirev.2020.106773

Chen, J., Günther, F., Grosse, G., Liu, L., and Lin, H. (2018). Sentinel-1 InSAR Measurements of Elevation Changes over Yedoma Uplands on Sobo-Sise Island, Lena Delta. *Remote Sensing* 10 (7), 1152. doi:10.3390/rs10071152

Fægri, K., and Iversen, J. (1989). *Textbook of Pollen Analysis*. fourth edition. Chichester: John Wiley & Sons.

Fedorova, I., Chetverova, A., Bolshiyanov, D., Makarov, A., Boike, J., Heim, B., et al. (2015). Lena Delta Hydrology and Geochemistry: Long-Term Hydrological Data and Recent Field Observations. *Biogeosciences* 12 (2), 345–363. doi:10.5194/bg-12-345-2015

Francis, D. R., Wolfe, A. P., Walker, I. R., and Miller, G. H. (2006). Interglacial and Holocene Temperature Reconstructions Based on Midge Remains in Sediments of Two Lakes from Baffin Island, Nunavut, Arctic Canada. *Palaeogeogr. Palaeoclimatol. Palaeoecol.* 236, 107–124. doi:10.1016/j.palaeo.2006.01.005

Fuchs, M., Grosse, G., Strauss, J., Günther, F., Grigoriev, M., Maximov, G. M., et al. (2018). Carbon and Nitrogen Pools in Thermokarst-Affected Permafrost Landscapes in Arctic Siberia. *Biogeosciences* 15 (3), 953–971. doi:10.5194/bg-15-953-2018

Fuchs, M., Nitze, I., Strauss, J., Günther, F., Wetterich, S., Kizyakov, A., et al. (2020). Rapid Fluvio-thermal Erosion of a Yedoma Permafrost Cliff in the Lena River Delta. *Front. Earth Sci.* 8, 336. doi:10.3389/feart.2020.00336

Grigoriev, M. N. (1988). The Role of Cryomorphogenesis in the Evolution of the Lena River Estuary Relief in the Holocene (Роль КриоморфоҐенеза В Лволюции Рельефа Устьевой Области Р. Лена В Голоцене). *Studies of Permafrost Strata and Cryogenic Phenomena (*Исследования Мерзлыч Толщ И КриоҐенныч Явлений*)*. Yakutsk: Institute of Permafrost of the Siberian Branch of the USSR Academy of Sciences, Yakutsk, 22–28.(in Russian).

Grimm, E. C. (2004). *TGView 2.0.2 (Software)*. Springfield, Illinois: Illinois State Museum.

Grosse, G., Robinson, J. E., Bryant, R., Taylor, M. D., Harper, W., DeMasi, A., et al. (2013). Distribution of Late Pleistocene Ice-Rich Syngenetic Permafrost of the Yedoma Suite in East and central Siberia, Russia. *U.S. Geological Survey Open File Report*, Open-File Report 2013-1078, 37.

Günther, F., Grosse, G., Maximov, G., Veremeeva, A., Haghshenas Haghighi, M., and Kizyakov, A. (2018). Repeat LiDAR for Tracking Extensive Thaw Subsidence on Yedoma Uplands. Book Of Abstracts, International Symposium 20 Years Of Lena-Delta Expeditions*, 17-19 October 2018*. St. Petersburg, RussiaSt. Petersburg: Arctic and Antarctic Research Institute, 22–24.

Guthrie, R. D. (1990). *Frozen Fauna of the Mammoth Steppe: The story of Blue Babe*. Chicago and London: The University of Chicago Press, 323.

Heiri, O., and Lotter, A. F. (2001). Effect of Low Count Sums on Quantitative Environmental Reconstructions: an Example Using Subfossil Chironomids. *J. Paleolimnology* 26, 343–350. doi:10.1023/A:1017568913302

Hill, M. O. (1973). Diversity and Evenness: a Unifying Notation and its Consequences. *Ecology* 54 (2), 427–432. doi:10.2307/1934352

Hoff, U., Biskaborn, B. K., Dirksen, V. G., Dirksen, O., Kuhn, G., Meyer, H., et al. (2015). Holocene Environment of Central Kamchatka, Russia: Implications from a Multi-Proxy Record of Two-Yurts Lake. *Glob. Planet. Change* 134, 101–117. doi:10.1016/j.gloplacha.2015.07.011

Hopkins, D. M. (1959). Cenozoic History of the Bering Land Bridge: The Seaway between the Pacific and Arctic Basins Has Often Been a Land Route between Siberia and Alaska. *Science* 129 (3362), 1519–1528. doi:10.1126/science.129.3362.1519

IBCAO grid (2021). Online source. Available at: https://www.gebco.net/data_and_products/gridded_bathymetry_data/arctic_ocean/((Accessed January 11, 2021).

Juggins, S. (2007). *C2 Version 1.5 User Guide. Software for Ecological and Paleoecological Data Analysis and Visualization*. Newcastle: Newcastle University.

Kanevskiy, M., Shur, Y., Fortier, D., Jorgenson, M. T., and Stephani, E. (2011). Cryostratigraphy of Late Pleistocene Syngenetic Permafrost (Yedoma) in Northern Alaska, Itkillik River Exposure. *Quat. Res.* 75, 584–596. doi:10.1016/j.yqres.2010.12.003

Katasonov, E. M. (2009). *Litologiya Merzlykh Chetvertichnykh Otlozhenii (Kriolotologiya) Yanskoi Primorkoi Nizmenosti (Lithology of Frozen Quaternary Deposits (Cryolithology) of the Yana lowland)*. Moscow, Russia: Production and Research Institute for Engineering Surveys and Construction (ПНИИИС) Publishers, 175 (in Russian).

Khazin, L. B., Khazina, I. V., Kuzmina, O. B., Ayunov, D. E., Golikov, N. A., and Tsibizov, L. V. (2019). A Borehole Record of Late Quaternary Permafrost on Kurungnakh Island (Lena Delta, Northeastern Siberia): Reconstruction of Deposition Environments. *Russ. Geology. Geophys.* 60 (7), 768–780. doi:10.1134/S004451341911010210.15372/RGG2019045

Kienast, F., Schirrmeister, L., Siegert, C., and Tarasov, P. (2005). Palaeobotanical Evidence for Warm Summers in the East Siberian Arctic during the Last Cold Stage. *Quat. Res.* 63, 283–300. doi:10.1134/S004451341911010210.1016/j.yqres.2005.01.003

Kienast, F., Wetterich, S., Kuzmina, S., Schirrmeister, L., Andreev, A. A., Tarasov, P., et al. (2011). Paleontological Records Indicate the Occurrence of Open Woodlands in a Dry Inland Climate at the Present-Day Arctic Coast in Western Beringia during the Last Interglacial. *Quat. Sci. Rev.* 30 (17-18), 2134–2159. doi:10.1016/j.quascirev.2010.11.024

Krammer, K., and Lange-Bertalot, H. (1986). Bacillariophyceae. Teil 1: Naviculaceae. *Süßwasserflora von Mitteleuropa*. Stuttgart: Gustav Fischer Verlag.

Krammer, K., and Lange-Bertalot, H. (1988). Bacillariophyceae. Teil 2: Bacillariaceae, Epitemiaceae, Surirellaceae. *Süßwasserflora von Mitteleuropa*. Stuttgart: Gustav Fischer Verlag.

Krammer, K., and Lange-Bertalot, H. (1991a). Bacillariophyceae. Teil 3: Centrales, Fragilariaceae, Eunotiaceae. *Süßwasserflora von Mitteleuropa*. Stuttgart: Gustav Fischer Verlag.

Krammer, K., and Lange-Bertalot, H. (1991b). Bacillariophyceae. Teil 4: Achnanthaceae, Kritische Ergänzungen zu Navicula (Lineolatae) und Gomphonema. Gesamtliteraturverzeichnis. *Süßwasserflora von Mitteleuropa*. Stuttgart: Gustav Fischer Verlag.

Kunitsky, V. V., Syromyatnikov, I. I., Schirrmeister, L., Skachov, Y. B., Grosse, G., Wetterich, S., et al. (2013). L'distye porody i termodenudatsiya v raione poselka Batagay, Yanskoe ploskogor'e, Vostochnaya Sibir' (Ice-rich permafrost and thermal denudation in the Batagay area, Yana Upland, East Siberia). *Kriosfera Zemli (Earth's Cryosphere)* 17 (1), 56–58.

Kuznetsova, T. V., Tumskoy, V. E., Schirrmeister, L., and Wetterich, S. (2019). Paleozoological Characteristics of Late Neopleistocene – Holocene Deposits of the Bykovsky Peninsula (Палеозоологическая ×рактеристика ПозднeнеоПлейстоцен–олоценовы× Отложений Быковского Полуострова *(*Северная Якутия*) Zoolog. J. (*ЗоолоГический журнал) 98 (11), 1268–1290. doi:10.1134/S0044513419110102

Laing, T. E., Rühland, K. M., and Smol, J. P. (1999). Past Environmental and Climatic Changes Related to Tree-Line Shifts Inferred from Fossil Diatoms from a lake Near the Lena River Delta, Siberia. *The Holocene* 9, 547–557. doi:10.1191/095968399675614733

Larocque, I. (2001). How many Chironomid Head Capsules Are Enough? A Statistical Approach to Determine Sample Size for Palaeoclimatic Reconstructions. *Palaeogeogr. Palaeoclimatol. Palaeoecol.* 172, 133–142. doi:10.1016/S0031-0182(01)00278-4

Margold, M., Jansen, J. D., Codilean, A. T., Preusser, F., Gurinov, A. L., Fujioka, T., et al. (2018). Repeated Megafloods from Glacial Lake Vitim, Siberia, to the Arctic Ocean over the Past 60,000 Years. *Quat. Sci. Rev.* 187, 41–61. doi:10.1016/j.quascirev.2018.03.005

Martin-Jézéquell, V., and Lopez, P. J. (2003). "Silicon - a central Metabolite for Diatom Growth and Morphogenesis,". *Silicon Biomineralization. Progress in Molecular and Subcellular Biology*. Editor W. E. G. Müller (Berlin, Heidelberg: Springer), 33, 99–124. doi:10.1007/978-3-642-55486-5_4

Moller Pillot, H. K. M. (2009). *Chironomidae Larvae. Biology and Ecology of the Chironomini*. Zeist, Netherlands: KNNV Publishing, 270.

Moller Pillot, H. K. M. (2013). *Chironomidae Larvae. Biology and Ecology of the Aquatic Orthocladiinae*. Zeist, Netherlands: KNNV Publishing, 312.

Morgenstern, A., Ulrich, M., Günther, F., Roessler, S., Fedorova, I. V., Rudaya, N. A., et al. (2013). Evolution of Thermokarst in East Siberian Ice-Rich Permafrost: A Case Study. *Geomorphology* 201, 363–379. doi:10.1016/j.geomorph.2013.07.011

Müller, S., Tarasov, P. E., Andreev, A. A., and Diekmann, B. (2009). Late Glacial to Holocene Environments in the Present-Day Coldest Region of the Northern Hemisphere Inferred from a Pollen Record of Lake Billyakh, Verkhoyansk Mts, NE Siberia. *Clim. Past* 5, 73–84. doi:10.5194/cp-5-73-2009

Nazarova, L. B., Pestryakova, L. A., Ushnitskaya, L. A., and Hubberten, H.-W. (2008). Chironomids (Diptera: Chironomidae) in Lakes of Central Yakutia and Their Indicative Potential for Paleoclimatic Research. *Contemp. Probl. Ecol.* 1, 335–345. doi:10.1134/S1995425508030089

Nazarova, L., Herzschuh, U., Wetterich, S., Kumke, T., and Pestryakova, L. (2011). Chironomid-based Inference Models for Estimating Mean July Air Temperature and Water Depth from Lakes in Yakutia, Northeastern Russia. *J. Paleolimnol* 45, 57–71. doi:10.1007/s10933-010-9479-4

Nazarova, L., Lüpfert, H., Subetto, D., Pestryakova, L., and Diekmann, B. (2013). Holocene Climate Conditions in central Yakutia (Eastern Siberia) Inferred from Sediment Composition and Fossil Chironomids of Lake Temje. *Quat. Int.* 290-291, 264–274. doi:10.1016/j.quaint.2012.11.006

Nazarova, L., Self, A. E., Brooks, S. J., van Hardenbroek, M., Herzschuh, U., and Diekmann, B. (2015). Northern Russian Chironomid-Based Modern Summer Temperature Data Set and Inference Models. *Glob. Planet. Change* 134, 10–25. doi:10.1016/j.gloplacha.2014.11.015

Nazarova, L., Bleibtreu, A., Hoff, U., Dirksen, V., and Diekmann, B. (2017a). Changes in Temperature and Water Depth of a Small mountain lake during the Past 3000 Years in Central Kamchatka Reflected by a Chironomid Record. *Quat. Int.* 447, 46–58. doi:10.1016/j.quaint.2016.10.008

Nazarova, L. B., Self, A. E., Brooks, S. J., Solovieva, N., Syrykh, L. S., and Dauvalter, V. A. (2017b). Chironomid Fauna of the Lakes from the Pechora River basin (East of European Part of Russian Arctic): Ecology and Reconstruction of Recent Ecological Changes in the Region. *Contemp. Probl. Ecol.* 10, 350–362. doi:10.1134/S1995425517040059

Nazarova, L., Grebennikova, T. A., Razjigaeva, N. G., Ganzey, L. A., Belyanina, N. I., Arslanov, K. A., et al. (2017c). Reconstruction of Holocene Environmental Changes in Southern Kurils (North-Western Pacific) Based on Palaeolake Sediment Proxies from Shikotan Island. *Glob. Planet. Change* 159, 25–36. doi:10.1016/j.gloplacha.2017.10.005

Nazarova, L., Syrykh, L. S., Frolova, R. J. L. A., Ibragimova, A. G., Grekov, I. M., Subetto, D. A., et al. (2020). Palaeoecological and Palaeoclimatic Conditions on the Karelian Isthmus (Northwestern Russia) during the Holocene. *Quat. Res.* 95, 65–83. doi:10.1017/qua.2019.88

Neretina, A. N., Gololobova, M. A., Neplyukhina, A. A., Zharov, A. A., Rogers, C. D., Horne, D. J., et al. (2020). Crustacean Remains from the Yuka mammoth Raise Questions about Non-analogue Freshwater Communities in the Beringian Region during the Pleistocene. *Sci. Rep.* 10, 859. doi:10.1038/s41598-020-57604-8

New, M., Lister, D., Hulme, M., and Makin, I. (2002). A High-Resolution Data Set of Surface Climate over Global Land Areas. *Clim. Res.* 21, 1–25. doi:10.3354/cr021001

Opel, T., Meyer, H., Wetterich, S., Laepple, T., Dereviagin, A., and Murton, J. (2018). Ice Wedges as Archives of winter Paleoclimate: A Review. *Permafrost and Periglac Process* 29, 199–209. doi:10.1002/ppp.1980

Opel, T., Murton, J. B., Wetterich, S., Meyer, H., Ashastina, K., Günther, F., et al. (2019). Past Climate and Continentality Inferred from Ice Wedges at Batagay Megaslump in the Northern Hemisphere's Most continental Region, Yana Highlands, interior Yakutia. *Clim. Past* 15, 1443–1461. doi:10.5194/cp-15-1443-2019

Overpeck, J. T., Webb, T., and Prentice, I. C. (1985). Quantitative Interpretation of Fossil Pollen Spectra: Dissimilarity Coefficients and the Method of Modern Analogs. *Quat. Res.* 23, 87–108. doi:10.1016/0033-5894(85)90074-2

Palagushkina, O. V., Nazarova, L. B., Wetterich, S., and Schirrmeister, L. (2012). Diatoms of Modern Bottom Sediments in Siberian Arctic. *Contemp. Probl. Ecol.* 5 (4), 413–422. doi:10.1134/S1995425512040105

Palagushkina, O. V., Wetterich, S., Schirrmeister, L., and Nazarova, L. B. (2017). Modern and Fossil Diatom Assemblages from Bol'shoy Lyakhovsky Island (New Siberian Archipelago, Arctic Siberia). *Contemp. Probl. Ecol.* 10, 380–394. doi:10.1134/S1995425517040060

Péwé, T. L. (1955). Origin of the upland silt Near Fairbanks, Alaska. *Geol. Soc. America Bull.* 66, 699–724. doi:10.1130/0016-7606(1955)66[699:ootusn]2.0.co;2

Pestryakova, L. A., Herzschuh, U., Gorodnichev, R., and Wetterich, S. (2018). The Sensitivity of Diatom Taxa from Yakutian Lakes (north-eastern Siberia) to Electrical Conductivity and Other Environmental Variables. *Polar Res.* 37, 1485625. doi:10.1080/17518369.2018.1485625

Pitulko, V., Pavlova, E., and Nikolskiy, P. (2017). Revising the Archaeological Record of the Upper Pleistocene Arctic Siberia: Human Dispersal and Adaptations in MIS 3 and 2. *Quat. Sci. Rev.* 165, 127–148. doi:10.1016/j.quascirev.2017.04.004

Plikk, A., Engels, S., Luoto, T. P., Nazarova, L., Salonen, J. S., and Helmens, K. F. (2019). Chironomid-based temperature reconstruction for the Eemian Interglacial (MIS 5e) at Sokli, northeast Finland. *J. Paleolimnol* 61, 355–371. doi:10.1007/s10933-018-00064-y

Proshkina-Lavrenko, A. I. (1974). Diatoms Of the USSR - Fossils And Modern *(*Диатомовые Водоросли СССР - ИскоЦаемые И СовременныеЦ. Leningrad: Nauka, 403.(in Russian).

Quinlan, R., and Smol, J. P. (2001). Chironomid-based Inference Models for Estimating End-Of-Summer Hypolimnetic Oxygen from South-central Ontario Shield Lakes. *Freshw. Biol.* 46, 1529–1551. doi:10.1046/j.1365-2427.2001.00763.x

Raschke, E. A., and Savelieva, L. A. (2017). Subrecent Spore-Pollen Spectra and Modern Vegetation from the Lena River Delta, Russian Arctic. *Contemp. Probl. Ecol.* 10 (4), 395–410. doi:10.1134/S1995425517040084

Reimer, P. J., Bard, E., Bayliss, A., Beck, J. W., Blackwell, P. G., Ramsey, C. B., et al. (2013). IntCal13 and Marine13 Radiocarbon Age Calibration Curves 0-

50,000 Years Cal BP. *Radiocarbon* 55, 1869–1887. doi:10.2458/azu_js_rc.55.16947

Reimer, P. J., Austin, W. E. N., Bard, E., Bayliss, A., Blackwell, P. G., Bronk Ramsey, C., et al. (2020). The IntCal20 Northern Hemisphere Radiocarbon Age Calibration Curve (0-55 Cal kBP). *Radiocarbon* 62 (4), 725–757. doi:10.1017/RDC.2020.41

Rogers, D. C., Zharov, A. A., Neretina, A. N., Kuzmina, S. A., and Kotov, A. A. (2021). A Review of Recently Discovered Remains of the Pleistocene Branchiopods (Anostraca, Notostraca) from NE Siberia and Arctic Canada. *Water* 13, 280. doi:10.3390/w13030280

Rothe, M., Kleeberg, A., and Hupfer, M. (2016). The Occurrence, Identification and Environmental Relevance of Vivianite in Waterlogged Soils and Aquatic Sediments. *Earth-Science Rev.* 158, 51–64. doi:10.1016/j.earscirev.2016.04.008

Schirrmeister, L., Siegert, C., Siegert, C., Kuznetsova, T., Kuzmina, S., Andreev, A., et al. (2002a). Paleoenvironmental and Paleoclimatic Records from Permafrost Deposits in the Arctic Region of Northern Siberia. *Quat. Int.* 89, 97–118. doi:10.1016/S1040-6182(01)00083-0

Schirrmeister, L., Siegert, C., Kunitzky, V. V., Grootes, P. M., and Erlenkeuser, H. (2002b). Late Quaternary Ice-Rich Permafrost Sequences as a Paleoenvironmental Archive for the Laptev Sea Region in Northern Siberia. *Int. J. Earth Sci.* 91, 154–167. doi:10.1007/s005310100205

Schirrmeister, L., Grosse, G., Schwamborn, G., Andreev, A. A., Meyer, H., Kunitsky, V. V., et al. (2003). Late Quaternary History of the Accumulation Plain North of the Chekanovsky Ridge (Lena Delta, Russia): A Multidisciplinary Approach. *Polar Geogr.* 27, 277–319. doi:10.1080/789610225

Schirrmeister, L., Kunitsky, V., Grosse, G., Wetterich, S., Meyer, H., Schwamborn, G., et al. (2011a). Sedimentary Characteristics and Origin of the Late Pleistocene Ice Complex on north-east Siberian Arctic Coastal Lowlands and Islands - A Review. *Quat. Int.* 241, 3–25. doi:10.1016/j.quaint.2010.04.004

Schirrmeister, L., Grosse, G., Schnelle, M., Fuchs, M., Krbetschek, M., Ulrich, M., et al. (2011b). Late Quaternary Paleoenvironmental Records from the Western Lena Delta, Arctic Siberia. *Palaeogeogr. Palaeoclimatol. Palaeoecol.* 299, 175–196. doi:10.1016/j.palaeo.2010.10.045

Schirrmeister, L., Froese, D., Tumskoy, V., Grosse, G., and Wetterich, S. (2013). "PERMAFROST and PERIGLACIAL FEATURES | Yedoma: Late Pleistocene Ice-Rich Syngenetic Permafrost of Beringia," in *The Encyclopedia of Quaternary Science*. Editor S. A. Elias (Amsterdam: Elsevier), 542–552. doi:10.1016/B978-0-444-53643-3.00106-0

Schirrmeister, L., Meyer, H., Andreev, A., Wetterich, S., Kienast, F., Bobrov, A., et al. (2016). Late Quaternary Paleoenvironmental Records from the Chatanika River valley Near Fairbanks (Alaska). *Quat. Sci. Rev.* 147, 259–278. doi:10.1016/j.quascirev.2016.02.009

Schirrmeister, L., Schwamborn, G., Overduin, P. P., Strauss, J., Fuchs, M. C., Grigoriev, M., et al. (2017). Yedoma Ice Complex of the Buor Khaya Peninsula (Southern Laptev Sea). *Biogeosciences* 14, 1261–1283. doi:10.5194/bg-14-1261-2017

Sher, A. V., Kuzmina, S. A., Kuznetsova, T. V., and Sulerzhitsky, L. D. (2005). New Insights into the Weichselian Environment and Climate of the East Siberian Arctic, Derived from Fossil Insects, Plants, and Mammals. *Quat. Sci. Rev.* 24, 533–569. doi:10.1016/j.quascirev.2004.09.007

Soloviev, P. A. (1959). *Kriolitozona Severnoy Chasti Leno-Amginskogo Mezhdurech'ya (The Permafrost of the Northern Part of the Lena-Amga Interfluve)*. Moscow: Academy of Science Press, 142.(in Russian).

Solovieva, N., Klimaschewski, A., Self, A. E., Jones, V. J., Andrén, E., Andreev, A. A., et al. (2015). The Holocene Environmental History of a Small Coastal lake on the north-eastern Kamchatka Peninsula. *Glob. Planet. Change* 134, 55–66. doi:10.1016/j.gloplacha.2015.06.010

Stockmarr, J. (1971). Tablets with Spores Used in Absolute Pollen Analysis. *Pollen et Spores* 13, 615–621.

Syrykh, L. S., Nazarova, L. B., Herzschuh, U., Subetto, D. A., and Grekov, I. M. (2017). Reconstruction of Palaeoecological and Palaeoclimatic Conditions of the Holocene in the South of the Taimyr According to an Analysis of lake Sediments. *Contemp. Probl. Ecol.* 10, 363–369. doi:10.1134/S1995425517040114

van Geel, B. (2001). "Non-pollen Palynomorphs,". *Terrestrial Algal and Siliceous Indicators, Tracking Environmental Changes Using lake Sediments*. Editors J. P. Smol, H. J. B. Birks, and W.M. Last (Dordrecht: Kluwer Academic Press), 3, 99–119.

Wasser, S. P., Kondratyeva, N. V., Masyuk, N. P., Palamar'-Mordvintseva, G. M., Vetrova, Z. I., Kordyum, E. L., et al. (1989). *Algae - Guide (*Водоросли - Справочник. Kiev: Naukova Dumka, 608.(in Russian).

Wetterich, S., Schirrmeister, L., and Pietrzeniuk, E. (2005). Freshwater Ostracodes in Quaternary Permafrost Deposits in the Siberian Arctic. *J. Paleolimnol* 34, 363–376. doi:10.1007/s10933-005-5801-y

Wetterich, S., Kuzmina, S., Andreev, A. A., Kienast, F., Meyer, H., Schirrmeister, L., et al. (2008a). Palaeoenvironmental Dynamics Inferred from Late Quaternary Permafrost Deposits on Kurungnakh Island, Lena Delta, Northeast Siberia, Russia. *Quat. Sci. Rev.* 27 (15), 1523–1540. doi:10.1016/j.quascirev.2008.04.007

Wetterich, S., Schirrmeister, L., Meyer, H., Viehberg, F. A., and Mackensen, A. (2008b). Arctic Freshwater Ostracods from Modern Periglacial Environments in the Lena River Delta (Siberian Arctic, Russia): Geochemical Applications for Palaeoenvironmental Reconstructions. *J. Paleolimnol* 39, 427–449. doi:10.1007/s10933-007-9122-1

Wetterich, S., Schirrmeister, L., Andreev, A. A., Pudenz, M., Plessen, B., Meyer, H., et al. (2009). Eemian and Late Glacial/Holocene Palaeoenvironmental Records from Permafrost Sequences at the Dmitry Laptev Strait (NE Siberia, Russia). *Palaeogeogr. Palaeoclimatol. Palaeoecol.* 279, 73–95. doi:10.1016/j.palaeo.2009.05.002

Wetterich, S., Rudaya, N., Tumskoy, V., Andreev, A. A., Opel, T., Schirrmeister, L., et al. (2011). Last Glacial Maximum Records in Permafrost of the East Siberian Arctic. *Quat. Sci. Rev.* 30, 3139–3151. doi:10.1016/j.quascirev.2011.07.020

Wetterich, S., Tumskoy, V., Rudaya, N., Andreev, A. A., Opel, T., Meyer, H., et al. (2014). Ice Complex Formation in Arctic East Siberia during the MIS3 Interstadial. *Quat. Sci. Rev.* 84, 39–55. doi:10.1016/j.quascirev.2013.11.009

Wetterich, S., Schirrmeister, L., Nazarova, L., Palagushkina, O., Bobrov, A., Pogosyan, L., et al. (2018). Holocene Thermokarst and Pingo Development in the Kolyma Lowland (NE Siberia). *Permafrost and Periglac Process* 29 (3), 182–198. doi:10.1002/ppp.1979

Wetterich, S., Rudaya, N., Kuznetsov, V., Maksimov, F., Opel, T., Meyer, H., et al. (2019a). Ice Complex Formation on Bol'shoy Lyakhovsky Island (New Siberian Archipelago, East Siberian Arctic) since about 200 Ka. *Quat. Res.* 92 (2), 530–548. doi:10.1017/qua.2019.6

Wetterich, S., Kizyakov, A., Fritz, M., Aksenov, A., Schirrmeister, L., and Opel, T. (2019b). Permafrost Research on Sobo-Sise Island (Lena Delta). *Rep. Polar Mar. Res.* 734, 102–113. doi:10.2312/BzPM_0734_2019

Wetterich, S., Kizyakov, A., Fritz, M., Wolter, J., Mollenhauer, G., Meyer, H., et al. (2020). The Cryostratigraphy of the Yedoma Cliff of Sobo-Sise Island (Lena delta) Reveals Permafrost Dynamics in the central Laptev Sea Coastal Region during the Last 52 Kyr. *The Cryosphere* 14, 4525–4551. doi:10.5194/tc-14-4525-2020

Wetterich, S., Meyer, H., Fritz, M., Mollenhauer, G., Rethemeyer, J., Kizyakov, A., et al. (2021). Northeast Siberian Permafrost Ice-Wedge Stable Isotopes Depict Pronounced Last Glacial Maximum Winter Cooling. *Geophys. Res. Lett.* 48, e2020GL092087. doi:10.1029/2020GL092087

Wiederholm, T. (1983). Chironomidae of the Holarctic Region. Keys and Diagnoses. Part 1. Larvae. *Entomologica Scand. Suppl.* 19, 1–457.

World Topo Base (2021). Online Source. Available at: https://www.arcgis.com/home/item.html?id=3a75a3ee1d1040838f382cbefce99125 Accessed. January 11, 2021.

Zabelina, M. M., Kiselev, I. A., Proshkina-Lavrenko, A. I., and Sheshukova, V. S. (1951). Diatoms. In: *Opredelitel' Presnovodnykh Vodoroslei SSSR (Guide for Identification of Freshwater Algae in Soviet Union)*. Moscow: Sovetskaya Nauka.(in Russian).

Conflict of Interest: The authors declare that the research was conducted in the absence of any commercial or financial relationships that could be construed as a potential conflict of interest.

The reviewer NS declared a past co-authorship with several of the authors LN, NR, LSy, and OP.

frontiers in Earth Science

ORIGINAL RESEARCH
published: 23 July 2021
doi: 10.3389/feart.2021.703339

Iron Redistribution Upon Thermokarst Processes in the Yedoma Domain

Arthur Monhonval[1], Jens Strauss[2], Elisabeth Mauclet[1], Catherine Hirst[1], Nathan Bemelmans[1], Guido Grosse[2,3], Lutz Schirrmeister[2], Matthias Fuchs[2] and Sophie Opfergelt[1]*

[1]Earth and Life Institute, Université Catholique de Louvain, Louvain-la-Neuve, Belgium, [2]Permafrost Research Section, Alfred Wegener Institute Helmholtz Centre for Polar and Marine Research, Potsdam, Germany, [3]Institute of Geosciences, University of Potsdam, Potsdam, Germany

Edited by:
Alexandra Veremeeva,
Institute of Physical-Chemical and Biological Problems in Soil Science (RAS), Russia

Reviewed by:
Paul Sanborn,
University of Northern British Columbia, Canada
Rinat Manasypov,
Tomsk State University, Russia

***Correspondence:**
Arthur Monhonval
arthur.monhonval@uclouvain.be

Specialty section:
This article was submitted to Cryospheric Sciences, a section of the journal Frontiers in Earth Science

Received: 30 April 2021
Accepted: 09 July 2021
Published: 23 July 2021

Citation:
Monhonval A, Strauss J, Mauclet E, Hirst C, Bemelmans N, Grosse G, Schirrmeister L, Fuchs M and Opfergelt S (2021) Iron Redistribution Upon Thermokarst Processes in the Yedoma Domain. Front. Earth Sci. 9:703339. doi: 10.3389/feart.2021.703339

Ice-rich permafrost has been subject to abrupt thaw and thermokarst formation in the past and is vulnerable to current global warming. The ice-rich permafrost domain includes Yedoma sediments that have never thawed since deposition during the late Pleistocene and Alas sediments that were formed by previous thermokarst processes during the Lateglacial and Holocene warming. Permafrost thaw unlocks organic carbon (OC) and minerals from these deposits and exposes OC to mineralization. A portion of the OC can be associated with iron (Fe), a redox-sensitive element acting as a trap for OC. Post-depositional thaw processes may have induced changes in redox conditions in these deposits and thereby affected Fe distribution and interactions between OC and Fe, with knock-on effects on the role that Fe plays in mediating present day OC mineralization. To test this hypothesis, we measured Fe concentrations and proportion of Fe oxides and Fe complexed with OC in unthawed Yedoma and previously thawed Alas deposits. Total Fe concentrations were determined on 1,292 sediment samples from the Yedoma domain using portable X-ray fluorescence; these concentrations were corrected for trueness using a calibration based on a subset of 144 samples measured by inductively coupled plasma optical emission spectrometry after alkaline fusion (R^2 = 0.95). The total Fe concentration is stable with depth in Yedoma deposits, but we observe a depletion or accumulation of total Fe in Alas deposits, which experienced previous thaw and/or flooding events. Selective Fe extractions targeting reactive forms of Fe on unthawed and previously thawed deposits highlight that about 25% of the total Fe is present as reactive species, either as crystalline or amorphous oxides, or complexed with OC, with no significant difference in proportions of reactive Fe between Yedoma and Alas deposits. These results suggest that redox driven processes during past thermokarst formation impact the present-day distribution of total Fe, and thereby the total amount of reactive Fe in Alas versus Yedoma deposits. This study highlights that ongoing thermokarst lake formation and drainage dynamics in the Arctic influences reactive Fe distribution and thereby interactions between Fe and OC, OC mineralization rates, and greenhouse gas emissions.

Keywords: permafrost, thaw, redox processes, carbon stabilization, arctic, subarctic

INTRODUCTION

Upon ice-rich permafrost thaw, substantial amounts of organic carbon (OC) stored in frozen deposits become potentially available for microbial mineralization (Strauss et al., 2017; Nitzbon et al., 2020; Turetsky et al., 2020). The Yedoma domain includes Yedoma Ice Complex deposits (50–90% volume percent ice, in the following referred as Yedoma deposits) that have never thawed since late Pleistocene deposition and Alas deposits that formed upon thermokarst processes during the Lateglacial and Holocene warmer and wetter periods (Schirrmeister et al., 2013; Strauss et al., 2013). The latest estimates show that the Yedoma domain stores around 327—466 Gt of OC despite covering only 8% of the circumarctic permafrost region (Hugelius et al., 2014; Strauss et al., 2017). Ongoing global warming in high northern latitudes will unlock OC frozen in ice-rich Yedoma deposits (with potential lake formation and drainage) and refrozen Alas deposits, exposing more OC to decomposition (Schneider von Deimling et al., 2015; Olefeldt et al., 2016). Thawing of present day Yedoma and Alas deposits triggers a cascade of processes, including the mineralization of previously locked carbon by microorganisms generating additional greenhouse gas emissions (Schuur et al., 2008).

For millennial-scale OC preservation, the interactions between OC and mineral surfaces, especially with iron (Fe) oxides surfaces, are of great importance in soils (Kaiser and Guggenberger, 2007; Kögel-Knabner et al., 2008; Kögel-Knabner et al., 2010; Adhikari and Yang, 2015) and sediments (Eglinton, 2012; Lalonde et al., 2012). In the Qinghai-Tibetan Plateau permafrost region, approximately 20% of the soil OC is stabilized by Fe (Mu et al., 2016) illustrating the important relationship between Fe and OC in permafrost terrain. Mineral-OC interactions contribute to stabilize OC through complexation, co-precipitation or aggregation processes and thus hinder microbial degradation of OC (Lutzow et al., 2006). The OC can be 1) physically protected within soil aggregates (involving Fe-Al oxy-(hydr)oxides, clay minerals, or carbonates), which means that OC is spatially inaccessible for microorganisms; or 2) physico-chemically protected in organo-mineral associations and/or as organo-metallic complexes. These organo-mineral associations result from the interaction of OC with mineral surfaces such as OC adsorbed onto Fe-oxides or clay minerals, using cation bridges such as Ca^{2+} or Mg^{2+}. Organo-metallic complexes result from the complexation of OC with metal ions (i.e., OC complexed with e.g., Fe^{3+}, Al^{3+}). Overall, several stabilizing mechanisms exist between reactive Fe (Fe-oxides or complexed Fe) and OC.

These mineral-protected pools of OC are of major concern to better understand OC mineralization rates in permafrost soils upon thawing (Opfergelt, 2020). The soil OC that interacts with reactive minerals (via aggregation, sorption, complexation, and/or co-precipitation) is less available for microbial decomposition, thus contributing to the “protected” or “stabilized” organic matter pool (Schmidt et al., 2011; Lalonde et al., 2012; Kleber et al., 2015, 2021; Salvadó et al., 2015). Yet, the “protected” OC pools are not permanent and may lose their mineral-protected status in redox changing environments (Kögel-Knabner et al., 2010; Colombo et al., 2014; Herndon et al., 2017; Huang and Hall, 2017; Opfergelt, 2020; Patzner et al., 2020). Iron-mediated OC decomposition in anoxic condition can counteract protection mechanisms of OC (Chen et al., 2020; Kappler et al., 2021). Thermokarst processes trigger redox changes in the environment (Kokelj and Jorgenson, 2013; Abbott and Jones, 2015), and Fe is a redox-sensitive element, consequently thawing of ice-rich permafrost deposits may redistribute and modify total Fe distribution, and the proportion of Fe distributed between Fe oxides and OC complexes. Overall, we expect biogeochemical Fe transformations to occur upon redox fluctuations in thermokarst-affected ice-rich permafrost soils, with potential direct implications for OC stabilization in Yedoma domain deposits (**Figure 1**), mirroring the impact of redox processes on Fe redistribution described for gradual thaw (i.e., gradual deepening of the active layer; Lipson et al., 2012; Herndon et al., 2020b; Patzner et al., 2020).

The dependence of Fe-bearing mineral solubilization, Fe translocation and Fe precipitation on redox conditions has been studied in polygonal permafrost soil of the Lena Delta (Fiedler et al., 2004), the Alaska North Slope (Lipson et al., 2012; Herndon et al., 2020b) and also in a thaw gradient site (i.e., palsa, bog, and fen) close to Abisko in northern Sweden (Patzner et al., 2020). These studies found that redox processes drive Fe solubilization under fluctuating water-table height. Similarly, the mobilization of Fe upon thermokarst lake formation and subsequent transport in the hydrological network has been observed in several studies (e.g., Audry et al., 2011; Pokrovsky et al., 2014; Manasypov et al., 2015). However, the influence of redox fluctuations on Fe distribution in deeper deposits from ice-rich permafrost regions during the late Pleistocene and Holocene periods remains unknown. Using modern day studies of Fe dynamics in permafrost as an analogue, we hypothesize that upon thermokarst processes, the fluctuating redox conditions due to subsidence, lake formation, drainage, subaerial exposure and/or deposition, and refreezing, will drive Fe solubilization, translocation and precipitation within former Yedoma deposits, potentially affecting Fe-OC interactions in the resulting Alas deposits. To test this hypothesis, a screening of total Fe concentrations in ice-rich permafrost landscape is needed to better evaluate the potential for Fe redistribution upon thaw. Being able to identify that thaw processes have occurred in the past with potential influence on Fe-OC interactions is valuable information in the context of a warming Arctic. Indeed, identifying potential redistribution of Fe-oxides and complexed Fe that took place in thawed, newly formed and subsequently refrozen deposits during the Lateglacial and Holocene warming periods may help to predict the fate of Fe-OC interactions upon current global warming and to better assess implications for OC stabilization. This information is relevant given that a large portion of the Arctic permafrost region is threatened by abrupt thaw and thermokarst processes (Olefeldt et al., 2016; Turetsky et al., 2020). Turetsky et al. (2020) emphasize that despite the fact that abrupt thaw will probably occur in <20% of the permafrost zone, this thaw could affect half of the permafrost OC through

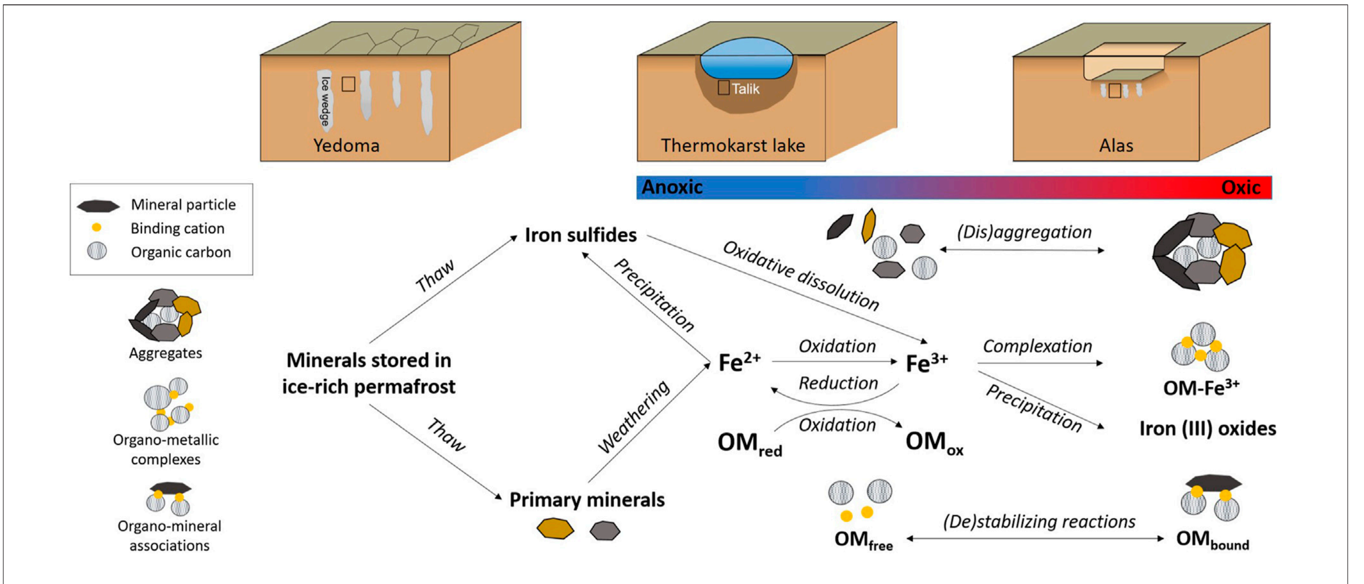

FIGURE 1 | Conceptual scheme of the biogeochemical iron (Fe) transformations expected upon thermokarst lake formation and drainage in ice-rich-permafrost (Yedoma) sediments and implications for organic matter (OM) stabilization. Black rectangles in the upper schematic representation of Yedoma, thermokarst lake and Alas profile indicate the sample location. Geochemical reactions shown are both abiotic and microbially mediated. OM_{red} represents reduced organic species, which can include CH_4, and OM_{ox} represents oxidized organic species, which can include CO_2.

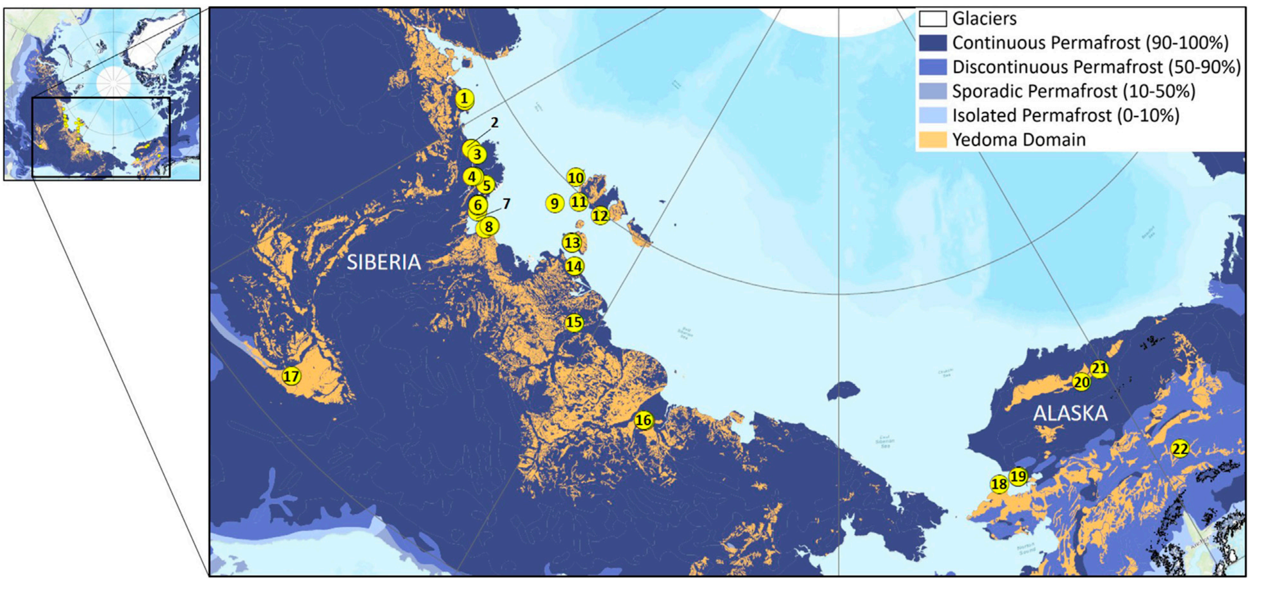

FIGURE 2 | Location of the studied permafrost sites from the Yedoma Domain. 1. Cape Mamontov Klyk; 2. Nagym (Ebe Sise Island); 3. Khardang Island; 4. Kurungnakh Island; 5. Sobo Sise Island; 6. Bykovsky Peninsula; 7. Muostakh Island; 8. Buor Khaya Peninsula; 9. Stolbovoy Island; 10. Belkovsky Island; 11. Kotel'ny Island; 12. Bunge Land; 13. Bol'shoy Lyakhovsky Island; 14. Oyogos Yar coast; 15. Kytalyk; 16. Duvanny Yar; 17. Yukechi; 18. Kitluk; 19. Baldwin Peninsula; 20. Colville; 21. Itkillik; 22. Vault Creek tunnel. Yedoma domain coverage from Strauss et al. (2016, 2017).

collapsing ground, lake formation, rapid erosion, and thaw slumping.

The aim of this study is to investigate the Fe redistribution upon thermokarst processes during the Lateglacial and Holocene and to highlight potential implications for interactions between Fe and OC in present day ice-rich permafrost sediments. To this goal, 1) we measured the total Fe concentration on 1,292 deposits samples across the ice-rich permafrost region, including Yedoma (never thawed) and Alas (previously thawed) deposits, and 2) we assessed the proportion of reactive Fe and the distribution between Fe oxides and Fe complexed with OC based on selective Fe extractions on a subset of Yedoma and Alas samples.

TABLE 1 | List of the studied sites from the Yedoma domain, associated label, number of samples analyzed with portable X-ray fluorescence and inductively coupled plasma optical emission spectrometry method, number of profiles sampled for each type of deposits and associated reference papers. Sites are located in Siberia (1–17) and Alaska (18–22). The site numbers 1 to 22 are located on the map in **Figure 2**. * Sobo Sise profiles are of Holocene age on top of Yedoma Ice Complex deposits. Labels identification for each profile are detailed in **Supplementary Table S1**.

Site Nb	Site name	Label	Samples analyzed with pXRF	Samples analyzed with ICP-OES	Yedoma profile	Alas profile	Fluvial profile	References papers
1	Cape Mamontov Klyk	Mak	80	-	2	1	0	Schirrmeister et al. (2008), (2011)
2	Nagym (Ebe Sise Island)	Nag	29	-	2	1	0	Schirrmeister et al. (2003b)
3	Khardang Island	Kha	31	1	1	0	0	Schirrmeister et al. (2007), (2011)
4	Kurungnakh Island	Bkh, KUR	143	2	2	2	0	Schirrmeister et al. (2003b), (2008); Wetterich et al. (2008)
5	Sobo sise Island	Sob	58	58	2*	1	1	Fuchs et al. (2018)
6	Bykovsky peninsula	Mkh, BYK	150	2	5	2	0	Andreev et al. (2002); Grosse et al.(2007); Schirrmeister et al. (2002), (2011)
7	Muostakh Island	Muo	11	-	1	0	0	Grigoriev et al. (2003); Schirrmeister et al. (2011)
8	Buor Khaya penisula	Buo	80	44	2	3	0	Schirrmeister et al. (2017)
9	Stolbovoy Island	Sto	16	1	3	1	0	Schirrmeister et al. (2003a); Grigoriev et al. (2003)
10	Belkovsky Island	Bel	12	-	0	2	0	Grigoriev et al. (2003); Schirrmeister et al. (2003a), (2011)
11	Kotel'ny Island	KyS	10	-	1	0	0	Grigoriev et al. (2003); Schirrmeister et al. (2003a), (2011)
12	Bunge land	Bun	8	-	0	0	1	Schirrmeister et al. (2010)
13	Bol'shoy lyakhovsky Island	TZ, R, L	150	3	11	4	0	Andreev et al. (2009); Wetterich et al. (2011a), (2014)
14	Oyogos Yar coast	Oy	50	1	1	1	0	Wetterich et al. (2009); Schirrmeister et al. (2011); Opel et al. (2017)
15	Kytalyk	KY, KH	50	4	2	1	0	Weiss et al. (2016)
16	Duvanny Yar	DY	143	5	5	1	0	Strauss, (2010)
17	Yukechi	Yuk-yul	87	2	2	2	0	Windirsch et al. (2020)
18	Kitluk	Kit	45	2	1	1	0	Unpublished data; Wetterich et al. (2012)
19	Baldwin peninsula	Bal	70	1	1	3	0	Jongejans et al. (2018)
20	Colville	Col	23	8	1	0	0	Grosse et al. (2015); unpublished data
21	Itkillik	Itk, It	22	10	1	0	0	Kanevskiy et al. (2011)
22	Vault creek tunnel	FAI	24	-	1	0	0	Schirrmeister et al. (2016)
Total	22		1,292	144	47	26	2	

ENVIRONMENTAL SETTINGS

The Yedoma domain is 1.4 million km^2 in extent and its Yedoma and thermokarst deposits contain between 327–466 Gt OC (Strauss et al., 2017). This region mainly includes areas of Alaska and Northeast Siberia which were not covered by ice sheets during the last glacial period (110–10 ka BP). For tens of millennia during the late Pleistocene, continuous periglacial weathering, transport, and sedimentation lead to the accumulation of several decameters thick permafrost deposits and syngenetic ice-wedge formation. The large syngenetic ice-wedges, often exceeding 50% of the soil volume, are a consequence of the late Pleistocene dry and cold climate which triggered regular frost cracking within the deposits. Subsequent filling of cracks with liquid water from rain or snowmelt resulted in the formation of vertical ice veins that over multiple millennia grew into up to 40˚m deep and several meters wide ice-wedges (Schirrmeister et al., 2013). The deposits also consist of ice-bearing sediments, which increase the total ice volume within Yedoma deposits (Strauss et al., 2017). These ice-rich deposits were then particularly sensitive to the rise in air temperature during the Pleistocene/Holocene transition period (starting around 14 ka BP; Walter et al., 2007). Ice-wedge degradation led to widespread thermokarst lake formation and subsequent lake drainage. Reworked sediments from former Yedoma deposits and newly formed peat deposits accumulated in thermokarst basins and refroze to form Alas deposits (Grosse et al., 2013). These Alas deposits are depleted in ice, compared to the original Yedoma ice-rich deposits, but still contain an important stock of OC (130–213 Gt C; Strauss et al., 2017). To perform this large-scale assessment of total Fe concentrations in Yedoma domain deposits, our set of samples (n = 1,292) covers many regions of the Yedoma domain (North, West, and Interior Alaska, the Kolyma region, the Indigirka region, the New Siberian Archipelago, the Laptev Sea coastal region, and Central Yakutia–**Figure 2**).

METHODS

Sampling

Depending on the sites, individual or multiple Yedoma/Alas deposit profiles were sampled (**Table 1**). Samples were obtained either from cores or from natural exposures. Coring

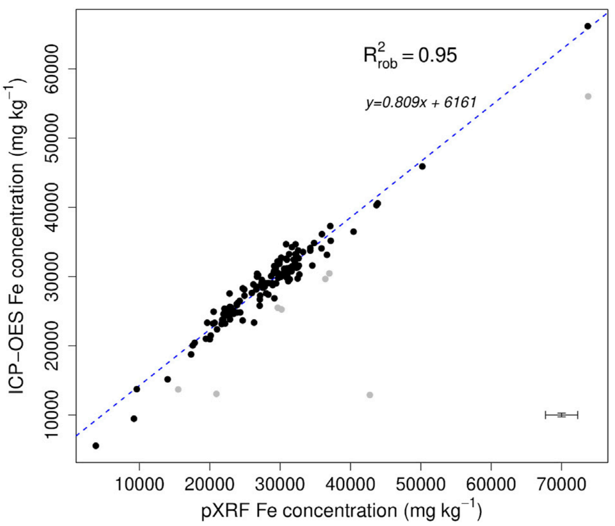

FIGURE 3 | Total Fe concentrations (mg kg^{-1}) measured by the inductively coupled plasma optical-emission spectrometry (ICP-OES) method as a function of those measured by the portable X-ray fluorescence (pXRF) method on the Yedoma domain deposits. Errors bars ($\pm 2\sigma$) are based on three repetitions of three samples for the ICP-OES method and five or three repetitions of twenty samples for the pXRF method. The robust linear regression is presented (blue line; alpha = 0.95; n = 144), excluding the grey points, and the equation is provided.

was conducted with various types of drilling rigs, from the surface during the winter season, and below the active layer during the summer season. Cliffs exposing deep permafrost deposits at coasts and river shores or headwall exposures in thaw slumps were sampled frozen with hammer and axes. Sub-profiles were sometimes needed to reconstruct a complete composite profile because of vertical discontinuities (i.e., ice wedges presence) or sections covered by thawed mud overburden. For any additional information related to sampling techniques of a specific site, please refer to the respective reference papers for each field site (**Table 1**). Recovered samples remained frozen or were air-dried in the field before transport to the lab. The particle size distribution of these Yedoma domain deposits (described in reference papers from **Table 1**) is below 2 mm; therefore no sieving was necessary.

Assessment of Bulk Iron Concentrations

We assessed the total Fe concentration on 1,292 samples from Yedoma domain deposits using a portable X-ray fluorescence (XRF) device (*Niton xl3t Goldd* + pXRF; ThermoFisher Scientific, Waltham, United States). The measurements were performed in laboratory (*ex situ*) conditions on air- or freeze-dried samples to avoid the introduction of additional variability (e.g., water content, sample heterogeneity). Briefly, samples are placed on a circular plastic cap (2.5 cm diameter) provided at its base with a thin transparent film (prolene 4 μm). Minimum sample thickness in the cap is set to 2 cm to prevent underestimation of the detected intensities (Ravansari et al., 2020) and total time of analysis is set to 90 s to standardize each measurement. The analysis is performed using a lead stand to protect operators from X-rays. To assess the precision of the pXRF method, we conducted three to five repetitions on twenty individual samples from different locations from Yedoma and Alas deposits (x-axis error bar from **Figure 3**).

To ensure trueness, the pXRF-measured concentrations were calibrated with another method. For a subset of 144 samples, we compared the total Fe concentrations measured by pXRF with Fe concentrations obtained using a method measuring Fe concentration in solution by inductively coupled plasma optical-emission spectrometry ICP-OES (iCAP 6500 ThermoFisher Scientific) after sample dissolution by alkaline fusion. Briefly, air- or freeze-dried sediment samples are carefully milled for homogenization. A portion of the milled sample (80 mg) is mixed with lithium metaborate and lithium tetraborate and heated up to 1,000°C for 10 min. The fusion bead is dissolved in HNO_3 2.2 N at 80°C and stirred until complete dissolution (Chao and Sanzolone, 1992). The loss on ignition is assessed at 1,000°C and total element content is expressed in reference to the sediment dry weight at 105°C. Trueness of the analytical measurement by ICP-OES is validated by repeated measurements on the USGS basalt reference material BHVO-2 (Wilson, 1997) as well as on certified soils GSS-1 and GSS-4 (National Research Centre for CRM, 1986). The offset, defined as the difference between certified and ICP-OES value over the certified value, is −0.8, −4.2, and −6.1% for the three certified materials, respectively. To assess the precision of the ICP-OES method, we conducted three repetitions on three individual samples from different locations from Yedoma and Alas deposits (y-axis error bar from **Figure 3**). The linear regression obtained based on Fe concentrations measured by pXRF and ICP-OES after alkaline fusion on this subset of 144 samples (robust R^2 = 0.95; **Figure 3**) was used to correct pXRF concentrations for trueness on the total set of samples (n = 1,292). This linear regression is dependent on the internal geometry of the pXRF device used and should not be used for other pXRF-measured data without a calibration check. All concentrations data can be found in the Yedoma domain Mineral Concentration Assessment (YMCA) dataset (Monhonval et al., 2020). Here, only pXRF concentration values corrected using the well-defined regression are used.

Selective Iron Extractions

To test the influence of permafrost thaw on the distribution of Fe-oxides and on Fe involved in complexes, we performed selective Fe extractions on a subset of samples from Yedoma and Alas deposits (n = 21) from three locations in Siberia: Sobo Sise Island, Buor Khaya Peninsula and Kytalyk (site number 5, 8, and 15 in **Figure 2**, respectively). Total Fe concentrations from Yedoma and Alas deposits in the subset are within similar range. Three standard procedures of selective Fe extraction from soil were used: dithionite-citrate-bicarbonate extraction (DCB), dark ammonium oxalate extraction (referred here as oxalate extraction), and sodium pyrophosphate extraction (referred here as pyrophosphate extraction). These extractions (DCB, oxalate, and pyrophosphate) are not fully quantitative (Rennert, 2019) but can be used as indicators of the Fe-oxides phases or complexed Fe within a particular soil or sediment. More specifically, 1) DCB extractions provide an estimate of the content of free Fe oxides in soils, i.e., poorly crystalline and crystalline Fe-oxides, and should not include structural Fe from clay minerals (Mehra and Jackson, 2013; McKeague and Day, 1966); 2) oxalate extractions target poorly crystalline Fe oxides (Blakemore et al., 1981), i.e., amorphous Fe oxides species and organo-metallic complexes; 3) pyrophosphate extractions are used as an indicator of Fe-organic complexes (Bascomb, 1968; Parfitt and Childs, 1988). A contribution of Fe oxide nanoparticulates in addition to the Fe involved in organic complexes cannot be excluded (Jeanroy and Guillet, 1981), even if limited by the centrifugation and the filtration of the extract.

Practically, Fe concentration was measured in solution by ICP-OES after the following extraction procedures: 1) for a DCB extraction, 0.75 g of milled sediment was mixed with 30 ml of citrate solution (sodium citrate $Na_3C_6H_5O_7$ $2H_2O$) 0.3 M buffered by sodium bicarbonate $NaHCO_3$. The sample tube was placed in a hot bath (85°C) and three successive additions of 0.75 g of sodium dithionite ($Na_2S_2O_4$) were used to reduce crystallized and amorphous Fe oxides. The tube was centrifuged and the solution was filtered (Whatman 41 filter, 20 μm retention size). The residue was rinsed three times with 20 ml of NaCl 1 M and centrifuged. The rinsing solutions were filtered and pooled with the first solution to obtain a final solution; 2) for an oxalate extraction, 0.4 g of milled sediment was mixed with 40 ml of oxalate extractant (ammonium oxalate $(NH_4)_2C_2O_4$ H_2O and oxalic acid $H_2C_2O_4$ $2H_2O$). The tube was agitated for 4 h in the dark, given that this reagent is UV-sensitive. The tube was centrifuged and the solution was filtered (Whatman 41 filter); 3) for a pyrophosphate extraction, 0.4 g of milled sediment was mixed with 40 ml of pyrophosphate solution (tetrasodium pyrophosphate decahydrate $Na_4P_2O_7$ $10H_2O$ 0.1 M). The tube was agitated for 16 h. Sodium sulfate (1.4 g) was added and the solution was centrifuged (30 min at 4,000 rpm) and filtered (Whatman 41 filter). To assess the precision of selective Fe extractions (i.e., DCB, oxalate and pyrophosphate), three repetitions of three different samples were performed. Samples were selected from Yedoma and Alas deposits from the Yukechi site (with similar matrix, not presented here). The mean and associated coefficient of variation (i.e., the ratio between standard deviation and the mean) were calculated for each sample and are summarized in **Supplementary Table S2**.

In the following, the Fe extracted using DCB, oxalate or pyrophosphate extraction methods will be referred to as Fe_d, Fe_o and Fe_p, respectively, whereas total Fe measured by XRF and corrected for trueness (*Assessment of Bulk Iron Concentrations*) will be referred to as Fe_t. The Fe_o/Fe_d ratio will be used to reflect the relative proportion of amorphous (short-range ordered) Fe oxyhydroxides and complexed Fe within the global pool of Fe oxides. The Fe_d/Fe_t ratio will be used for the proportion of free Fe oxides and complexed Fe relative to the total Fe, the Fe_o/Fe_t ratio indicates the proportion of amorphous Fe oxides and complexed Fe relative to the global Fe pool, and Fe_p/Fe_t ratio the proportion of Fe present in organo-metallic complexes relative to the global Fe pool.

Selective Carbon Extractions

The carbon selectively extracted by oxalate and pyrophosphate has been evaluated on the same solutions used for selective Fe extractions (*Selective Iron Extractions*). More specifically: 1) in the solution from the oxalate extraction, we evaluate the proportion of organic acids by measuring the absorbance at 430 nm on a Genesys 10 S VIS spectrophotometer, with the oxalate extractant solution as a blank. The optical density of the oxalate extract (ODOE) is mainly influenced by the extracted fulvic acids thereby indicating the concentration in organic acids present in solution (Daly, 1982); 2) in the solution from the pyrophosphate extraction, we measure the concentration of dissolved OC released after dispersion by pyrophosphate (referred as C_p) using a Shimadzu total organic carbon (TOC) analyzer (measuring non purgeable OC). This indicates the amounts of C participating in organo-metallic complexes in soils. To assess the precision of selective C extractions (i.e., ODOE and Cp), three repetitions of three different samples were performed. Samples were selected from Yedoma and Alas deposits from the Yukechi site. The mean and associated coefficient of variation (i.e., the ratio between the standard deviation and the mean) were calculated for each sample and are shown in **Supplementary Table S3**.

Statistical Analysis

We performed computations for statistical analysis using R software version R.3.5.1 (R Core Team, 2018). Robust linear regression (R^2_{rob}) presented in this study are implemented with an alpha of 0.95. In the following, the non-parametric statistical Wilcoxon test (median) is used in preference to the student test (mean) to statistically compare two distributions when data distribution do not follow the normality hypothesis (Shapiro-Wilk normality test p-value <0.05). Median and median absolute deviation (MAD) will be used to compare concentrations of Yedoma and Alas datasets. Mean and standard deviation (σ) will be used to compare concentrations among different sites.

RESULTS

Global Distribution of Iron Concentrations in Yedoma and Alas Deposits

The median total Fe concentration (±MAD, i.e., median absolute deviation) in never thawed Yedoma deposits (31.9 ± 3.0 g kg^{-1}; n = 814) and previously thawed, refrozen or newly formed Alas deposits (31.2 ± 8.2 g kg^{-1}; n = 470) shows no significant differences (p-value = 0.64, Wilcoxon test). However, the dispersion (i.e., MAD) of total Fe concentrations is more than two times larger for Alas deposits compared to Yedoma deposits (**Figure 4**). This implies that Alas deposits have higher probability to display either lower or higher total Fe concentrations at a certain depth, relative to Yedoma deposits. Along with this, **Figure 5** displays profile selections (i.e., based on Yedoma deposit profiles excluding active layer) of individual Yedoma, Alas or deltaic/fluvial deposits profiles and confirm the homogenous total Fe concentrations in Yedoma deposits and heterogeneous total Fe concentrations in Alas deposits as

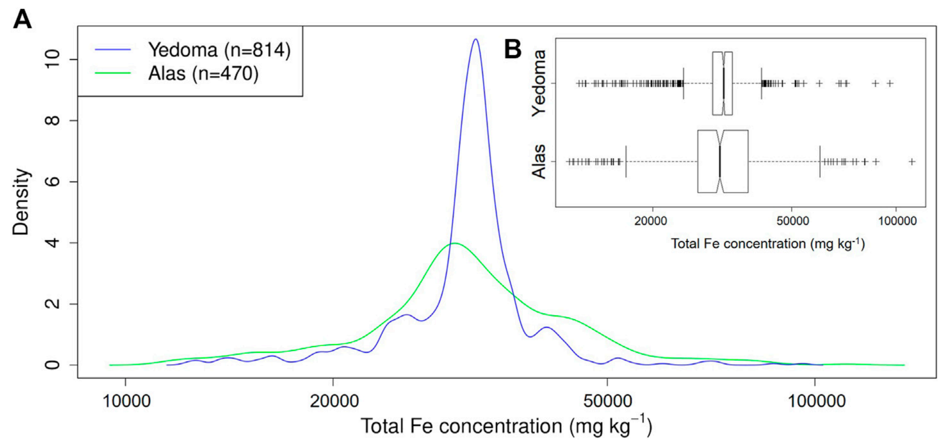

FIGURE 4 | (A) Density plot and **(B)** fligner test (boxplot) of the total iron (Fe) concentration within Yedoma (n = 814; blue line) and Alas (n = 470; green line) deposits.

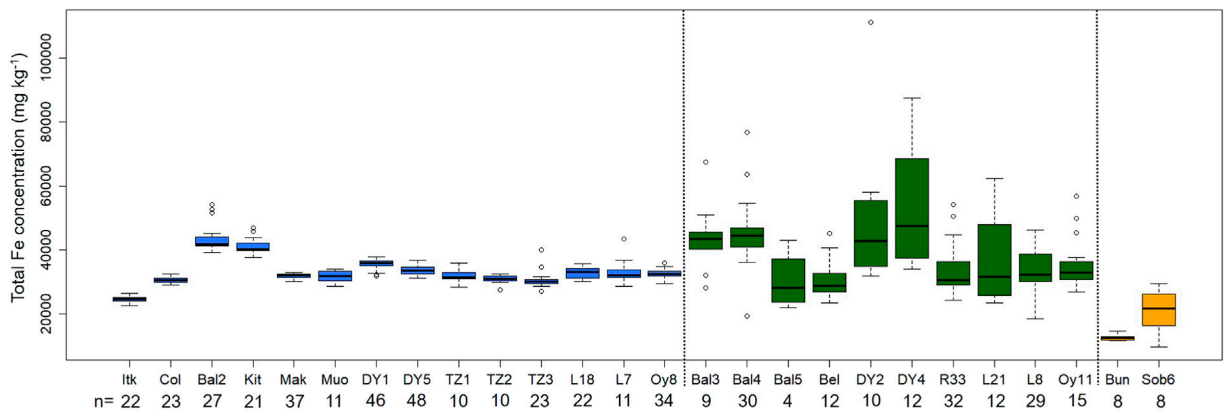

FIGURE 5 | Boxplot of the Fe concentration within selected profiles from different types of deposit: Yedoma Ice Complex (blue), Alas (green), and deltaic/fluvial deposits (orange). Yedoma Ice Complex deposit profiles were selected based on the absence of active layer deposits or fluvial deposits along the profile. Alas profiles located near Yedoma profiles selected (when possible) are shown. The number of samples for each boxplot is given below labels of the x-axis. The sample labels refer to **Table 1**.

mentioned above. **Figure 5** highlights some additional observations. First, profiles with sediments of deltaic/fluvial origins display significantly lower total Fe concentrations compared to Yedoma or Alas deposits (p-value < 0.005, Wilcoxon test). Deltaic deposits (Bun) and fluvial deposits (Sob14 T2-6) have a median total Fe concentration equal to 12.3 ± 0.8 g kg^{-1} and 21.7 ± 6.8 g kg^{-1}, significantly lower to the median values mentioned above for Yedoma and Alas deposits. Second, Yedoma deposits from Siberia (e.g., labeled Mak, Muo, DY, TZ, L, and Oy) show similar total Fe concentrations throughout the whole Siberia region, even for sites located thousands of km apart from each other. This is illustrated by equivalent mean total Fe concentrations (±2σ, i.e., two standard deviations) along the Yedoma deposit profiles from Cape Mamontov Klyk (Mak-12–19) 31.9 ± 1.3 g kg^{-1}, to Oyogos Yar coast (Oy-07-08) 32.6 ± 3.0 g kg^{-1}, Duvanny Yar (DY-05) 33.5 ± 2.8 g kg^{-1}, Sobo Sise Island (Sob14-T2-3) 31.6 ± 2.0 g kg^{-1}, Muostakh Island (Muo) 31.7 ± 3.7 g kg^{-1}, and even to the New Siberian Archipelago: Bol'shoy Lyakhovsky Island (L7-18) 32.7 ± 3.4 g kg^{-1} or Stolbovoy Island (Sto) 27.2 ± 1.2 g kg^{-1}. Note that the distance between profiles from Cape Mamontov Klyk (Mak-12–19) to Duvanny Yar (DY-05) is more than 1,500 km (see **Figure 2**). Lastly, **Figure 5** highlights that Yedoma deposit profiles from Alaska (i.e., labeled Itk, Col, Bal2 and Kit) display homogeneous total Fe concentrations along each profile (similarly to Yedoma deposits from Siberia) but with different mean total Fe concentrations between them. The Itkillik Yedoma exposure displays a mean of 24.6 ± 1.7 g kg^{-1} Fe, Colville Yedoma profile of 30.5 ± 1.9 g kg^{-1}, Baldwin Peninsula Yedoma deposits of 43.2 ± 7.4 g kg^{-1} Fe (the Fe concentration becomes 42.1 ± 3 g kg^{-1} Fe when excluding the three samples at the bottom of the profile considered as a separate unit), and 41.1 ± 4.7 g kg^{-1} Fe from a Yedoma exposure at the Kitluk River on the northern Seward Peninsula.

Variability of Iron Concentrations With Depth in Yedoma and Alas Deposits

The full dataset of total Fe concentration from Yedoma domain deposits is provided in the PANGAEA data repository (https://doi.pangaea.de/10.1594/PANGAEA.922724). Here, the depth-variations of total Fe concentrations in Yedoma domain deposits are investigated in detail and linked to the specific history of the deposits from deposition during late Pleistocene to post-depositional processes during Lateglacial and Holocene warmer periods. In each location, where both Yedoma and Alas deposits were available, the vertical total Fe concentration is compared between the Yedoma profile and the Alas profile (**Supplementary Presentation S1**). We present each profile with a simplified stratigraphic column, which highlights the successive layers along the sampled profile (i.e., Yedoma deposits, thermokarst deposits, fluvial deposits, active layer, or peat layer). The complexity in individual profiles arises from the multiple origins of Yedoma deposition during the late Pleistocene, as well as thermokarst, soil development, cryoturbation, peat formation, or flooding processes (as indicated by fluvial sandy layers) that affected the depositional and soil environment.

Ice-rich Yedoma deposits had homogeneous Fe concentrations throughout the whole deposit thickness, whereas Alas deposits were characterized by variable Fe concentrations with depth (**Supplementary Presentation S1**). This reflects the higher dispersion of Fe concentrations in Alas deposits compared to Yedoma deposits (**Figure 4**; *Global Distribution of Iron Concentrations in Yedoma and Alas Deposits*). For example, both Duvanny Yar Yedoma deposit profiles (DY-01 and DY-05) showed constant Fe concentrations despite their large thicknesses and despite the fact that they are located 2 km away from each other. DY-01 had a mean of 35.5 ± 2.77 $g\,kg^{-1}$ Fe (±2σ) for a total thickness of about 20 m and DY-05 of 33.5 ± 2.79 $g\,kg^{-1}$ Fe for an equivalent thickness. Conversely, DY-04 Alas profile displayed a mean of 53.3 ± 37.6 $g\,kg^{-1}$ (±2σ) for a deposit thickness of 3.5 m which points at the heterogeneity of the material inherent to Alas thawing history (**Supplementary Presentation S1**). Deposits with fluvial origins (i.e., characterized as sandy layers) showed depleted total Fe concentrations, as highlighted in **Supplementary Presentation S1**). Conversely, in sediments containing peat layers, total Fe concentrations either: 1) increased in active layer deposits or even in peat layers from underlying permafrost; 2) decreased, usually in the top horizons of the profile; or 3) remained with similar Fe concentration as deposits located above or below in the profile (**Supplementary Presentation S1**). The data further indicate a positive correlation between total Fe concentrations and TOC content (wt%; **Supplementary Figure S1**). An exception to this trend is observed for organic-rich samples (i.e., TOC >30 wt%) in the top surface layer (within the first centimeters) of the profile that show a depletion of total Fe concentrations.

Distribution of Selectively Extracted Iron and Carbon in Yedoma and Alas Deposits

The Fe concentrations in selective extractions by DCB, oxalate and pyrophosphate within a subset of selected Yedoma and Alas deposits are presented in **Table 2**. Robust and Pearson correlation matrix for all studied parameters (Fe_t, Fe_d, Fe_o, Fe_p) is presented in **Supplementary Figure S2**. Based on this subset of 21 samples from the Yedoma domain, the Fe_d/Fe_t ratios in Yedoma (n = 12) and Alas (n = 9) deposits have a median of 26.6 and 27.8%, respectively, and are not statistically different (p-value 0.46, Wilcoxon test). Taking the never thawed, previously thawed and newly formed deposits together, the mean of Fe_d/Fe_t, which represents the proportion of free Fe oxides out the global Fe pool (*Selective Iron Extractions*), equals 24.7%. Within those free oxides, poorly crystalline (i.e., amorphous) Fe oxides or complexed Fe reach 80.9% and therefore represent about 20% of the total Fe pool (Fe_o/Fe_t; **Table 2**). The distribution of reactive Fe-oxides varies within each profile; the Fe_o/Fe_t ratio ranges from 22.8 to 36.5% (Sob14 T2-2), 13.8–22.0% (Sob14 T2-5), 10–28.6% (KY T1-1) and 17.2–30.4% (KY T2-2), for two pairs of Yedoma-Alas profiles (**Table 2**); the Fe_p/Fe_o ratio in the same profiles indicates that more than a third of Fe amorphous phases are involved in complexes with OC.

The C selectively extracted by the oxalate and pyrophosphate is presented in **Table 2** and correlation matrix for all studied parameters (ODOE, C_p, TOC) is presented in **Supplementary Figure S2**. Positive correlations stand out between TOC content (in wt%) and C_p ($mg\,kg^{-1}$; R^2_{rob} = 0.80; **Figure 6A**), and between C_p and Fe_p (R^2_{rob} = 0.80; **Figure 6B**), resulting in a positive correlation between TOC content and Fe_p (R^2_{rob} = 0.77; **Figure 6C**). A positive correlation is also observed between ODOE and Fe_o (R^2_{rob} = 0.4; not shown), as well as between ODOE and Fe_p (R^2_{rob} = 0.77; **Figure 6D**). The total Fe concentration in these deposits (Fe_t) is not correlated with pyrophosphate-extractable Fe and C (Fe_p, C_p) or TOC (R^2_{rob} < 0.05), but is correlated with DCB- (Fe_d; R^2_{rob} = 0.76; **Figure 6E**) and oxalate-(Fe_o; R^2_{rob} = 0.34; not shown) extractable Fe.

DISCUSSION

Iron Distribution in Yedoma Deposits

In Yedoma deposits, total Fe concentrations are stable with depth in all profiles (from both Siberia and Alaska). The standard deviation, 2σ, ranges from 1.3 to 3.7 $g\,kg^{-1}$ Fe with depth for Cape Mamontov Klyk (Mak-12–19) and Muostakh Island (Muo), respectively (**Figure 5**; **Supplementary Presentation S1**). We suggest that the conditions of formation for these ice-rich deposits can explain the stable total Fe concentrations with depth within their profiles. First, Yedoma deposits have never thawed since their late Pleistocene deposition, thereby limiting the periods of redox fluctuations which may affect Fe solubility (Schwertmann, 1991; Colombo et al., 2014). We see this supported by evidence for a rapid syngenetic freezing (on geological timescale) of the transported particles after settlement during periods of Yedoma deposit aggradation

TABLE 2 | Concentrations in total Fe (Fe_t) and Fe selectively extracted by dithionite-citrate-bicarbonate (Fe_d), ammonium oxalate (Fe_o), pyrophosphate (Fe_p) in Yedoma and Alas deposits. Total organic carbon (TOC), optical density of oxalate extract (ODOE) and C extracted with pyrophosphate (C_p) are also presented. *Sobo Sise samples are Holocene age deposits on top of Yedoma Ice Complex deposits profile. ** The TOC data are from Fuchs et al. (2018) for Sobo Sise Island (Sob), from Schirrmeister et al. (2017) for Buor Khaya Peninsula (Buo) and from Weiss et al. (2016) for Kytalyk (KY).

Sample	Deposits	Depth	Fe_t	Fe_d	Fe_o	Fe_p	Fe_d/Fe_t	Fe_o/Fe_t	Fe_o/Fe_d	Fe_p/Fe_o	TOC**	ODOE	C_p
		cm	g kg^{-1}								wt%		g kg^{-1}
Sob14 T2-2–5	Yedoma*	43	30.3	9.75	10.2	4.65	0.322	0.337	1.048	0.456	3.26	0.335	13.1
Sob14 T2-2–19	Yedoma*	140	31.6	9.46	11.5	4.15	0.299	0.365	1.219	0.359	4.22	0.410	14.0
Sob14 T2-2–31	Yedoma*	230	30.0	6.45	6.83	1.84	0.215	0.228	1.058	0.270	2.68	0.369	9.74
KY (1–1) 9–14	Yedoma	11.5	27.2	7.41	5.65	2.77	0.272	0.207	0.762	0.491	2.40	0.093	7.16
KY (1–1) 40–45	Yedoma	42.5	32.8	10.0	3.29	0.217	0.305	0.100	0.329	0.066	0.61	0.029	1.26
KY (1–1) 90–95	Yedoma	92.5	30.8	8.25	8.81	5.45	0.268	0.286	1.069	0.618	4.94	0.409	45.8
Buo-02-A02	Yedoma	60	29.5	7.63	6.93	1.03	0.259	0.235	0.908	0.148	0.82	0.079	0.823
Buo-02-D18	Yedoma	450	20.0	0.941	0.634	0.421	0.047	0.032	0.674	0.664	4.08	0.129	5.64
Buo-02-D19	Yedoma	500	21.0	1.44	1.11	0.952	0.069	0.053	0.771	0.854	7.01	0.153	8.50
Buo-04-A01	Yedoma	100	32.2	8.72	4.06	0.644	0.271	0.126	0.465	0.159	0.86	0.062	2.33
Buo-04-B10	Yedoma	850	29.0	7.63	5.85	1.95	0.263	0.202	0.766	0.333	1.62	0.132	5.51
Buo-04-C23	Yedoma	1,350	23.2	4.78	2.42	0.622	0.206	0.104	0.506	0.257	0.21	0.033	1.53
Mean (Yedoma)							0.233	0.190	0.798	0.390			
1σ							0.088	0.108	0.274	0.236			
Sob14 T2-5–5	Alas	37.5	20.9	4.69	2.88	1.14	0.224	0.138	0.614	0.397	2.15	0.097	4.31
Sob14 T2-5–17	Alas	132	33.1	7.93	4.81	1.17	0.239	0.145	0.607	0.244	1.92	0.127	4.73
Sob14 T2-5–27	Alas	239	35.2	10.5	7.72	1.68	0.299	0.220	0.735	0.218	2.17	0.170	5.61
KY (2–2) 27–32	Alas	29.5	26.9	5.06	4.62	2.48	0.188	0.172	0.914	0.537	3.87	0.138	7.53
KY (2–2) 42–48	Alas	45	24.9	4.76	4.55	2.56	0.191	0.182	0.956	0.564	3.66	0.153	8.41
KY (2–2) 89–94	Alas	91.5	26.8	8.27	8.17	5.62	0.308	0.304	0.987	0.688	7.20	0.310	24.0
Buo-05-A04	Alas	80	26.0	7.23	7.35	0.650	0.278	0.282	1.017	0.088	2.31	0.128	3.00
Buo-05-B12	Alas	400	29.2	9.89	6.54	1.49	0.339	0.224	0.661	0.228	1.49	0.108	4.06
Buo-05-C26	Alas	830	30.3	9.90	9.17	1.46	0.326	0.302	0.926	0.159	1.64	0.116	3.71
Mean (Alas)							0.266	0.219	0.824	0.347			
1σ							0.057	0.065	0.168	0.208			
Mean (total)							0.240	0.198	0.785	0.366			
1σ							0.080	0.089	0.246	0.211			

(Schirrmeister et al., 2002) as well as overall dry conditions under late Pleistocene tundra steppe active layer conditions (Schirrmeister et al., 2013). Second, sediments along a single Yedoma profile likely result from materials with similar total Fe concentrations. Sediments contributing to Yedoma deposits are derived from a mix of lithologies being affected by intense periglacial weathering processes and getting deposited as unconsolidated sediments. The similar periglacial weathering, erosion, and sediment transport processes which were similar across large unglaciated permafrost domains in the Late Pleistocene may have contributed to the homogenization of mixed sediment lithologies before Yedoma aggradation. The origins of Yedoma sediments across the Yedoma domain have, for a long time, divided the scientific community and are still under debate (Schirrmeister et al., 2002, 2020; Murton et al., 2015). Yedoma deposits were, at first, characterized as homogeneous silty fine, ice- and organic-rich sediments with primary or secondary aeolian processes being the main contributor during the time of formation. Hence, Yedoma deposits were and still are often defined as loess or loess-related deposits (Pewe and Journaux, 1983; Tomirdiaro and Chernen'kiy, 1987; Murton et al., 2015). However, in addition to the established aeolian contribution to these ice-rich sediments, additional contributions from fluvial, colluvial, alluvial local sedimentation processes are identified in many regions of the Yedoma domain (e.g., Schirrmeister et al., 2020). It is now considered that the aggradation of Yedoma deposits is not the result of a single process of aeolian deposition, but rather the result of a polygenetic origin with probable seasonally differentiated deposition mechanisms controlled by local environmental conditions, including the contribution from local fluvial, colluvial, and alluvial sediments (Strauss et al., 2012; Schirrmeister et al., 2013, 2020). Similar heavy mineral composition between Yedoma deposits and the nearby mountain range support a contribution from local sediments during Yedoma deposits aggradation (e.g., Schwamborn et al., 2002; Siegert et al., 2002). The largely linear relationship between sample depth (or vertical position in an exposure) and calibrated ^{14}C age reported for Yedoma deposits (Schirrmeister et al., 2002; Wetterich et al., 2014) indicates that the material is supplied with a stable sedimentation rate. Our data are well in line with the supply of local sediments with similar Fe concentrations, which is consistent with the reported homogeneous mineralogy of Yedoma deposits with depth (Strauss et al., 2017).

Despite generally dry conditions, Yedoma deposits may have experienced short wetter periods during their formation (indicated by the presence of peat or peaty soil layers). It can be identified from some of the studied profiles, as in Cape Mamontov Klyk (Mak-2–10), Bol'shoy Lyakhovsky Island (1-3 TZ) or Sobo Sise Island (SobT2-2), that the formation of peat

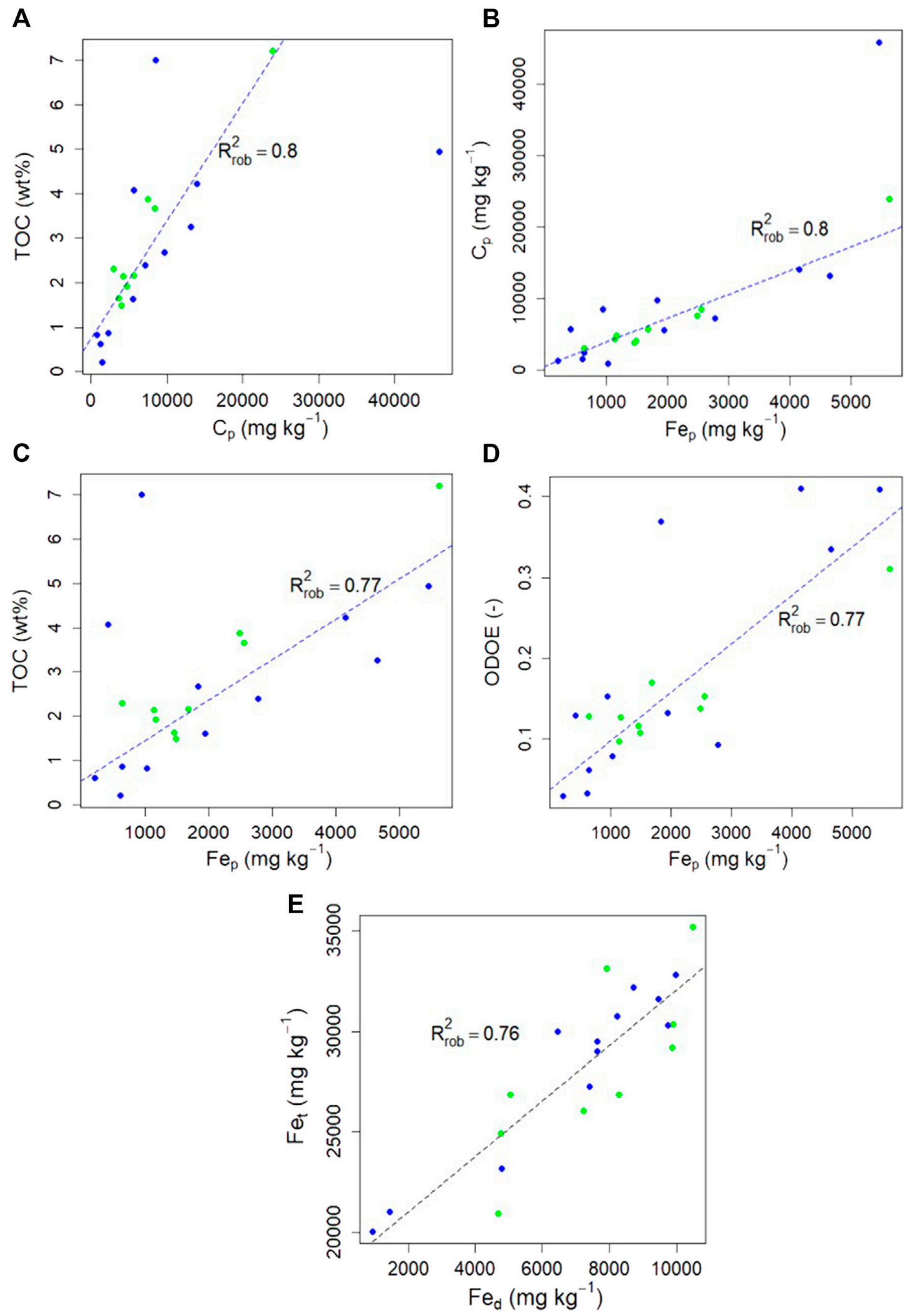

FIGURE 6 | Robust linear regression plots for Yedoma Ice Complex deposits (blue dots) and Alas deposits (green dots) between **(A)** Total organic carbon (TOC) content (wt%) vs C extracted with pyrophosphate (C_p) **(B)** C_p vs Fe selectively extracted by pyrophosphate (Fe_p) **(C)** TOC vs Fe_p **(D)** Optical density of oxalate extract (ODOE) vs Fe_p; and **(E)** Total Fe concentrations (Fe_t) vs Fe selectively extracted by dithionite-citrate-bicarbonate (Fe_d). Dashed lines represent the robust linear regression (alpha = 0.95; *n* = 21).

layers are associated with the highest total Fe concentrations (**Supplementary Presentation S1**). In Cape Mamontov Klyk, the highest Fe concentrations occurred in a sandy peat layer underlying the typical silty Yedoma deposits. In Bol'shoy Lyakhovsky Island, the highest total Fe concentrations occurred in a peat inclusion from a typical Yedoma Ice Complex unit. In Sobo Sise, the total Fe concentrations are the highest in a single peaty horizon of Holocene age overlying Yedoma deposits. The higher total Fe concentration highlighted in these deposits often correspond with peat layers or inclusions. The local redistribution of total Fe in Yedoma profiles can be explained with two hypotheses: 1) solubilization of Fe (from Fe oxide or complexed Fe dissolution) induced by the wetter conditions during short warmer periods and translocation of Fe to a peat layer where the microscale redox environment favors Fe oxide precipitation or 2) cryoturbation of a surface peat horizon where Fe was precipitated following a similar solubilization and precipitation process. The high TOC content in these Fe-rich samples (e.g., TOC: Mak-2–3 = 15.3 wt% and Sob14T2-2–11 = 7.6 wt%) supports the hypothesis that the presence of peat favors the precipitation of solubilized Fe. Field observations from Schirrmeister et al. (2008) indicate that the sandy-peat layer from Cape Mamontov Klyk (5–10 m above sea level; **Supplementary Presentation S1**) have brownish to reddish mottled layers, in a buried oxic gley–soil horizon, thereby supporting our hypothesis of Fe translocation upon water saturated conditions and Fe oxide precipitation in favorable oxic conditions. Water saturated conditions are suggested to favor the translocation of reduced Fe as already observed in previous studies (Fiedler et al., 2004; Riedel et al., 2013; Herndon et al., 2017). The accumulation of Fe is also found in active layer or Holocene deposits (located in the top of the Bykovsky Peninsula profiles-**Supplementary Presentation S1**), and comparable with Fe accumulation in organic-rich surface soils of ice-wedge polygon from arctic tundra (Herndon et al., 2020a). Thus, evidence for Fe accumulation also supports that higher TOC content, often observed in active layer, promotes Fe precipitation in favorable redox conditions. Despite the fact that Yedoma deposit formation predominantly took place during the interstadial Marine Isotope Stage (MIS) three and the stadial MIS 2, promoted by long-lasting continental cold and arid climate conditions, short thaw phases occurred during the late Pleistocene with potential impact on the formation of Yedoma deposits (Schirrmeister et al., 2002, 2013; Wetterich et al., 2014). Wetter conditions trigger anoxia, which improves vegetation growth, lowers organic matter mineralization rates and thus promotes peat accumulation (Keller and Medvedeff, 2016). In northern latitudes, phases of peat expansion triggered by increasing air temperatures and moisture supply were inferred from paleo proxies (from 57 ka to 45 ka BP and from 35 ka to 29 ka BP; Treat et al., 2019). Buried peat layers found in deep Yedoma deposits could be indirect evidence of these "short" warming and wetting periods (Treat et al., 2019), and our data highlight that this likely promoted Fe precipitation. However, our data show that the presence of peat layers in Yedoma deposits does not necessarily imply accumulation of Fe (**Supplementary Presentation S1**). Detecting the presence or absence of Fe accumulation in these peat layers is important to identify potential accumulation of reactive Fe, which in turn can promote OC stabilization. Based on the positive correlation between total Fe concentrations and reactive Fe concentrations in the deposits (R^2 = 0.76; **Figure 6E**), we argue that Fe accumulation in peat layers likely contributes to organic matter stabilization and hence to lower organic matter mineralization rates.

Our data highlight that Yedoma deposits from Siberia show similar total Fe concentrations (*Global Distribution of Iron Concentrations in Yedoma and Alas Deposits*; **Figure 5**) across deposits that span 1,500 km across Siberia (**Figure 2**). In Yedoma deposits from Alaska, the mean total Fe concentration differs from one Alaskan location to another, being higher in Western Alaska (Kitluk and Baldwin Peninsula: 41.1 ± 4.7 and 43.2 ± 7.4 g kg^{-1} Fe, respectively) than in Northern Alaska (Colville and Itkillik: 30.5 ± 1.9 and 24.6 ± 1.7 g kg^{-1} Fe, respectively; **Figure 5**; see **Figure 2** for locations). The mineralogical variation between loess in different parts of the world reflects the nature of the surficial geology and the effectiveness of sediment mixing processes in the individual source regions (Pye, 1995). Our data suggest that across the Siberian sites, the sediments contributing to the deposits are of similar chemical composition, or of mixed lithologies with a total Fe concentration similar to the Fe concentration in the continental crust (Börker et al., 2018). The total Fe concentration reported in the upper continental crust (39 g kg^{-1}; Rudnick and Gao, 2003), in continental sediments (40 g kg^{-1}; Rauch and Pacyna, 2009) and in a typical loess (24 g kg^{-1}; Rauch and Pacyna, 2009) are likely to yield a homogeneous total Fe concentration in Yedoma deposits (32 g kg^{-1}; this study) after sediment mixing by periglacial surface abrasion and polygenetic (aeolian, fluvial, colluvial, alluvial) transport and deposition. In contrast, in Alaska, the different mean total Fe concentration in different locations suggests a range of Fe contributions from different local lithologies, such as carbonates present in North Alaska close to the Brooks Range (Walker and Everett, 1991; Till et al., 2008). Overall, despite their different mean total Fe concentrations, both Siberia and Alaska Yedoma deposits present similar Fe concentrations with depth, and can be used to investigate the influence of thermokarst process with potential redistribution of Fe during Alas deposits formation.

Thawing Triggers Iron Mobility in Ice-Rich Deposits and Iron Redistribution in Alas Deposits

Our results show a larger variability in total Fe concentrations in Alas deposits relative to Yedoma deposits (**Figures 4**, **5**; **Supplementary Presentation S1** for both Siberia and Alaska. In contrast to never thawed Yedoma deposits (discussed in *Iron Distribution in Yedoma Deposits*), Alas deposits, have experienced intense thawing processes with potential effects on redox-sensitive elements (e.g., Fe). Alas deposits result from the impact of thaw and post-depositional processes on ice-rich Yedoma deposits, as well as newly formed Holocene deposits. Ground collapse during thawing of ice-rich deposits, caused by the volume loss after ground ice melt, often creates favorable conditions for thermokarst lake formation. Depending on local conditions, these lakes can persist for several decades, centuries, or even millennia, before they drain due to further permafrost degradation or dry out under unfavorable water balance conditions (e.g., shallow water bodies; Grosse et al., 2013). Moreover, several studies consider that thermokarst lakes form, drain and reform in a cycle ("thaw-lake cycle"); a process that would result in substantial changes to Alas deposits on millennial timescale because of repeatedly reworked sediments undergoing several alternating stages of lacustrine and subaerial wetland development (Jones et al., 2012). Field evidence of multiple thermokarst lake generations overlapping at sites can also be found in cores (e.g., Lenz et al., 2016). In summary, Alas deposits are the result of thermokarst dynamics during the Lateglacial and Holocene and associated reworking of deposits once or multiple times depending on overall thaw dynamics in the landscape. Additional complexity arises from the fact that thermokarst landforms undergo successional changes over time from initial towards advanced stages of degradation and possibly stabilization, during which the dominant physical and biogeochemical processes may change as these features evolve (Biskaborn et al., 2013; Kokelj and Jorgenson, 2013; Turetsky et al., 2020).

Relative to Yedoma deposits that have never thawed displaying homogeneous Fe concentrations with depth (*Iron Distribution in Yedoma Deposits*), Alas deposits from corresponding locations are characterized by changes in total Fe concentrations with depth (**Supplementary Presentation S1**). This likely results from Fe becoming mobile during post-depositional processes such as thermokarst events and subsequent drainage, affecting Fe distribution in reworked and newly formed deposits. It is well established that Fe can be mobilized in water-saturated soil (Riedel et al., 2013; Colombo et al., 2014; Pokrovsky et al., 2014; Manasypov et al., 2015; Herndon et al., 2020b). The loss of Fe from alluvial plain soil horizons is correlated to low redox potential (Eh) supporting the idea that leaching of redox-sensitive elements, such as Fe, occurred during fluctuating redox conditions in thermokarst lakes (Fiedler and Sommer, 2004). Moreover, redox gradients can occur over small scale, e.g., with relief changes between high-centered and low-centered polygons in polygonal permafrost soils (Fiedler et al., 2004), or over centimeter scale (Herndon et al., 2020). It follows that solubilization, translocation and precipitation are also the major processes involved in Fe mobility in Alas deposits. Here, the data support that 1) thermokarst lake formation after ice-rich Yedoma degradation has generated reducing conditions favoring the solubilization and translocation of dissolved Fe from oxides or complexed forms in the initial Yedoma deposit, 2) the subsequent thermokarst lake drainage and refreezing as well as peat accumulation generated suitable oxic conditions that promote Fe precipitation in Alas deposits. The Alas deposits therefore represent reworked and newly formed deposits, which have experienced local oxidation and precipitation of dissolved Fe in favorable environments depending on microscale redox potential. This is also supported by field observations of Alas deposits profiles (e.g., DY-02) with the typical brownish color given by Fe oxides (Wetterich et al., 2011b) in the layers enriched in total Fe concentration (**Supplementary Presentation S1**).

Grain-size distribution is commonly used as an indicator of major disturbances between the original Yedoma deposits and the reworked and newly formed Alas deposits induced by post-depositional processes (Strauss et al., 2012). This allows identifying contrasts between homogeneous grain-size distribution in Yedoma deposits (e.g., in Duvanny Yar DY-01 and DY-05) and the more heterogeneous distribution with coarser and finer particles in Alas deposits (e.g., DY-04 and DY-02 from the same location; Strauss, 2010; Strauss et al., 2012). The contrast between homogeneous distribution of total Fe concentration with depth in Yedoma deposits and the heterogeneous distribution of total Fe concentration with depth in Alas deposits (**Supplementary Presentation S1**) is in good agreement with the observations based on the grain-size distribution (**Supplementary Figure S3**), and supports that the reworking and new formation of the deposits is leading to changing conditions for the mobility of Fe. The degree of Fe redistribution within Alas deposits could be an indicator of the intensity of post-depositional processes. The study of such redistribution may give new clues on thermokarst dynamics, in particular 1) drainage rate after lake formation, 2) rapid refreezing after drainage, or 3) single or multiple thaw-lake cycles. In this way, these observations of Fe mobilization in the paleo-record act as an analogue for present day and future Fe distribution in thermokarst lake deposits.

Changing Iron and Organic Carbon Interactions During Post-Depositional Processes

The changing conditions for Fe mobility upon thermokarst processes potentially affect Fe-OC interactions and thereby OC stability in the reworked deposits (Colombo et al., 2014; Herndon et al., 2020b; Kleber et al., 2021). This study shows that, on average, 25% of total Fe is in Fe-oxide form (as crystalline or amorphous phases) and that out of these oxides, 80% is amorphous or complexed Fe (**Table 2**). Based on the subset of samples analyzed for the selective extractions of Fe (n = 21), it appears that the proportion of reactive Fe oxides to the global Fe pool is not significantly different between thawed and never thawed deposits, whether considering the total Fe-oxides (Fe_d/Fe_t; p-value = 0.46) or the amorphous Fe-oxides (Fe_o/Fe_t, p-value = 0.55; **Table 2**). The crystallinity of Fe-oxides phases in soils is not solely controlled by redox conditions, but other factors such as water budget, organic matter input, initial Fe phase composition, and time (potentially inducing Fe-oxide aging) are also important players (Cudennec and Lecerf, 2006; Winkler et al., 2018). In addition, microbial activity, especially from Fe-reducing microorganisms, may influence the crystallinity of Fe oxides and abundance of complexed Fe (Rivkina et al., 2020). As a result, both increases or decreases in Fe oxides crystallinity have been reported under redox fluctuations in wetlands soils (Winkler et al., 2018). This likely explains why our data indicate that the thawing history of the deposits is not leading to systematic changes in the crystallinity of Fe oxides. We observed that the concentration in reactive Fe oxides (Fe_d) in Yedoma and Alas deposits is positively correlated with their total Fe concentrations (**Figure 6E**). This result supports that total Fe accumulation (i.e., reported locally in Yedoma deposits and intensively in Alas deposits) is directly associated to the accumulation of reactive Fe oxides, thereby providing potential OC stabilizing phases in these deposits. The redistribution in total Fe concentration in the Alas deposits suggest that Fe accumulation likely occurred in oxic conditions favorable for oxy-hydroxide formation, whereas Fe depletion was likely associated with flooding conditions leading to dissolution in reducing conditions combined with subsequent loss of Fe via lateral or vertical leaching mechanisms.

The characterization of reactive Fe-oxides (crystalline, poorly crystalline and complexed Fe (Fe_d, Fe_o, Fe_p)) is a primary step

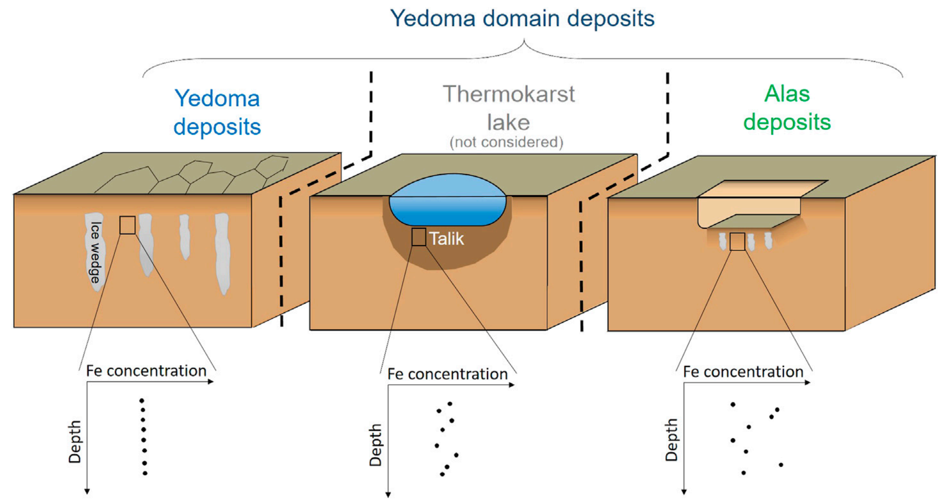

FIGURE 7 | Conceptual scheme of the depth-distribution of total Fe concentration in never thawed Yedoma Ice Complex deposits, in deposits subsequently to thaw processes, i.e., below thermokarst lake (not considered in this study) and in Alas deposits. Black rectangles in the upper schematic representation of Yedoma, thermokarst lake and Alas profile indicate the sample location. The spatial coverage of the geomorphologic features is not to scale.

required to track the potential driving factors linking mineral and organic components in soils and sediments. Interactions between Fe and OC, as Fe-OC complexes and as OC-Fe oxide associations, are supported by the positive correlation between 1) the complexed Fe (Fe_p) and the complexed carbon (**Figure 6B**), and 2) the complexed Fe and the ODOE which represents organic acids associated with amorphous Fe oxides and complexed Fe (**Figure 6D**). The more TOC is present in the deposit, the more carbon is present in complexed form (**Figure 6A**). Deciphering between the many OC stabilizing processes reported in the literature, such as physical and physico-chemical protection involving Fe oxides (aggregation, organo-mineral associations) and organo-metallic complexes (complexation) is of primary importance to better predict the fate of OC in a warming Arctic (e.g., Lutzow et al., 2006; Kögel-Knabner et al., 2008). Our work highlights that total Fe is redistributed upon thermokarst processes, but more importantly, we highlight the local (Yedoma) or intensive (Alas) redistribution of protective mechanisms associated to OC in ice-rich permafrost regions.

Implications of Thermokarst Processes for Iron Mobility and Interactions With Organic Carbon

The different steps of Fe mobility between Yedoma and Alas deposits can be summarized as follows (**Figure 7**): in Yedoma deposits that never thawed since deposition, the syngenetic freezing of sediments soon after deposition limits solubilization and translocation of Fe throughout the profile (**Supplementary Presentation S1**). Nonetheless, Yedoma deposits, which may have experienced short wetter periods (indicated by peat layers), show a local accumulation/depletion of Fe and therefore suggest Fe mobility and translocation mechanisms. In contrast, in Alas deposits, which have experienced intensive thermokarst processes, we observe a large variability of total Fe concentrations (**Figure 7**), suggesting sustained dissolution of Fe oxides and/or complexed Fe, Fe translocation and precipitation in redox favorable microscale environments with potential peat influence. Finally, fluvial deposits underlying Yedoma deposits or deposits showing marine to deltaic influence in coastal regions (e.g., Bunge Land; **Supplementary Presentation S1**) display low total Fe concentrations that either suggest depletion caused by lateral loss during flood events or a different sediment origin already depleted in Fe prior to deposition. These fluvial deposits are also characterized with very low TOC values which may not facilitate Fe precipitation. Overall, the redistribution of Fe between Yedoma and Alas deposits reflects the influence of the complex history of Yedoma deposits (polygenetic origin, potential short thawing periods during late Pleistocene) and the intense post-depositional processes of Alas deposits during Lateglacial to Holocene warmer periods (**Figure 8**).

The Fe-OC associations are not permanent: they may disappear in a wetter, reducing environment, or form in oxic conditions resulting in a redistribution of Fe throughout the sediment profile (Opfergelt, 2020; Patzner et al., 2020). Our results highlight that specific horizons from Alas deposits have a 2 to 3-fold increase in total Fe concentration (**Supplementary Presentation S1**) and therefore we could expect a 2 to 3-fold increase in reactive Fe, based on the positive correlation between total Fe concentrations and reactive Fe concentrations in the deposits ($R^2 = 0.76$; **Figure 6E**). In contrast, sandy layers, often depleted in TOC, have a 2.5-fold decrease in total Fe concentrations compared to the overlying typical Ice Complex deposits (**Supplementary Presentation S1**). The redistribution of stabilizing OC phases (i.e., Fe-oxides or complexed Fe) is key for the fate of OC in a warming Arctic. The changing Fe concentration between Yedoma and Alas deposits support the idea that future thermokarst processes in the Arctic will affect Fe-

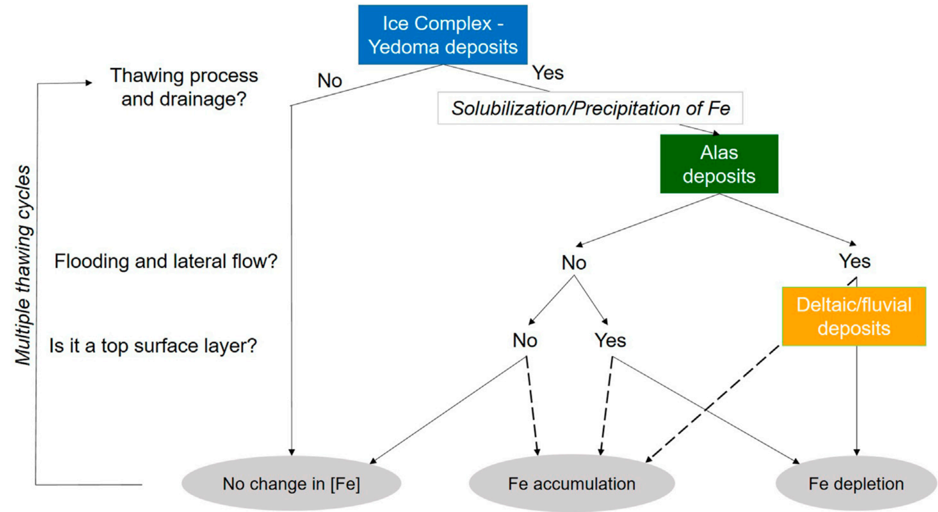

FIGURE 8 | Schematic representation of the iron dynamic within Yedoma domain deposits and the resulting impact for Fe concentration ([Fe]) in Yedoma Ice Complex (blue), Alas (green), and deltaic/fluvial deposits (orange). The "Yes" and "No" correspond to the answer of the question on the left side of the scheme. Dashed lines suggest the potential influence of peat to create favorable oxic conditions.

OC interactions. In this study, we contend that Alas deposits which have experienced past thawing processes are key witnesses to predict what may happen next with Fe-OC interactions during the current and future Arctic warming. More specifically, it can be expected that oxic conditions would favor Fe-oxides formation, generating Fe-OC interactions thereby contributing to mitigate OC decomposition, whereas flooding would generate reducing conditions and the lateral and vertical transport of dissolved Fe phases resulting in the depletion of total Fe concentrations, thereby contributing to decrease Fe-OC interactions, and limiting long-term OC stabilization. We also highlight that future permafrost thaw will be superimposed on deposits with a relict Fe distribution from the Holocene and Pleistocene. The paleo Fe distribution in the Yedoma domain may have a knock-on effect how Fe can be distributed during future thaw, and therefore is primed for variations in OC stabilization and OC mineralization rates. It is therefore essential to consider the permafrost history to predict the evolution of OC upon warming and permafrost thaw.

CONCLUSION

We determined the total Fe concentration (n = 1,292) and distribution of Fe-oxides and Fe involved in complexes (n = 21) in unthawed Yedoma deposits and previously thawed Alas deposits from the Yedoma domain. We found:

1) that the total Fe concentrations in never thawed Yedoma deposits are homogeneous with depth in Alaska and in Siberia, allowing for Fe concentrations in previously thawed Alas deposits to be compared with Yedoma deposits to test the impact of thermokarst processes on Fe mobility.
2) a local redistribution of total Fe concentration throughout Yedoma profiles (i.e., driven by short thaw phases upon Yedoma aggradation with potential peat influence) and an intensive total Fe redistribution in Alas deposits consequent to thermokarst lake formation and drainage, supporting that iron is mobile upon thaw. We suggest Fe mobility after Fe-oxides dissolution, i.e., Fe translocation within sediments followed by Fe-oxides re-precipitation in favorable microscale conditions or Fe leaching.
3) a positive correlation between the total Fe concentration and the reactive Fe concentration in both Yedoma and Alas deposits. On average, proportion of reactive Fe (i.e., Fe-oxides or complexed Fe) equals 25% of global Fe pool for both Yedoma and Alas deposits. The intensive redistribution of total Fe in Alas profiles imply that reactive Fe is redistributed upon thermokarst processes with direct implication on OC stabilization.

The Yedoma domain has been a highly dynamic environment since the late Pleistocene period until today, and will continue to be so with the projected rising temperatures. Our research suggests that similar processes (i.e., Fe solubilization, translocation and precipitation) occur in ice-rich permafrost degradation upon thermokarst processes as previously described for polygonal or thaw gradient permafrost landscapes. The total Fe accumulation/depletion, observed in Alas deposits is accompanied with an accumulation/depletion of reactive Fe and micro-scale implications for OC stabilization. We argue that the change from frozen to unfrozen state leads to the modifications of multiple environmental conditions (fluctuating redox conditions, subsidence, leaching, and drainage) with indirect impact on Fe-oxides distribution and hence on a portion of mineral-protected OC pools.

DATA AVAILABILITY STATEMENT

The datasets presented in this study can be found in online repositories. The names of the repository/repositories and accession number(s) can be found below: https://doi.pangaea.de/10.1594/PANGAEA.922724.

AUTHOR CONTRIBUTIONS

AM and SO conceived and planned the experimental work. AM realized the Fe concentration measurements by pXRF with the help of EM, and realized the selective Fe extractions with the help of NB. GG, LS, MF, and JS contributed with their expertise on permafrost stratigraphy, the sedimentological history of the sample deposits and provided the samples. CH contributed with her expertise on Fe in Arctic regions. AM performed the data processing. AM wrote the manuscript with input from all co-authors.

FUNDING

This project received funding from the European Union's Horizon 2020 research and innovation program under grant agreement No. 714617 to SO, and SO acknowledges funding from the Fund for Scientific Research FNRS in Belgium (FC69480). This work was embedded into the Action Group "The Yedoma Region" funded by the International Permafrost Association. Field sample collection was funded by a European Research Council (ERC) Starting Grant 338,335) to GG as well as Alfred Wegener Institute basic funding.

ACKNOWLEDGMENTS

The authors acknowledge the Mineral and Organic Chemical Analysis (MOCA) platform at UCLouvain for conducting chemical analysis, Benoît Pereira and Aubry Vandeuren for their expertise on portable X-Ray Fluorescence measurements, and the members of the WeThaw project for useful discussions. We thank Peter Kuhry from Stockholm University, as well as the Russian–German scientific collaborations like "System Laptev Sea", "Lena Delta" and other Russian-German expeditions for providing samples.

SUPPLEMENTARY MATERIAL

The Supplementary Material for this article can be found online at: https://www.frontiersin.org/articles/10.3389/feart.2021.703339/full#supplementary-material

Supplementary Presentation 1 | Depth-variation plot of total Fe concentrations (mg kg^{-1}) presented with the corresponding stratigraphic columns in never thawed Yedoma Ice Complex deposits **(left side: A, C, E, G, I, K, M, O)** and in previously thawed and newly formed Alas deposits **(right side: B, D, F, H, J, L, N, P)** from the following sites: Duvanny Yar **(A,B)**, Cape Mamontov Klyk **(C,D)**, Bol'shoy Lyakhovsky Island **(E,F)**, Bykovsky Peninsula **(G,H)**, Oyogos Yar coast **(I,J)**, Baldwin Peninsula **(K,L)**, Sobo Sise Island **(M,N)**, New Siberian Archipelago and Muostakh Island **(O,P)**. Samples with total organic carbon (TOC) content > 5wt% (plain circle) and < 5wt% (open circle) are identified (samples with missing information about TOC content are presented with a cross). The stratigraphic columns are based on descriptions provided in the reference papers listed in **Table 1** for each location. Labels for each profile are explained in **Supplementary Table S1**.

REFERENCES

Abbott, B. W., and Jones, J. B. (2015). Permafrost Collapse Alters Soil Carbon Stocks, Respiration, CH4, and N2O in upland Tundra. *Glob. Change Biol.* 21, 4570–4587. doi:10.1111/gcb.13069

Adhikari, D., and Yang, Y. (2015). Selective Stabilization of Aliphatic Organic Carbon by Iron Oxide. *Sci. Rep.* 5, 1–7. doi:10.1038/srep11214

Andreev, A. A., Grosse, G., Schirrmeister, L., Kuznetsova, T. V., Kuzmina, S. A., Bobrov, A. A., et al. (2009). Weichselian and Holocene Palaeoenvironmental History of the Bol'shoy Lyakhovsky Island, New Siberian Archipelago, Arctic Siberia. *Boreas.* 38, 72–110. doi:10.1111/j.1502-3885.2008.00039.x

Andreev, A. A., Schirrmeister, L., Siegert, C., Bobrov, A. A., Demske, D., Seiffert, M., et al. (2002). Paleoenvironmental Changes in Northeastern Siberia during the Late Quaternary - Evidence From Pollen Records of the Bykovsky Peninsula. *Polarforschung.* 70, 13–25. doi:10.2312/polarforschung.70.13

Audry, S., Pokrovsky, O. S., Shirokova, L. S., Kirpotin, S. N., and Dupré, B. (2011). Organic Matter Mineralization and Trace Element Post-Depositional Redistribution in Western Siberia Thermokarst lake Sediments. *Biogeosciences.* 8, 3341–3358. doi:10.5194/bg-8-3341-2011

Bascomb, C. L. (1968). Distribution of Pyrophosphate-Extractable Iron and Organic Carbon in Soils of Various Groups. *J. Soil Sci.* 19, 251–268. doi:10.1111/j.1365-2389.1968.tb01538.x

Biskaborn, B. K., Herzschuh, U., Bolshiyanov, D. Y., Schwamborn, G., and Diekmann, B. (2013). Thermokarst Processes and Depositional Events in a Tundra lake, Northeastern Siberia. *Permafrost Periglac. Process.* 24, 160–174. doi:10.1002/ppp.1769

Blakemore, L. C., Searle, P. L., and Daly, B. K. (1981). Methods for Chemical Analysis of Soils. *New Zealand Soil Bur. Scientific Rep. 10 A, second revision.*, 102. doi:10.7931/DL1-SBSR-10A

Börker, J., Hartmann, J., Amann, T., and Romero-Mujalli, G. (2018). Terrestrial Sediments of the Earth: Development of a Global Unconsolidated Sediments Map Database (GUM). *Geochem. Geophys. Geosyst.* 19, 997–1024. doi:10.1002/2017GC007273

Chao, T. T., and Sanzolone, R. F. (1992). Decomposition Techniques. *J. Geochemical Exploration.* 44, 65–106. doi:10.1016/0375-6742(92)90048-d

Chen, C., Hall, S. J., Coward, E., and Thompson, A. (2020). Iron-Mediated Organic Matter Decomposition in Humid Soils Can Counteract protection. *Nat. Commun.* 11, 2255. doi:10.1038/s41467-020-16071-5

Colombo, C., Palumbo, G., He, J.-Z., Pinton, R., and Cesco, S. (2014). Review on Iron Availability in Soil: Interaction of Fe Minerals, Plants, and Microbes. *J. Soils Sediments.* 14, 538–548. doi:10.1007/s11368-013-0814-z

Cudennec, Y., and Lecerf, A. (2006). The Transformation of Ferrihydrite into Goethite or Hematite, Revisited. *J. Solid State. Chem.* 179, 716–722. doi:10.1016/j.jssc.2005.11.030

Daly, B. K. (1982). Identification of Podzols and Podzolised Soils in New Zealand by Relative Absorbance of Oxalate Extracts of A and B Horizons. *Geoderma.* 28, 29–38. doi:10.1016/0016-7061(82)90038-6

Eglinton, T. I. (2012). A Rusty Carbon Sink. *Nature.* 483, 165–166. doi:10.1038/483165a

Fiedler, S., and Sommer, M. (2004). Water and Redox Conditions in Wetland Soils—Their Influence on Pedogenic Oxides and Morphology. *Soil Sci. Soc. Am. J.* 68, 10. doi:10.2136/sssaj2004.3260

Fiedler, S., Wagner, D., Kutzbach, L., and Pfeiffer, E.-M. (2004). Element Redistribution along Hydraulic and Redox Gradients of Low-Centered Polygons, Lena Delta, Northern Siberia. *Soil Sci. Soc. Am. J.* 68, 1002–1011. doi:10.2136/sssaj2004.1002

Fuchs, M., Grosse, G., Strauss, J., Günther, F., Grigoriev, M., Maximov, G. M., et al. (2018). Carbon and Nitrogen Pools in Thermokarst-Affected Permafrost Landscapes in Arctic Siberia. *Biogeosciences.* 15, 953–971. doi:10.5194/bg-15-953-2018

Grigoriev, M. N., Rachold, V., and Bolshiyanov, D. (2003). Russian-German Cooperation System Laptev Sea: the Expedition LENA 2002, Berichte zur

Polar- und Meeresforschung (Reports on Polar and Marine Research), *Alfred Wegener Inst. Polar Mar. Res.* 466, 341. doi:10.2312/BzPM_0466_2003

Grosse, G., Jones, B., and Arp, C. (2013). "8.21 Thermokarst Lakes, Drainage, and Drained Basins," in *Treatise on Geomorphology* (Elsevier), 325–353. doi:10.1016/B978-0-12-374739-6.00216-5

Grosse, G., Jones, B. M., Schirrmeister, L., Meyer, H., Wetterich, S., Strauss, J., et al. (2015). "Late Pleistocene and Holocene Ice-Rich Permafrost in the Colville River valley, Northern Alaska," in *EPIC3PAST Gateways 2015, Potsdam, 18 May 2015 - 22 May 2015, Geophysical Research Abstracts (Potsdam: EGU2015-10607)*. Available at: http://www.awi.de/pastgateways2015 (Accessed October 12, 2020).

Grosse, G., Schirrmeister, L., Siegert, C., Kunitsky, V. V., Slagoda, E. A., Andreev, A. A., et al. (2007). Geological and Geomorphological Evolution of a Sedimentary Periglacial Landscape in Northeast Siberia during the Late Quaternary. *Geomorphology.* 86, 25–51. doi:10.1016/j.geomorph.2006.08.005

Herndon, E., AlBashaireh, A., Singer, D., Roy Chowdhury, T., Gu, B., and Graham, D. (2017). Influence of Iron Redox Cycling on Organo-mineral Associations in Arctic Tundra Soil. *Geochimica et Cosmochimica Acta.* 207, 210–231. doi:10.1016/j.gca.2017.02.034

Herndon, E., Kinsman-Costello, L., Di Domenico, N., Duroe, K., Barczok, M., Smith, C., et al. (2020a). Iron and Iron-Bound Phosphate Accumulate in Surface Soils of Ice-Wedge Polygons in Arctic Tundra. *Environ. Sci. Process. Impacts.* 22, 1475–1490. doi:10.1039/D0EM00142B

Herndon, E., Kinsman-Costello, L., and Godsey, S. (2020b). "Biogeochemical Cycling of Redox-Sensitive Elements in Permafrost-Affected Ecosystems," in *In Geophysical Monograph Series*. Editors K. Dontsova, Z. Balogh-Brunstad, and G. Le Roux (Wiley), 245–265. doi:10.1002/9781119413332.ch12

Huang, W., and Hall, S. J. (2017). Elevated Moisture Stimulates Carbon Loss from mineral Soils by Releasing Protected Organic Matter. *Nat. Commun.* 8, 1–10. doi:10.1038/s41467-017-01998-z

Hugelius, G., Strauss, J., Zubrzycki, S., Harden, J. W., Schuur, E. A. G., Ping, C.-L., et al. (2014). Estimated Stocks of Circumpolar Permafrost Carbon with Quantified Uncertainty Ranges and Identified Data Gaps. *Biogeosciences.* 11, 6573–6593. doi:10.5194/bg-11-6573-2014

Jeanroy, E., and Guillet, B. (1981). The Occurrence of Suspended Ferruginous Particles in Pyrophosphate Extracts of Some Soil Horizons. *Geoderma.* 26, 95–105. doi:10.1016/0016-7061(81)90078-1

Jones, M. C., Grosse, G., Jones, B. M., and Walter Anthony, K. (2012). Peat Accumulation in Drained Thermokarst lake Basins in Continuous, Ice-Rich Permafrost, Northern Seward Peninsula, Alaska. *J. Geophys. Res.* 117, a. doi:10.1029/2011JG001766

Jongejans, L. L., Strauss, J., Lenz, J., Peterse, F., Mangelsdorf, K., Fuchs, M., et al. (2018). Organic Matter Characteristics in Yedoma and Thermokarst Deposits on Baldwin Peninsula, West Alaska. *Biogeosciences* 15, 6033–6048. doi:10.5194/bg-15-6033-2018

Kaiser, K., and Guggenberger, G. (2007). Sorptive Stabilization of Organic Matter by Microporous Goethite: Sorption into Small Pores vs. Surface Complexation. *Eur. J. Soil Sci.* 58, 45–59. doi:10.1111/j.1365-2389.2006.00799.x

Kanevskiy, M., Shur, Y., Fortier, D., Jorgenson, M. T., and Stephani, E. (2011). Cryostratigraphy of Late Pleistocene Syngenetic Permafrost (Yedoma) in Northern Alaska, Itkillik River Exposure. *Quat. Res.* 75, 584–596. doi:10.1016/j.yqres.2010.12.003

Kappler, A., Bryce, C., Mansor, M., Lueder, U., Byrne, J. M., and Swanner, E. D. (2021). An Evolving View on Biogeochemical Cycling of Iron. *Nat. Rev. Microbiol.* 19, 360–374. doi:10.1038/s41579-020-00502-7

Keller, J. K., and Medvedeff, C. A. (2016). "Soil Organic Matter," in *Wetland Soils: Genesis, Hydrology, Landscapes, and Classification*. Editors M.J. Vepraskas, C.B. Craft, and J.L. Richardson (Boca Raton, FL: CRC Press), 165–188.

Kleber, M., Bourg, I. C., Coward, E. K., Hansel, C. M., Myneni, S. C. B., and Nunan, N. (2021). Dynamic Interactions at the Mineral-Organic Matter Interface. *Nat. Rev. Earth Environ.* 2, 402–421. doi:10.1038/s43017-021-00162-y

Kleber, M., Eusterhues, K., Keiluweit, M., Mikutta, C., Mikutta, R., and Nico, P. S. (2015). Mineral-Organic Associations: Formation, Properties, and Relevance in Soil Environments," In *Advances in Agronomy* (Elsevier), 1–140. doi:10.1016/bs.agron.2014.10.005

Kögel-Knabner, I., Guggenberger, G., Kleber, M., Kandeler, E., Kalbitz, K., Scheu, S., et al. (2008). Organo-Mineral Associations in Temperate Soils: Integrating Biology, Mineralogy, and Organic Matter Chemistry. *J. Plant Nutr. Soil Sci.* 171, 61–82. doi:10.1002/jpln.200700048

Kögel-Knabner, I., Amelung, W., Cao, Z., Fiedler, S., Frenzel, P., Jahn, R., et al. (2010). Biogeochemistry of Paddy Soils. *Geoderma.* 157, 1–14. doi:10.1016/j.geoderma.2010.03.009

Kokelj, S. V., and Jorgenson, M. T. (2013). Advances in Thermokarst Research. *Permafrost Periglac. Process.* 24, 108–119. doi:10.1002/ppp.1779

Lalonde, K., Mucci, A., Ouellet, A., and Gélinas, Y. (2012). Preservation of Organic Matter in Sediments Promoted by Iron. *Nature* 483, 198–200. doi:10.1038/nature10855

Lenz, J., Wetterich, S., Jones, B. M., Meyer, H., Bobrov, A., and Grosse, G. (2016). Evidence of Multiple Thermokarst Lake Generations From an 11 800-Year-old Permafrost Core on the Northern S Eward P Eninsula, A Laska. *Boreas* 45, 584–603. doi:10.1111/bor.12186

Lipson, D. A., Zona, D., Raab, T. K., Bozzolo, F., Mauritz, M., and Oechel, W. C. (2012). Water-Table Height and Microtopography Control Biogeochemical Cycling in an Arctic Coastal Tundra Ecosystem. *Biogeosciences* 9, 577–591. doi:10.5194/bg-9-577-2012

Lützow, M. v., Kögel-Knabner, I., Ekschmitt, K., Matzner, E., Guggenberger, G., Marschner, B., et al. (2006). Stabilization of Organic Matter in Temperate Soils: Mechanisms and Their Relevance Under Different Soil Conditions - a Review. *Eur. J. Soil Sci.* 57, 426–445. doi:10.1111/j.1365-2389.2006.00809.x

Manasypov, R. M., Vorobyev, S. N., Loiko, S. V., Kritzkov, I. V., Shirokova, L. S., Shevchenko, V. P., et al. (2015). Seasonal Dynamics of Organic Carbon and Metals in Thermokarst Lakes from the Discontinuous Permafrost Zone of Western Siberia. *Biogeosciences* 12, 3009–3028. doi:10.5194/bg-12-3009-2015

McKeague, J. A., and Day, J. H. (1966). Dithionite- and Oxalate-Extractable Fe and Al as Aids in Differentiating Various Classes of Soils. *Can. J. Soil Sci.* 46, 13–22. doi:10.4141/cjss66-003

Mehra, O. P., and Jackson, M. L. (2013). Iron Oxide Removal from Soils and Clays by a Dithionite-Citrate System Buffered with Sodium Bicarbonate. *Clays Clay Miner*, 317–327. doi:10.1016/B978-0-08-009235-5.50026-7

Monhonval, A., Opfergelt, S., Mauclet, E., Pereira, B., Vandeuren, A., Grosse, G., et al. (2020). Data from: Yedoma Domain Mineral Concentrations Assessment (YMCA). *PANGAEA Digital Repository.* doi:10.1594/PANGAEA.922724

Mu, C. C., Zhang, T. J., Zhao, Q., Guo, H., Zhong, W., Su, H., et al. (2016). Soil Organic Carbon Stabilization by Iron in Permafrost Regions of the Qinghai-Tibet Plateau. *Geophys. Res. Lett.* 43 (10), 286–310. doi:10.1002/2016GL070071

Murton, J. B., Goslar, T., Edwards, M. E., Bateman, M. D., Danilov, P. P., Savvinov, G. N., et al. (2015). Palaeoenvironmental Interpretation of Yedoma Silt (Ice Complex) Deposition as Cold-Climate Loess, Duvanny Yar, Northeast Siberia. *Permafrost Periglac. Process.* 26, 208–288. doi:10.1002/ppp.1843

National research centre for CRM (1986). *Institute of Geophysical and Geochemical Exploration Component (GBW 07401- GBW 07404)*. Langfang, China.

Nitzbon, J., Westermann, S., Langer, M., Martin, L. C. P., Strauss, J., Laboor, S., et al. (2020). Fast Response of Cold Ice-Rich Permafrost in Northeast Siberia to a Warming Climate. *Nat. Commun.* 11, 2201. doi:10.1038/s41467-020-15725-8

Olefeldt, D., Goswami, S., Grosse, G., Hayes, D., Hugelius, G., Kuhry, P., et al. (2016). Circumpolar Distribution and Carbon Storage of Thermokarst Landscapes. *Nat. Commun.* 7, 13043. doi:10.1038/ncomms13043

Opel, T., Wetterich, S., Meyer, H., Dereviagin, A. Y., Fuchs, M. C., and Schirrmeister, L. (2017). Ground-ice Stable Isotopes and Cryostratigraphy Reflect Late Quaternary Palaeoclimate in the Northeast Siberian Arctic (Oyogos Yar Coast, Dmitry Laptev Strait). *Clim. Past Discuss.* 13, 587–611. doi:10.5194/cp-13-587-2017

Opfergelt, S. (2020). The Next Generation of Climate Model Should Account for the Evolution of mineral-organic Interactions with Permafrost Thaw. *Environ. Res. Lett.* 15, 091003. doi:10.1088/1748-9326/ab9a6d

Parfitt, R., and Childs, C. (1988). Estimation of Forms of Fe and Al - a Review, and Analysis of Contrasting Soils by Dissolution and Mossbauer Methods. *Soil Res.* 26, 121–144. doi:10.1071/sr9880121

Patzner, M. S., Mueller, C. W., Malusova, M., Baur, M., Nikeleit, V., Scholten, T., et al. (2020). Iron mineral Dissolution Releases Iron and Associated Organic Carbon during Permafrost Thaw. *Nat. Commun.* 11, 6329. doi:10.1038/s41467-020-20102-6

Pewe, T. L., and Journaux, A. (1983). Origin and Character of Loess-like silt in Unglaciated South- central Yakutia, Siberia, USSR. *US Geol. Surv. Prof. Pap.* 1262, 46. doi:10.3133/pp1262

Pokrovsky, O. S., Shirokova, L. S., Manasypov, R. M., Kirpotin, S. N., Kulizhsky, S. P., Kolesnichenko, L. G., et al. (2014). Thermokarst Lakes of Western Siberia: a Complex Biogeochemical Multidisciplinary Approach. *Int. J. Environ. Stud.* 71, 733–748. doi:10.1080/00207233.2014.942535

Pye, K. (1995). The Nature, Origin and Accumulation of Loess. *Quat. Sci. Rev.* 14, 653–667. doi:10.1016/0277-3791(95)00047-X

R Core Team (2018). *R: A Language and Environment for Statistical Computing*. Vienna, Austria: R Foundation for Statistical Computing. URL https://www.R-project.org/.

Rauch, J. N., and Pacyna, J. M. (2009). Earth's Global Ag, Al, Cr, Cu, Fe, Ni, Pb, and Zn Cycles. *Glob. Biogeochem. Cycles.* 23, a. doi:10.1029/2008GB003376

Ravansari, R., Wilson, S. C., and Tighe, M. (2020). Portable X-ray Fluorescence for Environmental Assessment of Soils: Not Just a point and Shoot Method. *Environ. Int.* 134, 105250. doi:10.1016/j.envint.2019.105250

Rennert, T. (2019). Wet-chemical Extractions to Characterise Pedogenic Al and Fe Species - a Critical Review. *Soil Res.* 57, 1. doi:10.1071/SR18299

Riedel, T., Zak, D., Biester, H., and Dittmar, T. (2013). Iron Traps Terrestrially Derived Dissolved Organic Matter at Redox Interfaces. *Proc. Natl. Acad. Sci.* 110, 10101–10105. doi:10.1073/pnas.1221487110

Rivkina, E. M., Fedorov-Davydov, D. G., Zakharyuk, A. G., Shcherbakova, V. A., and Vishnivetskaya, T. A. (2020). Free Iron and Iron-Reducing Microorganisms in Permafrost and Permafrost-Affected Soils of Northeastern Siberia. *Eurasian Soil Sci.* 53, 1455–1468. doi:10.1134/S1064229320100166

Rudnick, R. L., and Gao, S. (2003). Composition of the continental Crust. *Treatise Geochem.* 3, 1–64. doi:10.1016/B0-08-043751-6/03016-4

Salvadó, J. A., Tesi, T., Andersson, A., Ingri, J., Dudarev, O. V., Semiletov, I. P., et al. (2015). Organic Carbon Remobilized from Thawing Permafrost Is Resequestered by Reactive Iron on the Eurasian Arctic Shelf. *Geophys. Res. Lett.* 42, 8122–8130. doi:10.1002/2015GL066058

Schirrmeister, L., Dietze, E., Matthes, H., Grosse, G., Strauss, J., Laboor, S., et al. (2020). The Genesis of Yedoma Ice Complex Permafrost - Grain-Size Endmember Modeling Analysis from Siberia and Alaska. *E&g Quat. Sci. J.* 69, 33–53. doi:10.5194/egqsj-69-33-2020

Schirrmeister, L., Froese, D., Tumskoy, V., Grosse, G., and Wetterich, S. (2013). "Yedoma: Late Pleistocene Ice-Rich Syngenetic Permafrost of Beringia," in *Encyclopedia of Quaternary Science*. Editor S.A. Elias. 2nd edition (Amsterdam: Elsevier), 542–552. doi:10.1016/b978-0-444-53643-3.00106-0

Schirrmeister, L., Grosse, G., Kunitsky, V., Magens, D., Meyer, H., Dereviagin, A., et al. (2008). Periglacial Landscape Evolution and Environmental Changes of Arctic lowland Areas for the Last 60 000 Years (Western Laptev Sea Coast, Cape Mamontov Klyk). *Polar Res.* 27, 249–272. doi:10.1111/j.1751-8369.2008.00067.x

Schirrmeister, L., Grosse, G., Kunitsky, V. V., Fuchs, M. C., Krbetschek, M., Andreev, A. A., et al. (2010). The Mystery of Bunge Land (New Siberian Archipelago): Implications for its Formation Based on Palaeoenvironmental Records, Geomorphology, and Remote Sensing. *Quat. Sci. Rev.* 29, 3598–3614. doi:10.1016/j.quascirev.2009.11.017

Schirrmeister, L., Grosse, G., Kunitsky, V. V., Meyer, H., Dereviagyn, A. Y., and Kuznetsova, T. V. (2003a). Permafrost, Periglacial and Paleo-Environmental Studies on New Siberian Islands. *Rep. Polar Res.* 466, 195–314.

Schirrmeister, L., Grosse, G., Schwamborn, G., Andreev, A. A., Meyer, H., Kunitsky, V. V., et al. (2003b). Late Quaternary History of the Accumulation plain North of the Chekanovsky Ridge (Lena Delta, Russia): A Multidisciplinary Approach. *Polar Geogr.* 27, 277–319. doi:10.1080/789610225

Schirrmeister, L., Kunitsky, V., Grosse, G., Wetterich, S., Meyer, H., Schwamborn, G., et al. (2011). Sedimentary Characteristics and Origin of the Late Pleistocene Ice Complex on north-east Siberian Arctic Coastal Lowlands and Islands - A Review. *Quat. Int.* 241, 3–25. doi:10.1016/j.quaint.2010.04.004

Schirrmeister, L., Meyer, H., Andreev, A., Wetterich, S., Kienast, F., Bobrov, A., et al. (2016). Late Quaternary Paleoenvironmental Records from the Chatanika River valley Near Fairbanks (Alaska). *Quat. Sci. Rev.* 147, 259–278. doi:10.1016/j.quascirev.2016.02.009

Schirrmeister, L., Schwamborn, G., Overduin, P. P., Strauss, J., Fuchs, M. C., Grigoriev, M., et al. (2017). Yedoma Ice Complex of the Buor Khaya Peninsula (Southern Laptev Sea). *Biogeosciences* 14, 1261–1283. doi:10.5194/bg-14-1261-2017

Schirrmeister, L., Siegert, C., Kuznetsova, T., Kuzmina, S., Andreev, A., Kienast, F., et al. (2002). Paleoenvironmental and Paleoclimatic Records from Permafrost Deposits in the Arctic Region of Northern Siberia. *Quat. Int.* 89, 97–118. doi:10.1016/S1040-6182(01)00083-0

Schirrmeister, L., Wagner, D., Grigoriev, M., and Bolshiyanov, D. (2007). The Expedition LENA 2005 , Berichte zur Polar- und Meeresforschung (Reports on Polar and Marine Research), Bremerhaven, *Alfred Wegener Inst. Polar Mar. Res.* 550, 289. doi:10.2312/BzPM_0550_2007

Schmidt, M. W. I., Torn, M. S., Abiven, S., Dittmar, T., Guggenberger, G., Janssens, I. A., et al. (2011). Persistence of Soil Organic Matter as an Ecosystem Property. *Nature* 478, 49–56. doi:10.1038/nature10386

Schneider von Deimling, T., Grosse, G., Strauss, J., Schirrmeister, L., Morgenstern, A., Schaphoff, S., et al. (2015). Observation-based Modelling of Permafrost Carbon Fluxes with Accounting for Deep Carbon Deposits and Thermokarst Activity. *Biogeosciences* 12, 3469–3488. doi:10.5194/bg-12-3469-2015

Schuur, E. A. G., Bockheim, J., Canadell, J. G., Euskirchen, E., Field, C. B., Goryachkin, S. V., et al. (2008). Vulnerability of Permafrost Carbon to Climate Change: Implications for the Global Carbon Cycle. *BioScience* 58, 701–714. doi:10.1641/B580807

Schwamborn, G., Rachold, V., and Grigoriev, M. N. (2002). Late Quaternary Sedimentation History of the Lena Delta. *Quat. Int.* 89, 119–134. doi:10.1016/S1040-6182(01)00084-2

Schwertmann, U. (1991). Solubility and Dissolution of Iron Oxides. *Plant Soil* 130, 1–25. doi:10.1007/BF00011851

Siegert, C., Schirrmeister, L., and Babiy, O. (2002). The Sedimentological, Mineralogical and Geochemical Composition of Late Pleistocene Deposits from the Ice Complex on the Bykovsky peninsula, Northern Siberia. *Polarforsch* 70, 3–11.

Strauss, J., Laboor, S., Fedorov, A. N., Fortier, D., Froese, D., Fuchs, M., et al. (2016). Database of Ice-Rich Yedoma Permafrost (IRYP). doi:10.1594/PANGAEA.861733

Strauss, J. (2010). *Late Quaternary Environmental Dynamics at the Duvanny Yar Key Section, Lower Kolyma, East Siberia. Diploma Thesis*. Potsdam: Potsdam University.

Strauss, J., Schirrmeister, L., Grosse, G., Fortier, D., Hugelius, G., Knoblauch, C., et al. (2017). Deep Yedoma Permafrost: A Synthesis of Depositional Characteristics and Carbon Vulnerability. *Earth-Science Rev.* 172, 75–86. doi:10.1016/j.earscirev.2017.07.007

Strauss, J., Schirrmeister, L., Grosse, G., Wetterich, S., Ulrich, M., Herzschuh, U., et al. (2013). The Deep Permafrost Carbon Pool of the Yedoma Region in Siberia and Alaska. *Geophys. Res. Lett.* 40, 6165–6170. doi:10.1002/2013GL058088

Strauss, J., Schirrmeister, L., Wetterich, S., Borchers, A., and Davydov, S. P. (2012). Grain-size Properties and Organic-carbon Stock of Yedoma Ice Complex Permafrost from the Kolyma lowland, Northeastern Siberia. *Glob. Biogeochem. Cycles.* 26 (3). doi:10.1029/2011GB004104

Till, A. B., Dumoulin, J. A., Harris, A. G., Moore, T. E., Bleick, H. A., and Siwiec, B. R. (2008). Bedrock Geologic Map of the Southern Brooks Range, Alaska, and Accompanying Conodont Data. *U.S. Geol. Surv. Open-File Rep.*, 88, 2008 . Available at: http://pubs.usgs.gov/of/2008/1149/.

Tomirdiaro, S. V., and Chernen'kiy, O. (1987). *Cryogenic Deposits of East Arctic and Sub Arctic.* Russian: ANSSSR Far-East-Sci. Cent., 196.

Treat, C. C., Kleinen, T., Broothaerts, N., Dalton, A. S., Dommain, R., Douglas, T. A., et al. (2019). Widespread Global Peatland Establishment and Persistence over the Last 130,000 Y. *Proc. Natl. Acad. Sci. USA.* 116, 4822–4827. doi:10.1073/pnas.1813305116

Turetsky, M. R., Abbott, B. W., Jones, M. C., Anthony, K. W., Olefeldt, D., Schuur, E. A. G., et al. (2020). Carbon Release through Abrupt Permafrost Thaw. *Nat. Geosci.* 13, 138–143. doi:10.1038/s41561-019-0526-0

Walker, D. A., and Everett, K. R. (1991). Loess Ecosystems of Northern Alaska: Regional Gradient and Toposequence at Prudhoe Bay. *Ecol. Monogr.* 61, 437–464. doi:10.2307/2937050

Walter, K. M., Edwards, M. E., Grosse, G., Zimov, S. A., and Chapin, F. S. (2007). Thermokarst Lakes as a Source of Atmospheric CH4 during the Last Deglaciation. *Science* 318, 633–636. doi:10.1126/science.1142924

Weiss, N., Blok, D., Elberling, B., Hugelius, G., Jørgensen, C. J., Siewert, M. B., et al. (2016). Thermokarst Dynamics and Soil Organic Matter Characteristics Controlling Initial Carbon Release from Permafrost Soils in the Siberian Yedoma Region. *Sediment. Geology.* 340, 38–48. doi:10.1016/j.sedgeo.2015.12.004

Wetterich, S., Grosse, G., Schirrmeister, L., Andreev, A. A., Bobrov, A. A., Kienast, F., et al. (2012). Late Quaternary Environmental and Landscape Dynamics Revealed by a Pingo Sequence on the Northern Seward Peninsula, Alaska. *Quat. Sci. Rev.* 39, 26–44. doi:10.1016/j.quascirev.2012.01.027

Wetterich, S., Kuzmina, S., Andreev, A. A., Kienast, F., Meyer, H., Schirrmeister, L., et al. (2008). Palaeoenvironmental Dynamics Inferred from Late Quaternary Permafrost Deposits on Kurungnakh Island, Lena Delta, Northeast Siberia, Russia. *Quat. Sci. Rev.* 27, 1523–1540. doi:10.1016/j.quascirev.2008.04.007

Wetterich, S., Rudaya, N., Tumskoy, V., Andreev, A. A., Opel, T., Schirrmeister, L., et al. (2011a). Last Glacial Maximum Records in Permafrost of the East Siberian Arctic. *Quat. Sci. Rev.* 30, 3139–3151. doi:10.1016/j.quascirev.2011.07.020

Wetterich, S., Schirrmeister, L., and Kholodov, A. L. (2011b). The Joint Russian-German Expedition Beringia/Kolyma 2008 during the International Polar Year (IPY) 2007/2008. *Berichte zur Polar- Meeresforschung (Reports Polar Mar. Research), Bremerhaven, Germany, Alfred-Wegener Inst. Polar Mar. Res.* 636, 48. doi:10.2312/BzPM_0636_2011

Wetterich, S., Schirrmeister, L., Andreev, A. A., Pudenz, M., Plessen, B., Meyer, H., et al. (2009). Eemian and Late Glacial/Holocene Palaeoenvironmental Records from Permafrost Sequences at the Dmitry Laptev Strait (NE Siberia, Russia). *Palaeogeogr. Palaeoclimatol. Palaeoecol.* 279, 73–95. doi:10.1016/j.palaeo.2009.05.002

Wetterich, S., Tumskoy, V., Rudaya, N., Andreev, A. A., Opel, T., Meyer, H., et al. (2014). Ice Complex Formation in Arctic East Siberia during the MIS3 Interstadial. *Quat. Sci. Rev.* 84, 39–55. doi:10.1016/j.quascirev.2013.11.009

Wilson, S. A. (1997). Data Compilation for USGS Reference Material BHVO-2, Hawaian Basalt. *US Geol. Surv. Open-file Rep.* 2.

Windirsch, T., Grosse, G., Ulrich, M., Schirrmeister, L., Fedorov, A. N., Konstantinov, P. Y., et al. (2020). Organic Carbon Characteristics in Ice-Rich Permafrost in Alas and Yedoma Deposits, central Yakutia, Siberia. *Biogeosciences* 17, 3797–3814. doi:10.5194/bg-17-3797-2020

Winkler, P., Kaiser, K., Thompson, A., Kalbitz, K., Fiedler, S., and Jahn, R. (2018). Contrasting Evolution of Iron Phase Composition in Soils Exposed to Redox Fluctuations. *Geochimica et Cosmochimica Acta.* 235, 89–102. doi:10.1016/j.gca.2018.05.019

Conflict of Interest: The authors declare that the research was conducted in the absence of any commercial or financial relationships that could be construed as a potential conflict of interest.

The handling editor is currently organizing a Research Topic with one of the authors LS.

Publisher's Note: All claims expressed in this article are solely those of the authors and do not necessarily represent those of their affiliated organizations, or those of the publisher, the editors and the reviewers. Any product that may be evaluated in this article, or claim that may be made by its manufacturer, is not guaranteed or endorsed by the publisher.

frontiers in Earth Science

ORIGINAL RESEARCH
published: 11 August 2021
doi: 10.3389/feart.2021.704141

Geochemistry and Weathering Indices of Yedoma and Alas Deposits beneath Thermokarst Lakes in Central Yakutia

Mathias Ulrich[1]*, Loeka L. Jongejans[2,3], Guido Grosse[2,3], Birgit Schneider[4], Thomas Opel[5], Sebastian Wetterich[2], Alexander N. Fedorov[6,7], Lutz Schirrmeister[2], Torben Windirsch[2,3], Julia Wiedmann[2] and Jens Strauss[2]

[1]Institute for Geography, Geoinformatics and Remote Sensing, Leipzig University, Leipzig, Germany, [2]Permafrost Research Unit, Alfred Wegener Institute Helmholtz Centre for Polar and Marine Research, Potsdam, Germany, [3]Institute of Geosciences, University of Potsdam, Potsdam, Germany, [4]Institute for Geography, Physical Geography, Leipzig University, Leipzig, Germany, [5]Polar Terrestrial Environmental Systems, Alfred Wegener Institute Helmholtz Centre for Polar and Marine Research, Potsdam, Germany, [6]Laboratory of General Geocryology, Melnikov Permafrost Institute, Siberian Branch Russian Academy of Sciences, Yakutsk, Russia, [7]BEST International Centre, North-Eastern Federal University, Yakutsk, Russia

OPEN ACCESS

Edited by:
Daniel Nývlt,
Masaryk University, Czechia

Reviewed by:
Sophie Opfergelt,
Catholic University of Louvain, Belgium
Julien Fouché,
Montpellier SupAgro, France

***Correspondence:**
Mathias Ulrich
mathias.ulrich@uni-leipzig.de

Specialty section:
This article was submitted to Quaternary Science, Geomorphology and Paleoenvironment, a section of the journal Frontiers in Earth Science

Received: 01 May 2021
Accepted: 31 July 2021
Published: 11 August 2021

Citation:
Ulrich M, Jongejans LL, Grosse G, Schneider B, Opel T, Wetterich S, Fedorov AN, Schirrmeister L, Windirsch T, Wiedmann J and Strauss J (2021) Geochemistry and Weathering Indices of Yedoma and Alas Deposits beneath Thermokarst Lakes in Central Yakutia. Front. Earth Sci. 9:704141. doi: 10.3389/feart.2021.704141

Ice- and organic-rich deposits of late Pleistocene age, known as Yedoma Ice Complex (IC), are widespread across large permafrost regions in Northeast Siberia. To reconstruct Yedoma IC formation in Central Yakutia, we analyzed the geochemistry, sedimentology, and stratigraphy of thawed and frozen deposits below two thermokarst lakes in different evolutionary stages (a mature alas lake and a initial Yedoma lake) from the Yukechi site in the Lena-Aldan interfluve. We focused on inorganic geochemical characteristics and mineral weathering in two ~17 m long sediment cores to trace syngenetic permafrost aggradation and degradation over time. Geochemical properties, element ratios, and specific weathering indices reflect varying sedimentation processes and seasonal thaw depths under variable environmental conditions. Deeper thaw during the interstadial Marine Isotope Stage (MIS) 3 enabled increasing mineral weathering and initial thermokarst processes. Sedimentological proxies reflect high transport energy and short transport paths and mainly terrestrial sediment supply. The Yedoma formation resulted from fluvial, alluvial and aeolian processes. Low mean TOC contents in both cores contrast with Yedoma deposits elsewhere. Likely, this is a result of the very low organic matter content of the source material of the Yukechi Yedoma. Pronounced cryostructures and strongly depleted pore water stable isotopes show a perennially frozen state and preserved organic matter for the lower part of the Yedoma lake core, while changing permafrost conditions, conditions promoting weathering, and strong organic matter decomposition are suggested by our proxies for its middle and upper parts. For the alas lake core, less depleted water stable isotopes reflect the influence of recent precipitation, i.e. the infiltration of rain and lake water into the unfrozen ground. The FENG, $MIA_{(R)}$, and ICV weathering indices have proven to be promising proxies for the identification of conditions that promote mineral weathering to different degrees in the stratigraphy of the thawed and frozen Yedoma deposits, for which we assume a rather homogeneous chemical composition of the parent material. Our study highlights that the understanding of environmental conditions during Yedoma formation and degradation processes by specific geochemical proxies is crucial for assessing the potential decomposition and preservation of the frozen and unfrozen Yedoma inventories.

Keywords: inorganic geochemistry characteristics, weathering indices, thermokarst landscapes, Siberia (Russia), environmental reconstruction, permafrost, XRF (X-ray fluorescence analysis), talik

INTRODUCTION

Permafrost is a key element of the cryosphere and stores large amounts of organic carbon (OC) (Hugelius et al., 2014). The Arctic amplification of global warming affects permafrost regions by accelerating permafrost warming and thaw (Biskaborn et al., 2019). When frozen ground thaws, OC, nutrients and other formerly frozen chemical compounds will be reintroduced into active (bio)geochemical cycles (Opfergelt, 2020). Soil microbes could use these inventories to release greenhouse gases (GHG), which will accelerate climate warming and is known as the permafrost-carbon feedback (Schuur et al., 2015). It was shown that extensive remobilization of organic matter (OM) stored in permafrost occurred during the last major warming period at the Pleistocene-Holocene transition (Martens et al., 2020).

Permafrost degrades in different ways, depending on climate and permafrost conditions such as ground-ice content and ground temperature. The formation and development of thermokarst lakes is the most abundant form of permafrost degradation (Grosse et al., 2013). Today, millions of thermokarst lakes in different sizes and remnant lake basins can be found in the northern lowland permafrost regions of Canada, Alaska, Scandinavia, and Russia (Nitze et al., 2017; Muster et al., 2019). The two to four times higher heat storage capacity of water (compared to ice and dry ground) usually causes an ongoing increase of lake water volume and depth resulting in mean annual lake bottom temperatures above 0°C at the water-sediment interface (Grosse et al., 2013). This typically results in the formation of a talik, a body of perennially unfrozen ground occurring in a permafrost area. Anaerobic environments at the lake bottom and in the talik sediments beneath the lakes lead to specific sedimentary and geochemical conditions. Related microbial decomposition of OM and methane production contributes substantially to the current atmospheric carbon budget (Heslop et al., 2020). Hence, thermokarst lakes and taliks are important sources for atmospheric GHG, mainly carbon dioxide and methane (Walter-Anthony et al., 2018; Dean et al., 2020).

Widespread thermokarst basin (alas) formation in Central Yakutia during the late Pleistocene-Holocene transition and the Holocene Thermal Maximum (HTM) led to a lake-rich thermokarst landscape (Soloviev, 1973; Ulrich et al., 2017a; Ulrich et al., 2019). After thermokarst lake drainage, flat basins with steep-sided slopes and treeless grass-dominated meadows remained, which often contain shallow remnant thermokarst lakes. These alas landscapes have mainly developed in ice-rich and silt-dominated syngenetic late Pleistocene Yedoma Ice Complex (IC) deposits that cover large areas of Siberia, Alaska, and Canada. They can reach 50 m in thickness and usually contain huge ice wedges of several meters in width and height (Ulrich et al., 2014; Strauss et al., 2017). A striking feature of the East Siberian Yedoma IC is the relatively high OC content between 1.2 and 4.8 wt% (Schirrmeister et al., 2011). Strauss et al. (2017) calculated an amount of 398 Gt OC for the total circum-Arctic Yedoma domain (1.4 million km^2, including thermokarst lakes and basins). However, recent carbon inventory studies of Central Yakutian Yedoma deposits show significantly lower levels of OC (Ø 0.4–0.7 wt%; Windirsch et al., 2020; Jongejans et al., 2021a).

Simultaneously with the thermokarst-induced degradation of OM, geochemical processes and mineral weathering occur in different intensities and can be assessed relative to the chemical composition of the parent material (Zolkos and Tank, 2020). In cold climates, the physical weathering of clayey, silty and sandy source rocks and deposits determines the grain size of the material that is available for transport from local and regional sources (Schwamborn et al., 2012; Schirrmeister et al., 2020). Chemical weathering changes the mineral composition of the sediments, and thereby influences biogeochemical processes during thaw periods but is usually hampered by the permanent frozen conditions. Mineral weathering could even contribute to the fixation of carbon in the sediment (Zolkos et al., 2018; Zolkos and Tank, 2020). However, the effects of inorganic geochemical processes and mineral weathering during sedimentation, syngenetic permafrost aggradation, and thermokarst processes have been rarely studied so far in permafrost deposits (Lacelle et al., 2008; Kokelj et al., 2013; Zolkos et al., 2018; Zolkos and Tank, 2020) and especially for Yedoma IC deposits data are sparse (Zech et al., 2008). Furthermore, these processes are not yet included in climate prediction models and there are still uncertainties about the extent and impact of permafrost dynamics and degradation (Opfergelt, 2020; Turetsky et al., 2020).

The origin of Yedoma deposits, their degradation, and associated biogeochemical processes can be heterogeneous, but the sediment source is generally seen in the local environment (Schirrmeister et al., 2013; Schirrmeister et al., 2020). A knowledge gap remains how the late Pleistocene to Holocene permafrost landscape as well as related depositional and environmental conditions evolved in Central Yakutia. Furthermore, it is unclear how the various sedimentological and biogeochemical processes during Yedoma IC deposition and transformation as well as the formation of thermokarst lake basins affect the deposition and decomposition of OM. Consequently, it is essential to determine effects of organic and inorganic geochemical processes during permafrost degradation, in order to assess ongoing environmental changes and their potential impact on global climatic trends.

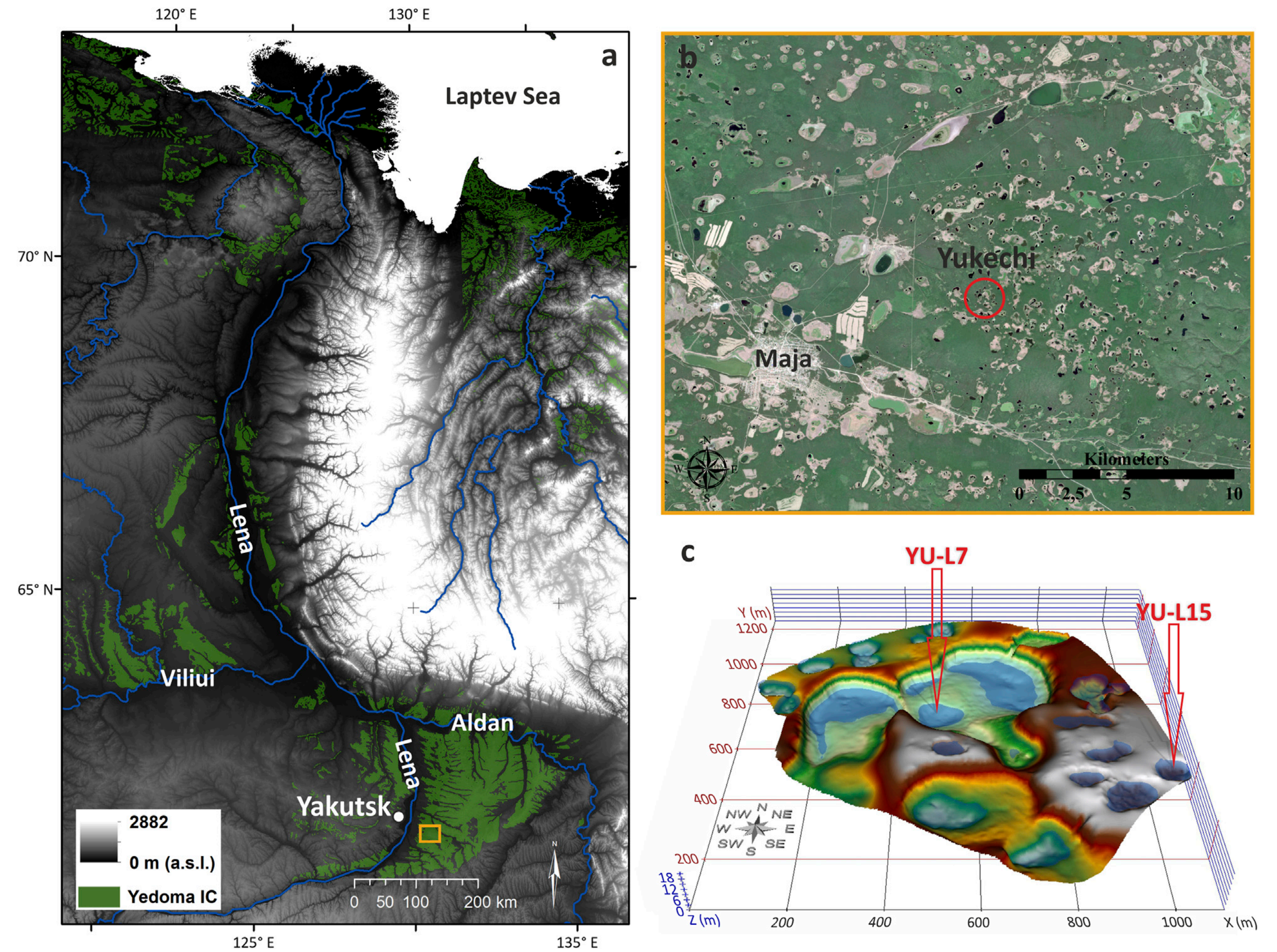

FIGURE 1 | Overview of the study area in Central Yakutia, Russia. **(A)** Location of the study area (orange square) near Yakutsk (Yedoma IC coverage after Strauss et al. (2016), Digital Elevation Model (DEM) generated using data from the ESA DUE Permafrost Project (Santoro and Strozzi, 2012). **(B)** Close up of the Yukechi study site within the typical Yakutian alas landscape (Sentinel-2 (ESA) 2017–07–29). **(C)** DEM with drilling locations on the alas lake (YU-L7) and the Yedoma lake (YU-L15). Height differences are obvious from the z-axis (Modified after Ulrich et al., 2017b).

In this study our major aims were 1) to reconstruct the late Pleistocene to Holocene depositional processes in the study area, 2) to define proxies of freeze and thaw conditions throughout sedimentation, syngenetic permafrost aggradation and subsequent degradation, and 3) to characterize inorganic geochemical processes and mineral weathering during Yedoma formation and degradation.

REGIONAL SETTING

The study area is located in the continuous permafrost zone, which in large parts of Yakutia is particularly characterized by Yedoma IC deposits (**Figure 1A**). Permafrost depths can reach several hundred meters here (Czudek and Demek, 1970). The active layer thickness reaches depths of up to 1.0 m below forests and up to 2.0 m in grassland areas (Iijima et al., 2010). The region is a low-relief landscape, characterized by numerous alas basins and thermokarst lakes in different evolutionary stages (Soloviev, 1959; Soloviev, 1973; Pestryakova et al., 2012; Tarasenko, 2013) and showed a remarkable increase in lake area of almost 50% during the last 15 years (Nitze et al., 2017; Ulrich et al., 2017b).

Central Yakutia is characterized by a strong continental climate with low annual precipitation (223 ± 54 mm), high seasonal temperature amplitudes, and a mean annual air temperature of −9.8 ± 1.8°C (based on Yakutsk weather station data for 1910–2014, see Ulrich et al., 2017b). The vegetation is characterized by taiga forest dominated by larch trees with inclusions of pine and birch trees. The alas basins form islands of steppe-like grasslands within the forested Yedoma uplands.

The drilling sites are located in the Lena-Aldan interfluve at approximately 200 m above sea level. Several terraces above the major rivers are differentiated by geomorphology,

FIGURE 2 | Photographs of the drilled lakes at the Yukechi study site during summer with views to Northwest: **(A)** YU-L7, **(B)** YU-L15.

cryolithology, and sediment genesis (Soloviev, 1959; Soloviev, 1973). The investigated Yukechi alas is located near the small city of Maja, about 50 km southeast of the Yakutian capital Yakutsk on the Abalakh terrace (**Figure 1B**) and is monitored for several decades by the Melnikov Permafrost Institute in Yakutsk (e.g., Bosikov 1998; Fedorov and Konstantinov, 2009; Fedorov et al., 2014). The Yukechi alas is about 300 by 500 m in size and about 10–15 m deep (**Figure 1C**). Two larger lakes and one smaller shallow lake exist within the alas (called alas lakes). The area around the alas is characterized by small and young thermokarst lakes on the Yedoma uplands (called Yedoma lakes) that are partly developing in former agricultural areas (Ulrich et al., 2017b).

A mature alas lake within the Yukechi alas (core YU-L7, 61.76397°N, 130.46442°E) and a nearby younger Yedoma lake (core YU-L15, 61.76086°N, 130.47466°E) located about 20 m above the alas ground level were selected as drilling sites. For both lakes, we assume a natural evolution (i.e., no direct anthropogenic interference with lake evolution). Furthermore, we assume a similar parent material for the sediments at the Yukechi study site, although they were altered upon thaw by compaction and degradation/weathering. During field work in March 2015, the alas lake had a diameter of about 100 m and a depth of about 2.3 m. The Yedoma lake was about 80 m in diameter and about 4.4 m deep (**Figure 2**). The lake ice on both lakes was about 70 cm thick and covered by about 35 cm of snow.

MATERIALS AND METHODS

Drilling and Sampling

The deposits below both lakes were drilled from the lake ice in March 2015 during a joint German-Russian field expedition. The drilling depths reached down to about 20–21 m below the lake-ice surface. We used a URB2-47 drilling rig without a core catching system. Due to partly unfrozen sediment layers, parts of the cores were lost during the drilling process. The retrieved core segments were pushed out with air pressure, described and stored in plastic bags and kept frozen until laboratory analysis. From here on, all core depths are given in centimeters as mean depth of a sampling interval below lake-ice surface (cm bls).

Sample Preparation

The frozen cores were split lengthwise using a band saw and were subsequently subsampled in a freezer room at −5°C. After cleaning, the cores were described visually and photographed (**Figure 3**). The sampling half was cut into subsamples and divided for further analysis. We did a regular sampling on both cores according to visual stratigraphy. Hence, the alas lake core YU-L7 was sampled in intervals between 20 and 70 cm ($n = 19$) and the Yedoma lake core YU-L15 at intervals between 10 and 40 cm ($n = 49$).

For the biogeochemical and sedimentological analyses, the gravimetric water and/or ice content was determined as the difference between wet mass of a sample (as ice for *in situ* frozen parts) and the dry sample mass and is expressed in

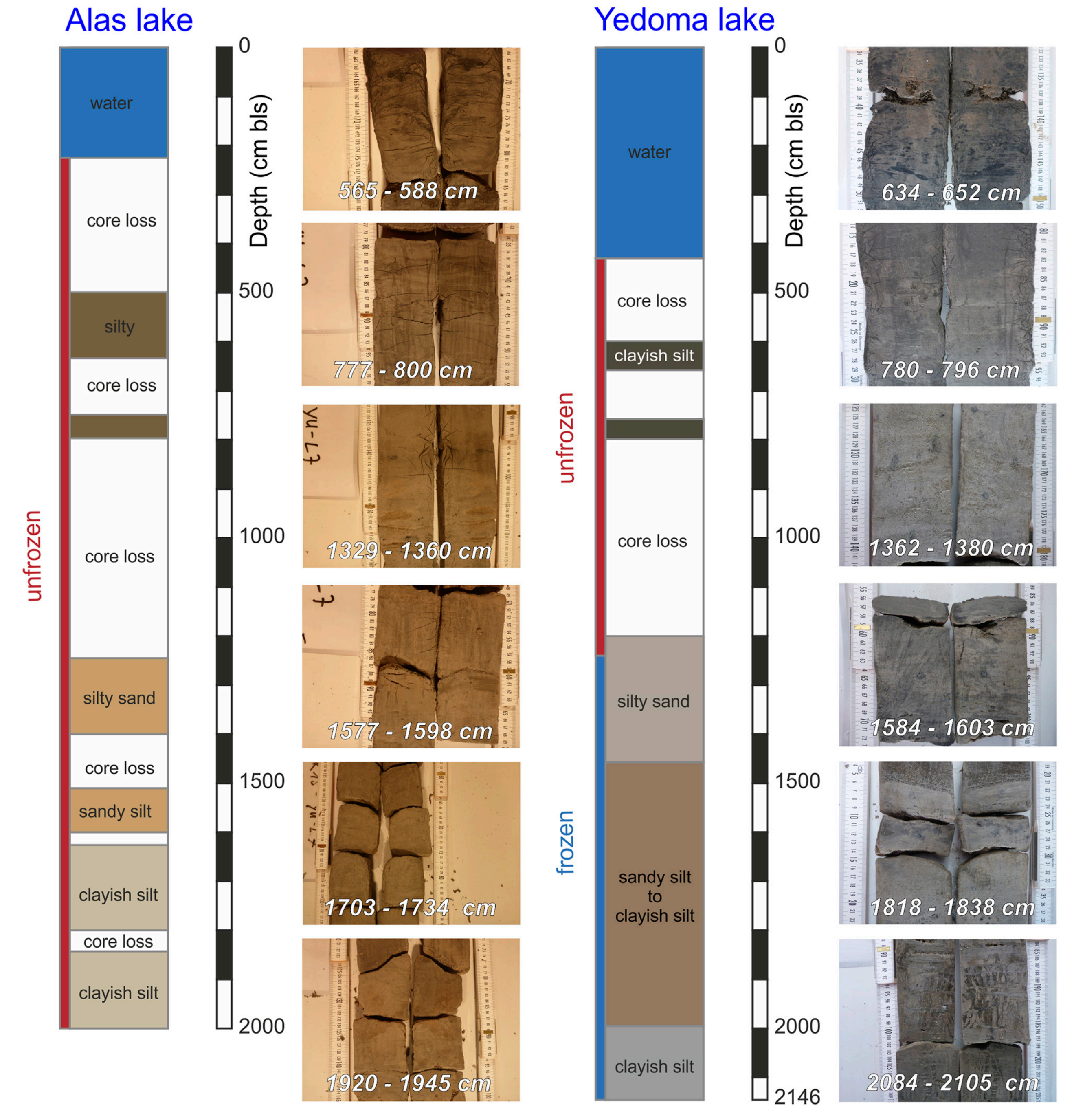

FIGURE 3 | Core profiles of the alas lake core YU-L7 and the Yedoma lake core YU-L15 with dominant sediment layers due to color, grain size and cryostructures.

weight percent (wt%). Unless stated otherwise, we will use the term gravimetric water/ice content (GW/IC) onwards, due to changing unfrozen and frozen conditions within the cores.

Radiocarbon Dating

We radiocarbon-dated seven samples from YU-L7 and eight from YU-L15 using Accelerator Mass Spectrometry (AMS) with the Mini Carbon Dating System (MICADAS) at Alfred Wegener Institute Helmholtz Centre for Polar and Marine Research (AWI) Bremerhaven, Germany (Mollenhauer et al., 2021). Macrofossils such as plant and wooden remains (i.e. roots, leaf fragments, twigs, *Larix* spp. (larch) needles) were picked and dated for nine samples. For the other six samples, bulk sediment was dated. The radiocarbon ages were calibrated using the OxCal4.4 software (Bronk Ramsey, 2009) with the IntCal20 calibration curve after Reimer et al. (2020), and are expressed in calibrated years before present (cal. yrs. BP).

Sedimentology and Biogeochemistry

All subsamples of the YU-L7 alas lake core (n = 19) were analyzed for sedimentology. Of the Yedoma lake core YU-L15, all samples above 1,362 cm and below 2064 cm bls were analyzed but only every second subsample from the middle part (n = 31).

A Bartington Magnetic Susceptibility Meter Model MS2 (Bartington Instruments, United Kingdom) was used to measure the mass-specific magnetic susceptibility (MS). The MS reflects differences in magnetizability of clastic material. Measurements were done at low frequency of 0.465 kHz in an external magnetic field in 10^{-8} m^3/kg.

Grain-size analyses were carried out on organic-free (treated with 35% H_2O_2) sub-samples using a Malvern Mastersizer 3000 (Malvern Instruments, United Kingdom) with an attached Malvern Hydro LV wet-sample dispersion unit. The proportions of sand, silt and clay fractions are given as sums between 2 mm and 63 µm, 63 and 2 µm and <2 µm, respectively. Grain-size parameters were calculated with the software Gradistat (Version 8.0; Blott and Pye, 2001).

We analyzed the total carbon (TC) content using an Elementar Vario EL III (Elementar Analysensysteme GmbH) (detection limit of 0.05 wt%). Furthermore, total organic carbon (TOC) measurements were performed using the Elementar Vario Max C (detection limit of 0.1 wt%). No external removal of the total inorganic carbon (TIC) is needed for this method. The TIC content was calculated as the difference of TOC and TC. All values of TC, TOC, TIC are calculated in wt% (n = 68).

The stable carbon isotope ratio ($\delta^{13}C$) was determined using a ThermoFisher Scientific Delta-V-Advantage gas mass spectrometer equipped with a FLASH elemental analyzer EA 2000 and a CONFLO IV gas mixing system in the Stable Isotope Laboratory at the AWI Potsdam, Germany. An aliquot per sample of 15 samples per core with TOC values above detection limit were measured. The $\delta^{13}C$ measurements have been calibrated by three international reference materials. The results are compared to the common Vienna Pee Dee Belemnite (VPDB) standard and expressed in per mill (‰ vs. VPDB; n = 30; measurement accuracy: equal or smaller than 0.15‰). The $\delta^{13}C$ values give information about plant metabolism, as they are generally very similar to those of the former vegetation. We interpret more negative $\delta^{13}C$ values as an indication of less-degraded OM, while less negative $\delta^{13}C$ values are linked to stronger decomposition processes (Schirrmeister et al., 2011; Strauss et al., 2015).

Pore-Water Hydrochemistry and Stable Water Isotopes

Pore water was extracted from sediment in order to measure stable water isotope ratios. The samples were thawed at 4°C and pore water was extracted using Rhizone soil moisture sampler (Eijkelkamp Soil & Water). The pore size of the membrane was between 0.12 and 0.18 µm. Several sediment subsamples did not hold enough water for pore water extraction. Thus, stable water isotope measurements could be carried out for 42 subsamples of YU-L15 and five subsamples for YU-L7.

Stable water isotopes, i.e. the ratios of hydrogen (δD) and oxygen ($\delta^{18}O$), were measured using a Finnigan MAT Delta-S mass spectrometer following standard procedures described in Meyer et al. (2000). The isotopic ratios of δD and $\delta^{18}O$ were calculated using the software ISODAT and expressed in per mill (‰) relative to the Vienna Standard Mean Ocean Water (VSMOW) value. The analytical precision is better than ±0.1‰ for $\delta^{18}O$ and ±0.1‰ for δD (Meyer et al., 2000). We furthermore calculated the second-order parameter deuterium excess d ($d = \delta D - 8 * \delta^{18}O$, Dansgaard, 1964). While $\delta^{18}O$ and δD in precipitation are considered as temperature proxies (lower values reflect lower temperatures, higher values reflect higher temperatures), d provides information on moisture generation processes, mainly relative humidity and sea surface temperature. Freeze-thaw processes in the active layer cause secondary fractionation processes, which may overprint the original isotopic signatures.

Inorganic Geochemistry

All samples were analyzed for their element concentrations by non-destructive X-ray fluorescence (XRF) spectrometry. Therefore, bulk samples were homogenized, mixed with a wax binder (CEREOX Licowax at a ratio of 4 to 1), and pressed into 32 mm pellets. Measurements were carried out using the Energy-Dispersive Polarisation XRF (EDPXRF) SPECTRO XEPOS (SPECTRO Analytical Instruments Ltd.) analyzer in a helium gas atmosphere. The contents of all elements from sodium to uranium were simultaneously determined and adjusted to sample weight. After intensive literature research, analyzing the measured single elements, and calculating a large number of ratios, we concentrated on six elemental ratios (S/Cl, Ca/Ti, Sr/Ca, Fe_2O_3/MnO, Si/Al, Zr/Al) for detailed discussion of sediment properties and permafrost conditions during Yedoma deposition as well as thermokarst and talik processes. We applied the oxide representation of iron and manganese because both, iron and manganese are characterized by several oxidation states compared to the other element ratios. Thus, the ratio in the oxidized form would be more understandable and easier to compare with literature data. The nominal values of the ratio differ only slightly but would lead to the same conclusions. All measured single element contents for both cores are presented in the **Supplementary Tables 1, 2**.

Mineral Weathering Indices

Multi-element weathering indices provide, relative to the parent material, semi-quantitative measures of mineral weathering intensity, which is directly dependent on, e.g., water availability and temperature conditions. They are traditionally calculated from the concentrations of several mobile (e.g., Ca, K, Na, Mg) and immobile elements (e.g., Al, Fe, Ti, Zr) (Schatz et al., 2015). From the large number of weathering indices (Schatz et al., 2015, *cf.* Table 1), we ultimately selected three indices that best correspond to geochemical conditions in frozen and thawed Yedoma deposits: the FENG, MIA, and ICV indices.

Feng (1997) developed the FENG index in particular for calcareous substrates. In contrast to many other indices, Ca is not taken into account in this index. Since the solution and relocation history of Ca is almost exclusively traced in the case of clearly calcareous initial substrates, misinterpretations can result (Buggle et al., 2011). By placing easily soluble elements in the denominator of the formula, an increase in the FENG index indicates increased weathering. In accordance to Feng (1997), the index is calculated in molar proportions using **Eq. 1**.

$$\mathrm{FENG} = (Al_2O_3+Fe_2O_3)/Na_2O + K_2O + MgO + P_2O_5 \quad (1)$$

Babechuk et al. (2014) proposed the mafic index of weathering (MIA) especially for Mg and Fe-containing minerals. The specific arrangement of the $MIA_{(R)}$ was used in consideration of predominantly reducing soil conditions. This takes into account the redox-dependent weathering behavior of iron. Under reducing conditions, Fe^{2+} responds as a mobile element and is leached along with Mg during the mafic weathering process (Babechuk et al., 2014). Hence, the $MIA_{(R)}$ index increases with increased weathering. In molar proportion and considering only the silicate-bound Ca (CaO*), the $MIA_{(R)}$ calculation is:

$$MIA_{(R)} = 100 \times \left[Al_2O_3/\left(Al_2O_3+Fe_2O_{3(T)}+MgO + CaO^* + Na_2O + K_2O\right)\right] \quad (2)$$

The index of composition variability (ICV) was defined by Cox et al. (1995) and can be applied as a measure of compositional maturity. The index measures the abundance of alumina in relation to other major cations (in molar proportions; Cox et al., 1995).

$$ICV = \left(Fe_2O_3 + K_2O + Na_2O + CaO + MgO + MnO + TiO_2\right)/Al_2O_3 \quad (3)$$

An index value close to 1 shows hardly any mineral conversions, while an index value less than 1 indicates several cycles of weathering, erosion and accumulation; i.e. the smaller the index, the stronger the weathering. This index is therefore inversely proportional to the FENG and the $MIA_{(R)}$ index.

Statistical Analyses

For the examination of relationships between sedimentology as well as organic and inorganic geochemistry of frozen and thawed Yedoma deposits, statistical analyses were performed. Descriptive statistics were carried out using the Python software packages Pandas (McKinney, 2010) and NumPy (Oliphant, 2006). For calculation of Pearson correlation matrices including p-values and to compare the two sediment cores by Mann–Whitney U nonparametric tests the Pingouin statistical package in Python 3 was used (Vallat, 2018). Principal component analysis (PCA) was performed on all pre-selected sedimentological, organic, and inorganic geochemical parameters. Ca, S and Cl were included, additionally, in order to evaluate the influence of these elements on individual elemental ratios. The PCA was carried out using the Python package Scikit-learn (Pedregosa et al., 2011). Since missing values are incompatible with Scikit-learn estimators, the missing values of the grain size parameters from the Yedoma lake core YU-L15 (see above) were initially replaced using the k-Nearest Neighbors approach. By default, an Euclidean distance metric that supports missing values was used to find the nearest neighbors. For more information on methodology see Troyanskaya et al. (2001). For running the PCA, all variables were standardized by subtracting the mean and scaling the actual data range to unit variance (i.e., z-transform). The resulting ordination diagram presents standardized metric scores (i.e. $scale_i = i \times 1.0/(i.max - i.min)$) and expresses the relationship among metrics as correlations. Additionally, all core samples were projected onto the ordination graph for interpretation purposes only, because they do not affect calculations. Finally, the sample scores on the first and second principal component (PC1 and PC2, respectively) were plotted against core depth.

RESULTS

Geochronology

Dating results are shown in **Table 1**. The mean calibrated ages of the YU-L7 alas core showed a general trend over depth ranging from 3,740 cal. yrs. BP at 520 cm bls, over 13,750 cal. yrs. BP at 758 cm bls to 43,020 cal. yrs. BP at 1,998 cm bls. The dating of plant remains at 1,560 cm bls showed an inverse age (49,070 ± 970 cal. yrs. BP). While the youngest calibrated age from the uppermost core part of YU-L7 came from plant remains dating, the other two dates resulted from bulk sediment dating. Three infinite ages at 1,278 cm bls (>24,570 yrs. BP), 1998 cm bls (>39,600 yrs. BP), and 1746 cm bls (>49,300 yrs. BP) generally fitted into the late Pleistocene age sequence.

The mean calibrated radiocarbon ages of the Yedoma lake core YU-L15 showed a relatively short age sequence during the interstadial Marine Isotope Stage (MIS) 3 with a bulk sediment ages of 41,870 cal. yrs. BP at 783 cm bls and 43,540 cal. yrs. BP at 1,917 cm bls. The dating of the plant remains at 1,917 cm bls (43,180 cal. yrs. BP) suggested an age similar to that of the bulk sediment from the same depth, thus confirming the period in which sediments were deposited in this core depth. Plant remains from the uppermost core sample were dated to a nearly modern age (140 ± 80 cal. yrs. BP). The inverse mean age at 1,395 cm bls (51,420 cal. yrs. BP) showed an age near the limit of the ^{14}C calibration curves (Reimer et al., 2020). Three infinite radiocarbon dates of the YU-L15 core also point to late Pleistocene age of the core (**Table 1**).

Sedimentology and Carbon Characteristics

Alas Lake Core YU-L7

Since the talik below the alas lake (lake depth 230 cm bls) could not be drilled through, the core YU-L7 was completely unfrozen. Generally, the sediments appeared relatively homogeneous and showed a brownish-grey to grey color with varying amounts of organic inclusions as well as blackish dots and streaks (**Figure 3**). The whole sediment sequence is composed of unimodally distributed, but poorly to very poorly sorted, clayish-silt to sandy-silt deposits (**Figure 4**). The mean of all grain size distributions (GSDs) is 40 ± 28 μm. The GW/IC (**Figure 5**) was relatively constant over the entire core (mean 23.2 ± 9.5 wt%) with a peak of 60.8 wt% at 1,258 cm bls as an exception. Taking into account the lithological,

TABLE 1 | Radiocarbon dating results for the alas lake core YU-L7 and the Yedoma lake core YU-L15. The mean calibrated ages are rounded to 10 years. Infinite and inverse ages are highlighted in italics.

Lab ID	Sample ID	Sediment condition	Mean depth (cm bls)	Dated material	^{14}C age (uncal. yrs. BP)	SD uncal. (±yrs)	Mean calibrated age, 2σ (cal. yrs. BP)	SD cal. (±years)
AWI.2422.1.1	YUL7_519-521	talik	520	Plant remains	3,473	48	3,740	70
AWI.2421.1.2	YUL7_745-751	talik	748	Bulk sediment	11,789	263	13,750	340
AWI.2420.1.1	YUL7_1276-1280	talik	1,278	Bulk sediment	*>24,570*			
AWI.2419.1.1	YUL7_1559-1562	talik	1,560.5	Plant remains	*46,472*	649	*49,070*	*970*
AWI.2418.1.1	YUL7_1745-1747	talik	1,746	Plant remains	*>49,300*			
AWI.2417.1.1	YUL7_1997-2000	talik	1,998.5	Plant remains	*>39,600*			
AWI.2417.2.2	YUL7_1997-2000	talik	1,998.5	Bulk sediment	39,714	311	43,020	270
AWI.2429.1.1	YUL15_598-601	talik	599.5	Plant remains	134	53	140	80
AWI.2428.1.1	YUL15_779-787	talik	783	Bulk sediment	37,122	247	41,870	180
AWI.2427.1.1	YUL15_1200-1215	talik	1,207.5	Plant remains	*>49,930*			
AWI.2426.1.1	YUL15_1393-1398	permafrost	1,395.5	Plant remains	*48,249*	515	*51,420*	*1,290*
AWI.2425.1.1	YUL15_1589-1593	permafrost	1,591	Plant remains	*>48,990*			
AWI.2424.1.1	YUL15_1915-1920	permafrost	1,917.5	Plant remains	39,120	1,178	43,180	830
AWI.2424.2.1	YUL15_1915-1920	permafrost	1,917.5	Bulk sediment	40,349	349	43,540	360
AWI.2423.1.1	YUL15_2140-2146	permafrost	2,143	Bulk sediment	*>24,570*			

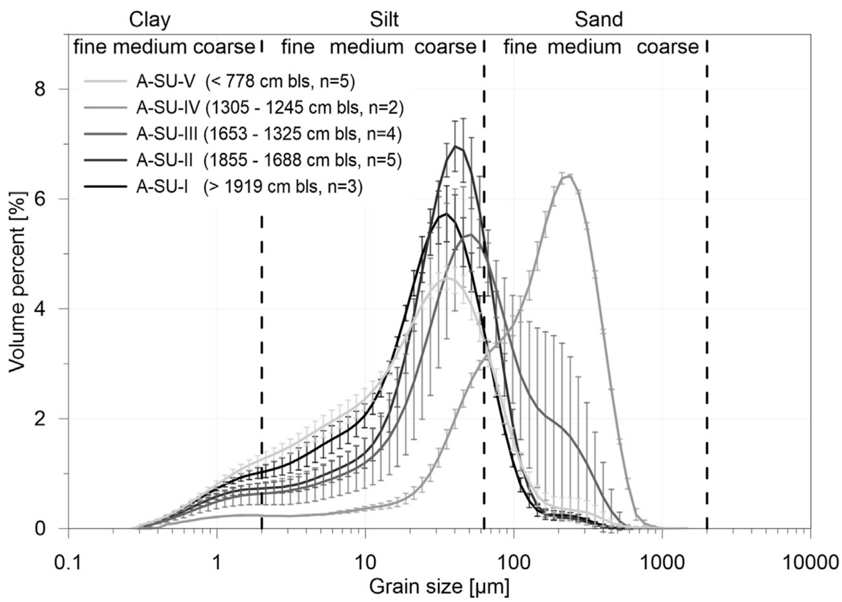

FIGURE 4 | Mean grain-size distributions for each sediment unit of the alas lake core YU-L7 (see also **Figure 5**). The error bars are indicating the standard deviations of individual measured grain sizes.

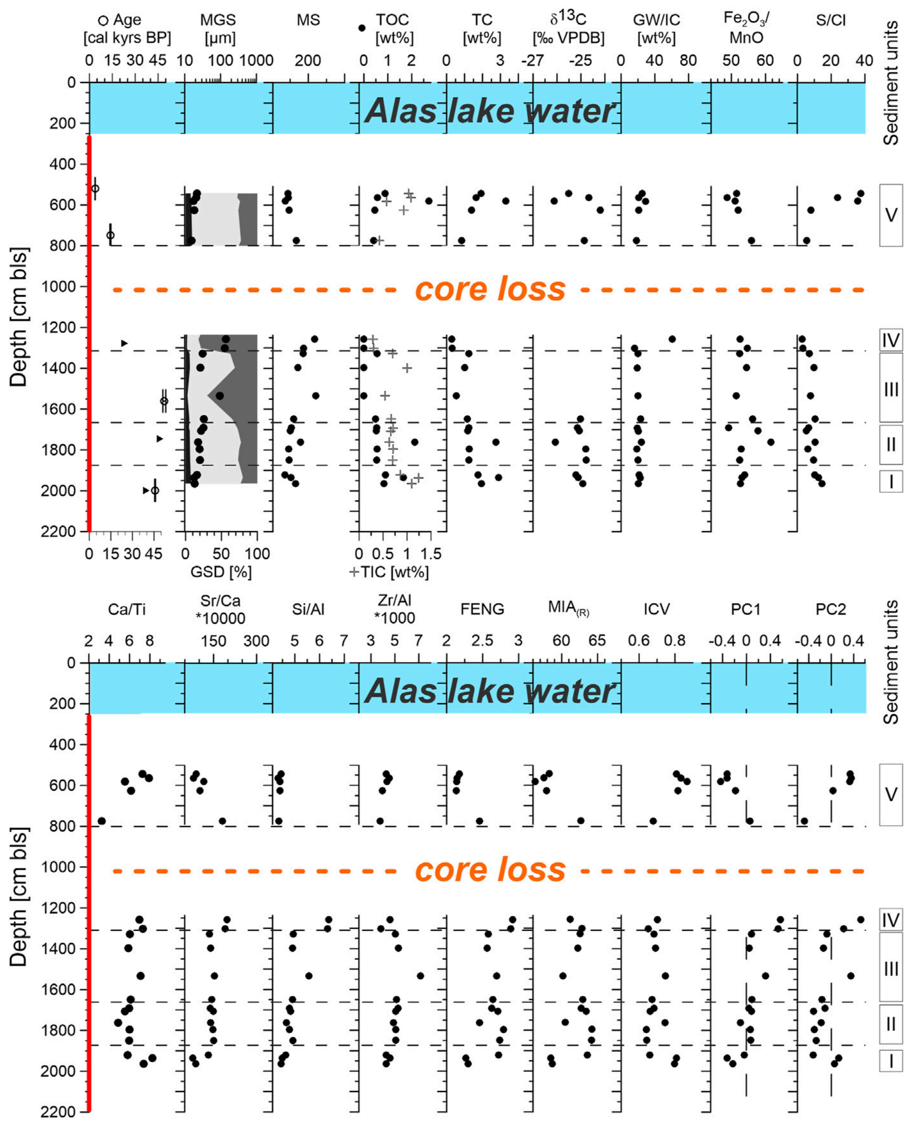

FIGURE 5 | Sedimentological parameters, organic and inorganic geochemistry as well as the weathering indices FENG, $MIA_{(R)}$, ICV and the Principal components (PC) of the alas lake core YU-L7 (MGS, Mean grain size; GSD, Grain-size distribution; MS, Mass-specific magnetic susceptibility; GW/IC, Ground water/ice content). Infinite radiocarbon dates are illustrated by triangles. Unfrozen core depth intervals are marked by red depth scale.

sedimentological, and biogeochemical properties and their characteristic simultaneous variations, the core was divided into five sediment units (A-SU).

The lowest unit (A-SU-I; >1,919 cm bls) was characterized by mean grain size values around 18–21 µm and by GSDs with a distinct peak in the coarse silt fraction (**Figure 4**). The MS decreased over the three unit samples, while TOC, TIC, and TC peaked at 1936 cm bls. The respective sample had a TOC content of 1.7 wt%, which is the third highest value in YU-L7. The $\delta^{13}C$ values varied only slightly around the average of the entire core of −25.1 ± 0.5‰.

In unit A-SU-II (1855–1,688 cm bls), the TOC showed a peak of 2.1 wt% at 1763 cm bls, but otherwise values of about 0.5 wt%. This TOC peak coincided with a positive peak in the MS and TC values, and a negative peak of $\delta^{13}C$ to −26.1‰. The TIC values, however, decreased upwards. The mean grain size slightly increased upwards because of a little increase in the sand content.

The mean grain size increased further within sediment unit A-SU-III (1,653–1,325 cm bls) and showed a peak of 94 µm at 1,534 cm bls related to a distinct increase in the sand content. A peak at the same depth was shown by the MS values. Striking in this sedimentary unit was the significant drop of the TOC values down to values below the detection limit of 0.1 wt%. Because of very low values in the OC content, it was not possible to measure $\delta^{13}C$ for this sediment unit. The TIC values remained constant here but showed a little high at 1,398 cm bls.

The two samples within sediment unit A-SU-IV (1,305–1,245 cm bls) were characterized as fine to medium

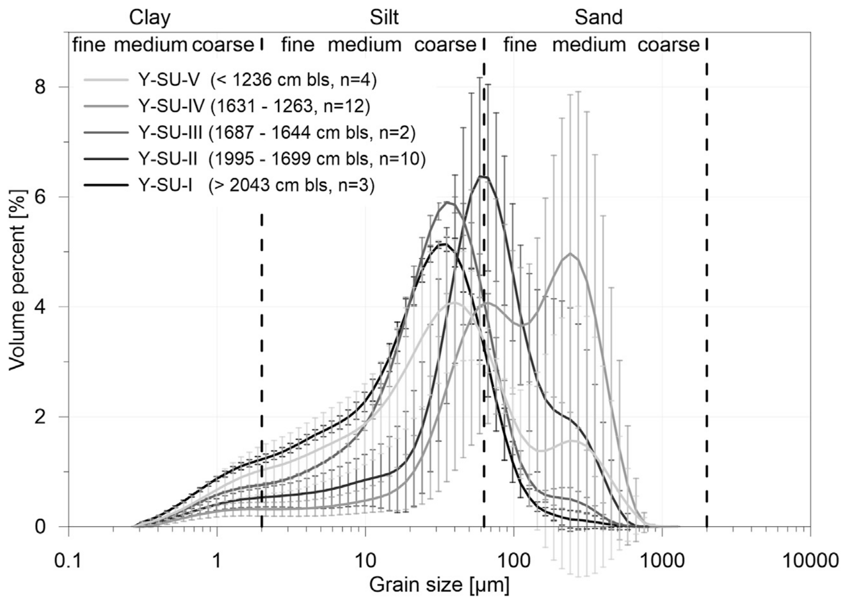

FIGURE 6 | Mean grain-size distributions for each sediment unit of the Yedoma lake core YU-L15 (see **Figure 7**). The error bars are indicating the standard deviations of individual measured grain sizes.

sand (**Figure 4**). Thus, they showed the highest mean grain sizes of the whole YU-L7 core with values of 132 and 141 µm. The MS values typically increased with the increased sand content but TC, TIC, and in particular TOC showed very low values within this sediment unit.

Within sediment unit A-SU-V (<778 cm bls), the clay content increased again while the sand content decreased considerably. Thus, the mean grain size decreased to lowest core values between 16 and 22 µm. This coincided with decreasing MS values. Higher clay content in this upper sediment unit was also reflected in broader GSDs. However, the TOC content showed its highest peak of the core with 2.7 wt% at 582 cm bls. This coincides with an increase of the TC and a negative peak of TIC and $\delta^{13}C$ to 0.57 wt% and −26.1‰, respectively (**Figure 5**).

Yedoma Lake Core YU-L15

The talik below the Yedoma lake reached a depth of about 1,250 cm bls during drilling. Thus, the core YU-L15 was frozen below 1,250 cm bls and unfrozen above, which also resulted in some core loss during drilling. Visually, the sediments appeared much more heterogeneous than the talik deposits below the alas lake and showed light grey to brownish- and blackish-grey colors with higher amounts of organic inclusions and lenses as well as noticeable blackish dots and streaks (**Figure 3**). The core was characterized by a generally decreasing GW/IC trend upwards and by distinct cryostructures in the middle to lower frozen core part. The cryostructures included structureless to micro-lenticular and also suspended ice. Larger ice veins and bands of few centimeters thickness are mainly vertical in the lowermost core part. Generally, the GSDs of the YU-L15 sediment samples were composed of uni- to bimodally distributed, very poorly sorted, clayish-silt to silty-sand deposits (**Figure 6**). The mean of all GSDs is 73 ± 51 µm. Considering the sedimentology, the biogeochemistry and also the cryostratigraphy, the YU-L15 core was divided into five sediment units (Y-SU; **Figure 7**).

The lowest sediment unit (Y-SU-I; >2,043 cm bls) was characterized by very low mean grain sizes between about 15 and 19 µm (**Figure 7**). The broad GSDs resulted from higher clay content in this sediment unit (**Figure 6**). The MS values were the lowest within the whole core. Striking in this unit were TOC values below detection limit and the highest TIC values (1.1–1.3 wt%) of the entire core. The ice contents were high in this unit with up to 68 wt%. The ice richness was represented by up to 3 cm thick-layered lenses and bands that were mainly vertically oriented (**Figure 3**).

Y-SU-II (1,995–1,699 cm bls) was characterized by a general increase in MS and mean grain size. The upper part of this unit was particularly characterized by high sand contents and a maximum mean grain size of 106 µm at 1,762 cm bls. The grain size variations in this unit were also evident in the strong varying and broad GSDs (**Figure 6**). In the lowermost part of this unit (1,992 cm bls), the TOC content showed a distinct peak with 1.4 wt%. Above it decreased and alternated between amounts under the detection limit and 0.5–0.9 wt%. The TIC and TC values decreased upwards as well, but the TIC peaked at 1,869 and 1,728 cm bls. The $\delta^{13}C$ values show very little variations around −25‰. A striking feature in this unit is the large peak in the gravimetric ice content to 80 wt% at 1817 cm bls. This goes along with a small peak in the TOC to 0.6 wt%. These properties were related to an approximately 5 cm thick ice-rich layer, with an obviously higher organic content than the sharply bordered sandy areas above and below (see **Figure 3**).

Strong parameter changes were obvious in unit Y-SU-III (1,687–1,644 cm bls). Except for MS, almost all parameters

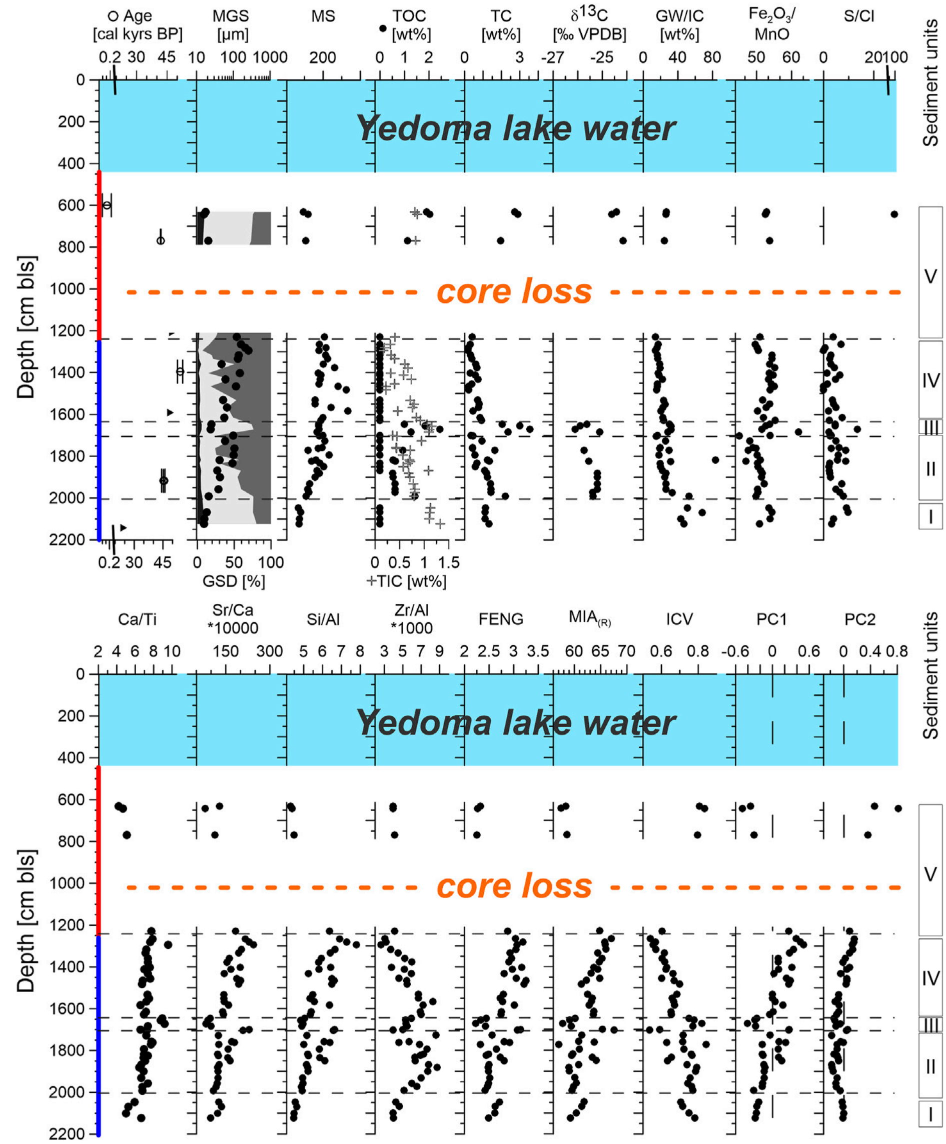

FIGURE 7 | Sedimentological parameters, organic and inorganic geochemistry as well as the weathering indices FENG, $MIA_{(R)}$, ICV and the Principal components (PC) of the Yedoma lake core YU-L15 (Mean grain size (MGS); Grain-size distribution (GSD); Mass-specific magnetic susceptibility (MS); Ground water/ice content (GW/IC)). Infinite radiocarbon dates are illustrated by triangles. Unfrozen core depth intervals are marked by red depth scale while frozen ones are marked in blue.

peaked considerably here. The suddenly increasing silt content to about 75% and the decreasing sand content cause a strong decrease in the mean grain size to about 25 µm. The broad GSDs are comparable to that of Y-SU-I but show little lower clay contents (**Figure 6**). The TOC content showed the highest values of the total core with its highest peak of 2.5 wt% at 1,672 cm bls (**Figure 7**). The strong TOC increase was complementary to maxima of TC und TIC up to 3.6 and 1.2 wt%, respectively. While $\delta^{13}C$ values fell below -26‰, the gravimetric ice content in this unit showed only little higher values around 30 wt% than above and below.

Unit Y-SU-IV (1,631–1,263 cm bls) was characterized by a high sand (up to 92%) and an upward decreasing GW/IC, ranging between 25 and 14 wt%. The ground ice in this unit was structureless and non-visible. With upwardly increasing sand contents, the mean grain size increased to a maximum value of 260 µm at 1,294 cm bls. However, alternating silt- and sand-rich areas within the core unit resulted in strong variations in the mean grains size and GSDs (**Figures 6**, **7**). The MS showed distinct peaks at 1,584, 1,483, and 1,377 cm bls that coincided with peaks in the sand content. This unit is characterized by consistent extremely low TOC amounts below the detection limit. TC also shows very low values decreasing further upwards. The TIC showed a strong decrease above unit Y-SU-III, but fluctuates upwards around a unit mean of about 0.5 wt%.

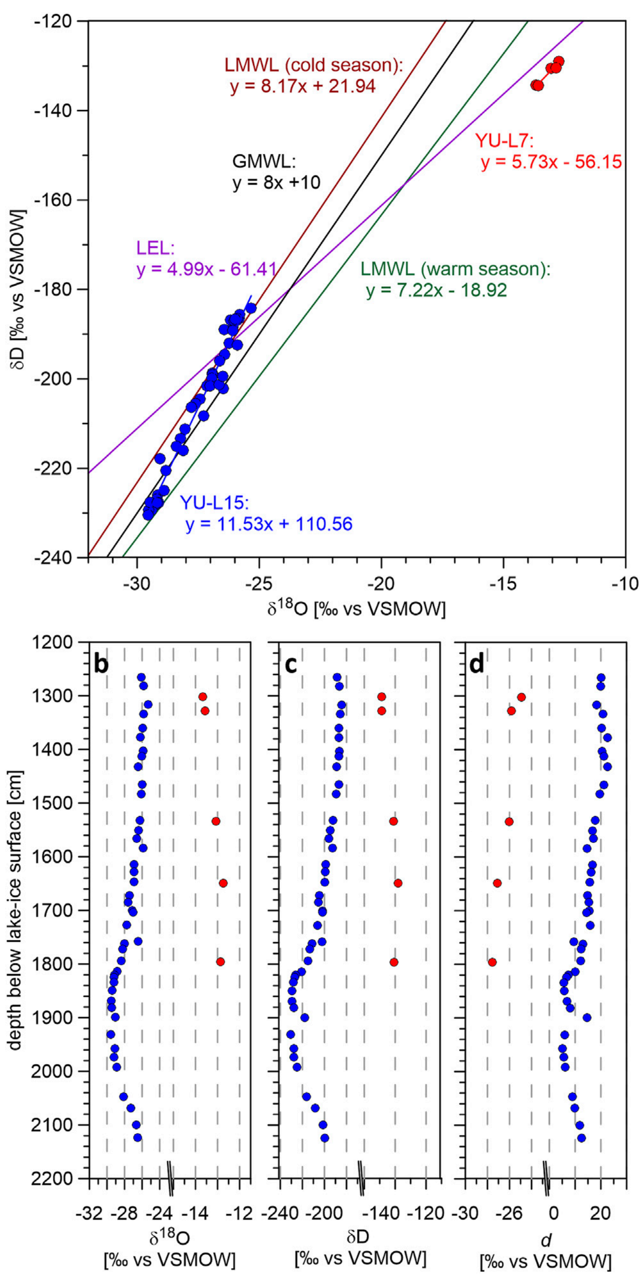

FIGURE 8 | Stable water isotopes of the alas lake core YU-L7 (red dots) and the Yedoma lake core YU-L15 (blue dots) samples. **(A)** Scatter plot of $\delta^{18}O$ and δD. Indicated are the GMWL (black), the LEL (purple), and the LMWL of Yakutsk for the warm season (green) and the cold season (brown). **(B–D)** $\delta^{18}O$, δD, and *d* (deuterium excess), respectively, against core depth. Note the breaks on the x-axes in **(B–D)**.

The uppermost unit Y-SU-V (<1,236 cm bls) represents unfrozen talik sediments and was characterized by silt-dominated GSDs with higher clay contents compared to the middle sediment units. Like the lowest unit Y-SU-I, the mean grain size of this talik unit showed values around 18 µm. The MS showed constant medium values. TOC, TC, and TIC showed high values up to 2.0, 2.9, and 0.9 wt%, respectively. The $\delta^{13}C$ values also showed higher values around −24‰ in this unit (**Figure 7**).

Stable Water Isotope Characteristics

Stable water isotopes were plotted in relation to the Global Meteoric Water Line (GMWL) (Craig, 1961) for each core (**Figure 8A**) and we used the season-specific Local Meteoric Water Line (LMWL) for Yakutsk from Papina et al. (2017). While the LMWL for the warm season exhibited a lower slope of 7.2 and a negative intercept of −18.9 in comparison to the GMWL, the LMWL for the cold season ran parallel but above the GMWL (**Figure 8A**). The Local Evaporation Line of Central Yakutia (LEL; Wetterich et al., 2008) reflects regional evaporation effects on the surface waters in the study area.

The $\delta^{18}O$ and δD values of the alas lake core YU-L7 strongly differed from the GMWL and LMWLs, respectively, but their slope (5.7) roughly corresponded to the LEL (slope of 5). The $\delta^{18}O$ values ranged from −13.7‰ at 1,302 cm bls to −12.9‰ at 1796 cm bls. The δD values ranged from −134‰ (1,649 cm bls) to −129‰ (1,328 cm bls). The *d* values varied between −27.6 and −24.9‰ and slightly decreased towards the bottom of the core.

The Yedoma lake core YU-L15 showed a much steeper slope (11.5) than GMWL, LMWLs, and LEL, respectively, with $\delta^{18}O$ values between −29.5‰ at 1,316.5 cm bls and −25.3‰ at 1,931.5 cm bls (**Figure 8B**). The δD values range between −230‰ (1,316.5 cm bls) and −184‰ (1931.5 cm bls). Notably, the isotopic values from the uppermost frozen deposits below the talik (1,265–1,483 cm bls) were highest, while the samples between 1820 and 1992 cm bls showed the lowest and most depleted isotopic values. Generally, the $\delta^{18}O$ and δD values decreased with depth until 1931.5 cm bls to −29.5‰ and to 230.4‰, but then increased again to the bottom layer to values that were more similar to the uppermost layers. The *d* values of the Yedoma lake core showed a similar course and lie between 5.1‰ (1957.5 cm bls) and 22.6‰ (1,377.5 cm bls).

Inorganic Geochemistry and Weathering Indices

Alas Lake Core YU-L7

The inorganic geochemical parameters in the YU-L7 core showed rather little variations (**Figure 5**). However, some noticeable peaks can be seen in all parameters. The by far highest but outlying S/Cl ratio of 37.6 was calculated for the uppermost unit A-SU-V at 582 cm bls. This peak coincides clearly with high TOC values. Below unit A-SU-V, the ratio showed less variations with minimum values in unit A-SU-IV but again higher values in the lowest sediment units (mean 11.9 ± 9.9).

Higher Ca/Ti ratios were calculated for the lowest und uppermost units. In between, the values stayed rather constant around the mean of 6.3 with a negative peak in unit A-SU-IV at 775 cm bls. The Sr/Ca ratio is inverse proportional to the Ca/Ti course, with low ratios in A-SU-I and A-SU-V and higher ratios in A-SU-IV. The mean Sr/Ca ratio of the alas lake core was 134 ± 35 (**Table 2**).

The Fe_2O_3/MnO ratio showed stronger variations than other parameters in the alas lake core. Particularly, at the transition

TABLE 2 | Overview of statistical characteristics for all analyzed parameters for the alas lake core YU-L7 and the Yedoma lake core YU-L15.

	YU-L7								YU-L15							
	Mean	**σ**	**Median**	**Min**	**25%**	**50%**	**75%**	**Max**	**Mean**	**σ**	**Median**	**Min**	**25%**	**50%**	**75%**	**Max**
GW/IC (wt%)	23.2	9.5	20.6	15.9	19.7	20.6	22.9	60.8	26.5	13.8	22.7	13.9	18.2	22.7	28.6	83.6
MS (10^{-8} m^3/kg)	127.4	49.4	106.5	71.7	93.1	106.5	149.5	241.1	174.9	57.7	177.9	67.4	137.4	177.9	200.9	331.9
TC (wt%)	1.5	0.8	1.2	0.3	1.1	1.2	1.8	3.3	1.1	0.8	0.8	0.2	0.4	0.8	1.3	3.6
TOC (wt%)	0.7	0.7	0.5	0.0	0.4	0.5	0.9	2.7	0.4	0.6	0.0	0.0	0.0	0.0	0.6	2.4
TIC (wt%)	0.7	0.3	0.7	0.3	0.6	0.7	1.0	1.2	0.7	0.3	0.7	0.2	0.4	0.7	0.8	1.3
Clay (%)	6.1	2.1	6.2	2.0	5.5	6.2	7.3	9.1	4.4	2.1	3.8	0.9	3.0	3.9	5.0	9.6
Silt (%)	65.4	19.4	73.2	17.9	67.0	73.2	76.2	79.8	46.4	20.8	48.5	7.1	27.8	48.5	59.5	80.3
Sand (%)	28.5	21.2	20.4	12.8	16.1	20.4	27.4	80.0	49.3	22.7	48.1	10.4	35.7	48.1	69.1	92.0
MGS (μm)	39.6	38.2	26.3	15.7	20.1	26.3	32.4	141.2	72.6	51.4	56.6	15.8	39.4	56.9	99.4	260.5
Sorting	4.3	0.9	4.5	2.0	4.4	4.5	4.7	4.9	3.7	0.9	4.0	1.6	3.4	4.0	4.2	4.9
Zr/Al	4.8	0.8	4.6	3.8	4.3	4.6	5.1	7.1	5.6	1.5	5.5	2.6	4.2	5.5	6.8	8.7
Si/Al	4.9	0.6	4.8	4.3	4.5	4.8	4.9	6.4	5.6	0.8	5.3	4.3	5.0	5.3	6.4	7.8
Fe_2O_3/MnO	53.4	3.0	52.6	48.8	51.8	52.6	54.5	61.6	52.0	2.7	51.9	45.0	50.3	51.9	53.8	62.0
Ca/Ti	6.3	1.1	6.0	3.3	5.9	6.0	7.2	8.2	7.1	1.0	7.2	4.2	6.7	7.2	7.5	9.6
Sr/Ca	134.2	35.1	140.0	77.4	109.3	140.0	150.2	196.9	149.8	40.7	143.4	79.8	122.8	143.4	179.8	243.8
S/Cl	11.9	9.9	9.6	2.7	6.4	9.6	11.5	37.6	7.4	14.7	4.0	0.0	2.4	4.0	6.4	98.7
FENG	2.5	0.3	2.6	2.1	2.3	2.6	2.7	2.9	2.7	0.3	2.7	2.2	2.5	2.7	3.0	3.2
ICV	0.7	0.1	0.7	0.6	0.7	0.7	0.8	0.9	0.7	0.1	0.7	0.5	0.6	0.7	0.8	0.8
$MIA_{(R)}$	61.1	2.5	62.3	56.3	58.6	62.3	62.9	64.2	62.0	2.7	61.8	57.0	59.7	61.8	64.1	67.6

GW/IC, Ground water/ice content; MS, Mass-specific magnetic susceptibility; TC, Total carbon; TOC, Total organic carbon; TIC, Total inorganic carbon; MGS, Mean grain size. The weathering indices FENG, $MIA_{(R)}$, ICV.

from A-SU-II to A-SU-III, reducing conditions (higher ratios) changed sharply to conditions of higher oxygen availability (lower ratios). A high Fe_2O_3/MnO ratio was especially prominent at 1763 cm bls, which corresponded to high TOC and lower $\delta^{13}C$ values (**Figure 5**). Smallest ratio values occurred at 1,692 and 564 cm bls. While the ratio stayed almost above 50 in the whole core and showed a generally upward decreasing trend.

Changes of the Si/Al ratio correlated clearly with the mean grain size in YU-L7 ($r = 0.97$, $p < 0.001$), which in particular points to the connection of sand and silicon input. The ratio increased with increasing sand content at 1,534 cm bls (A-SU-III) and in unit A-SU-IV (**Figure 5**). The Zr/Al ratio increased from A-SU-I together with the Si/Al until a maximum at 1,535 cm bls, but afterwards it decreased towards the top and showed even the lowest values in unit A-SU-IV.

All weathering index values suggest inhibited mineral weathering in the lowest and uppermost parts of the YU-L7 core (low values in FENG and $MIA_{(R)}$ and values close to 1.0 in ICV). Progressive weathering conditions are only shown by the increasing FENG and $MIA_{(R)}$ indices and the low ICV in particular at the transition from A-SU-I to A-SU-II between 1,921 and 1,796 cm bls and at the transition from A-SU-III to A-SU-IV between 1,302 and 1,257 cm bls (**Figure 5**).

Yedoma Lake Core YU-L15

Prominent maxima in the S/Cl ratio (98.7) were calculated for the uppermost sediment unit Y-SU-V representing the talik and unit Y-SU-III at 1,672 cm bls (13.4). However, the S/Cl ratio in the frozen part of the YU-L15 core was very low but slightly increasing within the lowest unit Y-SU_I (mean 7.4 ± 14.7).

The Ca/Ti ratio showed lowest values in Y-SU-I and Y-SU-V and a mean of 7.1 ± 1.0. In addition to a high ratio in Y-SU-III, another local maximum was shown at 1,294 cm bls (**Figure 7**). Low Sr/Ca ratio values were obvious for the lowest frozen and the uppermost unfrozen parts of the YU-L15 core. The ratio is slightly increasing in Y-SU-II to a high value of 230 at 1,700 cm bls, which marks the border to unit Y-SU-III. Noticeable in unit Y-SU-III (1,687–1,644 cm bls) is the strong drop in the Sr/Ca ratio to minimum values. Above Y-SU-III the Sr/Ca ratio was increasing again to a maximum of 243 at 1,294 cm bls. The mean Sr/Ca ratio of the Yedoma lake core was 149.8 ± 40.7 (**Table 2**).

While the Fe_2O_3/MnO ratio in the lower part of the YU-L15 core indicated a change from slightly reducing soil conditions in Y-SU-I to more oxidizing conditions in Y-SU-II with minimum values at 1,703 cm bls, the ratio remains relatively constant with values just over 50 in Y-SU-IV and the talik unit (Y-SU-V). Obvious, however, was the sharp and strong increase to a maximum ratio of 62 in Y-SU-III (1,684 cm bls).

A clear connection between changes of the Si/Al ratio and the mean grain size are obvious also for Yedoma lake core (($r = 0.93$, $p < 0.001$). The relatively high mean Si/Al ratio of YU-L15 (5.6 ± 5.3) reflected the sandy sediments below the Yedoma lake and the gradual increase of the sand content up to the talik boundary (~1,250 cm bls; **Figure 7**). The Zr/Al ratio in the Yedoma lake core was subjected to strong fluctuations. While the ratio increased in the lower core part, it showed rapidly changing maxima and minima from Y-SU-II to Y-SU-IV and then decreased again up to the unfrozen talik sediments.

The three weathering indices calculated for the Yedoma lake core showed high maximum values (minimum for ICV) and strong fluctuations (**Table 2**). The fluctuations of all three indices increased in the lower core part (Y-SU-I and Y-SU-II). Conditions promoting weathering have been indicated here by high values of the FENG and $MIA_{(R)}$ and low values of the ICV at

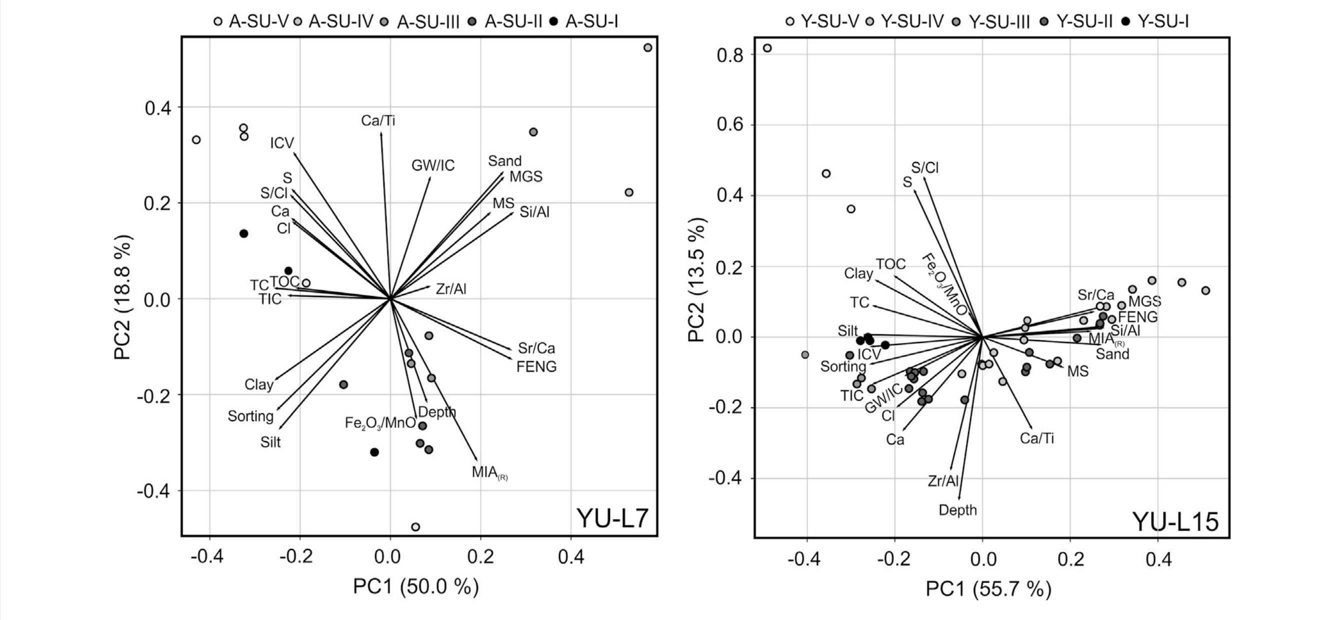

FIGURE 9 | PCA ordination biplots on all sedimentological and biogeochemical parameters for **(A)** the alas lake core YU-L7 and **(B)** the Yedoma lake core YU-L15. The sample scores are scaled in white, gray and black according to the sediment units given above the plots.

1,700 cm bls. A clearly opposite change in all values could then be observed within unit Y-SU-III (**Figure 7**). Above this, the FENG and $MIA_{(R)}$ indices rose again and the ICV decreased to maximum (minimum for ICV) values up to the talik boundary at 1,250 cm bls. Within the talik sediments (Y-SU-V), mineral weathering seemed to be inhibited again.

Parameter Correlations and Principal Component Analysis

Due to their inverse proportionality, a positive correlation (r) of the FENG or $MIA_{(R)}$ index with a variable corresponds to a negative correlation with the ICV. High negative (respectively positive for ICV) and statistically significant ($p < 0.05$) correlations are obvious for both cores between the weathering indices and TOC, TIC, TC, and the S/Cl ratio (see **Supplementary Tables 3, 4**). Further positive correlations for both sediment sequences exist between TOC and the clay and silt grain size fraction. For the YU-L15 Yedoma lake core, there are particularly high positive (respectively negative for ICV) and statistically high significant ($p < 0.001$) correlations between the three weathering indices and the sand content, the mean grain size, the Si/Al ratio, and the Sr/Ca ratio. A negative and high significant correlation between GW/IC and the sand content can only be seen in YU-L15 ($r = -0.64$, $p < 0.001$). In addition, also all three weathering indices show significant negative (resp. positive) correlation with GW/IC in YU-L15. In contrast to YU-L15, all weathering indices show significant ($p < 0.05$) positive (respectively negative) correlations with depth in the YU-L7 alas lake core.

The PCA of both cores show two major principal components (PC1 and PC2) that explain 68.8% (YU-L7) and 69.2% (YU-L15) of the total variance of all sedimentological and biogeochemical parameters. The sample scores on PC1 and PC2 are plotted against depth for both cores in **Figures 5**, **7**, illustrating their variations against the ordination results within the different sediment units. However, the ordination biplots (**Figure 9**) show different combinations of variables on the two axes. While the variables within the PCA for the Yedoma lake core YU-L15 are clustered quite clearly, for the alas lake core YU-L7 they show a broad distribution in small groups across the entire biplot. The vector lengths (i.e. PCA loadings) within the biplots indicate how strongly the individual variable is related to the displayed ordination. Hence, for both sediment cores, the highest positive loadings on PC1 are shown for Si/Al, Sr/Ca, Sand, the FENG index, and the MS. The $MIA_{(R)}$ index also shows a positive correlation with PC1 for YU-L15. High negative loadings on the first axis for both cores are shown for TC, clay, silt, sorting, TIC, and TOC. In addition, negative correlations with PC1 are also shown by the variables ICV and GW/IC for YU-L15 and the variables S/Cl, S, Ca and Cl for YU-L7. Variables with high positive loadings on PC2 for YU-L7 are Ca/Ti, ICV, and GW/IC and for YU-L15 S and S/Cl. Negative correlations with PC2 for YU-L7 are shown for $MIA_{(R)}$, Fe_2O_3/MnO, and depth, while for YU-L15, the variables depth, Zr/Al, Ca, Ca/Ti, and Cl are oriented along the negative range of PC2.

DISCUSSION

Origin of Ground Water and Ice

For our studied cores we found varying amounts of pore water/ice which is linked to the different host sediments and their respective water storage capacity (**Figure 8**). With a mean

GW/IC value of 26.5 ± 13.8 wt%, the Yedoma lake core contains slightly more water/ice in comparison to the alas lake core (mean: 23.2 ± 9.5 wt%). The deposits of the alas lake core were completely thawed already. Thus, no further ground subsidence is expected for the ground below the alas lake. The higher GW/IC in the Yedoma lake core results from the perennial frozen conditions, particularly of the lower parts of the YU-L15 core. This together with further vertical and lateral expansion of the lake and the talik, would lead to more thawing of the sediments and further ground subsidence below the Yedoma lake (Fedorov et al., 2014).

In general, the composition of stable water isotopes in thermokarst lakes is mostly influenced by precipitation, evaporation and occasionally by meltwater from the surrounding catchment and the underlying permafrost (e.g., Turner et al., 2014). Earlier measurements of stable water isotopes of lake water from different thermokarst lakes at the Yukechi study site show evaporation by enriched δ^{18}O (−13.8 to −8.8‰) and δD (−133.8 to −110.9‰) values, which is also seen in the LEL for Central Yakutia of δD = 5*δ^{18}O - 61.4 (sample nos. Yak-01 to Yak-05; Wetterich et al., 2008).

Because of ground thawing (i.e., talik development) and lake water infiltration, the lake water has a strong influence on the pore water isotope composition of the talik sediments. In comparison to Northern Yakutia, the influence of local air temperatures and resulting evaporation effects on lake water δ^{18}O are stronger due to much higher summer temperatures in Central Yakutia (Wetterich et al., 2008).

As shown in **Figure 8**, the δ^{18}O and δD values from the alas lake core YU-L7 (mean: −13.2 ± 0.4‰ and −131.7 ± 2.2‰, respectively) are distinctly less depleted than those from the Yedoma lake core YU-L15 (−27.4 ± 1.3‰ and −205.0 ± 15.4‰, respectively). Furthermore, the alas lake core data are clearly independent from the GMWL but align with the LEL. Overall, they are similar but slightly more depleted than stable isotope values of the nearby drilled alas sediment core presented in Windirsch et al. (2020). Despite the low number of samples (n = 5), both the slope of 5.73 (R^2 = 0.97) and the enriched isotopic composition with extremely negative d values suggest that the pore waters of the alas core originated from water infiltration from the alas lake above the thawed sediments. The alas lake water itself can be interpreted to represent a rather recent water source signal (i.e. precipitation), which is strongly affected by evaporative fractionation and further depends on cyclical water balance changes typical for the alas lakes in Central Yakutia (Ulrich et al., 2017b). The relatively homogenous isotope signals of YU-L7 result from the saturation of the sediments with surface water. This suggests subsurface water flow after talik development, which probably has also implications for local hydrology in a way that new flow paths through former impermeable layers are possible under warmer climate conditions (Johansson et al., 2015).

The Yedoma lake core (YU-L15) stable isotope data (n = 43) are highly correlated (R^2 = 0.97) with a δ^{18}O-δD slope of 11.53. The low δ^{18}O and δD and high d values indicate that the water/ice originates from intra-sedimental pore and segregation ice of the still frozen, i.e. intact, Yedoma IC below the lake. Hence, they represent the original isotopic composition during permafrost formation. An overprinting by isotopically different lake water can be ruled out. Furthermore, the high slope and the high d values indicate that neither evaporation nor freezing fractionation have played a major role before fixation of the isotope signals in permafrost. While the upper part (above 1,800 cm bls) of the Yedoma lake core is dominated by structureless non-visible pore ice, the sediments below 1,800 cm bls represent a larger variety of intra-sedimental cryostructures: from structureless non-visible ice to varying amounts of micro and macro ice lenses to almost pure ice lenses (**Figure 10**). Hence, distinct minima in δ^{18}O, δD, and d between 1,800 and 2,000 cm bls might be related to the higher amount of segregation ice even though the isotope profile below and above 1,800 cm bls do not differ considerably in terms of the δ^{18}O-δD slopes. Furthermore, changes in climate and hydrological conditions, their seasonal variations as well as active-layer dynamics may have contributed to this pattern.

Overall, the mean δ^{18}O and δD values of the Yedoma lake core are very similar to those of the nearby drilled on-land Yedoma core presented by Windirsch et al. (2020), whereas the mean d value of our core is lower, mainly driven by the distinct minimum between 1,800 and 2,000 cm bls. Nevertheless, our δ^{18}O-δD slope (11.53) differs distinctly from that of the Windirsch et al. (2020) core (6.61) and is much higher than season-specific LMWLs for Yakutsk (**Figure 8**). Generally, the low δ^{18}O and δD and the high d values are close to those of a nearby ice wedge (Windirsch et al., 2020) as well as other Central and Interior Yakutian MIS 3 ice wedges (Popp et al., 2006; Opel et al., 2019). This suggests a substantial contribution of winter precipitation (characterized by lower δ and higher d values) to the formation of the intra-sedimental ice. Comparable high pore ice d values have also been reported for some stratigraphic units exposed at the Batagay megaslump (Opel et al., 2019) and might therefore represent an over-regional pattern for Central and Interior Yakutia related to the extreme continentality of climate during MIS 3.

Organic Carbon Characteristics of Thawed and Frozen Yedoma Deposits at the Yukechi Study Site

Quantifying the OM content is important to estimate the relevance of the study site regarding potential future GHG release from Yedoma deposits (Turetsky et al., 2020). The TOC for the YU-L7 core has a mean value of 0.72 wt%, whereas the mean value for YU-L15 core lies at only 0.37 wt%. These values are in the marginal range of averaged TOC values reported by Strauss et al. (2013) for Siberian Yedoma deposits (3.0 + 1.6/−2.2 wt%), but fit well with results of previous studies carried in Central Yakutia (Ulrich et al., 2019; Windirsch et al., 2020). In both cores, TOC correlates negatively with grain size (YU-L7: r = −0.48, p < 0.05; YU-L15: r = −0.43, p < 0.01; **Supplementary Tables 1, 2**). TOC, TIC, and TC values show local peaks in the fine-grained sediment units; most prominent at the silt shift at 1,672 cm bls (Y-SU-III; **Figure 7**). Extreme low TOC values are rather linked to the sand-dominated units.

FIGURE 10 | Comparison of different cryostructures within the study region of Central Yakutia. **(Above)** Cryostructures of Y-SU-I at about 2,200 cm bls of the Yedoma lake core YU-L15 (this study) in comparison to **(Below)** cryostructures that have formed by the downward moisture migration in subaquatic deposits during talik re-freezing from the nearby alas basin Khara Bulgunnyakh (Ulrich et al., 2017a).

One explanation for the low TOC content can be a strong post-sedimentary OC decomposition during thermokarst processes (Strauss et al., 2015; Weiss et al., 2016). But this could only apply for the thawed YU-L7 core sediments. The cryostratigraphy and stable water isotope values for the middle and lower parts of core YU-L15 indicate that at least this part stayed frozen since accumulation. Therefore, a deep OM degradation is unlikely here. However, short-term and rather shallow OM degradation within the active layer after different sedimentation phases of YU-L15 could be an explanation. A subsequent slowly rising permafrost table would leave enough time for the carbon mobilization before the sediment would freeze.

Another explanation for the low TOC values is a low initial OC content. Windirsch et al. (2020) argued that the fluvial and alluvial deposition of coarse-grained (sandy), organic-poor sediments led to the low TOC content. In addition, plant growth and organic input could have been hampered by substrate quality and disturbance (i.e. accumulation) frequency.

Further OM decomposition processes within the sediments below both thermokarst lakes are possible and traceable by δ13C isotopes (Schirrmeister et al., 2011; Strauss et al., 2015). For the talik unit Y-SU-V of the Yedoma lake core, δ13C indicate lower quality and higher carbon decomposition rates (Strauss et al., 2015; Weiss et al., 2016). The high quality signal in the upper part of the YU-L7 core (−26.12‰) likely resulted from modern input by the alas lake above. However, Jongejans et al. (2021a) found higher C/N ratio in the Yedoma lake core and in the bottom of the alas lake core compared to the top and middle parts of YU-L7, which suggest that OM was at least better preserved in frozen sediments below the Yedoma lake compared to large parts of YU-L7.

Finally, the conditions that promote the weathering processes also lead to the gradual degradation of the OM, as can be indicated by the high significant correlations of the weathering indices with the TOC values (e.g., $r = -0.74$, $p < 0.001$ for FENG versus TOC, see **Supplementary Tables 3, 4**). However, analysis of close-by sediment cores drilled on dry land at the Yukechi site point against strong post-sedimentary decomposition of OM but rather for the input of organically poor and pre-decomposed material (Windirsch et al., 2020). Based on our data, a combination of the two can be assumed. Relatively few OM was deposited, which could then be decomposed comparatively quickly. Despite the low OC content of the Yukechi Yedoma IC sediments, Jongejans et al. (2021a) found substantial greenhouse gas production from sediments upon thawing. Their findings showed that the OM quality and turnover history are the main driver for GHG production (Jongejans et al., 2021a).

Applicability and Sensitivity of Specific Element Ratios

When comparing the two cores, it must be taken into account that the Yedoma lake core YU-L15 is significantly sandier than the alas lake core YU-L7 (**Table 2**; $p < 0.001$). Usually, there are more adsorption surfaces in silty substrates, depending on the element considered, but this could explain the generally higher element concentrations, and at least higher TOC content, in YU-L7 ($p < 0.01$). Thus, the comparison of weathering indices and elemental ratios is more suitable to compare different substrates than pure single element contents.

Previous studies from NE Siberia and Central Yakutia showed that Yedoma IC deposits are not only rich in carbonates (Schirrmeister et al., 2011) but also sulfides (Siegert, 1979; Siegert, 1987; Biskaborn et al., 2012; Ulrich et al., 2017a; Ulrich et al., 2019), the latter are common in the form of pyrite (FeS_2). Pyrite forms under reducing conditions and oxidizes relatively easily under oxygen-rich conditions. When the surface thaws and comes into contact with oxygen, sulfide oxidizes to sulfate and can then be easily removed, together with Fe, which is dissolved. Thus, individual surfaces can be detected that represent these short-term thawing processes and subsequent re-freezing (in case of the YU-L15 core) by increasing S and Fe values. Those are in particular prominent in the lower and upper parts of both cores (**Supplementary Tables 1, 2**). Furthermore, S naturally shows a close relation to the organic matrix, so that high S contents could be detected in the core sections with high TOC concentrations. Kokelj et al. (2013) reported S releases in the form of SO_4^{2-} during permafrost thaw and carbonate weathering from Late Pleistocene ice-rich glaciogenic sediments under oxidizing conditions on the Peel Plateau of northwestern Canada. The carbonate weathering includes sulfide oxidation, which leads to an increase in solute fluxes (Zolkos et al., 2018). With Cl^- as an ion that showed only minor increase with permafrost degradation, Kokelj et al. (2013) have shown that the SO_4^{2-}/Cl^- ratios have more than doubled since the 1960s in a Canadian Arctic river. This was resulting from an increase in retrogressive thaw slump (RTS) activities within its watershed due to increasing air temperatures. The following statements are possible if these findings are applied to our results. Since chloride is very easily soluble, it is removed faster than sulfate, which is only generated from sulfide through oxidation processes. The S/Cl ratio in the thawed core YU-L7 and within the talik of YU-L15 is thus higher than in the frozen part of YU-L15 (**Table 2**), where Cl is bound by the frozen state and has not been removed, yet. Therefore, individual maxima of the S/Cl ratio within YU-L15 suggest also brief thawing processes during pausing sedimentation. The syngenetically rising permafrost table has preserved the resulting S/Cl ratio.

The Ti/Ca ratio is often used as the primary weathering index, which increases as the degree of weathering increases, since the immobile Ti is more stable against weathering than the Ca, which is often bound in $CaCO_3$ (Fischer et al., 2012). Since we used the reverse Ca/Ti ratio, it drops when the weathering processes increases. When comparing the two cores, it becomes obvious that YU-L7 shows overall lower Ca/Ti values than YU-L15 ($p < 0.01$), which indicates a higher overall degree of mineral weathering in the alas lake core than in the Yedoma lake core. This is likely caused by the fact that YU-L7 is consistently thawed and is therefore subject to stronger and longer weathering than the frozen core part of YU-L15. Moreover, Ti is generally known to reflect detrital input (usually in lakes) as it is released from source rocks or deposits by physical weathering and minerals containing Ti are not sensitive to dissolution (Demory et al., 2005). Haberzettl et al. (2007) used the Ca/Ti ratio to interpret hydrological variability in lacustrine deposits from Southern Patagonia with the immobile Ti as a proxy for allochthonous clastic input. Using this method, we can differentiate between tendencies of lithogenic to carbonate deposition, with lower Ca/Ti values reflecting an intensified allochthonous input and higher values for autochthonous mineral precipitation.

The ratio of $(Sr/Ca)*10^4$ is used to separate lithogenic and biogenic Ca, whereby high ratios indicate lithogenic carbonate, while small ratios reflect the biogenic influence (mussel and snail shells). Overall, the Sr/Ca ratio of the alas lake core was showing much smaller values compared to the Yedoma lake core (**Table 2**; $p < 0.1$). This is suggesting a higher biogenic influence on the carbonate amount in the sediments below the alas lake and a predominantly lithogenic (clastic) carbonate input in the Yedoma deposits (Wien et al., 2005; Demina et al., 2019). Beside the predominantly lithogenic carbonate input in the Yedoma deposits, as supposed above, this ratio drops in Y-SU-III (1,672 cm bls) suggesting a short-term biogenic Ca input in this sediment unit. Moreover, if the $(Sr/Ca)*10^4$ ratio is >100, it is suggested to be an indication of the presence of aragonite (Sr-rich) rather than calcite (Wegwerth et al., 2014). Aragonite is mostly formed secondary by chemical precipitation from calcareous water. The prerequisite for this chemical precipitation is an increase in the $CaCO_3$ concentration until a supersaturated solution is reached (Wegwerth et al., 2014; Lampe et al., 2016). Aragonite precipitation is generally more characteristic of marine environments, but Roeser et al. (2016) were able to detect the accumulation of aragonite in lake sediments from NW Turkey in connection with very shallow lake levels and phases of increasing temperatures during the late Pleistocene (i.e. MIS3) and the early Holocene. The $CaCO_3$ precipitation from calcareous (ground-)water can only occur in thawed subsurface sediments as only then, a subsequent weathering process can be initiated. Thus, the Sr/Ca ratio, if compared with the FENG index, shows high correlations for YU-L7 and YU-L15 of $r = 0.83$ and $r = 0.91$, respectively. In this way, different phases of weathering of different degrees can be identified.

The Si/Al and Zr/Al ratios provide information about grain-size changes and can be used to estimate transport energy in sedimentary catchments (Lopez et al., 2006; Urbat, 2009; Bertrand et al., 2012). The amount of Si and Zr in surface sediments is controlled by their association with heavy minerals and are interpreted as signals of detrital input. However, Al is relatively insensitive to changes in the nature of the sediment sources, the size of the catchment area and hydrodynamic processes. Therefore, it represents the ideal element to interpret the lithogenic fraction of the sediment and to use it to normalize other lithophile elements (Bertrand et al., 2012). Increasing Si/Al and Zr/Al ratios during cold to moderate climate conditions may, therefore, reflect higher transport energy and terrestrial sediment supply, since silicate minerals cannot be weathered and removed as much under such conditions (Lopez et al., 2006; Urbat, 2009). The perennially frozen conditions below 1,250 cm bls in the YU-L15 core are reflected in overall high Si/Al ratios (**Table 2**; **Figures 5**, **7**). The Zr/Al ratio is understood in a similar context indicating cooler phases by high values. Bertrand et al. (2012) demonstrate that the Zr/Al ratio is in particular sensitive in proximal sediment environments of fjords in Northern Chilean Patagonia and increases with increasing transport energy. Especially in lower core parts of YU-L15 (below 1700 cm bls), the Zr/Al values are higher on average (almost twice as high), than in YU-L7 and the talik section of YU-L15. The relatively immobile Zr was only released and removed during increasing weathering processes (Urbat, 2009; Bertrand et al., 2012). Within both cores, the Zr/Al ratio decreases upwards, which suggests warmer conditions with longer lasting thawing cycles. Lower Zr/Al values (in particular within YU-L15), can be interpreted as old sediment surfaces, where higher summer temperatures could have favored deeper active layers.

Weathering Conditions Within Thawed and Frozen Yedoma Ice Complex Deposits

We consider similar chemical composition and hardly any post-sedimentary modification of the Yedoma deposits parent material, which have, as commonly acknowledged, rather local sources from where different transport mechanisms enabled the polygenetic Yedoma formation (e.g., Schirrmeister et al., 2013). This has been shown in Schirrmeister et al. (2020) by comparing grain-size distributions and endmembers of Yedoma deposits, which revealed a localized pattern and short-distance transport. As we studied a single Yedoma site, i.e. Yukechi, we assume the same general Yedoma formation conditions here and thus a rather homogeneous chemical composition. We further assume that alas deposits formed within and from Yedoma deposits, and are largely composed of taberal and re-located Yedoma deposits, although authigenic deposition during thermokarst lake stages is expected. Thus, any further diagenetic evolution of the material as reflected by increased weathering and expressed by the values of the weathering indices refers to the same base. Although variations between the single units of each core occur (see **Figures 5**, **7**) that allowed us to differentiate our proxies between the sediment units, with the still frozen sediments of YU-L15 as reference.

The applied weathering indices clearly indicate alternating freezing and thawing processes in the study area. Particularly during thawing phases, intensive chemical weathering processes took place due to the presence of (melt) water. Thus, all weathering indices indicated specific periods within both sediment sequences when weathering processes could have been more active. The good accordance of the indices is shown by their significant and high correlation coefficients in both cores (p < 0.001; see **Supplementary Tables 3, 4**). The correlations between the indices and the sand content, the mean grain size, the Si/Al, and the Sr/Ca ratio, suggests that weathering processes have mainly affected the lithogenic fraction of the sediments and thus the least pre-weathered portion. This would confirm the assumption that the parental material of the Yedoma IC deposits were hardly or not at all pre-weathered. Comparatively short transport routes and primary sedimentation under cold climatic conditions, i.e. conditions that are unfavorable for mineral weathering, could be reasons for this (Schirrmeister et al., 2020). However, these correlations are lower for the YU-L7 core, in particular with the $MIA_{(R)}$ index. This is probably due to the redox sensitivity of the $MIA_{(R)}$ index (Babechuk et al., 2014) and sustained reducing conditions in the talik zone. Contemporary sustained reducing conditions are found especially for the upper core sediments that are located immediately below the lakes. The significant negative correlation of the $MIA_{(R)}$ and FENG indices (positive for ICV; $p < 0.001$) with the GW/IC in YU-L15 confirms that (chemical) weathering processes stagnate under frozen conditions. The application of weathering indices can therefore be transferred very well to periglacial conditions in order to estimate past freezing processes.

The sampling of YU-L7 was not as detailed as for YU-L15 due to core loss. Nevertheless, homogeneous weathering conditions can be inferred from the relatively constant values of the indices. The uniform ICV values between 0.6 and 0.8 suggest only moderate mineral conversion for the YU-L7 sediments (Cox et al., 1995). Because these sediments were thawed completely, similar weathering processes likely took place throughout the YU-L7 sequence. At 1,762 cm bls and below about 1,900 cm bls, clear inhibited weathering processes are indicated by decisive indices. One explanation for this is the fluctuating expansion of the talik below the lake in connection with changing lake levels. Strongly changing lake levels including phases of complete drying out are typical for Central Yakutian alas lakes (Soloviev, 1959; Soloviev, 1973; Ulrich et al., 2017b). It is generally assumed that with loss of water bodies, taliks within the permafrost re-freeze relatively quickly from the sides (Grosse et al., 2013).

In general, the core YU-L15 is showing a much more differentiated picture for all utilized indices. Since we assume a largely homogeneous chemical composition of the parent material of both sediment sequences, we see the frozen sediments as a reference in our study on which we test our proxies comparatively. Most noticeable within YU-L15 is the significant jump in the index values within Y-SU-III. The frozen core section can clearly be structured from bottom up into three phases of weathering of different degrees (first: below about 1,700 cm bls; second: about 1,700–1,600 cm bls; and third: above about 1,600 cm bls). Starting from the lowest first phase, the weathering tendency increases to the third phase with a low during second phase. This suggests that weathering conditions have increased gradually from the bottom to top of the sediment sequence, which is associated with frequent changes of long-lasting thawing and subsequent freezing processes. Furthermore, we assume a deepening active layer caused by increasing ground temperatures, since the detected chemical weathering can take place more intensively only at higher positive temperatures and thawing permafrost (Zolkos et al., 2018).

Finally, our findings are supported by the Fe_2O_3/MnO ratio. The ratio of iron to manganese in sediments is known to change with the degree of oxidation (usually in lacustrine environments) during accumulation (Davison, 1993; Biskaborn et al., 2013). During reducing soil/sediment conditions, the Fe_2O_3/MnO ratio increases, since Mn is more soluble than Fe and is therefore faster mobilized. For YU-L7, the ratio is always above 50, which suggests sustained reducing conditions throughout the core (Lampe et al., 2016). For the frozen part of core YU-L15, a clear difference was obvious between the first and third weathering phases. Below about 1,700 cm bls, the ratio is significantly smaller than above, which in turn confirms the discussions of the FENG and $MIA_{(R)}$ value changes. It finally suggests that due to the long-lasting frozen state of the sediment units Y-SU-I and Y-SU-II of the Yedoma lake core, Mn was not reduced and discharged, which is reflected in lower Fe_2O_3/MnO ratios. The upper part of the frozen sediments has already been subject to several thawing phases and higher water availability due to rising temperatures, which is reflected in higher ratios. Since reducing anaerobic soil conditions significantly slows the degradation of organic matter (Knoblauch et al., 2012), higher TOC values for the areas of higher Fe_2O_3/MnO ratio could be expected. However, this correlation is not significant for the sediment cores presented here and ultimately cannot answer the question of the generally low TOC contents. In addition, higher TOC levels in the active layer can also be a sign of increasing plant production during warmer periods in the past (Schirrmeister et al., 2011).

Synthesis: Implications for Yedoma Ice Complex Deposition, Thermokarst Processes, and Paleo-Environmental Conditions

Our dating results do not allow a detailed age-depth model. Nevertheless, they suggest that the sediment sequence under the Yedoma lake was deposited quickly during MIS3. In contrast, the calibrated radiocarbon age range of the sediments under the alas lake points to a much longer sedimentation history, which extends from the MIS3 into the middle Holocene (**Table 1**). However, similar geochemical properties of both cores allow us to conclude that both sediment sequences originate from the same parent material and a primarily terrestrial sedimentation history. Evidence of higher terrestrial plants found throughout both cores by Jongejans et al. (2021b), indicated by the dominance of specific long-chained alkanes, corroborates the lack of lacustrine sediments even under the alas lake. The lenticular, layered and suspended cryostructures in the middle and lower section of the YU-L15 core (**Figure 10**) point to a gradual syngenetic freezing of the active layer of subaerial deposits, crack infilling and different rates of sedimentation (French and Shur, 2010).

Our PCA results are particularly helpful to discuss the general sedimentation environment of the Yedoma IC deposits at the Yukechi study site. In both cores, PC1 is generally determined by organic enrichment in connection with clayey-silty grain sizes on the one hand (negative sample scores) and sand-rich grain sizes, higher transport energy of sili-clastic material and conditions promoting weathering on the other hand (positive sample scores). The different distribution of the variables along PC2, however, reflects the differences between the two cores with regard to their depth-dependent thawed and/or frozen states and related redox conditions (**Figures 5**, **7**, **9**). We found that the sedimentation conditions gradually change from bottom to top, but return to conditions in the top most recent stratigraphic units comparable to those of the bottom sediment units.

For the East Siberian lowland region, Schirrmeister et al. (2013), Schirrmeister et al. (2020) developed the concept of a polygenetic Yedoma IC accumulation (including alluvial, fluvial and partly aeolian transportation) from nearby sources and syngenetic ground ice segregation, ice-wedge growth, peat aggradation, cryosol formation and cryoturbation. Furthermore, many paleo-environmental studies from NE Siberia discuss the MIS3 interstadial (57–29 ka BP), i.e. the main Yedoma IC formation period, as a climate optimum stage that was punctuated by strong climate fluctuations (Anderson and Lozhkin, 2001; Zech et al., 2008; Wetterich et al., 2014; Diekmann et al., 2017). For instance, plant macrofossils studied by Kienast et al. (2005) on Bykovsky Peninsula in the Central Laptev Sea region suggest relatively warm and moist summers even for Northern Yakutian regions with mean July temperatures above 12°C. Comparable variations in summer climate conditions in Central Yakutia could be the reason for the strong fluctuations in our proxy data, especially in the YU-L15 core. Warm and moist phases caused increased fluvial-alluvial sedimentation of sand-rich sediments, deeper active layer depths, increased mineral weathering and higher OM decomposition. In contrast, cooler and drier phases are dominated by aeolian sedimentation, inhibited weathering processes, and hampered decomposition of OM (Strauss et al., 2013; Jongejans et al., 2021b). The clearly unimodal GSDs with a high peak in the coarse silt to fine sand fraction (**Figures 4**, **6**) and the lack of stratification within both sediment sequences indicate the high aeolian component in our sediment cores (Péwé and Journaux, 1983; Murton et al., 2015). However, Schirrmeister et al. (2020) point out that the formation of finer-grained sediments in Yedoma deposits can also be the result of severe *in situ* frost weathering. But, high proportion of sand in the middle sediment units of both cores and especially in Y-SU-IV of the YU-L15 core (maximum mean grain size of 260 μm) can only be explained by fluvial-alluvial transport processes (Schirrmeister et al., 2020; Windirsch et al., 2020). These were intense short events of fluvial-alluvial deposition of large sediment amounts, which we suggest to be comparable to the short time frame covered by the Yedoma lake core and the proxy cyclicity represented by the sample score variations of PC1. A representative exception in the sedimentation history of the YU-L15 core is the unit Y-SU-III, which was defined as the second weathering phase, with low indices but exceptionally high TOC values and Fe_2O_3/MnO ratios. All proxies in this unit indicate that short-term thermokarst processes could have taken effect here (**Figure 7**) and that a shallow thermokarst lake may have developed and disappeared during a very short period (Ulrich et al., 2017a). A similar proxy pattern can be seen in the A-SU-II of the alas lake core at a depth of 1,763 cm bls. However, it cannot be conclusively clarified whether these short-term processes are the same in terms of time and thaw intensity.

For the transition to the MIS2 and the Last Glacial Maximum (LGM, 26.5–19 ka BP; Clark et al., 2009), significant summer and winter cooling and arid conditions are often described for NE Siberia (Wetterich et al., 2011). Such conditions are supposed to be typical for the formation of the NE Siberian Yedoma IC deposits (Schirrmeister et al., 2013; Schirrmeister et al., 2020). We cannot identify the MIS2 based on our dating and proxy data. A Holocene cover of the Yedoma IC deposits at the Yukechi study site is also not at all visible in the YU-L15 core and even difficult to identify in the YU-L7 core. Wetterich et al. (2020) describe several hiatuses for Northeast Siberian Yedoma deposits during MIS3-2 as typical regional disturbance leading to either low accumulation and/or fluvially-triggered or climate-triggered erosion of deposited IC material. We assume that for the Yukechi study site, climate-related thawing of the permafrost and successive changes of accumulation areas during the Lateglacial to Holocene transition and/or the HTM are the reason for the lack of younger deposits.

Various studies suggest that large alas basins in Central Yakutia formed during the pronounced climate warming after the LGM and during the HTM as a result of extensive thawing processes, ground-ice melting, and subsidence of Yedoma deposits (Soloviev, 1973; Ulrich et al., 2017a; Ulrich et al., 2019). During the formation of these thermokarst basins, younger OM likely was also deposited (e.g., mobilized from thermo-erosion processes and basin expansion) as seen by the two uppermost early and mid-Holocene dates from the YU-L7 core. In contrast, the inverse age at 1,560 cm bls of YU-L7 (**Table 2**) is interpreted as the result of old OM incorporation already during Yedoma deposition or thermokarst lake and talik development (Gaglioti et al., 2014). The calibrated radiocarbon dates from the uppermost core sample in YU-L15 (142 ± 49 cal. yrs. BP) suggest the deposition of modern sediments during the formation of the young thermokarst lake above, but could also reflect fresh input prior to the lake phase and cryoturbation.

The questions regarding the significantly lower sand proportion in the YU-L7 core remains. Biskaborn et al. (2013) and Ulrich et al. (2019) discussed that depositional activities and grain size fractionation during thermokarst (lake) basin development might have overprinted the original sediment characteristics of the Yedoma source sediments. Concerning this, distal sediment transport after lake bank erosion or a low-energy sedimentation milieu within an expanding thermokarst lake basin could have led to a homogeneous fractionation of finer-grained sediments in a basin center as represented by the YU-L7 core site.

CONCLUSION

Geochemical proxies and specific weathering indices were helpful in understanding the regionally varying history of formation and decay of the Yedoma IC, and provided more detailed information about the deposition, fixation, and degradation of the OM inventory of these permafrost deposits.

We were able to show that the combination of geochemical and sedimentological properties, element ratios and certain weathering indices, reflect changing sedimentation processes, seasonal thawing depths and environmental conditions. Deeper summer thawing enabled increasing mineral weathering and initial thermokarst processes during the interstadial MIS3. In particular, the FENG and $MIA_{(R)}$ indices have proven to be very promising proxies for Yedoma IC deposits. The ICV gives additional information about the general mineral weathering status. Grain-size distributions, certain sedimentological proxies (i.e. Si/Al, Sr/Ca) and a typical cryostratigraphy reflect high transport energy, short transport routes and terrestrial sediment supply as interactions of fluvial, alluvial and aeolian processes as well as syngenetic permafrost aggradation. With our study we show that frozen and thawed Yedoma deposits are more heterogeneous in their sedimentological and formation conditions at regional and circumarctic level than previously thought.

Nevertheless, all geochemical and sedimentological proxies of Yedoma sediments always seem to be mixed signals of original characteristics of parent material and the influence of permafrost degradation (seen by the radiocarbon dates). The latter applies above all to the talik areas of the studied sedimentary sequences. Dissolution and leaching of certain elements and also certain grain-size fractions are the results of extensive thermokarst formation. The talik sediment properties indicate, however, pure subsidence of the thawed sediment package during late Pleistocene and Holocene thaw-related formation of alas basin and lakes. Lacustrine processes and talik evolution have only marginally influenced the geochemical properties of the thawed sediments. Rather, the general geochemical and sedimentological properties of the Yedoma IC deposits seem to have been preserved in the alas deposits. A clear determination of thermokarst and/or taberal deposits in the sense of *in-situ* thaw of Yedoma deposits under a large body of water and the tracing of clear diagenetic changes within the sedimentary structures in this context is therefore not possible.

DATA AVAILABILITY STATEMENT

The original contributions presented in the study are included in the article/**Supplementary Material**, further inquiries can be directed to the corresponding author.

AUTHOR CONTRIBUTIONS

All authors listed have made a substantial, direct, and intellectual contribution to the work and approved it for publication.

FUNDING

We acknowledge support from Leipzig University for Open Access Publishing. This study is based on a joint field campaign of the ERC PETA-CARB project (starting grant No. 338335) and a Deutsche Forschungsgemeinschaft (DFG) project (DFG grant No. UL426/1-1), and was carried out in cooperation with the Melnikov Permafrost Institute, Siberian Branch of Russian Academy of Sciences. SW acknowledges further support from DFG (grant No. WE4390/7-1).

Additional support for this study was provided by the German Federal Environmental Foundation (DBU) and the Potsdam Graduate School.

ACKNOWLEDGMENTS

We greatly appreciate the efforts of all Russian and German colleagues in organizing and supporting the fieldwork and laboratory analyses. We thank in particular Pavel Konstantinov, Alexey R. Desyatkin, and Avksenty Kondakov for field and drilling assistance as well as Dyke Scheidemann, Mikaela Weiner, Hanno Meyer (Alfred Wegener Institute and the Isolab Facility) and Katja Pöhlmann (University of Leipzig) for laboratory assistance.

SUPPLEMENTARY MATERIAL

The Supplementary Material for this article can be found online at: https://www.frontiersin.org/articles/10.3389/feart.2021.704141/full#supplementary-material

REFERENCES

Anderson, P. M., and V. Lozhkin, A. (2001). The Stage 3 Interstadial Complex (Karginskii/Middle Wisconsinan Interval) of Beringia: Variations in Paleoenvironments and Implications for Paleoclimatic Interpretations. *Quat. Sci. Rev.* 20, 93–125. doi:10.1016/s0277-3791(00)00129-3

Babechuk, M. G., Widdowson, M., and Kamber, B. S. (2014). Quantifying Chemical Weathering Intensity and Trace Element Release from Two Contrasting Basalt Profiles, Deccan Traps, India. *Chem. Geol.* 363, 56–75. doi:10.1016/j.chemgeo.2013.10.027

Bertrand, S., Hughen, K. A., Sepúlveda, J., and Pantoja, S. (2012). Geochemistry of Surface Sediments from the Fjords of Northern Chilean Patagonia (44-47°S): Spatial Variability and Implications for Paleoclimate Reconstructions. *Geochim. Cosmochim. Acta* 76, 125–146. doi:10.1016/j.gca.2011.10.028

Biskaborn, B. K., Herzschuh, U., Bolshiyanov, D., Savelieva, L., and Diekmann, B. (2012). Environmental Variability in Northeastern Siberia During the Last ~ 13,300 Yr Inferred from lake Diatoms and Sediment-Geochemical Parameters. *Palaeogeogr. Palaeoclimatol. Palaeoecol.* 329–330, 22–36. doi:10.1016/j.palaeo.2012.02.003

Biskaborn, B. K., Herzschuh, U., Bolshiyanov, D. Y., Schwamborn, G., and Diekmann, B. (2013). Thermokarst Processes and Depositional Events in a Tundra lake, Northeastern Siberia. *Permafrost Periglac. Process.* 24 (3), 160–174. doi:10.1002/ppp.1769

Biskaborn, B. K., Smith, S. L., Noetzli, J., Matthes, H., Vieira, G., Streletskiy, D. A., et al. (2019). Permafrost is Warming at a Global Scale. *Nat. Commun.* 10, 264. doi:10.1038/s41467-018-08240-4

Blott, S. J., and Pye, K. (2001). GRADISTAT: a Grain Size Distribution and Statistics Package for the Analysis of Unconsolidated Sediments. *Earth Surf. Process. Landf.* 26 (11), 1237–1248. doi:10.1002/esp.261

Bosikov, N. P. (1998). Wetness Variability and Dynamics of Thermokarst Processes in Central Yakutia. *Collect. Nordicana* 57, 71.

Bronk Ramsey, C. (2009). Bayesian Analysis of Radiocarbon Dates. *Radiocarbon* 51 (1), 337–360. doi:10.1017/s0033822200033865

Buggle, B., Glaser, B., Hambach, U., Gerasimenko, N., and Marković, S. (2011). An Evaluation of Geochemical Weathering Indices in Loess-Paleosol Studies. *Quat. Int.* 240 (1–2), 12–21. doi:10.1016/j.quaint.2010.07.019

Clark, P. U., Dyke, A. S., Shakun, J. D., Carlson, A. E., Clark, J., Wohlfarth, B., et al. (2009). The Last Glacial Maximum. *Science* 325 (5941), 710–714. doi:10.1126/science.1172873

Cox, R., Lowe, D. R., and Cullers, R. L. (1995). The Influence of Sediment Recycling and Basement Composition on Evolution of Mudrock Chemistry in the Southwestern United States. *Geochim. Cosmochim. Acta* 59 (14), 2919–2940. doi:10.1016/0016-7037(95)00185-9

Craig, H. (1961). Isotopic Variations in Meteoric Waters. *Science* 133, 1702–1703. doi:10.1126/science.133.3465.1702

Czudek, T., and Demek, J. (1970). Thermokarst in Siberia and its Influence on the Development of Lowland Relief. *Quat. Res.* 1, 103–120. doi:10.1016/0033-5894(70)90013-x

Dansgaard, W. (1964). Stable Isotopes in Precipitation. *Tellus* 16, 436–468. doi:10.3402/tellusa.v16i4.8993

Davison, W. (1993). Iron and Manganese in Lakes. *Earth Sci. Rev.* 34 (2), 119–163. doi:10.1016/0012-8252(93)90029-7

Dean, J. F., Meisel, O. H., Martyn Rosco, M., Marchesini, L. B., Garnett, M. H., Lenderink, H., et al. (2020). East Siberian Arctic Inland Waters Emit Mostly Contemporary Carbon. *Nat. Commun.* 11, 1627. doi:10.1038/s41467-020-15511-6

Demina, L. L., Novichkova, E. A., Lisitzin, A. P., and Kozina, N. V. (2019). Geochemical Signatures of Paleoclimate Changes in the Sediment Cores from the Gloria and Snorri Drifts (Northwest Atlantic) Over the Holocene-Mid Pleistocene. *Geosciences* 9, 432. doi:10.3390/geosciences9100432

Demory, F., Oberhänsli, H., Nowaczyk, N. R., Gottschalk, M., Wirth, R., and Naumann, R. (2005). Detrital Input and Early Diagenesis in Sediments from Lake Baikal Revealed by Rock Magnetism. *Glob. Planet. Change* 46 (1-4), 145–166. doi:10.1016/j.gloplacha.2004.11.010

Diekmann, B., Pestryakova, L., Nazarova, L., Subetto, D., Tarasov, P. E., Stauch, G., et al. (2017). Late Quaternary lake Dynamics in the Verkhoyansk Mountains of Eastern Siberia: Implications for Climate and Glaciation History. *Polarforschung* 86, 97–110. doi:10.2312/polarforschung.86.2.97

Fedorov, A. N., Gavriliev, P. P., Konstantinov, P. Y., Hiyama, T., Iijima, Y., and Iwahana, G. (2014). Estimating the Water Balance of a Thermokarst lake in the Middle of the Lena River basin, Eastern Siberia. *Ecohydrol.* 7 (2), 188–196. doi:10.1002/eco.1378

Fedorov, A. N., and Konstantinov, P. Y. (2009). Response of Permafrost Landscapes of Central Yakutia to Current Changes of Climate, and Anthropogenic Impacts. *Geogr. Nat. Resour.* 30, 146–150. doi:10.1016/j.gnr.2009.06.010

Feng, Z.-D. (1997). Geochemical Characteristics of a Loess-Soil Sequence in Central Kansas. *Soil Sci. Soc. Am. J.* 61, 534–541. doi:10.2136/sssaj1997.03615995006100020023x

Fischer, P., Hilgers, A., Protze, J., Kels, H., Lehmkuhl, F., and Gerlach, R. (2012). Formation and Geochronology of Last Interglacial to Lower Weichselian Loess/palaeosol Sequences - Case Studies from the Lower Rhine Embayment, Germany. *E&G Quat. Sci. J.* 61 (1), 48–63. doi:10.23689/fidgeo-174810.3285/eg.61.1.04

French, H., and Shur, Y. (2010). The Principles of Cryostratigraphy. *Earth Sci. Rev.* 101, 190–206. doi:10.1016/j.earscirev.2010.04.002

Gaglioti, B. V., Mann, D. H., Jones, B. M., Pohlman, J. W., Kunz, M. L., and Wooller, M. J. (2014). Radiocarbon Age-Offsets In An Arctic Lake Reveal The Long-Term Response of Permafrost Carbon To Climate Change. *J. Geophys. Res.-Biogeo.* 119 (8), 1630–1651. doi:10.1002/2014JG002688

Grosse, G., Jones, B., and Arp, C. (2013). "8.21 Thermokarst Lakes, Drainage, and Drained Basins," in *Treatise on Geomorphology*. Editor J. F. Shroder (San Diego, CA: Academic Press), 325–353. doi:10.1016/b978-0-12-374739-6.00216-5

Haberzettl, T., Corbella, H., Fey, M., Janssen, S., Lücke, A., Mayr, C., et al. (2007). Lateglacial and Holocene Wet-Dry Cycles in Southern Patagonia: Chronology, Sedimentology and Geochemistry of a Lacustrine Record from Laguna Potrok Aike, Argentina. *Holocene* 17, 297–310. doi:10.1177/0959683607076437

Heslop, J. K., Walter Anthony, K. M., Winkel, M., Sepulveda-Jauregui, A., Martinez-Cruz, K., Bondurant, A., et al. (2020). A Synthesis of Methane Dynamics in Thermokarst Lake Environments. *Earth Sci. Rev.* 210, 103365. doi:10.1016/j.earscirev.2020.103365

Hugelius, G., Strauss, J., Zubrzycki, S., Harden, J. W., Schuur, E. A. G., Ping, C.-L., et al. (2014). Estimated Stocks of Circumpolar Permafrost Carbon with Quantified Uncertainty Ranges and Identified Data Gaps. *Biogeosciences* 11, 6573–6593. doi:10.5194/bg-11-6573-2014

Iijima, Y., Fedorov, A. N., Park, H., Suzuki, K., Yabuki, H., Maximov, T. C., et al. (2010). Abrupt Increases in Soil Temperatures Following Increased Precipitation in a Permafrost Region, Central Lena River basin, Russia. *Permafrost Periglac. Process.* 21, 30–41. doi:10.1002/ppp.662

Johansson, E., Gustafsson, L.-G., Berglund, S., Lindborg, T., Selroos, J.-O., Claesson Liljedahl, L., et al. (2015). Data Evaluation and Numerical Modeling of Hydrological Interactions between Active Layer, lake and Talik in a Permafrost Catchment, Western Greenland. *J. Hydrol.* 527, 688–703. doi:10.1016/j.jhydrol.2015.05.026

Jongejans, L. L., Liebner, S., Knoblauch, C., Mangelsdorf, K., and Strauss, J. (2021b). Dissolved Organic Carbon Content in Thawed Sediments underneath a Yedoma and Alas Thermokarst lake in Eastern Siberia. *PANGAEA*. doi:10.1594/PANGAEA.928136

Jongejans, L. L., Liebner, S., Knoblauch, C., Mangelsdorf, K., Ulrich, M., Grosse, G., et al. (2021a). Greenhouse Gas Production and Lipid Biomarker Distribution in Yedoma and Alas Thermokarst Lake Sediments in Eastern Siberia. *Glob. Change Biol.* 27 (12), 2822–2839. doi:10.1111/gcb.15566

Kienast, F., Schirrmeister, L., Siegert, C., and Tarasov, P. (2005). Palaeobotanical Evidence for Warm Summers in the East Siberian Arctic during the Last Cold Stage. *Quat. Res.* 63, 283–300. doi:10.1134/S004451341911010210.1016/j.yqres.2005.01.003

Knoblauch, C., Beer, C., Sosnin, A., Wagner, D., and Pfeiffer, E.-M. (2013). Predicting Long-Term Carbon Mineralization and Trace Gas Production from Thawing Permafrost of Northeast Siberia. *Glob. Change Biol.* 19 (4), 1160–1172. doi:10.1111/gcb.12116

Kokelj, S. V., Lacelle, D., Lantz, T. C., Tunnicliffe, J., Malone, L., Clark, I. D., et al. (2013). Thawing of Massive Ground Ice in Mega Slumps Drives Increases in Stream Sediment and Solute Flux across a Range of Watershed Scales. *J. Geophys. Res. Earth Surf.* 118, 681–692. doi:10.1002/jgrf.20063

Lacelle, D., Juneau, V., Pellerin, A., Lauriol, B., and Clark, I. D. (2008). Weathering Regime and Geochemical Conditions in a Polar Desert Environment, Haughton Impact Structure Region, Devon Island, Canada. *Can. J. Earth Sci.* 45 (10), 1139–1157. doi:10.1139/E08-063

Lampe, R., Janke, W., Schult, M., Meng, S., and Lampe, M. (2016). Multiproxy-Untersuchungen zur Paläoökologie und -hydrologie eines spätglazial- bis frühholozänen Flachsees im nordostdeutschen Küstengebiet (Glowe-Paläosee/Insel Rügen). *E&G Quat. Sci. J.* 65 (1), 41–75. doi:10.3285/eg.65.1.03

Lopez, P., Navarro, E., Marce, R., Ordoñez, J., Caputo, L., and Armengol, J. (2006). Elemental Ratios in Sediments as Indicators of Ecological Processes in Spanish Reservoirs. *Limnetica* 25 (1–2), 499–512.

Martens, J., Wild, B., Muschitiello, F., O'Regan, M., Jakobsson, M., Semiletov, I., et al. (2020). Remobilization of Dormant Carbon from Siberian-Arctic Permafrost During Three Past Warming Events. *Sci. Adv.* 6, eabb6546. doi:10.1126/sciadv.abb6546

McKinney, W. (2010). "Data Structures for Statistical Computing in Python," in Proceedings of the 9th Python in Science Conference, Austin, TX, USA, June 28–July 3. Editor S. van der Walt and K.J. Millman, 56–61. Available at: http://conference.scipy.org/proceedings/scipy2010/pdfs/mckinney.pdf.

Meyer, H., Schönicke, L., Wand, U., Hubberten, H. W., and Friedrichsen, H. (2000). Isotope Studies of Hydrogen and Oxygen in Ground Ice - Experiences with the Equilibration Technique. *Isotopes Environ. Health Stud.* 36, 133–149. doi:10.1080/10256010008032939

Mollenhauer, G., Grotheer, H., Gentz, T., Bonk, E., and Hefter, J. (2021). Standard Operation Procedures and Performance of the MICADAS Radiocarbon Laboratory at Alfred Wegener Institute (AWI), Germany. *Nucl. Instrum. Methods Phys. Res. Section B: Beam Interactions Mater. Atoms* 496, 45–51. doi:10.1016/j.nimb.2021.03.016

Murton, J. B., Goslar, T., Edwards, M. E., Bateman, M. D., Danilov, P. P., Savvinov, G. N., et al. (2015). Palaeoenvironmental Interpretation of Yedoma silt (Ice Complex) Deposition as Cold-Climate Loess, Duvanny Yar, Northeast Siberia. *Permafrost Periglac. Process* 26, 208–288. doi:10.1002/ppp.1843

Muster, S., Riley, W. J., Roth, K., Langer, M., Cresto Aleina, F., Koven, C. D., et al. (2019). Size Distributions of Arctic Waterbodies Reveal Consistent Relations in Their Statistical Moments in Space and Time. *Front. Earth Sci.* 7, 5. doi:10.3389/feart.2019.00005

Nitze, I., Grosse, G., Jones, B., Arp, C., Ulrich, M., Fedorov, A., et al. (2017). Landsat-Based Trend Analysis of lake Dynamics across Northern Permafrost Regions. *Remote Sens.* 9 (7), 640. doi:10.3390/rs9070640

Oliphant, T. E. (2006). *A Guide to NumPy*. United States: Trelgol Publishing.

Opel, T., Murton, J. B., Wetterich, S., Meyer, H., Ashastina, K., Günther, F., et al. (2019). Past Climate and Continentality Inferred from Ice Wedges at Batagay Megaslump in the Northern Hemisphere's Most continental Region, Yana Highlands, Interior Yakutia. *Clim. Past* 15, 1443–1461. doi:10.5194/cp-15-1443-2019

Opfergelt, S. (2020). The Next Generation of Climate Model Should Account for the Evolution of Mineral-Organic Interactions with Permafrost Thaw. *Environ. Res. Lett.* 15, 091003. doi:10.1088/1748-9326/ab9a6d

Papina, T., Malygina, N., Eirikh, A., Galanin, A., and Zheleznyak, M. (2017). Isotopic Composition And Sources of Atmospheric Precipitation In Central Yakutia. *Earth's Cryosphere* 21, 52–61. doi:10.21782/EC2541-9994-2017-1(52-61)

Pedregosa, F., Varoquaux, G., Gramfort, A., Michel, V., Thirion, B., Grisel, O., et al. (2011). Scikit-Learn: Machine Learning in Python. *J. Mach. Learn. Res.* 12, 2825–2830.

Pestryakova, L. A., Herzschuh, U., Wetterich, S., and Ulrich, M. (2012). Present-Day Variability and Holocene Dynamics of Permafrost-Affected Lakes in central Yakutia (Eastern Siberia) Inferred from Diatom Records. *Quat. Sci. Rev.* 51, 56–70. doi:10.1016/j.quascirev.2012.06.020

Péwé, T. L., and Journaux, A. (1983). *Origin and Character of Loess-Like Silt in Unglaciated South-Central Yakutia, Siberia, USSR*. *USGS Prof. Pap.* 1262, 1–45.

Popp, S., Diekmann, B., Meyer, H., Siegert, C., Syromyatnikov, I., and Hubberten, H.-W. (2006). Palaeoclimate Signals as Inferred from Stable-Isotope Composition of Ground Ice in the Verkhoyansk Foreland, Central Yakutia. *Permafrost Periglac. Process.* 17, 119–132. doi:10.1002/ppp.556

Reimer, P., Austin, W., Bard, E., Bayliss, A., Blackwell, P., Bronk Ramsey, C., et al. (2020). The IntCal20 Northern Hemisphere Radiocarbon Age Calibration Curve (0–55 cal kBP). *Radiocarbon* 62, 725–757. doi:10.1017/rdc.2020.41

Roeser, P., Franz, S. O., and Litt, T. (2016). Aragonite and Calcite Preservation in Sediments from Lake Iznik Related to Bottom lake Oxygenation and Water Column Depth. *Sedimentology* 63 (7), 2253–2277. doi:10.1111/sed.12306

Santoro, M., and Strozzi, T. (2012). Circumpolar Digital Elevation Models > 55° N with Links to Geotiff Images. *PANGAEA*. doi:10.1594/PANGAEA.779748

Schatz, A.-K., Scholten, T., and Kühn, P. (2015). Paleoclimate and Weathering of the Tokaj (Hungary) Loess-Paleosol Sequence. *Palaeogeogr. Palaeoclimatol. Palaeoecol.* 426, 170–182. doi:10.1016/j.palaeo.2015.03.016

Schirrmeister, L., Dietze, E., Matthes, H., Grosse, G., Strauss, J., Laboor, S., et al. (2020). The Genesis of Yedoma Ice Complex Permafrost - Grain-Size Endmember Modeling Analysis from Siberia and Alaska. *E&G Quat. Sci. J.* 69, 33–53. doi:10.5194/egqsj-69-33-2020

Schirrmeister, L., Froese, D., Tumskoy, V., Grosse, G., and Wetterich, S. (2013). "Yedoma: Late Pleistocene Ice-Rich Syngenetic Permafrost of Beringia," in *The Encyclopedia of Quaternary Science*. Editor S.A. Elias (Amsterdam: Elsevier) Vol. 3, 542–552.

Schirrmeister, L., Kunitsky, V., Grosse, G., Wetterich, S., Meyer, H., Schwamborn, G., et al. (2011). Sedimentary Characteristics and Origin of the Late Pleistocene Ice Complex on north-east Siberian Arctic Coastal Lowlands and Islands – A Review. *Quat. Int.* 241 (1–2), 3–25. doi:10.1016/j.quaint.2010.04.004

Schuur, E. A. G., McGuire, A. D., Schädel, C., Grosse, G., Harden, J. W., Hayes, D. J., et al. (2015). Climate Change and the Permafrost Carbon Feedback. *Nature* 520, 171–179. doi:10.1038/nature14338

Schwamborn, G., Schirrmeister, L., Frütsch, F., and Diekmann, B. (2012). Quartz Weathering in Freeze-Thaw Cycles: experiment and Application to the el'gygytgyn Crater Lake Record for Tracing Siberian Permafrost History. *Geografiska Annaler: Ser. A, Phys. Geogr.* 94, 481–499. doi:10.1111/j.1468-0459.2012.00472.x

Siegert, C. (1987). Greigite and Mackinawite in Quaternary Deposits of central Yakutia. *Mineral. Zh.* 9 (5), 75–81.

Siegert, C. (1979). "Minerologic-petrographic Characteristic of Alas Deposits," in *Structure and Absolute Geochronology of Alas Deposits in Central Yakutia*. Editor E. M. Katasonov (Moscow: Nauka), 44–61.

Soloviev, P. A. (1959). *Cryolithic Zone of the Northern Part of Lena-Amga Interfluve*. Moscow: Izdatel'stvo Akademii SSSR, 142.

Soloviev, P. A. (1973). Thermokarst Phenomena and Landforms Due to Frost Heaving in Central Yakutia. *Biuletyn Peryglacjalny* 23, 135–155.

Strauss, J., Laboor, S., Fedorov, A. N., Fortier, D., Froese, D., Fuchs, M., et al. (2016). Database of Ice-Rich Yedoma Permafrost (IRYP). *PANGAEA*. doi:10.1594/PANGAEA.861733

Strauss, J., Schirrmeister, L., Grosse, G., Fortier, D., Hugelius, G., Knoblauch, C., et al. (2017). Deep Yedoma Permafrost: A Synthesis of Depositional Characteristics and Carbon Vulnerability. *Earth Sci. Rev.* 172, 75–86. doi:10.1016/j.earscirev.2017.07.007

Strauss, J., Schirrmeister, L., Grosse, G., Wetterich, S., Ulrich, M., Herzschuh, U., et al. (2013). The Deep Permafrost Carbon Pool of the Yedoma Region in Siberia and Alaska. *Geophys. Res. Lett.* 40, 6165–6170. doi:10.1002/2013GL058088

Strauss, J., Schirrmeister, L., Mangelsdorf, K., Eichhorn, L., Wetterich, S., and Herzschuh, U. (2015). Organic-Matter Quality of Deep Permafrost Carbon - A Study from Arctic Siberia. *Biogeosciences* 12, 2227–2245. doi:10.5194/bg-12-2227-2015

Tarasenko, T. V. (2013). Interannual Variations in the Areas of Thermokarst Lakes in Central Yakutia. *Water Resour.* 40 (2), 111–119. doi:10.1134/S0097807813010107

Troyanskaya, O., Cantor, M., Sherlock, G., Brown, P., Hastie, T., Tibshirani, R., et al. (2001). Missing Value Estimation Methods for DNA Microarrays. *Bioinformatics* 17 (6), 520–525. doi:10.1093/bioinformatics/17.6.520

Turetsky, M. R., Abbott, B. W., Jones, M. C., Anthony, K. W., Olefeldt, D., Schuur, E. A. G., et al. (2020). Carbon Release through Abrupt Permafrost Thaw. *Nat. Geosci.* 13, 138–143. doi:10.1038/s41561-019-0526-0

Turner, K. W., Wolfe, B. B., Edwards, T. W. D., Lantz, T. C., Hall, R. I., and Larocque, G. (2014). Controls on Water Balance of Shallow Thermokarst Lakes and Their Relations with Catchment Characteristics: a Multi-Year, Landscape-Scale Assessment Based on Water Isotope Tracers and Remote Sensing in Old Crow Flats, Yukon (Canada). *Glob. Change Biol.* 20, 1585–1603. doi:10.1111/gcb.12465

Ulrich, M., Grosse, G., Strauss, J., and Schirrmeister, L. (2014). Quantifying Wedge-Ice Volumes in Yedoma and Thermokarst Basin Deposits. *Permafrost Periglac. Process.* 25, 151–161. doi:10.1002/ppp.1810

Ulrich, M., Matthes, H., Schirrmeister, L., Schütze, J., Park, H., Iijima, Y., et al. (2017b). Differences in Behavior and Distribution of Permafrost-Related Lakes in Central Yakutia and Their Response to Climatic Drivers. *Water Resour. Res.* 53 (2), 1167–1188. doi:10.1002/2016WR019267

Ulrich, M., Matthes, H., Schmidt, J., Fedorov, A. N., Schirrmeister, L., Siegert, C., et al. (2019). Holocene Thermokarst Dynamics in Central Yakutia - A Multi-Core and Robust Grain-Size Endmember Modeling Approach. *Quat. Sci. Rev.* 218, 10–33. doi:10.1016/j.quascirev.2019.06.010

Ulrich, M., Wetterich, S., Rudaya, N., Frolova, L., Schmidt, J., Siegert, C., et al. (2017a). Rapid Thermokarst Evolution During the Mid-Holocene in Central Yakutia, Russia. *Holocene* 27 (12), 1899–1913. doi:10.1177/0959683617708454

Urbat, I. (2009). Oceanic Anoxic Event (OAE) 1b - High Resolution Geochemical Studies, Mazagan Plateau and Vocontian Basin. PhD thesis. Cologne, Germany: University of Cologne, 125.

Vallat, R. (2018). Pingouin: Statistics in Python. *J. Open Source Softw.* 3 (31), 1026. doi:10.21105/joss.01026

Walter Anthony, K., Schneider von Deimling, T., Nitze, I., Frolking, S., Emond, A., Daanen, R., et al. (2018). 21st-Century Modeled Permafrost Carbon Emissions Accelerated by Abrupt Thaw beneath Lakes. *Nat. Commun.* 9, 3262. doi:10.1038/s41467-018-05738-9

Wegwerth, A., Dellwig, O., Kaiser, J., Ménot, G., Bard, E., Shumilovskikh, L., et al. (2014). Meltwater Events and the Mediterranean Reconnection at the Saalian-Eemian Transition in the Black Sea. *Earth Planet. Sci. Lett.* 404, 124–135. doi:10.1016/j.epsl.2014.07.030

Weiss, N., Blok, D., Elberling, B., Hugelius, G., Jørgensen, C. J., Siewert, M. B., et al. (2016). Thermokarst Dynamics and Soil Organic Matter Characteristics Controlling Initial Carbon Release from Permafrost Soils in the Siberian Yedoma Region. *Sediment. Geol.* 340, 38–48. doi:10.1016/j.sedgeo.2015.12.004

Wetterich, S., Herzschuh, U., Meyer, H., Pestryakova, L., Plessen, B., Lopez, C. M. L., et al. (2008). Evaporation Effects as Reflected in Freshwaters and Ostracod Calcite from Modern Environments in Central and Northeast Yakutia (East Siberia, Russia). *Hydrobiologia* 614, 171–195. doi:10.1007/s10750-008-9505-y

Wetterich, S., Kizyakov, A., Fritz, M., Wolter, J., Mollenhauer, G., Meyer, H., et al. (2020). The Cryostratigraphy of the Yedoma Cliff of Sobo-Sise Island (Lena delta) Reveals Permafrost Dynamics in the central Laptev Sea Coastal Region During the Last 52 kyr. *Cryosphere* 14, 4525–4551. doi:10.5194/tc-14-4525-2020

Wetterich, S., Rudaya, N., Tumskoy, V., Andreev, A. A., Opel, T., Schirrmeister, L., et al. (2011). Last Glacial Maximum Records in Permafrost of the East Siberian Arctic. *Quat. Sci. Rev.* 30, 3139–3151. doi:10.1016/j.quascirev.2011.07.020

Wetterich, S., Tumskoy, V., Rudaya, N., Andreev, A. A., Opel, T., Meyer, H., et al. (2014). Ice Complex Formation in Arctic East Siberia during the MIS3 Interstadial. *Quat. Sci. Rev.* 84, 39–55. doi:10.1016/j.quascirev.2013.11.009

Wien, K., Kölling, M., and Schulz, H. D. (2005). Close Correlation between Sr/Ca Ratios in Bulk Sediments from the Southern Cape Basin and the SPECMAP Record. *Geo. Mar. Lett.* 25, 265–271. doi:10.1007/s00367-005-0211-8

Windirsch, T., Grosse, G., Ulrich, M., Schirrmeister, L., Fedorov, A. N., Konstantinov, P. Y., et al. (2020). Organic Carbon Characteristics in Ice-Rich Permafrost in Alas and Yedoma Deposits, central Yakutia, Siberia. *Biogeosciences* 17, 3797–3814. doi:10.5194/bg-17-3797-2020

Zech, M., Zech, R., Zech, W., Glaser, B., Brodowski, S., and Amelung, W. (2008). Characterisation and Palaeoclimate of a Loess-Like Permafrost Palaeosol Sequence in NE Siberia. *Geoderma* 143 (3–4), 281–295. doi:10.1016/j.geoderma.2007.11.012

Zolkos, S., and Tank, S. E. (2020). Experimental Evidence that Permafrost Thaw History and Mineral Composition Shape Abiotic Carbon Cycling in Thermokarst-Affected Stream Networks. *Front. Earth Sci.* 8, 152. doi:10.3389/feart.2020.00152

Zolkos, S., Tank, S. E., and Kokelj, S. V. (2018). Mineral Weathering and the Permafrost Carbon-Climate Feedback. *Geophys. Res. Lett.* 45, 9623–9632. doi:10.1029/2018GL078748

Conflict of Interest: The authors declare that the research was conducted in the absence of any commercial or financial relationships that could be construed as a potential conflict of interest.

Publisher's Note: All claims expressed in this article are solely those of the authors and do not necessarily represent those of their affiliated organizations, or those of the publisher, the editors and the reviewers. Any product that may be evaluated in this article, or claim that may be made by its manufacturer, is not guaranteed or endorsed by the publisher.

frontiers in Earth Science

ORIGINAL RESEARCH
published: 24 August 2021
doi: 10.3389/feart.2021.680565

Check for updates

Geomorphology and InSAR-Tracked Surface Displacements in an Ice-Rich Yedoma Landscape

J. van Huissteden[1,2], K. Teshebaeva[1], Y. Cheung[1], R. Í. Magnússon[3], H. Noorbergen[4], S. V. Karsanaev[5], T. C. Maximov[5] and A. J. Dolman[1]*

[1]Earth Science Department, Faculty of Sciences, Vrije Universiteit, Amsterdam, Netherlands, [2]VOF Kytalyk Carbon Cycle Research, Epse, Netherlands, [3]Plant Ecology and Nature Conservation Group, Wageningen University, Wageningen, Netherlands, [4]Remote Sensing and GIS Department, NLR, Marknesse, Netherlands, [5]Institute for Biological Problems of the Cryolithozone, Siberian Branch Russian Academy of Sciences, Yakutsk, Russia

Ice-ridge Yedoma terrain is susceptible to vertical surface displacements by thaw and refreeze of ground ice, and geomorphological processes of mass wasting, erosion and sedimentation. Here we explore the relation between a 3 year data set of InSAR measurements of vertical surface displacements during the thaw season, and geomorphological features in an area in the Indigirka Lowlands, Northeast Siberia. The geomorphology is presented in a geomorphological map, based on interpretation of high resolution visible spectrum satellite imagery, field surveys and available data from paleo-environmental research. The main landforms comprise overlapping drained thaw lake basins and lakes, erosion remnants of Late Pleistocene Yedoma deposits, and a floodplain of a high-sinuosity anastomosing river with ancient river terrace remnants. The spatial distribution of drained thaw lake basins and Yedoma erosion remnants in the study area and its surroundings is influenced by neotectonic movements. The 3 years of InSAR measurement include 2 years of high snowfall and extreme river flooding (2017–2018) and 1 year of modest snowfall, early spring and warm summer (2019). The magnitude of surface displacements varies among the years, and show considerable spatial variation. Distinct spatial clusters of displacement trajectories can be discerned, which relate to geomorphological processes and ground ice conditions. Strong subsidence occurred in particular in 2019. In the wet year of 2017, marked heave occurred at Yedoma plateau surfaces, likely by ice accumulation at the top of the permafrost driven by excess precipitation. The spatial variability of surface displacements is high. This is explored by statistical analysis, and is attributed to the interaction of various processes. Next to ground ice volume change, also sedimentation (peat, colluvial deposition) and shrinkage or swelling of soils with changing water content may have contributed. Tussock tundra areas covered by the extreme 2017 and 2018 spring floods show high subsidence rates and an increase of midsummer thaw depths. We hypothesize that increased flood heights along Siberian lowland rivers potentially induce deeper thaw and subsidence on floodplain margins, and also lowers the drainage thresholds of thaw lakes. Both mechanisms tend to increase floodplain area. This may increase CH_4 emission from floodplains, but also may enhance carbon storage in floodplain sedimentary environments.

Keywords: InSAR (interferometric synthetic aperture radar), Yedoma, geomorphology, Thaw lakes, floodplain, neotectonics

OPEN ACCESS

Edited by:
*Annett Bartsch,
b.geos GmbH, Austria*

Reviewed by:
*Simon Zwieback,
University of Alaska Fairbanks, United States*
*Matthias Siewert,
Umeå University, Sweden*

****Correspondence:***
*J. van Huissteden
j.van.huissteden@vu.nl*

Specialty section:
This article was submitted to Cryospheric Sciences, a section of the journal Frontiers in Earth Science

Received: *14 March 2021*
Accepted: *06 August 2021*
Published: *24 August 2021*

Citation:
van Huissteden J, Teshebaeva K, Cheung Y, Magnússon RÍ, Noorbergen H, Karsanaev SV, Maximov TC and Dolman AJ (2021) Geomorphology and InSAR-Tracked Surface Displacements in an Ice-Rich Yedoma Landscape. Front. Earth Sci. 9:680565. doi: 10.3389/feart.2021.680565

INTRODUCTION

Permafrost is increasingly influenced by climate warming. Permafrost thaw is expected to enhance greenhouse gas emissions from permafrost soils and to decrease stability of soils, in particular in ice-rich permafrost areas (e.g. IPCC, 2013; AMAP, 2017). A specific type of ice-rich permafrost formation that occurs over large areas in Siberia and Alaska is Yedoma, also known as Ice Complex: periglacial loess and fluvial silt deposits that were deposited during Quaternary glacials in unglaciated terrain, which obtained large masses of excess ice by the growth of syngenetic ice wedges during sedimentation (Schirrmeister et al., 2013; Murton et al., 2015; Strauss et al., 2017). Yedoma contains a considerable carbon stock (Zimov et al., 2006; Strauss et al., 2017). These deep ice-rich deposits (several tens of meters and more) are very vulnerable to abrupt thaw (i.e. thermokarst) with rapid erosion, or more gradual subsidence, and may release carbon to the atmosphere as CO_2 and CH_4 (Schneider von Deimling et al., 2015; Vonk et al., 2013; Vonk et al., 2015). Surface displacements related to permafrost thaw also affect the stability of human infrastructure in permafrost areas. Structural instability can lead to severe environmental damage when urban, industrial or mining infrastructure is affected (e.g. Shiklomanov et al., 2017; Hjort et al., 2018).

Climate-related changes that may enhance permafrost thaw are higher air temperatures in winter and summer, and changes in precipitation that affect snow cover thickness, soil water saturation, water ponding, river flooding, fire frequency and vegetation change (e.g. reviews by Anisimov and Nelson, 1997; Nelson et al., 2002; Jorgenson et al., 2010; Nauta et al., 2014). Vegetation change also may delay permafrost thaw (Blok et al., 2010; Jorgenson et al., 2010; Kanevskiy et al., 2017). The effects of these climatic factors act unevenly across the landscape, since they are affected by geomorphologically determined terrain characteristics as slope, insolation, drainage and exposure to river flooding and erosion.

Net loss of ice by thaw of ice-rich permafrost over several years is reflected by a trend of surface subsidence, superimposed on the yearly surface displacements due to thaw at the top of the permafrost in summer (subsidence) and regrowth of ice in autumn and winter (frost heave). These surface displacements can be detected by synthetic aperture radar (SAR) interferometry from satellites (InSAR), and can assist in outlining areas that are most vulnerable to soil subsidence from permafrost thaw (Liu et al., 2010; Liu et al., 2012; Liu et al., 2014; Teshebaeva et al., 2020). Ice content is known to be an important parameter in surface subsidence (e.g. Jorgenson et al., 2010; Schneider von Deimling et al., 2015; Turetsky et al., 2019; van Huissteden, 2020), at least on a local scale. The soil ice distribution in Yedoma landscapes is also related to geomorphology and (cryo) stratigraphy of deposits, that determine duration and mode of ice accumulation: growth of wedge ice and small-scale cryostructure ice. This varies from large scale variation, e.g. large ice volumes in deep syngenetic wedges in Yedoma vs. lower ice volumes in deposits of Holocene thaw lake beds and floodplains (Kanevskiy et al., 2013; Morgenstern et al., 2013; Strauss et al., 2017), and variations determined by sedimentary patterns of floodplain and thaw lake sediments (Ulrich et al., 2014). Thus, the spatial variation of vulnerability to surface subsidence is expected to be strongly related to geomorphology.

Here, we present a geomorphological map of an Eastern Siberian Yedoma area in the Indigirka Lowlands, combined with InSAR surface displacement measures using Sentinel-1A/B data collected over 3 years. This time series is too short to quantify long term surface displacement trends. However, the data result from years with strongly contrasting seasonal weather patterns: 2 years of high winter precipitation resulting in pronounced spring flooding, and a year with low winter precipitation, early spring and warm summer. Therefore these data contain information that permits detection of differences in surface stability between terrain units, differences among years with contrasting weather patterns, and inferences on the processes that determine vertical surface displacements, such as ground ice thaw and accumulation, river flooding, erosion/sedimentation and soil processes. Also neotectonics influence the landscape on a large scale.

We explore the relation of surface displacements with geomorphological terrain units, and the interaction of these with the contrasting yearly weather patterns, by statistical analysis. Our analysis shows, that patterns of surface displacements vary with geomorphological position, and between years.

The carbon cycle and greenhouse gas emission impacts of geomorphological changes, changes in active layer thickness (ALT), soil subsidence and erosion as detected by InSAR are potentially large (e.g. Liu et al., 2010; Liu at al., 2014; Abbott and Jones, 2015; Natali et al., 2015). We discuss the potential carbon cycle effects of our findings in general terms.

STUDY AREA

The study area is located at the Kytalyk/Chokurdagh tundra research station (70°49′N, 147°29′E), approximately 30 km WNW of the town of Chokurdagh, and located just north of the Berelegh river, a tributary to the Indigirka river (**Figure 1**). From 2003 onwards, data were collected on the carbon balance of the tundra and permafrost soil (Van der Molen et al., 2007; Blok et al., 2010; Parmentier et al., 2011a; Parmentier et al., 2011b; Parmentier et al., 2011c; Nauta et al., 2014; Dean et al., 2020), as well as data on vegetation, heat balance, soils, soil ice content and environmental history (Juszak et al., 2014; Beermann et al., 2015; Juszak et al., 2016; Teltewskoi et al., 2016; Weiss et al., 2016; Juszak et al., 2017; Li et al., 2017; Wang et al., 2018; Magnússon et al., 2020). The site is located on continuous permafrost. It is dominated by three main terrain units: the Berelegh river plain, Yedoma terrace remnants dating from the Last Glacial, and Holocene drained thaw lake basins (DTLB). The area has recently (2007, 2017, 2018) experienced several high to extremely high spring snowmelt floods (This paper; Tei et al., 2020). The geomorphological map is based on high resolution visible spectrum images (Geo-Eye, Worldview), high resolution digital elevation models (DEMs) derived from radar satellites, and terrain surveys.

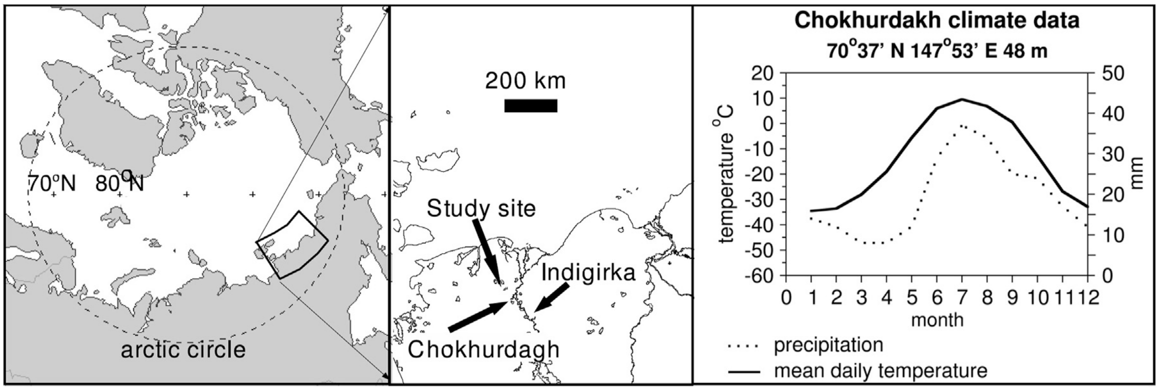

FIGURE 1 | Location of the study area and basic climatology 1970–2000 (right).

The permafrost is characterized by a shallow active layer, overlying continuous permafrost of over 300 m thickness. Near the surface, it is underlain by ice-rich Yedoma deposits (Schirrmeister et al., 2011), Holocene fluvial deposits of the Berelegh river and drained thaw lake basin fills (Alas deposits hereafter). The nearest weather station is that of Chokurdagh airport, WMO station code 21,946, 27 km away from the study site. The mean annual air temperature is −13.4°C, with an average July temperature of 10.3°C (1981–2010). Mean annual precipitation is 196 mm, with 76 mm falling in June to August (1981–2010) (Trouet and Van Oldenborgh, 2013).

The data from the weather station (**Figure 2A**, NOAA, 2020) show a conspicuous warming trend, in particular in the autumn months (October, November), winter and late winter (January, March, April). The winter precipitation shows marked variability in recent years, with three consecutive years of excessive snowfall in 2016–2018 (**Figure 2B**). The high snowfall winters of 2016–2017 and 2017–2018 are also demonstrated by the ERA5 reanalysis precipitation data in **Figure 2C**. The years 2017 and 2018 are similar in terms of precipitation and temperature. The year 2019 deviates from the previous 2 years, being considerably warmer and dryer than the previous years, both in summer and winter. This is demonstrated by the freezing and thawing degree days indices and cumulative winter and summer precipitation derived from the reanalysis data (**Figure 2D**).

The Berelegh river is an approximately west-east running tributary to the lower Indigirka river. The Berelegh is an anastomosing, multi-channel river with highly sinuous channels and wide marshy floodbasins with lakes. To the north of the floodplain, the landscape is dominated by Late Pleistocene-Holocene aged thaw lakes and drained thaw lake basins (DTLB's), and plateau-like erosion remnants of the Pleistocene Yedoma deposits. In the DTLB's, pingos are common. The DLTB relief is subdued with an elevation in the order of 10–12 m ASL; the DTLB floors are only a few meters higher than the floodplain surface (8–10 m), whilst the Yedoma plateaus rise some 10–25 m above the DTLB floors to elevations up to 35 m ASL. To the south of the Berelegh floodplain, the elevation of the Yedoma surface is higher (40–60 m ASL; Allaikhovsky Highland), and the area of lakes and DTLB is comparatively smaller (**Figure 3**; Schirrmeister et al., 2011).

The area is largely covered with Pliocene-Pleistocene deposits. At Chokurdagh and on the east side of the Indigirka river Mesozoic basaltic rock and Paleogene-Neogene sandstone crops out. In the Dzhelon-Sisi upland west of the study site, the Eocene Tastakh Formation consisting of clays and sands with coal lenses and gravel is exposed (Schirrmeister et al., 2011; Ren et al., 2013; Akhmetiev, 2015; Drachev, 2016). Below the Yedoma deposits, the Plio-Pleistocene Keremesit and Olyor Formations occur, which consist of fluvial and lacustrine silts and sands, with similar ice-rich characteristics as the Yedoma (Shmelev et al., 2017).

Tectonically, the area lies within the interaction zone of the Eurasian and North American plates (Imaeva et al., 2016a; Imaeva et al., 2016b; Drachev, 2016). The area is situated on the North American plate, consisting here of terranes of various origin. The Cenozoic sedimentary cover is bordered to the south by the Polousnyi mountain ridge, which is an active thrust belt with an WNW-ESE strike. To the SW of the area, the Chersky seismic belt is located (Fujita et al., 2009). Its seismic activity reaches to just south of the study area, with several reports of small (magnitude <4) earthquakes (Imaeva et al., 2016a; Imaeva et al., 2016b). To the north of the area, the intensely deformed Late Jurassic-Early Cretaceous South Anyui suture zone is buried beneath the Cenozoic sedimentary cover (Drachev, 2016).

DATA AND METHODS

Data

The SAR dataset used in this study was acquired by Sentinel-1 A/B C-band (~5.7 cm wavelength) satellite sensor, covering the seasonal time period from June to September for 2017–2019 years. We used 30 Sentinel-1A/B IW SLC SAR images acquired in descending orbits with an incidence angle of 37–39° and a pixel spacing of 2.3 × 14.1 m (range x azimuth).

A Digital Elevation Model (DEM) from TanDEM-X mission is used for InSAR processing, at 90 m spatial resolution. TanDEM-X (TerraSAR-X add-on for Digital Elevation Measurements) is an

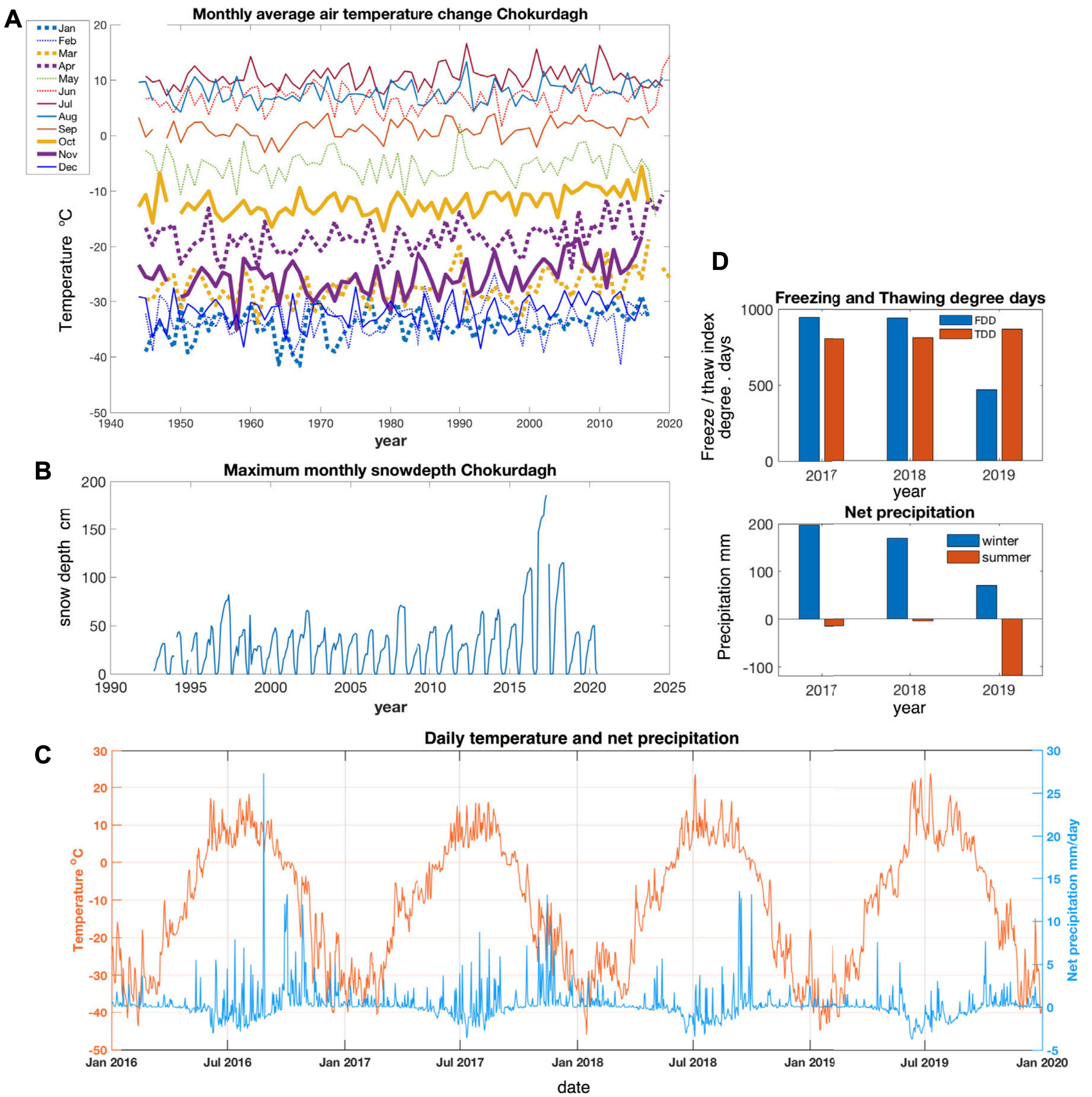

FIGURE 2 | (A): Mean monthly air temperatures (1944–2020) of Chokurdagh weather station. Thick lines represent months with a significant temperature trend (linear regression, $p < 0.01$). From 2017 onwards data are not always complete; months with >9 missing observation days are not included. **(B)**: Maximum monthly snow depth (cm) of Chokurdagh weather station, 1993–2020. **(C)**: Temperature and net precipitation (precipitation-evaporation) from ERA5 reanalysis (Hersbach et al., 2020); data of a 1° square around the study area, from 2016 to 2020. **(D)** above: freezing degree days (FDD) and thawing degree days (TDD), and below: winter (October-April) and summer (May-Sept) net precipitation totals for 2017–2019 derived from the ERA5 data.

Earth observation radar mission that consists of a SAR interferometer built by two almost identical satellites flying in close formation. With a typical separation between the satellites of 120–500 m a global Digital Elevation Model (DEM) was generated (Wessel et al., 2018).

In addition a high resolution global DEM from ALOS PRISM (Tadono et al., 2014; Takaku at al., 2016) with spatial resolution of 5 m is used for geomorphology analyses.

The high resolution visible spectrum images have a resolution 0.5 m in panchromatic mode and 1.8 m in multispectral mode and were acquired by the following satellites and dates: GeoEye-1, 0.41 m/1.64 m resolution in panchromatic, resp. multispectral mode, image date 2010-08-19), Worldview 2 (0.46 m/1.84 m panchrom./multispectral, date 2015-07-10 and 2019-08-01), Worldview 3 (0.31/1 0.24 m panchrom./multispectral, date 2018-07-05). The images from 2015 to 2019 were completely cloud-free. The image of 2015 was chosen as baseline for comparison with the velocity data, because it represents approximately average summer soil moisture conditions.

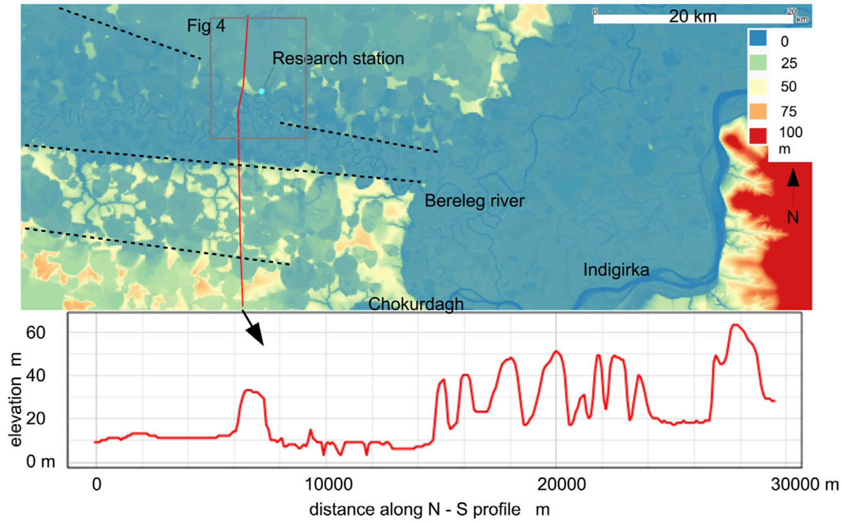

FIGURE 3 | Tandem-X elevation map of the study area and its surroundings. The elevation profile (below) is situated slightly west from Kytalyk Tundra Research Station (blue dot). The grey square indicates the map area of **Figure 4**. Broken black lines indicate possible tectonic lineaments.

InSAR Processing

The InSAR technique exploits multiple SAR images and applies appropriate data processing and analysis procedures to separate the contribution of the phase caused by the deformation, from the other phase components. The technique focuses on the identification of pixels in the SAR image characterized by small noise, which have typically two properties: the radar response is dominated by a strong reflecting object, and remains constant over time (Persistent Scatterer, PS) (Ferretti at al., 2001).

The SAR imagery is processed using ESA's Sentinel Application Platform (SNAP) S1-toolbox (Veci et al., 2014) and Stanford Method for Persistent Scatterers (StaMPS) by the University of Leeds (Hooper, 2008). We used statistical-cost, network-flow phase-unwrapping algorithm (SNAPHU) for unwrapping of the interferometric phase (Chen and Zebker, 2002). The topographic phase is removed using TanDEM-X 90 m DEM (Wessel et al., 2018).

The standard deviation of the mean line-of-sight InSAR velocity is estimated as 4–5 mm/yr. See Supplementary Information for further details on error sources and data processing. A drawback of the InSAR data is the uneven spatial distribution of data points, as is determined by the persistent scatterer algorithm in InSAR processing, which requires stable surface properties over time. This introduces a location bias. Winter data (with variable snow cover thickness) are not included, and the dynamic floodplain (ARF) with varying water cover has a low data point density.

We concentrate in our analysis on the thaw season surface displacement processes. However, summer subsidence may be compensated in winter by heave (**Supplementary Figures S1, S2**), as indicated by positive surface displacement between the last images of 2017 and 2018 and the first images of the next year. This is attributed to spatially varying ice accumulation in the active layer during the winter.

Soil Ice Content and Active Layer Thickness

Ice content data have been collected by Weiss et al. (2016) in 2012, and in 2013 by the authors. The samples were collected by hammering a steel pipe into the top of permafrost, and carefully extruding the sample in 5–10 cm increments. The samples are weighed and dried, to determine the gravimetric ice content. The ALT at selected sites was measured by probing with a thin steel rod (0.8 cm thickness). Gravelly or stony material is absent in the study area.

Geospatial Analysis

Geospatial data analysis was done with Quantum GIS version 2.18 (QGIS.org, 2016). A landform and surface micro-relief map is produced based on a synthesis of all satellite images, DEM data and field surveys made over the period 2004–2018. The main landform classes are: Yedoma remnant (YR hereafter), drained thaw lake basins (DTLB), active river floodplain (ARF) and river terrace (RT). **Table 1** shows further subdivisions in geomorphological details and micro-relief (mainly ice-wedge polygons and their morphology and degree of visibility; for slopes also erosion features such as rills).

Pond density classes were visually estimated. For the DTLB class, an estimate of the relative age was made based on overlapping relations, in combination with ice wedge polygon and surface micro-relief development, which can be used as indicator of age (Hinkel et al., 2003). Based on image time series, flooding frequency classes were derived (permanently flooded, seasonally flooded, extreme floods only and no

TABLE 1 | Subdivisions of the main geomorphological map units into subunits, and micro-relief classification for these units.

Main unit	Geomorphological subunits	Micro-relief classes
Yedoma remnant	plateau, slope, erosion gully	low/high centre polygons, obscured polygons, rill erosion, alluvial fan, colluvial deposition, ponds
Drained thaw lake basin	basin, shore platform, beach ridge, delta, active lake, pingo, and drainage channel	low/high centre polygons, obscured polygons, rill erosion, ponds
River floodplain	channel, point bar, levee, crevasse splay, flood basin, lake, pingo	low/high centre polygons, obscured polygons, ridge and swale topography
River terrace	terrace plateau, slope	low/high centre polygons, obscured polygons, rill erosion, ponds

flooding). ARF flooding frequency was checked by a longer time series of lower resolution Landsat images (Cheung, 2019). The visible spectrum images were also used to derive the normalized difference water index (NDWI, McFeeters, 1996) and normalized difference vegetation index NDVI (near infrared-red)/near infrared+red). NDWI (green + near infrared)/(green−near infrared), indicates the amount of open water within a pixel, NDVI indicates the amount of green biomass. The NDWI data of the 2015 image, with average wetness conditions and completely cloud-free, were combined with the landform data.

Statistical Analysis of InSAR and Terrain Data

The InSAR dataset contains both spatial and temporal variation, and interaction between these sources of variation. The analysis is based on the assumption that spatial variation is related to terrain characteristics expressed by the geomorphological map data, and the temporal variation is caused by the weather patterns throughout the observation years, affecting loss or gain of ice, water or sediment. Interaction between spatial and temporal variation is likely since the weather conditions may influence terrain units differently; e.g. by variation in soil drainage conditions that affect soil water content and thermal properties of the soil. To explore these relations, the InSAR data have been compared with the categorical scale data of the geomorphological map and ratio scale data derived from DEMs and visible spectrum images.

To characterize temporal variability of each data point, we performed a hierarchical cluster analysis (Euclidian distance, Ward's method, divisive algorithm), which groups all data points into dissimilar groups of displacement trajectories, based on the vertical displacements.

Next we applied two pathways of analyzing the relation between terrain characteristics and vertical displacements. The first pathway considers the interval/ratio scale data from the ALOS DEM and visible spectrum Worldview 2 image of 2015 separately. These data are elevation (ELEV), panchromatic greyscale (GS), NDVI and NDWI derived from the Worldview image. ELEV represents drainage conditions and geomorphology, NDVI and GS represent vegetation biomass and type. High values of NDWI indicate areas with much ponded water relative to vegetation, low GS also indicates presence of ponds. First we calculated the Pearson correlation coefficients between these terrain units and respectively the total summer displacement over the 3 years, and the total for each year separately. Next we applied principal component analysis on this dataset (mean and variance standardized) to explore which combination of properties explain most of the variance, and for dimensionality reduction.

The second pathway includes the categorical scale data in the geomorphological map. For relations of surface displacement with the categorical data of the geomorphological map we considered as potential driver variables:

- the large landform units (Drained thaw lake basins, river floodplain and terrace, Yedoma)
- erosion, sedimentation or ground ice thaw phenomena
- pond density
- river flooding classes

A one-way analysis of variance (ANOVA) for each combination of yearly InSAR data and the categorical classes Landform, EST, Pond density and Flooding) was applied, to detect which of the these categories are linked to surface displacements. A Tukey-Kramer multi-comparison was used to identify classes that differ significantly from others.

Next, the numerical and categorical data selected by PCA and ANOVA are combined into a generalized linear regression model which was fitted stepwise to the surface displacement data of each year separately, and to the summed surface displacement over all years (Σ years). Interaction terms were not included. The regression model gives information on the strength of relationships.

RESULTS

Landforms

The area is dominated by overlapping DTLB (54.5%) and the recent floodplain (ARF, 39.1%). Yedoma remnants (YR, 3.7%) and the river terrace (RT, 2.8%) make up a small fraction of the area. The YR are plateau-like features with a nearly flat upper surface, likely representing an older land surface. An isolated hill consisting of Yedoma deposits testifies former expansion of the Yedoma surface in the northern part of the study area (1 in **Figure 4**). This old surface slopes gently towards the river (**Supplementary Figure S3**). The Yedoma deposits have a Late Pleistocene age; calibrated ^{14}C ages of organic matter and bone at a lake bank exposure are 31,745 and 20,829 years BP, ages of

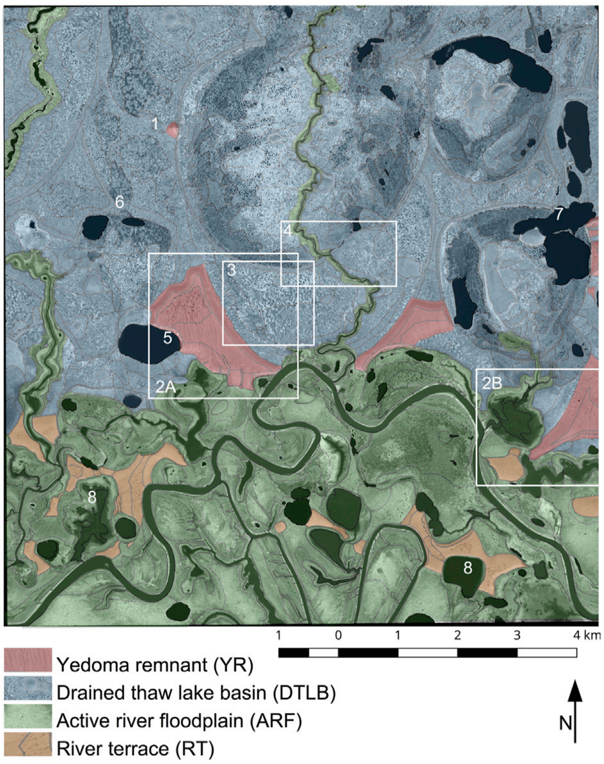

FIGURE 4 | Main landform classes in the study area. Backdrop: 2019 Worldview panchromatic image. Numbers refer to locations discussed in text, rectangles to locations of other figures. WorldView © 2019 MAXAR.

cryoturbated organic matter in the top of the succession are 1,674 and 11,449 years BP (Weiss et al., 2016). The youngest date likely contains young soil material.

The YR surface is generally well-drained, but on larger plateau areas low center polygons with intermittent ponded water occur. Tussock tundra vegetation dominates; surface drainage occurs through sedge-lined diffuse water courses, parallel to each other. On steeper slopes these grade into small rills between tussocks, and eventually in gullies where these rills concentrate.

The RT has similar surface characteristics as the YR. The RT may be the river valley equivalent of the YR, although traces of channel systems are not visible. In one location (2B in **Figure 4**; **Supplementary Figure S3B**), lateral continuity is suggested by a gradual slope from Yedoma plateau to terrace. Dating information from RT's is not available; a younger (Holocene) age than the Yedoma cannot be excluded. The RT is likely underlain by ice-rich permafrost, as shown by erosion features at RT edges.

The DTLB surface has a 10–20 m elevation difference with the YR surface. It is covered by overlapping drained lake basins. Differences in elevation up to 3 m are common, representing sedimentary features of the lakes, and elevation differences between individual basins. The basins differ in surface micro-relief, ranging from well-defined low center polygons in younger basins, to areas where ice wedge polygons are obscured by peat formation in older basins (Teltewskoi et al., 2016; Weiss et al., 2016). In the latter case ice wedges are visible by the formation of linear thaw ponds. A pattern that appears to develop over time on slightly sloping surfaces is a ribbed pattern with parallel, diffuse drainage channels with a dense sedge vegetation, alternating with ±0.5–1 m higher ridges covered by *Betula nana* heath (**Figure 5**). Well-drained areas are dominated by tussock tundra. Features indicating ground ice thaw (thaw ponds) are ubiquitous in DTLB's (**Figures 5**, **6**). Furthermore, *Sphagnum* peat growth is widespread, indicated on panchromatic images by light tones.

Individual basins are lined with a low ridge marking their former banks, interpreted as a beach ridge or ice shove ridge built up by material bulldozed ashore by a floating lake ice cover (**Figure 6**). The elevation difference between individual basins is small, 1 m or less. **Figure 6** also shows a fluvial delta, built into a lake by a channel connecting the lake with the river floodplain. At present, drainage through this channel has reversed, with flow towards the river, likely caused by river downcutting. Other relief elements are slightly elevated shore platforms that line the lake banks on the lake side, and a central bulge of the lake floor, shown as a better drained area in the center of the lake basin.

The overlapping relations of the lake basins were reconstructed, based on polygon maturity (Hinkel et al., 2003), surface elevation, and intersection of beach ridges (**Supplementary Figure S4**). Only from the older lake bed depicted in **Figures 5**, **6** ^{14}C dates are available (Schirrmeister et al., 2011; Weiss et al., 2016). Weiss et al. report a calibrated age of 3,251 years BP from a buried peat bed, and ages of 2,884 and 8,016 years BP for cryoturbated peat. Schirrmeister et al. (2013) report uncalibrated ages of 1,632 ± 32 and 2,144 ± 33 from peat. The age of 8,016 years BP indicates that the lake was drained in the Early Holocene. Renewed clastic sedimentation led to the burial of a peat bed after 3,251 years BP. Teltewskoi et al. (2016) report a calibrated basal ^{14}C age of 3,630 ± 40 for the surface of this lake bed.

Within the DTLB unit, lakes are common. Some of these are actively expanding thaw lakes (e.g. at 5 in **Figure 4**). Other lakes are remnants after partial lake drainage, or infilling of lakes with peat or clastic sediment (e.g. at 6 in **Figure 4**). These remnant lakes also may start to expand again, which occurred at 7 in **Figure 4**. New lakes are created by surface subsidence and merging of polygon ponds and thaw ponds; these are generally smaller and shallower lakes or ponds and have an irregular shape.

Pingos (bulgannyakhs) of all sizes occur abundantly on the drained lake basins (**Supplementary Figure S4**). Some consist of irregular shaped complexes. The pingos are of the hydrostatic type (Mackay, 1998). A field survey of pingos in the central section of the study area did not show any water seepage activity associated with these pingos, suggesting low or absent activity (Mackay, 1998).

Actively eroding slopes between YR and DTLB occur only near expanding lakes (5 in **Figure 4**); erosion is dominated by thaw slumps (e.g. at 1 and 5 in **Figure 4**). When lake bank erosion stops, slump activity continues for some time; at 1 in **Figure 4** lobes of thaw slump debris overriding the adjacent DTLB are found. Older slopes have lost their slump morphology by rill erosion and colluviation. Erosion occurs by rills between

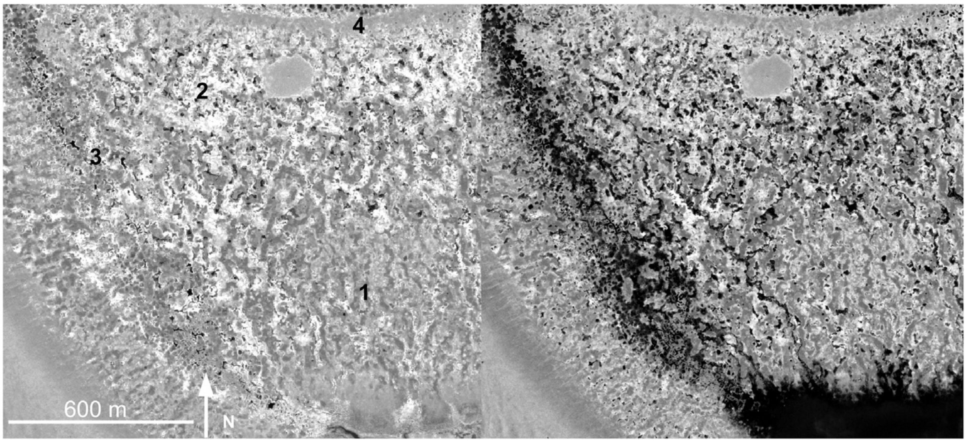

FIGURE 5 | Left: August 2019 Worldview image. Surface patterns in old drained thaw lake basins. 1: Ribbed pattern with sedge-lined diffuse drainage lines alternating with Betula nana heath (dark grey). 2. Area dominated by extensive Sphagnum growth and small thaw ponds. 3: Low and high centered polygons with pond formation by ice wedge thaw. 4. Stable low centered ponds in a younger basin (see also **Supplementary Figure S4**). Right: the same area with widespread flooding, July 2017. Location 2 of the image see **Figure 4** at nr 3. WorldView © 2019 MAXAR.

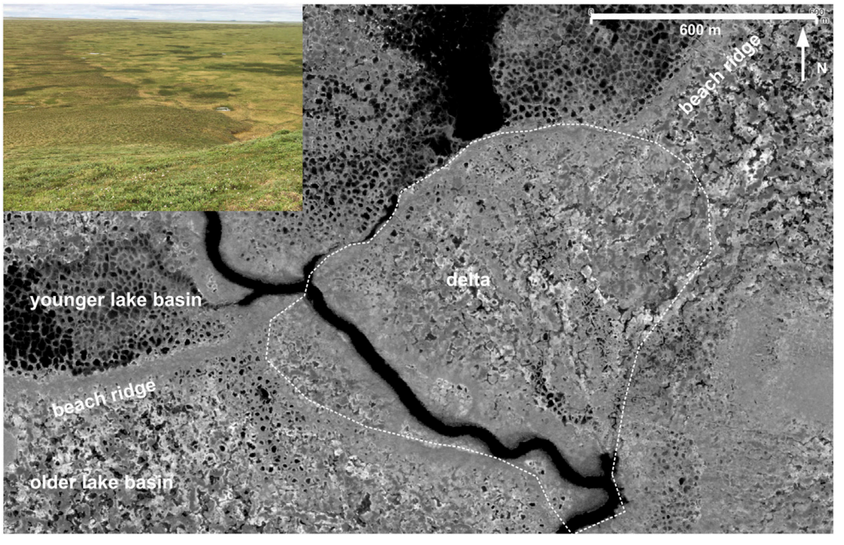

FIGURE 6 | Border between two lake basins with different age and surface micro-relief. The elevation difference is less than 1 m. The border of the younger lake is marked by a low ridge. In the center a former river delta. Inset: beach ridge of the same lake seen from point 1 in **Figure 4**; in the lower left corner the beach ridge is overridden by a thaw slump debris lobe, photo J. vanHuissteden. Location of the image frame: see **Figure 4** at nr 4. WorldView © 2019 MAXAR.

vegetation hummocks, along ice wedges and occasionally gully erosion. On lower slopes, colluviation and deposition of small alluvial fans likely dominates.

The ARF is separated by clear terrace scarps from the RT and often also from the adjacent DTLB surface; those separating ARF and RT are highest. This indicates two phases of downcutting of the river, after formation of the RT surface and after formation of the oldest DTLB's.

The ARF has a large proportion of lakes. By contrast to the lakes in DTLB, the water level and size of most of these lakes varies with the flood level of the river (e.g. **Figure 7**, Cheung, 2019). Many lakes likely have an origin as thaw lakes which have become connected with the river (1, 3 in **Figure 7**), or as thaw lakes eroding the RT unit (e.g. 2 in **Figure 7**). Several deeper lakes maintain a stable water level at low river stands. These lakes are not connected with outlet channels to the river channel, but nevertheless receive river water during high flood stages.

The river channel pattern is characterized as a high sinuosity river with multiple channels, but dominated by one main channel (**Figure 8**). At low stage, the non-lake floodplain surface in

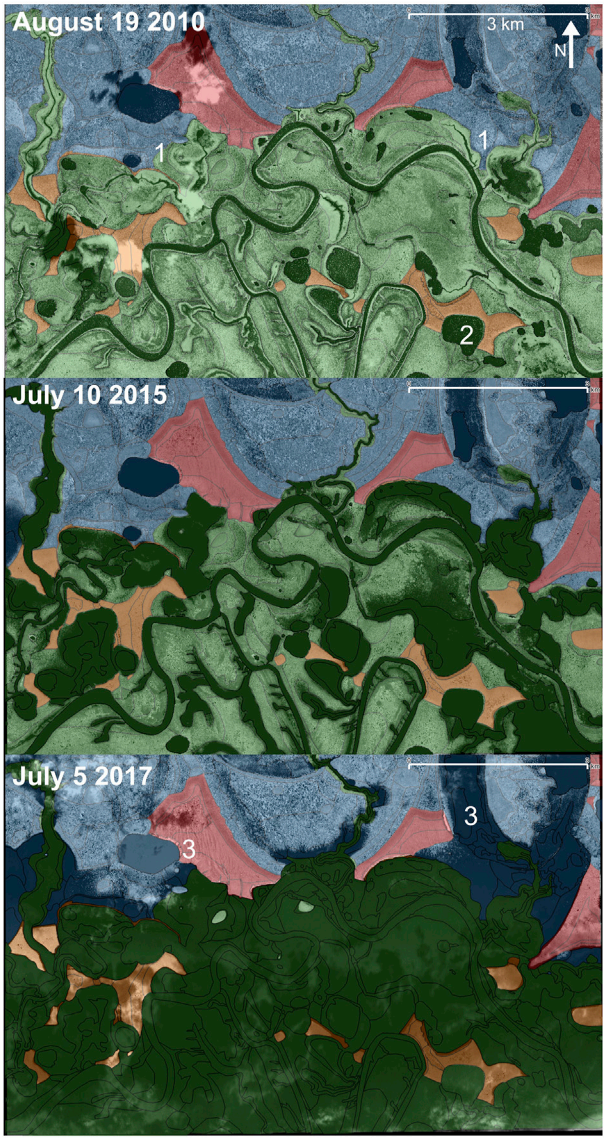

FIGURE 7 | Open water on the river floodplain at different river stages. Backdrop: geomorphological map units, see **Figure 4** for legend. Top: low stage, end of summer; mid: normal, ± bankfull river stage, below: extremely high flood, exceeding the normal floodplain limits. 1: river-connected thaw lakes; 2: thaw lake developed on floodplain in river terrace; 3: locations where connections between thaw lake and river is developing during high flood. WorldView © 2019 MAXAR.

between the channels consists of mostly vegetated, non-flooded flood basins, dominated by grasses and sedges, and channel levees with willow brushes. A part of these flood basins consist of point-bars with ridge and swale topography created by river bend expansion. The vegetation is denser and more productive than on similar flat areas outside the floodplain (DTLB, YR plateaus). The lowest floodplain levels (channel banks, drained lakes) are unvegetated. Ice wedge polygons are ubiquitous. At low stage in winter, the channel ice surface is some 2–3 m below the floodplain surface, exposing steep channel banks. These banks are sources of aeolian dust, as shown by streaks of dust over the winter snow surface.

Active sedimentation occurs on floodplain surfaces on levees and point bars, but also by suspended sediment and organic debris deposition in flood basins. Sediment cores in flood basins show successions of vegetation horizons, alternating with layers of fine-grained clastic material. In a core in flood basin sediments taken on a crevasse splay, a sedimentation rate of 0.48 ± 0.10 cm yr^{-1} was determined by radiocarbon dating of a vegetation horizon (185 ± 30 years, Groningen lab. nr. GrA59784, at depth of 90–95 cm). This sedimentation rate is corrected for a 15 vol. % excess ice content below the 0.5 m thick active layer.

Ice Content and Active Layer Depth

The ice content at the top of the permafrost varies strongly over short distances. The average ice content for DTLB is 42.60 ± 20.32% (n = 34), for YR 38.5 ± 18.46% (n = 12) and for ARF 26.45 ± 19.45% (n = 12). The YR and DTLB have approximately equal topsoil ice content. The ice content of ARF is lower than that of YR and DTLB; it differs significantly from that of DTLB (Tukey-Kramer test, p = 0.04). Fresh YR exposures show large ground ice masses in ice wedges. A 7 m deep borehole in DTLB sediments near the research station showed a decrease of ground ice after the top 3 m (G. Iwahana, pers. comm.).

On 19–20 July 2018, three transects of midsummer active layer thickness (ALT) were measured perpendicular to the maximum flood lines in 2017 and 2018 (**Figure 9**), and compared with ALT measurements in grids outside the flooded area. Transect 1–3 are located entirely on usually mesic tussock tundra, transect 4 in a wet area dominated by hummocky *Sphagnum* and *Salix* vegetation and a thicker surface organic horizon. The ALT for transect 1 to 3 show a significant increase at the flood limits (t-test, $p < 0.01$); this thickness increase is absent in the fourth transect. The grids ***a*** (100 × 100 m) and ***b*** (10 × 10 m) are active layer monitoring sites; grid ***a*** is located outside the flood limits (vegetation: tussock tundra and *Betula nana* heath), grid ***b*** (*Sphagnum* and *Salix*) inside the flood limits. The 100 point average of these grids, measured in the same week as the transects, are shown alongside the transect data. The average ALT of grid ***a*** is lower than that of transect 1–3 outside the flood limit; that of grid ***b*** is similar to transect 4.

Statistical Analysis of Velocity Data

The cumulative surface displacement over the thaw seasons of 2017–2019 are shown in **Figure 10**. There are clear regions where data points show similar displacement trends, either positive or negative. These displacement patterns vary among the years (**Supplementary Figure S5**). A hierarchical cluster analysis (Euclidian distance, Ward's method) using the displacements detected from the successive SAR images is used to cluster the data points into 11 groups of trajectories. In **Figure 11**, most clusters also represent fairly tight spatial clusters.

To evaluate relations of surface displacement with quantitative parameters of geomorphology, drainage and vegetation we have compared the total surface displacement over 3 years and the summed surface displacements over each year, with surface cover

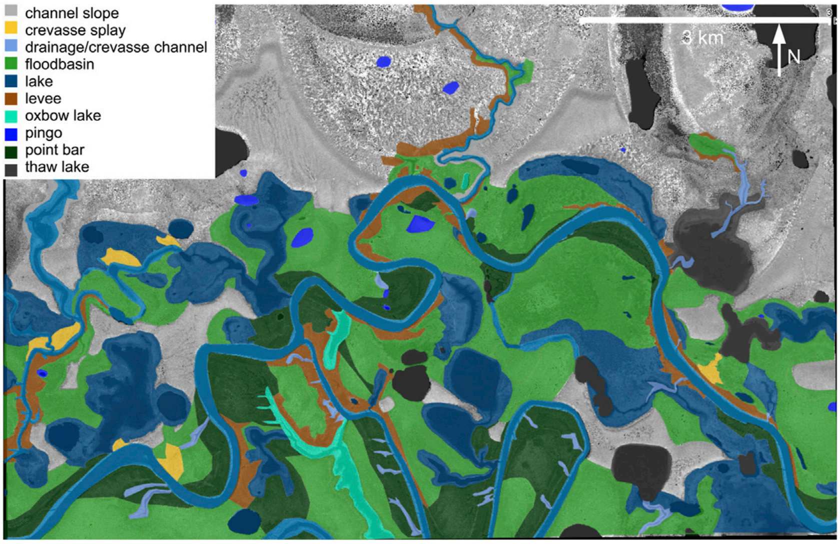

FIGURE 8 | Geomorphology of the active floodplain (ARF) with subunits. Backdrop: Lower half of Worldview 2019 image in **Figure 4**. Unclassified areas are the RT (old river terrace), YR and DTLB areas. WorldView © 2019 MAXAR.

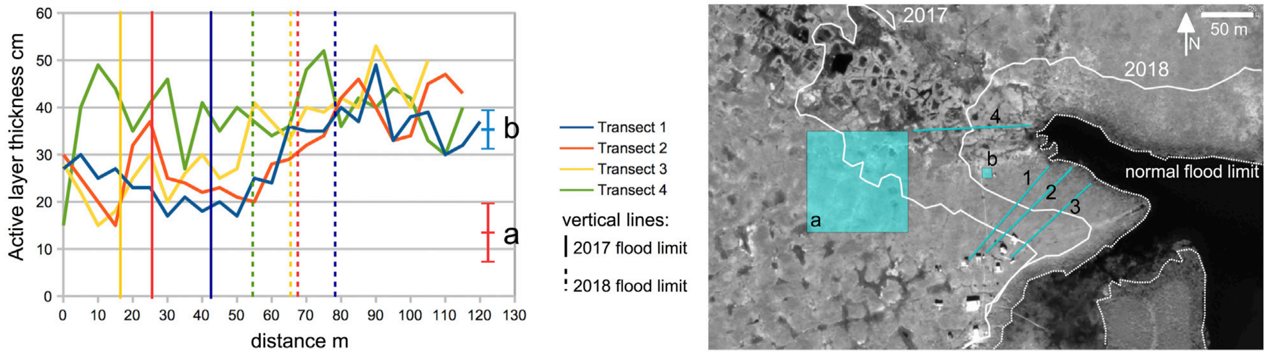

FIGURE 9 | Active layer thickness transects through the 2017 and 2018 flood limits. Left: ALT thicknesses plotted against distances from the start of the transects (from ± east to west). Right: location of the transects (1–4). The average and standard deviation of ALT of two gridded plots, one largely outside the flood limits (left, a) and one within the 2018 and 2017 limits (left, b), is indicated to the right of the transects in the graph on the left side. Scale bar 50 m. WorldView © 2019 MAXAR.

data derived from the Worldview image of 2015 (NDWI, Panchromatic greyscale (GS), NDVI) and the ALOS DEM. GS is related to both vegetation type and water ponding, NDVI reflects vegetation, NDWI water ponding. **Table 2** shows the correlations of surface displacement with the quantitative image data and DEM. NDWI, GS and NDVI correlate with surface displacement, but not equally among years and with varying signs. The surface displacement in 2017 correlates weakly negative with NDVI and NDWI; for 2018 there are no significant correlations; for 2019, positive correlations are found. Because of their relation with ponded water, GS - NDWI, and NDVI - NDWI correlate negatively.

Elevation has a strong positive correlation with surface displacement in 2017 (higher areas - less subsidence or more heave), but negative in 2019 (higher areas-more subsidence). Although there are significant correlations of displacement with vegetation-related parameters NDVI, greyscale and NDWI, these are weak in comparison to elevation. It indicates poor correlation with vegetation-related parameters and surface displacement, although this may have been affected to some extent by differences in spatial resolution between the InSAR and NDVI/NDWI data (see *Data and Methods*). Correlations of surface displacement between years have different signs; 2018 deviates, with negative correlation between the previous year and the next. These spatially different patterns of displacement in successive years is also visible in the trajectory clusters of **Figure 11**.

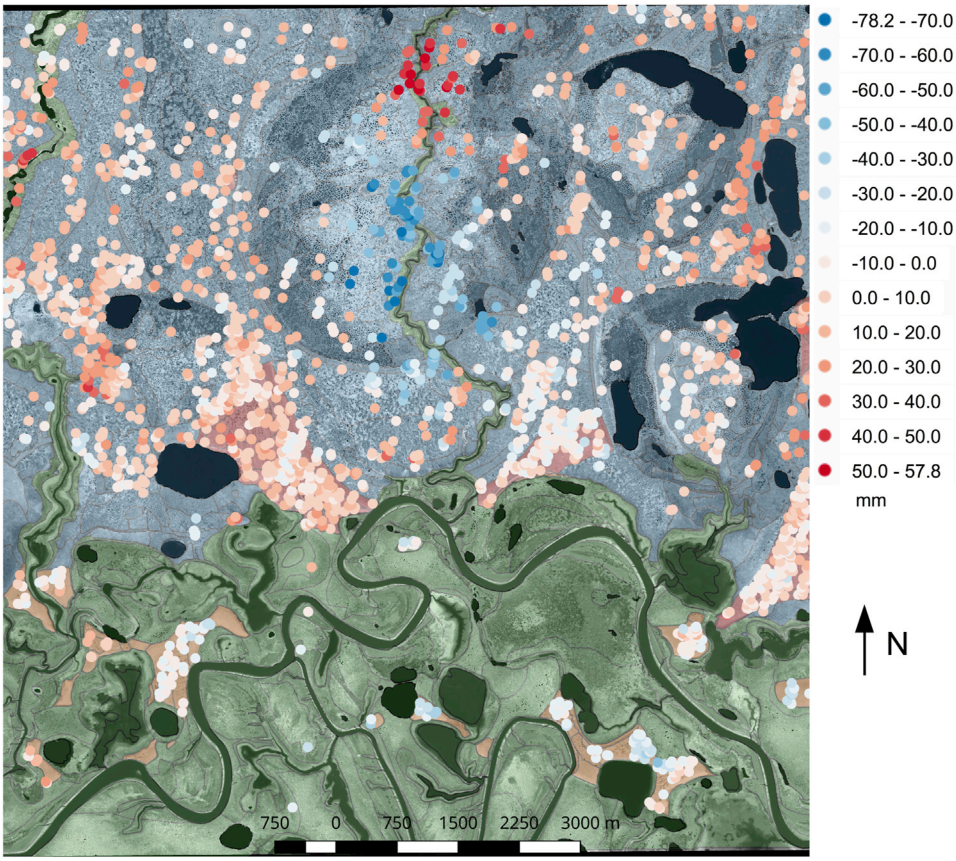

FIGURE 10 | Cumulative thawing season surface displacement over 3 years; subsidence (–) and heave (+) velocities in mm. Background: 2019 Worldview image with landform class (**Figure 4**). See also **Supplementary Figure S5** for cumulative displacement of every year and **Supplementary Figure S2** for average surface displacement velocities over 3 years. WorldView © 2019 MAXAR.

A principal component analysis on the standardized data shows that three components explain 95% of the total variance. The first principal component explains 60% of the variance, with a strong loading on the total surface displacement of 2019 (**Supplementary Figure S6**). The second principal component contains 27% of the variance, with the highest loading on the 2017 data. From the other variables, only elevation determines a small part of the total variance, in the third principal component (8% of total). This indicates that variability of the surface displacement is dominated by variability between years, related to elevation, but not to vegetation or drainage.

The categorical classes of the geomorphological tested in the further analysis are:

- the landform units (DTLB, ARF, YR, RT)
- erosion, sedimentation or ground ice thaw phenomena (EST hereafter)
- pond density (POND) classes (from 0-absent to 5 very high)
- river flooding (FLOOD) classes, ranging from none, flooding at extreme flood heights only (2017 and 2018 floods) and the normal seasonal flooding of the floodplain based on field surveys.

The ANOVA to detect the effect of the categorical classes of the geomorphological map (Landform, EST (erosion, sedimentation or ground ice thaw), POND and FLOOD) yields significant differences at the $p < 0.01$ level (**Table 3**, **Supplementary Figure S7**). A Tukey-Kramer multi-comparison was used to identify classes that differ significantly from others. The multi-comparison tests of class differences indicate significant differences ($p < 0.01$) for most of the classes, except for the EST and POND, where several classes do not differ significantly. In **Table 3**, only those classes have been listed that differ significantly from other classes within the same variable, and depart more than the uncertainty range (3 mm) from 0 mm displacement.

The categorical variables from the geomorphological map explain a significant amount of the variability of the InSAR surface displacement. However, the behavior of each class is not consistent between years. For the landform classes, the floodplain and river terrace (ARF, RT) shows the most consistent behavior with predominantly subsidence throughout all years. For EST, classes that indicate net sedimentation in non-flooded areas (colluvial deposition and peat growth) show clear, and among the years consistent, net positive surface displacement. However, sedimentary environments on the

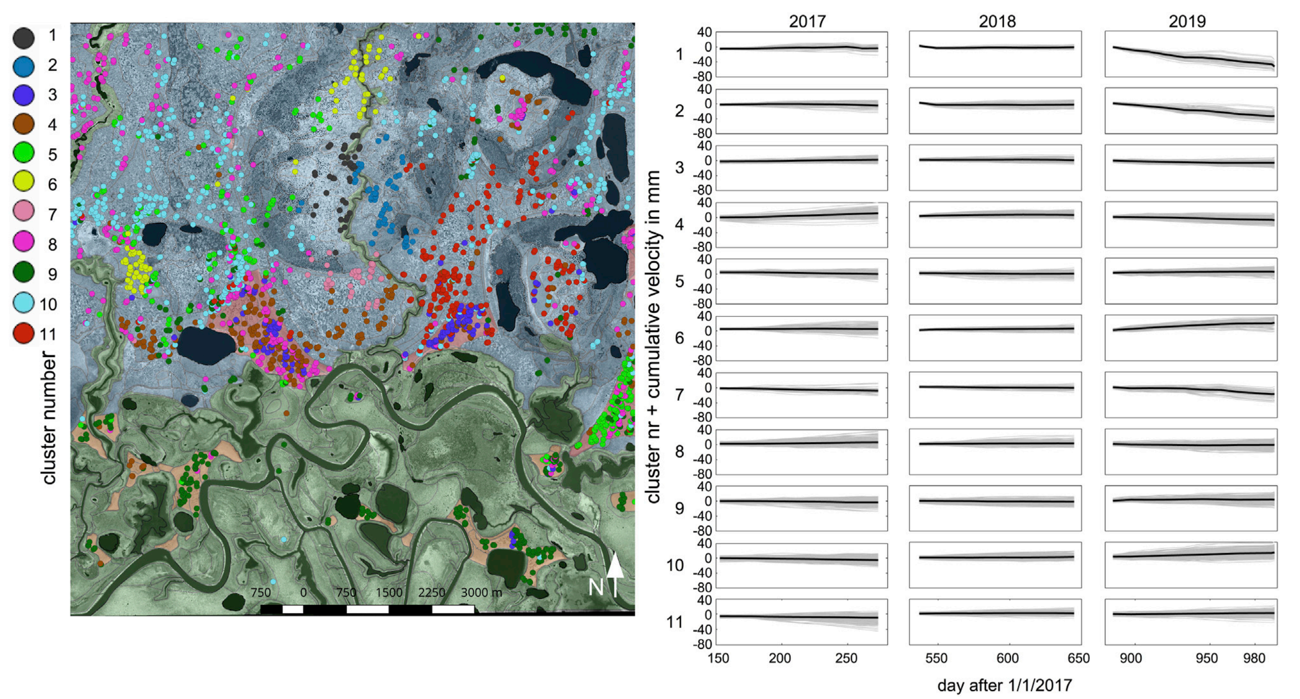

FIGURE 11 | Left: velocity trajectory clusters to which the InSAR data points were assigned by cluster analysis of single InSAR image data (see text), plotted on the geomorphological map underlain by Worldview image of 2019. Scale bar 3 km. Right: Graphs of cumulative velocities plotted against image date for each cluster for each year. Black lines in each graph represent the cluster average velocity over time, grey lines individual point trajectories.

TABLE 2 | Pearson correlation coefficients of yearly InSAR surface displacement sums and quantitative data derived from the Worldview 2015 image and ALOS DEM. Bold numbers are significantly strong correlations ($p < 0.01$).

	NDWI	Greyscale	NDVI	Elevation	∑ 2017	∑ 2018	∑ 2019	∑ all
NDWI	1.00	**−0.60**	**−0.98**	**−0.09**	**−0.08**	−0.04	**0.10**	0.03
Greyscale		1.00	**−0.71**	**0.07**	0.04	−0.04	**−0.13**	**−0.09**
NDVI			1.00	**0.10**	**0.07**	0.02	**−0.12**	0.06
Elevation				1.00	**0.27**	−0.03	**−0.13**	0.02
∑ 2017					1.00	**0.31**	**−0.16**	**0.47**
∑ 2018						1.00	**0.18**	**0.59**
∑ 2019							1.00	**0.75**
∑ all								1.00

Notes: NDWI: Normalized Difference Water Index, NDVI: Normalized Difference Vegetation Index.

TABLE 3 | Categorical variables and their classes used in anova, and multi-comparison (Tukey-Kramer) test results of differences between classes for each years and sum of all years.

	Landform	Erosion, sedimentation, ground ice thaw	Pond density	Flooding
classes	DTLB, YR, ARF, RT	none, GIT, DD, rills, gully, coll, sed, slump, pond	0 1 2 3 4 5	none extreme seasonal
2017	−RT −DTLB + ARF + YR	+ peat + coll		−extreme + seasonal
2018	−RT	+ peat + coll		+seasonal
2019	−ARF + DTLB −YR	+ peat + GIT + coll −none −sed	−1 + 4 +5	−extreme
all years	−ARF −RT	−none −sed −slump + coll	−1	−extreme + seasonal

Notes: Minus sign before class names indicate a significant departure from other classes and subsidence; plus sign significant departure from other classes and heave. Class abbreviations: DTLB, YR, ARF, RT explained in text above; GIT = ground ice thaw, DD = diffuse drainage, coll = colluvial deposition, sed = fluvial sedimentation, peat = Sphagnum peat formation, slump = thaw slumps, pond = expanding ponds.

TABLE 4 | General linear regression models of surface displacements with predictors elevation (ELEV), and categorical variables Landform group, EST (erosion/sedimentation/ground ice thaw), Pond density (PONDDENS) and Flooding.

Variable	Category	2017	2018	2019	All
Intercept		**–2.92 ± 0.99**	**3.19 ± 0.55**	**–2.92 ± 0.99**	**4.29 ± 0.58**
Elevation		**0.22 ± 0.05**	–0.05 ± 0.03	not included	not included
Landform	Yedoma remn.	**3.10 ± 0.87**	–1.14 ± 0.48	**–2.73 ± 1.05**	0.97 ± 0.33
	River terrace	**–3.74 ± 0.81**	**–7.51 ± 0.45**	1.82 ± 1.22	**–9.00 ± 1.46**
	Floodplain	–0.75 ± 2.34	**–3.77 ± 1.31**	**–17.67 ± 3.55**	**–21.63 ± 4.51**
EST	none	–1.80 ± 0.70	**–1.93 ± 0.39**	**–10.28 ± 1.06**	**–13.02 ± 1.24**
	expanding ponds	1.15 ± 2.03	**4.03 ± 1.13**	–5.65 ± 3.08	–4.00 ± 2.70
	diffuse drainage	1.53 ± 0.62	**1.16 ± 0.35**	**–7.20 ± 0.94**	**–4.38 ± 1.19**
	rills	–1.82 ± 0.76	–0.23 ± 0.42	**–3.64 ± 1.11**	**–5.66 ± 1.36**
	gullies	0.76 ± 1.21	–0.24 ± 0.68	–0.73 ± 1.79	–0.49 ± 2.21
	colluvium	**8.87 ± 2.64**	**5.44 ± 1.47**	2.89 ± 4.00	**17.59 ± 5.08**
	fluv. sediment.	1.48 ± 2.10	–2.84 ± 1.17	**–30.13 ± 3.19**	**–30.52 ± 4.00**
	peat growth	**10.21 ± 3.05**	**4.73 ± 1.70**	8.95 ± 4.63	**23.72 ± 5.92**
	thaw slumps	–3.86 ± 2.52	–0.93 ± 1.40	3.45 ± 3.82	0.56 ± 4.81
Pond density	1	1.21 ± 0.87	–0.28 ± 0.49	–2.62 ± 1.33	not included
	2	–1.27 ± 0.60	**–0.96 ± 0.33**	0.40 ± 0.87	not included
	3	**–2.22 ± 0.71**	–0.60 ± 0.40	0.81 ± 1.07	not included
	4	**–3.08 ± 0.73**	**–2.66 ± 0.41**	**3.89 ± 1.10**	not included
	5	–4.39 ± 2.46	0.63 ± 1.37	9.57 ± 3.73	not included
Flooding	seasonal	**17.21 ± 2.68**	**8.62 ± 1.50**	**18.75 ± 4.07**	**45.19 ± 5.16**
	extreme	–1.37 ± 1.88	–0.64 ± 1.05	–3.13 ± 2.84	–5.33 ± 3.63
Dispersion		73.5	29.5	170	277
Adjusted R^2		0.18	0.21	0.190	0.19
Model terms (constant omitted)		ELEV + LANDFORM + EST + PONDDENS + FLOODING	ELEV + LANDFORM + EST + PONDDENS + FLOODING	LANDFORM + EST + PONDDENS + FLOODING	LANDFORM + EST + FLOODING

Notes: Last three rows: model fit indicators and model terms. Coefficients: boldface = equation terms with coefficients differing significantly from zero (p < 0.01). Grey background rows: variables with different signs of significant coefficients between the years.

river floodplain or DTLB areas show net subsidence. Areas with inferred ground ice thaw (indicated by ice wedge thaw ponds) do not show subsidence, and even positive displacement in 2019. Pond density is the least predictive, only the "very low" density class (1 in **Table 3**) shows significant subsidence in 2019, while the high pond density classes 4 and 5 show heave in 2019. The FLOOD classes show consistent subsidence for data points that were flooded during the extreme floods in 2017 and/or 2018, while the seasonally flooded class shows heave in 2017 and 2018.

A generalized linear regression model (**Table 4**) was fitted stepwise to the surface displacement data of each year and the summed surface displacement over all years (Σ years), with Elevation (ELEV), and the categorical geomorphological map classes listed in **Table 4** as predictor variables. Elevation was included because of its contribution to the variance in the principal component analysis. Interaction terms were not included. All models capture a significant amount of the variance in the data ($p < 0.01$, F test).

For 2017 and 2019, all variables are retained by Akaike's (Akaike, 1974) criterion; for 2019, ELEV was removed from the model (**Table 2**). For Σyears, the model is reduced to LANDFORM, EST and FLOODING variables; for 2017, the positive coefficient for ELEV is significant.

Within the Landform group, the DTLB class was taken as the reference variable. For 2017, the coefficient for LANDFORM-YR is positive, in agreement with the positive coefficient of ELEV in that year and the higher elevation of YR. In 2019 however, the YR term has a strongly negative coefficient. Of the other LANDFORM groups, the ARF and RT have negative coefficients, indicating subsidence relative to DTLB throughout all years.

The EST variable includes processes that can result either positive or negative surface displacements. The widely occurring class with evidence of ground ice thaw (mostly ice wedge thaw) was taken as reference here. Colluvial deposition on slopes and peat growth show pronounced positive coefficients for 2017 and 2018, in line with expected positive displacement for these classes. However, fluvial sedimentation mostly linked to floodplain locations has a pronounced negative coefficient in 2019, indicating net subsidence. Areas of expanding ponds and diffuse drainage, where negative surface displacements might be expected by ground ice thaw or erosion, have positive coefficients in 2018. Most classes have clearly negative coefficients in 2019, except for peat growth and colluvial deposition.

The visually estimated pond density (POND, class 0 absence of ponds as reference class) does not have a large and consistent effect. Pond density classes 2, 3 and 4 (low, intermediate, high) have negative coefficients in 2017 and 2018, indicating subsidence. However, in 2018 only class 4 contributes significantly with a positive coefficient. POND is removed from the regression equation for Σyears. The FLOOD variable

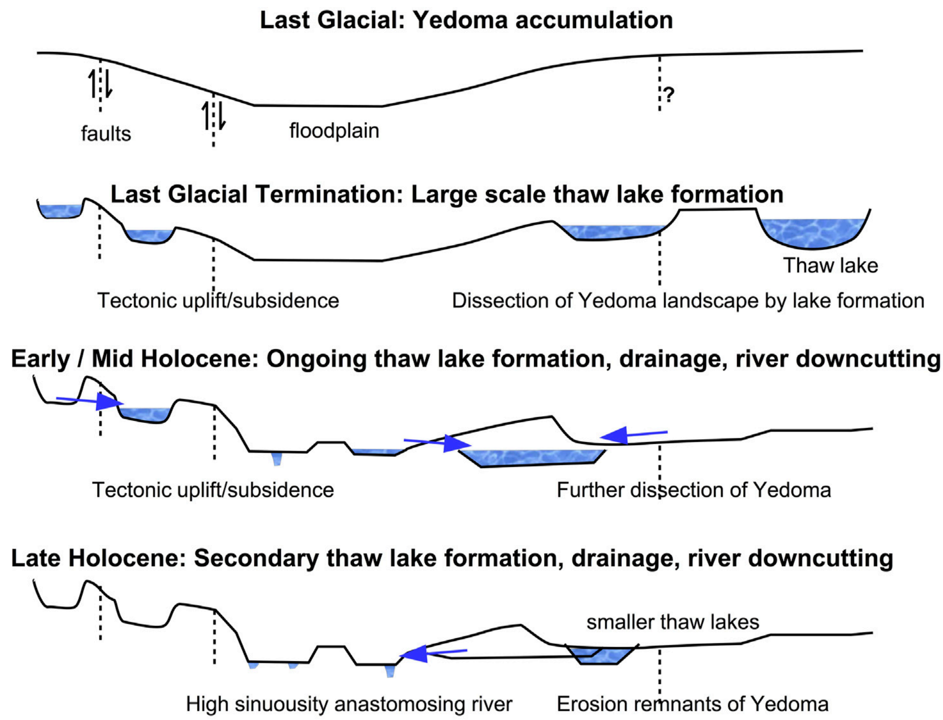

FIGURE 12 | Schematic summary of the Late Glacial and Holocene landscape development along a hypothetical North-South topographical profile across the study area.

(reference class No Flooding) is included for all years, with significant positive coefficients for the seasonally flooded class; the extreme flood class has all negative (but not significant) coefficients. Seasonally flooded points are all located in vegetated flood basins on the floodplain, whilst points reached by extreme floods only, are situated outside the floodplain but within the 2017 flood limits.

DISCUSSION

Geomorphology and Late Quaternary Development

Figure 12 summarizes the landscape development of our study area that we deduced from our geomorphological and geological data. Drained thaw lake basins (55%) and the present river floodplain of the Berelegh river (39%) dominate the study area. We assume that the ice-rich Yedoma deposits have had a much wider extension but have been reworked by ground ice thaw and erosion. This is based on an erosion remnant (at 1 in **Figure 4**), and presence of Yedoma hills north of the study area.

The original Yedoma surface had an elevation of 30–38 m above present sea level in the study area, sloping gently towards the river (**Supplementary Figure S3**). The erosion remnants at larger distance of 2 km do not indicate higher levels than 38 m, suggesting an essentially flat surface at distance from the river. The DTLB surfaces have an elevation between ±10 and ±14 m, indicating the removal of atleast 16 m of Yedoma deposits and ground ice over a large area, and subsequent redistribution in fluvial and lacustrine sediment. Remarkably, most of the Yedoma remnants occur at short distance from the river. A possible explanation that emerged from landscape-scale thaw lake modeling, is that expansion of thaw lakes close to rivers is restricted since the probability of early lake drainage is higher near the river, protecting Yedoma to large scale thaw lake erosion (Van Huissteden et al., 2011).

We assume that the RT unit is of the same age as the Yedoma surface. Its surface is higher by several meters (up to 20 m) than the highest DTLB surfaces (up to 14 m). Former fluvial channels are invisible on the terrace remnants, but may be obliterated by surface processes (sedimentation of loess, overbank river sediments, peat, or erosion).

Thaw lake formation started between at least 20,829 years BP (youngest ^{14}C date on Yedoma deposits) and 8,016 years BP (oldest ^{14}C on drained thaw lake basin fill) in the study area. In a recent analysis of Arctic-wide lake sediment basal dates (Brosius et al., 2021) two peaks in northern lake formation, including thaw lakes, were detected at 13,200 and 10,400 years ago, both following rapid increases in North Atlantic air temperature. This agrees well with the radiocarbon dates in our study area. The lake basin development in East Siberia is assumed to last until the end of the Boreal period (9.0–7.5 kyr BP, Romanovskii et al., 2004; Kaplina, 2009; Morgenstern et al., 2013).

Figures 4, **8** indicate the formation of large, elliptical to egg-shaped lake basin with smooth shores. This indicates the operation of wind-driven longshore currents during lake formation (Grosse et al., 2013), and a tendency to elongation in southerly direction. The overlapping relations of lake basins

(**Supplementary Figure S4**) show that lake basin formation was well underway before the large, prominent lake basins in the center of **Figure 4** have been formed. The lake basin at 3 in **Figure 4** was drained before 8,016 years BP, but overlaps older lake bottoms (**Supplementary Figure S4**, right side of the basin). This suggests an early, Late Glacial start of widespread lake formation, similar to the East Siberian area described by Morgenstern et al. (2013). After drainage of this lake, thaw lake activity shifted to the north with the formation of a new large lake basin at a slightly lower level (at 4 in **Figure 4**), indicating that the development of lakes continued after ca 8,000 years BP. This lake received river sediment, as shown by the presence of a delta (**Figure 7**). The presence of an elevated central bulge in many lake basins is attributed to a longer duration of sediment accumulation in the centre of expanding lakes, compared to near-shore areas where subsidence and sedimentation began later, as demonstrated by modeling by Kessler et al. (2012).

Present actively expanding thaw lakes are small compared to these older drained lake basins. They are restricted to the older basins floors, but may expand rapidly into remaining Yedoma (at 5 in **Figure 4**). At 7 in **Figure 4**, a remnant lake, left after lake drainage, appears to have been rejuvenated and is expanding again. Thaw lake formation and expansion needs large amounts of ground ice in the subsurface (Jorgenson and Shur, 2007; Morgenstern et al., 2008; Morgenstern et al., 2013), and therefore old thaw lake basin floors are less susceptible to rapid lake expansion. In the older lake basin floors significant accumulation of ice wedges and ice-rich organic deposits has occurred (Teltewskoi et al., 2016; Weiss et al., 2016) but most of the ground ice volume is restricted to the upper meters as shown by deeper boreholes (See *Results-Ice Content and Active Layer Depth*).

After major thaw lake expansion, a small 1–2 m high terrace scarp was created between ARF and DTLB, likely by fluvial downcutting. The downcutting occurred after the formation of the DTLB at 4 in **Figure 4**. Before drainage of this basin, a delta existed in this lake, with sediment supply from the river towards the lake through a feeder channel (**Figure 5**). Presently, the drainage is reversed towards the river. Fluvial downcutting should have facilitated this reversal, and subsequent lake drainage and the northward extension of the channel into the drained basin. The age of this river downcutting is assumed to be younger than Mid Holocene age, based on the age of the DTLB's.

On the ARF, several lakes have a morphology that suggest ground ice thaw as mechanism for their expansion: steep banks and rounded shapes, in particular bordering the RT unit. At 8 in **Figure 4**, thaw lakes developed within the river terrace. Some of these lakes are drained by the river channel during low flows (**Figure 7**, top), but others maintain a drainage threshold with the channel. Within the DTLB unit, lakes occur which appear to be thaw lakes that have been connected with the river quite recently, and drain during low stands (e.g. at 2A and 2B in **Figure 4**; see also **Figure 7** at 1 and 2). During extreme floods, also lakes at larger distance from the floodplain have become connected to the river (at 3 in **Figure 7** bottom).

On non-permafrost floodplains, lateral erosion is the primary mechanism for floodplain expansion (e.g. Howard, 1996). However, in our study area the capture of thaw lakes by subsidence and erosion of drainage thresholds may be induced by ground ice thaw during floods, representing a mechanism of floodplain expansion (see discussion of InSAR data). Capture of thaw lakes with subsequent avulsion of river channels through the former lakes may also be the cause of the irregular, patchy distribution of the river terrace (RT) unit on the floodplain, rather than the more common location of river terraces on valley sides. The height of the threshold between the lakes and the river system strongly affects river water input to the lakes, and as a consequence sediment and nutrient supply to the lake water (Marsh et al., 1999; Emmerton et al., 2007). Once connected to the floodplain, sedimentary infilling of these lakes may accelerate.

The compressional tectonic stress in the area has resulted in fault movements. In the DEM of **Figure 3**, two clear W-E trending lineaments can be discerned: the steep and nearly straight southern limit of the Berelegh floodplain, and a further terrain step of about 10 m to the south of it. Furthermore, there is a marked elevation difference between the Yedoma plateaus in the Allaikhovsky Highland (±50 m) to the south of the Berelegh river and the lower elevation of Yedoma plateau surfaces (30–38 m) north of the river. This suggests neotectonic movement along these lineaments, with a downward warping of the floodplain. On a North-South profile, the InSAR data indicate an average velocity of $-5.3 \pm 3.1\ \mathrm{mm\ yr^{-1}}$ north of the lineament bordering the Berelegh floodplain, south of this lineament $-0.17 \pm 3.2\ \mathrm{mm\ yr^{-1}}$, indicating a relative displacement of $-3.6\ \mathrm{mm\ yr^{-1}}$. The elevation differences of 12–20 m, likely developed since the Late Glacial, results in an estimate of the tectonic subsidence rate of 1–2 $\mathrm{mm\ yr^{-1}}$. Further lineaments, with a less clear terrain expression, occur north of the Berelegh valley (**Figure 3**), but apparently did not result in a large amount of displacement.

Tectonic subsidence may have contributed to the extensive lake formation in our study area by impeding drainage and creating more flood-prone areas. Jorgenson and Shur (2007) invoke a large scale water balance change at the Last Glacial termination to explain the rapid expansion of large thaw lakes. In a poorly drained subsiding basin this should have had larger impact than in an area without subsidence.

Tectonic movements resulting in base level changes, as well as climate change resulting in the change of the drainage basin water balance and sediment supply are likely causes of river downcutting, and may have acted in concert. For the prominent downcutting phase that formed the RT river terrace water balance changes at the Last Glacial Termination are a likely cause, next to tectonism. Jorgenson and Shur (2007) cite evidence for water balance changes at the LGT that also initiated thaw lake formation in Alaska. Another mechanism of floodplain erosion is catastrophic drainage of large thaw lakes, which could create peak flows larger than normal spring floods (Marsh and Neumann, 2001; Marsh et al., 2009; Arp et al., 2020). This likely occurred repeatedly in the drainage basin of the Berelegh river given the large DLTB areas north of the river.

Surface Displacements Detected by InSAR

We did not consider a tectonic component in the InSAR data analysis over the study area of **Figure 4**, which is entirely north of the most active lineaments. The principal component analysis shows that variation among years explains 87% of the variance in the first two principal components (**Supplementary Figure S6**). The large contrast between the weather conditions in 2019 and 2017–2018 (**Figure 2**) causes most of the variability. Terrain variable Elevation appears in the third principal component, which explains 8% of the variance while the contribution of vegetation (NDVI) or its ponded water component (NDWI) is negligible.

This is likely the result of variation in weather conditions. The year 2019 was exceptionally warm and dry (**Figure 2**), with a warm winter, an early spring and warm summer. The year 2017 and 2018 had high precipitation during the preceding winter. The net summer precipitation in 2017–2018 showed a small precipitation deficit, without long periods of warming in summer. By contrast, 2019 had a large summer precipitation deficit, and prolonged periods of hot weather. The dominance of the surface displacements in 2019 in the first principal component (60% variance), indicate that in particular warm and dry weather conditions induce surface subsidence on a large scale.

Although the yearly weather conditions dominate, the trajectory clusters in **Figure 11** show rather consistent spatial clustering, indicating that the terrain conditions contribute significantly to the spatial variation in surface displacements. This is also confirmed by the ANOVA and regression analysis. Weather conditions interact with terrain conditions. Several groups of weather and climate related processes could contribute to surface displacements:

1. Thaw or aggradation of ground ice (Liu et al., 2010; Liu et al., 2012; Liu et al., 2014), induced by changes in heat transport into the soil, by summer heat, a thick snow cover, change of surface vegetation, forest fire, flooding; e.g. Nauta et al., 2014; Liu et al., 2014; Jones et al., 2015; references in van Huissteden, 2020).
2. Shrinkage or swelling of soils on decrease or increase of soil water content. In particular fine-grained soils and peat are sensitive (e.g. Camporese et al., 2006; Succow and Joosten, 2012); this shrinkage/swelling can be detected by InSAR (Cuenca, 2008).
3. Surface displacements resulting from peat decomposition have been detected by InSAR (Cuenca, 2008). Decomposition of peat is affected by soil moisture and temperature (e.g. Succow and Joosten, 2012). The reverse process, peat accumulation, increases surface elevation. Sphagnum peat growth occurs widely in the study area, in particular within the DTLB unit (Magnússon et al., 2020).
4. Erosion and sedimentation are triggered by increased runoff and flooding; in permafrost areas the release of water by ground ice thaw on slopes triggers thaw slumps and active layer slides (Lewkowicz, 2007; Lewkowicz and Way, 2019).

The summer warmth and dryness in 2019 has contributed to significant surface subsidence compared to the previous years, for several of the clusters of data points in **Figure 11**, notably clusters. 1, 2 and 7. The regression analysis (**Table 3**) shows that in 2019 most categorical terrain variables have negative coefficients, indicating dominant subsidence. Most terrain classes show smaller positive coefficients, more negative coefficients, or reversals from positive to negative, notably the Yedoma landform class. A notable exception is Pond density class 4, of which the regression coefficient turns significantly positive in 2019, from negative in 2017–2018.

Both loss of ground ice and shrinkage of peat soils could have contributed to the pronounced surface subsidence in 2019. Trajectory clusters 1, 2 and to a lesser extent 7 all show pronounced subsidence in 2019 compared to 2017 and 2018. Clusters 1 and 2 are located in the large DLTB on the center-north of the study area (**Figure 11**), 7 in a neighboring area immediately to the south in an older DTLB. Both are areas with peat growth. Cluster 1 and 2 show low center polygons, cluster 7 represents an older DTLB area where polygons have been overgrown with peat (**Figure 6**). Shrinkage of peat during the dry summer therefore could have contributed to subsidence. However, small perennial frost mounds (without peat growth) in these clusters also show subsidence, indicating that ground ice thaw has occurred also.

Positive surface displacements in 2019 occur in cluster 6 and 10. Most of these points are areas with intermediate - high pond density and ice wedge polygons (cluster 6), or areas on the lower slopes of Yedoma remnants and higher ground in DTLB's (cluster 10). The lower slopes of the YR may have been subject to colluvial deposition or downslope creep of soil material by increased water release from thawing permafrost in 2019. In 2017 and 2018, areas with potential colluvial deposition and peat growth also showed aggradation (**Supplementary Figure S5** and **Table 3**). For areas with ponds in 2019, vegetation and Sphagnum peat growth may have been stimulated by decrease of water depth in ponds (Magnússon et al., 2020).

Positive surface displacements in 2017 correlate significantly with elevation (**Table 1**), the YR landform (**Supplementary Figure S6** and **Table 3**) and trajectory cluster 4 (**Figure 11**). This is less clear in 2018, and in 2019 elevation correlates negatively with surface displacement. Pronounced positive surface displacement data points in 2017 are located on higher, well-drained parts of the Yedoma surface and DTLB surfaces. These areas have dry soils in summer with a thick active layer, consisting of silt and organic matter. The release of large amounts of meltwater from the thick snowpack after the winter of 2017, followed by a summer with relatively high amounts of precipitation (**Figure 2**) likely increased soil moisture. Downward movement of this additional water towards the transition layer at the top of the permafrost contributes to ice lens formation and frost heave in summer (Mackay, 1983). In addition, swelling of the soil by high moisture content could have contributed to the surface heave.

Seasonal flooding may contribute to sedimentation in floodplain environments, reflected by the positive regression coefficients for seasonal flooding in the regression data for all years in **Table 4**. However, this is probably a spurious effect; the number of points on seasonally flooded floodplain areas is very small.

The areas outside the floodplain that are reached by extreme floods only, show significant subsidence in 2017 and 2019 in the ANOVA results (**Table 3**), but the regression coefficients for extreme flooding in **Table 4** remain just below the p = 0.01 significance level. The extreme flooding areas are represented by a low number of points, in clusters 4, 5, 9 and 10. Nevertheless, from **Figure 9** a pronounced increase of summer thaw depth of dry soils that were flooded in 2017 and 2018 (transect 1, 2 and 3 in **Figure 9**) can be inferred at flooded locations. It is unlikely that the thaw depth recovers later in summer. Ponded water and wet soil conditions after flooding result in increased heat flux into the soil by changing the heat balance at the surface and increasing the soil thermal conductivity (e.g. Westermann et al., 2016), creating a thaw depth legacy of the flooding after flood recession. Nearby floodplain areas that are seasonally flooded have a thicker late summer ALT than non-flooded areas (van Huissteden et al., 2005; van Huissteden et al., 2009). Therefore, flooding is expected to increase ALT throughout the summer and fall with loss of ground ice (**Figure 11**), by heat transfer from flood water into the soil. However, this depends on soil conditions; wet soil with a Sphagnum peat cover was not affected (transect 4 in **Figure 9**).

Also for the RT landform unit, subsidence is pronounced (**Figures 10**, **11**). During extreme floods, the RT are small isolated islands on the river floodplain surrounded by water (**Figure 7**). Prolonged flooding in 2017, 2018 likely adds to heat transfer in this unit.

Given the absence of river gaging data, it is difficult to specify a flood return period for the high floods of 2017 and 2018. However, the low terrace scarp bordering the floodplain, which limits most floods, was exceeded over a large distance in 2017 and 2018. Downstream in the Indigirka river, the return period of the 2017 flood level was estimated at ≥49 years (Tei et al., 2020). A study of Landsat images of the study area during the spring flood period dating back to 1999 did not show any higher flood limits than the 2017 flood (Cheung, 2019).

A higher frequency of extreme floods likely induces subsidence at ice-rich floodplain borders, making these areas in turn more flood-prone. Additionally, subsidence of drainage thresholds could facilitate the connection of thaw lakes and DTLB areas to the floodplain. The sites numbered 3 in **Figure 7** are critical areas in that respect. For the westernmost point, the drainage threshold was just not exceeded in 2017, for the easternmost point, the flood invaded two lakes in a large DTLB, and a channel connecting these lakes towards the floodplain is forming. We hypothesize that ground ice thaw by an increase of flood extremes will expand floodplains in ice-rich permafrost. A future increase of flood height and flooding frequency therefore may have a large impact on floodplain development in ice-rich permafrost floodplains (Shkolknik et al., 2017).

So far, we have only considered thaw season surface displacement processes. However, as **Supplementary Figures S1, S2** show, surface subsidence is compensated by spatially varying heave in winter. This is attributed to ice lens growth, determined by local water availability in the active layer. Points with strong subsidence in one or more thaw seasons may have gained in height overall years when winter heave is included. Overall, net subsidence dominates in the study area over 2017–2019, but there are marked areas where net heave occurred.

For instance, in the relatively young drained thaw lake basin in the north-central area of the study area, a cluster of points occurs with pronounced subsidence in 2019, resulting in considerable cumulative subsidence over the thaw season (**Figure 11** cluster 1, 2, **Figure 10**), but the net effect of winter heave and summer subsidence over 3 years is substantial heave. (**Supplementary Figure S2**). This is an area of active *Sphagnum* peat growth, with a high soil water content. Also the Yedoma surfaces show net heave over the 3 years, which is strongest in 2017 (cluster 3, 4 and 8 in **Figure 11**). This is mainly driven by soil water accumulation in 2017 as discussed above.

Pingos that were visited in the study area do not show any recent growth activity. Compared to normal DTLB surfaces, pingos tend to subside a few mm over the years in the thaw season (t-test, $p < 0.01$) and also on average over the 3 years, which is like the result of slope processes and loss of ice.

Carbon Cycle Implications

The InSAR data presented here do not allow estimates on the carbon loss or greenhouse gas emissions from thawing permafrost, since this would require quantitative data on soil moisture conditions, active layer depth and carbon content of the soil. However, general trends can be inferred:

1. Increased flooding enhances ground ice thaw and active layer depth along floodplain limits and may expand floodplains. This enhances CH_4 emission (van Huissteden et al., 2005; van Huissteden et al., 2009), by exposing old permafrost carbon to anaerobic decomposition, and potentially by creating a more productive wetland vegetation through nutrient supply by flood water. Carbon emission in floodplain environments is fueled by higher ecosystem productivity of floodplains; most of the released fluvial-derived carbon is of recent origin (Dean et al., 2020). However, floodplain subsidence and capture of thaw lakes also creates storage space for burial and sequestration of organic-rich sediments (Emmerton et al., 2007; Van Huissteden et al., 2013; Vonk et al., 2015). In this location a sedimentation rate of organic-rich silt of 0.5 cm $year^{-1}$ was recorded in a borehole. However, tectonic subsidence also contributes to the sedimentation rate.
2. Outside floodplain areas, warm or wet summer conditions contribute to thaw of ice-rich permafrost, subsidence and enhanced exposure of permafrost organic matter to aerobic or anaerobic decomposition (e.g. Dorrepaal et al., 2009; Natali et al., 2015). However, the net effect on carbon loss and the ratio between CO_2 and CH_4 emission is not straightforward, since multiple interactions on various time scales between vegetation primary production, nutrient liberation by permafrost carbon decomposition and soil water content occur (Natali et al., 2015). Subsidence therefore cannot be used as a proxy for carbon loss.
3. Wet soil conditions enhance subsidence, as shown by increased subsidence in 2017–2018 in areas with intermediate-high pond density. On the other hand, during the warm/dry year the well-drained Yedoma was more prone to subsidence, and areas with high pond density showed positive surface displacement, probably linked to enhanced vegetation growth/peat accumulation (see at 3 below). Thaw ponds in the DTLB unit in this area release mostly contemporary CH_4 and CO_2 carbon from recent vegetation and soil (Nauta et al., 2014; Dean et al., 2020). This indicates that release of old carbon is minor. However, the loss of recent vegetation and soil carbon by pond formation may be substantial, and the release of CH_4 decreases the greenhouse gas sink or increases the net greenhouse gas emission of the area. Greenhouse gas emission of ponds is

partly compensated by recolonization of ponds by vegetation (Magnússon et al., 2020); see also previous section).

4. Some of the areas where peat formation by Sphagnum mosses occurs, showed pronounced subsidence in dry and warm 2019. This suggest dryer conditions by shrinkage and/or ground ice thaw. Dry conditions may limit peat growth and its carbon sequestration.
5. Both warm and wet years enhance mass wasting and colluviation on slopes of Yedoma landforms. Mass wasting by thaw slumps, active layer slides and gully erosion exposes permafrost and vegetation carbon to decomposition; sedimentation of mass wasted material and colluviation buries soil and vegetation carbon (Grosse et al., 2011; Abbott and Jones, 2015).

CONCLUSION

In our study area, erosion remnants of a paleo-surface of the Glacial Yedoma landscape testify of the former morphology of this landscape. The Yedoma surface extended with gentle slopes into the present river floodplain, where an old terrace level testifies of the floodplain surface at that time. The fluvial downcutting that created this terrace could relate to tectonic movements and/or change of the water balance of the drainage basin.

The formation of thaw lakes during the Late Glacial and Early Holocene eroded most of the Yedoma deposits, leaving only minor erosion remnants near the river floodplain. Probably formation of large thaw lakes was enhanced by tectonic subsidence. The Yedoma remnants were preserved preferentially near the river floodplain, because drainage by fluvial erosion limited the growth of thaw lakes. Catastrophic lake drainage could have contributed to floodplain erosion.

The potential for short-term geomorphological changes is shown by the InSAR surface displacement data. These data, and midsummer active layer thickness data collected after the floods of 2017 and 2018, show that heat transfer into the permafrost by flooding during high flood stages results in subsidence along floodplain margins, lowering drainage thresholds of thaw lakes near the river. We hypothesize that flood-induced subsidence is an important mechanism for floodplain expansion if future climate change increases spring flood heights.

Variability between the observation years contributes most to the variance of the InSAR data, but interacts with the local terrain characteristics. Surface displacement patterns differ considerably between the wet years 2017 and 2018, and the warm and dry year 2019. In general, during the wet years well-drained, elevated terrain appears less sensitive to subsidence by ground ice thaw and even may show heave. During the warm and drier year 2019, overall subsidence is more prominent.

Subsidence or heave are generally caused by changes in the ice volume at the top of the permafrost. Increased soil water availability in wet years contributes to gain of ice at the top of the permafrost, in particular at relatively dry sites. However, variations in soil moisture content also may contribute to surface displacement by shrinking or swelling of peat and fine-grained Yedoma soils. Peat growth and colluvial deposition on lower slopes result in positive surface displacement. However, detailed observations on changes in ice content and sedimentation are necessary to constrain contribution of each of these processes.

The relation between subsidence and the carbon cycle is not simple because of the many soil - vegetation interactions on various time scales. Combined with water ponding, subsidence increases CH_4 emission. Carbon cycle implications of floodplain expansion are the creation of a larger storage space for organic-rich fluvial sedimentation, but also expansion of areas with a high CH_4 emission.

DATA AVAILABILITY STATEMENT

The raw data supporting the conclusion of this article will be made available by the authors, without undue reservation.

AUTHOR CONTRIBUTIONS

JH did the geomorphological interpretation of the satellite images and field data, the statistical analysis and wrote most of the text. KT analyzed the radar images and computed the InSAR data. YC analyzed river flood levels from older Landsat image data, the data were provided by NLR and her work was supervised by HN. RM participated in fieldwork, discussions and provided a part of high resolution satellite image data. SK participated in fieldwork organization and data collection. TM and AD supervised fieldwork organization and contributed to discussion of the research results.

FUNDING

This research was financed by the User Support Program Space Research of the Netherlands Space Office, Grant No. ALW-GO/16-13, “Radar mapping of permafrost degradation and methane emission hotspots”, and by the Netherlands Polar Program of the Dutch Research Council (NWO), grant number ALWPP.2016.008. The geomorphological work was initiated and funded by the PAGE21 (Changing Permafrost in the Arctic and its Global Effects in the 21st Century) Large-scale integrating project EU FP7-ENV-2011 Grant Nr 282700.

ACKNOWLEDGMENTS

The authors acknowledge the European Space Agency (ESA) for Sentinel-1 images used in this study. We thank the crew of the Sakha Republic Nature Conservancy and Fisheries Inspection at Chokurdagh for their valuable support in the field. ERA5 reanalysis data have been provided under the terms of the Copernicus Products License Agreement version 1.2.

SUPPLEMENTARY MATERIAL

The Supplementary Material for this article can be found online at: https://www.frontiersin.org/articles/10.3389/feart.2021.680565/full#supplementary-material

REFERENCES

Abbott, B. W., and Jones, J. B. (2015). Permafrost Collapse Alters Soil Carbon Stocks, Respiration, CH4, and N2O in upland Tundra. *Glob. Change Biol.* 21 (12), 4570–4587. doi:10.1111/gcb.13069

Akaike, H. (1974). A New Look at the Statistical Model Identification. *IEEE Trans. Automat. Contr.*, 19 (6):716–723. doi:10.1109/TAC.1974.1100705

Akhmetiev, M. A. (2015). High-latitude Regions of Siberia and Northeast Russia in the Paleogene: Stratigraphy, flora, Climate, Coal Accumulation. *Stratigr. Geol. Correl.* 23 (4), 421–435. doi:10.1134/s0869593815040024

Amap (2017). "Snow,Water,Ice and Permafrost in the Arctic (SWIPA) 2017," in *Arctic Monitoring and Assessment Programme* (AMAP). Oslo, Norway, 269.

Anisimov, O., and Nelson, F. (1997). Influence of Climate Change on Permafrost in the Northern Hemisphere. *Russ. Meteorology Hydrol.* 5, 47–53.

Arp, C. D., Jones, B. M., Hinkel, K. M., Kane, D. L., Whitman, M. S., and Kemnitz, R. (2020). Recurring Outburst Floods from Drained Lakes: an Emerging Arctic hazard. *Front. Ecol. Environ.* 18 (7), 384–390. doi:10.1002/fee.2175

Beermann, F., Teltewskoi, A., Fiencke, C., Pfeiffer, E-M., and Kutzbach, L. (2015). Stoichiometric Analysis of Nutrient Availability (N, P, K) within Soils of Polygonal Tundra. *Biogeochemistry* 122 (2-3), 211–227. doi:10.1007/s10533-014-0037-4

Blok, D., Heijmans, M. M. P. D., Schaepman-strub, G., Kononov, A. V., Maximov, T. C., and Berendse, F. (2010). Shrub Expansion May Reduce Summer Permafrost Thaw in Siberian Tundra. *Glob. Change Biol.* 16 (4), 1296–1305. doi:10.1111/j.1365-2486.2009.02110.x

Brosius, L. S., Anthony, K. M. W., Treat, C. C., Lenz, J., Jones, M. C., Bret-Harte, M. S., et al. (2021). Spatiotemporal Patterns of Northern lake Formation since the Last Glacial Maximum. *Quat. Sci. Rev.* 253, 106773. doi:10.1016/j.quascirev.2020.106773

Camporese, M., Ferraris, S., Putti, M., Salandin, P., and Teatini, P. (2006). Hydrological Modeling in Swelling/shrinking Peat Soils. *Water Resour. Res.* 42 (6). doi:10.1029/2005wr004495

Chen, C. W., and Zebker, H. A. (2002). Phase Unwrapping for Large SAR Interferograms: Statistical Segmentation and Generalized Network Models. *IEEE Trans. Geosci. Remote Sensing* 40 (8), 1709–1719. doi:10.1109/tgrs.2002.802453

Cheung, Y. (2019). *Siberian Permafrost. A Temporal and Spatial Analysis on Flooding Frequency and Thaw Lakes*. Amsterdam: Vrije Universteit Faculty os Science/HAS University of Applied Sciences/NLR.

Cuenca, M. C. (2008). "Hanssen R Subsidence Due to Peat Decomposition in the Netherlands, Kinematic Observations from Radar Interferometry," in Proc. Fringe 2007 Workshop, 1–6.

Dean, J. F., Meisel, O. H., Martyn Rosco, M., Marchesini, L. B., Garnett, M. H., Lenderink, H., et al. (2020). East Siberian Arctic Inland Waters Emit Mostly Contemporary Carbon. *Nat. Commun.* 11 (1), 1627. doi:10.1038/s41467-020-15511-6

Dorrepaal, E., Toet, S., van Logtestijn, R. S. P., Swart, E., van de Weg, M. J., Callaghan, T. V., et al. (2009). Carbon Respiration from Subsurface Peat Accelerated by Climate Warming in the Subarctic. *Nature* 460 (7255), 616–619. doi:10.1038/nature08216

Drachev, S. S. (2016). Fold Belts and Sedimentary Basins of the Eurasian Arctic. *arktos* 2 (1), 21. doi:10.1007/s41063-015-0014-8

Emmerton, C. A., Lesack, L. F., and Marsh, P. (2007). Lake Abundance, Potential Water Storage, and Habitat Distribution in the Mackenzie River Delta, Western Canadian Arctic. *Water Resour. Res.* 43 (5). doi:10.1029/2006wr005139

Ferretti, A., Prati, C., and Rocca, F. (2001). Permanent Scatterers in SAR Interferometry. *IEEE Trans. Geosci. Remote Sensing* 39 (1), 8–20. doi:10.1109/36.898661

Fujita, K., Koz'min, B. M., Mackey, K. G., Riegel, S. A., McLean, M. S., and Imaev, V. S. (2009). 4. Göttingen, Germany: Copernicus Publications, 117–145. doi:10.5194/smsps-4-117-2009Seismotectonics of the Chersky Seismic Belt, Eastern Sakha Republic (Yakutia) and Magadan District, Russia*Stephan Mueller Spec. Publ. Ser.*

Grosse, G., Harden, J., Turetsky, M., McGuire, A. D., Camill, P., Tarnocai, C., et al. (2011). Vulnerability of High-Latitude Soil Organic Carbon in North America to Disturbance. *J. Geophys. Res.* 116. doi:10.1029/2010jg001507

Grosse, G., Jones, B., and Arp, C. (2013). "8.21 Thermokarst Lakes, Drainage, and Drained Basins," in *Treatise on Geomorphology* Editors J. Shroder, R. Giardino, and J. Harbor (San Diego, CA: Academic Press) 8, 325–353. doi:10.1016/b978-0-12-374739-6.00216-5

Hersbach, H., Bell, B., Berrisford, P., Hirahara, S., Horányi, A., Muñoz-Sabater, J., et al. (2020). The ERA5 Global Reanalysis. *Q.J.R. Meteorol. Soc.* 146 (730), 1999–2049. doi:10.1002/qj.3803

Hinkel, K. M., Eisner, W. R., Bockheim, J. G., Nelson, F. E., Peterson, K. M., and Dai, X. (2003). Spatial Extent, Age, and Carbon Stocks in Drained Thaw lake Basins on the Barrow Peninsula, Alaska. *Arctic, Antarctic, Alpine Res.* 35 (3), 291–300. doi:10.1657/1523-0430(2003)035[0291:seaacs]2.0.co;2

Hjort, J., Karjalainen, O., Aalto, J., Westermann, S., Romanovsky, V. E., Nelson, F. E., et al. (2018). Degrading Permafrost Puts Arctic Infrastructure at Risk by Mid-century. *Nat. Commun.* 9 (1), 5147. doi:10.1038/s41467-018-07557-4

Hooper, A. (2008). A Multi-Temporal InSAR Method Incorporating Both Persistent Scatterer and Small Baseline Approaches. *Geophys. Res. Lett.* 35. doi:10.1029/2008GL034654

Howard, A. D. (1996). "Modeling Channel Evolution and Floodplain Morphology," in *Floodplain Processes*. Editors M Anderson, E Walling, and P. D Bates (Chichester: Wiley), 15–62.

Imaeva, L. P., Imaev, V. S., and Koz'min, B. M. (2016a). Structural-dynamic Model of the Chersky Seismotectonic Zone (continental Part of the Arctic-Asian Seismic belt). *J. Asian Earth Sci.* 116, 59–68. doi:10.1016/j.jseaes.2015.11.010

Imaeva, L. P., Imaev, V. S., Mel'nikova, V. I., and Koz'min, B. M. (2016b). Recent Structures and Tectonic Regimes of the Stress-Strain State of the Earth's Crust in the Northeastern Sector of the Russian Arctic Region. *Geotecton.* 50 (6), 535–552. doi:10.1134/s0016852116060030

IPCC (2013). *Climate Change 2013: The Physical Science Basis. Contribution of Working Group I to the Fifth Assessment Report of the Intergovernmental Panel on Climate Change*. Cambridge University Press. doi:10.1017/CBO9781107415324

Jones, B. M., Grosse, G., Arp, C. D., Miller, E., Liu, L., Hayes, D. J., et al. (2015). Recent Arctic Tundra Fire Initiates Widespread Thermokarst Development. *Sci. Rep.* 5, 15865. doi:10.1038/srep15865

Jorgenson, M. T., and Shur, Y. (2007). Evolution of Lakes and Basins in Northern Alaska and Discussion of the Thaw lake Cycle. *J. Geophys. Res. Earth Surf.* 112 (F2). doi:10.1029/2006jf000531

Jorgenson, M. T., Romanovsky, V., Harden, J., Shur, Y., O'Donnell, J., Schuur, E. A. G., et al. (2010). Resilience and Vulnerability of Permafrost to Climate changeThis Article Is One of a Selection of Papers from the Dynamics of Change in Alaska's Boreal Forests: Resilience and Vulnerability in Response to Climate Warming. *Can. J. For. Res.* 40 (7), 1219–1236. doi:10.1139/x10-060

Juszak, I., Erb, A. M., Maximov, T. C., and Schaepman-Strub, G. (2014). Arctic Shrub Effects on NDVI, Summer Albedo and Soil Shading. *Remote sensing Environ.* 153, 79–89. doi:10.1016/j.rse.2014.07.021

Juszak, I., Eugster, W., Heijmans, M. M. P. D., and Schaepman-Strub, G. (2016). Contrasting Radiation and Soil Heat Fluxes in Arctic Shrub and Wet Sedge Tundra. *Biogeosciences* 13, 4049–4064. doi:10.5194/bg-13-4049-2016

Juszak, I., Iturrate-Garcia, M., Gastellu-Etchegorry, J.-P., Schaepman, M. E., Maximov, T. C., and Schaepman-Strub, G. (2017). Drivers of Shortwave Radiation Fluxes in Arctic Tundra across Scales. *Remote sensing Environ.* 193, 86–102. doi:10.1016/j.rse.2017.02.017

Kanevskiy, M., Shur, Y., Jorgenson, M. T., Ping, C.-L., Michaelson, G. J., Fortier, D., et al. (2013). Ground Ice in the Upper Permafrost of the Beaufort Sea Coast of Alaska. *Cold Regions Sci. Tech.* 85, 56–70. doi:10.1016/j.coldregions.2012.08.002

Kanevskiy, M., Shur, Y., Jorgenson, T., Brown, D. R. N., Moskalenko, N., Brown, J., et al. (2017). Degradation and Stabilization of Ice Wedges: Implications for Assessing Risk of Thermokarst in Northern Alaska. *Geomorphology* 297, 20–42. doi:10.1016/j.geomorph.2017.09.001

Kaplina, T. N. (2009). Alasnye Komplexy Severnoy Yakutii (Alas Complex of Northern Yakutia). *Kriosfera Zemli (Earth Cryosphere)* 13, 3–17.

Kessler, M., and Plug, L. J., and Walter Anthony, K. M. (2012). Simulating the Decadal-to Millennial-scale Dynamics of Morphology and Sequestered Carbon Mobilization of Two Thermokarst Lakes in NW Alaska. *J. Geophys. Res. Biogeosciences* 117 (G2). doi:10.1029/2011jg001796

Lewkowicz, A. G. (2007). Dynamics of Active-Layer Detachment Failures, Fosheim Peninsula, Ellesmere Island, Nunavut, Canada. *Permafrost Periglac. Process.* 18 (1), 89–103. doi:10.1002/ppp.578

Lewkowicz, A. G., and Way, R. G. (2019). Extremes of Summer Climate Trigger Thousands of Thermokarst Landslides in a High Arctic Environment. *Nat. Commun.* 10 (1), 1329. doi:10.1038/s41467-019-09314-7

Li, B., Heijmans, M. M., Blok, D., Wang, P., Karsanaev, S. V., Maximov, T. C., et al. (2017). Thaw Pond Development and Initial Vegetation Succession in Experimental Plots at a Siberian lowland Tundra Site. *Plant and Soil* 420 (1-2), 147–162. doi:10.1007/s11104-017-3369-8

Liu, L., Schaefer, K., Zhang, T., and Wahr, J. (2012). Estimating 1992–2000 Average Active Layer Thickness on the Alaskan North Slope from Remotely Sensed Surface Subsidence. *J. Geophys. Res. Earth Surf.* 117 (F1). doi:10.1029/2011jf002041

Liu, L., Zhang, T., and Wahr, J. (2010). InSAR Measurements of Surface Deformation over Permafrost on the North Slope of Alaska. *J. Geophys. Res. Earth Surf.* 115 (F3). doi:10.1029/2009jf001547

Liu, L., Jafarov, E. E., Schaefer, K. M., Jones, B. M., Zebker, H. A., Williams, C. A., et al. (2014). InSAR Detects Increase in Surface Subsidence Caused by an Arctic Tundra Fire. *Geophys. Res. Lett.* 41 (11), 3906–3913. doi:10.1002/2014gl060533

Mackay, J. R. (1983). Downward Water Movement into Frozen Ground, Western Arctic Coast, Canada. *Can. J. Earth Sci.* 20, 120–134. doi:10.1139/e83-012

Mackay, J. R. (1998). Pingo Growth and Collapse, Tuktoyaktuk Peninsula Area, Western Arctic Coast, Canada: A Long-Term Field Study. *Géographie physique et Quaternaire* 52 (3), 271–323.

Magnússon, R. Í., Limpens, J., Huissteden, J., Kleijn, D., Maximov, T. C., Rotbarth, R., et al. (2020). Rapid Vegetation Succession and Coupled Permafrost Dynamics in Arctic Thaw Ponds in the Siberian Lowland Tundra. *J. Geophys. Res. Biogeosci.* 125 (7), e2019JG005618. doi:10.1029/2019jg005618

Marsh, P., Lesack, L. F. W., and Roberts, A. (1999). Lake Sedimentation in the Mackenzie Delta, NWT. *Hydrol. Process.* 13 (16), 2519–2536. doi:10.1002/(sici)1099-1085(199911)13:16<2519::aid-hyp935>3.0.co;2-t

Marsh, P., and Neumann, N. N. (2001). Processes Controlling the Rapid Drainage of Two Ice-Rich Permafrost-Dammed Lakes in NW Canada. *Hydrol. Process.* 15 (18), 3433–3446. doi:10.1002/hyp.1035

Marsh, P., Russell, M., Pohl, S., Haywood, H., and Onclin, C. (2009). Changes in Thaw lake Drainage in the Western Canadian Arctic from 1950 to 2000. *Hydrol. Process.* 23 (1), 145–158. doi:10.1002/hyp.7179

McFeeters, S. K. (1996). The Use of the Normalized Difference Water Index (NDWI) in the Delineation of Open Water Features. *Int. J. remote sensing* 17 (7), 1425–1432. doi:10.1080/01431169608948714

Morgenstern, A., Grosse, G., and Schirrmeister, L. (2008). *Genetic, Morphological, and Statistical Characterization of Lakes in the Permafrost-Dominated Lena Delta*.

Morgenstern, A., Ulrich, M., Günther, F., Roessler, S., Fedorova, I. V., Rudaya, N. A., et al. (2013). Evolution of Thermokarst in East Siberian Ice-Rich Permafrost: A Case Study. *Geomorphology* 201, 363–379. doi:10.1016/j.geomorph.2013.07.011

Murton, J. B., Goslar, T., Edwards, M. E., Bateman, M. D., Danilov, P. P., Savvinov, G. N., et al. (2015). Palaeoenvironmental Interpretation of Yedoma Silt (Ice Complex) Deposition as Cold-Climate Loess, Duvanny Yar, Northeast Siberia. *Permafrost Periglac. Process.* 26 (3), 208–288. doi:10.1002/ppp.1843

Natali, S. M., Schuur, E. A. G., Mauritz, M., Schade, J. D., Celis, G., Crummer, K. G., et al. (2015). Permafrost Thaw and Soil Moisture Driving CO 2 and CH 4 Release from upland Tundra. *J. Geophys. Res. Biogeosci.* 120 (3), 525–537. doi:10.1002/2014jg002872

Nauta, A. L., Heijmans, M. M. P. D., Blok, D., Limpens, J., Elberling, B., Gallagher, A., et al. (2014). Permafrost Collapse after Shrub Removal Shifts Tundra Ecosystem to a Methane Source. *Nat. Clim Change* 5 (1), 67–70. doi:10.1038/nclimate2446

Nelson, F. E., Anisimov, O. A., and Shiklomanov, N. I. (2002). Climate Change and hazard Zonation in the Circum-Arctic Permafrost Regions. *Nat. Hazards* 26 (3), 203–225. doi:10.1023/a:1015612918401

NOAA (2020). Gobal Summary of the Day. Available at: https://www.ncei.noaa.gov/access/search/data-search/global-summary-of-the-day (Accessed July, , 2020).

Parmentier, F., Van Der Molen, M., Van Huissteden, J., Karsanaev, S., Kononov, A., Suzdalov, D., et al. (2011b). Longer Growing Seasons Do Not Increase Net Carbon Uptake in the Northeastern Siberian Tundra. *J. Geophys. Res. Biogeosciences* 116 (G4). doi:10.1029/2011jg001653

Parmentier, F. J. W., van Huissteden, J., Kip, N., Op den Camp, H. J. M., Jetten, M. S. M., Maximov, T. C., et al. (2011c). The Role of Endophytic Methane-Oxidizing Bacteria in Submerged Sphagnum in Determining Methane Emissions of Northeastern Siberian Tundra. *Biogeosciences* 8 (5), 1267–1278. doi:10.5194/bg-8-1267-2011

Parmentier, F. J. W., van Huissteden, J., van der Molen, M. K., Schaepman-Strub, G., Karsanaev, S. A., Maximov, T. C., et al. (2011a). Spatial and Temporal Dynamics in Eddy Covariance Observations of Methane Fluxes at a Tundra Site in Northeastern Siberia. *J. Geophys. Res.* 116 (G3). doi:10.1029/2010jg001637

QGIS.org (2016). *QGIS Geographic Information System*. Open Source Geospatial Foundation Project.

Ren, J., Niu, B., Wang, J., Jin, X., and Xie, L. (2013). *1: 5000000 International Geological Map of Asia*. Beijing: Geological Publishing House.,

Romanovskii, N., Hubberten, H-W., Gavrilov, A., Tumskoy, V., and Kholodov, A. (2004). Permafrost of the East Siberian Arctic Shelf and Coastal Lowlands. *Quat. Sci. Rev.* 23 (11-13), 1359–1369. doi:10.1016/j.quascirev.2003.12.014

Schirrmeister, L., Pestryakova, L., Wetterich, S., and Tumskoy, V. (2011). *Joint Russian-German Polygon Project East Siberia 2011-2014: The Expedition Kytalyk 2011AWI, Potsdam/Yakutsk*.

Schirrmeister, L., Froese, D., Tumskoy, V., Grosse, G., and Wetterich, S. (2013). *Encyclopedia of Quaternary Science*. 2nd edition. Elsevier, 542–552. doi:10.1016/b978-0-444-53643-3.00106-0PERMAFROST and PERIGLACIAL FEATURES | Yedoma: Late Pleistocene Ice-Rich Syngenetic Permafrost of Beringia

Schneider von Deimling, T., Grosse, G., Strauss, J., Schirrmeister, L., Morgenstern, A., Schaphoff, S., et al. (2015). Observation-based Modelling of Permafrost Carbon Fluxes with Accounting for Deep Carbon Deposits and Thermokarst Activity. *Biogeosciences* 12 (11), 3469–3488. doi:10.5194/bg-12-3469-2015

Shiklomanov, N. I., Streletskiy, D. A., Swales, T. B., and Kokorev, V. A. (2017). Climate Change and Stability of Urban Infrastructure in Russian Permafrost Regions: Prognostic Assessment Based on GCM Climate Projections. *Geographical Rev.* 107 (1), 125–142. doi:10.1111/gere.12214

Shkolnik, I., Pavlova, T., Efimov, S., and Zhuravlev, S. (2017). Future Changes in Peak River Flows across Northern Eurasia as Inferred from an Ensemble of Regional Climate Projections under the IPCC RCP8.5 Scenario. *Clim. Dyn.* 50, 215–230. doi:10.1007/s00382-017-3600-6

Shmelev, D., Veremeeva, A., Kraev, G., Kholodov, A., Spencer, R. G. M., Walker, W. S., et al. (2017). Estimation and Sensitivity of Carbon Storage in Permafrost of North-Eastern Yakutia. *Permafrost Periglac. Process.* 28 (2), 379–390. doi:10.1002/ppp.1933

Strauss, J., Schirrmeister, L., Grosse, G., Fortier, D., Hugelius, G., Knoblauch, C., et al. (2017). Deep Yedoma Permafrost: A Synthesis of Depositional Characteristics and Carbon Vulnerability. *Earth-Science Rev.* 172, 75–86. doi:10.1016/j.earscirev.2017.07.007

Succow, M., and Joosten, H. (2012). *Landschaftsökologische Moorkunde*.

Tadono, T., Ishida, H., Oda, F., Naito, S., Minakawa, K., and Iwamoto, H. (2014). Precise Global DEM Generation by ALOS PRISM. *ISPRS Ann. Photogramm. Remote Sens. Spat. Inf. Sci.* II-4 (4), 71–76. doi:10.5194/isprsannals-ii-4-71-2014

Takaku, J., Tadono, T., Tsutsui, K., and Ichikawa, M. (2016). Validation of "Aw3D" Global Dsm Generated from Alos Prism. *ISPRS Ann. Photogramm. Remote Sens. Spat. Inf. Sci.* III-4, 25–31. doi:10.5194/isprsannals-iii-4-25-2016

Tei, S., Morozumi, T., Nagai, S., Takano, S., Sugimoto, A., Shingubara, R., et al. (2020). An Extreme Flood Caused by a Heavy Snowfall over the Indigirka River basin in Northeastern Siberia. *Hydrological Process.* 34 (3), 522–537. doi:10.1002/hyp.13601

Teltewskoi, A., Beermann, F., Beil, I., Bobrov, A., De Klerk, P., Lorenz, S., et al. (2016). 4000 Years of Changing Wetness in a Permafrost Polygon Peatland (Kytalyk, NE Siberia): A Comparative High-Resolution Multi-Proxy Study. *Permafrost Periglac. Process.* 27 (1), 76–95. doi:10.1002/ppp.1869

Teshebaeva, K., van Huissteden, K. J., Puzanov, A. V., Balykin, D. N., Sinitsky, A. I., and Kovalevskaya, N. (2020). Permafrost Seasonal Surface Changes Revealed from Sentinel-1 InSAR Time-Series, Yamal peninsula. *Proc. IAHS* 382, 183–187. doi:10.5194/piahs-382-183-2020

Trouet, V., and Van Oldenborgh, G. J. (2013). KNMI Climate Explorer: a Web-Based Research Tool for High-Resolution Paleoclimatology. *Tree-Ring Res.* 69 (1), 3–13. doi:10.3959/1536-1098-69.1.3

Turetsky, M. R., Abbott, B. W., Jones, M. C., Walter Anthony, K., Olefeldt, D., Schuur, E. A. G., et al. (2019). Permafrost Collapse Is Accelerating Carbon Release. *Nature* 569, 32–34. doi:10.1038/d41586-019-01313-4

Ulrich, M., Grosse, G., Strauss, J., and Schirrmeister, L. (2014). Quantifying Wedge-Ice Volumes in Yedoma and Thermokarst Basin Deposits. *Permafrost Periglac. Process.* 25 (3), 151–161. doi:10.1002/ppp.1810

Van der Molen, M. K., Van Huissteden, J., Parmentier, F. J. W., Petrescu, A. M. R., Dolman, A. J., Maximov, T. C., et al. (2007). The Growing Season Greenhouse Gas Balance of a continental Tundra Site in the Indigirka Lowlands, NE Siberia. *Biogeosciences* 4 (6), 985–1003. doi:10.5194/bg-4-985-2007

Van Huissteden, J., Berrittella, C., Parmentier, F. J. W., Mi, Y., Maximov, T. C., and Dolman, A. J. (2011). Methane Emissions from Permafrost Thaw Lakes Limited by lake Drainage. *Nat. Clim Change* 1 (2), 119–123. doi:10.1038/nclimate1101

van Huissteden, J., Maximov, T. C., and Dolman, A. J. (2009). Correction to "High Methane Flux from an Arctic Floodplain (Indigirka Lowlands, Eastern Siberia)". *J. Geophys. Res.* 114, a–n. doi:10.1029/2009JG001040

van Huissteden, J., Maximov, T. C., and Dolman, A. J. (2005). High Methane Flux from an Arctic Floodplain (Indigirka Lowlands, Eastern Siberia). *J. Geophys. Res.* 110, a–n. doi:10.1029/2005JG000010

van Huissteden, J. (2020). "Thawing Permafrost," in *Permafrost Carbon in a Warming Arctic*. Springer Nature AG. doi:10.1007/978-3-030-31379-1

Van Huissteden, J., Vandenberghe, J., Gibbard, P. L., Lewin, J., Elias, A., and Mock, C. (2013). *PERMAFROST and PERIGLACIAL FEATURES | Periglacial Fluvial Sediments and Forms*. 2nd edition. Amsterdam: The Encyclopedia of Quaternary Science, 490–499. doi:10.1016/b978-0-444-53643-3.00108-4

Veci, L., Prats-Iraola, P., Scheiber, R., Collard, F., Fomferra, N., and Engdahl, M. (2014). *The sentinel-1 Toolbox*, 1–3.

Vonk, J. E., Mann, P. J., Davydov, S., Davydova, A., Spencer, R. G. M., Schade, J., et al. (2013). High Biolability of Ancient Permafrost Carbon upon Thaw. *Geophys. Res. Lett.* 40 (11), 2689–2693. doi:10.1002/grl.50348

Vonk, J. E., Tank, S. E., Bowden, W. B., Laurion, I., Vincent, W. F., Alekseychik, P., et al. (2015). Reviews and Syntheses: Effects of Permafrost Thaw on Arctic Aquatic Ecosystems. *Biogeosciences* 12 (23), 7129–7167. doi:10.5194/bg-12-7129-2015

Wang, P., Limpens, J., Nauta, A., van Huissteden, C., Quirina van Rijssel, S., Mommer, L., et al. (2018). Depth-based Differentiation in Nitrogen Uptake between Graminoids and Shrubs in an Arctic Tundra Plant Community. *J. Veg Sci.* 29 (1), 34–41. doi:10.1111/jvs.12593

Weiss, N., Blok, D., Elberling, B., Hugelius, G., Jørgensen, C. J., Siewert, M. B., et al. (2016). Thermokarst Dynamics and Soil Organic Matter Characteristics Controlling Initial Carbon Release from Permafrost Soils in the Siberian Yedoma Region. *Sediment. Geology.* 340, 38–48. doi:10.1016/j.sedgeo.2015.12.004

Wessel, B., Huber, M., Wohlfart, C., Marschalk, U., Kosmann, D., and Roth, A. (2018). Accuracy Assessment of the Global TanDEM-X Digital Elevation Model with GPS Data. *ISPRS J. Photogrammetry Remote Sensing* 139, 171–182. doi:10.1016/j.isprsjprs.2018.02.017

Westermann, S., Langer, M., Boike, J., Heikenfeld, M., Peter, M., Etzelmüller, B., et al. (2016). Simulating the thermal Regime and Thaw Processes of Ice-Rich Permafrost Ground with the Land-Surface Model CryoGrid 3. *Geosci. Model. Dev.* 9 (2), 523–546. doi:10.5194/gmd-9-523-2016

Zimov, S. A. A., Davydov, G. M., Zimova, E. A. G., Davydova, F. S., Schuur, E. A. G., Dutta, K., et al. (2006). Permafrost Carbon: Stock and Decomposability of a Globally Significant Carbon Pool. *Geophys. Res. Lett.* 33 (20). doi:10.1029/2006gl027484

Conflict of Interest: The authors declare that the research was conducted in the absence of any commercial or financial relationships that could be construed as a potential conflict of interest.

Publisher's Note: All claims expressed in this article are solely those of the authors and do not necessarily represent those of their affiliated organizations, or those of the publisher, the editors and the reviewers. Any product that may be evaluated in this article, or claim that may be made by its manufacturer, is not guaranteed or endorsed by the publisher.

frontiers in Earth Science

METHODS
published: 03 September 2021
doi: 10.3389/feart.2021.703304

Mineral Element Stocks in the Yedoma Domain: A Novel Method Applied to Ice-Rich Permafrost Regions

Arthur Monhonval[1], Elisabeth Mauclet[1], Benoît Pereira[1], Aubry Vandeuren[1], Jens Strauss[2], Guido Grosse[2,3], Lutz Schirrmeister[2], Matthias Fuchs[2], Peter Kuhry[4] and Sophie Opfergelt[1]*

[1]Earth and Life Institute, Université Catholique de Louvain, Louvain-la-Neuve, Belgium, [2]Permafrost Research Section, Alfred Wegener Institute Helmholtz Centre for Polar and Marine Research, Potsdam, Germany, [3]Institute of Geosciences, University of Potsdam, Potsdam, Germany, [4]Department of Physical Geography, Stockholm University, Stockholm, Sweden

OPEN ACCESS

Edited by:
Ko Van Huissteden,
Vrije Universiteit Amsterdam,
Netherlands

Reviewed by:
Trofim Maximov,
Institute for Biological Problems of Cryolithozone, Siberian Branch (RAS), Russia
Evgeny Abakumov,
Saint Petersburg State University, Russia

***Correspondence:**
Arthur Monhonval
arthur.monhonval@uclouvain.be

Specialty section:
This article was submitted to Cryospheric Sciences, a section of the journal Frontiers in Earth Science

Received: 30 April 2021
Accepted: 18 August 2021
Published: 03 September 2021

Citation:
Monhonval A, Mauclet E, Pereira B, Vandeuren A, Strauss J, Grosse G, Schirrmeister L, Fuchs M, Kuhry P and Opfergelt S (2021) Mineral Element Stocks in the Yedoma Domain: A Novel Method Applied to Ice-Rich Permafrost Regions. Front. Earth Sci. 9:703304. doi: 10.3389/feart.2021.703304

With permafrost thaw, significant amounts of organic carbon (OC) previously stored in frozen deposits are unlocked and become potentially available for microbial mineralization. This is particularly the case in ice-rich regions such as the Yedoma domain. Excess ground ice degradation exposes deep sediments and their OC stocks, but also mineral elements, to biogeochemical processes. Interactions of mineral elements and OC play a crucial role for OC stabilization and the fate of OC upon thaw, and thus regulate carbon dioxide and methane emissions. In addition, some mineral elements are limiting nutrients for plant growth or microbial metabolic activity. A large ongoing effort is to quantify OC stocks and their lability in permafrost regions, but the influence of mineral elements on the fate of OC or on biogeochemical nutrient cycles has received less attention and there is an overall lack of mineral element content analyses for permafrost sediments. Here, we combine portable X-ray fluorescence (pXRF) with a bootstrapping technique to provide i) the first large-scale Yedoma domain Mineral Concentrations Assessment (YMCA) dataset, and ii) estimates of mineral element stocks in never thawed (since deposition) ice-rich Yedoma permafrost and previously thawed and partly refrozen Alas deposits. The pXRF method for mineral element quantification is non-destructive and offers a complement to the classical dissolution and measurement by optical emission spectrometry (ICP-OES) in solution. Using this method, mineral element concentrations (Si, Al, Fe, Ca, K, Ti, Mn, Zn, Sr and Zr) were assessed on 1,292 sediment samples from the Yedoma domain with lower analytical effort and lower costs relative to the ICP-OES method. The pXRF measured concentrations were calibrated using alkaline fusion and ICP-OES measurements on a subset of 144 samples (R^2 from 0.725 to 0.996). The results highlight that i) the mineral element stock in sediments of the Yedoma domain (1,387,000 km^2) is higher for Si, followed by Al, Fe, K, Ca, Ti, Mn, Zr, Sr, and Zn, and that ii) the stock in Al and Fe (598 ± 213 and 288 ± 104 Gt) is in the same order of magnitude as the OC stock (327–466 Gt).

Keywords: thaw, alas, thermokarst, mineralogy, late pleistocene – holocene, arctic, X-ray fluorescence, bootstrapping technique

INTRODUCTION

The ice-rich deposits of the Yedoma domain hold more than 25% (213 Gt) of the frozen organic carbon (OC) of the northern circumpolar permafrost region, while covering only about 8% of its total soil area (c. 1.4 of 17.8 million km^2; Schirrmeister et al., 2013; Hugelius et al., 2014; Strauss et al., 2017). This carbon- and ice-rich region is particularly vulnerable to abrupt thawing processes (Nitzbon et al., 2020; Turetsky et al., 2020). This is the reason why Yedoma deposits are considered as a potential "tipping element" for future climate warming (Lenton, 2012). The key features of Yedoma deposits relative to other permafrost deposits are i) their ground ice properties, with 50–90% volume percent ice (Schirrmeister et al., 2013) and ii) their large spatial extent and thickness, resulting in a large total volume (Strauss et al., 2017). Thawing of ice-rich sediments has severe geomorphological consequences for the landscape (Kokelj and Jorgenson, 2013). Striking examples are collapsing river and coastal bluffs (Günther et al., 2015; Kanevskiy et al., 2016; Fuchs et al., 2020). But a spatially more important process is thermokarst lake formation, caused by surface subsidence due to excess ground ice melting in Yedoma deposits and leading to the formation of vast thermokarst depressions. The process not only affects the superficial soil horizons but also deep mineral horizons (Strauss et al., 2013; Walter Anthony et al., 2018). Thermokarst processes were highly active during the Deglacial and early Holocene period (Walter et al., 2007; Brosius et al., 2021) and shaped the Yedoma domain region with numerous lakes. Following drainage of lakes, a widespread process across lake-rich lowlands (Grosse et al., 2013), renewed permafrost aggradation and new soil development could occur in the drained thermokarst lake basins also called Alas. The Yedoma domain therefore includes Yedoma deposits never affected by thaw and frozen deposits that accumulated after Yedoma degradation in Alas landforms (Olefeldt et al., 2016; Strauss et al., 2017).

In permafrost soils, between ~30% (Mueller et al., 2015) and ~80% (Dutta et al., 2006) of the total soil OC is associated to minerals through various mechanisms, as detailed below. It is well known that interactions between minerals and OC can have a stabilizing effect on OC (Kaiser and Guggenberger, 2003; Lutzow et al., 2006; Kögel-Knabner et al., 2008; Gentsch et al., 2018; Wang et al., 2019). Mineral-protected OC is less bioavailable than mineral free OC (Schmidt et al., 2011; Kleber et al., 2015), thereby contributing to the long term carbon storage (Hemingway et al., 2019). Mineral protection of OC includes aggregation, adsorption and/or complexation or co-precipitation processes (Kaiser and Guggenberger, 2003). These protection mechanisms involve i) clay minerals, Fe-, Al-, Mn-oxy-(hydr) oxides, or carbonates (aggregation); ii) clay minerals and Fe-, Al-, Mn-oxy-(hydr)oxides using polyvalent cation bridges such as Fe^{3+}, Al^{3+}, Ca^{2+} or Sr^{2+} (adsorption); or iii) Fe^{3+}, Fe^{2+} and Al^{3+} ions (complexation). In addition, mineral elements (e.g., Si, Al, Fe, Ca, K, Mn, Zn, Sr) drive nutrient supply to plants or microorganisms, including algae such as diatoms. Nutrient supply is essential for plants growth and/or microbes metabolic activity and therefore indirectly influences C storage or degradation. It remains however unclear how mineral-OC interactions and nutrient supply will evolve upon permafrost thaw (Opfergelt, 2020), especially in ice-rich permafrost regions. This is mainly due to a lack of knowledge about the mineral element content in permafrost regions, relative to the well-known OC stocks in permafrost soils (Harden et al., 2012; Hugelius et al., 2014; Strauss et al., 2017; Hugelius et al., 2020; Kuhry et al., 2020) and the increasing knowledge on N stocks (Fuchs et al., 2018; Fuchs et al., 2019; Fouché et al., 2020; Hugelius et al., 2020).

To improve our understanding on the potential effects mineral elements can have on OC from permafrost regions, it is essential to have better knowledge on mineral element stocks in these regions, and on the changes in mineral element stocks upon thawing with changing conditions for mineral weathering (Zolkos and Tank, 2020). Ice-rich permafrost regions are particularly well suited areas to study the impact of thawing processes on the mineral elemental stocks in deposits. Indeed, "never" (since deposition) thawed deposits can be compared with previously thawed deposits resulting from thermokarst processes during warmer and wetter periods in the Deglacial and early Holocene periods (13–9 ka BP; Morgenstern et al., 2013; Walter et al., 2007). Assessing the evolution of the mineral element stocks between never thawed (since deposition) and previously thawed, refrozen as well as newly formed deposits will contribute to a better understanding of the impact of past thawing processes on the evolution of the pool of mineral elements available for mineral-OC interactions. It also provides insights into how ongoing permafrost thaw and thermokarst processes may impact mineral elements and what the potential implications are for the fate of OC in ice-rich deposits (Strauss et al., 2017). This is particularly relevant given that thermokarst processes are projected to spread across the Arctic and will potentially unlock additional OC stocks (Lacelle et al., 2010; Abbott and Jones, 2015; Schneider von Deimling et al., 2015; Nitzbon et al., 2020; Turetsky et al., 2020).

The objective of this study is to provide a method to assess the mineral element content on a large sample set in order to cover the different types of deposits from the Yedoma domain. Using this method, we provide a Yedoma domain Mineral Concentrations Assessment (YMCA) dataset for ten mineral elements (Si, Al, Fe, Ca, K, Ti, Mn, Zn, Sr, and Zr) and the stocks for these mineral elements in deposits from ice-rich permafrost regions. This assessment comprises "never" thawed since syngenetic freezing Yedoma Ice Complex deposits (in the following referred as Yedoma) and at least once previously thawed and then refrozen drained thermokarst lake basin deposits (in the following referred as Alas).

MATERIALS

Environmental Settings

The Yedoma domain is part of the permafrost region characterized by organic- and ice-rich deposits as well as thermokarst features. Today, the Yedoma domain predominantly covers areas in Siberia and Alaska (**Figure 1**)

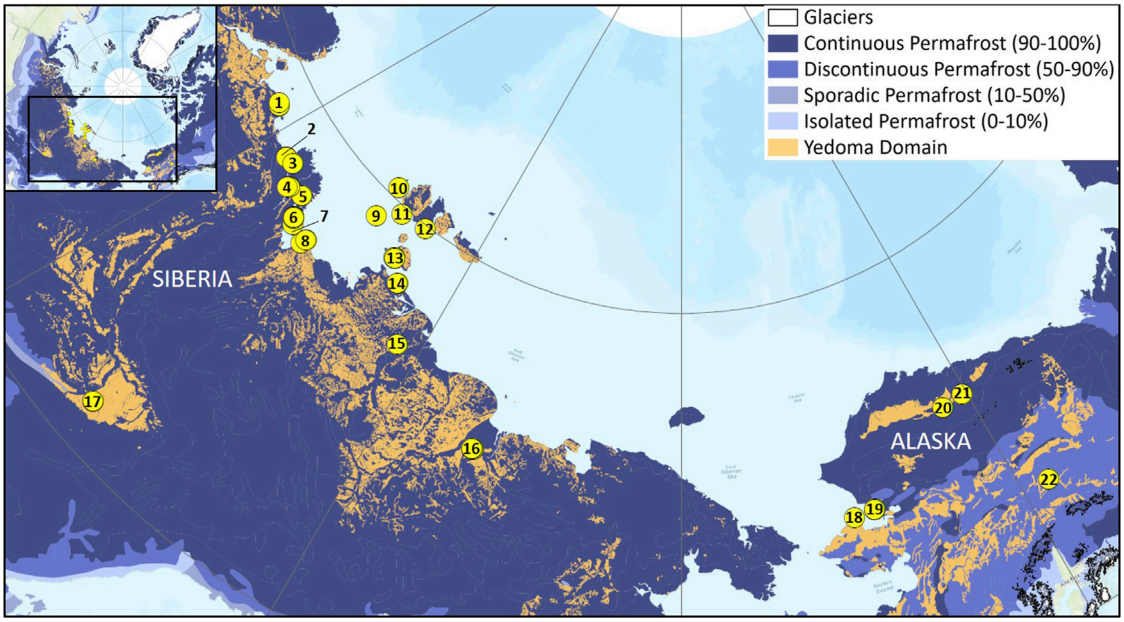

FIGURE 1 | Studied permafrost sites from the Yedoma domain. 1) Cape Mamontov Klyk; 2) Nagym (Ebe Sise Island); 3) Khardang Island; 4) Kurungnakh Island; 5) Sobo Sise Island; 6) Bykovsky Peninsula; 7) Muostakh Island; 8) Buor Khaya Peninsula; 9) Stolbovoy Island; 10) Belkovsky Island; 11) Kotel'ny Island; 12) Bunge Land; 13) Bol'shoy Lyakhovsky Island; 14) Oyogos Yar coast; 15) Kytalyk; 16) Duvanny Yar; 17) Yukechi; 18) Kitluk; 19) Baldwin Peninsula; 20) Colville; 21) Itkillik; 22) Vault Creek tunnel. Permafrost coverage layer is derived from the Circum-Arctic map of permafrost and ground-ice conditions shapefile (Brown et al., 1997). Yedoma domain coverage from Strauss et al. (2016) (Database of Ice-Rich Yedoma Permafrost - IRYP).

which were not covered with ice sheets during last glacial period (110 ka – 10 ka BP; Schirrmeister et al., 2013).

Recent estimates indicate that the current Yedoma domain has an extent of ~1.4 million km^2 and contains between 327 and 466 Gt OC (Strauss et al., 2017). Frozen deposits from the Yedoma domain alone store probably at least as much carbon as the tropical forest biomass (Lai, 2004). These deposits were formed by long-term continuous sedimentation and syngenetic freezing. Yedoma deposits were first described as homogeneous silty fine, ice-, and organic-rich sediments derived from aeolian processes (i.e., loess or loess-related deposits) (Pewe and Journaux, 1983; Tomirdiaro and Chernen'kiy, 1987; Murton et al., 2015). Current evidence indicates that depositional processes are polygenetic including alluvial and aeolian deposition and re-deposition, as well as *in situ* weathering during the late Pleistocene cold stages (Konishchev and Rogov, 1993; Schirrmeister et al., 2013). Despite evidence of homogeneity of Yedoma deposit aggradation, grain-size analyses show the large diversity of Yedoma deposits, pointing at multiple origins and transport pathways of sediments as well as a diverse interplay of (post)depositional sedimentary processes (Strauss et al., 2012; Schirrmeister et al., 2020; Sizov et al., 2020). For tens of millennia, continuous sedimentation led to the accumulation of several tens of meters thick permafrost deposits with characteristic syngenetic ice-wedge formation. Harsh, cold late Pleistocene winter climate triggered the formation of vertical frost cracks within surface deposits in which snow melt water percolated during spring and refroze into vertical ice veins in the permafrost. Over time and with annual repetition of this process, many meters wide and up to 40 m high ice-wedges were formed. Those large volumes of icy sediments together with the rise in temperature during the Holocene Thermal Maximum (HTM between 11 and 5 ka BP depending on the region; HTM reached at 7.6–6.6 ka BP in North Alaska and variable with time in Siberian regions) (Velichko et al., 2002; Kaufman et al., 2004; Porter and Opel, 2020) lead to a vast reshaping of the landscape with formation of thermokarst lakes and drained Alas basins (Grosse et al., 2013). Alas deposits in drained thermokarst lake basins are composed of reworked Yedoma deposits as well as Holocene accumulation during sub-aquatic and sub-aerial phases (Strauss et al., 2017; Windirsch et al., 2020). The Yedoma domain area includes 30% of unthawed Yedoma deposits composed of homogeneous silty deposits with polygenetic origins (eolian, alluvial or colluvial deposition) between large ice-wedges. Alas deposits have experienced thawing processes and drainage during early Holocene until more recently and account for 56% of the Yedoma domain area. Deltaic deposits (4%) as well as lakes and rivers (10%) complete the Yedoma domain deposits area distribution (**Figure 2**).

In this study, mineral element stocks are evaluated in Yedoma and Alas deposits (for a mean deposit thickness of 19.6 and 5.5 m, respectively; **Figure 3A**), but the evaluation does not include sediments underlying extant thermokarst lakes, active layer sediments or fluvial sediments (**Figure 3B**).

Sample Collection

This large-scale mineral element concentration assessment from Yedoma and Alas deposits is based on samples collected in two major Arctic regions, Alaska and Siberia. More specifically, the dataset includes 22 locations and compiles 75 different profiles from West, North and Interior Alaska, the Kolyma region, the Indigirka region, the New Siberian Archipelago, the Laptev Sea coastal regions, and Central Yakutia (**Figure 1**). About 64% of the profiles are from Yedoma deposits, 33% from Alas deposits and 3% from deltaic deposits, and the sites cover a range of geomorphological settings (**Supplementary Table S1**). For each location, Yedoma and Alas deposits profiles were sampled if both types of deposit were present. In total, 1,292 different samples were analyzed for their mineral element concentration. Sampling strategies were as follows: during the cold season, frozen samples were collected by drilling from the surface down with drilling rigs, whereas during the mid-summer season, drilling was performed in frozen ground below the existing thawed active layer. Cliffs or headwall exposures along coasts, rivers, or lakes were cleaned and frozen *in situ* sediments sampled with hammer and ax. For headwall or cliff sampling, sub-profiles from different vertical exposures were included when needed to reconstruct a complete stratigraphical composite profile. Additional information on specific site sampling techniques can be found in the reference papers cited in **Table 1**. Recovered samples were air- or freeze-dried before being stored and archived. The number of samples collected in each location and the number of samples analyzed with the different methods presented in *Methods* are provided in **Supplementary Table S1**.

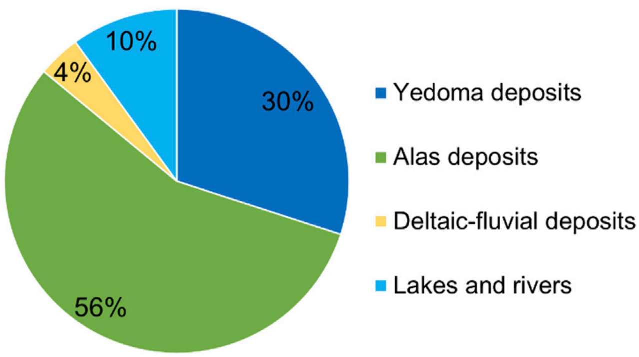

FIGURE 2 | Distribution of the area coverage (percentage) in the Yedoma domain region. The total Yedoma domain area is estimated at 1,387,000 km^2 (based on Strauss et al. (2017)).

METHODS

Total Elemental Analysis by ICP-OES Measurement After Alkaline Fusion

Inductively coupled plasma optical-emission spectrometry (ICP-OES) is a classical method to assess mineral element concentrations in solutions from the environment accurately. Solid phases such as soil samples should be first digested prior to ICP-OES analysis. Here, soils were digested by alkaline fusion. Briefly, air- or freeze-dried soil samples were carefully milled for homogenization (agate mill). We mixed a portion of the milled sample (80 mg) with Lithium metaborate and Lithium tetraborate and heated it up to 1,000°C for 10 min. Then we dissolved the fusion bead in HNO_3 2.2N at 80°C and stirred until complete dissolution (Chao and Sanzolone, 1992). We measured the mineral element concentrations in that solution by ICP-OES (iCAP 6500 Thermo Fisher Scientific). We assessed the loss on ignition at 1,000°C, the sum of oxides was between 98 and 102%, and the total element content in soils is expressed in reference to the soil dry weight at 105°C. To assess the accuracy (i.e., trueness and precision) of the method, the analytical measurement was validated by repeated measurements on three certified materials; i) USGS basalt reference material BHVO-2 (Wilson, 1997), ii) GBW07401 podzolitic soil, and iii) GBW07404 limy-yellow soil (National Research Center for CRM, 1986; **Supplementary Table S2**). To assess the precision of the method on a matrix similar to samples from the Yedoma domain, we conducted three

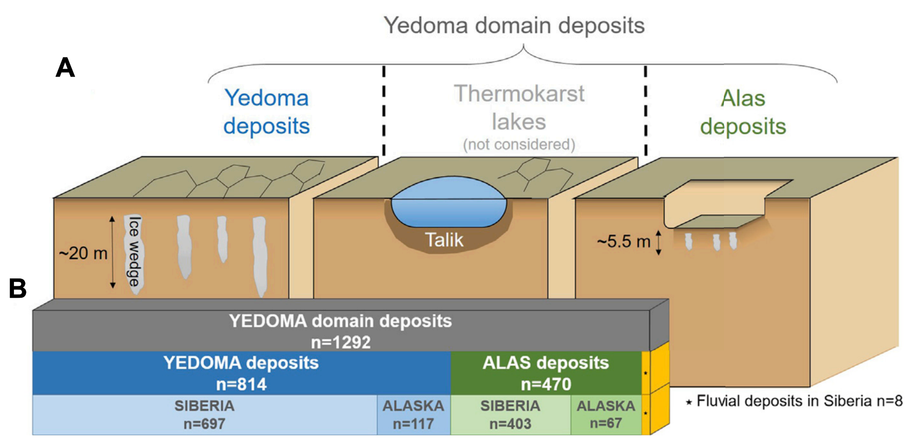

FIGURE 3 | (A) Schematic view of Yedoma and Alas (drained thermokarst lake basins) deposits considered for mineral element stock calculations (modified from Nitzbon et al. (2020)); sediments underlying thermokarst lakes or river floodplains are excluded. **(B)** Number of samples from Yedoma domain deposits included in the Yedoma domain Mineral Concentrations Assessment (YMCA) dataset (see *Yedoma Domain Mineral Concentrations Assessment Dataset*).

TABLE 1 | Studied locations from the Yedoma domain with associated labels, the number of profiles assessed for each type of deposits and the associated reference papers for site description. The site numbers (Site Nb) 1–17 are from Siberia, and 18–22 are from Alaska (located on the map in **Figure 1**). The labels are used in the Yedoma domain Mineral Concentrations Assessment (YMCA) dataset (doi:10.1594/PANGAEA.922724) (see *Yedoma Domain Mineral Concentrations Assessment Dataset* for details). Information on site geomorphology, number of samples collected in each location, and samples selected for specific analyses (*Methods*) are given in **Supplementary Table S1**

Site Nb	Site name	Label	Yedoma deposits	Alas deposits	Deltaic deposits	Reference papers
1	Cape Mamontov Klyk	Mak	2	1	0	Schirrmeister et al. (2008), 2011
2	Nagym (Ebe Sise Island)	Nag	2	1	0	Schirrmeister et al. (2003)
3	Khardang Island	Kha	1	0	0	Schirrmeister et al. (2007), 2011
4	Kurungnakh Island	Bkh, KUR	2	2	0	Schirrmeister et al. (2003), 2008; Wetterich et al. (2008)
5	Sobo Sise Island	Sob	2[a]	1	1	Fuchs et al. (2018)
6	Bykovsky Peninsula	Mkh, BYK	5	2	0	Andreev et al., (2002); Grosse et al. (2007); Schirrmeister et al. (2002), 2011
7	Muostakh Island	Muo	1	0	0	Grigoriev et al. (2003); Schirrmeister et al., (2011)
8	Buor Khaya Peninsula	Buo	2	3	0	Schirrmeister et al. (2017)
9	Stolbovoy Island	Sto	3	1	0	Grigoriev et al. (2003); Schirrmeister et al. (2003b)
10	Belkovsky Island	Bel	0	2	0	Grigoriev et al. (2003); Schirrmeister et al. (2003b), 2011
11	Kotel'ny Island	KyS	1	0	0	Grigoriev et al. (2003); Schirrmeister et al. (2003b), 2011
12	Bunge Land	Bun	0	0	1	Schirrmeister et al. (2010)
13	Bol'shoy Lyakhovsky Island	TZ, R, L	11	4	0	Andreev et al. (2009); Wetterich et al. (2011), 2014
14	Oyogos Yar coast	Oy	1	1	0	Opel et al., (2017); Schirrmeister et al. (2011); Wetterich et al. (2009)
15	Kytalyk	KY, KH	2	1	0	Weiss et al. (2016)
16	Duvanny Yar	DY	5	1	0	Strauss, (2010)
17	Yukechi	Yuk-Yul	2	2	0	Windirsch et al. (2020)
18	Kitluk	Kit	1	1	0	Unpublished data; Wetterich et al. (2012)
19	Baldwin Peninsula	Bal	1	3	0	Jongejans et al. (2018)
20	Colville	Col	1	0	0	Grosse et al. (2015); unpublished data
21	Itkillik	Itk, It	1	0	0	Kanevskiy et al. (2011)
22	Vault Creek Tunnel	FAI	1	0	0	Schirrmeister et al. (2016a)

[a]*Sobo Sise Yedoma profiles were collected from the top of Yedoma hills but radiocarbon dating indicates that those are actually cover deposits of Holocene age.*

TABLE 2 | Precision of the element concentrations expressed as pooled standard deviations (i.e., two pooled standard deviations, expressed in mg kg^{-1}) for the 10 elements considered. The values are based on three repetitions of three identical samples for both ICP-OES and raw concentrations from pXRF method. The coefficient of variation (CV; expressed in %), defined as the ratio of the standard deviation to the mean is also provided.

		Si	Al	Fe	Ca	K	Ti	Mn	Zn	Sr	Zr
ICP-OES	$\pm 2SD_{pooled}$ (mg kg^{-1})	±1858	±417	±275	±758	±510	±55	±8.5	±6.8	±3.0	±25
	CV (%)	0.29	0.43	0.50	0.99	2.01	0.71	0.85	4.31	1.05	4.21
pXRF	$\pm 2SD_{pooled}$ (mg kg^{-1})	±5,887	±3,830	±401	±627	±386	±210	±27	±8.2	±5.17	±11.3
	CV (%)	1.15	3.75	0.74	0.84	1.51	2.88	2.91	5.72	1.97	2.04

repetitions on three individual samples from Yedoma and Alas deposits. For each mineral element, standard deviations on the repetitions, expressed in mg kg^{-1}, are available in **Table 2**.

Out of the 1,292 deposit samples retrieved from the Yedoma domain (*Sample Collection*), a subset of 144 samples was analyzed by ICP-OES after alkaline fusion to determine their mineral element concentrations (sample list is provided in **Supplementary Table S3**). We used this subset of analysis to calibrate element concentrations measured by portable X-ray fluorescence (*Total Elemental Analysis by ex situ Direct Measurement by Portable X-Ray Fluorescenc*) for accurate determination of concentration values. For this first assessment, we measured the following elements on the subset of samples (except for Zn, which was measured on 119 out of the 144 samples): Si, Al, Fe, Ca, Mg, Cr, Ba, K, Ti, P, Cu, Mn, Ni, Zn, Sr, and Zr.

Total Elemental Analysis by *ex situ* Direct Measurement by Portable X-Ray Fluorescence

X-ray fluorescence (XRF) spectrometry is an elemental analysis technique with broad environmental and geologic applications, from pollution assessments to mining industries (Weindorf et al., 2014a; Rouillon and Taylor, 2016; Young et al., 2016; Ravansari et al., 2020). In addition, there is a growing use of portable XRF for soil science (McLaren et al., 2012; Ravansari and Lemke, 2018). Portable XRF is used primarily for solid elemental analysis (soils, sediments, rocks or even plastics) but can also deal with oil chemical characterization (Weindorf et al., 2014a). XRF is based on the principle that individual atoms emit photons of a characteristic energy or wavelength upon excitation by an external X-ray energy source. By counting the number of photons of each energy emitted from a sample, the elements present may be identified and quantified (Anzelmo and Lindsay, 1987; **Supplementary Figure S1**). XRF-scanning results represent elements intensities in "counts per second" (cps) which are proportional to chemical concentrations in the sample but depend also on sample properties (Röhl and Abrams, 2000), ice and water content (Tjallingii et al., 2007; Weindorf et al., 2014b) and interactions between elements called "matrix effect" (Weltje and Tjallingii, 2008; Fritz et al., 2018).

In situ pXRF measurement often involves variability from uncontrolled environmental factors, such as water content, organic matter content or sample heterogeneity (Shand and Wendler, 2014; Weindorf et al., 2014b; Ravansari et al., 2020). To avoid such variability in water content, measurements were performed on dried samples in laboratory (*ex situ*) conditions with the handheld device in the laboratory. The particle size distribution of these Yedoma domain deposits (described in reference papers from **Table 1**) is below 2 mm: therefore no sieving was necessary. For the pXRF measurement, the dried sample is placed on a circular plastic cap (2.5 cm diameter) provided at its base with a transparent thin film (prolene 4 μm). To avoid the underestimation of the detected intensities, sample thickness in the cap needs to be higher than 5 mm to 2 cm, depending on the element of interest (Ravansari et al., 2020). For a precise measurement, the sample thickness in the cap is set to >2 cm. Above 2 cm, the width is considered as "infinitely thick" for all elements. Measurements on the 1,292 samples from the Yedoma domain were performed using the pXRF device *Niton xl3t Goldd+* (Thermo Fisher Scientific), which has two specific internal calibration modes called *mining* and *soil*. Each internal calibration is dealing with different energy range and filters to scan the complete energetic spectrum from low to high-energetic fluorescence values. Both modes were used on each sample and depending on the element, the calibration with the best correlation with the ICP-OES method (*Total Elemental Analysis by ICP-OES Measurement After Alkaline Fusion*) was kept for further calculations (*Mineralogy by X-Ray Diffraction*). To standardize the analysis, total time of measurement was set to 90 s. We conducted the analysis in laboratory conditions, using a lead stand to protect the operator from X-rays.

In theory, the pXRF device used to generate this dataset can measure simultaneously elements of atomic mass from Mg to U. Because ambient air annihilates fluorescence photons that do not have enough energy, low atomic mass elements from Na and lighter cannot be quantified by pXRF. Note that Na quantification would be possible in controlled void conditions during analysis (Weindorf et al., 2014a). In this study, we focussed on the concentrations in 16 elements (Si, Al, Fe, Ca, Mg, Cr, Ba, K, Ti, P, Cu, Mn, Ni, Zn, Sr, Zr) by pXRF and by the ICP-OES method (*Total Elemental Analysis by ICP-OES Measurement After Alkaline Fusion*) to allow for quality check, calibration and correction. Some elements are at the limit of detection (LOD) for pXRF device (e.g., Cu, Ni). The LOD was reached when the sample was lacking a specific mineral element. LOD concentrations were set to 0.7 times the minimal concentration measured for this element, which is an arbitrary number but conventionally used for data statistical treatment (Reimann et al., 2008). Depending on the considered element, pXRF measured concentrations were highly precise but not always accurate (far from the true value) (**Figure 4**). Trueness was achieved after correction using a regression with concentration values measured by the ICP-OES method to avoid systematic bias (**Figure 4**; *Linear Regression for Accurate Mineral Element Concentration Measurements*). Using a well-defined regression to correct pXRF measurements for trueness allowed using the pXRF method to measure mineral element concentrations on a large number of Yedoma and Alas sample (n = 1,292), i.e., providing a valuable method to assess the mineral element content on a large sample set (**Figure 4**). Raw pXRF concentrations cannot be used for absolute quantification if not corrected with a reliable and accurate method. Here, only pXRF concentration values corrected using a well-defined regression were used (*Linear Regression for Accurate Mineral Element Concentration Measurements*). Because of poor correlation (R^2 < 0.5) between pXRF and accurate ICP-OES method for Mg, Cr, Ba, P, Cu and Ni, as discussed in *Linear Regression for Accurate Mineral Element Concentration Measurements*, these elements were not considered further in this study.

To assess the precision (i.e., random errors) of the pXRF method, three repetitions were conducted on three individual samples from different locations. Between each repetition, instrument/sample repositioning is used to mitigate the "nugget effect" due to heterogeneity in the sample (Ravansari and Lemke, 2018). Pooled standard deviations (SD_{pooled}, weighted average of standard deviations), expressed in mg kg^{-1}, of the repetitions for the ten elements used for stock calculation (*Linear Regression for Accurate Mineral Element Concentration Measurements*) are available in **Table 2**. Given the influence of sample matrix on pXRF measurements, the precision of the pXRF method was also evaluated based on three to five repetitions on 20 individual samples and on average 2.6 times larger than based on three repetitions on three samples (**Supplementary Table S4**). The coefficient of variation was 20% smaller for Al but 6.5 times larger for Ca based on 20 samples. To ensure a cautious evaluation of the dataset, we decided to report the precision on the data in Supplementary Presentation S1 based on the precisions from **Table 2** for ICP-OES measurements, and from **Supplementary Table S4** for pXRF measurements to use the largest set of sample with precision data available.

Mineralogy by X-Ray Diffraction

The X-ray diffraction (XRD) method allows the characterization of the presence of crystalline mineral phases. We assessed the mineralogy of 39 finely ground bulk samples and six clay fraction samples (samples selected in Siberia and Alaska detailed in

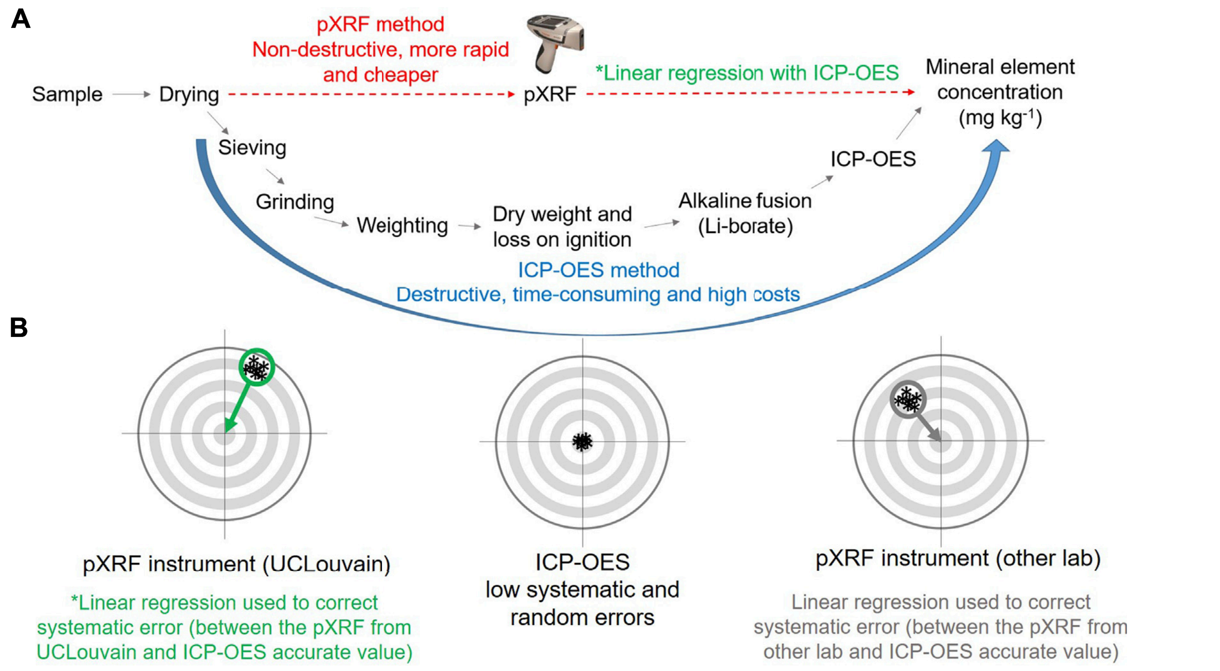

FIGURE 4 | (A) Comparison between two methods to assess mineral element concentrations in deposit samples: the inductively coupled plasma optical-emission spectrometry (ICP-OES) method (large blue arrow) is destructive and time-consuming (involving several steps), whereas the portable X-ray fluorescence (pXRF) method (dotted red arrows) is non-destructive and allows a fast and reliable determination of element concentrations on a large set of samples in a cost-effective way when a correction with a linear regression is applied. **(B)** The pXRF bias (i.e., systematic error) is corrected with a linear regression specific to each pXRF device. Portable XRF devices from each lab require their own linear regression to correct for accurate value. The linear regression is obtained from a selection of samples (here 11 % of the samples) analysed by both methods, pXRF and ICP-OES.

Supplementary Table S1). The mineralogy of bulk samples was determined on powder (Cu Kα, Bruker Advance D8). Clay fraction mineralogy was assessed after K^+ and Mg^{2+} saturation, ethylene glycol (eg) solvation and thermal treatments at 300 and 550°C (Robert and Tessier, 1974). The clay size fraction (<2 μm) was recovered after sonication, sieving at 50 μm to remove the sand fraction, and dispersion with Na^+-resins to separate silt (2–50 μm) and clay fractions (Rouiller et al., 1972).

Mean-Bootstrapping Technique for Mineral Element Stocks Calculations

Calculations of mineral element stocks are based on a mean-bootstrapping technique. From the corrected mineral element concentrations obtained via linear regression of pXRF measurements (YMCA dataset; *Yedoma Domain Mineral Concentrations Assessment (YMCA) Dataset*), the aim is to calculate the mineral element stock in Yedoma and Alas deposits individually, in order to estimate total mineral element budget at the Yedoma domain scale. This technique has been used to estimate OC budget from Yedoma and Alas deposits (Strauss et al., 2013) and was further improved by Jongejans and Strauss (2020). Because Yedoma domain deposits contain large ice volumes, stock calculations need to take into account not only the bulk density (BD) of the samples but also total thickness and total wedge-ice volume (WIV) of the deposits. In order to avoid overestimation of the mineral stocks, WIV was subtracted from the total Yedoma domain deposit volume, since the proportion of mineral elements locked inside ice-wedges is negligible. Indeed, Opel et al. (2018) indicate the minor contribution of mineral particles during ice-wedge formation. Fritz et al. (2011) further indicate that ion concentrations in ice is generally low, dominated by HCO_3^- (55%) and Cl^- (37%) for anions and Na^+ (58%) and Ca^{2+} (30%) for cations. Note that a flush of highly labile mineral elements (e.g., Na^+, Ca^{2+}, Cl^-) locked inside ice-wedges may increase nutrient supply for a short time scale upon Yedoma deposits degradation compared to long-term solid-liquid interactions upon thaw. Assumptions and calculations for BD determination, WIV estimations, deposits thickness, and coverage are fully explained in Strauss et al. (2013) and are summarized here. The bootstrapping statistical method use resampled (10,000 times) observed values (mineral element concentrations, BD, WIV and deposits thickness (**Supplementary Figure S2**)) and derive the mean afterward. The BD determination for each sample was obtained by using an inverse relationship with porosity (ϕ) **Eq. 1** (Strauss et al., 2013):

$$BD = (\phi - 1) \times \rho_s \tag{1}$$

whereas ρ_s is the solid fraction density. We assume that pore volume in ice-saturated samples is directly measured with segregated ice volume. For samples where no BD determination is available, BD is inferred from the total

TABLE 3 | Summary of key parameters for Yedoma deposits and Alas deposits. Parameters include thicknesses (in meters) and wedge ice volume (WIV, in %) from Strauss et al. (2013). Mineral element stock estimations are based on a mean thickness of 19.6 m for Yedoma and 5.5 m for Alas deposits.

	Yedoma deposits		Alas deposits	
	Thickness (m)	WIV (vol%)	Thickness (m)	WIV (vol%)
Mean	19.6	49.1	5.5	7.8
Median	15.1	51.9	4.6	7.6
Min	4.6	34.7	1.2	0.8
Max	46	59	13.4	12.8
N	19	10	10	7

organic carbon (TOC) content using equation **Eq. 2** (Strauss et al., 2013):

$$BD = 1.126^{-0.061\times TOC} \tag{2}$$

If neither BD or TOC is available, BD is fixed to 0.88 103 and 0.93 103 kg m^{-3} for Yedoma and Alas deposits, respectively, i.e., the mean BD measured in such deposits (Strauss et al., 2013). These values are comparable with other studies on BD of Yedoma deposits (0.98 103 kg m^{-3}; Dutta et al., 2006). The WIV estimations were performed using ice-wedge width from field measurements (Strauss et al., 2013), ice-wedge polygon size determinations from high-resolution satellite, and additional geometrical tools (assuming ice-wedges have an isosceles triangular or rectangular shape depending on the type of ice-wedge; see Strauss et al. (2013), Ulrich et al. (2014)). Thickness used for mineral element stock estimations in Yedoma domain deposits are based on mean profile depths of the sampled Yedoma (n = 19) and Alas (n = 10) deposits (**Table 3**; Strauss et al., 2013). Since the 10,000 step bootstrapping technique randomly picks one thickness at a time with replacement, we evaluated the stock estimation for a mean thickness of 19.6 m deep in Yedoma deposits and 5.5 m deep in Alas deposits.

The core Yedoma domain extent was estimated to ~1,387,000 km^2, based on digital Siberian Yedoma region map (Romanovskii, 1993) and the distribution of Alaskan ice-rich silt deposits equivalent to Yedoma (Jorgenson et al., 2008). The Yedoma deposit extent is estimated to 410,000 km^2, i.e., 30% of the Yedoma domain, based on the fact that 70% of the Yedoma domain area is affected by degradation (Strauss et al., 2013). Considering 10% of the area of the Yedoma domain covered with lakes and rivers, 4% covered with other deposits including deltaic and fluvial unfrozen sediments, this leaves 56% (780,000 km^2) of the Yedoma domain covered by frozen thermokarst deposits in drained thermokarst lakes (**Figure 2**). Using these parameters, the overall mineral element stock is determined with **Eq. 3** included into the bootstrapping calculation:

$$Mineral\ element\ stock\ [Gt] = \frac{thickness\ [m] \times coverage\ [m^2] \times BD\left[10^3 \frac{kg}{m^3}\right] \times \frac{100-WIV}{100}\,[-] \times mineral\ concentration \left[\frac{mg_{Min\ element}}{kg_{dry\ soil}}\right]}{1,000,000,000} \tag{3}$$

Because Yedoma and Alas deposits have different properties for BD, ice content, and deposit thickness, mineral element stocks were estimated for each deposit type individually. For each bootstrapping step, the sample mineral element concentration and specific BD were paired (as they are not independent) and a specific stock was estimated based on one value for WIV and thickness. The stock was then multiplied by total coverage for total mineral stock estimation to the Yedoma domain scale. From these input parameters, multiple mineral element stocks were computed, one for each bootstrapping step. Eventually, from those multiple steps (n = 10,000), a mineral element stock distribution was estimated from which the mean represents the best stock estimation of the considered mineral element. The error estimates in this study represent 2 standard deviations (mean ±2σ), with the assumption of a normal distribution. Computations were performed using R software (boot package; R Core Team, 2018). Supplementary information on input parameters (deposit thickness, WIV) are available in **Supplementary Figure S2**.

DATA PROCESSING AND RESULTS

Linear Regression for Accurate Mineral Element Concentration Measurements

Mineral element concentrations were measured with both the ICP-OES method (*Total Elemental Analysis by ICP-OES Measurement After Alkaline Fusion*) and the pXRF method (*Total Elemental Analysis by ICP-OES Measurement After Alkaline Fusion*) on a subset of samples (n = 144) from Yedoma domain deposits (**Supplementary Tables S1, S3**). Linear regressions can be computed from this subset of data and parameters of the regression are estimated and based on a robust linear regression (alpha = 0.95; **Table 4**). Among the 16 mineral elements measured, 10 elements (Si, Al, Fe, Ca, K, Ti, Mn, Zn, Sr and Zr) display high correlations between pXRF and ICP-OES method with R^2 ranging from 0.725 (Al) to 0.996 (Ca; **Table 4**). Linear regression plots for these elements are presented in **Supplementary Presentation S1**. The other six elements (Mg, Ba, Cr, Cu, Ni and P) present weak (R^2 < 0.5) or no correlations between the two methods. According to these correlations, the mineral element stock quantification was performed on the 10 elements reliably measured by pXRF (Si, Al, Fe, Ca, K, Ti, Mn, Zn, Sr and Zr), and the other six elements are not discussed further in this study.

The uncertainty based on three identical samples on the ICP-OES measurement after alkaline fusion was lower than pXRF measurements, except for Ca, K, and Zr (**Table 2**). Nonetheless, the advantages of a non-destructive, rapid and cheaper method predominate for a large-scale mineral concentration assessment given that the coefficient of variation (2.1–8.7%) on the pXRF measurement was satisfying to differentiate between high and low concentrations values measured in these deposits (i.e., comparing the horizontal error bar with the total range of values represented on the X-axis in **Supplementary Presentation S1**).

In this dataset, the risk of overestimating the element concentration by pXRF in organic-rich samples (Shand and Wendler, 2014) is limited. Among the 1,292 Yedoma and Alas samples used in this study to build the YMCA dataset (*Yedoma*

TABLE 4 | Robust linear regression adjusted R^2 (alpha = 0.95) between concentrations measured from pXRF and ICP-OES method in Yedoma domain deposits (n = 144 for all elements, except for Zn where n = 119).

Element	Si	Al	Fe	Ca	K	Ti	Mn	Zn	Sr	Zr
Adjusted R^2	0.835	0.725	0.949	0.996	0.941	0.728	0.875	0.844	0.965	0.907

Domain Mineral Concentrations Assessment Dataset), less than 0.5% of the samples were characterized by TOC content similar to or higher than 40 wt% (**Table 5**). Overestimation of the concentration was only observed for a single sample for Fe (**Supplementary Presentation S1C**) and for three samples for Ca (**Supplementary Presentation S1D**) out of the 144 samples from the subset (for samples with TOC content >40 wt%), and not observed for Si, Al, K, Ti, Mn, Zn, Sr and Zr.

Since the points corresponding to these organic-rich samples were excluded from the robust linear regressions (**Supplementary Presentation S1**), we assume that the matrix effect is not a source of significant bias to correct pXRF measurements of element concentrations using these regressions. Thus, the pXRF method can be applied for this first large-scale mineral element assessment of Yedoma domain deposits.

Yedoma Domain Mineral Concentrations Assessment Dataset

Robust linear regression equations with reliable R^2 (**Table 4**) were applied for each pXRF-measured concentration to correct concentrations values for trueness (**Figure 4** and **Supplementary Presentation S1**). The resulting YMCA dataset, freely available under doi:10.1594/PANGAEA.922724 (Monhonval et al., 2020), compiles 1,292 samples for the following elements: Si, Al, Fe, Ca, K, Ti, Mn, Zn, Sr and Zr.

In addition to the corrected mineral element concentrations, the YMCA dataset combines a wide range of relevant existing information on these 1,292 samples. Site and samples properties are integrated from AWI (Alfred Wegener Institute) Potsdam and Stockholm University data. We associated the lithology of the underlying bedrock, and the type of unconsolidated sediments at the surface characterizing each site from a spatial join using Arc Map 10.4. Specifically, coordinates from each site are joined based on their spatial location to Global Lithology Map (GLiM; Hartmann and Moosdorf, 2012) and Global Unconsolidated Sediments Map (GUM; Börker et al., 2018). Typically, we included the lithology of the underlying bedrock to evaluate its potential control on the mineral element concentrations in the deposits.

The attribute columns of this dataset are organized as follows: i) all site and sample properties (sample ID, description (identifying active layer (AL)), type of deposit, site location, number of profile, GPS coordinates, country, GLiM-lithology, GUM-unconsolidated sediment type, GUM-age, sample depth below surface level (b.s.l) or height above sea/river level (a.s.l), sediment characteristics, BD, gravimetric and absolute ice content, TOC values); and ii) corrected pXRF concentrations based on linear regressions from *Linear Regression for Accurate Mineral Element Concentration Measurements*. **Table 5** summarizes corrected mineral element concentration values as well as BD, TOC and ice content from the whole Yedoma domain region, with no differentiation between Yedoma and Alas deposits samples (n = 1,292).

Yedoma Domain Deposits Mineralogy

The main mineral phases (i.e., primary and secondary minerals) identified in selected Yedoma, Alas and fluvial deposits are presented in **Table 6**. The following minerals were identified in all bulk samples: quartz, feldspar plagioclase, micas and kaolinite. Chlorite was identified in Siberian deposits from Sobo Sise, Buor Khaya and Kytalyk. Calcite and dolomite were only detected in Alaskan Yedoma deposits from Colville and Itkillik. The mineralogy is generally similar along the profile depth for each location (**Supplementary Figure S3**). In these silty-fine sediments, the clay content ranges between 6 and 18% (silt content 67–79%; sand content 3–55%), i.e., well in line with Strauss et al. (2012). The diffractograms on clay fractions from Buor Khaya highlighted the presence of kaolinite, illite, and smectite (**Supplementary Figure S3D–I**). These data highlight the co-existence in these deposits of highly stable minerals such as quartz with more weatherable minerals such as dolomite, calcite, or feldspar plagioclase (Goldich, 1938; Wilson, 2004; Cornelis et al., 2011), and the presence of clay minerals characterized by higher specific surface area relative to the other mineral constituents (i.e., smectite, kaolinite, illite) (Kahle et al., 2004; Saidy et al., 2012).

Mineral Element Stocks in the Yedoma Domain

The quantification of mineral element stocks is a major step to assess the distribution of mineral elements in the Yedoma domain. We performed mineral elements stock estimations with the bootstrapping technique (*Mineralogy by X-Ray Diffraction*). For example, the mean Fe stock from Yedoma deposits (n = 814) is 147 ± 43 Gt (±2σ) using the theoretical normal distribution (mean-bootstrapping technique; **Figure 5**).

Based on the YMCA dataset, the bootstrapping technique was applied to calculate the stocks in Yedoma deposits for the 10 elements (Si, Al, Fe, Ca, K, Ti, Mn, Zn, Sr, and Zr), basing on the same input parameters for BD, thickness, WIV and coverage. The estimate mean and standard deviation derived the best estimation of the Yedoma deposit stocks for each specific mineral element. With a similar approach, mineral element stocks (Si, Al, Fe, Ca, K, Ti, Mn, Zn, Sr, and Zr) were estimated in Alas deposits. The element stocks in the Yedoma domain were obtained by adding element stocks in Yedoma and Alas deposits (**Table 7**). The results highlight that the mineral element with the largest stock in

TABLE 5 | Statistical summary of YMCA dataset (n = 1,292) for bulk density (BD), total organic carbon content (TOC), absolute ice content, and corrected mineral element concentrations (Si, Al, Fe, Ca, K, Ti, Mn, Zn, Sr and Zr) in Yedoma domain deposit samples (grouping Yedoma and Alas deposits together). Columns stand for N (number of data); Missing (missing data); MIN (minimum value reported); Q (quantiles); Q1 (first quantile); Q3 (third quantile); MEDIAN; MEAN; MAX (maximum value reported); SD (standard deviation); MAD (median absolute deviation standardised to conform with the normal distribution); IQR (interquartile range standardised to conform with the normal distribution); CV (coefficient of variation (%)); CVR (robust coefficient of variation (%)).

	Units	N	Missing	Min	Q_0.05	Q1	Median	MEAN-log	Mean	Q3	Q_0.95	Max	SD	Mad	IQR	CV	CVR
BD	g cm^{-3}	1,292	0	0.0379	0.721	0.943	0.988	1.076	1.143	1.322	2.055	2.429	0.397	0.1083	0.2814	34.74	10.96
TOC	wt%	1,182	110	0.07	0.1	1.11	1.942	1.87	3.747	3.748	13.09	44.36	5.950	1.606	1.955	159	82.74
Abs. ice content	%	703	589	0	17.76	28.83	37.5	36.66	38.94	47.8	64.69	103.9	14.99	14.08	14.06	38.48	37.56
Si	mg kg^{-1}	1,292	0	-19310[a]	241,400	284,000	301,000	290,400	295,200	316,900	335,700	444,700	40,750	24,170	24,330	13.8	8.031
Al	mg kg^{-1}	1,292	0	6,480	48,630	61,210	66,460	63,700	64,820	70,600	77,100	101,000	9,978	6,914	6,957	15.39	10.4
Fe	mg kg^{-1}	1,292	0	9,591	18,770	28,270	31,680	30,970	32,140	34,470	45,810	111,000	9,234	4,586	4,600	28.73	14.48
Ca	mg kg^{-1}	1,292	0	2086	5,316	7,972	10,380	11,490	13,910	15,520	32,910	102,000	11,540	4,667	5,594	82.94	44.97
K	mg kg^{-1}	1,292	0	2097	11,820	17,680	19,290	18,300	18,720	20,640	22,580	30,380	3,270	2,192	2,194	17.47	11.36
Ti	mg kg^{-1}	1,292	0	100.2	2,112	3,715	4,171	3,867	4,015	4,480	5,081	10,970	940.1	536.9	567.5	23.41	12.87
Mn	mg kg^{-1}	1,292	0	118.6	275.8	409	498	490	569.9	568.2	775.1	48,690	1,395	118.8	118	244.8	23.86
Zn	mg kg^{-1}	1,292	0	22.1	29.88	58.45	70.86	67.01	71.28	83.37	103.8	686.8	28.81	18.47	18.48	40.41	26.07
Sr	mg kg^{-1}	1,292	0	32.82	96.03	158.1	186	185	196.2	242.5	308.1	392.5	63.53	59.81	62.57	32.38	32.16
Zr	mg kg^{-1}	1,292	0	43.74	158.6	242.8	278.5	269.4	280.1	314	399.8	711	73.48	53.03	52.8	26.23	19.04

[a]*For Si, excessive organic rich samples may result in lower concentration values and consequently in negative concentration value after correction. Only positive values have been considered for stock calculations.*

the Yedoma domain is Si (2,739 ± 986 Gt) followed by Al, Fe, K, Ca, Ti, Mn, Zr, Sr, and Zn (**Figure 6**). In comparison, the estimated OC stock in the Yedoma domain reaches around 324–466 Gt (Strauss et al., 2017; **Figure 6**).

Overall, Yedoma and Alas deposits (**Table 7**) represent 86% of the total Yedoma domain area (**Figure 2**): this means that mineral element stocks are based on 86% of the deposits. The remaining surfaces of the Yedoma domain correspond to deltaic deposits (4%) or lakes and rivers (10%). Element stocks in deltaic deposits have not been estimated in this study due to the scarce number of available mineral concentration data in deltaic deposits (0.6% of the YMCA dataset) and the lack of empirical estimations of their thickness, or their ice volume (even if ice volume is probably negligible in these deposits). Waterbodies, lakes and rivers are not considered in this assessment focusing on the mineral element content in surface solid materials vulnerable to thaw or already thawed in the past. Sediments underlying lakes and rivers are therefore outside the scope of this evaluation and would only become relevant if drainage occurs. Absolute stock estimates (in Gt) allow direct comparison between Yedoma and Alas deposits, despite their different thickness (19.6 and 5.5 m, respectively), WIV and coverage. Mineral element density estimations (kg m^{-3}) are available (**Supplementary Table S5**) in which thickness and WIV have been neglected: this estimation is the product of mineral element concentrations and BD using bootstrapping technique.

ADVANTAGES AND LIMITATIONS OF THE METHODOLOGICAL APPROACH

Portable X-Ray Fluorescence

The main advantage of the pXRF method is to ensure a non-destructive, more rapid (less steps involved; **Figure 4**) and cheaper method for mineral element concentration measurement compared to the ICP-OES measurements after alkaline fusion. This is beneficial when dealing with large-scale assessments involving thousands of archive samples from the Yedoma domain. The concentrations of 10 elements could be reliably measured in these deposits (i.e., Si, Al, Fe, K, Ca, Ti, Mn, Zr, Sr, and Zn). The main limitation of the pXRF method is that raw concentration data cannot be used before applying a linear regression to correct for systematic error. This drawback related to inaccurate raw pXRF measurements can be rectified by correcting the raw pXRF values with accurate values obtained with the ICP-OES method after alkaline fusion (calibration based on 144 samples in this study). This correction can only be applied when the correlation between pXRF and ICP-OES concentrations is satisfactory (here, $R^2 > 0.7$). In these deposits, the concentrations of some elements (Mg, P, Cu, Ni, Ba) could not be assessed due to poor pXRF-ICP-OES correlation ($R^2 < 0.5$). Linear regressions used to correct raw pXRF concentrations depend on internal geometry of the pXRF device used. This means that each pXRF device needs its own linear regression and that a single linear regression equation cannot be used with different pXRF devices. Moreover, pXRF measurements are also matrix-dependent. The matrix (i.e., organic content, bulk density) of a sample can affect

TABLE 6 | Mineralogical composition in Yedoma (Y) and Alas and fluvial (A) deposits of Siberia and Alaska (Q, Quartz; Pl, Plagioclase; Ch, Chlorite; M, Mica; I, Illite; K, Kaolinite; D, Dolomite; Ca, Calcite; Sm, Smectites). The diffractograms for each profile (n = number of diffractogram per profile) are presented in **Supplementary Figure S3**.

Site	n	Fraction	Profile label	Mineralogy	Supplementary Figure 3
Sobo Sise	13	Bulk	Sobo T2-2 (Y), T2-3 (Y), T2-5 (A), T2-6 (A)	Q, Pl, Ch, M, K	A)
Buor Khaya	3	Bulk	Buo-02 (Y)	Q, Pl, Ch, M, K	B)
Buor Khaya	6	Bulk	Buo-04 (Y)	Q, Pl, Ch, M, K	C)
Buor Khaya	6	Clay	Buo-04 (Y)	Q, Pl, Ch, I, K, Sm	D) to I)
Kytalyk	4	Bulk	KY T1-1 (Y), KY T2-2 (A)	Q, Pl, Ch, M, K	J)
Colville	3	Bulk	Col (Y)	Q, Pl, M, K, D, Ca	K)
Itkillik	10	Bulk	Itk (Y)	Q, Pl, M, K, D, Ca	L)

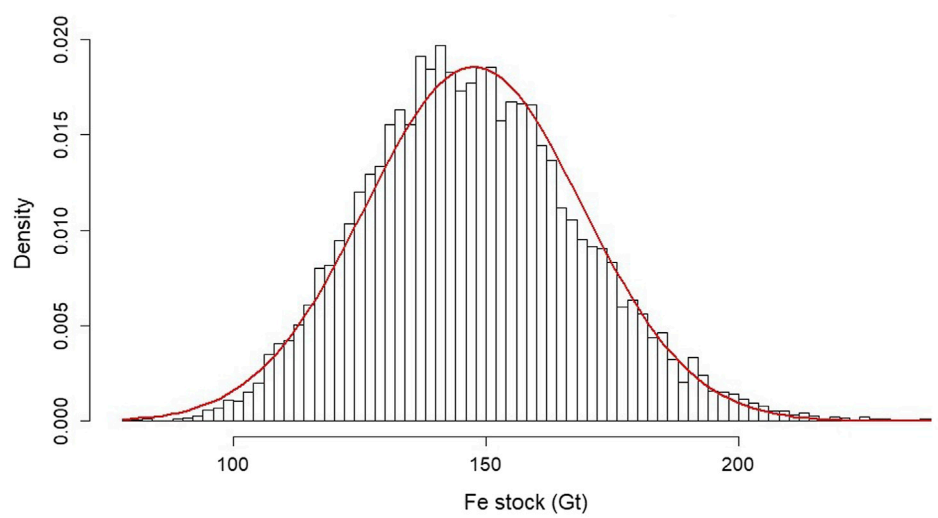

FIGURE 5 | Distribution of the iron stock (Gt) in Yedoma deposits (n = 814). The histogram results from the bootstrapping technique (n = 10,000; **Supplementary Figure S2**). The theoretical normal distribution is shown in red.

pXRF-measured concentrations and therefore linear regressions must be calibrated with samples from the same matrix (here, we used a subset of 11% of samples from the Yedoma domain). For some other elements, pXRF measurements are not possible due to the low atomic mass of these elements (N, Na).

Mean-Bootstrapping Technique

The main advantage of the mean-bootstrapping technique is to ensure a reliable calculation of non-parametric uncertainty estimates. The bootstrapping technique allows to include variability in mineral element concentrations and BD, WIV and thickness of the deposits. However, standard deviations from stock estimations (**Table 7**) are markedly large because of the conservative (observation-based) approach using all measurement for bootstrapping and deriving the mean afterwards. The only fixed parameter included in mineral element stock calculation (**Eq. 3**) is coverage. The coverage is set to 410,000 and 780,000 km^2 for Yedoma and Alas deposits, respectively. These estimations are subject to uncertainty but are the best current estimates, identical to the ones used in Strauss et al. (2013) to allow direct comparison with OC stocks. However, with the ongoing Arctic warming, these coverage estimations are dedicated to change with time. Because mineral element stocks are based on different WIV, thickness and coverage, the mineral element density expressed in kg m^{-3} allows to compare Yedoma and Alas deposits for an identical one cubic meter of sediments (without ice-wedges volume) (**Supplementary Table S5**).

IMPLICATIONS UPON PERMAFROST THAW

Implications for the Evolution of Mineral-Organic Carbon Interactions

The YMCA dataset allows investigating the evolution of selected element to OC ratio upon thermokarst processes resulting from permafrost thaw, i.e., between Yedoma and Alas deposits. Organo-mineral associations with Fe-, Al-, Mn-oxides or clay

TABLE 7 | Mineral elements stock (Gt) summary in Yedoma, Alas and Yedoma domain deposits (n = 814, 470 and 1,284, respectively). Mean and associated 2 standard deviations (σ; absolute value) are provided. Total stocks are the addition from the stocks in Yedoma and Alas deposits. Note, fluvial/deltaic deposits stocks were not estimated because of lack of data and spatial coverage (n = 8).

Element	Stock (Gt)					
	Yedoma deposits		Alas deposits		Total Yedoma domain	
	Mean	±2σ	Mean	±2σ	Mean	±2σ
Si	1,413	408	1,327	578	2,739	986
Al	309	88.9	289	124	598	213
Fe	147	42.6	140	60.9	288	104
Ca	70.8	20.9	51.7	23.2	123	44.1
K	90.0	25.7	84.0	36.8	174	62.4
Ti	19.0	5.45	17.5	7.68	36.5	13.1
Mn	2.57	0.852	2.34	1.02	4.90	1.87
Zn	0.327	0.0941	0.311	0.137	0.638	0.231
Sr	0.963	0.278	0.935	0.409	1.90	0.687
Zr	1.36	0.393	1.25	0.543	2.61	0.936

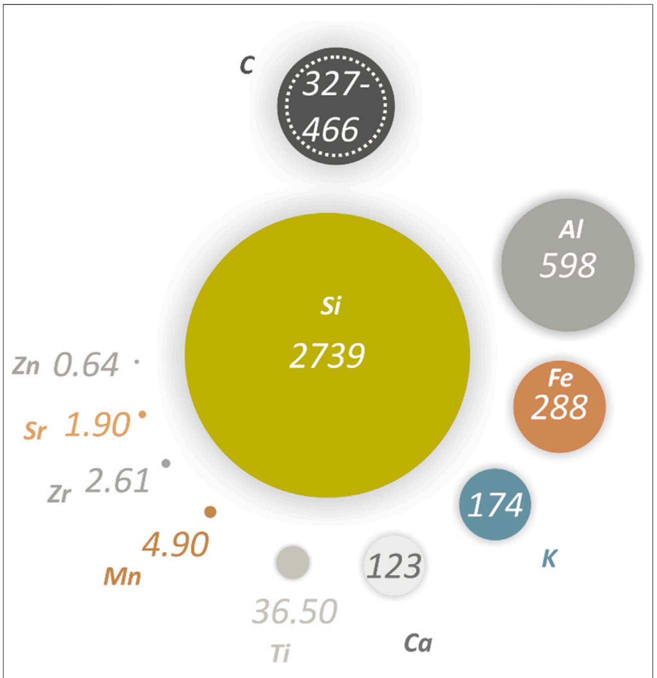

FIGURE 6 | Mineral element stocks (in Gt) in the Yedoma domain deposits (including Yedoma and Alas deposits) for Si, Al, Fe, K, Ca, Ti, Mn, Zr, Sr, and Zn. The surface area of the circles is proportional to the stock of the element considered. The organic carbon stock in the Yedoma domain (Strauss et al., 2017) is provided for comparison (the dotted line represents the lower range of the estimate, i.e., 327 Gt).

minerals using polyvalent cations bridging between OC and mineral surfaces (e.g., Ca^{2+}, Sr^{2+} in neutral and alkaline soils or Fe^{3+} and Al^{3+} in acid soils), or organo-metallic complexes involving Fe^{3+}, Fe^{2+} and Al^{3+} ions are well known to contribute to OC stabilization (Lutzow et al., 2006). Some mineral elements such as Fe or Mn are known for an inhibition effect on methane production (Lovley and Phillips, 1987; Beal et al., 2009; Herndon et al., 2015; Sowers et al., 2018), despite microbial function being considered as a larger part of the limitation for methane production (Monteux et al., 2020). The present dataset highlights a decrease of the Fe/TOC ratio and the Al/TOC ratio from Yedoma to Alas in Alaska, and virtually no change in these ratios in the Siberian Yedoma domain (**Figures 7A,B**). Providing evidence for changes in Fe/TOC or Al/TOC ratios upon thermokarst processes in a portion of the Yedoma domain highlights the need for further investigations regarding the evolution of interactions between OC and Fe or Al upon thawing.

In addition, the clay minerals present in these Yedoma domain deposits (confirmed by XRD; **Table 6**) can be associated to the formation of aggregates, thereby contributing to spatial inaccessibility of OC for decomposer organisms due to occlusion in aggregates (Lutzow et al., 2006). Iron oxides are also known to contribute to the formation of aggregates (Eusterhues et al., 2005; Kleber et al., 2015). Changing Fe/TOC ratio between Yedoma and Alas in Alaska (**Figures 7A,B**) reinforces the need to further investigate the potential role of the evolution of aggregates for OC availability upon thawing (Monhonval et al., 2021). Changing conditions for mineral protection of OC upon thawing is likely to influence OC microbial degradation (Gentsch et al., 2015; Herndon et al., 2017; Kögel-Knabner et al., 2010; Opfergelt, 2020), thereby contributing to modulate the permafrost carbon feedback (Schuur et al., 2015).

Implications for Mineral Weathering and Nutrient Supply to Ecosystems

The YMCA dataset allows investigating the change in concentration of soluble elements such as Ca upon thermokarst processes resulting from permafrost thaw, i.e., between Yedoma and Alas deposits. As shown on a density plot (**Figure 7C**), sediments from Alas deposits are characterized by lower Ca concentrations compared to Yedoma deposits. This was observed between Yedoma and Alas deposits in Alaska, and in Siberia (**Figure 7C**).

Higher Ca concentrations in Yedoma and Alas deposits from Alaska relative to the deposits from Siberia can be explained by the local lithology, i.e., carbonate rocks from the northern Brooks Range contributing to the deposits in Alaska (Till et al., 2008). The lithology of the bedrock, beneath Quaternary deposits, inferred from the GLiM map, is similar between Yedoma and Alas deposits (**Supplementary Figure S4**). This can likely be explained by the fact that the Yedoma and Alas deposits from the Yedoma domain mainly originate from the same source material on local to regional scales (Grosse et al., 2007; Strauss et al., 2017). Since most of the studied regions are covered by thick Quaternary deposits, mineral element concentrations are likely more influenced by the mixing of the unconsolidated sediments contributing to the Quaternary deposits rather than by the lithology of the underlying bedrock. The lithological similarity between

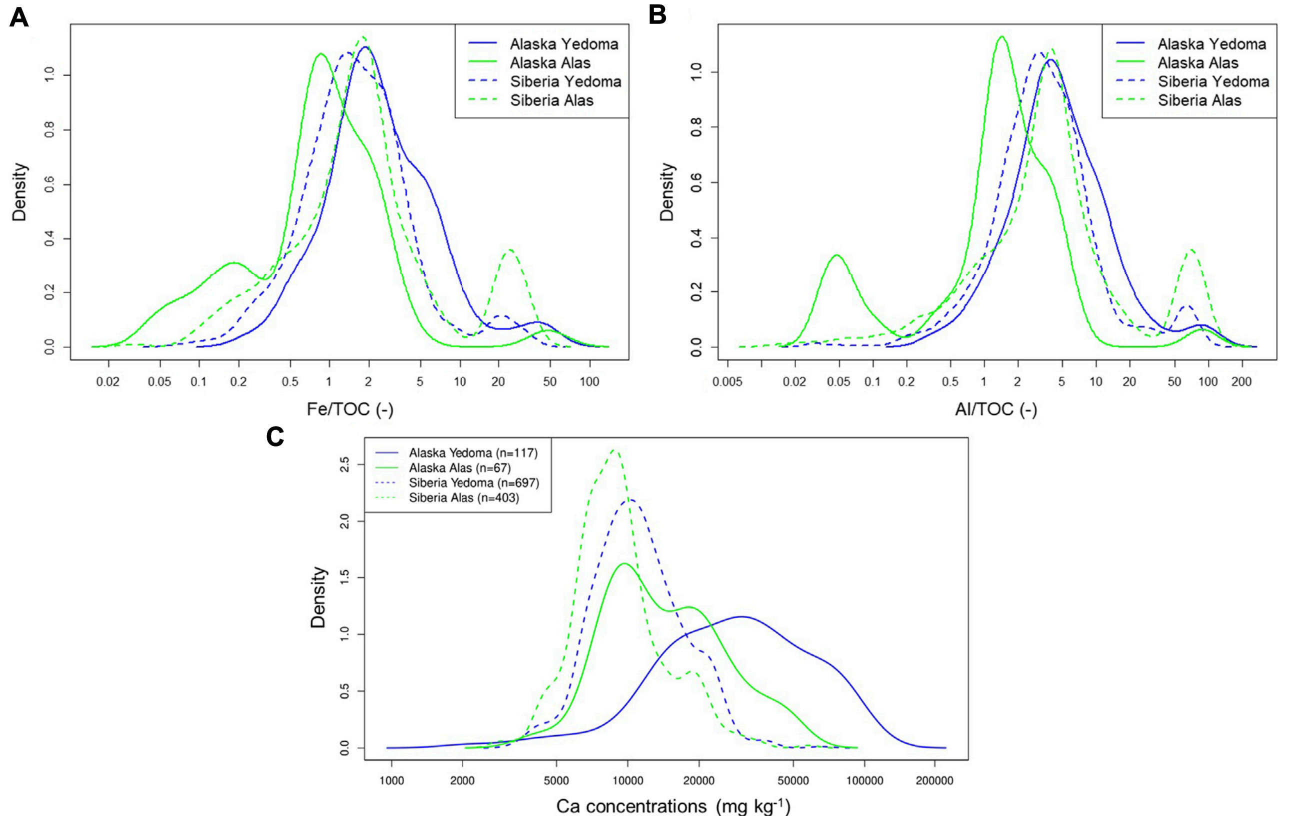

FIGURE 7 | Empirical density histogram of **(A)** Fe/total organic carbon (TOC) ratio, **(B)** Al/TOC ratio and **(C)** Ca concentrations (mg kg^{-1}) in Yedoma domain deposits in Alaska (full line) and Siberia (dashed line) for Yedoma (blue line) and Alas (green line) deposits. The X-axis is a log scale.

Yedoma and Alas deposits can also be explained by the fact that Alas deposits are dominated by reworked sediments from former Yedoma deposits (Schirrmeister et al., 2020). Therefore, Ca depletion in Alas deposits relative to Yedoma deposits from one region is not lithology dependent but potentially results from mineral weathering and leaching processes of soluble elements such as Ca during former thawing periods. Indeed, Alas formation history includes lake formation and drainage, and the dynamism of such formation over the past thousands of years may lead to leaching processes of soluble elements, a commonly observed process in non-cryogenic soils (Stumm and Morgan, 1995) and cryogenic soils (Ping et al., 2005).

The co-existence of more weatherable (dolomite, calcite, or feldspar plagioclase) and less weatherable (quartz) mineral constituents in Yedoma deposits (**Table 6**) is likely to lead to an increasing contribution from mineral weathering to the inorganic carbon budget (Zolkos and Tank, 2020) upon thermokarst processes. The balance between carbonate or silicate mineral weathering is known to influence the short-term and long-term atmospheric CO_2 consumption (Berner et al., 1983). Locally, the oxidation of sulfides such as pyrite present in low amount, not detected here but reported in beach deposits (Schirrmeister et al., 2010), can lead to the formation of sulfuric acid and the subsequent weathering of carbonate mineral without involving atmospheric CO_2 consumption (Zolkos and Tank, 2020).

The YMCA dataset provides total mineral element concentrations, including i) a mineral element reservoir known to be rapidly available to vegetation and microorganisms in permafrost soils (Ping et al., 1998, 2005), and ii) a mineral element reservoir providing a longer term supply of nutrients through mineral weathering (Zolkos and Tank, 2020). Indeed, the weathering of minerals such as dolomite, calcite, or feldspar plagioclase is expected to release soluble cations such as Ca available to supply nutrients to terrestrial and aquatic Arctic ecosystems, or to interact with OC (*Implications for the Evolution of Mineral-Organic Carbon Interactions*). Among the 10 elements included in the YMCA dataset, macro- (e.g., K, Ca) and micro-nutrients (e.g., Fe, Mn, Zn) are required for plant nutrition and also regulate other vital processes for plants and microorganisms growth and metabolic activity (DalCorso et al., 2014). Briefly, K regulates vital processes, such as photosynthesis, water and nutrient transportation, or protein synthesis (Marschner, 2012). Ca is a major second messenger in plant signal transduction, mediating stress- and developmental processes (Liese and Romeis, 2013). Micro-elements are required as cofactor for some essential proteins (Fe; Morgan and Connolly, 2013), play an essential role as a photosynthetic function or in metallo-protein conformation (Mn; Yang et al., 2008) or can have enzymatic functions (Zn; Lindsay, 1972). Some non-essential elements, such as Si and Al, can stimulate plant growth by playing with abiotic-biotic stress resistance and symbiosis (Richmond and Sussman, 2003; DalCorso et al., 2014). In aquatic ecosystems, silicon is a limiting nutrient for diatoms and other siliceous organisms, thereby controlling diatom abundance and community structure in the ocean, and as a result, food web and CO_2 uptake by photosynthesis (Smetacek, 1999; Yool and Tyrrell, 2003). The leaching of the more mobile cations such as Ca or K can be estimated by comparing ratios between mobile and immobile elements: this is why assessing the concentration of elements considered as immobile such as Ti or Zr can be useful to evaluate the advance of weathering in a soil relative to its parent material, and thereby the soil mineral reserve (Kurtz et al., 2000; Hodson, 2002; Jiang et al., 2018). However, the reserve in important nutrients such as P, N, S, and Mg in the Yedoma domain could not be estimated with the method used in this study (Sect. 5). The YMCA dataset is a first step needed in order to evaluate the impact of widespread rapid permafrost thaw through thermokarst processes (Turetsky et al., 2020) on the mineral element concentrations in the deposits and the potential implications for OC and mineral nutrient supply.

CONCLUSION

This study presents a method combining portable X-ray fluorescence with a bootstrapping technique to generate the first mineral element inventory of permafrost deposits from the ice-rich Yedoma region, i.e., never thawed Yedoma deposits and previously thawed Alas deposits for a mean thickness of 19.6 and 5.5 m, respectively. In the resulting Yedoma domain Mineral Concentrations Assessment (YMCA) dataset, the total concentrations of 10 mineral elements (Si, Al, Fe, Ca, K, Ti, Mn, Zn, Sr, Zr) in Yedoma domain deposits have been quantified in 75 different profiles. The associated mineral elements stocks are shown to be in the same order of magnitude for Al and Fe than for OC, and to decrease from Si, Al, Fe, K, Ca, Ti, Mn, Zr, Sr, to Zn. This dataset allows tracking dynamic processes controlling mineral element concentrations in thawing environments, as illustrated by lower Ca concentration in Alas deposits relative to Yedoma deposits highlighting potential Ca leaching upon thawing. Providing the YMCA dataset is contributing to improve the knowledge on the mineral constituents in ice-rich permafrost, i.e., a necessary step to better understand the evolution of mineral-OC interactions, mineral weathering and mineral nutrient supply to ecosystems upon permafrost thaw. The YMCA dataset is particularly relevant given the increasing occurrence of abrupt thaw in ice-rich permafrost regions.

DATA AVAILABILITY STATEMENT

The datasets presented in this study can be found in online repositories. The names of the repository/repositories and accession number(s) can be found below: https://doi.pangaea.de/10.1594/PANGAEA.922724.

AUTHORS CONTRIBUTION

AM, SO, and JS conceived the project. JS, GG, LS, MF, and PK retrieved samples from Alaska and Siberia from many different field expeditions. AM did the pXRF measurements with the help of EM. AM, SO, EM, BP, and AV contributed to set up the YMCA database. AM analyzed the data and calculated to the stocks based on the code developed by JS for carbon stock estimation using mean-bootstrapping. AM wrote the manuscript with contributions from all co-authors.

FUNDING

This project received funding from the European Union's Horizon 2020 research and innovation program under grant agreement No. 714617 to SO, and SO acknowledges funding from the Fund for Scientific Research FNRS in Belgium (FC69480). This work was embedded into the Action Group "The Yedoma Region" funded by the International Permafrost Association. Field sample collection was funded by a European Research Council (ERC) Starting Grant (338335) to GG as well as Alfred Wegener Institute basic funding. Kytalyk samples were collected with support of the European Union FP7—ENVIRONMENT project PAGE21 (grant agreement 282700) and the EU FP7 INTERACT Integrating Activity.

ACKNOWLEDGMENTS

The authors acknowledge Hélène Dailly, Anne Iserentant, Elodie Devos and Laurence Monin from the MOCA analytical platform at UCLouvain for mineral elemental analysis. We thank Waldemar Schneider (AWI logistics) and Dmitry Melnichenko (Hydrobase Tiksi) for many years of logistical support, and Catherine Hirst, Maxime Thomas, and Pierre Delmelle for fruitful scientific discussions. We thank the two reviewers for their constructive comments.

SUPPLEMENTARY MATERIAL

The Supplementary Material for this article can be found online at: https://www.frontiersin.org/articles/10.3389/feart.2021.703304/full#supplementary-material

Supplementary Presentation S1 | Robust linear regressions (blue line) between element concentrations obtained by the ICP-OES method as a function of the raw concentrations obtained by the pXRF method. The data are presented for the 10 elements considered: Si (A), Al (B), Fe (C), Ca (D), K (E), Ti (F), Mn (G), Zn (H), Sr (I), and Zr (J) with n = 144 for all elements, except for Zn where n = 119. Grey points (which include organic-rich samples; TOC >40 wt%) were excluded from the robust linear regression. Errors bar (±2 pooled σ) were calculated based on three repetitions of three samples for ICP-OES method and on three to five repetitions of 20 samples for pXRFmethod. Robust linear regression R^2 and equation are provided for each element.

REFERENCES

Abbott, B. W., and Jones, J. B. (2015). Permafrost Collapse Alters Soil Carbon Stocks, Respiration, CH4, and N2O in upland Tundra. *Glob. Change Biol.* 21, 4570–4587. doi:10.1111/gcb.13069

Andreev, A. A., Grosse, G., Schirrmeister, L., Kuznetsova, T. V., Kuzmina, S. A., Bobrov, A. A., et al. (2009). Weichselian and Holocene Palaeoenvironmental History of the Bol'shoy Lyakhovsky Island, New Siberian Archipelago, Arctic Siberia. *Boreas* 38, 72–110. doi:10.1111/j.1502-3885.2008.00039.x

Andreev, A. A., Schirrmeister, L., Siegert, C., Bobrov, A. A., Demske, D., Seiffert, M., et al. (2002). Paleoenvironmental Changes in Northeastern Siberia during the Late Quaternary - Evidence from Pollen Records of the Bykovsky Peninsula. *Polarforschung* 70, 13–25. doi:10.2312/polarforschung.70.13

Anzelmo, J. A., and Lindsay, J. R. (1987). X-ray Fluorescence Spectrometric Analysis of Geologic Materials Part 1. Principles and Instrumentation. *J. Chem. Educ.* 64, A181. doi:10.1021/ed064pA181

Börker, J., Hartmann, J., Amann, T., and Romero-Mujalli, G. (2018). Global Unconsolidated Sediments Map Database v1.0 (Shapefile and Gridded to 0.5° Spatial Resolution). doi:10.1594/PANGAEA.884822

Beal, E. J., House, C. H., and Orphan, V. J. (2009). Manganese- and Iron-dependent Marine Methane Oxidation. *Science* 325, 184–187. doi:10.1126/science.1169984

Berner, R. A., Lasaga, A. C., and Garrels, R. M. (1983). The Carbonate-Silicate Geochemical Cycle and its Effect on Atmospheric Carbon Dioxide over the Past 100 Million Years. *Am. J. Sci.* 283, 641–683. doi:10.2475/ajs.283.7.641

Brosius, L. S., Anthony, K. M. W., Treat, C. C., Lenz, J., Jones, M. C., Bret-Harte, M. S., et al. (2021). Spatiotemporal Patterns of Northern lake Formation since the Last Glacial Maximum. *Quat. Sci. Rev.* 253, 106773. doi:10.1016/j.quascirev.2020.106773

Brown, J., Ferrians, O. J., Heginbottom, J. A., Melnikov, E. S., and Akerman, J. (1997). *Circum-Arctic Map of Permafrost and Ground-Ice conditionsCircum-Pacific Map Series CP-45, Scale 1:10,000,000, Tech. Rep.* (Washington, DC: U.S.Geological Survey in Cooperation with the Circum-Pacific Council for Energy and Mineral Resources). doi:10.13140/RG.2.1.2994.9040

Chao, T. T., and Sanzolone, R. F. (1992). Decomposition Techniques. *J. Geochemical Exploration* 44, 65–106. doi:10.1016/0375-6742(92)90048-d

Cornelis, J.-T., Delvaux, B., Georg, R. B., Lucas, Y., Ranger, J., and Opfergelt, S. (2011). Tracing the Origin of Dissolved Silicon Transferred from Various Soil-Plant Systems towards Rivers: a Review. *Biogeosciences* 8, 89–112. doi:10.5194/bg-8-89-2011

DalCorso, G., Manara, A., Piasentin, S., and Furini, A. (2014). Nutrient Metal Elements in Plants. *Metallomics* 6, 1770–1788. doi:10.1039/c4mt00173g

Dutta, K., Schuur, E. A. G., Neff, J. C., and Zimov, S. A. (2006). Potential Carbon Release from Permafrost Soils of Northeastern Siberia. *Glob. Change Biol.* 12, 2336–2351. doi:10.1111/j.1365-2486.2006.01259.x

Eusterhues, K., Rumpel, C., and Kogel-Knabner, I. (2005). Organo-mineral Associations in sandy Acid forest Soils: Importance of Specific Surface Area, Iron Oxides and Micropores. *Eur. J. Soil Sci.* 56, 050912034650049–050912034650763. doi:10.1111/j.1365-2389.2005.00710.x

Fouché, J., Christiansen, C. T., Lafrenière, M. J., Grogan, P., and Lamoureux, S. F. (2020). Canadian Permafrost Stores Large Pools of Ammonium and Optically Distinct Dissolved Organic Matter. *Nat. Commun.* 11, 4500. doi:10.1038/s41467-020-18331-w

Fritz, M., Unkel, I., Lenz, J., Gajewski, K., Frenzel, P., Paquette, N., et al. (2018). Regional Environmental Change versus Local Signal Preservation in Holocene Thermokarst lake Sediments: A Case Study from Herschel Island, Yukon (Canada). *J. Paleolimnol.* 60, 77–96. doi:10.1007/s10933-018-0025-0

Fritz, M., Wetterich, S., Meyer, H., Schirrmeister, L., Lantuit, H., and Pollard, W. H. (2011). Origin and Characteristics of Massive Ground Ice on Herschel Island (Western Canadian Arctic) as Revealed by Stable Water Isotope and Hydrochemical Signatures. *Permafrost Periglac. Process.* 22, 26–38. doi:10.1002/ppp.714

Fuchs, M., Grosse, G., Strauss, J., Günther, F., Grigoriev, M., Maximov, G. M., et al. (2018). Carbon and Nitrogen Pools in Thermokarst-Affected Permafrost Landscapes in Arctic Siberia. *Biogeosciences* 15, 953–971. doi:10.5194/bg-15-953-2018

Fuchs, M., Lenz, J., Jock, S., Nitze, I., Jones, B. M., Strauss, J., et al. (2019). Organic Carbon and Nitrogen Stocks along a Thermokarst Lake Sequence in Arctic Alaska. *J. Geophys. Res. Biogeosci.* 124, 1230–1247. doi:10.1029/2018JG004591

Fuchs, M., Nitze, I., Strauss, J., Günther, F., Wetterich, S., Kizyakov, A., et al. (2020). Rapid Fluvio-thermal Erosion of a Yedoma Permafrost Cliff in the Lena River Delta (Accepted). *Front. Earth Sci.*

Gentsch, N., Mikutta, R., Shibistova, O., Wild, B., Schnecker, J., Richter, A., et al. (2015). Properties and Bioavailability of Particulate and Mineral-Associated Organic Matter in Arctic Permafrost Soils, Lower Kolyma Region, Russia: Organic Matter Stabilization in Permafrost Soils. *Eur. J. Soil Sci.* 66, 722–734. doi:10.1111/ejss.12269

Gentsch, N., Wild, B., Mikutta, R., Čapek, P., Diáková, K., Schrumpf, M., et al. (2018). Temperature Response of Permafrost Soil Carbon Is Attenuated by mineral protection. *Glob. Change Biol.* 24, 3401–3415. doi:10.1111/gcb.14316

Goldich, S. S. (1938). A Study in Rock-Weathering. *J. Geology* 46, 17–58. doi:10.1086/624619

Grigoriev, M. N., Rachold, V., and Bolshiyanov, D. (2003).Russian-German cooperation System Laptev Sea : the expedition LENA 2002 , Berichte zur Polar- und Meeresforschung (Reports on Polar and Marine Research), *Alfred Wegener Inst. Polar Mar. Res.* 466, 341. doi:10.2312/BzPM_0466_2003

Grosse, G., Jones, B., and Arp, C. (2013). *Treatise on Geomorphology*. Elsevier, 325–353. doi:10.1016/B978-0-12-374739-6.00216-58.21 Thermokarst Lakes, Drainage, and Drained Basins

Grosse, G., Jones, B. M., Schirrmeister, L., Meyer, H., Wetterich, S., Strauss, J., et al. (2015). Late Pleistocene and Holocene Ice-Rich Permafrost in the Colville River valley, Northern Alaska. EPIC3PAST Gateways 2015, Potsdam, 18, *Geophysical Research Abstracts* (Potsdam: EGU2015-10607). Available at: http://www.awi.de/pastgateways2015 (Accessed October 12, 2020).

Grosse, G., Schirrmeister, L., Siegert, C., Kunitsky, V. V., Slagoda, E. A., Andreev, A. A., et al. (2007). Geological and Geomorphological Evolution of a Sedimentary Periglacial Landscape in Northeast Siberia during the Late Quaternary. *Geomorphology* 86, 25–51. doi:10.1016/j.geomorph.2006.08.005

Günther, F., Overduin, P. P., Yakshina, I. A., Opel, T., Baranskaya, A. V., and Grigoriev, M. N. (2015). Observing Muostakh Disappear: Permafrost Thaw Subsidence and Erosion of a Ground-Ice-Rich Island in Response to Arctic Summer Warming and Sea Ice Reduction. *The Cryosphere* 9, 151–178. doi:10.5194/tc-9-151-2015

Harden, J. W., Koven, C. D., Ping, C.-L., Hugelius, G., David McGuire, A., Camill, P., et al. (2012). Field Information Links Permafrost Carbon to Physical Vulnerabilities of Thawing. *Geophys. Res. Lett.* 39. doi:10.1029/2012GL051958

Hartmann, J., and Moosdorf, N. (2012). *Global Lithological Map Database v1.0 (Gridded to 0.5° Spatial Resolution)*. doi:10.1594/PANGAEA.788537

Hemingway, J. D., Rothman, D. H., Grant, K. E., Rosengard, S. Z., Eglinton, T. I., Derry, L. A., et al. (2019). Mineral protection Regulates Long-Term Global Preservation of Natural Organic Carbon. *Nature* 570, 228–231. doi:10.1038/s41586-019-1280-6

Herndon, E., AlBashaireh, A., Singer, D., Roy Chowdhury, T., Gu, B., and Graham, D. (2017). Influence of Iron Redox Cycling on Organo-mineral Associations in Arctic Tundra Soil. *Geochimica et Cosmochimica Acta* 207, 210–231. doi:10.1016/j.gca.2017.02.034

Herndon, E. M., Mann, B. F., Roy Chowdhury, T., Yang, Z., Wullschleger, S. D., Graham, D., et al. (2015). Pathways of Anaerobic Organic Matter Decomposition in Tundra Soils from Barrow, Alaska. *J. Geophys. Res. Biogeosci.* 120, 2345–2359. doi:10.1002/2015JG003147

Hodson, M. E. (2002). Experimental Evidence for Mobility of Zr and Other Trace Elements in Soils. *Geochimica et Cosmochimica Acta* 66, 819–828. doi:10.1016/S0016-7037(01)00803-1

Hugelius, G., Loisel, J., Chadburn, S., Jackson, R. B., Jones, M., MacDonald, G., et al. (2020). Large Stocks of Peatland Carbon and Nitrogen Are Vulnerable to Permafrost Thaw. *Proc. Natl. Acad. Sci. USA* 117, 20438–20446. doi:10.1073/pnas.1916387117

Hugelius, G., Strauss, J., Zubrzycki, S., Harden, J. W., Schuur, E. A. G., Ping, C.-L., et al. (2014). Estimated Stocks of Circumpolar Permafrost Carbon with Quantified Uncertainty Ranges and Identified Data Gaps. *Biogeosciences* 11, 6573–6593. doi:10.5194/bg-11-6573-2014

Jiang, K., Qi, H.-W., and Hu, R.-Z. (2018). Element Mobilization and Redistribution under Extreme Tropical Weathering of Basalts from the Hainan Island, South China. *J. Asian Earth Sci.* 158, 80–102. doi:10.1016/j.jseaes.2018.02.008

Jongejans, L. L., and Strauss, J. (2020). Bootstrapping Approach for Permafrost Organic Carbon Pool Estimation. doi:10.5281/zenodo.3734247

Jongejans, L. L., Strauss, J., Lenz, J., Peterse, F., Mangelsdorf, K., Fuchs, M., et al. (2018). Organic Matter Characteristics in Yedoma and Thermokarst Deposits on Baldwin Peninsula, West Alaska. *Biogeosciences* 15, 6033–6048. doi:10.5194/bg-15-6033-2018

Jorgenson, M. T., Yoshikawa, K., Kanveskiy, M., Shur, Y., Romanovsky, V., Marchenko, S., et al. (2008). *Permafrost Characteristics of Alaska*.

Kahle, M., Kleber, M., and Jahn, R. (2004). Retention of Dissolved Organic Matter by Phyllosilicate and Soil clay Fractions in Relation to mineral Properties. *Org. Geochem.* 35, 269–276. doi:10.1016/j.orggeochem.2003.11.008

Kaiser, K., and Guggenberger, G. (2003). Mineral Surfaces and Soil Organic Matter. *Eur. J. Soil Sci.* 54, 219–236. doi:10.1046/j.1365-2389.2003.00544.x

Kanevskiy, M., Shur, Y., Fortier, D., Jorgenson, M. T., and Stephani, E. (2011). Cryostratigraphy of Late Pleistocene Syngenetic Permafrost (Yedoma) in Northern Alaska, Itkillik River Exposure. *Quat. Res.* 75, 584–596. doi:10.1016/j.yqres.2010.12.003

Kanevskiy, M., Shur, Y., Strauss, J., Jorgenson, T., Fortier, D., Stephani, E., et al. (2016). Patterns and Rates of riverbank Erosion Involving Ice-Rich Permafrost (Yedoma) in Northern Alaska. *Geomorphology* 253, 370–384. doi:10.1016/j.geomorph.2015.10.023

Kaufman, D., Ager, T. A., Anderson, N. J., Anderson, P. M., Andrews, J. T., Bartlein, P. J., et al. (2004). Holocene thermal Maximum in the Western Arctic (0-180°W). *Quat. Sci. Rev.* 23, 529–560. doi:10.1016/j.quascirev.2003.09.007

Kleber, M., Eusterhues, K., Keiluweit, M., Mikutta, C., Mikutta, R., and Nico, P. S. (2015).Mineral-organic Associations: Formation, Properties, and Relevance in Soil Environments. In Advances in Agronomy. Elsevier, 1–140. doi:10.1016/bs.agron.2014.10.005

Kögel-Knabner, I., Amelung, W., Cao, Z., Fiedler, S., Frenzel, P., Jahn, R., et al. (2010). Biogeochemistry of Paddy Soils. *Geoderma* 157, 1–14. doi:10.1016/j.geoderma.2010.03.009

Kögel-Knabner, I., Guggenberger, G., Kleber, M., Kandeler, E., Kalbitz, K., Scheu, S., et al. (2008). Organo-mineral Associations in Temperate Soils: Integrating Biology, Mineralogy, and Organic Matter Chemistry. *J. Plant Nutr. Soil Sci.* 171, 61–82. doi:10.1002/jpln.200700048

Kokelj, S. V., and Jorgenson, M. T. (2013). Advances in Thermokarst Research. *Permafrost Periglac. Process.* 24, 108–119. doi:10.1002/ppp.1779

Konishchev, V. N., and Rogov, V. V. (1993). Investigations of Cryogenic Weathering in Europe and Northern Asia. *Permafrost Periglac. Process.* 4, 49–64. doi:10.1002/ppp.3430040105

Kuhry, P., Bárta, J., Blok, D., Elberling, B., Faucherre, S., Hugelius, G., et al. (2020). Lability Classification of Soil Organic Matter in the Northern Permafrost Region. *Biogeosciences* 17, 361–379. doi:10.5194/bg-17-361-2020

Kurtz, A. C., Derry, L. A., Chadwick, O. A., and Jo Alfano, M. (2000). Refractory Element Mobility in Volcanic Soils. *Geology* 28, 683–686. doi:10.1130/0091-7613(2000)028<0683:remivs>2.3.co;2

Lacelle, D., Bjornson, J., and Lauriol, B. (2010). Climatic and Geomorphic Factors Affecting Contemporary (1950-2004) Activity of Retrogressive Thaw Slumps on the Aklavik Plateau, Richardson Mountains, NWT, Canada. *Permafrost Periglac. Process.* 21, 1–15. doi:10.1002/ppp.666

Lai, R. (2004). Soil Carbon Sequestration in Natural and Managed Tropical Forest Ecosystems. *J. Sust. For.* 21, 1–30. doi:10.1300/J091v21n01_01

Lenton, T. M. (2012). Arctic Climate Tipping Points. *Ambio* 41, 10–22. doi:10.1007/s13280-011-0221-x

Liese, A., and Romeis, T. (2013). Biochemical Regulation of *In Vivo* Function of Plant Calcium-dependent Protein Kinases (CDPK). *Biochim. Biophys. Acta (Bba) - Mol. Cel Res.* 1833, 1582–1589. doi:10.1016/j.bbamcr.2012.10.024

Lindsay, W. L. (1972). "Zinc in Soils and Plant Nutrition," in *"Zinc in Soils and Plant Nutrition," in Advances in Agronomy*. Editor N. C. Brady (Academic Press), 147–186. doi:10.1016/S0065-2113(08)60635-5

Lovley, D. R., and Phillips, E. J. P. (1987). Competitive Mechanisms for Inhibition of Sulfate Reduction and Methane Production in the Zone of Ferric Iron Reduction in Sediments. *Appl. Environ. Microbiol.* 53, 2636–2641. doi:10.1128/aem.53.11.2636-2641.1987

Lützow, M. v., Kögel-Knabner, I., Ekschmitt, K., Matzner, E., Guggenberger, G., Marschner, B., et al. (2006). Stabilization of Organic Matter in Temperate Soils: Mechanisms and Their Relevance under Different Soil Conditions - a Review. *Eur. J. Soil Sci.* 57, 426–445. doi:10.1111/j.1365-2389.2006.00809.x

Marschner, P. (2012). *Marschner's Mineral Nutrition of Higher Plants*. doi:10.1016/C2009-0-63043-9

McLaren, T. I., Guppy, C. N., Tighe, M. K., Forster, N., Grave, P., Lisle, L. M., et al. (2012). Rapid, Nondestructive Total Elemental Analysis of Vertisol Soils Using Portable X-ray Fluorescence. *Soil Sci. Soc. America J.* 76, 1436–1445. doi:10.2136/sssaj2011.0354

Monteux, S., Keuper, F., Fontaine, S., Gavazov, K., Hallin, S., Juhanson, J., et al. (2020). Carbon and Nitrogen Cycling in Yedoma Permafrost Controlled by Microbial Functional Limitations. *Nat. Geosci.* 13, 794–798. doi:10.1038/s41561-020-00662-4

Monhonval, A., Opfergelt, S., Mauclet, E., Pereira, B., Vandeuren, A., Grosse, G., et al. (2020). *Yedoma Domain Mineral Concentrations Assessment (YMCA)*. doi:10.1594/PANGAEA.922724

Monhonval, A., Strauss, J., Mauclet, E., Hirst, C., Bemelmans, N., Grosse, G., et al. (2021). Iron Redistribution upon Thermokarst Processes in the Yedoma Domain. *Front. Earth Sci.* 9, 629. doi:10.3389/feart.2021.703339

Morgan, J. B., and Connolly, E. L. (2013). Plant-Soil Interactions: Nutrient Uptake. *Nat. Educ. Knowl.* 482. , 2013 Available at: https://www.nature.com/scitable/knowledge/library/plant-soil-interactions-nutrient-uptake-105289112/ (Accessed November 2, 2020).

Morgenstern, A., Ulrich, M., Günther, F., Roessler, S., Fedorova, I. V., Rudaya, N. A., et al. (2013). Evolution of Thermokarst in East Siberian Ice-Rich Permafrost: A Case Study. *Geomorphology* 201, 363–379. doi:10.1016/j.geomorph.2013.07.011

Mueller, C. W., Rethemeyer, J., Kao-Kniffin, J., Löppmann, S., Hinkel, K. M., and G. Bockheim, J. (2015). Large Amounts of Labile Organic Carbon in Permafrost Soils of Northern Alaska. *Glob. Change Biol.* 21, 2804–2817. doi:10.1111/gcb.12876

Murton, J. B., Goslar, T., Edwards, M. E., Bateman, M. D., Danilov, P. P., Savvinov, G. N., et al. (2015). Palaeoenvironmental Interpretation of Yedoma Silt (Ice Complex) Deposition as Cold-Climate Loess, Duvanny Yar, Northeast Siberia. *Permafrost Periglac. Process.* 26, 208–288. doi:10.1002/ppp.1843

National Research Centre for CRM (1986). *Institute of Geophysical and Geochemical Exploration Component (GBW 07401- GBW 07404*.

Nitzbon, J., Westermann, S., Langer, M., Martin, L. C. P., Strauss, J., Laboor, S., et al. (2020). Fast Response of Cold Ice-Rich Permafrost in Northeast Siberia to a Warming Climate. *Nat. Commun.* 11, 2201. doi:10.1038/s41467-020-15725-8

Olefeldt, D., Goswami, S., Grosse, G., Hayes, D., Hugelius, G., Kuhry, P., et al. (2016). Circumpolar Distribution and Carbon Storage of Thermokarst Landscapes. *Nat. Commun.* 7, 13043. doi:10.1038/ncomms13043

Opel, T., Meyer, H., Wetterich, S., Laepple, T., Dereviagin, A., and Murton, J. (2018). Ice Wedges as Archives of winter Paleoclimate: A Review. *Permafrost and Periglac Process* 29, 199–209. doi:10.1002/ppp.1980

Opel, T., Wetterich, S., Meyer, H., Dereviagin, A. Y., Fuchs, M. C., and Schirrmeister, L. (2017). Ground-ice Stable Isotopes and Cryostratigraphy Reflect Late Quaternary Palaeoclimate in the Northeast Siberian Arctic (Oyogos Yar Coast, Dmitry Laptev Strait). *Clim. Past* 13, 587–611. doi:10.5194/cp-13-587-2017

Opfergelt, S. (2020). The Next Generation of Climate Model Should Account for the Evolution of mineral-organic Interactions with Permafrost Thaw. *Environ. Res. Lett.* 15, 091003. doi:10.1088/1748-9326/ab9a6d

Pewe, T. L., and Journaux, A. (1983). Origin and Character of Loesslike silt in Unglaciated South-central Yakutia, Siberia, U.S.S.R. *US Geol. Surv. Prof. Pap.* 1262. doi:10.3133/pp1262

Ping, C.-L., Michaelson, G. J., Kimble, J. M., and Walker, D. A. (2005). Soil Acidity and Exchange Properties of Cryogenic Soils in Arctic Alaska. *Soil Sci. Plant Nutr.* 51, 649–653. doi:10.1111/j.1747-0765.2005.tb00083.x

Ping, C. L., Bockheim, J. G., Kimble, J. M., Michaelson, G. J., and Walker, D. A. (1998). Characteristics of Cryogenic Soils along a Latitudinal Transect in Arctic Alaska. *J. Geophys. Res.* 103, 28917–28928. doi:10.1029/98JD02024

Porter, T. J., and Opel, T. (2020). Recent Advances in Paleoclimatological Studies of Arctic Wedge- and Pore-ice Stable-water Isotope Records. *Permafrost and Periglac Process* 31, 429–441. doi:10.1002/ppp.2052

R Core Team (2018). *R: A Language and Environment for Statistical Computing*. Vienna, Austria: R Foundation for Statistical Computing. available at: https://www.R-project.org/.

Ravansari, R., and Lemke, L. D. (2018). Portable X-ray Fluorescence Trace Metal Measurement in Organic Rich Soils: pXRF Response as a Function of Organic Matter Fraction. *Geoderma* 319, 175–184. doi:10.1016/j.geoderma.2018.01.011

Ravansari, R., Wilson, S. C., and Tighe, M. (2020). Portable X-ray Fluorescence for Environmental Assessment of Soils: Not Just a point and Shoot Method. *Environ. Int.* 134, 105250. doi:10.1016/j.envint.2019.105250

Reimann, C., Filzmoser, P., Garrett, R., and Dutter, R. (2008). *Statistical Data Analysis Explained*: Applied Environmental Statistics with R |.

Richmond, K. E., and Sussman, M. (2003). Got Silicon? the Non-essential Beneficial Plant Nutrient. *Curr. Opin. Plant Biol.* 6, 268–272. doi:10.1016/s1369-5266(03)00041-4

Robert, M., and Tessier, D. (1974). Méthode de préparation des argiles des sols pour des études minéralogiques. *Méthode Préparation Argiles Sols Pour Études Minéralogiques* 25, 859–882.

Röhl, U., and Abrams, L. J. (2000). High-resolution, Downhole, and Nondestructive Core Measurements from Sites 999 and 1001 in the Caribbean Sea: Application to the Late Pleistocene. *Therm. Maximum* 165, 191–203.

Romanovskii, N. N. (1993). *Fundamentals of Cryogenesis of Lithosphere*. Moscow: Moscow University Press.

Rouiller, J., Burtin, G., and Souchier, B. (1972). La dispersion des sols dans l'analyse granulométrique. *Méthode utilisant les résines échangeuses d'ions* 14, 194–205.

Rouillon, M., and Taylor, M. P. (2016). Can Field Portable X-ray Fluorescence (pXRF) Produce High Quality Data for Application in Environmental Contamination Research?. *Environ. Pollut.* 214, 255–264. doi:10.1016/j.envpol.2016.03.055

Saidy, A. R., Smernik, R. J., Baldock, J. A., Kaiser, K., Sanderman, J., and Macdonald, L. M. (2012). Effects of clay Mineralogy and Hydrous Iron Oxides on Labile Organic Carbon Stabilisation. *Geoderma* 173-174 (174), 104–110. doi:10.1016/j.geoderma.2011.12.030

Schirrmeister, L., Dietze, E., Matthes, H., Grosse, G., Strauss, J., Laboor, S., et al. (2020). The Genesis of Yedoma Ice Complex Permafrost - Grain-Size Endmember Modeling Analysis from Siberia and Alaska. *E&g Quat. Sci. J.* 69, 33–53. doi:10.5194/egqsj-69-33-2020

Schirrmeister, L., Froese, D., Tumskoy, V., Grosse, G., and Wetterich, S. (2013). PERMAFROST and PERIGLACIAL FEATURES | Yedoma: Late Pleistocene Ice-Rich Syngenetic Permafrost of Beringia. in Encyclopedia of Quaternary Science. 2nd edition. Elsevier, 542–552. doi:10.1016/b978-0-444-53643-3.00106-0

Schirrmeister, L., Grosse, G., Kunitsky, V., Magens, D., Meyer, H., Dereviagin, A., et al. (2008). Periglacial Landscape Evolution and Environmental Changes of Arctic lowland Areas for the Last 60 000 Years (Western Laptev Sea Coast, Cape Mamontov Klyk). *Polar Res.* 27, 249–272. doi:10.1111/j.1751-8369.2008.00067.x

Schirrmeister, L., Grosse, G., Kunitsky, V. V., Fuchs, M. C., Krbetschek, M., Andreev, A. A., et al. (2010). The Mystery of Bunge Land (New Siberian Archipelago): Implications for its Formation Based on Palaeoenvironmental Records, Geomorphology, and Remote Sensing. *Quat. Sci. Rev.* 29, 3598–3614. doi:10.1016/j.quascirev.2009.11.017

Schirrmeister, L., Grosse, G., Kunitsky, V. V., Meyer, H., Dereviagyn, A. Y., and Kuznetsova, T. V. (2003a). Permafrost, Periglacial and Paleo-Environmental Studies on New Siberian Islands. *Rep. Polar Res.* 466, 195–314.

Schirrmeister, L., Grosse, G., Schwamborn, G., Andreev, A. A., Meyer, H., Kunitsky, V. V., et al. (2003b). Late Quaternary History of the Accumulation Plain North of the Chekanovsky Ridge (Lena Delta, Russia): A Multidisciplinary Approach. *Polar Geogr.* 27, 277–319. doi:10.1080/789610225

Schirrmeister, L., Kunitsky, V., Grosse, G., Wetterich, S., Meyer, H., Schwamborn, G., et al. (2011). Sedimentary Characteristics and Origin of the Late Pleistocene Ice Complex on north-east Siberian Arctic Coastal Lowlands and Islands - A Review. *Quat. Int.* 241, 3–25. doi:10.1016/j.quaint.2010.04.004

Schirrmeister, L., Meyer, H., Andreev, A., Wetterich, S., Kienast, F., Bobrov, A., et al. (2016). Late Quaternary Paleoenvironmental Records from the Chatanika River valley Near Fairbanks (Alaska). *Quat. Sci. Rev.* 147, 259–278. doi:10.1016/j.quascirev.2016.02.009

Schirrmeister, L., Schwamborn, G., Overduin, P. P., Strauss, J., Fuchs, M. C., Grigoriev, M., et al. (2017). Yedoma Ice Complex of the Buor Khaya Peninsula (Southern Laptev Sea). *Biogeosciences* 14, 1261–1283. doi:10.5194/bg-14-1261-2017

Schirrmeister, L., Siegert, C., Kuznetsova, T., Kuzmina, S., Andreev, A., Kienast, F., et al. (2002). Paleoenvironmental and Paleoclimatic Records from Permafrost Deposits in the Arctic Region of Northern Siberia. *Quat. Int.* 89, 97–118. doi:10.1016/S1040-6182(01)00083-0

Schirrmeister, L., Wagner, D., Grigoriev, M., and Bolshiyanov, D. (2007). *The Expedition LENA 2005 , Berichte zur Polar- und Meeresforschung (Reports on Polar and Marine Research), Bremerhaven*, 550. Bremerhaven: Alfred Wegener Institute for Polar and Marine Research, 289. doi:10.2312/BzPM_0550_2007

Schmidt, M. W. I., Torn, M. S., Abiven, S., Dittmar, T., Guggenberger, G., Janssens, I. A., et al. (2011). Persistence of Soil Organic Matter as an Ecosystem Property. *Nature* 478, 49–56. doi:10.1038/nature10386

Schneider von Deimling, T., Grosse, G., Strauss, J., Schirrmeister, L., Morgenstern, A., Schaphoff, S., et al. (2015). Observation-based Modelling of Permafrost Carbon Fluxes with Accounting for Deep Carbon Deposits and Thermokarst Activity. *Biogeosciences* 12, 3469–3488. doi:10.5194/bg-12-3469-2015

Schuur, E. A. G., McGuire, A. D., Schädel, C., Grosse, G., Harden, J. W., Hayes, D. J., et al. (2015). Climate Change and the Permafrost Carbon Feedback. *Nature* 520, 171–179. doi:10.1038/nature14338

Shand, C. A., and Wendler, R. (2014). Portable X-ray Fluorescence Analysis of mineral and Organic Soils and the Influence of Organic Matter. *J. Geochemical Exploration* 143, 31–42. doi:10.1016/j.gexplo.2014.03.005

Sizov, O., Konstantinov, A., Volvakh, A., and Molodkov, A. (2020). Timing and Sedimentary Record of Late Quaternary Fluvio-Aeolian Successions of the Tura-Pyshma Interfluve (SW Western Siberia, Russia). *Geosciences* 10, 396. doi:10.3390/geosciences10100396

Smetacek, V. (1999). Diatoms and the Ocean Carbon Cycle. *Protist* 150, 25–32. doi:10.1016/S1434-4610(99)70006-4

Sowers, T. D., Stuckey, J. W., and Sparks, D. L. (2018). The Synergistic Effect of Calcium on Organic Carbon Sequestration to Ferrihydrite. *Geochem. Trans.* 19, 4. doi:10.1186/s12932-018-0049-4

Strauss, J., Laboor, S., Fedorov, A. N., Fortier, D., Froese, D., Fuchs, M., et al. (2016). Database of Ice-Rich Yedoma Permafrost (IRYP). doi:10.1594/PANGAEA.861733

Strauss, J. (2010). Late Quaternary Environmental Dynamics at the Duvanny Yar Key Section, Lower Kolyma, East Siberia Diploma Thesis. Potsdam: Potsdam University.

Strauss, J., Schirrmeister, L., Grosse, G., Fortier, D., Hugelius, G., Knoblauch, C., et al. (2017). Deep Yedoma Permafrost: A Synthesis of Depositional Characteristics and Carbon Vulnerability. *Earth-Science Rev.* 172, 75–86. doi:10.1016/j.earscirev.2017.07.007

Strauss, J., Schirrmeister, L., Grosse, G., Wetterich, S., Ulrich, M., Herzschuh, U., et al. (2013). The Deep Permafrost Carbon Pool of the Yedoma Region in Siberia and Alaska. *Geophys. Res. Lett.* 40, 6165–6170. doi:10.1002/2013GL058088

Strauss, J., Schirrmeister, L., Wetterich, S., Borchers, A., and Davydov, S. P. (2012). Grain-size Properties and Organic-carbon Stock of Yedoma Ice Complex Permafrost from the Kolyma lowland, Northeastern Siberia. *Glob. Biogeochem. Cycles* 26 (3). doi:10.1029/2011GB004104

Stumm, W., and Morgan, J. J. (1995). *Aquatic Chemistry: Chemical Equilibria and Rates in Natural Waters*, 3rd Edition | Wiley.

Till, A. B., Dumoulin, J. A., Harris, A. G., Moore, T. E., Bleick, H. A., and Siwiec, B. R. (2008). *Bedrock Geologic Map of the Southern Brooks Range, Alaska, and Accompanying Conodont Data*, 70.

Tjallingii, R., Röhl, U., Kölling, M., and Bickert, T. (2007). Influence of the Water Content on X-ray Fluorescence Core-Scanning Measurements in Soft marine Sediments: XRF Core Scanning. *Geochem. Geophys. Geosystems* 8. doi:10.1029/2006gc001393

Tomirdiaro, S. V., and Chernen'kiy, O. (1987). *Cryogenic Deposits of East Arctic and Sub Arctic*. SSSR Far-East-Sci. Cent., 196.

Turetsky, M. R., Abbott, B. W., Jones, M. C., Anthony, K. W., Olefeldt, D., Schuur, E. A. G., et al. (2020). Carbon Release through Abrupt Permafrost Thaw. *Nat. Geosci.* 13, 138–143. doi:10.1038/s41561-019-0526-0

Ulrich, M., Grosse, G., Strauss, J., and Schirrmeister, L. (2014). Quantifying Wedge-Ice Volumes in Yedoma and Thermokarst Basin Deposits. *Permafrost Periglac. Process.* 25, 151–161. doi:10.1002/ppp.1810

Velichko, A. A., Catto, N., Drenova, A. N., Klimanov, V. A., Kremenetski, K. V., and Nechaev, V. P. (2002). Climate Changes in East Europe and Siberia at the Late Glacial-Holocene Transition. *Quat. Int.* 91, 75–99. doi:10.1016/S1040-6182(01)00104-5

Walter Anthony, K., Schneider von Deimling, T., Nitze, I., Frolking, S., Emond, A., Daanen, R., et al. (2018). 21st-century Modeled Permafrost Carbon Emissions Accelerated by Abrupt Thaw beneath Lakes. *Nat. Commun.* 9, 3262. doi:10.1038/s41467-018-05738-9

Walter, K. M., Edwards, M. E., Grosse, G., Zimov, S. A., and Chapin, F. S. (2007). Thermokarst Lakes as a Source of Atmospheric CH4 during the Last Deglaciation. *Science* 318, 633–636. doi:10.1126/science.1142924

Wang, X., Toner, B. M., and Yoo, K. (2019). Mineral vs. Organic Matter Supply as a Limiting Factor for the Formation of mineral-associated Organic Matter in forest and Agricultural Soils. *Sci. Total Environ.* 692, 344–353. doi:10.1016/j.scitotenv.2019.07.219

Weindorf, D. C., Bakr, N., and Zhu, Y. (2014a). Advances in Portable X-ray Fluorescence (PXRF) for Environmental, Pedological, and Agronomic Applications. in Advances in Agronomy. Elsevier, 1–45. doi:10.1016/B978-0-12-802139-2.00001-9

Weindorf, D. C., Bakr, N., Zhu, Y., Mcwhirt, A., Ping, C. L., Michaelson, G., et al. (2014b). Influence of Ice on Soil Elemental Characterization via Portable X-Ray Fluorescence Spectrometry. *Pedosphere* 24, 1–12. doi:10.1016/S1002-0160(13)60076-4

Weiss, N., Blok, D., Elberling, B., Hugelius, G., Jørgensen, C. J., Siewert, M. B., et al. (2016). Thermokarst Dynamics and Soil Organic Matter Characteristics Controlling Initial Carbon Release from Permafrost Soils in the Siberian Yedoma Region. *Sediment. Geology* 340, 38–48. doi:10.1016/j.sedgeo.2015.12.004

Weltje, G. J., and Tjallingii, R. (2008). Calibration of XRF Core Scanners for Quantitative Geochemical Logging of Sediment Cores: Theory and Application. *Earth Planet. Sci. Lett.* 274, 423–438. doi:10.1016/j.epsl.2008.07.054

Wetterich, S., Grosse, G., Schirrmeister, L., Andreev, A. A., Bobrov, A. A., Kienast, F., et al. (2012). Late Quaternary Environmental and Landscape Dynamics Revealed by a Pingo Sequence on the Northern Seward Peninsula, Alaska. *Quat. Sci. Rev.* 39, 26–44. doi:10.1016/j.quascirev.2012.01.027

Wetterich, S., Kuzmina, S., Andreev, A. A., Kienast, F., Meyer, H., Schirrmeister, L., et al. (2008). Palaeoenvironmental Dynamics Inferred from Late Quaternary Permafrost Deposits on Kurungnakh Island, Lena Delta, Northeast Siberia, Russia. *Quat. Sci. Rev.* 27, 1523–1540. doi:10.1016/j.quascirev.2008.04.007

Wetterich, S., Rudaya, N., Tumskoy, V., Andreev, A. A., Opel, T., Schirrmeister, L., et al. (2011). Last Glacial Maximum Records in Permafrost of the East Siberian Arctic. *Quat. Sci. Rev.* 30, 3139–3151. doi:10.1016/j.quascirev.2011.07.020

Wetterich, S., Schirrmeister, L., Andreev, A. A., Pudenz, M., Plessen, B., Meyer, H., et al. (2009). Eemian and Late Glacial/Holocene Palaeoenvironmental Records from Permafrost Sequences at the Dmitry Laptev Strait (NE Siberia, Russia). *Palaeogeogr. Palaeoclimatol. Palaeoecol.* 279, 73–95. doi:10.1016/j.palaeo.2009.05.002

Wetterich, S., Tumskoy, V., Rudaya, N., Andreev, A. A., Opel, T., Meyer, H., et al. (2014). Ice Complex Formation in Arctic East Siberia during the MIS3 Interstadial. *Quat. Sci. Rev.* 84, 39–55. doi:10.1016/j.quascirev.2013.11.009

Wilson, M. J. (2004). Weathering of the Primary Rock-Forming Minerals: Processes, Products and Rates. *Clay miner.* 39, 233–266. doi:10.1180/0009855043930133

Wilson, S. A. (1997). Data Compilation for USGS Reference Material BHVO-2, Hawaiian Basalt. *US Geol. Surv. Open-file Rep.* 2.

Windirsch, T., Grosse, G., Ulrich, M., Schirrmeister, L., Fedorov, A. N., Konstantinov, P. Y., et al. (2020). Organic Carbon Characteristics in Ice-Rich Permafrost in Alas and Yedoma Deposits, central Yakutia, Siberia. *Biogeosciences* 17, 3797–3814. doi:10.5194/bg-17-3797-2020

Yang, Z. B., You, J. F., and Yang, Z. M. (2008). Manganese Uptake and Transportation as Well as Antioxidant Response to Excess Manganese in Plants. *Zhi Wu Sheng Li Yu Fen Zi Sheng Wu Xue Xue Bao* 33, 480–488.

Yool, A., and Tyrrell, T. (2003). Role of Diatoms in Regulating the Ocean's Silicon Cycle. *Glob. Biogeochem. Cycles* 17, a–n. doi:10.1029/2002GB002018

Young, K. E., Evans, C. A., Hodges, K. V., Bleacher, J. E., and Graff, T. G. (2016). A Review of the Handheld X-ray Fluorescence Spectrometer as a Tool for Field Geologic Investigations on Earth and in Planetary Surface Exploration. *Appl. Geochem.* 72, 77–87. doi:10.1016/j.apgeochem.2016.07.003

Zolkos, S., and Tank, S. E. (2020). Experimental Evidence that Permafrost Thaw History and Mineral Composition Shape Abiotic Carbon Cycling in Thermokarst-Affected Stream Networks. *Front. Earth Sci.* 8. doi:10.3389/feart.2020.00152

Conflict of Interest: The authors declare that the research was conducted in the absence of any commercial or financial relationships that could be construed as a potential conflict of interest.

frontiers in Earth Science

ORIGINAL RESEARCH
published: 03 September 2021
doi: 10.3389/feart.2021.718153

Mercury in Sediment Core Samples From Deep Siberian Ice-Rich Permafrost

*Clara Rutkowski[1,2], Josefine Lenz[1,3], Andreas Lang[2], Juliane Wolter[1,4], Sibylle Mothes[5], Thorsten Reemtsma[5], Guido Grosse[1,6], Mathias Ulrich[7], Matthias Fuchs[1], Lutz Schirrmeister[1], Alexander Fedorov[8], Mikhail Grigoriev[9], Hugues Lantuit[1,6] and Jens Strauss[1]**

[1]Permafrost Research Section, Alfred Wegener Institute Helmholtz-Centre for Polar and Marine Research, Potsdam, Germany, [2]Department of Geography and Geology, Paris Lodron University Salzburg, Salzburg, Austria, [3]Water and Environmental Research Center, Institute of Northern Engineering, University of Alaska Fairbanks, Fairbanks, AK, United States, [4]Institute of Biochemistry and Biology University of Potsdam, Potsdam, Germany, [5]Department of Analytical Chemistry, Helmholtz-Centre for Environmental Research—UFZ, Leipzig, Germany, [6]Institute of Geosciences, University of Potsdam, Potsdam, Germany, [7]Institute for Geography, Leipzig University, Leipzig, Germany, [8]Laboratory of Permafrost Landscapes, Melnikov Permafrost Institute Siberian Branch of the Russian Academy of Sciences, Yakutsk, Russia, [9]Laboratory of General Geocryology, Melnikov Permafrost Institute Siberian Branch of the Russian Academy of Sciences, Yakutsk, Russia

OPEN ACCESS

Edited by:
Timothy Ferdelman, Max Planck Institute for Marine Microbiology (MPG), Germany

Reviewed by:
Tetsuo Sueyoshi, National Institute of Polar Research, Japan
Kyra St.Pierre, University of British Columbia, Canada

***Correspondence:**
Jens Strauss
jens.strauss@awi.de

Specialty section:
This article was submitted to Biogeoscience, a section of the journal Frontiers in Earth Science

Received: *31 May 2021*
Accepted: *13 August 2021*
Published: *03 September 2021*

Citation:
Rutkowski C, Lenz J, Lang A, Wolter J, Mothes S, Reemtsma T, Grosse G, Ulrich M, Fuchs M, Schirrmeister L, Fedorov A, Grigoriev M, Lantuit H and Strauss J (2021) Mercury in Sediment Core Samples From Deep Siberian Ice-Rich Permafrost. Front. Earth Sci. 9:718153. doi: 10.3389/feart.2021.718153

We determine Hg concentrations of various deposits in Siberia's deep permafrost and link sediment properties and Hg enrichment to establish a first Hg inventory of late Pleistocene permafrost down to a depth of 36 m below surface. As Arctic warming is transforming the ice-rich permafrost of Siberia, sediment is released and increases the flux of particulates to the Arctic shelf seas through thawing coasts, lakeshores, and river floodplains. Heavy metals within soils and sediments are also released and may increasingly enter Arctic waters and the biological food chain. High levels of mercury (Hg) have been reported from shallow soils across the Arctic. Rapid thawing is now mobilizing sediment from deeper strata, but so far little is known about Hg concentrations in deep permafrost. Here, forty-one samples from sediment successions at seven sites and of different states of permafrost degradation on Bykovsky Peninsula (northern Yakutian coast) and in the Yukechi Alas region (Central Yakutia) were analyzed for Hg, total carbon, total nitrogen, and total organic carbon as well as grain-size distribution, bulk density, and mass specific magnetic susceptibility. We show average Hg concentrations of 9.72 ± 9.28 $\mu g\ kg^{-1}$ in the deep sediments, an amount comparable to the few previous Arctic studies existing, and a significant correlation of Hg content with total organic carbon, total nitrogen, grain-size distribution, and mass specific magnetic susceptibility. Hg concentrations are higher in the generally sandier sediments of the Bykovsky Peninsula than in the siltier sediments of the Yukechi Alas. The ratio of Hg to total organic carbon in this study is 2.57 $g\ kg^{-1}$, including samples with very low carbon content. We conclude that many deep permafrost sediments, some of which have been frozen for millennia, contain elevated concentrations of Hg and the stock of Hg ready to be released by erosion is of significance for the Arctic ecosystem. The Hg mobilized may accumulate on the way to or in the shallow sea, and where it enters into active biogeochemical cycles of aquatic systems it may concentrate in food webs. Our study highlights the need for better understanding Hg stocks and Hg release from permafrost.

Keywords: arctic, pollutants, heavy metal, arctic warming, polar regions

INTRODUCTION

Climate change and thus environmental transitions have an enormous impact on polar regions (Schuur et al., 2008; Jones et al., 2020) and their local populations (Ramage et al., 2021). This study focuses on a very sensitive part of the terrestrial Arctic: Ice-bearing deposits in Yedoma permafrost landscapes, tens of meters thick. Yedoma landscapes are characterized mostly by fine sandy to silty, ice-rich deposits of late Pleistocene age. They occur in areas that were not glaciated during the last ice ages and accumulated sediments for thousands of years (Kostyukevich, 1993; Grosse et al., 2013; Strauss et al., 2013). Syngenetic ice wedges and intrasedimentary ice are characteristic for Yedoma deposits (Grosse et al., 2013). The frozen sediment layers have preserved organic matter (OM) and associated contaminants, generally acting as an organic carbon (OC) sink (Lindgren et al., 2018; Walz et al., 2018).

Since the late 1970s, permafrost temperatures have increased between 0.5 and 2°C worldwide (Larsen et al., 2014; Biskaborn et al., 2019); the deep and ice-rich Yedoma permafrost from the late Pleistocene is suggested as a major source of greenhouse gas emission when it thaws (Schuur et al., 2015; Strauss et al., 2017). Besides climate relevant substances such as methane and carbon dioxide, other freeze-locked elements and compounds will also be released as permafrost degrades. Among these are nutrients (Beermann et al., 2015) but also harmful contaminants, such as heavy metals, including mercury (Hg).

Hg is a natural element of the lithosphere and its primary mechanism of mobilization and release to the environment is through volcanism, as well as via weathering and erosion of continental rock (Streets et al., 2011). Its distribution through the atmosphere and hydrosphere also allows its uptake in ecosystems. Such Hg can then be re-emitted (secondary emission) via soil respiration, biomass incineration, and oceans (gas exchange or as aerosolized droplets from sea spray-wind interaction) (Driscoll et al., 2013). Anthropogenic sources are more diverse but they have augmented the hemisphere-wide natural flux immensely (Pirrone et al., 2009; Streets et al., 2011) and Hg concentration in atmospheric deposition has increased threefold since industrialization (Driscoll et al., 2013). Hg deposition is usually in the form of inorganic Hg^{2+} complexes (Schroeder and Munthe, 1998; Xin et al., 2007). When Hg binds to OC, it is incorporated into the carbon cycle and can travel among several carbon pools. The storage of Hg in OC has increased by approximately 20% since pre-industrial times (Smith-Downey et al., 2010). Especially the Arctic tundra and its uptake of gaseous Hg^0 during summer months is suggested to be a globally important Hg sink (Obrist et al., 2017). The role of plants in the accumulation of atmospheric Hg in permafrost soils has been stressed in a number of recent studies (Jiskra et al., 2019; Obrist et al., 2017; Olson et al., 2019). Non-vascular plants such as mosses and lichens have been shown to take up large amounts of atmospheric Hg (Olson et al., 2019). This looks to be one major explanation for the elevated Hg concentrations found in permafrost soils as compared with soils from lower latitudes (non-permafrost soils). The accumulation of Hg in permafrost soils has occured over the course of millennia (Obrist et al., 2017).

Organomercury compounds are liposoluble and penetrate biological membranes easily (Carneado et al., 2015). The most hazardous and neurotoxic form of organomercury is methylated Hg (MeHg) (Schroeder and Munthe, 1998), in particular CH_3Hg^+ (monomethylmercury). The methylation process is mainly driven by bacteria (biogenic) and occurs generally under reducing conditions that usually occur in wetlands, waterlogged sediments, coastal shallow water zones, and upper ocean layers (Driscoll et al., 2013). Water-saturated unfrozen soils in the Arctic permafrost region offer similar conditions. The increasing disposability of nutrients and the rise of microbial activities in thawing permafrost therefore lead to augmented methylation of the available Hg, particularly in water surroundings (MacMillan et al., 2015; St. Pierre et al., 2018). In light of the high toxicity of organomercury compounds (Ha et al., 2017) there is a need for improving our understanding of Hg pools to help constrain the hazard potential to human health posed by Hg liberation through arctic climate change.

Other studies (Burke et al., 2017; Obrist et al., 2017; Schuster et al., 2018) highlight the importance of elevated Hg concentrations in Arctic soils and thermokarst lake sediments, but to date insufficient data are available for the Russian Arctic (Lim et al., 2020), especially for deep deposits of the Yedoma landscape which degrades with ongoing climate warming. Current estimates of potential Hg release with ongoing permafrost thaw are based almost entirely on data from shallow (top one to three m) sediments (e.g., Schuster et al., 2018; Lim et al., 2020; Schaefer et al., 2020) but climate driven transformation processes in Yedoma regions affect also deeper sediment layers (Schirrmeister et al., 2020).

Our study aims to estimate Hg quantities in deep permafrost from a Yedoma-dominated landscape. The objective of this paper is a first examination of Hg at depth to enable a rough risk assessment in terms of future Hg release to Arctic ecosystems. We determine Hg in seven deep cores from two Siberian permafrost regions: 1) the Bykovsky Peninsula southeast of the Lena Delta near the city of Tiksi, and 2) the Yukechi Alas, 50 km southeast of the city of Yakutsk. Our set of cores includes permafrost at different stages of degradation, from varying sedimentary origins, and with differing periglacial properties. We explore: 1) if Hg concentrations in deep permafrost soils of Yedoma landscapes differ from those of shallow levels, and 2) to what extent permafrost landscape features (late Pleistocene permafrost vs. Holocene permafrost, lake or lagoon deposits vs. dry Alas or Yedoma deposits) show distinct Hg patterns.

STUDY AREA

To enable comparison of different states of permafrost degradation in Holocene and late Pleistocene (10^4–10^5 years old) deposits, two study sites on the Lena River in Siberia, Russia were chosen (**Figure 1A**): the Bykovsky Peninsula to

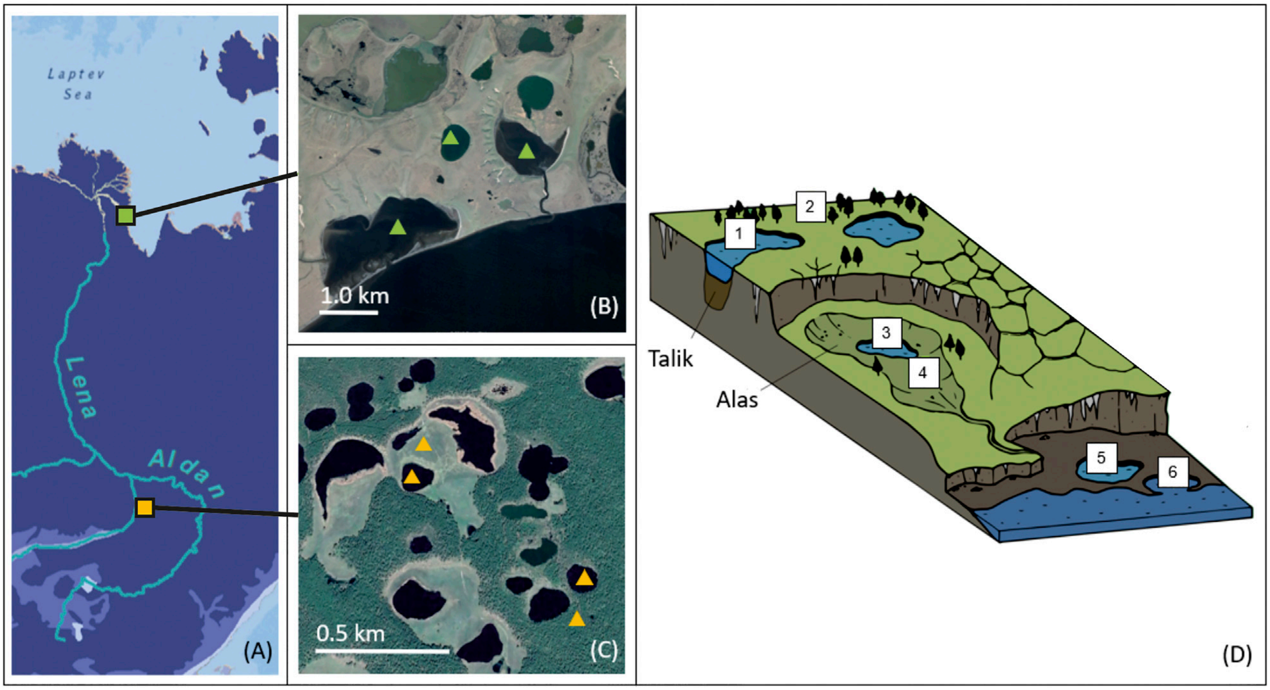

FIGURE 1 | Drilling location overview **(A)** and details of the study sites at Bykovsky Peninsula **(B)** and the Yukechi Alas in Yakutia **(C)**; environmental sketch of study sites and different states of permafrost degradation in Siberia **(D)**. The numbers indicate: 1) Yedoma upland: unfrozen zone in Yedoma permafrost (talik), 2) late Pleistocene Yedoma (frozen), 3) Alas basin: talik below thermokarst lake (unfrozen), 4) drained lake basin, 5) Thermokarst setting: talik below thermokarst lake (unfrozen), 6) lagoonal setting: talik below seawater-flooded thermokarst basins (unfrozen). The triangle symbols in **Figures 1B,C** indicate the location of the single drilling sites in the orthophotos.

the north (**Figure 1B**) and the Yukechi Alas about 1,000 km further south (**Figure 1C**). Within each site, sediment cores from different permafrost landscape elements were selected and sampled (see also **Supplementary Figure A**).

Yukechi Alas

The Yukechi Alas is located within the zone of continuous permafrost and about 50 km southeast of Yakutsk, the capital of the Sakha Republic (Yakutia). The region of Central Yakutia is dominated by alluvial and lacustrine accumulation on the right bank of the Lena River (**Figure 1A**) (Soloviev, 1973). Large parts of the Central Yakutian lowland remained unglaciated during the late Pleistocene, allowing aggradation of massive silty and sandy deposits under cold conditions, forming Yedoma. Today, large syngenetic ice wedges up to 50–60 m in height underlie between 30 and 60% of the massive alluvial terraces (Kostyukevich, 1993; Brouchkov et al., 2004). Alas landscapes appear as result of thermokarst processes, where ground ice or frozen soil thaws extensively. This leads to permafrost degradation and surface deformation since the Holocene (Soloviev, 1973). Part (D) of **Figure 1** shows some typical thermokarst landforms in Central Yakutia: Alas lakes (3) and drained Alas basins (4), surrounded by the older Yedoma landscape of mid to late Pleistocene age (2). The Yedoma landscape at the Yukechi study site also contains lakes, sometimes with thawed talik layers below (1) and vertical soil displacements caused by melting ice wedges (not numbered). The Lena River and shallow thermokarst lakes are the most important water sources for the local population because permafrost inhibits upwelling of ground water (Fedorov and Konstantinov, 2003). The Lena River and its tributaries are also the main sediment supplier of this area. The study site is at 200–220 m above sea level (a.s.l.) and local relief between Yedoma upland surfaces and the Yukechi Alas basin floors is 10–15 m. Several Alas generations with a depth of 8–10 m occur and are dominated by thermokarst lakes and flat plains (see **Supplementary Figure B(A)**). New lakes and depressions develop continuously as a result of active thermokarst processes (Fedorov and Konstantinov, 2003). Newly formed taliks (perennially unfrozen areas in the permafrost realm) below young thermokarst lakes in Yedoma uplands (Fedorov et al., 2014; Ulrich et al., 2017; Ulrich et al., 2019) are also indicative of ongoing thaw processes.

The Yukechi Alas is situated within the taiga biome with larch forests interspersed with pine and birch, a well-developed shrub layer (willows, alder, rose, various Ericaceae) and often well-developed moss layers dominating on Yedoma uplands. The studied alas itself has azonal grassland vegetation, in which non-vascular plants (mosses, lichens) play a minor role, except along the shores and in shallow parts of alas lakes. The regional vegetation has been influenced by anthropogenic clearing of forest and use of alas grasslands for pasture and agriculture during the 20th century (Crate et al., 2017) and a high natural fire frequency throughout the Holocene (Katamura et al., 2009). The current larch and pine forests and surface fire regime have been present in the region for at least 6,500 years (Katamura et al., 2009), and alas depressions have started to develop around the same time (Ulrich et al., 2017).

Bykovsky Peninsula

The Bykovsky Peninsula is located southeast of the Lena River Delta (Northern Yakutia). This area is also characterized by widespread Yedoma and thermokarst landscapes. The latter include brackish lakes close to the seashore and lagoons (**Figure 1(D5,D6)**). The peninsula is elongated in the NNW-SSE direction, is part of a late Pleistocene coastal plain, and represents a typical setting for the coastal lowlands of the Laptev Sea (Grosse et al., 2005). The local topography of the peninsula varies from 0 m up to 45 m a.s.l. (Schirrmeister et al., 2018) and the total length of the shoreline is about 150 km. Cliffs and low-lying thermokarst basins are the typical backshore coastal landforms. Thermokarst basins resulting from thawing of ice-rich permafrost cover about 46% of the peninsula (Grosse et al., 2005) and will prospectively transform into lakes and lagoons (see **Supplementary Figure B(B)**). Within the basins, ice-wedge polygonal structures can easily be detected from remote sensing imagery (Grosse et al., 2005; Schneider et al., 2009; Strauss et al., 2018). Some cliffs are relatively stable and covered by vegetation; others are near vertical, reaching tens of meters in height, and often expose large syngenetic ice wedges and ice-rich Yedoma deposits. In general, the deposits of the Bykovsky Peninsula are poorly sorted sandy silt (Schirrmeister et al., 2002; Strauss et al., 2018; Schirrmeister et al., 2020) with frequent intercalations of peat and paleosols (Lantuit et al., 2011). Many retrogressive thaw slumps and thermokarst basins indicate the degraded state of the permafrost (see **Supplementary Figure B(C)**). Subaquatic permafrost exists on and around the peninsula and undergoes complex thaw processes (Overduin et al., 2016). Recent transitions from thermokarst lakes to lagoons in this area and consequent talik dynamics are described by Angelopoulos et al. (2020).

This study site is situated in the tundra biome, with dwarf shrubs, sedges, grasses, and herbs growing above a well-developed moss layer. Lichens are present, but usually do not have a high cover. In contrast to the region around Yukechi Alas, the regional vegetation on Bykovsky Peninsula has not been subjected to anthropogenic land use and has been less impacted by fires throughout the Holocene (Nitze et al., 2018).

MATERIALS AND METHODS

Sediment Cores and Subsampling

For this study, we investigated sediment cores from each of the landscape elements that are numbered in **Figure 1D** to gain insight into different permafrost degradation states. Winter fieldwork in the Yukechi Alas was conducted in March 2015. We drilled four sediment cores with a drilling rig (Geotechnika URB 4T) from lake ice or ground surface to depths between 19.80 and 22.35 m. For Hg analyses, we took five to seven subsamples from each core (**Table 1**). The YU-L7 sediment core (total length: 17.7 m) derives from a small residual Alas lake located within the Yukechi Alas basin (**Figure 1(D3)**). Here, we took five subsamples. Depth is given as depth below surface and includes lake depth. The sediment core starts at 2.30 m below the lake-ice surface (b.l.s.). Another five subsamples were taken from the YU-L15 sediment core (total length: 17.06 m) beneath a young thermokarst lake on late Pleistocene Yedoma deposits (**Figure 1(D1)**). The top of the sediment is at 4.40 m b.l.s. At 22.35 m YED-1 is the longest of all Central Yakutian cores. We drilled into the dry Yedoma surface surrounding the Yukechi Alas (**Figure 1(D2)**) and investigated seven subsamples of this core. The ALAS-1 sediment core came from the dry bottom of the Yukechi Alas center (**Figure 1(D4)**). This core has a total length of 19.80 m and five subsamples were taken. Except for YED-1, some core loss occurred in all cores where unfrozen sediment was encountered; e.g. in ALAS-1, material was lost in the upper part between 2.25 and 9.34 m below surface (b.s.). Detailed stratigraphic descriptions of the YU-L7 and YU-L15 cores are available in Jongejans et al. (2021); Ulrich et al. (2021). Detailed stratigraphic descriptions of the terrestrial cores can be found in Windirsch et al. (2020).

In April 2017, we drilled three 27.45–32.30 m long cores on Bykovsky Peninsula with an URB 4T drilling rig. Two of the cores originate from thermokarst lagoons (**Figure 1(D6)**), while the third originates from a thermokarst lake (**Figure 1(D5)**) (Strauss et al., 2018). PG2410 contains sediment from below the 1.20 m deep Uomullyakh-Kyuel Lagoon and is 32.30 m long. Here, we analyzed seven subsamples. PG2411, a sediment core from below the 3.30 m deep Polar Fox Lagoon, has a total length of 27.45 m and we took six subsamples. Uomullyakh-Kyuel Lagoon is a former thermokarst lake and due to coastal erosion is now part of the coastline. Polar Fox Lagoon is a partially drained thermokarst lake close to the coastline. A channel has developed allowing exchange with sea water (Angelopoulos et al., 2020). The third north Yakutian core, PG2412, is the longest of all cores and it comes from the thermokarst lake Goltsovoye. Its total length is 31.55 m and it starts at a depth of 5.10 m b.l.s. We also investigated six subsamples of this core. **Figure 2** gives another schematic overview of all seven core locations, complemental to **Figure 1**.

The cores were cryolithologically described in the field, wrapped in foil, and stored frozen in thermo-boxes. We kept all core material frozen during transport and storage and cores were sampled at a temperature of −10°C in the cold chamber in Potsdam. We cut the cores in half using a band saw and cleaned, photographed, described, and sampled them approximately every 3 m except where no material was available or visible stratigraphic changes occurred. Sediment columns of 5–10 cm thickness were sampled for analyses and the center depth of each column is given as sample depth. To avoid contamination, nitrile gloves were used during subsampling and the outermost few millimeters of the sediment columns sampled were removed using a ceramic knife. The samples were stored in plastic sample bags, covered with lint-free cloth to avoid contamination and freeze-dried in a Zirbus

TABLE 1 | Sedimentary cores, location detail, and corresponding landscape elements (**Figure 2**).

Sample ID	Landscape unit	Coordinates	Core depth below surface (m.b.s.)	No of subsamples
YUK15-YU-L7	Alas lake in a drained lake basin	61.76397°N, 130.46442°E	20.00	5
YUK15-YU-L15	Yedoma lake of first generation	61.76086°N, 130.47466°E	21.46	5
YUK15-YED-1	Dry Yedoma hill	61.75967°N, 130.47438°E	22.35	7
YUK15-ALAS-1	Dry Alas center in a refrozen drained lake basin	61.76490°N, 130.46503°E	19.80	5
BYK17-PG2410	Deposits under brackish water of the flooded Uomullyakh-Kyuel Lagoon	71.730,869°N, 129.274,831°E	33.50	7
BYK17-PG2411	Deposits under brackish water of the flooded Polar Fox Lagoon	71.74303°N, 129.3383°E	30.75	6
BYK17-PG2412	Sediments from Goltsovoye Lake (thermokarst) and talik below	71.74515°N, 129.30217°E	36.65	6

Sublimator 3-4-5. Afterwards, we split the samples for homogenization with a planetary mill (FRITSCH pulverisette 5) in agate jars and non-destructive analyses, like determining grain-size distribution. In total, we took 41 samples. Further details on the stratigraphic successions and sampling procedures can be found in Strauss et al. (2018), on Goltsovoye Lake (PG2412) in Jongejans et al. (2020), and in Jenrich et al. (2021) for the lagoon locations (PG2410 and PG2411).

Biogeochemical Parameters

Soil Total Mercury

We determined the soil total mercury (STHg) in solid material by thermal decomposition, amalgamation and atomic absorption spectrophotometry using a Direct Mercury Analyzer (DMA-80; MLS GmbH). The solid samples are combusted at about 750°C under a flow of oxygen, and the Hg in the off-gases is trapped as amalgam on a gold sieve. In a subsequent step, Hg is released and its amount is determined by atomic absorption spectroscopy. IAEA 456, a marine sediment, was used as reference material, six times within two consecutive days of measurement. The detection limit of the most sensitive cuvette was <0.003 ng. For each sample, we measured STHg at least three times and up to six times if the results showed larger variations. Relative standard deviation of the replicates ranged from 0.4 to 11.7%, with a median of 3.0% and a mean of 3.7%.

Hg species (Hg^0, Hg^{2+}, CH_3Hg^+) were analyzed in three samples with higher Hg content using gas chromatography with atomic emission detection (GC-AED) as described in Frohne et al. (2012).

Carbon and Nitrogen

For the measurement of total carbon (TC) and total nitrogen (TN), we put 5.0–5.8 mg of the homogenized sample material into zinc capsules, added tungsten oxide for better combustion and put them in the catalytic tube of an element analyzer (Elementar Vario EL III). We used empty capsules for background detection and included reference standards every 30 measurements to ensure correct results. The device has a specific accuracy and a detection minimum of 0.1 wt%.

TOC was determined using pyrolysis, the thermo-chemical fission of organic compounds, with pure nitrogen (99.996%) as carrier gas and an Elementar varioMAX C Analyzer. We measured different glutamic acids as reference material as well as empty containers at the beginning and always after 30 measurements for background determination. We measured TC, TN, and TOC twice per sample and calculated total inorganic carbon (TIC) content as the difference between TC and TOC.

Sedimentological Methods

Dry Bulk Density

Bulk density ρ_b is the ratio of mass to volume of the dry sample and is a standard parameter for soil description. ρ_b of ice-saturated sediment was determined following Strauss et al. (2012) for all samples with a water content of more than 20 wt% (= "water saturated").

Mass Specific Magnetic Susceptibility

The mass specific magnetic susceptibility (MS) is a frequently used stratigraphic parameter and allows detecting variations of

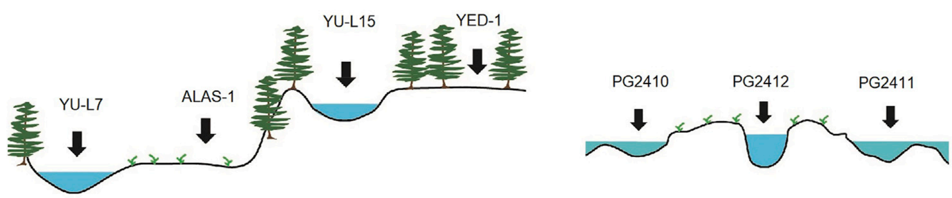

FIGURE 2 | Schematic overview of coring locations (**Table 1**). Left: Yukechi Alas; bottom positions (YU-L7 and ALAS-1) below the dry Yedoma permafrost surface and top positions (YU-L15 and YED-1) with both terrestrial and thermokarst lake cores. Right: Bykovsky Peninsula; PG2410 and PG 2411 from lagoonal open water bodies, and PG2412 from a thermokarst lake.

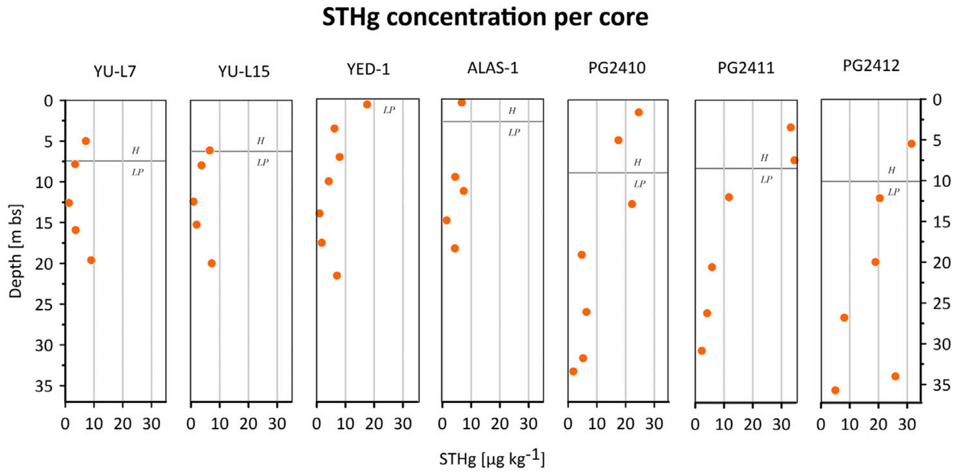

FIGURE 3 | Soil total Hg concentration plotted against depth for all seven cores investigated. H, Holocene; LP, late Pleistocene. Further information on lithology (grain size, frozen or unfrozen) can be found in **Supplementary Figure A**.

magnetic minerals within sediment layers. We measured MS with a Magnetic Susceptibility Meter (Bartington Instruments MS2, Sensor Type MS 2B) on the freeze-dried samples with a frequency of 0.465 kHz. MS is given as x10^{-8} m^3 kg^{-1}.

Grain Size

The grain-size distribution is a central sedimentological parameter. In general, trace elements are expected to be enriched in finer sediments (e.g., Martin and Meybeck, 1979; Mwamburi, 2003). Prior to grain-size analyses, we removed all organic remains by using hydrogen peroxide. The samples were sieved for particles >1 mm and for analyzing the finer fraction a laser particle sizer (Malvern Mastersizer 3000) was employed and tetrasodium pyrophosphate was used for grain dispersal. Size distributions and other statistical parameters were calculated after Folk and Ward (1957) using GRADISTATv8 (Blott and Pye, 2001) for particles <1 mm; when particles >1 mm were included R studio was used.

Statistical Analyses

We carried out all statistical analyses using R studio (RStudio Team, 2020). To test a correlation between STHg and TOC, TIC, TN, clay content, silt content, sand content, and MS, we used the Spearman rank correlation coefficient (r_s). This is a non-parametric procedure, not requiring a linear relationship between variables (Zar, 2005). The correlation is considered weak for $r_s < 0.3$, moderate for $0.3 < r_s < 0.5$ and strong for $r_s = 0.5$ or above. The decisive level of significance (α) was 0.01.

Our second research question implies two null hypotheses: There are no significant differences in STHg accumulation between Holocene and late Pleistocene landscape elements ($H_{0,1}$) or between both study areas ($H_{0,2}$). To test these, a Mann-Whitney *U* test for paired nonparametric data (Nachar, 2008) was performed. Here, a hypothesis is to be rejected when α exceeds 0.05.

RESULTS

In addition to the specific descriptions below, we listed a full set of sedimentological and chemical results in the appendix and they are plotted for each core as multiplots (**Supplementary Figure C**). Throughout the following, the given variability measures are the standard deviation.

Biogeochemistry

Soil Total Mercury

The mean Hg concentration of all samples is 9.72 ± 9.28 µg kg^{-1}. The minimum value of 0.86 ± 0.09 µg kg^{-1} was detected in YU-L15 (12.42 m b.s.), the maximum concentration of 34.52 ± 4.02 µg kg^{-1} in PG2411 (7.35 m b.s.). Concentrations clearly differ between the two study areas. Within each area there are no obvious patterns related to the landscape units studied.

At Yukechi, the arithmetic mean Hg concentration of all samples is 5.21 ± 3.66 µg kg^{-1}. Below 5 m the STHg concentration shows a similar trend in cores YU-L7, YU-L15, and YED-1 (**Figure 3**) with decreasing concentrations from 25 to 10 m depth and then increasing above. ALAS-1 shows values in the same range, between 0 and 10 µg kg^{-1}, but a slightly different pattern. We selected the cores to represent different landscape units and thus the similarity in Hg patterns shows no significant dependence on present day environment.

With a mean of 14.95 ± 10.94 µg kg^{-1} the STHg concentration in sediments from the Bykovsky Peninsula is higher compared to Yukechi, with values up to 34.52 µg kg^{-1}, and shows a wider range. Values generally increase towards the surface (up core; **Figure 3**). One sample from the lower part of PG2412 (33.85 m b.s.) shows a noticeably high STHg value. It originates from the vicinity of an organic rich deposit (wood remains; see **Supplementary Figure A**). Particularly in PG2411 an abrupt increase in STHg concentration above the transition of late Pleistocene sand to Holocene silt is apparent (see **Figure 3**

TABLE 2 | Mean concentration of TC, TN, TOC, and TIC in the sediment samples from the Yukechi Alas (22 samples from 4 cores) and the Bykovsky Peninsula (19 samples from 3 cores).

	TC (wt%)	TN (wt%)	TOC (wt%)	TIC (wt%)
Yukechi Alas	1.33 ± 0.69	0.11 ± 0.06	0.63 ± 0.57	0.70 ± 0.41
Bykovsky Peninsula	2.58 ± 2.25	0.16 ± 0.12	2.13 ± 2.22	0.45 ± 1.21

and **Supplementary Figure A**); the increase is less in PG2010 and PG2412.

The values plotted in **Figure 3** display the mean of all STHg measurements per sample. The standard deviation ranged from 0.04 to 4.02 μg kg^{-1} (0.4–18.9%) but this deviation plots within the symbol size for most samples and is therefore not shown.

The Hg speciation analysis (Hg^0, Hg^{2+}, $MeHg^+$) in three samples with relatively high Hg concentrations (all from the Bykovsky Peninsula) revealed that, as expected, all detectable Hg is in the form of Hg^{2+}. Still, the presence of methylated species in regularly thawing near-surface layers of terrestrial cores (YED-1, ALAS-1) cannot be excluded.

Total Carbon, Total Nitrogen, and Total Organic Carbon

TC, TN, and TOC concentrations are listed in **Table 2** (see also **Supplementary Table A** and **Supplementary Figure C**). Distinct differences in TC, TN, and TOC are visible between both study regions whereas environmental setting or state of permafrost degradation within a region seem less important. The general down core trends at Yukechi show decreasing values in the upper half and increasing values below, whereas the TC, TN, and TOC values decrease with depth in the cores from Bykovsky Peninsula. TN and TOC values for samples below detection limit (<0.1 wt%) were assumed to be 0.05 wt%. The trend of TIC with depth is less consistent within the study areas.

Sedimentology

Lithology, Water Content, and Bulk Density

Detailed descriptions of sediment characteristics for Yukechi can be found in Jongejans et al. (2020); Windirsch et al. (2020); Ulrich et al. (2021). In brief, the sediment cores analyzed revealed different types of permafrost including Yedoma deposits (silty sediment from the late Pleistocene), thermokarst sediments, fluvial sediments (sandy sediments from the late Pleistocene and Holocene), lake/lagoon sediments, and alas deposits.

Sediments recovered by coring from the Yukechi Alas showed the following characteristics: Core YU-L15 reveals silty to silty-sand Ice-Complex deposits of late Pleistocene age (Ulrich et al., 2021). Sediments of the YU-L7 core were unfrozen when recovered and contain predominantly silt with clay and sand beds in places. Core YED-1 contains silty and sandy layers and was largely frozen when recovered. Part of an ice wedge is present between 7 and 10 m b.s. while the lowest meter of the YED-1 core is characterized by dense horizontal micro ice lenses. The ALAS-1 core is characterized by unfrozen silt to silty sand in the upper half and frozen silt below. The ALAS-1 core revealed a frozen organic layer more than half a meter thick at the top. Ice lenses up to 3 mm thick were found throughout the core.

Core PG2410 revealed three frozen layers. The upper 8 m consist of dark grey to black silt, with layers of coarse sand intercalated. The rest of the core contains greenish grey to medium grey sand with individual pebbles in the depth interval 9–14 m b.s. The second core from a lagoon, PG2411, contained prominent gravel up to 4 cm in diameter in a coarse-grained section between about 22 and 28 m b.s. Smaller pebbles can be found throughout. Detailed descriptions of the sediment characteristics of these two lagoon cores can be found in Jenrich et al. (2021). The mostly unfrozen sediment core PG2412 shows alternating fine, medium, and coarse sand layers, with pebbles in places. An organic layer with macroscopic wood remains was recovered between 34 and 35 m b.s. The range of water contents and mean dry bulk density (for water saturated samples only) are listed in **Table 3**.

Mass-Specific Magnetic Susceptibility

MS values show similar trends in all cores from the Yukechi Alas with variable values throughout each core, but the general trend increases from the top to the middle of the cores and decreases from the middle to the bottom. The highest MS of all Yukechi cores was measured in the ALAS-1 core at a depth of 14.75 m b.s. with a value of 257×10^{-8} m^3 kg^{-1}, the minimum was 56×10^{-8} m^3 kg^{-1} in YU-L7 (5.00 m b.s.).

At Bykovsky Peninsula most of the sediments of PG2410, PG2411, and PG2412 show a MS lower than 50×10^{-8} m^3 kg^{-1}. Maximum values occur in a depth range between 26.60 and 33.30 m b.s. The highest MS of 234×10^{-8} m^3 kg^{-1} was measured in PG2410 at 33.25 m b.s.; the lowest MS was 20×10^{-8} m^3 kg^{-1} in PG2412 (33.85 m b.s.).

Grain-Size Distributions

The fine fractions (<1 mm) of all samples show poor to very poor sorting and a dominance of silty to sandy grain sizes (see **Supplementary Figure D**; weight proportions of clay, silt, and sand, and fractions >1 mm are listed in **Supplementary Table B**). In sediment successions from Yukechi, sandy silt is predominant with mostly unimodal and poorly sorted size distributions. Sediment sequences from Bykovsky on average show coarser grain sizes, dominated by sand, more diverse (bi- to polymodal) size distributions, and very poor sorting. The Bykovsky cores also reveal fine layers with clay contents up to 18.5%, whereas the highest clay content in Yukechi sediments is only 9.2%. Particles >1 mm in diameter were found in all cores from Bykovsky, predominantly in PG2410 and PG2411 with >10 wt%; just one sample from Yukechi core YU-L7 contained larger clasts.

Statistical Mann-Whitney *U* test

The second research question implied two null hypotheses: There are no significant differences in STHg accumulation between Holocene and late Pleistocene landscape elements ($H_{0,1}$) or between both study areas ($H_{0,2}$). Based on the Mann-Whitney U test we reject both null hypotheses. The test for $H_{0,1}$ revealed $W = 223$ and $\alpha = 0.01$. The test for $H_{0,2}$ resulted in $W = 319$ and $\alpha < 0.1$.

TABLE 3 | Water content and dry bulk density for all water-saturated samples of the seven studied sediment cores. Note that water content represents ground-ice content in the frozen parts of all cores except YU-L7, which was completely unfrozen during drilling.

		Water content [wt%]		ρb [g/cm³]
		Min	Max	Mean
Yukechi Alas	YU-L15	15.70	38.56	1.27 ± 0.16
	YU-L7	12.47	22.60	1.43
	YED-1	21.34	57.48	1.11 ± 0.29
	ALAS-1	15.46	23.51	1.43 ± 0.03
Bykovsky	PG2410	9.83	25.64	1.36 ± 0.04
	PG2411	9.16	47.74	0.95 ± 0.26
	PG2412	14.88	54.35	1.08 ± 0.42

DISCUSSION

We sought to answer two concrete research questions: 1) Is there a difference in Hg concentration in deep permafrost soils of Yedoma landscapes compared to shallow levels? 2) To what extent can distinct permafrost landscape features (late Pleistocene permafrost vs. Holocene permafrost, lake or lagoon deposits vs. dry Alas or Yedoma deposits) be clearly distinguished in terms of their Hg enrichment?

First, we discuss both questions and then further aspects, particularly the relation of Hg to TOC, TN and sedimentation regime. Conclusive, we give an outlook to potentially initiated Hg dynamics in the Arctic with ongoing permafrost thaw.

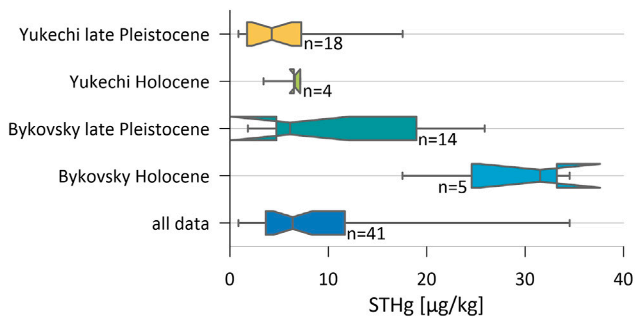

FIGURE 4 | Distribution of the STHg concentration per study site; each site is divided into Holocene and late Pleistocene samples. The notches illustrate the 95% confidence around the median (middle line). A bigger confidence interval than the quartiles causes the ear-like features. The whiskers show the data range.

Mercury Content Compared to Other Arctic Studies

We found detectable Hg concentrations in the deep permafrost deposits from Siberian Yedoma-characterized landscapes. The number of samples were limited in this study, however, we can expect them to be unaffected by anthropogenic Hg input. Most of our samples are of pre-industrial age, as derived from radiocarbon age determination by Jongejans et al. (2020), Windirsch et al. (2020) and Ulrich et al. (2021) (see also **Supplementary Figure C**). In our study, the STHg concentration ranges from 0.86 to 34.52 $\mu g\, kg^{-1}$ with a mean of 9.72 ± 9.28 $\mu g\, kg^{-1}$. The median is 6.38 $\mu g\, kg^{-1}$. This amount is lower compared to that found in the investigation of Alaskan near-surface permafrost layers (upper 3 m) described by Schuster et al. (2018); those samples contained an average of 43 ± 30 $\mu g\, kg^{-1}$ STHg, but were within the same order of magnitude as our samples. We have only a few subsamples from a similar depth because we looked more at deep deposits, so a direct comparison would be insufficient, but the sediment layers that are closest to the surface revealed also higher mean STHg concentrations in our study (17.64 ± 10.40 $\mu g\, kg^{-1}$ in all subsamples from the uppermost 3.5 m). For comparison, 55 ± 11 $\mu g\, kg^{-1}$ were found in near-surface peat cores from permafrost mires in the Stordalen area (Northern Sweden) and 66 ± 24 $\mu g\, kg^{-1}$ in lake sediments from the same region (pre-industrial layers in both cases) (Rydberg et al., 2010). Munthe et al. (2007) found 2-5 fold higher Hg concentrations in recent lake sediment layers compared to historical ones in Scandinavia. However, our Yukechi cores also show similar STHg concentrations in the deepest layers compared to the near-surface samples, as **Figure 3** shows. The uppermost section from the YED-1 land surface core contains the highest STHg of this core, while in ALAS-1 (also drilled from the land surface) this section is unremarkable. Based on our findings, we suggest that young layers on the land surface, relatively recently affected by atmospheric deposition, do not necessarily contain strikingly higher STHg concentrations.

Differences Between the Study Areas

In consequence of our rejected null-hypotheses, we report that there are differences in STHg concentration with respect to both geochronology and study location. However, the difference between the study areas is more pronounced than between the stratigraphical units as shown by the boxplots in **Figure 4**. The Holocene material from Yukechi is similar to the late Pleistocene material from Bykovsky in STHg, but much lower than Bykovsky's Holocene layers. We cannot see clear differences in Hg concentrations between the different landscape elements within one study area. For example, the cores from the Yukechi Alas showed similar trends of Hg with depth, independent from whether they derived from a thermokarst lake, a dry alas basin, dry Yedoma surface or a first-generation lake in Yedoma remains (see **Figure 3**; **Supplementary Figure C**).

As noticed by e.g., Douglas et al. (2005), Hg enrichment in Artic areas close to the sea is elevated. Recent studies by St. Pierre at al. (2015) or Douglas and Blum (2019) show evidence for this in Arctic soils and snowpacks, respectively. They explain their findings, inter alia, with the springtime atmospheric Hg depletion events (AMDEs). Every year during springtime, the amount of gaseous elemental Hg (GEM) in the air is lower than usual, particularly along polar coasts. Involving oxidizing reactions with halogens, the GEM is rapidly deposited to the environment and therefore vanishes from the atmosphere (Steffen et al., 2008). As those photochemical processes with halogen are strongly linked to the Arctic open water areas, the soil is also characterized by higher Hg enrichment compared to Arctic inland areas (St. Pierre et al., 2015). Analogous to this, the Arctic coastal spring snowpack is also enriched in Hg until snowmelt. The majority of the GEM is re-emitted to the atmosphere earlier, but about 9–24% are further transported with spring runoff and, inter alia, deposited to the ground or uptaken by vegetation (Douglas and Blum, 2019). St. Pierre et al. (2015) also reported, that lichens in the Canadian Arctic were highly enriched in Hg compared to underlying soils. As other non-vascular plants (e.g., moss), lichens take up more Hg than vascular plants (Olson et al., 2019). Although the surface of Bykovsky Peninsula is not highly covered with lichens, they are more present there than in the Yukechi Alas region. Also, the moss layer on the North Yakutian peninsula is denser developed than in Central Yakutia, where the landscape is more anthropogenically influenced. Hg uptaken by non-vascular vegetation gets incorporated into the soil with ongoing sedimentation over thousands of years. This, together with the mentioned correlation of Hg and the proximity to Arctic open waters supports our findings of higher Hg concentrations in the North Yakutian sediment, close to the Laptev Sea. Interestingly the alas sediment core (ALAS-1) does not show distinctly lower Hg concentrations overall, although non-vascular plants play little to no role in the current vegetational cover. However, the uppermost and youngest investigated layer of the deposits is only half as concentrated in Hg than compared to the uppermost layer of the Yedoma core (YED-1) which derives from a more moss-dominated surrounding. In addition, according to Ulrich et al. (2017) and Katamura et al. (2009), the development of alas depressions as well as the current forest and grassland vegetation is younger than the rest of the investigated layers in both cores. Therefore, the vegetational influence to Hg enrichment might have changed over the last 6,500 years in the Yukechi Alas. Furthermore, natural wild fires occurred throughout the Holocene until today (Katamura et al., 2009; Glückler et al., 2021), which also leads to depletion of mercury in soil surface and vegetation.

Total Mercury/Total Organic Carbon Ratio

In modern literature, the ratio of STHg/TOC (R_{HgC}) is used for a first rough estimation of the Arctic Hg reservoir. TOC data are available for several areas in the Arctic zone (e.g., Schuster et al., 2018; Lim et al., 2020) and it has been shown that Hg strongly correlates with OM (Sanei et al., 2012; Lim et al., 2019). Our data also show a strong positive correlation between STHg and TOC (r_s = 0.78, p < 0.01).

Schuster et al. (2018) found a median R_{HgC} of 1.6 μg Hg g C^{-1} in Alaskan Arctic shallow permafrost soils to a depth of three m. Therefore, they estimated the permafrost region of the Northern Hemisphere to contain twice as much Hg as all other soils, the atmosphere, and the ocean combined. Lim et al. (2020) suggest a lower value for the Northern Hemisphere Hg pool, based on studies in the Western Siberian lowlands. They calculated a lower median R_{HgC} of 0.19 Gg Hg Pg C^{-1} for organic soils and 0.63 Gg Hg Pg C^{-1} for mineral soils.

We calculate a total R_{HgC} mean for all samples of 2.57 μg Hg g C^{-1}. This observation could lead to the assumption of a larger Arctic STHg pool (at least when including deeper permafrost deposits) than suggested by Schuster et al. (2018). Excluding all samples with TOC below detection limit (we assumed a value of 0.05 wt%), the mean R_{HgC} becomes considerably lower, namely 0.77 μg Hg g C^{-1}. Charbonnier et al. (2020) point out that this ratio must be interpreted carefully because post-depositional degradation of OM does not necessarily affect the Hg concentration, which could lead, in turn, to a misleadingly high STHg/TOC ratio. Giesler et al. (2017) also state that a higher R_{HgC} value can indicate an increase in post-depositional OM decomposition, but that the latter is, in turn, also linked to the enrichment of Hg in soil as a by-product.

Because our two study sites show clear differences in STHg/TOC as well, we are skeptical about this method for a pan-Arctic Hg reservoir estimation. Across the cores from the Bykovsky Peninsula, the mean R_{HgC} is 2.02 μg Hg g C^{-1} with a clearly visible correlation between Hg and TOC (**Figure 5A**); it is higher for the Yukechi study site (3.05 μg Hg g C^{-1}), but with no correlation (**Figure 5B**). In general, we assume that OM decomposition, weathering, and biological activity are significantly reduced in the frozen Yukechi sediments, but the higher R_{HgC} might also be caused by the higher number of samples from this study site with TOC below detection limit.

Our number of samples and study sites is limited compared to the whole Arctic region. Nonetheless, if we combine our mean R_{HgC} of 2.57 μg Hg g C^{-1} with the estimation of the OC pool in the Siberian Yedoma regions (211 Gt OC stored in the frozen deposits; Strauss et al. (2013)), we could estimate a total STHg pool of approximately 542 gigagram (1 Gg = 10^6 kg = 1,000 t) in those areas. Lim et al. (2020) suggest a similar pan-Arctic permafrost Hg pool of 597 Gg (384–750 Gg) in the upper 3 m. Further studies could refine those findings.

Our statistical test revealed a non-significant weak negative correlation between STHg and TIC (r_s = -0.18, p = 0.24). Therefore, we disregard TIC in our further discussion.

Sedimentation Regime as Potential Controlling Factor

Grain-size distribution reveals information about transport and sedimentation regimes and might allow conclusions about depositional conditions. Strauss et al. (2012) established an interpretation of grain-size distribution diagrams from

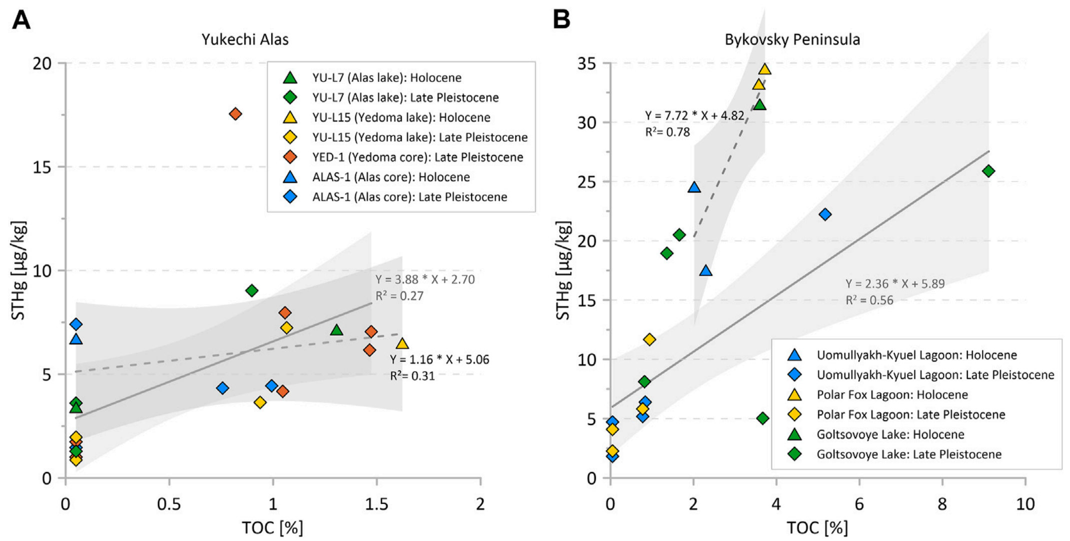

FIGURE 5 | Plot of STHg vs. TOC, **(A)** for all samples from the Yukechi Alas with a R_{HgC} of 3.05 µg Hg g C^{-1} but no clear correlation; **(B)** for all samples from the Bykovsky Peninsula. The correlation is positive with a R_{HgC} of 2.02 µg Hg g C^{-1}. The equations of the linear regressions and the R^2 are given in color: Holocene is the black dashed line, late Pleistocene is grey.

Yedoma environments in terms of sedimentation regimes. Every peak in the curves is caused by a different deposition process. A sand maximum, for example, indicates a higher energy level during transport, because a certain energy level is needed to transport coarse particles. We found a distinct maximum in the sandy regime in all samples from the Bykovsky Peninsula and the Yukechi study site. The bi- to multi-modal grain-size distributions (see **Supplementary Figure D**) suggest that more than one process influenced sediment transport and deposition, which is typical for Siberia's deep ice-bearing permafrost deposits that developed under a very cold and highly continental climate (e.g., Schirrmeister et al., 2011; Strauss et al., 2017). Based on grain-size distribution, the aeolian and alluvial/fluvial transport and depositional processes seem to dominate in these study areas, which is consistent with the findings of Strauss et al. (2012). Schirrmeister et al. (2020) support the hypothesis of polygenetic sedimentation regimes in those types of landscapes, involving alluvial, fluvial, and aeolian transport, *in situ* frost weathering, as well as post-depositional processes.

Water and air fluxes are also suggested to be the main transport media of Hg^{2+} from uplands (watershed area) to reducing zones (wetlands, coastal areas, etc.). Even if the transport by riverine fluxes might be small on a global scale, it can be a substantial pathway in coastal areas (Driscoll et al., 2013; Zolkos et al., 2020).

Although the material of the Bykovsky cores is sandier on average, it is also more poorly sorted and contains more clay. This has an impact on the STHg, as well. As **Figure 6A** shows, there is a positive correlation between STHg and clay content ($r_s = 0.58$, $p < 0.01$). This is in accordance with most statements in literature about elemental deposition in sediments and can be explained by the increased specific surface area and the structural properties of clays (Whitney, 1975; Zonta et al., 1994) as well as ionic charge (clay´s net charge is often negative (Barton and Karathanasis, 2002) which allows binding to positive Hg ions, as for example Hg^{2+}). On the contrary, the Spearman test revealed a weak but not significant correlation for STHg vs. silt content (0.3, p-value > 0.01) and a moderate negative correlation for STHg and sand content (−0.47, p-value < 0.1). **Figure 6B** shows that the correlation of mean grain size and STHg is negative exponential. In consequence, STHg increases with finer mean grain size, or higher clay content. This leads us to the statement that in the finer-grained and more organic-rich Holocene sediments, Hg is significantly enriched. The siltier sediment in Yedoma landscapes tends to contain less Hg. Still, we found comparable levels of Hg in late Pleistocene sediments, too, but always accompanied by elevated TOC levels.

Our results showed that an enhanced MS (100×10^{-8} m^3 kg^{-1} and above) is accompanied by relatively low STHg and vice versa (see **Figure 6C**). Spearman's rank correlation coefficient with subsequent significance testing revealed a strong negative correlation of −0.71 ($p < 0.01$). The correlation between MS and heavy metal concentration (not only in Arctic regions) has already been discussed, by e.g., Hanesch and Scholger (2002); Schmidt et al. (2005); Wang and Qin (2005). These results indicate that the correlation of heavy metals with MS is variable, presumably dependent upon the minerals present. Because there are mostly anaerobic and thus reducing conditions in these predominantly deep permafrost deposits and additionally low signals for MS, less oxidized minerals might dominate here. In contrast, more oxidized minerals are expected to be found in samples with higher MS and thus under less reducing conditions (Mullins, 1977). This observation might suggest that less oxidized minerals (in a reducing Arctic environment) are associated with enhanced STHg concentration. Even though the reduction of Hg^{2+} results in

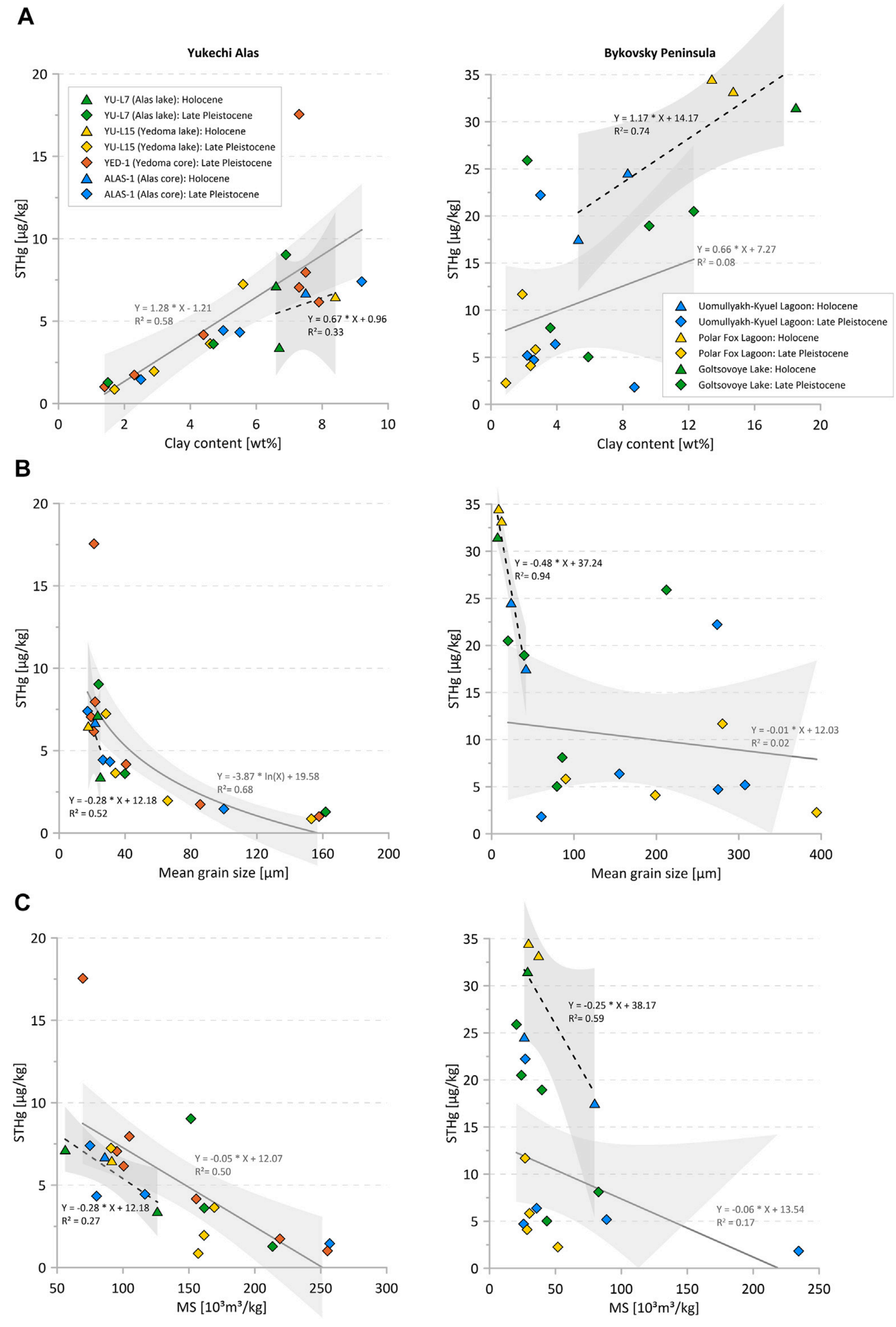

FIGURE 6 | Correlation of STHg with **(A)** clay: A positive correlation occurs between clay content and STHg concentration; **(B)** mean grain size: The correlation between the mean grain size and STHg is clearer in the Yukechi Alas than on Bykovsky Peninsula, caused by sorting quality. Grain-size distribution is better sorted in the Yukechi Alas; **(C)** MS: The correlation here is negative in general but, again, clearer in the Yukechi Alas. The equations of the linear regressions and the R^2 are given in color: Holocene is the black dashed line, late Pleistocene is grey. The legend given in **(A)** is the same in **(B)** and **(C)**.

volatile elemental Hg^0, a loss of STHg via volatilization is only probable for topsoil layers interacting with the atmosphere. Nonetheless, because an enrichment of Hg or less degradation under anaerobic conditions is unlikely, we cannot give a reliable reason for the observed negative correlation of MS and STHg in this study without further investigations.

Correlation of Total Mercury and Total Nitrogen

TN was relatively low in general but comparable to what was observed in other Arctic studies (e.g., Lenz et al., 2013; Schirrmeister et al., 2013). Moreover, the TN concentration in sediment has been found to be positively correlated with carbon concentration (Faure, 1986), which we could also confirm in this study. Spearman's rank correlation for TN vs. TC is 0.75, while for TN vs. TOC it is 0.87 ($p < 0.01$).

We found a strong linear positive correlation between TN and STHg ($r_s = 0.72$, $p < 0.01$), but we cannot distinguish if there is a direct biochemical connection or if that observation can only be explained by the positive correlation of both TN and STHg with TC/TOC and clay content. A strong positive correlation of Hg and N in mineral soils and litter was reported from non-Arctic studies, e.g., in the Sierra Nevada by Obrist et al. (2009), but the authors also highlight that comparing the factors determining Hg contents across different sites is challenging. An analysis of nitrogen speciation would enable a deeper analysis and interpretation of TN and its composition.

Biogeochemical Dynamics of Mercury Potentially Initiated by Thawing Arctic Permafrost

We confirmed the positive correlation between Hg concentration and clay content for Arctic permafrost environments in this study, but above all, between Hg and TOC. Clay particles often have a net negative chemical charge (Barton and Karathanasis, 2002). For instance, in case of erosion, Hg is transported as particle-bound Hg^{2+}. The interaction with TOC is more complex and has been discussed in the scientific literature already: Positive ions such as Hg^{2+} also bind to negatively charged OM components. Most Hg bound to soil organic matter (SOM) occurs with reduced sulfur groups (Giesler et al., 2017). Furthermore, SOM is considered to be a natural chelation agent for the biochemical process of organic acids binding metal ions (Sohalscha et al., 1967; Nowack and VanBriesen, 2005), which might also explain the coupling of soil carbon and Hg^{2+}, but uncertainties still exist (Giesler et al., 2017). Nevertheless, the mineralization of SOM leads to the reduction of Hg^{2+} to Hg^0 as a byproduct of soil respiration (Driscoll et al., 2013). Direct photolysis also leads to the reduction of Hg^{2+} to Hg^0 (Ravichandran, 2004). Because Hg^0 is volatile this causes re-emission to the atmosphere, at least from surface soil layers. The retention time of Hg in the atmosphere is about 0.5 to 1 year, so from there it can be redeposited globally or at least within the hemisphere (Driscoll et al., 2013).

At the same time, current permafrost thaw and active layer deepening results in increasing mineralization of freeze-locked OM, increasing microbial activity and vulnerability to erosional processes. As a consequence of this biogeochemical correlations, rapid, deep thaw of deposits in Yedoma environments releases significant amounts of OC and nitrogen (e.g., Kanevskiy et al., 2016; Fuchs et al., 2020). Hence, the release of significant Hg amounts into aquatic ecosystems via sediment transport is also likely. Under reducing conditions as for example in wetlands, coastal zones, and (nearly) water saturated permafrost deposits after thawing, bacterially mediated methylation processes occur, mostly driven by sulfate-reducing bacteria (Ullrich et al., 2001; Skyllberg et al., 2006). Methylation is a key step of the global Hg cycle in aquatic systems, particularly of inorganic Hg (mostly Hg^0 or Hg^{2+}) to $MeHg^+$ (Ullrich et al., 2001). So even if the input of already methylated species like CH_3Hg^+ into the ocean via fluvial or erosional fluxes is relatively small (Driscoll et al., 2013), the potential of producing toxic Hg species in surface water and shallow ocean layers increases with the input of inorganic Hg as found in our samples. This is proven by e.g., Lehnherr et al. (2011) and Soerensen et al. (2016). In contrast to Driscoll et al. (2013); St. Pierre et al. (2018) confirmed already elevated aquatic MeHg concentration downstream of Arctic retrogressive thaw slump debris tongues and MacMillan et al. (2015) found significantly higher MeHg levels in Canadian thaw ponds on top of degrading ice wedges. In addition, due to climate change, the season for Hg methylation is extending, as annual thawing begins earlier and freezing starts later (Stern et al., 2012). MeHg is toxic for humans and animals, as it enters the central nervous system via the digestive tract (Ha et al., 2017) and accumulates along the food chain (Carneado et al., 2015). Human exposure is mainly through consumption of fish and other seafood, an important part of the traditional diet of Arctic communities (Duhaime et al., 2004). Thus, MeHg input to the polar ecosystem with ongoing permafrost thaw poses a significant hazard to local populations. In 2017, about 4.9 million people were living on permafrost soils with about 20% of these living on the coast (Ramage et al., 2021).

Dissolved organic matter (DOM) also plays an important role in transporting metal pollutants, because humic matter has redox properties that bind cations like Hg^{2+} to anionic OM (Tipping, 2002). Munthe et al. (2007) reported increased Hg levels in fish from lakes with higher DOM. It is likely that parts of OC in the investigated aquatic environments are present as DOM with a strong ionic binding to metal ions (Ravichandran, 2004).

Terrestrial inputs by sediment of degrading permafrost enriched with OM, are one of the major sources of particulate Hg into Arctic streams (Schuster et al., 2011; Sonke et al., 2018; St. Pierre et al., 2018; Lim et al., 2019; Zolkos et al., 2020), which contribute more than 10% of the global river discharge into the Arctic oceans (Zolkos et al., 2020). Mu et al. (2019) and Zolkos et al. (2020) investigated the average export of Hg by the major Arctic rivers from 2012–2015 and 2012–2017, respectively. Both found an annual Hg export to the Arctic Ocean of about 20,000 $kg\ yr^{-1}$, of which 7,500 $kg\ yr^{-1}$ (6,591 $kg\ yr^{-1}$, respectively) are delivered by the Lena River. Furthermore, Lim et al. (2020) investigated a south to north transect in the Western Siberian lowlands and found that Hg concentrations in soil increased with latitude. Our findings confirm that. Thus it appears that those deposits with a higher Hg enrichment are also located closer to the oceanic ecosystem and also have a more direct impact on the oceanic ecosystem and thus further methylation processes.

To provide a rough risk assessment based on the findings in this study, we state the following: The amount of STHg found in this study is not alarmingly high (critical Hg concentration for contaminated soils is 1.5 mg kg^{-1} according to EU guidelines (Hein et al., 2011)). Still, we highlight that Arctic permafrost soils described in other studies contain more clay or more TOC (especially in relation to the TOC-poor Yukechi site) than our samples. Hence, we assume that higher Hg levels can be found in other permafrost regions of the Arctic with more TOC. Nevertheless, there is a natural background signal in the Arctic Ocean due to anthropogenic emissions coupled with exported MeHg, and it will be biomagnified through food webs.

CONCLUSION

The sediment cores from Siberian permafrost deposits in this study contained 9.72 ± 9.28 μg STHg kg^{-1} on average. Probably most of this STHg is inorganic Hg^{2+}, but the formation of CH_3Hg^+ after thawing or entering the Arctic Ocean is expected. The mean STHg concentration in the samples from the Yukechi study site is 5.21 ± 3.66 μg kg^{-1}, while the samples from the coastal area of Bykovsky contain nearly three times as much, namely 14.95 ± 10.94 μg kg^{-1}. The trend of STHg versus depth was quite similar in all four cores from the Yukechi Alas. The upper half of the cores showed decreasing concentrations, with the lowest STHg in the middle and a downward increase in the lower half. In contrast, all three cores from the Bykovsky Peninsula exhibited decreasing concentrations with depth, but with higher values in the near-surface layers. Therefore, at first glance the difference seems distinct between both study sites, but not between the single cores. However, our plots and statistics show that the varying deposition phases (mainly distinguished by age, location, and grain size distribution) lead to differences in STHg concentrations as well. According to our data, Holocene thermokarst and lagoonal deposits contain more STHg than late Pleistocene fluvial sands, while late Pleistocene Yedoma deposits consist partially of STHg similar to that found in Holocene alas deposits but with a lower average.

Moreover, we found a correlation of STHg with MS (negative) and clay content, TOC, and TN (all positive). Although the samples from Bykovsky contained coarser sediments in general, they were also less sorted and therefore partly contained a higher concentration of clay compared to the samples from Central Yakutia. Associated with the higher clay content, the Hg concentration was also higher in the cores from Bykovsky. The state of the investigated sections of the cores (whether originally frozen or not) was not obviously decisive for elemental enrichment or conservation.

Based on our study, the increasing thermokarst processes and coastal erosion in Arctic permafrost regions will liberate the available Hg and very likely enable the increase of highly toxic CH_3Hg^+ in the terrestrial ecosystem, the Arctic Ocean, and the food chain. The amount of approximately 10 μg Hg kg^{-1} in the studied Central Yakutian permafrost deposits is not expected to lead to immense and alarming injections of the metal pollutant Hg into the environment. Nonetheless, with regard to our R_{HgC} and the TOC levels from other studies, we suggest the Yedoma Hg pool contains about 542 Gg, but this value comes with significant uncertainties. Other Arctic studies revealed more TOC and TN in sediments. Due to the positive correlation of these indicators with STHg, the circum-Arctic pool might be even larger as our findings suggest.

DATA AVAILABILITY STATEMENT

The original contributions presented in the study are included in the article/**Supplementary Material**, further inquiries can be directed to the corresponding author.

AUTHOR CONTRIBUTIONS

CR and JS designed the research and wrote the paper; CR performed research. JL, AL, JW and HL contributed towards ideas and data analysis and TR and SM contributed mercury analytics. JS, GG, MU, LS, AF, and MG participated in the expeditions to retrieve the cores. All co-authors commented on and contributed to the article.

FUNDING

This work is embedded into the CACOON project as a part of the Changing Arctic Ocean (CAO) program (#03F0806A, German Federal Ministry of Education and Research, BMBF). CR was supported by the University of Salzburg ("Stipendium für kurzfristige wissenschaftliche Arbeiten"), JL was supported by the National Science Foundation (NSF Grant #1500931), JW was supported by the German Research Foundation (DFG Research Grant No. WO 2420/2-1), GG was supported by the European Research Council (Starting Grant #338335). MU was supported by the German Research Foundation (DFG Grant No.: UL426/1-1). AF was supported by the Russian Foundation for Basic Research (ID-No. 18-45-140046). The Nunataryuk project (EU H2020, #773421) is acknowledged for fruitful discussion. We thank MPI Yakutsk for fieldwork assistance and UFZ Leipzig for their help with lab work. This work is part of the research focus "Permafrost BioGeoChemistry" at AWI Potsdam.

SUPPLEMENTARY MATERIAL

The Supplementary Material for this article can be found online at: https://www.frontiersin.org/articles/10.3389/feart.2021.718153/full#supplementary-material

REFERENCES

Angelopoulos, M., Overduin, P. P., Westermann, S., Tronicke, J., Strauss, J., Schirrmeister, L., et al. (2020). Thermokarst Lake to Lagoon Transitions in Eastern Siberia: Do Submerged Taliks Refreeze? *J. Geophys. Res. Earth Surf.* 125 (10). doi:10.1029/2019jf005424

Barton, C., and Karathanasis, A. (2002). *Clay Minerals* Encyclopedia Of Soil Science. Marcel Dekker, Inc. AH rights reserved.

Beermann, F., Teltewskoi, A., Fiencke, C., Pfeiffer, E.-M., and Kutzbach, L. (2015). Stoichiometric Analysis of Nutrient Availability (N, P, K) within Soils of Polygonal Tundra. *Biogeochemistry* 122 (2), 211–227. doi:10.1007/s10533-014-0037-4

Biskaborn, B. K., Smith, S. L., Noetzli, J., Matthes, H., Vieira, G., Streletskiy, D. A., et al. (2019). Permafrost Is Warming at a Global Scale. *Nat. Commun.* 10 (1), 264. doi:10.1038/s41467-018-08240-4

Blott, S. J., and Pye, K. (2001). GRADISTAT: a Grain Size Distribution and Statistics Package for the Analysis of Unconsolidated Sediments. *Earth Surf. Process. Landforms* 26 (11), 1237–1248. doi:10.1002/esp.261

Brouchkov, A., Fukuda, M., Fedorov, A., Konstantinov, P., and Iwahana, G. (2004). Thermokarst as a Short-Term Permafrost Disturbance, Central Yakutia. *Permafrost Periglac. Process.* 15 (1), 81–87. doi:10.1002/ppp.473

Burke, S. M., Zimmerman, C. E., Branfireun, B. A., Koch, J. C., and Swanson, H. K. (2017). Patterns and Controls of Mercury Accumulation in Sediments from Three Thermokarst Lakes on the Arctic Coastal Plain of Alaska. *Aquat. Sci.* 80 (1). doi:10.1007/s00027-017-0553-0

Carneado, S., Peró-Gascón, R., Ibáñez-Palomino, C., López-Sánchez, J. F., and Sahuquillo, A. (2015). Mercury(ii) and Methylmercury Determination in Water by Liquid Chromatography Hyphenated to Cold Vapour Atomic Fluorescence Spectrometry after Online Short-Column Preconcentration. *Anal. Methods* 7 (6), 2699–2706. doi:10.1039/c4ay02929a

Charbonnier, G., Adatte, T., Föllmi, K. B., and Suan, G. (2020). Effect of Intense Weathering and Postdepositional Degradation of Organic Matter on Hg/TOC Proxy in Organic-rich Sediments and its Implicationsfor Deep-Time Investigations. *Geochem. Geophys. Geosyst.* 21 (2). doi:10.1029/2019gc008707

Crate, S., Ulrich, M., Habeck, J. O., Desyatkin, A. R., Desyatkin, R. V., Fedorov, A. N., et al. (2017). Permafrost Livelihoods: A Transdisciplinary Review and Analysis of Thermokarst-Based Systems of Indigenous Land Use. *Anthropocene* 18, 89–104. doi:10.1016/j.ancene.2017.06.001

Douglas, T. A., and Blum, J. D. (2019). Mercury Isotopes Reveal Atmospheric Gaseous Mercury Deposition Directly to the Arctic Coastal Snowpack. *Environ. Sci. Technol. Lett.* 6 (4), 235–242. doi:10.1021/acs.estlett.9b00131

Douglas, T. A., Sturm, M., Simpson, W. R., Brooks, S., Lindberg, S. E., and Perovich, D. K. (2005). Elevated Mercury Measured in Snow and Frost Flowers Near Arctic Sea Ice Leads. *Geophys. Res. Lett.* 32 (4), a–n. doi:10.1029/2004GL022132

Driscoll, C. T., Mason, R. P., Chan, H. M., Jacob, D. J., and Pirrone, N. (2013). Mercury as a Global Pollutant: Sources, Pathways, and Effects. *Environ. Sci. Technol.* 47 (10), 4967–4983. doi:10.1021/es305071v

Duhaime, G., Chabot, M., Fréchette, P., Robichaud, V., and Proulx, S. (2004). The Impact of Dietary Changes Among the Inuit of Nunavik (Canada): a Socioeconomic Assessment of Possible Public Health Recommendations Dealing with Food Contamination. *Risk Anal.* 24 (4), 1007–1018. doi:10.1111/j.0272-4332.2004.00503.x

Faure, G. (1986). *Principles of Isotope Geology*. New York: Wiley.

Fedorov, A., and Konstantinov, P. (2003). "Observations of Surface Dynamics with Thermokarst Initiation, Yukechi Site, Central Yakutia," in Paper presented at the Proceedings of the 8th International Conference on Permafrost, Zurich, Switzerland, 21-25 July 2003.

Fedorov, A. N., Gavriliev, P. P., Konstantinov, P. Y., Hiyama, T., Iijima, Y., and Iwahana, G. (2014). Estimating the Water Balance of a Thermokarst lake in the Middle of the Lena River basin, Eastern Siberia. *Ecohydrol.* 7 (2), 188–196. doi:10.1002/eco.1378

Folk, R. L., and Ward, W. C. (1957). Brazos River Bar [Texas]; a Study in the Significance of Grain Size Parameters. *J. Sediment. Res.* 27 (1), 3–26. doi:10.1306/74d70646-2b21-11d7-8648000102c1865d

Frohne, T., Rinklebe, J., Langer, U., Du Laing, G., Mothes, S., and Wennrich, R. (2012). Biogeochemical Factors Affecting Mercury Methylation Rate in Two Contaminated Floodplain Soils. *Biogeosciences* 9 (1), 493–507. doi:10.5194/bg-9-493-2012

Fuchs, M., Nitze, I., Strauss, J., Günther, F., Wetterich, S., Kizyakov, A., et al. (2020). Rapid Fluvio-Thermal Erosion of a Yedoma Permafrost Cliff in the Lena River Delta. *Front. Earth Sci.* 8. doi:10.3389/feart.2020.00336

Giesler, R., Clemmensen, K. E., Wardle, D. A., Klaminder, J., and Bindler, R. (2017). Boreal Forests Sequester Large Amounts of Mercury over Millennial Time Scales in the Absence of Wildfire. *Environ. Sci. Technol.* 51 (5), 2621–2627. doi:10.1021/acs.est.6b06369

Glückler, R., Herzschuh, U., Kruse, S., Andreev, A., Vyse, S. A., Winkler, B., et al. (2021). Wildfire History of the Boreal forest of South-Western Yakutia (Siberia) over the Last Two Millennia Documented by a lake-sediment Charcoal Record. *Biogeosciences* 18, 4185–4209. doi:10.5194/bg-18-4185-2021

Grosse, G., Robinson, J., Bryant, R., Taylor, M., Harper, W., DeMasi, A., et al. (2013). *Distribution of Late Pleistocene Ice-Rich Syngenetic Permafrost of the Yedoma Suite in East and Central Siberia*. Russia.

Grosse, G., Schirrmeister, L., Kunitsky, V. V., and Hubberten, H.-W. (2005). The Use of CORONA Images in Remote Sensing of Periglacial Geomorphology: an Illustration from the NE Siberian Coast. *Permafrost Periglac. Process.* 16 (2), 163–172. doi:10.1002/ppp.509

Ha, E., Basu, N., Bose-O'Reilly, S., Dórea, J. G., McSorley, E., Sakamoto, M., et al. (2017). Current Progress on Understanding the Impact of Mercury on Human Health. *Environ. Res.* 152, 419–433. doi:10.1016/j.envres.2016.06.042

Hein, H., Klaus, S., Meyer, A., and Schwedt, G. (2011). *Richt- und Grenzwerte im deutschen und europäischen Umweltrecht: Wasser - Boden - Abfall - Gefahrstoffe - Luft - Lärm*. Düsseldorf: Springer-VDI-Verlag GmbH & Co. KG.

Jenrich, M., Angelopoulos, M., Grosse, G., Overduin, P. P., Schirrmeister, L., Nitze, I., et al. (2021). Thermokarst Lagoons: A Core-Based Assessment of Depositional Characteristics and Estimate of Carbon Pools on Bykovsky Peninsula. *Front. Earth Sci.* 9. doi:10.3389/feart.2021.637899

Jiskra, M., Sonke, J. E., Agnan, Y., Helmig, D., and Obrist, D. (2019). Insights from Mercury Stable Isotopes on Terrestrial-Atmosphere Exchange of Hg(0) in the Arctic Tundra. *Biogeosciences* 16 (20), 4051–4064. doi:10.5194/bg-16-4051-2019

Jones, B. M., Irrgang, A. M., Farquharson, L. M., Lantuit, H., Whalen, D., Ogorodov, S., et al. (2020). "Coastal Permafrost Erosion," in *Arctic Report Card 2020*. Editors R. L. Thoman, J. Richter-Menge, and M. L. Druckenmiller.

Jongejans, L. L., Liebner, S., Knoblauch, C., Mangelsdorf, K., Ulrich, M., Grosse, G., et al. (2021). Greenhouse Gas Production and Lipid Biomarker Distribution in Yedoma and Alas Thermokarst lake Sediments in Eastern Siberia. *Glob. Change Biol.* doi:10.1111/gcb.15566

Jongejans, L. L., Mangelsdorf, K., Schirrmeister, L., Grigoriev, M. N., Maksimov, G. M., Biskaborn, B. K., et al. (2020). n-Alkane Characteristics of Thawed Permafrost Deposits below a Thermokarst Lake on Bykovsky Peninsula, Northeastern Siberia. *Front. Environ. Sci.* 8. doi:10.3389/fenvs.2020.00118

Kanevskiy, M., Shur, Y., Strauss, J., Jorgenson, T., Fortier, D., Stephani, E., et al. (2016). Patterns and Rates of riverbank Erosion Involving Ice-Rich Permafrost (Yedoma) in Northern Alaska. *Geomorphology* 253, 370–384. doi:10.1016/j.geomorph.2015.10.023

Katamura, F., Fukuda, M., Bosikov, N. P., and Desyatkin, R. V. (2009). Forest Fires and Vegetation during the Holocene in central Yakutia, Eastern Siberia. *J. For. Res.* 14 (1), 30–36. doi:10.1007/s10310-008-0099-z

Kostyukevich, V. V. (1993). A Regional Geochronological Study of Late Pleistocene Permafrost. *Radiocarbon* 35 (3), 477–486. doi:10.1017/s0033822200060501

Lantuit, H., Atkinson, D., Paul Overduin, P., Grigoriev, M., Rachold, V., Grosse, G., et al. (2011). Coastal Erosion Dynamics on the Permafrost-Dominated Bykovsky Peninsula, north Siberia, 1951-2006. *Polar Res.* 30 (1), 7341. doi:10.3402/polar.v30i0.7341

Larsen, J. N., Anisimov, O. A., Constable, A., Hollowed, A. B., Maynard, N., Prestrud, P., et al. (2014). *Polar Regions*. New York, USA: Retrieved from CambridgeU.K.

Lehnherr, I., St. Louis, V. L., Hintelmann, H., and Kirk, J. L. (2011). Methylation of Inorganic Mercury in Polar marine Waters. *Nat. Geosci* 4 (5), 298–302. doi:10.1038/ngeo1134

Lenz, J., Fritz, M., Schirrmeister, L., Lantuit, H., Wooller, M. J., Pollard, W. H., et al. (2013). Periglacial Landscape Dynamics in the Western Canadian Arctic: Results from a Thermokarst lake Record on a Push Moraine (Herschel

Island, Yukon Territory). *Palaeogeogr. Palaeoclimatol. Palaeoecol.* 381-382, 15–25. doi:10.1016/j.palaeo.2013.04.009

Lim, A. G., Jiskra, M., Sonke, J. E., Loiko, S. V., Kosykh, N., and Pokrovsky, O. S. (2020). A Revised Pan-Arctic Permafrost Soil Hg Pool Based on Western Siberian Peat Hg and Carbon Observations. *Biogeosciences* 17 (12), 3083–3097. doi:10.5194/bg-17-3083-2020

Lim, A. G., Sonke, J. E., Krickov, I. V., Manasypov, R. M., Loiko, S. V., and Pokrovsky, O. S. (2019). Enhanced Particulate Hg export at the Permafrost Boundary, Western Siberia. *Environ. Pollut.* 254 (Pt B), 113083. doi:10.1016/j.envpol.2019.113083

Lindgren, A., Hugelius, G., and Kuhry, P. (2018). Extensive Loss of Past Permafrost Carbon but a Net Accumulation into Present-Day Soils. *Nature* 560 (7717), 219–222. doi:10.1038/s41586-018-0371-0

MacMillan, G. A., Girard, C., Chételat, J., Laurion, I., and Amyot, M. (2015). High Methylmercury in Arctic and Subarctic Ponds Is Related to Nutrient Levels in the Warming Eastern Canadian Arctic. *Environ. Sci. Technol.* 49 (13), 7743–7753. doi:10.1021/acs.est.5b00763

Martin, J.-M., and Meybeck, M. (1979). Elemental Mass-Balance of Material Carried by Major World Rivers. *Mar. Chem.* 7 (3), 173–206. doi:10.1016/0304-4203(79)90039-2

M., H., and R., S. (2002). Mapping of Heavy Metal Loadings in Soils by Means of Magnetic Susceptibility Measurements. *Environ. Geology.* 42 (8), 857–870. doi:10.1007/s00254-002-0604-1

Mu, C., Zhang, F., Chen, X., Ge, S., Mu, M., Jia, L., et al. (2019). Carbon and Mercury export from the Arctic Rivers and Response to Permafrost Degradation. *Water Res.* 161, 54–60. doi:10.1016/j.watres.2019.05.082

Mullins, C. E. (1977). Magnetic Susceptibility of the Soil and its Significance in Soil Science - a Review. *J. Soil Sci.* 28 (2), 223–246. doi:10.1111/j.1365-2389.1977.tb02232.x

Munthe, J., Wängberg, I., Rognerud, S., Fjeld, E., Verta, M., Porvari, P., et al. (2007). *Mercury in Nordic Ecosystems*.

Mwamburi, J. (2003). Variations in Trace Elements in Bottom Sediments of Major Rivers in Lake Victoria's basin, Kenya. *Lakes Reserv Res. Manage.* 8 (1), 5–13. doi:10.1046/j.1440-1770.2003.00212.x

Nachar, N. (2008). The Mann-Whitney U: A Test for Assessing whether Two Independent Samples Come from the Same Distribution. *Tqmp* 4 (1), 13–20. doi:10.20982/tqmp.04.1.p013

Nitze, I., Grosse, G., Jones, B. M., Romanovsky, V. E., and Boike, J. (2018). Remote Sensing Quantifies Widespread Abundance of Permafrost Region Disturbances across the Arctic and Subarctic. *Nat. Commun.* 9, 5423. doi:10.1038/s41467-018-07663-3

Nowack, B., and VanBriesen, J. M. (2005). "Chelating Agents in the Environment," in *Biogeochemistry of Chelating Agents*. Editors B. Nowack and J. M. VanBriesen (Washington, DC: ACS Publications). doi:10.1021/bk-2005-0910.ch001

Obrist, D., Agnan, Y., Jiskra, M., Olson, C. L., Colegrove, D. P., Hueber, J., et al. (2017). Tundra Uptake of Atmospheric Elemental Mercury Drives Arctic Mercury Pollution. *Nature* 547 (7662), 201–204. doi:10.1038/nature22997

Obrist, D., Johnson, D. W., and Lindberg, S. E. (2009). Mercury Concentrations and Pools in Four Sierra Nevada forest Sites, and Relationships to Organic Carbon and Nitrogen. *Biogeosciences* 6 (5), 765–777. doi:10.5194/bg-6-765-2009

Olson, C. L., Jiskra, M., Sonke, J. E., and Obrist, D. (2019). Mercury in Tundra Vegetation of Alaska: Spatial and Temporal Dynamics and Stable Isotope Patterns. *Sci. total Environ.* 660, 1502–1512. doi:10.1016/j.scitotenv.2019.01.058

Overduin, P. P., Wetterich, S., Günther, F., Grigoriev, M. N., Grosse, G., Schirrmeister, L., et al. (2016). Coastal Dynamics and Submarine Permafrost in Shallow Water of the central Laptev Sea, East Siberia. *The Cryosphere* 10 (4), 1449–1462. doi:10.5194/tc-10-1449-2016

Pirrone, N., Cinnirella, S., Feng, X., Finkelman, R. B., Friedli, H. R., Leaner, J., et al. (2009). "Global Mercury Emissions to the Atmosphere from Natural and Anthropogenic Sources," in *Mercury Fate and Transport in the Global Atmosphere: Emissions, Measurements and Models*. Editors R. Mason and N. Pirrone (Boston, MA: Springer US), 1–47. doi:10.1007/978-0-387-93958-2_1

Ramage, J., Jungsberg, L., Wang, S., Westermann, S., Lantuit, H., and Heleniak, T. (2021). Population Living on Permafrost in the Arctic. *Popul. Environ.* 43, 22–38. doi:10.1007/s11111-020-00370-6

Ravichandran, M. (2004). Interactions between Mercury and Dissolved Organic Matter-Aa Review. *Chemosphere* 55 (3), 319–331. doi:10.1016/j.chemosphere.2003.11.011

RStudio Team (2020). *RStudio*. Boston, MA: Integrated Development for R. RStudio, PBC. Availableat: http://www.rstudio.com/.

Rydberg, J., Klaminder, J., Rosén, P., and Bindler, R. (2010). Climate Driven Release of Carbon and Mercury from Permafrost Mires Increases Mercury Loading to Sub-arctic Lakes. *Sci. Total Environ.* 408 (20), 4778–4783. doi:10.1016/j.scitotenv.2010.06.056

Sanei, H., Grasby, S. E., and Beauchamp, B. (2012). Latest Permian Mercury Anomalies. *Geology* 40 (1), 63–66. doi:10.1130/g32596.1

Schaefer, K., Elshorbany, Y., Jafarov, E., Schuster, P. F., Striegl, R. G., Wickland, K. P., et al. (2020). Potential Impacts of Mercury Released from Thawing Permafrost. *Nat. Commun.* 11 (1), 4650. doi:10.1038/s41467-020-18398-5

Schirrmeister, L., Dietze, E., Matthes, H., Grosse, G., Strauss, J., Laboor, S., et al. (2020). The Genesis of Yedoma Ice Complex Permafrost - Grain-Size Endmember Modeling Analysis from Siberia and Alaska. *E&g Quat. Sci. J.* 69 (1), 33–53. doi:10.5194/egqsj-69-33-2020

Schirrmeister, L., Froese, D., Tumskoy, V., Grosse, G., and Wetterich, S. (2013). *PERMAFROST and PERIGLACIAL FEATURES | . Yedoma: Late Pleistocene Ice-Rich Syngenetic Permafrost of Beringia*, 542–552. doi:10.1016/b978-0-444-53643-3.00106-0

Schirrmeister, L., Grigoriev, M. N., Strauss, J., Grosse, G., Overduin, P. P., Kholodov, A., et al. (2018). Sediment Characteristics of a Thermokarst Lagoon in the Northeastern Siberian Arctic (Ivashkina Lagoon, Bykovsky Peninsula). *arktos* 4 (1), 1–16. doi:10.1007/s41063-018-0049-8

Schirrmeister, L., Kunitsky, V., Grosse, G., Wetterich, S., Meyer, H., Schwamborn, G., et al. (2011). Sedimentary Characteristics and Origin of the Late Pleistocene Ice Complex on north-east Siberian Arctic Coastal Lowlands and Islands–A Review. *Quat. Int.* 241 (1-2), 3–25. doi:10.1016/j.quaint.2010.04.004

Schirrmeister, L., Siegert, C., Kuznetsova, T., Kuzmina, S., Andreev, A., Kienast, F., et al. (2002). Paleoenvironmental and Paleoclimatic Records from Permafrost Deposits in the Arctic Region of Northern Siberia. *Quat. Int.* 89 (1), 97–118. doi:10.1016/s1040-6182(01)00083-0

Schmidt, A., Yarnold, R., Hill, M., and Ashmore, M. (2005). Magnetic Susceptibility as Proxy for Heavy Metal Pollution: a Site Study. *J. Geochemical Exploration* 85 (3), 109–117. doi:10.1016/j.gexplo.2004.12.001

Schneider, J., Grosse, G., and Wagner, D. (2009). Land Cover Classification of Tundra Environments in the Arctic Lena Delta Based on Landsat 7 ETM+ Data and its Application for Upscaling of Methane Emissions. *Remote Sensing Environ.* 113 (2), 380–391. doi:10.1016/j.rse.2008.10.013

Schroeder, W. H., and Munthe, J. (1998). Atmospheric Mercury-An Overview. *Atmos. Environ.* 32 (5), 809–822. doi:10.1016/S1352-2310(97)00293-8

Schuster, P. F., Schaefer, K. M., Aiken, G. R., Antweiler, R. C., Dewild, J. F., Gryziec, J. D., et al. (2018). Permafrost Stores a Globally Significant Amount of Mercury. *Geophys. Res. Lett.* 45 (3), 1463–1471. doi:10.1002/2017gl075571

Schuster, P. F., Striegl, R. G., Aiken, G. R., Krabbenhoft, D. P., Dewild, J. F., Butler, K., et al. (2011). Mercury export from the Yukon River Basin and Potential Response to a Changing Climate. *Environ. Sci. Technol.* 45 (21), 9262–9267. doi:10.1021/es202068b

Schuur, E. A. G., Bockheim, J., Canadell, J. G., Euskirchen, E., Field, C. B., Goryachkin, S. V., et al. (2008). Vulnerability of Permafrost Carbon to Climate Change: Implications for the Global Carbon Cycle. *BioScience* 58 (8), 701–714. doi:10.1641/b580807

Schuur, E. A. G., McGuire, A. D., Schädel, C., Grosse, G., Harden, J. W., Hayes, D. J., et al. (2015). Climate Change and the Permafrost Carbon Feedback. *Nature* 520 (7546), 171–179. doi:10.1038/nature14338

Skyllberg, U., Bloom, P. R., Qian, J., Lin, C.-M., and Bleam, W. F. (2006). Complexation of Mercury (II) In Soil Organic Matter: EXAFS Evidence For Linear Two-Coordination With Reduced Sulfur Groups. *Environ. Sci. Technol.*, 40 (13), 4174–4180.

Smith-Downey, N. V., Sunderland, E. M., and Jacob, D. J. (2010). Anthropogenic Impacts on Global Storage and Emissions of Mercury from Terrestrial Soils: Insights from a New Global Model. *J. Geophys. Res.* 115 (G3). doi:10.1029/2009jg001124

Soerensen, A. L., Jacob, D. J., Schartup, A. T., Fisher, J. A., Lehnherr, I., St. Louis, V. L. V. L., et al. (2016). A Mass Budget for Mercury and Methylmercury in the

Arctic Ocean. *Glob. Biogeochem. Cycles* 30 (4), 560–575. doi:10.1002/2015gb005280

Sohalscha, E. B., Appelt, H., and Schatz, A. (1967). Chelation as a Weathering Mechanism-I. Effect of Complexing Agents on the Solubilization of Iron from Minerals and Granodiorite. *Geochimica et Cosmochimica Acta* 31 (4), 587–596. doi:10.1016/0016-7037(67)90035-X

Soloviev, P. A. (1973). Thermokarst Phenomena and Landforms Due to Frostheaving in Central Yakutia. *Biuletyn Peryglacjalny* 23, 135–155.

Sonke, J. E., Teisserenc, R., Heimbürger-Boavida, L.-E., Petrova, M. V., Marusczak, N., Le Dantec, T., et al. (2018). Eurasian River spring Flood Observations Support Net Arctic Ocean Mercury export to the Atmosphere and Atlantic Ocean. *Proc. Natl. Acad. Sci. USA* 115 (50), E11586–E11594. doi:10.1073/pnas.1811957115

Steffen, A., Douglas, T., Amyot, M., Ariya, P., Aspmo, K., Berg, T., et al. (2008). A Synthesis of Atmospheric Mercury Depletion Event Chemistry in the Atmosphere and Snow. *Atmos. Chem. Phys.* 8 (6), 1445–1482. doi:10.5194/acp-8-1445-2008

Stern, G. A., Macdonald, R. W., Outridge, P. M., Wilson, S., Chételat, J., Cole, A., et al. (2012). How Does Climate Change Influence Arctic Mercury? *Sci. Total Environ.* 414, 22–42. doi:10.1016/j.scitotenv.2011.10.039

St. Pierre, K. A., St. Louis, V. L., Lehnherr, I., Wang, S., La Farge, C., et al. (2015). Importance of Open Marine Waters to the Enrichment of Total Mercury and Monomethylmercury in Lichens in the Canadian High Arctic. *Environ. Sci. Technol.* 49 (10), 5930–5938. doi:10.1021/acs.est.5b00347

St. Pierre, K. A., Zolkos, S., Shakil, S., Tank, S. E., St. Louis, V. L. V. L., and Kokelj, S. V. (2018). Unprecedented Increases in Total and Methyl Mercury Concentrations Downstream of Retrogressive Thaw Slumps in the Western Canadian Arctic. *Environ. Sci. Technol.* 52 (24), 14099–14109. doi:10.1021/acs.est.8b05348

Strauss, J., Grigoriev, M., Maximov, G., Pravkin, S., and Schirrmeister, L. (2018). *Drilling Campaign on Bykovsky Peninsula: Spring 2017.*

Strauss, J., Schirrmeister, L., Grosse, G., Fortier, D., Hugelius, G., Knoblauch, C., et al. (2017). Deep Yedoma Permafrost: A Synthesis of Depositional Characteristics and Carbon Vulnerability. *Earth-Science Rev.* 172, 75–86. doi:10.1016/j.earscirev.2017.07.007

Strauss, J., Schirrmeister, L., Grosse, G., Wetterich, S., Ulrich, M., Herzschuh, U., et al. (2013). The Deep Permafrost Carbon Pool of the Yedoma Region in Siberia and Alaska. *Geophys. Res. Lett.* 40 (23), 6165–6170. doi:10.1002/2013GL058088

Strauss, J., Schirrmeister, L., Wetterich, S., Borchers, A., and Davydov, S. P. (2012). Grain-size Properties and Organic-carbon Stock of Yedoma Ice Complex Permafrost from the Kolyma lowland, Northeastern Siberia. *Glob. Biogeochem. Cycles* 26 (3). doi:10.1029/2011gb004104

Streets, D. G., Devane, M. K., Lu, Z., Bond, T. C., Sunderland, E. M., and Jacob, D. J. (2011). All-time Releases of Mercury to the Atmosphere from Human Activities. *Environ. Sci. Technol.* 45 (24), 10485–10491. doi:10.1021/es202765m

Tipping, E. (2002). *Cation Binding by Humic Substances*, Vol. 12. Cambridge University Press.

Ulrich, M., Jongejans, L. L., Grosse, G., Schneider, B., Opel, T., Wetterich, S., et al. (2021). Geochemistry and Weathering Indices of Yedoma and Alas Deposits beneath Thermokarst Lakes in Central Yakutia. *Front. Earth Sci.* 9. doi:10.3389/feart.2021.704141

Ullrich, S. M., Tanton, T. W., and Abdrashitova, S. A. (2001). Mercury in The Aquatic Environment: A Review of Factors Affecting Methylation. *Crit. Rev. Environ. Sci. Technol.*, 31 (3), 241–293.

Ulrich, M., Matthes, H., Schirrmeister, L., Schütze, J., Park, H., Iijima, Y., et al. (2017). Differences in Behavior and Distribution of Permafrost-related Lakes in C Entral Y Akutia and Their Response to Climatic Drivers. *Water Resour. Res.* 53 (2), 1167–1188. doi:10.1002/2016wr019267

Ulrich, M., Matthes, H., Schmidt, J., Fedorov, A. N., Schirrmeister, L., Siegert, C., et al. (2019). Holocene Thermokarst Dynamics in Central Yakutia - A Multi-Core and Robust Grain-Size Endmember Modeling Approach. *Quat. Sci. Rev.* 218, 10–33. doi:10.1016/j.quascirev.2019.06.010

Walz, J., Knoblauch, C., Tigges, R., Opel, T., Schirrmeister, L., and Pfeiffer, E.-M. (2018). Greenhouse Gas Production in Degrading Ice-Rich Permafrost Deposits in Northeastern Siberia. *Biogeosciences* 15 (17), 5423–5436. doi:10.5194/bg-15-5423-2018

Wang, X. S., and Qin, Y. (2005). Correlation between Magnetic Susceptibility and Heavy Metals in Urban Topsoil: a Case Study from the City of Xuzhou, China. *Environ. Geol.* 49 (1), 10–18. doi:10.1007/s00254-005-0015-1

Whitney, P. R. (1975). Relationship of Manganese-Iron Oxides and Associated Heavy Metals to Grain Size in Stream Sediments. *J. Geochemical Exploration* 4 (2), 251–263. doi:10.1016/0375-6742(75)90005-9

Windirsch, T., Grosse, G., Ulrich, M., Schirrmeister, L., Fedorov, A. N., Konstantinov, P. Y., et al. (2020). Organic Carbon Characteristics in Ice-Rich Permafrost in Alas and Yedoma Deposits, central Yakutia, Siberia. *Biogeosciences* 17 (14), 3797–3814. doi:10.5194/bg-17-3797-2020

Xin, M., Gustin, M., and Johnson, D. (2007). Laboratory Investigation of the Potential for Re-emission of Atmospherically Derived Hg from Soils. *Environ. Sci. Technol.* 41 (14), 4946–4951. doi:10.1021/es062783f

Zar, J. H. (2005). *Spearman Rank Correlation* Encyclopedia Of Biostatistics.

Zolkos, S., Krabbenhoft, D. P., Suslova, A., Tank, S. E., McClelland, J. W., Spencer, R. G. M., et al. (2020). Mercury export from Arctic Great Rivers. *Environ. Sci. Technol.* 54 (7), 4140–4148. doi:10.1021/acs.est.9b07145

Zonta, R., Zaggia, L., and Argese, E. (1994). Heavy Metal and Grain-Size Distributions in Estuarine Shallow Water Sediments of the Cona Marsh (Venice Lagoon, Italy), 151(1), 19–28.

Conflict of Interest: The authors declare that the research was conducted in the absence of any commercial or financial relationships that could be construed as a potential conflict of interest.

Publisher's Note: All claims expressed in this article are solely those of the authors and do not necessarily represent those of their affiliated organizations, or those of the publisher, the editors and the reviewers. Any product that may be evaluated in this article, or claim that may be made by its manufacturer, is not guaranteed or endorsed by the publisher.

ORIGINAL RESEARCH
published: 22 September 2021
doi: 10.3389/feart.2021.704447

Numerical Assessments of Excess Ice Impacts on Permafrost and Greenhouse Gases in a Siberian Tundra Site Under a Warming Climate

Hotaek Park[1,2]*, *Alexander N. Fedorov*[3], *Pavel Konstantinov*[3] *and Tetsuya Hiyama*[2]

[1]Institute of Arctic Climate and Environmental Research, JAMSTEC, Yokosuka, Japan, [2]Institute for Space-Earth Environmental Research, Nagoya University, Nagoya, Japan, [3]Melnikov Permafrost Institute, Siberian Branch of the Russian Academy of Sciences, Yakutsk, Russia

Excess ice that exists in forms such as ice lenses and wedges in permafrost soils is vulnerable to climate warming. Here, we incorporated a simple representation of excess ice in a coupled hydrological and biogeochemical model (CHANGE) to assess how excess ice affects permafrost thaw and associated hydrologic responses, and possible impacts on carbon dioxide and methane (CH_4) fluxes. The model was used to simulate a moss-covered tundra site in northeastern Siberia with various vertical initializations of excess ice under a future warming climate scenario. Simulations revealed that the warming climate induced deepening of the active layer thickness (ALT) and higher vegetation productivity and heterotrophic respiration from permafrost soil. Meanwhile, excess ice temporarily constrained ALT deepening and thermally stabilized permafrost because of the highest latent heat effect obtained under these conditions. These effects were large under conditions of high excess ice content distributed in deeper soil layers, especially when covered by moss and thinner snow. Once ALT reached to the layer of excess ice, it was abruptly melted, leading to ground surface subsidence over 15–20 years. The excess ice meltwater caused deeper soil to wet and contributed to talik formation. The anaerobic wet condition was effective to high CH_4 emissions. However, as the excess ice meltwater was connected to the subsurface flow, the resultant lower water table limited the CH_4 efflux. These results provide insights for interactions between warming climate, permafrost excess ice, and carbon and CH_4 fluxes in well-drained conditions.

Keywords: land surface model, subsurface flow, subsidence, permafrost excess ice, carbon and methane fluxes

OPEN ACCESS

Edited by:
Ko Van Huissteden, Vrije Universiteit Amsterdam, Netherlands

Reviewed by:
Michelle Walvoord, United States Geological Survey (USGS), United States
Boris K. Biskaborn, Alfred Wegener Institute Helmholtz Centre for Polar and Marine Research (AWI), Germany

***Correspondence:**
Hotaek Park
park@jamstec.go.jp

Specialty section:
This article was submitted to Cryospheric Sciences, a section of the journal Frontiers in Earth Science

Received: 03 May 2021
Accepted: 07 September 2021
Published: 22 September 2021

Citation:
Park H, Fedorov AN, Konstantinov P and Hiyama T (2021) Numerical Assessments of Excess Ice Impacts on Permafrost and Greenhouse Gases in a Siberian Tundra Site Under a Warming Climate. Front. Earth Sci. 9:704447. doi: 10.3389/feart.2021.704447

INTRODUCTION

The warming climate has resulted in changes in the Arctic system. A representative change is permafrost warming (Biskaborn et al., 2019), which is closely related to changes in ecological, hydrological, and biogeochemical functions. The changes are in turn fed back to global climate through altered water, energy, and carbon fluxes. For example, permafrost is estimated to store approximately 1,300 Pg of carbon, which is considerably larger than the current atmospheric carbon pool (Hugelius et al., 2014). If thawed and mobilized, this carbon could become a major source of greenhouse gas emissions (Schuur et al., 2008). Field observations have monitored increases in carbon dioxide (CO_2) release from permafrost soils to the atmosphere (Turetsky et al., 2019, 2020), and numerical models also projected the deepening active layer thickness (ALT)-induced increase in organic carbon thawing under future warming scenarios (Koven et al., 2011, 2015; Lawrence et al., 2012; Nitzbon et al., 2020). These results imply that future climate conditions will accelerate the permafrost thaw through positive feedback.

The ice-rich permafrost, formed by ice wedge and Yedoma, is vulnerable to climate change (Jorgenson et al., 2006; Liljedahl et al., 2016). The warming temperature enhances permafrost degradation and melting of ground ice, inducing landscape changes such as subsidence and thermokarst. The thermokarst processes can yield spatially heterogeneous thaw lakes and thermo-erosional gullies, influenced by the microtopography of the terrain. The ground-ice melt supplies water to the thaw lakes in conjunction with snowmelt water and precipitation, so that the thaw lakes tend to continuously grow once initiated (Fedorov et al., 2014), causing severe permafrost degradation within a few years or decades (Ulrich et al., 2017). Thaw lake growth significantly alters landscape scales of water and energy fluxes. *In situ* measurements and remote sensing observations in several Arctic sites have documented the thermokarst-associated changes in local and regional hydrology (Liljedahl et al., 2016), with implications for a range of ecosystem functions such as, for example, the decomposition of organic carbon (Lara et al., 2015).

The contribution of thermokarst landscape evolution to hydrological processes in a warming climate is likely further amplified by ground subsidence inducing greater snow accumulation, reduced winter heat loss, and increased ground ice melt (Aas et al., 2019). A variety of numerical modeling studies have addressed the hydrologic processes changed by permafrost degradation, separately identifying lateral fluxes of subsurface water as well as redistribution of snow and surface water, with groundwater flow and related heat advection (Kurylyk et al., 2016; Sjöberg et al., 2016; Grant et al., 2017; Bisht et al., 2018). Some studies assessed the influence of microtopography on the biogeochemical processes in polygonal tundra areas (Cresto Aleina et al., 2013; Kumar et al., 2016; Abolt et al., 2018). These modeling studies have improved our understanding of thermokarst associated processes and feedbacks. The knowledge gained in earlier studies has become an important resource for recent model development that can simulate more realistic ice-rich permafrost thaw dynamics and successive fine-scale ground subsidence (Aas et al., 2019; Nitzbon et al., 2020). However, the improved models have limitations in terms of representations at regional and global scales. To overcome these limitations, the Community Land Model (CLM) included land subsidence related to permafrost thaw and ground ice melt in a global simulation (Lee et al., 2014). Using a sub-grid tiling approach allows land surface models to represent lateral fluxes of heat, water, and snow in the degrading permafrost terrain (Qiu et al., 2018; Aas et al., 2019; Cai et al., 2020; Nitzbon et al., 2020).

Previous observational and modeling studies have provided evidence of continuously degrading permafrost under climate warming (Liljedahl et al., 2016; Cai et al., 2020). The model projections likely have biases that arise from assumptions about model parameters and limitations in representing the inherent distribution of ground ice relevant to permafrost degradation. Nonetheless, one of the advantages of incorporating excess ice in the model is that we can capture features of changes in permafrost landscapes and hydrology that result from thawing permafrost and melting excess ice. Therefore, we incorporated a simple framework of excess ice melt and subsidence (Bowling et al., 2008) into a coupled hydrological and biogeochemical model (CHANGE: Park et al., 2011, 2018). The objective of this study was to examine the impact of excess ice melt on permafrost hydrology and associated changes in CO_2 and methane (CH_4) fluxes under future climate scenarios following the strongest representative concentration pathways (RCP8.5) in a tundra site in northeastern Siberia using the improved CHANGE model. We also quantified the contribution of excess ice meltwater to the surface–subsurface hydrologic system, which is likely achieved because of the inclusion of a water tracer scheme within CHANGE to track pathways of water originating from precipitation and ground ice meltwater (Park et al., 2021).

METHODS

General Model Description

CHANGE is a process-based land surface model that calculates momentum, water, heat, and carbon fluxes in the atmosphere–vegetation–snow–soil system, soil hydrothermal states, snow hydrology, and stomatal physiology and photosynthesis, in combination with interactions and feedbacks between components and processes within the system (Park et al., 2011, 2018). The model simulates snow accumulation and melt, and the meltwater is partitioned into soil infiltration and surface runoff, even during precipitation events. The infiltrated water can move up or down within the soil, depending on the water potential gradient between soil layers, in which a portion is used for plant transpiration and the excess vertically infiltrated water at either the permafrost table or the bottom soil boundary layer is converted to lateral water flux that is assumed to be subsurface flow. CHANGE calculates the energy balance over the canopy, snow, and soil surface separately and also solves the water budget at both the canopy and soil based on the mass conservation principle. The soil evaporation, transpiration, and rainfall interception by the canopy, which consists of evapotranspiration, are calculated by the balance solution, and their summation is evapotranspiration. The model explicitly represents the dynamics of water and heat flows in permafrost soil considering the freezing/thawing phase transitions in a soil column of 70.4 m depth to explicitly capture thermal inertia in deep ground. The heat flux into the soil–snow is obtained by solving an energy balance equation and is used as the upper boundary condition for the solution of the heat conduction. Zero heat flux is prescribed as the lower boundary condition. The effects of soil organic carbon (SOC) on the soil thermal and hydraulic dynamics are represented by the parameterization of the vertical distribution of SOC within the soil depth of 1.2 m. The calculated ice content in frozen soil layers is used for the parameterization of effective porosity that represents the soil water stress conditions associated with drying and/or freezing, which is coupled to stomatal conductance and the maximum rate of carboxylation, consequently controlling plant productivity as well as phenology. CHANGE mechanistically calculates leaf photosynthesis via the Farquhar biochemical model (Farquhar et al., 1980) as a function of absorbed light, leaf temperature, CO_2 concentration within the leaf, and Rubisco enzyme capacity for photosynthesis. Leaf stomatal conductance, which is needed for the water flux, is coupled to the leaf photosynthesis and concentrations of CO_2 and water vapor (Collatz et al., 1991). The model calculates photosynthesis and stomatal conductance separately for sunlit and shaded leaves. CHANGE simulates biogeochemical processes across multiple biomes, including the carbon and nitrogen cycles in vegetation, litter, and soil. The carbon absorbed by photosynthesis is partitioned into vegetation components, and the coupled nitrogen cycle allows nitrogen limitation to influence plant productivity that is associated with the dynamics of SOC. The decomposition rate of SOC, controlled by soil temperature and moisture, in turn affects productivity through nitrogen availability.

Mosses covering the subarctic soil surface strongly affect water and heat fluxes because of their high water holding capacity and the provision of insulation. CHANGE was coupled with a moss process module, enabling an explicit representation of heat, water, and carbon exchanges in the ecosystem (Park et al., 2018). The moss cover that is assumed to be uniformly distributed over the soil surface is divided into three vertical layers for the calculations of heat and water flows. The temperature of each moss layer is calculated using the heat conduction equation, which is forced by the heat flux into the moss surface from the atmosphere and snow bottom layer, solving the energy budget equation (Launiainen et al., 2015; Park et al., 2018). The dynamics of water content between moss layers are calculated by the water budget equation, and then the fraction of liquid and ice water in individual moss layers is estimated by the simulated temperature. The estimation of thermal properties (i.e., heat conductivity and capacity) in the moss layers is dependent on the separated water and ice fractions. The moss net CO_2 exchange depends on climatic conditions and moss water content and temperature, based on the prognostic moss leaf area index over the annual time series. Therefore, the model assumes that the seasonal cycle of photosynthetic parameters of the moss layers was negligible, and all changes were considered to be instantaneous and reversible.

CHANGE includes a water tracer model that is designed to illustrate the spatiotemporal variability of water originating from precipitation and ground ice in the hydrologic system and quantify their contributions to hydrological processes (Park et al., 2021). It therefore has an ability to assess the contribution ratio of excess ice meltwater to the subsurface flow under future climate warming, which is important to understand the dynamics of hydrological processes.

Excess Ground Ice Model

CHANGE extended the soil column to a depth of 70.4 m, discretizing into 31 soil layers by default. The soil surface (e.g., ~0.37 m) over which the soil water gradient is generally strong forms six soil layers based on an exponential equation, and then the soil layers have a 0.2-m node spacing to 3.2 m. The deepest remnant layers in turn form thicker node depths based on the exponential equation. The soil layers from the surface to 6 m are treated as hydrologically active with the remaining deeper layers representing bedrock. In the active soil layers, the appearance of permafrost operates the parameterization of ice blocking, thereby constraining the hydrological activity in the relevant soil layers regardless of the model configuration. The maximum ALT is updated during the model calculation period including spinup, and the frozen soil below the active layer which is defined as permafrost soil. Excess ice is initially distributed within the configured soil layers and below the ALT, with the same ice fraction (**Table 1**), which increases both the volume of the whole soil layer (including saturated soil moisture) and the soil layer thickness accordingly (Bowling et al., 2008; Lee et al., 2014). The increase in the soil layer thickness is linearly proportional to the volumetric content of excess ice. As excess ice melts in response to climatic warming, the soil layer thickness decreases, which corresponds to surface subsidence because of excess ice melt (Cai et al., 2020). The water holding capacity of the soil layer is simultaneously decreased by the melting. The subsidence induced changes in saturated soil moisture and soil layer thickness directly affect hydraulic characteristics such as hydraulic conductivity and saturated soil water suction. These changes influence the vertical fluxes of soil water and ultimately the moisture content of the soil layers, as described in the **Supplementary Appendix**. Because excess ice is located below the ALT, however, there is little to no change in excess ice and related variables during model spinup.

The excess ice substantially affects soil thermal conductivity and soil heat capacity, which is immediately linked to soil temperature through their influences on heat flux and phase change. Following Lee et al. (2014), CHANGE adopted the thermal parameterization that includes the influence of the excess ice, as described in the **Supplementary Appendix**. Because the excess ice is prescribed as an initial condition, it only melts and does not grow again. As thawing occurs at a layer, permafrost soil of the layer is preferentially thawed, and thereafter excess ice. These assumptions allow simplification of the model calculation. The excess ice meltwater is added to liquid water of the soil layer or an unsaturated layer above if the soil layer is saturated. The liquid water then participates in the hydrologic system of transpiration and subsurface flow generation in the way of soil water movement.

TABLE 1 | Summary of experimental configurations used in this study.

Experiments	Excess ice		Moss cover	Blowing snow
	Content	Table		
CNTR	–	–	included	included
$EXICE_{T1\_C15}$	15%	1 m	included	included
$EXICE_{T1\_C30}$	30%	1 m	included	included
$EXICE_{T3\_C15}$	15%	3 m	included	included
$EXICE_{T3\_C30}$	30%	3 m	included	included
$EXCL_{MOS\_BLS}$	–	–	excluded	excluded
$EXCL_{MOS}$	–	–	excluded	included

Methane Flux Model

The coupling of a CH_4 biogeochemistry model integrated in the community land model (CLM4Me, Riley et al., 2011) to CHANGE was made to examine interactions of climate–excess ice–CH_4 fluxes. CLM4Me has been improved by integrating several new process representations and parameterization, and the improved versions have been tested and evaluated at global and site scales (Meng et al., 2012; Melton et al., 2013). Because the detailed descriptions of CLM4Me have been provided in previous studies (Riley et al., 2011), we here describe the major characteristics of CLM4Me, including the major modifications. In the model calculation, CLM4Me first controls the initialization of boundary conditions, inundation, and impact of redox conditions and then calculates CH_4 production, oxidation, transport through aerenchyma, ebullition, aqueous and gaseous diffusion, and the overall mass balance for unsaturated and saturated soils. Above all, mechanistically modeling net surface CH_4 emissions requires representing a time series of changing inundated fraction. CHANGE can optionally use a parameterization based on TOPMODEL (Beven and Kirkby, 1979) that includes a groundwater model calculating changes in water table controlled by water recharge and lateral flow. As the water table becomes higher, more of the surface area becomes saturated, thereby flooding the regions with higher topographic index first. Here, the saturated fraction (f_{sat}) calculated as in Gedney and Cox (2003) was alternated with the inundated fraction that is required in CLM4Me. The water table depth is calculated, and the probability distribution function of the topographic index within the site is then used to describe the relative frequency of occurrence of the topographic indices. f_{sat} of the site can be found by integrating the probability distribution function of the topographic index. This is determined by numerical integration because a two-parameter gamma distribution is used for the probability distribution function. An exponential distribution of f_{sat} is fitted to the parameters of the gamma distribution. f_{sat} is allowed to change at each time step, in which the calculation is made four times in total in the saturated and unsaturated fractions for CH_4 and O_2. The total soil CH_4 quantity is conserved by evolving CH_4 to the atmosphere when f_{sat} decreases and averaging a portion of the unsaturated concentration into the saturated concentration when f_{sat} increases. In addition, our simulation neglected the solution of the CH_4 and O_2 mass balance for water bodies.

Model Experiments

Several simulations were conducted for the years 1980–2099, based on various modeling setups of excess ice, as summarized in **Table 1**. The case "CNTR" is the standard version of the model that excludes the process of excess ice. The cases that included excess ice had different settings for the surface depth and content of excess ice along the thickness of 3 m. We combined two types of daily forcing data for running the model – the forcing data for the current climate from 1980 to 2013 were yielded by the combination of observations at the study site and ERA-Interim reanalysis data (Miyazaki et al., 2015) and the future forcing data from 2014 to 2099 were obtained from a single ensemble member of a projection simulation (RCP8.5) with Hadgem2-ES. Individual experiments were spun up for 1,200 years using the detrended forcing data of the initial 20 years and a CO_2 concentration of 350 ppm. Through the spinup runs, the model determines dynamic equilibriums for soil temperature and moisture and vegetation carbon and nitrogen. A static land cover type of arctic grass was defined for the simulation, while the vegetation phenology was prognostic based on the estimated carbon and nitrogen contents.

The RCP8.5 scenario is a high greenhouse gas emissions scenario (Moss et al., 2010), which resulted in strong warming in the study site; for example, air temperature increased 3°C and there was three times higher precipitation in the 2090s when compared with the 1980s (**Figure 1A**). It is noted that projections by climate models tend to contain biases in the Arctic, particularly excessive winter snowfall that likely results in unexpected thicker snow depth, as identified by the CNTR experiment (**Figure 1B**). The snow depth leads to excessive soil insulation that likely results in rapid permafrost thawing in combination with the warmer air temperature than when the climate biases are removed. To explore the response of permafrost to the precipitation-induced snow depth change of strong emission scenarios, we conducted additional experiments that reduced precipitation by 50% when compared with the default condition (**Table 1**), which was called "the treated experiment." Although the reduced precipitation produced lower snow depth during the winter than the original experiment (**Figure 1B**), the future snow depth of the treated experiment was considerably larger than the maximum snow depth (i.e., 40 cm) observed under the present climate.

Site Description and Observations

The Tiksi field site is located in northeastern Siberia (71.4°N, 128.5°E), near the mouth of the Lena River and 5 km west of the Laptev Sea coast (**Figure 2**). The study site receives about 173 mm of precipitation annually, with 60% in the form of rain during the summer (June to September). Annual mean air temperature is about −13.5°C with an annual amplitude from an average of −33.3°C in January to an average of 7.5°C in August. Strong wind speed results in usually heterogeneous and shallow snow cover, recording maximum snow depths of about 40 cm. The site represents a typical lowland tundra landscape, characterized by small lakes and low flat plains of wet tundra, and hill slopes and mountains of dry tundra. Various vegetation types, such as non-tussock sedge, dwarf-shrubs, and moss, are distributed on flat plains and the lower parts of relatively gentle slopes. The top and steep-sloping part of the mountains is covered by gravel with lichen. Continuous and ice-rich permafrost underlies the ground. The thermo-erosion induced by the climate warming increases the expansion of thermokarst lakes and small ponds (Liljedahl et al., 2016). The tundra soil consists of water-/ice-saturated sandy peat, with the water table close to the surface. The mineral soil is a clay loam consisting of 35% silt, 32% sand, and 33% clay. The quantity of organic matter around the site is significantly heterogeneous, with values ranging between 3 and 85 kg m^{-3}, and mean SOC values of 35 kg m^{-3} in the soil layer above 50 cm.

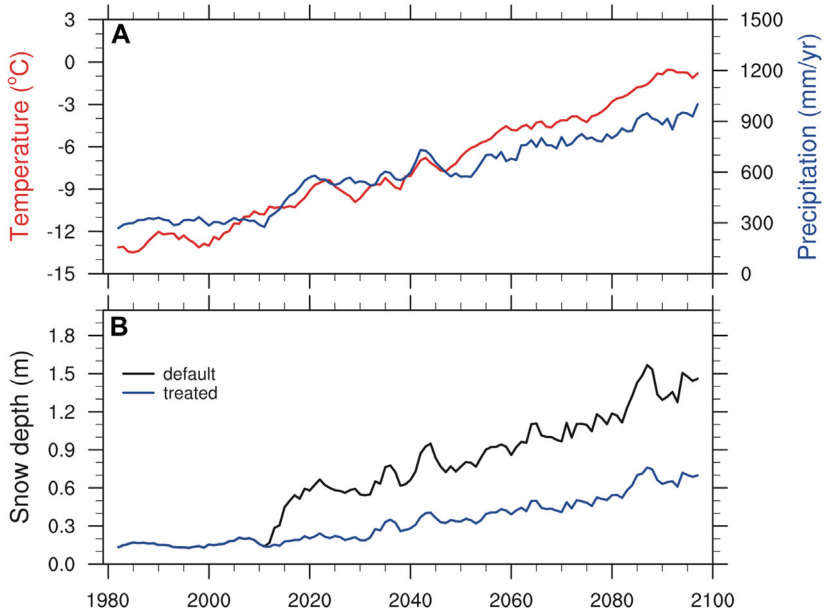

FIGURE 1 | Variations in annual precipitation (blue) and annual mean air temperature (red) **(A)** and snow depth **(B)** simulated by the original forcing climate (default experiment) and when precipitation was reduced by 50% when compared with the original data (treated experiment). Air temperature and precipitation until 2013 were yielded by the combination of *in situ* observations and ERA-Interim reanalysis data (Miyazaki et al., 2015), and thereafter those were obtained from a single ensemble member of a projection simulation (RCP8.5) with Hadgem2-ES (Collins et al., 2008), as described in *Model Experiments* section.

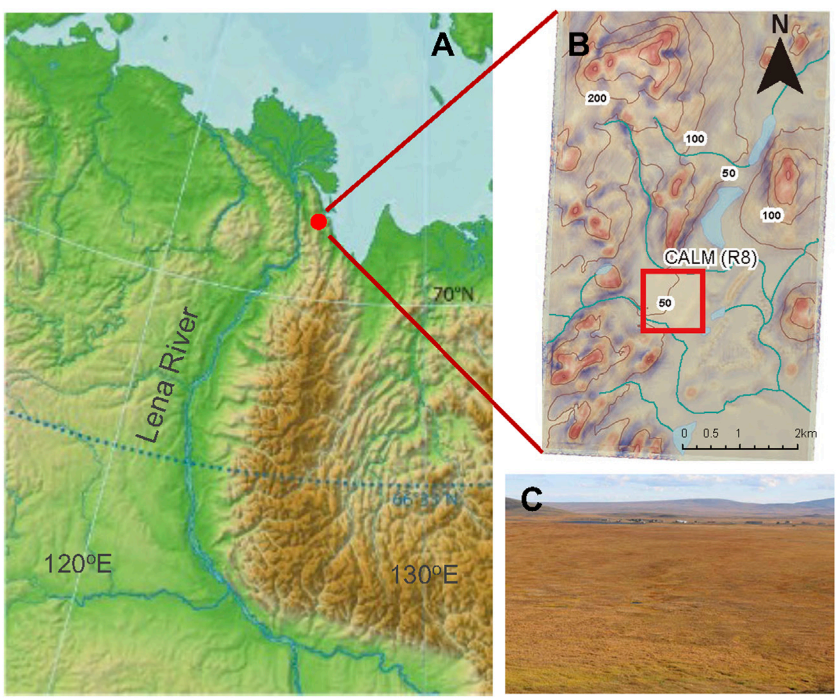

FIGURE 2 | The study area showing the topography in the northeastern Siberia including the Tiksi region (red dot, **A**) in the main map and the topography map **(B)** and landscape (Iijima et al., 2016) **(C)** of the study site. The landscape photo was taken in August 2015.

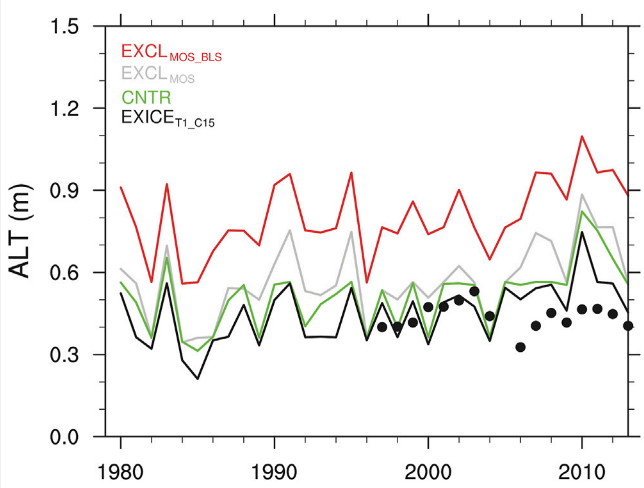

FIGURE 3 | Simulated active layer thickness (ALT) based on different model settings compared with the observational records (dots). This comparison makes it possible to quantify the influence of excess ice, blowing snow, and moss cover on ALT through relative comparisons between simulations. Because the simulations from 2014 onwards were forced by the warming climate scenario RCP8.5, the comparison between observation and simulation is available until 2013.

Various meteorological variables have been recorded from a 10-m high observational tower since 1997. The meteorological variables (i.e., shortwave and longwave radiation, air temperature, precipitation, relative humidity, wind speed, and air pressure) were measured at different heights on the tower; however, heat, water vapor, and CO_2 and CH_4 fluxes have not been observed directly at this site.

The heterogeneous surface and subsurface properties of the study site likely produce large spatial variations in the soil thermal regime. ALT was monitored at a 1 km × 1 km CALM site established in 1998 (Iijima et al., 2016). The measurement was performed in grids with 100-m intervals, once a year in mid-September using a metal rod. Another site of moss-covered ground consisting of 12 points was established near the CALM site, to further monitor ALT in 2006. Two observation plots monitoring soil temperature were established in 2004 – the first plot was located in a flat and very wet area and the second was in a flattened wet area and a narrow valley about 500 m from the first site. The landscape of the plots was polygonal tundra, with low shrub, sedge, and moss cover. Moss cover was dominated by sphagnum. Each plot was equipped with two TR-52 single-channel temperature loggers (T&D Corp., Matsumoto, Japan). The temperature sensors were placed on the soil surface and in permafrost at depths of 0.5 and 0.6 m.

RESULTS

Model Performance

The CHANGE-simulated results for water and carbon fluxes and soil moisture and temperature profiles, which have previously been validated to observational records in this study site, showed statistically satisfactory performances for seasonal and interannual variability (Park et al., 2018). Although the CH_4 process was newly added to CHANGE in this study, deficiencies in the observational data constrain the validation of model performance. Here, the ALTs simulated under various model settings were compared against the observational records, which enabled us to address the influence of climatic and surface conditions on ALT. The comparison between the simulated ALT and the observation shows that CHANGE captured the interannual variability of the observed ALT with +6 cm deviation during the period of 1997–2013 simulated by the current forcing climate (**Figure 3**). The observational values were averaged by records of points with different microclimates, soil properties, and vegetation characteristics. The one-dimensional CHANGE cannot accurately simulate the influences of these heterogeneities. This scale problem is one plausible reason for the difference in ALT between the simulated and observed values (Park et al., 2018). ALT was influenced more by snow cover than by moss cover (**Figure 3**). For example, the ALT simulated by EXCL$_{MOS_BLS}$ that excluded blowing snow was approximately 30 cm deeper than that by EXCL$_{MOS}$ that considered blowing snow, indicating the large cooling effect of thinner snow depth caused by blowing snow on ALT. The effect of moss cover on ALT was not larger than that of the blowing snow; CNTR, which considered moss cover, resulted in 5 cm lower ALT than EXCL$_{MOS}$. Meanwhile, the comparison between CNTR and EXICE$_{T1_C15}$ showed small differences in ALT, revealing the slight impact of excess ice on ALT. Because the excess ice was located 1 m deeper than the ALT, it was part of the permafrost. Therefore, the latent heat effect was dominant at the ALT bottom (i.e., the permafrost table). Instead, the excess ice has a large cooling effect on permafrost temperature. The differences in ALT between the experiments (**Figure 3**) suggest that the representation of moss cover and blowing snow is an inevitable consideration in models for the correct projection of permafrost dynamics in tundra regions influenced by climate change. Previous studies highlighted the critical impact of SOC on ALT. For example, a simulation for Samoylov Island of northern Siberia, close to this study site, addressed that the inclusion of SOC reduced ALT by 50 cm relative to the exclusion (Chadburn et al., 2015).

Model Experiments

Active Layer Thickness and Subsidence

The simulated ALT exhibited evident deepening during 1980–2099, driven by the warming climate (**Figure 4C**). The deepening was initiated from 2014 forced by the RCP8.5 climate conditions and became mostly significant from 2040 onwards when excess ice began to melt (**Figure 4B**). The rate of deepening increased over time, particularly under conditions of moss-free cover and excess ice exclusion (**Figure 4C**), where the resultant higher heat fluxes into the soil column were effective for the warming of permafrost. EXCL$_{MOS_BLS}$ of the default experiment resulted in 12 m of ALT during 2080–2099, which was considerably larger than that of the other simulations (**Table 2**). Comparison of the experimental ALTs confirmed

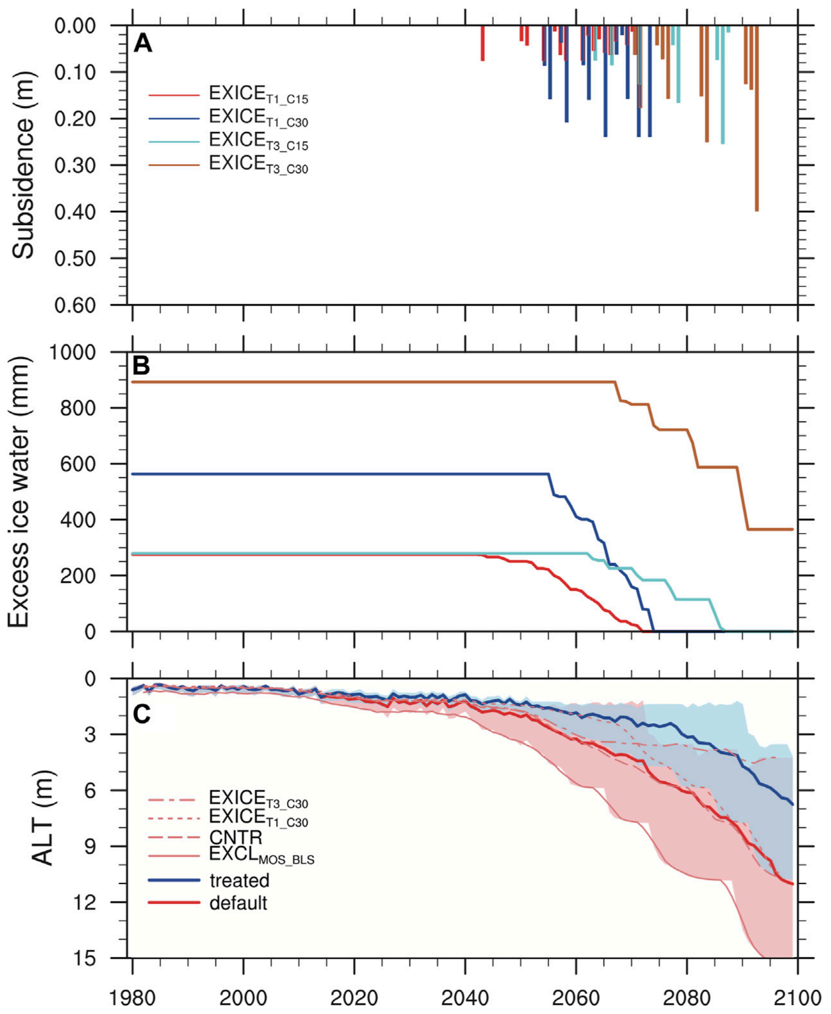

FIGURE 4 | Interannual variability in estimated annual subsidence **(A)** caused by excess ice melt in the default experiment, including excess-ice water content **(B)** and active layer thickness (ALT) in the experiment **(C)**. The colored lines of excess-ice water content **(B)** are consistent with the legends in panel **(A)**. The shaded areas of ALT represent the range of maximum and minimum values among seven simulations in the default and treated experiments, and the thick lines in the figure indicate the average values of individual experiments. The different types of thin lines in the default experiment exhibit 3-year running averaged ALT for individual simulations.

that the presence of excess ice limited the ALT (**Table 2**). The limitation was largest in the cases with 30% ice contents of 3 m table; for example, ALT of EXICE$_{T3_C30}$ was 4 m during 2080–2099, which was three times lower than that of EXCL$_{MOS_BLS}$ because of the larger latent heat requirements for the excess ice melt. The surface soil layers repeat seasonally thawing and freezing even under the strong future emission scenarios, and the warming climates likely develop annually unfrozen talik layers beneath the ALT. It is therefore defined that ALT in this study is the maximum depth of unfrozen soil including talik.

The treated experiments that reduced precipitation by 50% showed a time series of ALT variability similar to that of the default experiments. The absolute values of ALT under the same conditions were 45% larger on average in the default experiments than in the treated ones during 2080–2099 (**Table 2**), indicating the impact of snow on the ALT caused by the increased soil temperature. In the case of EXICE$_{T1_C15}$, for example, the snow depths in the two future periods (2030–2049 and 2080–2099) were considerably higher than in the present climate, despite later snow accumulation (**Figures 5A,C**). The thicker snow depth evidently has a larger insulation effect, preserving permafrost warming formed during summer and resulting in deeper ALT. A modeling study that treated snowfall magnitudes and snow seasons differently identified that changes in snow depth had larger impacts on thermal conditions of continuous rather than discontinuous permafrost and on colder Siberia than warmer North America (Park et al., 2015). The default experiment resulted in ALT of approximately 8 m on average during 2080–2099. The deeper ALT was also influenced by talik that was formed at the soil depth of 1 m or lower (**Figures 5B,D**). A large volume of water stored in the talik soil layers increases heat capacity and thermal conductivity, effectively dampening the annual temperature cycle (Subin et al., 2013; Lee et al., 2014),

TABLE 2 | Comparison of simulated components between simulations in individual experiments, averaged for the period 2080–2099. The annual methane (CH_4) fluxes were averaged for the period of 2014–2099 forced by RCP8.5.

Experiment		ALT (m)	Subsurface flow (mm/y)	Water table (m)	NPP (g C m^{-2} y^{-1})	HR (g C m^{-2} y^{-1})	CH_4 flux (g C m^{-2} y^{-1})
Default exp.	CNTR	8.6	287.3	4.87	781.8	785.2	38.8
	$EXICE_{T1\_C15}$	8.0	282.4	4.54	781.9	781.7	44.4
	$EXICE_{T1\_C30}$	7.5	302.0	4.01	781.8	787.1	47.0
	$EXICE_{T3\_C15}$	6.8	277.5	3.58	779.3	784.0	39.3
	$EXICE_{T3\_C30}$	4.09	222.4	1.80	773.3	790.7	41.3
	$EXCL_{MOS\_BLS}$	12.9	345.4	5.26	823.2	831.7	38.3
	$EXCL_{MOS}$	10.9	326.2	5.28	785.2	792.2	36.7
Treated exp.	CNTR	4.52	125.8	3.08	828.2	809.3	40.7
	$EXICE_{T1\_C15}$	3.54	128.2	2.04	826.7	822.2	45.7
	$EXICE_{T1\_C30}$	2.63	103.6	1.26	814.0	851.6	49.6
	$EXICE_{T3\_C15}$	3.74	129.3	2.27	826.9	813.0	41.2
	$EXICE_{T3\_C30}$	3.35	123.9	1.96	826.1	815.3	42.3
	$EXCL_{MOS\_BLS}$	8.23	207.2	5.21	878.4	876.4	36.6
	$EXCL_{MOS}$	6.92	171.8	4.73	821.0	816.3	34.8

*ALT: active layer thickness; NPP: net primary productivity; HR: heterotrophic respiration. For an explanation of treatment codes, see **Table 1**.*

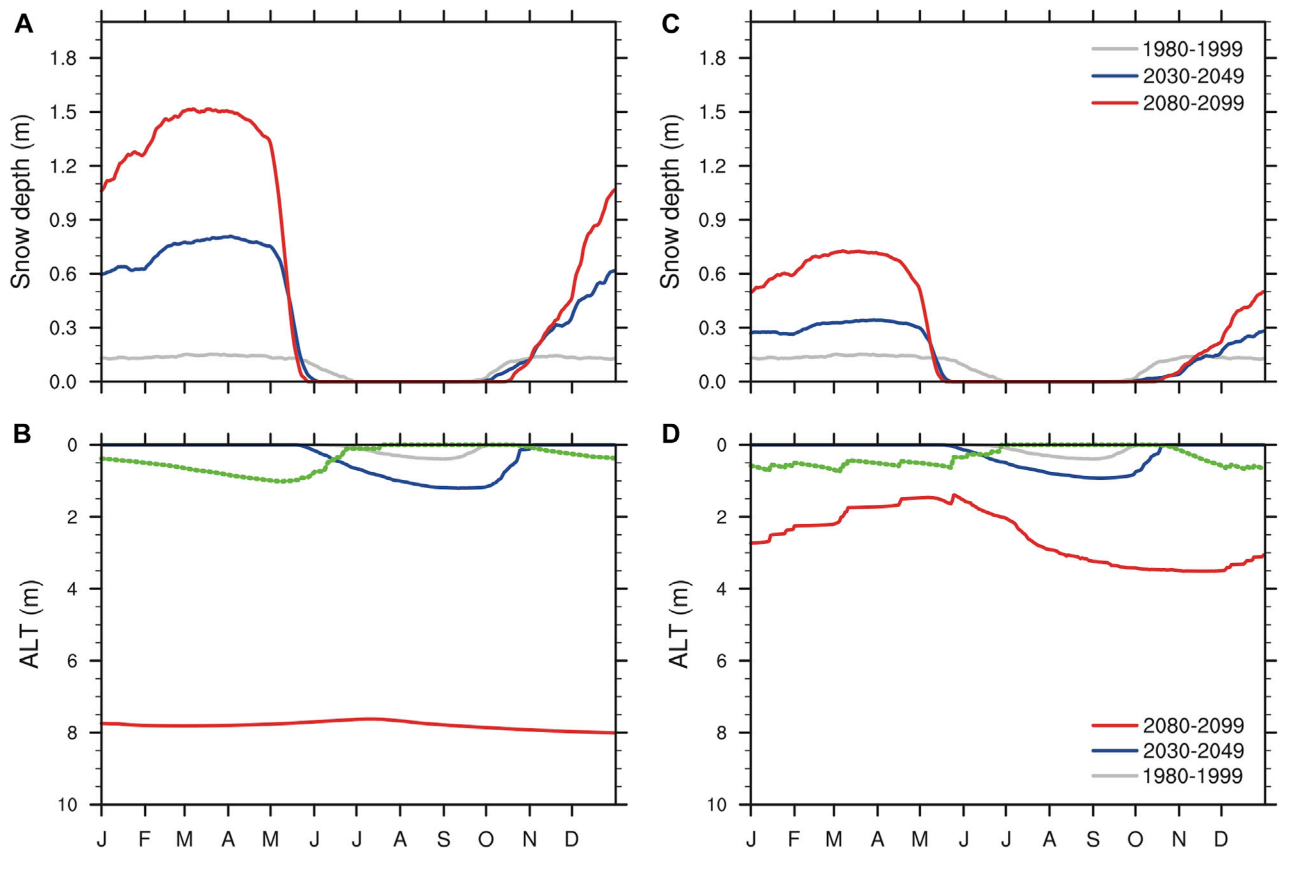

FIGURE 5 | Comparisons of seasonal snow depths **(A,C)** and active layer thickness (ALT) **(B,D)** for the three decadal averages in the case of $EXICE_{T1\_C15}$ of the default **(left panels)** and treated **(right)** experiments. The green lines in **(B, D)** represent the surface depth of talik.

as identified in the seasonal ALT of the default experiment (**Figure 5B**). Interestingly, the talik was also found for the treated experiment with relatively thin snow depth (**Figure 5D**), which highlights the strong influence of the warming temperature on the talik, with high insulation effect of the snow depth and moss cover.

The different setups of simulations in both experiments showed that excess ice in this study site preserved the initial

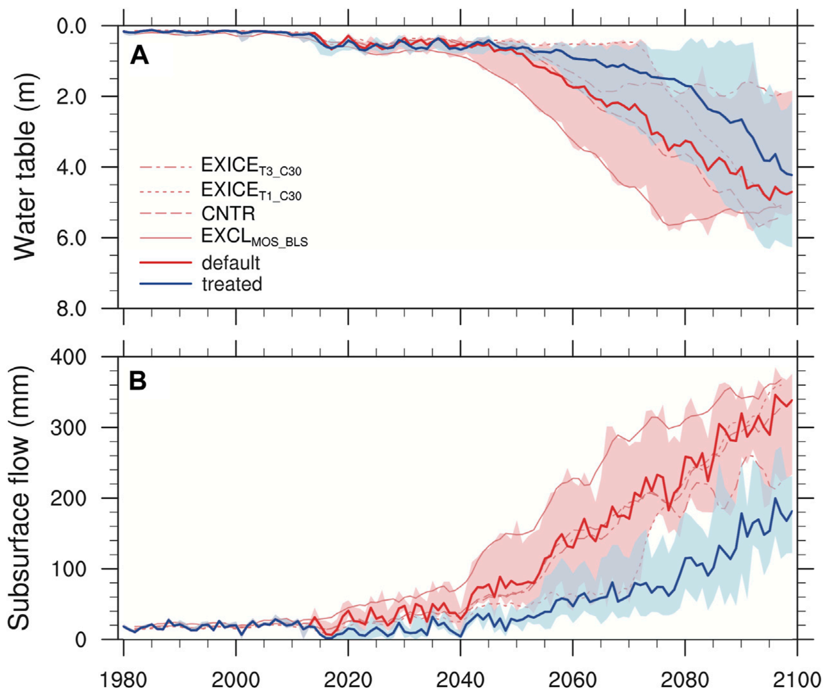

FIGURE 6 | Interannual variability of water table **(A)** and subsurface flow **(B)** in the default (red) and treated (blue) experiments. The shaded areas and colored lines are the same as those in **Figure 4**.

state until 2040 because of the combined effects of less extreme emission scenario, the insulation of moss cover, and higher latent heat of excess ice, and thereafter it mostly melted by the end of the 21st century (**Figures 4A,B**). However, the melting time series showed evident differences between the simulations (**Figure 4B**). The timing and magnitude of excess ice melt was influenced by the distribution and amount of the initial excess ice; for example, the case $EXICE_{T1\_C15}$ with lower excess ice resulted in advanced excess ice melt by approximately 10 years relative to the case of $EXICE_{T1\_C30}$ (**Figure 4B**). In the case of $EXICE_{T3\_C30}$, interestingly, a portion of excess ice remained until 2099 (**Figure 4B**) because of the higher latent heat effect associated with the higher excess ice content distributed at the deeper soil layer.

The excess ice melt resulted in land surface subsidence. The estimated annual subsidence ranged from 2 to 40 cm in the default simulations (**Figure 4A**). A simulation for Samoylov Island of northern Siberia, close to this study site, estimated surface subsidence of 35 cm by around 2030 and more than 1 m by the end of this century, based on the RCP4.5 warming scenario (Aas et al., 2019). Our results for subsidence show discontinuous occurrence in the time series of individual simulations. As permafrost thaws under the warming climate, excess ice simultaneously melts in nature. However, CHANGE used a physics model where excess ice starts to melt after permafrost of a soil layer is completely thawed. As the permafrost layer becomes active, the soil layer has already stored enough heat to rapidly melt the excess ice. Therefore, the physics model resulted in stepwise patterns of subsidence.

Water Flows

Permafrost and excess ice that are located at the base of the active layer greatly impede water flow below the layer. This leads to a relatively wet active layer and high water level. The simulations exhibited high water levels until 2040 (**Figure 6A**) when the excess ice was still intact (**Figure 4**); the water level rapidly lowered after the excess ice melted (**Figure 6A**). In the physics model, excess ice meltwater is added to soil moisture. The meltwater causes the base of the active layer to wet, so that the model groundwater becomes more active, leading to higher subsurface flow as observed in the simulations (**Figure 6B**). The runoff abruptly increased after 2040, although there were differences in the amount of runoff between the simulations (**Figure 6B**). In the treated experiments, the annual subsurface flow averaged 141.4 mm during 2080–2099, which corresponded to 31% of the annual precipitation averaged during the same period.

As the ALT thickens, the meltwater from both excess ice and permafrost increases. Substantial amounts of unfrozen liquid water, defined as older soil moisture in the tracer scheme, is stored in permafrost soil. As the permafrost thaws, the liquid water becomes active and is involved in talik formation and subsurface flow. The tracer model quantified the largest contribution of the old soil moisture, which was the initial unfrozen water in the model setting, to the subsurface flow during 2080–2099 (**Figure 7D**). The excess ice meltwater accounted for 26% of the subsurface flow during the same period, which was not identified in the present climate. Both the old soil moisture and excess ice meltwater maintained high

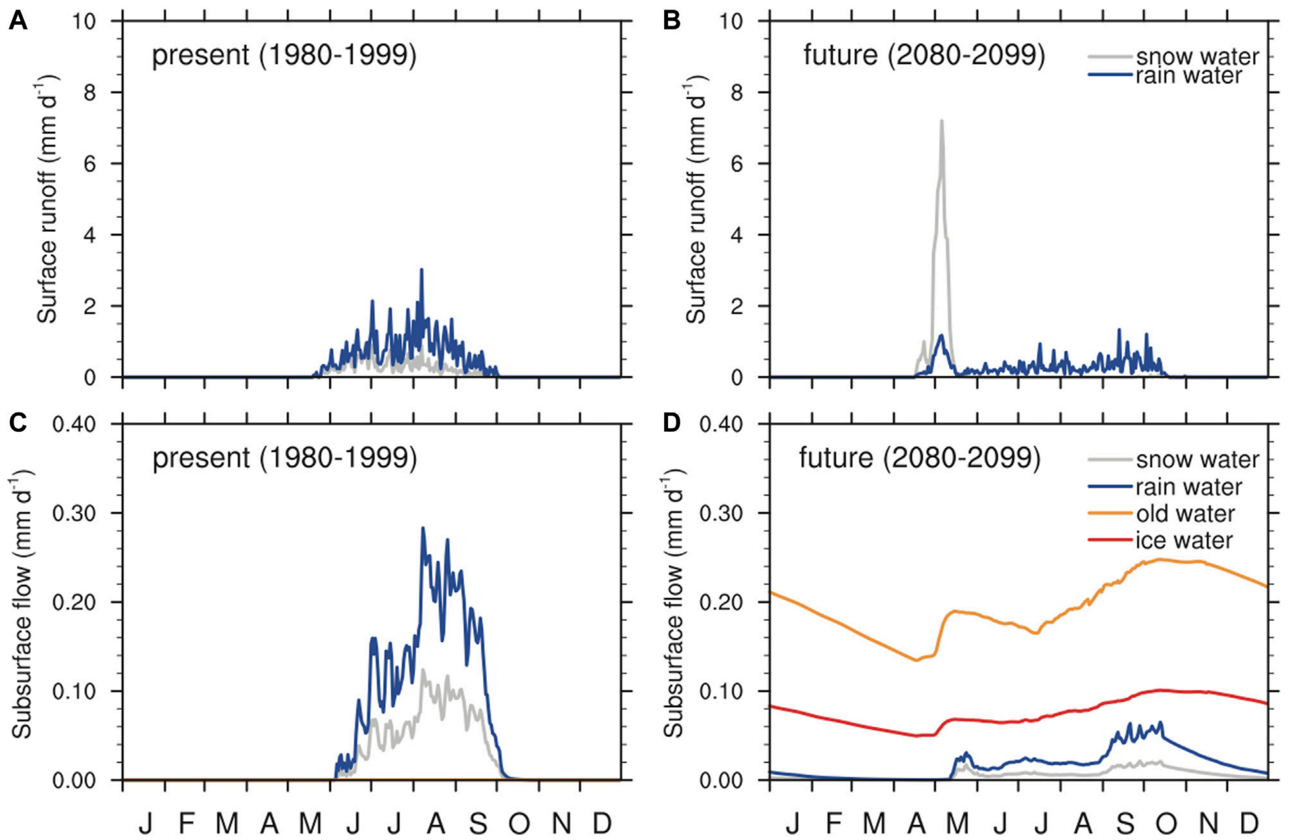

FIGURE 7 | Contribution of source waters to the averaged seasonal surface **(A,B)** and subsurface **(C,D)** runoffs in the present (1980–1999, left) and future (2080–2099, right) climates in the case of $EXICE_{T1\_C15}$ of the treated experiment. The contributions of source waters to runoffs were separated by the tracer scheme in CHANGE. The old water in **(D)** indicates the water that was existent as unfrozen type in the soil column by the initial model setup.

contribution rates to the subsurface flow with changing seasons, strongly implicating the talik in the runoff processes. The influence of the snow meltwater and rainwater on subsurface flow considerably decreased in the future when compared with the high fractions in the current climate (**Figures 7B,D**). The simulated results also displayed low fractions of the snow meltwater and rainwater constituting deeper soil moisture in the future, particularly at 1.6 m or deeper, while the excess ice meltwater increased at the same soil depths relative to the current climate (**Figure 8**).

The future warming climate resulted in a drier environment in the upper soil layers relative to the present (**Figure 8**), despite the larger precipitation (**Figure 1A**). As ALT thickens, the higher conversion of excess ice meltwater to subsurface flow, as described above, was related to soil drying. The dried soil layers need more water for soil wetting. A portion of the available precipitation is used for soil wetting, which ultimately reduces water flowing to the deeper soil layers. In terms of soil moisture distribution, evapotranspiration increases moisture loss from the upper soil layers, thereby resulting in increased soil drying. The dry soil resulted in the decline of the water table (**Figure 6A**). The water table exhibited the declining trend toward the end of the 21st century, in which the interannual variability was also similar to the patterns of the subsurface flow and ALT, representing their interaction.

Carbon Dioxide and Methane Fluxes

Soil moisture in the upper soil layers (i.e., 0–1 m) during 2080–2099 mainly distributed within the range of 0.2–0.3 $m^3\ m^{-3}$, although it was drier than during 1980–1999 (**Figure 8A**). The future soil moisture was never low enough to constrain vegetation productivity or SOC decomposition. The simulated net primary productivity (NPP) of the study site continuously increased during the study period (**Figure 9A**), with slight differences in values between the model experiments during 2080–2099 (**Table 2**). The increase in NPP was large from 2014 when it was forced by the warming climate of RCP8.5. In the warming climate, there was no large difference in the annual mean NPPs of the two experiments. Interestingly, however, NPP of the default experiment showed slightly lower values than the treated one from 2060 onwards, despite the larger precipitation in the default experiment. The deeper ALT in the default relative to the treated experiment was linked to the decrease in soil moisture, as demonstrated by the lower water table (**Table 2**), which likely somewhat limits ecohydrological functions. The high precipitation during the summer season wets a large fraction of the vegetation, limiting temporary photosynthesis by plants

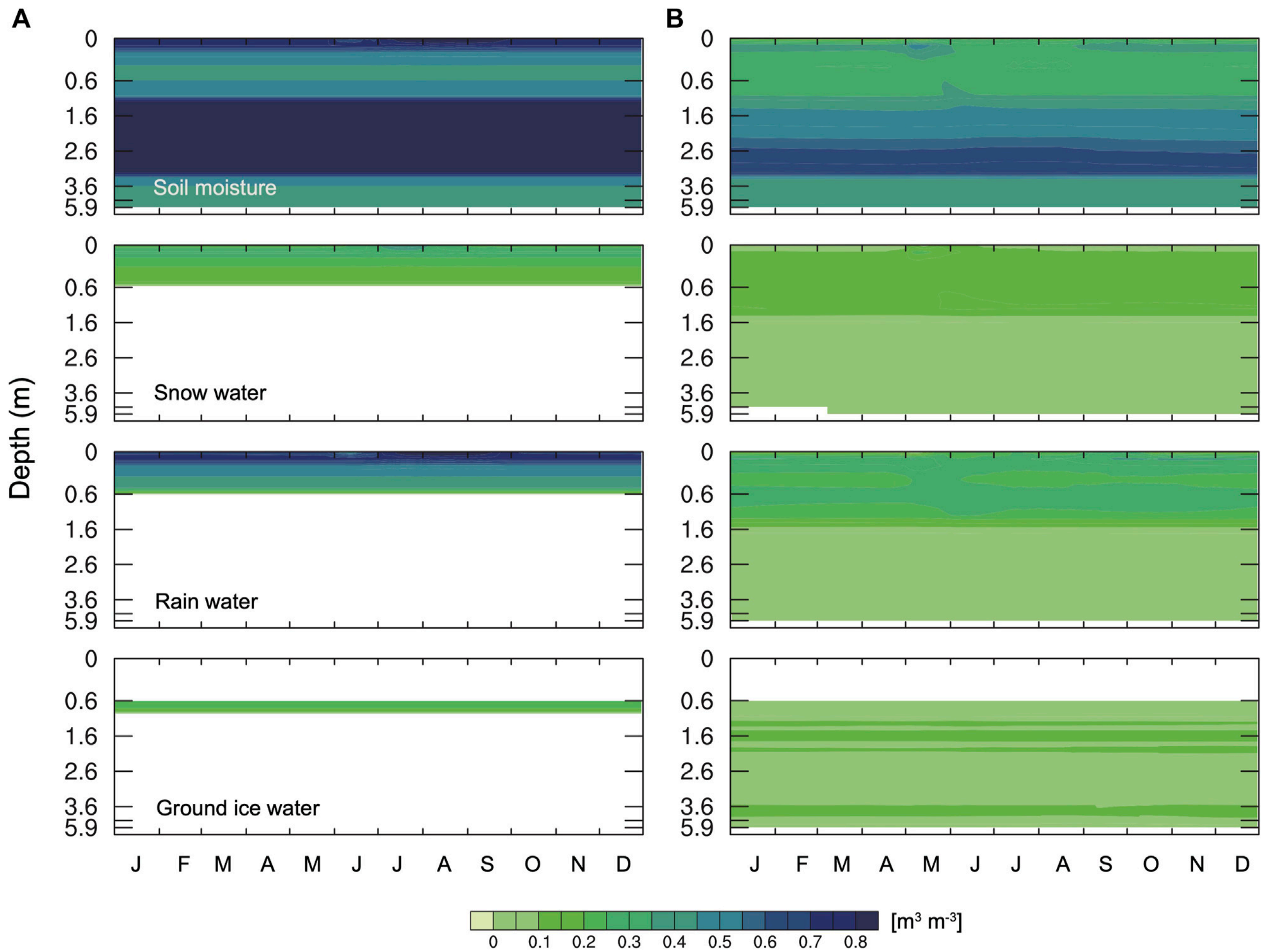

FIGURE 8 | Seasonal variations in source waters composition of soil moisture in the soil column in the present (1980–1999, **A**) and future (2080–2099, **B**) climates in the case of CNTR of the treated experiment. The profiles of the tracer scheme separated source water were averaged in the two analyzed periods.

(Park and Hattori, 2004). The simulated heterotrophic respiration (HR) exhibited similar variations to those identified for NPP (**Figure 9B**).

The simulated CH_4 efflux displayed complex interannual variability and decadal trends (**Figure 9C**), considerably different to those identified for the simulated NPP and HR (**Figures 9A,B**). The warming climate forced increasing CH_4 emission and HR from the permafrost soil to the atmosphere until 2040 when permafrost was still stable (**Figure 4C**), and the water level was relatively high (**Figure 6A**). Then, CH_4 effluxes generally tended to decrease, although the timing was quite different according to the simulations; for example, CNTR of the default experiment represented the earliest decrease of CH_4 efflux by 2040, because of the decreased soil moisture induced by the early permafrost thawing, while the experiments with excess ice simulated higher CH_4 effluxes until the mid-2070s. The excess ice meltwater temporarily creates a wetted soil that efficiently generates CH_4 effluxes. The model effectively simulated higher CH_4 effluxes during excess ice melt. In contrast, the high conversion of excess ice meltwater to subsurface flow induced soil drying, as explained above, resulting in an abrupt decrease in CH_4 effluxes because of the aerobic conditions. Despite of the soil drying, both NPP and HR continuously increased responding to the warming climate, inconsistent with the decreasing CH_4 efflux. The precipitation in the future climate (**Figure 1A**) was as large as to alleviate the drying of the surface soil layers (**Figure 8B**), which contributed to higher vegetation productivity and respiration. The same variations in CH_4 effluxes were identified in the treated experiments as those in the default experiments, although the timing of the projected higher CH_4 effluxes was later relative to the default experiments. These model experimental results suggest that excess ice is an important component in the complex interannual variability of CH_4 efflux.

Sensitivity Analysis

The excess ice constrained the deepening of ALT; the magnitude of this response fluctuated depending on the ice content (**Figure 4B**). For example, at the cases that the surface of

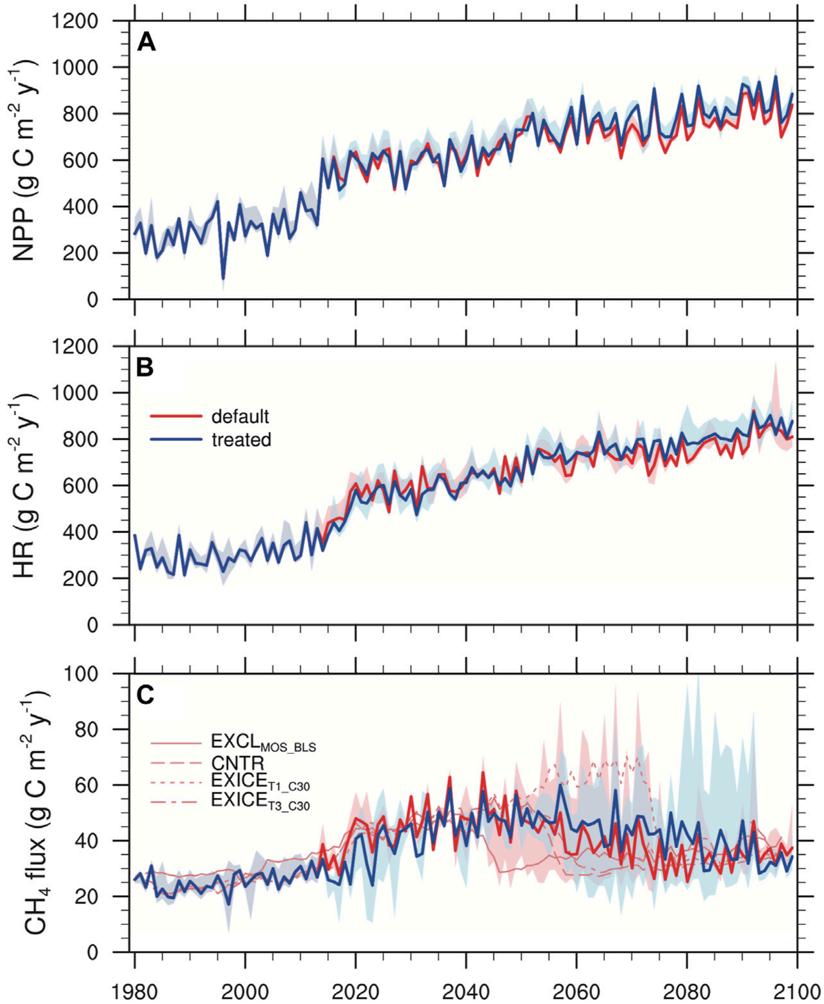

FIGURE 9 | Interannual variability of simulated net primary productivity (NPP) **(A)**, heterotrophic respiration (HR) **(B)**, and methane (CH_4) flux **(C)** for the default (red) and treated (blue) experiments. The shaded areas and colored lines are the same as those in **Figure 4**.

excess ice was 1 m, $EXICE_{T1\_C30}$ with excess ice content of 30% lowered ALT by 50 cm relative to $EXICE_{T1\_C15}$ with 15% during 2080–2099 (**Table 2**). At the cases of 3 m, the difference in ALT between $EXICE_{T3\_C15}$ and $EXICE_{T3\_C30}$ increased ALT by 2.7 m during the same period (**Table 2**), indicating larger latent heat effect by higher excess ice content.

The permafrost including excess ice impedes water flowing downward, wetting soil layers above the permafrost table and thereby resulting in a higher water level (**Figure 6A**). Under those conditions, the warming temperature warms the active soil layers, consequently increasing SOC decomposition. Excess ice melt contributed to increased CH_4 efflux, with a larger response obtained for high ice content than for low ice content (**Table 2**). The depth of the excess ice table was also closely associated with the CH_4 efflux, which was lower for an ice table depth of 3 m than of 1 m (**Table 2**). As the table of excess ice deepens, the thicker soil column intuitively slows the soil wetting and warming. These conditions are effective for limiting the CH_4 efflux. Even though soil wetting and warming are extended to the deeper layers, CH_4 efflux under the changed conditions might not be large because of smaller SOC storage in the deeper soil layers. The maximum estimated ALT was 60 cm during the model spinup of 1,200 years. SOC is mainly stored in the active layers. As ALT is thickened by the warming climate, SOC also flows down. However, the amount of SOC flowing to 3 m was low, hence the low CH_4 efflux.

DISCUSSION

Because of the lack of excess ice datasets and observational evidence, our model projections of excess ice melt and associated processes likely have biases that arise from model settings and simplifications of the excess ice initialization. However, the sensitivity experiments can potentially improve our understanding of the impacts of excess ice melt on hydrological and biogeochemical processes. The water tracer model in CHANGE tracks pathways of excess ice meltwater in the soil system and assesses their contribution to hydrological processes.

The excess ice and permafrost act as a barrier to water infiltration because of the low conductivity of icy soils, storing the inflowing precipitation water within the active layers. The large volume of stored water induces higher heat capacity and conductivity, dampening the annual soil temperature cycles (Subin et al., 2013), in which warming climate forces permafrost thawing and excess ice melt. As soon as the excess ice melts, the ALT bottom layers are wetted by the melt water. The wetted soil moisture was connected to the subsurface flow (Liljedahl et al., 2016). Once excess ice melts, there is no additional water production from the soil layer. During these processes, subsidence occurs, and the excess ice meltwater is linked to the upper soil moisture that is mainly the result of precipitation (i.e., snowmelt and rainwater). However, evapotranspiration and the recharge of soil moisture preferentially use precipitation water inflowing from the surface, and thus there is limited connectivity of the precipitation to the deeper soil moisture. As a result, the soil column tends to be dried as ALT deepens, and the water level is lowered. CHANGE captured both the weakening signal of the connectivity of surface soil moisture to the deeper soil, and the hydrological regime of thawed permafrost tipping as a consequence of melted excess ice to a dominance of unsaturated soil condition (Aas et al., 2019; Nitzbon et al., 2020). The excess ice has a contrary effect of temporarily limiting rapid soil drying in the melting stage. At the bottom of the active layer, the excess ice melt water-induced wetting reduces water input from the upper soil layers because of the reversed large moisture gradient. The moisture gradient gradually decreases with the increasing subsurface flow, so that soil is dried. The excess ice melting lasted for 15–20 years dependent on the excess ice settings. In practice, the model setups that excluded excess ice simulated earlier soil drying than experiments that included the excess ice (**Figure 6A**).

The simulated regime of soil moisture is strongly dependent on the assumptions for the modeling. Under water-logged conditions, the melting of excess ice would develop deep water-filled troughs, and potentially form thermokarst lakes and ponds (Nitzbon et al., 2020). Furthermore, excess ice melt and associated ground subsidence increases the lateral hydrological connectivity of the natural landscape, causing higher water levels in the depressed lowlands. However, models lacking in the representation of thermokarst-inducing processes likely underestimate permafrost thaw dynamics and resultant carbon fluxes. A modeling study highlighted differences of 2–12 times in SOC decomposition between two experiments that included and excluded thermokarst-inducing processes in northeastern Siberia (Nitzbon et al., 2020). As mentioned before, CHANGE employed one-dimensional physics of permafrost thaw dynamics considering only the vertical heterogeneity of excess ice. It was assumed that the excess ice meltwater was connected to soil moisture dynamics and subsurface flow generation. The simplistic representation of CHANGE likely yields biased projections for the subsurface hydrology crucially influenced by heterogeneous microtopography, lateral hydrological connectivity and ground subsidence. In reality, CHANGE simulated wetter soil and higher subsurface flow after the melt of excess ice (**Figure 7**) and subsequent higher carbon releases (**Figure 9**). However, our simulations provide important insights for excess ice melt and associated changing hydrology and carbon fluxes under well-drained conditions. Following the simulated results, the default experiments with large precipitation produced large HR and CH_4 (**Figure 9**) until 2040 when permafrost was stable, while larger production of HR and CH_4 was found in the treated experiments after this time. However, the differences between the two experiments were not large. This is probably because of the relatively similar moisture environments in their upper soil layers that were relatively sensitive to precipitation. Although the default experiments simulated dry soil and lower water table level (**Figure 6**), the high precipitation was efficient in alleviating drying of the upper soil layers.

The CH_4 fluxes showed different variations than that of HR. After 2060 when excess ice melted, the interannual variability of CH_4 effluxes was large and exhibited considerable differences between simulations (**Figure 9**). Earlier occurrence of high CH_4 efflux was found in the simulations with the surface of excess ice of 1 m than in ones with 3 m. Moreover, CH_4 efflux was further increased in the simulations with higher volumetric contents of excess ice. These results indicate that the initialization of excess ice greatly affects CH_4 efflux. Therefore, the model projection of CH_4 efflux utterly relies on the initial settings of excess ice. Because of the scarcity of observational data, however, this study employed the active layer-dependent excess ice initialization for modeling, together with statistical and empirical knowledge of the vertical extent and depth of excess ice as used in previous modeling studies (Lee et al., 2014; Aas et al., 2019; Cai et al., 2020). These configurations of excess ice still likely deviated from the actual ice features. We do not therefore expect the modeled excess ice melt and CH_4 efflux in this study to be an adequate representation of reality. However, our simulations could be used to infer the timing and magnitude of excess ice melt and associated carbon and CH_4 fluxes, and possible changes in soil hydrology under the well-drained condition.

Locally developing thermokarst lakes have recently been observed in this study site (Liljedahl et al., 2016), which could have been induced by natural or anthropogenic disturbances like the accumulation of snow in topographic depressions, the removal of vegetation or moss cover, and forest and tundra fires (Jones et al., 2015; Nauta et al., 2015; Abolt et al., 2018). Here, our model results provide evidence for the early excess ice melt as a result of higher insulation of thicker snow and thus enhanced soil drying. The simulation that excluded moss cover also estimated considerably earlier excess ice melt than the undisturbed case. In contrast, the high cooling by moss cover limited ALT deepening, hence stable permafrost. A simulation including excess ice initialization for the Lena River delta close to our site estimated the initiation of excess ice melt before 2020 (Cai et al., 2020). The melt timing is quite fast relative to our result showing stable permafrost until 2040 (**Figure 4**). The different model structure and settings make it impossible to directly compare the two results. Considering that the model used by Cai et al. (2020) did not consider the influence of moss cover, here we could expect further easy warming of permafrost under the moss-free condition. Park et al. (2018) found that 4-cm-thick moss cover reduced the ALT by 14 cm relative to the moss-free case. These results suggest that model improvement including moss cover as a land component is required for realistic representation of permafrost features under warming climate conditions.

Recent observations reported complex landscape development in the terrestrial Arctic, such as thermokarst ponds and lakes of meter-scale distribution (Liljedahl et al., 2016; Ulrich et al., 2017). To represent the small-scale permafrost features, models employed sub-tile interactive setups that simulated microtopographic changes associated with degradation of ice-rich permafrost, considering the lateral water flux (Aas et al., 2019; Nitzbon et al., 2020). The sub-tile representation of excess ground ice within permafrost soil was used for the global simulation without the lateral flux (Cai et al., 2020). The sub-tiling approach preferentially needs available observational data for the model simulation, which is substantially consistent with the requirements of our model. Therefore, the introduction of the tiling system could be a direction for the future development of CHANGE, particularly by configuring an optional function whereby lateral heat and water fluxes could be switched on and off dependent on topography. Laterally coupled tiling likely builds more potential for better modeling subscale variability of soil and snow, consequently improving permafrost–water–carbon feedbacks.

CONCLUSION

This study coupled an excess ice scheme to CHANGE and examined the impacts of excess ice on permafrost, soil water dynamics, and carbon and methane fluxes in a Siberian tundra site under the strong future emission scenarios. The model results indicated that the warming air temperature and higher snow depth were major factors deriving ALT increasing and the resultant permafrost degradation. Under the warming permafrost, in contrast, excess ice thermally stabilized permafrost until it melts, which was further significant under the conditions of larger excess ice content and moss cover. As excess ice melts, however, the meltwater was connected to hydrologic and thermal regimes, and the resultant wetted and warm soil was positively fed back to higher subsurface flow, permafrost degradation, and temporarily higher CH_4 efflux. These results provide insights for interactions and feedbacks between climate change, permafrost excess ice, and carbon fluxes in a well-drained condition.

The insights obtained by this study represented that the magnitude and timing of excess ice melt are largely dependent on the model settings. The model parameterization and initialization of excess ice remain necessarily simplistic, which highlights the importance of the connectivity of the excess ice meltwater to the subsurface flow and subsequent implications for carbon fluxes. Therefore, future model improvement emphasizes the necessity of coupling tiling hierarchy to CHANGE, which would enable a more comprehensive examination of the possible trajectory of the permafrost carbon–climate feedback under changing climate.

DATA AVAILABILITY STATEMENT

The raw data supporting the conclusions of this article will be made available by the authors, without undue reservation.

AUTHOR CONTRIBUTIONS

HP developed the ideas, wrote most of this paper and drew most of the figures. All authors participated in data processing and preliminary analysis; HP and TH coordinated the model experiments and analyzed the simulation results; AF and PK collected and analyzed *in situ* observational data.

FUNDING

This study was partly supported by the Japan Society for the Promotion of Science KAKENHI Grant Number 17H01870, 19H05668, and 21H04934. It was also supported by JST Belmont Forum Grant Number JPMJBF2003, Japan, and the Arctic Challenge for Sustainability II (ArCS II; JPMXD1420318865) project funded by the Ministry of Education, Culture, Sports, Science and Technology (MEXT), Japan.

ACKNOWLEDGMENTS

We thank Catherine Dandie, from Edanz (https://jp.edanz.com/ac) for editing a draft of this manuscript.

SUPPLEMENTARY MATERIAL

The Supplementary Material for this article can be found online at: https://www.frontiersin.org/articles/10.3389/feart.2021.704447/full#supplementary-material

REFERENCES

Aas, K. S., Martin, L., Nitzbon, J., Langer, M., Boike, J., Lee, H., et al. (2019). Thaw Processes in Ice-Rich Permafrost Landscapes Represented with Laterally Coupled Tiles in a Land Surface Model. *The Cryosphere* 13, 591–609. doi:10.5194/tc-13-591-2019

Abolt, C. J., Young, M. H., Atchley, A. L., and Harp, D. R. (2018). Microtopographic Control on the Ground thermal Regime in Ice Wedge Polygons. *The Cryosphere* 12, 1957–1968. doi:10.5194/tc-12-1957-2018

Beven, K. J., and Kirkby, M. J. (1979). A physically based, variable contributing area model of basin hydrology/Un modèle à base physique de zone d'appel variable de l'hydrologie du bassin versant. *Hydrological Sci. Bull.* 24, 43–69. doi:10.1080/02626667909491834

Bisht, G., Riley, W. J., Wainwright, H. M., Dafflon, B., Yuan, F., and Romanovsky, V. E. (2018). Impacts of Microtopographic Snow Redistribution and Lateral Subsurface Processes on Hydrologic and thermal States in an Arctic Polygonal Ground Ecosystem: a Case Study Using ELM-3D v1.0. *Geosci. Model. Dev.* 11, 61–76. doi:10.5194/gmd-11-61-2018

Biskaborn, B. K., Smith, S. L., Noetzli, J., Matthes, H., Vieira, G., Streletskiy, D. A., et al. (2019). Permafrost Is Warming at a Global Scale. *Nat. Commun.* 10, 264. doi:10.1038/s41467-018-08240-4

Bowling, L. C., Cherkauer, K. A., and Adam, J. C. (2008). "Current Capabilities in Soil thermal Representations within a Large-Scale Hydrology Model for Regions of Continuous Permafrost," in Proceeding of Ninth International Conference of Permafrost, 177–182.

Cai, L., Lee, H., Aas, K. S., and Westermann, S. (2020). Projecting Circum-Arctic Excess-Ground-Ice Melt with a Sub-grid Representation in the Community Land Model. *The Cryosphere* 14, 4611–4626. doi:10.5194/tc-14-4611-2020

Chadburn, S., Burke, E., Essery, R., Boike, J., Langer, M., Heikenfeld, M., et al. (2015). An Improved Representation of Physical Permafrost Dynamics in the JULES Land-Surface Model. *Geosci. Model. Dev.* 8, 1493–1508. doi:10.5194/gmd-8-1493-2015

Collins, W. J., Bellouin, N., Doutriaux-Boucher, M., Gedney, T., Hinton, J., Jones, C. D., et al. (2008). Evaluation of the HadGEM2 model. Met Office Hadley Centre Technical Note no. HCTN 74. Available at: Met Office, FitzRoy Road, Exeter EX1 3PB. http://www.metoffice.gov.uk/publications/HCTN/index.html

Collatz, G. J., Ball, J. T., Grivet, C., and Berry, J. A. (1991). Physiological and Environmental Regulation of Stomatal Conductance, Photosynthesis and Transpiration: a Model that Includes a Laminar Boundary Layer. *Agric. For. Meteorology* 54, 107–136. doi:10.1016/0168-1923(91)90002-8

Cresto Aleina, F., Brovkin, V., Muster, S., Boike, J., Kutzbach, L., Sachs, T., et al. (2013). A Stochastic Model for the Polygonal Tundra Based on Poisson-Voronoi Diagrams. *Earth Syst. Dynam.* 4, 187–198. doi:10.5194/esd-4-187-2013

Farquhar, G. D., Von Caemmerer, S., and Berry, J. A. (1980). A Biochemical Model of Photosynthetic CO2 Assimilation in Leaves of C3 Species. *Planta* 149, 78–90. doi:10.1007/BF00386231

Fedorov, A. N., Gavriliev, P. P., Konstantinov, P. Y., Hiyama, T., Iijima, Y., and Iwahana, G. (2014). Estimating the Water Balance of a Thermokarst lake in the Middle of the Lena River basin, Eastern Siberia. *Ecohydrol.* 7, 188–196. doi:10.1002/eco.1378

Gedney, N., and Cox, P. M. (2003). The Sensitivity of Global Climate Model Simulations to the Representation of Soil Moisture Heterogeneity. *J. Hydrometeor* 4, 1265–1275. doi:10.1175/1525-7541(2003)004<1265:tsogcm>2.0.co;2

Grant, R. F., Mekonnen, Z. A., Riley, W. J., Wainwright, H. M., Graham, D., and Torn, M. S. (2017). Mathematical Modelling of Arctic Polygonal Tundra with Ecosys : 1. Microtopography Determines How Active Layer Depths Respond to Changes in Temperature and Precipitation. *J. Geophys. Res. Biogeosci.* 122, 3161–3173. doi:10.1002/2017jg004035

Hugelius, G., Strauss, J., Zubrzycki, S., Harden, J. W., Schuur, E. A. G., Ping, C.-L., et al. (2014). Estimated Stocks of Circumpolar Permafrost Carbon with Quantified Uncertainty Ranges and Identified Data Gaps. *Biogeosciences* 11, 6573–6593. doi:10.5194/bg-11-6573-2014

Iijima, Y., Park, H., Konstantinov, P. Y., Pudov, G. G., and Fedorov, A. N. (2016). Active-layer Thickness Measurements Using a Handheld Penetrometer at Boreal and Tundra Sites in Eastern Siberia. *Permafrost Periglac. Process.* 28, 306–313. doi:10.1002/ppp.1908

Jones, B. M., Grosse, G., Arp, C. D., Miller, E., Liu, L., Hayes, D. J., et al. (2015). Recent Arctic Tundra Fire Initiates Widespread Thermokarst Development. *Sci. Rep.* 5, 15865. doi:10.1038/srep15865

Jorgenson, M. T., Shur, Y. L., and Pullman, E. R. (2006). Abrupt Increase in Permafrost Degradation in Arctic Alaska. *Geophys. Res. Lett.* 33, L02503. doi:10.1029/2005gl024960

Koven, C. D., Lawrence, D. M., and Riley, W. J. (2015). Permafrost Carbon−climate Feedback Is Sensitive to Deep Soil Carbon Decomposability but Not Deep Soil Nitrogen Dynamics. *Proc. Natl. Acad. Sci. USA.* 112, 3752–3757. doi:10.1073/pnas.1415123112

Koven, C. D., Ringeval, B., Friedlingstein, P., Ciais, P., Cadule, P., Khvorostyanov, D., et al. (2011). Permafrost Carbon-Climate Feedbacks Accelerate Global Warming. *Proc. Natl. Acad. Sci.* 108, 14769–14774. doi:10.1073/pnas.1103910108

Kumar, J., Collier, N., Bisht, G., Mills, R. T., Thornton, P. E., Iversen, C. M., et al. (2016). Modeling the Spatiotemporal Variability in Subsurface thermal Regimes across a Low-Relief Polygonal Tundra Landscape. *The Cryosphere* 10, 2241–2274. doi:10.5194/tc-10-2241-2016

Kurylyk, B. L., Hayashi, M., Quinton, W. L., McKenzie, J. M., and Voss, C. I. (2016). Influence of Vertical and Lateral Heat Transfer on Permafrost Thaw, Peatland Landscape Transition, and Groundwater Flow. *Water Resour. Res.* 52, 1286–1305. doi:10.1002/2015wr018057

Lara, M. J., McGuire, A. D., Euskirchen, E. S., Tweedie, C. E., Hinkel, K. M., Skurikhin, A. N., et al. (2015). Polygonal Tundra Geomorphological Change in Response to Warming Alters Future CO 2 and CH 4 Flux on the Barrow Peninsula. *Glob. Change Biol.* 21, 1634–1651. doi:10.1111/gcb.12757

Launiainen, S., Katul, G. G., Lauren, A., and Kolari, P. (2015). Coupling Boreal forest CO2, H2O and Energy Flows by a Vertically Structured forest Canopy - Soil Model with Separate Bryophyte Layer. *Ecol. Model.* 312, 385–405. doi:10.1016/j.ecolmodel.2015.06.007

Lawrence, D. M., Slater, A. G., and Swenson, S. C. (2012). Simulation of Present-Day and Future Permafrost and Seasonally Frozen Ground Conditions in CCSM4. *J. Clim.* 25, 2207–2225. doi:10.1175/jcli-d-11-00334.1

Lee, H., Swenson, S. C., Slater, A. G., and Lawrence, D. M. (2014). Effects of Excess Ground Ice on Projections of Permafrost in a Warming Climate. *Environ. Res. Lett.* 9, 124006. doi:10.1088/1748-9326/9/12/124006

Liljedahl, A. K., Boike, J., Daanen, R. P., Fedorov, A. N., Frost, G. V., Grosse, G., et al. (2016). Pan-Arctic Ice-Wedge Degradation in Warming Permafrost and its Influence on Tundra Hydrology. *Nat. Geosci.* 9, 312–318. doi:10.1038/ngeo2674

Melton, J. R., Wania, R., Hodson, E. L., Poulter, B., Ringeval, B., Spahni, R., et al. (2013). Present State of Global Wetland Extent and Wetland Methane Modelling: Conclusions from a Model Inter-comparison Project (WETCHIMP). *Biogeosciences* 10, 753–788. doi:10.5194/bg-10-753-2013

Meng, L., Hess, P. G. M., Mahowald, N. M., Yavitt, J. B., Riley, W. J., Subin, Z. M., et al. (2012). Sensitivity of Wetland Methane Emissions to Model Assumptions: Application and Model Testing against Site Observations. *Biogeosciences* 9, 2793–2819. doi:10.5194/bg-9-2793-2012

Miyazaki, S., Saito, K., Mori, J., Yamazaki, T., Ise, T., Arakida, H., et al. (2015). The GRENE-TEA Model Intercomparison Project (GTMIP): Overview and experiment Protocol for Stage 1. *Geosci. Model. Dev.* 8, 2841–2856. doi:10.5194/gmd-8-2841-2015

Moss, R. H., Edmonds, J. A., Hibbard, K. A., Manning, M. R., Rose, S. K., van Vuuren, D. P., et al. (2010). The Next Generation of Scenarios for Climate Change Research and Assessment. *Nature* 463, 747–756. doi:10.1038/nature08823

Nauta, A. L., Heijmans, M. M. P. D., Blok, D., Limpens, J., Elberling, B., Gallagher, A., et al. (2015). Permafrost Collapse after Shrub Removal Shifts Tundra Ecosystem to a Methane Source. *Nat. Clim Change* 5, 67–70. doi:10.1038/nclimate2446

Nitzbon, J., Westermann, S., Langer, M., Martin, L. C. P., Strauss, J., Laboor, S., et al. (2020). Fast Response of Cold Ice-Rich Permafrost in Northeast Siberia to a Warming Climate. *Nat. Commun.* 11, 2201. doi:10.1038/s41467-020-15725-8

Park, H., Fedorov, A. N., Zheleznyak, M. N., Konstantinov, P. Y., and Walsh, J. E. (2015). Effect of Snow Cover on Pan-Arctic Permafrost thermal Regimes. *Clim. Dyn.* 44, 2873–2895. doi:10.1007/s00382-014-2356-5

Park, H., and Hattori, S. (2004). Modeling Scalar and Heat Sources, Sinks, and Fluxes within a forest Canopy during and after Rainfall Events. *J. Geophys. Res.* 109, D14301. doi:10.1029/2003JD004360

Park, H., Iijima, Y., Yabuki, H., Ohta, T., Walsh, J., Kodama, Y., et al. (2011). The Application of a Coupled Hydrological and Biogeochemical Model (CHANGE) for Modeling of Energy, Water, and CO2exchanges over a Larch forest in Eastern Siberia. *J. Geophys. Res.* 116, D15102. doi:10.1029/2010JD015386

Park, H., Launiainen, S., Konstantinov, P. Y., Iijima, Y., and Fedorov, A. N. (2018). Modeling the Effect of moss Cover on Soil Temperature and Carbon Fluxes at a Tundra Site in Northeastern Siberia. *J. Geophys. Res. Biogeosci.* 123, 3028–3044. doi:10.1029/2018JG004491

Park, H., Tanoue, M., Ichiyanagi, K., Iwahana, G., and Hiyama, T. (2021). *Tracer Model-Based Quantitative Separation of Precipitation and Permafrost Waters*

Used for Evapotranspiration in a Boreal forest. Washington: ESSOAr. doi:10.1002/essoar.105063.1

Qiu, C., Zhu, D., Ciais, P., Guenet, B., Krinner, G., Peng, S., et al. (2018). ORCHIDEE-PEAT (Revision 4596), a Model for Northern Peatland CO2, Water, and Energy Fluxes on Daily to Annual Scales. *Geosci. Model. Dev.* 11, 497–519. doi:10.5194/gmd-11-497-2018

Riley, W. J., Subin, Z. M., Lawrence, D. M., Swenson, S. C., Torn, M. S., Meng, L., et al. (2011). Barriers to Predicting Changes in Global Terrestrial Methane Fluxes: Analyses Using CLM4Me, a Methane Biogeochemistry Model Integrated in CESM. *Biogeosciences* 8, 1925–1953. doi:10.5194/bg-8-1925-2011

Schuur, E. A. G., Bockheim, J., Canadell, J. G., Euskirchen, E., Field, C. B., Goryachkin, S. V., et al. (2008). Vulnerability of Permafrost Carbon to Climate Change: Implications for the Global Carbon Cycle. *BioScience* 58, 701–714. doi:10.1641/B580807

Sjöberg, Y., Coon, E., K. Sannel, A. B., Pannetier, R., Harp, D., Frampton, A., et al. (2016). Thermal Effects of Groundwater Flow through Subarctic Fens: A Case Study Based on Field Observations and Numerical Modeling. *Water Resour. Res.* 52, 1591–1606. doi:10.1002/2015wr017571

Subin, Z. M., Koven, C. D., Riley, W. J., Torn, M. S., Lawrence, D. M., and Swenson, S. C. (2013). Effects of Soil Moisture on the Responses of Soil Temperatures to Climate Change in Cold Regions*. *J. Clim.* 26, 3139–3158. doi:10.1175/JCLI-D-12-00305.1

Turetsky, M. R., Abbott, B. W., Jones, M. C., Anthony, K. W., Olefeldt, D., Schuur, E. A. G., et al. (2020). Carbon Release through Abrupt Permafrost Thaw. *Nat. Geosci.* 13, 138–143. doi:10.1038/s41561-019-0526-0

Turetsky, M. R., Abbott, B. W., Jones, M. C., Walter Anthony, K., Olefeldt, D., Schuur, E. A. G., et al. (2019). Permafrost Collapse Is Accelerating Carbon Release. *Nature* 569, 32–34. doi:10.1038/d41586-019-01313-4

Ulrich, M., Matthes, H., Schirrmeister, L., Schütze, J., Park, H., Iijima, Y., et al. (2017). Differences in Behavior and Distribution of Permafrost-related Lakes in C Entral Y Akutia and Their Response to Climatic Drivers. *Water Resour. Res.* 53, 1167–1188. doi:10.1002/2016WR019267

van Genuchten, M. T. (1980). A Closed-form Equation for Predicting the Hydraulic Conductivity of Unsaturated Soils. *Soil Sci. Soc. America J.* 44, 892–898. doi:10.2136/sssaj1980.03615995004400050002x

Conflict of Interest: The authors declare that the research was conducted in the absence of any commercial or financial relationships that could be construed as a potential conflict of interest.

The handling editor is currently organizing a Research Topic with one of the authors AF.

Publisher's Note: All claims expressed in this article are solely those of the authors and do not necessarily represent those of their affiliated organizations, or those of the publisher, the editors and the reviewers. Any product that may be evaluated in this article, or claim that may be made by its manufacturer, is not guaranteed or endorsed by the publisher.

frontiers in Earth Science

ORIGINAL RESEARCH
published: 24 September 2021
doi: 10.3389/feart.2021.683730

Degradation of Arable Soils in Central Yakutia: Negative Consequences of Global Warming for Yedoma Landscapes

Roman Desyatkin[1]*, *Nikolai Filippov*[1], *Alexey Desyatkin*[1], *Dmitry Konyushkov*[2] and *Sergey Goryachkin*[3]

[1]*Laboratory of Ecosystem Research of Cold Regions, Institute of Biological Problems of the Cryolithozone, Siberian Branch of the Russian Academy of Sciences, Yakutsk, Russia,* [2]*Department of Genesis, Geography, Classification and Digital Cartography of Soils, Dokuchaev Soil Science Institute, Russian Academy of Sciences, Moscow, Russia,* [3]*Department of Soil Geography and Evolution, Institute of Geography, Russian Academy of Sciences, Moscow, Russia*

OPEN ACCESS

Edited by:
Go Iwahana,
University of Alaska Fairbanks,
United States

Reviewed by:
Nicolas Jelinski,
University of Minnesota Twin Cities,
United States
Chien-Lu Ping,
University of Alaska Fairbanks,
United States

***Correspondence:**
Roman Desyatkin
rvdes@ibpc.ysn.ru
rvdes@mail.ru

Specialty section:
This article was submitted to Cryospheric Sciences, a section of the journal Frontiers in Earth Science

Received: *22 March 2021*
Accepted: *23 August 2021*
Published: *24 September 2021*

Citation:
Desyatkin R, Filippov N, Desyatkin A, Konyushkov D and Goryachkin S (2021) Degradation of Arable Soils in Central Yakutia: Negative Consequences of Global Warming for Yedoma Landscapes. Front. Earth Sci. 9:683730. doi: 10.3389/feart.2021.683730

Global warming, which is especially intensive (up to 0.08°C yr^{-1}) in permafrost area of Central Yakutia, has dramatic consequences for scarce arable land resources in this region. In Yedoma landscapes, intense permafrost thawing on arable fields unprotected by forest vegetation transforms the surface microtopography with the formation of residual thermokarst mounds (byllars) of 6–10 m in diameter surrounded by a polygonal network of hollows of 0.3–1.5 m in depth above melting ice wedges. This process also takes place on former croplands abandoned in the recent decades because of socioeconomic reasons. It is accompanied by a significant transformation of the previously highly likely homogeneous soil cover composed of Cambic Turbic Cryosols (Sodic) into differentiated complexes of permafrost-affected Stagnic Cambisols or Calcic Solonetzes (Turbic) on the mounds and Calcic Stagnic Solonetzes (Turbic) in the microlows. Surface soil horizons on the mounds have a strongly to very strongly alkaline reaction (pH 8.5–9.5) and low (<2%) organic carbon content; a wavy line of effervescence is found at a depth of 15–30 cm. Soils in the microlows have a close to neutral reaction in the upper horizons (pH 6.2–7.5); higher organic carbon content (2–3%); more pronounced textural differentiation of the profile with the formation of typical natric Btn and, in some cases, overlying eluvial E horizons; deeper (50–60 cm) line of effervescence; and clear stagnic features in the lower part of the profile. In the case of shallow embedding by ice wedge, the lowermost part of the soil in the microlow is characterized by the low bulk density (1.04 g cm^{-3}) because of the appearance of hollows after thawing of the ice-rich transient layer and melting of the top of ice wedges. This may be indicative of the further soil subsidence in the future and the appearance of initial thermokarst lakes (dyuedya) within the Yedoma terrain with its transformation into the alas type of landscape. Rapid thermokarst-driven development of microtopography followed by differentiation of the soil cover with increasing soil alkalinity on the microhighs and soil textural differentiation and overmoistening of deep layers in the microlows prevents the return of abandoned arable land to agriculture in Yedoma landscapes.

Keywords: permafrost thawing, abandoned arable land, Cambic Turbic Cryosols, Calcic Stagnic Solonetzes, thermokarst formation, boreal forest zone

INTRODUCTION

Global climate change poses a serious challenge for humankind (IPCC, 2014). It is a well-known factor of changes in world agriculture and food supply (Rosenzweig and Parry, 1994). In the recent decades, unprecedented climate changes have taken place in the Arctic and the adjacent area of continental permafrost (Schuur and Mack, 2018). The rise in temperature in the northern high-latitude regions has been 2.5 times faster than on the entire Earth (IPCC, 2014). This phenomenon has attracted the attention of specialists in agriculture sending them in search of new opportunities for sustainable farming in these traditionally poorly cultivated areas both in the entire Circumpolar North (Poeplau et al., 2019) and in its particular regions (Stevenson et al., 2014; Lader et al., 2019). Some tendencies of the development of agriculture in cold regions seem to be very optimistic; thus, in 2012–2017, the number of farms in Alaska increased by up to 30% (Crampton, 2019). However, it is also known that cropland areas of the North display different tendencies. Thus, in most of northern Russia regions, a pronounced decrease in cropland area took place in the recent past (Lyuri and Goryachkin, 2008). The reasons for this decrease may be different. In this study, we consider adverse effects of natural processes taking place due to climate warming in the permafrost environment of Central Yakutia.

By the early 1640s, vast territories of Siberia were colonized by the Russian state. In the second half of the 17th century, after the integration of lands in the middle Lena reaches, Russian arable farming began to be practiced in this harsh environment (Safronov, 1961). Early-ripening varieties of grain crops—spring wheat, rye, and oats—were sown. Despite very unstable harvests from year to year, the area of arable land was gradually expanded to meet the needs of population. By the time of the collapse of the Soviet state, cropland area reached more than 140 thousand hectares (Desyatkin, 2004). After the collapse of the Soviet Union, state-owned agricultural enterprises ceased to exist. Since then, cropland area in the middle Lena basin has been decreasing from year to year. At present, there are no more than 40 thousand hectares of regularly cultivated cropland. Under conditions of global climate change, abandoned arable land is subjected to a strong transformation of the soil cover (Desyatkin, 2018).

In the presence of ice-rich permafrost with ice wedges (Yedoma, Ice Complex deposits), an increase in the depth of seasonal soil thawing leads to the melting of underground ice (Jorgenson et al., 2015; Veremeeva et al., 2021). In this case, not only the release of additional moisture previously stored in the permafrost (Jorgenson, 2013) but also the formation of deep thermokarst hollows above melting ice wedges take place (Jorgenson et al., 2015). These processes are well known for permafrost-affected terrain involved in agriculture in Alaska (Péwé, 1954). Degradation of the Yedoma ice complex proceeds until the ice reserves are completely depleted (Shur and Jorgenson, 2007). As a rule, thermal erosion of the Yedoma ice complex is associated with physical soil erosion and redeposition of soil material and proceeds at a relatively fast rate leading to the formation of young thermokarst landscapes and changing the water budget of permafrost territories (Desyatkin and Desyatkin, 2019).

The entire territory of the Republic of Sakha (Yakutia) lies in the permafrost zone. Especially, noticeable processes of transformation of the soil cover occur in the most developed agricultural regions of Central Yakutia—the Lena–Amga interfluve and, to a smaller extent, the Tabaga area on the left bank of the Lena River (Boike et al., 2016). As a result of the collapse of large agricultural enterprises in the early 1990s, thousands of hectares of arable land developed from under taiga vegetation on the Yedoma ice complex have been abandoned in the recent decades in these regions. The thermokarst process on arable land leads to the transformation of the soil cover over large areas removed from the agricultural use.

In this study, we analyzed the change in morphological features and some properties of soils affected by agricultural land use and climate change in the Yedoma landscape of Central Yakutia and considered them in the context of climate-induced soil changes in other cold regions. However, we did not make a direct comparison of soils under intact forests and under cropland and did not evaluate the rate of these changes but instead focused on soil features occurring after decades of soil use in arable farming.

MATERIALS AND METHODS

Study Area

The research area is located in Central Yakutia, northeast Russia. The first study site—Churapcha—is located to the east of the Lena River, in the central part of the Lena–Amga interfluve near the town of Churapcha, on the medium-level ancient erosional–accumulative Abalakh terrace. The second site—Tabaga—is found to the west of the Lena River on the medium-level Tabaga terrace of approximately the same elevation near the village of Tabaga (**Figure 1**).

These terraces are composed of the Quaternary loamy and loamy sandy lacustrine–alluvial sediments with ice wedges (**Figure 2**) underlain by alluvial sands. The entire area lies in the zone of continuous permafrost with a thickness over 400 m and with temperatures at the base of the layer of annual temperature fluctuations varying from –1 to –5°C (Brown et al., 1997).

The climate of the Lena-Amga interfluve belongs to the Dwc type according to the Köppen–Geiger climate classification system (Beck et al., 2018) and is characterized by the following parameters (Churapcha/Yakutsk[1] weather stations): mean annual air temperature −10.3/−7.5°C, mean air temperature of the warmest month (July) 18.7/20°C, and mean air temperature of the coldest month (January) −42.5/−36.3°C. Thus, the annual amplitude of mean monthly temperatures reaches 61.2/56.3°C. The mean annual precipitation is 296/280 mm with a monthly minimum (5/6 mm) in February

[1]Yakutsk meteorological station is the nearest one (~30 km) for the Tabaga site.

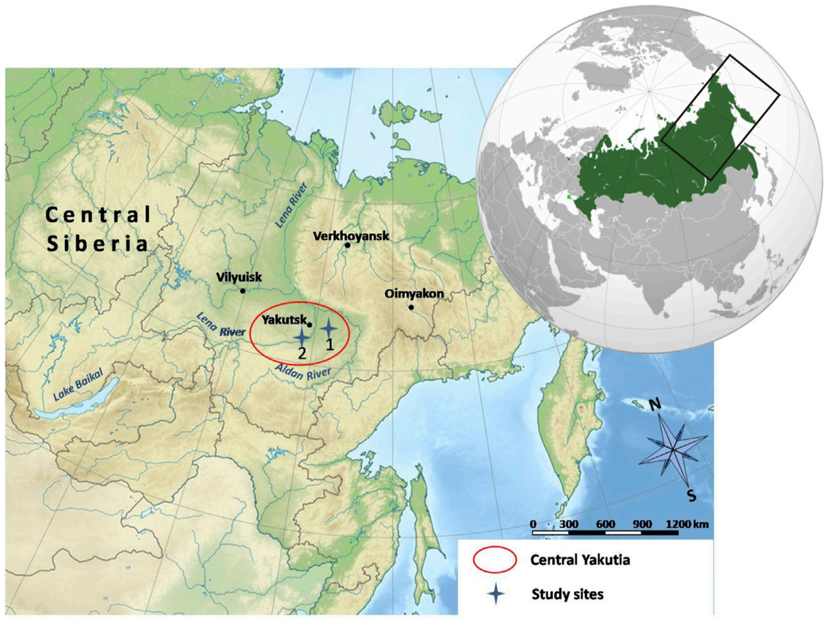

FIGURE 1 | Study area. Key sites: (1) Churapcha and (2) Tabaga.

FIGURE 2 | The upper boundary of an ice wedge lies at a depth of about 2 m.

and a maximum (52/47 mm) in July/August, respectively (https://en.climate-data.org/asia/russian-federation/sakha-republic-875/).

In the past 30 years, climate warming in Central Yakutia has been clearly pronounced. The rate of the rise in the mean annual air temperature (up to 0.08°C/yr) in this area is one of the highest in Russia. In the 1960s–1970s, the warming was not so noticeable; it accelerated in the 1980s (Skachkov, 2000). The last decade of the 20th century with the mean annual air temperature of –8.7°C was the warmest decade in the history of meteorological observations in Central Yakutia (Grigor'ev et al., 2010).

Since the appearance of permafrost (about 500–700 ka ago), soils have been developing within a thin active layer in the absence of drainage and active removal of the products of pedogenesis and weathering. Under these conditions, soil

FIGURE 3 | The initial stage of thermokarst degradation of the soil cover of abandoned arable land in the area of Churapcha with typical Yedoma-alas landscape. Photo by K. Abrosimov.

solutions migrate only within the active layer, and the products of weathering and soil formation are gradually accumulated in it. Against the background of dry continental climate, this has resulted in the widespread soil salinization (Desyatkin, 1993).

Partial degradation of ground ice in this area in the Holocene led to the development of thermokarst Yedoma–alas landscape with lakes and meadows (**Figure 3**) (Veremeeva et al., 2021). Alases (thermokarst depressions) are characterized by herbaceous vegetation, under which a group of specific soils are developed (Desyatkin, 1991); some of them are saline (Desyatkin, 2008). Alases of different sizes (from dozens of meters to several kilometers) are scattered amidst the predominant boreal forest vegetation. On the map of terrestrial ecoregions of the world (Olson et al., 2001), this territory is shown as "Boreal forests/Taiga." Russian specialists name this territory as the Central Yakutia taiga-alas soil province (Elovskaya and Konorovskii, 1978). Forest vegetation in the region is represented by larch (*Larix cajanderi* L.) and birch (*Betula pendula* R.) forests with herbs in the ground cover (Timofeev et al., 1994).

Owing to the recent rise in air temperatures, the depth of seasonal soil thawing has increased throughout the studied area (Desyatkin et al., 2015). When the depth of seasonal soil thawing reaches the upper boundary of ice wedges of the Yedoma ice complex, their melting begins. This leads to the appearance of initial forms of alas development—byllars—residual thermokarst mounds of up to 7–10 m in diameter and 0.5–1.6 m in height relative to the polygonal network of thermokarst hollows (microlows) forming above melting ice wedges (**Figures 4**, **5A**) (Gavril'ev et al., 2005). In some places, ice melting leads to the formation of young and relatively small thermokarst lakes, dyuedya (**Figure 5B**). These processes were described in more detail earlier (Jones et al., 2009; Desyatkin et al., 2013). The appearance of the mound–hollow microrelief on the flat surface of abandoned arable land leads to land degradation and difficulty of its use for arable farming; it also causes transformation of the formerly more or less homogeneous soil cover of agricultural fields developed in the 1960s after clearing of forest vegetation.

Both study sites, as well as the entire territory of Central Yakutia, belong to the zone of high-risk farming under severe climatic conditions: a short growing season (65–100 days in dependence of the natural weather cycles), typical late spring and early summer (until June 15) and early autumn (after August 10–15) frosts, and wide interannual fluctuations of precipitation (from 75 to 250 mm during the warm season). In addition, farming is threatened by the periodic mass reproduction of locusts (up to 1,200–1,500 insects/m^2). For these reasons, the yield of cereal crops in different years varies from 0.3–0.5 to 1.5–2.8 t/ha. The gross harvest of meadow roughage during the 11-year solar cycle ranges from 0.2–0.3 to 1.5–1.8 t/ha. Under these conditions, the traditional branch of agriculture—cattle breeding and horse breeding—lacks solid fodder base and experiences wide fluctuations in the number of cattle and horses (Neustroev et al., 2017).

Field studies of the influence of initial thermokarst landforms on the morphogenetic properties of soils were performed in July 2012 on the arable field abandoned in the early 1990s, 1.5 km southeast of the town of Churapcha (site 1), and in August 2012, near Tabaga (site 2), where the cropland was abandoned in the early 1980. At the Churapcha site, soil pits were examined on the top (pit C-01-12) and slope (pit C-02-12) of a thermokarst mound (byllar) and in the bottom of a thermokarst hollow (microlow) between neighboring byllars (pit C-03-12); the hollow system had a polygonal pattern (**Figure 4**). On the tops of some byllars, the network of frost cracks could be observed.

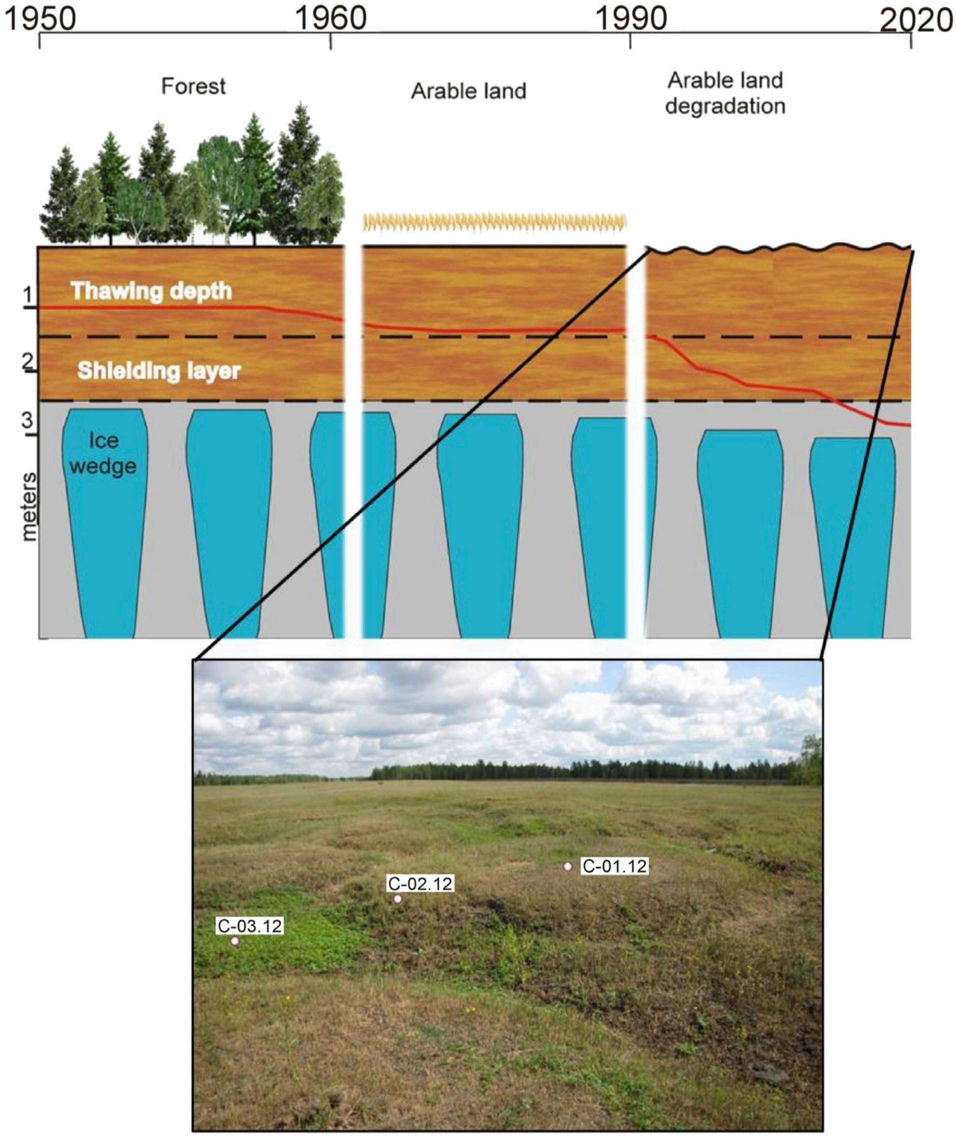

FIGURE 4 | Development scheme, general view, and location of studied soil pits on the former arable field (Churapcha site) abandoned in the early 1990s and subjected to thermokarst with the formation of byllar microtopography.

At the Tabaga site, a trench crossing the top of byllar (pit T-2.1), the slope of neighboring byllar (pit T-2.2), and the microlow between byllars (pit T-2.3) were examined. In this case, the byllar microtopography was less pronounced: the diameter of thermokarst mounds was about 3–5 m, and the amplitude of heights between their tops and microlows was about 0.5 m (**Figure 5A**). However, on an adjacent former arable field, the development of thermokarst processes was much more intense and led to the formation of thermokarst badland and initial small deeply (4–6 m) incised thermokarst lakes (dyuedya) (**Figure 5B**).

Methods

In the field, morphological descriptions of the soil profiles and measurements of thawing depths were conducted. Designation of soil horizons and soil names followed the Guidelines for Soil Description (FAO, 2006) and the WRB system (IUSS WG WRB, 2015). Physical soil samples were taken from every horizon and air-dried. Bulk density, pH, particle-size distribution, and organic carbon content were determined in the samples taken with a cutting ring of 100 cm^3 in volume from each soil horizon in triplicate.

The pH of soil water suspensions (1: 2.5) was measured with an F-8 pH meter (Horiba, Japan) after shaking the suspensions for 2 h, or once mixing by hand and standing for 30 min. The bulk density was determined by the gravimetric method with the soil drying in a thermostat at 105°C.

The organic carbon content was determined by wet combustion using Tyurin's method. This procedure is similar

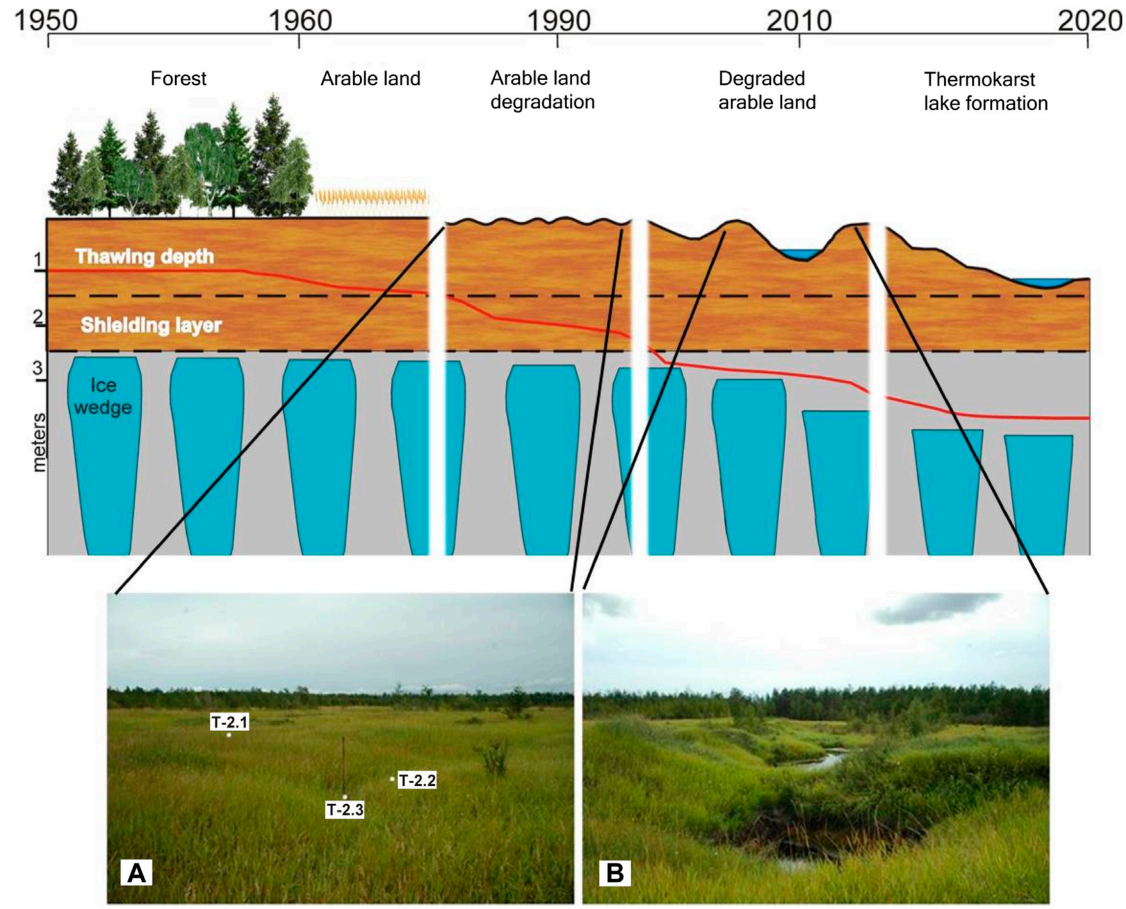

FIGURE 5 | Development scheme, general view, and location of studied soil pits on the former arable field (Tabaga site) abandoned in the 1970s–1980s and subjected to thermokarst with the formation of **(A)** byllar and **(B)** dyuedya microtopography.

to the Walkley–Black method and involves the combustion of the organic matter with a 1 : 1 mixture of 0.14 M $K_2Cr_2O_7$ and concentrated H_2SO_4 at 150°C for 20 min and titration with ferrous sulfate solution or colorimetric measurement on a SPECOL 211 spectrometer at 590 nm (van Reeuwijk, 2002).

Particle-size distribution analysis for Tabaga site was applied to the fine earth fraction (<2 mm). After ultrasound dispersion and sieving, oxidation of organic matter by H_2O_2, removal of carbonates by HCl, and shaking with dispersing agent ($NaPO_3$ + Na_2CO_3), the sand fraction was separated from other fractions using a 63-μm sieve. The clay (<2 μm) and silt (2–63 μm) fractions were determined by pipette method (van Reeuwijk, 2002). The same pretreatment was applied to samples from the Churapcha site. However, the fractions were determined according to the Russian system of particle-size classes: sand, 1–0.05 mm; silt, 0.05–0.001 mm; and clay, <0.001 mm. In this study, the original data on the Churapcha site are recalculated to the international scale (2000–63–2 μm) using Shein's model (Shein, 2009).

The determination of the cation exchange capacity and exchangeable bases was conducted in accordance with the methodological guidance of "Procedures for Soil Analyses" (van Reeuwijk, 2002) by the ammonium acetate method using a programmable mechanical vacuum extractor (Model 24VE). In the non-carbonate and non-saline soil samples, the exchangeable bases were displaced by 1 M NH_4OAc solution (pH 7.0), sample weight 2.5 g for mineral specimens and 1 g for organic specimens. In saline and calcareous soils, the preliminary washing of the samples with 80% ethanol was performed. Then, exchangeable bases were displaced by 1 M NH_4OAc (pH 8.2). The cation exchange capacity (CEC) was determined using a solution of 0.9 M NaOAc (pH 8.2). The concentrations of Ca^{2+}, Mg^{2+}, K^+, and Na^+ in the solution were measured on an atomic emission spectrometer with inductively coupled plasma Spectro CirosCCD (Germany, Spectro Analytical Instruments GmbH).

RESULTS

The whole sets of morphological, micromorphological, and analytical data for the Tabaga and Churapcha sites were presented in two guidebooks (Desyatkin et al., 2013, 2017). For the Tabaga site, this information is accessible on the Web

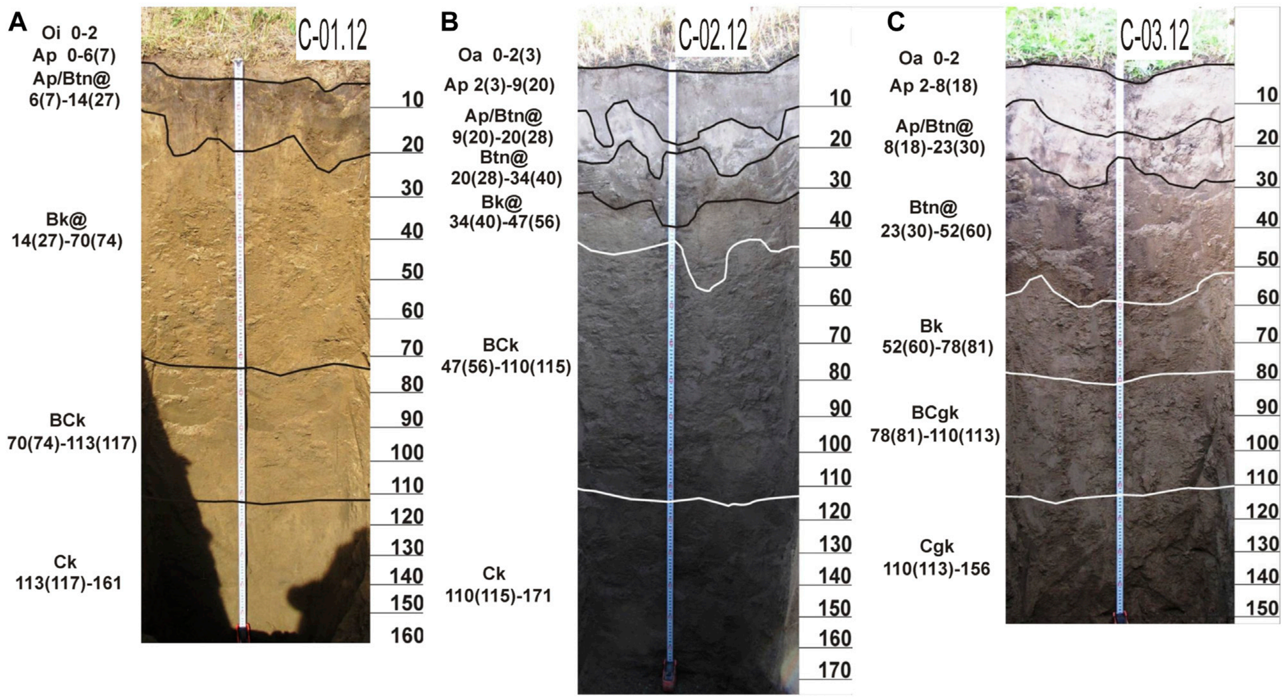

FIGURE 6 | Horizonation of soil profiles studied at the Churapcha site: **(A)** top of byllar, pit C-01-12; **(B)** slope of byllar, pit C-02-12; and **(C)** microlow between byllars, pit C-03-12.

(https://www3.ls.tum.de/fileadmin/w00bds/boku/downloads/wrb/Guide_Sakha_final.pdf).

Field Data. Soil Profiles

Churapcha site. A general view of the studied soil profiles and their horizonation is presented in **Figure 6**. Brief descriptions of the specificity of soil morphology are given below.

Pit C-01-12 (61°59.136′ N, 132°29.807′ E) was examined on the top of a byllar within the abandoned arable field 1.5 km northwest of the town of Churapcha on July 17, 2012. The soil was developed under steppe herbs (*Artemisia commutata, Vicia cracca* L., *Potentilla anserina* L., *Taráxacum officinále*, etc.) covering about 45–50% of the surface; cryogenic cracks of up to 10 cm in width were seen on the soil surface. The parent material was represented by calcareous loesslike loam. From the depth of 161 cm, the parent material was in the frozen state.

In the WRB system, this soil can be classified as a Calcic Solonetz (Loamic, Turbic) with the profile Oi—Ap—Ap/Btn@—Bk@—BCk—Ck in the FAO system of horizon designation. This profile, as well as the other two studied profiles, cannot be classified as Cryosols in spite of the presence of frozen horizons. This is because the maximum thawing depth (in September) is deeper than 2 m.

Note the presence of a thin litter layer (O) consisting of weakly decomposed residues of herbs on the mineral soil surface. The former plow (Ap) horizon is differentiated; in its upper part, the modern humus (Ap) horizon of gray color with brownish tint is formed. The lower part of the plow horizon is mixed by cryogenic processes with the strongly compacted subsoil now representing a solonetzic (Btn) horizon. Fragments of the plowpan are marked by the darkest color in the profile. This horizon (Ap/Btn@) is dissected by cryogenic fissures filled with tongues and pockets of humified material. The underlying carbonate-accumulative (Bk@) horizon represents effervescing loesslike loam of yellowish (pale brown) color with a total thickness of 47–56 cm; this horizon is considerably thicker than in the other two soil pits. The transitional BCk horizon with residual carbonates represents a slightly dry, dense, strongly effervescing silt loam with coarse angular blocky structure; its thickness is up to 43 cm. The parent material (Ck) is a grayish, wet, moderately compact, calcareous silt loam with coarse blocky structure. The thawing depth on the day of the soil description was 161 cm; the ice content in the underlying seasonally frozen layer (Ck) was low.

Pit C-02-12 (61°59.136′ N, 132°29.807′ E) was described 4 m away from pit C-01-12 on the slope of southwestern aspect of the same byllar on July 17, 2012. Steppe herbs with a higher participation of *Potentilla anserina* L. and grasses *Poa praténsis* L. and *Elytrígia répens* L. covered 65–70% of the surface. The soil developed from the same parent material (calcareous loesslike loam); the thawing depth reached 171 cm.

The soil had the following horizonation: Oa—Ap—AEp/Btn@—Btn@—Bk@—BCk—Ck—Ckf. It was also classified as a Calcic Solonetz (Albic, Loamic, Turbic).

The uppermost brown-colored horizon of this soil is densely penetrated by roots and contains abundant plant residues of different decomposition degrees. As a result of deformation of the surface microtopography, this soil is now in a relatively well-drained slope position, which could enhance leaching processes and the removal of labile fractions of the organic matter from the former plow horizon. This horizon acquired a light gray color with brownish tint. The underlying solonetzic (Btn) horizon has a thickness of about 12–14 cm [from 20 (28) to 34 (40) cm] and is less disturbed by the cryogenic processes in comparison with the soil on the top of the byllar. This horizon clearly differs from the whitish overlying layer and from the underlying carbonate-accumulative (Bk) horizon. The transitional BCk horizon has the greatest thickness (42 cm) among the three studied soils. The thawing depth in this soil reached 171 cm.

Pit C-03-12 (61°59.136′ N, 132°29.807′ E) was examined on the same day in the bottom of the microlow between neighboring byllars, 3 m from pit C-02-12. This soil developed under mesophytic steppe herbs with a predominance (up to 70%) of *Potentilla anserina* L.; almost the entire surface (90–95%) was covered by plants. The parent material—calcareous loesslike loam—was in the frozen state from the depth of 156 cm.

The soil profile consisted of the following horizons: Oa—Ap—AEp/Btn@—Btn@—Bk—BCgk—Cgk. It was classified as a Calcic Stagnic Solonetz (Albic, Loamic, Turbic).

In this soil, the illuvial (solonetzic) Btn horizon is found somewhat deeper and has a greater thickness than that in the soils of the byllar. The light-colored zone of eluviation is also thicker. Thus, the upper- and middle-profile horizons are somewhat extended under the impact of the subsidence of the lower horizons because of the melting of the ice wedge found below the soil profile. The thickness of the middle-profile carbonate-accumulative (Bk) horizon is reduced. The lower part of the profile is marked by the presence of stagnic features.

The depth to the horizon of parent material (Ck) with minimal indications of pedogenetic transformation in the three studied profiles is approximately the same (about 110 cm). In general, though the sequences of the major horizons in the three studied profiles look similar, their thicknesses are different. The thickness of the upper part of the profile with the zones of eluviation and illuviation of substances is somewhat greater on the slope of byllar than on its top and gains maximum in the soil of the microlow between neighboring byllars. The soil on the top of byllar was formally classified as Solonetz because of the high percentage of sodium in the soil exchange complex (see below). However, weak differentiation in clay makes it closer to Sodic Cambisols.

Tabaga site. The trench examined at the Tabaga site (61°48′55.7″ N, 129°31′51.5″ E) included three reference soil profiles (**Figure 7**). In 2013, they were demonstrated to the participants of the WRB “Mammoth” tour (Desyatkin et al., 2013). After discussion in the field and careful examination of field and laboratory data, the classification position of these soils in the WRB system given by Desyatkin et al.(2013) was specified by field tour participants, and in this study, we use the soil names approved by them.

The surface microtopography at the Tabaga site was less pronounced than at the Churapcha site, and the size of thermokarst mounds (byllars) and microlows between them was somewhat smaller. Steppe herbs covered almost 100% of the surface and had a more mesophytic character in the microlows. However, despite more homogeneous surface conditions, the differentiation of the soil profiles within the studied trench was very distinct (**Figure 7**).

Pit T-2.1 (profile 2-1 in the guidebook) characterized a part of the trench crossing the top of byllar. It had the following horizonation: A—Bwk—BCkg@—BCkg—2BCkg. The humus horizon (former plow layer) had a brownish-black color, silt loamy texture, and fine subangular blocky structure. Its lower boundary was abrupt and slightly wavy. The middle-profile horizons (Bwk, BCkg@, BCkg) were characterized by dull yellow to yellowish-gray color, platy to subangular blocky structure, some horizontal layering, and distinct effervescence because of the abundance of dispersed calcite grains and few fine (d ~ 2 mm) soft carbonate nodules (in the Bwk horizon). It was classified as Stagnic Cambisol (Sodic, Turbic, Pisocalcic, Episiltic).

Pit T-2.2 (profile 2-3 in the guidebook) characterized the soil on the slope of adjacent byllar. Its horizonation (A—E—Btn—Bk—BCk) displayed a pronounced differentiation into the eluvial and clay-illuvial parts. This profile was less cryoturbated, and the depth of effervescence (60 cm) occupied an intermediate position. It was classified as Calcic Mollic Solonetz (Albic, Siltic, Turbic).

Pit T-2.3 (profile 2-2 in the guidebook) characterized the soil in the microlow with the following horizonation: A—AE@—EA@—E@—EB—Btn—BCk. It had a much thicker (30–46 cm) and darker humus horizon, distinct features of cryoturbation in the middle-profile horizons, and a pronounced differentiation into the eluvial (AE@—E@) and clay-illuvial (EB@—Btn) parts. The depth of effervescence was much deeper (120 cm). It was classified as Mollic Hyposalic Solonetz (Glossalbic, Humic, Siltic, Turbic).

Descriptions of these soil profiles at the initial stage of arable land degradation were given by Gavril’ev et al. (2005). Our research attests to the acceleration of transformation processes.

In general, the patterns of the lateral differentiation of the soils by the elements of byllar microtopography at the two studied sites have much in common. The least differentiated soil profiles with a shallow depth of effervescence are observed on the tops of byllars. The thickness of the humus horizon noticeably increases in the soils of the microlows. The eluvial-illuvial differentiation enhances on the slopes of byllars and in the microlows between them. At both sites, it has led to the appearance of the bleached eluvial (E) horizon. At the Churapcha site, stagnic features in the soil profiles are clearly pronounced in the microlow. At the Tabaga site, they are observed in the lower part of the soil under the top of the byllar and are absent in the soils on its slope and in the microlow, which were excavated to a shallower depth. It is probable that they should appear in deeper horizons. Note, however, that the redistribution of soil water by the elements of the less pronounced byllar microtopography at the Tabaga site should be less active than that at the Churapcha site.

Laboratory Data. Bulk Density, Soil Reaction, Particle-Size Distribution, and Organic Carbon Content

Laboratory data on soil reaction (pH), organic carbon content, particle size distribution, and bulk density (**Table 1**) are informative indicators of soil transformation during the

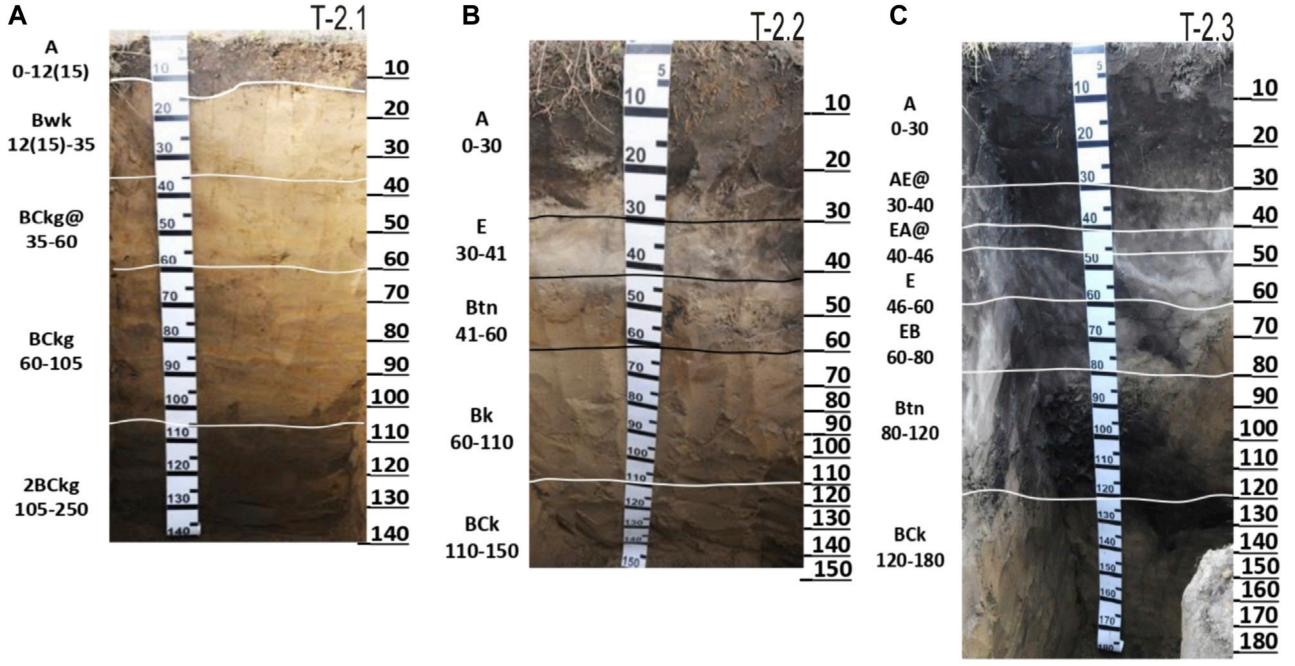

FIGURE 7 | Horizonation of soil profiles studied at the Tabaga site: **(A)** top of byllar, pit T-2.1; **(B)** slope of byllar, pit T-2.2; and **(C)** microlow between byllars, pit T-2.3.

development of thermokarst processes. We also use information on the proportion of sodium and magnesium cations in the sum of exchangeable cations.

Soil reaction. As can be seen from **Table 1**, the pH values of the soils on the top of byllars at both sites indicate a very strongly alkaline reaction throughout the profile (pH_{water} > 9.5). Slightly lower pH values characterize the soils on the slopes of byllars, but a different distribution of pH values is observed in the soils of microlows, in which the upper horizons have a neutral reaction because of leaching of carbonates and, evidently, the absence (or low content) of exchangeable sodium. In the soil of the microlow at the Churapcha site, a general decrease in alkalinity is observed throughout the soil profile. In the analogous soil at the Tabaga site, where the redistribution of moisture by the elements of the microtopography is less pronounced (because of their smaller sizes), the soil reaction in the deep part of the profile reaches strongly alkaline values. Microlows are the areas of concentration of surface runoff, and thermokarst-driven loosening of the lower part of the soil at the Churapcha site (see below) enhances infiltration of water with dissolved substances and its withdrawal from the soil profile into thermokarst voids (**Figure 8**).

The organic carbon content in the soil profiles is generally very low (0.4–0.6%), except for the topmost thin organic horizons (Churapcha site) and humus horizons. The maximum C_{org} content in the humus horizons at both sites is observed in the soils of microlows (2.77% at the Churapcha site and 2.95% at the Tabaga site). The uneven distribution of C_{org} in the soil of the microlow at the Tabaga site is noted. A local maximum (2.40%) at the depth of 40–46 cm (pit T-2.3., EA@ horizon) is explained by the influence of cryoturbation with a deep penetration of humus tongue.

The proportion of sodium and magnesium cations in the sum of exchangeable cations is indicative of the possibility of manifestation of the solonetzic process. Soils of the Churapcha site have more sodium and magnesium in their exchange complex than soils of the Tabaga site. However, the Btn horizons of soils at both sites have the high content of sodium and magnesium cations in their exchange complex.

Particle-size distribution data attest to a coarser texture and higher content of sand fractions in the soils of the Tabaga site. The contents of clay and silt fractions in the soils of the Churapcha site vary within 30–56% with clear maximums of the clay content in the clay-illuvial (Btn) horizons. At the Tabaga site, silt fractions predominate throughout the soil profiles, except for the BCkg@ horizon of pit T-2.1 with a predominance (44–51%) of sand fractions. Similar to the Churapcha site, maximum values of the clay content are observed in the Btn horizon of the soil developed in the microlow. Thus, the processes of clay illuviation are most pronounced in this geomorphic position.

Bulk density is found to be dynamic. Thus, on cultivated fields, freshly tilled soil is most friable; then, it compacts, and its bulk density gradually comes to an equilibrium state. As it is known, during thermokarst transformation of soils under the impact of melting of subsurface ice wedges, soil subsidence takes place in some areas (above ice wedges), whereas other areas keep their former position (byllars or thermokarst mounds). By studying the bulk density of the soils on different elements of the microtopography, it is possible to determine the effect of

TABLE 1 | Laboratory data on soil samples from the Churapcha and Tabaga key sites.

Pit no.	Horizon	Depth, cm	pH_{H2O}	C_{org}, %	Clay	Silt	Sand	Bulk density, g cm^{-3}
					%			
Churapcha key site								
C-01-12, top of byllar	Oi	0–2	8.16	13.61	—	—	—	0.21
	Ap	2–6 (7)	9.5	1.88	29	59	12	1.19
	Ap/Btn@	6–14 (27)	9.69	0.92	31	62	7	1.38
	Bk@	14 (27)–70	9.66	0.43	30	58	12	1.31
	BCk	70–113	9.6	0.67	30	56	14	1.27
	Ck	113–161	9.54	0.82	30	59	11	1.53
C-02-12, slope of byllar	Oa	0–2 (3)	7.65	16.31	—	—	—	0.25
	Ap	2–9 (20)	9.15	1.39	26	64	10	1.27
	AEp/ Btn@	9–20 (28)	8.69	1.19	13	70	18	1.46
	Btn@	20–34 (40)	9.54	1.29	36	54	10	1.24
	Bk@	34–47 (56)	9.64	0.49	35	57	8	1.49
	BCk	47–110 (115)	9.6	0.42	29	62	9	1.49
	Ck	110–171	9.06	0.46	30	60	10	1.44
C-03-12, microlow	Oa	0–2	6.13	21.19	—	—	—	0.31
	Ap	2–8 (18)	6.19	2.77	20	66	15	1.25
	AEp/ Btn@	8–23 (30)	7.34	1.51	25	66	9	1.39
	Btn@	23–52 (60)	8.65	0.73	41	51	8	1.31
	Bk	52–78 (81)	8.9	0.45	32	61	8	1.31
	BCgk	78–110 (113)	8.96	0.53	31	60	9	1.36
	Cgk	110–156	8.92	0.56	30	61	9	1.04
Tabaga key site								
T-2.1, top of byllar	A	0–12 (15)	8.80	1.64	6	60	34	1.27
	Bwk	12 (15)–35	9.30	0.33	9	59	32	1.54
	BCkg@	35–60	9.75	0.28	11	38	51	1.50
	BCkg	60–105	9.75	0.42	12	44	44	1.42
	2BCkg	105–250	9.60	0.42	16	57	27	N.d.
T-2.2, slope of byllar	A1	0–22	7.35	2.01	15	53	32	1.48
	A2	22–30	8.55	1.66	15	53	32	1.49
	E	30–41	8.55	0.33	6	56	38	1.58
	Btn	41–60	9.45	0.65	15	53	32	1.64
	Bk	60–110	9.55	0.59	18	53	29	N.d.
	BCk	110–150	9.50	0.29	13	45	42	N.d.
T-2.3, microlow	A1	0–4	6.95	2.95	16	50	34	1.21
	A2	4–20	7.20	1.96	16	51	33	1.55
	A3	20–30	7.50	2.23	18	53	29	1.34
	AE@	30–40	7.70	1.67	16	53	31	1.38
	EA@	40–46	8.70	2.40	11	55	34	N.d.
	E	46–60	8.65	0.75	8	54	38	1.47
	EB	60–80	7.75	1.34	12	58	30	1.13
	Btn1	80–100	8.80	0.53	20	51	29	1.60
	Btn2	100–120	9.00	0.47	20	44	36	N.d.
	BCk	120–180	9.55	0.54	16	47	37	N.d

degradation of subsurface ice on the spatial and vertical differentiation of bulk density values.

Bulk density values of the soil on the top of byllar at the Churapcha site are generally typical of the permafrost-affected solonetzic pale soils (in Russian soil classification system) or Cambic Turbic Cryosols (Aric, Loamic, Sodic). A thin [0–6 (7) cm] gray-humus horizon forming in place of the former plow layer has the bulk density of 1.19 g/cm^3 (**Table 1**). Below, there is a dense subsurface eluvial–solonetzic horizon representing the former plowpan (Ap/Btn@) with an increased bulk density. In the underlying calcareous Bk and BCk horizons, bulk density is about 1.3 g/cm^3. It increases in the lowermost suprapermafrost horizon (Ck) up to 1.53 g/cm^3. In general, analogous bulk density values are typical of native pale soils (Cambic Turbic Cryosols) under taiga vegetation (Elovskaya and Konorovskii, 1978). The reduction in the thickness of the former plow layer may be

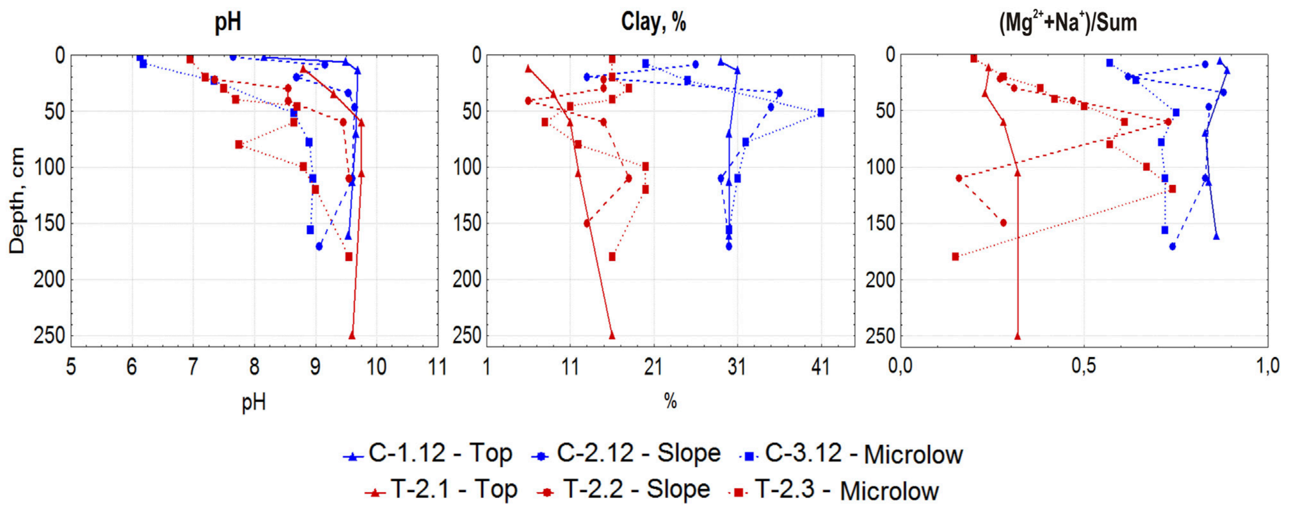

FIGURE 8 | Distribution of pH values, clay content, and the portion of (Na^+ + Mg^{2+}) in the exchange complex of soils studied at the Churapcha (blue lines) and Tabaga (red lines) sites.

due to a combination of factors, such as the initially not deep plowing and the action of water erosion under conditions of terrain deformation because of thermokarst development in the recent decades.

As a result of subsidence of the soil on the slope of the byllar, a significant rearrangement of bulk density values has taken place. The compaction of the surface (former plow) and subsurface (subplow) horizons occurs because of the development of a relatively thick soddy horizon in the absence of its mechanical loosening and strengthening of the solonetzic properties in the former subplow layer due to the increased washing of the upper soil layer. At the same time, the bulk density of the underlying solonetzic horizon (20–40 cm) somewhat decreases due to the removal of soluble salts from the upper horizons. The genetic horizons in the lower half of the soil profile on the microslope of the byllar undergo compaction, which may be related to the vertical compression of the soil upon subsidence of the tightly bound upper soil horizons in local areas after the considerable soil subsidence in the microlow because of ice melting.

The melting of ice wedges that serve as the basement for overlying sediments in the microlows leads to the most considerable subsidence of the soil in the microlow. This subsidence also involves some soils on the adjacent slopes. The bulk density of the soil in the microlow in the upper meter does not change much in comparison with the soil of the byllar. At the same time, the lower part of the soil of the microlow is subjected to a strong decompaction; its bulk density is only 1.04 g/cm^3. Such a strong loosening of this soil is explained by the downward collapse of the lowermost soil horizons following the collapse of the ice-rich permafrost-protective transient layer overlying the melting ice wedge under the action of heat wave with positive soil temperatures because of climate warming.

At the Tabaga site, bulk density values are generally somewhat higher. A tendency for soil loosening is only observed in the upper part of the humus horizon. Below, bulk density values tend to increase to reach maximum values (up to 1.64 g/cm^3) in the solonetzic (Btn) horizons. We have not found a decrease in the bulk density of the lower horizons in the soil of the microlow (pit T-2.3). It is probable that the effect of the soil loosening above melting ice wedge can be observed in the deeper part of this soil, or even beyond the soil profile.

DISCUSSION

The results obtained from this study attest to considerable variation of soil properties following the differentiation of surface topography owing to the development of thermokarst on the arable field.

It is known for at least 70–80 years that after development of permafrost-affected soils into cropland after clear-cutting and wildfires, the permafrost table descends downwards (Péwé, 1954; Tomirdiaro, 1978; Yoshikawa et al., 2002; Iwahana et al., 2005; Shur and Jorgenson, 2007). However, the same studies stated that after returning to the natural environment, the permafrost table rises up again. The experience of geocryologists in Central Yakutia showed that the permafrost table did not move upward after the abandonment of formerly arable land, and this was related to climate warming (Gavriliev et al., 2001; Gavriliev, 2008; Iijima et al., 2010).

Our studies confirm this statement. It is probable that, in the current era, we are observing, the transition of "ecosystem-driven permafrost" to "climate-driven ecosystem-protected permafrost" (according to Shur and Jorgenson, 2007) in Central Yakutia. This means an irreversible trend of permafrost degradation in the areas of former cropland.

The progressing development of thermokarst processes predetermines the change in the character of soil formation and in the classification status of permafrost-affected soils. The soils studied on the top of byllars represent postagrogenic soils, or the remains of the formerly cultivated soils, in which the surface plow and the underlying subplow horizons had been formed in several decades of the soil cultivation. The beginning of the soil cultivation dates back to the mid-1960s, when the native larch–birch forests (charany) were cleared out, and arable fields were organized in their place (Desyatkin, 2004).

The soils of these forests in their natural state were investigated by A. A. Krasyuk, who found that permafrost-affected solods [~Luvic Turbic Cryosols (Albic, Loamic)] develop under birch groves and podzolized solonetzic soils (~Natric Turbic Cryosols (Albic, Loamic)) develop under larch stands (Krasyuk and Ognev, 1927). Later, V.G. Zol'nikov (1954) and L.G. Elovskaya (1964) considered the soils under larch forests as soddy forest soils [~Mollic Turbic Cryosols (Loamic)] or as permafrost-affected pale (palevye) soils [~Cambic Turbic Cryosols (Loamic, Humic, Sodic)]. Under forest vegetation, the thawing depth in these soils was less than 2 m, and there were clear features of cryoturbation in their profiles, so they fitted the concept of Cryosols in the WRB (IUSS Working Group WRB, 2015). Taking into account these classical studies of experts in Yakutian soils and the results obtained from this study, we suppose that "permafrost-affected solonetzic pale soils" [Cambic Turbic Cryosols (Sodic, Luvic)] in the case of Churapcha site and "permafrost-affected solonetzic dark pale soils" [Mollic Turbic Cryosols (Sodic, Luvic)] in the case of Tabaga site predominated within currently degrading arable fields around Churapcha and Tabaga, respectively. In the course of their cultivation, the surface plow and subplow horizons were formed in the soil profiles. Unfortunately, we currently have no reliable information on the spatial variation of relevant soil features under intact forests. These data should be gained at the next stage of the study. This is particularly important for correct evaluation of the rates of soil changes during the agrogenic (arable farming) and postagrogenic (cessation of soil tillage because of thermokarst development) stages.

After the abandoning of the fields and the cessation of tillage, a thin litter layer composed of mainly weakly decomposed remains of herbs has formed on the soil surface. The former plow horizon has been transformed into the gray-colored humus horizon. The subplow layer has been mixed by cryoturbation with the underlying solonetzic horizon containing fragments of the former plowpan marked by the darkest color. This layer is also marked by the most distinct cryogenic fissures, along which the tongues of humified material from the upper horizon penetrate deeper into the soil. Such a profile was examined on the top of byllar at the Churapcha site.

This "normal" pattern of the postagrogenic soil development was complicated by the progressing thawing of permafrost because of the removal of the protecting cover of forest vegetation and forest litter and warming of the climate. At present, the maximum thawing depth exceeds 2 m at both study sites, and the soils do not fit the definition of Cryosols, though the soils in winter freeze down to the permafrost table. When the seasonal thawing depth reached the surface of underlying ice wedges, their melting began, which caused a sharp differentiation of the surface microtopography and the appearance of residual mounds (byllars) between the polygonal networks of hollows (microlows) above the ice wedges. In turn, this triggered the differentiation of the soil properties by the elements of the newly formed microtopography.

It is evident that the soil on the top of byllars (pits C-01-12 and T-2.1) receives the minimum amount of atmospheric moisture. This convex landform does not favor the accumulation of snow. It is probable that the surface soil horizon could be somewhat eroded, so that the thickness of the former plow layer has decreased. This is clearly manifested in profile T-2.1. Leaching processes are not active, and the soil is characterized by the highest pH values attesting to the presence of exchangeable sodium.

The soil on the microslope of byllars (pits C-02-12 and T-2.2) receives more moisture with surface runoff. Its upper part is characterized by somewhat lower pH values. However, deep vertical infiltration is impeded by the presence of the dense solonetzic horizon. It can be supposed that lateral soil water flow toward the adjacent microlow takes place above this horizon. Note that the natric horizon and the upper boundary of the calcic horizon (the line of effervescence) in this soil are found somewhat deeper.

The soil of the microlows (pits C-03-12 and T-2.3) between neighboring byllars receives the maximum amount of water due to the accumulation of snow and surface and soil runoff from the adjacent slopes. Soluble salts and exchangeable sodium are removed from their upper part with the neutral soil reaction. At the same time, the former solonetzic Btn horizon is still preserved in the profile, which is marked by the increased bulk density. Note a considerable decrease in bulk density values in the lower part of the profile in pit C-03-12, which can be explained by the soil loosening related to the thawing of ice-rich transient layer and the appearance of hollow space under the soil profile owing to the ice wedge melting. This should favor deep water infiltration. At the Tabaga site, the soil of the microlow is characterized by the maximum accumulation of organic carbon at a considerable depth, which may be due to soil erosion at the top of the byllar, cryoturbation, and humus migration into the Btn horizon.

Thus, dynamic indicators (bulk density, pH, and organic carbon content) of the state of soils along the studied microcatenas clearly attest to their differentiation in the lateral and vertical directions because of the development of thermokarst microtopography. This is also accompanied by the differentiation of the vegetation cover with its mesophytic character and higher density in the microlow. It is probable that the removal of soluble salts and sodium from this soil with its neutral reaction will favor the further accumulation of humus and deepening of the humus horizon. The postagrogenic transformation of the soil on the top of byllars proceeds much slower. However, in the case of the fast melting of ground ice under conditions of the absence of local drainage network, the transformation of the entire system into the dyuedya lake—the initial stage of the development of alas lakes—may be expected at the Churapcha site; such lakes and thermokarst badland already have appeared on the adjacent field at the Tabaga site (**Figure 5B**).

If we compare the climate-induced change of soils and cropland in Central Yakutia with those in other cold regions

(Péwé, 1954; Poeplau et al., 2019; Stevenson et al., 2014; Archegova et al., 2004; Kaverin et al., 2019; Alekseev and Abakumov, 2018), we can see both similarities and differences. In Central Alaska, the similar change—the occurrence of thermokarst mounds—took place (Péwé, 1954), but after decades of cultivation, the contrast in microtopography decreased and even disappeared. This may be related to the fact that Central Alaska is not the area of the widespread development of the Yedoma landscapes, and melting ice lenses do not create the same problem for agriculture as melting ice wedges. As well as in Central Yakutia, the permafrost table does not return to the previous depth after the abandoning of former cropland in the north of European Russia and West Siberia (Alekseev and Abakumov, 2018; Kaverin et al., 2019). However, the warming in other regions may not result in strong cryogenic deformation of abandoned croplands, most likely because of a lower ice content in the underlying permafrost. At the same time, such soil processes as acidification, paludification, podzolization, and peat accumulation, which are characteristic for soils of cold humid regions, are not much better for agriculture than the solonetz development in alkaline soils in the ultra-continental climate of Central Yakutia. Intense cryogenic fissuring and cryoturbation of topsoil horizons may gradually destroy the dense solonetzic/plowpan horizon, and the soil will evolve into a typical Cambisol. However, in the case of the fast melting of ground ice under conditions of the absence of a local drainage network, the transformation of the entire system into the dyuedya lake—the initial stage of the development of alas lakes—may be expected.

CONCLUSION

Under the conditions of global climate change, the degradation of the Yedoma ice complex is observed on arable fields of Central Yakutia with the formation of initial forms of alas development—byllars, or residual thermokarst mounds surrounded by the hollows above the polygonal network of melting ice wedges, and in some places, dyuedya or young thermokarst lakes confined to the intersections of actively melting ice wedges. Thus, thermokarst processes on arable land lead to a considerable transformation of the surface topography and soil cover of the former arable fields.

The abandonment of croplands under the conditions of the recent continuous warming of the climate does not result in the restoration of the initial landscape but strengthens negative impacts on soils. As a result of thermokarst, the development of microtopography, and downward shift of the permafrost table, the morphology of soils is reconstructed with a change in their classification position. The Cryosols are transformed into Solonetzes and eroded Cambisols, and the large spatial contrast in soil properties, such as pH, bulk density, and organic carbon content, appears in the soil profiles.

Upon subsidence of the soils of slopes and microlows, their middle- and lower-profile horizons become compacted, whereas the lowermost horizons above permafrost are loosened because of the collapse of the underlying sediment above the melting ice wedges. The soils of slopes and microlows also display considerable changes in the distribution of pH in their profiles. The soil cover becomes more heterogeneous, and such contrasts in the soil properties at small distances are very negative for the use of these soils for crop growing.

The global warming in the studied region with very cold climate resulted in the total degradation of the cropland because of the development of byllar microtopography and melting of buried ice wedges. Those specialists anticipating better conditions for agriculture in cold areas because of climate warming could learn from this experience for more accurate predictions. However, in other cold regions beyond the areas with the Yedoma ice complex deposits, the situation may be more optimistic.

DATA AVAILABILITY STATEMENT

The original contributions presented in the study are included in the article/supplementary material, further inquiries can be directed to the corresponding author.

AUTHOR CONTRIBUTIONS

Conceptualization, RD; field and laboratory data acquisition, NF and AD; data analysis and interpretation, all authors; writing—original draft preparation, RD and AD; writing—review and editing, DK and SG; visualization, NF and AD; project administration, RD. All authors have read and agreed to the published version of the manuscript.

FUNDING

This study was supported by the Russian Foundation for Basic Research (project no. 19-29-05151) (data collection, conceptual generalization, and text writing). It was also performed within the framework of the Russian governmental assignment of the Institute of Geography no. 0148-2019-0006 (WRB classification and data arrangement according to international standards).

ACKNOWLEDGMENTS

We are grateful to all our colleagues for their help in completing this study, especially to Peter Schad for his help in determining the classification position of soils in the WRB system.

REFERENCES

Alekseev, I., and Abakumov, E. (2018). Permafrost-affected Former Agricultural Soils of the Salekhard City (Central Part of Yamal Region). *Czech Polar Rep.* 8 (1), 119–131. doi:10.5817/cpr2018-1-9

Archegova, I., Kotelina, N., and Mazhitova, G. (2004). "Agricultural Use of Tundra Soils in the Vorkuta Area, Northeast European Russia," in *Cryosols. Permafrost-Affected Soils*. Editor J. M. Kimble (Berlin Heidelberg: Springer-Verlag), 661–676. doi:10.1007/978-3-662-06429-0_34

Beck, H. E., Zimmermann, N. E., McVicar, T. R., Vergopolan, N., Berg, A., and Wood, E. F. (2018). Present and Future Köppen-Geiger Climate Classification Maps at 1-km Resolution. *Sci. Data* 5, 180214. doi:10.1038/sdata.2018.214

Boike, J., Grau, T., Heim, B., Günther, F., Langer, M., Muster, S., et al. (2016). Satellite-Derived Changes in the Permafrost Landscape of Central Yakutia, 2000-2011: Wetting, Drying, and Fires. *Glob. Planet. Change* 139, 116–127. doi:10.1016/j.gloplacha.2016.01.001

Brown, J., Ferrians, O. J., Jr., Heginbottom, J. A., and Melnikov, E. S. (1997). *Circum-Arctic Map of Permafrost and Ground Ice Conditions*. Washington, DC: USGS in Cooperation with the Circum-Pacific Council for Energy and Mineral Resources, Circum-Pacific Map Series CP-45. scale 1:10,000,000.

Crampton, L. (2019). Alaska's Agriculture Boom Is Driven by a Local-First Spirit. Available online: https://www.politico.com/story/2019/04/30/alaskas-agriculture-boom-is-driven-by-a-local-first-spirit-1381727.

Desyatkin, R., Fedorov, A., Desyatkin, A., and Konstantinov, P. (2015). Air Temperature Changes and Their Impact on Permafrost Ecosystems in Eastern Siberia. *Therm. Sci.* 19 (Suppl. 2), 351–360. S351–S360. doi:10.2298/TSCI150320102D

Desyatkin, R. V. (2018). Climate Change and Dynamics of Permafrost Ecosystems of the Center of the Continental Cryolithozone of the Northern Hemisphere. *Her. Russ. Acad. Sci.* 88 (6), 494–501. doi:10.1134/S1019331618060072

Desyatkin, R. V., and Desyatkin, A. R. (2019). The Effect of Increasing Active Layer Depth on Changes in the Water Budget in the Cryolithozone. *Eurasian Soil Sci.* 52 (11), 1447–1455. doi:10.1134/S1064229319110036

Desyatkin, R. V. (2004). "Ecological Problems of the Use of Alas Land in Agriculture," in *Measures on Implementation of the State Program on the Socio-Economic Development of Rural Areas up to 2006* (Moscow: Timiryazev Agric. Acad.), 40–52. [in Russian].

Desyatkin, R. V., Goryachkin, S. V., Konyushkov, D. E., Krasilnikov, P. V., Lebedeva, M. P., Bronnikova, M. A., et al. (2017). *Cryosols in Perspective: A View from the Permafrost Heartland.* Guidebook-Monograph for Field Excursions of the VII International Conference on Cryopedology. Moscow-Yakutsk: Inst. Geogr. RAS.

Desyatkin, R. V., Goryachkin, S. V., Konyushkov, D. E., Krasilnikov, P. V., Lebedeva, M. P., Bronnikova, M. A., et al. (2013). *Diversity of Soils of Cold Ultra-Continental Climate.* Guidebook-Monograph for the "Mammoth" Ultra-Continental WRB Field Workshop. Sakha-Yakutia, August 17-23, 2013 Moscow-Yakutsk: Inst. Geogr. RAS. Available online: https://www3.ls.tum.de/fileadmin/w00bds/boku/downloads/wrb/Guide_Sakha_final.pdf.

Desyatkin, R. V. (1991). Soil Formation in Alases. *Soviet Soil Sci.* 23 (4), 9–19.

Desyatkin, R. V. (2008). *Soil Formation in Thermokarst Depressions—Alases of the Cryolithozone*. Novosibirsk: Nauka. [in Russian].

Desyatkin, R. V. (1993). Syngenetic Soil Salinization During Alas Development. *Eurasian Soil Sci.* 25 (4), 38–46.

Elovskaya, L. G., and Konorovskii, A. K. (1978). *Regionalization and Reclamation of Permafrost-Affected Soils of Yakutia*. Novosibirsk: Nauka, 175. [in Russian].

Elovskaya, L. G. (1964). *Soils of Arable Farming Regions in Yakutia and the Ways to Improve Their Fertility*. Yakutsk Knizhn. Izd.[in Russian].

Food and Agriculture Organization of the United Nations (2006). *Guidelines for Soil Description*. 4th ed. Rome: FAO.

Gavril'ev, P. P., Ugarov, I. S., and Efremov, P. V. (2005). Cryogenic Processes and Tolerance of the Ice Complex Deposits in Central Yakutia Towards Modern Climate Change and Surface Disturbance. *Nauka i Obrazovanie* 40 (4), 84–87.

Gavriliev, P. P. (2008). "Inter-alas Agricultural Landscapes and Active Layer Trends and Dynamics in Response to a Warming Climate in Central Yakutia," in *Proceedings of the Ninth International Conference on Permafrost*. Editors D. L. Kane and K. M. Hinkel (Fairbanks: Univ. of Alaska, Institute of Northern Engineering), 499–505.

Gavriliev, P. P., Ugarov, I. S., and Efremov, P. V. (2001). *Permafrost-Ecological Characteristics of Taiga Agrolandscapes, Central Yakutia*. Izd. Inst. Merzlotoved. Zemli Sib Yakutsk: Izd. Inst. Merszlotoved. Zemli Sib. Otd. Ross. Akad. Nauk. [in Russian].

Grigor'ev, M. N., Skachkov, Yu. B., Fedorov, A. N., Desyatkin, R. V., and Maksimov, T. Kh. (2010). *A Review of Modern Climate and Environmental Changes in the Sakha (Yakutia) Republic*. Yakutsk: Izd. Inst. Merzlotoved. Zemli Sib. Otd. Ross. Akad. Nauk. [in Russian].

Iijima, Y., Fedorov, A. N., Park, H., Suzuki, K., Yabuki, H., Maximov, T. C., et al. (2010). Abrupt Increases in Soil Temperatures Following Increased Precipitation in a Permafrost Region, Central Lena River Basin, Russia. *Permafrost Periglac. Process.* 21, 30–41. doi:10.1002/ppp.662

Intergovernmental Panel on Climate Change (2014). *Climate Change 2014: Synthesis Report. Contribution of Working Groups I, II and III to the Fifth Assessment Report of the Intergovernmental Panel on Climate Change*. Editors Core Writing Team R. K. Pachauri and L. A. Meyer (Geneva, Switzerland: IPCC).

IUSS Working Group WRB (2015). *World Reference Base for Soil Resources 2014, update 2015. International Soil Classification System for Naming Soils and Creating Legends for Soil Maps*. World Soil Resources Reports No. 106 (Rome: FAO).

Iwahana, G., Machimura, T., Kobayashi, Y., Fedorov, A. N., Konstantinov, P. Y., and Fukuda, M. (2005). Influence of Forest Clear-Cutting on the Thermal and Hydrological Regime of the Active Layer Near Yakutsk, Eastern Siberia. *J. Geophys. Res.* 110, G02004. doi:10.1029/2005jg000039

Jones, A., Stolbovoy, V., Tarnocai, C., Broll, G., Spaargaren, O., and Montanarella, L. (2009). *Soil Atlas of the Northern Circumpolar Region* (Luxembourg: Office for Official Publications of the European Communities).

Jorgenson, M. T. (2013). "Thermokarst Terrains," in *Treatise on Geomorphology. Glacial and Periglacial Geomorphology*. Editors J. F. Shroder, R. Giardino, and J. Harbor (USA, San Diego: Academic Press), Vol. 8, 313–324. doi:10.1016/b978-0-12-374739-6.00215-3

Jorgenson, M. T., Kanevskiy, M., Shur, Y., Moskalenko, N., Brown, D. R. N., Wickland, K., et al. (2015). Role of Ground Ice Dynamics and Ecological Feedbacks in Recent Ice Wedge Degradation and Stabilization. *J. Geophys. Res. Earth Surf.* 120 (11), 2280–2297. doi:10.1002/2015JF003602

Kaverin, D. A., Pastukhov, A. V., and Panjukov, A. N. (2019). Soil Temperature Regime in Postagrogenic Ecosystems Under the Expansion of Self-Restoring Succession of Tundra Vegetation (European Northeast of Russia). *Earth's Cryosphere* XXIII (5), 50–56. doi:10.21782/EC2541-9994-2019-5(50-5610.21782/kz1560-7496-2019-5(58-66)

Krasyuk, A. A., and Ognev, G. N. (1927). "Soils of the Lena–Amga Interfluve (Yakutsk Okrug)," in *Materials of the Commission on the Study of Yakutian Autonomous Soviet Socialist Republic*. Moscow: Izd. Akad. Nauk SSSR. [in Russian].

Lader, R., Walsh, J. E., Bhatt, U. S., and Bieniek, P. A. (2019). Agro-climate Projections for a Warming Alaska. *Earth Interactions* 22, 1–24.

Lyuri, D. I., and Goryachkin, S. V. (2008). "Global Land Use Change and its Specificity in Permafrost-Affected Regions: Consequences for Cryosols," in *Ninth International Conference on Permafrost. Institute of Northern Engineering*. Editors D. L. Kane and K. M. Hinkel (Fairbanks: University of Alaska Fairbanks), 1093–1097.

Neustroev, M. P., Ivanov, R. V., and Abramov, A. F. (2017). *The Agricultural System in the Republic of Sakha (Yakutia) for the Period 2016-2020: Methodological Manuals*. Yakutsk: YANIISH. [in Russian].

Olson, D. M., Dinerstein, E., Wikramanayake, E. D., Burgess, N. D., Powell, G. V. N., Underwood, E. C., et al. (2001). Terrestrial Ecoregions of the World: a New Map of Life on Earth. *BioScience* 51, 933–938. doi:10.1641/0006-3568(2001)051[0933:teotwa]2.0.co;2

Péwé, T. L. (1954). Effect of Permafrost on Cultivated Fields, Fairbanks Area, Alaska. *U.S. Geol. Surv. Bull.* 989-F, 315–351. doi:10.3133/b989f

Poeplau, C., Schroeder, J., Gregorich, E., and Kurganova, I. (2019). Farmers' Perspective on Agriculture and Environmental Change in the Circumpolar North of Europe and America. *Land* 8, 190. doi:10.3390/land8120190

Rosenzweig, C., and Parry, M. L. (1994). Potential Impact of Climate Change on World Food Supply. *Nature* 367, 133–138. doi:10.1038/367133a0

Safronov, F. G. (1961). *Russian Peasants in Yakutia in the 17th–Beginning of the 20th Centuries AD*. Yakutsk: Izd. Sib. Otd. Akad. Nauk SSSR. [in Russian].

Schuur, E. A. G., and Mack, M. C. (2018). Ecological Response to Permafrost Thaw and Consequences for Local and Global Ecosystem Services. *Annu. Rev. Ecol. Evol. Syst.* 49, 279–301. doi:10.1146/annurev-ecolsys-121415-032349

Shein, E. V. (2009). The Particle-Size Distribution in Soils: Problems of the Methods of Study, Interpretation of the Results, and Classification. *Eurasian Soil Sci.* 42 (3), 286–293. doi:10.1134/s1064229309030053

Shur, Y. L., and Jorgenson, M. T. (2007). Patterns of Permafrost Formation and Degradation in Relation to Climate and Ecosystems. *Permafrost Periglac. Process.* 18, 7–19. doi:10.1002/ppp.582

Skachkov, Yu. B. (2000). "Modern Climate Changes in Central Yakutia," in *Climate and Permafrost: Integrated Studies in Yakutia* (Yakutsk: Izd. Inst. Merzlotoved. Zemli Sib. Otd. Ross. Akad. Nauk), 55–63. [in Russian].

Stevenson, K. T., Rader, H. B., Alessa, L., Kliskey, A. D., Pantoja, A., Clark, M., et al. (2014). Sustainable Agriculture for Alaska and the Circumpolar North: Part II. Environmental, Geophysical, Biological and Socioeconomic Challenges. *Arctic* 67, 296–319. doi:10.14430/arctic4408

Timofeev, P. A., Isaev, A. P., and Shcherbakov, I. P. (1994). *Forests of the Middle Taiga Subzone of Yakutia*. Yakutsk: Izd. Yakutsk. Nauchn. Tsentra Sib. Otd. Ross. Akad. Nauk. [in Russian].

Tomirdiaro, S. V. (1978). *Natural Processes and Development of the Territory in the Permafrost Zone*. Moscow: Nedra. [in Russian].

van Reeuwijk, L. P. (2002). *Procedures for Soil Analyses*. Sixth edition. Wageningen: Int. Soil Ref. Inform. Centre.

Veremeeva, A., Nitze, I., Günther, F., Grosse, G., and Rivkina, E. (2021). Geomorphological and Climatic Drivers of Thermokarst Lake Area Increase Trend (1999-2018) in the Kolyma Lowland Yedoma Region, North-Eastern Siberia. *Remote Sensing* 13, 178. doi:10.3390/rs13020178

Yoshikawa, K., Bolton, W. R., Romanovsky, V. E., Fukuda, M., and Hinzman, L. D. (2002). Impacts of Wildfire on the Permafrost in the Boreal Forests of Interior Alaska. *J. Geophys. Res.* 108, 8148. doi:10.1029/2001JD000438

Zol'nikov, V. G. (1954). "Soils of the Eastern Part of Central Yakutia and Their Use," in *Materials on the Environmental Conditions and Agriculture in Central Yakutia* (Moscow: Izd. Akad. Nauk SSSR), 1, 35–221. [in Russian].

Conflict of Interest: The authors declare that the research was conducted in the absence of any commercial or financial relationships that could be construed as a potential conflict of interest.

Publisher's Note: All claims expressed in this article are solely those of the authors and do not necessarily represent those of their affiliated organizations, or those of the publisher, the editors, and the reviewers. Any product that may be evaluated in this article, or claim that may be made by its manufacturer, is not guaranteed or endorsed by the publisher.

frontiers in Earth Science

ORIGINAL RESEARCH
published: 27 October 2021
doi: 10.3389/feart.2021.718904

Types and Micromorphology of Authigenic Carbonates in the Kolyma Yedoma Ice Complex, Northeast Siberia

Victor V. Rogov[1,2], Anna N. Kurchatova[1,3] and Natalia A. Taratunina[2,4]*

[1]Institute of the Earth's Cryosphere, Siberian Branch of the Russian Academy of Sciences, Tyumen, Russia, [2]Department of Geography, Lomonosov Moscow State University, Moscow, Russia, [3]Tyumen Industrial University, Tyumen, Russia, [4]Institute of Geography, Russian Academy of Sciences, Moscow, Russia

The study focuses on authigenic carbonates that are widespread in different deposition environments and are a component part of the terrestrial biogeochemical cycle of carbon. Samples from the Kolyma Yedoma Ice Complex that formed during the Sartan Cryochrone (MIS 2), the coldest period of the Late Pleistocene, in the northeastern Siberian lowlands, have been studied utilizing scanning electron microscopy and energy-dispersive spectroscopy with replica technique. The samples bear signatures of irreversible multistage cryogenic changes in structure and composition, with the formation of authigenic minerals. Authigenic carbonates as secondary phases in the Ice Complex deposits are remarkable by local changes in chemical, physical, and other properties, which induce gradual changes in the lattice and conversion of one mineral species to another. As a result, the sediments may contain stable and metastable minerals. Crystalline species like calcite or aragonite precipitate from aqueous solutions and their presence are restricted to free pore space in segregation ice. Metastable phases may be produced as an initial reaction product between the CO_2 and the aqueous phase, while mineral surfaces and small pores act as possible nucleation sites. Organic matter is also an important agent in the cryometamorphism of sediments, including precipitation of authigenic phases due to the freezing of colloids and high-molecular compounds.

Keywords: Yedoma Ice Complex, replica techniques, authigenic carbonates, Sartan Cryochrone (MIS 2), the Kolyma Lowland

OPEN ACCESS

Edited by:
Lutz Schirrmeister, Alfred Wegener Institute Helmholtz Centre for Polar and Marine Research (AWI), Germany

Reviewed by:
Sebastian Wetterich, Alfred Wegener Institute Helmholtz Centre for Polar and Marine Research (AWI), Germany
Georg Schwamborn, Istanbul Technical University, Turkey

****Correspondence:***
Anna N. Kurchatova
kanni@mail.ru

Specialty section:
This article was submitted to Cryospheric Sciences, a section of the journal Frontiers in Earth Science

Received: *01 June 2021*
Accepted: *21 September 2021*
Published: *27 October 2021*

Citation:
Rogov VV, Kurchatova AN and Taratunina NA (2021) Types and Micromorphology of Authigenic Carbonates in the Kolyma Yedoma Ice Complex, Northeast Siberia. Front. Earth Sci. 9:718904. doi: 10.3389/feart.2021.718904

INTRODUCTION

Authigenic minerals in sediments are formed by physicochemical and biochemical reactions during and after deposition in various environmental settings. The mineralogical alteration of sediments soon after the deposition (early diagenesis) is controlled primarily by their original compositions and relative percentages of four main components: chemically passive and active minerals, organic matter, and pore fluids. Chemically passive phases are commonly predominant and mostly include primary minerals (quartz, feldspar, garnet, and ilmenite) except for a few relatively reactive Fe- and Ca-bearing silicates. Chemically active minerals encompass such inorganic phases as Fe, Al, and Mn hydroxides, mix gels, amorphous silica, carbonates, and water-soluble salts, which are in equilibrium with pore fluids only at the time of precipitation (Curtis, 1990; Buggle et al., 2011).

The decay of organic matter produces CO_2 and H_2S, NH_3, CH_4, and other reactive components, which become involved in the alteration of sediments and control the chemical environment, though are as low as a few percents or less (Davidson and Janssens, 2006). As for pore fluids, they commonly acquire higher pH during early diagenesis (Tranter, 2003).

The rate of physicochemical changes and the redistribution of components differ in subaquatic and subaerial settings. The authigenic minerals that precipitate in subaquatic conditions, when sediments undergo compaction and pore water is squeezed out, locally cement detrital mineral grains and form concretions accumulating impurities (Zn, Co, Cu, etc.). Precipitation of calcium carbonate in sediments is driven by the generation of subseafloor alkalinity, which is typically the result of microbial respiration of organic carbon in the absence of oxygen; the oxygen penetration depth for the majority of the seafloor is less than 1 m (D'Hondt et al., 2015; Turchyn et al., 2021).

Subaerial diagenesis requires hydration of sediments to maintain ion exchange between surface-active components (clay minerals, collomorphic oxide phases, organic complexes, etc.) and the ensuing formation of soluble and amorphous phases. Calcification as the process of the accumulation of authigenic carbonates in subaerial settings is dominant in many soils in arid or semiarid environments. Both abiogenic sources of Ca (primary minerals ann groundwater) and atmospheric or biogenic (decaying organic matter and rhizomicrobial respiration) sources of CO_2 are involved in carbonate authigenesis in soils (Kolesár and Čurlik, 2015). Various types of microscale secondary carbonates are preserved in loess-paleosol sequences. Their abundance and distribution within loess profiles can indicate moisture regime changes, dust accumulation characteristics, and the extent and intensity of leaching processes (Becze-Deák et al., 1997; Barta, 2011; Durand et al., 2018).

Unlike unfrozen areas, the diagenetic reactions in permafrost mostly involve bound water that affects the surface of organic-mineral particles, whereas free water-sediment interactions are restricted to the active layer. Another difference is that the reactions at negative temperatures are slow, but the low rates are compensated by the high contents of agents in limited volume. Chemical reactions in perennially or seasonally frozen sediments occur, respectively, at long-lasting negative temperatures or during freezing and thawing (single brief events or repeated cycles) (Yershov, 1998). The processes during the freezing and thawing cycles in the active layer have been quite well studied (Siegert, 1981; Konishchev and Rogov, 1993; Ostroumov et al., 2001; Rogov, 2009).

Note that it is hard to discriminate between diagenetic processes and soil formation in subaerial settings (Lupachev, Gubin, 2012). Soil formation processes, which reflect the main physicochemical and biochemical reactions during and after deposition, influence the precipitation of authigenic minerals. These minerals are abundant in frozen soils and permafrost of Central Yakutia (Siegert, 1981) and the northeastern Siberian lowlands (Alekseev et al., 2003).

In general, the main aim of this topic is to elucidate authigenic carbonate accumulations in the Yedoma Ice Complex from the Kolyma Lowland, Northeast Siberia i) to document the *in situ* crystals of carbonates in Yedoma silt, ii) to report shape and characteristics of the crystals deposited in the textural ice and pore space of the frozen sediments, and iii) to discuss the processes involved in the precipitation of cryogenic carbonates. Their features and distribution patterns in permafrost have implications for the formation conditions of genetically different frozen sediments, both inside and outside the present permafrost limits, and for ecological factors that provide the terrestrial biogeochemical cycle of carbon (Strauss et al., 2013).

MATERIALS AND METHODS

The microstructure of Yedoma Ice Complex was studied in samples from the well-known sites of the Kolyma Lowland: Kolymskoe, Plakhinskii Yar, Duvanny Yar, Zelyony Mys, and Kur'ishka (**Figure 1**). Currently, a large number of publications mainly by Russian researchers exist that give detailed description of these sites since the 1970s; therefore, in this article, the authors will not describe their lithological and stratigraphic units (e.g., Arkhangelov et al., 1979; Vasil'chuk, 2005; Kaplina, 2011). The distribution of Yedoma in the northeastern Siberian lowlands has been recently mapped (Veremeeva et al., 2021). One of the last summary publications concerning the Yedoma Ice Complex from the Kolyma Lowland (on the base of stratotype site Duvanny Yar) to test the processes and environmental conditions of silt deposition has been given by Murton et al., 2015.

We chose specific sampling sites to study the undisturbed structure of the frozen sediments. The cubic monoliths (15 × 15 × 15 cm) were cut at a certain height (above river level, arl), which allows considering the age of the samples tested as Sartan Cryochrone (Q_{III}^4 or MIS 2, Marine Isotope Stage) for each site.

The samples are typical for the Yedoma silt and are characterized by uniform fine grain sizes (up to 75% of coarse silt) and high ice contents. The mineral composition consists of rock-forming quartz, orthoclase, and plagioclase of the light fraction (92–97%); accessory rutile, apatite, zircon, and sporadic Cr-spinel; sericite and montmorillonitic clay minerals. Yedoma deposits are non-saline and have 7–10 pH (Lupachev and Gubin, 2012); mean TOC (total organic carbon) is 3.0 + 1.6/ –2.2 wt% (Strauss et al., 2013).

Samples were prepared by the replica technique that enables studying the microstructure of finely dispersed deposits and involves minimal disturbance to their morphology by forming a thin plastic film on the sample surface (Bates and Comer, 1955). The authors have modified the replica technique to investigate the frozen ground in the scanning electron microscope (Rogov and Kurchatova, 2013). Currently, replicas for SEM imaging are made as follows. A frozen specimen is split in the cooling chamber at a negative temperature, and its fresh cleavage plane is coated with polystyrol dissolved in dichloroethane. Then, the specimen is exposed to a specified negative temperature until the solvent evaporates and thaws after drying. The plastic film with the surface print (impression

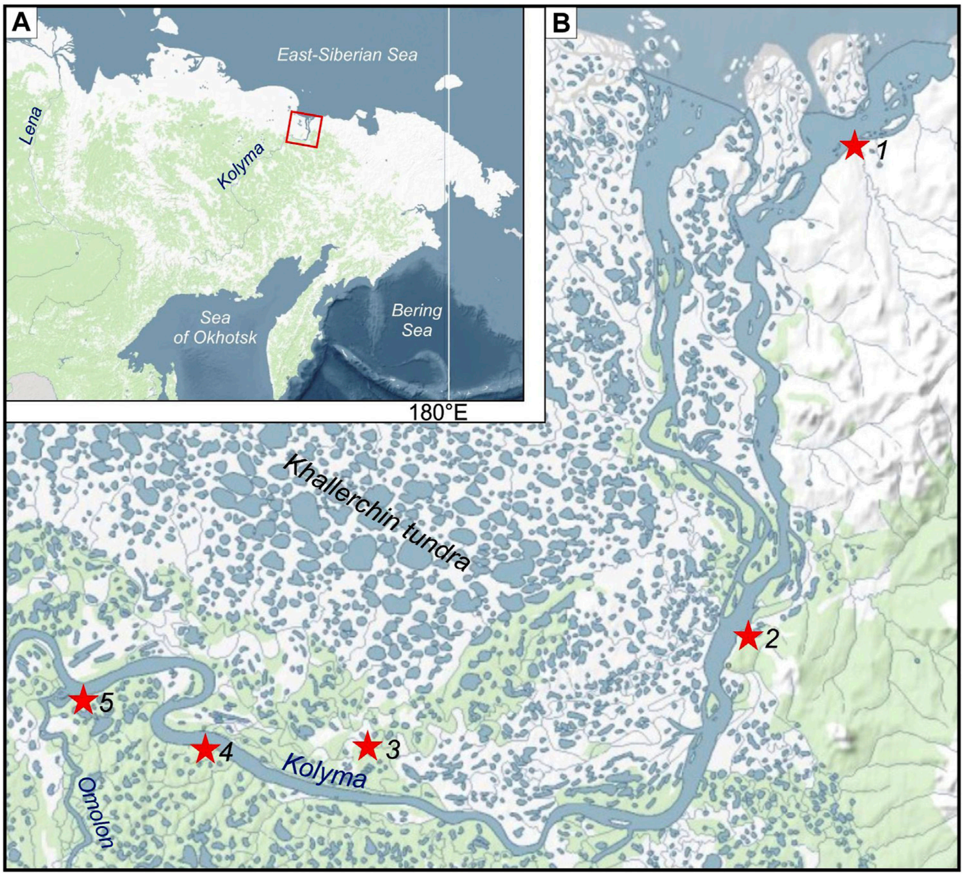

FIGURE 1 | Study area **(A)** and location of the sampling sites at the Kolyma Lowland **(B)**. Sites are numbered: 1 = Kur'ishka; 2 = Zelyony Mys; 3 = Plakhinskii Yar; 4 = Duvanny Yar; 5 = Kolymskoe.

replica) is removed mechanically from the thawed specimen, rinsed in distilled water, and examined under optical or scanning electron microscopes in the laboratory (i.e., at room temperature). The replica technique allows for the study shapes and sizes of particles and aggregates, their surface microtopography, and qualitative and quantitative relations among the components of frozen ground in the initial undisturbed state.

The samples were sputter-coated with gold in a Quorum Q150R S an automatic rotary pumped coater and examined with TM3000 (Hitachi) scanning electron microscope equipped with an energy-dispersive X-ray system SwiftED3000 (Oxford). Determination of the composition of authigenic minerals in replicas was carried out in the Earth Cryosphere Institute, Tyumen Scientific Center of the Siberian Branch of the Russian Academy of Sciences (SB RAS).

RESULTS

The microstructure formation in perennially frozen ground results in their deposition and freezing conditions, including grain size, mineralogy, water content, water chemistry, temperature, and time of freezing (during or after deposition). The sediment particles within a seasonal freezing and thawing layer acquire a particular morphology during diagenesis due to the exposition to cryogenic deformation (frost cracking). The types of microstructure in seasonally and perennially frozen ground control their cryostructures.

The sediments commonly freeze in wet conditions and contain mostly basal-type pore ice and waved microlenses of segregated ice that sometimes are difficult to distinguish. Latent lenticular microstructure of samples from the Zelyony Mys site has been observed using SEM (**Figure 2A**). The well-preserved diatoms valves, which indicated *in situ* deposition in the polygonal ponds or thermokarst lakes, were found in these samples. Segregated ice can form only due to the expansion of the soil skeleton when the bonds between mineral particles break down (dilatancy). Since the breakage follows weak zones, the resulting voids represent the pattern of particles and their relationships, i.e., the types of microstructure. Ice contents of Yedoma silt usually increase from latent lenticular microstructure to a braided one (**Figure 2B**). Silt preserves elements of the primary sedimentary structure; however, some mineral grains are reoriented, displaced, and

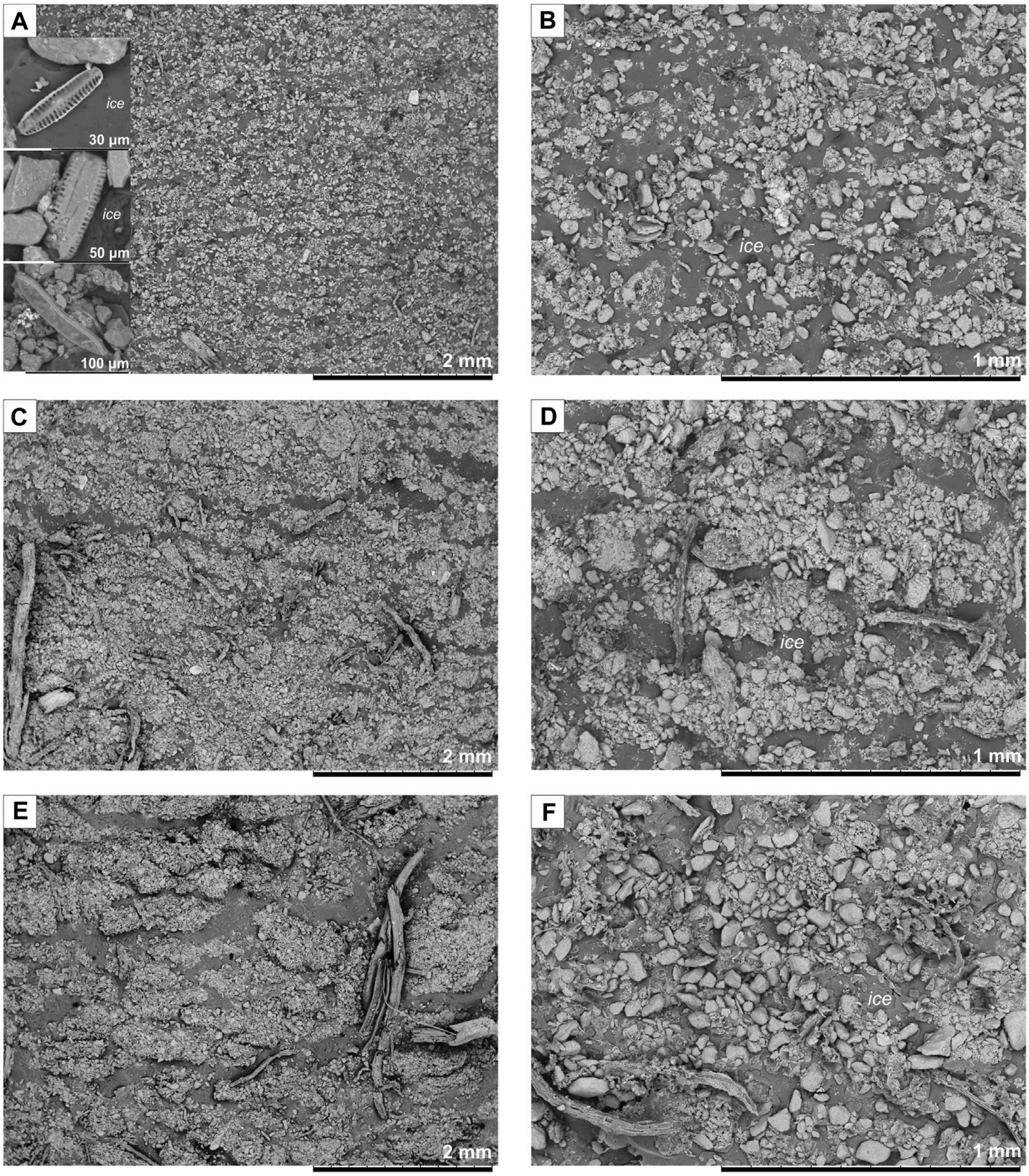

FIGURE 2 | Microstructure of Ice Complex deposits: **(A,B)** latent lenticular microstructure, Zelyony Mys site, sampled at 35 m arl; **(C,D)** braided microstructure, Plakhinskii Yar site, sampled at 12 m arl; **(E,F)** irregular reticulate microstructure, Kolymskoe site, sampled at 25 m arl. arl = above river level.

aggregated. The structure patterns are the most prominent in the layers, with high percentages of silt and plant remaining (**Figure 2C**). The silt unit from the Kolymskoe site has high ice content: lenses of segregated ice formed in diverse ways. Ice crystals are platy in thin lenses and become purer upward in thick bands, indicating freezing from the surface. The silt unit comprises sand-, silt-, or clay-size particles, sometimes cemented with mud and organic material or silt particles cemented with iron and plant remnants. The particle density between ice layers increases by cyclic freezing; their contacts change from volumetric to point-like and by coagulation and cementation, they form circular features (Yershov, 1998). Poorly decomposed fine *in situ* roots are pervasive.

Different types of water freeze up successively during cyclic freezing of silt sediments and syncryogenic stratum formation; aqueous solutions acquire more complex compositions, and authigenic minerals precipitate. The following types of secondary carbonates have been observed under a SEM-EDX study in the Sartan Yedoma Ice Complex deposits from the Kolyma Lowland:

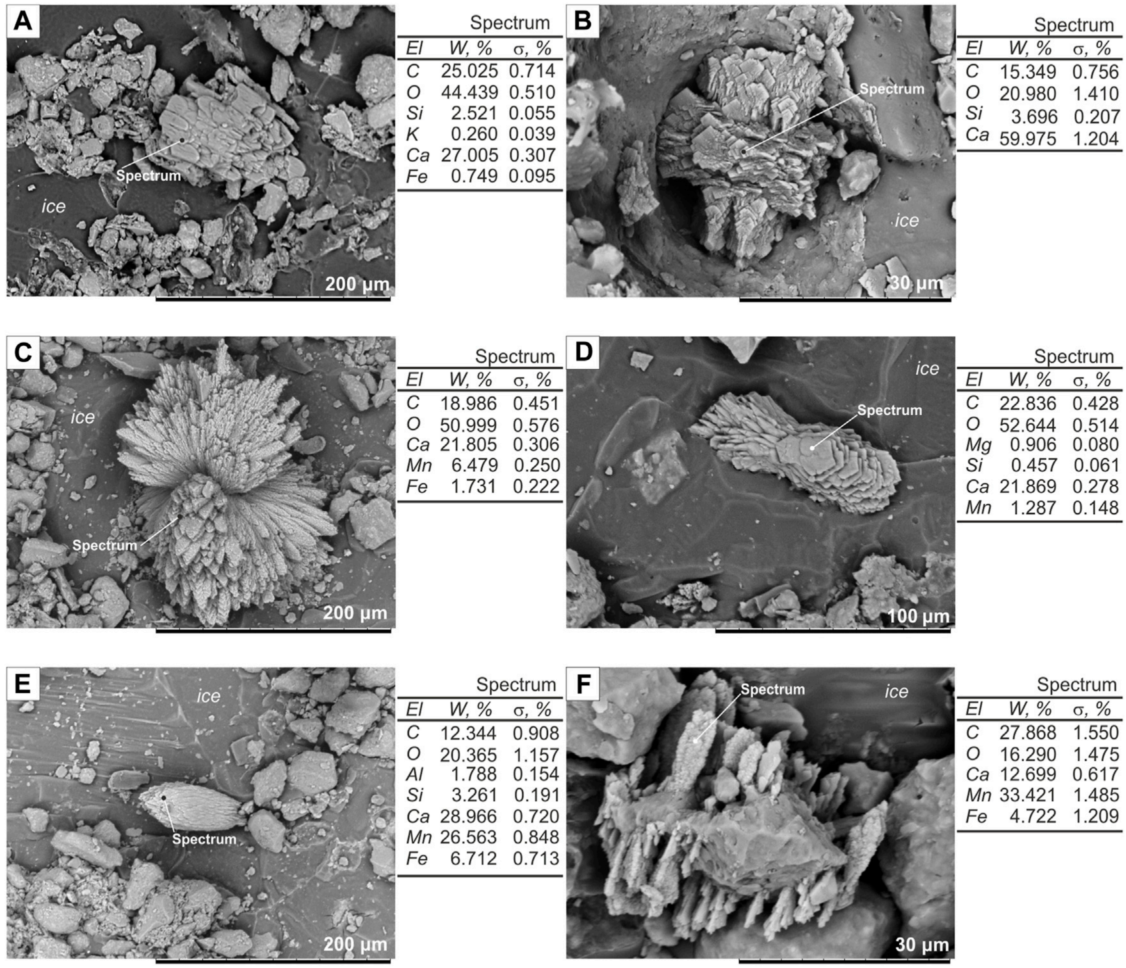

FIGURE 3 | Morphology of the authigenic carbonates under SEM-EDX. El = element; W% = weight percent; σ% = error. **(A)** Parallel intergrowth of calcite crystals, Kur'ishka site, sampled at 17 m arl; **(B)** polysynthetic twinning of rhombohedral calcite crystals, Duvanny Yar site, sampled at 36 m arl; **(C)** rosette-like aragonite aggregate, Kur'ishka site, sampled at 19 m arl; **(D)** twinning of acicular and prismatic aragonite crystals, Kolymskoe sampled at 25 m arl; **(E)** columnar manganocalcite intergrowth, Kur'ishka site, sampled at 21 m arl; **(F)** Ca-rhodochrosite druse, Kur'ishka site, sampled at 29 m arl

1) Calcium carbonate ($CaCO_3$) polymorphs are characterized by parallel intergrowth and polysynthetic twinning of scalenohedral to rhombohedral calcite crystals (**Figures 3A,B**); radiated rosette-like aggregate and twinning of aragonite with a prismatic or acicular (needle-like) habit of crystals (**Figures 3C,D**). $CaCO_3$ aggregates have a size ranging from 50 to 100 µm on average and are located in ice layers or at contacts with mineral grains, with coarser sizes of crystals in larger aggregates.
2) Isomorphic series of manganocalcite $(Ca,Mn)CO_3$ (Mn: Ca = 1 : 1) and Ca-rhodochrosite ($MnCO_3$, with up to 17% Ca) look like columnar intergrowth in ice layers (**Figure 3E**) or druses on the surface of mineral grains (**Figure 3F**). Unlike the calcium carbonate polymorphs, the grains in parallel-columnar aggregates are uneven in size (decreasing toward one end), and some platy crystals have granular surfaces. Ca-rhodochrosite aggregates are sporadic and more often appear as small druses on mineral surfaces.
3) Carbonate compounds of alternating compositions have high Fe, Al, and Si (**Figures 4A,B**) and films around mineral grains, cement in aggregates, or amorphous flakes, often with metal impurities (Zn).
4) Siderite ($FeCO_3$), as colloidal spherules, are commonly located at the contact with grassroots or moss remains and also around fungal hyphae (**Figure 4C**); early sediment alteration produces siderite concretions (**Figure 4D**).

Iron sulfides in the form of amorphous FeS_{am} and crystalline greigites ($FeS{\cdot}F_2S_3$) were observed in the samples from the Kur'ishka site as an indicator of anaerobic environments (**Figures 4E,F**). FeS_{am} has a characteristic microstructure, consisting of several µm large aggregates of curved, wrinkled sheets. These sheets are coated by completely amorphous material, the wavy, fluffy surface of which can also be observed in high-resolution SEM images. Greigite forms

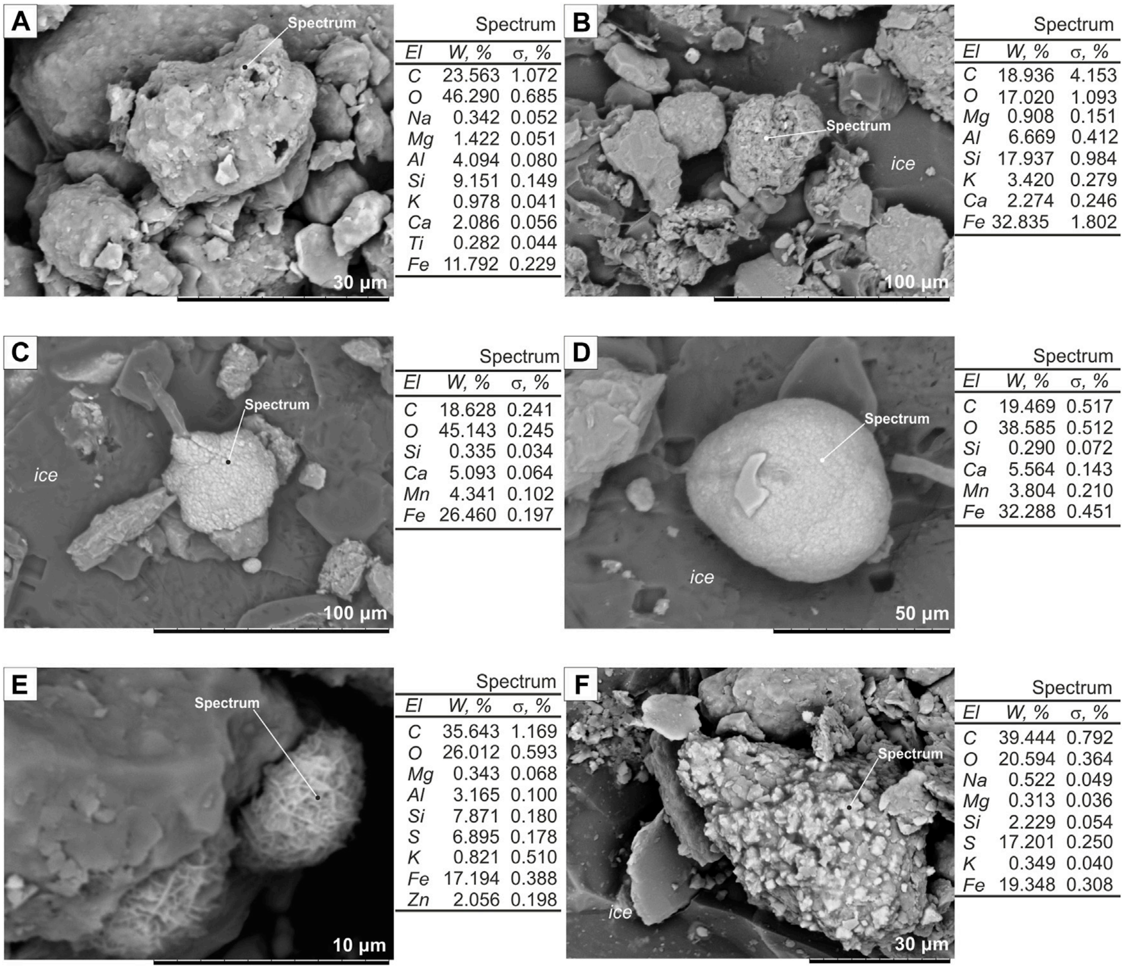

(A) Spectrum

El	W, %	σ, %
C	23.563	1.072
O	46.290	0.685
Na	0.342	0.052
Mg	1.422	0.051
Al	4.094	0.080
Si	9.151	0.149
K	0.978	0.041
Ca	2.086	0.056
Ti	0.282	0.044
Fe	11.792	0.229

(B) Spectrum

El	W, %	σ, %
C	18.936	4.153
O	17.020	1.093
Mg	0.908	0.151
Al	6.669	0.412
Si	17.937	0.984
K	3.420	0.279
Ca	2.274	0.246
Fe	32.835	1.802

(C) Spectrum

El	W, %	σ, %
C	18.628	0.241
O	45.143	0.245
Si	0.335	0.034
Ca	5.093	0.064
Mn	4.341	0.102
Fe	26.460	0.197

(D) Spectrum

El	W, %	σ, %
C	19.469	0.517
O	38.585	0.512
Si	0.290	0.072
Ca	5.564	0.143
Mn	3.804	0.210
Fe	32.288	0.451

(E) Spectrum

El	W, %	σ, %
C	35.643	1.169
O	26.012	0.593
Mg	0.343	0.068
Al	3.165	0.100
Si	7.871	0.180
S	6.895	0.178
K	0.821	0.510
Fe	17.194	0.388
Zn	2.056	0.198

(F) Spectrum

El	W, %	σ, %
C	39.444	0.792
O	20.594	0.364
Na	0.522	0.049
Mg	0.313	0.036
Si	2.229	0.054
S	17.201	0.250
K	0.349	0.040
Fe	19.348	0.308

FIGURE 4 | Cryometamorphic features: **(A)** Fe-colloidal film on mineral grain surface, Kur'ishka site, sampled at 15 m arl; **(B)** aggregate cement, Plakhinskii Yar site, sampled at 12 m arl; **(C)** colloidal siderite around fungal hyphae, Zelyony Mys site, sampled at 35 m arl; **(D)** siderite concretion, Zelyony Mys site, sampled at 35 m arl; **(E)** amorphous iron sulfide (FeSam), Kur'ishka site, sampled at 21 m arl; **(F)** octahedral greigites coating a silt particle, Kur'ishka site, sampled at 21 m arl.

irregularly shaped aggregations on the mineral surface coated by the colloidal film.

DISCUSSION

Mineral grains in subaerial sediments subject to cryogenesis during cyclic freezing and thawing experience physical, chemical, and biochemical changes under the effect of pore moisture phase transitions. The features of deposits in such conditions shape up when mineral grains, especially quartz, break upon freezing (Konishchev, 1982; Konishchev and Rogov, 1993; Schwamborn et al., 2012). Finer sediments have larger surface areas of grain contacts with water and related physical and chemical interactions. Cyclic freezing-thawing accelerates chemical weathering because the migration of bound water toward the freezing front and subsequent melting of segregation ice maintain high water reactivity at low temperatures and generally decrease the contents of free water in pore fluids.

The lower part of the active layer in moistened tundra landscapes has an anaerobic (reducing) composition and low pH. Hydrolysis, which is especially rapid in layered and framework silicates, leads to concurrent chemical weathering of sediments and ionic decomposition of water (Oelkers and Schott, 1995; Tranter, 2003):

$$\underset{\text{anorthite}}{CaAl_2Si_2O_8\,(s)} + 2CO_2\,(aq) + 2H_2O\,(l) \Leftrightarrow Ca^{2+}\,(aq) + 2HCO_3^-\,(aq) + \underset{\text{weathered feldspar}}{H_2Al_2Si_2O_8\,(s)}$$

The H^+ ions released by the water dissociation enter the lattices of newly formed clay particles, while the OH^- and silica groups interact to produce silicic acid. Furthermore, some H_2O molecules react with dissolved atmospheric carbon dioxide and provide HCO_3^- inputs to the solution. In solution, carbonate minerals are precipitated during dissolved Ca-HCO_3/CO_3 saturation when the ion activity product is greater than the solubility product. In polar soils, this typically occurs during evaporation/sublimation or cryoconcentration due to the freezing of soil solutions or films (Tranter, 2003). The freezing of the active layer leads to water desorption, compositional complexity of carbonates, and successive precipitation of authigenic minerals at various geochemical barriers. Cryometamorphism develops in several stages for freezing.

Stage I: pH increases slightly to neutral values due to the high contents of CO_2 at the near-zero temperature. Freezing under a closed system imparts a concentration of solutes in the residual water, leading to an increase in calcite saturation index. Calcium precipitates from the aqueous solution with high contents of CO_2 as calcite on the thermodynamic barrier. Precipitation of carbonates upon freshwater freezing (with the ensuing calcitization) is a common process in permafrost: for example, up to 0.5–2.0 kg/m^2 of salts (mainly $CaCO_3$) form upon aufeis fields after ice melting (Lacelle et al., 2009; Fotiev, 2009). As noted, calcites are presented by the parallel aggregates often located along the ice layer and also by polysynthetic twins that are typical for them. Crystals are easily recognized by the rhombohedral and scalenohedral habits.

The precipitation of calcite increases relatively the contents of Mg^{2+} in free water during freezing (Anisimova, 1981), which is favorable for the formation of aragonite, another calcium carbonate polymorph. As calcite growth rates decrease, aragonite growth rates stay constant and this phase becomes the dominant mineral phase in solutions with a high Mg/Ca ratio (up to five against 0.25 in freshwater) and low supersaturation (De Choudens-Sanchez and Gonzalez, 2009). Crystals show a prismatic or acicular (needle-like) habit as is usually displayed for inorganic origin. Rosette- and sheaf-like aragonite clusters prevail.

Furthermore, freezing in a closed system can produce manganocalcite with ~1 : 1 Ca: Mn and finally Ca-rhodochrosite, as Ca^{2+} becomes isomorphically substituted by manganese. The process accelerates as the amount of free water reduces, resulting in smaller sizes of mineral grains. The accumulation of manganese is fairly widespread in the form of authigenic carbonates of complex composition in the Pleistocene-Holocene sediments of shelf-continental lithogenesis (Kuleshov, 2016).

Thus, the calcium carbonates that form at the first stage of freezing make up the series "calcite—aragonite—manganocalcite—Ca rhodochrosite." The redistribution of soluble compounds takes place during the ice segregation in freezing grounds. The mobile components are accumulated on the interface of a growing ice lens. A part of soluble substances transforms into fixed forms in zones of cryoconcentration.

Stage II: freezing involves pore fluids with complex organic-mineral compounds (low-molecular complexes of iron with fulvic acid, silica gel, Mn hydroxides, and colloidal clay minerals). Migration of bound water and desorption of collomorph phases produce clay films on grain surfaces and cause cementing of clasts with Fe-Al-carbonate material. Locally, Ba, Zn, Co, and other elements become adsorbed on geochemical barriers of clay and, possibly, Mn hydroxides in compositionally complex flake-like amorphous phases. Lower crystallization temperatures of organic-mineral complexes are indicated by the presence of NaCl compounds entrapped from freezing solutions.

The Kolyma Ice Complex deposits contain an assemblage of iron sulfides with manganic calcite cement, which were also discovered in the central Yakutian permafrost (Siegert, 1981). SEM images reveal two varieties (**Figures 4E,F**, respectively): aggregates of amorphous sulfide (FeS_{am}), possibly, sheet-like features as mackinawite-type structural elements that can form early during precipitation of colloids in reduced conditions (Csákberényi-Malasicsa et al., 2012), and octahedral greigite ($FeS{\cdot}F_2S_3$) crystals.

Stage III: further freezing affects high-molecular solutions in living cells, especially fungal hyphae. Several fungi can produce organic acids with chelating properties; as a result of the interaction between oxalic acid and cations, crystals of metal oxalates are produced (Baran, 2016). Therefore, fungi usually induce drastic changes in the microenvironment near their hyphal network. For instance, a modification of pH is an essential environmental factor influencing the redox state and the stability of iron ions and their solubility. Indeed, according to laboratory experiments (Varadachari et al., 1994), oxalic acid produces insoluble salts only reacting with divalent cations such as Ca^{2+}, while oxalates from the reaction with trivalent cations result in soluble salts. Only Fe^{3+} can react with oxalic acid, which could be why fungal iron oxalate is rarely found in soils, even though fungi produce high amounts of oxalic acid and iron is the most abundant metal on Earth (Comensoli et al., 2017).

Authigenic carbonates as secondary phases in the Ice Complex deposits are remarkable by local changes in chemical, physical, and other properties, which induce gradual changes in the lattice and conversion of one mineral species to another. As a result, the sediments may contain stable and metastable minerals. Crystalline species like calcite or aragonite precipitated from solutions and their presence is restricted to free pore space in segregation ice. Metastable phases commonly form aggregates and polysynthetic twins, which reflect the freezing kinetics and the contrasting properties of the growth medium.

CONCLUSION

1) The Kolyma Yedoma Ice Complex that was formed during the Sartan Cryochrone (MIS 2), the coldest period of the Late Pleistocene, contains authigenic carbonates of several generations: polymorphic (calcite and aragonite) and isomorphic (manganocalcite, rhodokhrosite, and siderite) calcium carbonates and complex Fe-Al compounds.
2) Growth of authigenic mineral aggregates is constrained by the interstitial space and the thickness of ice lenses and is generally consistent with the predominance of silt-size grains. The morphology of new phases depends on the rate of pore moisture freezing; Ca carbonate crystals are the largest (50–100 μm on average). Secondary carbonates are represented by polysynthetic twins, parallel intergrowth, and druses or aggregates.
3) Cryogenesis leads to irreversible changes in the structure and composition (cryometamorphism) of sediments and the formation of metastable hydrates or colloids in anoxic areas of the active layer (closed system). The freezing sediments change in several successive stages: cryoconcentration of the residual solutions of pore water; migration of bound water and desorption of organic-mineral complexes; Ca-rich silicate weathering.

DATA AVAILABILITY STATEMENT

The original contributions presented in the study are included in the article/**Supplementary Material**; further inquiries can be directed to the corresponding author.

AUTHOR CONTRIBUTIONS

AK and VR were responsible for sample preparation, analysis of the results, and writing of the article. NT contributed to laboratory research and technical support.

SUPPLEMENTARY MATERIAL

The Supplementary Material for this article can be found online at: https://www.frontiersin.org/articles/10.3389/feart.2021.718904/full#supplementary-material

REFERENCES

Anisimova, N. P. (1981). *Cryological and Hydrochemical Features of Permafrost*. Novosibirsk: Nauka, 152. (in Russian).

Arkhangelov, A. A., Rogov, V. V., and Lyanos-Mas, A. V. (1979). Cryostratigraphy and Facies of the Duvan Yar Ice Complex. *Problemy Kriolitologii* VIII, 145–157. (in Russian).

Baran, E. J. (2016). Natural Iron Oxalates and Their Analogous Synthetic Counterparts: A Review. *Geochemistry* 76, 449–460. doi:10.1016/j.chemer.2016.06.005

Bates, T. F., and Comer, J. J. (1955). Electron Microscopy of clay Surfaces. *Clays Clay Miner* 3, 1–25. doi:10.1346/ccmn.1954.0030102

Becze-Deák, J., Langohr, R., and Verrecchia, E. P. (1997). Small Scale Secondary CaCO3 Accumulations in Selected Sections of the European Loess belt. Morphological Forms and Potential for Paleoenvironmental Reconstruction. *Geoderma* 76, 22. doi:10.1016/S0016-7061(96)00106-1

Buggle, B., Glaser, B., Hambach, U., Gerasimenko, N., and Marković, S. (2011). An Evaluation of Geochemical Weathering Indices in Loess-Paleosol Studies. *Quat. Int.* 240, 12–21. doi:10.1016/j.quaint.2010.07.019

Butler, I. B., Rickard, D., and Grimes, S. (2000). "Framboidal Pyrite: Self-Organisation in the Fe-S System," in Journal of Conference Abstracts, 5, 276–277.

Comensoli, L., Bindschedler, S., Junier, P., and Joseph, E. (2017). Iron and Fungal Physiology. *Adv. Appl. Microbiol.* 98, 31–60. doi:10.1016/bs.aambs.2016.11.001

Csákberényi-Malasics, D., Rodriguez-Blanco, J. D., Kis, V. K., Rečnik, A., Benning, L. G., and Pósfai, M. (2012). Structural Properties and Transformations of Precipitated FeS. *Chem. Geology* 294-295, 249–258. doi:10.1016/j.chemgeo.2011.12.009

Curtis, C. D. (1990). Aspects of Climatic Influence on the clay Mineralogy and Geochemistry of Soils, Palaeosols and Clastic Sedimentary Rocks. *J. Geol. Soc.* 147 (2), 351–357. doi:10.1144/gsjgs.147.2.0351

Davidson, E. A., and Janssens, I. A. (2006). Temperature Sensitivity of Soil Carbon Decomposition and Feedbacks to Climate Change. *Nature* 440, 165–173. doi:10.1038/nature04514

De Choudens-Sanchez, V., and Gonzalez, L. A. (2009). Calcite and Aragonite Precipitation under Controlled Instantaneous Supersaturation: Elucidating the Role of CaCO3 Saturation State and Mg/Ca Ratio on Calcium Carbonate Polymorphism. *J. Sediment. Res.* 79 (6), 363–376. doi:10.2110/jsr.2009.043

D'Hondt, S., Inagaki, F., Zarikian, C. A., Abrams, L. J., Dubois, N., Engelhardt, T., et al. (2015). Presence of Oxygen and Aerobic Communities from Sea Floor to Basement in Deep-Sea Sediments. *Nat. Geosci.* 8, 299–304. doi:10.1038/ngeo2387

Fotiev, S. M. (2009). *Cryometamorphism of Rocks and Groundwaters: Results and Conditions*. Novosibirsk: Geo, 279. (in Russian).

Kaplina, T. N. (2011). Ancient Alas Complexes of Northern Yakutia. *Kriosfera Zemli* XV (2), 3–13. (in Russian).

Keys, J. R., and Williams, K. (1981). Origin of Crystalline, Cold Desert Salts in the McMurdo Region, Antarctica. *Geochimica et Cosmochimica Acta* 45 (12), 2299–2309. doi:10.1016/0016-7037(81)90084-3

Kolesár, M., and Čurlik, J. (2015). Origin, Distribution and Transformation of Authigenic Carbonates in Loessic Soils. *Ejss* 4 (1), 38–43. doi:10.18393/ejss.50910

Konishchev, V. N. (1982). Characteristics of Cryogenic Weathering in the Permafrost Zone of the European USSR. *Arctic Alpine Res.* 14 (3), 261–265. doi:10.2307/1551158

Konishchev, V. N., and Rogov, V. V. (1993). Investigations of Cryogenic Weathering in Europe and Northern Asia. *Permafrost Periglac. Process.* 4, 49–64. doi:10.1002/ppp.3430040105

Kuleshov, V. N. (2016). in *Isotope Geochemistry: The Origin and Formation of Manganese Rocks and Ores*. Editor J. B. Maynard (Amsterdam: Elsevier), 5–62. doi:10.1016/B978-0-12-803165-0.00002-1

Lacelle, D., Lauriol, B., and Clark, I. D. (2009). Formation of seasonal cave ice and associated cryogenic carbonates in Caverne de l'Ours, Quebec, Canada. Kinetic isotope effects and pseudo-biogenic crystal structures. *J. Cave Karst Stud.* 71 (1), 48–62.

Lupachev, A. V., and Gubin, S. V. (2012). Suprapermafrost Organic-Accumulative Horizons in the Tundra Cryozems of Northern Yakutia. *Eurasian Soil Sc.* 45, 45–55. doi:10.1134/s1064229312010115

Murton, J. B., Goslar, T., Edwards, M. E., Bateman, M. D., Danilov, P. P., Savvinov, G. N., et al. (2015). Palaeoenvironmental Interpretation of Yedoma Silt (Ice Complex) Deposition as Cold-Climate Loess, Duvanny Yar, Northeast Siberia. *Permafrost Periglac. Process.* 26 (3), 208–288. doi:10.1002/ppp.1843

Oelkers, E. H., and Schott, J. (1995). Experimental Study of Anorthite Dissolution and the Relative Mechanism of Feldspar Hydrolysis. *Geochimica et Cosmochimica Acta* 59 (24), 5039–5053. doi:10.1016/0016-7037(95)00326-6

Ostroumov, V., Ostroumova, N., Sorokovikov, V., Hoover, R., Van Vliet-Lanoë, B., and Siegert, Ch. (2001). Redistribution of Soluble Components during Ice Segregation in Freezing Ground. *Cold Regions Sci. Tech.* 32 (2-3), 175–182. doi:10.1016/S0165-232X(01)00031-3

Rogov, V. V. (2009). *Fundamentals of Cryogenesis*. Novosibirsk: Geo, 202. (in Russian).

Rogov, V. V., and Kurchatova, A. N. (2013). Method of Manufacturing Replica for Analyses of Microstructure of Frozen Rocks in Scanning Electron Microscope. RU Patent 2528256 C1. Available at: http://www.freepatent.ru/images/img_patents/2/2528/2528256/patent-2528256.pdf.

Schwamborn, G., Schirrmeister, L., Frütsch, F., and Diekmann, B. (2012). Quartz Weathering in Freeze-Thaw Cycles: experiment and Application to the El'gygytgyn Crater lake Record for Tracing Siberian Permafrost History. *Geografiska Annaler: Ser. A, Phys. Geogr.* 94 (4), 481–499. doi:10.1111/j.1468-0459.2012.00472.x

Siegert, Kh. G. (1981). "Mineral Formation in Permafrost," in *Structure and Thermal Regime of Permafrost* (Novosibirsk: Nauka), 14–21. (in Russian).

Strauss, J., Schirrmeister, L., Grosse, G., Wetterich, S., Ulrich, M., Herzschuh, U., et al. (2013). The Deep Permafrost Carbon Pool of the Yedoma Region in Siberia and Alaska. *Geophys. Res. Lett.* 40 (23), 6165–6170. doi:10.1002/2013GL058088

Tranter, M. (2003). "Geochemical Weathering in Glacial and Proglacial Environments," in Holland, H.D., Turekian, K.K. (Eds.), *Treatise on Geochemistry: Surface and Ground Water, Weathering, and Soils*. Elsevier, pp. 189–205. doi:10.1016/b0-08-043751-6/05078-7

Turchyn, A. V., Bradbury, H. J., Walker, K., and Sun, X. (2021). Controls on the Precipitation of Carbonate Minerals within marine Sediments. *Front. Earth Sci.* 9. doi:10.3389/feart.2021.618311

Varadachari, C., Barman, A. K., and Ghosh, K. (1994). Weathering of Silicate Minerals by Organic Acids II. Nature of Residual Products. *Geoderma* 61, 251–268. doi:10.1016/0016-7061(94)90052-3

Vasil'chuk, Y. K. (2005). Heterochroneity and Heterogeneity of the Duvanny Yar Edoma. *Doklady Earth Sci.* 402, 568–573. doi:10.1594/PANGAEA.919525

Veremeeva, A., Nitze, I., Günther, F., Grosse, G., and Rivkina, E. (2021). Geomorphological and Climatic Drivers of Thermokarst Lake Area Increase

Trend (1999-2018) in the Kolyma Lowland Yedoma Region, North-Eastern Siberia. *Remote Sensing* 13, 178. doi:10.3390/rs13020178
Yershov, E. D. (1998). *General Geocryology*. Cambridge: Cambridge University Press, 580.

Conflict of Interest: The authors declare that the research was conducted in the absence of any commercial or financial relationships that could be construed as a potential conflict of interest.

Publisher's Note: All claims expressed in this article are solely those of the authors and do not necessarily represent those of their affiliated organizations, or those of the publisher, the editors and the reviewers. Any product that may be evaluated in this article, or claim that may be made by its manufacturer, is not guaranteed or endorsed by the publisher.

frontiers in Earth Science

ORIGINAL RESEARCH
published: 28 October 2021
doi: 10.3389/feart.2021.758360

Circum-Arctic Map of the Yedoma Permafrost Domain

Jens Strauss[1], Sebastian Laboor[1], Lutz Schirrmeister[1], Alexander N. Fedorov[2], Daniel Fortier[3], Duane Froese[4], Matthias Fuchs[1], Frank Günther[1,5], Mikhail Grigoriev[6], Jennifer Harden[7], Gustaf Hugelius[8,9], Loeka L. Jongejans[1,5], Mikhail Kanevskiy[10], Alexander Kholodov[11], Viktor Kunitsky[6], Gleb Kraev[12,13], Anatoly Lozhkin[14], Elizaveta Rivkina[15], Yuri Shur[10], Christine Siegert[1], Valentin Spektor[6], Irina Streletskaya[16], Mathias Ulrich[17], Sergey Vartanyan[14], Alexandra Veremeeva[15], Katey Walter Anthony[10], Sebastian Wetterich[1], Nikita Zimov[18] and Guido Grosse[1,5]*

[1]Permafrost Research Section, Alfred Wegener Institute Helmholtz Centre for Polar and Marine Research, Potsdam, Germany, [2]Laboratory of Permafrost Landscapes, Melnikov Permafrost Institute, Yakutsk, Russia, [3]Geography Department, Université de Montréal, Montréal, QC, Canada, [4]Department of Earth and Atmospheric Sciences, University of Alberta, Edmonton, AB, Canada, [5]Institute of Geosciences, University of Potsdam, Potsdam, Germany, [6]Laboratory of General Geocryology, Melnikov Permafrost Institute, Yakutsk, Russia, [7]Scientist Emeritus, Formerly United States Geological Survey, Menlo Park, CA, United States, [8]Department of Physical Geography, Stockholm University, Stockholm, Sweden, [9]Bolin Centre for Climate Research, Stockholm University, Stockholm, Sweden, [10]Institute of Northern Engineering, University of Alaska Fairbanks, Fairbanks, AK, United States, [11]Geophysical Institute, University of Alaska Fairbanks, Fairbanks, AK, United States, [12]Yamal-Nenets Center of Arctic Research, Salekhard, Russia, [13]Institute of Geography of the Russian Academy of Sciences, Moscow, Russia, [14]North-East Interdisciplinary Scientific Research Institute, Magadan, Russia, [15]Institute of Physicochemical and Biological Problems in Soil Science, Russian Academy of Sciences, Pushchino, Russia, [16]Geographical Faculty, Lomonosov Moscow State University, Moscow, Russia, [17]Institute for Geography, Leipzig University, Leipzig, Germany, [18]North-East Science Station, Pacific Geographical Institute of the Russian Academy of Sciences, Cherskii, Russia

OPEN ACCESS

Edited by:
Nozomu Takeuchi,
Chiba University, Japan

Reviewed by:
Yoshihiro Iijima,
Mie University, Japan
Kazuyuki Saito,
Japan Agency for Marine-Earth Science and Technology (JAMSTEC), Japan

***Correspondence:**
Jens Strauss
jens.strauss@awi.de

Specialty section:
This article was submitted to Cryospheric Sciences, a section of the journal Frontiers in Earth Science

Received: 13 August 2021
Accepted: 11 October 2021
Published: 28 October 2021

Citation:
Strauss J, Laboor S, Schirrmeister L, Fedorov AN, Fortier D, Froese D, Fuchs M, Günther F, Grigoriev M, Harden J, Hugelius G, Jongejans LL, Kanevskiy M, Kholodov A, Kunitsky V, Kraev G, Lozhkin A, Rivkina E, Shur Y, Siegert C, Spektor V, Streletskaya I, Ulrich M, Vartanyan S, Veremeeva A, Anthony KW, Wetterich S, Zimov N and Grosse G (2021) Circum-Arctic Map of the Yedoma Permafrost Domain. Front. Earth Sci. 9:758360. doi: 10.3389/feart.2021.758360

Ice-rich permafrost in the circum-Arctic and sub-Arctic (hereafter pan-Arctic), such as late Pleistocene Yedoma, are especially prone to degradation due to climate change or human activity. When Yedoma deposits thaw, large amounts of frozen organic matter and biogeochemically relevant elements return into current biogeochemical cycles. This mobilization of elements has local and global implications: increased thaw in thermokarst or thermal erosion settings enhances greenhouse gas fluxes from permafrost regions. In addition, this ice-rich ground is of special concern for infrastructure stability as the terrain surface settles along with thawing. Finally, understanding the distribution of the Yedoma domain area provides a window into the Pleistocene past and allows reconstruction of Ice Age environmental conditions and past mammoth-steppe landscapes. Therefore, a detailed assessment of the current pan-Arctic Yedoma coverage is of importance to estimate its potential contribution to permafrost-climate feedbacks, assess infrastructure vulnerabilities, and understand past environmental and permafrost dynamics. Building on previous mapping efforts, the objective of this paper is to compile the first digital pan-Arctic Yedoma map and spatial database of Yedoma coverage. Therefore, we 1) synthesized, analyzed, and digitized geological and stratigraphical maps allowing identification of Yedoma occurrence at all available scales, and 2) compiled field data and expert knowledge for creating Yedoma map confidence classes. We used GIS-techniques to vectorize maps and harmonize site information based on expert knowledge. We included a range of attributes for Yedoma areas based on lithological and stratigraphic information from the source maps and assigned three different confidence levels of the presence of Yedoma (confirmed, likely, or uncertain). Using a spatial buffer of 20 km around mapped Yedoma occurrences, we derived an extent of the Yedoma domain. Our result is a vector-based map of the current pan-Arctic Yedoma domain that covers approximately 2,587,000 km^2, whereas Yedoma deposits are found within 480,000 km^2 of this region. We estimate that 35% of the total Yedoma area today is located in the tundra zone, and 65% in the taiga zone. With this Yedoma mapping, we outlined the substantial spatial extent of late Pleistocene Yedoma deposits and created a unique pan-Arctic dataset including confidence estimates.

Keywords: late Pleistocene, syngenetic permafrost, Beringia, Siberia, Alaska, Yukon

1 INTRODUCTION

Vast portions of the Arctic and sub-Arctic regions (hereafter pan-Arctic), predominantly in Siberia, the Far East of Russia, Alaska and Yukon, are covered by ice-rich fine-grained permafrost deposits that contain large late Pleistocene syngenetic ice wedges (Sher et al., 1971; Kanevskiy et al., 2011; Schirrmeister et al., 2013). Accompanied by wedge-ice growth in polygonal tundra-steppe landscapes, the sedimentation process was driven by cold continental climatic and environmental conditions in unglaciated regions during the late Pleistocene, inducing the accumulation of the unique Yedoma deposits up to 50 m thickness. Because of the fast incorporation of material into syngenetic permafrost and ice wedge growth during its formation, Yedoma deposits include a high volume of ground ice (including pore, segregated, and wedge ice) and preserved organic matter consisting of floral and faunal fossil remains that are perennially frozen and distinct from the recent organic matter cycles and have remained relict for tens of thousands to hundreds of thousands of years (Schirrmeister et al., 2011; Strauss et al., 2017). The first descriptions of Yedoma deposits date back to the early 19th century, when Arctic explorers described these deposits erroneously as buried glacial ice remnants based on the obvious high amount of "pure" ice that was observed in coastal exposures (von Kotzebue, 1821).

The permafrost region and the Yedoma domain in particular have been characterized as a very large and potentially vulnerable organic carbon pool (Schuur et al., 2015). Recently, the Yedoma domain has even been discussed as one of the potential climate tipping elements (Lenton et al., 2019). Scientific interest in Yedoma is rising as, besides the vulnerability of its frozen organic matter pool to degradation, melt of the high excess ground ice upon Yedoma thaw will cause substantial ground volume loss. Resulting surface subsidence will pose a serious threat to any infrastructure built on permafrost (de Grandpré et al., 2012; Hjort et al., 2018; Streletskiy et al., 2019; Chen et al., 2021; Schneider von Deimling et al., 2021). More broadly, Yedoma thaw implies substantial consequences for landscape reorganization by surface subsidence (Günther et al., 2015; Antonova et al., 2018), thermal erosion (Kanevskiy et al., 2016; Fuchs et al., 2020; Shur et al., 2021b; Morgenstern et al., 2021), thermokarst formation (Jones et al., 2011; Nitze et al., 2017; Ulrich et al., 2017; Veremeeva et al., 2021), and relief inversion as well as land loss by coastal erosion (Günther et al., 2013; Farquharson et al., 2018). Such changes of the periglacial landscape inventory certainly affect surface and sub-surface drainage patterns across scales, trigger ecosystem responses, and thus alter floral and faunal species composition and distribution (Pastick et al., 2019; Jones et al., 2020).

Previous studies estimated that Yedoma deposits cover about one million km^2 of a large region in central and eastern Siberia (Romanovskii, 1993; Zimov et al., 2006), especially Yakutia (Grigoriev and Kunitsky, 2000; Konishchev, 2011), although these estimates are generally based on maps with scales smaller than 1:10,000,000. During the late Pleistocene, the extent of Yedoma and Yedoma-like deposits may have been up to three million km^2 (Zimov et al., 2006; Walter et al., 2007; Strauss et al., 2017). Detailed compilations of current Yedoma distribution were started by using Quaternary geological maps at scales of 1:500,000 to 1:1,000,000 for Northeast Siberia (Grosse et al., 2013). Map analysis and field studies showed that significant areas of Yedoma deposits were reworked by thermokarst and thermal erosion due to the climate warming at the end of the Pleistocene and beginning of the Holocene with extensive thermokarst lake formation, expansion, and drainage (Kaplina, 2009; Morgenstern et al., 2013; Lenz et al., 2016). Estimations of Yedoma and drained lake basin coverage in the Yana-Indigirka and Kolyma Lowlands show that the modern area of drained lake basins could reach up to 80–100% in low-lying relief regions with Yedoma remnants covering now less than 20% while in elevated regions 40–55% of Yedoma uplands remained (Veremeeva, 2016; Veremeeva et al., 2021). Building on previous efforts, the objective of our present study is to compile the first detailed circum-Arctic digital map of the Yedoma domain coverage using high and medium resolution geological and stratigraphical maps from the regions of former Beringia, the unglaciated landmass consisting of today's Siberian (Russia), Alaskan (United States) and Yukon (Canada) territories.

1.1 Terminology

1.1.1 Origin of the Term Yedoma

There is no clear agreement on the origin of the term "Yedoma" and its association with ice-rich fine-grained sediments. One version is that "Yedoma" was originally used by local people in Yakutia in a geomorphological sense to describe hills composed of Ice Complex deposits, which are "eaten" (Russian root yed from yest' = to eat, to reduce, to erode) by thermokarst that is forming typical landforms of alternating hills with lake depressions. However, there is no absolute confidence regarding this meaning. The term Yedoma was also used in the north-European part of Russia, where its originality from "samoyed" (Finnish language "erämaa") is hypothesized with the meaning of remote forests or pasture and something "far away" or "wilderness" (Chudinov, 1910).

1.1.2 Previous Scientific Use of the Term Yedoma

As summarized by Kanevskiy et al. (2011) and Schirrmeister et al. (2013), the terminology used in scientific publications for the ice-rich, syngenetically frozen deposits of late Pleistocene age varies across Beringia. These deposits are often referred to as "Ice Complex", "Yedoma", or "Edoma" in Siberia, while in North America other terms such as "muck" or "upland silt" are partially considered as equivalent terms (Péwé, 1975; Shur et al., 2004; Froese et al., 2009). The term "muck", originating from gold mining operations, seems to have the broader meaning of an overburden material including ice-rich deposits of Holocene age (Péwé, 1975), but with remnants dating back to at least 700 ka in Yukon (Froese et al., 2008). Solov'ev (1959) defined "Ice Complex" as frozen deposits of various age, composition, genesis, and thickness, with syngenetic ice wedges. Ice Complexes formed in the Pleistocene and the oldest directly dated Ice Complexes are the mid-Pleistocene Yukagir Suite of Bol'shoy Lyakhovsky Island (New Siberian Islands) with an age of about 2,00,000 years (Tumskoy, 2012; Wetterich et al., 2019). The lower Ice Complex of the Batagay Megaslump was even dated to an age of about 650 000 years (Murton et al., 2021). Usually, the Yedoma Ice Complex formed in late Pleistocene during the period 60,000-12,500 years (Sher et al., 1971; Sher et al., 1987; Schirrmeister et al., 2002a; Kaplina, 2009; Strauss et al., 2017). It is considered a dominant relief-forming deposit in many regions of western Beringia. The term "Yedoma Suite", describing the late Pleistocene Ice Complex, was first introduced into the regional stratigraphic scheme of northeastern Siberia (Sher et al., 1987). As there are many usages and viewpoints of "Yedoma" in literature, it is difficult to agree on one overall definition. Especially, uncertainties using this term in mining and scientific traditions complicate a circum-Arctic Yedoma study. Nevertheless, it is agreed that ice constitutes the largest portion of Yedoma deposits with 60–95 volume percent (vol %) including pore, segregated, and wedge ice (Kanevskiy et al., 2011; Schirrmeister et al., 2013; Strauss et al., 2013; Ulrich et al., 2014; Kanevskiy et al., 2016; Strauss et al., 2017; Wetterich et al., 2019; Schirrmeister et al., 2020; Wetterich et al., 2020; Kanevskiy et al., Forthcoming 2021). Further, clastic and organic Yedoma components (Schirrmeister et al., 2011; Schirrmeister et al., 2013) suggest aeolian, fluvial, or slope sedimentation with simultaneous freezing (i.e. syngenetic permafrost formation).

1.1.3 Yedoma Definition

Our summary definition considers that Yedoma deposits are perennially frozen (permafrost), fine-grained, organic-bearing, and ice-rich sediments of late Pleistocene age, that they can reach thickness of up to tens of meters and are framed by large syngenetic ice wedges, and that they are preserved in remnant Yedoma uplands. With this definition, we cover the Yedoma Suite and other types of the late Pleistocene Ice Complexes and late Pleistocene muck, being located in West, Central and East Siberia, in Chukotka and the Russian Far East as well as in Alaska and Yukon areas. Even though syngenetic Pleistocene permafrost sediments mostly have large ice wedges, this is not true for all cases (e.g. Fraser and Burn, 1997; Froese et al., 2009).

1.1.4 Yedoma Domain

Analogue to the permafrost region, where "just" a part of the sediments are perennial frozen (e.g. >90% coverage in the continuous permafrost region below the active layer), the "Yedoma domain" term refers to the region where Yedoma deposits are expected to occur but may also include drained lake basins, river valleys etc. Thus, this region is an outline of the maximum extent of Yedoma deposits during the late Pleistocene.

2 MATERIALS AND METHODS

We continued the work of Grosse et al. (2013) to extend their digital database of Yedoma distribution in East and Central Siberia by updating and merging different sources such as maps, scientific descriptions and synthesizing scientific literature.

2.1 Digitization of Maps

Our study focused on extracting geologic units from existing maps that are labeled as Yedoma or that we interpreted as Yedoma, based on cryolithology, ground ice conditions, geochronology, geomorphologic, and spatial associations (**Figure 1**). For compiling this map, we used maps of the previous Yedoma coverage estimates, included the digitized areas from Grosse et al. (2013), and extracted areas of potential Yedoma distribution from additional surface geological and Quaternary geological maps:

- 1:500,000 Geological maps of Yakutia (**Supplementary Table S2**)
- 1:1,000,000 Quaternary formation maps of Russia (**Supplementary Table S3**)
- 1:2,500,000 Quaternary map of the territory of Russian Federation (**Supplementary Table S4**)
- Permafrost Characteristics of Alaska
- Late Quaternary Aeolian Deposits of Northern North America: Age and Extent, Geological Survey of Canada (Wolfe et al., 2009), used in version 1 of the map available at Strauss et al. (2016)
- Yukon Digital Surficial Geology Compilation as digital 1:50,000 (50k), 1:100,000–125,000 (100k–125k) and 1:250,000 (250k) datasets (replaced the "Late Quaternary Aeolian Deposits of Northern North America" in this dataset, Yukon Geological Survey, 2014)
- Dataset "The Lena River Delta - inventory of lakes and geomorphological terraces" by Morgenstern, et al. (2011)
- Digital Database and Maps of Quaternary Deposits in East and Central Siberia by Bryant et al. (2017).

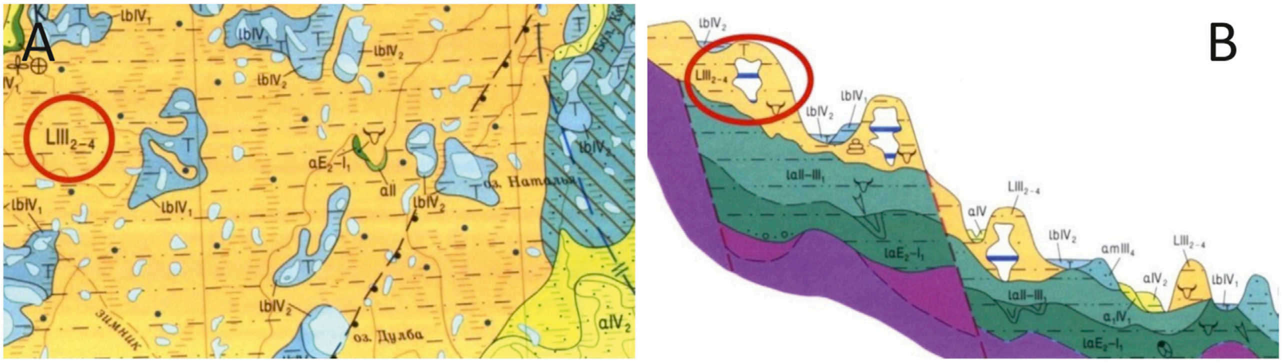

FIGURE 1 | Example subsets of the maps with Yedoma units. This example from Grosse et al. (2013) was taken from map R-(55)-57. **(A)** Map view: Orange-colored unit LIII$_{2-4}$ (label circled in red) is described in the legend as loess-like deposits (L) of late Pleistocene stratigraphy (III), specifically covering the periods Zyryan, Kargin, and Sartan (2–4). The lithologic signature (dash-dot-dash) illustrates that this unit consists of mostly silty to fine-sandy deposits, and the dark blue dots indicate very high ground ice contents. Abundance of lakes (light blue) and lacustrine deposits (medium and dark blue, lbIV$_1$ and lbIV$_2$) within the unit indicate degradation of at least the upper part of the Yedoma unit by Holocene thermokarst. **(B)** Cross-profile view: the same unit LIII$_{2-4}$ (red circle) is shown to blanket terrace slopes. Bison skull symbol indicates the presence of fossil bones of the mammoth fauna. White features with blue stripes (e.g. in the red circle) indicate the presence of large syngenetic ice wedges typical for Yedoma.

- Quaternary deposits map of Yana-Indigirka and Kolyma lowlands tundra zone, R-55-57, based on Landsat imagery by Veremeeva (2021).
- Sedimentological, biogeochemical and geochronological data of Yedoma and thermokarst deposits in West-Alaska by Jongejans et al. (2018a) and Jongejans et al. (2018b).

Supplementary Figure S5 shows the approximate map frames of the used sources. The digitization was done using GIS techniques (ArcGIS) and semiautomated vectorization of raster images (Adobe Photoshop and Illustrator). Using digitized geologic maps does not violate the spatial resolution of the specific data. Even though the digital form of the map removes the constraints imposed by the scale of a paper map, the detail and accuracy represents various scale-specific generalization levels of each map. Similarly, where this database is used in combination with other data of higher resolution, the resolution of the combined output will be limited by the lower resolution of these data.

The original geological Quaternary maps of Russia were issued by the Department of Natural Resources of the Russian Federation or its predecessor the Department of Geology of the Soviet Union and have their foundation in decades of geological field and remote sensing work and mapping at scales 1:50,000 to 1:500,000 by Russian geologists and cartographers in the respective regions.

We eventually merged the Yedoma spatial units extracted from across these multiple maps into a single data layer for the pan-Arctic domain. We further synthesized data on the thickness of Yedoma for our database using deposit thickness information provided on the maps and from published datasets from drill cores and exposures.

2.1.1 Geological Maps of Yakutia, Scale 1:500,000

We used nine geological maps of Yakutia of scale 1:500,000 to refine the spatial distribution of Yedoma deposits. The data were digitized and edited at a scale of 1:500,000. The Yedoma identification criteria are shown in the supplement (**Supplementary Table S2**).

2.1.2 Russian Quaternary Formation Maps, Scale 1: 1,000,000 Map

We used 23 Quaternary formation maps of scale 1:1,000,000 to refine the spatial distribution of Yedoma deposits. The data was edited at a scale of 1:1,000,000. On these maps, we also extracted point features, which contain information about boreholes in potential Yedoma deposits. Yedoma selection criteria are listed in **Supplementary Table S3**.

2.1.3 Quaternary Map of the Territory of Russian Federation, Scale 1:2,500,000

The 1:2,500,000 scaled map published in 2010 by the Ministry of Natural Resources and Ecology of the Russian Federation, Federal Agency of Mineral Resources was used to extract the areas declared as "Ice loess (Yedoma) deposits" (**Supplementary Table S4**).

2.1.4 Alaskan Permafrost Map, Scale 1:7,200,000

For Yedoma deposits in Alaska, we used the "Permafrost Characteristics of Alaska" map, scale 1:7,200,000 published by Jorgenson et al. (2008). Here, we extracted the areas declared as "loess" and "ice rich" (**Supplementary Table S5, S6**). To reduce the area of this highly generalized Yedoma polygon features and to improve the Yedoma domain estimate, we used the "Global Lakes and Wetlands Database" (GLWD) (Lehner and Döll, 2004) and clipped the Yedoma domain polygon with GLWD lake polygons. Moreover, we used Yedoma distribution maps for Alaska derived from extensive geomorophologic mapping in the field and literature synthesis by Kanevskiy et al. (2011; 2016; Forthcoming 2021) for a visual plausibility check.

2.1.5 Yukon Loess Map

For the western Yukon loess, we used the map "Loess of Northern North America" published by Wolfe et al. (2009) in the dataset

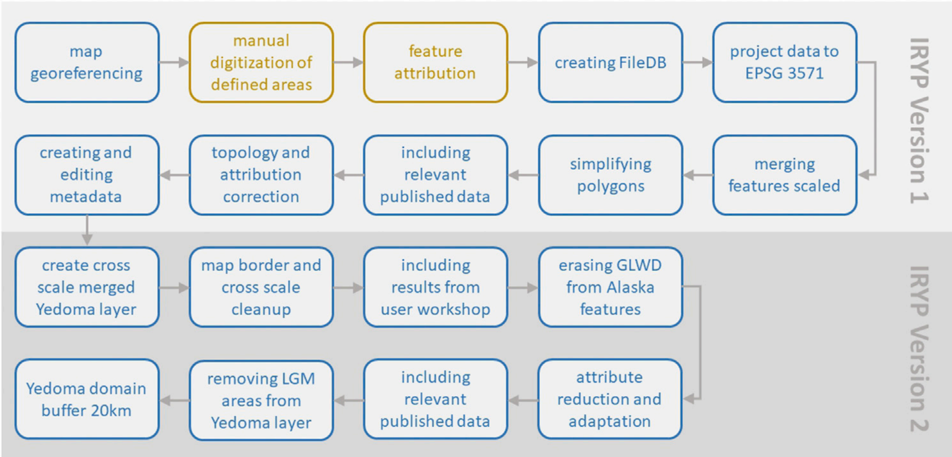

FIGURE 2 | Workflow of the major steps of the Ice-Rich Yedoma Permafrost (IRYP) mapping from the scanned Russian maps or Alaskan and Canadian datasets to data interpretation, data harmonization to compiling the overall map. Software applied in these steps included ArcGIS (blue) and Avenza MAPublisher (yellow).

version in Strauss et al. (2016). In this version, we refined it by using the Yukon Digital Surficial Geology Compilation (Yukon Geological Survey, 2014). We selected the Yukon 1:50,000, 1:100,000–125,000 and 1:250,000 maps. The selection criteria are shown in the supplement (**Supplementary Table S8**). We clipped this with late Pleistocene glacial areas to avoid overestimation.

2.1.6 Inclusion of Other Datasets

There are a few datasets with more detailed mapping. For example, Veremeeva (2021) used Landsat images that allow the area of the Yedoma uplands and alases (partially to fully drained depressions formed by thermokarst, i.e. ground-ice melt induced surface subsidence and lake formation) to be clearly identified. We included this detailed dataset in our circum-Arctic version. Moreover, we used the difference between our first estimate for this region compared to Veremeeva (2021) as an indicator for and potential overestimation of Yedoma coverage, also caused by ongoing degradation (thermokarst and other processes).

For the Baldwin Peninsula, one of the first (1826) sites where Yedoma was encountered scientifically (at Cape Blossom (Beechey, 1831, see; Shur et al., Forthcoming 2021a), we integrated the Yedoma areas defined in the land cover classification map published by Jongejans et al. (2018) (**Supplementary Table S1**). We used data from Morgenstern et al. (2011) for refining the Lena Delta and Bryant et al. (2017) as well as Grosse et al. (2013) for East and Central Siberia.

2.2 Dataset Merging and Harmonization

To harmonize the different datasets and to avoid merging artifacts, we applied map edge cleaning while merging data from different database layers. For the digitalization and spatial integration, we used Adobe Photoshop CS6 (Version: 13.0 x64), Adobe Illustrator CS6 (Version 16.0.3 x64), Avenza MAPublisher 9.5.4 (Illustrator Plug-In) and ESRI ArcGIS 10.2.2 for Desktop (Advanced License). The applied working steps were done as described in **Figure 2** and the **Supplementary Methods** in detail.

To improve working efficiency with many georeferenced maps in a map view, overlapping map parts, legends, and further information were clipped. For georeferencing, we used map corner coordinates as control points. For older maps, more (up to 50) control points had to be set at grid intersections. Then, to simplify further data processing, the geological maps were reprojected using WGS84 as datum to a common projection. In order to define the relevant map contents, we used different sources from different continents for our study. Even if having the same publisher, which is the case for the Russian geological maps, the maps were compiled with diverse geological foci and during different times. For every map, we defined the relevant categories, and for the Russian maps, the legend content had to be translated to English. After this, we used Avenza MAPublisher (Adobe Illustrator) for vectorization. From the Russian geological maps in 1:500,000 scale, we digitized 818 (multi-)polygon features. For the 1:1,000,000 maps, about 2,138 (multi-) polygon features and 75 point features of deposit thickness were digitized, and from geological maps of scale 1:2,500,000, we deduced about 771 (multi-)polygon features. We connected the digitized polygons to the specific relevant attributes. We provided information for stratigraphic units that were assigned to Yedoma in **Supplementary Tables S5–S8**, as well as in Grosse et al. (2013 table D1).

Subsequently, the Yedoma database was built by merging (projection: EPSG: 3571 WGS 1984 North Pole LAEA Bering_Sea) the different data extracts. We defined topology rules to identify and solve errors like gaps between bordering areas and areas overlapping within a layer. Some content errors have been resolved by checking the dataset manually. For the Alaskan dataset, we cut out lakes and used the "Global Lakes and Wetlands Database" to clip lake polygons. We removed overlaps of the generated Yedoma polygons with areas of LGM glaciation. This removed a large portion of the areas generated from the

Yukon Digital Surficial Geology Compilation, and a few small areas in Western Siberia.

2.3 Field Sites and Photos

For Yedoma ground truthing, we synthesized available field sites from scientific literature data on Yedoma characteristics and occurrences. Our database includes more than 360 boreholes and exposures. These points were summarized by Schirrmeister et al. (2011), Kanevskiy et al. (2011) and updated with additional points by Strauss et al. (2013) and Strauss et al. (2017). For Chukotka we use a field guide compiled by Kotov and Brazhnik (1991).

As an additional visualization opportunity, we initiated the Yedoma photo database as a feature collection, having a point as spatial representation. (**Supplementary Figure S2**). This point feature class (collection/compilation of points in a geospatial layer) includes the spatial location of photos showing Yedoma, which were taken by several members of the International Permafrost Association (IPA) Yedoma Action Group. The picture's credits and license information are given in the attribute table.

To get a general impression of Yedoma thickness, which is needed for volume estimation, we included the data synthesized by Strauss et al. (2013; 2017). We compiled field and literature data for available Yedoma depth estimates and updated this with newly available or newly recognized depth estimates (see **Supplementary Table S9**).

2.4 Inclusion of Expert Knowledge

During the International Conference on Permafrost (ICOP) held in Potsdam in 2016, a 2-day Yedoma workshop took place (**Supplementary Figure S3**). Preliminary maps were discussed and checked by a group of experts. For this reason, the IRYP map was split into four regions: Western and Central Siberia (supervised by I. Streletskaya), East Siberia/Yakutia (supervised by V. Kunitsky and C. Siegert), Far East Siberia and Chukotka (supervised by D. Shmelev and G. Kraev) and Alaska and Canada (supervised by Y. Shur and D. Froese). We used first-hand field knowledge from various Yedoma sites and scientific literature in order to decide if digitized areas should be attributed to Yedoma.

2.5 Confidence Estimation and Area Estimate Harmonization

Despite studies on Yedoma mystery and controversy for more than 150 years (Shur et al., Forthcoming 2021a), we had to agree on a technical way to compile Yedoma deposits on the broad scale, including local peculiarities. To account for this level of controversy and uncertainty, we implemented a Yedoma confidence classification system based on source details and additional information such as ancillary data on lithology and stratigraphy, which can be attributed to Yedoma. This data is often available in the original source maps and helped us to define our confidence level four our Yedoma classification of a specific area or region. We included a range of attributes for Yedoma area polygons based on lithological and stratigraphical information from the original source maps as well as a confidence level for our classification of an area as Yedoma (three levels: confirmed, likely, or uncertain, corresponding to high, medium, and low confidence). We based the confidence level on the amount of independent sources providing information about the sites. In case that just the stratigraphic context of the maps matched the Yedoma description, we classified the Yedoma as "uncertain" (**Table 1**). When one map explicitly defined a certain area as Yedoma, and this classified polygon intersected with polygons of other maps, or if lithologic and stratigraphic context were plausible for Yedoma, we used the classification "likely". We reached the level "confirmed" when field data was available, or it was mentioned on the map explicitly as Yedoma, or the context of lithology and close field data fit, or experts agreed that this is Yedoma.

As the Alaskan Yedoma domain is mapped in less detail when compared to the Siberian (see **Figure 3**) or the Canadian datasets, and thus including much more alas basins and other areas, we applied a correction factor of 0.5 for the Alaskan area estimation to avoid overestimation of the Yedoma area (**Supplementary Table S10**). This factor is a first guess based on findings from Veremeeva (2021) reducing our mapped areas by 50%, even though it is in Siberia with better spatial resolution (**Supplementary Table S10**).

2.6 Estimating the Yedoma Domain Outline

For getting the outline of the maximum Yedoma domain, and to be able to compare it to older regional estimates (**Supplementary Figure S4**), we decided to add a buffer of 20 km to each digitized Yedoma polygon and merge these areas. This buffer distance was chosen as the average to compensate for the lower resolution of older maps as well as a reasonable distance to account for the fact that natural borders are never as sharp as illustrated in the maps. The buffer was clipped with the coastline and the resulting area is shown in **Figure 4**.

3 RESULTS

3.1 Coverage and Regional Classification

We estimated the Northern Hemisphere Yedoma domain to cover approximately 2,587,000 km^2 located between the Yamal Peninsula in Russia all the way to the Yukon, Canada (**Figure 4**). In this domain, we estimate that 480,000 km^2 to be underlain by Yedoma. 35% of the total Yedoma area today is located in the tundra zone, and 65% in the taiga and boreal ecozone (tree line from Walker et al., 2005).

Our database includes more than 360 boreholes and exposures and more than 13,600 digitized Yedoma areas. For the area calculations please note the above-mentioned Alaskan correction factor of 0.5. The globally northernmost Yedoma occurrence was found on 138.9°E, 76.19°N (Kotelny Island, confidence class: confirmed), the easternmost in 136.0°W, 62.88°N (close to the village of Pelly Crossing, Canada, confidence class: uncertain), the southernmost in Central Yakutia 127.3°, 61.0° (close to the village Sinsk, Yakutia, confidence class: confirmed), and the westernmost 83.0°E, 70.3°N (Yenisei River, confidence class: uncertain). If only including the confirmed areas, the latitudinal extent stretches from 76.19°N to 61.0°N and longitudinal extent from 141°W to 83.28°E.

TABLE 1 | Confidence classification scheme. In the column "confidence ID", the first number is connected to the confidence classification' and the second number to the confidence source.

Confidence classification	conf_source (the source that constitutes the confidence)	Confidence ID (classification and source)
confirmed (1)	1_field data	11
confirmed (1)	2_explicit classification in map	12
confirmed (1)	3_context of lithology and field data	13
confirmed (1)	4_expert_knowledge	14
likely (2)	1_intersection with explicit classification of 2.5M map	21
likely (2)	2_lithologic and stratigraphic context	22
uncertain (3)	1_stratigraphic context	31

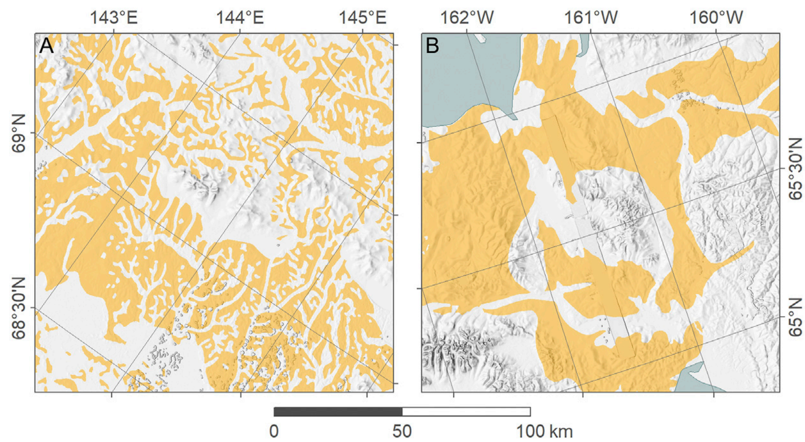

FIGURE 3 | Different levels of detail/fragmentation of Siberian **(A)** and Alaskan **(B)** Yedoma dataset with the same scale. For improving the level of detail of the Alaskan dataset, we excluded lake areas (clipping lake areas) as well as using a correction factor of 0.5 for the area calculation.

Separated from east to west (a bit misleading as we are crossing the international date line), 19% of the Yedoma area is found in North America (18.5% Alaska, 0.1% in Canada) and 81% in northern Asia.

3.2 Confidence

We found 83% (399,060 km^2) of our digitized Yedoma areas to be confirmed, 5% (21,873 km^2) to be likely and 12% (58,808 km^2) to be uncertain. Looking at the Yedoma domain (**Figure 4**) and its confidence estimates (**Figure 5**), Yakutia proves to be the heartland of Yedoma.

3.3 Available Products

All products from the present Yedoma mapping attempt are based on the Ice-Rich Yedoma Permafrost (IRYP) database. A preliminary version was published by Strauss et al. (2016) and with this study, we enhanced and finalized the database. All reported results and products of this study are based on this second version (IRYPv2).

The main product of this study is the map (**Figure 4** and map version in the supplement) and its confidence estimate (**Figure 5** and map version in the supplement).

Moreover, we worked closely together with the geospatial visualization team of the Alfred Wegener Institute (Germany; maps@awi.de) and the Arctic Permafrost Geospatial Centre (APGC; https://apgc.awi.de/) to make a WebGIS available allowing for interaction with the spatial data sets (**Supplementary Figure S1**). We further published a visual tool called the Yedoma picture database (**Supplementary Figure S2**) that is hosted and visualized by the APGC and PANGAEA, whose pictures were used for the confidence assessment.

4 DISCUSSION

4.1 Previous Large Scale Mapping of Yedoma Distribution

Various maps of Yedoma distribution exist in the literature. However, most of them are small-scale (1:10,000,000 or smaller) maps that tend to under or overestimate the spatial extent of Yedoma. The Yedoma map most widely referred to is that of Romanovskii (1993) (**Supplementary Table S1** and **Supplementary Figure S4**), but the first Yedoma map, to our knowledge, was published by Tormidiaro (1980) (**Supplementary Table S1** and **Supplementary Figure S4**). In another adaptation of the small-scale map of Yedoma distribution, Konishchev (2011) separated the Yedoma deposits into three categories of spatial

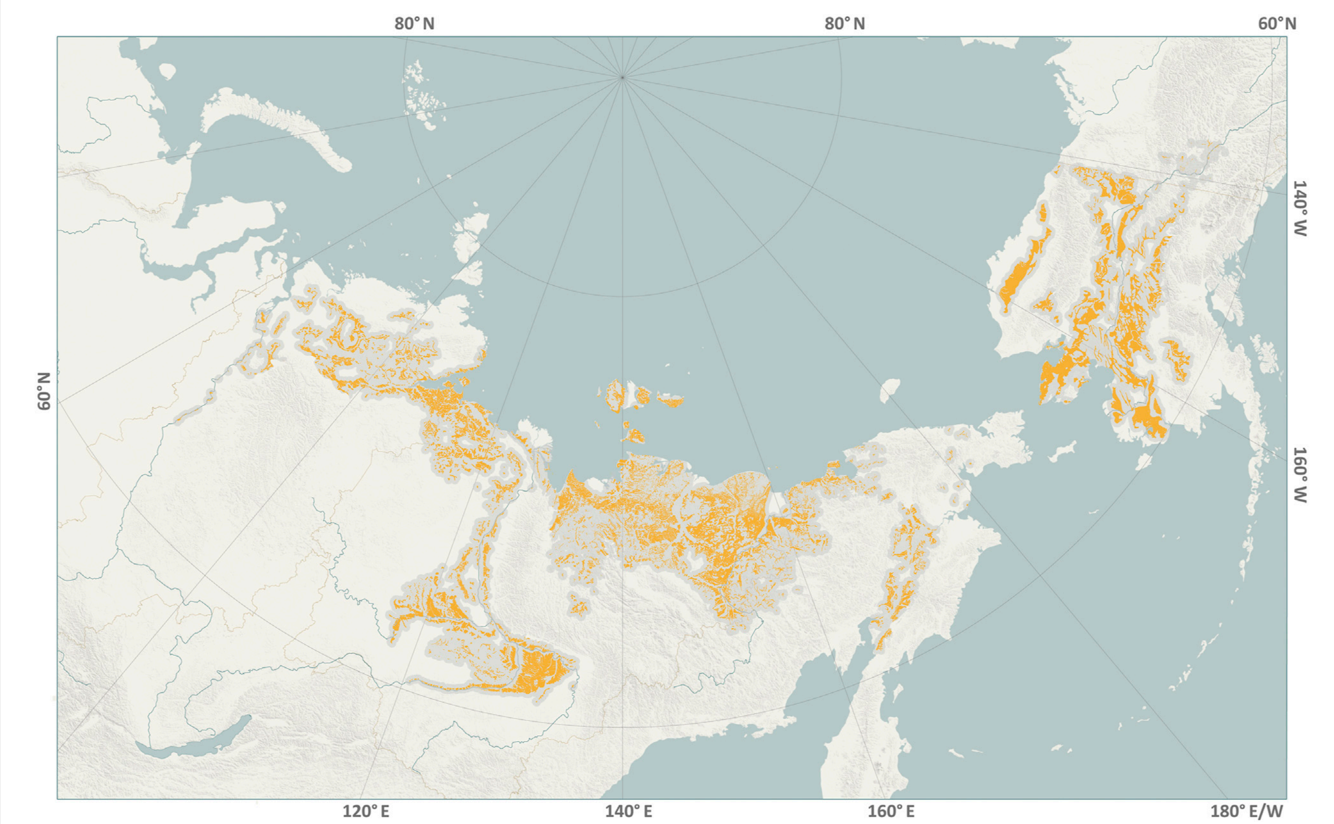

FIGURE 4 | Yedoma Northern Hemisphere Distribution. The grey area illustrates the Yedoma domain outline visualized with a 20 km buffer around all digitized areas. An A0 map version of this map is available in the supplement, and a geospatial PDF on https://apgc.awi.de/. The blank area on the map is considered as an area where Yedoma does not exist.

distribution, ranging from widely distributed to fragmented to sporadic (**Supplementary Table S1**).

The area covered by Yedoma in Romanivskii's (not including spatially not quantified "Yedoma in river valleys) map is 1,141,390 km^2. This map has been subsequently adapted by Siegert and Romanovskii (1996) and was furthermore published by Schirrmeister et al. (2002b), showing Yedoma extent in central and northeastern Siberian lowlands and indicating additional Yedoma occurrences in formerly unglaciated valleys. Besides Romanovskii (1993), we digitized the maps by Tormidiaro (1980), Grigoriev and Kunitsky (2000) and Konishchev (2011) (**Supplementary Figure S4** and **Supplementary Table S11**).

There are two other citable estimates for the extent of the Yedoma region in Siberia: 1,000,000 km^2 assumed by Zimov et al. (2006), and 1,186,000 km^2 estimated by Strauss et al. (2013). In our study, we estimated an extent of 1,957,885 km^2 for the Siberian Yedoma domain, which is by about 49, 42 and 39% more than found in Zimov et al. (2006), Romanovskii (1993), and Strauss et al. (2013), respectively. The main reason for this is that we included a broader east-to-west extent, as well as that Romanovskii's (1993) not quantifiable signatures on Yedoma distribution in river valleys (**Supplementary Table S1**).

4.2 Previous Regional Mapping of Yedoma Distribution

Several maps of regional Yedoma extent exist, for example, for the Yana-Indigirka and Kolyma lowlands (Tomirdiaro, 1980), or Yakutia (Grigoriev and Kunitsky, 2000) (**Supplementary Table S1**). The areas of all these maps are not comparable to our new numbers, as field studies and high-resolution satellite imagery clearly indicate that the Yedoma deposit cover in the Yedoma domain is not uniform, but can range from complete to heavily fragmented remnants (e.g. **Figure 3**). For example, Grosse et al. (2006) indicated that only about 22% of the Yedoma surface area in the Lena Anabar lowland near Cape Mamontov Klyk was preserved in its original state. Within the Yana-Indigirka lowland, the Yedoma area on Buor-Khaya Peninsula is 15% (Günther et al., 2013) and on Shirokostan Peninsula 42% (Tarasenko et al., 2013). In the State Geological Map from the year 2000, 31% is covered by alases and 27% by Yedoma in the Indigirka-Kolyma region (Shmelev et al., 2017). Following Lomachenkov (1966), 65–75% of the Yana-Indigirka region is covered by alases and 25% by Yedoma. For the Kolyma Lowland tundra zone, Veremeeva and Glushkova (2016) found a coverage of 72% for alases and 16% for Yedoma. Strauss et al. (2013) generalized the Yedoma domain for Northern Yakutia and found 56% covered by alas and 30% by Yedoma deposits.

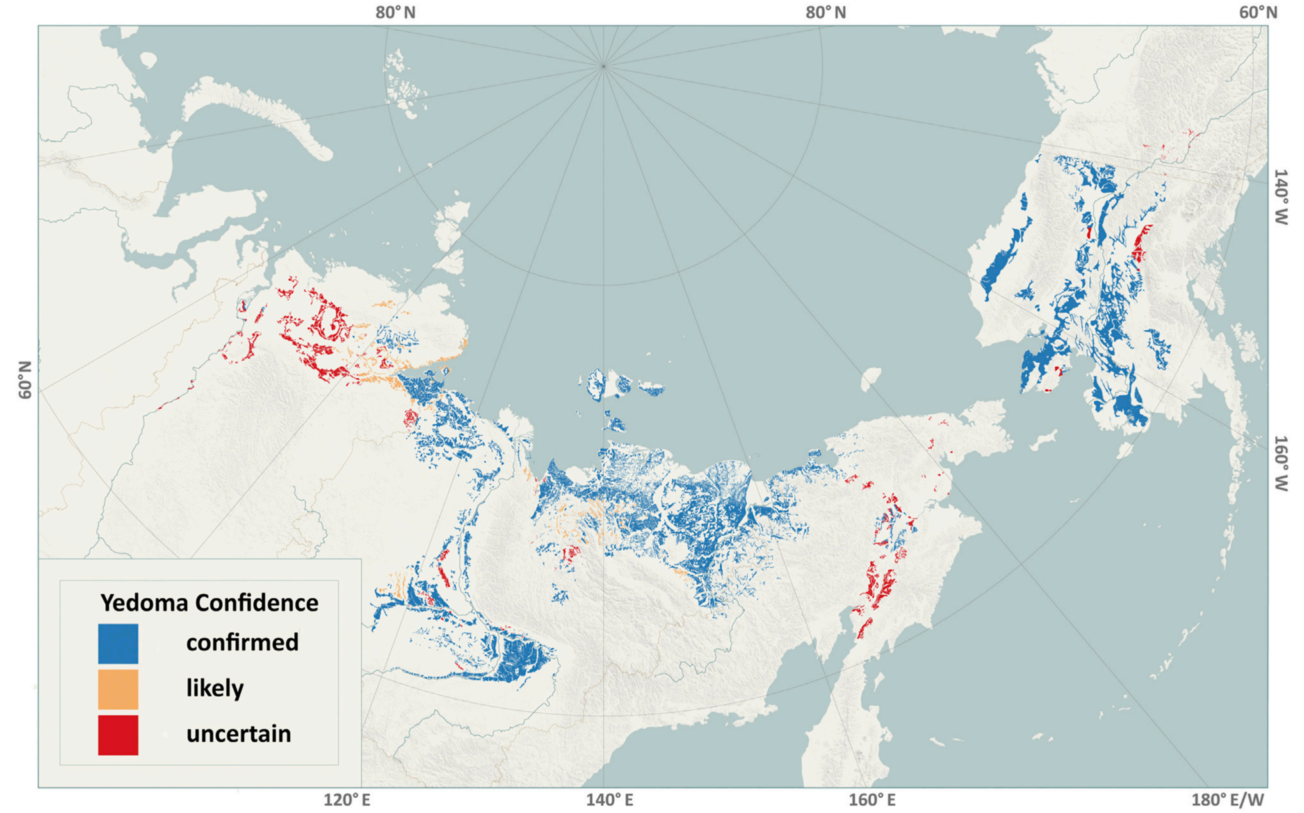

FIGURE 5 | Spatial distribution of the confidence classes: confirmed (blue), likely (orange) and uncertain (red). An A0 map version of this map is available in the supplement, and a geospatial PDF on https://apgc.awi.de/.

This fragmentation in Yedoma extent varies by location and map source. In most cases it is captured in high-resolution scales of 1:1,000,000 and better. Examples for a much higher resolution mapping are Veremeeva (2021), who published an update for the Yana-Indigirka and Kolyma Lowlands (**Supplementary Table S1**) as well as Jongejans et al. (2018b) for the Baldwin Peninsula, and Morgenstern et al. (2011) for Lena Delta Yedoma.

4.3 Applicability

The spatial dataset of Yedoma distribution will have broad applications. A range of studies citing the first version of the IRYP dataset (Strauss et al., 2016) suggest that an accurate spatial Yedoma extent dataset is useful in the context of modelling, reconstructing paleo-environmental dynamics and past ecosystems such as the mammoth-steppe-tundra, or assessments of ground ice distribution and future thermokarst vulnerability (e.g. Wild et al., 2019; Nitzbon et al., 2020; Douglas et al., 2021).

Moreover, the map is a crucial improvement needed to refine the present-day Yedoma permafrost organic matter inventory as included in Hugelius et al. (2013) or Strauss et al. (2017).

4.4 Dataset Limitations

Our data set is a significant improvement to previous mapping attempts of the Yedoma region. However, when mapping such a large area in uninhabited terrain, several potential sources of errors need to be discussed such as the fragmentation of Yedoma, the resolution of the final product, the definition of Yedoma itself.

4.4.1 Map Resolution

The fragmentation of the Yedoma extent can be captured in high-resolution scales of 1:1,000,000 and higher. In the State Geological Map (2000) of the Indigirka-Kolyma region (R-55-57), 31% is occupied by alases and 27% by Yedoma, while the more detailed estimate on the same study region using Landsat images reveal an alas area of 50% and a Yedoma area of 13% (Shmelev et al., 2017; Veremeeva, 2021). Therefore, the coverage of Yedoma could be about two times overestimated on maps of 1,000,000 scale due to the high level of initial Yedoma relief dissection by thermokarst and thermal erosion, which could be mapped on a more detailed scale using remote sensing data. Taking our estimate (based on a map of the region which was also quantified by Veremeeva (2021)), our database included 50% more Yedoma area compared to the identical region like in Veremeeva (2021) (**Supplementary Table S10**). For our map, we included Veremeeva's (2021) update for this specific region, but having this in mind, the rest of our circum-Arctic Yedoma mapping approach is potentially overestimating the Yedoma distribution. Moreover, since the year of the map's data acquisition, the degradation of Yedoma deposits likely continued. Especially when considering that the Yedoma domain belongs to one of the hotspots of warming, with a temperature increase of more than ~4°C (NASA Visualization Studio, 2021) since von Bunge's (1883) first steps to the todays accepted interpretation of how the ground ice in Yedoma was formed.

4.4.2 Yedoma Existence Under Overlying Sediments

Another important point of discussion was mentioned by Grosse et al. (2013). They pointed to a need to carefully evaluate the Yedoma coverage from the fact that a two-dimensional surface source map, as true for nearly every classical map, cannot properly represent the total spatial extent of geologic horizons that potentially overlap in three dimensions. The Yedoma units represented in the maps (and thus the ones in our database) are likely those that crop out close to the land surface. Although thermokarst depressions and lakes indicate that the entire underlying Yedoma has thawed out in many cases, shallow lakes may not have fully degraded Yedoma below yet (Shmelev et al., 2017; Walter Anthony et al., 2021). Similarly, younger aeolian or alluvial deposits may cover late Pleistocene Yedoma surfaces. Therefore, it is still unclear whether there are any Yedoma remains beneath the lacustrine and alluvial sediments. Such geological situations would make the identified extent of Yedoma in our database a conservative estimate at the lower end.

4.4.3 General Map Accuracy

As also summarized by Grosse et al. (2013), the general accuracy of the Yedoma distribution shown in this database is tied to several potential general error sources: 1) uncertainties in the original geologic and cryostratigraphic mapping, 2) uncertainties in converting and scaling the original field and remote sensing data to a paper map product, 3) uncertainties in the technical conversion from a paper map to a digital geodatabase, and 4) uncertainties in interpretation of Quaternary geological units across multiple map tiles as a Yedoma unit.

Our study cannot influence the uncertainties mentioned in (1) and (2) and assumes that quality control of the original geologic, stratigraphic, and cartographic work was rigorous. For (3), geometric uncertainties are mostly included, such as the accuracy of georeferencing the maps, and the line thickness of geologic boundaries and their digitization accuracy. To estimate transparently and to minimize errors in (4), we relied on existing scientific literature, our field data and field knowledge of Yedoma and the involvement of expert assessment. Therefore, we introduced the confidence classes, making use of the fact that most of the maps provide evidence that a certain unit is ice-rich, syngenetic, late Pleistocene Yedoma by cryostratigraphic signatures. In a few cases, no signature for high ground-ice content or syngenetic ice wedges was included. However, it was possible to trace such units by comparing them with neighboring polygons in directly adjacent map tiles, connecting them to field or literature data, or intersecting this with other maps and inferring that they are the same units if spatially connected.

4.4.4 Yedoma and Yedoma-like Deposit Definitions

Another important topic to address here are the scientific differences and viewpoints on Yedoma, Ice Complex and muck definitions. This is quite clear for the Yedoma core region, but gets more difficult to the Yedoma domain borders, meaning the easternmost and westernmost sites (**Figure 5**). The key features of Canadian mucks (eastern edge of Beringia) are that they are primarily found in the extensive-discontinuous permafrost zone. In contrast to the East Siberian Yedoma core area, they are also strongly controlled by aspect (north-facing sites and narrow valleys with relict ice) and they also occur in high relief landscapes. Following our definition, the Holocene part like organics (sologenic) are not included here (Fraser and Burn, 1997; Froese et al., 2009). On the other side, the Western Taymyr to Yamal Peninsula coast is the westernmost area of distribution of Yedoma (Sopochnaya Karga, Marre-Sale, Dikson, Krestyanka River). In contrast to the Yakutian Yedoma, the Western Taymyr Yedoma is less thick (up to 12 m), and includes smaller syngenetic ice wedges (Streletskaya et al., 2007). Nevertheless, the grain-size fractions and cryogenic structure of the Yedoma deposits of Western Taymyr are similar to sections in Yakutia and Alaska (Tomirdiaro and Chernen'kiy, 1987). Here, we see these differences as regional expressions of Yedoma, marking differences in source areas, sedimentation rates, moisture availability and climate during aggradation of these fine-grained ice-rich sediments across Beringia. Secondly, we feel there is more to gain by considering these as regional variants of processes that were active across the region during the Late Pleistocene.

4.4.5 Yedoma Thickness

One important step forward in our dataset and map is for the first time the inclusion of Yedoma thickness, which is needed for volume estimation. However, published data on Yedoma thickness are rather scarce. Synthesized by Strauss et al. (2013; 2017), we compiled field and literature data for available Yedoma depth estimate and updated this with newly available or newly recognized depth estimates (see **Supplementary Table S9**). Moreover, as visualized in the example in **Figure 6**, it is difficult to quantify the depth of Yedoma deposits if the base is not reached by the cliff or drilling. Local heterogeneity and depths ranging from 5 to 50 m (mean 17 m, **Supplementary Table S9**) make it impossible at this current stage to visualize the thickness spatially explicit. There are first approaches to use the depth of thermokarst basins for Yedoma depth estimation such as the study by Veremeeva and Glushkova (2016). For the Kolyma Lowland tundra region, they showed that average depths of Yedoma-alas relief dissection by thermokarst and thermal erosion are 20–25 m between highest elevation of Yedoma uplands and alas levels. This is consistent with Yedoma thickness data of studied exposures and boreholes. Average heights of Yedoma upland and alas relief for low, moderate and high Yedoma fraction regions in Kolyma Lowland tundra correspond to different elevation levels but have similar relative elevation differences between average Yedoma and alas heights across all relief types, which are about 10 m (Veremeeva et al., 2021).

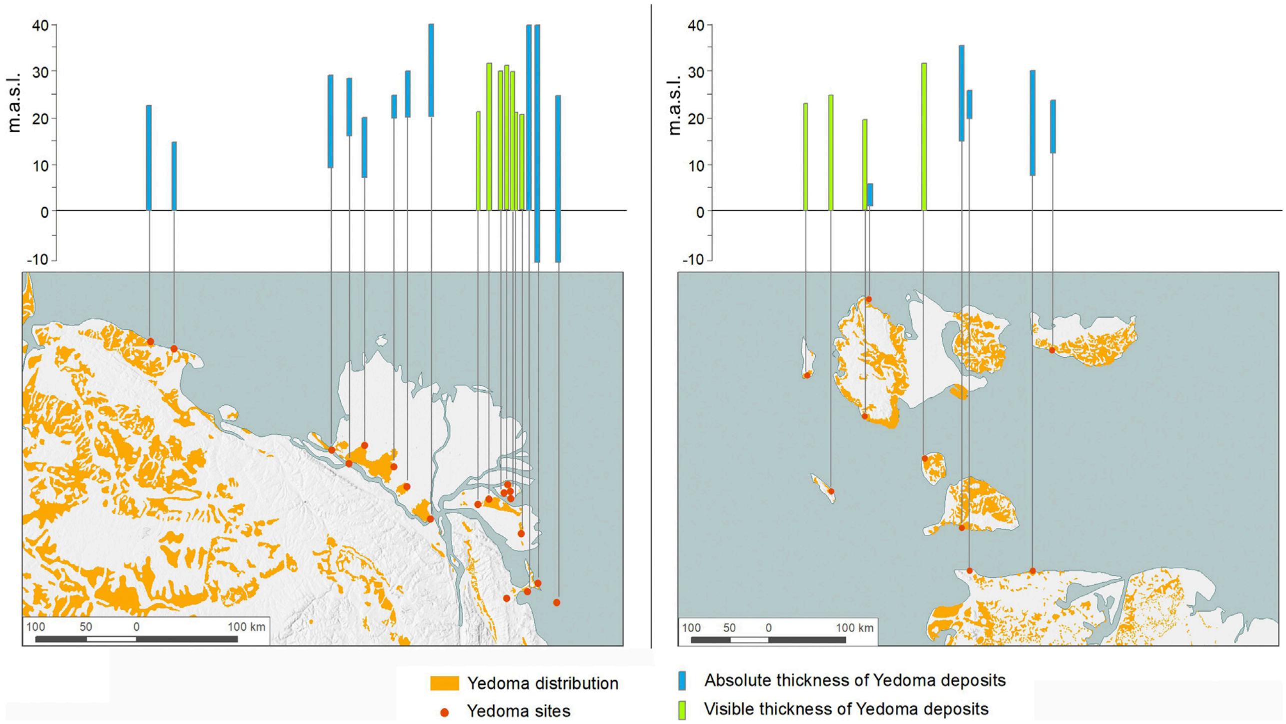

FIGURE 6 | Yedoma thickness exemplarily visualized for **(left)** the Lena-Anabar coastal region, and **(right)** the New Siberian Islands region. The Yedoma distribution is according to **Figure 4**. Absolute thickness refers to sites where both upper and lower boundaries of the Yedoma are known, and visible thickness refers to sites with known thickness above sea level and an unknown lower Yedoma boundary below sea level. Please find available depth data in **Supplementary Table S9**.

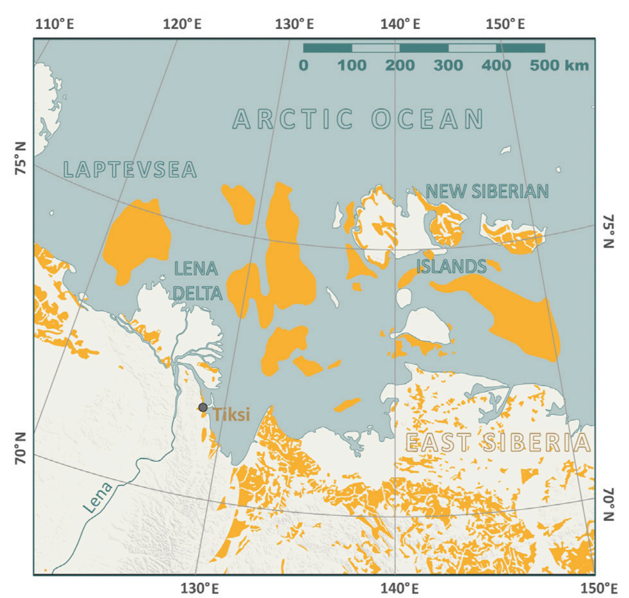

FIGURE 7 | Potential areas with subsea remnants of the Yedoma domain in the Laptev and East Siberian seas based on the 1:2,500,000 Quaternary map of the territory of Russian Federation. The subsea areas are not included in our mapping and total area calculation approach due to the high uncertainties.

4.4.6 Subsea Yedoma Deposits

Another unsolved question is the quantification of potentially preserved Yedoma under today's sea coverage. The area of this potential subsea Yedoma is highly uncertain: there are only several maps estimating potential areas in the Laptev Sea (1:1,000,000 Quaternary geological map S-52 and S-53,54, and the 1:2,500,000 Quaternary map of the territory of Russian Federation), visualized in Astakhov et al. (2021) and the western part of the East Siberian Sea as indicated in Walter et al. (2007). Although we did not include the potential subsea regions in our map or any submarine Yedoma remnant area estimate in our calculations, we here show an example of potential regions with submarine Yedoma remnants (**Figure 7**). The outline of the areas shown here enclose 77,620 km^2.

5 OUTLOOK

Our Yedoma mapping includes a large and diverse amount of available geospatial data from which the Yedoma extent could be extracted. Additional datasets and maps are likely to become available in the future. In particular, Soviet and Russian geological mapping efforts over many decades have been included in geological maps of 1:200,000 scale, however, many of these are not yet published or available for the Northeast Siberian Yedoma regions. A substantial treasure of data on Yedoma distribution and thickness is likely buried in largely inaccessible data from prospecting drilling campaigns focused on engineering, infrastructure planning, exploration, or hydrogeological studies in Siberia as well as in North America. Making such datasets accessible and digitally available would provide a tremendous boost to understanding the distribution of ice-rich syngenetic permafrost at much higher levels of spatial detail. Additional scientific studies on Yedoma exposures and drill cores will further enhance knowledge on Yedoma distribution and thickness and can be integrated in future updates of this new pan-Arctic map and database. A highly promising approach will be the application of geomorphic mapping of Yedoma coverage based on terrain texture and thermokarst and thermal erosion features associated with Yedoma deposits using high-resolution satellite images and digital elevation models. Such remote sensing datasets also allow enhanced quantification of the spatial heterogeneity of remnant Yedoma uplands well below the resolution of currently used mapping scales in this study.

6 CONCLUSION

The Yedoma geospatial database and map strongly reduces uncertainties in Yedoma distribution. We quantified the Yedoma domain for a land area of 2,587,000 km^2 in Central and East Siberia, Alaska and Yukon with areas of digitized Yedoma deposits of 480,000 km^2. Today's Yedoma areas are highly fragmented, which mainly resulted from permafrost degradation processes during the Lateglacial and Holocene such as thermokarst, thermal erosion, and fluvial and coastal erosion. This first complete, digital circum-Arctic Yedoma map is an important step forward to understand the past and present spatial heterogeneity of Yedoma deposits, which is of utmost importance for assessing vulnerabilities and risks in a rapidly warming Arctic.

DATA AVAILABILITY STATEMENT

The datasets presented in this study can be found in online repositories. The names of the repository/repositories and accession number(s) can be found in the article/ **Supplementary Material**.

AUTHOR CONTRIBUTIONS

JS and GG designed this study. SL, GG and USGS volunteers conducted all digitizing, data archiving and visualizations. JS, GG, and LS drafted the first versions of the manuscript. All authors contributed data to this study and contributed to manuscript finalization.

FUNDING

This project is part of the Action Group "The Yedoma Region: A Synthesis of Circum-Arctic Distribution and Thickness" (funded by the International Permafrost Association (IPA) to JS) and is embedded in the Permafrost Carbon Network (working group Carbon Stocks). We acknowledge funding by the European Research Council (Starting Grant PETA-CARB #338335) and by the Helmholtz Impulse and Networking Fund (ERC_0013) to GG. IS research is embedded into the Development program of the Interdisciplinary Scientific and Educational School of M.V. Lomonosov Moscow State University "Future Planet and Global Environmental Change" and the program "The cryosphere evolution under climate change and anthropogenic impact" (#121051100164-0). GK was supported by the Russian Foundation For Basic Research (grant 18-05-60279) in the framework of the State Assignment of the Institute of Geography (0148-2019-0004).

ACKNOWLEDGMENTS

We thank the University of Alaska Fairbanks, U.S. Geological Survey and the Alfred Wegener Institute for Polar and Marine Research for their support since starting this digital data compilation in 2013. Moreover, we thank the Arctic Geospatial Centre (APGC) for the fruitful collaboration on developing and hosting the products connected to our study. For realizing the WebGIS, we want to thank Antonie Haas.

SUPPLEMENTARY MATERIAL

The Supplementary Material for this article can be found online at: https://www.frontiersin.org/articles/10.3389/feart.2021.758360/full#supplementary-material

REFERENCES

Antonova, S., Sudhaus, H., Strozzi, T., Zwieback, S., Kääb, A., Heim, B., et al. (2018). Thaw Subsidence of a Yedoma Landscape in Northern Siberia, Measured *In Situ* and Estimated from TerraSAR-X Interferometry. *Remote Sensing* 10, 494. doi:10.3390/rs10040494

Astakhov, V., Pestova, L., and Shkatova, V. (2021). Loessoids of Russia: Varieties and Distribution. *Quat. Int.* doi:10.1016/j.quaint.2021.01.005

Beechey, F. W., Bentley, R., and Colburn, H. (1831). *Narrative of a Voyage to the Pacific and Beering's Strait, to Co-operate with the Polar Expeditions : Performed in His Majesty's Ship Blossom, under the Command of Captain F.W. Beechey in the Years 1825, 26, 27, 28*. London: Henry Colburn and Richard Bentley.

Bryant, R., Robinson, J. E., Demasi, A., Harper, W., Kyker-Snowman, E., Schirrmeister, L., et al. (2017). *Digital Database and Maps of Quaternary Deposits in East and Central Siberia*. Siberia: USGS.

Chen, L., Voss, C., Fortier, D., and Mckenzie, J. (2021). "Surface Energy Balance of Sub-arctic Roads with Varying Snow Regimes and Properties in Permafrost Regions," in *Permafrost Periglacial Process*. John Wiley & Sons Ltd doi:10.1002/ppp.2129

Chudinov, A. N. (1910). *Slovar' Inostrannykh Slov, Voshedshikh V Sostav Russkogo Yazyka (Dictionary of Foreign Words Introduced to Russian)*. Saint Petersburg: Gubinsky publishers, 676.

de Grandpré, I., Fortier, D., Stephani, E., and Burn, C. R. (2012). Degradation of Permafrost beneath a Road Embankment Enhanced by Heat Advected in Groundwater. *Can. J. Earth Sci.* 49, 953–962. doi:10.1139/e2012-018

Douglas, T. A., Hiemstra, C. A., Anderson, J. E., Barbato, R. A., Bjella, K. L., Deeb, E. J., et al. (2021). Recent Degradation of interior Alaska Permafrost Mapped with Ground Surveys, Geophysics, Deep Drilling, and Repeat Airborne Lidar. *The Cryosphere* 15, 3555–3575. doi:10.5194/tc-15-3555-2021

Farquharson, L. M., Mann, D. H., Swanson, D. K., Jones, B. M., Buzard, R. M., and Jordan, J. W. (2018). Temporal and Spatial Variability in Coastline Response to Declining Sea-Ice in Northwest Alaska. *Mar. Geology.* 404, 71–83. doi:10.1016/j.margeo.2018.07.007

Fraser, T. A., and Burn, C. R. (1997). On the Nature and Origin of "muck" Deposits in the Klondike Area, Yukon Territory. *Can. J. Earth Sci.* 34, 1333–1344. doi:10.1139/e17-106

Froese, D. G., Westgate, J. A., Reyes, A. V., Enkin, R. J., and Preece, S. J. (2008). Ancient Permafrost and a Future, Warmer Arctic. *Science* 321, 1648. doi:10.1126/science.1157525

Froese, D. G., Zazula, G. D., Westgate, J. A., Preece, S. J., Sanborn, P. T., Reyes, A. V., et al. (2009). The Klondike Goldfields and Pleistocene Environments of Beringia. *GSA Today* 19, 4–10. doi:10.1130/gsatg54a.1

Fuchs, M., Nitze, I., Strauss, J., Günther, F., Wetterich, S., Kizyakov, A., et al. (2020). Rapid Fluvio-Thermal Erosion of a Yedoma Permafrost Cliff in the Lena River Delta. *Front. Earth Sci.* 8. doi:10.3389/feart.2020.00336

Grigoriev, M. N., and Kunitsky, V. V. (2000). Ice Complex of the Arctic Coasts of Yakutia as a Sediment Source on the continental Shelf. *Hydrometeorological and Biogeochemical Research in the Arctic Region*. Vladivostok, Russia: Dalnauka Press, 109–116.

Grosse, G., Robinson, J. E., Bryant, R., Taylor, M. D., Harper, W., Demasi, A., et al. (2013). *Distribution of Late Pleistocene Ice-Rich Syngenetic Permafrost of the Yedoma Suite in East and central Siberia, Russia*. Reston, Virginia: U.S. Geological Survey. doi:10.3133/ofr20131078

Grosse, G., Schirrmeister, L., and Malthus, T. J. (2006). Application of Landsat-7 Satellite Data and a DEM for the Quantification of Thermokarst-Affected Terrain Types in the Periglacial Lena-Anabar Coastal lowland. *Polar Res.* 25, 51–67. doi:10.3402/polar.v25i1.6238

Günther, F., Overduin, P. P., Sandakov, A. V., Grosse, G., and Grigoriev, M. N. (2013). Short- and Long-Term Thermo-Erosion of Ice-Rich Permafrost Coasts in the Laptev Sea Region. *Biogeosciences* 10, 4297–4318. doi:10.5194/bg-10-4297-2013

Günther, F., Overduin, P. P., Yakshina, I. A., Opel, T., Baranskaya, A. V., and Grigoriev, M. N. (2015). Observing Muostakh Disappear: Permafrost Thaw Subsidence and Erosion of a Ground-Ice-Rich Island in Response to Arctic Summer Warming and Sea Ice Reduction. *The Cryosphere* 9, 151–178. doi:10.5194/tc-9-151-2015

Hjort, J., Karjalainen, O., Aalto, J., Westermann, S., Romanovsky, V. E., Nelson, F. E., et al. (2018). Degrading Permafrost Puts Arctic Infrastructure at Risk by Mid-century. *Nat. Commun.* 9, 5147. doi:10.1038/s41467-018-07557-4

Hugelius, G., Bockheim, J. G., Camill, P., Elberling, B., Grosse, G., Harden, J. W., et al. (2013). A New Data Set for Estimating Organic Carbon Storage to 3 M Depth in Soils of the Northern Circumpolar Permafrost Region. *Earth Syst. Sci. Data* 5, 393–402. doi:10.5194/essd-5-393-2013

Jones, B. M., Irrgang, A. M., Farquharson, L. M., Lantuit, H., Whalen, D., Ogorodov, S., et al. (2020). Arctic Report Card: Update for 2020 - the Sustained Transformation to a Warmer, Less Frozen and Biologically Changed Arctic Remains clear. [Online]. Available at: https://arctic.noaa.gov/Report-Card/Report-Card-2020/ArtMID/7975/ArticleID/904/Coastal-Permafrost-Erosion (Accessed 08 2021, 08).

Jones, B. M., Grosse, G., Arp, C. D., Jones, M. C., Walter Anthony, K. M., and Romanovsky, V. E. (2011). Modern Thermokarst lake Dynamics in the Continuous Permafrost Zone, Northern Seward Peninsula, Alaska. *J. Geophys. Res.* 116, G00M03. doi:10.1029/2011jg001666

Jongejans, L. L., Strauss, J., Lenz, J., Peterse, F., Mangelsdorf, K., Fuchs, M., et al. (2018a). Organic Matter Characteristics in Yedoma and Thermokarst Deposits on Baldwin Peninsula, West Alaska. *Biogeosciences* 15, 6033–6048. doi:10.5194/bg-15-6033-2018

Jongejans, L. L., Strauss, J., Lenz, J., Peterse, F., Mangelsdorf, K., Fuchs, M., et al. (2018b). Sedimentological, Biogeochemical and Geochronological Data of Yedoma and Thermokarst Deposits in West-Alaska. *PANGAEA*. doi:10.1594/PANGAEA.892310

Jorgenson, M. T., Yoshikawa, K., Kanevskiy, M., Shur, Y., Romanovsky, V., Marchenko, S., et al. (2008). "Permafrost Characteristics of Alaska," in Proceedings of the 9th International Conference on Permafrost, Fairbanks, Alaska, June 29 - July 3**,** 121–122.

Kanevskiy, M., Shur, Y., Bigelow, N. H., Bjella, K. L., Douglas, T. A., Jones, B. M., et al. (Forthcoming 2021). Yedoma Cryostratigraphy of Recently Excavated Sections of the CRREL Permafrost Tunnel Near Fairbanks, Alaska. *Front. Earth Sci.* submitted.

Kanevskiy, M., Shur, Y., Fortier, D., Jorgenson, M. T., and Stephani, E. (2011). Cryostratigraphy of Late Pleistocene Syngenetic Permafrost (Yedoma) in Northern Alaska, Itkillik River Exposure. *Quat. Res.* 75, 584–596. doi:10.1016/j.yqres.2010.12.003

Kanevskiy, M., Shur, Y., Strauss, J., Jorgenson, T., Fortier, D., Stephani, E., et al. (2016). Patterns and Rates of riverbank Erosion Involving Ice-Rich Permafrost (Yedoma) in Northern Alaska. *Geomorphology* 253, 370–384. doi:10.1016/j.geomorph.2015.10.023

Kaplina, T. (2009). Alas Complex of Northern Yakutia. *Kriosfera Zemli (Earth Cryosphere)* 13 (4), 3–17.

Konishchev, V. N. (2011). Permafrost Response to Climate Warming. *Kriosfera Zemli (Earth Cryosphere)* 15 (4), 13–16.

Kotov, A. N., and Brazhnik, S. N. (1991). "Underground Ice and Cryomorphogenesis, Scientific Excursion Guide in the Onemen Bay (Outcrop of Cape Rogozhny)," in *Scientific Seminar "Cryolitogenesis", Interdepartmental Lithological Committee of the USSR Academy of Sciences*. Magadan: Anadyr, 1–31.

Lehner, B., and Döll, P. (2004). Development and Validation of a Global Database of Lakes, Reservoirs and Wetlands. *J. Hydrol.* 296, 1–22. doi:10.1016/j.jhydrol.2004.03.028

Lenton, T. M., Rockström, J., Gaffney, O., Rahmstorf, S., Richardson, K., Steffen, W., et al. (2019). Climate Tipping Points - Too Risky to Bet against. *Nature* 575, 592–595. doi:10.1038/d41586-019-03595-0

Lenz, J., Wetterich, S., Jones, B. M., Meyer, H., Bobrov, A., and Grosse, G. (2016). Evidence of Multiple Thermokarst lake Generations from an 11 800-year-old Permafrost Core on the Northern S Eward P Eninsula, A Laska. *Boreas* 45, 584–603. doi:10.1111/bor.12186

Lomachenkov, V. S. (1966). "On the Main Stages of Geologic Development of the Lena-Kolyma Coastal lowland during the Late Quaternary and Recent Epochs," in *The Quaternary Period in Siberia*. Editor V. N. Saks (Moscow: Nauka), 283–288.

Morgenstern, A., Overduin, P. P., Günther, F., Stettner, S., Ramage, J., Schirrmeister, L., et al. (2021). Thermo-erosional Valleys in Siberian Ice-rich Permafrost. *Permafrost and Periglac Process* 32, 59–75. doi:10.1002/ppp.2087

Morgenstern, A., Röhr, C., Grosse, G., and Grigoriev, M. N. (2011). The Lena River Delta - Inventory of Lakes and Geomorphological Terraces. *PANGAEA*. doi:10.1594/PANGAEA.758728

Morgenstern, A., Ulrich, M., Günther, F., Roessler, S., Fedorova, I. V., Rudaya, N. A., et al. (2013). Evolution of Thermokarst in East Siberian Ice-Rich Permafrost: A Case Study. *Geomorphology* 201, 363–379. doi:10.1016/j.geomorph.2013.07.011

Murton, J. B., Opel, T., Toms, P., Blinov, A., Fuchs, M., Wood, J., et al. (2021). A Multimethod Dating Study of Ancient Permafrost, Batagay Megaslump, East Siberia. *Quat. Res.*, 1–22.(in press) doi:10.1017/qua.2021.27

NASA Visualization Studio (2021). Global Temperature Anomalies from 1880 to 2020. [Online]. NASA. Available at: https://svs.gsfc.nasa.gov/4882 (Accessed 08 2021, 08).

Nitzbon, J., Westermann, S., Langer, M., Martin, L. C. P., Strauss, J., Laboor, S., et al. (2020). Fast Response of Cold Ice-Rich Permafrost in Northeast Siberia to a Warming Climate. *Nat. Commun.* 11, 2201. doi:10.1038/s41467-020-15725-8

Nitze, I., Grosse, G., Jones, B., Arp, C., Ulrich, M., Fedorov, A., et al. (2017). Landsat-Based Trend Analysis of Lake Dynamics across Northern Permafrost Regions. *Remote Sensing* 9, 640. doi:10.3390/rs9070640

Pastick, N. J., Jorgenson, M. T., Goetz, S. J., Jones, B. M., Wylie, B. K., Minsley, B. J., et al. (2019). Spatiotemporal Remote Sensing of Ecosystem Change and Causation across Alaska. *Glob. Change Biol.* 25, 1171–1189. doi:10.1111/gcb.14279

Péwé, T. L. (1975). Quaternary Geology of Alaska. Professional Paper 835 doi:10.3133/pp835

Romanovskii, N. N. (1993). *Fundamentals of Cryogenesis of Lithosphere*. Moscow: Moscow University Press.

Schirrmeister, L., Dietze, E., Matthes, H., Grosse, G., Strauss, J., Laboor, S., et al. (2020). The Genesis of Yedoma Ice Complex Permafrost - Grain-Size

Endmember Modeling Analysis from Siberia and Alaska. *E&g Quat. Sci. J.* 69, 33–53. doi:10.5194/egqsj-69-33-2020

Schirrmeister, L., Froese, D., Tumskoy, V., Grosse, G., and Wetterich, S. (2013). "Permafrost and Periglacial Features | Yedoma: Late Pleistocene Ice-Rich Syngenetic Permafrost of Beringia," in *Encyclopedia of Quaternary Sciences*. Editor S. A. Elias. 2 ed (Amsterdam: Elsevier), 542–552. doi:10.1016/B978-0-444-53643-3.00106-0

Schirrmeister, L., Grosse, G., Wetterich, S., Overduin, P. P., Strauss, J., Schuur, E. A. G., et al. (2011a). Fossil Organic Matter Characteristics in Permafrost Deposits of the Northeast Siberian Arctic. *J. Geophys. Res.* 116, G00M02. doi:10.1029/2011jg001647

Schirrmeister, L., Kunitsky, V., Grosse, G., Wetterich, S., Meyer, H., Schwamborn, G., et al. (2011b). Sedimentary Characteristics and Origin of the Late Pleistocene Ice Complex on north-east Siberian Arctic Coastal Lowlands and Islands - A Review. *Quat. Int.* 241, 3–25. doi:10.1016/j.quaint.2010.04.004

Schirrmeister, L., Siegert, C., Kunitzky, V. V., Grootes, P. M., and Erlenkeuser, H. (2002a). Late Quaternary Ice-Rich Permafrost Sequences as a Paleoenvironmental Archive for the Laptev Sea Region in Northern Siberia. *Int. J. Earth Sci.* 91, 154–167. doi:10.1007/s005310100205

Schirrmeister, L., Siegert, C., Kuznetsova, T., Kuzmina, S., Andreev, A., Kienast, F., et al. (2002b). Paleoenvironmental and Paleoclimatic Records from Permafrost Deposits in the Arctic Region of Northern Siberia. *Quat. Int.* 89, 97–118. doi:10.1016/S1040-6182(01)00083-0

Schneider von Deimling, T., Lee, H., Ingeman-Nielsen, T., Westermann, S., Romanovsky, V., Lamoureux, S., et al. (2021). Consequences of Permafrost Degradation for Arctic Infrastructure - Bridging the Model gap between Regional and Engineering Scales. *The Cryosphere* 15, 2451–2471. doi:10.5194/tc-15-2451-2021

Schuur, E. A. G., Mcguire, A. D., Schädel, C., Grosse, G., Harden, J. W., Hayes, D. J., et al. (2015). Climate Change and the Permafrost Carbon Feedback. *Nature* 520, 171–179. doi:10.1038/nature14338

Sher, A. V., Kaplina, T. N., and Ovander, M. G. (1987). *Decisions of Interdepartmental Stratigraphic Conference on the Quaternary of the East USSR*. Magadan: USSR Academy of Sciences, Far Eastern Branch, North-Eastern Complex Research Institute, 29–62.

Sher, A. V. (1971). "Unified Regional Stratigraphic Chart for the Quaternary Deposits in the Yana-Kolyma lowland and its Mountainous Surroundings - Explanatory Note," in *Mammals and Stratigraphy of the Pleistocene of the Extreme Northeast of the USSR and North America*. Moscow: Nauka.

Shmelev, D., Veremeeva, A., Kraev, G., Kholodov, A., Spencer, R. G. M., Walker, W. S., et al. (2017). Estimation and Sensitivity of Carbon Storage in Permafrost of North-Eastern Yakutia. *Permafrost Periglac. Process.* 28, 379–390. doi:10.1002/ppp.1933

Shur, Y., Fortier, D., Jorgenson, T., Kanevskiy, M., Schirrmeister, L., Strauss, J., et al. (Forthcoming 2021a). Yedoma Permafrost Genesis: More Than 150 Years of Mystery and Controversy. *Front. Earth Sci.*

Shur, Y., Jones, B. M., Kanevskiy, M., Jorgenson, T., Jones, M. K. W., Fortier, D., et al. (2021b). Fluvio-thermal Erosion and thermal Denudation in the Yedoma Region of Northern Alaska: Revisiting the Itkillik River Exposure. *Permafrost and Periglac Process* 32, 277–298. doi:10.1002/ppp.2105

Shur, Y., French, H. M., Bray, M. T., and Anderson, D. A. (2004). Syngenetic Permafrost Growth: Cryostratigraphic Observations from the CRREL Tunnel Near Fairbanks, Alaska. *Permafrost Periglac. Process.* 15, 339–347. doi:10.1002/ppp.486

Siegert, C., and Romanovskii, N. N. (1996). "The Late Pleistocene 'Ice Complex' a Phenomenon of the Non Glaciated Areas of Northern Eurasia," in First Annual Workshop of the EST Scientific Program: Quaternary Environment of the Eurasian North, QUEEN, Strasbourg, France, November 29–December 2, 1996. Kiel: Christian-Albrechts-Universität, 122–123.

Solov'ev, P. (1959). *Kriolitozona Severnoy Chasti Leno-Amginskogo Mezhdurech'ya (The Permafrost of the Northern Part of the Lena-Amga Interfluve)*. Moscow: Academy of Science Press.

Strauss, J., Laboor, S., Fedorov, A. N., Fortier, D., Froese, D. G., Fuchs, M., et al. (2016). *Database of Ice-Rich Yedoma Permafrost (IRYP)*. PANGAEA. doi:10.1594/PANGAEA.861733

Strauss, J., Schirrmeister, L., Grosse, G., Fortier, D., Hugelius, G., Knoblauch, C., et al. (2017). Deep Yedoma Permafrost: A Synthesis of Depositional Characteristics and Carbon Vulnerability. *Earth-Science Rev.* 172, 75–86. doi:10.1016/j.earscirev.2017.07.007

Strauss, J., Schirrmeister, L., Grosse, G., Wetterich, S., Ulrich, M., Herzschuh, U., et al. (2013). The Deep Permafrost Carbon Pool of the Yedoma Region in Siberia and Alaska. *Geophys. Res. Lett.* 40, 6165–6170. doi:10.1002/2013GL058088

Streletskaya, I., Gusev, E., Vasiliev, A., Kanevskiy, M., Anikina, N. Y., and Derevyanko, L. (2007). New Results of Quaternary Sediment Studies of Western Taymyr. *Kriosfera Zemli (Earth Cryosphere)* 11 (3), 14–28.

Streletskiy, D. A., Suter, L. J., Shiklomanov, N. I., Porfiriev, B. N., and Eliseev, D. O. (2019). Assessment of Climate Change Impacts on Buildings, Structures and Infrastructure in the Russian Regions on Permafrost. *Environ. Res. Lett.* 14, 025003. doi:10.1088/1748-9326/aaf5e6

Tarasenko, T. V., Kravtsova, V. I., and Pizhankova, E. I. (2013). "Study of Thermokarst Lakes Dynamics in the Coastal Part of the Yana-Indigirka lowland Using Remote Data", in: Proceedings of the Conference Geocryological mapping: Problems and prospects, Moscow, Russia, June 5–6, 2013, 135–138.

Tomirdiaro, S. V., and Chernen'kiy, B. I. (1987). *Cryogenic-eolian Deposits of East Arctic and Sub-arctic*. Moscow: Nauka.

Tomirdiaro, S. V. (1980). *Loess-ice Formations in East Siberia during the Late Pleistocene and Holocene*. Moscow: Nauka Press.

Tumskoy, V. (2012). Peculiarities of Cryolithogenesis in Northern Yakutia (Middle Neopleistocene to Holocene). *Kriosfera Zemli (Earth Cryosphere)* 16 (1), 12–21.

Ulrich, M., Grosse, G., Strauss, J., and Schirrmeister, L. (2014). Quantifying Wedge-Ice Volumes in Yedoma and Thermokarst basin Deposits. *Permafrost Periglac. Process.* 25, 151–161. doi:10.1002/ppp.1810

Ulrich, M., Matthes, H., Schirrmeister, L., Schütze, J., Park, H., Iijima, Y., et al. (2017). Differences in Behavior and Distribution of Permafrost-related Lakes in C Entral Y Akutia and Their Response to Climatic Drivers. *Water Resour. Res.* 53, 1167–1188. doi:10.1002/2016WR019267

Veremeeva, A., and Glushkova, N. (2016). Formation of Relief in the Regions of Ice Complex Deposits Distribution: Remote Sensing and GIS Studies in the Kolyma lowland Tundra. *Kriosfera Zemli (Earth Cryosphere)* 20 (1), 14–24.

Veremeeva, A., Nitze, I., Günther, F., Grosse, G., and Rivkina, E. (2021). Geomorphological and Climatic Drivers of Thermokarst Lake Area Increase Trend (1999-2018) in the Kolyma Lowland Yedoma Region, North-Eastern Siberia. *Remote Sensing* 13, 178. doi:10.3390/rs13020178

Veremeeva, A. (2021). Quaternary Deposits Map of Yana-Indigirka and Kolyma Lowlands Tundra Zone, R-55-57, Based on Landsat Imagery. *PANGAEA*. doi:10.1594/PANGAEA.927292

von Bunge, A. (1883). "Natural History News from the Polar Station at the Mouth of the Lena River. From a Letter to the Academician Leopold von Schrenck," in *Bull. Imp. Acad. Sci.* 11, 581–622.

von Kotzebue, O. (1821). *Entdeckungs-Reise in die Süd-See und nach der Berings-Straße zur Erforschung einer nordöstlichen Durchfahrt: unternommen in den Jahren 1815, 1816, 1817 und 1818, auf Kosten des Herrn Reichs-Kanzlers Grafen Rumanzoff auf dem Schiffe Rurick unter dem Befehle des Lieutenants der Russisch Kaiserlichen Marine Otto von Kotzebue*. Weimar: Gebrüder Hoffmann.

Walker, D. A., Raynolds, M. K., Daniëls, F. J. A., Einarsson, E., Elvebakk, A., Gould, W. A., et al. (2005). The Circumpolar Arctic Vegetation Map. *J. Vegetation Sci.* 16, 267–282. doi:10.1111/j.1654-1103.2005.tb02365.x

Walter Anthony, K. M., Lindgren, P., Hanke, P., Engram, M., Anthony, P., Daanen, R. P., et al. (2021). Decadal-scale Hotspot Methane Ebullition within Lakes Following Abrupt Permafrost Thaw. *Environ. Res. Lett.* 16, 035010. doi:10.1088/1748-9326/abc848

Walter, K. M., Edwards, M. E., Grosse, G., Zimov, S. A., and Chapin, F. S. (2007). Thermokarst Lakes as a Source of Atmospheric CH4 during the Last Deglaciation. *Science* 318, 633–636. doi:10.1126/science.1142924

Wetterich, S., Kizyakov, A., Fritz, M., Wolter, J., Mollenhauer, G., Meyer, H., et al. (2020). The Cryostratigraphy of the Yedoma Cliff of Sobo-Sise Island (Lena delta) Reveals Permafrost Dynamics in the central Laptev Sea Coastal Region during the Last 52 Kyr. *The Cryosphere* 14, 4525–4551. doi:10.5194/tc-14-4525-2020

Wetterich, S., Rudaya, N., Kuznetsov, V., Maksimov, F., Opel, T., Meyer, H., et al. (2019). Ice Complex Formation on Bol'shoy Lyakhovsky Island (New Siberian Archipelago, East Siberian Arctic) since about 200 Ka. *Quat. Res.* 92, 530–548. doi:10.1017/qua.2019.6

Wild, B., Andersson, A., Bröder, L., Vonk, J., Hugelius, G., Mcclelland, J. W., et al. (2019). Rivers across the Siberian Arctic Unearth the Patterns of Carbon Release from Thawing Permafrost. *Proc. Natl. Acad. Sci. USA* 116, 10280–10285. doi:10.1073/pnas.1811797116

Wolfe, S. A., Gillis, A., and Robertson, L. (2009). Late Quaternary Aeolian Deposits of Northern North America: Age and Extent. *Geol. Surv. Can. Open File* 6006. doi:10.4095/226434

Yukon geological survey (2014). in *Yukon Digital Surficial Geology Compilation*. Editors P. S. Lipovsky and J. D. Bond.

Zimov, S. A., Davydov, S. P., Zimova, G. M., Davydova, A. I., Schuur, E. A. G., Dutta, K., et al. (2006). Permafrost Carbon: Stock and Decomposability of a Globally Significant Carbon Pool. *Geophys. Res. Lett.* 33, L20502. doi:10.1029/2006GL027484

Conflict of Interest: The authors declare that the research was conducted in the absence of any commercial or financial relationships that could be construed as a potential conflict of interest.

Publisher's Note: All claims expressed in this article are solely those of the authors and do not necessarily represent those of their affiliated organizations, or those of the publisher, the editors and the reviewers. Any product that may be evaluated in this article, or claim that may be made by its manufacturer, is not guaranteed or endorsed by the publisher.

frontiers in Earth Science

ORIGINAL RESEARCH
published: 29 October 2021
doi: 10.3389/feart.2021.727315

Reconstructing Permafrost Sedimentological Characteristics and Post-depositional Processes of the Yedoma Stratotype Duvanny Yar, Siberia

Denis Shmelev[1]*, *Maria Cherbunina*[2], *Victor Rogov*[3], *Sophie Opfergelt*[4], *Arthur Monhonval*[4] *and Jens Strauss*[5]

[1]*Institute of Physicochemical and Biological Problems in Soil Science, Russian Academy of Sciences, Pushchino, Russia,* [2]*Geology Department, Lomonosov Moscow State University, Moscow, Russia,* [3]*Geography Department, Lomonosov Moscow State University, Moscow, Russia,* [4]*Earth and Life Institute, Université Catholique de Louvain, Louvain-la-Neuve, Belgium,* [5]*Permafrost Research Section, Alfred Wegener Institute Helmholtz Centre for Polar and Marine Research, Potsdam, Germany*

OPEN ACCESS

Edited by:
Go Iwahana,
University of Alaska Fairbanks,
United States

Reviewed by:
Barbara Woronko,
University of Warsaw, Poland
Georg Schwamborn,
Istanbul Technical University, Turkey

***Correspondence:**
Denis Shmelev
shmelevdenis_msu@mail.ru

Specialty section:
This article was submitted to Sedimentology, Stratigraphy and Diagenesis, a section of the journal Frontiers in Earth Science

Received: *18 June 2021*
Accepted: *30 September 2021*
Published: *29 October 2021*

Citation:
Shmelev D, Cherbunina M, Rogov V, Opfergelt S, Monhonval A and Strauss J (2021) Reconstructing Permafrost Sedimentological Characteristics and Post-depositional Processes of the Yedoma Stratotype Duvanny Yar, Siberia. Front. Earth Sci. 9:727315. doi: 10.3389/feart.2021.727315

Cryogenic weathering is a key driver of periglacial sediment composition and properties. Selective mineral-grain weathering caused by freeze-thaw cycles in permafrost environments has the ability to dominate this process, leading to silt-rich grain-size distributions. The cryogenic weathering index (CWI) is a promising tool to quantify cryogenic weathering and freezing conditions. It considers the low resistance of quartz to freeze-thaw cycles compared to feldspars. Using this approach, this study aims to decipher post-depositional weathering by reconstructing cryogenic late Pleistocene Yedoma origins of the Yedoma stratotype exposure Duvanny Yar. To estimate the recent environmental endmember and to determine the initial mineral composition of sediment until freezing, the distribution of CWI in the active layer was studied. In addition to CWI, we studied mineral composition, heavy mineral distribution, grain size distribution and grain morphology. We suggest that cryogenic weathering likely altered polygenetic deposits (fluvial, nival, colluvial, lacustrine, alluvial, and aeolian processes) during sediment and ground ice accumulation. Moreover, we found two CWI distribution peaks in the late Pleistocene - Holocene sediments at the boundaries between glacial and interglacial ages. In conclusion, we see that the Duvanny Yar sediment facies varied by CWI, but also with grain-size distribution, suggesting environmental changes during formation. Nevertheless, post-depositional processes like cryogenic weathering have influenced sediment characteristics and should be considered in paleoenvironmental reconstructions.

Keywords: cryogenic weathering, Kolyma lowland, Arctic, permafrost, late Pleistocene, Holocene

INTRODUCTION

The permafrost region (including permafrost-free areas) of the Northern Hemisphere land area is estimated to be 21 million km^2 (22% of the exposed land area), and modelling studies indicate that 13.9 million km^2 are actually underlain by permafrost (Obu et al., 2019). In general, frozen soils are characterized by specific properties caused by their accumulation and freezing. Cryogenic weathering of permafrost, i.e., the processes of selective mineral destruction that occur during alternating freeze-thaw cycles, has been shown previously (Konishchev, 1981; Konishchev and Rogov, 1993; Rogov, 2000; Konishchev, 2013). A process of cryogenic weathering (mineral-grain destruction due to changing thickness of water films, ice pressure, and the pressure of gas-liquid inclusions) was found to be a key process of cryolithogenes (rock-like sediments, caused by freezing). Looking closer at the influence of mineral composition on weathering effectiveness, an increasing resistance of minerals to cryogenic weathering was found in this order: quartz < amphibole < pyroxene < feldspars < mica (Konishchev, 1981). An accepted view is that quartz is more resistant than feldspar to chemical weathering, the process involving chemical reactions of minerals with water and acidity leading to the dissolution of the minerals. For cryogenic weathering, this is the opposite: quartz is less resistant than feldspar (Konishchev and Rogov, 1993; Schwamborn et al., 2012). Konishchev and Rogov (1993) argued that during freeze-thaw cycles cryogenic weathering depends primarily on the thickness and properties of the unfrozen water film, and less on the mechanical properties of the mineral itself. Due to different surface energy (charge) quartz is assumed to have thicker water films compared to feldspar (Rogov, 2000). Rogov (2000) suggested that when gas-liquid inclusions, generally containing salt, freeze, they create weak points, leading to the weathering of quartz minerals during freeze-thaw cycles.

Cryogenic weathering is important in the permafrost region, especially in ice-bearing permafrost areas. Especially the Yedoma domain could be a prime candidate for cryogenic weathering. The Duvanny Yar site in northeastern Siberia is a well-known stratotype of a typical Yedoma landscape with traces of permafrost dated back to the Pliocene in the form of ice-wedge casts and cryoturbations (Sher, 1971; Arkhangelov, 1977; Sher et al., 1979). During the Last Glacial Maximum (LGM, 22,000–14,000 yrs BP) winter temperatures in the Arctic were found to be 10–15°C lower than today (Meyer et al., 2015), and permafrost temperatures were up to 20°C colder than modern permafrost temperatures (Kaplina, 2009; Konishchev, 2013). Starting in late Pleistocene times, Yedoma deposits accumulated in a tundra-steppe landscape *via* cryogenic weathering and different transport and deposition mechanisms until the late Pleistocene to Holocene transition period (~12,000 yrs BP) (Sher, 1971; Arkhangelov, 1977; Sher et al., 1979; Tomirdiaro, 1980; Schirrmeister et al., 2011; Strauss et al., 2012; Murton et al., 2015; Strauss et al., 2017). Yedoma deposits largely formed due to polygenetic deposition with syngenetic frost cracking and ground ice accumulation (Ulrich et al., 2014). A relatively constant sedimentation rate and significant syngenetic ice development in Yedoma deposits accumulated sediments up to 50 m thick (Kanevskiy et al., 2011; Schirrmeister et al., 2013). Two key layers are generally distinguished within Yedoma outcrops (e.g., Chukochiy cape, Duvanny Yar, Mus-Khaya): the one formed during the Marine Isotope Stage (MIS) 3–4 (75,000–50,000 and 50,000–25,000 yrs BP) with thick and infrequent ice wedges, and the one formed during the MIS-2 (25,000–12,000 yrs BP) with thin and frequent ice wedges (Arkhangelov, 1977; Konishchev, 1983; Katasonov, 2009). Thermal degradation was starting in the late glacial (mainly Holocene) warming. This intensified the degradation of Yedoma deposits. The main degradation process during this period was thermokarst (Olefeldt et al., 2016), i.e., the deep thawing of Yedoma ice wedges leading to shallow lake formation and permafrost subsidence (Grosse et al., 2013). When the lake drains, the sediments in the thawed depression refreeze under subaerial conditions. Sediments in thermokarst depressions are considered to be alas deposits (Walter et al., 2007; Kaplina, 2009). Moreover, the surfaces of the Yedoma uplands have been reworked by Holocene thawing and refreezing. Thus, a Holocene cover layer up to 2–3 m thick (Sher, 1997; Kaplina, 2009) was developed.

It is considered that Yedoma formation at the Duvanny Yar stratotype involves polygenetic origins such as aeolian, fluvial, colluvial sediments (Sher, 1997; Schirrmeister et al., 2011; Strauss et al., 2012), as described for other Yedoma deposits (Strauss et al., 2017; Schirrmeister et al., 2020). However, there are still unsolved questions regarding the influence of post-depositional processes at the Duvanny Yar site. An alternative explanation for a sediment considered dominated by aeolian deposition (Tomirdiaro, 1980; Gubin, 1999; Murton et al., 2015) could be that post-depositional cryogenic weathering processes may have affected grain morphology. This hypothesis can be tested by using the cryogenic weathering index (CWI) developed by Konishchev (1981) as a proxy for the intensity of cryogenic transformation. Given that multiple repeated freeze-thaw processes in the active layer can also affect the mineral distributions in the grain-size fractions, there is also a need to investigate the variability of the CWI in modern active layers.

Applying the CWI, the aim of this study is to decipher the Yedoma depositional environment and the post-depositional processes involved at the Duvanny Yar Yedoma stratotype by determining the role of cryogenic weathering in the formation of Yedoma deposits and the cover layers.

STUDY AREA

We studied the Yedoma deposit stratotype in northeastern Siberia, the Duvanny Yar exposure. In addition, samples of the modern active layer, collected in various landscapes and geomorphological conditions, were included as benchmarks for assessing the impact of cryogenic weathering on the mineral distribution in the grain size fractions of the deposits.

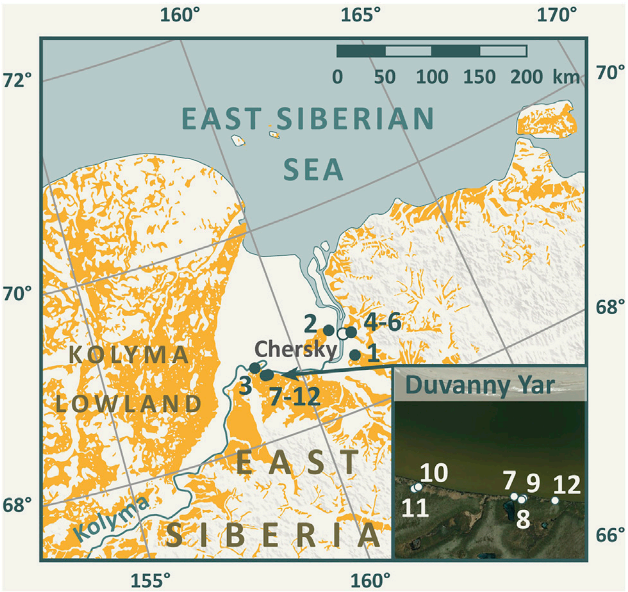

FIGURE 1 | Location of the study sites. The yellowish background is part of the Yedoma map (Strauss et al., 2021), where ice rich Yedoma occurrence is likely. Numbers show the locations of (1) Malchikovskaya channel, (2) Lake Akhmelo, (3) Mouth of the Omolon River, (4–6) Mount Rodinka and (7–12) the Duvanny Yar exposure. 7–12 are shown as a close up in the inset on the lower right.

The Kolyma lowland's relief is dominated by low hills (50–100 m above sea level [asl], **Figure 1**). This coastal lowland deposits show widespread degradation by thermokarst processes. Polygons, frost cracks, pingos, thermokarst lakes, alases, and baidzerakhs (called thermokarst mounds, the inter-wedge sediment remnants left after ice wedges melt; **Figure 2**) are evidence of widespread cryogenic processes and warming-caused permafrost degradation.

We collected the samples for our study at the Duvanny Yar site, a permafrost outcrop on the right bank of the Kolyma River. The site was first described by Barandova (1957) and Biske (1957), and subsequently investigated by several researchers (Sher, 1971; Strauss, 2010; Wetterich et al., 2014). The left bank of the Kolyma river beside Duvanny Yar site is presented by late Pleistocene 15–20 m above river level (arl) terrace called Alyoshkina Zaimka (Sher et al., 1979; Murton et al., 2015). This surface is covered by poorly silty sand with ice-less cryostructures.

The exposure is located within a typical Yedoma landscape. The outcrop is about 9 km long and up to 55 m high. Seven gentle Yedoma hills of late Pleistocene ice-rich silty sediment (**Figure 2**) and four drained Holocene thermokarst lakes (alas depressions) were distinguished by Sher et al. (1979). Four stratigraphic units were identified (**Figure 3**) by Sher et al. (1979). The first unit is described as interglacial lacustrine silts with ice-wedge casts at the river level, which deposited in middle Pleistocene. Peat sediments represent a second unit from the middle Pleistocene/beginning of late Pleistocene. The third unit is associated with late Pleistocene Yedoma deposits. The top of the exposure is composed of a Holocene cover layer.

The deposits of the Duvanny Yar exposure were studied previously by other researchers, which allow us to link the units by absolute (radiocarbon) age. In the lower part (12 m arl) of VIth Yedoma hills a buried peat layer up to 1.5 m thick is found with a radiocarbon age of 42,000–44,000 yrs BP (Zanina et al., 2011; Gubin and Zanina, 2013). The peat is overlaid by a sandy layer (**Unit A**). Three paleo soil horizons are found in Unit A (MIS-3 deposits) and located at 1–1,5 m arl, 18–28 m arl and 30–32 m arl. Radiocarbon age are within range of 38,000–28,000 yrs BP; the oldest paleo soil is similar to the age from the Yedoma ice wedges (ca 33,000–37,000 yrs BP), and the youngest paleo soil corresponds to the MIS-3 termination (28,000 yr BP) (Gubin and Zanina, 2013; Wetterich et al., 2014).

The age referencing within **Unit B** is most difficult. Unit B accumulation is expected to have begun at 28,000 yrs BP (Zanina et al., 2011). The younger ^{14}C and optically stimulated luminescence (OSL)-obtained dates of Yedoma from the Duvanny Yar exposure usually vary from 17,000 to 22,000 yrs BP (Kaplina, 2009; Zanina et al., 2011; Murton et al., 2015). All ice samples from upper ice wedges show ages younger than 25,000 yrs BP; the youngest dates are 14–16,000 yrs BP (Vasil'chuk, 2005; Vasil'chuk, 2013).

The Holocene cover layer (**Unit C**) is 13,500 ± 160 yrs BP, as dated from the paleo soil at the Yedoma top, and 13,080 ± 160 ^{14}C BP as dated from soil about 51 m arl (Gubin, 1999; Zanina et al., 2011). The youngest ^{14}C dates from near-surface silt vary from 840 ± 40 to 70 ± 30 ^{14}C BP (Murton et al., 2015).

METHODS

We studied the composition (mineralogy, grain size, morphology) and structure of cryogenic silt and clay using the abovementioned sample material.

Sampling

Fieldwork was conducted at the Duvanny Yar site during summer 2013 on the Yedoma hills called the VIth hill (N 68.62998, E 159.13582) and the VIIth hill (N 68.62732, E 159.19460) (Sher et al., 1979) (**Figure 1**, **Supplementary Figure S3**). During our field season, the lower part of the exposure was under water. We described the cryolithological structures of the exposure and collected 36 sediment samples by hammer and axe. For a same depth, some samples were taken close to the ice wedge, and some further within the mineral part. We transferred the air-dried samples to our laboratories for further analysis.

In addition, 14 samples of the modern active layer were collected in various landscapes and geomorphological conditions at the following sites: Malchikovskaya channel (Kolyma floodplain, active layer depth (ALD), ALD up to 60 cm), lake Akhmelo (sandy forest-tundra, Khallercha level, ALD up to 110 cm), the mouth of the Omolon (Yedoma hill, ALD 30–40 cm), the slope of the Rodinka mountain (larch forest). The annual number of freeze-thaw cycles are 14–15 for all sites (Shmelev et al., 2015, **Supplementary Table S3**). Samples were collected from various depths of the active layer in the August–September period. On the Rodinka mountain slope,

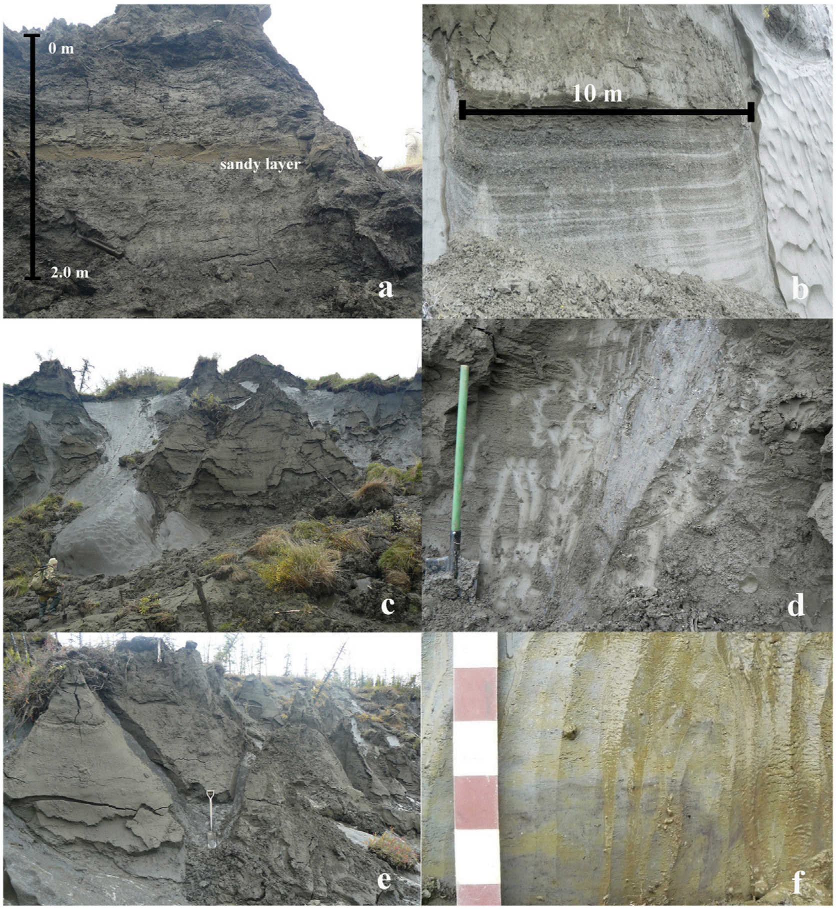

FIGURE 2 | Cryolithological features of the Duvanny Yar exposure. **(A)**–sandy layer at 8–10 m above the Kolyma level, **Unit A**; **(B)**–low-center polygon deposit, **Unit A; (C)**–the exterior of **Unit B**; **(D)**–mineral part of **Unit B**; **(E)**–baidzerakh and ice wedges, **Unit B**; **(F)**–organic inclusions and cryoturbation traces, **Unit C**.

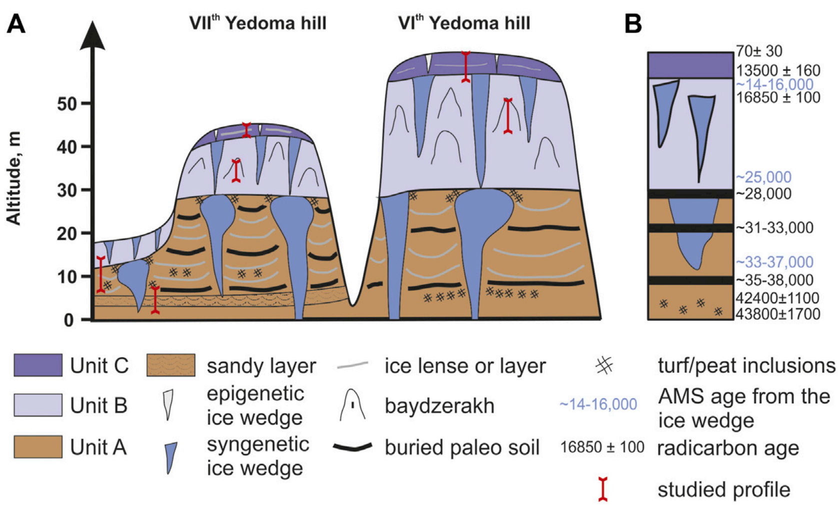

FIGURE 3 | Scheme of the Duvanny Yar exposure. The VIth and the VIIth Yedoma hill correspond to previously described exposures (Sher et al., 1979). **(A)**–geological cross-section. **(B)**–review of Duvanny Yar deposit dating.

TABLE 1 | Classification of grain roundness according to Khabakov (1933) and according to Krumbein (1941).

Roundness classes (Khabakov, 1933)	Description of shape	Roundness classes (Krumbein, 1941)	Description of shape
0	sharp-angular	0.0–0.1	Crushed/broken grain edges
1	angular	0.1–0.2	Grain surfaces and edges fresh and angular
2	angular-rounded	0.2–0.4	Lightly rounded grains with angular edges and surface
3	rounded	0.4–0.6	Moderately rounded
4	well-rounded	0.7–1.0	Very well rounded

samples were collected from a depth of 10 cm at the top of the mountain, in the middle part of the slope and at the foot of the mountain in order to evaluate the change in the mineral distribution in sediment during denudation.

Mineral Composition and Heavy Mineral Distribution

Sediment samples (n = 38) were sieved to separate the 10–50 µm and 51–100 µm fractions. Following Schwamborn et al. (2012), Schwamborn et al. (2014) the mineral compositions in the 10–50 µm and 51–100 µm grain-size fractions were determined by X-ray phase analysis with a Dron-3M (Shlykov, 1991).

We separated heavy and light mineral fractions in a centrifuge using a heavy liquid (bromoform, $CHBr_3$ with a density of 2.89 g/ cm^3). Based on the data obtained, the coefficient of heavy residue (CHR) was calculated as a function of the heavy residue of minerals in the 10–50 µm (HM1) and 51–100 µm (HM2) grain-size fractions (Konishchev, 1981).

$$\mathrm{CHR} = \frac{\mathrm{HM1}}{\mathrm{HM2}} \quad (1)$$

This coefficient shows the role of sediment sorting during sedimentation. The greater the transport capacity during deposition (high-energy conditions), the greater the CHR values and the grain size. Lower CHR values reflect decreasing transport capacity (Konischev, 1981; see **Supplementary Figure S3**).

The mineral composition and the CHR were determined on the samples from Duvanny Yar (n = 36) and on the samples of modern active layer (n = 5).

Grain-Size Parameters

The grain-size distribution (GSD) was determined on the samples from Duvanny Yar (n = 50) by a "Mastersizer 3000" Laser Particle Sizer (Malvern Instruments). Following the procedure described in Strauss et al. (2012), and in order to measure only mineral grains and to disaggregate the sample, organic components were removed by adding hydrogen peroxide (H_2O_2). The organic-free samples were diluted and washed to neutral pH values by centrifugation. The resulting GSD comprises 101 grain-size classes. We used GSD results to calculate grain-size parameters (mean diameter and sorting) used for the lithostratigraphical classification. GSD parameters were calculated after Folk and Ward (1957) using the Gradistat software (Blott and Pye, 2001).

Grain Morphology

The morphology of 100–250 µm particles was studied on the samples from Duvanny Yar (n = 24) with a Tesla Scanning Electron Microscope (SEM). We studied 30 to 40 mineral grains in each sample. The mineral grains and aggregates consisting of mineral and organic particles were studied. Individually, the roundness of quartz grains was assessed using a five-number scale according to Khabakov (1933) (**Table 1**), i.e., well correlated to a classical scheme by Krumbein (1941) (**Table 1**).

For grain-shape quantification (roundness), we used average and most-frequently-encountered (mode) values on a scale ranging from 0 to 4. The morphological features of grain shapes (relief and shape of grain edges) were described and classified according to Mahaney (2002) and Woronko and Pisarska-Jamroży (2016). The grain relief is the contrast between a mineral and its surroundings due to difference in refractive index, and classified as low, medium or high (Mahaney, 2002; Vos et al., 2014). Low relief is recognized as surfaces being smooth with near to no topographic irregularities while medium relief indicates a surface being affected by collisions or weathering processes (diagenetic environments) resulting in a somewhat irregular surface. High relief is recognized on a grain with a highly irregular surface, which mostly belongs in a glacial environment where glacial grinding and crushing has affected the grains. According to Konishchev and Rogov (1993) the 101–250 µm grain-size fraction is determined as the fraction that is most actively processed by cryogenic destruction of minerals, especially when looking at quartz and feldspar. We studied this fraction in detail for identification of signals and evidences of cryogenic weathering at sedimentation and freezing of deposits.

Cryogenic Weathering Index

The grain-size fractions determined in *Mineral Composition and Heavy Mineral Distribution* are used to calculate the cryogenic weathering index (CWI) (Konishchev, 1981). Using the CWI it is possible to quantify the intensity of cryogenic sediment transformation. We calculate the CWI as follows (**Eq. 2**):

$$\mathrm{CWI} = \frac{\frac{Q_1}{F_1}}{\frac{Q_2}{F_2}} \quad (2)$$

where Q_1 and F_1 are the quartz and feldspar contents in the 10–50 µm fraction (in %) and Q_2 and F_2 represent the quartz and feldspar contents in the 51–100 µm size fraction. CWI values > 1 indicate active cryogenic weathering during sedimentation. The greater the value, the more cryogenic weathering during sedimentation has occurred. CWI values < 1 indicate a low

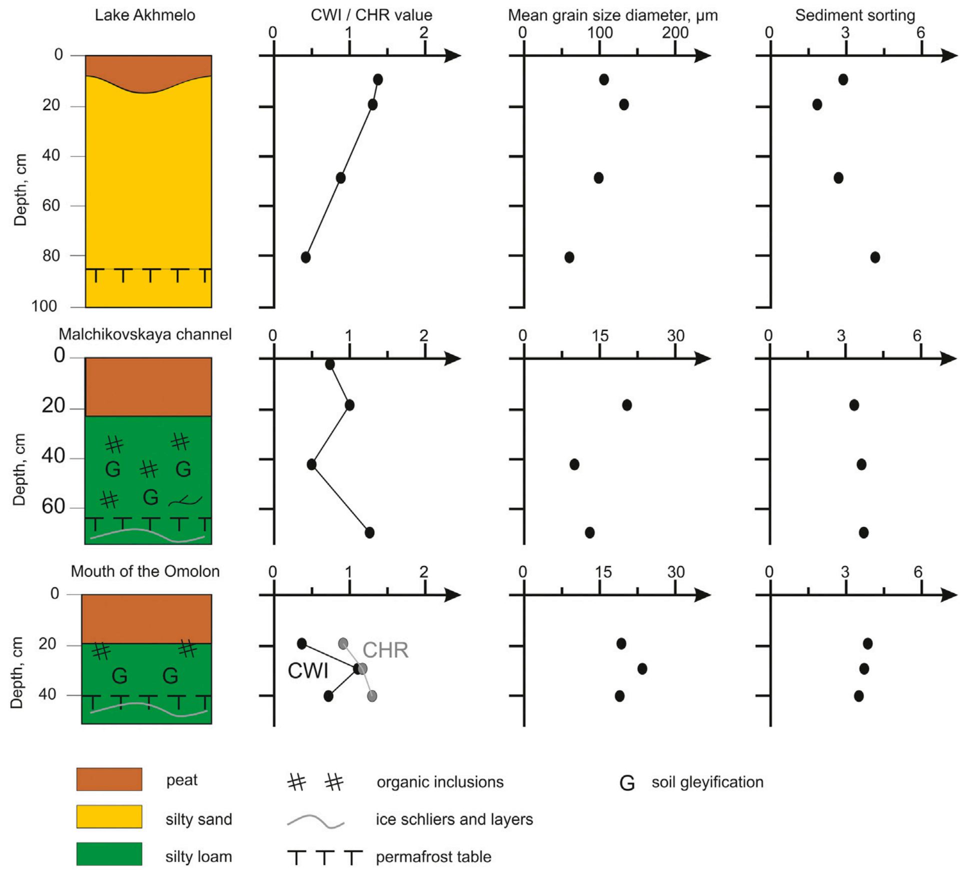

FIGURE 4 | Sediment parameters analysis of the active layer sediments. CWI = cryogenic weathering index; CHR = coefficient of heavy residue. Please note that the mean grain size axis for Lake Akhmelo is different from the others.

influence of cryogenic weathering. The CWI was determined on the samples from Duvanny Yar (n = 24) and on the samples of modern active layer (n = 14).

RESULTS

Mineral Composition, Grain Size Distribution and Cryogenic Weathering Index in Modern Active Layer Samples

For the Lake Akhmelo site (**Figure 1**, no. 2), the highest CWI values are typical in the upper 20 cm (up to CWI of 1.4), whereas in the lower part of the section the CWI decreases to 0.5 (**Figure 4**). This reflects the most favorable conditions for cryogenesis in the upper part of the active layer (the greatest number of transitions through 0°C and highest temperature amplitudes). At the same time, the granulometric composition is almost unchanged throughout the entire active layer; the mean grain size varies in the region of 50–150 μm. The particle distribution is monomodal (**Figure 5**). In samples with high CWI values, quartz accumulates in a finer fraction (silt), whereas in samples with low CWI quartz accumulates in fractions of fine sand. The mineral particles are characterized by clean surfaces with fresh cracks (**Figure 6A**). Besides the sample in 50 cm depth (moderately sorted), all samples are poorly sorted.

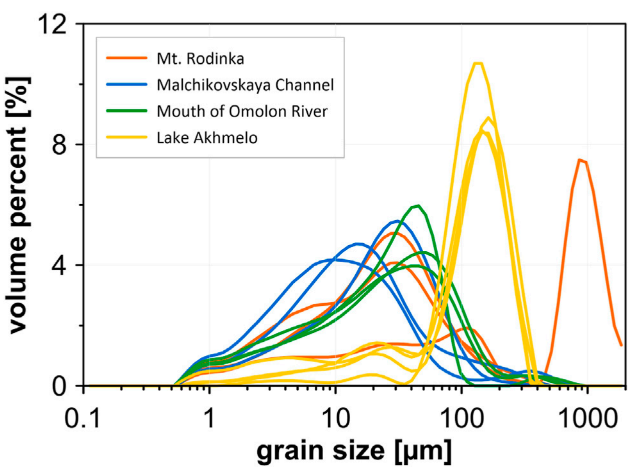

FIGURE 5 | Grain size distribution of the active layer sediments.

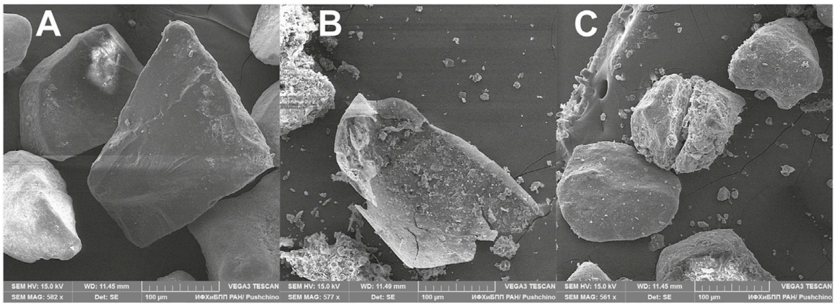

FIGURE 6 | Grain morphology images from a raster electron microscope on the active layer sediments. **(A)**–fresh quartz surface (Lake Akhmelo, depth 20 cm); **(B)**–disintegration of cryogenic aggregate (Malchikovskaya channel, depth 10 cm); **(C)**–disintegration of quartz grain (mouth of the Omolon River, depth 20 cm).

We studied the processes of cryogenic transformation of mineral particles in the conditions of active modern sedimentation at the Kolyma floodplain (Malchikovskaya channel site, **Figure 1**, no. 1). Here, the CWI values vary from 0.5 to 1.2 (**Figure 4**), and there is a clear relationship with the grain composition of the sediments. Cryogenic values (CWI—1.0–1.2) are associated with fine sediments in the silt fraction. Here, non-cryogenic revealing values (CWI values 0.5–0.7) are associated with coarse sediments–sand with organic inclusions and loam. The particle distribution is unimodal with a peak per fraction of 0.001–0.01 mm and 0.01–0.1 mm (**Figure 5**). The surface of the mineral particles is covered by aggregates (smaller particles and organic residues). These aggregates are cut by cracks into separate parts (**Figure 6B**).

At the mouth of the Omolon site (**Figure 1**, no. 3), the thickness of the active layer at the time of the study was 40 cm. Upper 20 cm of active layer is presented by water-saturated turf and moss layer. The CWI values vary in a large range from 0.4 to 1.1 by only 20 cm (**Figure 4**). The particle distribution is unimodal with a peak per fraction of 0.001–0.01 mm and 0.01–0.1 mm (**Figure 5**). There are both particles covered by aggregates (like as Malchikovskaya channel site), and particles with clean and fresh surfaces. Some quartz grains are broken in half (**Figure 6C**).

We studied the influence of denudation and slope processes on cryogenesis on the northwestern slope of the Mt Rodinka (**Figure 1**, no. 4–6). The granulometric features and CHR indicates a lateral transportation from the top to the foothill. The CHR values increase from the top of the Mt. Rodinka (CHR = 1.13), where the source rock is destroyed through the middle part of the slope (CHR = 1.62) to the bottom of the slope, where the maximum is reached (CHR = 2.76). The mean grain size also decreases from the top (196.6 μm) to the bottom (19.6 μm). The CWI values change very much: 0.6 at the top, 1.6 in the middle part of the slope, 0.5 at the bottom of the slope. Thus, the active lateral transportation of the sediment interferes with the cryogenic processing of the substance in the active layer. The particle distribution is unimodal (**Figure 5**).

Grain Size Distribution of the Duvanny Yar Exposure

Analyses of GSD show homogeneous composition (**Figure 7**). **Unit A, Unit B,** and **Unit C** are composed of very fine sand or very coarse silt sediments. All samples are characterized by a main peak between 20 and 60 μm and a secondary peak in the 4–8 μm range. Some samples (mainly from **Unit C**) have a small peak in the fine and middle sand fraction (200–600 μm). The mean grain-size diameter and standard deviation is 25.3 ± 7 μm. The sediments are poorly to very-poorly sorted with a mean sorting degree after Falk and Ward (1957) of 3.0 ± 0.5 (**Figure 8**). **Unit B** exhibits coarser grain sizes than the other two units (mean diameter is 29.9 for **Unit B,** 21.4 for **Unit A,** and 20.8 μm for **Unit C**), **Unit C** is better sorted (3.6 ± 0.5).

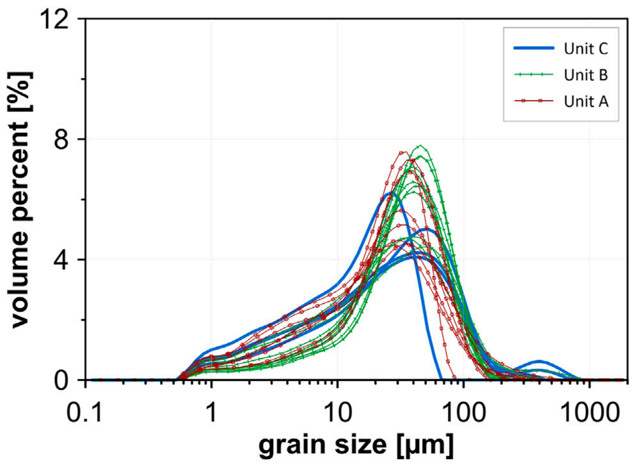

FIGURE 7 | Grain size distribution on the Duvanny Yar sediments. Unit A and Unit B–late Pleistocene Yedoma, Unit C–Holocene Cover Layer.

Cryolithological Structure of the Duvanny Yar Exposure

In this section we follow our cryostratigraphic classification of two different Yedoma facies and the Holocene cover layer. These units are marked as **Unit A, Unit B,** and **Unit C**, respectively (**Figure 3**). **Unit A** is located in the lower part of the exposure from 5 to 25 m asl. The layer is characterized by thick ice wedges with a visible width of 5–8 m and distances between the wedges 10–15 m. The uppermost parts of the wedges are penetrated by

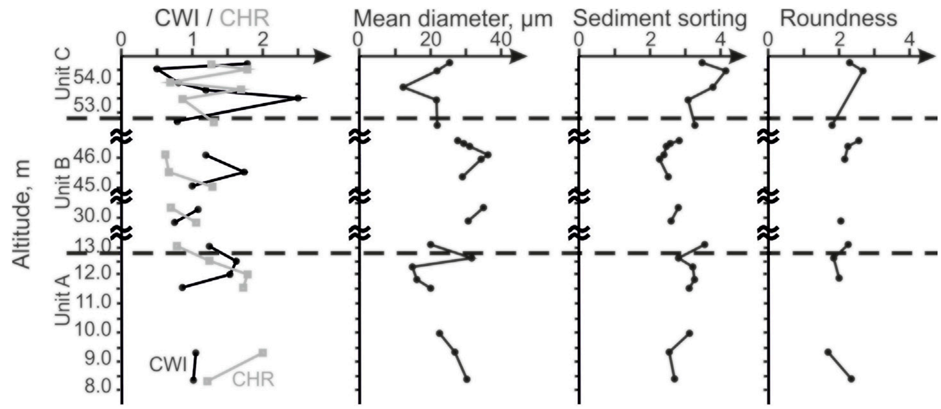

FIGURE 8 | Sediment parameters analysis on the Duvanny Yar sediments: CHR = coefficient of heavy residue; CWI = cryogenic weathering index. Unit A and Unit B–late Pleistocene Yedoma, Unit C–Holocene Cover Layer.

wedge tails from the overlaying **Unit B.** The ice of the lower wedges is dark-grey and muddy with vertical foliation and layers less than 1–2 cm wide.

Unit A involves at least two distinct sediment facies. The first type is dominated by a sandy layer, which extends across the exposure at 8–10 m arl (**Figure 2A**). This layer is a yellow and dark-yellow, silty fine sand with inclusions of bluish-grey silt. The lower part consists of 2–5 cm thick ice-rich layers. The thickness of this sand varies from 1 to 2 m. The sandy layer is a marking horizon of the Duvanny Yar exposure (Sher, 1971; Vasil'chuk, 2005; Gubin and Zanina, 2013).

The second sampled **Unit A** sediment facies consists of dark-brown and black ice- and organic-rich silts with peat layers and buried soils. This includes 5–8 m thick ice wedges. The heads of the ice wedges are surrounded by lightly-decomposed brown peat containing wood and roots. These sediments are similar to modern deposits formed in centers of low-center polygons of boggy polygonal tundra (**Figure 2B**). The cryostructure includes up to 2–5 cm thick horizontal ice lenses, and micro-lenticular and non-visible (called structureless) cryostructures between the ice lenses. The distance between these layers is 40–60 cm. In the lower part (at 11–13 m arl) the organic layer is 30–40 cm thick. **Unit A** is overlain by **Unit B** silts**,** while ice-wedge roots of **Unit B** penetrate into the underlying deposits.

Unit B is located in the high parts of the studied Yedoma hills above **Unit A** (**Figure 3**). We observed the most characteristic **Unit B** outcrops in the central parts of the studied Yedoma hills in thermocirques (**Figure 2C**). **Unit B** is different from **Unit A** by thinner (1–2 m width) ice wedges located closer to each other (3–5 m) than in **Unit A**. The ice wedges are dark grey and contain sediment inclusions, gas bubbles, and vertical foliation. The uppermost parts of the ice wedges are penetrated by very thin (0.5–3 cm thick) milky-colored ice wedges. At the boundary between ice wedges, inclined, 1–3 cm wide ice lenses are present in the sediment. Moreover, the mineral component of **Unit B** is composed of homogeneously grey and dark-grey silts with structureless and lenticular cryostructures and rootlets up to 10 cm long (**Figure 2D**). Organic layers 30–50 cm thick composed of roots and peat inclusions occur. Sparse anoxic soil environments are indicated by blue vivianite spots. **Unit B** is significantly influenced by thermokarst and thermoerosion processes and its outcrops are within thermocirques 500–1,000 m wide and 20–30 m deep. In fact, this is the area where baidzerakhs are present (**Figure 2E**). The mean baidzerakh size is 5–10 m high and up to 20–30 m wide at the base. Sporadically, the baidzerakh contain leftover parts of ice wedges.

Unit C is located on top of the Yedoma remains and overlies **Unit B** (**Figure 3**). **Unit C** was formed in the early Holocene as the result of deep thawing and subsequent re-freezing of the upper Yedoma deposits. The main difference between **Unit C** and alas deposits is that the thawing did not lead to ice wedge degradation and lake formation; therefore, the repeated freezing of water-saturated deposits formed an ice-rich permafrost layer called a transient or protective layer. **Unit C** contains thin milky-colored ice wedges ~0.5–1.0 m thick and is overlain by the 0.5–1.0 m thick modern active layer and soil. Ice wedges from **Unit C** sometimes penetrate the top of **Unit B** wedges. The organic peat inclusions and traces of cryoturbation occur at the bottom (**Figure 2F**).

The sediment composition of **Unit C** is similar to that of **Unit B** because it consists of reworked former Yedoma deposits. The main feature of **Unit C** is its cryostructural diversity, including the whole variety from structureless to crystal and suspended and pure ice layers.

Mineral Composition and Heavy Mineral Distribution of the Duvanny Yar Exposure

The mineral composition of the Duvanny Yar deposit can be characterized as homogeneous for all units of the exposure (**Table 2**). The heavy mineral fraction includes pyroxene, hornblende, pyrope, pyrite, magnetite, and individual grains of apatite, goethite, and siderite. The heavy mineral concentration is low and varies from 1.3 to 8.5%. The main light minerals are quartz (up to 50% of grains), feldspars, illite, chlorite and clay minerals (mainly smectite), dolomite, and

TABLE 2 | Mineral composition in 10–100 μm grain size classes of Duvanny Yar sediments (this study) and comparison to Kolyma alluvium and Chersky Yedoma deposits (Shmelev et al., 2013).

Location	Deposits	Heavy minerals	Light minerals
Duvanny Yar	Unit A	Pyroxene, hornblende, pyrope, magnetite, goethite	Quartz, feldspars, illite, chlorite, clay minerals, calcite
	Unit B	Pyroxene, hornblende, pyrite, apatite, pyrope	Quartz, feldspars, illite, chlorite, clay minerals, zeolite
	Unit C	Pyroxene, pyrite, magnetite, pyrope, siderite	Quartz, feldspars, illite, chlorite, clay minerals, zeolite, dolomite
Chersky (Panteleikha mouth)	Late Pleistocene Yedoma	Hornblende, siderite	Quartz, feldspars, chlorite, illite, zeolite, clay minerals, calcite, dolomite
Kolyma-Ambolikha floodplain	Holocene Kolyma alluvium	Hornblende	Quartz, feldspars, chlorite, illite

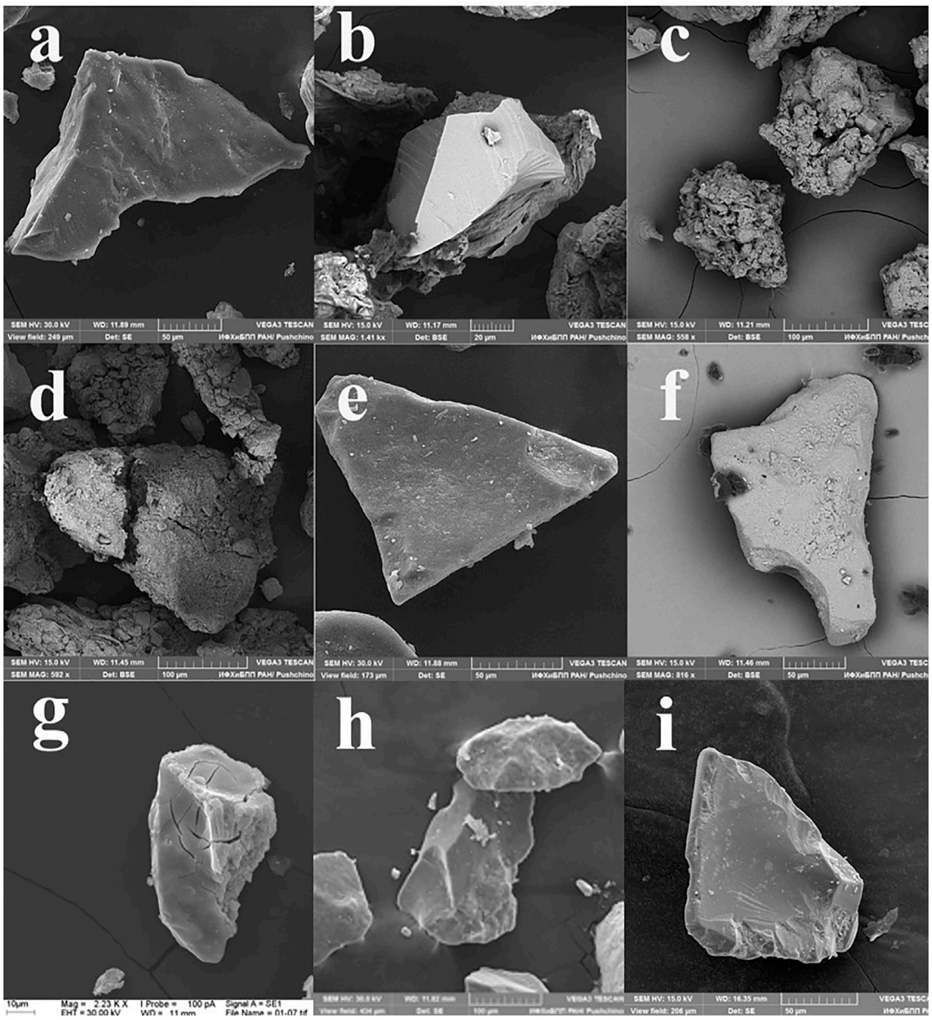

FIGURE 9 | Grain morphology images from a raster electron microscope on the Duvanny Yar sediments. **(A)**–fresh surface; **(B)**–sharp, coarse grain edge; **(C)**–cryogenic aggregate; **(D)**–obvious crack; **(E)**–fresh surface; **(F)**–nodular edge; **(G)**–radial fractures on quarts grain; **(H)**–fresh surface with nodular edge; **(I)**–fresh conchoidal surface with shell fracture.

calcite (occasionally). In one sample (sandy layer of **Unit A**) kaolinite was present. The sandy layer CHR values are >1.0. Within **Unit A**, the CHR varies between 1.25 and 2.71. The CHR values decrease toward the top of **Unit A** with the maximum values adjacent to ice wedges. At the final stage the wedges were covered by peat layers.

TABLE 3 | Roundness and microstructures of the Duvanny Yar samples.

Units	Mean roundness of grain according to Khabakov (1933)	Description	Microstructure
A	2	angular rounded shapes with matte surface and medium relief	Fresh conchoidal surfaces with concentric ripples like a shell, high-frequency and radial fractures and craters Sharp and jagged edges
sandy layer A	2.16	rounded shapes with matte surface and high relief	Some silty particles on surface, fresh jagged fractures
B	2.45	rounded grain with low and medium relief	Cryogenic aggregates (mineral and organic particles) with big cracks and craters; rounded edges
C	1.87	rounded long grain with low and medium relief	Fresh surfaces, nodular and shell edges, high-frequency fractures

The **Unit B** CHR values range from 0.69 to 1.84 (**Figure 8**). Similar to **Unit A**, the **Unit B** maximum values are located adjacent to ice wedges, where they can reach 1.70–1.84. The CHR values of the mineral layer are low at 0.69–1.04.

Grain Morphology of the Duvanny Yar Exposure

In **Unit A** extended angular rounded shapes (slightly rounded grains with angular edges and surface) with matte surface dominate; mean rounded degree values are 2.16 for the sandy layer and 2.00 for samples from a low center polygon (**Figure 2B**). The mode value for **Unit A** is 2. The grains are characterized by high relief in sand deposits and medium relief in ice-rich silts. Fresh conchoidal surfaces with concentric ripples like a shell (**Figure 9A**) with high-frequency and radial fractures and craters (**Figure 9G**) have been observed. Often we were able to identify the point of origin of grain destruction. The grain edge is mostly sharp and jagged (**Figure 9B**), but nodular edges are ovserved also (**Figure 9H**).

Unit B is characterized by more rounded grain shapes with a mean rounded degree value up to 2.45. Here, the mode value is 3. The grain relief in **Unit B** is low to medium. Fresh or weathered surfaces are absent and significant parts of grains are covered by aggregates in the form of adhering particles. Such a formation is called a "cryogenic aggregate" (Rogov, 2000) (**Figure 9C**). Big cracks crossing the grains and rounded edges have been identified (**Figure 9D**).

In **Unit C** the weathering evidence is more clearly developed. The grain shape varies within a broad range; the degree of rounding reaches up to 2.57 with a mode value of 3 between ice lenses. The mean value for **Unit C** is 1.85, with a mode value of 2. The grain shapes are more elongated than in **Unit A**. The grain morphology can be characterized by low and medium relief, fresh surfaces (**Figure 9E**), nodular (**Figure 9F**), high-frequency fractures and shell edges (**Figure 9I**). **Table 3** presents the results of the grain morphology studies.

Cryogenic Weathering Index Distribution of the Duvanny Yar Exposure

In the **Unit A** sediment column we observe CWI values increasing from 0.88 to 1.55, with maximum values in the upper part. The CWI values from sediments collected at a boundary with ice wedges (at a 20–30 cm distance from them) are lower (0.77–1.11) compared to samples at the same height but further away from the wedge. In the center of the mineral part, the CWI values increase towards the top. Moreover, CWI values are positively correlated with the visible ice contents. In **Unit B,** at a height of 1 m above the boundary with **Unit A**, the CWI value is 1.32 in the mineral part and 0.78 same depth, but close to the ice wedges (**Supplementary Figure S1**).

The sandy layer of **Unit A** (**Figure 8**) is characterized by low CWI values between 0.98 and 1.01, suggesting a weaker influence of cryogenic weathering. Mean **Unit A** CWI values are 1.10 ± 0.3 (n = 7).

The lithological and cryostructural **Unit B** features are homogeneous, but the CWI values vary across a wide range between 0.66 and 1.70. The maximum CWI value in **Unit B** occurs near the ice wedges. Adjacent sediment samples show low CWI values that do not exceed 1.10. The mean **Unit B** CWI value is 1.05 ± 0.5 (n = 10) (**Figure 8**).

Unit C is composed similar to the upper layer of the Yedoma exposure (**Unit B**), which thawed, subsided, and re-froze during the Holocene. Despite the lithological affinity, the CWI values of this Holocene cover layer (**Unit C**) are significantly higher than in the underlying deposits and reach the overall maximum here. Thus, in ice-free layers CWI values can range between 1.88–2.51, while in layers with pure ice and suspended cryostructures the CWI decreases to 0.52–0.84. The CWI values in the lower active layer range from 1.00 to 1.77. Remarkably, the uppermost **Unit B** sediments (at 45–50 m arl) show CWI values of 0.65 (**Figure 8**). This variation happens over short distances (2–3 m). The mean **Unit C** CWI value is 1.29 ± 0.5 (n = 7).

DISCUSSION

Deciphering Accumulation and Post-deposition Process Using Cryogenic Weathering Index of Modern Active Layer

The analysis of samples of the modern active layer allowed us to determine the main features of cryogenic weathering during sedimentation. A first driver of CWI in the active layer is a gradual decrease of the CWI values with depth at stable surfaces that were deposited outside the cryogenic impact, like in subaquatic environments. The most favorable temperature conditions for cryogenic weathering are great temperature amplitudes and number of temperature cycles through 0°C (Shmelev, 2015; see **Supplementary Table S2**). These are observed in the upper near-surface layer, where sediment is transformed (Lake Akhmelo; **Figure 4**).

A second driver of CWI are the dependence of cryogenic processing and CWI values with the sedimentation rate. The cryogenic weathering is most active at significant temperature amplitudes and a large number of transitions after 0°C. According to the analysis of the active layer's temperature regime, the most favorable temperature conditions are in the near-surface layer (Shmelev, 2015; see **Supplementary Table S2**). Thus, the sedimentation rate will influence on the cryogenic weathering. The faster sediments are deposited on top of the old surface (sedimentation), the faster the deeper sediment will leave the near-surface zone. At the same time, the stabilization of the surface or even its partial washout because of erosion processes will increase the time of the sediment in conditions favorable for cryogenic weathering, which will lead to increase of CWI values. For the Malchikovskaya Channel and the mouth of the Omolon River, we found the CWI values to be higher for sediments with bigger mean grain size. We explain this by the cycles of rapid sedimentation. Rapid sedimentation leads to the burial of the near-surface layer, because of which the sediment leaves the favorable conditions for cryogenic weathering. At loctions with good temperature insulation, like by thick moss cover, peat layers or water saturation, this significantly impedes cryogenic weathering due dampened temperature amplitudes.

An important feature of the grain-size composition of active layer samples is their multimodal distribution. Such a distribution may be the result of cryogenic weathering, which leads to the formation of a secondary peak in the grain size composition associated with the silty fraction. Our analysis of the mineral composition of samples from the Malchikovskaya Channel revealed that the content of feldspars by grain size fractions (100–51 microns and 50–10 microns) does not change severely, but in cryogenic samples (CWI >1) the quartz particles are more in the silt fraction. Of course a silt peak can have more than one explanation, and likely is the sum of different processes (like multiple transport cycles/dynamics, hydrodynamic sorting and more). But also quartz weathering likely contributed to the formation of a secondary peak in the grain size distribution.

We want to note that during transport in a fluvial environment, especially when mixed-grain sediment is transported, intense abrasion and production of silt fractions takes place. But quartz is more resistant to mechanical destruction than feldspar. At intense abrasion, feldspar should mainly be destroyed and accumulate in a finer fraction, and we expect quartz to be increased (relatively) in a coarser fraction. However, the higher CWI values mean that more quartz concentrate in the fine grain-size fractions, feldspars concentrate in the coarser fraction. That is why high CWI values indicate the dominant role of cryogenic weathering.

On the slope of Mt. Rodinka, the same mineralogical composition and distribution of minerals by grain fractions are established. The CWI values increase downhill with 0.6 at the top and 1.6 at the middle part of slope. At the same time, cryoturbation processes lead to mixing of sediments and smoothing of the results of the cryogenic weathering leading to a CWI of 0.5 at the bottom of the slope. As we applied a transect sampling (up, middle, down the slope) we were not able to include a profile sketch and diagram on **Figure 4**.

Deciphering Accumulation and Post-deposition Process Using Cryogenic Weathering Index of Unit A

A comparison of the mineral composition of the Duvanny Yar deposits to modern alluvial deposits and Yedoma deposits located in the lower streams of the Kolyma River (at Chersky location) (Shmelev et al., 2013) shows obvious differences. In the Duvanny Yar exposure, pyrope, pyrite, magnetite, goethite, and siderite are present, while in the Yedoma deposits at Chersky these minerals are absent (except siderite). The composition of the light minerals is also different: chlorite is more abundant than hydromica illite in the alluvial deposits of the lower streams of the Kolyma River, while clay minerals are more abundant in the Yedoma deposits of Duvanny Yar (**Table 2**) (Shmelev et al., 2013). Based on this we show a different mineralogical provenance, meaning a different source of Duvanny Yar Yedoma deposit sediments compared to the middle and lower Kolyma River Yedoma. Moreover, looking at the mineral composition of the Duvanny Yar Yedoma deposits, a homogeneous mineralogical composition indicates a constant source of sediments for the entire late Pleistocene to Holocene period. The warm interstadial MIS-3, exposed in Unit A of Duvanny Yar, shows warm and wet conditions [changing to more dry and aerial signals during MIS-2 (Kaplina, 2011; Zanina et al., 2011; Murton et al., 2015)]. Higher CHR values and good roundness, reflected by increasing mean grain-size diameter (**Figure 8**), indicate that the lower sand layer in ice-rich silts under buried soil was deposited by highly energetic processes under warmer permafrost conditions. Strauss et al. (2012) offer an explanation associated with increased stream velocity during a period of flooding. In the "low-center polygon" setting of Unit A the gradual drying of the polygon was accompanied by the development of cryogenic weathering and permafrost conditions. During this time, the permafrost conditions around frost cracks were warmer including deep seasonal thawing and higher ground temperatures.

The above-mentioned warmer conditions are revealed by lower CWI values here than in the center of the mineral part. We suggest that this is caused by seasonally percolating and flowing water in the active layer. According to Vasil'chuk, (2005), Vasil'chuk, (2013) ice-wedge development during long periods of subaerial bog-floodplain sedimentation was interrupted by subaqueous conditions. The fine mean grain-size diameter and good sediment sorting reveal sedimentation in subaquatic conditions (like alluvial floodplain deposition). Evidence for these conditions is found in the Unit A CHR distribution. Here, the maximum CHR values occur close to the ice wedges

(**Supplementary Figure S1**); this could be caused by the influence of flowing water (high-energy conditions). On the vertical scale, slow drying of the low-center polygon is confirmed by 1) decreasing ice contents and cryostructure changes from suspended, thick layers to structureless, thin lenses, 2) increasing CWI values, and 3) decreasing CHR values towards the top of the stratigraphic boundary between Unit A and Unit B (reduction of transporting energy, sedimentation in "calm" conditions: shallow drying lakes and puddles, may be a signal of aerial conditions and aeolian processes).

Thus, we hypothesize that Unit A accumulated under the impact of fluvial processes (according to grain shapes and GSD) under high-energy conditions, influenced by flowing water. This is consistent with the high ice content (visible ice content of 50–70%) and layered, reticulate, and crystal cryostructures, which are typical of wet conditions. Moreover, seasonal streams and creeks flowing above the top of the ice wedges caused periodic thermoerosion of the wedges. This comes with intensive cryogenic weathering (high CWI values). Generally, the depositional environment may be characterized as wet polygonal tundra and corresponds to proposed reconstructions for MIS-3 Yedoma (Zanina et al., 2011; Wetterich et al., 2014). It is possible that the natural conditions during the accumulation and freezing of Unit A were close to the modern ones observed at the Malchikovskaya channel site. Grain size is characterized mainly by a bimodal grain-size distribution, which can be caused by cryogenic weathering. At the same time, in general, the deposits are characterized by good sorting. This regularity of the grain size distribution is typical of all the studied Units at the Duvanny Yar.

Accumulation and Post-deposition Process Using Cryogenic Weathering Index of Unit B

The stratigraphic boundary between Unit A and Unit B is distinct, according to both cryogenic structures (dominance of ice-poor structures in Unit B) and lithology (change of sediment color). This is caused by the environmental shift after the MIS-3 termination to harsher stadial MIS-2 conditions at 28,000 yrs BP (Konishchev, 1983; Wetterich et al., 2014). The shift from warmer and wetter conditions (warm interstadial MIS-3) to dryer and cooler conditions (late MIS-3, MIS-2) (Zanina et al., 2011; Wetterich et al., 2014) corresponds to cryogenic weathering activation. This is nicely shown by the CWI peak at the boundary between Unit A and Unit B in our data. Based on our analyses we hypothesize that the Unit B accumulation was accompanied by drying of the interstadial landscape and the dominance of subaerial conditions (according to grain shapes, visible ice content, CHR distribution). The seasonal water in frost cracks above the ice wedges dried up, resulting in the freezing of sediments above the ice wedges. The maximum CWI values located close to the ice wedges support this (**Supplementary Figure S1**). Environmental drying caused an increased role of aeolian processes, which is also reflected by rising mean grain diameter, better sorting, and rounded grain morphologies. The lower CHR values reveal decreasing transport energy. We consider low CHR values (<1.0) to be a signal of dominating aeolian processes during deposition. Concerning the post-depositional change of the sediments, we explain the great variety of CWI values within the mineral part of Unit B as reflecting a period characterized by either a relatively high sedimentation rate. This causes a short exposure time in the paleo active layer resulting in a low rate of cryogenic weathering, or a low deposition rate and long residence time of the sediments in the active layer for active cryogenic weathering. We see the decreasing trend of coarse grains with low CWI values because of fast freezing. In general, the CHR decreases in Unit B likely reflect decreasing transport capacity during deposition.

We interpret the fraction >50 μm as a signal of aeolian input, and not a consequence of cryogenic destruction. A constraint on this interpretation is that this is only valid for the mineral part where low CWI values occur. For mineral layers closer to ground ice intensive, cryogenic weathering shown by high CWI values, complicates the interpretation of the grain-size curves.

Decreasing fluvial/alluvial signals correspond to a time around 14,000–15,000 yrs BP, when a terrace called the Alyoshkina terrace was deposited. This terrace was composed of sediments at a lower elevation than the Yedoma surface (15–20 m arl), underlain by relatively ice-poor silty sands. The Alyoshkina accumulated at the left bank of Kolyma River beside the Duvanny Yar exposure as an alluvial terrace, causing Kolyma channel migration during the MIS-2 period (Sher et al., 1979). This shows that alluvial or fluvial silty sands cannot have been simultaneously deposited at elevations of 15–20 m arl at the Alyoshkina terrace and at 50–100 m arl across the Omolon-Anyuy Yedoma plain (including Duvanny Yar) without extremely high river floods, at a time when the Kolyma River level was increasing at only a few meters per decade (Murton et al., 2015).

Accumulation and Post-deposition Process Using Cryogenic Weathering Index of Unit C

Unit C accumulated in the early Holocene during deep thawing and subsequent freezing of the Yedoma top, which formed in the LGM (19,000–14,000 yrs BP). The mineral part of Unit C originated from Unit B, but thawed and refroze during the Holocene. We explain the maximum CWI values by initially active cryogenic weathering of Yedoma deposits in the LGM and intensification of this weathering during Holocene thawing and re-freezing cycles. Finally, Yedoma accumulation was accompanied by the activation of aeolian processes.

The CWI values of near-surface silt samples (53–55 arl) correlates to visible ice content (high or low) and cryostructures (structureless-lensed-layered-suspended). Active-layer wetting led to gradual termination of aeolian sedimentation, because the grain size classes suitable for wind transport were protected by water and vegetation. In Unit C the CHR varies from 0.69 to 1.83, but there is no clear association with cryostructures or lithology.

CONCLUSION

Generally, the Cryogenic Weathering Index (CWI) seems to be a helpful tool in the toolbox for deciphering post-depositional processes in all freeze-thaw affected environments. Our data and literature data that, after being deposited polygenetically, sediments were affected by post-depositional processes dominated by cryogenic weathering. Holocene warming caused thawing of the upper Yedoma layers and re-deposition of these deposits, but also intensified cryogenesis due to more freeze thaw cycling.

The paleo-permafrost dynamics at Duvanny Yar accumulation is reflected in the CWI distribution. Two main peaks associated to cryogenic weathering activation links to environmental shift in MIS-3–MIS-2 boundary (change from wet to dry conditions) and in LGM (maximum climate cooling). The CWI distribution within selected Yedoma units depends from the ratio between sedimentation rate, sediment watering and soil cover (peat). The dependence of the CWI values from many factors is confirmed by the research of the modern active layer, then the CWI values wide varies within the active layer.

DATA AVAILABILITY STATEMENT

The original contributions presented in the study are included in the article/**Supplementary Material**, further inquiries can be directed to the corresponding author.

AUTHOR CONTRIBUTIONS

DS, MC and VR collected the data. DS and JS outlined the paper, SO and AM contributed with the other authors to the interpretation of the data. All authors contributed to the discussion of data and manuscript writing.

FUNDING

This investigation is part of the activities of the IPA Action Group “The Yedoma Region: A Synthesis of Circum-Arctic Distribution and Thickness”. Research has been supported by RFBR projects no. 16-35-00403 and 16-05-00612. JS was supported by the European Research Council (Starting Grant #338335) and the German Federal Ministry of Education and Research (BMBF, CACOON project, 03F0806A). SO and AM acknowledges support by the European Union’s Horizon 2020 research and innovation program (grant agreement No. 714617). SO acknowledges support from the “Fonds National de la Recherche Scientifique” (FNRS, Belgium, FC69480).

ACKNOWLEDGMENTS

In memory of V. N. Konishchev, who passed away in July 2020. His investigations of cryogenic weathering and consultations were the basis for this paper. We thank O. Zanina, A. Lupachev, S. Gubin, and S. Davydov for consultation during fieldwork and laboratory studies. Most labwork was done in the Geography faculty at Moscow State University and the Institute of Physicochemical and Biological Problems in Soil Science (Pushchino).

SUPPLEMENTARY MATERIAL

The Supplementary Material for this article can be found online at: https://www.frontiersin.org/articles/10.3389/feart.2021.727315/full#supplementary-material

REFERENCES

Arkhangelov, A. A. (1977). “Underground Glaciation of the Kolyma Lowland,” in *Problems of Cryolithology*. Editor A. Popov (Moscow: Moscow State University), 26–57.

Barandova, Y. P. (1957). Geomorphological Sketch of the Eastern Part of the Kolyma Lowland. *Mater. Geology. Resour. Northeast USSR* (Magadan: Sevvostgeologiya), 208–222.

Biske, S. F. (1957).Quaternary Deposits of the Kolyma Lowlands *Materials for Geology and Resources of Northeast USSR*. Magadan: Sevvostgeologiya.

Blott, S. J., and Pye, K. (2001). GRADISTAT: A Grain Size Distribution and Statistics Package for the Analysis of Unconsolidated Sediments. *Earth Surf. Process. Landforms* 26, 1237–1248. doi:10.1002/esp.261

Folk, R. L., and Ward, W. C. (1957). Brazos River Bar [Texas]; a Study in the Significance of Grain Size Parameters. *J. Sediment. Res.* 27, 3–26. doi:10.1306/74d70646-2b21-11d7-8648000102c1865d

Grosse, G., Jones, B., and Arp, C. (2013). “8.21 Thermokarst Lakes, Drainage, and Drained Basins,” in *Treatise in Geomorphology*. Editor J. F. Shroder (San Diego: Academic Press), 325–353. doi:10.1016/b978-0-12-374739-6.00216-5

Gubin, S. V. (1999). *Late Pleistocene Soil Formations in Loess-Ice Deposits of Northeast Eurasia*. Abstract of doctor dissertation. Pushchino.

Gubin, S., and Zanina, O. (2013). Variation of Soil Cover during the Ice Complex deposit Formation, Kolyma Lowland (Part 1). *Earth Cryosphere* 17, 48–56.

Kanevskiy, M., Shur, Y., Fortier, D., Jorgenson, M. T., and Stephani, E. (2011). Cryostratigraphy of Late Pleistocene Syngenetic Permafrost (Yedoma) in Northern Alaska, Itkillik River Exposure. *Quat. Res.* 75, 584–596. doi:10.1016/j.yqres.2010.12.003

Kaplina, T. (2009). Alas Complex of Northern Yakutia. *Kriosfera Zemli (Earth Cryosphere)* 13, 3–17.

Kaplina, T. (2011). Northern Yakutia, Pleistocene, Ancient Ice Complex, Thermokarst, Ancient Alas Complex. *The Earth’s Cryosphere* 15, 3–13.

Katasonov, E. M. (2009). *Litologiya Merzlykh Chetvertichnykh Otlozhenii (Kriolitologiya) Yanskoi Primorskoi Nizmennosti - (Lithology of Frozen Quaternary Deposits (Cryolithology) of the Yana Coastal Plain)*. Moscow: OAO PNIIIS.

Khabakov, A. (1933). *Kratkaya Instruktsiya Dlya Polevogo Issledovaniya Konglomeratov (Short Instruction for the Field Study of Conglomerates)*. Moscow: Gos. nauchn.-technol. geologo-razvedochn. izdatelstvo.

Konishchev, V. N. (1983).*Cryolithological Evidences of the Heterogeneous Structure of “Ice Complex” Deposits in the Dyvanny Yar Section Problems of Cryolithology*. Moscow: MGU, 56–64.

Konishchev, V. N. (1981). *Formirovanie Sostava Dispersnih Porod V Kriolitosfere [Formation of the Composition of Dispersed Rocks in the Cryolithosphere]*. Novosibirsk: Nauka, 197.

Konishchev, V. N., and Rogov, V. V. (1993). Investigations of Cryogenic Weathering in Europe and Northern Asia. *Permafrost Periglac. Process.* 4, 49–64. doi:10.1002/ppp.3430040105

Konishchev, V. (2013). The Nature of Cyclic Structure of the Ice Complex, East Siberia. *Geogr. Environ. Sustain.* 6, 4–20. doi:10.24057/2071-9388-2013-6-3-4-20

Krumbein, W. C. (1941). Measurement and Geological Significance of Shape and Roundness of Sedimentary Particles. *J. Sediment. Res.* 11, 64–72. doi:10.1306/d42690f3-2b26-11d7-8648000102c1865d

Mahaney, W. C. (2002). *Atlas of Sand Grain Surface Textures and Applications*. USA: Oxford University Press.

Meyer, H., Opel, T., Laepple, T., Dereviagin, A. Y., Hoffmann, K., and Werner, M. (2015). Long-term winter Warming Trend in the Siberian Arctic during the Mid- to Late Holocene. *Nat. Geosci* 8, 122–125. doi:10.1038/Ngeo2349

Murton, J. B., Goslar, T., Edwards, M. E., Bateman, M. D., Danilov, P. P., Savvinov, G. N., et al. (2015). Palaeoenvironmental Interpretation of Yedoma Silt (Ice Complex) Deposition as Cold-Climate Loess, Duvanny Yar, Northeast Siberia. *Permafrost Periglac. Process.* 26, 208–288. doi:10.1002/ppp.1843

Obu, J., Westermann, S., Bartsch, A., Berdnikov, N., Christiansen, H. H., Dashtseren, A., et al. (2019). Northern Hemisphere Permafrost Map Based on TTOP Modelling for 2000-2016 at 1 Km2 Scale. *Earth-Science Rev.* 193, 299–316. doi:10.1016/j.earscirev.2019.04.023

Olefeldt, D., Goswami, S., Grosse, G., Hayes, D., Hugelius, G., Kuhry, P., et al. (2016). Circumpolar Distribution and Carbon Storage of Thermokarst Landscapes. *Nat. Commun.* 7, 13043. doi:10.1038/ncomms13043

Rogov, V. V. (2000). Specific Features of the Morphology of Skeletal Particles of Cryogenic Alluvium. *The Earth's Cryosphere* 4, 67–73.

Schirrmeister, L., Dietze, E., Matthes, H., Grosse, G., Strauss, J., Laboor, S., et al. (2020). The Genesis of Yedoma Ice Complex Permafrost - Grain-Size Endmember Modeling Analysis from Siberia and Alaska. *E&g Quat. Sci. J.* 69, 33–53. doi:10.5194/egqsj-69-33-2020

Schirrmeister, L., Froese, D., Tumskoy, V., Grosse, G., and Wetterich, S. (2013). "PERMAFROST and PERIGLACIAL FEATURES | Yedoma: Late Pleistocene Ice-Rich Syngenetic Permafrost of Beringia," in *Encyclopedia of Quaternary Sciences*. Editor S. A. Elias. 2 ed (Amsterdam: Elsevier), 542–552. doi:10.1016/b978-0-444-53643-3.00106-0

Schirrmeister, L., Kunitsky, V., Grosse, G., Wetterich, S., Meyer, H., Schwamborn, G., et al. (2011). Sedimentary Characteristics and Origin of the Late Pleistocene Ice Complex on north-east Siberian Arctic Coastal Lowlands and Islands - A Review. *Quat. Int.* 241, 3–25. doi:10.1016/j.quaint.2010.04.004

Schwamborn, G., Meyer, H., Schirrmeister, L., and Fedorov, G. (2014). Past Freeze and Thaw Cycling in the Margin of the El'gygytgyn Crater Deduced from a 141 M Long Permafrost Record. *Clim. Past* 10, 1109–1123. doi:10.5194/cp-10-1109-2014

Schwamborn, G., Schirrmeister, L., Frütsch, F., and Diekmann, B. (2012). Quartz Weathering in Freeze-Thaw Cycles: experiment and Application to the El'gygytgyn Crater lake Record for Tracing Siberian Permafrost History. *Geografiska Annaler: Ser. A, Phys. Geogr.* 94, 481–499. doi:10.1111/j.1468-0459.2012.00472.x

Sher, A. V., Kaplina, T. N., Giterman, R. E., Lozhkin, A. V., Arkhangelov, A. A., Kiselyov, S. V., et al. (1979). *Late Cenozoic of the Kolyma Lowland 14th Pacific Science Congress: Academy of Science*: Moscow: VINITI. 116.

Sher, A. V. (1971). *Mammals and Stratigraphy of the Pleistocene of the Extreme Northeast of the USSR and North America*. Moscow: Nauka.

Sher, A. V. (1997). "Yedoma as a Store of Paleoenvironmental Records in Beringia," in *Beringia Paleoenvironmental Workshop*. Editors S. Elias and J. Brigham-Grette, 140–144.

Shlykov, V. G. (1991). *X-ray Studies of Grounds*. Moscow: MGU, 184.

Shmelev, D., Kraev, G., Veremeeva, A., and Rivkina, E. (2013). Carbon Pool of Permafrost in north-eastern Yakutia. *Earth's Cryophere* 17, 50–59.

Shmelev, D. (2015). The Role of Cryogenesis in the Formation of Texture and Composition of Frozen Late Quaternary Deposits in Antarctic Oases and Northeast Yakutia. *Earth's Cryophere* 19, 37–52.

Strauss, J. (2010). *Late Quaternary Environmental Dynamics at the Duvanny Yar Key Section, Lower Kolyma, East Siberia*. Potsdam: University of Potsdam.

Strauss, J., Schirrmeister, L., Grosse, G., Fortier, D., Hugelius, G., Knoblauch, C., et al. (2017). Deep Yedoma Permafrost: A Synthesis of Depositional Characteristics and Carbon Vulnerability. *Earth-Science Rev.* 172, 75–86. doi:10.1016/j.earscirev.2017.07.007

Strauss, J., Schirrmeister, L., Wetterich, S., Borchers, A., and Davydov, S. P. (2012). Grain-size Properties and Organic-carbon Stock of Yedoma Ice Complex Permafrost from the Kolyma lowland, Northeastern Siberia. *Glob. Biogeochem. Cycles* 26, GB3003. doi:10.1029/2011GB004104

Tomirdiaro, S. V. (1980). *Loess-ice Formations in East Siberia during the Late Pleistocene and Holocene*. Moscow: Nauka Press.

Strauss, J., Laboor, S., Schirrmeister, L., Fedorov, A. N., Fortier, D., Froese, D., et al. (2021). Circum-Arctic Map of the Yedoma Permafrost Domain. *Front. Earth Sci.* 9, 758360. doi:10.3389/feart.2021.758360

Ulrich, M., Grosse, G., Strauss, J., and Schirrmeister, L. (2014). Quantifying Wedge-Ice Volumes in Yedoma and Thermokarst basin Deposits. *Permafrost Periglac. Process.* 25, 151–161. doi:10.1002/ppp.1810

Vasil'chuk, Y. K. (2013, Syngenetic Ice Wedges: Cyclical Formation, Radiocarbon Age and Stable Isotope Records by Yurij K. Vasil 'chuk, *Monograph Synopsis.* 24, 82–93. doi:10.1002/ppp.1764

Vasil'chuk, Y. K. (2005). Heterochroneity and Heterogeneity of the Duvanny Yar Edoma. *Doklady Earth Sci.* 402, 568–573.

Vos, K., Vandenberghe, N., and Elsen, J. (2014). Surface Textural Analysis of Quartz Grains by Scanning Electron Microscopy (SEM): From Sample Preparation to Environmental Interpretation. *Earth-Science Rev.* 128, 93–104. doi:10.1016/j.earscirev.2013.10.013

Walter, K. M., Edwards, M. E., Grosse, G., Zimov, S. A., and Chapin, F. S. (2007). Thermokarst Lakes as a Source of Atmospheric CH4 during the Last Deglaciation. *Science* 318, 633–636. doi:10.1126/science.1142924

Wetterich, S., Tumskoy, V., Rudaya, N., Andreev, A. A., Opel, T., Meyer, H., et al. (2014). Ice Complex Formation in Arctic East Siberia during the MIS3 Interstadial. *Quat. Sci. Rev.* 84, 39–55. doi:10.1016/j.quascirev.2013.11.009

Woronko, B., and Pisarska-Jamroży, M. (2016). Micro-Scale Frost Weathering of Sand-Sized Quartz Grains. *Permafrost Periglac. Process.* 27, 109–122. doi:10.1002/ppp.1855

Zanina, O. G., Gubin, S. V., Kuzmina, S. A., Maximovich, S. V., and Lopatina, D. A. (2011). Late-Pleistocene (MIS 3-2) Palaeoenvironments as Recorded by Sediments, Palaeosols, and Ground-Squirrel Nests at Duvanny Yar, Kolyma lowland, Northeast Siberia. *Quat. Sci. Rev.* 30, 2107–2123. doi:10.1016/j.quascirev.2011.01.021

Conflict of Interest: The authors declare that the research was conducted in the absence of any commercial or financial relationships that could be construed as a potential conflict of interest.

Publisher's Note: All claims expressed in this article are solely those of the authors and do not necessarily represent those of their affiliated organizations, or those of the publisher, the editors and the reviewers. Any product that may be evaluated in this article, or claim that may be made by its manufacturer, is not guaranteed or endorsed by the publisher.

frontiers in Earth Science

ORIGINAL RESEARCH
published: 05 November 2021
doi: 10.3389/feart.2021.739365

Microbial and Geochemical Evidence of Permafrost Formation at Mamontova Gora and Syrdakh, Central Yakutia

M. Yu. Cherbunina[1]*, E. S. Karaevskaya[2], Yu. K. Vasil'chuk[3], N. I. Tananaev[4], D. G. Shmelev[1], N. A. Budantseva[3], A. Y. Merkel[5], A. L. Rakitin[6], A. V. Mardanov[6], A. V. Brouchkov[1] and S. A. Bulat[7,8]

[1]Faculty of Geology, Lomonosov Moscow State University, Moscow, Russia, [2]Arctic and Antarctic Research Institute (AARI), St. Petersburg, Russia, [3]Faculty of Geography, Lomonosov Moscow State University, Moscow, Russia, [4]The Melnikov Permafrost Institute, Siberian Branch of the Russian Academy of Sciences, Yakutsk, Russia, [5]Winogradsky Institute of Microbiology, Research Center of Biotechnology, Russian Academy of Sciences, Moscow, Russia, [6]Institute of Bioengineering, Research Center of Biotechnology, Russian Academy of Sciences, Moscow, Russia, [7]Petersburg Nuclear Physics Institute Named by B.P. Konstantinov of NRC "Kurchatov Institute", Gatchina, Russia, [8]Institute of Physics and Technology, Ural Federal University, Ekaterinburg, Russia

OPEN ACCESS

Edited by:
Ko Van Huissteden, Vrije Universiteit Amsterdam, Netherlands

Reviewed by:
Mary E. Edwards, University of Southampton, United Kingdom
Sebastian Wetterich, Alfred Wegener Institute Helmholtz Centre for Polar and Marine Research (AWI), Germany

***Correspondence:**
M. Yu. Cherbunina
cherbuninamariya@gmail.com

Specialty section:
This article was submitted to Cryospheric Sciences, a section of the journal Frontiers in Earth Science

Received: *10 July 2021*
Accepted: *14 October 2021*
Published: *05 November 2021*

Citation:
Cherbunina MY, Karaevskaya ES, Vasil'chuk YK, Tananaev NI, Shmelev DG, Budantseva NA, Merkel AY, Rakitin AL, Mardanov AV, Brouchkov AV and Bulat SA (2021) Microbial and Geochemical Evidence of Permafrost Formation at Mamontova Gora and Syrdakh, Central Yakutia. Front. Earth Sci. 9:739365. doi: 10.3389/feart.2021.739365

Biotracers marking the geologic history and permafrost evolution in Central Yakutia, including Yedoma Ice Complex (IC) deposits, were identified in a multiproxy analysis of water chemistry, isotopic signatures, and microbial datasets. The key study sections were the Mamontova Gora and Syrdakh exposures, well covered in the literature. In the Mamontova Gora section, two distinct IC strata with massive ice wedges were described and sampled, the upper and lower IC strata, while previously published studies focused only on the lower IC horizon. Our results suggest that these two IC horizons differ in water origin of wedge ice and in their cryogenic evolution, evidenced by the differences in their chemistry, water isotopic signatures and the microbial community compositions. Microbial community similarity between ground ice and host deposits is shown to be a proxy for syngenetic deposition and freezing. High community similarity indicates syngenetic formation of ice wedges and host deposits of the lower IC horizon at the Mamontova Gora exposure. The upper IC horizon in this exposure has much lower similarity metrics between ice wedge and host sediments, and we suggest epigenetic ice wedge development in this stratum. We found a certain correspondence between the water origin and the degree of evaporative transformation in ice wedges and the microbial community composition, notably, the presence of *Chloroflexia* bacteria, represented by *Gitt-GS-136* and *KD4-96* classes. These bacteria are absent at the ice wedges of lower IC stratum at Mamontova Gora originating from snowmelt, but are abundant in the Syrdakh ice wedges, where the meltwater underwent evaporative isotopical fractionation. Minor evaporative transformation of water in the upper IC horizon of Mamontova Gora, whose ice wedges formed by meltwater that was additionally fractionated corresponds with moderate abundance of these classes in its bacterial community.

Keywords: ice comlex, yedoma, Central Yakutia, microbial community, stable water isotopes, hydrochemistry, ancient DNA

1 INTRODUCTION

Permafrost soils contain around 1,000 Pg of organic carbon, close to 50% of its total terrestrial storage (Schuur et al., 2015). Microbial activity stimulated by increasing air and ground temperatures and associated permafrost degradation is likely to increase trace gas release and accelerate climate change, threatening global carbon goals (Natali et al., 2021). The microbial community structure of permafrost soils draws substantial attention as a potential control in carbon release to the atmosphere (McCalley et al., 2014; Hultman et al., 2015; Tveit et al., 2015; Brouillette, 2021; Emerson et al., 2021). Permafrost microbiota are frozen in permafrost, and its biological performance upon permafrost thaw corresponds to their strategies and metabolic versatility (Ernakovich et al., 2015; Mackelprang et al., 2017; Zhou et al., 2020; Perez-Mon et al., 2021). Metagenomics and 16S RNA sequencing are widely used in permafrost microbial community studies, although 40–50% of the permafrost-derived DNA is relict (Carini et al., 2017; Liang et al., 2019). Viability or metabolic activity of the derived cells cannot be concluded from DNA-based methods, it is shown that dead cell's DNA has a minor effect on the community structure (Carini et al., 2017; Burkert et al., 2019). The Northern Hemisphere permafrost was subject to significant alterations in the last 650 ka (Konischev, 2011; Vaks et al., 2013; Murton et al., 2021a), potentially affecting the microbial communities. Taxonomic diversity and ecological functionality of microbiota in various permafrost strata could have either remained unchanged and reflect the environmental conditions around freezing time or undergone adaptation to potential thawing and refreezing.

Recent studies suggest that both composition and diversity of permafrost microbiota vary with the age of deposits (Mackelprang et al., 2017; Burkert et al., 2019; Liang et al., 2019), the ice content (Burkert et al., 2019), and are subject to dispersal limitation and both homogenous and variable selection (Bottos et al., 2018). The permafrost origin is additionally important in driving the community structure, since significant differences in community composition were reported from late Pleistocene lacustrine-alluvial and Ice Complex (Yedoma) sediments (Rivkina et al., 2016). Recently, the transition from Pleistocene to Holocene was shown to initiate a major threshold-type shift in the composition and structure of permafrost microbial community in Central Yukon (Saidi-Mehrabad et al., 2020). These results draw particular attention to the potential effect of climate change on microbial activity and trace gas production. Our study is a follow-up to numerous preceding research efforts in Central Yakutia, Northern Eurasia, focusing on microbiota and climate-relevant gas production (Cherbunina et al., 2018; Kim et al., 2019; Hughes-Allen et al., 2021). This region is underlain by thick ice-rich horizon, known as Ice Complex, a series of fine-grained Pleistocene deposits of disputed origin (Solovev, 1959; Péwé and Journaux, 1983; Ivanov, 1984; Sukhodrovsky, 2002; Vasil'chuk et al., 2004; Schirrmeister et al., 2020). Under changing climate, landscapes on Ice Complex deposits are subject to intensified thermal disturbance and thermokarst development (Sejourné et al., 2015; Saito et al., 2018; Zakharova et al., 2018).

Previous studies on Central Yakutia ICs using 16S rRNA gene sequencing from ice wedge material have shown lower diversity and dominance of anaerobic species and psychrophilic bacteria with older age (Rakitin et al., 2020). Electron microscopy of ice wedge-derived material combined with X-ray microanalysis evidence high diversity and organic origin of bacteriomorphic particles, including those with signs of low-temperature damage to the cellular structures (Filippova et al., 2014). Recently, bacterial communities from both Pleistocene ice wedges and Miocene alluvial sands have been described (Brouchkov et al., 2017; Ivanova et al., 2017; Filippova et al., 2019).

The microbial community structure in permafrost soils is supposed to be relatively stable over time (Shade et al., 2013), but rapidly shift to a new stable state under changing conditions, experiencing threshold behavior (Saidi-Mehrabad et al., 2020). Ground freezing and permafrost development are natural thresholds, but they can occur either simultaneously with sediment accumulation, or significantly later. Moreover, frozen ground can be subject to thermal degradation and subsequent refreezing, in which case the structure of microbial communities is expected to reflect natural conditions of the post-degradation period. Massive ice wedges are known to be formed predominantly from snow meltwater, but, other surface water sources might interfere as well, i.e., shallow groundwater or thermokarst lake water. New species associated with such water sources can be introduced to the initial microbial community and could serve, if identified, as markers of both thermal degradation and/or water origin. Ice-rich deposits of central Yakutia accumulated during a prolonged cold epoch from marine isotope stages (MIS) 4 to MIS 2 and were subject to partial thermal degradation during MIS 3 and during the Holocene, which should have been reflected in the microbial composition of these deposits and associated ice wedges.

In our study, our aim was to describe and quantify the microbial community composition and structure with 16S rRNA gene sequencing and bioinformatic metrics, and to relate these community features to the geological history of the "Ice Complex" (IC) deposits and the origin of massive ice wedges at two key locations in Central Yakutia, Northern Eurasia: Mamontova Gora and Syrdakh, both well described in the preceding literature (Ravsky et al., 1960; Baranova and Biske, 1964; Markov, 1973; Svitoch, 1983; Baranova et al., 1976; Péwé et al., 1977; Ershov, 1989; Lazukov, 1989).

Three hypotheses were tested in the present study: 1) the composition and structure of microbial communities are similar in host deposits and ice wedges that formed syngenetically, and strongly differ when ice wedges formed epigenetically; 2) the composition of microbial communities can be related to the water origin of the ice wedges, and indicate if the IC strata were subject to thawing and subsequent refreezing (epigenetic freezing); 3) the similarity in microbial community composition and structure can be indicative of similar age of the IC strata in different locations, or their contemporaneous accumulation and freezing.

2 STUDY SITES

Central Yakutia occupies the interfluve surface of the Lena and Aldan Rivers in North-East Siberia, Russia, underlain by thick

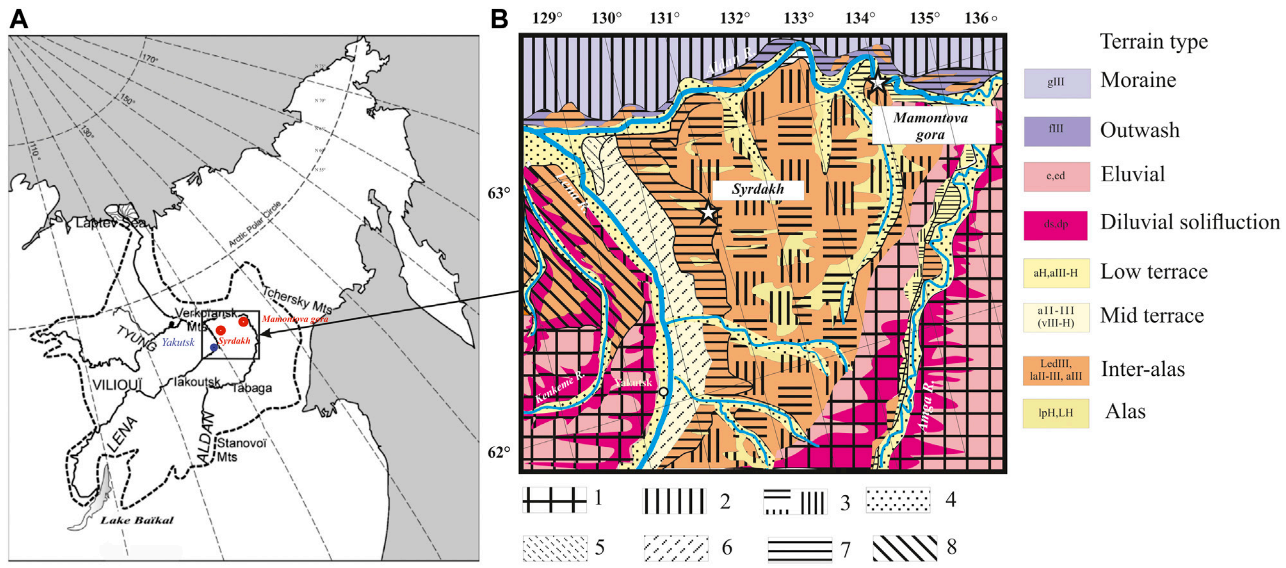

FIGURE 1 | Location of the study sites **(A)** Study region **(B)** Schematic geomorphological map of the Lena-Aldan interfluve with main genetic types of deposits and corresponding terrains (based on Ivanov, 1984, Solovev, 1959; Pravkin et al., 2018; Fedorov et al., 2018). Legend: the types of terrain are indicated by color, geomorphological levels by hatching: 1) denudation plain, 2) glacial-fluvioglacial plain, 3) erosion-accumulative Abalakh plain, 4) low terraces of Lena and Aldan, 5) Kerdem terrace (III), 6) Bestyakhskaya terrace (IV), 7) Tyungyulun terrace (V), 8) Magan terrace.

continuous permafrost. Its thickness varies from 150 to 200 m in the middle Lena River valley, from 200 to 400 m under the accumulative terrace sequence on the right (east) bank of the Lena River, and up to 500 m under the left-bank (west) denudation plain (Ivanov, 1984; Nikolaev et al., 2011). The IC deposits, or ice-rich late Pleistocene sediments of disputed origin hosting thick ice wedges down to 50 m depth, and are widespread in the region (Fedorov and Konstantinov, 2009; Konischev, 2011; Schirrmeister et al., 2013). Numerous episodes of the IC thermal disturbance are reported at the Pleistocene-Holocene transition and during the Holocene optimum, leading to widespread thermokarst development (Fradkina et al., 2005; Katamura et al., 2006; Katamura et al., 2009; Pestryakova et al., 2012; Nazarova et al., 2013; Ulrich et al., 2017a; Ulrich et al., 2017b; Ulrich et al., 2019).

Data from the two major ground ice exposures are presented in this study: Mamontova Gora and Syrdakh (**Figure 1**; **Supplementary Figures S1–S5**). The well-described Mamontova Gora exposure (N63°01.169′, E133°55.787′) serves as a reference section for the Miocene-Pleistocene unconformity in East Siberian stratigraphy (Baranova and Biske, 1964). The Aldan River creates this exposure by undercutting the Central Yakutian terrace sequence at its northern margin, where six main terrace levels and a contemporary floodplain are observed (Markov, 1973). This study investigates the deposits of the 50 m terrace (V terrace), and to a lesser extent the 80-m terrace (VI terrace) and the right-bank floodplain of the Aldan River. The lowest part of the outcrop is the Miocene (N_2) sandy stratum which is exposed slightly above the shoreline, overlain by Middle Pleistocene (Q_2) sands

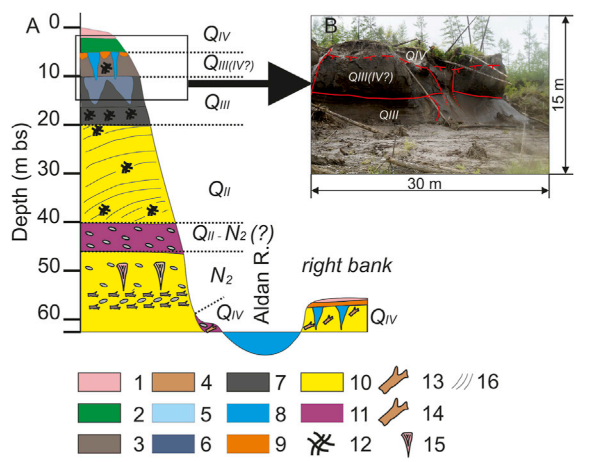

FIGURE 2 | Mamontova Gora outcrop: **(A)** Geological section across the Aldan River in the area of the V terrace of the Mamontova Gora outcrop. **(B)** thermocirque, exposing two generations of thick ice wedges (photo by D.G. Shmelev). Legend: 1) active layer, 2) icy dark gray loams—cover layer, 3) icy dark gray, black loams with organic matter and thick-schlieren cryostructure, 4) thawed clays and silts; 5) wedge ice, milky white, 6) wedge ice, muddy, 7) loam with massive cryostructure, gray and dark gray, 8) water (here its the Aldan R and it is Syrdakh lake for **Figure 3**), 9) peat, 10) sands medium to coarse-grained, 11) gravel-pebble deposits with sandy interlayers, 12) organic inclusions (plant remains), 13) wood remains, 14) pebbles and boulders, 15) pseudomorphs, 16) lithological bedding.

(**Figure 2**). These middle Pleistocene sands are overlain by the late Pleistocene loams (Q_3) hosting two generations of thick ice wedges (Kuznetsov, 1976).

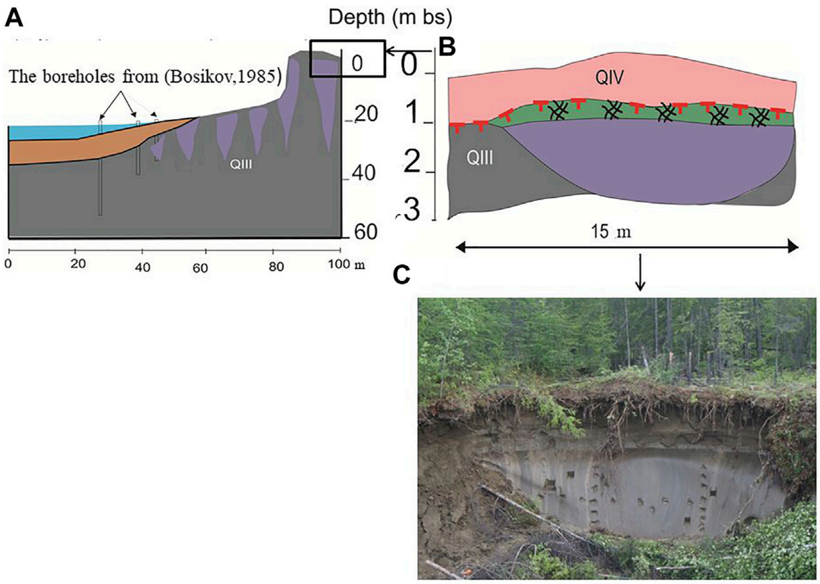

FIGURE 3 | Geological section of the Syrdakh Ice Complex: **(A)** schematic section of the coastal slope with archival boreholes (Bosikov, 1985); **(B)** geological section of the outcrop exposed in a thermo-erosional gully **(C)** the photo of the outcrop (by M. Cherbunina). Legend for the figure, see above (**Figure 2**).

Syrdakh *alas*, a local name for thermokarst depression, is located on the Lena-Aldan interfluve, about 85 km to NE from Yakutsk (**Figure 3**). This alas has an elongated form, around 2 km long and 1 km wide, and depression depth is approx. 30 m. Previous studies have observed massive ice wedges close to the shoreline of the Syrdakh Lake. Four boreholes have encountered ice wedges at depths from 2.2 to 16.6 m, and their toes occurred at deepest at several meters below the lake bottom (**Figures 3A,B**). On inter-alas surfaces, the ice-wedge depth reached 45 and 34 m near the Oner and Syrdakh Lakes, respectively (Bosikov, 1985). Our study on Syrdakh site is based on a ice wedge outcrop (N62°32.638′, E130°57.915′), exposed in a thermo-erosional gully, around 6 m deep and 10–15 m wide.

3 MATERIALS AND METHODS

3.1 Field Sampling

The field work was carried out at 2016–2017. To determine the composition and properties of ice and sediments, at least six monoliths were taken from one genetic horizon and were transported to the laboratory in frozen state (n = 70 for sediments and n = 18 for ice). Ice wedges from both IC horizons, as well as modern ice veins from the active layer of the Aldan River floodplain, and ice wedge from Syrdakh exposure, were sampled in vertical and horizontal profiles for stable water isotope analyses (**Supplementary Figure S7**). Ice samples were melted in the field, collected in 15 ml plastic vials without headspace, sealed and stored at cool place at near zero temperature (total n = 75, the results for most of them (n = 65) were previously discussed in Vasil'chuk et al. (2017) , Vasil'chuk et al. (2019) and in Budantseva and Vasil'chuk (2017). Microbiological samples were taken from the cleaned exposure wall, heated with butane blowtorch flame, carried over to sterile Whirl–Pak® Nasco bags (Nasco, Modesto), and kept frozen at −5°C (mimicking natural conditions) in 36-L Coleman® isothermal containers with saturated NaCl solution as a cooling agent until delivered to the laboratory. In the lab, samples were stored at −20°C in a freezer. Sampling point locations are shown on **Supplementary Figure S6** (n = 10 for sediments and n = 2 for ice are presented in this study and 3 samples (n = 2 for ice and 1 for the active layer soil is previously published in Rakitin et al., 2020).

3.2 Laboratory Analysis

3.2.1 Physical and Chemical Analysis

For sediments, wet bulk density, further referred to as bulk density, was determined by directly measuring the volume and weight of frozen samples. Soil dry weight was measured after oven-drying the samples at 105°C for 24 h (Yershov, 1998). Gravimetric ice content was recalculated from the frozen sample weight and dry soil weight and is given as weight percentage (wt%). For grain size analysis, the samples were treated with hydrogen peroxide to remove organic material. Subsequently, the organic-free samples were diluted and washed to neutral pH values. The grain size distribution (GSD) was analysed optically using Fritsch Laser Particle Sizer Analysette 22 and was displayed in 62 size classes between 0.15 and 1,027.24 μm. GSD parameters, including the mean grain size diameter (MGSD) were calculated using the Gradistat software (Blott and Pye, 2020). The total carbon (TC) in soils and soil particles of the ice (in wt%) was detected by an elemental analyzer (Vario EL CHNS analyser, Germany) The standard deviation for TC was ±0.1% for repeated measurements. Inorganic carbon content in Quaternary deposits of North-Eastern Russia is typically less than 10–15% of TC (Schirrmeister et al., 2011),

TABLE 1 | The list of samples for microbiological analysis of the outcrops of Mamontova Gora and Syrdakh.

Sample name	Sample point	Type of sediment	The age of sediment accumulation	Freezing period	Type of freezing
C-3	Mamontova Gora, VI terrace	Sand	Miocene	Middle Pleistocene	Epicryogenic
C-4	Mamontova Gora, V terrace, the lower horizon of IC	Loam (host)	Late Pleistocene	Late Pleistocene	Syncryogenic
C-5	Mamontova Gora, V terrace	Sand	Miocene	Middle Pleistocene	Epicryogenic
C-6	Mamontova Gora, 80-m terrace (VI)	Sand	Miocene	Middle Pleistocene	Epicryogenic
C-7	Mamontova Gora, V terrace	Sand	Middle Pleistocene	Middle Pleistocene	Syncryogenic
C-8	Mamontova Gora, V terrace	Sand	Middle Pleistocene	Middle Pleistocene	Syncryogenic
C-9	Mamontova Gora, V terrace, the upper horizon of IC	Loam (host)	? Late Pleistocene, Holocene	? Late Pleistocene, Holocene	?
C-10	Mamontova Gora, (V), the upper horizon of IC	Ice	? Late Pleistocene, Holocene	? Late Pleistocene, Holocene	?
C-11	Mamontova Gora, (V), the lower horizon of IC	Loam (host)	Late Pleistocene	Late Pleistocene	Syncryogenic
C-12	Syrdakh	Loam (cover)	Holocene	Holocene	Epicryogenic
C-12a	Syrdakh	Loam (cover)	Holocene	Holocene	Epicryogenic
led-S	Syrdakh	Ice	Late Pleistocene	Late Pleistocene	Syncryogenic

while recent studies show larger values up to 22% at Batagay IC (Shepelev at al., 2020).

Ice wedge samples were melted at room temperature and filtered through pre-weighed filters. Filters with retained sediment were dried at 105°C for 24 h and weighted, sediment dry weight was recorded. The pH values were measured electrometrically (US EPA, 2017) using an Expert 001 ion meter (Econix-Expert Ltd., Russia). Total content of dissolved inorganic anions (Cl^-, SO_4^{2-}, HCO_3^-), and cations (Ca^{2+}, Mg^+, Na^+, K^+) in ice filtrates and aqueous dry soil suspensions was measured using Russian standard methods. Hydrocarbonates content (GOST 31957-2012, 2019) was recalculated from total alkalinity, measured by titration with 20% accuracy. Major anions were measured by capillary ion electrophoresis (GOST 31867-2012, 2019; GOST 31869-2012, 2019), with accuracy ca. 15%, using 'Kapel' capillary ion electrophoresis system (Lumex, Russia). Analytical results were expressed in mg/L and recalculated to milliequivalents per liter (meq/L) as per standard practices. Then, equivalent masses were totalled separately across anions and cations and equalled 100% each, from where %-equivalent masses (%-eq.) were calculated for each anion and cation.

3.2.2 Radiocarbon Dating

Radiocarbon dating of the two samples from Mamontova Gora and Syrdakh IC was done by the Laboratory of Radiocarbon Dating and Electron Microscopy of the Institute of Geography of the Russian Academy of Sciences (IGAN) and the Center for Applied Isotope Research, University of Georgia (Athens, United States) using accelerator mass spectrometry (AMS). The calibration programme CALIB REV7.1.0 using the IntCal13 curve (Reimer et al., 2013), was used to calibrate these radiocarbon dates. The dates obtained at various facilities in the 1980's and 1990's and published without calibration were calibrated in Calib 8.2 (Stuiver et al., 2021) using the IntCal20 calibration datasets (Reimer et al., 2020).

3.2.3 Stable Water Isotopic Composition

Stable water isotope analysis was done by isotope ratio mass spectrometry with constant helium flux (CF-IRMS), with Finnigan Delta-V Plus mass spectrometer using gas-bench device, at the isotope laboratory of the Department of Geography, Moscow State University (MSU). Calibration was made using the V-SMOW and SLAP international standards, as well as the MSU internal standard, snow from the Garabashi glacier (Mount Elbrus area), with $\delta^{18}O = -15.60‰$, $\delta^2H = -110.0‰$. The measurement errors were ±0.6 and ±0.1‰ for δ^2H and $\delta^{18}O$, respectively.

3.2.4 Profiling of Prokaryotic Communities Based on 16S rRNA Gene

gDNA (genomic DNA) isolation of samples C-3–C-12 (**Table 1**; **Supplementary Figure S6**) and primary amplification of the studied samples, depending on the type and age of the samples, was carried out in the "clean" rooms of the Institute of Geophysics of the Environment (IGOS) of the University of Grenoble-Alpes in Grenoble, France (IGE, CNRS-UGA, Grenoble) (Bulat et al., 2004). Cell disruption and gDNA isolation were performed mechanically using the FastPrep instrument (MPBiomedicals, United States) and the PowerSoilDNAisolationKIT (MoBioLabs, United States) with E matrix (beads) (MPBiomedicals, United States), as well as using the FastDNASpinKitforSoil kit according to the manufacturer's method (MPBiomedicals, United States). The concentration was measured using a Qubit 2.0 fluorometer with a dsDNAHSreagentKIT (Invitrogen™, United States).

DNA for other samples (led-S, C-12a showed at **Table 1**; **Supplementary Figure S6**) was isolated using the FastDNA SpinKit and FastPrep-24 bead beating grinder (MP Bio, United States) and according to the manufacturer's instructions. The libraries of the V4 region of the 16S rRNA gene for Illumina MiSeq high-throughput sequencing were prepared using PCR with following primer system: forward (5′-CAAGCAGAAGACGGCATACGAGATGTGACTGGA GTTCAGACGTGTGCTCTTCCGATCT XXXXXX ZZZZ GTGBCAGCMGCCGCGGTAA-3′), containing, respectively, the 5′ Illumina Linker Sequence, Index1, Heterogeneity Spacer (Fadrosh et al., 2014), and 515F primer sequence (Hugerth et al., 2014); and the reverse primer (5′-AATGATACGGCGACCACCGAGATCTAC ACTCTTTCCCTACACGACGCTCTTCCGATCT XXXXXX

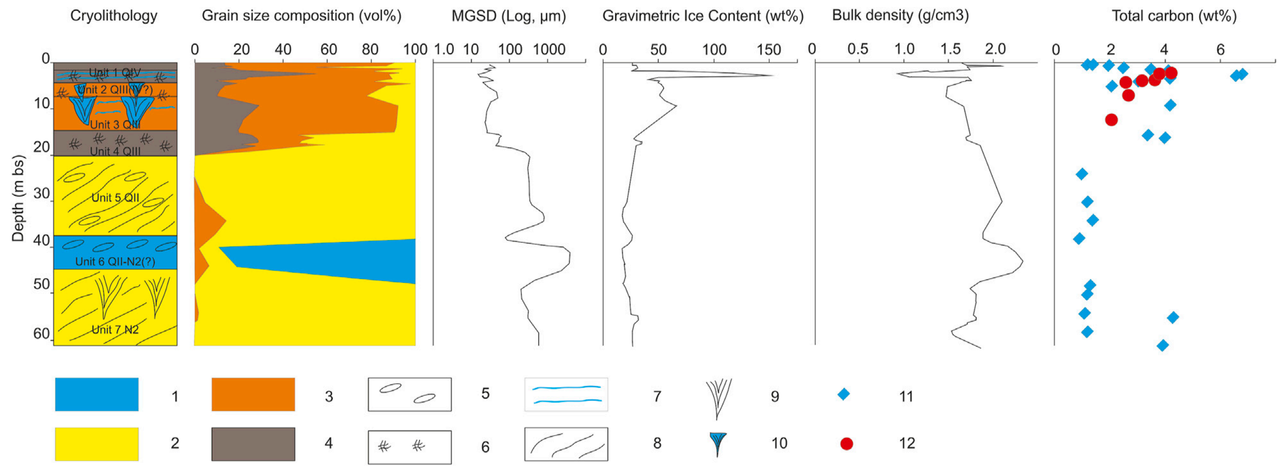

FIGURE 4 | Characteristics of the Mamontova Gora outcrop (Vterrace). Legend: 1)pebbles, 2)sand, 3)silt, 4)loam, 5)boulders and gravels, 6)peat and organic inclusions, 7)ice layers, 8)lithological layering, 9)pseudomorphs, 10)ice wedges, 11)total carbon content is the sediments, 12)total carbon content in soil particles of the ice wedges (relative to the dried soil particles).

ZZZZ GACTACNVGGGTMTCTAATCC-3′), containing the 3′ Illumina Linker Sequence, Index 2, Heterogeneity Space, and the Pro-mod-805R primer sequence, respectively. This primer set covers 86% of 16S rRNA gene sequence diversity of the Archaea and 84.3% of the Bacteria (Merkel et al., 2019). For each DNA sample, two libraries were prepared, which were sequenced in parallel using the MiSeq Reagent Micro Kit v2 (300-cycles) MS-103-1002 (Illumina, San Diego, CA, United States) on a MiSeq sequencer (Illumina, San Diego, CA, United States) according to the manufacturer's instructions. The primary processing of raw reads was carried out as described earlier (Kallistova et al., 2020).

3.3 Data Treatment

All 16S rRNA gene sequence reads were processed by the SILVAngs 1.4 pipeline (Quast et al., 2013) using the default settings: 98% similarity threshold was used for creating operational taxonomic units (OTUs) tables, and 93% was the minimal similarity to the closest relative that was used for classification (other reads were assigned as "No Relative"). Abundance data were further treated in RStudio software (RStudio Team, 2021), an open-source GUI to R programming language (RCore Team, 2021). Statistical and graphical analyses relied on packages "tidyverse" (Wickham et al., 2019), "ggplot2" (Wickham, 2016). Dissimilarity and similarity-based distance metrics, function *vegdist()*, package "vegan" (Oksanen et al., 2020). Heatmaps were prepared using function *pheatmap()*, package "pheatmap" (Kolde, 2018). UniFrac and Principle Coordinate Analysis (PCoA) were also carried out in QIIME2 via q2-diversity function (Lozupone and Knight, 2005; Lozupone et al., 2007; Lozupone et al., 2011). The significance of weighted and unweighted unifrac matrices was calculated with Permanova test (Anderson, 2001).

4 RESULTS

4.1 Stratigraphy

4.1.1 Mamontova Gora

At the Mamontova Gora site, an outcrop of the V terrace of Aldan River was studied in one location where numerous thermal denudation features, thaw slump scars, up to 20 m deep and about 200 m in diameter, exposed a two-horizons ice wedge structure (**Figure 2**). The complete outcrop profile including the underlying sediments is shown in **Figure 4**. In this profile, the following strata were described, top to bottom [as meters below surface (m bs)]:

Unit 1 (0–1.5 m bs): Silty brown loams, thawed from the surface down to 0.9 m (active layer depth at the time of description). The ice content in the frozen part of the active layer ranges between 27 and 31 wt%, decreasing towards the surface. The stratum is heterogenous, and there is clear separation in color and TC content between the active layer, and transient layer (Shur et al., 2005). The TC content is between 2.5 and 3.5 wt % in the transient layer and varies from 1.4 to 2.0 wt% in the active layer.

Unit 2 (1.5–3.7 m bs): "Ice Complex I" (ice wedges and host deposits, upper horizon). The host deposits are dark grey, heavy, silty loams with thick-schlieren cryostructure and with peat interbeds locally. The ice content in loams is from 45 to 50 wt %, TC from 4.1 to 4.2 wt%; peat layers have higher ice content, from 129 to 160 wt% and higher TC, from 6.6 to 6.8 wt%. Particulate TC content in soil particles of the ice wedge ranges from 3.7 to 4.2 wt%, relative to the dried soil particles. This unit gave a median ^{14}C date of 43.3 cal ka BP (this study, **Supplementary Table S1**). The 0.5–2 m wide and up to 3 m long wedges penetrate into the lower horizon.

Unit 3 (3.7–15.7 m bs): "Ice Complex II" (ice wedges and host deposits, lower horizon). Host deposits are dark grey, ice-rich, silty loams and grey sandy loams. Ice wedges are up 5 m thick, the

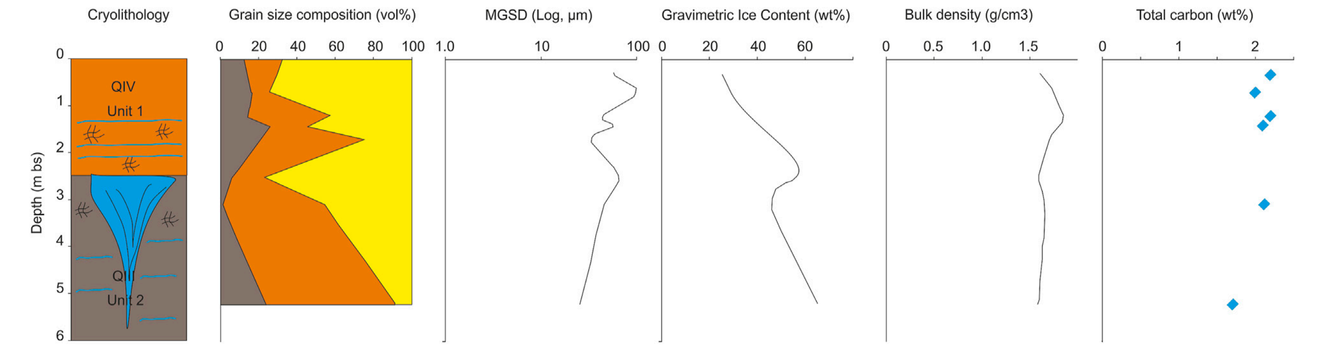

FIGURE 5 | Characteristics of the Syrdakh outcrop. Legend for the figure see above (**Figure 4**).

size of the polygonal grid is about 10–15 m. Syngenetic origin is indicated by layered cryostructures in the host sediments that turn upward adjacent to the wedge owing to the ice growth which was also noted earlier by Popp et al. (2006). Ice content varies from 49 to 66 wt%, TC from 2.1 to 4.2 wt%. The soil particles fraction content changes from 1.9 to 2.4 vol%, particulate TC content in soil particles of the ice wedge ranges from 2.1 to 3.2 wt % and decreases down the profile.

Unit 4 (15.7–19.0 m bs): Blueish-grey heavy ferruginous loams with high peat content, covered with a film of 1–2 mm similar to biogenic mats when interacting with air. Ice content is from 28 to 35 wt%, TC from 3.4 to 4.0 wt%. The lattice-like cryostructures are observed here with cell size of 3–4 by 7–10 cm.

Unit 5 (19.0–38.4 m bs): Light grey sands, mainly coarse-grained, with horizontal layers and cross-bedding structures, ferruginous nodules, and interbedded with dark grey sandy loams. Ice content is low, varying from 18 to 24 wt%. Cryostructure is massive for the sands, and horizontally layered for the loams, with a width of 1–3 mm and a distance between them of 5–8 mm.

Unit 6 (38.4–46.2 m bs): Well-rounded gravel-pebble deposits with sandy interbeds. Ice content is from 18 to 20 wt%, TC from 0.9 to 1.4 wt%.

Unit 7 (below 46.2 m bs): Yellowish-grey mixed sand, from fine to coarse, with massive cryostructure containing wood residues, pebbles, and ferruginous interlayers. Ice content varies from 19 to 32 wt%, TC ranges from 0.7 to 4.3%. Ice wedge casts were described previously in this stratum (Markov, 1973).

The highest VI Aldan River terrace was not studied in detail during our field expedition. Only basal sandy deposits were sampled for microbiological analyses, as their appearance is close to the lowest layer (Unit 7 above) of the V terrace. Its ice content varies from 19 to 31 wt%, TC from 0.9 to 3.5 wt%. Therefore, samples were taken here to allow inter-comparison of microbial composition between two terrace levels and similar deposits.

4.1.2 Syrdakh

At the Syrdakh site, two main strata were exposed in the visible section of the profile (**Figure 5**):

Unit 1 (0–2.7 m bs): Interbedded loams and sandy loams. The active layer at the time of observations was 1.2 m deep with inclusions of poorly decomposed organic matter in the form of a bluish felt. The ice content in the frozen part of the active layer varies from 25 to 29 wt%, TC is 2.0 wt%. The transient layer has abundant peat inclusions, and TC content around 2.1 to 2.2 wt%. Cryostructure is massive, with thick ice layers toward the layer base. This layer gave a median ^{14}C date of 10.6 cal ka BP (this study, **Supplementary Table S1**).

Unit 2 (2.7–5.1 m bs): "Ice Complex" (ice wedges and host sediments). Ice wedges have apparent vertical layering. Host sediments are loams with schlieren and the lattice-like

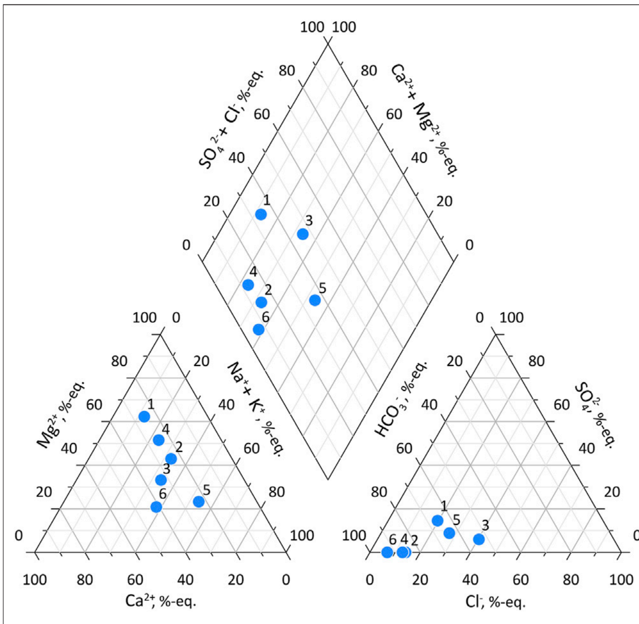

FIGURE 6 | Piper diagram of the chemical composition of ice wedges of the Mamontova Gora outcrop according to the authors (this article) and Kuznetsov (1976), %-equiv. 1) ice wedge of the upper tier (our results), 2) ice wedge of the upper tier (Kuznetsov, 1976), 3) ice wedge of the lower tier (our results), 4) ice wedge of the lower tier (Kuznetsov, 1976), 5) modern ice of the floodplain (our results), 6) Holocene ice of a 6–9 m terrace (Kuznetsov, 1976).

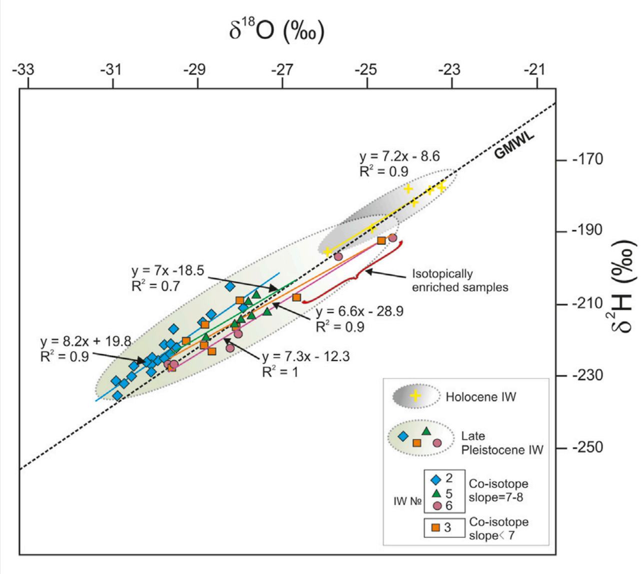

FIGURE 7 | Ratio of $\delta^{18}O$ and $\delta^{2}H$ values in late Pleistocene and Holocene ice wedges of an outcrop of a V terrace on the right bank of the Aldan River (Mamontova Gora outcrop). Sampling profiles 2 and 3 refer to the lower tier of the ice complex, 6 and 5 to the upper tier. GMWL, global meteoric water line.

cryostructures. Ice content ranges between 46 and 65 wt%, the TC content ranges from 1.2 to 2.1 wt%.

4.2 Water and Sediment Chemistry

At Mamontova Gora, samples were taken from two Ice Complex (IC) horizons, and from ice veins in the contemporary Aldan River floodplain ca. 4–5 m above the low-flow water stage. At the Syrdakh site, a single sample was collected from the exposed ice wedge. The two IC horizons differ in their chemical composition (**Figure 6**), as previously discussed by Kuznetsov (1976). The total dissolved solids (TDS) content varies from 393 to 687 mg L^{-1} and is slightly higher in the upper IC layer. Hydrochemical type of the "Ice Complex I" wedge ice is HCO_3-Mg (n = 1), "Ice Complex II" ice, HCO_3-Ca (n = 2) or HCO_3-Na-K (n = 3). Contemporary ice vein of the Aldan River floodplain is HCO_3-Na-K (n = 1). We have also observed high Cl^{-} content in the 'Ice Complex II' ice, up to 40%-eq.

Chemistry of aqueous soil extracts prepared from sediments is uniform across the studied profiles. TDS content ranges from 90 to 390 mg per 100 g dried soil in the "Ice Complex I" host deposits, from 60 to 350 mg in the "Ice Complex II" deposits, and from 100 to 180 mg in the I (9 m) Aldan River terrace sediments (Kuznetsov, 1976). The water type is HCO_3-Ca, rarely HCO_3-Mg "Ice Complex I" or HCO_3-Na-K ("Ice Complex II").

Water type of the aqueous soil extract in samples collected from Syrdakh exposure is HCO_3-Na-K in the upper horizons, and HCO_3-Ca in the lower horizons, surrounding the ice wedges, and with lower TDS compared to the Mamontova Gora samples, from 51 to 121 mg per 100 g dried soil.

Increased sodium content is typical for ice-containing sediments of the region (Anisimova and Pavlova, 2014). Water and sediment chemistry of the Mamontova Gora exposure was studied previously (Kuznetsov, 1976; Vasil'chuk et al., 2004; Vasil'chuk et al., 2017) as one of the proxies of ice origin and tracers of landscape evolution. According to Kuznetsov (1976), ice wedges of the V Aldan River terrace, classified as late Pleistocene, have higher TDS content, from 230 to 640 mg L^{-1}, than lower-lying wedges of the I terrace, or Holocene wedges, from 71 to 219 mg L^{-1}. Dominant water type in late Pleistocene ice wedges was HCO_3-Mg, in Holocene ice wedges, HCO_3-Ca. Total dissolved solids content in samples collected from an "Ice Complex II" late Pleistocene ice wedge (Vasil'chuk et al., 2017), varied from 80 to 476 mg L^{-1}. Hydrochemical type was HCO_3-Ca, switching to HCO_3-Mg between 7.0 and 7.8 m from the surface. The pH value varied over a wide range, from 4.4 to 7.6.

4.3 Water Stable Isotope Composition

Both upper and lower ice wedge generations of the V Aldan River terrace, a contemporary ice wedge of the Aldan River floodplain, as well as ice wedge of the Syrdakh outcrop were sampled. The results are partially presented and discussed in (Vasil'chuk, 1988; Vasil'chuk, 1992; Budantseva and Vasil'chuk, 2017; Vasil'chuk et al., 2017; Vasil'chuk et al., 2019), therefore here only a brief overview is given adding data on upper ice wedge horizon.

The upper "Ice Complex I" ice wedges have $\delta^{18}O$ values from −29.6 to −24.4‰ and −28.8 to −27.4‰ for two profiles $\delta^{2}H$ values from −227 to −192‰, −219 to −207‰ with a slight difference in variance between the profiles (**Figure 7**; **Supplementary Figure S7B**). The atmospheric origin of ice with insignificant participation of non-atmospheric waters was previously suggested based on the one of the profiles (Vasil'chuk et al., 2019). Nonetheless, in several samples highly enriched in heavy isotopes, deuterium excess, or d-excess, descends below 3.0, which may indicate participation of surface water from active layer or mixed snowmelt and shallow marshes waters that underwent sufficiently strong evaporative loss.

The lower "Ice Complex II" ice wedges show highly variable stable isotope composition (**Figure 7**; **Supplementary Figure S7B**). The $\delta^{18}O$ values from −29.58 to −24.69‰ were observed in one location, while from −30.89 to −27.89‰ in the other location about 3 m apart, close to $\delta^{18}O$ from −31.5 to −28.5‰, previously reported in (Popp et al., 2006). Isotopically heavier values were

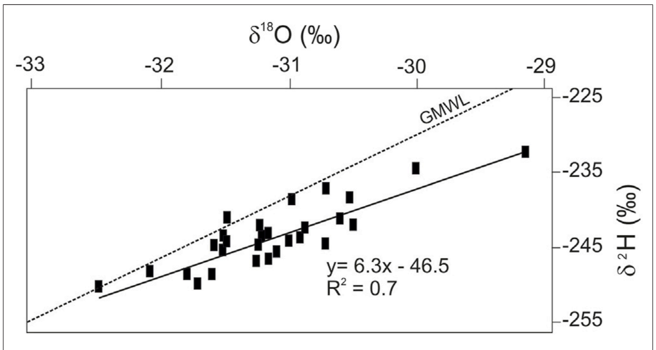

FIGURE 8 | Ratio of $\delta^{18}O$ and $\delta^{2}H$ values in the late Pleistocene ice wedges of the Syrdakh outcrop. GMWL, global meteoric water line.

TABLE 2 | Characteristics of the amplicon libraries of the Mamontova Gora and Syrdakh.

Sample name	Number of sequences	# OTUs	Number of taxonomic paths	Chao1	Good's coverage	Shannon index	Simpson index
C-3	5,312	850	135	179	0.70	3.13	0.10
C-4	9,244	5,168	616	636	0.65	4.81	0.04
C-5	5,214	1,163	180	221	0.61	3.03	0.10
C-6	14,353	2,154	194	180	0.71	3.27	0.09
C-7	4,239	445	67	81	0.80	2.29	0.20
C-8	6,031	523	83	118	0.64	1.99	0.26
C-9	6,046	3,581	423	524	0.59	3.97	0.08
C-10	5,818	4,660	571	730	0.63	5.17	0.01
C-11	8,043	4,749	547	591	0.65	4.56	0.05
C-12	4,683	2,363	225	342	0.58	3.59	0.07
C-12a	12,219	1,737	298	301	0.70	3.82	0.06
led-S	7,946	1,725	460	560	0.60	4.37	0.04

obtained for the upper parts of the ice wedge, conflicting with previously published results, where $\delta^{18}O$ values from −29 to −25.9‰ were obtained in the upper part of the wedge, and from −22.7 to −16.5‰ in the high-TDS bottom toes of an ice wedge (Vasil'chuk and Vasil'chuk, 1998).

Holocene and contemporary ice wedges from the Aldan River floodplain are generally isotopically heavier, with $\delta^{18}O$ values from −25.9 to −23.2‰, and $\delta^{2}H$ values from −196 to −178‰ (**Figure 7**; **Supplementary Figure S7C**).

At Syrdakh, along the vertical profile, $\delta^{18}O$ and $\delta^{2}H$ values varied narrowly in a range from −31.8 to −30‰ and from −251 to −231‰, respectively (**Figure 8**; **Supplementary Figure S7D**). Horizontal $\delta^{18}O$ variations were in the range from −32.5 to −29.2% at a 0.5 m depth, and from −31.5 to −30.5 at a 1.2 m depth. Isotopic composition of Syrdakh ice suggest its atmospheric origin and is in the typical regional range for snow. At the same time, *d*-excess values vary from 3 to 12‰ and fall below 5‰ on multiple occasions, which reflects the relatively frequent participation of non-meteoric water in ice formation, for example, evaporated water from interpolygonal ponds.

4.4 Prokaryotic Communities

A sample list with additional information is given in **Table 1**. Characteristics of amplicon libraries and alpha diversity of prokaryotic communities are summarized in **Table 2**.

Microbial communities of the studied samples are mainly represented by bacteria. Archaea are minor and constitute no more than 0.6% in all samples. The bacterial communities differ both in the composition of dominant groups and in their ratio. Each of the nine phyla of bacteria exceeded 3% abundance in one or several studied geological units: *Acidobacteria*, *Actinobacteria*, *Bacteroidetes*, *Chloroflexi*, *Firmicutes*, *Gemmatimonadetes*, *Proteobacteria*, *Parcubacteria*, *Verrucomicrobia* (**Figure 9**).

A number of reads per sample varied from ~4,200 and ~14,300 after using all quality filters. The coverage for the studied microbial communities ranged from 0.58 to 0.80, estimated by Good's coverage index, meaning that between 20 and 42% of reads were from OTUs that appear only once in the samples. Such coverage is insufficient for a complete description of the phylogenetic diversity of studied microbial communities. However, all major existing groups have been identified. The diversity of prokaryotes was estimated with the Shannon index, which varied within a wide range from very moderate to relatively high values, from 2 to over 5.2. Sampling points are shown in **Supplementary Figure S6**.

4.4.1 Mamontova Gora

Miocene Alluvial Sands (Samples C-3, C-5 From the "Unit 7" of V Terrace, C-6 From the VI Terrace)

The dominant phylum in all three samples was *Proteobacteria* (58–61%), represented mainly by the class *Gammaroteoabcteria* (44–58%), the other predominant phyla were *Bacteroidota* (3–24%) and *Actinobacteriota* (7–24%). *Firmicutes* constitute a significant part only in C-6 community (9%) whereas C-5 was characterized by a high presence of the *Patescibacteria* phylum (14%). At the genus level, the main feature of these three samples is high abundance of *Gallionella* (6–19%) and *Sideroxydans* (3–6%), which are almost completely absent in other samples. A distinctive feature of samples C-3 and C-5 is the presence of *Salinibacterium* (5–6%).

Middle Pleistocene Alluvial Sands, Overlying Miocene Sands (Samples C-7, C-8 From Unit 5)

There are three dominant phyla in these samples: *Firmicutes* (31–43%), *Bacteroidota* (34–35%) and *Proteobacteria* (17–31%), in both cases almost equally represented by *Gammaproteobacteria* and *Alphaproteobacteria*. Phylum *Firmicutes* is almost entirely represented by *Desulfosporosinus* genus and this is the characteristic feature of these samples. Phylum *Bacteroidota* is exclusively represented by uncultivated microorganisms of env.OPS 17 group which is typical for other samples where this phylum is highly present. Another distinctive feature of these samples is the relatively high abundance of *Diaphorobacter* (7–10%).

"Ice Complex II" Late Pleistocene Deposits (Samples C-4, C-11) From Unit 3

The late Pleistocene samples are characterized by a high degree of community complexity, with Shannon Index from 4.6 to 4.8,

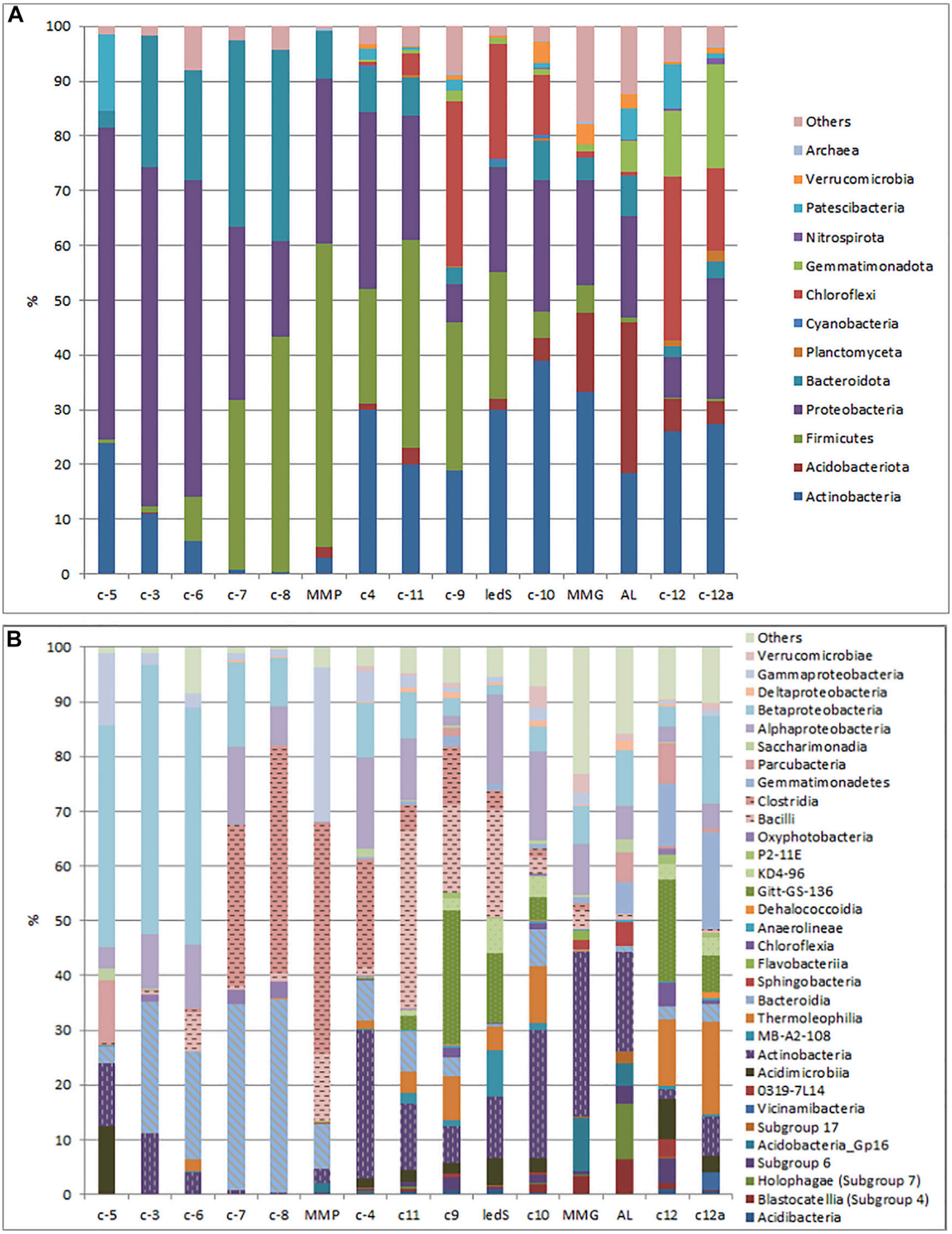

FIGURE 9 | Relative abundance of prokaryotic phyla **(A)** and classes **(B)** in different horizons of Mammoth Mountain and Syrdakh (the samples AL, MMG and MMP correspond to previously studied samples of the ice complex of Mamontova Gora:an active layer (AL), an ice wedge of the upper (MMG) and lower horizons (MMP) (Rakitin et al., 2020).

mainly represented by *Actinobacteriota* (20–30%), *Proteobacteria* (22–32%), *Firmicutes* (21–38%), and *Bacteroidota* (7–8%). At the genus level, these two samples are very different from each other. For example, the most common genus in sample C-4 is *Clostridium* (16%), whereas in sample C11, *Bacillus* (21%).

"Ice Complex I" Deposits of Uncertain Age (Late Pleistocene or Holocene) (Samples C-9, C-10 From Unit 2)

The sample C-10 was taken from the same ice wedge of the upper IC horizon as the sample "MMG" described in Rakitin et al. (2020), but closer to the base of the ice wedge. The community of this sample is the most complex among studied, Shannon Index value is 5.2. The phyla *Actinobacteriota* (39%), *Proteobacteria* (23%), *Chloroflexi* (11%), *Bacteroidota* (7%), and *Firmicutes* (5%) form the backbone of the community. Unlike sample C-9, there are no clearly dominant genera of microorganisms here. Each genus makes up no more than 4% of all microorganisms. The sample C-9, obtained from hosti loams, has the same dominant phyla but in different proportions: *Actinobacteria* (7%), *Proteobacteria* (6%), *Chloroflexi* (30%), *Bacteroidota* (7%), and *Firmicutes* (27%). At the genus level, there are two clearly dominant groups: uncultured *Chloroflexi* of the Gitt-GS-136 cluster (24%) and *Bacillus* genus (12%).

4.4.2 Syrdakh

Ice Complex Late Pleistocene Ice Wedge (Sample Led-S From Unit 2)

The Ice Complex sample from Syrdakh exposure was dominated by the phyla *Actinobacteriota* (30%), *Firmicutes* (23%), *Chloroflexi* (21%), and *Proteobacteria* (19%). In contrast to other studied samples, phylum *Bacteroidota* is almost absent from this sample. Another distinctive feature of this community is the abundance of phylogenetically deep cluster of uncultured *Actinobacteriota* named MB-A2-108 (8%). Besides, at the genus level there are several widely represented groups: *Bacillus* (9%), uncultured *Chloroflexi* of the Gitt-GS-136 cluster (13%), uncultured *Chloroflexi* of the KD4-96 cluster (6%).

Overlying Loams (Samples C-12, C-12a From Unit 1)

The phyla *Chloroflexi* (15–30%), *Actinobacteriota* (26–28%), *Proteobacteria* (7–22%), *Acidobacteriota* (4–6%), and *Bacteroidetes* (2–3%) are dominant in these samples. Also, phylum *Gemmatimonadota* (12–19%) is abundant in these samples, unlike other studied communities. This phylum is almost entirely represented by uncultivated microorganisms. Among *Actinobacteria*, a significant part of the community in both samples is represented by uncultivated groups of *Actinobacteria*, *Thermoleophilia* and *Acidimicrobiia* classes. At the genus level, uncultured *Chloroflexi* of the Gitt-GS-136 cluster (7–19%) are also highly abundant.

5 DISCUSSION

5.1 Age and Origin of the Mamontova Gora and Syrdakh Deposits

5.1.1 Geological Evidence

Starting from Miocene, the Mamontova Gora region experienced tectonic subsidence compensated by sedimentation, and a monotonous sandy stratum accumulated since that time (Ivanova et al., 2015). The sands of the VI Aldan River terrace do not contain cryogenic formations. Their age is considered pre-Quaternary (Baranova and Biske, 1964), while others subdivide this stratum into three sub-horizons: Miocene, transitional and lower Pliocene (Ravsky, 1960). These same sands are exposed at the base of the V Aldan River terrace. Miocene flora from the Mamontova Gora basal sands dates to Middle Miocene (Nikitin, 2007). During that time, according to paleobotanical data, the climate was warm, with mean annual temperature about +12°C, mild winters with frosts not lower than −20°C, and precipitation from 1,000 to 1,500 mm (Biske and Baranova, 1976).

In the late Pliocene, the climate was still humid, but winters were getting colder, it is assumed that mean annual temperatures were below 3°C. Permafrost was most likely absent in the region during this time (Fradkina et al., 2005; see **Supplementary Figures S8, S9**). Stable depositional environment shifted to tectonic stability or, possibly, uplift and erosion. Monotonous cross-bedded sands are overlain by a pebble horizon, with erosional base contact and multiple unconformities. The similar pebble horizon is dated back to Middle Neopleistocene in the close Chuyskaya Gora exposure on the right bank of the Aldan River ca. 400 km downstream from Mamontova Gora (Ivanova et al., 2015). In the Batagay megaslump exposure at least one episode of permafrost thaw and erosion occurred sometime between MIS 16 and 6 (Murton et al., 2021b).

Markov (1973) attributes the accumulation of sediments of the upper part of the VI terrace level to late Pliocene, while the alluvium of the V terrace accumulated during the Middle Pleistocene. These alluvial layers contain traces of syngenetic frost cracking (Katasonov and Ivanov, 1973; Ershov, 1989), as well as wedge ice in the upper part of these sands, directly below the overlying thermokarst basin deposits (Markov, 1973). A single available U/Th date, 300 ± 5.7 ka BP, was obtained from loamy interbeds in this pebble layer (Katasonov and Ivanov, 1973). The middle Pleistocene environment during MIS 6, 170–130 ka BP, was characterized by a cold and severe climate in southern and northern Siberia (Chlachula, 2003; Andreev et al., 2004). The lacustrine loamy deposits which overlay the alluvial sands yield the U/Th date of 176 ± 2 ka BP (Katasonov and Ivanov, 1973). Ice Complex deposits of Central Yakutia accumulated during the MIS 4-2, a prolonged cryochron comprising the Zyryan stadial (MIS 4), the Kargin interstadial (MIS 3) and the Sartan stadial (MIS 2). Despite numerous detailed studies and the abundance of published radiocarbon dates (Tananaev, 2021), the age and origin of the Mamontova Gora Ice Complex deposits are still debated. Radiocarbon dates from host deposits enclosing the ice range from 36.7 cal ka BP (IM-155) to 47.4 cal ka BP (SI-1972) at depths from 3 to 8.8 m (Péwé et al., 1977; Kostyukevich et al., 1984). A series of AMS ^{14}C dates from organic matter dispersed in wedge ice of "Ice Complex II," from 14.9 to 21.9 cal ka BP, suggest their epigenetic origin (Vasil'chuk et al., 2004). Palaeoclimatic data obtained from the Central Yakutian Ice Complex evidence severe winters, and overall cold and dry environment for time intervals around 41, 21, and 13 cal ka BP (Popp et al., 2006).

The upper IC horizon, "Ice Complex I," remains poorly studied, because it was only rarely found exposed in the thermal denudation scars of the Mamontova Gora. The age and genesis of these deposits remain unclear. On one hand, according to visual descriptions, host deposits of the upper IC horizon are, from their appearance lenses of lacustrine loams of the lower IC horizon subject to thawing during the Holocene and subsequently frozen with the development of ice wedges of epigenetic origin. The AMS ^{14}C date 43.3 cal ka BP from the host loams, and similar stable water isotopic composition to the lower IC horizons, oppose this interpretation.

The age of Ice Complex at the Syrdakh site can be estimated from 16.6 cal ka BP (IM-433) to 23.6 cal ka BP (IM-433), from Ener and Syrdakh lakes, respectively (Tananaev, 2021). Dispersed organic material from Syrdakh ice yields AMS ^{14}C date of 21.7 cal ka BP (KIA 26367) at 2 m depth, contemporaneous to the enclosing loams and supporting its syngenetic origin (Popp et al., 2006). Age distribution in an ice wedge in a nearby Ulakhan Syrdakh lake, 13.1 cal ka BP (KIA 26364) in the ice wedge margin and 3.8 cal ka BP (KIA 26365) in the ice wedge center, suggests that even if initial freezing and massive ice formation proceeded syngenetically, at least two later episodes of ice wedge development occurred in the region. These cold spells correspond respectively to Younger Dryas and Subboreal stage of the Holocene, signals of which are widely present in published regional paleoclimate proxies (Fradkina et al., 2005; Katamura et al., 2006; Nazarova et al., 2013).

The late Pleistocene-Holocene transition, between 11 and 9 ka BP, led to the widespread development of thermokarst lakes in Central Yakutia (Ulrich et al., 2019). The obtained (in this study) date of 10.6 cal ka BP years for the deposits overlying the ice complex is logical and associated with the accumulation of precipitation in the conditions of climatic warming of the Holocene. The Holocene climatic optimum in Central Yakutia falls on the period between 6.7 and 5.0 ka BP years, as evidenced by the data of the paleoarchives on diatom records (Pestryakova et al., 2012; Ulrich et al., 2017a).

5.1.2 Soil and Water Chemistry Evidence

Soil Carbon

The content of TC is quite high, with a maximum in the loams of the upper horizon, reaching 6.6–6.8 wt% in peat interlayers (for unpeat interlayers, the value is about 4.0 wt%). In the lower horizon, these values are slightly lower, 3.4–4.0 wt%. High values of the content of organic matter are typical for the Yedoma sediments, the values in the active layer correspond to those previously described for Central Yakutia (Shepelev et al., 2016), but significantly higher than the data obtained for the Yukechi ice complex, which is very poor in terms of the content of organic matter (less than 1 wt%), dated 18–49 thousand years ago (Windirsch et al., 2020). Higher carbon contents in the upper horizon can be associated with more convenient conditions for the accumulation of organic matter, for example, due to the thawing of the lower IC horizon with the formation of lakes, the re-deposition of matter from other places, or with its better preservation. In Strauss et al. (2015), a higher total organic content was also observed in thermokarst deposits formed during the thawing of ice complexes. The available dating of 43.6 cal ka BP years, from the host deposits of the upper horizon, similar to the lower IC horizon (see above) may indicate the absence of new accumulation of organic matter at the time of the formation of the upper IC horizon (otherwise there would be younger dating). In this case, higher TC values are most likely associated with its better preservation. The more intensive decomposition or leaching of soil carbon could significantly reduce its content in the underlying layers. In the ice complex of the Syrdakh outcrop we observe lower values of carbon content, 2.1–2.2 wt%. The TC content is low in syngenetic ice complex deposits of Syrdakh, which were not subjected to melting and re-freezing.

Stable Water Isotope Evidence and Hydrochemical Evidence

Stable water isotopic composition of ice wedges is used to provide proxy-data for paleoclimatic and paleoenvironmental reconstructions (Rozanski et al., 1997; Sturm et al., 2010). In North-East Siberia, contemporary ice wedges are reported to have consistently heavier composition, getting significantly lighter toward late Pleistocene (Vasil'chuk, 1991; Vasil'chuk, 1992; Meyer et al., 2002; Wetterich et al., 2008; Meyer et al., 2010; Opel et al., 2011; Boereboom et al., 2013). Under warmer Holocene conditions and in different depositional environments, i.e., under riverine influence on flood plains, other mechanisms could have been involved, as suggested by the data from Mamontova Gora floodplain wedges (Opel et al., 2018).

Our stable water isotope data on Mamontova Gora wedge ice shows a pronounced difference between Holocene floodplain wedges and both Ice Complex horizons. Isotopic composition becomes increasingly lighter with depth and, therefore, age of the horizon. Water sources in ground ice can be deduced from both isotopic composition and basic water chemistry.

The slope of the regression line, in coordinates δ^2H-$\delta^{18}O$, reflects not only the nature of water (atmospheric nature according to the GMWL correspondence, isotopically transformed water according to the displacement of values relative to the GLMW—this is mainly due to evaporation processes that reduce the slope of the line), but also ice formation processes in a closed or an open system. So, we get the highest ratio coefficient (8.2) for the lower generation wedge of Mamontova Gora which we interpret forming from winter snow, and a low slope coefficient (6.6) for the other profile from this wedge, which we can interpret as water source form surface or evaporated waters (seasonal thawed layer, or swamps with polygonal ponds). In principle, such low coefficients are also characteristic of ice formation in a closed system. The upper horizon of wedges is characterized by co-isotope slopes 7–8, which corresponds to the atmospheric origin of ice and insignificant participation of waters of non-atmospheric origin. The lowest values of the slope of the regression line, equal to 6.3 are obtained for Syrdakh ice, which probably reflect the relatively constant participation in the ice wedge formation of non-meteoric water. Ice segregation in a closed system, i.e., freezing lake basin (Fotiev, 2015), can also be involved in ice accumulation. High abundance of alkalis, Na^+ and K^+, shows important cryogenic metamorphization effect. Increased Cl^- content positively related with total dissolved solids suggests closed system conditions in the subsurface compartment. Otherwise, in open system chlorides are expected to leach from soils during the repetitive freeze/thaw cycles (Ivanov and Vlasov, 1974).

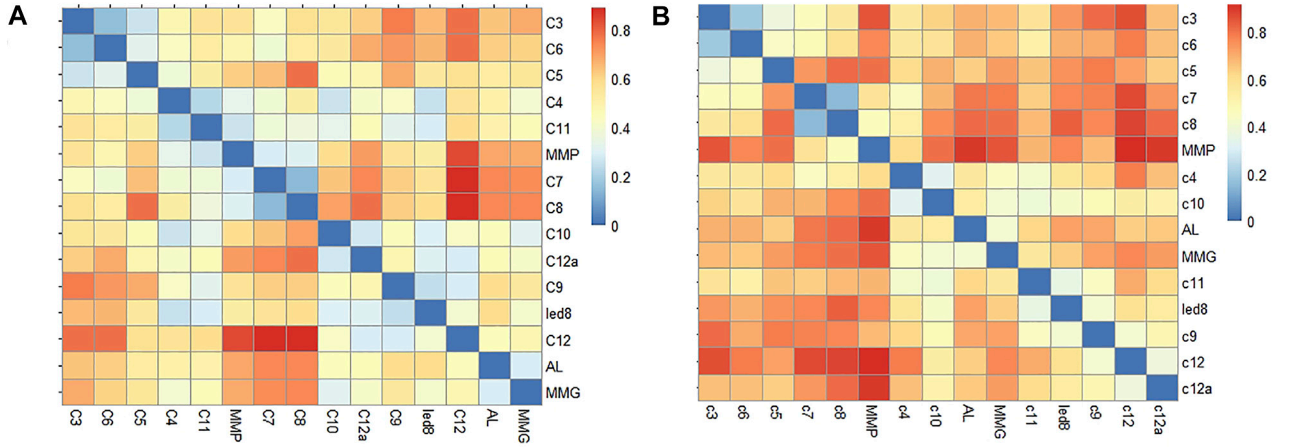

FIGURE 10 | Bray-Curtis dissimilarity heatmap for phyla **(A)** and classes **(B)**. The samples AL, MMG and MMP correspond to previously studied samples of the ice complex of Mamontova Gora: an active layer (AL), an ice wedge of the upper (MMG) and lower horizons (MMP). For numerical values see **Supplementary Tables S2, S3**

In general, high TDS content suggests dominant water origin of wedge ice from the subsurface compartment, while variations in major ion composition and ratios might relate to alternating ice segregation mechanisms or variable degree of cryogenic metamorphization. The latter leads to an increase in Na^+ content, and alters the ratios between major ions, especially cations, and between alkaline Earth metals, Ca^{2+} and Mg^{2+} being the most affected (Ivanov and Vlasov, 1974). Point grouping in both the Na^+ and Cl^--normalized molar ratios of Ca^{2+} and Mg^{2+} plots (**Figure 6**) suggest higher degree of cryogenic metamorphization in contemporary ice and several samples of the "Ice Complex II" wedge ice. High pH variability, along with extremely high Fe and DOC concentrations, above 40 and 53 mg L^{-1}, respectively, suggest an important impact of soil solutions in ground ice chemistry through the fixation of colloidal complexes produced through Al-Fe-humus release process (Pereverzev, 2009). High sodium carbonate content in the underlying lacustrine deposits, uncommon in loess layers, is seen by Kuznetsov (1976) as evidence for the subaerial loess origin, while for us it may also explain high Na content in the upper horizons of the "lower-generation" wedge ice through pore water filtration to the freezing front under epigenetic freezing.

Our results suggest, that at the Mamontova Gora exposure, the lower IC horizon, "Ice Complex II," is a non-homogenous and polygenetic feature, where the isotopically lighter ice wedges were formed from snow meltwater with insignificant input from other atmospheric waters, while heavier ice wedges correspond to water origin from evaporated surface and shallow groundwater sources, i.e., lacustrine waters or soil moisture in the sub-lacustrine talik, interpolygonal ponds and shallow marshes. The isotopic composition of the Late Pleistocene ice wedges in Central Yakutia shows that snowmelt water was the dominant water source for ice wedge growth and yields the isotopic signal of winter precipitation. Surface waters, especially from alas lakes and shallow marshes, as suggested by their significant evaporative transformation, could also have a local effect on the isotopic composition of wedge ice.

5.2 Microbial Communities vs. Deposits

The bacterial communities of the studied horizons differ both in the composition of the dominant groups and in their ratio. Similarity patterns assessed using Bray-Curtis dissimilarity and phylogenetic (weighted UniFrac) metrics are not entirely identical at the class and phylum levels (**Figures 10**, **11**; **Supplementary Tables S2, S3**).

5.2.1 Neogene-Middle Pleistocene Alluvial Sands

The most ancient sediments, Miocene alluvial sands (C-3, C-5, C-6) yield one of the lowest Shannon Index values (3.0–3.3), and rather high similarity coefficients at the phylum level. The greatest similarity is between samples C-3 and C-6, belonging to the same VI terrace (dissimilarity 15%), sample C-5 of a V terrace is characterized by a lower similarity (dissimilarity 26–32%) with them. These sediments were deposited under warm and humid conditions of the Miocene and underwent epigenetic freezing only in the middle Pleistocene (see above, **Section 5.1**). According to the UniFrac distance metric, they are also combined with the syngenetic riverbed sands deposits (C-7, C-8) of V terrace. It is interesting that at the same time they show significant differences at the phyla and class levels, reaching a discrepancy of 39–57% with samples C-3 and C-5, and up to 78% with sample C-5. In middle Pleistocene sands (C-7, C-8), the Shannon Index values are lower (1.99–2.29), and less OTUs are allocated—this seems to be quite natural considering their synchronous formation and freezing. In addition, the samples of these sands have the highest similarity among the samples at the phylum level (dissimilarity 14%), which is explained by a fact that in fact these are the sub-samples from a single monolith. The profiles of the main communities remain the same for the Miocene alluvial sands and Pleistocene ones, but their ratio changes dramatically; in the sands formed in the much more

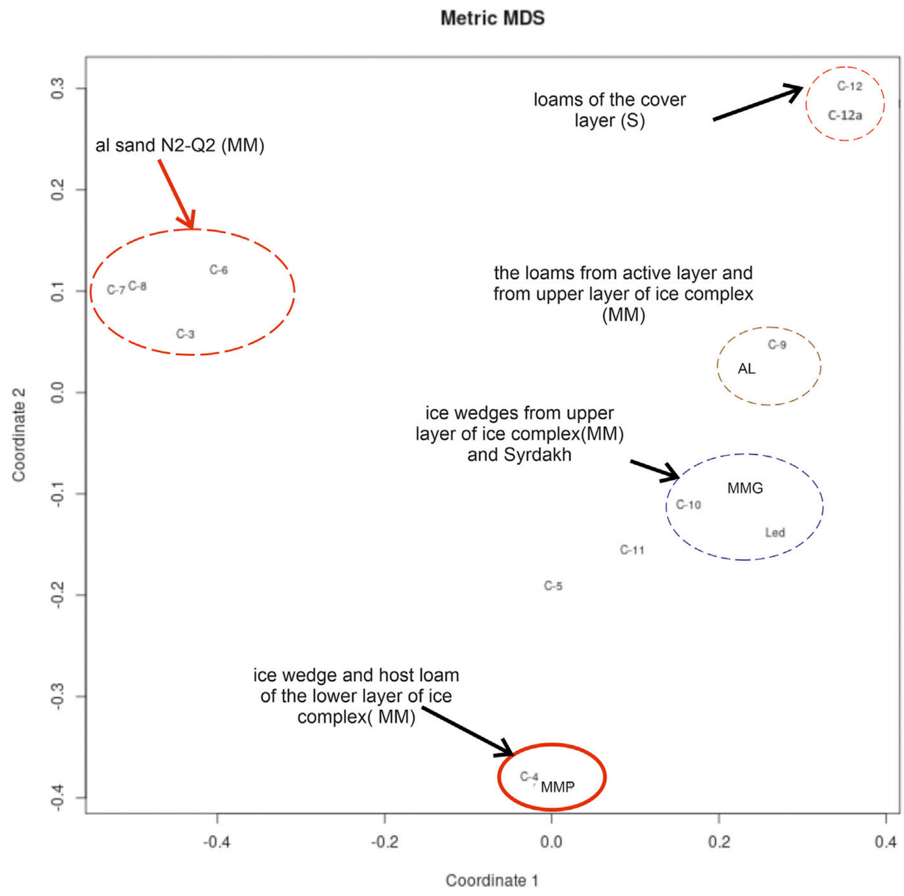

FIGURE 11 | Principal coordinate analysis (PCoA) scores plot of beta diversity based on UniFrac distance metric. MM for Mamontova Gora, S for Syrdakh. The samples AL, MMG and MMP correspond to previously studied samples of the ice complex of Mamontova Gora: an active layer (AL), an ice wedge of the upper (MMG) and lower horizons (MMP).

severe climatic conditions of the middle Pleistocene (C-7, C-8), which were subjected to freezing synchronously with their accumulation, representatives of the phylum *Firmicutes* (with dominance of class *Clostridia*, genera *Desulfosporosinus*) begin to dominate (up to 43%), which either were completely absent, or were present in a minor amount in the Neogene sands formed in warm conditions (maximum 8%).

Published results on the Neogene sand community of a V Aldan River terrace (Brouchkov et al., 2017) show the same basic profiles at the phylum level, with a minor number of *Firmicutes*, the absence of *Actinobacteritota*, but with a predominance of *Bacteroidota*. In the Middle Pleistocene sands, *Firmicutes* phyla increases in abundance (up to 43%), while it was absent, or present in only a minor amount, in the Neogene sands formed under warmer conditions (maximum 8%). *Actinobacteriota* also remain in trace amounts, but the proportion of the phylum *Bacteroidota* slightly increases from Neogene to Middle Pleistocene sands. A large proportion of *Betaproteobacteria*, detected predominantly in samples C-3, C-5 and C-6, indicates the adaptability of communities to life at low temperatures and low nutrient content (Johnson et al., 2007). *Actinobacteria* and cold-loving obligate anaerobic, capsule-forming *Bacteroidetes* are also mainly distributed in strata of the Arctic permafrost (Jansson, Taş, 2014; Taş et al., 2018).

5.2.2 Ice Complexes: Ice Wedges

The studied samples from ice wedges of the Mamontova Gora exposure demonstrate significant differences in the community composition of the lower and upper Ice Complex horizons, further confirming that these are different generations of ice wedges with different origin (**Figures 10, 11**). We assume that the observed differences are related more to the genesis than the differential preservation of DNA since the microbial community structure within an epoch is relatively stable over time (Shade et al., 2013), while once the system surpasses a threshold, microbial parameters rapidly shift to a new stable state (Saidi-Mehrabad et al., 2020).

The group of samples from the upper "Ice Complex I" ice wedges (C-10 from this study, and ice sample of upper IC horizon (MMG) from Rakitin et al. (2020), are clustered together with Syrdakh ice wedge (led-S), based on the UniFrac distance metric, and are significantly distanced from the lower "Ice Complex II" (MMP in Rakitin et al., 2020). Bray-Curtis dissimilarity index at the phylum level between the lower IC ice wedges and all other samples varies from 0.52 to 0.68, while intra-group dissimilarity values are from 0.30 to 0.32. The maximum dissimilarity of 0.40 is between Syrdakh and previously studied MMG samples, mostly owing to closer position of the MMG sample to the active layer, allowing infiltration of organisms from the active layer (Rakitin et al., 2020).

These two groups of samples differ in both diversity metrics and compositional profiles. The ice of the lower "Ice Complex II" horizon yields a poor prokaryotic community, with the dominance of *Firmicutes* (54.5%) followed by *Proteobacteria* (31.4%). The communities of other named samples more diverse: the highest Shannon Index value, 5.17, is observed in the upper "Ice Complex I" horizon, it is slightly lower, 4.37, for the Syrdakh IC sample. At the phylum level, in addition to their greater diversity, the main difference between these groups is the emergence of photosynthetic anoxygenic gram-negative bacteria *Chloroflexia* in samples C-10 and led-S Syrdakh). This phylum can be associated with photosynthetically active aquatic ecosystem (11–21%), with prevailing Gitt-GS-136 and KD4-96 classes, which are most often found in soil or river sediments, freshwater lakes (Mehrshad et al., 2018), and were also widespread in taberal sediments, including recently thawed ones, together with *Actinobacteriota* (*Gaiellales*, 0319-7L-14) (Winkel et al., 2019).

We find a certain correspondence between the water origin ant the degree of evaporative transformation in ice wedges and the microbial community composition. Isotopically lighter ice wedges of the lower "Ice Complex II" horizon originating from snow meltwater yield also a poor, slightly diverse communities. Ice wedges at Syrdakh are same meltwater additionally fractionated by evaporation in surface or subsurface compartments. The *Chloroflexia* bacteria is absent in the first case but are abundant (21%) in the second. Minor evaporative transformation of waters in the upper 'Ice Complex I' horizon, corresponds with moderate presence of *Chloroflexia* (11%) in its bacterial community. This inter-relation can be driven by higher water temperature associated with higher evaporation, and with this, higher photosynthetic activity in the water later stored in ice wedges.

Besides, we observe the high similarity between the microbial communities of Syrdakh and the upper "Ice Complex I" horizon at Mamontova Gora, that may reflect their similar genesis and/or age. The enclosing sediments of the Syrdakh ice wedges have ^{14}C dates between 23.6 and 16.6 cal ka BP. The similar calibrated age interval, from 21 to 14.9 cal ka BP, is attributed to ice wedges of the lower "Ice Complex II" horizon of the Mamontova Gora exposure (Vasil'chuk et al., 2004). Host deposits of this "Ice Complex II" horizon date to 47–35 cal ka BP.

5.2.3 Ice Complex: Host Deposits and Cover Layer

The highest similarity coefficients at the phyla level, Bray-Curtis index 0.22, were obtained for loams of the lower horizon, samples C-4 and C-11 (**Figure 10**; **Supplementary Tables S2, S3**). They are mainly represented by the same phyla, differing in the contribution of the phylum *Firmicutes:* 38% for C-4 vs. 21% for C-11. Starting from sample c11 and further up the vertical profile, the ratio remains in which *Bacilli* (*Bacillus sp.*) prevail over *Clostridia* (*Clostridium sensu stricto 13*) several times. *Chloroflexi* in C-11 (up to 3.9%), the share of the *Thermoleophila* class among *Actinobacteriota* is higher. On the Unifrac cluster plot, samples C-4 and C-11 are plotted far from each other, in contrast to C-4 vs MMP (**Figure 11**).

The *Firmicutes* species in the studied samples were observed in significant quantities only in syncryogenically frozen deposits: Middle Pleistocene sands, samples C-7 and C-8; late Pleistocene loams C-4 and C-11. But they are almost absent in the epigenetically frozen sediments formed in warm and humid Miocene conditions (samples C-3, C-5, C-6). This observation leads us to the suggestion that representatives of this phylum may be a marker of syngenetic freezing of deposits. The prevalence of the phylum *Firmicutes*, detected using the same primers and technique in clay permafrost layer from Western Spitsbergen, corresponding to the end of The Last Glacial Maximum, supports our hypothesis of *Firmicutes* as a marker of syngenetic sediment formation (Karaevskaya et al., 2021). Other studies of syngenetically frozen deposits exposed in the CRREL Permafrost Tunnel, Alaska, United States, showed that the content of *Firmicutes* OTUs, primarily from the spore-forming *Clostridia* and *Bacilli* classes, increased from an average relative abundance of 13% in the youngest age category (19 cal ka BP) to 79% in the oldest samples (33 cal ka BP) (40–60% for 27 cal ka BP) (Kanevskiy et al., 2008; Mackerlprang et al., 2017). Microbial community structure from the CRREL tunnel is close to that of our samples from the lower "Ice Complex II" horizon of Mamontova Gora.

The host loams of the upper "Ice Complex I" horizon of Mamontova Gora, sample C-9, have a high similarity coefficient to late Pleistocene loams of the lower IC layer, notably, the C-11 loam, located above C-4 sample in the vertical profile, at the dissimilarity level of phyla 0.32 and 0.42, respectively. UniFrac metrics, however, plots them close to the active layer sample even though the Bray-Curtis index at the phylum level, 0.58, is low (**Figure 11**; **Supplementary Tables S2, S3**). The reason for discrepancy between these coefficients is not very clear and requires further study. On the one hand, the significant differences in the microbial community composition between the active layer and the underlying frozen strata are typical (Müller et al., 2018), but on the other hand the close distance on Unifrac metris is logical too, since it deals with phylogenetic distances between observed organisms as well.

At the phylum level, *Cloroflexi* and *Firmicutes* are almost completely absent from the active layer but comprise up to 57% of the community in the underlying loams (sample C-9), which mostly differs from loams of lower horizon at the phylum level by the presence of the *Chloroflexi* phylum up to 30% (*Gitt-GS-136* and *KD4-96 classes*). The fact that phototrophic bacteria are typical aquatic microorganisms, rarely occurring in dry soil, but developing very actively when flooded with water, confirms the hypothesis about the partial thawing of the ice complex deposits, followed by freezing. The fact that this thawing occurred in the Holocene is contradicted by the available dating and isotopic oxygen-deuterium results, which show similar data for the upper and lower ice (see above), in addition. We assume the IC of Mamontova Gora thawed in MIS 3 and was followed by refreezing of the deposits forming the new unit. The redeposition of material could take place there as it is shown in Kaplina (2011) for North Yakutia. This explains our dating in 43.3 cal ka BP of the upper IC horizon which fits in the range of data of the lower IC horizon. Therefore, the presence of the phylum *Firmicutes* in the upper loam is logical, since they are inherited communities of syngenetically frozen deposits of the lower horizon, In addition, a large amount of *Chloroflexi* (15–30%) can be noted in loams dated of 10.6 cal ka BP (our study), overlying the Syrdakh ice complex (C-12, C-12a), and the complete absence of *Firmicutes* there. If we adhere to the hypotheses about the formation of overlying loams due to the thawing of the IC (Vtyurin, 1975; Kaplina, 2011) during the Holocene optimum, then the presence of *Chloroflexi* (*Gitt-GS-136* and *KD4-96* classes) can be considered as a biotracer of this process indicating a likely watering of the territory, waterlogging due to excessive moisture, which commonly leads to thawing.

Freezing of loam deposits of the upper stage in the Holocene was, accordingly, epicryogenic, when the reconstructed temperature is characterized by values approximately equal to the present or slightly lower.

5.2.4 Deposits of Ice Complexes. Soils vs. Ice Wedges

High similarity at the phyla level of host loam and ice wedge ice of the lower generation, as well a similar composition of the main bacterial profiles at this level (dissimilarity 0.26) and clustering together the C-4 and MMP samples according to Unifrac, confirm the simultaneous formation and freezing of sediments and ice wedge. The C-11 sample, located closer to the upper part of the lower tier, that showed some distance from C-4 along Unifrac (and is closer to the sediments of upper tier of IC), but having a sufficiently high coefficient of similarity with the upper loam at the phylum level (0.32) can most likely be interpreted as undergone short-term thawing and immediately frozen.

As for the ratio of the upper ice wedge to the host sediments, the low dissimilarity (0.45) most likely indicates the non-simultaneous formation of loams relative to the upper ice wedge, as the ice wedge was formed epigenetically.

6 CONCLUSION

Our conclusions reflect on the hypotheses suggested in the Introduction:

1) The composition and structure of microbial communities are similar in host deposits and ice wedges under syngenetic sedimentation, and strongly differ under epigenetic formation of ice wedges.

High similarity coefficients were obtained between ice wedges and host sediments (Bray-Curtis dissimilarity 0.26 at the phylum level) of the lower IC unit of Mamontova Gora, while significant differences for observed for the wedges and host sediments of the upper IC generation (0.45), which is also confirmed by Beta diversity results based on the UniFrac distance metric, which considers phylogenetic distances between observed organisms in the computation.

2) The composition of microbial communities can be related to the water origin in the ice wedges and mark the IC strata subject to thawing and subsequent refreezing (epigenetic freezing).

We found a certain correspondence between the water origin and the degree of evaporative transformation in ice wedges and the microbial community composition. The *Chloroflexia* bacteria represented mostly by *Gitt-GS-136, KD4-96* classes is absent in the lower generation ice wedges of Mamontova Gora originating from snow meltwater, and are abundant at the Syrdakh IC (21%), formed by the meltwater additionally fractionated by evaporation in surface or subsurface compartments. Minor evaporative transformation of waters in the upper "Ice Complex I" layer, corresponds with moderate abundance of *Chloroflexia* (11%) in its bacterial community. This inter-relation can be driven by higher water temperature associated with higher evaporative loss alongside with higher photosynthetic activity in the surficial water, later stored in ice wedges upon freezing.

For the soils, the abundance of the uncultured *Chloroflexi* of the *Gitt-GS-136* and *KD4-96* classes, is characteristic only to the layers that underwent thawing and refreezing. These bacteria were previously found both in freshwater bodies and in taberal sediments, including those recently thawed, and in our study, were abundantly present, up to 30% of the microbial community, in the loams from the upper generation IC Mamontova Gora, presumably thawed in MIS 3 interstadial, and in cover layer of Syrdakh IC, thawed during Holocene.

3) The similarity in microbial community composition and structure can be indicative of similar age of the IC strata in different locations, or their contemporaneous accumulation and freezing.

Different microbial communities of sediments and ice of the upper and lower generations of Mamontova Gora mark different stages of its formation. Based on the similarity of the communities for the upper IC layer of the Mamontova Gora and the Syrdakh IC, it can be concluded that these ice formations are somewhat synchronous. Still to confirm this we need data on the microbial communities of the host deposits of the Syrdakh IC.

In addition, the following interesting results were found that require further research:

1) Microbial diversity did not decrease monotonically down the profile according to sediment age. Thus, the lowest diversity with regard to soils was found in the Middle Pleistocene sands, and not Miocene sands. This may be caused by the deposition and long-term existence of the latter in a warm humid climate which creates favorable conditions for microbial diversity, rich species composition accumulated in the warm epoch was higher. Despite the destruction of cells later under harsh cold conditions, we suggest more DNA preserved from this stratum than from the later sediments formed in the more harsh conditions. These sediments were frozen only in the Middle Pleistocene, while the sands of the Middle Pleistocene

were formed in much colder conditions synchronously with freezing (syngenetic freezing).

2) An abundant number of representatives of the phylum *Firmicutes* (the dominance of *Clostridia* is replaced by *Bacilli* at the beginning of the late Pleistocene) is characteristic only of sediments that were formed syngenetically: their accumulation and freezing took place at the same time in very harsh conditions.
3) The composition of microbial communities of the host syncryogenic loam deposits of the lower layer of the Mamontova Gora IC (dated to 47.4–36,7 cal ka BP) is similar to the composition of microbial communities (phylum level) in the syncryogenic deposits of the CRREL Permafrost Tunnel in Alaska, dated to 33–27 cal ka BP which makes such marker as microbial community similarity very promising to paleoreconstructions.
4) Absence of archaea in all samples earlier than late Pleistocene, which is probably due to their poor preservation.

DATA AVAILABILITY STATEMENT

Metagenomic data uploaded to Genbank (https://www.ncbi.nlm.nih.gov) as bioproject number PRJNA734507 (SRX11067028-SRX11067041). The data on isotopes that support the findings of this study are openly available in PANGAEA at https://doi.org/10.1594/PANGAEA.921024.

AUTHOR CONTRIBUTIONS

MC conceived the project and wrote the original draft of the manuscript. MC and DS participated in the field work and collected the data. SB and AYM performed DNA isolation. AYM supervised and provided bioinformatics analysis. AYM, EK, and MC performed microbiological interpretations. YV and NB performed isotopic analysis and interpretations. NT performed water and sediment chemistry interpretations. AR and AVM participated in bioinformatics analysis. MC, EK, AYM, and AB supported overall proxy data interpretation. All authors discussed the results and contributed to the final manuscript.

FUNDING

The reported study was funded by RFBR according to the research project 21-55-75004. The research of YV and NB was financially supported by the Russian Scientific Foundation (grant No. 19-17-00126, isotope analysis). The work of AR and AVM was supported by Ministry of Education and Science of the Russian Federation. The work of BS was carried out with the partial support from the Act 211 Government of the Russian Federation, Agreement no. 02.A03.21.0006.

ACKNOWLEDGMENTS

We thank Samsonova Vera, Karzhavin Vladimir, Pankov Alexander, Andreevskaya Maya and Alexander Osipov for their for their invaluable assistance in field work.

SUPPLEMENTARY MATERIAL

The Supplementary Material for this article can be found online at: https://www.frontiersin.org/articles/10.3389/feart.2021.739365/full#supplementary-material

REFERENCES

Anderson, M. J. (2001). A New Method for Non-parametric Multivariate Analysis of Variance. *Austral Ecol.* 26, 32–46. doi:10.1111/j.1442-9993.2001.01070.pp.x

Andreev, A., Grosse, G., Schirrmeister, L., Kuzmina, S., Novenko, E., Bobrov, A., et al. (2004). Late Saalian and Eemian Palaeoenvironmental History of the Bol'shoy Lyakhovsky Island (Laptev Sea Region, Arctic Siberia). *Boreas* 33 (4), 319–348. doi:10.1080/03009480410001974

Anisimova, N. P., and Pavlova, N. A. (2014). *Hydrogeochemical Studies of Permafrost in Central Yakutia*. NovosibirskGeo: Academic Publishing House, 189.

Baranova, Y. P., Ilinskaya, I. A., Nikitin, V. P., Pneva, G. P., Fradkina, A. F., Shvareva, N. Ya., et al. (1976). "Miocene of Mammoth Mountain". in *Stratigraphy. Fossil flora* Moscow: Nauka Publ., 376.

Baranova, Y. P., and Biske, S. F. (1964). "History of the Development of the Relief of Siberia and the Far East". in *Northeastern USSR*. Moscow: Nauka, 290.

Biske, S. F., and Baranova, Y. P. (1976). "The Main Features of the Paleogeography of Beringia in the Pre-quaternary Cenozoic," in *Beringia in the Cenozoic*.Vladivostok: Far East Scientific Center of the Academy of Sciences of the USSR, 121–128.

Blott, S. J., and Pye, K. (2020). GRADISTAT: a Grain Size Distribution and Statistics Package for the Analysis of Unconsolidated Sediments. *Biogeosciences* 17, 3797–3814. doi:10.1002/esp.261

Boereboom, T., Samyn, D., Meyer, H., and Tison, J.-L. (2013). Stable Isotope and Gas Properties of Two Climatically Contrasting (Pleistocene and Holocene) Ice Wedges from Cape Mamontov Klyk, Laptev Sea, Northern Siberia. *The Cryosphere* 7 (1), 31–46. doi:10.5194/tc-7-31-2013

Bosikov, N. P. (1985). Evolution of Alases of Central Yakutia, Extended Abstract of Cand. Sci.(Geol.–Mineral.). Dissertation. Yakutsk: IMZ SB RAS 1991, 1–128.

Bottos, E. M., Kennedy, D. W., Romero, E. B., Fansler, S. J., Brown, J. M., Bramer, L. M., et al. (2018). Dispersal Limitation and Thermodynamic Constraints Govern Spatial Structure of Permafrost Microbial Communities. *FEMS Microbiol. Ecol.* 94 (8), fiy110. doi:10.1093/femsec/fiy110

Brouchkov, A., Kabilov, M., Filippova, S., Baturina, O., Rogov, V., Galchenko, V., et al. (2017). Bacterial Community in Ancient Permafrost Alluvium at the Mammoth Mountain (Eastern Siberia). *Gene* 636, 48–53. doi:10.1016/j.gene.2017.09.021

Brouillette, M. (2021). How Microbes in Permafrost Could Trigger a Massive Carbon Bomb. *Nature* 591 (7850), 360–362. doi:10.1038/d41586-021-00659-y

Budantseva, N. A., and Vasil'chuk, Y. K. (2017). Weighting of the Isotopic Composition of Ice Wedges in Central Yakutia Due to Active Evaporation of Surface Waters. *Arctic and Antarctica* 3, 53–68. doi:10.7256/2453-8922.2017.3.24541

Bulat, S. A., Alekhina, I. A., Blot, M., Petit, J.-R., De Angelis, M., Wagenbach, D., et al. (2004). DNA Signature of Thermophilic Bacteria from the Aged Accretion Ice of Lake Vostok, Antarctica: Implications for Searching for Life in Extreme Icy Environments. *Int. J. Astrobiology* 3 (1), 1–12. doi:10.1017/S1473550404001879

Burkert, A., Douglas, T. A., Waldrop, M. P., and Mackelprang, R. (2019). Changes in the Active, Dead, and Dormant Microbial Community Structure across a

Pleistocene Permafrost Chronosequence. *Appl. Environ. Microbiol.* 85 (7), e02646. doi:10.1128/AEM.02646-18

Carini, P., Marsden, P. J., Leff, J. W., Morgan, E. E., Strickland, M. S., and Fierer, N. (2017). Relic DNA Is Abundant in Soil and Obscures Estimates of Soil Microbial Diversity. *Nat. Microbiol.* 2, 16242. doi:10.1038/nmicrobiol.2016.242

Cherbunina, M. Y., Shmelev, D. G., Brouchkov, A. V., Kazancev, V. S., and Argunov, R. N. (2018). Patterns of Spatial Methane Distribution in the Upper Layers of the Permafrost in Central Yakutia. *Mosc. Univ. Geol. Bull.* 73 (1), 100–108. doi:10.3103/S0145875218010027

Chlachula, J. (2003). The Siberian Loess Record and its Significance for Reconstruction of Pleistocene Climate Change in north-central Asia. *Quat. Sci. Rev.* 22 (18-19), 1879–1906. doi:10.1016/S0277-3791(03)00182-3

Emerson, J. B., Varner, R. K., Wik, M., Parks, D. H., Neumann, R. B., Johnson, J. E., et al. (2021). Diverse Sediment Microbiota Shape Methane Emission Temperature Sensitivity in Arctic Lakes. *Nat. Commun.* 12, 5815. doi:10.1038/s41467-021-25983-9

US EPA (2017). EPA Method150.3: Determination of pH in Drinking Water, EPA 815-B-17-001. Available at http://www.regulations.gov; docket Accessed February 2017, 17.

Ernakovich, J. G., and Wallenstein, M. D. (2015). Permafrost Microbial Community Traits and Functional Diversity Indicate Low Activity at *In Situ* Thaw Temperatures. *Soil Biol. Biochem.* 87, 78–89. doi:10.1016/j.soilbio.2015.04.009

Ershov, E. D. (1989). *Geocryology of USSR, Eastern Siberia and Far East* (Moscow: Nedra), 515.

Fadrosh, D. W., Ma, B., Gajer, P., Sengamalay, N., Ott, S., Brotman, R. M., et al. (2014). An Improved Dual-Indexing Approach for Multiplexed 16S rRNA Gene Sequencing on the Illumina MiSeq Platform. *Microbiome* 2 (1), 6. doi:10.1186/2049-2618-2-6

Fedorov, A. N., and Konstantinov, P. Y. (2009). Response of Permafrost Landscapes of Central Yakutia to Current Changes of Climate, and Anthropogenic Impacts. *Geogr. Nat. Resour.* 30 (2), 146–150. doi:10.1016/j.gnr.2009.06.010

Fedorov, A., Vasilyev, N., Torgovkin, Y., Shestakova, A., Varlamov, S., Zheleznyak, M., et al. (2018). Permafrost-Landscape Map of the Republic of Sakha (Yakutia) on a Scale 1:1,500,000. *Geosciences* 8, 465. doi:10.3390/geosciences8120465

Filippova, S. N., Surgucheva, N. A., Kolganova, T. V., Cherbunina, M. Y., Brushkov, A. V., Mulyukin, A. L., et al. (2019). Isolation and Identification of Bacteria from an Ice Wedge of the Mamontova Gora Glacial Complex (Central Yakutia). *Biol. Bull. Russ. Acad. Sci.* 46, 234–241. doi:10.1134/S1062359019030026

Fotiev, S. M. (2015). Genesis and mechanism of formation of repeated-intrusive massive ice layers. *Earth Cryosphere* 19, 27–36.

Filippova, S. N., Surgucheva, N. A., Sorokin, V. V., Cherbunina, M. Y., Karnysheva, E. A., Brushkov, A. V., et al. (2014). Diversity of Bacterial Forms in Ice Wedge of the Mamontova Gora Glacial Complex (Central Yakutiya). *Microbiology* 83, 85–93. doi:10.1134/S0026261714020076

Fradkina, A. F., Alekseev, M. N., Andreev, A. A., and Klimanov, V. A. (2005). Chapter 5: East Siberia (Based on Data Obtained Mainly in Central Yakutia). *Geol. Soc. America Spec. Pap.* 382, 89–103. doi:10.1130/0-8137-2382-5.89

GOST 31867-2012 (2019). *Drinking Water. Determination of Anions Content by Chromatography and Capillary Electrophoresis Method* Moscow: Standartinform Publ., 11.

GOST 31869-2012 (2019). *Water. Methods for the Determination of Cations (Ammonium, Barium, Potassium, Calcium, Lithium, Magnesium, Sodium, Strontium) Content Using Capillary Electrophoresis* Moscow: Standartinform Publ., 23.

GOST 31957-2012 (2019). *Water. Methods for Determination of Alkalinity and Mass Concentration of Carbonates and Hydrocarbonates* Moscow: Standartinform Publ., 30.

Hugerth, L. W., Wefer, H. A., Lundin, S., Jakobsson, H. E., Lindberg, M., Rodin, S., et al. (2014). DegePrime, a Program for Degenerate Primer Design for Broad-Taxonomic-Range PCR in Microbial Ecology Studies. *Appl. Environ. Microbiol.* 80 (16), 5116–5123. doi:10.1128/AEM.01403-14

Hughes-Allen, L., Bouchard, F., Laurion, I., Séjourné, A., Marlin, C., and Hatté, C. (2021). Seasonal Patterns in Greenhouse Gas Emissions from Thermokarst Lakes in Central Yakutia (Eastern Siberia). *Limnol Oceanogr* 66, S98–S116. doi:10.1002/lno.11665

Hultman, J., Waldrop, M. P., Mackelprang, R., David, M. M., McFarland, J., Blazewicz, S. J., et al. (2015). Multi-omics of Permafrost, Active Layer and Thermokarst Bog Soil Microbiomes. *Nature* 521 (7551), 208–212. doi:10.1038/nature14238

Ivanov, A. V., and Vlasov, N. A. (1974). Influence of Cryogenic Processes on the Formation of Sodium Bicarbonate Waters. *Gidrochimicheskie Materialy (Hydrochemical Materials). L: Gidrometeoizdat.* 61, 56–61.

Ivanov, M. S. (1984). *Cryogenic Structure of Quaternary Deposits of the Lena–Aldan Depression*. Novosibirsk: Nauka.

Ivanova, T. I., Kuzmina, N. P., and Cherbunina, M. Y. (2017). Microbial Community of the Active Soil Layer from the Mammoth Mountain Outcrop (Central Yakutia). *Bullet. North-Eastern Scientific CenterFar East Branch Russian Academy of Sciences* 4, 95–103.

Ivanova, V. V., Nikol'skii, P. A., Tesakov, A. S., Basilyan, A. E., Belolyubskii, I. N., and Boeskorov, G. G. (2015). Geochemical Indicators of Paleoclimatic Changes in the Cenozoic Deposits of the Lower Aldan Basin. *Geochem. Int.* 53, 358–368. doi:10.1134/S0016702915020044

Jansson, J. K., and Taş, N. (2014). The Microbial Ecology of Permafrost. *Nat. Rev. Microbiol.* 12 (6), 414–425. doi:10.1038/nrmicro3262

Johnson, S. S., Hebsgaard, M. B., Christensen, T. R., Mastepanov, M., Nielsen, R., Munch, K., et al. (2007). Ancient Bacteria Show Evidence of DNA Repair. *Proc. Natl. Acad. Sci.* 104, 14401–14405. doi:10.1073/pnas.0706787104

Kallistova, A., Merkel, A., Kanapatskiy, T., Boltyanskaya, Y., Tarnovetskii, I., Perevalova, A., et al. (2020). Methanogenesis in the Lake Elton saline Aquatic System. *Extremophiles* 24 (4), 657–672. doi:10.1007/s00792-020-01185-x

Kanevskiy, M., Fortier, D., Shur, Y., Bray, M., and Jorgenson, T. (2008). "Detailed Cryostratigraphic Studies of Syngenetic Permafrost in the Winze of the CRREL Permafrost Tunnel, Fox, Alaska," in Proceedings of the Ninth International Conference on Permafrost, June-July 29-3, 2008 Fairbanks, Alaska: Institute of Northern Engineering, University of Alaska Fairbanks, 889–894.

Kaplina, T. (2011). Ancient Alas Complexes of Northern Yakutia (Part 2). *Kriosfera Zemli* XV, 20–30

Karaevskaya, E., Demidov, N., Kazantsev, V., Elizarov, I., Khaloshin, A., Petrov, A., ..., and Wetterich, S. (2021). Bacterial Communities of Frozen Quaternary Sediments of marine Origin on the Coast of Western Spitsbergen. *Geofi zicheskie Protsessy i Biosfera (Geophysical Process. Biosphere)* 20 (2), 75–98. doi:10.21455/gpb2021.2-5

Katamura, F., Fukuda, M., Bosikov, N. P., and Desyatkin, R. V. (2009). Charcoal Records from Thermokarst Deposits in Central Yakutia, Eastern Siberia: Implications for forest Fire History and Thermokarst Development. *Quat. Res.* 71 (1), 36–40. doi:10.1016/j.yqres.2008.08.003

Katamura, F., Fukuda, M., Bosikov, N. P., Desyatkin, R. V., Nakamura, T., and Moriizumi, J. (2006). Thermokarst Formation and Vegetation Dynamics Inferred from a Palynological Study in Central Yakutia, Eastern Siberia, Russia:TFAVDI]2.0. *Arctic, Antarctic, and Alpine ResearchCO* 38 (4), 561. doi:10.1657/1523-0430(2006)38[561:tfavdi]2.0.co;2

Katasonov, E. M., and Ivanov, M. S. (1973). *Cryolithology of Central Yakutia. Guide to field excursion along the Lena and Aldan Rivers* Yakutsk: Permafrost Institute, Siberian Branch, Academy of Sciences of the USSR, 37.

Kim, K., Yang, J.-W., Yoon, H., Byun, E., Fedorov, A., Ryu, Y., et al. (2019). Greenhouse Gas Formation in Ice Wedges at Cyuie, Central Yakutia. *Permafrost and Periglac Process* 30 (1), 48–57. doi:10.1002/ppp.1994

Kolde, R., Franzosa, E. A., Rahnavard, G., Hall, A. B., Vlamakis, H., Stevens, C., et al. (2018). Host Genetic Variation and its Microbiome Interactions within the Human Microbiome Project. *Genome Med.* 10, 6. doi:10.1186/s13073-018-0515-8

Konishchev, V. N. (2011). Permafrost Response to Climate Warming. *Krios. Zemli* 15 (4), 15–18.

Kostyukevich, V. V., Dneprovskaya, O. A., and Ivanov, I. Y. (1984). Radiocarbon Dates from the Laboratory of the Permafrost Institute of the Siberian Division of the USSR Academy of Sciences: Byull. *Komis. Po Izuch. Chetvertich. Perioda.* (53), 172–174.

Kuznetsov, Y. V. (1976). "Cryolithological Structure and Hydrochemical Composition of the Upper Pleistocene and Holocene Deposits of Mamontovaya," in *GoraCollection: Geocryological Conditions of the Formation of the Upper Pleistocene and Holocene Deposits in the North-East of the USSR. Tr. SVKNII DVNTS AS USSR*. Magadan: Publishing house of the SVKNII DVNTS AS USSR, 74, 12–21.

Lazukov, G. I. (1989). *The Pleistocene of the USSR's Territory*. Moscow: Vysshaya Shkola, 320.

Liang, R., Lau, M., Vishnivetskaya, T., Lloyd, K. G., Wang, W., Wiggins, J., et al. (2019). Predominance of Anaerobic, Spore-Forming Bacteria in Metabolically Active Microbial Communities from Ancient Siberian Permafrost. *Appl. Environ. Microbiol.* 85 (15), e00560. doi:10.1128/AEM.00560-19

Lozupone, C. A., Hamady, M., Kelley, S. T., and Knight, R. (2007). Quantitative and Qualitative β Diversity Measures Lead to Different Insights into Factors that Structure Microbial Communities. *Appl. Environ. Microbiol.* 73 (5), 1576–1585. doi:10.1128/AEM.01996-06

Lozupone, C., and Knight, R. (2005). UniFrac: a New Phylogenetic Method for Comparing Microbial Communities. *Appl. Environ. Microbiol.* 71 (12), 8228–8235. doi:10.1128/AEM.71.12.8228-8235.2005

Lozupone, C., Lladser, M. E., Knights, D., Stombaugh, J., and Knight, R. (2011). UniFrac: an Effective Distance Metric for Microbial Community Comparison. *Isme J.* 5 (2), 169–172. doi:10.1038/ismej.2010.133

Mackelprang, R., Burkert, A., Haw, M., Mahendrarajah, T., Conaway, C. H., Douglas, T. A., et al. (2017). Microbial Survival Strategies in Ancient Permafrost: Insights from Metagenomics. *Isme J.* 11, 2305–2318. doi:10.1038/ismej.2017.93

Markov, K. K. (1973). *Cross-section of the Newest Sediments*. Moscow, Russia: Moscow University Press.

McCalley, C. K., Woodcroft, B. J., Hodgkins, S. B., Wehr, R. A., Kim, E.-H., Mondav, R., et al. (2014). Methane Dynamics Regulated by Microbial Community Response to Permafrost Thaw. *Nature* 514 (7523), 478–481. doi:10.1038/nature13798

Mehrshad, M., Salcher, M. M., Okazaki, Y., Nakano, S. I., Šimek, K., Andrei, A. S., et al. (2018). Hidden in plain Sight-Highly Abundant and Diverse Planktonic Freshwater Chloroflexi. *Microbiome* 6 (1), 176. doi:10.1186/s40168-018-0563-8

Merkel, A. Y., Tarnovetskii, I. Y., Podosokorskaya, O. A., and Toshchakov, S. V. (2019). Analysis of 16S rRNA Primer Systems for Profiling of Thermophilic Microbial Communities. *Microbiology* 88, 671–680. doi:10.1134/S0026261719060110

Meyer, H., Dereviagin, A., Siegert, C., Schirrmeister, L., and Hubberten, H.-W. (2002). Palaeoclimate Reconstruction on Big Lyakhovsky Island, north Siberia?hydrogen and Oxygen Isotopes in Ice Wedges. *Permafrost Periglac. Process.* 13 (2), 91–105. doi:10.1002/ppp.416

Meyer, H., Schirrmeister, L., Andreev, A., Wagner, D., Hubberten, H.-W., Yoshikawa, K., et al. (2010). Lateglacial and Holocene Isotopic and Environmental History of Northern Coastal Alaska - Results from a Buried Ice-Wedge System at Barrow. *Quat. Sci. Rev.* 29 (27-28), 3720–3735. doi:10.1016/j.quascirev.2010.08.005

Müller, O., Bang-Andreasen, T., White, R. A., III, Elberling, B., Taş, N., Kneafsey, T., et al. (2018). Disentangling the Complexity of Permafrost Soil by Using High Resolution Profiling of Microbial Community Composition, Key Functions and Respiration Rates. *Environ. Microbiol.* 20 (12), 4328–4342. doi:10.1111/1462-2920.14348

Murton, J. B. (2021a). "Permafrost and Climate Change". in *Climate Change: Observed Impacts on Planet Earth*Snipp, M. (2016). "What does data sovereignty imply: what does it Look like?," in *In indigenous data sovereignty: toward an agenda*. 3rd Edn Editors TM Letcher Amsterdam, Netherlands: Elsevier, 281–326. doi:10.1016/B978-0-12-821575-3.00014-1

Murton, J., Opel, T., Toms, P., Blinov, A., Fuchs, M., Wood, J., et al. (2021b). A Multimethod Dating Study of Ancient Permafrost, Batagay Megaslump, East Siberia. *Quat. Res.*, 1–22. doi:10.1017/qua.2021.27

Natali, S. M., Holdren, J. P., Rogers, B. M., Treharne, R., Duffy, P. B., Pomerance, R., et al. (2021). Permafrost Carbon Feedbacks Threaten Global Climate Goals. *Proc. Natl. Acad. Sci. USA* 118 (21), e2100163118. doi:10.1073/pnas.2100163118

Nazarova, L., Lüpfert, H., Subetto, D., Pestryakova, L., and Diekmann, B. (2013). Holocene Climate Conditions in central Yakutia (Eastern Siberia) Inferred from Sediment Composition and Fossil Chironomids of Lake Temje. *Quat. Int.* 290-291, 264–274. doi:10.1016/j.quaint.2012.11.006

Nikitin, V. P. (2007). Paleogene and Neogene Strata in Northeastern Asia: Paleocarpological Background. *Russ. Geology. Geophys.* 48 (8), 675–682. doi:10.1016/j.rgg.2006.06.002

Nikolaev, A. N., Fedorov, P. P., and Desyatkin, A. R. (2011). Effect of Hydrothermal Conditions of Permafrost Soil on Radial Growth of Larch and pine in Central Yakutia. *Contemp. Probl. Ecol.* 4 (2), 140–149. doi:10.1134/S1995425511020044

Oksanen, J., Blanchet, G., Friendly, M., Kindt, R., Legendre, P., McGlinn, D., et al. (2020). vegan: Community Ecology Package. R package version 2.5-7 Available at: https://CRAN.R-project.org/package=vegan (Accessed March 3, 2021).

Opel, T., Dereviagin, A. Y., Meyer, H., Schirrmeister, L., and Wetterich, S. (2011). Palaeoclimatic Information from Stable Water Isotopes of Holocene Ice Wedges on the Dmitrii Laptev Strait, Northeast Siberia, Russia. *Permafrost Periglac. Process.* 22 (1), 84–100. doi:10.1002/ppp.667

Opel, T., Meyer, H., Wetterich, S., Laepple, T., Dereviagin, A., and Murton, J. (2018). Ice Wedges as Archives of winter Paleoclimate: A Review. *Permafrost and Periglac Process* 29 (3), 199–209. doi:10.1002/ppp.1980

Pereverzev, V. N. (2009). Genetic Features of Soils on Sorted Sand Deposits of Different Origins in the Kola Peninsula. *Eurasian Soil Sc.* 42, 976–983. doi:10.1134/S1064229309090038

Perez-Mon, C., Qi, W., Vikram, S., Frossard, A., Makhalanyane, T., Cowan, D., et al. (2021). Shotgun metagenomics reveals distinct functional diversity and metabolic capabilities between 12 000-year-old permafrost and active layers on Muot da Barba Peider (Swiss Alps). *Microb. genomics* 7 (4), 1–13. doi:10.1099/mgen.0.000558

Pestryakova, L. A., Herzschuh, U., Wetterich, S., and Ulrich, M. (2012). Present-day Variability and Holocene Dynamics of Permafrost-Affected Lakes in Central Yakutia (Eastern Siberia) Inferred from Diatom Records. *Quat. Sci. Rev.* 51, 56–70. doi:10.1016/j.quascirev.2012.06.020

Péwé, T. L., and Journaux, A. (1983). "Origin and Character of Loesslike silt in Unglaciated South-central Yakutia, Siberia, U.S.S.R". in *Prof. Publ. 1262* Washington, DC: U.S. Government Printing Office, 46. doi:10.3133/pp1262

Péwé, T. L., Journaux, A., and Stuckenrath, R. (1977). Radiocarbon Dates and Late-Quaternary Stratigraphy from Mamontova Gora, Unglaciated Central Yakutia, Siberia, U.S.S.R. *Quat. Res.* 8 (1), 51–63. doi:10.1016/0033-5894(77)90056-4

Popp, S., Diekmann, B., Meyer, H., Siegert, C., Syromyatnikov, I., and Hubberten, H.-W. (2006). Palaeoclimate Signals as Inferred from Stable-Isotope Composition of Ground Ice in the Verkhoyansk Foreland, Central Yakutia. *Permafrost Periglac. Process.* 17 (2), 119–132. doi:10.1002/ppp.556

Pravkin, S. A., Bolshiyanov, D. Yu., Pomortsev, O. A., Savelyeva, L. A., Molodkov, A. N., Grigoriev, M. N., et al. (2018). Relief, Structure and Age of Quaternary Deposits of the River valley. Lena in the Yakutsk bend. *Earth Sci.* 63 (2), 209–229. doi:10.21638/11701/spbu07.2018.206

Quast, C., Pruesse, E., Yilmaz, P., Gerken, J., Schweer, T., Yarza, P., et al. (2013). The SILVA Ribosomal RNA Gene Database Project: Improved Data Processing and Web-Based Tools. *Nucleic Acids Res.* 41, D590–D596. doi:10.1093/nar/gks1219

Rakitin, A., Beletsky, A., Mardanov, A., Surgucheva, N., Sorokin, V., Cherbunina, M., et al. (2020). Prokaryotic Community in Pleistocene Ice Wedges of Mammoth Mountain. *Extremophiles* 24 (1), 93–105. doi:10.1007/s00792-019-01138-z

Ravsky, E. I., and Alexeev, M. N. (1960). "Quaternary of the Eastern Siberia," in *Chronology and Climates of the Quaternary Period* Moscow: Academy of Sciences of the USSR Publ., 149–161.

RCore Team (2021). R: The R Project for Statistical Computing. R Foundation for Statistical Computing Website. Available at https://www.R-project.org/ (Accessed March 3, 2021).

Reimer, P. J., Austin, W. E. N., Bard, E., Bayliss, A., Blackwell, P. G., Bronk Ramsey, C., et al. (2020). The IntCal20 Northern Hemisphere Radiocarbon Age Calibration Curve (0-55 Cal kBP). *Radiocarbon* 62, 725–757. doi:10.1017/RDC.2020.41

Reimer, P. J., Bard, E., Bayliss, A., Beck, J. W., Blackwell, P. G., Ramsey, C. B., et al. (2013). IntCal13 and Marine13 Radiocarbon Age Calibration Curves 0-50,000 Years Cal BP. *Radiocarbon* 55, 1869–1887. doi:10.2458/azu_js_rc.55.16947

Rivkina, E., Petrovskaya, L., Vishnivetskaya, T., Krivushin, K., Shmakova, L., Tutukina, M., et al. (2016). Metagenomic Analyses of the Late Pleistocene Permafrost - Additional Tools for Reconstruction of Environmental Conditions. *Biogeosciences* 13 (7), 2207–2219. doi:10.5194/bg-13-2207-2016

Rozanski, K., Johnsen, S. J., Schotterer, U., and Thompson, L. G. (1997). Reconstruction of Past Climates from Stable Isotope Records of Palaeo-Precipitation Preserved in continental Archives. *Hydrological Sci. J.* 42 (5), 725–745. doi:10.1080/02626669709492069

RStudio Team (2021). *RStudio*. Boston, MA: Integrated Development Environment for R. RStudio, PBC. Available at: http://www.rstudio.com/ (Accessed March 3, 2021).

Saidi-Mehrabad, A., Neuberger, P., Hajihosseini, M., Froese, D., and Lanoil, B. D. (2020). Permafrost Microbial Community Structure Changes across the Pleistocene-Holocene Boundary. *Front. Environ. Sci.* 8, 133. doi:10.3389/fenvs.2020.00133

Saito, H., Iijima, Y., Basharin, N., Fedorov, A., and Kunitsky, V. (2018). Thermokarst Development Detected from High-Definition Topographic Data in Central Yakutia. *Remote sensing* 10 (10), 1579. doi:10.3390/rs10101579

Schirrmeister, L., Dietze, E., Matthes, H., Grosse, G., Strauss, J., Laboor, S., et al. (2020). The Genesis of Yedoma Ice Complex Permafrost - Grain-Size Endmember Modeling Analysis from Siberia and Alaska. *E&g Quat. Sci. J.* 69, 33–53. doi:10.5194/egqsj-69-3310.5194/egqsj-69-33-2020

Schirrmeister, L., Froese, D., Tumskoy, V., Grosse, G., and Wetterich, S. (2013). "PERMAFROST and PERIGLACIAL FEATURES | Yedoma: Late Pleistocene Ice-

Rich Syngenetic Permafrost of Beringia," in *Encyclopedia of Quaternary Science*. 2nd edition (Amsterdam: Elsevier), 542–552. doi:10.1016/B978-0-444-53643-3.00106-0

Schirrmeister, L., Grosse, G., Wetterich, S., Overduin, P. P., Strauss, J., Schuur, E. A. G., et al. (2011). Fossil Organic Matter Characteristics in Permafrost Deposits of the Northeast Siberian Arctic. *J. Geophys. Res.* 116 (G2), 1–16. doi:10.1029/2011JG001647

Schuur, E. A. G., McGuire, A. D., Schädel, C., Grosse, G., Harden, J. W., Hayes, D. J., et al. (2015). Climate Change and the Permafrost Carbon Feedback. *Nature* 520 (7546), 171–179. doi:10.1038/nature14338

Sejourné, A., Costard, F., Fedorov, A., Gargani, J., Skorve, J., Massé, M., et al. (2015). Evolution of the banks of Thermokarst Lakes in Central Yakutia (Central Siberia) Due to Retrogressive Thaw Slump Activity Controlled by Insolation. *Geomorphology* 241, 31–40. doi:10.1016/j.geomorph.2015.03.033

Shade, A., Gregory Caporaso, J., Handelsman, J., Knight, R., and Fierer, N. (2013). A Meta-Analysis of Changes in Bacterial and Archaeal Communities with Time. *Isme J.* 7, 1493–1506. doi:10.1038/ismej.2013.54

Shepelev, A. G., Kizyakov, A., Wetterich, S., Cherepanova, A., Fedorov, A., Syromyatnikov, I., et al. (2020). Sub-Surface Carbon Stocks in Northern Taiga Landscapes Exposed in the Batagay Megaslump, Yana Upland, Yakutia. *Land* 9, 305. doi:10.3390/land9090305

Shepelev, A. G., Starostin, E. V., Fedorov, A. N., and Maximov, T. (2016). Preliminary Analysis of Stocks of Organic Carbon and Nitrogen in the Upper Part of the Ice Complex in Central Yakutia. *Nauka i Obrazovanie* 82 (2), 35–42.

Shur, Y., Hinkel, K. M., and Nelson, F. E. (2005). The Transient Layer: Implications for Geocryology and Climate-Change Science. *Permafrost Periglac. Process.* 16 (1), 5–17. doi:10.1002/ppp.518

Solovev, P. A. (1959). *The Cryolithozone of the Northern Part of the Lena–Amga Interstream Area*. Moscow: Publ. House Acad. of Sciences.

Strauss, J., Schirrmeister, L., Mangelsdorf, K., Eichhorn, L., Wetterich, S., and Herzschuh, U. (2015). Organic-matter Quality of Deep Permafrost Carbon - a Study from Arctic Siberia. *Biogeosciences* 12 (7), 2227–2245. doi:10.5194/bg-12-2227-2015

Stuiver, M., Reimer, P. J., and Reimer, R. W. (2021). CALIB 8.2 [WWW program]. Available at: http://calib.org (Accessed September 12, 2021)

Sturm, C., Zhang, Q., and Noone, D. (2010). An Introduction to Stable Water Isotopes in Climate Models: Benefits of Forward Proxy Modelling for Paleoclimatology. *Clim. Past* 6 (1), 115–129. doi:10.5194/cp-6-115-2010

Sukhodrovsky, V. L. (2002). On the Genesis of the Ice Complex and Alas Relief. *Earth Cryosphere* 6 (1), 56–61.

Svitoch, A. A. (1983). Main Features and Features of the Pleistocene Paleogeography. *Bull. Comm. Study Quat. Period* 52, 143–147.

Tananaev, N. (2021). *Radiocarbon Dates from Central Yakutia*. figshare. Dataset. doi:10.6084/m9.figshare.14261372.v2

Taş, N., Prestat, E., Wang, S., Wu, Y., Ulrich, C., Kneafsey, T., et al. (2018). Landscape Topography Structures the Soil Microbiome in Arctic Polygonal Tundra. *Nat. Commun.* 9 (1), 1–13. doi:10.1038/s41467-018-03089-z

Tveit, A. T., Urich, T., Frenzel, P., and Svenning, M. M. (2015). Metabolic and Trophic Interactions Modulate Methane Production by Arctic Peat Microbiota in Response to Warming. *Proc. Natl. Acad. Sci. USA* 112 (19), E2507–E2516. doi:10.1073/pnas.1420797112

Ulrich, M., Matthes, H., Schirrmeister, L., Schütze, J., Park, H., Iijima, Y., et al. (2017b). Differences in Behavior and Distribution of Permafrost-related Lakes in C Entral Y Akutia and Their Response to Climatic Drivers. *Water Resour. Res.* 53 (2), 1167–1188. doi:10.1002/2016WR019267

Ulrich, M., Matthes, H., Schmidt, J., Fedorov, A. N., Schirrmeister, L., Siegert, C., et al. (2019). Holocene Thermokarst Dynamics in Central Yakutia - A Multi-Core and Robust Grain-Size Endmember Modeling Approach. *Quat. Sci. Rev.* 218, 10–33. doi:10.1016/j.quascirev.2019.06.010

Ulrich, M., Wetterich, S., Rudaya, N., Frolova, L., Schmidt, J., Siegert, C., et al. (2017a). Rapid Thermokarst Evolution during the Mid-holocene in Central Yakutia, Russia. *The Holocene* 27 (12), 1899–1913. doi:10.1177/0959683617708454

Vaks, A., Gutareva, O. S., Breitenbach, S. F. M., Avirmed, E., Mason, A. J., Thomas, A. L., et al. (2013). Speleothems Reveal 500,000-year History of Siberian Permafrost. *Science* 340 (6129), 183–186. doi:10.1126/science.1228729

Vasil'chuk, Y. K. (1992). *Oxygen Isotope Composition of Ground Ice (Application to Paleogeocryological Reconstructions)*. Moscow: Theoretical Problems Department, Russian Academy of Sciences and Lomonosov Moscow University Publications. 1, 420; 2, 264.

Vasil'chuk, Y. K. (1988). "Paleological Permafrost Interpretation of Oxygen Isotope Composition of Late Pleistocene and Holocene Wedge ice of Yakutia". in *Transactions (Doklady) of the USSR Academy of Sciences. Earth Science Sections* New York, NY: Scripta Technica, Inc. A Wiley Company 298 (1), 56–59.

Vasil'chuk, Y. K. (1991). Reconstruction of the Paleoclimate of the Late Pleistocene and Holocene of the Basis of Isotope Studies of Subsurface Ice and Waters of the Permafrost Zone. *Water Resour.* 17 (6), 640–647.

Vasil'chuk, Y. K., Kim, J.-C., and Vasil'chuk, A. C. (2004). AMS ^{14}C Dating and Stable Isotope Plots of Late Pleistocene Ice-Wedge Ice. *Nucl. Instr. Methods Phys. Res. Section B: Beam Interactions Mater. Atoms* 223-224, 1650–1654. doi:10.1016/j.nimb.2004.04.120

Vasil'chuk, Y. K., and Vasil'chuk, A. C. (1998). ^{14}C and 18O in Siberian Syngenetic Ice-Wedge Complexes. *Radiocarbon* 40, 2883–2893. doi:10.1017/S0033822200018853

Vasil'chuk, Y. K., Shmelev, D. G., Cherbunina, M. Y., Budantseva, N. A., Broushkov, A. V., and Vasil'chuk, A. C. (2019). New Oxygen Isotope Diagrams of Late Pleistocene and Holocene Ice Wedges in Mamontova Gora and Syrdakh Lake, Central Yakutia. *Dokl. Earth Sc.* 486 (1), 580–584. doi:10.1134/S1028334X19050283

Vasil'chuk, Yu. K., Shmelev, D. G., Budantseva, N. A., Cherbunina, M. Yu., Brouchkov, A. V., Vasil'chuk, A. K., and Chizhova, Yu. N. (2017). Oxygen Isotopic and Deuterium Composition of Syngenetic Ice Wedges in the Mamontova Gora and Syrdakh Sections and Reconstruction of Late Pleistocene winter Temperatures in Central Yakutia. *Arctic and Antarctic* (2), 112–135. doi:10.7256/2453-8922.2017.2.23189

Vtyurin, B. I. (1975). *Ground Ice of the USSR*. Moscow: Nauka, 215.

Wetterich, S., Kuzmina, S., Andreev, A. A., Kienast, F., Meyer, H., Schirrmeister, L., et al. (2008). Palaeoenvironmental Dynamics Inferred from Late Quaternary Permafrost Deposits on Kurungnakh Island, Lena Delta, Northeast Siberia, Russia. *Quat. Sci. Rev.* 27, 1523–1540. doi:10.1016/j.quascirev.2008.04.007

Wickham, H., Averick, M., Bryan, J., Chang, W., McGowan, L., François, R., et al. (2019). Welcome to the Tidyverse. *Joss* 4 (43), 1686. doi:10.21105/joss.01686

Wickham, H. (2016). *Programming with Ggplot2*. Cham: Springer, 241–253. doi:10.1007/978-3-319-24277-4_12

Windirsch, T., Grosse, G., Ulrich, M., Schirrmeister, L., Fedorov, A. N., Konstantinov, P. Y., et al. (2020). Organic Carbon Characteristics in Ice-Rich Permafrost in Alas and Yedoma Deposits, central Yakutia, Siberia. *Biogeosciences* 17, 3797–3814. doi:10.5194/bg-17-3797-2020

Winkel, M., Sepulveda-Jauregui, A., Martinez-Cruz, K., Heslop, J. K., Rijkers, R., Horn, F., et al. (2019). First Evidence for Cold-Adapted Anaerobic Oxidation of Methane in Deep Sediments of Thermokarst Lakes. *Environ. Res. Commun.* 1 (2), 021002. doi:10.1088/2515-7620/ab1042

Yershov, E. D. (1998). "General Geocryology". in *Studies in Polar Research* New York, NY: Cambridge Univ. Press, 580.

Zakharova, E. A., Kouraev, A. V., Stephane, G., Franck, G., Desyatkin, R. V., and Desyatkin, A. R. (2018). Recent Dynamics of Hydro-Ecosystems in Thermokarst Depressions in Central Siberia from Satellite and *In Situ* Observations: Importance for Agriculture and Human Life. *Sci. Total Environ.* 615, 1290–1304. doi:10.1016/j.scitotenv.2017.09.059

Zhou, L., Zhou, Y., Yao, X., Cai, J., Liu, X., Tang, X., et al. (2020). Decreasing Diversity of Rare Bacterial Subcommunities Relates to Dissolved Organic Matter along Permafrost Thawing Gradients. *Environ. Int.* 134, 105330. doi:10.1016/j.envint.2019.105330

Conflict of Interest: The authors declare that the research was conducted in the absence of any commercial or financial relationships that could be construed as a potential conflict of interest.

Publisher's Note: All claims expressed in this article are solely those of the authors and do not necessarily represent those of their affiliated organizations, or those of the publisher, the editors and the reviewers. Any product that may be evaluated in this article, or claim that may be made by its manufacturer, is not guaranteed or endorsed by the publisher.

frontiers in Earth Science

ORIGINAL RESEARCH
published: 09 November 2021
doi: 10.3389/feart.2021.741473

Forest Steppe-Like Vegetation Near Cherskiy (West Beringia) During the Early Pleistocene Olyorian Period Reconstructed Using Plant Macrofossils

Frank Kienast[1]* and Sergei P. Davydov[2]

[1]Senckenberg Research Institute and Natural History Museum, Research Station of Quaternary Palaeontology, Weimar, Germany, [2]Pacific Geographical Institute, Far East Branch of Russian Academy of Sciences, North-East Science Station, Cherskiy, Russia

OPEN ACCESS

Edited by:
Alexandra Veremeeva, Institute of Physical-Chemical and Biological Problems in Soil Science (RAS), Russia

Reviewed by:
Subir Bera, University of Calcutta, India
Mary E Edwards, University of Southampton, United Kingdom

***Correspondence:**
Frank Kienast
frank.kienast@senckenberg.de

Specialty section:
This article was submitted to Paleontology, a section of the journal Frontiers in Earth Science

Received: 14 July 2021
Accepted: 18 October 2021
Published: 09 November 2021

Citation:
Kienast F and Davydov SP (2021) Forest Steppe-Like Vegetation Near Cherskiy (West Beringia) During the Early Pleistocene Olyorian Period Reconstructed Using Plant Macrofossils. Front. Earth Sci. 9:741473. doi: 10.3389/feart.2021.741473

The lower Kolyma region is known for rich Early Olyorian large mammal assemblages including plesiomorphic musk ox, reindeer, horse, broad-fronted moose, steppe mammoth and cave bear. Data on the vegetation in zonal habitats from the Olyorian period are, in contrast, scarce. Earlier palynological results from classical Olyorian sites indicated predominant grassland vegetation with scattered larch occurrences but are, due to limited taxonomical resolution, uncertain. Plant macrofossil data were, so far, only available from azonal, aquatic habitats. Here, we describe Olyorian palaeo-vegetation from an exposure near Cherskiy, Nizhnekolymsky District, Sakha Republic, Russia. The macrofossil-based reconstruction of palaeo-vegetation revealed the existence of an open forest steppe comprising a mosaic of sparse larch groves in a dry grassland composed of tundra steppes, degraded meadow steppes and saline meadows. In the larch groves, light demanding shrubs and dwarf shrubs such as shrub birch (*Betula* cf. *fruticosa*, *B. nana* ssp. *exilis*), raspberry (*Rubus idaeus*), cowberry (*Vaccinium vitis-idaea*), and crowberry (*Empetrum nigrum*) formed the understory. Ruderal pioneer plants point to open ground as result of disturbances, possibly due to the activity of large herbivores. The nitrophytic ruderal species *Urtica dioica*, in particular, suggests locally increased nutrient supply from animal excretions. Also, the abundant remains of *Chenopodium* cf. *prostratum* might be explained by disturbances and nutrient enrichment, but *Chenopodium* is also characteristic of salt accumulation in the soil owing to high evaporation under arid conditions, which are also indicated by alkali grass (*Puccinellia* sp.). The presence of trees and shrubs indicates interglacial-like temperature conditions but the dominance of dry grassland species and the occurrence of facultatively halophytic plants (*Chenopodium prostratum*, *Puccinellia* sp.) suggests aridity, which is more typical of cold stages. During the early Pleistocene, i.e., prior to the Early-Middle Pleistocene transition (EMPT) culminating around 900 ka ago, the duration of climate cycles was shorter and the amplitude of climate fluctuations was smaller. Ice-rich permafrost formed only after the EMPT during increasingly extreme cold stages, and, during warm stages, its thawing resulted in paludification of the active layer. Prior to the EMPT, the climate in West

Beringia was constantly relatively dry, more or less moderate and more stable than thereafter. In contrast to modern tundra and northern taiga in the study region, dry habitats apparently prevailed during the time of deposition of the plant macro-remains.

Keywords: olyorian, early-middle pleistocene transition, paleobotany, plant macrofossils, mammoth-steppe, megaherbivores, beringia, centre of origin

INTRODUCTION

Due to continental climate and the consequent lack of extensive glaciation, Beringia was a refugium for arctic biota during Pleistocene warm stages and center of dispersal during cold stages, when cold-adapted taxa spread over much of Eurasia far into the middle latitudes. Also, the intercontinental faunal exchange between Eurasia and the New World took place via the Beringian landmass during phases of global sea level lowering. As result of ice sheet formation in Northern Europe and North America and the fixation of tremendous water masses, the huge and shallow Laptev, East Siberian, Chukchi and Bering shelves in the North of Yakutia and in the East of Chukotka became, at such times, fully exposed and together formed the Beringian landmass.

Apart from being a refugium during the late Middle and Late Pleistocene, the western part of Beringia is furthermore regarded as center of development or center of origin of preadapted late Pleistocene mammoth faunal complex components, like *Ovibos* (resp. *Praeovibos*), *Rangifer*, *Gulo*, *Alopex* and advanced forms of *Mammuthus*, which evolved there during the late Early to the early Middle Pleistocene giving rise to define the Northeast Siberian land mammal age Olyorian (Sher, 1986; Kahlke, 1999).

The Olyorian comprises a long period of time for the evolution of the mammoth faunal complex spanning from the late Early to the early Middle Pleistocene (early Eopleistocene to early Neopleistocene according to the Russian nomenclature), i.e., 1.4–0.5 Ma (Sher, 1971; Sher, 1986), though without exactly defined lower and upper boundaries. The type locality of the Olyorian is situated at the Chukochya River in the Kolyma lowlands about 150 km NW of Cherskiy (**Figure 1**; Sher, 1986). Classical Olyorian sites in NE Siberia are furthermore located at the Krestovka River (**Figure 1**; Sher et al., 1979) as well as at the Adycha River (Kaplina et al., 1983) and in the surroundings of Cherskiy, where important Olyorian sites are known from Tretiy Ruchey between Zeleniy Mys and the town of Cherskiy (Sher et al., 2011) as well as the Cherskiy Ovrag (Davydov, 2007) from where plant remains are described in the present paper.

As part of the regional Northeast Siberian (West Beringian) Quaternary sequence, the Olyorian mammal age can be further separated into two faunal units on the base of the evolutionary succession of collared lemmings (Sher, 1997). The lower Olyorian (Chukochyan) is characterized by the presence of the predecessor of modern collared lemmings *Predicrostonyx compitalis* and the likewise archaic vole *Allophaiomys pliocaenicus* and is correlated with the late part of the reverse polarity Matuyama Chron in the palaeomagnetic record including the inserted magnetically normal Jaramillo event. The upper Olyorian (Akanian) is defined by the occurrence of the more advanced collared lemming *Dicrostonyx renidens* and corresponds with the earliest part of the normal polarity Brunhes Chron although also including the Matuyama/Brunhes reversal and the uppermost Matuyama Chron.

The Olyorian is characterized by a unique assemblage of large mammals, which appeared for the first time in this region and, in the case of *Gulo*, *Rangifer* and *Mammuthus primigenius*, for the first time worldwide. Remains of an "archaic northern elephant" in Chukochyan deposits and of a more advanced form in Akanian sediments (Sher, 1986) represent a distinct mammoth lineage. They are actually morphologically very advanced pre-empting an evolutionary level of mammoths that occurred outside Beringia only 300–400 ka later (Sher, 1986; Kahlke, 1999). Genomic analyses based on ancient DNA with an age of more than 1 million years prove the affiliation of lower Olyorian mammoth remains at the Krestovka and Adycha sites to the steppe-mammoth lineage (van der Valk et al., 2021). Genomic data from another, only 650,000-year-old, thus Akanian, mammoth found at the Chukochya site reveal that it was an early representative of the woolly mammoth (*M. primigenius*), which thus evolved in Western Beringia and descended from the Adycha lineage of the steppe-mammoth (van der Valk et al., 2021).

Numerous bones of a very large horse assigned to *Equus* (*Plesippus*) *verae* are characteristic of both units, the Chukochyan and the Akanian. According to recent cladistic analyses of morphometrical measurements of cranial and postcranial elements of 30 extinct and extant horse taxa, *Plesippus* must be placed within the genus *Equus* (Cirilli et al., 2021). *Equus verae* belongs to the stenonine clade, which comprises modern zebras and asses and descends from *E. stenonis* and, as all Old-World Equids, from its North American progenitor *E. simplicidens*. *Equus suessenbornensis*, occurring in Central Europe later during the Middle Pleistocene, coincides morphometrically with *E. verae* and is regarded successor of an Asian parent form (Forsten, 1986 referred to in; Kahlke, 1999). In addition to the large *E. verae*, the sympatric occurrence of a second, smaller, equid in Olyorian deposits is reported (Sher et al., 1979). From the upper (Akanian) unit, also caballine horses are described (Sher, 1986).

Remains of a giant moose (*Cervalces* sp.) and of *Bison* sp. were regularly found in both units. Both taxa were, at this time, widespread over the Eurasian middle and high latitudes as is documented by abundant findings, e.g., at the Epivillafranchian site of Untermassfeld in Germany (Kahlke et al., 2011). Also cave bears had an extensive distribution in middle latitudes at this time, but the discovery of a mandible determined as *Ursus savini* ssp. *nordostensis* near Cherskiy represents the northernmost and easternmost find of spelaeoid bears worldwide (Sher et al., 2011).

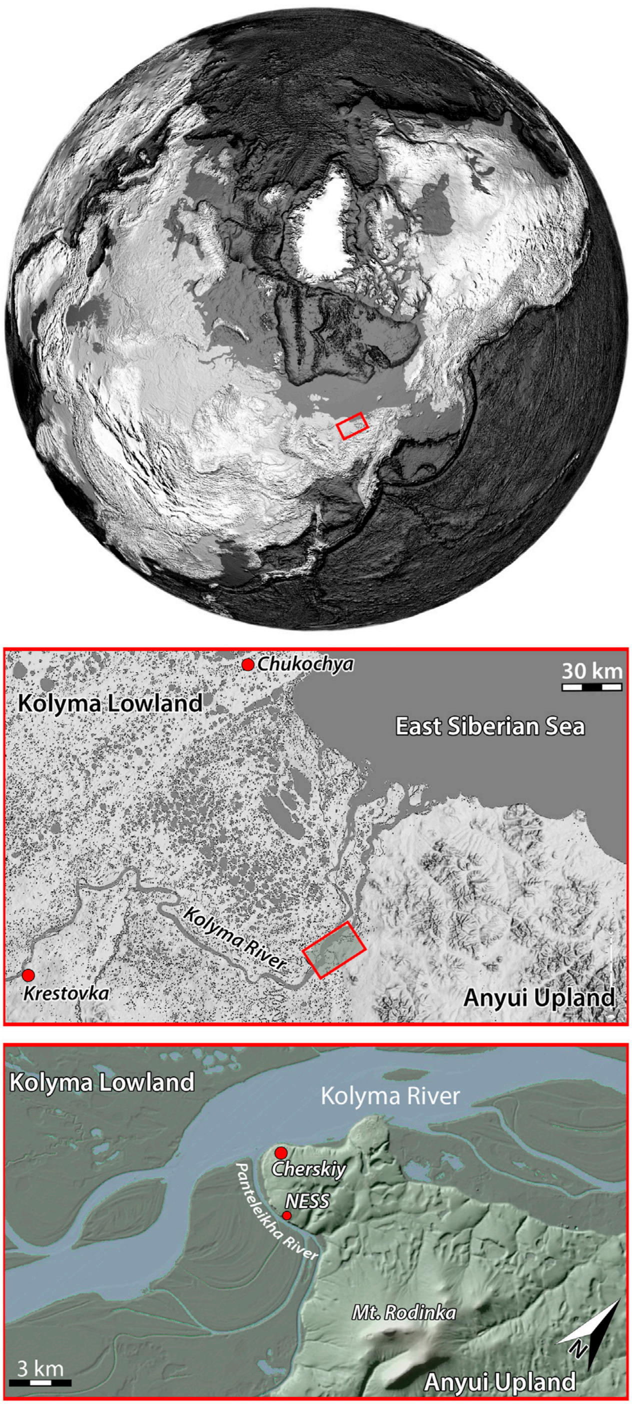

FIGURE 1 | Location in the western part of Beringia (upper part), topography and regional context of the study site at the junction of the Northeast Siberian coastal lowlands and the Far Eastern Anyui uplands (central part) as well as location of the Chukochya and Krestovka sites. The study site is situated in close proximity to the North East Science Station (NESS) Cherskiy at the westernmost edge of the Anyui Upland (lower part). Upper part adapted from the NGDC, NOAA Satellite and Information Service, available at http://www.ngdc.noaa.gov/mgg/global/; central and lower part Digital Elevation Model adapted from the Arctic DEM Explorer available at https://livingatlas2.arcgis.com/arcticdemexplorer.

The Olyorian findings of *Rangifer* ex. gr. *tarandus* are, together with fossils from Cape Deceit, Kotzebue Sound, Western Alaska, the oldest known reindeer fossils worldwide suggesting the origin of reindeer in Beringia (Sher, 1986; Kahlke, 1999). An archaic form of another typically arctic faunal element is represented in Olyorian deposits as well: the oldest finds of *Praeovibus beringiensis* indicate the origin of musk ox in NE Siberia (Sher, 1971). *Praeovibos* can be considered as early morphotype of the extant *Ovibos moschatus* as is suggested by ancient DNA studies (Campos et al., 2010). Apart from *Praeovibos*, postcranial remains of another, smaller Ovibovine were also detected in Olyorian deposits and might possibly represent *Soergelia* (Sher et al., 1979), which is proven for the upper unit Akanian (Sher, 1986). *Soergelia* was widely distributed in NE Siberia (Sher, 1971; Boeskorov, 2019) and probably originated in the NE Siberian Arctic (Kahlke, 1999). Thus, it is regarded a Beringian bovid as well.

Even *Saiga*, undoubtedly an immigrant from the zonal steppe belt, was already present in West Beringia during Olyorian times. The Olyorian finds of *Saiga* are the worldwide oldest known fossils of that genus so far (Kahlke, 1999). As saiga is, more than any other Beringian faunal element, indicative of zonal steppe grasslands, it can be assumed that it evolved in the inner continental steppe belt.

Some large mammals expanded into the region from the inner continental steppe belt, as is the case of *Saiga*, *Equus* and *Cervalces*. Several of the listed taxa evolved, however, in Beringia during the Early Pleistocene developing adaptations to environmental conditions making them fit for huge range expansions across the Holarctic and far into the mid latitudes during later cold climate phases, which became, in the course of the Early-Mid Pleistocene Transition, progressively longer and colder. The Olyorian faunal complex is therefore regarded as an important predecessor of the late-Pleistocene *Mammuthus-Coelodonta* faunal complex (Kahlke, 1999).

Only limited data are available on the habitat conditions for large herbivores in Beringia during the Olyorian period. Palaeobotanical and entomological data from the Krestovka and the Chukochya sites suggest that climate and vegetation changed only slightly within the deposition period of the sequence (Giterman et al., 1982). According to palynological results from the Krestovka sequence, non-arboreal pollen with Poaceae, *Artemisia*, Chenopodiaceae and Caryophyllaceae were most abundant throughout the studied sequence indicating open grassland vegetation and aridity. The existence of such environments is confirmed by entomological data revealing the prevalence of grassland dwellers in Chukochyan deposits and the existence of few taiga species suggesting that groves of trees and shrubs persisted. The percentage of arboreal taxa in the pollen spectra, mainly *Alnus* (*alnobetula* ssp.) *fruticosa*, *Betula*, sp., *Betula* Sect. *Nanae* and *Pinus pumila* with rare *Larix*, declined from up to 40% at the base of the sequence to nearly 5% in the middle part and then slowly increased towards the top of the sequence. Available plant macrofossil data represent only azonal, aquatic vegetation presumably from small ponds (Giterman et al., 1982). Due to the limitations of pollen data in northern environments, like overrepresentation of long-distance-transported pollen in conjunction with low local pollen production and the lack of taxonomic differentiation (Birks and Birks, 2000), plant macrofossil data are, however, especially valuable for the reconstruction of vegetation and environmental conditions in particular when they represent zonal vegetation.

In the present paper, we use plant macrofossils sampled from Early Olyorian (Chukochyan) deposits in a gully near Cherskiy, to reconstruct zonal vegetation and environmental conditions existing at the life-time of the cold pre-adapted Beringian faunal complex.

STUDY AREA

The sampled outcrop "Cherskiy Ovrag" is situated near the North-East Science Station of the Pacific Geographical Institute and about 3 km east of Cherskiy at the right bank of the Panteleikha River, a tributary of the Kolyma River (**Figure 1**). The study site is located at the northeastern edge of Yakutia at the junction to the Anyui Upland macroslope. Starting from the left bank of the Panteleikha River, the Kolyma lowland extends over hundreds of km to the west and merges with the Yana-Indigirka lowland, together forming the vast Northeast Siberian coastal lowlands.

Geology and Permafrost

The bedrock exposed at the study site and at other sites along the right banks of the Kolyma and Panteleikha Rivers in the vicinity of Cherskiy is composed of Triassic sedimentary rocks cut through by small intrusions of Jurassic granitoids, and less often by Cretaceous effusive bodies. Subsequently, these bedrocks and the Neogene weathering crust were covered with permafrost sediments of various Pleistocene ages (Sher et al., 1979; Davydov, 2007; Sher et al., 2011). The major portion of rocks in the study area is overlain by thick ice-rich silty-sandy deposits of the late Pleistocene Yedoma Formation (Sher et al., 1979; Davydov et al., 2009) or by products of their Holocene transformation. Currently, these deposits are widely eroded and disturbed by industrial extraction of rock debris at the right banks of the Panteleikha and Kolyma Rivers. In particular, these disturbances exposed a formerly buried relief with fragments of ancient erosional channels cutting into the Neogene weathering crust. These channels resemble gullies, so-called ovrags (овраГи) in Russian.

The entire territory of Yakutia is situated in the zone of continuous permafrost. Owing to the lack of inland glaciations, ice-bonded permafrost deposits (Ice Complex), penetrated by thick ice wedges and consisting of up to 90% of ice, formed on the Northeast Siberian coastal lowlands during cold phases of the Late Pleistocene (Tomirdiaro, 1980; Romanovskii et al., 2004). The adjacent shelves, which were subaerially exposed during Pleistocene cold stages, are still underlain by relict permafrost down to depths of 300–700 m (Romanovskii et al., 2004). The upper part of the Ice Complex largely eroded in the course of the Holocene resulting in characteristic thermokarst landforms. In recent years, Ice Complex deposits older than Late Pleistocene became exposed near Batagay in the Yana Highlands illustrating the continuity of cold continental climate in Northern Yakutia back until, at least, the Middle Pleistocene (Ashastina et al., 2017; Murton et al., 2017, 2021). Ice wedge casts in Olyorian deposits and in underlying Kutuyakh deposits at the Bolshaya Chukochya and Krestovka sites indicate that continuous permafrost existed at the time of their deposition, thus already during the Early Pleistocene (Giterman et al., 1982).

Climate

Climate in Yakutia is cold continental, i.e., the annual mean temperature is everywhere negative with very cold winters. The lowest temperature of the Northern hemisphere was measured in Verkhoyansk in the Yakutian Yana Highlands. The temperature during the growing season is the main factor controlling modern vegetation. During the summer, the temperature is relatively high in inland areas such as the Central Yakutian Plain and the Yana Highlands but considerably decreases towards the coast due to the cooling effect of the sea and increasing cloud cover. This maritime effect increases also eastwards at the Chukchi Peninsula. The region around Cherskiy is, thus, a transitional area, covering an E-W continentality gradient from inland Yakutia to Chukotka and, due to the proximity to the coast, a N-S gradient in terms of summer temperature and vegetation illustrated by the polar tree line, which is only 25 km to the Northwest. Climatic data from the weather station in Cherskiy (WMO 25123) indicate a mean annual air temperature of −9.7C, a mean temperature of the coldest month of −33.5C and a mean temperature of the warmest month (July) of 13.9C. The mean seasonal temperature gradient varies within 45.0–49.0C. The annual precipitation is very low with about 215 mm (Russia's Weather Server, 2021) but, due to low evapotranspiration, the prevention of downward percolation by permafrost and additional moisture supply by thawing permafrost, the active layer is, on zonal sites, wet.

Vegetation

The zonal vegetation in the study area is sparse northern taiga and near-tundra woodland (forest tundra) composed of the extremely cold-tolerant deciduous larch (*Larix gmelinii* var. *gmelinii*; synonym with after GBIF https://www.gbif.org/species/2686192) with shrub alder (*Alnus alnobetula* ssp. *fruticosa*), shrub birches (*Betula divaricata*, *B. fruticosa*, *B. exilis*), more than a dozen species of shrub willows (*Salix* spp.) and Ericaceae (*Vaccinium vitis-idaea*, *Rhododendron tomentosum*, *Arctous alpina*) in the understorey (Troeva et al., 2010). The tree line is situated only about 25 km to the North where the floristically rich subarctic tundra of the Kolyma Lowland extends, a huge wetland that is covered with countless thermokarst lakes (**Figure 1**, middle part). The region is also known for the presence of extrazonal relict steppe patches considered as potential analogues of Pleistocene vegetation (Yurtsev, 1982). Detailed lists of the local flora were provided by Yurtsev, (1974), Kozhevnikov (1981), Zaslavskaya and Petrovskii (1994), Maksimovich (1998) and Davydov et al. (2020). In the lower Kolyma region, steppe patches are restricted to specific sites in southern exposures and to coarsely clastic substrate. One of the most extensive steppe patches in the whole region is immediately adjacent to the sampling site. An outline of the vegetation occurring in the study area is given by Kienast (2016).

MATERIAL AND METHODS

The Cherskiy Ovrag

In the course of quarrying rock debris from the Neogene weathering crust for airstrip reconstruction at the nearby Cherskiy Airport, ancient erosional channels were uncovered by bulldozers. These channels or gullies (ovrags) represent former erosive cuts into the bedrock that were subsequently filled with Pleistocene permafrost deposits. The extraction of rock gave access to Late Pleistocene Yedoma sediments and, in their lower parts, to fossiliferous Early Olyorian deposits rich in vertebrate fossils (**Figure 2**).

S.P. Davydov (2007) studied systematically the stratigraphical sequence and collected large mammal remains that became exposed as result of quarrying or of natural erosion in these gullies between the years 2000 and 2018. The above-lying Ice Complex deposits contained numerous bones of typical Late Pleistocene mammoth faunal representatives such as *Mammuthus primigenius*, *Bison priscus*, *Rangifer tarandus* and *Equus* sp.

The Olyorian deposits underlying the Ice Complex revealed a quite different faunal composition. 25 percent of all mammal bones recorded at the Cherskiy Ovrag originated from Ovibovini (Sher et al., 2011), which is in stark contrast to late Pleistocene assemblages in NE Siberia, where musk oxen play only a minor role in the large mammal composition in favor of the then much more abundant bison (Sher, 1971). Most of these Ovibovini remains can be assigned to the extinct *Praeovibos beringiensis* Sher et al. (2011), which is, according to Campos et al. (2010), considered as an archaic morphotype of the extant musk ox. Furthermore, bones of the large, archaic, stenonine horse *Equus* (subgen. *Plesippus*) *verae*, a large caballoid horse (*Equus* subgen. *Equus*), likewise large bodied Bison and mammoth forms, broad-fronted moose (*Cervalces* sp.), an ancient maral (*Cervus* sp.) and hare (*Lepus* sp.) were found at the site (Davydov, 2007). Finally, a mandible and a canine of *Ursus savinii nordostensis*, a small extinct cave bear, was found in the Cherskiy Ovrag indicating a much more extended range of cave bears than formerly expected (Sher et al., 2011).

From one of the gullies that were formerly sampled for large mammal bones, P. Nikolskyi screened fine sandy and silty sediments for the analysis of small mammals, which are crucial for biostratigraphical dating. The results, published by Sher et al. (2011), revealed, beside *Lemmus* sp. remains, the presence of the extinct vole *Allophaiomys reservatus* and a plesiomorphic collared lemming (*Predicrostonyx compitalis*) characteristic of the lower Olyor (Chukochyan). Two other teeth stem either from a more advanced form of *P. compitalis* or from its Late Olyorian successor *Dicrostonyx renidens*. Thus, both large and small mammal remains indicate an age of the studied sediments belonging to the Early Olyorian (Chukochyan).

Plant Macrofossil Analyses

From the layers earlier screened for small mammal remains, we took material for plant macrofossil analyses in 2015 (**Figure 2**). At the time of sampling, only a small section of the outcrop was accessible and we took the sample from the only observable organic-rich horizon, which apparently contained plant remains. The sampled sediments were wet-sieved using various mesh sizes from 250 μm up to 1 mm and then air-dried. The residue was then manually screened for identifiable plant remains using a zoom binocular (Olympus SZX 16) with variable magnification between 7 and 115 times. Identification of plant remains was conducted using modern plant material from the carpological collection of the Herbarium Senckenbergianum (IQW) as a reference. The residue contained many woody remains, mainly bark fragments, which probably originate from conifers (most likely larch), but they were not identified in further detail as we did not have modern material in the reference collection available and the taxa in question are represented by other, easily identifiable organs such as seeds, fruits and needles.

RESULTS

We recovered 750 plant macrofossils from altogether 33 plant taxa. The abundance of individual taxa was not considered in detail because the number of preserved seeds and fruits does not necessarily reflect the actual percentage of plant taxa in the former vegetation but depends on taphonomic circumstances and other coincidences. The studied assemblage represents plants from a wide spectrum of habitats co-occurring in distances of few dozens to hundreds of meters probably during a period of few years. As the plant remains are partly tiny and are well preserved, a redeposition over long distances can be excluded. Plant species only occur under environmental conditions that meet their requirements and together with other plants with similar requirements. Their find thus indicates the presence of these conditions, habitats and communities even when the original set of plant species is incomplete and fragmentary. The recovered taxa were assigned to discrete plant communities according to the phytosociological classification following the ecological requirements of their modern representatives. They are listed in **Table 1** in the order of their probable occurrence in certain plant communities.

Open Woodland Vegetation–*Ledo palustris-Laricetalia cajanderi*

We found several boreal woody plants characteristic of the northern larch woodland that constitutes the zonal vegetation in the area today (Krestov et al., 2009). Several needles, fascicles and seeds indicate the presence of the Dahurian larch (*Larix gmelinii* s.l., **Figure 3**), which is competitive only under extreme cold continental climate in regions with continuous permafrost such as north-eastern Yakutia. We furthermore detected a pyrene

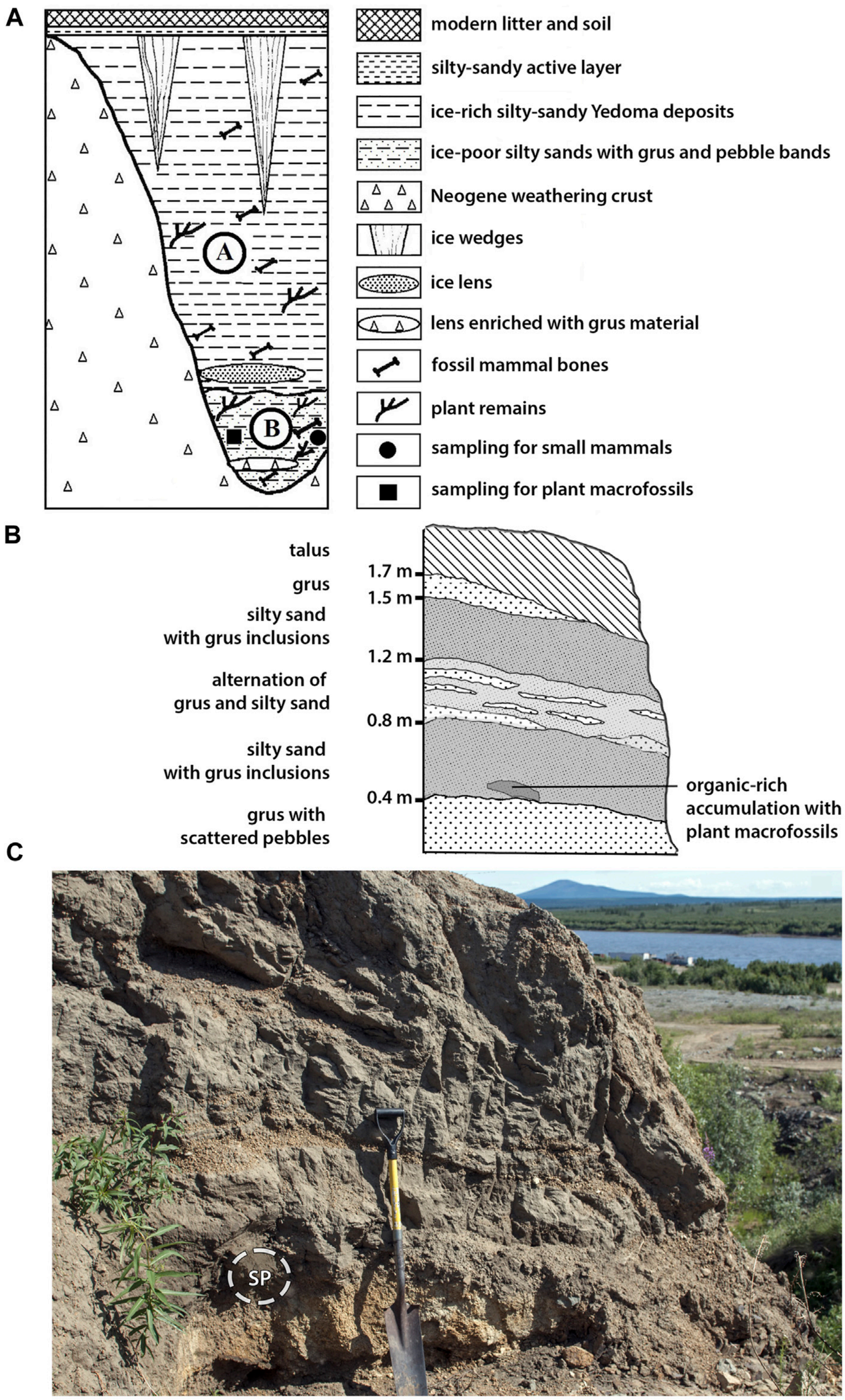

FIGURE 2 | (A) Scheme of the original stratigraphic sequence at the Cherskiy Ovrag reconstructed on the basis of long-term monitoring by S.P. Davydov. The upper unit A–the late Pleistocene Yedoma Ice Complex—became eroded in the frame of industrial exposure and subsequent thawing, which gave access to the underlying unit B–the Olyorian sequence. **(B)** Sketch and description of the Olyorian section (unit B) exposed at the time of sampling. **(C)** Photo of the studied exposure and sampling point (SP) within the sequence. In the background, the Panteleikha River and Mt. Panteleikha are visible.

TABLE 1 | List of the identified plant macrofossils and their classification into plant communities (syntaxa).

Vegetation	Taxon	Number of detected remains
Open larch woodland *Ledo palustris-Laricion cajanderi*	*Larix gmelinii* s.l.	32
	Betula cf. *fruticosa*	5
	Betula nana ssp. *exilis*	1
	Rubus idaeus	1
	Stellaria cf. *longifolia*	4
	Vaccinium vitis-idaea	1
Tundra steppe vegetation *Carici rupestris-Kobresietea bellardii*	*Empetrum nigrum*	2
	Arnica frigida	2
	Silene involucrata	6
	Ranunculus pedatifidus var. *affinis*	29
	Saxifraga cernua	23
	Papaver Sect. *Scapiflora*	42
	Phlox sibirica	5
	Smelowskia sp.	63
	Artemisia sp.	1
	Draba sp.	158
	Selaginella rupestris	1
	Festuca sp.	4
	Poa sp.	31
Meadow steppes *Festucetalia lenensis*	cf. *Koeleria* sp.	1
	Rumex Subgen. *acetosella*	2
	Androsace septentrionalis	17
	Potentilla arenosa	117
	Carex duriuscula	38
	Sibbaldianthe bifurca	2
nitrophile ruderals and saline meadows *Artemisietea vulgaris; Asteretea tripolii*	*Chenopodium* cf. *prostratum*	103
	Puccinellia sp.	5
	Urtica dioica	1
	Polygonum aviculare	1
Wetland and aquatic vegetation *Scheuchzerio-Caricitea nigrae; Charetea fragilis*	*Juncus biglumis*	2
	Luzula kjellmaniana	1
	Equisetum palustre	7
	Carex sp.	34
	Characeae	8
	sum	750

Dotted lines illustrate transitional synecological preferences, i.e., taxa may occur in two adjacent, ecologically similar communities.

of *Rubus idaeus*, which is characteristic for dry forest edges and glades, and frequently occurs after wildfires. The presence of birches is indicated by ancient fruits corresponding to those of *Betula* cf. *fruticosa* and *B. nana* ssp. *exilis*. Some wingless nutlets resemble those of tree birches (**Figure 3**), but it cannot be excluded that the remains stem from *B. divaricata* or even from *Alnus alnobetula* ssp. *fruticosa*, which have similar demands and often occur together. Shrub birches form the understorey of open larch forests and, as secondary woods, replace larches after disturbances such as wildfires and north of the tree line. Furthermore, *Vaccinium vitis-idaea* and *Empetrum nigrum* were detected as seeds. Both dwarf-shrubs are likewise typical for the understorey of open dry boreal woods and advance also beyond the tree line. Among forbs, we found seeds of *Stellaria longifolia*, which mainly occurs in the herb layer of boreal woodland. The shrubs and dwarf shrubs are light-demanding suggesting an open character of the groves.

Grassland Vegetation

The majority of identified plant remains originate from herbaceous taxa, which can be assigned to several grassland communities that together formed the ancient ecosystem or palaeo-biome mammoth steppe, steppe-tundra or tundra-steppe, in Beringia during Pleistocene cold stages (Yurtsev, 1972; Yurtsev, 1982; Yurtsev, 2001; Guthrie, 1982; Kienast, 2013). As the term tundra-steppe was only recently defined for the English description of the plant-sociological class *Carici rupestris-Kobresietea bellardii* occurring at dry places in the Arctic or in the alpine belt of mountains (Kucherov and Daniels, 2005), we will use, for description of the zonal vegetation during Pleistocene cold stages, the term mammoth steppe as proposed by Guthrie. As all biomes, the mammoth steppe can be regarded as a mosaic of different communities such as tundra steppe, meadow steppe and saline meadows occurring as a function of moisture, substrate, exposition, disturbances and other environmental factors. In the following, we will describe the grassland communities reconstructed on the base of phytosociology of modern vegetation.

Tundra Steppe Vegetation–*Carici rupestris-Kobresietea bellardii*

As mentioned above, tundra steppes are characteristic for dry, exposed places in the Arctic such as pingos as well as for equivalent habitats in mountains above the tree line. Tundra steppe communities often merge into steppe communities and a differentiation is sometimes difficult. In the Olyorian plant macrofossil assemblage of the Cherskiy Ovrag, remains of *Ranunculus pedatifidus* var. *affinis*, *Smelowskia* sp., *Saxifraga cernua, Silene involucrata, Phlox sibirica, Arnica frigida, Draba* sp., *Artemisia* sp., *Papaver* Sect. *Scapiflora*, and *Selaginella rupestris* were detected (**Figure 4**). They indicate, for the time of deposition, cold and dry conditions and, in particular, a thin snow cover in winter. Some species within the *Draba* and *Papaver*

FIGURE 3 | Olyorian macrofossils of woodland plants. 1–*Larix gmelinii* s.l., needle fragment, 2–*L. gmelinii* s.l., spur branch fragment with young needles preserved, 3–*L. gmelinii* s.l., seed from two sides, wing is not preserved but the attachment scar of the former wing is distinct, 4–*Betula* cf. *fruticosa*, nutlet with partly preserved wings from both sides, 5–*Betula* cf. Sect *Albae*, nutlet, wings are not preserved but maximum width in upper third suggests assignment to tree birch, 6–*Betula nana* s.l., nutlet with completely preserved wings from both sides, 7–*Empetrum nigrum*, seed from two sides, 8–*Vaccinium vitis-idaea*, seed from both sides, 9–*Stellaria longifolia*, seed from both sides, 10–*Rubus idaeus*, pyrene from two sides.

Sect. *Scapiflora* clades occur, aside from tundra steppes, also in Arctic pioneer vegetation (*Thaspithea rotundifolii*). Tundra steppe communities were a constitutive component in the vegetation complex of the Yakutian coastal lowlands during the last cold stage and were, in earlier publications, designated as *Kobresia*-meadows or as dry arctic upland vegetation (Kienast et al., 2005; Kienast, 2013) and later defined as tundra-steppe by Kucherov and Daniels (2005).

Meadow Steppe Vegetation–*Festucetalia lenensis*

During the cold stages of the Late Pleistocene, meadow steppes formed the primary vegetation in the extreme continental inner-Yakutian Yana Highlands, where the seasonal temperature gradient was higher and precipitation was likely even lower than in the Kolyma basin (Ashastina et al., 2018). The above-reported cryoxeric tundra steppe communities (*Kobresietea*) were largely absent there during the Late Pleistocene and completely replaced by meadow steppes (Ashastina et al., 2018). Remains of *Androsace septentrionalis, Potentilla arenosa, Festuca* sp., cf. *Koeleria* sp., *Poa* sp. and *Rumex* Subgen. *acetosella* are represented in the Olyorian palaeobotanical record from Cherskiy (**Figure 4**). Steppe vegetation reconstructed from plant macrofossil spectra in West Beringia was, in earlier papers (e.g., Kienast et al., 2005), subsumed under the European/West Asian steppes *Festuco-Brometea*. A revision of the phytosociological classification of Asian steppe vegetation followed only later (Ermakov et al., 2006) according to which the Eastern steppes of Mongolia, Transbaikalia and Yakutia form an own class (*Cleistogenetea squarrosae*) comprising two orders, true steppes (*Stipetalia krylovii*) and meadow steppes *Festucetalia lenensis*. True steppes have their northernmost occurrence currently in Central Yakutia, whereas meadow steppes primarily occur in less dry, more northern or mountainous areas often in a mosaic with herb-rich larch groves. In the study region at the lower Kolyma, appearances of thermophilic wormwood-grass-herb vegetation can be attributed to meadow steppes (Davydov et al., 2020). In the paleo-record of Northern Yakutia, they indicate warm and dry habitats such as south-exposed slopes. Some of the meadow steppe taxa found in the Cherskiy Ovrag occur in tundra-steppe communities as well.

Degraded and Saline Grassland–*Artemisietea vulgaris* and *Asteretea tripolii*

Several of the detected species, particularly *Potentilla* cf. *bifurca*, *Carex duriuscula*, *Chenopodium* cf. *prostratum*, *Polygonum aviculare,* and *Puccinellia* sp., (**Figure 4**) indicate either degradation of grassland vegetation or salt influence or both. *Sibbaldianthe bifurca* is regarded, together with *Carex duriuscula*, *Chenopodium prostratum*, and *Polygonum aviculare*, as indicator of overgrazing in severely degraded steppes of Mongolia and Russia (Hilbig, 1995; Abaturov et al., 2005). The plant community occurs today on disturbed, nutrient-rich, heavily compacted ground near yurts or resting places for livestock, often in the range of seasonally dry drainage channels. Such sites are, due to arid climate conditions, often slightly saline. The presence of alkali grass (*Puccinellia* sp.) in the Olyorian palaeo-record suggests salt accumulation in the soil due to high evaporation and resulting capillary rise of solutes. *Puccinellia* sp. was one of the most abundant taxa in Late Quaternary cold stage plant macrofossil assemblages from the Arctic coastal lowlands of Yakutia, which were situated, during the time of deposition, far inland and were affected by more continental, arid climate (Kienast et al., 2005; Kienast et al., 2011). Salt accumulation in the soil is due to the combined effect of aridity, a lack of drainage in depressions and permafrost preventing percolation of solutes (Yelovskaya et al., 1966). Also, the other listed plant taxa are, to a certain degree, halotolerant. *Chenopodium prostratum* is together with *Puccinellia* described from saline meadows on solonchak (salty soils) along the shore lines of shrinking lakes and ponds in relict steppe landscapes at the middle course of the Indigirka River often disturbed by horses seeking salt (Yurtsev, 1982). The species occurs, in the steppe zone, also in nitrophilous forb communities together with *Sibbaldianthe bifurca* and *Urtica dioica*. *Urtica dioica* occurs in various floodplain, woodland and forb communities as well as in moist eutrophic ruderal vegetation (Ellenberg, 1996). The occurrence of the species is controlled by the access to solved nitrogen and phosphorus (Šrůtek and Teckelmann, 1998) – nutrients that are, in modern taiga and tundra soils, deficient (Guthrie, 1982; Chapin et al., 1995) but might have been released by Pleistocene herbivores via urine and faeces (Weber, 1914; Johnson, 2009; Mania et al., 2010). The detection of an ancient *Urtica dioica* seed in the Olyorian assemblage (**Figure 3**) therefore indicates zoogenic nutrient enrichment of the ground suggesting that disturbances and compaction is likewise the result of the work of megaherbivores, which were abundant in the study area during the Olyorian period.

Arctic Wetland Vegetation–*Scheuchzerio-Caricitea*

The remaining taxa in the plant macrofossil assemblage of the Cherskiy Ovrag, *Juncus biglumis*, *Luzula kjellmaniana*, *Equisetum palustre*, Characeae, and *Carex* sp., can be assigned to wetland vegetation as it is typical for modern arctic tundra. The plants might have occurred near or, in the case of Characeae, in ponds or adjacent to snowbeds. As the fruits of *Carex* were only poorly preserved, we could not identify the remains down to the species level. Sedges occur in a variety of habitats in the high latitudes ranging from steppes like *C. pediformis, C. obtusata* or *C. duriuscula*, over tundra steppes like *C. rupestris* or *C. argunensis* to wetlands like *C. aquatilis* ssp. *stans* or *C. chodorrhiza*. The assignment of *Carex* remains to wetland vegetation is thus to be regarded tentative. Wetland plants are, in the studied assemblage, underrepresented suggesting that permanently wet habitats were, during the time of deposition, less common than today.

DISCUSSION

The composition of the studied Olyorian plant macrofossil assemblage of the Cherskiy Ovrag reflects predominant grassland vegetation consisting of meadow steppes and tundra steppes interspersed with wooded patches composed of cold-resistant deciduous trees and shrubs (*Larix gmelinii* s.l. and *Betula*). The results give the impression of a mosaic-like open landscape with sparse larch groves and are consistent with pollen and entomological data from the Krestovka site, about 160 km to the southwest of Cherskiy (**Figure 1**; Giterman et al., 1982), for the Olyorian mammal age. Like the Cherskiy Ovrag, the Krestovka site is situated at the junction of the Kolyma lowland and an upland, in this case the Yukagir Plateau, and the Chukochyan deposits at the Krestovka site display a similar lithology mainly comprising alluvial sand interspersed with sandy silt beds. In the pollen data, low levels of shrub taxa and larch are consistent with our data. Also, the abundance of Poaceae, *Artemisia,* Chenopodiaceae and Caryophyllaceae in the pollen spectra confirm steppe-like vegetation as reconstructed with our macrofossil data from the Cherskiy Ovrag. As described in the introduction, plant macrofossils from the Krestovka site mainly originate from aquatic plants such as *Sparganium*, *Menyanthes* and several *Potamogeton* species (Sher et al., 1979). The few terrestrial plant remains stem from *Larix* and *Rubus;* both taxa are preserved also in the studied deposits of the Cherskiy Ovrag.

In our results, the zonal vegetation, i.e., the vegetation that correlates with the macroclimate and that attains dominance under this climate, is represented by dry grassland, i.e., tundra steppe and meadow steppe. The majority of identified plant remains in both abundance and diversity belong to dry grassland taxa, which cannot tolerate shading, as occurring in closed woodlands, or surplus moisture in the active layer, as in tundra wetlands.

Among the mammals preserved in Olyorian deposits, there are several grassland taxa, which indicate an open landscape and steppe-like vegetation as well. *Saiga*, an immigrant from the zonal steppe belt, indicates dry climate, a thin snow cover, a firm ground or, respectively, a dry active layer and widespread grassland vegetation. Chenopodiaceae, detected in both the pollen and macrofossil data (*Chenopodium prostratum*), are, besides other steppe forbs, considered the basic food of saiga (Kahlke, 1999; Abaturov et al., 2005). The presence of the giant moose *Cervalces* with its iconic huge antlers suggests vegetation was open rather than consisting of closed taiga forests. Remains of steppe mammoth (*M. trongontheri*), and bones of archaic giant horses (*E. verae*) are also clue for open grassland and steppe like vegetation existing during the time of deposition. Steppe mammoths had already evolved abrasion-resistant teeth as an effective adaptation to relatively hard grass-rich diet and are thus indicators of steppe-like vegetation.

In the presented Early Olyorian (Early Pleistocene) plant macrofossil assemblage, the presence of trees and shrubs indicates interglacial-like temperature conditions but the dominance of dry grassland species and the occurrence of halotolerant plants suggests aridity, which is actually rather

FIGURE 4 | Olyorian macrofossils of grassland and ruderal plants. 1–*Arnica frigida*, modern cypsela without pappus as reference, 1–*A. frigida*, fragment of cypsela, upper part with preserved pappus ring, 3–*A. frigida*, fragment of cypsela, basal part with abscission scar, 4–*Artemisia* sp., cypsela from two sides, 5–*Saxifraga cernua*, ancient seed, 6–*Potentilla arenosa*, nutlets, 7–*Ranunculus pedatifidus* ssp. *affinis*, nutlet fragment (carpel) from two sides, 8–*Silene involucrata*, seed from two sides, 9–*Phlox sibirica*, valve fragment of seed pod, 10–*Smelowskia* sp., seed from both sides, 11–*Androsace septentrionalis*, seed from two sides, 12–*Rumex* Subgen. *acetosella*, nutlet from two sides, 12a–*R.* Subgen. *acetosella*, detail of nutlet surface, 13–*Selaginella rupestris*, megaspore from two sides, 14–*Draba* sp., seed from both sides, 15–*Papaver* Sect. *Scapiflora*, seed, 16–*Poa* sp., caryopsis from two sides, note the circular hilum near the base at the left picture, 17–*Festuca* sp., caryopsis from two sides, note the linear hilum at the centre of the fruit, 18–*Koeleria* sp., caryopsis from two sides, 19–*Puccinellia* sp., caryopsis from two sides, 20–*Chenopodium* cf. *prostratum*, seed from both sides, 21–*Polygonum aviculare*, nutlet from two sides, 22–*Carex duriuscula*, ancient nutlet from both sides, 22a–detail of surface, 23–*C. duriuscula*, modern nutlet for comparison, 23a–detail of surface, 24–*Sibbaldianthe bifurca*, nutlet from two sides, 25–*Urtica dioica*, ancient seed from two sides.

characteristic of cold stages. The palaeontological data suggest that the described grass and forb dominated open forest steppe persisted over a long period of time, i.e., during the entire Olyorian age as is indicated by pollen data from both the Chukochyan and the Akanian units at the Krestovka site continuously dominated by herb pollen, mainly from Poaceae, *Artemisia* and Chenopodiaceae and with only a small amount of larch and birch over all of the sequence (Giterman et al., 1982).

The Olyorian mammal age comprised a long period of time spanning from the late Early to the early Middle Pleistocene, i.e., 1.4–0.5 Ma (Sher, 1986) and, thus, included the Early-Middle Pleistocene transition (EMPT), which occurred about 1.25–0.7 Ma ago (between MIS 37, and MIS 18). The EMPT is described as a shift from relatively low-amplitude 41 kyr lasting climate cycles with a more or less symmetrical curve of warming and cooling to high-amplitude 100 kyr cycles with a more sawtooth-like pattern as result of abrupt warming followed by a slow descent of temperature (Pisias and Moore, 1981; Clark et al., 2006; Cohen and Gibbard, 2019). Prior to the EMPT, the amplitude of climate fluctuations was smaller and the duration of climate cycles was shorter, which possibly resulted, in West Beringia, in relatively dry, cool but more moderate climate that became progressively colder in the course of the EMPT but remained more stable than in other parts of the Holarctic. The palynological record from the composite sediment core of Lake El'gygytgyn, ICPD Site 5,011-1, about 467 km SE of the Cherskiy Ovrag provides valuable information on the regional history of vegetation and climate in West Beringia over the EMPT interval, i.e., between 1,091 and 715 kyr (Zhao et al., 2018). The pollen data indicate shrub tundra and cold steppe communities alternatingly dominating over the major part of the studied Early Olyorian period until MIS 24 (from 1,091 until 930 kyr) with Poaceae, Cyperaceae and *Artemisia* pollen and high contents of *Selaginella rupestris* spores prevailing during cold phases and increased amounts of *Betula* and *Alnus* (shrub birch and shrub alder) with sporadic occurrences of *Larix* during warm stages. The data suggest a gradual opening of the vegetation cover during this time period with a continuous but decreasing presence of larch in scattered woodland stands. The (supra-) regional pollen data thus indicate that the local vegetation we reconstructed for the Cherskiy Ovrag, consisting of grasslands in a mosaic with scattered woodlands, was widespread and existed over a long period of time. A hiatus in the pollen record comprised MIS 23.

MIS 22 around 890 kyr ago was a turning point in the West Beringian vegetation history as recorded in the El'gygytgyn core. Cold steppe biome scores in the pollen record significantly increased from this point in time onwards indicating accelerated aridification. The long-term cooling and aridification trend observed in the El'gygytgyn record corresponds with global ice-sheet expansion, sea-level lowering, coast-line shifts, shelf exposure and an intensified Siberian High and is considered additionally strengthened by the Tibetan Plateau uplift (Zhao et al., 2018).

The boundary between the lower and upper Olyorian, i.e., between the Chukochyan and Akanian was not yet exactly defined and is not preserved in a continuous geological record. But MIS 22 is a good candidate for this boundary as it represents the first high-amplitude glaciation that followed the 100 kyr periodicity. The switch from 41 to 100 kyr periodicity entailed long-lasting environmental changes resulting in the strengthening of aridification and the expansion of cold steppe vegetation and drove the evolution of cold and drought-resistant herbivores. The Chukochyan period therefore likely corresponds to the time prior to MIS 22. This phase was, according to the El'gygytgyn pollen record, characterized by a gradual expansion of grassland vegetation and the persistence of more or less scattered larch and shrub birch woodlands reflecting rather slow cooling and relative climatic stability. This relative stability of cold and dry climate over such a long period of time possibly resulted in the evolution of cold-adapted grazers and, eventually, of the mammoth steppe ecosystem.

The openness of vegetation is consequently not necessarily exclusively a function of climate in West Beringia but was probably also the result of megafaunal influence. The impact of the large herbivores on vegetation is documented in the macrofossil assemblage by plant taxa that are considered ruderal in modern vegetation, i.e., that occur at severely disturbed sites on nutrient-rich, compacted ground. Such taxa as *Carex duriuscula*, *Chenopodium prostratum*, *Sibbaldianthe bifurca* and *Polygonum aviculare* are resistant to overgrazing and trampling and are hardly competitive without regular disturbances of the plant cover, e.g., by herbivores. Steppe vegetation is fostered by the removal of woody plants due to decreasing shading and increasing insolation and evaporation. Steppes therefore replace woodlands in extremely continental areas at the middle courses of the Yana and Indigirka Rivers in Yakutia after wildfires (Yurtsev, 1982). In the Olyorian assemblage, the absence of any charcoal precludes that wildfire was the reason for the low percentage of trees and shrubs. Instead, the presence of nitrophilous pioneer plants such as *Sibbaldianthe bifurca* and *Urtica dioica* is rather an indication for zoogenic impact. Megaherbivores, especially proboscideans, are considered ecosystem engineers, which maintain vegetation openness, and in wooded landscapes, create mosaics of different structural types of vegetation with high habitat and species diversity (Johnson, 2009). Due to consumption of woody plants in winter and increased nutrient turnover, grasses and forbs are fostered by the presence of megaherbivores. The continuous existence of grassland vegetation and megaherbivores such as the steppe mammoth and, later, the evolution of the woolly mammoth in the study region demonstrates the importance of the unglaciated Arctic of Beringia as a cold laboratory for the evolution of the mammoth steppe biome – the ice-age ecosystem that, during the Middle and Late Pleistocene, spread over large proportions of the Northern hemisphere. Therefore, West Beringia can be regarded as the cradle of the mammoth steppe biome.

CONCLUSION

- A plant macrofossil assemblage from the Cherskiy Ovrag reveals the predominance of grassland vegetation composed of tundra steppes, meadow steppes and saline meadows in West Beringia during the Early Olyorian.
- The presence of larch and (shrub) birch as well as of dwarf shrubs, characteristic of the understorey of woodlands, indicates a mosaic-like interspersion of shrublands and larch groves in an altogether open landscape.
- Halotolerant plants indicate salt accumulation in the soil due to seasonally high evaporation.
- Nitrophytic ruderal plants suggest zoogenic impact on vegetation by nutrient enrichment, disturbances and compaction of the ground.

DATA AVAILABILITY STATEMENT

The original contributions presented in the study are included in the article/Supplementary Materials, further inquiries can be directed to the corresponding author.

AUTHOR CONTRIBUTIONS

SPD, as employee of the North East Science Station Cherskiy, continuously had access to the sections of the Cherskiy Ovrag over a long period of time, i.e., since 2001. He regularly studied the lithology and sedimentology of the sections, which were only temporarily and each time partially exposed and collected, over the years, numerous fossil mammal bones from both exposed units, the lower Olyorian (early Pleistocene) and the upper Yedoma (late Pleistocene). In the present paper, the description of topography, geology, lithology, geocryology and mammal remains recovered in the Cherskiy Ovrag base on the observations made by SPD in the course of his long-time monitoring. Sampling of organic-rich material was conducted by both authors, SPD and FK in 2015. FK conducted sieving of the sediment, screening of identifiable plant remains, identification of plant remains, their ecological interpretation, reconstruction of palaeo-vegetation and discussion of the results. FK wrote the article with contributions of SPD **Figure 1**, **3**, **4** are made by FK **Figure 2** bases on earlier publications of SPD and was adapted by both authors for the present paper.

FUNDING

The fieldwork was conducted with means from the Deutsche Forschungsgemeinschaft (DFG) in the frame of the research project TUNDRA-STEPPE (DFG project number 247453756) and was also partially conducted in the frame of the research project AAAA-A19-119030790003-1, Russia.

ACKNOWLEDGMENTS

We thank Elena Troeva, Kseniia Ashastina, North Eastern Federal University Yakutsk (NEFU) and the Alfred Wegener Institute for Polar and Marine Resarch Potsdam (AWI) for help in preparing, conducting and logistics of the fieldworks as well as Nikita and Sergey Zimov for hospitality and inspiring discussions. We are grateful to the anonymous reviewers who helped us to improve the article.

REFERENCES

Abaturov, B. D., Larionov, K. O., Kolesnikov, M. K., and Nikonova, O. A. (2005). State and Food Provision of Saigas on Pastures with Vegetation of Various Types. *Zoologichesky Zhurnal* 84 (3), 377–390.

Ashastina, K., Kuzmina, S., Rudaya, N., Troeva, E., Schoch, W. H., Römermann, C., et al. (2018). Woodlands and Steppes: Pleistocene Vegetation in Yakutia's Most continental Part Recorded in the Batagay Permafrost Sequence. *Quat. Sci. Rev.* 196, 38–61. doi:10.1016/j.quascirev.2018.07.032

Ashastina, K., Schirrmeister, L., Fuchs, M., and Kienast, F. (2017). Palaeoclimate Characteristics in interior Siberia of MIS 6-2: First Insights from the Batagay Permafrost Mega-Thaw Slump in the Yana Highlands. *Clim. Past* 13 (7), 795–818. doi:10.5194/cp-13-795-2017

Birks, H. H., and Birks, H. J. B. (2000). Future Uses of Pollen Analysis Must Include Plant Macrofossils. *J. Biogeogr.* 27 (1), 31–35. doi:10.1046/j.1365-2699.2000.00375.x

Boeskorov, G. G. (2019). To the Distribution and Taxonomy of a Fossil Soergelia, *Soergelia* Sp. (Caprinae, Bovidae, Artiodactyla, Mammalia), in Yakutia. *Zoologichesky Zhurnal* 98 (10), 1148–1155.

Campos, P. F., Sher, A., Mead, J. I., Tikhonov, A., Buckley, M., Collins, M., et al. (2010). Clarification of the Taxonomic Relationship of the Extant and Extinct Ovibovids, *Ovibos, Praeovibos, Euceratherium* and *Bootherium*. *Quat. Sci. Rev.* 29, 2123–2130. doi:10.1016/j.quascirev.2010.05.006

Chapin, F. S., III, Shaver, G. R., Giblin, A. E., Nadelhoffer, K. J., and Laundre, J. A. (1995). Responses of Arctic Tundra to Experimental and Observed Changes in Climate. *Ecology* 76, 694–711. doi:10.2307/1939337

Cirilli, O., Pandolfi, L., Rook, L., and Bernor, R. L. (2021). Evolution of Old World Equus and Origin of the Zebra-Ass Clade. *Sci. Rep.* 11 (1), 10156. doi:10.1038/s41598-021-89440-9

Clark, P. U., Archer, D., Pollard, D., Blum, J. D., Rial, J. A., Brovkin, V., et al. (2006). The Middle Pleistocene Transition: Characteristics, Mechanisms, and Implications for Long-Term Changes in Atmospheric pCO2. *Quat. Sci. Rev.* 25, 3150–3184. doi:10.1016/j.quascirev.2006.07.008

Cohen, K. M., and Gibbard, P. L. (2019). Global Chronostratigraphical Correlation Table for the Last 2.7 Million Years, Version 2019 QI-500. *Quat. Int.* 500, 20–31. doi:10.1016/j.quaint.2019.03.009

Davydov, S., Davydova, A., Schelchkova, M., Makarevich, R., Fyodorov-Davydov, D., Loranty, M., et al. (2020). Essential mineral Nutrients of the High-Latitude Steppe Vegetation and the Herbivores of mammoth Fauna. *Quat. Sci. Rev.* 228, 106073. doi:10.1016/j.quascirev.2019.106073

Davydov, S. P. (2007). "Features of Buried Fossil Fauna of mammoth Theriological Complex in Valleys of Low-Order Streams of the North East of Kolyma Lowland," in Proceedings of the IV International Mammoth Conference, Yakutsk, June 18–22.

Davydov, S. P., Boeskorov, G. G., Sher, A. V., Bakulina, N. T., Davydova, A. I., and Schelchkova, M. V. (2009). "Mammoth Fauna Burial Places of the Northeast Kolyma Lowland Submontane Zone," in P*roceedings of the International Conference Environmental Development of East Asia during the Pleistocene – Holocene (Boundaries, Factors, Stages of Human Mastering)*, Editor P.Y. Baklanov (Dal'nauka, Vladivostok, Russia), 49–51.

E.I. Troeva, A.P. Isaev, M.M. Cherosov, and N.S. Karpov (Editors) (2010). *The Far North: Plant Biodiversity and Ecology of Yakutia* (Dordrecht: Springer), 389.

Ellenberg, H. (1996). *Vegetation Mitteleuropas mit den Alpen in ökologischer, dynamischer und historischer Sicht*. 5th ed. Stuttgart: Eugen Ulmer, 1096.

Ermakov, N., Chytrý, M., and Valachovič, M. (2006). Vegetation of the Rock Outcrops and Screes in the forest-steppe and Steppe Belts of the Altai and Western Sayan Mts., Southern Siberia. *phyto* 36, 509–545. doi:10.1127/0340-269x/2006/0036-0509

Forstén, A. (1986). A Review of the Süssenborn Horses and the Origin of Equus Hydruntinus, *Quartärpaläontologie*, 6. Berlin, 43–52.

Giterman, R. E., Sher, A. V., and Matthews, J. V., Jr. (1982). "Comparison of the Development of Tundra-Steppe Environments in West and East Beringia: Pollen and Macrofossil Evidence from Key Sections," in *Paleoecology of Beringia*. Editors D.M. Hopkins, J.V. Matthews-Jr., C.E. Schweger, and S.B. Young (New York: Academic Press), 43–73. doi:10.1016/b978-0-12-355860-2.50011-9

Guthrie, R. D. (1982). "Mammals of the mammoth Steppe as Paleoenvironmental Indicators," in *Paleoecology of Beringia*. Editors D.M. Hopkins, J.V. Matthews-Jr., C.E. Schweger, and S.B. Young (New York: Academic Press), 307–326. doi:10.1016/b978-0-12-355860-2.50030-2

Hilbig, W. (1995). *The Vegetation of Mongolia*. Amsterdam: SPB Academic Publications, 258.

Johnson, C. N. (2009). Ecological Consequences of Late Quaternary Extinctions of Megafauna. *Proc. R. Soc. B.* 276, 2509–2519. doi:10.1098/rspb.2008.1921

Kahlke, R.-D. (1999). *The History of the Origin, Evolution and Dispersal of the Late Pleistocene Mammuthus-Coelodonta Faunal Complex in Eurasia (Large Mammals)*. Hot Springs, South Dakota: Mammoth Site, 219.

Kahlke, R.-D., García, N., Kostopoulos, D. S., Lacombat, F., Lister, A. M., Mazza, P. P. A., et al. (2011). Western Palaearctic Palaeoenvironmental Conditions during the Early and Early Middle Pleistocene Inferred from Large Mammal Communities, and Implications for Hominin Dispersal in Europe. *Quat. Sci. Rev.* 30, 1368–1395. doi:10.1016/j.quascirev.2010.07.020

Kaplina, T. N., Kartashova, G. G., Nikitin, V. P., and Shilova, G. N. (1983). New Data on the Sand Unite of the Tuostakh Depression. *Bulleten Komissii po izucheniyu chetvertichnogo perioda (Bulletin Quat. Commission)* 52, 107–122. in Russian.

Kienast, F. (2016). Studies of Modern Vegetation and Sampling of Permafrost Deposits for Palaeobotanical Studies at the Lower Kolyma. *Rep. Polar Mar. Res.* 697, 87–160.

Kienast, F. (2013). "PLANT MACROFOSSIL RECORDS | Arctic Eurasia," in *The Encyclopedia of Quaternary Science*. Editor S.A. Elias (Amsterdam: Elsevier), Vol. 3, 733–745. doi:10.1016/b978-0-444-53643-3.00213-2

Kienast, F., Schirrmeister, L., Siegert, C., and Tarasov, P. (2005). Palaeobotanical Evidence for Warm Summers in the East Siberian Arctic during the Last Cold Stage. *Quat. Res.* 63 (3), 283–300. doi:10.1016/j.yqres.2005.01.003

Kienast, F., Wetterich, S., Kuzmina, S., Schirrmeister, L., Andreev, A. A., Tarasov, P., et al. (2011). Palaeontological Records Indicate the Occurrence of Open Woodlands in a Dry Inland Climate at the Present-Day Arctic Coast in Western Beringia During the Last Interglacial. *Quat. Sci. Rev.* 30, 2134–2159.

Kozhevnikov, Y. P. (1981). "Botanical and Environmental Observations in the Kolyma Region at the Middle Course of the Berezovka River and the Cherskiy Settlement," in *Biology and Ecology of Plants of the Kolyma basin* (Vladivostok: Far East Branch Acad. Sci. USSR), 99–117. in Russian.

Krestov, P. V., Ermakov, N. B., Osipov, S. V., and Nakamura, Y. (2009). Classification and Phytogeography of Larch Forests of Northeast Asia. *Folia Geobot* 44, 323–363. doi:10.1007/s12224-009-9049-6

Kucherov, I. B., and Daniëls, F. J. A. (2005). Vegetation of the Classes *Carici-Kobresietea* and *Cleistogenetea Squarrosae* in Central Chukotka. *phyto* 35 (4), 1019–1066. doi:10.1127/0340-269x/2005/0035-1019

Maksimovich, S. V. (1998). Ecology of Steppe Soils and Vegetation in Far Northeastern Yakutia (Tundra and forest-tundra Zone). *Earth's Cryosphere* 2 (2), 26–32. in Russian.

Mania, D., Mai, D. H., Seifert-Eulen, M., Thomae, M., and Altermann, M. (2010). The Special Environmental and Climatic Character of the Late Middle Pleistocene Interglacial of Neumark Nord (Geisel Valley). *Hercynia N. F.* 43, 203–256.

Murton, J. B., Edwards, M. E., Lozhkin, A. V., Anderson, P. M., Savvinov, G. N., Bakulina, N., et al. (2017). Preliminary Paleoenvironmental Analysis of Permafrost Deposits at Batagaika Megaslump, Yana Uplands, Northeast Siberia. *Quat. Res.* 87 (2), 314–330. doi:10.1017/qua.2016.15

Murton, J. B., Opel, T., Toms, P., Blinov, A., Fuchs, M., Wood, J., et al. (2021). A Multimethod Dating Study of Ancient Permafrost, Batagay Megaslump, East Siberia. *Quat. Res.*, 1–22. doi:10.1017/qua.2021.27

Pisias, N. G., and Moore, T. C. (1981). The Evolution of Pleistocene Climate: A Time Series Approach. *Earth Planet. Sci. Lett.* 52, 450–458. doi:10.1016/0012-821x(81)90197-7

Romanovskii, N., Hubberten, H.-W., Gavrilov, A. V., Tumskoy, V. E., and Kholodov, A. L. (2004). Permafrost of the East Siberian Arctic Shelf and Coastal Lowlands. *Quat. Sci. Rev.* 23, 1359–1369. doi:10.1016/j.quascirev.2003.12.014

Russia's Weather Server (2021). *Weather of Russia*. Available at: meteo.infospace.ru.

Sher, A. V. (1971). Mammals and Stratigraphy of the Pleistocene of the Far North-East of the USSR and North America. Moscow: Nauka. in Russian). In English: Pleistocene mammals and stratigraphy of the Far Northeast USSR and North America. *International Geology Review* 16 (7-10), 1-284.

Sher, A. V. (1986). Olyorian Land Mammal Age of Northeastern Siberia. *Palaeontographia Italica* 74, 97–112.

Sher, A. V., Kaplina, T. N., Giterman, R. E., Lozhkin, A. V., Arkhangelov, A. A., Kiselyov, S. V., et al. (1979). "Scientific Excursion on Problem "Late Cenozoic of the Kolyma Lowland"," in *XIV Pacific Science Congress* (Moscow: Academy of Sciences USSR), 115.

Sher, A. V. (1997). "Late-Quaternary Extinction of Large Mammals in Northern Eurasia:A New Look at the Siberian Contribution," *Past and Future Rapid Environmental Changes*. Editors B. Huntley, W. Cramer, AV Morgan, H C Prentice, and JRM Allen (New York, United States: Springer), 319–339. doi:10.1007/978-3-642-60599-4_25

Sher, A. V., Weinstock, J., Baryshnikov, G. F., Davydov, S. P., Boeskorov, G. G., Zazhigin, V. S., et al. (2011). The First Record of "Spelaeoid" Bears in Arctic Siberia. *Quat. Sci. Rev.* 30 (17-18), 2238–2249. doi:10.1016/j.quascirev.2010.10.016

Šrůtek, M., and Teckelmann, M. (1998). Review of Biology and Ecology of *Urtica Dioica*. *Preslia, Praha* 70, 1–19.

Tomirdiaro, S. V. (1980). *Loess-ice Formation in Eastern Siberia during the Late Pleistocene and Holocene*. Moscow: Nauka, 184.

van der Valk, T., Pečnerová, P., Díez-del-Molino, D., Bergström, A., Oppenheimer, J., Hartmann, S., et al. (2021). Million-year-old DNA Sheds Light on the Genomic History of Mammoths. *Nature* 591, 265–269. doi:10.1038/s41586-021-03224-9

Weber, C. A. (1914). Die Mammutflora von Borna. – *Abhandlungen des Naturwissenschaftlichen Vereins zu Bremen* 23, 1–69.

Yelovskaya, L. G., Konorovsky, A. K., and Savinov, D. D. (1966). *Salt-Rich Soils above Permafrost (Kryosols) in Central Yakutia*. Moscow: Nauka. In Russian.

Yurtsev, B. A. (1972). "Phytogeography of Northeastern Asia and the Problem of Transberingian Floristic Interrelations," in *Floristics and Paleofloristics and Asia and Eastern North America*. Editor A. Graham (Amsterdam: Elsevier), 19–54.

Yurtsev, B. A. (1974). Steppe Communities of Chukotka Tundra and the Pleistocene "Tundra-steppe". *Botanicheskii Zhurnal* 59 (4), 484–501. in Russian.

Yurtsev, B. A. (1982). "Relics of the Xerophyte Vegetation of Beringia in Northeastern Asia," in *Paleoecology of Beringia*. Editors D.M. Hopkins, J.V. Matthews-Jr., C.E. Schweger, and S.B. Young (New York: Academic Press), 157–177. doi:10.1016/b978-0-12-355860-2.50018-1

Yurtsev, B. A. (2001). The Pleistocene "Tundra-Steppe" and the Productivity Paradox: the Landscape Approach. *Quat. Sci. Rev.* 20, 165–174. doi:10.1016/s0277-3791(00)00125-6

Zaslavskaya, T. M., and Petrovskii, V. V. (1994). Vascular Plants in the Environs of the Settlement of Cherskiy (North Yakutia). *Botanicheskii Zhurnal* 79 (2), 65–79. in Russian.

Zhao, W., Tarasov, P. E., Lozhkin, A. V., Anderson, P. M., Andreev, A. A., Korzun, J. A., et al. (2018). High-latitude Vegetation and Climate Changes during the Mid-pleistocene Transition Inferred from a Palynological Record from Lake El'gygytgyn, NE Russian Arctic. *Boreas* 47, 137–149. doi:10.1111/bor.12262

Conflict of Interest: The authors declare that the research was conducted in the absence of any commercial or financial relationships that could be construed as a potential conflict of interest.

Publisher's Note: All claims expressed in this article are solely those of the authors and do not necessarily represent those of their affiliated organizations, or those of the publisher, the editors and the reviewers. Any product that may be evaluated in this article, or claim that may be made by its manufacturer, is not guaranteed or endorsed by the publisher.

frontiers
in Earth Science

ORIGINAL RESEARCH
published: 19 November 2021
doi: 10.3389/feart.2021.723382

The Ice-Rich Permafrost Sequences as a Paleoenvironmental Archive for the Kara Sea Region (Western Arctic)

I. D. Streletskaya[1], A. A. Pismeniuk[1,2], A. A. Vasiliev[3,4], E. A. Gusev[2], G. E. Oblogov[3,4] and N. A. Zadorozhnaya[3]*

[1]Faculty of Geography, Lomonosov Moscow State University, Moscow, Russia, [2]All-Russia Institute for Geology and Mineral Resources of the World Ocean (VNIIOkeangeologia), Saint Petersburg, Russia, [3]Earth Cryosphere Institute of Tyumen Scientific Centre SB RAS, Tyumen, Russia, [4]Tyumen State University, Tyumen, Russia

OPEN ACCESS

Edited by:
Duane Froese,
University of Alberta, Canada

Reviewed by:
Alexander Kholodov,
University of Alaska Fairbanks, United States
Oksana Zanina,
Institute of Physical-Chemical and Biological Problems in Soil Science (RAS), Russia

****Correspondence:***
I. D. Streletskaya
irinastrelets@gmail.com

Specialty section:
This article was submitted to Cryospheric Sciences, a section of the journal Frontiers in Earth Science

Received: *10 June 2021*
Accepted: *11 October 2021*
Published: *19 November 2021*

Citation:
Streletskaya ID, Pismeniuk AA, Vasiliev AA, Gusev EA, Oblogov GE and Zadorozhnaya NA (2021) The Ice-Rich Permafrost Sequences as a Paleoenvironmental Archive for the Kara Sea Region (Western Arctic). Front. Earth Sci. 9:723382. doi: 10.3389/feart.2021.723382

The Kara Sea coast and part of the shelf are characterized by wide presence of the ice-rich permafrost sequences containing massive tabular ground ice (MTGI) and ice wedges (IW). The investigations of distribution, morphology and isotopic composition of MTGI and IW allows paleoenvironmental reconstructions for Late Pleistocene and Holocene period in the Kara Sea Region. This work summarizes result of long-term research of ice-rich permafrost at eight key sites located in the Yamal, Gydan, Taimyr Peninsulas, and Sibiryakov Island. We identified several types of ground ice in the coastal sediments and summarized data on their isotopic and geochemical composition, and methane content. We summarized the available data on particle size distribution, ice chemical composition, including organic carbon content, and age of the enclosing ice sediments. The results show that Quaternary sediments of the region accumulated during MIS 5 – MIS 1 and generally consisted of two main stratigraphic parts. Ice-rich polygenetic continental sediments with syngenetic and epigenetic IW represent the upper part of geological sections (10–15 m). The IW formed in two stages: in the Late Pleistocene (MIS 3 – MIS 2) and in the Holocene cold periods. Oxygen isotope composition of IW formed during MIS 3 – MIS 2 is on average 6‰ lower than that of the Holocene IW. The saline clay with rare sand layers of the lower part of geological sections, formed in marine and shallow shelf anaerobic conditions. MTGI present in the lower part of the sections. The MTGI formed under epigenetic freezing of marine sediments immediately after sea regression and syngenetic freezing of marine sediments in the tidal zone and in the conditions of shallow sea.

Keywords: permafrost, massive tabular ground ice, ice wedges, Kara Sea coast, stable isotope, paleogeography

INTRODUCTION

The ice-rich Quaternary deposits including ground ice of various types are widely present at the Western Siberia coast and the Kara Sea shelf. Despite that permafrost studies in Western Siberia were conducted for more than a hundred years, the conditions of the Quaternary sediments and ground ice genesis are still under debate.

Over the last 200 thousand years of Quaternary history, marine sedimentation has repeatedly changed with continental sedimentation on the coastal plains of the Western Arctic (Molodkov and Bolikhovskaya, 2009). Many geological sections of marine Pleistocene deposits include massive tabular ground ice (MTGI). The origin of these extensive ice bodies in Western Siberia is under continued debate. Some studies argued that it is buried glacial ice of Late Pleistocene (Solomatin, 1982; Kaplyanskaya and Tarnogradsky, 1986; Gataullin, 1988; Forman et al., 2002; Astakhov, 2009). The authors of this work support non-glacial genesis of the ice (Streletskaya and Leibman, 2003) and explain the position of the MTGI at the interface between two lithologic units: sandy sediments beneath and clay sediments above the ice body. Water segregation and intrusion through the deposits leave evidence of both water sources and the aquifer properties in the resulting MTGI. The following line of evidence support this explanation: i) MTGI bodies are found in littoral clay sediments of the Late Pleistocene (Streletskaya et al., 2008; Streletskaya et al., 2009); ii) heavy stable isotope composition and relationship between oxygen and hydrogen isotopes show that the MTGI in the marine sediments were formed *in-situ* within the ground (Streletskaya et al., 2012a; Streletskaya et al., 2013); iii) chemical signatures of the sediments and the MTGI indicate the possibility of intrusive origin of the MTGI (Streletskaya and Leibman, 2003; Streletskaya et al., 2006; Oblogov, 2016); iiii) high concentrations of methane trapped in the air bubbles within the MTGI and the stable isotope analysis of methane are indicative of ground ice formation (Streletskaya et al., 2018; Dvornikov et al., 2019; Oblogov et al., 2020; Semenov et al., 2020).

Upper 10–15 m of the Late Pleistocene - Holocene sections typically consist of ice-rich continental sediments of polygenetic origin containing syngenetic Ice Wedges (IW) of two ages (Late Pleistocene and Holocene). The formation of syngenetic IW occurs as a result of the snow and meltwater refreezing in the frost cracks (Mackay, 1974). In Nothwest Siberia and Yenisei North frost cracks form primarily between mid-January and mid-March (Podborny, 1978). Meltwater entering the cracks freezes rather rapidly preventing isotopic fractionation (Michel, 1990). The stable oxygen isotopic composition of ice wedges is correlated with mean winter and January temperatures (Vasil'chuk, 1992; Nikolaev and Mikhalev, 1995; Vasil'chuk, 2006; Streletskaya et al., 2015). In the Kara region many authors have described syngenetic polygonal-wedge ice occurring in the Pleistocene-Holocene mainly silty sediments (Danilov, 1978; Karpov, 1986; Kanevskiy et al., 2005; Vasil'chuk, 2006; Kritsuk, 2010). The most extensive complexes of ice-rich deposits containing syngenetic IW are found in the northern East Siberian lowlands, where they are called Ice Complex formations. The issue of terminology, genesis and distribution of ice complex (or "yedoma") causes a lot of discussion (Popov, 1953; Tomirdiaro, 1980; Péwé and Journaux, 1983; Schirrmeister et al., 2003; Bolshiyanov et al., 2008). Currently, the point of view about the polygenetic origin of this unique phenomenon is becoming more and more popular (Bolikhovsky, 1987; Romanovskiy, 1993; Kanevskiy et al., 2011). By the sediments of the ice complex, we mean ice-rich mainly silty, silty-sandy sediments with inclusions of organic remains, containing syngenetic IW. In contrast to Yakutia, the ice complex of West-Siberian North has a smaller thickness (up to 12 m), includes smaller IW and formed in the last stage of the Pleistocene and Holocene.

Ongoing debate about the origin of ice and insufficiently detailed studied of ice-rich permafrost sequences require further attention. This review summarizes the data on the ice-rich sediments of the Western Siberia coast obtained during numerous expeditions. The main goal of this study is therefore to identify the major characteristics of the ground ice and Quaternary deposits of Western Siberia, and to characterize permafrost evolution from the Late Pleistocene to the present. The specific objectives are to: i) collect all available data of the permafrost sections of Western Yamal, Gydan, and Yenisei North; ii) describe the cryostratigraphy of frozen sediments; iii) establish the conditions for the formation of ice-rich sediments and ground ice; iiii) develop a conceptual model of the Western Arctic paleogeography and show the difference with the ice complex formation in the East Siberia. This work summarized materials collected by authors during expeditions to the Kara Sea region over the last 16 years. **Table 1** presents location of key sites (**Figure 1**), time of fieldworks and main publications for each study site previously conducted by authors.

METHODS

Fieldwork

Eight Quaternary sections of the Western Siberia coast were documented, photographed and sketched, indicating the height of all layers and sampling locations. The sediments were collected at 0.3–1.0 m intervals for grain-size, organic matter and biostratigraphic indicators. Peat, wood fragments, and animal bones were collected for dating. The ground ice was sampled across the bedding of the ice body (the IW and MTGI is sampled along the horizontal and vertical profiles). When possible, the samples were transported to the laboratory in a frozen state. In the field, preliminary preparation and preservation of samples for transportation to the laboratory was carried out. Some of the samples in the form of monoliths of frozen sediments and ice were transported to laboratories in mobile refrigerators.

The gravimetric ice content (wt%) was estimated immediately after thawing by relating the weight of the frozen sample to the weight of the dry sample, expressed as weight percentage (%). More than 1,000 sediment samples were collected.

Stable Water Isotopes ($\delta^{18}O$, δD)

Stable isotopes $\delta^{18}O$ and δD from 344 samples were determined using Finnigan MAT Delta-S mass spectrometer at the isotope laboratory of the Institute for Polar and Marine Research (Potsdam, Germany). Isotopic composition is expressed in ppm (‰) relative to the V-SMOW standard (**Supplementary Table S2**). The analytical precision is better than ±0.8‰ for δD and ±0.1‰ for $\delta^{18}O$ (Meyer et al., 2000). The isotopic values of individual parameters are plotted in the δD – $\delta^{18}O$ diagram and compared to the Global Meteoric Water Line (GMWL) to determine the genesis of ground ice. The deviation of points from the GMWL is estimated by the amount of excess deuterium (d_{exc}).

TABLE 1 | Location of studied ice-rich permafrost sites and corresponding site-specific publications.

Location	Coordinates N	Coordinates E	Years of field studies	Main publications
MS – Marre-Sale Polar Station	69°41	66°48	2004–2019	Kanevskiy et al. (2005), Streletskaya et al. (2006), Streletskaya et al. (2013), Streletskaya et al. (2018); Oblogov et al. (2020)
EM - Ery-Maretayakha River Mouth	71°50	75°13	2010	Oblogov et al. (2012), Streletskaya et al. (2012a), Streletskaya et al. (2013)
MA-Matyuisale trading post	72°00	76°25	2010	Pismeniuk et al. (2019)
PS - Paha-Sale Cape	71°17	77°34	2010	Oblogov et al. (2012), Streletskaya et al. (2012b), Streletskaya et al. (2013)
SB - Sibiryakov Island	72°43	79°06	2008–2009	Gusev et al. (2011), Gusev et al. (2013), Streletskaya et al. (2012a), Oblogov, (2016)
DI – Dikson Settlement	73°30	80°33	2008–2010	Streletskaya et al. (2007), Streletskaya et al. (2011), Streletskaya et al. (2013), Oblogov, (2016)
KR – Khrestyanka River Mouth	72°58	80°51	2007	Streletskaya et al. (2007), Streletskaya et al. (2013), Oblogov, 2016
SK - Sopochnaya Karga Cape	71°53	82°40	2007–2010, 2014	Streletskaya et al. (2007), Streletskaya et al. (2011), Streletskaya et al. (2013), Oblogov, (2016)

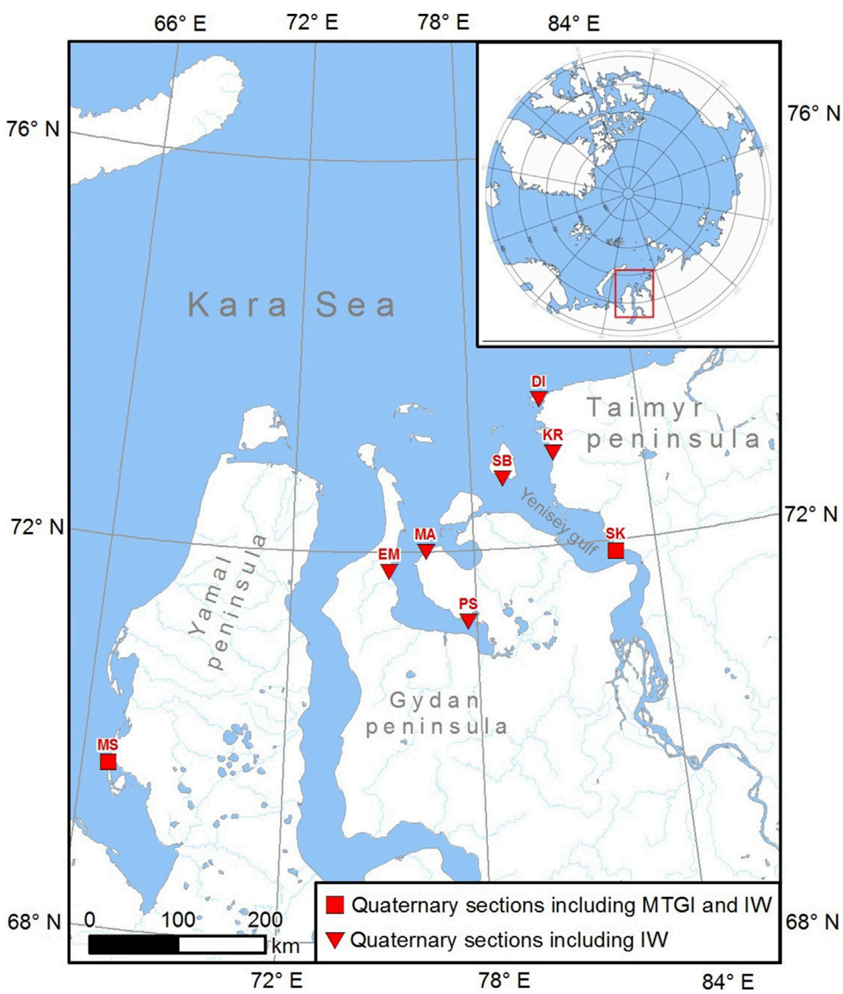

FIGURE 1 | Study region and location of key sites indicated in **Table 1**.

OSL and Radiocarbon Dating

Quaternary sediments were dated using radiocarbon dating (^{14}C), small samples was dated using accelerating mass spectrometry (AMS), and optical infrared stimulated luminescence (IR-OSL). The shells of marine and freshwater mollusks were dated by ^{14}C methods and AMS; wood remains, peat and mammalian bone remains by ^{14}C; enclosing parental strata such as sands and silts by IR-OSL.

Radiometric dating of 41 samples was held in in Geomorphology and Palaeogeography Laboratory of Polar Regions and the World Ocean (KÖPPENLab, Institute of Earth Sciences, St. Petersburg State University). Radiocarbon dating using the AMS was determined at the AMS Laboratory at the University of Arizona (two samples). Direct dates were calibrated using the «OxCal 4.4» program (https://c14.arch.ox.ac.uk). All radiocarbon dates through this paper are reported as uncalibrated ages (**Supplementary Table S1**).

OSL dates has been obtained from nine samples in IR-OSL in the Laboratory of Geochronology of the Quaternary Period, Institute of Geology, Tallinn University of Technology (IG TTU) (**Supplementary Table S1**).

Lithology and Geochemistry

The complex of lithological and geochemical analyses of soil and ground ice were conducted in the Laboratory of Lithology and Geochemistry of All-Russian Research Institute for Geology and Mineral Resources of the World Ocean (VNIIOceangeologia) in St. Petersburg, Russia. Grain size was determined by sieving and pipette analysis. The ion composition of the Quaternary deposits was determined from the water extract. Ground ice melts were preliminarily filtered to remove suspended matter. Subsequently, both in the water extract and in the ice filtrates, the concentrations of K, Na, Sr were determined by flame photometry, and Ca, Mg, Cl, SO_4, HCO_3 were determined by titration. Mineralization of ice was calculated from the sum of the cations and anions concentrations. Total organic carbon (TOC) was determined on Shimadzu TOC-VCSH analyzer using an IR detector with preliminary catalytic oxidation.

Methane concentrations were also determined in the two key study sites in the ground ice (Marre-Sale and Sopochnaya Karga Cape) and in enclosing ice sediments (Marre-Sale). Out of 920 samples collected at the Marre-Sale, 214 were collected from ground ice, 393 from frozen sediments. 25 samples were collected from ground ice at Sopochnaya Karga Cape. During 2012–2013 field seasons, the degassing of ice monolith samples was performed using a dynamic method of degassing by SUOK-DG degassing unit (Patent (19) RU (11) 2348931 (13) C1). Gas composition was determined by chromatography with flame ionization detector (FID) Shimadzu GC-2014 (Japan). After 2013, samples were degassed using a «head space» method (Alperin and Reeburgh, 1985) in the field and sent to the laboratory. Concentration of methane in gas phase was also determined in the Institute of Physical, Chemical, and Biological Problems in Soil Science RAS (Pushchino, Russia) using a gas chromatograph HPM.4 (Russia) with flame ionization detector. The difference of results obtained by two methods did not exceed the measurement accuracy. To determine the genesis of the MTGI, six samples collected at Marre-Sale were analyzed for δD (CH_4) content in the ISOLAB B.V. laboratory, Netherlands. Summary characteristics of the ground ice chemical composition provided in the **Supplementary Table S2**.

RESULTS

Marre-Sale Polar Station (MS)

The westernmost key site is located on the Yamal Peninsula near the Marre-Sale polar station. The Quaternary section here is well-studied and remains a reference for permafrost research (Forman et al., 2002; Kanevskiy et al., 2005; Streletskaya et al., 2006; Streletskaya et al., 2009; Kritsuk, 2010; Slagoda et al., 2012).

Two complexes of Quaternary deposits were investigated in the coastal cliff exposure about 30 m high (**Figure 2**). The upper complex on average 10 m thick consists of the Late Pleistocene-Holocene continental (alluvial, lacustrine) non-saline sands and sandy loams. Holocene sands, sandy loams and fragmentary peat found from the surface to 2–4 m depth (Unit 1). These deposits formed from 8.2 to 1.2 ka BP (**Supplementary Table S1**) (Forman et al., 2002; Slagoda et al., 2012). Sodium ions and bicarbonate ions predominate in the composition of water-soluble salts. The TOC content varies from 0.1 to 0.4%.

Holocene deposits are overlaying the Late Pleistocene deposits represented by sandy loams with layers of silt with inclusions of dark organic matter, lenses and pieces of peat and plant roots (2.0–10.0 m; Unit 2). The lower boundary of the complex contains an interlayer (0.2–0.3 m) of coarse-grained sands with fragments of wood, dark-colored pebbles and lenses of pure ice (2–5 cm). The salinity of sediments does not exceed 0.05%, sodium and bicarbonate ions dominate the composition of water-soluble salts. The values of TOC vary from 0.4 to 0.6%. The deposits have belt-like cryogenic structure. Interlayers are characterized by low ice content and a massive cryogenic structure (the Wt% is 16–20%), highly icy interlayers have small vertically oriented ice lenses (the Wt% is 35–55%). The average methane concentrations in the upper complex of Quaternary deposits are between 147 ppmV (0.08 ml/kg) and 269 ppmV (0.11 ml/kg) (Streletskaya et al., 2018).

The upper complex of continental deposits contains syngenetic IW of different ages. Larger wedges, 2.0–2.5 m wide at the top and 6–7 m long, form a grid with a polygon side of 10–20 m. The ends of the wedges penetrate the MTGI. According to S. Forman (2002), active formation of syngenetic IW occurred in MIS 3. The content of stable isotopes in the Upper Pleistocene ice wedges varies from −27.0‰ to −16.6‰ for oxygen, and from −208.0‰ to −123.7‰ for deuterium. The deuterium excess is 7.8‰ (**Supplementary Table S2**). Smaller Holocene wedges, 0.5–1.0 m wide at the top and 1.5–2.0 m long, form a grid with a polygon side of 6–8 m. The dating of peat fragments from IW gave an age close to 8 ka BP (**Supplementary Table S1**) (Forman et al., 2002). The stable isotope composition in Holocene ice wedges for oxygen varies in the range from −22,8‰ to −11.1‰ and for deuterium from −170.8‰ to −89.9‰ (**Supplementary Table S2**). The deuterium excess is 8.2‰. Mineralization of IW are about 84 mg/L for Holocene and 70 mg/L for Late Pleistocene IW respectively (**Supplementary Table S2**). Methane concentrations are 40 ppmV (0.04 ml/kg) in Pleistocene IW and 146 ppmV (0.16 ml/kg) in Holocene IW respectively (Streletskaya et al., 2018).

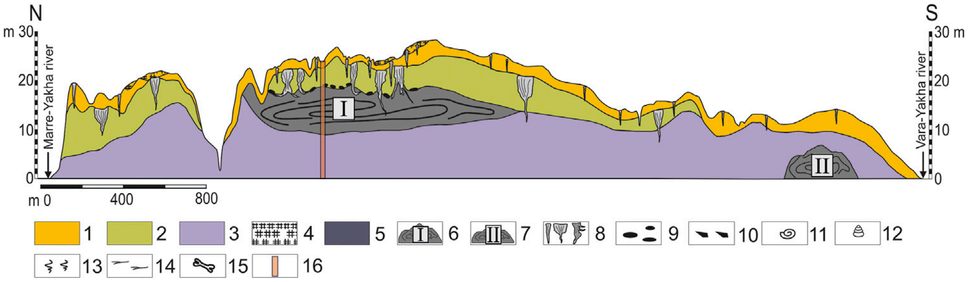

FIGURE 2 | Generalized cross-section of the exposure at Marre–Sale polar station (redrawn after to Forman et al. (2002), Kanevskiy et al. (2005), Streletskaya et al. (2006), Streletskaya et al. (2009), Kritsuk (2010)). Legend: 1 — Unit 1 – alluvial, eolian, deluvial solifluction (or slope), lacustrine deposits (MIS 1); 2 — Unit 2 – undifferentiated alluvial, alluvial-marine, lacustrine, slope deposits (MIS 2–3); 3 — Unit 3 – undifferentiated marine, lagoon-marine deposits (MIS 6–4); 4 — peat (without distinction as to age); 5 — bedrocks; 6 — MTGI (1 type); 7 — MTGI (2 type); 8 — ice wedges shown outside of scale (without distinction as to age); 9 — rounded pebble; 10 — coarse gravel; 11 — sea mollusks; 12 — fresh-water lacustrine shells; 13 — detritus inclusions; 14 — wood debris inclusions; 15 — the place of mammoth carcass find; 16 — sections of grain size sampling in accordance with the **Figure 10**.

The lower complex represented by the saline marine clays and loams, which formed prior to MIS 3 (Unit 3). The salinity of clays varies from 0.02 to 0.30% with sodium chloride composition. The layer has no visible organic inclusions; the mean TOC is 0.84%. The clays have a large-scale reticulate cryostructure (Wt% is 30–60%). Marine clays were freezing epigenetically after of retreating sea. Average concentration of methane in clay (or loam) is 3,875 ppmV (2.02 ml/kg) (Streletskaya et al., 2018).

Two types of MTGI are included in the lower complex of marine sediments. The MTGI of first type located in the contact of the saline marine clays and continental sandy-clayey sediments. MTGI is 3–10 m thick and 300 m long. Sandy loam and sand alternating with dislocated ice layers up to 1.5 m thick represent it. The particle size distribution of mineral inclusions in ice varies: sandy inclusions are from 10 to 91%, silty - from 6 to 62%, clay - from 10 to 36%. In general, the amount of sand particles in the MTGI decreases with depth, while the proportion of clay and silt increases. Heavy minerals of the sand fraction in clay are well sorted. The cryostructure of the ice-soil interlayers in the MTGI is microlenticular. Folded deformations are often observed within MTGI. The layer contains inclusions of well-decomposed organic matter. The TOC content in MTGI increases to 1.1–1.3%, in presence of silty and clay particle inclusion within the ice, but only 0.16%, where sandy particles dominate. Salinity of clay layer in MTGI reaches 0.7%. The composition of the salts remains sodium chloride. The content of stable isotopes in the MTGI varies from −21.5‰ to −17.2‰ for oxygen, and from −165‰ to −129‰ for deuterium (**Supplementary Table S2**). The deuterium excess is 7.9‰. The second type is the clear homogeneous MTGI in marine clay with 6–8 m thick and 150–200 m long, visible part submerging below the sea level. The transition from overlying clay sediments to MTGI is marked by the change in cryostructure from layered to reticulate and coarse-block (block size about 30 × 20 cm, ice lenses 0.5–1 cm thick). The MTGI have rare mineral inclusions. Based on the results of mineralogical analysis clay particles predominate, the presence of marcasite indicates hydrogen sulfide contamination of freezing water. The isotope composition (**Supplementary Table S2**) of ice varies from −21.9 to −7.5‰ for oxygen and from −163.7 to −67.9‰ for deuterium (D), d_{excess} is 6.4‰. MTGI has unevenly distributed rounded and horizontally elongated air bubbles of 1–2 mm in diameter. The air bubbles contain methane. Methane concentrations from bubbles into MTGI are on average 1,413 ppmV (1.57 ml/kg) for the first type and 558 ppmV (0.62 ml/kg) for the second type respectively (Streletskaya et al., 2018). Mineralization of MTGI varies from 23 to 260 mg/L for the first type and from 32 to 218 mg/L for the second type of ice respectively (**Supplementary Table S2**).

Ery-Maretayakha River Mouth (EM)

The cross-section (**Figure 3**) of the western coast of the Gydan Bay is exposed in the coastal cliff consisting of thermo-denudation surfaces (15–28 m a.s.l) and the thermo-abrasive cliff descending to the modern beach near the Ery Maretayakha River mouth (Oblogov et al., 2012; Streletskaya et al., 2013). Two layers of IW are exposed in the section. Vasil'chuk (1992) obtained dates of the Late Pleistocene peat-mineral complex at Mongatalyangyakha river mouth, close to the section from 34.8 (3.5 m a.s.l.) to 26.3 (5.9 m a.s.l.) ka BP (**Supplementary Table S1**). As a result, the age of the lower part of the Ery-Maretayakha section relates to MIS 3 (Kargino horizon in the modern Pleistocene stratigraphic scheme of West Siberia).

The upper part of the EM section to a depth of 4.7 m consists of ice-rich frozen lacustrine deposits. Partially decomposed peat alternate with large interlayers of pure ice near the surface. The age of the peat is 9.5 ka BP (**Supplementary Table S1**) (Oblogov et al., 2012). Lower, ice-rich sandy silts (Unit 1) contain peat, plant roots and fossils of fresh-water mollusks (the silt particles content is more than 54%). The value of TOC reaches 0.9%. The peat deposits are dated to the Early Holocene (**Supplementary Table S1**). The cryogenic structure is belt-like; the Wt% is on average 53%. Holocene IW are 1.2 m wide at the top and 3.6 m long. Late Pleistocene IW are 2.5 m wide at the top and more than 10 m long. The isotopic composition of the upper-layer IW

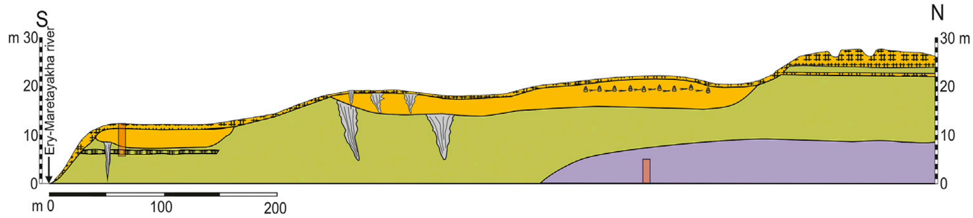

FIGURE 3 | Generalized cross-section of the exposure at Ery-Maretayakha River mouth (adopted from Oblogov et al. (2012)). See legend for **Figure 2**.

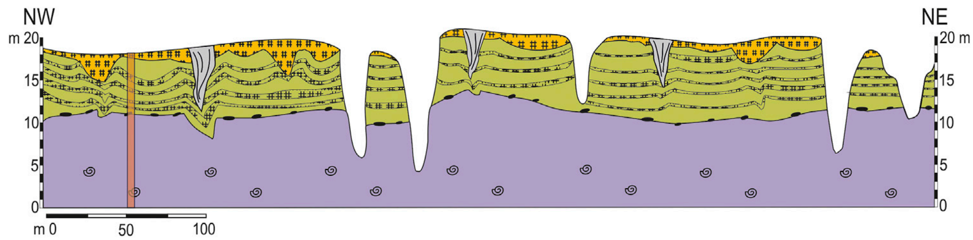

FIGURE 4 | Generalized cross-section of the exposure at Matyuisale trading post (redrawn after to Pismeniuk et al. (2019)). See legend for **Figure 2**.

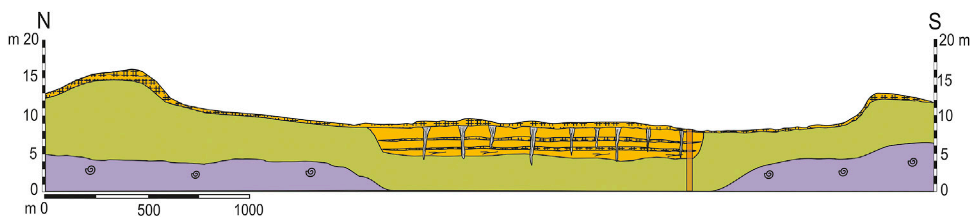

FIGURE 5 | Generalized cross-section of the exposure at Pakha-Sale Cape (redrawn after to Oblogov et al. (2012)). See legend for **Figure 2**.

changes from −23.6 to −18.3‰ for oxygen and from −179.9 to −134.3‰ for deuterium; the deuterium excess changes from 9 to 12‰ (**Supplementary Table S2**). Mineralization of Holocene ice is 212 mg/L (**Supplementary Table S2**).

Unit 2 represents Late Pleistocene alluvial silty sandy loams. The sandy fraction in the unit increases with depth, in contrast TOC decreases to 0.2%. Closer to the river mouth silty and sandy loams alternate with fine-grained sands and peat with massive cryostructure. The Wt% decreases with depth from 54 to 27%. The peat interlayer in sandy sediments has the age of 26.3 ka BP (**Supplementary Table S1**). The content of oxygen and hydrogen stable isotopes in the Late Pleistocene ice wedge does not change with depth and is from −24.6 to −22.6‰ for oxygen and from −193.1 to −176.5‰ for deuterium; the deuterium excess does not exceed 6–7‰. Mineralization of Late Pleistocene ice is 126 mg/L (**Supplementary Table S2**).

In the northern part of the section, the sandy silts from the 20 m depth cover ice-rich clays (Unit 3). The clays have a high content of TOC (0.89%) and the Wt% from 26 to 33%. The clays have reticulate cryogenic structure, which indicates the epigenetic freezing of deposits.

Matyuisale Trading Post (MA)

The cross-section near the Matyuisale trading post consists of two units (**Figure 4**). The upper is peat-mineral complex with the inclusion of ice wedges; the lower one is represented by saline marine clays. The peat layers dated from 41.2 ka BP at 7 m a.s.l. to 8.7 ka BP at 9.1 m a.s.l. (**Supplementary Table S1**). Accordingly, continental conditions were established in the region of 41–42 thousand years ago.

The thickness of the peat-mineral complex (Unit 2) varies along the section from 5 to 10 m. It represents alternating layers of peat, yellow-brown sands, sandy loams and loams with belt-like cryogenic structure. The deposits are silty with silt particles comprising up to 85%. There is a lot of visible organic matter in the sediments; the organic carbon content varies from 0.49% in silty clays to 2.15% in sandy loams. The Wt% of the sediments in the upper part varies from 39.8 to 71.8%. At the boundary with the underlying saline clays, brown-gray silty sandy loam with

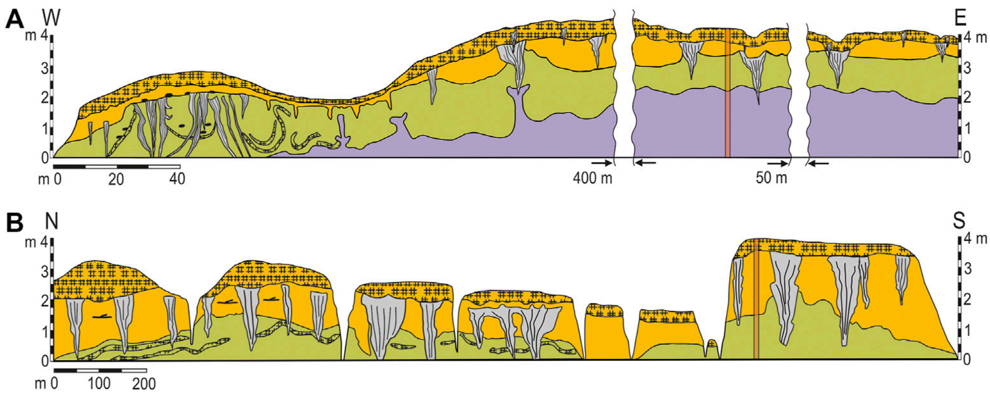

FIGURE 6 | Generalized Quaternary section of the exposure at Sibiryakov island (**A** – southern coast; **B** – western coast) (redrawn after to Streletskaya et al. (2012b), Oblogov (2016)). See legend for **Figure 2**.

interlayers of fine-grained sand and a distinct 0.1 m pebble horizon is present. The TOC in the layer is about 0.41%. The Wt% sediments at the lithological boundary with clays is 36.1%.

In the upper part of the peat-mineral complex, ice wedges are 1.5–2.0 m wide at the top and more than 5 m long. Stable isotope content in ice varies from −19.2 to −17.2‰ for oxygen and from −143.5 to −127.9‰ for deuterium (**Supplementary Table S2**). The deuterium excess is on average 9‰. The ice mineralization is 37 mg/L (**Supplementary Table S2**). At the lateral contacts of some wedges with the enclosing sediments, a distinct iron framing, repeating the shape of the wedge is observed. This indicates that its formation occurred along the ice-wedge casts of an older ice wedge. Late Pleistocene IW completely thawed in the area. The Holocene ice wedges occasionally infiltrated into ice-wedge casts.

In the lower part of the section (up to 15 m a.s.l.) dark gray saline clays are exposed (Unit 3). Cryogenic structure differs across the section from reticular to prismatic. There is no visible organic matter in the clays, but the values of TOC are quite high (0.48–0.53%). The clays have a high content of sedimentary marine (NaCl) salts, which indicates their marine genesis. Salinity is more than 0.37%. The marine unit contains very rare fragments of mollusks (Hiatella arctica, Macoma calcarea, etc.). The Wt% varies from 36.1% (11 m a.s.l.) in sandy loams to 16.4% (6 m a.s.l.) at the boundary with clays.

Pakha-Sale Cape (PS)

In the 10–17 m high coastal cliff from Paha-Sale Cape to Nyada-Sale Cape, Late Pleistocene-Holocene continental sediments cover older marine unit (**Figure 5**).

The lens of lacustrine sediments (Unit 1) up to 4–6 m thick and 1,200 m long contains organic-rich sandy loams (the TOC reaches 1%) with a layered cryostructure. Light sandy loams at 2–4 m depth transform into heavy sandy loam. The silt particles content increases from 35% at 1.4 m depth to 56% at 3.7 m depth. The Wt% increases from 33% at 1.4 m depth to 64.7% at 3.2 m depth. The cryostructure of the sandy loam is finely reticulate, postcryogenic. These are deposits characteristic of the talik. The lake was filled with sediments from the Early to Middle Holocene (from 8.8 to 6 ka BP; **Supplementary Table S2**). Lacustrine deposits include IW complex. Ice-wedges have the 0.2–0.5 m wide at the top and the 2–5 m long. The IW isotopic values are on average −19.1‰ for oxygen and −146.2‰ for deuterium; the deuterium excess is 7.2‰. Mineralization of ice is 17 mg/L (**Supplementary Table S2**). Gray fine-grained sands of Unit 2 underlie silty sandy loam. The sands have the massive cryostructure. The Wt% is 22.4%. Marine clays with a rich fauna of marine mollusks (Unit 3) underlie the section. The Wt% at the contact of clays and silty sandy loam is 64.1%.

Sibiryakov Island (SB)

Sibiryakov Island located at the northern part of the Yenisei Gulf. It is relatively flat with average height decreases from the central part (25–33 m a.s.l.) to the coastal area (3–5 m a.s.l.).

Southern coastal cliff about 2.0–4.5 m a.s.l. consists of three units (**Figure 6A**). Holocene peat with an admixture of sand up to 0.5–1.5 m thick form the uppermost layer. Peat began to form at the surface around 3.7 ka BP (**Supplementary Table S1**). Under the peat layer, a layer of gray oblique-bedded sandy loams and sands (Unit 1) is located and has plant remains. The cryostructure is massive or lenticular. The upper and lower boundaries are gradual. The Unit 2 is composed of stratified iron rich sands up to1.2–2.0 m thick with traces of deformation, inclusions of pebbles, gravel, plants and peat. The content of water-soluble salts in sands does not exceed 0.06%. The average value of TOC in the sands is 0.26%. The deposits have massive cryogenic structure. The Wt% is 21–30%. Content of silt fraction in deposits reaches 75%. The amount of TOC increases to 1.3%. The unit dated from 13.3 to 31.4 ka BP (**Supplementary Table S1**). Sands overlie dark gray saline (salinity is 0.7%) silty sandy loam of marine genesis (Unit 3). The deposits formed in MIS 3, the older date is 45.8 ka BP obtained by the IR-OSL method (**Supplementary Table S1**).

The western coastal cliff up to 3.5 m a.s.l. (**Figure 6B**) consists of two units. Autochthonous peat is exposed from the surface to a depth of 0.5–1.5 m. Below the section, peat is replaced by layered

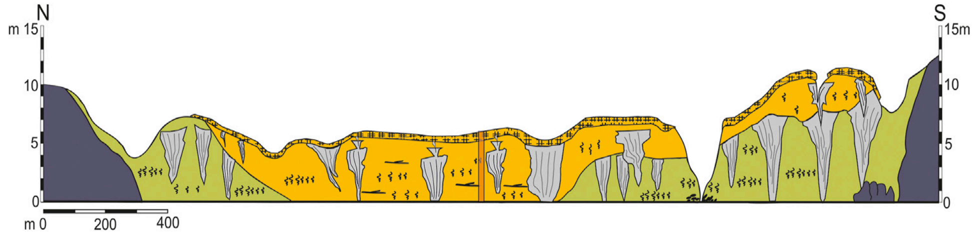

FIGURE 7 | Generalized cross-section of the exposure at Dikson village (redrawn after to Streletskaya et al. (2013)). See legend for **Figure 2**.

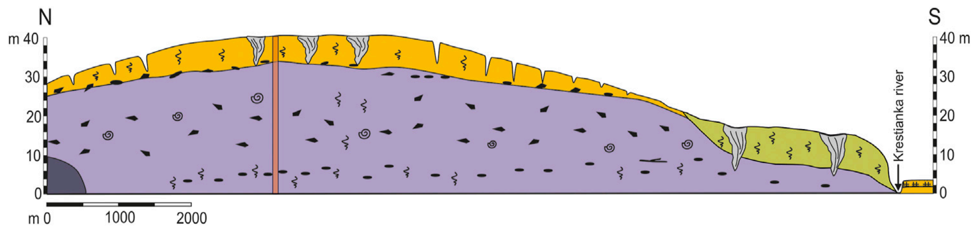

FIGURE 8 | Generalized cross-section of the exposure at Khrestianka River mouth (redrawn after to Streletskaya et al. (2013)). See legend for **Figure 2**.

gray silty sandy loam (0.5–3.0 m thick) with traces of iron, lenses of sand, inclusions of peat and wood. The date from sandy loams, obtained by the IR-OSL method, is 8.6 ka BP (Gusev et al., 2013). Ice wedge casts are present. The postcryogenic texture indicates syngenetic formation and freezing of the sediments. Sandy loams have massive cryogenic structure (Wt% less than 25%), sandy loams are ice-rich (Wt% is 90%) with a lenticular-mesh cryostructure only at contacts with ice wedges. From a 2.5 m depth sandy loams are ice rich with lenticular and suspended cryostructure (the Wt% is more than 60%). The sands underlying the sandy loam have a massive cryostructure (the Wt% is 30%).

In the sandy loams, ice wedges up to 2 m height spaced by 8–10 m were found. The width of the IW at the top does not exceed 1.5 m. The sandy loam enclosing ice wedges are strongly iron-rich, some of the IW repeat the form of ice wedge casts, penetrate into the sediments of Unit 2 and possibly sediments of Unit 3. The isotope content in ice wedges varies from −22.1 to −16‰ for oxygen and from −167.5 to −121‰ for deuterium. Mineralization of ice is about 58 mg/L (**Supplementary Table S2**).

Dikson (DI)

The most complete section of Quaternary sediments was studied in the Dikson area where two layers of IW are exposed in the coastal cliff (**Figure 7**).

The Quaternary section consists of two units containing syngenetic IW. According to the results of radiocarbon dating (**Supplementary Table S1**), the Holocene unit accumulated 9.8 to 3.7 ka BP (Gusev et al., 2011). The deposits are homogeneous in particle size distribution and consist of silty-sized particles, which number increases with depth from 82 to 96%. The TOC in the sediments of upper unit 1 is 0.6–1.2% and reaches 2.1% due to inclusions of peat and wood fragments. In the deposits including Late Pleistocene IW (Unit 2), the TOC is about 0.6%. Organic matter is uniform in the section. The ice-rich deposits (Wt% is over 86%) have a rhythmically layered structure typical for syngenetic deposits.

The visible thickness of the deposits is about 10 m, but the IW continues below the sea level. The width of the Late Pleistocene wedges at the top reaches 6 m, the thickness - 10 m and more. The width of the wedges of the Holocene unit at the top is up to 4 m, the thickness varies from 2–3 to 7 m. Late Pleistocene IW in the area have a width from 0.4 to 3 m at top and more than 5 m thickness. The isotopic composition of Pleistocene IW show changes of values from -26.8 to -22,9‰ for oxygen and from -205 to -175‰ for deuterium. The isotopic values of the Holocene IW varies from -21.2‰ to -14.8‰ for oxygen and from -159‰ to -108‰ for deuterium (**Supplementary Table S2**) (Streletskaya et al., 2011). Ice mineralization increases from 47 mg/L (Holocene IW) to 360.5 mg/L (Late Pleistocene IW) (**Supplementary Table S2**).

Khrestianka River Mouth (KR)

Quaternary deposits are overlaying Permian bedrocks in the 12–40 m high coastal cliff of the Yenisei Bay from Cape Makarevich to the Khrestianka River mouth (**Figure 8**).

Holocene deposits (Unit 1) are exposed in the southern part of the section. The main section part is a levelled surface of the Yenisei terrace 35–40 m high with baydzherakhs (residual-thermokarst mounds). To the south, the surface of the terrace descends to 18–23 m high and turns into the slope of the Krestyanka River valley (12–20 m a.s.l.). The upper part of the

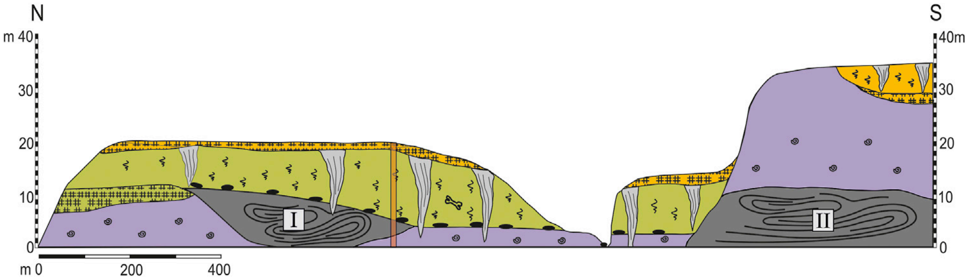

FIGURE 9 | Generalized cross-section of the exposure at Sopochnaya Karga Cape (redrawn after to Streletskaya at al. (2013)). See legend for **Figure 2**.

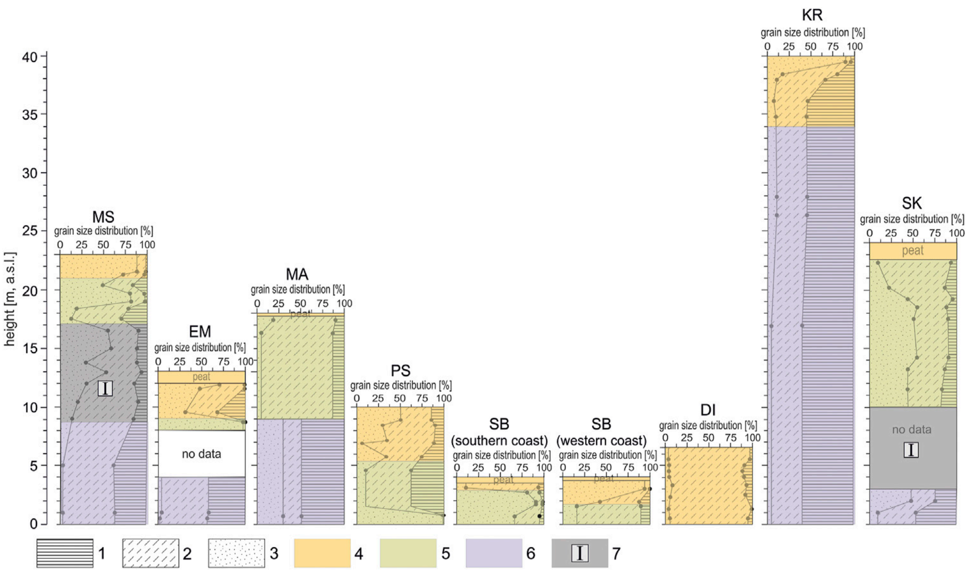

FIGURE 10 | Grain size distribution patterns of studied ice-rich permafrost sequences. Legend: 1–3 – Grain size composition in accordance with the V.V.Okhotin (1933) classification: 1 – clay, loam; 2 – sandy loam; 3 – sand; 4–6 – Units: 4 – Unit 1 – alluvial, eolian, deluvial solifluction (or slope), lacustrine deposits (MIS 1); 5 – Unit 2 – undifferentiated alluvial, alluvial-marine, lacustrine, slope deposits (MIS 2–3); 6 – Unit 3 – undifferentiated marine, lagoon-marine deposits (MIS 6–4); 7 – MTGI (1 type).

section contains dark brown silty sandy loams (Unit 2) with peat fragments 5–7 m thick. Silt fraction in deposits reaches 83%. Sandy loams contain 0.05–0.14% of soluble salts with prevailing sodium and chloride ion composition. Sandy loams have numerous detritus; the TOC content is 0.7–0.9%. The deposits are ice rich (the Wt% reaches 80%), have belt-like cryostructure and contain large syngenetic IW. Ice wedges are about 9 m thick and 3–4 m wide at the top and form the polygonal topography. The average values of the isotope composition vary from −23.5 to −22.0‰ for oxygen and from −179.7 to −167.7‰ for deuterium. Within a single wedge, isotopic composition is rather similar (Streletskaya et al., 2011). Deuterium excess is from 8.2 to 10.2‰) (**Supplementary Table S2**). The lower part is represented by marine clays of Pre-Kargino age (Unit 3). The age and genesis of this unit were previously discussed (Streletskaya et al., 2013; Gusev et al., 2016; Oblogov, 2016).

Sopochnaya Karga Cape (SK)

Several exposures of Quaternary deposits containing MTGI and ice wedges (**Figure 9**) were studied 6 km from Sopochnaya Karga Cape (Streletskaya et al., 2011; Streletskaya et al., 2013).

The upper part of the section from the surface to 1–2 m depth is represented by poorly decomposed peat. The formation of this layer began about 11 ka BP (Gusev et al., 2011). In the southern part of the section at 30–35 m a.s.l., Holocene lacustrine deposits (Unit 1) with IW 5 m thick and 0.4 to 3.0 m wide are exposed. These deposits are ice-rich (the Wt% exceeds 80%) and have distinctive belt-like cryogenic structure. The underlying peat layer is dated to the Holocene optimum (**Supplementary Table S1**) (Streletskaya et al., 2012b). The range of $\delta^{18}O$ in Holocene IW is −23.3‰ to −17.1‰, and the range of δD is −175‰ to −122‰. The deuterium excess is 11.6‰ (Streletskaya et al., 2011). Ice mineralization from Holocene IW is 22 mg/L (Supplementary

Table 2). Methane concentrations in Holocene ice wedges on average are 74 ppmV (0.08 ml/kg) (Streletskaya et al., 2018).

Stratified yellow-gray silty sandy loams and sands with interlayers of peat 4–10 m thick are located below (Unit 2). These deposits contain plant roots; the TOC reaches 2.0%. Salinity does not exceed 0.06%. Bicarbonate and sodium ions prevail among the ions. The amount of silt particles and organic impurities decrease with depth, sandy loam turns into coarse-grained and gravelly sands. Grain-size and mineral analysis of the gravel horizon present at the contact of clays and sands suggests alluvial channel of a large river downstream. The carcass of a woolly mammoth was found at a depth of 6 m in 2012. The dates of it ranged from 42.2 ka BP to 47.3 ka BP (Maschenko et al., 2017; **Supplementary Table S1**). In the north of the section central part, under the sandy loam stratum, peat interlayers are exposed, the age is more than 42.3 ka BP (Streletskaya et al., 2013). Sandy loam and sands (MIS 3- MIS 2) contain syngenetic IW about 10 m thick and 2–3 m wide at the top. The lower narrow parts of the wedges penetrate into the clays by 0.5–1.0 m, in some parts of the section they continue below sea level. The values of isotopic composition range from −26.9 to −21.7‰ for $\delta^{18}O$ and −204.8 to −164.8‰ for δD. The deuterium excess is 7.2‰ (**Supplementary Table S2**) (Streletskaya et al., 2011). Ice mineralization in Late Pleistocene IW varies from 57 mg/L to 266 mg/L. Methane mean concentration in Pleistocene IW is 55 ppmV (0.06 ml/kg) (Streletskaya et al., 2018).

Dark gray clays (Unit 3) are underlain the section and have a visible thickness from 2 to 30 m. The sediments are saline (salinity up to 1.5%) and are classified as marine by the composition of water-soluble salts. The amount of the TOC in the clay deposits is 0.8–1.0%. The Wt% of clays varies along the section from 30–53 to 130%. Along the section, MTGI 35 m thick is exposed. The lower boundary of the ice layer is below the sea level. The MTGI represents frequent alternation of pure ice layers and relatively ice-rich soil. Inside the ice-soil layer large irregular mineral blocks of 0.4–1.0 m by 0.1–0.4 m^2 are present. Blocks contain dark gray clay with inclusions of pebbles and boulders with a diameter up to 0.4 m. Mineralization of ice varies from 311 mg/L to 1,068 mg/L(**Supplementary Table S2**). Ion composition shows the prevalence of bicarbonate-ions. Among cations, sodium-ions dominate, with concentrations increasing towards the center of MTGI. Stable isotope content in ice is rather constant and is −23‰ for oxygen and −174‰ for deuterium. The deuterium excess is on average 5.8‰ (**Supplementary Table S2**). This MTGI is similar to the first type of MTGI exposed at Marre-Sale, but has smaller methane concentration with an average of 301 ppmV (0.33 ml/kg) (Streletskaya, 2018). The MTGI of second type has the same characteristics as MTGI (II) of the Marre-Sale section.

DISCUSSION

Cryolithology

Three major sedimentary units were determined. Grain size composition of the studied sediments and the boundaries between the identified sedimentary units summarized in **Figure 10**.

Marine clays deposits formed during MIS 6-4 were found in the lower parts of the sections in almost all of the studied sites and comprise the oldest sedimentary unit (Unit 3). The deposits are represented by heavy loams and clays with a reticular, incompletely reticulated, or massive cryogenic structure with few inclusions of boulders and pebbles. On average, the ice content of mineral interlayers of loamy deposits is 20–30%, the total ice content is 40–50%. The deposits include a faunal complex characteristic of the Arctic seas margins. Freezing of the clay strata began after the sea regression, accompanied by frost cracking and the formation of the lower epigenetic parts of ice wedges. The transition from subaquatic to subaerial conditions marked by strong iron oxidizing along the edges of block units in the upper part of the clay horizon. With an increase in depth, iron oxidizing becomes less intensive and is confined mainly to fractured zones. The size of mineral blocks increases with depth, and the ice content of deposits decreases, which indicates a slowing of the freezing rate. In some outcrops, for example the SK section, a sedimentation break is observed which is marked by the development of erosion processes. As a result, there was a partial removal of the upper part of the clay strata.

The marine clays of Unit 3 in the MS and SK sites includes massive accumulations of very ice-rich sediments or practically pure ice with a relatively small amount of mineral inclusions - massive tabular ground ice (MTGI). Plicative and disjunctive deformations are often observed in ice-rich formations. The transition from overlying clays to MTGI is emphasized by a change in the cryostruture of the deposits from layered to irregularly meshy and coarse-blocks (block size about 30 × 20 cm, lenses 0.5–1 cm thick). Heavy minerals of the sand fraction in clay impurities in the MTGI are distinguished by almost perfect sorting. This distribution of particles is typical for sediment formed in shallow sea or near-delta part of river involving longshore currents and wave processing. The most probable origin hypothesis of the MTGI bodies occurring in marine clays is injection. This assumption can explain many structural features, such as high thickness and length, the presence of plicative and disjunctive deformations, and a large number of mineral inclusions.

Loamy-clayey marine deposits of Unit 3 are overlain by horizons of unsorted alluvial-marine, lacustrine, slope deposits of various compositions accumulated during MIS 2–3 (Unit 2). In the KR section, brown-gray loams and clays with a comminuted structure and oxidized iron along the cracks, represent this unit. In the SK section, sediments of this age compose the second terrace of the Yenisei River and are represented by layered sandy loams and fine sands of 4–10 m thick. A well-preserved mammoth carcass was discovered in these sediments, the radiocarbon age of which was about 37–44 ka BP (Maschenko et al., 2017). Alluvial-lacustrine sediments include large syngenetic IW up to 10 m long and 3–4 m wide at the top. In the DI site, silty ice-rich deposits of the MIS 2 (Sartan age), containing thick ice wedges form a specific stratum of the Ice Complex ("yedoma"). The lower narrow ends of ice wedges penetrate into the Unit 3. The syngenetic nature of accumulation and freezing is indicated by the layering of the deposits, which is emphasized by the belt cryogenic structure. Ice-rich deposits often have a microscale cryogenic structure with vertically oriented lenses and a total ice content of 30–55%. Less icy sandy deposits are characterized by a massive cryostructure with a total ice content of 15–20%. Sandy ice-rich sediments in the MS section contain lenses and interlayers of pure glassy ice. This horizon is classified as Type 1 of MTGI. The horizon is an alternation of sub-horizontal (dislocated) layers of ice from a few centimeters to 1.5 m thick in sandy, sandy loam deposits.

Alluvial, alluvial-marine, lacustrine, and slope deposits of Unit 2 in all sections are overlain by a horizon of sandy, sandy loam alluvial, lacustrine, aeolian, deluvial deposits, or by peat of Holocene age (Unit 1). Cryostructure of sandy loams and sands are mainly massive, as well as semi-layered or oblique, consistent with sedimentary bedding. Ice content varies from 15% in sands to 70–80% in silty syngenetic sediments. The silty sandy loam and sandy deposits of Unit 1 are enveloping, for example, as in the MS and KR sections. Often, deposits of Unit 1 occur locally as inserts in earlier deposits, such as the lacustrine deposits in the PS site and in the southern part of the SK site. The Unit 1 deposits contains the complex of ice wedges. In the DI site, silty syngenetic sediments of the Holocene age are similar with composition, cryostructure, and other features to the underlying Pleistocene deposits. In the PS site, the embedding of Holocene lacustrine sediments with a thickness of 4–6 m and visible length of about 1,200 m was investigated. The lens consists of sandy loam saturated with organic matter. With increasing depth, light sandy loams turn into heavy sandy loams, the amount of organic content decreases, the content of silt particles increases from 35% at 1.4 m depth to 56% 3.7 m depth. Ice content increases with depth from 33% at 1.4 m depth to 65% 3.2 m depth. The cryostructure of sandy loam is layered. Lacustrine sandy loam transforms into silty sandy loam, characterized by a fine-mesh post-cryogenic structure (during thawing the sediments crumbles into small pieces). These deposits characteristic of the talik formed under lake.

Geochronology and Stratigraphy

Results of radiocarbon dating showed the formation of ice wedges occurred from more than 47 ka BP near Sopochnaya Karga Cape to about 3.6 ka BP on Sibiryakov Island (**Supplementary Table S1**). The stratification of ice rich sequences varies from site to site (**Figures 2–9**). In some cases, the ice-rich continental sediments cover ice-rich marine sediments with MTGI dated over 70 ka BP (Molodkov and Bolikhovskaya, 2009). The key outcrops have similar structure in terms of the sequence of lithological complexes, the change in the genesis and age of the enclosing sediments and the presence of organic material. Part of the sections of the Late Pleistocene - Holocene lies directly on the bedrock of the folded complex of Taimyr (DI), while the main part of the reference sections lies on the Cenozoic sedimentary rock material of the West Siberian basin.

The geochronological referencing of the studied complexes to local stratigraphic subdivisions (units) of Western Siberia was made based on the most typical to the region Kazantsevo horizon (MIS 5), the stratotypes of which are reliably dated along the Yenisei River to the south of the study area (Gusev et al., 2016), as well as at the study area (Streletskaya et al., 2007). At the base of the coastal cliffs of the Yenisei, Yenisei Gulf, Yamal and Gydanskaya Bay, basement loams of the Middle and Late Pleistocene are often exposed, which sometimes include thick MTGI. Ice wedges are usually found stratigraphically higher, in MIS 3 – MIS 1 sediments. Holocene sediments containing IW are discoveres in all key sites. The filling of thermokarst depression in some sections (EM, PS, SK) occurred in two stages. Deposits accumulated during the first stage in the beginning of the Holocene. They got into the lake during the destruction of coasts formed by dusty sandy silts with high ice content. Peat accumulates in the second stage of filling depressions. Holocene organic and peat-bearing sediments, accumulating mainly from the Early Holocene, top the section but in some places these settings persisted throughout the Holocene.

Geochemical Study of Ground Ice

Late Pleistocene IW and enclosing sediments have mineralization of ice from 25 to 266 mg/L with prevailing hydrocarbonate and calcium ions. The chloride content does not exceed 30% in the DI and MS areas, its content in IW of other key sites is much lower (in EM – 10%; in SK – 16%). Holocene IW and enclosing sediments is also have low salinity. Mineralization of ice is 17–360 mg/L with prevailing hydrocarbonate, chloride and sodium ions. The chloride content exceeds 30%, and it reaches 50% among the anions in the DI, SB and MS sections. The exception is Holocene IW of the EM section where the chloride content does not exceed several percent. The low mineralization and the predominance of hydrocarbonates most likely indicate the atmospheric nature of the water which formed IW in the Late Pleistocene and Holocene.

For chlorides, a direct correlation was established between the concentrations of ions in the snow cover with the average and total concentrations in atmospheric precipitation over the period of the snow cover occurrence. Forming over the sea surface, winter precipitation can contain sea salts, which are transported over large distances. The chemical composition of ice in Holocene and modern ice wedges (MS, SB, and DI) is dominated by the "marine" elements (Cl and Na), which reflects the closer position of the coastline (Kotov, 1991; Streletskaya and Vasiliev, 2009; Vasil'chuk, 2016). Winter precipitation was formed in the continental conditions, when the land occupied the modern shelf during the last cold stage (MIS 2) to 120 m depth. Domination of chloride and sodium ions in chemical composition of Late Pleistocene IW determines the increasing proximity of the sea in the Holocene. The large variability in mineralization and ion content in Holocene IW is determined by the dynamics of the sea ice cover. At EM, MA, PS, SK sections the amount of chloride in ice wedges is less owing to the preservation of ice in the Yenisei Bay and Gydan Bay in summer. In glacial cores of the ice field of the Nordaustlandet (Svalbard) and Vavilov glacier (Severnaya Zemlya), variations of the main «sea» components in the ice content correlate in time with the dynamics of the sea ice cover (Korzun, 1985).

The chemical composition of MTGI reflects the composition of groundwater before freezing (Anisimova, 1981; Streletskaya and Leibman, 2003; Vasil'chuk, 2016; Ivanova, 2012).

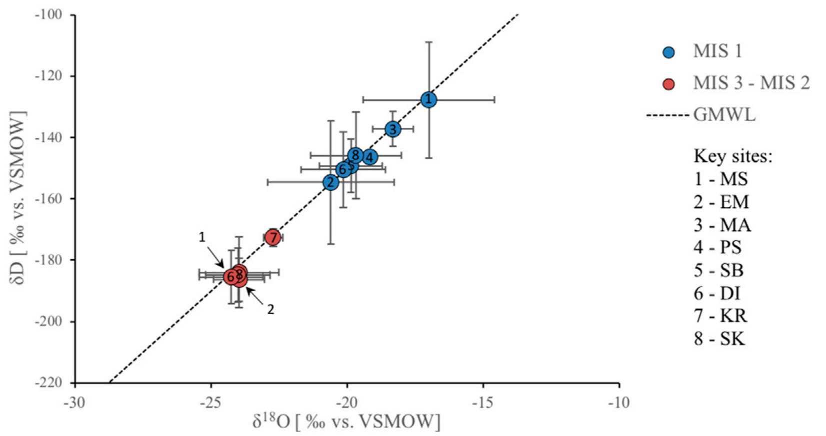

FIGURE 11 | Compilation of stable isotope data ($\delta\ ^{18}O$, δ D) in Late Pleistocene and Holocene generations of syngenetic ice wedges (IW) exposed at the Kara Sea. Ice-wedge data sources: Holocene (MIS 1) and Late Pleistocene (MIS 2–3) (see **Supplementary Table S1**). Data are shown with respect to the Global Meteoric Water Line (GMWL) (Craig, 1961).

Mineralization of MTGI of both types varies from 23 to 1,068 mg/L and depends on the degree of "pollution" of the formation ice with mineral inclusions, but mostly determined by a mechanism of MTGI formation. Mineralization in MTGI of first type depends on the amount of mineral admixture in the ice: less and more mineralized interlayers alternate. Mineralization in MTGI of second type increases with depth, sodium predominates among cations, and its content increases to 92% with depth. In all samples, the sodium ion predominates among the anions. An increase in mineralization with depth is typical for freezing of closed talik systems (Anisimova, 1981). Mineralization of MTGI is in a wide range, but the composition of the salts dominated by sodium chloride. The results of geochemical analysis make it possible to confirm the subsoil conditions for the MTGI formation (MS and SK).

Methane in Frozen Sediments and Ground Ice

The methane content in ground ice and frozen sediments has been studied in the Marre-Sale and Sopochnaya Karga sections. Detailed characteristics of methane concentration were provided in previous works (Streletskaya et al., 2018; Oblogov et al., 2020). Sediment type have a strong influence on the methane concentration in permafrost. The highest methane concentrations are characteristic for marine clays of the Pre-Kargino time (MIS 3 and older). Here, the methane content averages 3,875 ± 3,468 ppmv (mean ± standard deviation), the minimum methane content is typical for sandy sediments of MIS 2 – MIS 1 - 195 ± 265 ppmv. Thus, despite the high variability, the methane content can serve as an indicator of the formation conditions of deposits and can be useful as an indicator for the geological and geocryological classification. The methane content in IW also differs depending on their age. In the Holocene IW, the methane content of 146 ± 241 ppmv is higher than in Late Pleistocene IW of 40 ± 82 ppmv. Large difference in the methane content in IW can also be useful to estimate the IW age. The MTGI represents a high methane content - up to 1,500 ± 2,400 ppmv. For instance, the methane content in the MTGI is about 100–1,000 times higher than in the ice sheets of Antarctica and Greenland (Raynaud, 2012). This confirms the non-atmospheric, subsoil genesis of the MTGI.

Stable-Isotope Composition of Ground Ice

Ice wedges have been widely used to reconstruct winter climate conditions across Siberia at glacial/interglacial timescales (Vasil'chuk, 1992; Streletskaya et al., 2013; Meyer et al., 2015; Streletskaya et al., 2015; Opel et al., 2017; Porter and Opel, 2020). Stable isotope compositions for different generations of ice wedges were analyzed for a reconstruction of the palaeoclimate environment. The stable isotope variations of relict ice wedges are used for qualitative inferences of winter temperature. It is given for ice wedges of nine geocryological sections. The isotopic composition of ice wedges on Kara Sea coasts is highly variable throughout time, ranging between −27‰ and −11‰ for $\delta^{18}O$ and from −208‰ to −90‰ for δD. We have observed a relatively constant stable isotopic composition within a single IW. For all ice wedges including recent ice wedges, the mean d_{excess} varies between 5 and 12‰. Recent ice wedges, sampled in the active layer have heavier isotopic compositions around −17.0‰ for $\delta^{18}O$ and −121.0‰ for δD (Streletskaya et al., 2011).

The Holocene ice wedges characterized by relatively heavy isotopic composition. The ice wedges of the Pakha-Sale Cape, Gydan Bay show a mean isotopic composition around −20.4‰ for $\delta^{18}O$ and −154.2‰ for δD. The ice wedges of the Dikson and Sopochnaya Karga show a same isotopic composition around −20.6‰ for $\delta^{18}O$ and −154.0‰ for δD (**Figure 11**).

The accuracy of paleotemperature estimates based on isotope trends in relict ground ice depends on the assumptions that the precipitation seasonality of relict ice and the relationship between

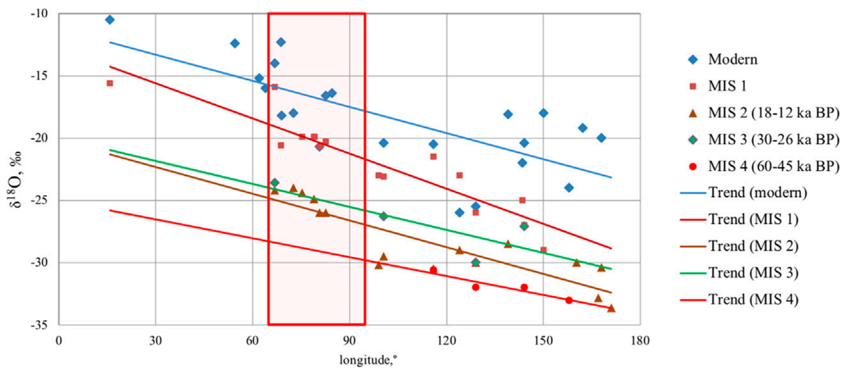

FIGURE 12 | Spatial distributions of oxygen stable isotopes $\delta^{18}O$, ‰ and their trend lines in ice-wedges-formed at different times in the Russian Arctic (after Streletskaya et al. (2015)). The study area is marked with a red rectangle.

precipitation-isotope ratios and air temperatures were constant. Ice-rich permafrost can be very resilient and survive even several interglacials (Wetterich et al., 2019).

Non temperature-related effects in the isotope record under the land–ocean configuration (e.g., sea level, ice sheet topography) which was different from today with possible differences in moisture source and trajectory of moist air parcels were previously discussed (Jouzel, 1999). We have summarized mean ice-wedge $\delta^{18}O$ data across the northern high latitudes for several periods: MIS 3 (30–26 ka BP), MIS 2 (18–12 ka BP), Holocene (last 12 ka BP), and modern (last several decades) in order to examine broad spatial and temporal patterns.

Temperature estimates (Vasil'chuk, 1992) show that average January temperature in the Dikson area dropped to −40 ± 3°C during Late Pleistocene IW formation. This is approximately 12–15° lower than the average January air temperatures (according to the Dikson meteorological station, the average January temperature is −25.5°C). Calculation of the average January air temperature using the same equation (Vasil'chuk, 1992) showed that for the Taimyr central regions (Cape Sabler), winter temperatures 18,000 years were the same or slightly lower (Derevyagin et al., 1999). The isotopic composition of the Late Pleistocene – Holocene IW in western Taimyr is close to the isotopic composition of IW on the Laptev and East Siberian coasts (Magens, 2005; Romanenko et al., 2011).

The isotopic composition of Holocene ice wedges reflects a higher temperature in winter and the influence of the sea. Active cracking and growth of syngenetic IW are associated with dry winters in the Holocene. Holocene ice wedges are heavier than older ones by an average of 6 ppm in oxygen isotope content depending on the location.

The similarity of ice formation conditions from Taimyr to Alaska makes it possible to use isotope data as correlation markers (Romanenko et al., 2011). The number of stable oxygen isotopes in Late Pleistocene ice wedges decreases from west to east (**Figure 12**) by 1–2‰; we observe the same reduction of isotopic composition in Holocene ice. The isotopic composition of ice wedges in the Late Pleistocene deposits, formed 12–25 ka BP, varies along the meridian in a narrow range. The direction of atmospheric transport from west to east has remained unchanged since the end of the Pleistocene.

Syngenetic IW with similar isotope content grew on Sverdrup Island and other Arctic islands (Tarasov et al., 1995, Romanenko et al., 2011). Severe winters at the time of ice formation are reconstructed based on the light isotopic composition of ice. The evidence of the hard continental conditions at the end of the Pleistocene on the Kara Sea shelf is the existence of relict subsea permafrost.

The content of stable oxygen isotopes in the MTGI of first type ($\delta^{18}O$) varies from −22 to −17‰ and for δD from −165.2 to −129‰. Deuterium excess changes from 5 to 10‰. Ice soils at the contact of the continental and marine units of the Marre-Sale sediments lay on the Global Meteoric Water Line (GLMW) along with data on ice wedges. The values of oxygen isotopes in the MTGI (SK) do not change extremely along the section and average −23‰, the values of d_{exc} are from 2 to 9‰. Thus, the MTGI of type I formation can be explained by the freezing of meteoric waters in an open system.

The MTGI of second type overlain by marine saline deposits have isotopic values that do not fall on the GMWL; their distribution is described by a line with a slope far from 8, which apparently indicates freezing of the initial waters in a closed system. The values of stable isotopes in the ice (MS) $\delta^{18}O$ varies from −22 to −7.5‰ and for δD - from −164‰ to −68‰. Deuterium excess varies from −1 to 12‰. With depth, isotopic compositions of ice becomes lighter. Values of the d_{exc} less than 10‰ are typical for ice formed during freezing of groundwater, or for surface water subjected to evaporative fractionation. The results of the isotopic composition in MTGI of second type support the in-ground conditions if ice formation.

CONCLUSION

Eight reference sections containing ground ice were investigated in the north of Western Siberia. The upper part of the Quaternary section in the north of Western Siberia can be attributed to ice-rich permafrost. The total ice content of the upper part of the section due to segregation ice, IW and MTGI can reach 40–50%. In the lower part of the section, the ice content decreases to 30%.

The most typical section of Quaternary deposits was represented by the two-layered strata. The upper part of the section consists of continental sandy and sandy loam deposits formed during MIS 2 – MIS 1 (Sartan time and Holocene). Below this section, marine and coastal-marine sandy-loamy and clayey deposits formed during MIS 3 – MIS 5 (Kargino and Pre-Kargino times). Ice wedges were forming during MIS 3 – MIS 1 periods (Kargino, Sartan and Holocene horizons of the section). MTGI occurs at the border of the MIS 3 – MIS 2 horizon and Pre-Kargino horizons, as well as within the Pre-Kargino clay deposits.

In contrast to the Ice Complex of Eastern Siberia (Schirrmeister et al., 2011), the formation of ice rich permafrost in the Kara Sea coast occurred in two stages: marine stage with characteristic marine and coastal conditions (MIS 5 – MIS 3) and continental stage (MIS 3 – MIS 2). The MIS 3 – MIS 2 regression was accompanied by rapid cooling, dry climate and generation of syngenetic IW on the land and drained shelf area. The shelf of the Kara Sea was drained to the 110–120 m isobath (Stein et al., 2002) and the coastline retreated hundreds of kilometers north of its present position. At the same time epigenetic freezing of marine and coastal-marine sediments and MTGI formation occurred. The Holocene transgression of the Kara Sea proceeded unevenly with some fluctuations in the rate of sea level rise (Gornitz, 2009). During the climatic optimum of the Holocene degradation of the Late Pleistocene ice wedges occurred at the Kara Sea coast and caused erosion and slope processes. After thawing of the Pleistocene PWI ice ground-wedge casts were formed. Subsequent cooling in the Late Holocene caused freezing and formation of new generation of IW. The Holocene ice wedges are smaller in size and formed under more warmer climatic conditions than in Late Pleistocene.

Ground ice is a paleoenviromental archive that allows to establish sedimentation and ground ice formation at the end of the Late Pleistocene - Holocene. Base on isotopic composition of IW it was established that from MIS 4 to the present western atmospheric transport dominated in the Russian Western Arctic. There is a pronounced geographic trend in the isotopic composition of ice with highest $\delta^{18}O$ values found in the western and lowest values in the eastern part of the study region. Based on isotopic composition of ice wedges, winter air temperatures in MIS 3 – MIS 2 were 10–15°C lower than modern ones.

The chemical composition of IW is determined by the chemical composition of winter atmospheric precipitation and possible geochemical changes in the IW upper parts during the permafrost degradation. The presence of a strong “marine signal” with a high sodium chloride content in the Holocene IW may indicate the proximity of the sea during the IW formation and, in contrast, the remoteness of the sea during the Late Pleistocene IW formation.

High methane content in permafrost sediments is inherent in clayey sediments of marine origin; in continental sediments, the methane content is substantially lower. Thus, the methane content can also be used as an indicator for evaluation the genesis of sediments. The methane content in MTGI is 100–1,000 times higher than in glacial ice. This confirms the non-glacial genesis of the MTGI.

DATA AVAILABILITY STATEMENT

The original contributions presented in the study are included in the article/**Supplementary Material**, further inquiries can be directed to the corresponding author.

AUTHOR CONTRIBUTIONS

All authors contributed in data collection, processing, interpretation, and writing the manuscript.

FUNDING

This work is supported by State Scientific Program # 121041600043-4 and Research Program GM 1.5 «The cryosphere evolution under climate change and anthropogenic impact» No 121051100164-0.

ACKNOWLEDGMENTS

We sincerely thank P.B. Semenov and B.G. Vanshtein from VNIIokeangeologia (Saint Petersburg, Russia) who made quality control of the samples; Elizaveta Rivkina who determined concentration of methane in the Institute of Physical, Chemical, and Biological Problems in Soil Science RAS (Pushchino, Moscow Region, Russia); and Hanno Meyer who analyzed the isotope composition of ground ice in Isotope Laboratory of the Alfred Wegener Institute for Polar and Marine Research (Potsdam, Germany).

SUPPLEMENTARY MATERIAL

The Supplementary Material for this article can be found online at: https://www.frontiersin.org/articles/10.3389/feart.2021.723382/full#supplementary-material

REFERENCES

Alperin, M. J., and Reeburgh, W. S. (1985). Inhibition Experiments on Anaerobic Methane Oxidation. *Appl. Environ. Microbiol.* 50, 940–945. doi:10.1128/aem.50.4.940-945.1985

Anisimova, N. P. (1981). *Cryohydrogeochemistry of the Frozen Zone*. Novosibirsk: Nauka.

Astakhov, V. I. (2009). The Mid- and Late Neopleistocene of the Glacial Zone of Western Siberia: Problems in Stratigraphy and Paleogeography. *Bull. Comm. Quat. Period.* 69, 8–24.

Bolikhovsky, V. F. (1987). "Edoma Sediments of Western Siberia," in *New Data on the Geochronology of the Quaternary Period* (Moscow: Nauka).

Bolshiyanov, D. Yu., Makarov, A. S., Gusev, E. A., and Schneider, W. (2008). Problems of Ice Complex Origination and Former "Sannikovs Lands" Existence in the Laptev Sea. *Problemy Arktiki i Antarktiki.* 1, 151–160.

Craig, H. (1961). Isotopic Variations in Meteoric Waters. *Science.* 133, 1702–1703. doi:10.1126/science.133.3465.1702

Danilov, I. D. (1978). *Pleistocene of marine Subarctic plains*. Moscow: Moscow University Press.

Derevyagin, A. Y., Chizhov, A. B., Brezgunov, V. S., Hubberten, H. W., and Siegert, C. (1999). Isotopic Composition of Ice Wedges on Cape Sabler (Taimyr Lake). *Kriosfera Zemli.* 3, 41–49.

Dvornikov, Y. A., Leibman, M. O., Khomutov, A. V., Kizyakov, A. I., Semenov, P., Bussmann, I., et al. (2019). Gas-Emission Craters of the Yamal and Gydan Peninsulas: A Proposed Mechanism for lake Genesis and Development of Permafrost Landscapes. *Permafrost and Periglac Process.* 30, 146–162. doi:10.1002/ppp.2014

Forman, S. L., Ingólfsson, Ó., Gataullin, V., Manley, W., and Lokrantz, H. (2002). Late Quaternary Stratigraphy, Glacial Limits, and Paleoenvironments of the Marresale Area, Western Yamal Peninsula, Russia. *Quat. Res.* 57, 355–370. doi:10.1006/qres.2002.2322

Gataullin, V. N. (1988). *Upper Quaternary Deposits of the Western Coast of the Yamal Peninsula, Russia. [PhD Thesis Abstract]*. St. Petersburg: Federal Geological Institute.

Gornitz, V. (2009). "Sea Level Change, Post-Glacial," in *Encyclopedia of Paleoclimatology and Ancient Environments* (Dordrech: Springer).

Gusev, E. A., Anikina, N. Y., Arslanov, K. A., Bondarenko, S. A., Derevyanko, L. G., Molodkov, A. N., et al. (2013). Quaternary Deposits and Paleogeography of Sibiryakov Island During the Past 50 000. *Izvestija Russkogo Geograficheskogo Obcshestva.* 145 (4), 65–79.

Gusev, E. A., Molodkov, A. N., Streletskaya, I. D., Vasiliev, A. A., Anikina, N. Y., Bondarenko, S. A., et al. (2016). Deposits of the Kazantsevo Transgression (MIS 5) in the Northern Yenisei Region. *Russ. Geology. Geophys.* 57 (4), 586–596. doi:10.1016/j.rgg.2015.05.013

Gusev, E. A., Arslanov, H. A., Maksimov, F. E., Molodkov, A. N., Kuznetsov, V. Yu., Smirnov, S. B., et al. (2011). New Geochronological Data on NeoPleistocene - Holocene Sediments From Lower Yenisey Area. *Problemy Arktiki i Antarktiki.* 2, 36–44.

Ivanova, V. V. (2012). Geochemical Features of Formation of Massive Ground Ice Bodies (New Siberia Islands, Siberian Arctic) as the Evidence of Their Genesis. *Kriosfera Zemli.* 6 (1), 56–70.

Jouzel, J. (1999). Calibrating the Isotopic Paleothermometer. *Science.* 286 (5441), 910–911. doi:10.1126/science.286.5441.910

Kanevskiy, M., Shur, Y., Fortier, D., Jorgenson, M. T., and Stephani, E. (2011). Cryostratigraphy of Late Pleistocene Syngenetic Permafrost (Yedoma) in Northern Alaska, Itkillik River Exposure. *Quat. Res.* 75, 584–596. doi:10.1016/j.yqres2010.12.003

Kanevskiy, M. Z., Streletskaya, I. D., and Vasiliev, A. A. (2005). Regularities in the Formation of the Cryogenic Structure of the Quaternary Deposits of the Western Yamal (On the Example of the Marre-Sale District). *Earth's Cryosphere.* 9, 16–27.

Kaplanskaya, F. A., and Tarnogradskiy, V. D. (1986). Remnants of the Pleistocene Ice Sheets in the Permafrost Zone as an Object for Paleoglaciological Research. *Polar Geogr. Geology.* 10, 257–266. doi:10.1080/10889378609377295

Karpov, Y. G. (1986). *Ground Ice of the Yenissei North*. Novosibirsk: Nauka.

Korzun, A. V. (1985). *Geochemical Processes in Glacial and Underground Ice in Northern Eurasia [phd. Thesis]*. Moscow: MSU.

Kotov, A. N. (1991). "«Chemical Composition of Ice Wedges in Chukotka»," in *Comprehensive Geocryological Investigations of Chukotka*. Editor M. I. Tishin (Magadan: SEKNII DVO AN SSSR), 39–48.

Kritsuk, L. N. (2010). *Ground Ice of Western Siberia*. Moscow: Nauchnij mir.

Mackay, J. R. (1974). Ice-Wedge Cracks, Garry Island, Northwest Territories. *Can. J. Earth Sci.* 11, 1366–1383. doi:10.1139/e74-133

Magens, D. (2005). *Late Quaternary Climate and Environmental History of Siberian Arctic – Permafrost Records from Cape Mamontovy Klyk, Laptev Sea. [diplom Thesis]. [Kiel]*. Kiel: University of Kiel.

Maschenko, E. N., Potapova, O. R., Vershinina, A., Shapiro, B., Streletskaya, I. D., Vasiliev, A. A., et al. (2017). The Zhenya Mammoth (Mammuthus Primigenius (Blum.)): Taphonomy, Geology, Age, Morphology and Ancient DNA of a 48,000 Year Old Frozen Mummy From Western Taimyr, Russia. *Quat. Int.* 445, 104–134. doi:10.1016/j.quaint.2017.06.055

Meyer, H., Opel, T., Laepple, T., Dereviagin, A. Y., Hoffmann, K., and Werner, M. (2015). Long-Term Winter Warming Trend in the Siberian Arctic During the Mid- to Late Holocene. *Nat. Geosci.* 8 (2), 122–125. doi:10.1038/ngeo2349

Meyer, H., Schönicke, L., Wand, U., Hubberten, H. W., and Friedrichsen, H. (2000). Isotope Studies of Hydrogen and Oxygen in Ground Ice - Experiences With the Equilibration Technique. *Isotopes Environ. Health Stud.* 36, 133–149. doi:10.1080/10256010008032939

Michel, F. A. (1990). Isotopic Composition of Ice-Wedge Ice in Northwestern Canada. *Nordicana.* 54, 1–9.

Molodkov, A., and Bolikhovskaya, N. (2009). Climate Change Dynamics in Northern Eurasia Over the Last 200ka: Evidence From Mollusc-Based ESR-Chronostratigraphy and Vegetation Successions of the Loess-Palaeosol Records. *Quat. Int.* 201, 67–76. doi:10.1016/j.quaint.2008.05.028

Nikolayev, V. I., and Mikhalev, D. V. (1995). An Oxygen-Isotope Paleothermometer from Ice in Siberian Permafrost. *Quat. Res.* 43 (1), 14–21. doi:10.1006/qres.1995.1002

Oblogov, G. E. (2016). *Evolution of the Permafrost Zone of the Coast and Shelf of the Kara Sea in the Late Neopleistocene – Holocene. [phd. thesis]*. Tyumen: Earth Cryosphere Institute.

Oblogov, G. E., Streletskaya, I. D., Vasiliev, A. A., Gusev, E. A., and Arslanov, H. A. (2012). Quaternary Deposits and Geocryological Conditions of Gydan Bay Coast of the Kara Sea. *Tenth Int. Conf. Permafrost.* 3, 293–297.

Oblogov, G. E., Vasiliev, A. A., Streletskaya, I. D., Zadorozhnaya, N. A., Kuznetsova, A. O., Kanevskiy, M. Z., et al. (2020). Methane Content and Emission in the Permafrost Landscapes of Western Yamal, Russian Arctic. *Geosciences.* 10 (10), 412–421. doi:10.3390/geosciences10100412

Okhotin, V. V. (1933). *Granulometric Classification of Soils Based on Their Physical and Mechanical Properties*. Leningrad: Lengostransizdat.

Opel, T., Wetterich, S., Meyer, H., Dereviagin, A. Y., Fuchs, M. C., and Schirrmeister, L. (2017). Ground-ice Stable Isotopes and Cryostratigraphy Reflect Late Quaternary Palaeoclimate in the Northeast Siberian Arctic (Oyogos Yar Coast, Dmitry Laptev Strait). *Clim. Past.* 13 (6), 587–611. doi:10.5194/cp-13-587-2017

Péwé, T. L., and Journaux, A. (1983). *Origin and Character of Loess-Like Silt in Unglaciated South-Central Yakutia, Siberia, USSR*. USGS Professional Paper. Washington, 1262, 1–45. doi:10.3133/pp1262

Pismeniuk, A., Streletskaya, I., and Gusev, E. (2019). "Quaternary Deposits of the Gydan peninsula Coast of Western Siberia and Their cryogenic Structure," in Abstracts of International Conference "Solving the puzzles from Cryosphere".

Podborny, E. E. (1978). "«The Time and Activity of thermal-contraction Cracks Formation»," in *Cryolitology Problems*. Editor A. I. Popov (Moscow: Moscow University Press), 132–140.

Popov, A. I. (1953). The peculiar Characteristics of the Lithogenesis of Alluvial plains in Severe Climatic Conditions. *Izvestiya Akademii Nauk SSSR, Geogr. Ser.* 2, 29–41.

Porter, T. J., and Opel, T. (2020). Recent Advances in Paleoclimatological Studies of Arctic Wedge- and Pore-ice Stable-Water Isotope Records. *Permafrost and Periglac Process.* 31 (31), 429–441. doi:10.1002/ppp.2052

Raynaud, D. (2012). The Integrity of the Ice Record of Greenhouse Gases With a Special Focus on Atmospheric CO_2. *Led. I Sneg.* 2 (118), 5–14

Romanenko, F. A., Nikolaev, V. I., and Arkhipov, V. V. (2011). Changes in the Isotope Composition of Ice Deposits of the East Siberian Sea Coast: Geographical Aspect. *Led i Sneg.* 1 (113), 93–104.

Romanovskiy, N. N. (1993). *Fundamentals of Cryogenesis of the Lithosphere*. Moscow: Moscow State University.

Schirrmeister, L., Grosse, G., Schwamborn, G., Andreev, A. A., Meyer, H., Kunitsky, V. V., et al. (2003). Late Quaternary History of the Accumulation plain north of the Chekanovsky Ridge (Lena Delta, Russia): a Multidisciplinary Approach. *Polar Geogr.* 27 (4), 277–319. doi:10.1080/789610225

Schirrmeister, L., Kunitsky, V., Grosse, G., Wetterich, S., Meyer, H., Schwamborn, G., et al. (2011). Sedimentary Characteristics and Origin of the Late Pleistocene Ice Complex on north-east Siberian Arctic Coastal Lowlands and Islands - A Review. *Quat. Int.* 241, 3–25. doi:10.1016/j.quaint.2010.04.004

Semenov, P. B., Pismeniuk, A. A., Malyshev, S. A., Leibman, M. O., Streletskaya, I. D., Shatrova, E. V., et al. (2020). Methane and Dissolved Organic Matter in the Ground Ice Samples from Central Yamal: Implications to Biogeochemical Cycling and Greenhouse Gas Emission. *Geosciences.* 10 (11), 450. doi:10.3390/geosciences10110450

Slagoda, E. A., Opokina, O. L., Rogov, V. V., and Kurchatova, A. N. (2012). Structure and Genesis of Underground Ice in Upper Pleistocene-Holocene Deposits of Cape Marre-Sale (Western Yamal). *Earth's Cryosphere.* 16 (2), 9–22.

Solomatin, V. I. (1982). *«Buried Ice, Patterns of Formation and Structure», in Layered Ice of the Permafrost Zone*. Yakutsk: IM SO AN SSSR, 97–104.

Stein, R., Niessen, F., Dittmers, K., Levitan, M., Schoster, F., Simstich, J., et al. (2002). Siberian River Run-Off and Late Quaternary Glaciation in the Southern Kara Sea, Arctic Ocean: Preliminary Results. *Polar Res.* 21 (2), 315–322. doi:10.3402/polar.v21i2.6493

Streletskaya, I. D., Gusev, E. A., Vasiliev, A. A., Kanevskiy, M. Z., Anikina, N. Yu., and Derevyanko, L. G. (2007). New Results of Quaternary Sediment Studies of Western Taymyr. *Earth's Cryosphere.* 6 (3), 14–28.

Streletskaya, I. D., Gusev, E. A., Vasiliev, A. A., Rekant, P. V., and Arslanov, Kh. A. (2012a). Late Pleistocene-Holocene Ground Ice in Quaternary Deposits on the Kara Shelf as a Record of Paleogeographic Conditions. *Bull. Comm. Quat. Period.* 72, 28–59.

Streletskaya, I. D., Vasiliev, A. A., Slagoda, E. A., Opokina, O. L., and Oblogov, G. E. (2012b). Ice Wedges on Sibiryakov Island (Kara Sea) Bulletin of Moscow University. *Ser. Geogr.* 3, 57–63.

Streletskaya, I. D., Kanevskiy, M. Z., and Vasiliev and, A. A. (2006). Massive Ground Ice in Dislocated Quaternary Sediments of Western Yamal. *Earth's Cryosphere.* 10, 68–78.

Streletskaya, I. D., and Leibman, M. O. (2003). "«Cryogeochemical Model of Tabular Ground Ice and Cryopegs Formation at Central Yamal, Russia»," in Proceedings of the Eighth International Conference on Permafrost 2. Editors M. Phillips, S. M. Springman, and L. U. Arenson (Lisse: Balkema), 1111–1115.

Streletskaya, I. D., Shpolyanskaya, N. A., Kritsuk, L. N., and Surkov, A. V. (2009). Cenozoic Deposits of the Western Yamal and the Problem of Their Genesis. Vestnik of the Moscow State University. *Ser. Geogr.* 3, 50–57.

Streletskaya, I. D., and Vasiliev, A. A. (2009). Isotopic Composition of Ice Wedges of West Taymir. *Earth's Cryosphere.* 8 (3), 59–69.

Streletskaya, I. D., Vasiliev, A. A., and Kanevskiy, M. Z. (2008). "«Freezing of marine Sediments and Formation of continental Permafrost at the Coasts of Yenisey Gulf»," in Proceedings of Ninth International Conference on Permafrost 2. Editors D. L. Kane and K. M. Hinkel (Fairbanks: Institute of Northern Engineering, University of Alaska Fairbanks), 1722–1726.

Streletskaya, I. D., Vasiliev, A. A., Oblogov, G. E., and Tokarev, I. V. (2015). Reconstruction of Paleoclimate of Russian Arctic in Late Pleistocene–Holocene on the Basis of Isotope Study of Ice Wedges. *Earth's Cryosphere.* 19 (2), 86–94.

Streletskaya, I., Gusev, E., Vasiliev, A., Oblogov, G., and Molodkov, A. (2013). Pleistocene-Holocene Palaeoenvironmental Records From Permafrost Sequences at the Kara Sea Coast (Nw Siberia, Russia). *Geogr. Environ. Sustain.* 6, 60–76. doi:10.24057/2071-9388-2013-6-3-60-76

Streletskaya, I., Vasiliev, A., and Meyer, H. (2011). Isotopic Composition of Syngenetic Ice Wedges and Palaeoclimatic Reconstruction, Western Taymyr, Russian Arctic. *Permafrost Periglac. Process.* 22, 101–106. doi:10.1002/ppp.707

Streletskaya, I., Vasiliev, A., Oblogov, G., and Streletskiy, D. (2018). Methane Content in Ground Ice and Sediments of the Kara Sea Coast. *Geosciences.* 8 (12), 434. doi:10.3390/geosciences8120434

Tarasov, P. E., Andreev, A. A., Romanenko, F. A., and Sulerzhitskii, L. D. (1995). Palynostratigraphy of Upper Quaternary Deposits of Sverdrup Island, the Kara Sea. *Stratigr. Geol. Correl.* 3, 190–196. doi:10.1016/0037-0738(94)00119-F

Tomirdiaro, S. V. (1980). *The Loess-Ice Formation of East Siberia in the Late Pleistocene*. Moscow: Nauka.

Vasil'chuk, Y. K. (1992). *Oxygen Isotope Composition of Ground Ice (Application to Paleogeocryological Reconstructions)*. Moscow: Geological Faculty of Moscow State University.

Vasil'chuk, Y. K. (2006). *Ice Wedge: Heterocyclity, Heterogeneity, Heterochroneity*. Moscow: Moscow University Press.

Vasil'chuk, Y. K. (2016). Geochemical Composition of Ground Ice of the Russian Arctic. *Arktika i Antarktika.* 2, 99–115. doi:10.7256/2453-8922.2016.2.21378

Wetterich, S., Rudaya, N., Kuznetsov, V., Maksimov, F., Opel, T., Meyer, H., et al. (2019). Ice Complex Formation on Bol'shoy Lyakhovsky Island (New Siberian Archipelago, East Siberian Arctic) Since about 200 Ka. *Quat. Res.* 92 (2), 530–548. doi:10.1017/qua.2019.6

Conflict of Interest: The authors declare that the research was conducted in the absence of any commercial or financial relationships that could be construed as a potential conflict of interest.

frontiers in Earth Science

ORIGINAL RESEARCH
published: 25 November 2021
doi: 10.3389/feart.2021.710257

14,000-year Carbon Accumulation Dynamics in a Siberian Lake Reveal Catchment and Lake Productivity Changes

Lara Hughes-Allen[1,2]*, Frédéric Bouchard[1,3], Christine Hatté[4], Hanno Meyer[2], Lyudmila A. Pestryakova[5], Bernhard Diekmann[2], Dmitry A. Subetto[6,7] and Boris K. Biskaborn[2]*

[1]CNRS, GEOPS, Université Paris-Saclay, Orsay, France, [2]Alfred Wegener Institute Helmholtz Centre for Polar and Marine Research, Potsdam, Germany, [3]Centre d'études nordiques (CEN), Université Laval, Québec, Canada, [4]Laboratoire des Sciences du Climat et de L'Environnement (LSCE), CEA CNRS UVSQ, Université Paris-Saclay, Gif-sur-Yvette, France, [5]North-Eastern Federal University of Yakutsk, Yakutsk, Russia, [6]Herzen State Pedagogical University of Russia, Saint Petersburg, Russia, [7]Institute for Water and Environmental Problems, Siberian Branch of the Russian Academy of Sciences, Barnaul, Russia

OPEN ACCESS

Edited by:
Lutz Schirrmeister,
Alfred Wegener Institute Helmholtz Centre for Polar and Marine Research (AWI), Germany

Reviewed by:
Mathias Ulrich,
Leipzig University, Germany
Darrell Kaufman,
Northern Arizona University, United States

***Correspondence:**
Lara Hughes-Allen
lara.hughes-allen@universite-paris-saclay.fr
Boris K. Biskaborn
Boris.biskaborn@awi.de

Specialty section:
This article was submitted to Cryospheric Sciences, a section of the journal Frontiers in Earth Science

Received: 15 May 2021
Accepted: 29 October 2021
Published: 25 November 2021

Citation:
Hughes-Allen L, Bouchard F, Hatté C, Meyer H, Pestryakova LA, Diekmann B, Subetto DA and Biskaborn BK (2021) 14,000-year Carbon Accumulation Dynamics in a Siberian Lake Reveal Catchment and Lake Productivity Changes. Front. Earth Sci. 9:710257. doi: 10.3389/feart.2021.710257

A multi-proxy paleolimnological analysis of a sediment core sequence from Lake Malaya Chabyda in Central Yakutia (Eastern Siberia, Russia) was conducted to investigate changes in lake processes, including lake development, sediment and organic carbon accumulation, and changes in primary productivity, within the context of Late Pleistocene and Holocene climate change. Age-depth modeling with ^{14}C indicates that the maximum age of the sediment core is ~14 cal kBP. Three distinct sedimentary units were identified within the sediment core. Sedimentological and biogeochemical properties in the deepest section of the core (663–584 cm; 14.1–12.3 cal kBP) suggests a lake environment mostly influenced by terrestrial vegetation, where organic carbon accumulation might have been relatively low (average ~100 g OC m^{-2} a^{-1}), although much higher than the global modern average. The middle section of the core (584–376 cm; 12.3–9.0 cal kBP) is characterized by higher primary productivity in the lake, much higher sedimentation, and a remarkable increase in OC delivery (average ~300 g OC m^{-2} a^{-1}). Conditions in the upper section of the core (<376 cm; < 9.0 cal kBP) suggest high primary productivity in the lake and high OC accumulation rates (average ~200 g OC m^{-2} a^{-1}), with stable environmental conditions. The transition from organic-poor and mostly terrestrial vegetation inputs (TOC/TN_{atomic} ratios ~20) to conditions dominated by aquatic primary productivity (TOC/TN_{atomic} ratios <15) occurs at around 12.3 cal kBP. This resulted in an increase in the sedimentation rate of OC within the lake, illustrated by higher sedimentation rates and very high total OC concentrations (>30%) measured in the upper section of the core. Compact lake morphology and high sedimentation rates likely resulted in this lake acting as a significant OC sink since the Pleistocene-Holocene transition. Sediment accumulation rates declined after ~8 cal k BP, however total OC concentrations were still notably high. TOC/TN_{atomic} and isotopic data ($\delta^{13}C$) confirm the transition from terrestrial-influenced to aquatic-dominated conditions during the Early Holocene. Since the mid-Holocene, there was likely higher photosynthetic uptake of CO_2 by algae, as suggested by heavier (isotopically enriched) $\delta^{13}C$ values (>−25‰).

Keywords: paleolimnology, lake sediment core, late Pleistocene, Holocene, Eastern Siberia, organic carbon accumulation, stable carbon isotope (13C)

INTRODUCTION

Permafrost is a dominant landscape feature in Siberia, Alaska, and Canada, occupying more than 20 million square kilometers and representing 24% of land cover within the northern hemisphere (Brown et al., 1997). Regional climate conditions, landscape cover, and other factors control the spatial extent and thickness of permafrost, and ground ice content can vary widely across landscapes (Grosse et al., 2016; Strauss et al., 2017). The Yedoma ice complex (referred to as "Yedoma" in the following) is a particular type of ice-rich (50–90 vol%), relatively low organic content (2–4 wt%) permafrost that can reach depths of up to 40 m (Schirrmeister et al., 2013; Hugelius et al., 2014). Permafrost landscapes of all types are sensitive to changes in temperature and other local disturbances including forest fires and forest removal for agricultural purposes as well as lake formation and development (Grosse et al., 2013; Ulrich et al., 2019), which can have widespread implications for local and regional hydrology and the global carbon cycle (Walter Anthony et al., 2016). Yedoma is particularly susceptible to localized abrupt thaw based on its high ice content (Vonk et al., 2013). The Arctic is currently warming at a disproportionately high rate and magnitude compared to global averages, with mean annual air temperature predicted to increase by as much as 5.4°C within the 21st century in the absence of significant and directed global effort to reduce greenhouse gas emissions (Pörtner et al., 2019). This will likely herald a period of dynamic changes within permafrost landscapes.

The surface of Yedoma landscapes in many places is covered by ponds and lakes that document thermokarst processes (Strauss et al., 2017). In addition to the dominance of thermokarst lakes in Yakutia, lake formation can occur within the dune landscape which is widespread in the lower section of the Vilyui River and the middle part of the Lena River (Pestryakova et al., 2012). These sand dunes (also called tukulans) likely originated during the early stages of the interglacial epochs and dune lakes can often form in deflation basins (Pestryakova et al., 2012). Similar to thermokarst lakes, the high heat capacity of water relative to the air causes preferential thawing of surrounding permafrost as well as settling of sand to facilitate minor deepening of the lake (Sumgin et al., 1940; Kachurin, 1961; Zhirkov, 1983). While the genesis of dune lakes clearly differs from thermokarst lakes, there is overlap in the developmental history between these two lake types. There is, however, a relative paucity of studies which examine the paleolimnological history of dune lakes located in permafrost landscapes, and in particular differences in the potential for release of stored carbon upon permafrost thawing between these lakes and thermokarst lakes. Permafrost thaw can release substantial amounts of organic and mineral matter, including carbon, to surrounding terrestrial and aquatic ecosystems (Vonk et al., 2015). Soils across northern permafrost regions could contain twice as much carbon as currently exists in the atmosphere (Schuur et al., 2015). Total global terrestrial (non-marine) stores alone are estimated to hold 1,672 Pg of carbon (PgC), with Yedoma deposits accounting for more than 500 Pg C of this total (Hugelius et al., 2014). Permafrost carbon stores consist primarily of the remnants of terrestrial vegetation such as leaves and root detritus as well as microorganisms which have accumulated in the perennially frozen soil over thousands of years (Davidson and Janssens, 2006; Vonk and Gustafsson, 2013; Schuur et al., 2015). Lakes, however, store both terrestrial material (allochthonous) and also the organic matter (OM) that was produced by algae in the aquatic ecosystem (autochthonous) (Schuur et al., 2015). However, there is a lack of studies which study long-term carbon storage in Siberian lakes (Mendonça et al., 2017). Lakes can also act as hotspots for greenhouse gas emissions in permafrost landscapes. These emissions originate from the mineralization of OM (both allochthonous and autochthonous) stored within lake sediments (Bouchard et al., 2015; Hughes-Allen et al., 2021; Prėskienis et al., 2021) and understanding past lake dynamics can inform predictions about future greenhouse gas emissions from permafrost landscapes.

Paleolimnological studies often rely on proxy analyses based on carbon concentrations, carbon isotopes, and nitrogen concentrations. However, the applicability of these variables for interpretation of the relationships between carbon accumulation, carbon degradation, and the permafrost catchment are not fully understood (Biskaborn et al., 2019a). Therefore, the general approach of our study was to gain insights into how these variables can contribute to a better understanding of carbon dynamics in Siberian lake systems, facilitating future paleolimnological studies. Here, we present the results from a multi-proxy analysis of an approximately 6.6 m-long sediment core, covering the last 14,000 years, from Lake Malaya Chabyda within the Central Yakutia region to understand the history and processes of carbon accumulation through time within a permafrost landscape. The specific objectives of the study were: 1. present the development history of Lake Malaya Chabyda, 2. quantify and understand the accumulation of organic carbon in the lake, 3. distinguish between organic matter produced within the lake itself and within the surrounding catchment, 4. discern carbon preservation trends based on climate variability and changing lake dynamics.

STUDY SITE

Lake Malaya Chabyda (Озеро Малая цабыда) (61.9569 °N, 129.4091 °E) is located approximately 15 km southwest of the City of Yakutsk (Central Yakutia, Eastern Siberia). This lake is at 188 m a.s.l, has an area of 0.24 km^2, and a max depth of 3 m (Kumke et al., 2007). During initial surveying in July 2005, Lake Malaya Chabyda had a pH of 6.71, a conductivity of 131 (µS/cm),

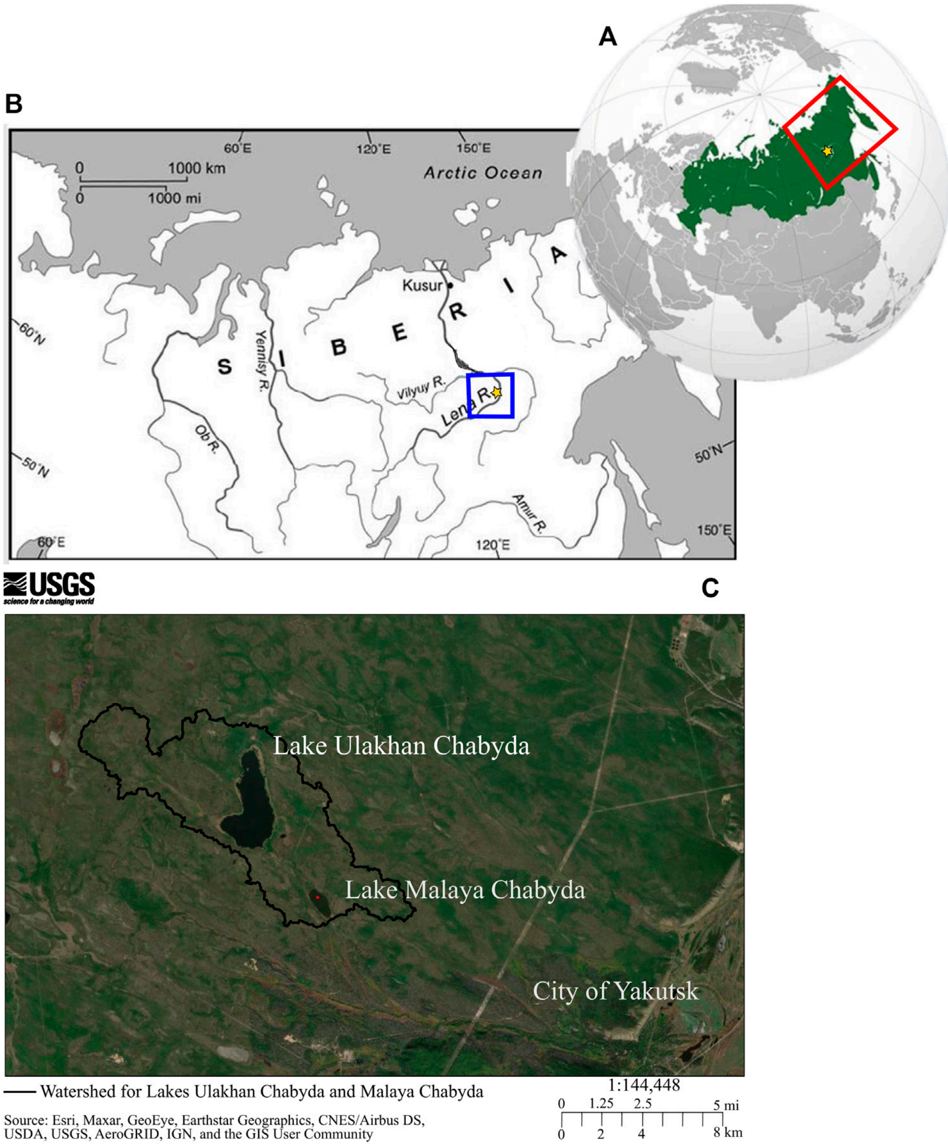

FIGURE 1 | (A) Map showing general location of the study site (red box) within the Russia Federation (green) **(B)** Location of study site (blue box). Note the Lena River and the city of Yakutsk (yellow star) **(C)** Locations of Lakes Ulakhan Chabyda and Malaya Chabyda, near the city of Yakutsk. Lake catchment is outline in black. Coring site location is indicated by red circle.

and a temperature of 18°C (Pestryakova et al., 2012). The lake catchment is 10 km^2 and also includes Lake Ulakhan Chabyda (Tarasov et al., 1996), which is a lake four times larger than Lake Malaya Chabyda, approximately 3 km to the northwest (**Figure 1**). Lake Ulakhan Chabyda has an area of 2.1 km^2, an average depth of 0.5 m and a maximum depth of 2.0 m. There are no surface inflows into Lake Ulakhan Chabyda (Pestryakova et al., 2012), but this lake does discharge into Lake Malaya Chabyda during times of high water (i.e. after spring melting). Lake Malaya Chabyda sits on massifs of spear-shaped dunes which have been fixed in place by vegetation growth since the onset of the Holocene. Both lakes sit on the former Lena River erosion-accumulation plain, within the central Yakutian Depression. This plain is composed of Quaternary loams overlying Cambrian limestones (Pestryakova et al., 2012).

Central Yakutia is characterized by an extreme subarctic continental climate with long, cold, and dry winters (January mean temperature around −40°C) and relatively warm summers (July mean temperature around +20°C). The winter season, characterized by the presence of ice cover on local lakes, generally extends from late September until early May (Hughes-Allen et al., 2021). The biologically productive summer season is short, lasting from the middle of June to the beginning of August (Nazarova et al., 2013). The low annual precipitation (190–230 mm) is mostly constrained to the summer season. Average snow depth for winter months (January to April) ranges from 24 cm in January to a maximum of 30 cm in March, and then decreasing to 10 cm at the end of April (1980-2020 recorded values from Yakutsk weather station) (A. Fedorov pers. comm.). Yearly evaporation rates exceed total precipitation in this region (Fedorov et al., 2014b). Between 1996 and 2016, the mean annual air temperature of Central Yakutia increased by 0.5–0.6 °C per decade (Gorokhov and Fedorov, 2018).

Permafrost in this region is continuous, thick (>500 m deep), and the upper 30–50 m (Pleistocene-age fluvial and aeolian sediments) can be extremely rich in ground ice (50–90% by volume) (Ivanov, 1984). The active layer typically reaches depths of 0.5–2.0 m, varying depending on landscape factors that include vegetation cover type, general topography, soil type, and subsurface water content (Ulrich et al., 2017b). Central Yakutia is dominated by a middle taiga landscape regime (Fedorov et al., 2014) and larch, pine, and birch forests are prevalent (Ulrich et al., 2017a). Grasslands are abundant in unforested areas, including land cleared for farming, ranching, or in the remnant depressions of old thaw lakes known as '*alases*'. After the cold temperatures and low precipitation of the Younger Dryas, Central Yakutia experienced a slow, but relatively persistent increase in temperature and precipitation (Müller et al., 2009; Biskaborn et al., 2012; Nazarova et al., 2013). These conditions resulted in widespread permafrost degradation (Biskaborn et al., 2012), including the development of 'alas' depressions that are now widespread in Central Yakutia (Soloviev, 1959; Brouchkov et al., 2004). The grasslands in the alases consist of halophytic steppe-like and bog plant communities (Ulrich et al., 2017b).

Nearly half of the landscape has been affected by thermokarst since the Early Holocene, resulting in the formation of thousands of partly drained 'alas' depressions (Soloviev, 1959; Brouchkov et al., 2004). However, recent thermokarst activity related to natural landscape evolution, increasing air temperatures and/or human-induced landscape modifications (agriculture, clear-cutting, and infrastructure) is also occurring in the region, resulting in the development of numerous small, fast-developing lakes and retrogressive thaw slumps along lake shores (Fedorov et al., 2014; Séjourné et al., 2015). Dune lakes are found in the lower section of the Vilyui River and the middle section of the Lena River, where there are abundant unvegetated massifs of undulating and cross-bedded quartz loamy sand that can be up to 25 m thick. These dune features are fairly common in the Lena watershed and can account for nearly 30 percent of the landscape in some areas (Galanin et al., 2018). Central Yakutian dunes are considered to be aeolian in origin and likely formed at the end of the last glacial epoch between 27.0–12.0 cal kBP on Lower Cambrian carbonates, although the actual abundance of $CaCO_3$ in the dune sand is not known. Lakes are found in deflation and aeolian-dammed basins (Pestryakova et al., 2012).

METHODS

Field Sampling

Eight overlapping sediment cores, representing an approximately 6.6 m–long composite sequence (**Supplementary Figure S1**), were collected on March 24, 2013 from Lake Malaya Chabyda in Central Yakutia (exact coring location 61°57.509′ 129°24.500′). Sampling was conducted during a German–Russian Expedition ("Yakutia 2013") as the cooperation between the North Eastern Federal State University in Yakutsk (NEFU) and the Alfred Wegener Institute Helmholtz Centre for Polar and Marine Research (AWI).

Two parallel drilling holes, approximately 1 m apart, were used alternatingly to obtain core sections which overlap by approximately 20 cm. To penetrate ca. 1 m of lake ice cover, 250-mm-diameter holes were drilled using a hand-held Jiffy ice auger. Water depth was measured using an Echo sounder (HONDEX PS-7 LCD) and a calibrated rope for verification. Each individual core sample consisted of a 100 cm-long core collected at 2 m water depth using a Russian peat corer and supported by an UWITEC gravity coring system. Core samples were taken alternatingly from the first drill hole and then the second until the entire length of the core was obtained. Care was taken when coring to ensure that there was 20 cm of overlap between core sections. Cores were stored in waterproof sealed, transparent PVC plastic tubes in cool and dark conditions. After the field season, the cores were transported to Potsdam, Germany and stored at 4°C in the cold rooms at AWI. The cores did not experience any visible drying or surface oxidation during storage.

Sediment Core Subsampling and Dating

After XRF scanning in early 2014, subsampling of the cores for laboratory analyses began in November 2018 with a simple visual description and photography of the eight cores sections. One-cm-thick discrete subsamples were then taken at approximately 10 cm intervals using an inox spatula. Each subsample was split into two parts containing approximately equal amounts of material (4–10 g) and weighed. One subsample was kept in the cold room for potential future analysis. The remaining subsample was used for all subsequent analysis.

Four bulk samples and three organic vegetal macro remains were extracted from the sediment cores sections and sent for ^{14}C dating to the MICADAS radiocarbon lab at AWI, Germany (**Table 1**). These samples were placed in glass containers and dried at 50 °C and analyzed for radiocarbon dating using accelerator mass spectrometry (AMS) after using an acid treatment (method outlined in (Vyse et al., 2020). We applied Bacon in R (Blaauw and Christen, 2011) and the IntCal20 calibration curve (Reimer et al., 2020) to model the age-depth relationship. The surface of the core represents 2013 CE (the time of core retrieval) and the linear relationship of the samples from the bottom to the top of the core shows that there is no significant reservoir effect in the lake.

X-Ray Fluorescence (XRF) Analysis

High–resolution X–ray fluorescence (XRF) analyses were carried out with 10 mm resolution on the entire sequence using an Avaatech XRF core scanner at AWI (Bremerhaven, Germany) with a Rh X-ray tube at 10 kV (without filter, 12 s, 1.5 mA) and 30 kV (Pd-thick filer, 15 s, 1.2 mA). The sediment surface was cleaned, leveled, and covered with a 4 μm ultralene foil to avoid sediment desiccation prior to XRF scanning. Individual element counts per second (CPS)

TABLE 1 | Radiocarbon (^{14}C) dated samples from Lake Malaya Chabyda sediment core.

Lab ID	Sample label	Composite depth (cm)	14C age (yr)	14C error (yr)	Methods and material
AWI-2601.1.1	PG2201-2_a200-300_80–81	66.5	1802	70	ABA, wood
AWI-2786.1.1	PG2201-2_b280-380_75–76	141.5	3,564	38	ABA, wood
AWI-2602.1.2	PG2201-2_d440-540_59.5-60	285.5	7,691	32	A, bulk
AWI-2606.1.2	PG2201-2_f600-700_10–10.5	396.25	8,460	37	A, bulk
AWI-2605.1.1	PG2201-2_f600-700_77–78	463.5	8,548	106	ABA, wood
AWI-2609.1.2	PG2201-2_h780-880_9.5-10	573.25	10,218	39	A, bulk
AWI-2608.1.2	PG2201-2_h780-880_97–97.5	661.25	12,184	38	A, bulk

were transformed using a centered log transformation (CLR) and element ratios were transformed using an additive log ratio (ALR) to account for compositional data effects and reduce effects from variations in sample density, water content, and grain size (Weltje and Tjallingii, 2008). Statistical analysis was completed using the *Python* programming language (*Python* Software Foundation, https://www.python.org/). XRF analysis of the sequence indicated 24 detectable elements and a subset of these were selected for analysis based on low element Chi-Square (χ^2) values. χ^2 values are produced by the WinAxil Software to help determine the goodness of fit of the mathematical model. Provided that the χ^2 value does not exceed 3, it is considered acceptable. These selected elements include the major rock forming elements of Silicon (Si) (Chi^2 1.4), Calcium (Ca) (Chi^2 6.3), Titanium (Ti) (Chi^2 1.3), Rubidium (Rb) (Chi^2 0.6), Strontium (Sr) (Chi^2 0.7), Zircon (Zr) (Chi^2 0.6) and the redox sensitive, productivity indicating elements of Manganese (Mn) (Chi^2 1.3), Iron (Fe) (Chi^2 2.5), and Bromine (Br) (Chi^2 0.8).

Grain Size Analysis

All subsequent analyses took place after the extracted subsamples had been freeze–dried until completely dry (approximately 48 h). Grain size analysis was conducted on 16 samples that were chosen to span the entire sequence at relatively regular intervals. The samples were first treated for 5 weeks with H_2O_2 (0.88 M) in order to isolate clastic material. After treatment, seven samples were eliminated from the analysis because the remaining inorganic sediment fraction was too low for detection by the laser grain size analyzer. The remaining samples were homogenized using an elution shaker for 24 h and then analyzed using a Malvern Mastersizer 3,000 laser. Standard statistical parameters (mean, median, mode, sorting, skewness, and kurtosis) were determined using GRADISTAT 9.1 (Blott and Pye, 2001).

Dry Bulk Density, Sedimentation and Organic Carbon Accumulation Calculations

Total organic carbon concentrations (see below) were used to determine the organic *vs* mineral matter content (OM *vs* MM) in each sample, assuming that bulk OM contains about 50% of organic carbon (Pribyl, 2010). OM and MM concentrations were used to derive average particle densities, based on values of 1.25 g cm^{-3} and 2.65 g cm^{-3} for OM and MM, respectively (Avnimelech et al., 2001). Dry bulk density (DBD, in g cm^{-3}) values were then inferred by multiplying particle densities by porosity values, which had been calculated using wet and dry weights (thus the water content before and after sediment drying by freeze drying). Sedimentation rate (SR, in cm a^{-1}) was calculated using the R function "accrate.depth", which estimated mean sedimentation rate derived from the age-depth model at 0.5 cm increments downcore. All iterations at each depth from the bacon modelling output where then used in a student t-test to calculate the 95% confidence range and the *p*-values for SR at each 0.5 cm increment. Sediment mass accumulation rate (MAR, in g cm^{-2} a^{-1}) was obtained by multiplying DBD by SR. Finally, the organic carbon accumulation rate (OCAR, in g OC m^{-2} a^{-1}) was inferred as the adjusted product of MAR and the total organic carbon concentration. OCAR and MAR uncertainties were calculated from the 95% uncertainty ranges of SR.

Biogeochemical Analysis

Total carbon (TC), total organic carbon (TOC), and total nitrogen (TN) analyses were completed after the freeze–dried subsamples were ground in a Pulverisette 5 (Fritsch) planetary mill at 3,000 rpm for 7 min. TC and TN were measured in a carbon–nitrogen–sulphur analyzer (Vario EL III, Elementar). Five mg of sample material were encapsulated in tin (Sn) capsules together with 10 mg of tungsten–(VI)–oxide. The tungsten–(VI)–oxide ensures complete oxidation of the sample during the measurement process. Duplicate capsules were prepared and measured for each subsample. Blanks and calibration standards were placed every 15 samples to ensure analytical accuracy (<± 0.1 wt%). Between each sample the spatula was cleaned with KIMTECK fuzz-free tissues and isopropyl.

Analysis of TOC began by removing the inorganic carbon fraction by placing each subsample in a warm hydrochloric acid solution (1.3 M) for at least 3 hours and then transferring the sample to a drying oven. The TC measured for each subsample in the previous analysis was used to determine the amount of sample required for the TOC analysis. The appropriate amount of sample was weighted in a ceramic crucible and analyzed using the Vario Max C, Elementar. The TOC/TN ratio was converted to the TOC/$TN_{atomic\ ratio}$ by multiplying the TOC/TN ratio by 1.167 (atomic weight of carbon and nitrogen) (Meyers and Arbor, 2001). Total inorganic carbon (TIC) analysis was completed using a Vario SoilTOC cube elemental analyzer after combustion at 400°C (TOC) and 900°C (TIC) (Elementar Corp, Germany).

Calculation of $\delta^{13}C$ was completed twice for a subset of samples using two different methodologies. The analysis completed at the AWI Potsdam ISOLAB Facility removed carbonate by treating the samples with hydrogen chloride (12 M HCl) for 3 hours at 97°C, then adding purified water and decanting and washing three times. Once the chloride content was below 500 parts per million (ppm), the samples were filtered over a glass microfiber (Whatman Grade GF/B, nominal particle retention of 1.0 μm). The residual sample was dried overnight in a drying cabinet at 50°C. The dry samples were manually ground for homogenization and weighted into tin capsules and analyzed using a ThermoFisher Scientific Delta–V–Advantage gas mass spectrometer equipped with a FLASH elemental analyzer Andreev and Klimanov, 2000 and a CONFLO IV gas mixing system. In this system, the sample is combusted at 1,020°C in O_2 atmosphere so that the OC is quantitatively transferred to CO_2, after which the isotope ratio is determined relative to a laboratory standard of known isotopic composition. Capsules for control and calibration were run in between. The isotope composition is given in permil (‰) relative to Vienna Pee Dee Belemnite (VPDB).

The analysis of a small subset of samples which took place at Laboratoire des sciences du climat et de l'environnement Isotopic Laboratory for methodological comparison underwent a slightly different treatment, as follows. The sediment underwent a soft leaching process to remove carbonate using pre-combusted glass beakers, HCl 0.6N at room temperature, ultra-pure water and drying at 50°C. The samples were then crushed in a pre-combusted glass mortar for homogenization prior to carbon content and δ13 C analysis. The handling and chemical procedures are common precautions employed with low-carbon-content sediments. Analysis was performed online using a continuous flow EA-IRMS coupling, that is, a Fisons Instrument NA 1500 Element Analyzer coupled to a ThermoFinigan Delta + XP Isotope-Ratio Mass Spectrometer. Two in-house standards (oxalic acid, δ13C = −19.3% and GCL, _13C = −26.7%) were inserted every five samples. Each in-house standard was regularly checked against international standards. The measurements were at least triplicated for representativeness. The external reproducibility of the analysis was better than 0.1%, typically 0.06%. Extreme values were checked twice.

Those samples for which the carbonate was leeched at the room temperature, with lower HCl concentration (0.6N), and without a filtration step (samples analyzed at Laboratoire des sciences du climat et de l'environnement Isotopic Laboratory) had $\delta^{13}C$ values 0.1–1.0‰ (average 0.5‰) higher than the samples treated at the higher temperature (97.7°C). However, the plotted $\delta^{13}C$ curve is nearly identical for the subset of samples which were subjected to both treatments (**Supplementary Figure S2**). There is some heterogeneity in the amount of offset between the two treatment methods. This might be related to an asymmetrical distribution of hot acid-soluble organic compounds throughout the sediment core. A correction of ca. +0.5‰ was applied to the results of the high temperature treatment. These values were then combined with the low temperature results to provide a complete dataset for the whole core. The standard deviation of the typical measurement error (1σ) is generally better than $\delta^{13}C = \pm 0.15$‰.

Statistical Analysis

A hierarchical agglomerative cluster analysis was performed in order to divide the sediment core sequence into distinct units. XRF elemental data (CLR values for Ca, Fe, Ti, Mn, Sr, Zr, Rb, Br, and Si), $\delta^{13}C$, TN (wt%), C (wt%), TOC (wt%), and TIC (wt%) were used to perform the cluster analysis (**Supplementary Figure S3**).

A principal component analysis (PCA) was completed on a subset of XRF elements (Ca, Sr, Fe, Zr, and Ti), and biogeochemical parameters (TOC (wt%), C (wt%), TN (wt%), TOC/TN_{atomic}) to explore the dimensionality of the dataset and the relationships between the included variables. All values were z-transformed. The data when considered for the whole core, do not have a Gaussian distribution, but the data do approach a normal distribution when considered by unit. Therefore, the PCA was performed individually for each unit, rather than on the whole core. Only a subset of XRF elements were included in the PCA in order to reduce dimensionality, while preserving as much variability as possible. All variables were then plotted onto an ordination plot for interpretation purposes (**Supplementary Figure S4**). The clustering analysis and PCA analysis were performed using the *Python* programming language (*Python* Software Foundation, https://www.python.org/). Packages used include: numpy (Harris et al., 2020) and pandas (The pandas development team, 2020).

RESULTS

Chronology and Sedimentation Rates

The results of the ^{14}C dating analysis of seven samples indicate that the oldest lake sediments at the base of the core were deposited around 14.1 cal kBP according to the age depth model (**Figure 2**). The middle horizon (dark brown clayey silt with laminated sections) decreases in age consistently from 12.3 cal kBP at 584 cm depth to ~9.0 cal kBP at 376 cm depth. The upper horizon (homogenous, brown, clayey silt) decreased from ~9.0 cal kBP at 376 cm depth to present-day at the top of the sediment core. Mean 95% confidence over the entire core was 874 years 100% of the dates overlap with the age-depth model (95% ranges). It is possible that the bulk-sediment radiocarbon dates are older by multiple centuries or even millennia than recorded due to reworking of old organic material (Strunk et al., 2020). However, based on the linear alignment of dated samples until the time of sampling, we can assume neglectable effects from the presence of old carbon in the samples.

The age depth model indicates a higher average sedimentation rate (SR) of 0.13 cm a^{-1} below 290 cm, and a lower average SR of 0.07 cm a^{-1} in the upper horizon. Considering the dry bulk density (DBD) of each sample, instantaneous sediment mass accumulation rates (MARs) range from 0.05 g cm^{-2} a^{-1} above 300 cm depth to 0.09 g cm^{-2} a^{-1} below 300 cm depth. Considering each unit separately, average MAR values are 0.09 g cm^{-2} a^{-1} for Unit 1, 0.1 g cm^{-2} a^{-1} for Unit 2, and 0.06 g cm^{-2} a^{-1} for Unit 3. Each individual unit displays quite distinct OCAR trends (**Figure 5**). Average OCAR is lowest in Unit 1 (~100 g m^{-2} a^{-1}), highest in Unit 2 and the bottom of Unit

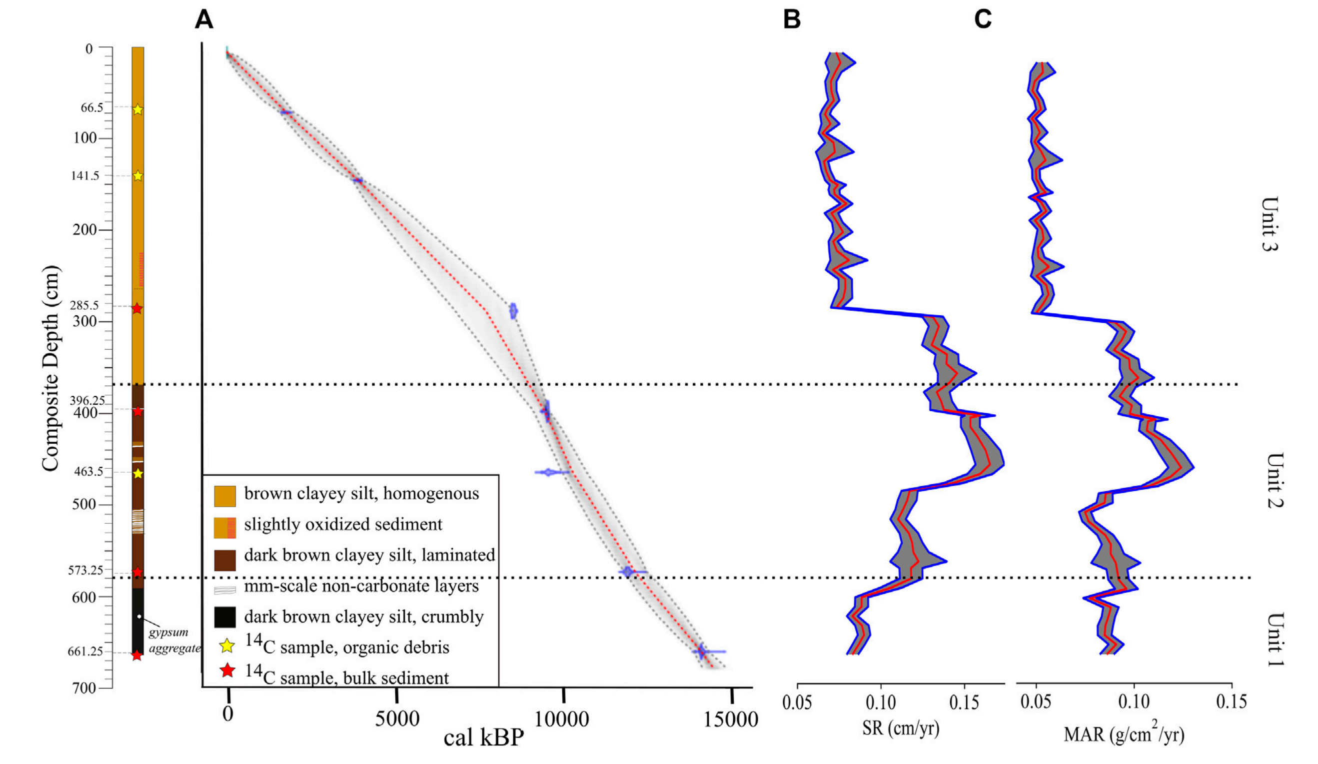

FIGURE 2 | (A) General stratigraphy and **(B)** age-depth model of the sediment core, based on radiocarbon dating of 7 samples, shown as green/yellow stars (see details in **Table 1**). **(C)** Inferred sedimentation and mass accumulation rate (SR and MAR) curves along the core, based on the age-depth model.

3 (~300 g m^{-2} a^{-1}), while Unit 3 values fall between Unit 1 and Unit 2 (~200 g m^{-2} a^{-1}).

General Stratigraphy

The composite sequence is separated into three broad stratigraphic units based on the sedimentological and biogeochemical analyses (**Figure 2**) and the cluster analysis (**Supplementary Figure S2**). Due to an existing talik (area of unfrozen ground surrounded by permafrost) below Lake Malaya Chabyda (Bakulina et al., 2000), the entire sequence was unfrozen. From bottom to top, stratigraphic zones are described as follows:

- Unit 1 (663–584 cm) (14.1 cal kBP–12.3 cal kBP). The bottom 80 cm of the sequence consists of dark brown massive (i.e., not laminated) clayey silt. The lower section (663–619 cm) is notably dry and has a 'crumbly' texture. A small gypsum aggregate particle was found within this unit (623 cm) and identified using a binocular microscope. The upper section (636–584 cm) appears less dry and displays mm-scale, sections of lighter grayish brown.
- Unit 2 (584–376 cm) (12.3 cal kBP–9.0 cal kBP). This unit is composed of dark brown, laminated, clayey silt with interstratified light brown to white laminations. These laminations are well-defined horizontal layers of non–calcareous sediment (based on room temperature HCl (10%) test), each one being approximately 1 cm thick and continuous across the width of the sediment cores. The light-colored laminations are notably visible at three sections of the unit, i.e., between 550 and 505 cm depth, and near 450 and 435 cm depth. Above 400 cm depth, the core transitions to homogenous light colored clay characteristic of Unit 3.
- Unit 3 (376–0 cm) (9.0 cal kBP–CE 2013). This unit is uniformly lighter brown, silty, homogenous (non-laminated) clay. Traces of oxidation were observed between ~265 and 225 cm depth.

Grain-Size Distribution

The grain size of the sediment core ranges from uni–, bi–, to trimodally distributed, and spans a size range from medium silt to very-fine sandy coarse silt. The mean grain size for the entire core is 29.05 μm (±6 μm), with a minimum size of 14.4 μm at 156 cm depth and a maximum size of 40.9 μm at 624 cm depth (**Figure 3**). The sorting ranges from poorly to very-poorly sorted. Sorting becomes generally more poorly sorted below 400 cm depth (**Figure 3**). The grain size distribution of clay, silt, and sand remains fairly consistent throughout the length of the core, with silt dominating the distribution (~80%) throughout the entire core (**Figure 3**).

Biogeochemistry

From the base of the sequence to the top of Unit 1 (584 cm depth), TOC content decreases consistently from 17 to 6.5 wt% (**Figure 4**).

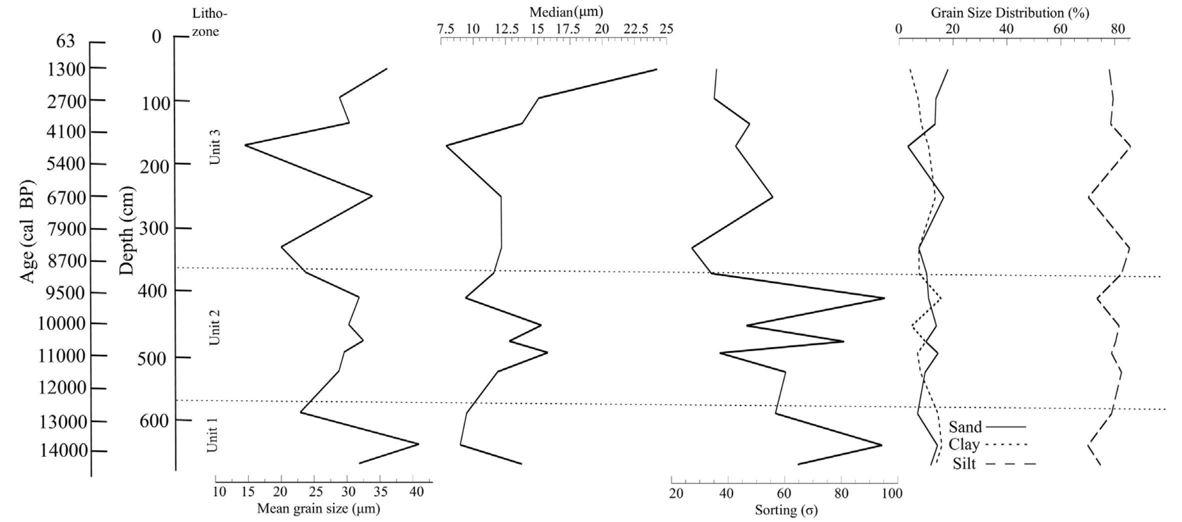

FIGURE 3 | Analysis of mean and median grain size, as well as sorting and grain size distribution (% of clay, silt and sand) of 16 samples.

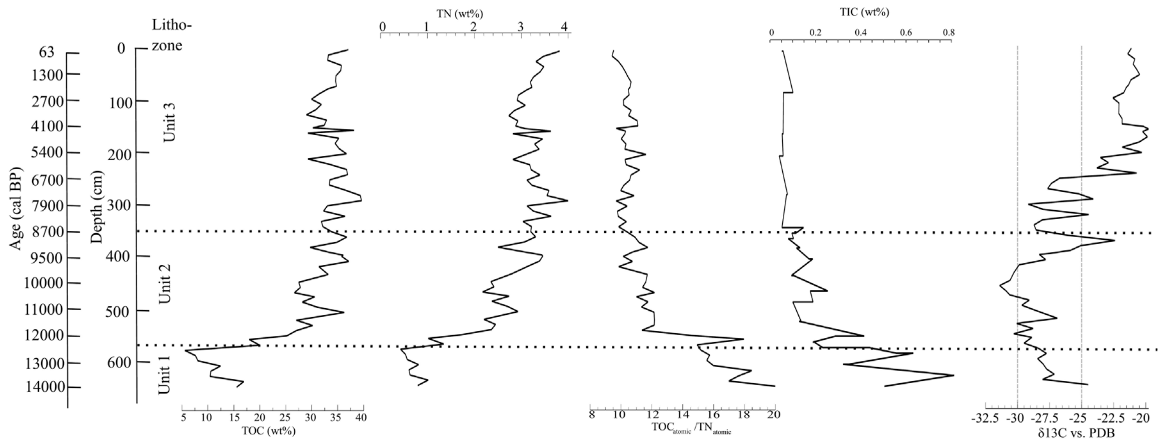

FIGURE 4 | Biogeochemical proxies measured of 78 discrete samples, including total organic carbon (TOC), total nitrogen (TN), TOC/TN_{atomic} ratio, total inorganic carbon (TIC) and $\delta^{13}C$ trends (vertical dashed lines represent the usual isotopic signature of C3 land plants; see **Figure 7**).

There is a sharp increase in TOC content from the lowest value of 6.5% at 584 cm depth (top of Unit 1) to ~35 wt% at just above 500 cm depth (base of Unit 2). The TOC content is relatively stable in the upper two units (Unit 2 and Unit 3) of the sediment sequence, remaining between 30–40 wt%. OCAR, controlled by both TOC and MAR, is at its lowest for the whole core (~63 g OC m^{-2} a^{-1}) at the top of Unit 1 (**Figure 5**). It then increases substantially throughout Unit 2 and the base of Unit 3, with highest values of 397 g OC m^{-2} a^{-1} around 400 cm depth. Above a depth of ~300 cm, OCAR decreases and stabilizes between 150 and 200 g OC m^{-2} a^{-1}. Considering each unit separately, OCAR average values are 101 g OC m^{-2} a^{-1} (ranging from 63 to 158 g OC m^{-2} a^{-1}) for Unit 1, 293 g OC m^{-2} a^{-1} (ranging from 168 to 397 gOC m^{-2} a^{-1}) for Unit 2, and 205 g OC m^{-2} a^{-1} (ranging from 144 to 354 g OC m^{-2} a^{-1}) for Unit 3.

Similar to TOC, TN is lowest in Unit 1 at the base of the core (below 1 wt%) and increases steadily throughout Unit 2 to approximately 3 wt% (**Figure 4**). TN is relatively stable throughout Unit 3 at approximately 3.5 wt%. There is less variability in TN above 150 cm depth and a steadily increasing trend to a maximum value of nearly 4 wt% at the top of the core (**Figure 4**). The TOC/TN_{atomic} is highest at the bottom of the sequence (TOC/TN_{atomic} = 20) and decreases consistently throughout Unit 1. After a transient peak at 570 cm depth (TOC/TN_{atomic} = 18), the TOC/TN_{atomic} ratio is very stable in the top two horizons of the sediment sequence, remaining at nearly 12 (**Figure 4**). The TOC/TN_{atomic} ratio is highest for Unit 1 (20), while Unit 2 and Unit 3 have similar values of 14 and 12, respectively (**Figure 6**). TIC content is low throughout the entire sequence (0.0–2.4 wt%), although Unit 1 (below 584 cm) has

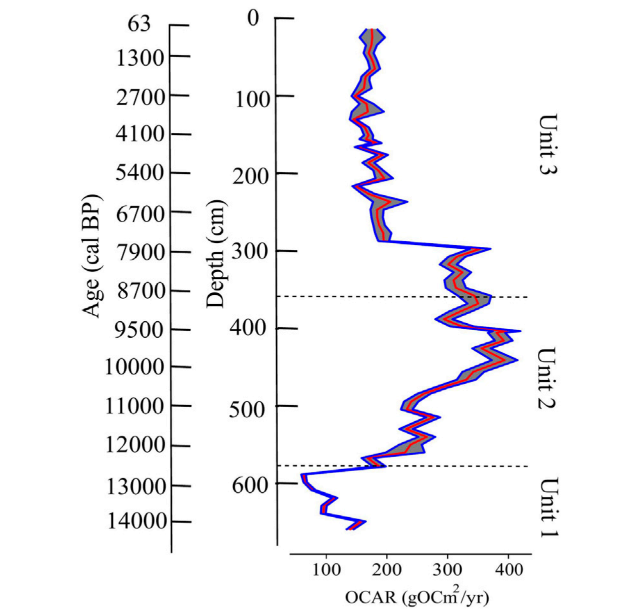

FIGURE 5 | Organic carbon accumulation rate (OCAR, in g OC m^{-2} a^{-1}) for each biogeochemical subsample along the core (see **Figure 4**), inferred from the age-depth model, as well as sedimentation and mass accumulation rates (see **Figure 2**).

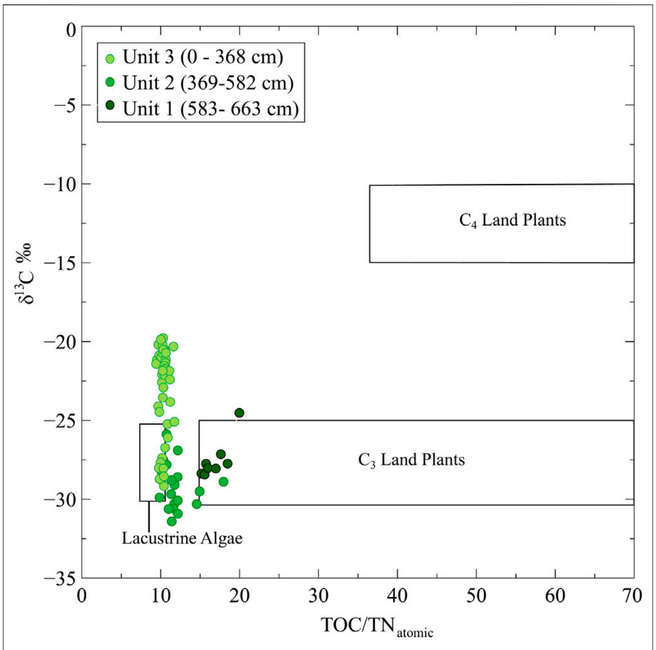

FIGURE 7 | $\delta^{13}C$ versus TOC/TN_{atomic} ratio of 78 discrete samples. Lacustrine algae, C_3 land plant, and C_4 land plant designations from Meyers and Teranes, 2002.

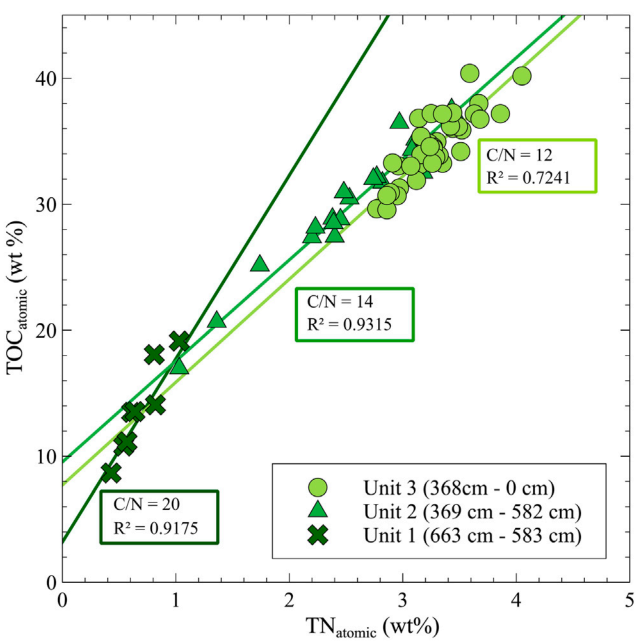

FIGURE 6 | Carbon (wt%) versus nitrogen (wt%) ratio by unit.

slightly higher average values compared to the other units (Unit 1 average: 1.9 wt% versus Unit 2 average: 0.6 wt%, Unit 3 average: 0.7 wt%) (**Figure 4**).

$\delta^{13}C$ values decrease consistently throughout Unit 1 (**Figure 4**). In the overlying units, $\delta^{13}C$ values increase from the lowest value (−31.9‰) at 475 cm depth (middle of Unit 2) until approximately 150 cm depth (middle of Unit 1) to −20.3‰. Above 150 cm depth, $\delta^{13}C$ values decrease slightly and then remain stable until the top of the core (**Figure 4**). Although identifying the distinct sources of organic material in a lacustrine environment is complicated by competing signals from the lake and catchment, the relationship between TOC/TN_{atomic} and $\delta^{13}C$ values can help further distinguish OM origin (Meyers and Teranes, 2002). Unit 1 plots within the C_3 land plant zone, while Units 2 and 3 plot within the lacustrine algae zone (**Figure 7**). Again, much of Unit 3 plots above typical values for lacustrine algae.

Inorganic Elemental Composition

The main rock forming elements analyzed include rubidium (Rb) (Kalugin et al., 2013), zirconium (Zr) (Marshall et al., 2011), titanium (Ti) (Balascio et al., 2011), silicon (Si) (Marshall et al., 2011; Martín-Puertas et al., 2011), calcium (Ca) and strontium (Sr) (Bouchard et al., 2011) and associated ratios. CLR transformed values of Rb and Zr have almost identical profiles (**Figure 8**). Unit 1 has the highest values of Rb and Zr with low variability. Unit 2 and Unit 3 have low values and very high variability. Ti has similar values in Unit 1 and Unit 3, but there is a notable decrease in Unit 2, with higher variability. Si values increase slightly through Unit 1, then decrease from the bottom of Unit 2 until the middle of Unit 3. Si values increase from 250 cm depth (6.7 cal kBP) to 100 cm depth (2.7 cal kBP), where the values remain consistent until the top of the core (**Figure 8**). Ca and Sr are high in Unit 1 with relatively low variability (**Figure 8**). The bottom half of Unit 2 shows a decrease

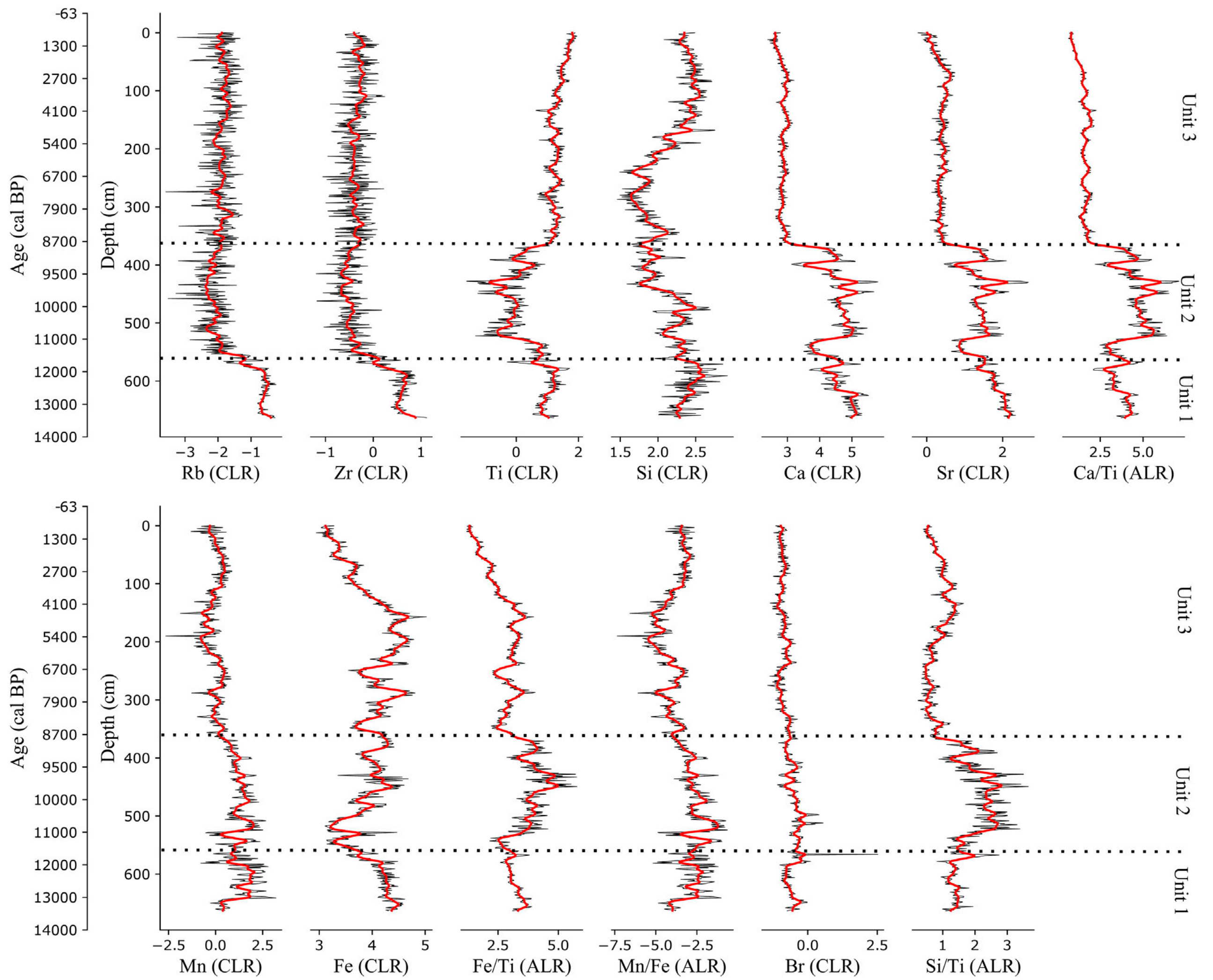

FIGURE 8 | XRF profiles of selected elements and elemental ratios along the core. The thin black lines represent continuous measurements (sampling interval of 10 mm), and the thicker red lines represent the 5-point running mean.

in Ca and Sr; values return to similar levels seen in Unit 1 in the upper half of Unit 2. These values decrease into Unit 3, where they are low with low variability. Ca/Ti, follows a similar trend to Ca. Unit 2 has the highest values, while Unit 3 has consistently low values and low variability (**Figure 8**).

Redox sensitive elements analyzed include manganese (Mn) and iron (Fe) (Haberzettl et al., 2007; Bouchard et al., 2011). Mn values are consistent throughout the entire core, with some small changes in the variability of the values between units. Fe values in Unit 1 are high, with low variability. There is a low peak in the lower half of Unit 2, with values returning to Unit 1 levels by the top of Unit 2. Fe values fluctuate between high and low peaks from the bottom of Unit 3 until approximately 150 cm depth (4.0 cal kBP), where values decrease consistently. Fe/Ti (**Figure 8**), which also represents reducing conditions as well as a possible reduction in grain-size (Marshall et al., 2011; Davies et al., 2015), decreases throughout Unit 1. Fe/Ti increases in the lower half of Unit 2, reaching the highest values at approximately 550 cm depth (~11.7 cal kBP), before decreasing in the upper half of Unit 2 and stabilizing in the lower half of Unit 3. Fe/Ti values decrease consistently throughout the upper half of Unit 3. Oxygenation of the water column is represented by Mn/Fe (Melles et al., 2012). The highest values are present in the lower half of Unit 2 around 500 cm depth (~11.0 cal kBP). Values decrease above 500 cm depth until the middle of Unit 3 at around 200 cm depth (~5.4 cal kBP), where values increase again until the top of the sediment core (**Figure 8**).

Elements and elemental ratios that are sensitive to changes in organic content include bromine (Br) (Kalugin et al., 2007, 2013; Bouchard et al., 2011) and silicon/titanium (Si/Ti) (Melles et al., 2012). Br values decrease throughout Unit 1 (**Figure 8**). Values in Unit 2 increase from the bottom of this unit until a large peak at 520 cm depth, after which, the values decrease. Unit 3 has decreasing Br values until 250 cm depth, after which there is a sharp, but brief increase. Br values decrease from approximately

230 cm depth until the top of the sediment core. Si/Ti, which is particularly sensitive to increases in biogenic silica (notably diatoms) (Melles et al., 2012), follows a different pattern. Unit 2 has the highest Si/Ti values (**Figure 8**). Unit 3 has Si/Ti values which are slightly lower than Unit 1, with a slight increase that peaks around 100 cm depth (2.6 cal kBP).

PCA Analysis

For Unit 1, PC1 accounted for 56.8% of explained variance, while PC 2 accounted for 22.7% variance (**Supplementary Figure S4A**). Ca, Sr, and TOC/TN_{atomic} are positioned together in the upper left quadrant, while Fe, C (wt%), TOC (wt%), and TN (wt%) are positioned together in the lower left quadrant. Zr is positioned in the upper right quadrant, while Ti is positioned in the lower right quadrant. $\delta^{13}C$ is very well negatively correlated to PC2.

For Unit 2, PC1 accounted for 39.6% of explained variance, while PC 2 accounted for 24.4% of explained variance (**Supplementary Figure S4B**). Ca and Sr are positioned together in the upper left quadrant, while TOC/TN_{atomic}, Zr, and Ti are positioned together in the bottom left quadrant. C (wt%), TOC (wt%), and TN (wt%) are very well positively correlated to PC1. Fe and $\delta^{13}C$ are well negatively correlated to PC 2.

For Unit 3, PC 1 accounted for 32.8% of explained variance, while PC2 accounted for 22.4% of explained variance (**Supplementary Figure S4C**). Sr is very well negatively correlated to PC 1, while Ca, TOC/TN_{atomic}, and Fe are positioned together in the lower left quadrant. C (wt%), TOC (wt%), and TN (wt%) are positioned together in the lower right quadrant. TOC (wt%) and C (wt%) are very well correlated. Ti is positioned in the upper right quadrant. Zr and $\delta^{13}C$ are very well positively correlated to PC 2.

DISCUSSION

Multiproxy-Inferred Paleolimnological History

Unit 1 (Late Pleistocene)

The observed depositional history of Lake Malaya Chabyda starts in Unit 1, which spans a time frame from approximately 14.1 – 12.3 cal kBP (Late Pleistocene). The TOC/TN_{atomic} ratio at the bottom of the core represents the maximum (20) measured in the entire recovered sequence, indicating a stronger contribution of carbon produced by vascular land plants than aquatic algae (**Figure 6**) (Meyers, 1994). Both, the TOC (average = 12 wt%) and TN (average = 0.68 wt%) values are lower in Unit 1 compared to Unit 2 and Unit 3, although relatively high compared to other sites in this region (Vyse et al., 2021). Combined with moderate MAR values (average = 0.09 g cm^{-2} a^{-1}), this resulted in the lowest OCAR values (average = 101 g OC m^{-2} a^{-1}) for the whole core (**Figure 2**, **Figure 5**). During the time of deposition, this region was still experiencing cold temperatures associated with the Late Pleistocene deglaciation period in the Northern Hemisphere and active microbial decomposition would have been restricted to a short period of time after spring thawing and before the onset of winter cold temperatures. Therefore, microbial decomposition would not have been particularly abundant, limiting significant OM degradation (Davidson and Janssens, 2006). As a result, the lower levels of TOC observed in Unit 1 cannot be explained solely by more active microbial decomposition compared to Unit 2 and Unit 3. It is more likely that Unit 1 experienced lower OC input compared to the upper two units. It is also possible that longer periods of ice cover compared to Unit 2 and Unit 3 restricted *in situ* autotrophic production (algae) in the lake. However, these TOC values are high compared to other reported values from Yedoma permafrost (Windirsch et al., 2020; Vyse et al., 2021; **Figure 8**). Moderately high $\delta^{13}C$ values, high TIC values, and relatively low TOC (**Figure 4**) compared to Units 2 and 3 corroborate lower levels of bioproductivity within the lake and indicate input from sources of inorganic carbon during this time (Schirrmeister et al., 2011), as shown in other lake records from Yakutia (Biskaborn et al., 2012). These trends could also reflect an increase in accumulation of authigenic $CaCO_3$, which was not explored in this study, but remains a possibility.

Unit 1 is massive, exhibiting no layering, and has fairly homogenous elemental composition for most of the elements examined using XRF. Analysis of detrital elements Rb, Zr, Si, and Ti indicate that Unit 1 had the highest level of terrestrial input compared to Unit 2 and Unit 3. Higher mineral detrital input coupled with low TOC, high TOC/TN_{atomic} ratio, and moderate $\delta^{13}C$ values indicate overall low productivity within the lake. The absence of soil stabilizing vegetation surrounding the lake due to prevalent cold conditions could have facilitated the input of clastic material from the catchment (Subetto et al., 2002; Nazarova et al., 2013). Si/Ti ratios and preliminary inspections of smear-slides (one slide for each unit) suggest that there are diatoms present in all units, indicating that there was an aquatic system at the core location (Vyse et al., 2020). This matches with a continuous diatom record over 14 cal kBP from Lake Ulakhan Chabyda (**Figure 1**) 4 km northwest of Lake Malaya Chabyda (Pestryakova et al., 2012; Herzschuh et al., 2013). High Ti values can also indicate increased run-off from precipitation events and/or increased aeolian deposition (Davies et al., 2015). This could have been the case at the study site, with active soil erosion and transport associated with poorly developed vegetation cover during this period of cold, Late Pleistocene climate (Biskaborn et al., 2021b). Precipitation was generally low in the study site region during the time of deposition, making increased aeolian deposition more likely than increased run-off from precipitation events (Biskaborn et al., 2012). Relatively high Ca, Ca/Ti, and Sr values can be indicative of a persistent alkaline environment under semi-arid conditions, which can be attributed to Lake Malaya Chabyda during the deposition of Unit 1. These conditions are also observed in neighboring lakes (Ulkahan Chabyda and Temje Lake) (Herzschuh et al., 2013; Nazarova et al., 2013). Both low precipitation and/or strong summer insolation would enhance evaporation. Additionally, during this period, there were open landscapes, strong winds, and, as a result, increased evaporation from the surface of the lakes. The absence of soil cover and swamps around the lake contributed to the absence of humic acids in the surface runoff and the water in the lake was predominantly alkaline, with low bioproductivity and ultra-oligotrophic in contrast to the later Holocene period. It is also possible that changes in Ca, Ca/Ti, and Sr trends throughout the core are more related to changes in regional sources for these elements.

The Mn/Fe ratio for the Lake Malaya Chabyda core is generally higher and more variable in the lower sections of the core, specifically in Unit 1. Higher Mn/Fe compared to the rest of the core indicates predominately oxic conditions as Mn is more readily reduced (dissolved) under anoxic conditions compared to Fe (Davies et al., 2015; Vyse et al., 2020). Shallow lake depth (i.e. light can penetrate to the bottom of the lake) as well as low productivity and stronger lake water mixing could be responsible for maintaining oxygenated bottom waters and a shallow lake could experience evaporation indicated by the proxies described above.

Grain-size distribution and sorting provide information about the dominant denudation, erosional, and transport processes at the study site. Grain size ranges from coarse silt to fine silt and poor to very-poorly sorted sediments are present throughout the entire core (**Figure 3**), indicating either a relatively short sediment transport distance or the influence of a combination of different erosional and transport processes (Folk and Ward, 1957). It is also possible that the early lake had a very different shore structure than is present today and that active slumping and abrasive processes could have taken place, creating a large amount of unsorted mineral matter input to the lake. A longer transport distance or the influence of a single dominant transport process, such as aeolian activity, would likely have resulted in stronger sorting of grain sizes throughout the core (Biskaborn et al., 2013). Unit 1 sediments are slightly more "poorly sorted" compared to Unit 2 and Unit 3. This is perhaps related to higher detrital input from the surrounding catchment. The polymodal nature of the grain size distributions suggests that the source sediments are heterogeneous and polygenetic in origin (**Supplementary Figure S5**) (Schirrmeister et al., 2011; Wang et al., 2015; Ulrich et al., 2019). According to grain-size results, there is no sand-dominated material that could have clearly confirmed the sand-dune origin ('tukulan') of the lake, as sand percentage remained <20% along the whole core, including at its base (**Figure 3**). In fact, the top of the core has the highest percentage of sand (18%). However, we expect that such sand-rich deposits lie deeper, in older sediments.

Unit 2 (Late Pleistocene-Holocene Transition)

The proxy analyses suggest that Unit 2, spanning the Late Pleistocene-Early Holocene transition (~12.3 – 9.0 cal kBP), was deposited under variable limnological conditions. Unit 2 has a consistently high level of TOC (30 – 36 wt%; average 31 wt%), and its TOC/TN_{atomic} ratio (average of 14, ranging from <10 to 18) is close to the 4 – 10 range indicating production by phytoplankton or algae (Meyers, 1994; Ulrich et al., 2019) (**Figure 6**). There is a consistent reduction in TIC throughout Unit 2, while $\delta^{13}C$ first decreases slightly, then increases in the upper half of Unit 2 (**Figure 4**). $\delta^{13}C$ values can vary inversely to water depth and/or in a direct relationship with primary productivity (Meyers, 2003), suggesting that Lake Malaya Chabyda could have experienced lake deepening and then shallowing and/or a decrease followed by an increase in primary productivity within the lake as is supported by strongly increasing Si/Ti values (**Figure 8**). During the Holocene, increasing thermokarst activity likely caused lake deepening, followed by lake shallowing as thermokarst activity stabilized and the lake depression began to be filled by sediments (Andreev et al., 2003). Analysis of these proxies nonetheless suggests a transition to a dominance of lacustrine versus terrestrial carbon source between 12.3 cal kBP and 9.0 cal kBP (Biskaborn et al., 2013).

Sedimentation experienced an initial decrease in the bottom half of Unit 2 (MAR decreasing from 0.09 g cm^{-2} a^{-1} bottom of Unit 2 to 0.07 g cm^{-2} a^{-1} at 500 cm depth), before peaking above 0.1 g cm^{-2} a^{-1} at 453 cm depth (**Figure 2**). MAR then decreases slightly until about 300 cm depth. OC delivery was high during the Early Holocene (average OCAR ~292 g OC m^{-2} a^{-1} above 574 cm of composite depth, i.e., after ~12 cal kBP). Such rates are clearly well above the reported values for high-latitude lake basins and notably higher than global modern values (Vyse et al., 2021 and references therein).

Unit 2 is the only unit in the Lake Malaya Chabyda sediment core which exhibits any clear layering or laminations (**Figure 2**). The subsection of Unit 2 between 535 cm depth and 500 cm depth exhibits the most pronounced layers, with mm scale alternations between light colored non calcareous layers (determined using dilute acid) and the brown, massive clayey silt layers. The presence of these layers indicates a lack of bioturbation and enhanced preservation of OM (Melles et al., 2012). Analysis of detrital elements, Rb and Zr indicate that Unit 2 experienced lower levels of detrital input compared to Unit 1 and higher rate of deposition of organic material produced within the lake, i.e., by algae. Unit 2 has the lowest Ti values compared to Unit 1 and Unit 3, further suggesting a decrease in detrital input. This signal could also be related to a decrease in the relative proportion of detrital inputs due to an increase in accumulation of lighter OM produced within the lake coupled with a decrease the detrital input (Balascio et al., 2011; Davies et al., 2015). This signal is also corroborated by a slight decrease in SR between Unit 1 and Unit 2 and a decrease in MAR between Unit 1 and Unit 2. A shift in bulk sediment deposition from mainly allochthonous in Unit 1 to mainly autochthonous sources in Unit 2 is likely indicative of an increase in biological activity within the lake contributing to an increase in the deposition of OM compared to sediment input from the surrounding catchment. In the Holocene, vegetation cover and soils are formed within the catchment area, resulting in a weakening of the processes of denudation and erosion (Andreev et al., 2003). Only dissolved substances enter the surface runoff, and groundwater and sedimentation begin to be dominated by intra-reservoir processes, particularly, the bioproductivity of the lake ecosystem (Subetto et al., 2017).

Values of Ca and Sr in Unit 2 are more variable but have slightly lower average values compared to Unit 1. There is a low peak in both elements at approximately 530 cm depth (approximately 11.3 cal kBP) suggesting that the lake did not experience any significant evaporative stages or that there were changes in the availability and input source of Ca-rich clastic material. These variabilities in Ca and Sr could also be associated with changing wind directions and reallocation of sediment sources controlled by migrating dune features, as well as changing patterns of detrital input from the surrounding catchment. These variabilities may also be due to a change in the hydrochemical characteristics of the water in the lake. Above this low peak, Ca and Sr values return to Unit 1 levels, but with higher variability, suggesting continued changes within the catchment that affected the source and/or availability of Ca and Sr source materials. Unit 2 has the highest values for Ca/Ti, which can indicate carbonate deposition (Davies et al., 2015). Ca/Ti can be controlled by in-lake (autochthonous) carbonate precipitation, biologically mediated calcite production, and/or input of additional old carbonate from catchment sources. Haberzettl et al. (2007) suggest that high Ca/Ti values indicate lower lake levels, resulting in a proliferation of biologically induced calcite production (i.e., *P. lenticularis*) related to warmer water temperatures and higher concentrations of nutrients. Warmer water temperatures and higher concentrations of nutrients could be related to shallow lake conditions for Unit 2. These hypotheses are corroborated by $\delta^{13}C$, which increases consistently throughout Unit 2, suggesting a decrease in water depth and/or an increase in biological activity (Meyers, 2003).

The Mn/Fe ratio for Unit 2 decreases consistently throughout the entire unit. Oxygen-depleted conditions could be related to continued microbial activity beneath the winter-ice cover and/or higher levels of primary productivity associated with mixing of the bottom waters in the summer season (Hughes-Allen et al., 2021). This is a possible scenario as the Early Holocene experienced very cold winters (Meyer et al., 2015) and thus prolonged periods ice cover (Biskaborn et al., 2012). The Early Holocene is also associated with an increase in thermokarst lake development in central Yakutia related to warm summers. Warm summer temperatures, like prolonged periods of ice cover, can cause periods of anoxic bottom waters (Hughes-Allen et al., 2021). This is also supported by PCA biplots (**Supplementary Figure S4**), suggesting a strong relationship between redox-sensitive elements (Fe) and organic matter proxies in the lower units 1 and 2 (Heinecke et al., 2017).

Unit 2 has the highest Si/Ti values compared to the other two units, which is also indicative of high levels of biological activity. The depositional characteristics of Unit 2 suggest that a transition occurred at approximately 12.3 cal kBP from the preferential deposition of terrestrial carbon and low lake primary productivity conditions of Unit 1 to preferential deposition of aquatic carbon and high lake primary productivity in Unit 2.

Unit 3 (Early Holocene to Present)

The proxy analyses indicate that Unit 3, deposited since the Early Holocene (~9.0 cal kBP), was formed with some variability in lake depth, bottom water oxygen availability, and biological activity. Unit 3 is more homogenous than Unit 1 and Unit 2, both in terms of a lack of discernable laminations or other features and homogeneity within the biogeochemical metrics analyzed. Average TOC content is >34 wt% (ranging from 29 to 39 wt%) in this unit, higher than elsewhere along the core and an order of magnitude above most of the reported values for lakes across Yedoma regions (Vyse et al., 2021). Presumably, this period heralded higher levels of bioproductivity and increased nutrient supply to an expanding lake at the study site. The mean TOC/TN_{atomic} ratio of Unit 3 is 12, which indicates some dominance of production by phytoplankton or algae (Meyers, 1994; Ulrich et al., 2019) (**Figure 6**) with minor contribution from vascular plants in the lake catchment area (Heinecke et al., 2017). Shallower lake waters would have amplified the influence of carbon from the lake catchment on the TOC/TN_{atomic} ratio. This value suggests a dominance of lacustrine rather than terrestrial carbon input between 9.0 cal kBP and present day (Biskaborn et al., 2013).

OC delivery decreased after 7.9 cal kBP, as shown by an average OCAR of 205 g OC m^{-2} a^{-1} for Unit 3. This was the result of lower sedimentation (average MAR decreasing from ~0.1 g cm^{-2} a^{-1} at the top of Unit 2 to ~0.04 g cm^{-2} a^{-1} in the upper section of Unit 3). Still, OCAR values of 200 g OC m^{-2} a^{-1} are notably in the upper range of global modern values and significantly higher than elsewhere across high-latitude regions (Vyse et al., 2021; **Figure 8**). TIC remains consistently low throughout Unit 3, while $\delta^{13}C$ increases in the lower half of the unit, before decreasing and then stabilizing in the upper half of the unit. This could indicate decreasing lake levels followed by increasing lake levels. Changes in $\delta^{13}C$ could also be controlled by changes in primary productivity. In this case, primary productivity would have decreased briefly, then increased from the bottom to the top of Unit 3 (Meyers, 2003).

The profiles for detrital elements Rb and Zr are nearly identical to Unit 2 and offer no strong indications of changing catchment regimes or erosional transport. However, Ti values are much higher compared to Unit 2, returning to Unit 1 levels. It is possible that Ti deposition was more sensitive to increases in detrital input. Ti can be also be associated with increased run-off from rain events (Corella et al., 2012) and/or increased aeolian deposition (Bakke et al., 2009) and it is possible that the observed trends are linked to changes in these processes.

Unit 3 has the lowest values for elements Ca and Sr, suggesting a distinctly lacustrine environment that did not experience any significant evaporative events. Ca/Ti, which is also associated with evaporative events, is also consistently low and less variable throughout Unit 3. Mn/Fe values decrease from the bottom of Unit 3 until approximately 200 cm depth (5.4 cal kBP), suggesting increasing lake depth and more frequent periods of anoxic bottom water conditions (Davies et al., 2015). As lake depth increases, unfrozen lake water persists during winter and microbial activity can continue under the ice cover. The ice cover does not allow gas exchange with the atmosphere, creating an anoxic environment at the water-sediment interface (Hughes-Allen et al., 2021). Anoxic conditions can also occur in the summer related to high levels of primary productivity. Unit 3 has the lowest Si/Ti values (between 390 cm depth and 175 cm depth) compared to the rest of the core, and relatively low levels of Br, which can be related to decreases in the input of biogenic silica (Melles et al., 2012) and organic content (Kalugin et al., 2007, 2013; Bouchard et al., 2011), respectively. These low values for elements normally associated with high biological activity suggest that primary productivity is not high enough to account solely for an increase in anoxic bottom water conditions. Mn/Fe values increase from 200 cm depth until approximately 75 cm depth (1.9 cal kBP), where they remain stable until the top of the sediment core. Increasing Mn/Fe values suggest less frequent anoxic conditions, which might have resulted from moderate lake depth decrease, enhanced wind activity, and/or shorter periods of ice-cover allowing for more water column mixing (Hughes-Allen et al., 2021). Si/Ti values also increased during the same time period, potentially indicating a slight increase in the deposition of biogenic silica, which could be related to an increase in primary productivity. Perhaps a decrease in lake depth, that was not so drastic as to cause Lake Malaya Chabyda to freeze to the lake bottom in the winter, caused an increase in water temperature and increased nutrient concentrations during the biologically productive ice-free seasons. These analyses suggest that Unit 3 was deposited under very stable sediment deposition conditions, although there was some variability in lake depth, bottom water oxygen availability, and biological activity. Lacustrine algae were the main source of OC deposited in the lake during this period.

Lake Malaya Chabyda Carbon Accumulation Rates

Total organic carbon concentration (TOC) is a crucial proxy for understanding the abundance of OM in sediments, including the proportion of OM that evaded remineralization during the sedimentation process. The concentration of OM in sediment is generally equivalent to twice the recorded TOC value (Meyers, 2003). Therefore, TOC values can suggest initial production of biomass as well as subsequent levels of degradation. Moreover, since TOC concentrations are expressed in % weight, therefore influenced by mineral/clastic matter inputs (artificially diluted or concentrated), it can be useful to infer organic carbon (OC) accumulation rates (expressed as mg OC cm^{-2} a^{-1} or g OC m^{-2} a^{-1}) when reliable age-depth model and estimations of sediment dry bulk density for each sample are available (Meyers, 2003).

High TOC values, high TOC/TN_{atomic} ratios, and low $\delta^{13}C$ generally reflect OM which have not undergone significant decomposition under anaerobic conditions (Schirrmeister et al., 2011; Ulrich et al., 2019). Although Unit 1 showed the highest TOC/TN_{atomic} ratio (20), it also had a lower weight percent of carbon (<20 percent C) compared to Unit 2 and Unit 3 (greater than 30 percent C for both units). Unit 1 can therefore be classified as a mineral sediment (<20% C). Mineral sediments lose 6–13% on average of their OC within 1 decade after exposure due to thawing or other processes (Schirrmeister et al., 2011). Moreover, the inferred OCARs for Unit 1 indeed represent the lowest values of the whole sequence, with an average of ~100 g OC m^{-2} a^{-1} (ranging from 63 to 158 g OC m^{-2} a^{-1}; **Figure 5**). These low values are nevertheless higher than reported rates for temperate latitudes, such as the Great Lakes in North America (e.g., Meyers, 2003), and much higher than several arctic/subarctic sites, such as northern Québec (Ferland et al., 2012, 2014), Finland (Pajunen, 2000), Greenland (Anderson et al., 2009; Sobek et al., 2014), as well as southeastern and northeastern Siberia (Martin et al., 1998; Vyse et al., 2021).

Unit 2 and Unit 3 have greater than 20% carbon and are therefore classified generally as organic sediments. Unit 2, in particular, exhibited significant layering, which suggest a lack of bioturbation and enhanced preservation of OM and/or seasonal changes in sedimentation processes. Organic deposits, including deposits that are aquatic in origin (i.e. fluvial, alluvial, and lacustrine), typically exhibit decade-long losses of 17 – 34% of their OC after exposure by thawing or other processes (Schirrmeister et al., 2011). Some studies suggest that input of ancient carbon into aquatic systems may augment or even galvanize remineralization of modern dissolved OC (Vonk and Gustafsson, 2013; Mann et al., 2015; Strauss et al., 2017). This effect is likely due, in part, to low levels of carbon decomposition during deposition (i.e. colder conditions) and before thawing (Vonk et al., 2013). A significant portion of the Lake Malaya Chabyda sediment core is classified as organic sediment, which is predicted to lose comparatively high percentages of their OC upon potential exposure. Jongejans et al. (2021) found that although the OC content of the Yukechi Yedoma ice complex sediments was relatively low, there was substantial greenhouse gas release upon thawing. These findings point to OM quality and decomposition history and more important drivers of greenhouse gas release than OM content alone (Jongejans et al., 2021). Although a lake currently exists, proxy evidence discussed above suggest that Lake Malaya Chabyda did experience high levels of evaporation, which might have brought the lake close to desiccation in the past. Changing temperature and precipitation regimes, lower precipitation and higher temperatures for example, might make drying out more likely in the future for this relatively small and shallow lake. In this case, it is important to consider OM quality and possible future greenhouse gas release. Furthermore, inferred OCARs for Unit 2 show a strong increase from the base (187 g OC m^{-2} a^{-1}) to the top (321 g OC m^{-2} a^{-1}) of this unit, in accordance with developing lacustrine conditions and enhanced biological productivity from algae (i.e., mostly autochthonous source of OM). OC accumulation rates for Unit 3 are slightly lower, but still quite high (average of ~200 g OC m^{-2} a^{-1}, ranging from 144 to 354 g OC m^{-2} a^{-1}) compared to other reported values in both temperate and high-latitude regions (Meyers, 2003; Vyse et al., 2021 and references therein). As Lake Malaya Chabyda is located in a semiarid climate, with high summer temperatures and humid climate, the primary production in its ecosystems can be quite high, resulting in strong accumulation of organic matter in bottom sediments (Biskaborn et al., 2021b). Given the significant increase of OCAR (**Figure 5**) and TOC accumulation (**Figure 4**) around 11 cal kBP, Lake Malaya Chabyda likely transitioned to an OC sink at approximately the Pleistocene-Holocene transition. However, data about lake morphology (especially the ratio between lake area and mean depth) and C emissions, which control the net C balance (Ferland et al., 2012), are not available for this site. Ferland et al. (2012) found that sediments in large and shallow lakes (i.e., Lake

Ulakhan Chabyda), experience higher rates of decomposition compared to smaller lakes. This is due, in part, to the greater exposure of sediments in these lakes to warmer surface waters which accommodate higher rates of sediment decomposition. Additionally, small lakes, especially those with steeper bathymetry, can have high sedimentation rates and sediment focusing, which reduces the efficiency of sediment decomposition. These characteristics of small lakes lead to generally lower rates of OC degradation and enhanced long-term burial and storage of carbon. Compared to the nearby Lake Ulakhan Chabyda, notably larger but shallower (see study area above), Lake Malaya Chabyda likely acted as a more efficient C sink (per m^2) with its 'compact' morphology (Ferland et al., 2014). The relatively high sedimentation rate recorded within Lake Malaya Chabyda, especially between 13 cal kBP – 7.9 cal kBP, likely also contributed to the lake acting as an efficient C sink, in part by reducing O_2 exposure time (Ferland et al., 2014).

$\delta^{13}C$ values can provide information about sources of OM and past productivity trends, as well as identify changes in the availability of nutrients in surface waters (Meyers, 2003; Ulrich et al., 2019). As phytoplankton preferentially use the lighter carbon isotope (^{12}C), an increase in productivity causes an initial, but relatively brief decrease in $\delta^{13}C$ in the lake water. However, as the phytoplankton deplete dissolved inorganic carbon stores in the lake, the $\delta^{13}C$ values of the residual inorganic carbon in the lake water increases, causing enrichment in the $\delta^{13}C$ values of the newly created OM (Meyers and Teranes, 2002). Re-equilibration between lake water DIC and atmospheric CO_2 will occur over time, resulting in the deposition of OM not enriched in $\delta^{13}C$ in the sediment layer. $\delta^{13}C$ values decrease slightly from the bottom of the core until a low point at approximately 450 cm depth (10.0 cal kBP) (middle of Unit 2). This $\delta^{13}C$ trend is complicated by the high levels of TOC and a TOC/TN_{atomic} value of 14 in Unit 2, which would normally accompany more enriched $\delta^{13}C$ values (Meyers and Arbor, 2001). It is possible that these low $\delta^{13}C$ values around 450 cm depth are related to changes in the $\delta^{13}C$ signature of available DIC in the lake and/or to changes in the degradation pathways of the $\delta^{13}C$. It is also possible that low algae production in the lake resulted from long periods of ice cover and/or low temperatures unfavorable to primary production.

$\delta^{13}C$ values increase consistently from 450 cm depth (10.0 cal kBP) to 150 cm depth (4.0 cal kBP), where they remain stable to the top of the core, suggesting a continuous increase in primary productivity. However, this assumption is complicated by the fact that water from Lake Ulakhan Chabyda can flow into Lake Malaya Chabyda during times of high water. As Lake Malaya Chabyda is relatively small, it is possible that this influx of water could affect the $\delta^{13}C$ signal in the sediment core. An increase in $\delta^{13}C$ values can also be related to an increase in nutrient delivery from soil erosion and/or active layer development. Perhaps the continued expansion of Lake Malaya Chabyda by thermokarst processes has increased the availability of nitrates and phosphates, which could have enhanced primary productivity, resulting in an increase in $\delta^{13}C$ values (Meyers and Teranes, 2002).

The TOC/TN_{atomic} vs $\delta^{13}C$ relationship (**Figure 7**) suggests that the majority of carbon deposited between 14.1–12.3 cal kBP (Unit 1) was from terrestrial (C_3) land plants (Meyers and Arbor, 2001; Ulrich et al., 2019). This suggests that the bioproductivity in the lake was very low at the time of deposition (Heinecke et al., 2017) and therefore not recorded in the sediment core. Also possible is that detrital input to the lake was very high during this time, as discussed above. Moderate MAR combined with low TOC resulted in relatively lower OCAR values within Unit 1 (**Figure 2C**; **Figure 5**). The dominance of vascular plant carbon also suggests higher input from the lake catchment to the lake compared to the upper two units. Thermokarst lakes usually do not have a classical littoral zone and the edges of the lakes are often overgrown with aquatic vegetation and surrounded by peat bogs. Therefore, there is no direct mineral runoff from the catchment area, as it is filtered by the peatlands. However, there can be significant input of organic matter coming from the surrounding peatlands to the lake. The OM found in Units 2 and 3 plots more toward an origin of lacustrine algae. Many of the points in Unit 3 plot above the expected values for lacustrine algae. The relatively high values (>−25‰) generally occur above 250 cm depth (6.7 cal kBP). Enriched $\delta^{13}C$ values can occur is alkaline lacustrine systems where there is limited availability of dissolved atmospheric CO_2 ($\delta^{13}C$ = −8.5‰), therefore HCO_3- ($\delta^{13}C$ = 1‰) becomes the dominant source of inorganic carbon for lake algae, shifting the isotopic signature to higher (more enriched) values (Meyers, 2003). This effect might have been limited in Lake Malaya Chabyda, where modern pH is slightly acidic (pH = 6.71). This change in carbon source is reflected by comparatively heavier isotopic compositions for lake algae than normally expected (Meyers, 2003). Periods of very high bioproductivity resulting in a depletion in dissolved CO_2 can be responsible for a shift from CO_2 to HCO_3^-, among other possible explanations (Meyers, 2003).

Connections Between the Lake Environment, Permafrost Dynamics, and Climatic Conditions

Lake development and thermokarst activity began in earnest in Eastern Siberia between 15.0–10.0 cal kBP (Nazarova et al., 2013; Ulrich et al., 2019), with the postglacial period experiencing gradual rising temperatures and permafrost thaw (Schirrmeister et al., 2011; Biskaborn et al., 2019b). However, this period was also punctuated by periods of colder temperatures and low precipitation (Andreev et al., 2003; Nazarova et al., 2013). Andreev et al. (2003) recorded a transient climate amelioration during the Allerød in Eastern Siberia based on pollen spectra collected from a sediment core from Lake Ulakhan Chabyda (9.75 m depth). They suggest that mean July temperatures in this area were 1.5–2°C below present values and January temperatures were −2– −5°C colder (mean annual temperatures −3– −4°C colder than present). However, subsequent low precipitation levels (150 mm/year lower than modern conditions) and colder temperatures (Andreev et al., 2003) likely slowed the development of many nascent thermokarst lakes that were created during this relatively brief warm period before the onset of the Younger Dryas. Paleoclimatic estimates suggest that mean summer temperature decreased by 3°C and January mean temperature decreased by 6–7°C during the Younger Dryas (Andreev et al., 2003). It is possible that these environmental conditions lead to the signal, recorded in Unit 1 (14.1 cal kBP–12.3 cal kBP), of higher inputs of terrestrial plants from the surrounding catchment rather than deposition of OM produced in the lake. We also see lower values of Br, associated with organic matter production, and Si/Ti, usually related to biogenic silica production, in Unit 1 compared to the other two units. Dry, cold conditions, associated with permafrost stability in the catchment (i.e., no or rare thermokarst activity) and persistent ice cover, were likely favorable to increased detrital input from the catchment to the lake relative to organic matter, as recorded by the XRF signals.

Environmental conditions during the time of deposition of Unit 2 (12.3 cal kBP–9.0 cal kBP) encompassed the Younger Dryas cool period. Conditions during the height of the Younger Dryas were likely colder and dryer than today and then experienced a slow, but persistent warming associated with the end of the Younger Dryas and the transition to the Early Holocene warm period (Andreev et al., 2003; Katamura et al., 2006; Biskaborn et al., 2012; Ulrich et al., 2019). Müller et al. (2009) records the peak of the episodic cooling and drying related to the Younger Dryas between 12.4–11.3 cal kBP based on pollen records from a sediment core taken from Lake Billyakh (approximately 400 km north-west of Lake Malaya Chabyda). However, the conditions were likely still warmer and wetter than the period before the Allerød climate amelioration (15–13.5 cal kBP) (Müller et al., 2009). It is difficult to see evidence of the Younger Dryas in the proxy data analyzed for the Malaya Chabyda sediment core. The transition to the Holocene climate optimum began around 11.3 cal kBP in Eastern Siberia as recorded in the pollen record, peaking between 6.7–5 cal kBP (Müller et al., 2009; Nazarova et al., 2013; Biskaborn et al., 2016). This transition, likely associated with enhanced thermokarst activity, is reflected in the increased deposition of OM produced within the lake, as well as a reduction in detrital input from the surrounding catchment (e.g., Bouchard et al., 2017, and references therein). Proxies (e.g., Mn/Fe) also indicate potentially stronger depletion in bottom-water oxygen caused by enhanced water column stratification during this time (Bouchard et al., 2011). Velichko et al. (1997) reconstructed January and July temperatures that were still 1°C and 0.5°C lower than present values combined with 25 mm/yr lower annual precipitation.

Lake development processes, including thermokarst, generally increase across the region at the time of the Early Holocene warm period, which corresponds to the lower boundary of Unit 3 (9.0 cal kBP–CE 2013) (Müller et al., 2009; Nazarova et al., 2013). Nazarova et al. (2013) hypothesize that temperatures between 8–4.8 cal kBP were likely warmer than present day and record an increase in the sedimentation rate in Lake Temje consistent with increased biological production. July temperatures are recorded to be 1.5°C warmer than today, with the warmest temperatures occurring between 6.7–5 cal kBP. Our results show an increase in sedimentation rates at approximately 10.0 cal kBP, based on the age depth model, and higher TOC values after 9.5 cal kBP, resulting in notably higher OC accumulation rates during the first half of the Holocene. The upper half of Unit 2 seems to be distinctly lacustrine and the development of the lake basin was likely facilitated by rising precipitation levels and associated permafrost thaw (Nazarova et al., 2013; Schirrmeister et al., 2013; Ulrich et al., 2019).

Temperatures dropped below modern values in Central Yakutia after approximately 4.5 cal kBP with the low peak estimated to have occurred between 3.0 and 2.0 cal kBP (Biskaborn et al., 2012; Nazarova et al., 2013). This cooler episode ("Neoglacial") has also been reported elsewhere across the circumpolar North, for example, in the Canadian Arctic (Fortier et al., 2006; Bouchard et al., 2020). After this cool period, there is a general warming trend, interspersed with short-term temperature fluctuations to present-day values (Biskaborn et al., 2021a). It is possible that the enriched $\delta^{13}C$ observed in the upper half of Unit 3 are in response to warmer temperatures and favorable growing conditions.

CONCLUSION

- Here we present an in-depth and high-resolution analysis of a nearly 7-m-long sediment core which spans the Pleistocene-Holocene transition and encompasses a continuous Holocene time series. There was considerable variation in biogeochemical proxies both between and within three stratigraphic units.
- A shift occurred between 12.5 cal kBP to 11.0 cal kBP from predominately terrestrial land plant contribution to lacustrine algae contribution, which is recorded in OM deposition.
- Unit 2 and Unit 3 have high TOC values, high TOC/TN_{atomic} ratios, and low $\delta^{13}C$, generally indicating OM which have not undergone significant decomposition under anaerobic conditions.
- There is high carbon content, including TOC (wt%) for this sediment core compared to other similar sites in Central Yakutia, and elsewhere across the Arctic. OCARs are above the highest reported values for temperate and high-latitude regions, for both past (Holocene and Late Pleistocene) and modern conditions. Lake Malaya Chabyda might have thus acted as a significant OC sink since the Pleistocene-Holocene transition.
- Increases in lake depth and nutrient availability from the catchment increased bioproductivity within the lake and organic matter preservation and storage relative to decomposition. Compact lake morphology (relatively small surface-to-depth ratio), associated with higher sedimentation rates and less exposure to warmer and oxygen-rich shallow waters, likely contributed to notably high OC preservation.

DATA AVAILABILITY STATEMENT

The datasets presented in this study can be found in online repositories. The names of the repository/repositories and accession number(s) can be found below: Pangaea doi.pangaea.de/10.1594/PANGAEA.933411.

AUTHOR CONTRIBUTIONS

FB and BB developed the project idea. BB, LP, BD, and DS collected the sediment core. LP and DS provided logistical support for field work and shipment of the sediment core. LH-A conducted laboratory analyses along with HM and CH. LH-A wrote the manuscript with contributions from FB, BB and CH, HM and DS.

ACKNOWLEDGMENTS

The authors would like to thank the Melnikov Permafrost Institute (Yakutsk) for their collaboration and fieldwork assistance. We are also grateful to A. Rudolf (AWI) for his calculation of lake catchment area. D. Scheidemann (AWI) and J. Lindemann (AWI) provided laboratory support and analyses. Many thanks to G. Fougeron for his invaluable and patient help with statistical analysis and python programming. DS was supported by Ministry of Education of the Russian Federation (project No. FSZN-2020-16). LH-A and FB are supported by the Agence nationale de la recherche (ANR) through the Make Our Planet Great Again initiative (Programme d'investissements d'avenir – project no. ANR-17-MPGA-0014).

SUPPLEMENTARY MATERIAL

The Supplementary Material for this article can be found online at: https://www.frontiersin.org/articles/10.3389/feart.2021.710257/full#supplementary-material

REFERENCES

Anderson, N. J., D'Andrea, W., and Fritz, S. C. (2009). Holocene Carbon Burial by Lakes in SW Greenland. *Glob. Chang. Biol.* 15, 2590–2598. doi:10.1111/j.1365-2486.2009.01942.x

Andreev, A. A., and Klimanov, V. A. (2000). Quantitative Holocene Climatic Reconstruction from Arctic Russia. *J. Paleolimnol.* 24, 81–91. doi:10.1023/A:1008121917521

Andreev, A. A., Tarasov, P. E., Siegert, C., Ebel, T., Klimanov, V. A., Melles, M., et al. (2003). Late Pleistocene and Holocene Vegetation and Climate on the Northern Taymyr Peninsula, Arctic Russia. *Boreas* 32, 484–505. doi:10.1080/03009480310003388

Avnimelech, Y., Ritvo, G., Meijer, L. E., and Kochba, M. (2001). Water Content, Organic Carbon and Dry Bulk Density in Flooded Sediments. *Aquacultural Eng.* 25, 25–33. doi:10.1016/S0144-8609(01)00068-1

Bakke, J., Lie, Ø., Heegaard, E., Dokken, T., Haug, G. H., Birks, H. H., et al. (2009). Rapid Oceanic and Atmospheric Changes during the Younger Dryas Cold Period. *Nat. Geosci* 2, 202–205. doi:10.1038/ngeo439

Bakulina, N. T., Spektor, V. B., Novikov, N. I., Kurchatova, A. N., and Spektor, V. V. (2000). "Section of Benthic Deposits in the Malaya Tchabyda Lake," in *Proceeding of the International Conference '"Lakes of Cold Regions"', Part IV, Paleoclimatology, Paleolimnology and Paleoecology* Yakutsk, Russia.

Balascio, N. L., Zhang, Z., Bradley, R. S., Perren, B., Dahl, S. O., and Bakke, J. (2011). A Multi-Proxy Approach to Assessing Isolation basin Stratigraphy from the Lofoten Islands, Norway. *Quat. Res.* 75, 288–300. doi:10.1016/j.yqres.2010.08.012

Biskaborn, B. K., Herzschuh, U., Bolshiyanov, D., Savelieva, L., and Diekmann, B. (2012). Environmental Variability in Northeastern Siberia during the Last ~ 13,300 Yr Inferred from lake Diatoms and Sediment-Geochemical Parameters. *Palaeogeogr. Palaeoclimatol. Palaeoecol.* 329-330, 22–36. doi:10.1016/j.palaeo.2012.02.003

Biskaborn, B. K., Herzschuh, U., Bolshiyanov, D. Y., Schwamborn, G., and Diekmann, B. (2013). Thermokarst Processes and Depositional Events in a Tundra Lake, Northeastern Siberia. *Permafrost Periglac. Process.* 24, 160–174. doi:10.1002/ppp.1769

Biskaborn, B. K., Narancic, B., Stoof-Leichsenring, K. R., Pestryakova, L. A., Appleby, P. G., Piliposian, G. T., et al. (2021a). Effects of Climate Change and Industrialization on Lake Bolshoe Toko, Eastern Siberia. *J. Paleolimnol.* 65, 335–352. doi:10.1007/s10933-021-00175-z

Biskaborn, B. K., Nazarova, L., Kröger, T., Pestryakova, L. A., Syrykh, L., Pfalz, G., et al. (2021b). Late Quaternary Climate Reconstruction and Lead-Lag Relationships of Biotic and Sediment-Geochemical Indicators at Lake Bolshoe Toko, Siberia. *Front. Earth Sci.* 9, 703, 2021b . Available at: https://www.frontiersin.org/article/10.3389/feart.2021.737353. doi:10.3389/feart.2021.737353

Biskaborn, B. K., Nazarova, L., Pestryakova, L. A., Syrykh, L., Funck, K., Meyer, H., et al. (2019a). Spatial Distribution of Environmental Indicators in Surface Sediments of Lake Bolshoe Toko, Yakutia, Russia. *Biogeosciences* 16, 4023–4049. doi:10.5194/bg-16-4023-2019

Biskaborn, B. K., Smith, S. L., Noetzli, J., Matthes, H., Vieira, G., Streletskiy, D. A., et al. (2019b). Permafrost Is Warming at a Global Scale. *Nat. Commun.* 10, 1–11. doi:10.1038/s41467-018-08240-4

Biskaborn, B. K., Subetto, D. A., Savelieva, L. A., Vakhrameeva, P. S., Hansche, A., Herzschuh, U., et al. (2016). Late Quaternary Vegetation and lake System Dynamics in north-eastern Siberia: Implications for Seasonal Climate Variability. *Quat. Sci. Rev.* 147, 406–421. doi:10.1016/j.quascirev.2015.08.014

Blaauw, M., and Christen, J. A. (2011). Flexible Paleoclimate Age-Depth Models Using an Autoregressive Gamma Process. *Bayesian Anal.* 6, 457–474. doi:10.1214/ba/1339616472

Blott, S. J., and Pye, K. (2001). GRADISTAT: A Grain Size Distribution and Statistics Package for the Analysis of Unconsolidated Sediments. *Earth Surf. Process. Landforms* 26, 1237–1248. doi:10.1002/esp.261

Bouchard, F., Fortier, D., Paquette, M., Boucher, V., Pienitz, R., and Laurion, I. (2020). Thermokarst lake Inception and Development in Syngenetic Ice-Wedge Polygon Terrain during a Cooling Climatic Trend, Bylot Island (Nunavut), Eastern Canadian Arctic. *The Cryosphere* 14, 2607–2627. doi:10.5194/tc-14-2607-2020

Bouchard, F., Francus, P., Pienitz, R., and Laurion, I. (2011). Sedimentology and Geochemistry of Thermokarst Ponds in Discontinuous Permafrost, Subarctic Quebec, Canada. *J. Geophys. Res.* 116–130. doi:10.1029/2011JG001675

Bouchard, F., Laurion, I., Preskienis, V., Fortier, D., Xu, X., and Whiticar, M. J. (2015). Modern to Millennium-Old Greenhouse Gases Emitted from Ponds and Lakes of the Eastern Canadian Arctic (Bylot Island, Nunavut). *Biogeosciences* 12, 7279–7298. doi:10.5194/bg-12-7279-2015

Bouchard, F., Macdonald, L. A., Turner, K. W., Thienpont, J. R., Medeiros, A. S., Biskaborn, B. K., et al. (2017). Paleolimnology of Thermokarst Lakes: a Window into Permafrost Landscape Evolution. *Arctic Sci.* 3, 91–117. doi:10.1139/as-2016-0022

Brouchkov, A., Fukuda, M., Fedorov, A., Konstantinov, P., and Iwahana, G. (2004). Thermokarst as a Short-Term Permafrost Disturbance, Central Yakutia. *Permafrost Periglac. Process.* 15, 81–87. doi:10.1002/ppp.473

Brown, J., Ferrians, O. J., Heginbottom, J. A., and Melnikov, E. S. (1997). Circum-Arctic Map of Permafrost and Ground-Ice Conditions *Circum-Pacific Map Series CP-45, scale 1:10,000,000, 1 sheet. US Geological Survey in Cooperation with the Circum-Pacific Council for Energy and Mineral Resources*. doi:10.3133/cp45

Corella, J. P., Brauer, A., Mangili, C., Rull, V., Vegas-Vilarrúbia, T., Morellón, M., et al. (2012). The 1.5-ka Varved Record of Lake Montcortès (Southern Pyrenees, NE Spain). *Quat. Res.* 78, 323–332. doi:10.1016/j.yqres.2012.06.002

Davidson, E. A., and Janssens, I. A. (2006). Temperature Sensitivity of Soil Carbon Decomposition and Feedbacks to Climate Change. *Nature* 440, 165–173. doi:10.1038/nature04514

Davies, S. J., Lamb, H. F., and Roberts, S. J. (2015). "Micro-XRF Core Scanning in Palaeolimnology: Recent Developments," in *BT - Micro-XRF Studies of Sediment Cores: Applications of a Non-destructive Tool for the Environmental Sciences*. Editors I. W. Croudace and R. G. Rothwell (Dordrecht: Springer Netherlands).

Fedorov, A. N., Ivanova, R. N., Park, H., Hiyama, T., and Iijima, Y. (2014). Recent Air Temperature Changes in the Permafrost Landscapes of Northeastern Eurasia. *Polar Sci.* 8, 114–128. doi:10.1016/j.polar.2014.02.001

Ferland, M.-E., Prairie, Y. T., Teodoru, C., and del Giorgio, P. A. (2014). Linking Organic Carbon Sedimentation, Burial Efficiency, and Long-Term Accumulation in Boreal Lakes. *J. Geophys. Res. Biogeosci.* 119, 836–847. doi:10.1002/2013JG002345

Ferland, M. E., Giorgio, P. A., Teodoru, C. R., and Prairie, Y. T. (2012). Long-term C Accumulation and Total C Stocks in Boreal Lakes in Northern Québec. *Glob. Biogeochem. Cycles* 26, GB0E04. doi:10.1029/2011GB004241

Folk, R. L., and Ward, W. C. (1957). Brazos River Bar [Texas]; a Study in the Significance of Grain Size Parameters. *J. Sediment. Res.* 27, 3–26. doi:10.1306/74D70646-2B21-11D7-8648000102C1865D

Fortier, D., Allard, M., and Pivot, F. (2006). A Late-Holocene Record of Loess Deposition in Ice-Wedge Polygons Reflecting Wind Activity and Ground Moisture Conditions, Bylot Island, Eastern Canadian Arctic. *The Holocene* 16, 635–646. doi:10.1191/0959683606hl960rp

Galanin, A. A., Pavlova, M. R., and Klimova, I. V. (2018). Late Quaternary Dune Formations (D'olkuminskaya Series) in Central Yakutia (Part 1). *Kz* XXII, 3–14. doi:10.21782/KZ1560-7496-2018-63-15

Gorokhov, A. N., and Fedorov, A. N. (2018). Current Trends in Climate Change in Yakutia. *Geogr. Nat. Resour.* 39, 153–161. doi:10.1134/S1875372818020087

Grosse, G., Goetz, S., Mcguire, A. D., Romanovsky, V. E., and Schuur, E. A. G. (2016). Changing Permafrost in a Warming World and Feedbacks to the Earth System. *Environ. Res. Lett.* 11, 040201. doi:10.1088/1748-9326/11/4/040201

Grosse, G., Jones, B., and Arp, C. (2013). Thermokarst Lakes, Drainage, and Drained Basins," in. *Treatise on Geomorphology*, 326–349. doi:10.1016/B978-0-12-374739-6.00216-5

Haberzettl, T., Corbella, H., Fey, M., Janssen, S., Lücke, A., Mayr, C., et al. (2007). Lateglacial and Holocene Wet-Dry Cycles in Southern Patagonia: Chronology, Sedimentology and Geochemistry of a Lacustrine Record from Laguna Potrok Aike, Argentina. *The Holocene* 17, 297–310. doi:10.1177/0959683607076437

Heinecke, L., Mischke, S., Adler, K., Barth, A., Biskaborn, B. K., Plessen, B., et al. (2017). Climatic and Limnological Changes at Lake Karakul (Tajikistan) during the Last ~29 Cal Ka. *J. Paleolimnol.* 58, 317–334. doi:10.1007/s10933-017-9980-0

Herzschuh, U., Pestryakova, L. A., Savelieva, L. A., Heinecke, L., Böhmer, T., Biskaborn, B. K., et al. (2013). Siberian Larch Forests and the Ion Content of Thaw Lakes Form a Geochemically Functional Entity. *Nat. Commun.* 4, 2408. doi:10.1038/ncomms3408

Hugelius, G., Strauss, J., Zubrzycki, S., Harden, J. W., Schuur, E. A. G., Ping, C.-L., et al. (2014). Estimated Stocks of Circumpolar Permafrost Carbon with Quantified Uncertainty Ranges and Identified Data Gaps. *Biogeosciences* 11, 6573–6593. doi:10.5194/bg-11-6573-2014

Hughes-Allen, L., Bouchard, F., Laurion, I., Séjourné, A., Marlin, C., Hatté, C., et al. (2021). Seasonal Patterns in Greenhouse Gas Emissions from Different Types of Thermokarst Lakes in Central Yakutia (Eastern Siberia). *Limnol. Oceanogr.* 66, S98–S116. doi:10.1002/lno.11665

Ivanov, M. S. (1984). *Cryogenic Structure of Quaternary Sediments in the Lena-Aldan Depression*. Novosibirsk: Nauka. (in Russian).

Jongejans, L. L., Liebner, S., Knoblauch, C., Mangelsdorf, K., Ulrich, M., Grosse, G., et al. (2021). Greenhouse Gas Production and Lipid Biomarker Distribution in Yedoma and Alas Thermokarst lake Sediments in Eastern Siberia. *Glob. Change Biol.* 27, 2822–2839. doi:10.1111/gcb.15566

Kachurin, S. P. (1961). *Thermokarst on the Territory of USSR*. Moscow, Russia: Publ. House USSR Acad. Sci.

Kalugin, I., Darin, A., Rogozin, D., and Tretyakov, G. (2013). Seasonal and Centennial Cycles of Carbonate Mineralisation during the Past 2500 Years from Varved Sediment in Lake Shira, South Siberia. *Quat. Int.* 290-291, 245–252. doi:10.1016/j.quaint.2012.09.016

Kalugin, I., Daryin, A., Smolyaninova, L., Andreev, A., Diekmann, B., and Khlystov, O. (2007). 800-yr-long Records of Annual Air Temperature and Precipitation over Southern Siberia Inferred from Teletskoye Lake Sediments. *Quat. Res.* 67, 400–410. doi:10.1016/j.yqres.2007.01.007

Katamura, F., Fukuda, M., Bosikov, N. P., Desyatkin, R. V., Nakamura, T., and Moriizumi, J. (2006). Thermokarst Formation and Vegetation Dynamics Inferred from a Palynological Study in Central Yakutia, Eastern Siberia, Russia. *Arctic, Antarctic, Alpine Res.* 38, 561–570. doi:10.1657/1523-0430(2006)38[561:tfavdi]2.0.co;2

Kumke, T., Ksenofontova, M., Pestryakova, L., Nazarova, L., and Hubberten, H.-W. (2007). Limnological Characteristics of Lakes in the Lowlands of Central Yakutia, Russia. *J. Limnol.* 66, 40–53. doi:10.4081/jlimnol.2007.40

Mann, P. J., Eglinton, T. I., McIntyre, C. P., Zimov, N., Davydova, A., Vonk, J. E., et al. (2015). Utilization of Ancient Permafrost Carbon in Headwaters of Arctic Fluvial Networks. *Nat. Commun.* 6, 7856. doi:10.1038/ncomms8856

Marshall, M. H., Lamb, H. F., Huws, D., Davies, S. J., Bates, R., Bloemendal, J., et al. (2011). Late Pleistocene and Holocene Drought Events at Lake Tana, the Source of the Blue Nile. *Glob. Planet. Change* 78, 147–161. doi:10.1016/j.gloplacha.2011.06.004

Martin, P., Granina, L., Martens, K., and Goddeeris, B. (1998). Oxygen Concentration Profiles in Sediments of Two 1120 Ancientlakes: Lake Baikal (Siberia, Russia) and Lake Malawi (East Africa). *Hydrobiologia* 367, 163–174. doi:10.1023/A:1003280101128

Martín-Puertas, C., Valero-Garcés, B. L., Mata, M. P., Moreno, A., Giralt, S., Martínez-Ruiz, F., et al. (2011). Geochemical Processes in a Mediterranean Lake: a High-Resolution Study of the Last 4,000 Years in Zoñar Lake, Southern Spain. *J. Paleolimnol.* 46, 405–421. doi:10.1007/s10933-009-9373-0

Melles, M., Brigham-Grette, J., Minyuk, P. S., Nowaczyk, N. R., Wennrich, V., DeConto, R. M., et al. (2012). 2.8 Million Years of Arctic Climate Change from Lake El'gygytgyn, NE Russia. *Science* 337, 315–320. doi:10.1126/science.1222135

Mendonça, R., Müller, R. A., Clow, D., Verpoorter, C., Raymond, P., Tranvik, L. J., et al. (2017). Organic Carbon Burial in Global Lakes and Reservoirs. *Nat. Commun.* 8, 1694. doi:10.1038/s41467-017-01789-6

Meyer, H., Opel, T., Laepple, T., Dereviagin, A. Y., Hoffmann, K., and Werner, M. (2015). Long-term winter Warming Trend in the Siberian Arctic during the Mid- to Late Holocene. *Nat. Geosci* 8, 122–125. doi:10.1038/ngeo2349

Meyers, P. A. (2003). Applications of Organic Geochemistry to Paleolimnological Reconstructions: A Summary of Examples from the Laurentian Great Lakes. *Org. Geochem.* 34, 261–289. doi:10.1016/S0146-6380(02)00168-7

Meyers, P. A., and Arbor, A. (2001). Sediment Organic Matter. *Track. Environ. Chang. Using Lake Sediments. Vol. 2 Phys. Geochemical Methods* 2, 239–269.

Meyers, P. A. (1994). Preservation of Elemental and Isotopic Source Identification of Sedimentary Organic Matter. *Chem. Geology.* 114, 289–302. doi:10.1016/0009-2541(94)90059-0

Meyers, P. A., and Teranes, J. L. (2002). "Sediment Organic Matter," in *Tracking Environmental Change Using Lake Sediments. Developments in Paleoenvironmental Research*. Editors W. M. Last and J. P. Smol 2 (Dordrecht: Springer), 239–269. doi:10.1007/0-306-47670-3_9

Müller, S., Tarasov, P. E., Andreev, A. A., and Diekmann, B. (2009). Late Glacial to Holocene Environments in the Present-Day Coldest Region of the Northern Hemisphere Inferred from a Pollen Record of Lake Billyakh, Verkhoyansk Mts, NE Siberia. *Clim. Past* 5, 74–94. doi:10.5194/cpd-4-1237-2008

Nazarova, L., Lüpfert, H., Subetto, D., Pestryakova, L., and Diekmann, B. (2013). Holocene Climate Conditions in central Yakutia (Eastern Siberia) Inferred from Sediment Composition and Fossil Chironomids of Lake Temje. *Quat. Int.* 290-291, 264–274. doi:10.1016/j.quaint.2012.11.006

Pajunen, H. (2000). Lake Sediments: Their Carbon Store and Related Accumulations Rates. *Spec. Pap. Geol. Surv. Finl.* 29, 39–69.

Pestryakova, L. A., Herzschuh, U., Wetterich, S., and Ulrich, M. (2012). Present-day Variability and Holocene Dynamics of Permafrost-Affected Lakes in central Yakutia (Eastern Siberia) Inferred from Diatom Records. *Quat. Sci. Rev.* 51, 56–70. doi:10.1016/j.quascirev.2012.06.020

Pörtner, H.-O., Roberts, D. C., Masson-Delmotte, V., Zhai, P., Tignor, M., Poloczanska, E., et al. (2019). *IPCC Special Report on the Ocean and Cryosphere in a Changing Climate*.

Prėskienis, V., Laurion, I., Bouchard, F., Douglas, P. M. J., Billett, M. F., Fortier, D., et al. (2021). Seasonal Patterns in Greenhouse Gas Emissions from Lakes and Ponds in a High Arctic Polygonal Landscape. *Limnol. Oceanogr.* 66, S117–S141. doi:10.1002/lno.11660

Pribyl, D. W. (2010). A Critical Review of the Conventional SOC to SOM Conversion Factor. *Geoderma* 156, 75–83. doi:10.1016/j.geoderma.2010.02.003

Reimer, P. J., Austin, W. E. N., Bard, E., Bayliss, A., Blackwell, P. G., Bronk Ramsey, C., et al. (2020). The IntCal20 Northern Hemisphere Radiocarbon Age Calibration Curve (0-55 Cal kBP). *Radiocarbon* 62, 725–757. doi:10.1017/RDC.2020.41

Schirrmeister, L., Froese, D., Tumskoy, V., Grosse, G., and Wetterich, S. (2013). Permafrost and Periglacial Features | Yedoma: Late Pleistocene Ice-Rich Syngenetic Permafrost of Beringia. *Encycl. Quat. Sci.* 3, 542–552. doi:10.1016/b978-0-444-53643-3.00106-0

Schirrmeister, L., Grosse, G., Wetterich, S., Overduin, P. P., Strauss, J., Schuur, E. A. G., et al. (2011). Fossil Organic Matter Characteristics in Permafrost Deposits of the Northeast Siberian Arctic. *J. Geophys. Res.* 116–132. doi:10.1029/2011JG001647

Schuur, E. A. G., McGuire, A. D., Schädel, C., Grosse, G., Harden, J. W., Hayes, D. J., et al. (2015). Climate Change and the Permafrost Carbon Feedback. *Nature* 520, 171–179. doi:10.1038/nature14338

Séjourné, A., Costard, F., Fedorov, A., Gargani, J., Skorve, J., Massé, M., et al. (2015). Evolution of the banks of Thermokarst Lakes in Central Yakutia (Central Siberia) Due to Retrogressive Thaw Slump Activity Controlled by Insolation. *Geomorphology* 241, 31–40. doi:10.1016/j.geomorph.2015.03.033

Sobek, S., Anderson, N. J., Bernasconi, S. M., and Del Sontro, T. (2014). Low Organic Carbon Burial Efficiency in Arctic lake Sediments. *J. Geophys. Res. Biogeosci.* 119, 1231–1243. doi:10.1002/2014JG002612

Soloviev, P. A. (1959). *The Cryolithozone of Northern Part of the Lena-Amga Interfluve*. Moscow: USSR Acad. Sci. Publ.

Strauss, J., Schirrmeister, L., Grosse, G., Fortier, D., Hugelius, G., Knoblauch, C., et al. (2017). Deep Yedoma Permafrost: A Synthesis of Depositional Characteristics and Carbon Vulnerability. *Earth-Science Rev.* 172, 75–86. doi:10.1016/j.earscirev.2017.07.007

Strunk, A., Olsen, J., Sanei, H., Rudra, A., and Larsen, N. K. (2020). Improving the Reliability of Bulk Sediment Radiocarbon Dating. *Quat. Sci. Rev.* 242, 106442. doi:10.1016/j.quascirev.2020.106442

Subetto, D. A., Nazarova, L. B., Pestryakova, L. A., Syrykh, L. S., Andronikov, A. V., Biskaborn, B., et al. (2017). Paleolimnological Studies in Russian Northern Eurasia: A Review. *Contemp. Probl. Ecol.* 10, 327–335. doi:10.1134/S1995425517040102

Subetto, D. A., Wohlfarth, B., Davydova, N. N., Sapelko, T. V., Björkman, L., Solovieva, N., et al. (2002). Climate and Environment on the Karelian Isthmus, Northwestern Russia, 13000-9000 Cal. Yrs BP. *Boreas* 31, 1–19. doi:10.1111/j.1502-3885.2002.tb01051.x

Sumgin, M. I., Kachurin, S. P., and Tolstikhin, N. I. (1940). *General Permafrost Studies*. Moscow, Russia: Publ. House USSR Acad. Sci., 340.

Tarasov, P. E., Harrison, S. P., Saarse, L., Pushenko, M. Y., Andreev, A. A., Aleshinskaya, Z. V., et al. (1996). *Lake Status Records from the FSU, Database Documentation Version 2*. Boulder, USA: IGBP PAGES/World Data Center-A for Paleoclimatology Data. Contribution Series # 96-032.

Ulrich, M., Matthes, H., Schirrmeister, L., Schütze, J., Park, H., Iijima, Y., et al. (2017a). Differences in Behavior and Distribution of Permafrost-related Lakes in C Entral Y Akutia and Their Response to Climatic Drivers. *Water Resour. Res.* 53, 1167–1188. doi:10.1002/2016WR019267.Received

Ulrich, M., Matthes, H., Schmidt, J., Fedorov, A. N., Schirrmeister, L., Siegert, C., et al. (2019). Holocene Thermokarst Dynamics in Central Yakutia - A Multi-Core and Robust Grain-Size Endmember Modeling Approach. *Quat. Sci. Rev.* 218, 10–33. doi:10.1016/j.quascirev.2019.06.010

Ulrich, M., Wetterich, S., Rudaya, N., Frolova, L., Schmidt, J., Siegert, C., et al. (2017b). Rapid Thermokarst Evolution during the Mid-holocene in Central Yakutia, Russia. *The Holocene* 27, 1899–1913. doi:10.1177/0959683617708454

Velichko, A. A., Andreev, A. A., and Klimanov, V. A. (1997). Climate and Vegetation Dynamics in the Tundra and forest Zone during the Late Glacial and Holocene. *Quat. Int.* 41-42, 71–96. doi:10.1016/S1040-6182(96)00039-0

Vonk, J. E., and Gustafsson, Ö. (2013). Permafrost-carbon Complexities. *Nat. Geosci* 6, 675–676. doi:10.1038/ngeo1937

Vonk, J. E., Mann, P. J., Davydov, S., Davydova, A., Spencer, R. G. M., Schade, J., et al. (2013). High Biolability of Ancient Permafrost Carbon upon Thaw. *Geophys. Res. Lett.* 40, 2689–2693. doi:10.1002/grl.50348

Vonk, J. E., Tank, S. E., Bowden, W. B., Laurion, I., Vincent, W. F., Alekseychik, P., et al. (2015). Reviews and Syntheses: Effects of Permafrost Thaw on Arctic Aquatic Ecosystems. *Biogeosciences* 12, 7129–7167. doi:10.5194/bg-12-7129-2015

Vyse, S. A., Herzschuh, U., Andreev, A. A., Pestryakova, L. A., Diekmann, B., Armitage, S. J., et al. (2020). Geochemical and Sedimentological Responses of Arctic Glacial Lake Ilirney, Chukotka (Far East Russia) to Palaeoenvironmental Change since ~51.8 Ka BP. *Quat. Sci. Rev.* 247, 106607. doi:10.1016/j.quascirev.2020.106607

Vyse, S. A., Herzschuh, U., Pfalz, G., Pestryakova, L. A., Diekmann, B., Nowaczyk, N., et al. (2021). Sediment and Carbon Accumulation in a Glacial lake in Chukotka (Arctic Siberia) during the Late Pleistocene and Holocene: Combining Hydroacoustic Profiling and Down-Core Analyses. *Biogeosciences Discuss.* 16, 4791–4816. doi:10.5194/bg-2021-39

Walter Anthony, K., Daanen, R., Anthony, P., Schneider von Deimling, T., VonPing, C., Ping, C.-L., et al. (2016). Methane Emissions Proportional to Permafrost Carbon Thawed in Arctic Lakes since the 1950s. *Nat. Geosci* 9, 679–682. doi:10.1038/NGEO2795

Wang, R., Zhang, Y., Wünnemann, B., Biskaborn, B. K., Yin, H., Xia, F., et al. (2015). Linkages between Quaternary Climate Change and Sedimentary Processes in Hala Lake, Northern Tibetan Plateau, China. *J. Asian Earth Sci.* 107, 140–150. doi:10.1016/j.jseaes.2015.04.008

Weltje, G. J., and Tjallingii, R. (2008). Calibration of XRF Core Scanners for Quantitative Geochemical Logging of Sediment Cores: Theory and Application. *Earth Planet. Sci. Lett.* 274, 423–438. doi:10.1016/j.epsl.2008.07.054

Zhirkov, I. (1983). Morphogenetic Classification as the Basis of Rational Use, protection and Reproduction of Natural Resources of Lakes of the Cryolithozone (On the Example of Central Yakutia)/Questions of Rational Use and protection of Natural Resources of Different Type. *Yakutsk*, 4–47.

Conflict of Interest: The authors declare that the research was conducted in the absence of any commercial or financial relationships that could be construed as a potential conflict of interest.

Publisher's Note: All claims expressed in this article are solely those of the authors and do not necessarily represent those of their affiliated organizations, or those of the publisher, the editors and the reviewers. Any product that may be evaluated in this article, or claim that may be made by its manufacturer, is not guaranteed or endorsed by the publisher.

frontiers in Earth Science

ORIGINAL RESEARCH
published: 10 December 2021
doi: 10.3389/feart.2021.750298

Check for updates

Thermokarst Landscape Development Detected by Multiple-Geospatial Data in Churapcha, Eastern Siberia

Yoshihiro Iijima[1]*, *Takahiro Abe*[1], *Hitoshi Saito*[2], *Mathias Ulrich*[3], *Alexander N. Fedorov*[4,5], *Nikolay I. Basharin*[4], *Alexey N. Gorokhov*[5,6] and *Victor S. Makarov*[4,6,7]

[1]Graduate School of Bioresources, Mie University, Mie, Japan, [2]College of Economics, Kanto-Gakuin University, Kanagawa, Japan, [3]Institute for Geography, Leipzig University, Leipzig, Germany, [4]Melnikov Permafrost Institute, SBRAS, Yakutsk, Russia, [5]BEST International Centre, North-Eastern Federal University, Yakutsk, Russia, [6]Institute for Biological Problem in Cryolithozone, SBRAS, Yakutsk, Russia, [7]Scientific Research Institute of Applied Ecology of the North, M.K. Ammosov North-Eastern Federal University, Yakutsk, Russia

OPEN ACCESS

Edited by:
Duane Froese,
University of Alberta, Canada

Reviewed by:
Lin Liu,
The Chinese University of Hong Kong, China
Bernhard Rabus,
Simon Fraser University, Canada

***Correspondence:**
Yoshihiro Iijima
yiijima@bio.mie-u.ac.jp

Specialty section:
This article was submitted to Cryospheric Sciences, a section of the journal Frontiers in Earth Science

Received: 30 July 2021
Accepted: 09 November 2021
Published: 10 December 2021

Citation:
Iijima Y, Abe T, Saito H, Ulrich M, Fedorov AN, Basharin NI, Gorokhov AN and Makarov VS (2021) Thermokarst Landscape Development Detected by Multiple-Geospatial Data in Churapcha, Eastern Siberia. Front. Earth Sci. 9:750298. doi: 10.3389/feart.2021.750298

Thermokarst is a typical process that indicates widespread permafrost degradation in yedoma landscapes. The Lena-Aldan interfluvial area in Central Yakutia in eastern Siberia is now facing extensive landscape changes with surface subsidence due to thermokarst development during the past few decades. To clarify the spatial extent and rate of subsidence, multiple spatial datasets, including GIS and remote sensing observations, were used to analyze the Churapcha rural locality, which has a typical yedoma landscape in Central Yakutia. Land cover classification maps for 1945 and 2009 provide basic information on anthropogenic disturbance to the natural landscape of boreal forest and dry grassland. Interferometric synthetic aperture radar (InSAR) with ALOS-2/PALSAR-2 data revealed activated surface subsidence of 2 cm/yr in the disturbed area, comprising mainly abandoned agricultural fields. Remote sensing with an unmanned aerial system also provided high-resolution information on polygonal relief formed by thermokarst development at a disused airfield where InSAR analysis exhibited extensive subsidence. It is worth noting that some historically deforested areas have likely recovered to the original landscape without further thermokarst development. Spatial information on historical land-use change is helpful because most areas with thermokarst development correspond to locations where land was used by humans in the past. Going forward, the integrated analysis of geospatial information will be essential for assessing permafrost degradation.

Keywords: ALOS-2/PALSAR-2, UAS, interferometric SAR (InSAR), permafrost degradation, subsidence, Central Yakutia

INTRODUCTION

Permafrost landscapes in Central Yakutia (Eastern Siberia, Russia) are primarily sensitive to Arctic warming (Fedorov et al., 2014b; Miller et al., 2021; Overland and Wang, 2021). Very ice-rich permafrost deposits, such as the yedoma ice complex (Schirrmeister et al., 2013; Strauss et al., 2013; Strauss et al., 2017), are extensively distributed throughout this region. Ice wedges developed under the lacustrine environment in the Lena-Aldan interfluvial region during Pleistocene glacial periods (Bosikov 1991). The permafrost in Central Yakutia faces a risk of rapid, strong warming and thawing processes and thermal erosion. The thawing of ice-rich deposits leads to strong ground subsidence, namely “thermokarst” (Soloviev, 1959; Tarasenko, 2013; Ulrich et al., 2017; Ulrich et al., 2019), and landscape reorganization from flat boreal forest to a rugged open surface with ponding (Czudek and Demek, 1970; Bosikov, 1991).

In Central Yakutia, climate warming initiated extensive thawing and thermokarst processes during the Pleistocene-Holocene transition and the climatic optimum in the middle Holocene (7,000–4000 BP; Katamura et al., 2009; Ulrich et al., 2019). This old permafrost degradation turned into the present-day climax landscape known as an "alas" (Bosikov, 1991), comprising concave grassland with shallow lakes. The grassland in alases has historically been used for livelihood in Central Yakutia (Crate et al., 2017). Excavations of archaeological sites have shown traces of human habitation here for at least 5,000 years, and Tungusic linguistic groups (hunter-gatherers and reindeer herders) inhabited this region from the 11th to 13th centuries. In the 17th century, Central Yakutia belonged to Russia, and in the 20th century, agricultural land was expanded under the economic policy when it was part of the Soviet Union. During this period, the climate was colder on average and hydrological cyclical. Hence, thermokarst was unlikely to develop (Crate et al., 2017), and the natural landscape was relatively stable. With the collapse of the Soviet Union in the 1990s and related large-scale land use changes, the climate was also turned into a warming state (Fedorov et al., 2014b). In addition, increased precipitation was observed in the subsequent decade (after 2000), causing extensive forest degradation due to a warmed and saturated active layer under wet climate conditions (Iijima et al., 2014; Iijima et al., 2016). Both anthropogenic and natural environmental changes have contributed to the warming of permafrost with deepening of the active layer and melting of underground ice, which has led to subsequent land surface displacement by thermokarst. Changes in landforms and ecosystems due to thermokarst development have drastically changed Central Yakutia's natural and social landscape. The changes of the last 2 decades are taking a heavy toll on cattle and horse farming, agricultural land use, and residential environments that were highly dependent on the local ecosystem (Crate et al., 2017; Takakura et al., 2021).

To evaluate landscape changes associated with permafrost degradation, it is necessary to detect topographic changes caused by thermokarst formation. To analyze surface subsidence accompanied by the very rapid formation of thermokarst over a few years, a spatial resolution of <1.0 m is needed. A limitation of detecting the spatial extent of thermokarst development is that the smallest topographical features are not fully seen in traditional remote sensing images only because of their relatively coarse spatial resolution. In recent years, high-resolution imaging by unmanned aerial systems (UASs) and commercial satellites taking multispectral images has become available. From these images, the distribution of thermokarst development can be obtained with much more precision (Saito et al., 2018). However, even with multiple years of fine-scale images, detecting the topographic subsidence rate is challenging.

The spatial extent of thermokarst development has been detected by combining temporal variation in satellite and aerial images with detailed field measurements as ground truth during the last 2 decades. Recently, a study with the results of a field survey showed that thawing subsidence of permafrost due to surface disturbance in the Alaskan North Slope could be determined using interferometric synthetic aperture radar (InSAR) and light detection and ranging techniques. These methods showed thermokarst development over the coastal tundra (Liu et al., 2015) and extensive areas affected by wildfires in Alaska (Iwahana et al., 2016), its temporal evolution with a resolution of a few centimeters, and its spatial distribution with a resolution of 10 m (Iwahana et al., 2016). Subsequent studies on the ground surface deformation of permafrost zones using SAR images and InSAR analysis have been reported for other permafrost zones (Antonova et al., 2018; Chen et al., 2018; Strozzi et al., 2018).

Combining this spatial information will make it possible to provide a more vivid picture of permafrost degradation based on those backgrounds. However, due to the lack of collaborative field studies and remote sensing analyses, consistent results regarding the relationship between the thermokarst subsidence rate and intensity of natural and social disturbances are still scarce for continuous permafrost zones, particularly in Central Yakutia. The purpose of this study is, thus, to combine multiple spatial data sets to clarify thermokarst development in very ice-rich Yedoma deposits of Central Yakutia.

STUDY SITE

The present study targeted thermokarst landforms in the Churapcha locality on the right bank of the Lena River in Central Yakutia (**Figure 1A**). Dry grasslands and abandoned arable lands, which may be at risk of thermokarst development, are widely distributed around the settlement of Churapcha (**Figure 1**). The population of Churapcha has increased from 8,769 in 2010 to 10,202 in 2020 (SakhaSTAT, 2021). The recent population growth has caused settlement expansion in the town's vicinity into the dry grasslands and abandoned arable lands. These sites were selected to assess thermokarst development associated with socially disturbed areas.

Churapcha is located about 180 km east of Yakutsk on an almost flat surface of the Abrakh terrace at the top of the interfluve of the Taata and Kokhara Rivers at about 170–220 m asl (**Figure 1A**). The permafrost thickness is estimated at 540 m in Churapcha (Ivanov, 1984). Old alas depressions are widely distributed with a relative depth of about 7–8 m (Saito et al., 2018). The sediments of the ice complex contain syngenetic polygonal ice wedges up to 12–14 m in depth, which lie at a depth of 2.2–2.3 m below the surface. The width of the upper parts of the ice wedges varies from 1.5 to 3.0 m. The volumetric ice content (ice-wedge) in the upper part of the permafrost is approximately 17% at the disused airfield site and 25% in the abandoned arable land areas located south of the Churapcha locality, as estimated by the method of Gasanov (1969) and field measurements by the Melnikov Permafrost Institute.

The regional climate is extremely continental with a pronounced warming trend. Climatological data (1991–2020)

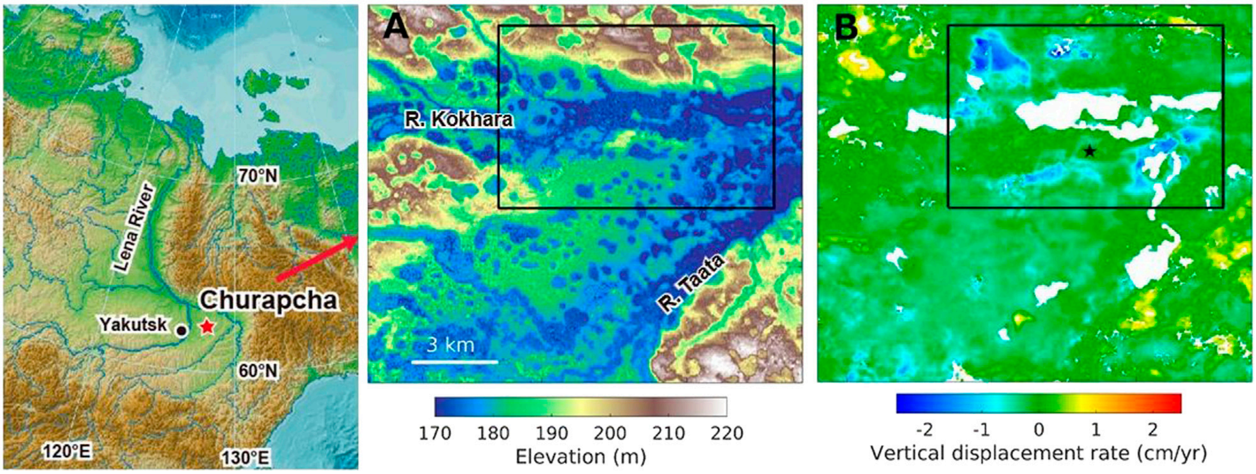

FIGURE 1 | Study area: **(A)** Elevation around Churapcha. **(B)** Vertical displacement rate derived from ALOS-2 InSAR stacking. The black rectangle indicates the area shown in **Figure 2**. The black star in **(B)** indicates the location of the InSAR reference point.

from the Churapcha meteorological station show that the mean annual air temperature is −9.6°C, while monthly mean temperatures for January and July are −39.9°C and 19.3°C, respectively. The average yearly number of freezing days (mean daily air temperature below 0°C) is 109 days. The amount of precipitation is 257 mm/yr, with 185 mm occurring during the warm period (May to September). However, during 2005–2020, the mean annual air temperature increased to −8.9°C, and the total precipitation reached 275 mm/yr.

At the meteorological station, the mean annual ground temperature at a depth of 3.2 m was −2.1 ± 0.7°C for 1967–2014. Permafrost temperature was rather colder ranging from −3 to −6°C before the 1980s (Ivanov, 1984). Our recently ongoing monitoring sites in forest and meadow areas near Churapcha show soil temperature ranges from −2 to −3°C and −1.5 to −2°C, respectively, at 3.2 m depth. The active layer thickness was 1.3 and 2.0 m in September 2015 for the forests and meadows, respectively (Iijima et al., 2017). Increasing air temperatures and corresponding ground temperature rise have been observed in Central Yakutia since the early 1990s (Fedorov et al., 2014b). The increase in the active layer thickness in open areas has caused rapid thermokarst subsidence since the 1990s and enhancing after the 2000s (Fedorov and Konstantinov, 2003; Gavriliev and Ugarov, 2009).

MATERIALS AND METHODS

SAR Data Processing

InSAR is a powerful tool for examining surface displacement using two SAR images acquired at different times with an accuracy of a few centimeters. InSAR is used for detecting surface deformation related to permafrost, such as the seasonal thaw/freeze cycle (e.g., Liu et al., 2010; Short et al., 2011), thermokarst (e.g., Liu et al., 2015; Antonova et al., 2018; Chen et al., 2018; Abe et al., 2020), and wildfires (Liu et al., 2014; Iwahana et al., 2016; Molan et al., 2018; Michaelides et al., 2019; Yanagiya and Furuya, 2020). To examine long-term displacement by thermokarst development, the L-band InSAR is more suitable than the C- and X-band InSAR for coherence (e.g., Strozzi et al., 2018; Abe et al., 2020; Yanagiya and Furuya, 2020).

In this study, L-band SAR data obtained by the PALSAR-2 instrument on the ALOS-2 satellite were processed using the GAMMA software (Wegmüller and Werner, 1997). ALOS-2 obtained six scenes of the stripmap mode 3 with 10-m resolution (path 124, frame 1,240, beam F2_5, **Table 1**) over Churapcha in 2015–2020. The off-nadir angle at the center of the SAR image is approximately 28 deg. Our InSAR processing procedures are the same as those of previous studies (Strozzi et al., 2018; Abe et al., 2020). We generated Single Look Complex (SLC) data from ALOS-2 Lv1.1 data. After performing co-registration between two SLC images, we reproduced interferograms and selected 11 of them. We excluded interferograms in which the image acquisition period of the pair was over 4 years apart or during the same year for the stacking analysis (**Table 1**). The topographically related phase was removed using ALOS World 3D -30 m- (AW3D30). The vertical accuracy of AW3D30 digital surface model is less than ca. 5 m. Goldstein–Werner's adaptive spectral filter with an exponent of 0.7 was applied to smooth the signals (Goldstein and Werner, 1998), and phase unwrapping by minimum cost flow was performed (Costantini, 1998). The spatial resolution after terrain-corrected geocoding projected onto the UTM coordinate was set to 30 m. Finally, the line of sight (LOS, distance between satellite and ground) change detected by InSAR was converted to a vertical displacement by dividing it by the cosine of the incidence angle because vertical displacement is assumed to be dominant in thermokarst. The reference point in interferograms was set to an alas located in the southeast of Churapcha (**Figure 1B**). Alas is considered to be the climax geomorphological stage of thermokarst development (Bosikov 1991). Hence, we assumed that the bottom of an alas is less likely

TABLE 1 | Interferometric pairs used in this study. B-perp stands for the distance perpendicular to the line of sight between the positions of the satellite at different times.

No	Primary (yyyy/mm/dd)	Secondary (yyyy/mm/dd)	Interval (days)	B-perp (m)
1	2015/08/11	2017/09/19	770	–79.12
2	2015/08/11	2018/07/10	1,164	–153.08
3	2015/08/11	2018/08/21	1,106	21.40
4	2015/09/22	2017/09/19	728	–140.50
5	2015/09/22	2018/07/10	1,022	–214.45
6	2015/09/22	2018/08/21	1,064	–39.96
7	2017/09/19	2018/07/10	294	–73.95
8	2017/09/19	2018/08/21	336	100.53
9	2017/09/19	2020/07/07	1,022	45.64
10	2018/07/10	2020/07/07	728	119.59
11	2018/08/21	2020/07/07	686	–54.88

to be displaced inter-annually in comparison with inter-alas areas on ice-rich permafrost (Abe et al., 2020). In fact, the place of the alas bottom shows no polygonal terrain in the recent Worldview image (**Supplementary Figure S1**), and it is not a wetland landscape. Thus, the alas bottom is considered to be appropriate as a reference point as no further surface displacement is expected.

Tropospheric and ionospheric disturbances contaminated each interferogram. These disturbances are sometimes interfered with to extract surface displacement. Regarding the tropospheric effect, the GACOS product was used to reduce its noise (Yu et al., 2017; Yu et al., 2018). The impacts of ionospheric disturbances are often shown as a linear long-wavelength trend. Our analysis area was spatially limited to ~10 × 10 km and, we were able to model and subtract the trend by fitting a 2D linear function.

Finally, after generating and correcting interferograms, we performed a weighted stacking analysis for the number of days in the thawing season (from 1 June to 30 September) among the total number of days for the two images (Abe et al., 2020). This weighting reflects the actual period that contributes to the signals of surface subsidence rather than using the total number of days for the two images. The spatial resolution of the stacked interferograms was left at 30 m per pixel. Error analysis of the stacking result was conducted based on Equation 10 in Emardson et al. (2003), which is also used in Rouyet et al. (2019) and Abe et al. (2020). Used the eleven interferograms and error of each interferogram given as the variance of the phase, the 2σ error of the stacking result was estimated to be 0.26 cm/yr.

UAS Remote Sensing

Aerial images were obtained using a DJI Phantom 4 UAS with a digital camera (12.4 megapixels) at the disused airfield site near the settlement of Churapcha on September 14, 2016 and September 15, 2017 (Saito et al., 2018). Images were captured at an altitude of about 100 m above ground level, with an overlap of more than nine images. In total, 94 and 167 images were acquired for 2016 and 2017. We also measured ground control points (GCPs) with a global navigation satellite system receiver (Emlid Reach RTK). The geodetic data were processed based on the kinematic method using RTKLIB (ver. 2.4.3). The standard deviations of the GCP analysis were less than 0.01 m in total across three dimensions for the GCP measurements in 2017 (Saito et al., 2018).

The aerial images were processed using SfM-MVS (Structure from Motion-Multi View Stereo) photogrammetry software (Agisoft Metashape, Professional Edition). We obtained orthorectified images and digital surface models (DSMs). The residual errors (root-mean-squared error) at the GCPs were 16.5 cm in total across three dimensions for 2017. We co-registered the orthorectified images and DSMs for 2016 to those for 2017. The residual errors for 2016 were 7.8 cm. We then compared the images and DSMs to detect the differences in water area and topography.

Fine-Scale Satellite Images

We used additional optical satellite imagery taken in late summer to detect the initiation and development of high-centered polygonal relief and water bodies resulting from thermokarst processes in Churapcha. ALOS-PRISM took an image on September 15, 2007 in the panchromatic band with 2.5-m resolution. The WorldView series includes images taken on September 4, 2011, September 4, 2018, and August 27, 2019 by the panchromatic band with 0.5-m resolution.

GIS Data on Landscape Change

The land cover classification map of the area around Churapcha was compiled in a GIS format by Gorokhov et al. (2011). The first map in 1945 was initially drawn based on aerial photographic interpretation by Soloviev (1959). This first map was later became known to the world by Czudek and Demek (1970). Another map in 2009 was produced at a scale of 1:25,000 and is based on aerial photographs and satellite visible images (Terra/ASTER in 2007, IKONOS and GoeEys-1 in 2009). There are four terrain classes (alas, inter-alas, small valley, and lake) and sub-classification with 13 vegetation and anthropogenic landscape categories (**Table 2**).

RESULTS

InSAR Stacking Result

Figure 1 shows the elevation and vertical displacement rate maps derived from AW3D30 and ALOS-2 InSAR stacking over an area of ~10 × 10 km that includes Churapcha. The elevation ranges

TABLE 2 | Landscape characteristics of Churapcha in 1945 and 2009 (after Gorokhov et al., 2011). The targeted area is shown in **Figures 2C,D**.

Terrain	Vegetation	1945		2009	
		km^2	%	km^2	%
Alas	Dry grassland	19.2	15.2	8	6.3
	Wet grassland	7.4	5.9	9	7.1
	Settlement	0.3	0.2	1.9	1.5
Inter-alas	Larch forest mossum	11.3	8.9	11	8.7
	Larch forest vacciniosum	39.8	31.3	22.8	17.9
	Larch-Birch and Birch-Larch secondary forest	21.3	16.7	30.3	23.8
	Dry grassland	16.4	12.9	11.4	9
	Field	2.8	2.2	7.5	5.9
	Routs and cut-through	0.2	0.2	1.9	1.5
	Settlement	1.1	0.9	6.9	5.5
Small valley	Small valley grassland	5.2	4.1	3.6	2.8
Lake	Alas lakes	1.7	1.3	11.9	9.4
	Inter-alas lakes	0.3	0.2	0.8	0.6

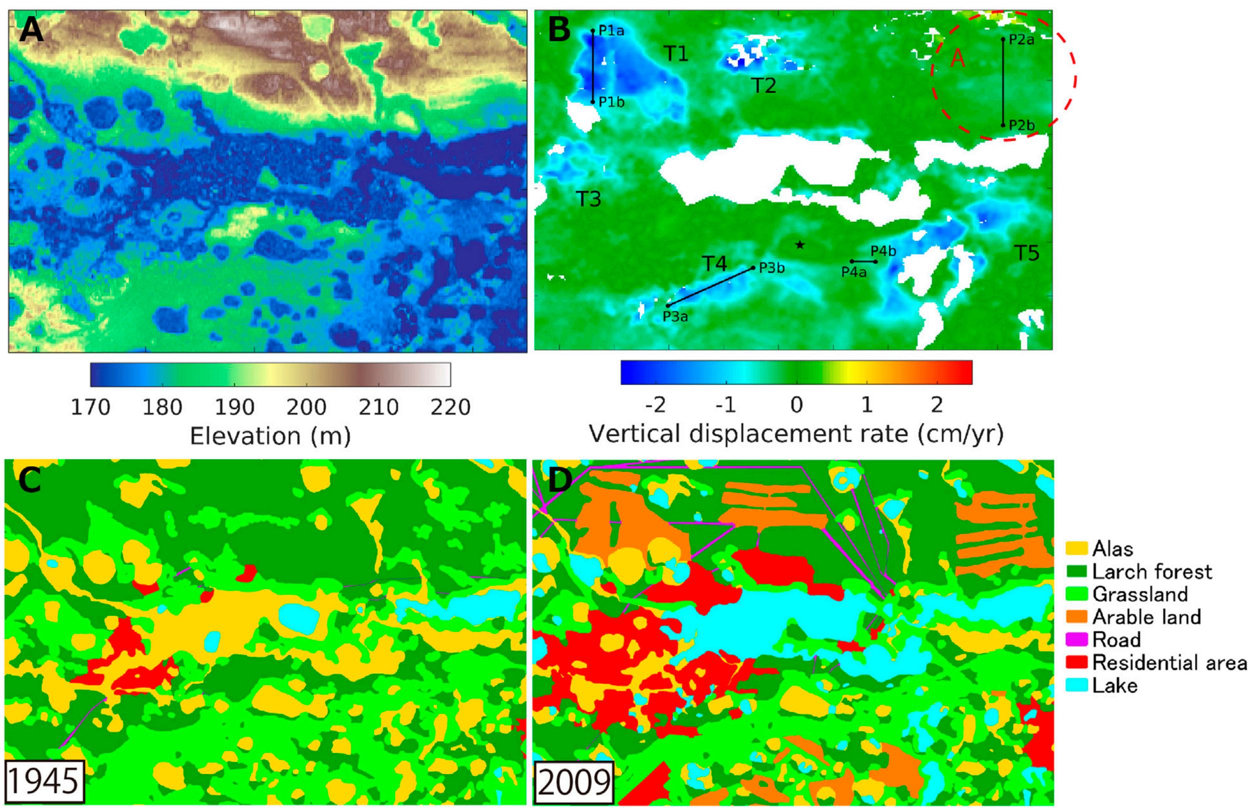

FIGURE 2 | Enlarged view of **(A)** elevation and **(B)** vertical displacement rate in Churapcha. P1-P4 indicate transect lines showing profiles in **Figure 3**. The star indicates the location of the InSAR reference point. The red dotted oval labeled A indicates an area of arable land where surface subsidence was not detected. **(C)** and **(D)** indicate land classification in 1945 and 2009, partially modified from Gorokhov et al. (2011).

from 170 to 230 m. The north, west, and southeast area has a slightly higher elevation, while the Central part is relatively lower than the surrounding area (**Figure 1A**). The result of the stacked interferogram (**Figure 1B**) indicates clear signals of surface subsidence around Churapcha. The signs indicating the subsidence are also southwest of Churapcha.

In contrast, positive signals exist in the northwest and southeast Churapcha. The distribution of the positive signals mainly corresponds to the extent of the larch forest. Inter-annual surface uplift is unlikely to occur within a larch forest, and thus these signals are considered to be due to some tropospheric effects.

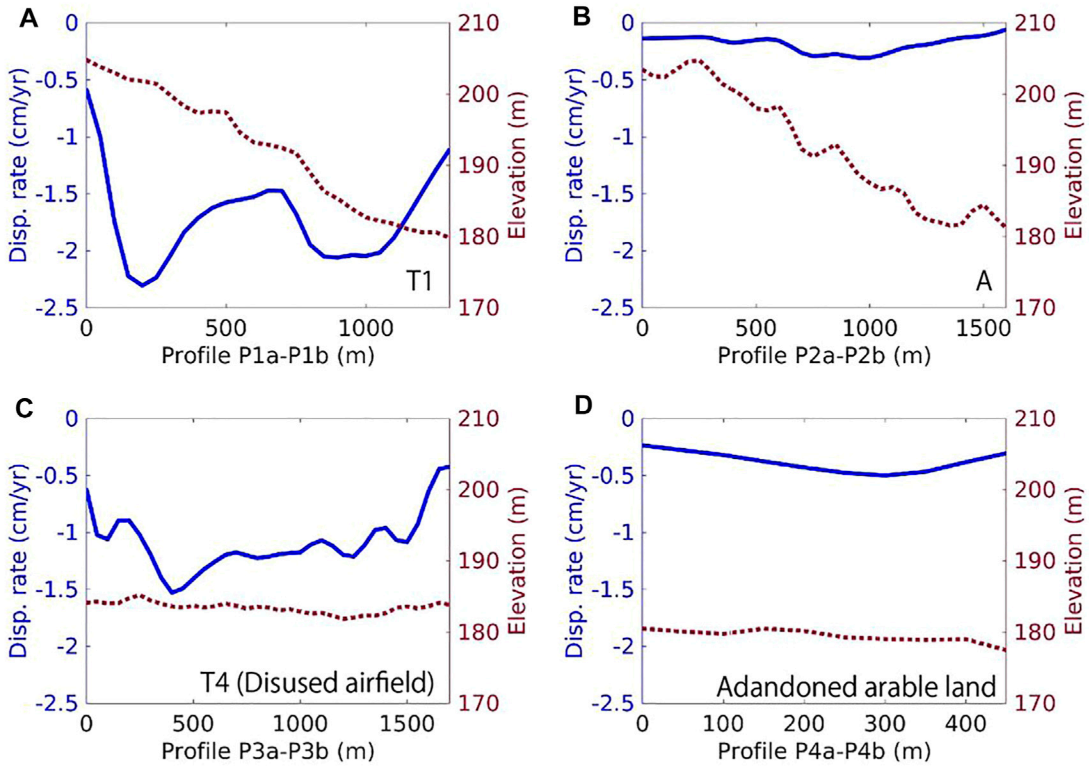

FIGURE 3 | Comparison of the surface displacement rate and elevation along the transect lines P1-P4 in **Figure 2B**.

Figure 2 shows an enlarged view of the elevation and vertical displacement rate of the Churapcha settlement in **Figure 1**. There are some lakes in the central part of the area, and the elevation in the north is relatively higher than the other area (**Figure 2A**). The stacked interferogram shows that five significant signals of surface subsidence rate (areas T1-T5) were identified, up to 2.4 cm/yr (**Figure 2B**). Land classification by Gorokhov et al. (2011) shows that significant land classifications in 1945 were grassland, larch forest, and alases (**Figure 2C**). The classification in 2009 (**Figure 2D**) shows that the number of lakes has increased, and the residential area has expanded distinctly. Some portions of grassland and larch forest were cultivated and changed to agricultural fields. Compared with these changes, the identified surface subsidence signals are in agricultural fields (T1 and T2) and grassland (T3, T4, and T5). The displacement rate of areas T1 and T2 was larger than that of areas T3, T4, and T5. In contrast, no subsidence signals exist in the arable land area in the northeast of the study area (encircled and labeled with A in **Figure 2B**), which has the same elevation and land classification as T1 and T2.

A comparison of the elevation and displacement rate along four transect lines (P1-P4) is shown in **Figure 3**. In particular, the transect lines of P1 and P2 (T1 and A, respectively) run along the north-south direction on south-facing slopes (**Figures 3A,B**). However, while both sites are located in abandoned agricultural fields on comparable elevations and relief positions on the Abrakh terrace, only T1 showed subsidence rates up to 2.4 cm/yr, but no displacement could be detected for A (**Figures 3A,B**).

For comparison with our previous studies (Saito et al., 2018), the transect lines of P3 and P4 were set in a disused airfield and abandoned agricultural field. The elevation profiles along lines P3 and P4 show that the two areas are almost flat (**Figures 3C,D**). Subsidence in area T4 (disused airfield) was detected at a rate of up to 1.5 cm/yr, while it was up to 0.5 cm/yr in the abandoned agricultural field (**Figures 3C,D**).

Fine-Scale Mapping Based on UAS Remote Sensing

We obtained the respective orthorectified images and DSMs with spatial resolutions of 3.0 and 6.0 cm for 2016 and 4.0 and 8.0 cm for 2017. High-centered polygons with an average diameter of 11.6 m (Saito et al., 2018) were observed over the entire area of the images (**Figure 4**). Over the 2 years, little topographic change was observed from the difference between DSMs. The only difference for water areas was that they were more extensive in 2016 (**Figure 4**). The size of the water area was also affected by the precipitation amounts in each year. The summer season (June, July, and August) precipitations in 2016 and 2017 were 168 and 99 mm, respectively, in the study area. The larger precipitation in 2016 likely resulted in larger water areas in 2016.

Figure 5 shows the elevation difference of rectangle area in **Figure 4** between 2016 and 2017 DSMs. The difference was

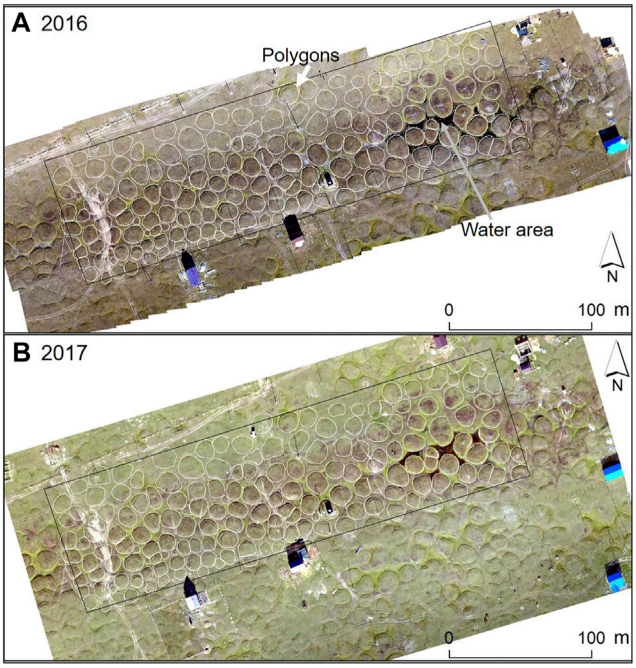

FIGURE 4 | Orthorectified images taken by UAS at the disused airfield site (T4 in **Figure 2B**) for **(A)** 2016 and **(B)** 2017. White lines in both photos denote the boundary of polygons.

calculated only inside the high-centered polygons (**Figure 4** and **Supplementary Figure S2**) since the difference of DSMs between 2016 and 2017 provides unrealistic positive values (uplifting) in most of the trough parts. The reverse tendency was probably due to the low quality of photogrammetry in 2016. The photos taken under the cloudy condition in the late afternoon likely caused the overestimation of deeper trough shape (lower elevation). As a result of **Figure 5**, most of the difference indicates subsidence with a mean difference of −8 cm/366 days.

The previous study (Saito et al., 2018) showed that the estimated average subsidence rate was 2.1 cm/yr in the disused airfield (**Figure 4**) and 3.9 cm/yr in the abandoned arable land (Saito et al., 2018). Considering the residual errors of the SfM-MVS photogrammetry of 7.8 and 16.5 cm for 2016 and 2017, respectively, the comparison is mostly within the error. Thus, the small topographic changes (less than 20 cm) triggered by the subsidence in only a 1-year interval may have observational uncertainties by UAS remote sensing.

DISCUSSION

Effect of Land Use History on Thermokarst Development

In the settlement of Churapcha, the landscape on the terraced terrain, where yedoma permafrost has been preserved, differs greatly on a north to south transect (**Figure 2**). The northern part of the settlement is dominated by larch forest taiga, while natural grassland dominates the southern area. As of 1945, much of the land had been made up of old alases interspersed with terraced terrain, whereas there had been a few young thermokarst lakes (**Figure 2C**; Czudek and Demek, 1970; Gorokhov et al., 2011). In contrast, anthropogenic development, such as expanding residential development and agricultural fields, has spread north and south. Many young thermokarst lakes emerged simultaneously and continue to do so. Landscape changes between two periods (**Table 2**) show that the original boreal forest (larch forest with vaccinium) on higher elevations classified as inter-alas, has been decreasing (−13.4%), while settlements (+5.9%) and agricultural fields (+3.7%) have been expanding. The area of alas and inter-alas lakes has also increased (+8.1 and 0.4%, respectively). The inter-alas lakes show a slight total area increase, which indicates the extensive emergence of young thermokarst lakes (**Figure 2D**). According to an assessment of lake dynamics at the Yukechi site in the Lena-Aldan interfluvial area in Central Yakutia over 70 years (Ulrich et al., 2017), which is located about 100 km to the east, anthropogenic disturbance and deforestation was initiated, and the climate forced rapid and continuous thermokarst lake development in Central Yakutia. They quantified a mean radial growth of 1.2 ± 1.0 m/yr of and a mean subsidence rate of 6.2 ± 1.4 cm/yr. The Churapcha locality is also considered to follow a similar temporal evolution of thermokarst development.

Churapcha is the location of an unpaved airport on inter-alas grassland (T4) that was used until the early 1990s. In addition, the locality has also seemed stably used as agricultural fields in the open areas of the northern boreal forest and in the southern grassland (**Figures 2C,D**; Gorokhov et al., 2011; Saito et al., 2018). Similar land use without any signs of permafrost degradation and

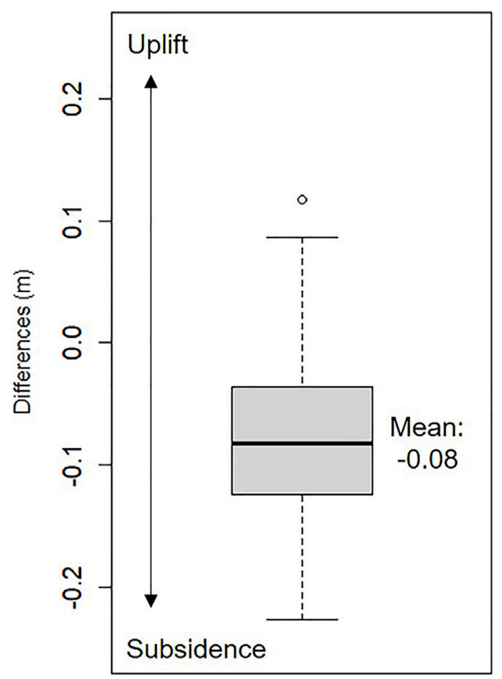

FIGURE 5 | (new). Box plot of elevation difference at the center part of polygons between 2016 and 2017 DSM.

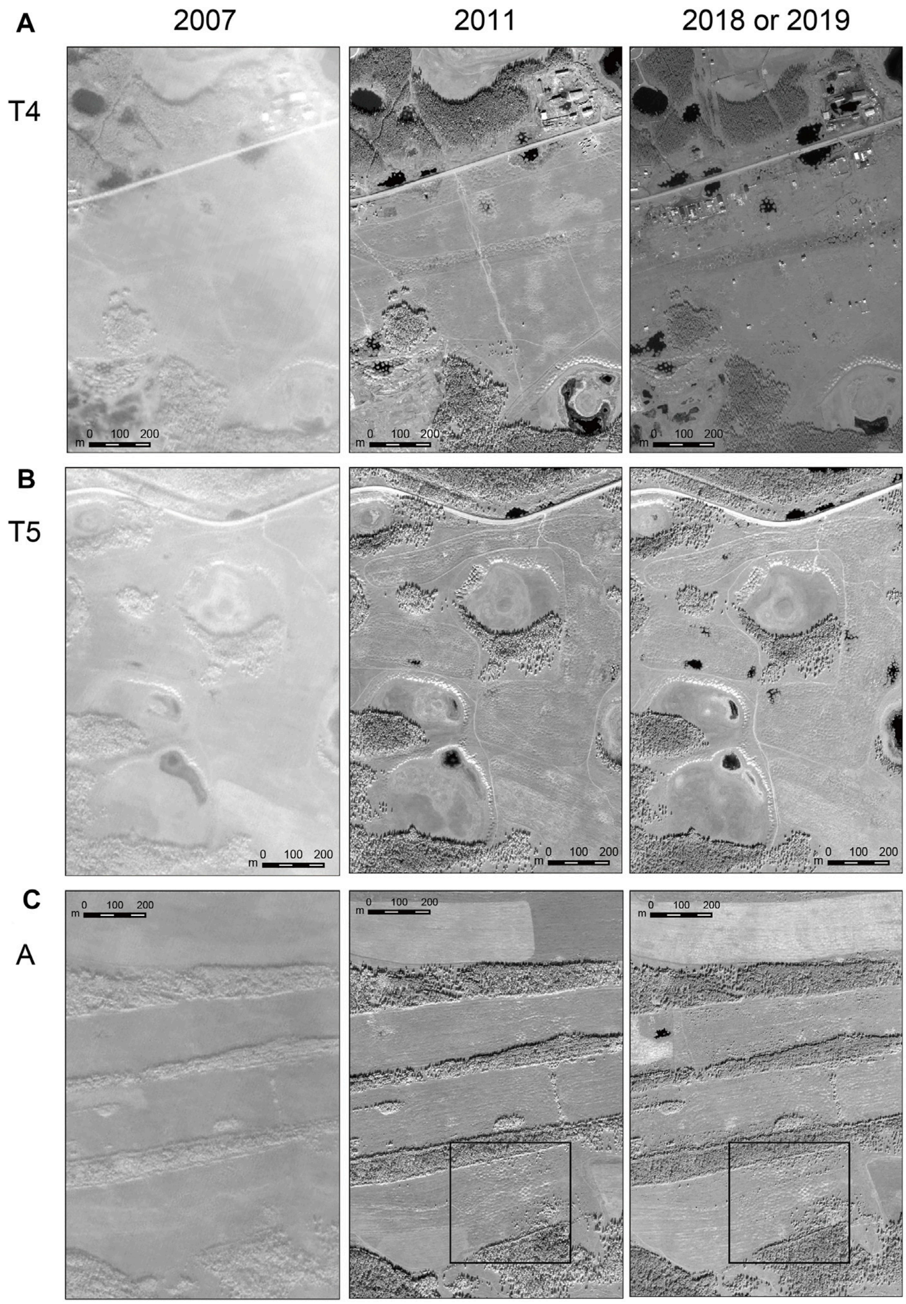

FIGURE 6 | Comparison of the visible images in areas **(A)** T4, **(B)** T5, and **(C)** A (as shown in **Figure 2B**), derived from ALOS-PRISM in September 2007 **(left)**, WorldView in September 2011 **(center)**, and WorldView in September 2018 or August 2019 **(right)**. The rectangle in **(C)** shows the enlarged area in **Figure 8**.

thermokarst processes was widespread in Central Yakutia until the 1980s (Crate et al., 2017). In contrast, extensive surface subsidence due to increasing thermokarst processes seems to be related to a clear warming shift in the region since the 1990s. Reports from the Yukechi site (Fedorov et al., 2014a) indicate that the surface subsidence in the 1990s was minor when the thermokarst lakes had just emerged. In contrast, the subsidence rate increased significantly after 2000, when lakes began to expand rapidly. These recent changes indicate that the status of thermokarst development since the 1990s would be very effectively detected by combining multiple spatial analyses.

Thermokarst Development After 2000 Detected by Multiple Spatial Data

Thermokarst development has been active in Central Yakutia since the early 2000s (Iijima et al., 2010; Fedorov et al., 2014a; Ulrich et al., 2017; Czerniawska and Chlachula, 2020). In addition to the expansion of young thermokarst lakes, the development of polygonal relief due to continuous surface subsidence in the early stage of thermokarst formation with the beginning of ice-wedge complex thawing ("dyede" in the Sakha language, Desyatkin et al., 2009) has been observed in various parts of the open field in Churapcha. The InSAR results show that monotonous topographic subsidence has continued for the previous 5 years (2015–2020), indicating that the thermokarst has been actively developing. However, it is also clear that there are some differences in its progression even within the region.

We compare the landscape changes due to surface subsidence and polygonal landform development detected by InSAR and UAS remote sensing at several sites in **Figure 2B** with satellite imagery from 2007 (ALOS-PRISM), 2011, and the present (WorldView) in **Figure 6**. The disused airfield (T4) shows thermokarst initiation with less polygonal relief and small ponding areas in 2007 (**Figure 6A**). In contrast, we can find intense development of polygonal relief on the former runway (long and narrow rectangle area) and newly developed lakes along the northern road and in the southwestern grassland in 2011. In particular, it is noted that thermokarst lakes have expanded, implying a deepening of their bathymetry in the recent image. Moreover, it is noteworthy that the number of new houses and buildings has been increasing in these areas despite the obvious and significant landscape changes due to the progression of thermokarst during the last decade.

The same change is obvious for the abandoned agricultural field (T5; **Figure 6B**). Thermokarst lakes had already emerged in their exact current locations as of 2007. The lakes were initially small but appear to have constantly increased in size until recently. High-centered polygons are developed in a plot of land used as agricultural fields, where vehicle tracks are visible. The extent of the polygons coincides well with the large subsidence seen in area T5 (**Figure 2B**).

Saito et al. (2018) examined thermokarst subsidence in areas T4 and T5 using a UAS and SfM-MVS and estimated a subsidence rate of 2.1 cm/yr for the disused airfield and 3.9 cm/yr for the abandoned arable land from 1990 to 2017. According to our InSAR stacking results (**Figures 3C,D**), both average subsidence rates during 2015–2020 (1.5 cm/yr at P3 and 0.5 cm/yr at P4) were lower than those reported in Saito et al. (2018). One of the possible reasons is interannual changes in the subsidence rate. Fedorov et al. (2014a) demonstrated the acceleration of subsidence at polygon centers after 2000, particularly in 2004–2008 during wet climate periods at the Yukechi site. Compared to that period, the speed of the active layer deepening shows a slow or recovering trend, and this may indicate the possibility that the recent period of relative stability is somewhat small compared to the long-term subsidence rate likely because of drier climate. It is also clear that the significant subsidence rate indicated by InSAR analysis is difficult to estimate from the difference of the DSMs taken in two consecutive years. **Figure 7** shows the subsidence rate of InSAR in area T4 compared to the UAS ortho-images and DSM. The orthorectified images and DSM show that the polygons are distributed over the entire area. In particular, the polygon troughs are showing the lowest terrain heights, which are about 2 m lower than the surrounding area. The InSAR magnified images indicate that a subsidence rate of 0.5–2 cm/yr is widespread over the entire area, and areas of high subsidence correspond to regions with deep polygon development. Based on the line transect diagram (A-B) in **Figure 7**, there is an obvious correspondence between the magnitude of the InSAR subsidence rate and the level of polygon development. Areas with high elevations and less pronounced polygon development at side A show low subsidence rates, while areas with well-developed polygons near the center show high subsidence rates. On side B, the polygons are well developed. However, there is a water area, which may correspond to the fact that the subsidence was not well reproduced by InSAR. Thus, although it is difficult to calculate the subsidence rate from year to year based on the accuracy of the images and the DSM itself, the high-resolution spatial information is beneficial for confirming the locations where the InSAR results can be verified.

In contrast, the stacked interferogram (**Figure 2B**) shows that no subsidence signal was detected in area A. However, numerous high-centered polygons in area A were identified by Worldview high-resolution optical images in 2011 (**Figure 6C**). **Figure 8** shows enlarged pan-sharpened images in area A by Worldview-2 in 2011 and Worldview-3 in 2019 with a resolution of 50 cm. High-centered polygons in cultivated areas are shown in both images, confirming that thermokarst has been developing in area A. However, the polygons in 2019 were more ambiguous than in 2011, and it is apparent that larch regeneration is also spreading, which would indicate a slight stabilization of the surface. The cultivated agricultural land in the north showed extensive subsidence at T1 (**Figures 2B**, **3A**). Both areas T1 and A are south-facing slopes with similar topography and relief positions on the potentially ice-rich Abrakh terrace surfaces. Based on these conditions, it is not surprising that thermokarst development has progressed at both locations. However, if thermokarst development is slowing down in area A, it can be pointed out that the reason may reflect differences in soil and ground ice distribution rather than a climatic trend. Area A is located on the terrace edge near the Taata River (**Figure 1A**), suggesting the existence of a depositional environment here, different from that of T1. The average diameter of polygons in areas T4 and T5 also differ by approximately 4 m, suggesting that the ice wedges were formed under different conditions (Saito et al., 2018).

Effectiveness of InSAR Analysis for Detecting Thermokarst Development

The application of InSAR analysis to the vicinity of Yakutsk, East Siberia, Russia, mark a starting point in quantifying land surface subsidence related to the thawing of permafrost (Abe et al., 2020; Yanagiya and Furuya, 2020). These previous studies used stacking InSAR analysis with SAR images from 2006–2010 (ALOS-PALSAR) and 2015–2018 (ALOS-2/PALSAR-2). Their results showed that, compared with regions showing relatively small surface displacements, open areas showing obvious thermokarst subsidence signals had average subsidence rates of 1–3 cm/yr (Abe et al., 2020). According to their field survey at the Mayya settlement (about 100 km southeast of Churapcha), the ground

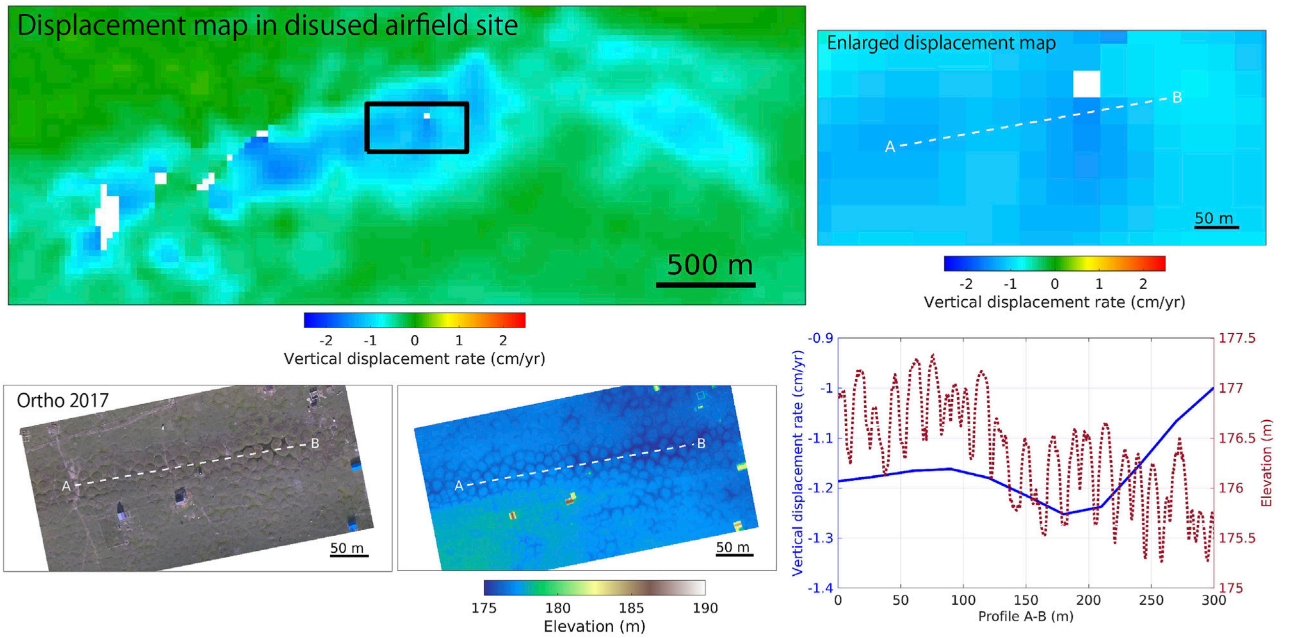

FIGURE 7 | Comparison between InSAR and UAS maps at area T4. The displacement map **(upper left)** is the same as **Figure 2B** with 30-m resolution. **(upper right)** Enlarged displacement map **(lower left)** Orthorectified and DSM maps in 2017. **(lower-right)** comparison between elevation and vertical displacement rate along line transect **(A–B)**.

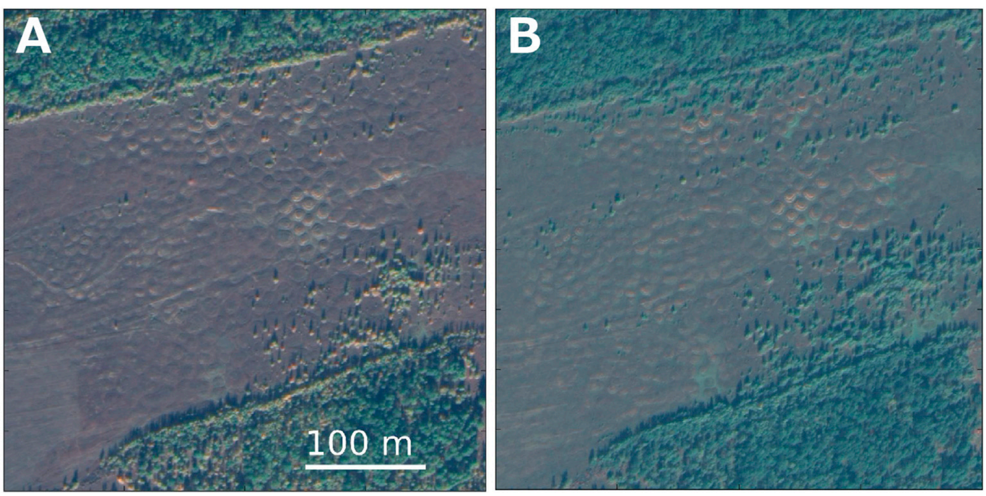

FIGURE 8 | Comparison of the pan-sharpened images in arable land area A in **Figure 2B** derived from the **(A)** Worldview-2 image on September 11, 2011 and **(B)** Worldview-3 image on August 27, 2019.

truth data identified polygonal landforms in the deforested areas where thermokarst subsidence signals were found. The ground surface displacements obtained from two field surveys in subsequent autumns showed good agreement with the displacements obtained from InSAR analysis. This result confirms that InSAR successfully detects the spatio-temporal distribution of subsidence signals in open land, logging land, and agricultural land, including non-forested urban areas in Central Yakutia.

In the present study, several open areas near Churapcha also showed a clear subsidence trend at the rate of 0.5–2 cm/yr (**Figure 1B**, **Figure 2B**, and **Figure 3**). The rate is somehow comparable to the estimation at T4 and T5 by Saito et al. (2018). How can these interannual subsidence rates be evaluated in relation to the annual freeze-thaw cycle? As for seasonal subsidence, we additionally performed InSAR analysis using two pairs within the warm season in the certain year, a pair between autumn to next early summer and a pair 3 years apart (**Supplementary Figure S3**). The subsidence distribution in (**Supplementary Figure S3A**) is exactly similar to the ones in the stacked interferogram. Since the melting of yedoma ice occurs in the latter half of the thawing season, this result may represent a part of the thermokarst process; Zwieback and Meyer (2021) discuss the same point in their InSAR results for Alaska. Since the signal distribution in **Supplementary Figure S3B** does not show very clear subsidence, it appears that the surface subsidence associated with ground-ice melting has not yet occurred in this period. Seasonal subsidence during July to August tends to be a little less than 1 cm/month. **Supplementary Figure S3C** suggests the net change in subsidence associated with melting of the ground ice in 2017 and subsequent frost heaving, and then seasonal ice melting mainly within the active layer in 2018. It is similar to the distribution of subsidence in the stacked interferogram. The subsidence rate is more extensive than **Supplementary Figure S3A**, which suggests that there is still more subsidence after September 22, 2015 and/or that the 2017 subsidence is more significant. As for the InSAR results for images 3 years apart (**Supplementary Figure S3D**), the displacement distribution shows the same trend as the stacking result. It represents about 3 years of displacement. The large positive areas are forests or lakes, which appear differently in the other images, so they are possibly noise. Area A shows slight subsidence (**Supplementary Figures S3C,D**), so we might have found more subsidence if we had images from the end of September instead of 20 July. Based on the results, the seasonal change component tends to show the effect of yedoma ice melting in the late summer rather than the effect of annual frost heaving and subsidence. The subsidence rate for stacking analyses in this study is probably underestimated in this case due to the availability of data for the late summer.

Based on the fine-scale satellite images, these landscapes are mostly affected by polygonal land deformation, indicating thermokarst development. In addition, these are not natural areas but have been developed by human activity within the past 70 years. This subsidence progression was consistent with the InSAR results as an average value for the entire target area. Still, the results suggest that continued observations and additional observation points are needed for more detailed verification.

CONCLUSION

In the present study, we evaluated the distribution of topographic subsidence caused by thermokarst development in the area around Churapcha, in Central Yakutia, which is characterized by a typical yedoma landscape. In an attempt to understand the rapidly progressing thermokarst development, multiple spatial data sources were used.

The results of the InSAR stacking analysis show that the interannual trend of surface subsidence by thawing permafrost and melting of yedoma ice mainly occurred in deforested areas and agricultural fields. The agricultural fields have expanded significantly north and south of Churapcha during the past 70 years. However, extensive thermokarst processes and the widespread development of high-centered polygonal relief make it difficult for the local people to continue using these areas. Thermokarst has also developed in areas where people have already built structures. This situation makes it particularly important to provide information about permafrost degradation to the local population, also in order to be able to take countermeasures.

The thermokarst development in Central Yakutia has progressed since the 2000s. InSAR analysis using the ALOS series of satellites, which has been in operation since the early 2000s, can detect topographic changes over the years. However, even in the stripmap mode of ALOS-2, the effective resolution is limited to approximately 30 m due to noise influences, which is insufficient to map the displacement to actual landscape changes. By comparing with the DSMs and high-resolution images from the UAS, which have a resolution of the order of less than 10 cm, we can effectively examine the development of thermokarst in the area where the InSAR displacement appeared. On the other hand, for short-term (1 year) differences in DSMs, the amount of displacement could not be detected with the vertical accuracy of InSAR due to the low data quality of the 2016 DSM. Therefore, to improve the accuracy of the topographic displacement validation, it is necessary to detect the cumulative displacement over 5–10 years. In this case, clear photography and accurate GCP geocoding in the space of about 1 km^2 will be necessary to compare with InSAR results. In addition, because most fields with thermokarst development correspond to areas affected by anthropogenic activity in the past, spatial information on historical land-use change in GIS format is also helpful. Going forward, the integrated analysis of geospatial information will be essential for assessing permafrost degradation.

DATA AVAILABILITY STATEMENT

The original contributions presented in the study are included in the article/**Supplementary Materials**, further inquiries can be directed to the corresponding author.

AUTHOR CONTRIBUTIONS

YI, TA, HS, MU, and AF designed the study. YI and TA acquired funding. YI, HS, NB, and AF participated in field investigations. TA and MU conducted InSAR analyses. HS, NB, and AF conducted SfM analyses using UAS data. AG and VM applied the land classifications in the GIS format. YI, TA, and HS wrote the original draft of the manuscript. All authors contributed to the review and editing of the manuscript.

FUNDING

This research was supported by the three Japanese grants: JSPS KAKENHI Grant JP19H00556, Arctic Challenge for Sustainability II Program Grant JPMXD1420318865, JST SICORP Grant JPMJSC1902, and JSPS International Fellowship for Research in Japan (L18558). This study was also supported by ERI JURP 2021-B-03 in Earthquake Research Institute, the University of Tokyo and the HYPE-ERAS project, which is funded by FORMAS (project No. 2019-02332), RFBR (project No. 20-55-71005), JST (grant No. JPMJBF2003) through the Belmont Forum Collaborative Research Action: Resilience in Rapidly Changing Arctic Systems.

ACKNOWLEDGMENTS

We express sincere thanks to Dr. Aleksey Desyatkin for help with fieldwork in 2016 and 2017. ALOS-2/PALSAR-2 SLC data are shared among PIXEL (PALSAR Interferometry Consortium to Study our Evolving Land surface), and provided from JAXA under a cooperative research contract with PIXEL. The ownership of ALOS-2/PALSAR-2 data belongs to JAXA.

SUPPLEMENTARY MATERIAL

The Supplementary Material for this article can be found online at: https://www.frontiersin.org/articles/10.3389/feart.2021.750298/full#supplementary-material

REFERENCES

Abe, T., Iwahana, G., Efremov, P. V., Desyatkin, A. R., Kawamura, T., Fedorov, A., et al. (2020). Surface Displacement Revealed by L-Band InSAR Analysis in the Mayya Area, Central Yakutia, Underlain by Continuous Permafrost. *Earth Planets Space* 72, 138. doi:10.1186/s40623-020-01266-3

Antonova, S., Sudhaus, H., Strozzi, T., Zwieback, S., Kääb, A., Heim, B., et al. (2018). Thaw Subsidence of a Yedoma Landscape in Northern Siberia, Measured *In Situ* and Estimated from TerraSAR-X Interferometry. *Remote Sensing* 10, 494. doi:10.3390/rs10040494

Bosikov, N. P. (1991). *Alas Evolution of Central Yakutia*. Yakutsk: Permafrost Institute SD USSR AS. 128p. (In Russian).

Chen, J., Liu, L., Zhang, T., Cao, B., and Lin, H. (2018). Using Persistent Scatterer Interferometry to Map and Quantify Permafrost Thaw Subsidence: A Case Study of Eboling Mountain on the Qinghai-Tibet Plateau. *J. Geophys. Res. Earth Surf.* 123, 2663–2676. doi:10.1029/2018jf004618

Costantini, M. (1998). A Novel Phase Unwrapping Method Based on Network Programming. *IEEE Trans. Geosci. Remote Sensing* 36, 813–821. doi:10.1109/36.673674

Crate, S., Ulrich, M., Habeck, J. O., Desyatkin, A. R., Desyatkin, R. V., Fedorov, A. N., et al. (2017). Permafrost Livelihoods: A Transdisciplinary Review and Analysis of Thermokarst-Based Systems of Indigenous Land Use. *Anthropocene* 18, 89–104. doi:10.1016/j.ancene.2017.06.001

Czerniawska, J., and Chlachula, J. (2020). Climate-Change Induced Permafrost Degradation in Yakutia, East Siberia. *Arctic* 73, 509–528. doi:10.14430/arctic71674

Czudek, T., and Demek, J. (1970). Thermokarst in Siberia and its Influence on the Development of Lowland Relief. *Quat. Res.* 1, 103–120. doi:10.1016/0033-5894(70)90013-x

Desyatkin, A. R., Takakai, F., Fedorov, P. P., Nikolaeva, M. C., Desyatkin, R. V., and Hatano, R. (2009). CH4emission from Different Stages of Thermokarst Formation in Central Yakutia, East Siberia. *Soil Sci. Plant Nutr.* 55, 558–570. doi:10.1111/j.1747-0765.2009.00389.x

Emardson, T. R., Simons, M., and Webb, F. H. (2003). Neutral Atmospheric Delay in Interferometric Synthetic Aperture Radar Applications: Statistical Description and Mitigation. *J. Geophys. Res.* 108 (B5), 2231. doi:10.1029/2002JB001781

Eshqi Molan, Y., Kim, J.-W., Lu, Z., Wylie, B., and Zhu, Z. (2018). Modeling Wildfire-Induced Permafrost Deformation in an Alaskan Boreal Forest Using InSAR Observations. *Remote Sensing* 10, 405. doi:10.3390/rs10030405

Fedorov, A., and Konstantinov, P. (2003). "Observations of Surface Dynamics with Thermokarst Initiation, Yukechi Site, Central Yakutia", in Proceedings of the 8th International Conference on Permafrost, Zurich, Switzerland, July 21-25, 2003 (Lisse, Netherlands: AA Balkema). 239–243.

Fedorov, A. N., Gavriliev, P. P., Konstantinov, P. Y., Hiyama, T., Iijima, Y., and Iwahana, G. (2014a). Estimating the Water Balance of a Thermokarst lake in the Middle of the Lena River basin, Eastern Siberia. *Ecohydrol.* 7, 188–196. doi:10.1002/eco.1378

Fedorov, A. N., Ivanova, R. N., Park, H., Hiyama, T., and Iijima, Y. (2014b). Recent Air Temperature Changes in the Permafrost Landscapes of Northeastern Eurasia. *Polar Sci.* 8, 114–128. doi:10.1016/j.polar.2014.02.001

Gasanov, S. S. (1969). Estimating of the Volumetric Macro Ice Bodies Content of Permafrost in the Development of Placer deposit. *Kolyma* 6, 41–42.

Gavriliev, P. P., and Ugarov, I. S. (2009). Reaction of Central Yakutian Ice Complex on Climate Warming. *Earth Cryosphere* XIII, 24–30. (In Russian).

Goldstein, R. M., and Werner, C. L. (1998). Radar Interferogram Filtering for Geophysical Applications. *Geophys. Res. Lett.* 25, 4035–4038. doi:10.1029/1998gl900033

Gorokhov, A. N., Fedorov, A. N., Skorve, D., and Makarov, V. S. (2011). Assessment of the Anthropogenic Landscape Variability in the Vicinity of the Churapcha Village (Central Yakutia) Based on Remote Sensing Data. *Probl. Reg. Ecol. Evol. Dyn. Geosystems, UDC* 504, 54. (In Russian).

Iijima, Y., Fedorov, A. N., Park, H., Suzuki, K., Yabuki, H., Maximov, T. C., et al. (2010). Abrupt Increases in Soil Temperatures Following Increased Precipitation in a Permafrost Region, central Lena River basin, Russia. *Permafrost Periglac. Process.* 21, 30–41. doi:10.1002/ppp.662

Iijima, Y., Nakamura, T., Park, H., Tachibana, Y., and Fedorov, A. N. (2016). Enhancement of Arctic Storm Activity in Relation to Permafrost Degradation in Eastern Siberia. *Int. J. Climatol.* 36, 4265–4275. doi:10.1002/joc.4629

Iijima, Y., Ohta, T., Kotani, A., Fedorov, A. N., Kodama, Y., and Maximov, T. C. (2014). Sap Flow Changes in Relation to Permafrost Degradation under Increasing Precipitation in an Eastern Siberian Larch forest. *Ecohydrol.* 7, 177–187. doi:10.1002/eco.1366

Iijima, Y., Park, H., Konstantinov, P. Y., Pudov, G. G., and Fedorov, A. N. (2017). Active-Layer Thickness Measurements Using a Handheld Penetrometer at Boreal and Tundra Sites in Eastern Siberia. *Permafrost Periglac. Process.* 28, 306–313. doi:10.1002/ppp.1908

Ivanov, M. S. (1984). *The Cryogenic Structure of Quarternary Deposits of the Leno-Aldan Depression*. Novosibirsk: Nauka. 125p. (In Russian).

Iwahana, G., Uchida, M., Liu, L., Gong, W., Meyer, F., Guritz, R., et al. (2016). InSAR Detection and Field Evidence for Thermokarst after a Tundra Wildfire, Using ALOS-PALSAR. *Remote Sensing* 8, 218. doi:10.3390/rs8030218

Katamura, F., Fukuda, M., Bosikov, N. P., and Desyatkin, R. V. (2009). Charcoal Records from Thermokarst Deposits in Central Yakutia, Eastern Siberia: Implications for forest Fire History and Thermokarst Development. *Quat. Res.* 71, 36–40. doi:10.1016/j.yqres.2008.08.003

Liu, L., Jafarov, E. E., Schaefer, K. M., Jones, B. M., Zebker, H. A., Williams, C. A., et al. (2014). InSAR Detects Increase in Surface Subsidence Caused by an Arctic Tundra Fire. *Geophys. Res. Lett.* 41, 3906–3913. doi:10.1002/2014gl060533

Liu, L., Schaefer, K. M., Chen, A. C., Gusmeroli, A., Zebker, H. A., and Zhang, T. (2015). Remote Sensing Measurements of Thermokarst Subsidence Using InSAR. *J. Geophys. Res. Earth Surf.* 120, 1935–1948. doi:10.1002/2015jf003599

Liu, L., Zhang, T., and Wahr, J. (2010). InSAR Measurements of Surface Deformation over Permafrost on the North Slope of Alaska. *J. Geophys. Res.* 115, F03023. doi:10.1029/2009jf001547

Michaelides, R. J., Schaefer, K., Zebker, H. A., Parsekian, A., Liu, L., Chen, J., et al. (2019). Inference of the Impact of Wildfire on Permafrost and Active Layer

Thickness in a Discontinuous Permafrost Region Using the Remotely Sensed Active Layer Thickness (ReSALT) Algorithm. *Environ. Res. Lett.* 14, 035007. doi:10.1088/1748-9326/aaf932

Miller, J. R., Fuller, J. E., Puma, M. J., and Finnegan, J. M. (2021). Elevation-dependent Warming in the Eastern Siberian Arctic. *Environ. Res. Lett.* 16, 024044. doi:10.1088/1748-9326/abdb5e

Overland, J. E., and Wang, M. (2021). The 2020 Siberian heat wave. *Int. J. Climatol.* 41, E2341–E2346. doi:10.1002/joc.6850E2346

Rouyet, L., Lauknes, T. R., Christiansen, H. H., Strand, S. M., and Larsen, Y. (2019). Seasonal Dynamics of a Permafrost Landscape, Adventdalen, Svalbard, Investigated by InSAR. *Remote Sensing Environ.* 231, 111236. doi:10.1016/j.rse.2019.111236

Saito, H., Iijima, Y., Basharin, N., Fedorov, A., and Kunitsky, V. (2018). Thermokarst Development Detected from High-Definition Topographic Data in Central Yakutia. *Remote Sensing* 10, 1579. doi:10.3390/rs10101579

SakhSTAT SakhSTAT (2021). Available at: https://sakha.gks.ru/about (Accessed July 19, 2021).

Schirrmeister, L., Froese, D., Tumskoy, V., Grosse, G., and Wetterich, S. (2013). “PERMAFROST and PERIGLACIAL FEATURES | Yedoma: Late Pleistocene Ice-Rich Syngenetic Permafrost of Beringia,” in *The Encyclopedia of Quaternary Science*. Editor S. A. Elias (Amsterdam: Elsevier), 542–552. doi:10.1016/b978-0-444-53643-3.00106-0

Short, N., Brisco, B., Couture, N., Pollard, W., Murnaghan, K., and Budkewitsch, P. (2011). A Comparison of TerraSAR-X, RADARSAT-2 and ALOS-PALSAR Interferometry for Monitoring Permafrost Environments, Case Study from Herschel Island, Canada. *Remote Sensing Environ.* 115, 3491–3506. doi:10.1016/j.rse.2011.08.012

Soloviev, P. A. (1959). *Permafrost of Northern Part of the Lena-Amga Interfluve*. Moscow: USSR Academy of Sciences.

Strauss, J., Schirrmeister, L., Grosse, G., Fortier, D., Hugelius, G., Knoblauch, C., et al. (2017). Deep Yedoma Permafrost: A Synthesis of Depositional Characteristics and Carbon Vulnerability. *Earth-Science Rev.* 172, 75–86. doi:10.1016/j.earscirev.2017.07.007

Strauss, J., Schirrmeister, L., Grosse, G., Wetterich, S., Ulrich, M., Herzschuh, U., et al. (2013). The Deep Permafrost Carbon Pool of the Yedoma Region in Siberia and Alaska. *Geophys. Res. Lett.* 40, 6165–6170. doi:10.1002/2013gl058088

Strozzi, T., Antonova, S., Günther, F., Mätzler, E., Vieira, G., Wegmüller, U., et al. (2018). Sentinel-1 SAR Interferometry for Surface Deformation Monitoring in Low-Land Permafrost Areas. *Remote Sensing* 10, 1360. doi:10.3390/rs10091360

Takakura, H., Fujioka, Y., Ignatyeva, V., Tanaka, T., Vinokurova, N., Grigorev, S., et al. (2021). Differences in Local Perceptions about Climate and Environmental Changes Among Residents in a Small Community in Eastern Siberia. *Polar Sci.* 27, 100556. doi:10.1016/j.polar.2020.100556

Tarasenko, T. V. (2013). Interannual Variations in the Areas of Thermokarst Lakes in Central Yakutia. *Water Resour.* 40, 111–119. doi:10.1134/S0097807813010107

Ulrich, M., Matthes, H., Schirrmeister, L., Schütze, J., Park, H., Iijima, Y., et al. (2017). Differences in Behavior and Distribution of Permafrost-related Lakes in C Entral Y Akutia and Their Response to Climatic Drivers. *Water Resour. Res.* 53, 1167–1188. doi:10.1002/2016wr019267

Ulrich, M., Matthes, H., Schmidt, J., Fedorov, A. N., Schirrmeister, L., Siegert, C., et al. (2019). Holocene Thermokarst Dynamics in Central Yakutia - A Multi-Core and Robust Grain-Size Endmember Modeling Approach. *Quat. Sci. Rev.* 218, 10–33. doi:10.1016/j.quascirev.2019.06.010

Wegmüller, U., and Werner, C. L. (1997). “Gamma SAR Processor and Interferometry Software,” in Proceedings of the 3rd ERS symposium, Florence, Italy, March 14-21, 1997 (European Space Agency, Spec Publ), 1687–1692.

Yanagiya, K., and Furuya, M. (2020). Post-wildfire Surface Deformation at Batagay, Eastern Siberia, Detected by L-Band and C-Band InSAR. 125, e2019JF005473. doi:10.1029/2019JF005473

Yu, C., Li, Z., Penna, N. T., and Crippa, P. (2018). Generic Atmospheric Correction Model for Interferometric Synthetic Aperture Radar Observations. *J. Geophys. Res. Solid Earth* 123, 9202–9222. doi:10.1029/2017jb015305

Yu, C., Penna, N. T., and Li, Z. (2017). Generation of Real-time Mode High-resolution Water Vapor fields from GPS Observations. *J. Geophys. Res. Atmos.* 122, 2008–2025. doi:10.1002/2016jd025753

Zwieback, S., and Meyer, F. J. (2021). Top-of-permafrost Ground Ice Indicated by Remotely Sensed Late-Season Subsidence. *The Cryosphere* 15, 2041–2055. doi:10.5194/tc-15-2041-2021

Conflict of Interest: The authors declare that the research was conducted in the absence of any commercial or financial relationships that could be construed as a potential conflict of interest.

Publisher's Note: All claims expressed in this article are solely those of the authors and do not necessarily represent those of their affiliated organizations, or those of the publisher, the editors and the reviewers. Any product that may be evaluated in this article, or claim that may be made by its manufacturer, is not guaranteed or endorsed by the publisher.

frontiers in Earth Science

ORIGINAL RESEARCH
published: 17 December 2021
doi: 10.3389/feart.2021.741556

Permafrost Dynamics and Degradation in Polar Arctic From Satellite Radar Observations, Yamal Peninsula

Kanayim Teshebaeva[1], Ko J. van Huissteden[1], Helmut Echtler[2], Alexander V. Puzanov[3], Dmitry N. Balykin[3], Anton I. Sinitsky[4], Nelley M. Kovalevskaya[3] and Han A. J. Dolman[1]*

[1]Faculty of Science, Department of Earth Sciences, Earth and Climate Cluster, Vrije Universiteit, Amsterdam, Netherlands, [2]GFZ, German Research Center for Geosciences, Potsdam, Germany, [3]Siberian Branch of the RAS, Institute for Water and Environmental Problems, Barnaul, Russia, [4]Arctic Research Center of the Yamal-Nenets Autonomous District, Salekhard, Russia

OPEN ACCESS

Edited by:
Qingbai Wu,
Chinese Academy of Sciences (CAS), China

Reviewed by:
Tonghua Wu,
Chinese Academy of Sciences (CAS), China
Huijun Jin,
Northeast Forestry University, China

***Correspondence:**
Kanayim Teshebaeva
kanayim@gmail.com

Specialty section:
This article was submitted to Cryospheric Sciences, a section of the journal Frontiers in Earth Science

Received: 14 July 2021
Accepted: 15 November 2021
Published: 17 December 2021

Citation:
Teshebaeva K, van Huissteden KJ, Echtler H, Puzanov AV, Balykin DN, Sinitsky AI, Kovalevskaya NM and Dolman HAJ (2021) Permafrost Dynamics and Degradation in Polar Arctic From Satellite Radar Observations, Yamal Peninsula. Front. Earth Sci. 9:741556. doi: 10.3389/feart.2021.741556

We investigate permafrost surface features revealed from satellite radar data in the Siberian arctic at the Yamal peninsula. Surface dynamics analysis based on SRTM and TanDEM-X DEMs shows up to 2 m net loss of surface relief between 2000 and 2014 indicating a highly dynamic landscape. Surface features for the past 14 years reflect an increase in small stream channels and a number of new lakes that developed, likely caused by permafrost thaw. We used Sentinel-1 SAR imagery to measure permafrost surface changes. Owing to limited observation data we analyzed only 2 years. The InSAR time-series has detected surface displacements in three distinct spatial locations during 2017 and 2018. At these three locations, 60–120 mm/yr rates of seasonal surface permafrost changes are observed. Spatial location of seasonal ground displacements aligns well with lithology. One of them is located on marine sediments and is linked to anthropogenic impact on permafrost stability. Two other areas are located within alluvial sediments and are at the top of topographic elevated zones. We discuss the influence of the geologic environment and the potential effect of local upwelling of gas. These combined analyses of InSAR time-series with analysis of geomorphic features from DEMs present an important tool for continuous process monitoring of surface dynamics as part of a global warming risk assessment.

Keywords: permafrost, active layer, InSAR time-series, subsidence, Dynamic Landscape

1 INTRODUCTION

Rapid thaw of permafrost, by climate warming, has huge impacts on natural environments, human activities, and global climate in the Arctic. Ice-rich permafrost thaw is causing soil subsidence and has a devastating effect on infrastructure (Anisimov et al., 2014; Nauta et al., 2015; French, 2017; Hjort et al., 2018). Despite recent intensifying research in Arctic environments, these hold still strong surprises for us, shown by the recent discoveries of CH_4 emitting outburst craters in the permafrost.

The feedbacks of permafrost degradation on climate, such as the Arctic carbon feedback, and in land surface changes still require better quantification (Schuur et al., 2015). This scientific challenge calls for innovative methods to measure permafrost change over large areas. Some of recent studies used Synthetic Aperture Radar Interferometry (InSAR) to quantify permafrost surface changes (Liu et al., 2010, Liu et al., 2015 X.; Chen et al., 2013; Short et al., 2014; Bartsch et al., 2019).

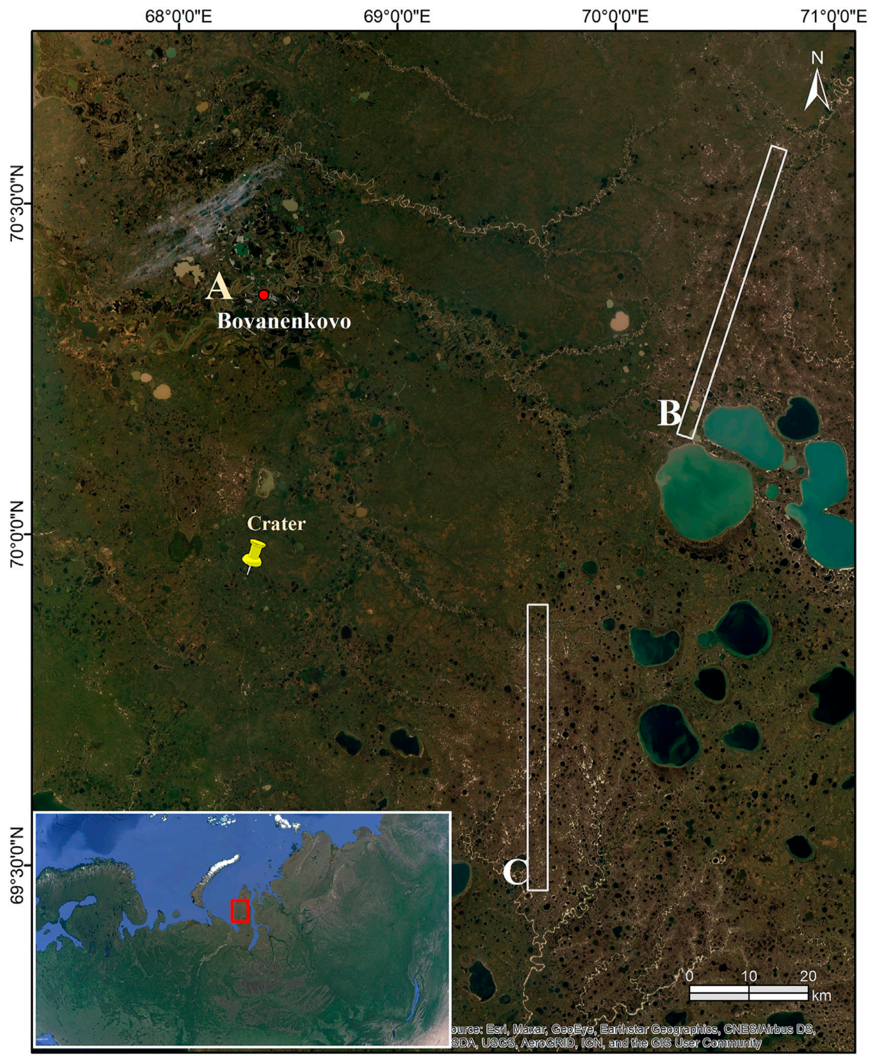

FIGURE 1 | Study area located in the Yamal peninsula of the western Siberia. The map is based on optical Landsat data showing location of the Bovanenkovo field and 2014 crater.

The focus of this study is an area of 2014 outburst crater on the Yamal peninsula in Western Siberia (Leibman et al., 2014a; Olenchenko et al., 2015; Kizyakov et al., 2017). The crater is located in close vicinity of the Bovanenkovo gas condensate field and is formed by a powerful release of natural gas in the permafrost structure (Leibman et al., 2014a).

Detailed assessment of permafrost thaw progression and impact of extreme years using the InSAR technique have been applied by Bartsch et al. (2019) in the central Yamal. This study evaluated InSAR observations with meteorological data, borehole temperature, active-layer thickness measurements, and land-cover classification.

The InSAR technique has the potential for monitoring near-surface permafrost processes and seasonal variations. However, permafrost is a subsurface phenomenon and is still difficult to monitor due to the complexity of the exchange system that includes differences in soil properties and surface cover (Zhang et al., 2004; Duguay et al., 2005).

The objective of our study is to locate areas of active surface displacement and infer surface processes related to permafrost thaw, using InSAR time-series at regional scale. We correlate InSAR observations with available geomorphological and geological data and on-site data collection. To better understand permafrost thaw and landscape evolution in the region we combine this with information on geological subsurface structure that may interact with surface processes. We hypothesize two possibilities on the origin of the surface subsidence and degradation in the region. The first hypothesis is based on classical heterogeneous ice distribution in subsiding zones: higher ice content causing high thaw and subsidence potential. Second, we hypothesize that the natural gas seepage from a deep origin contributes to subsurface heat flow and steep

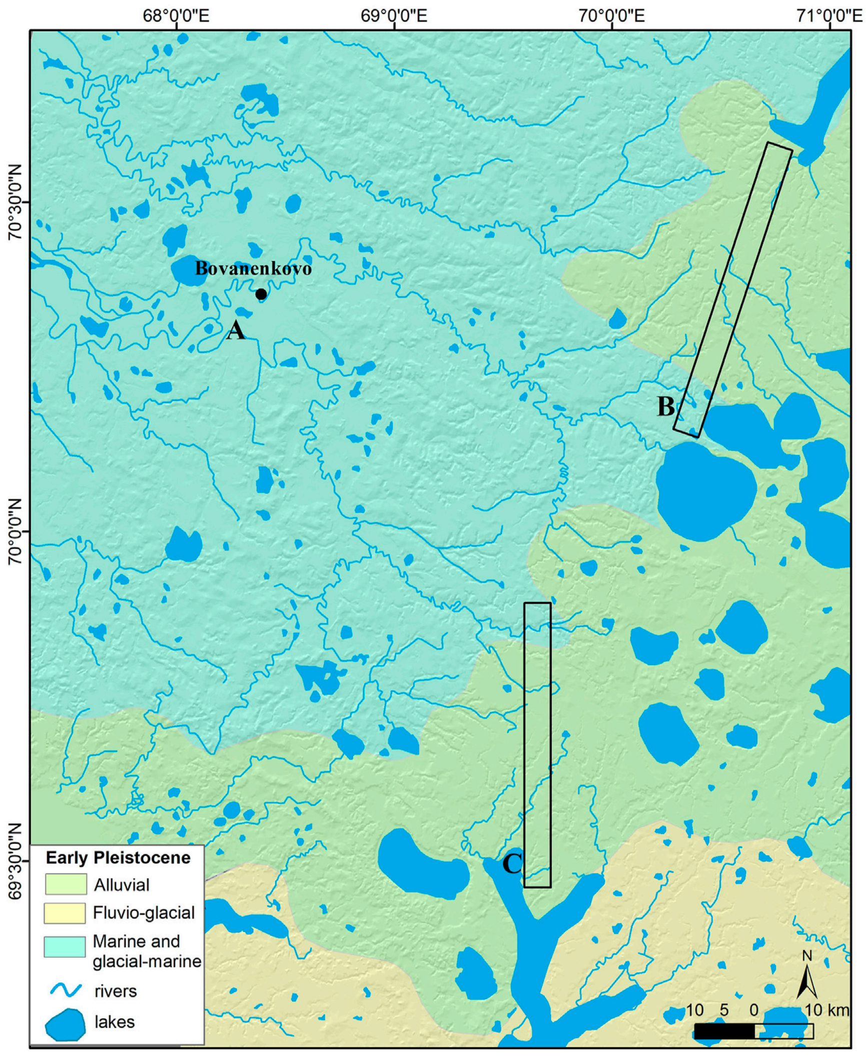

FIGURE 2 | Geology map of the study area. The map is modified after Food and Agriculture Organization (FAO) of the United Nations project defined geology map of the western Siberia.

thermal gradients, causing higher temperatures or thaw of the permafrost layer from the subsurface.

2 STUDY AREA

The study area is located near the Bovanenkovo gas field in the central part of the Yamal peninsula (**Figure 1**). The Yamal peninsula is situated northeast of the Ural mountain and is the polar extension at the northwestern rim of the West Siberian basin. The West Siberian basin is a huge sedimentary basin formed by almost continuous subsidence during Mesozoic and Tertiary (Zonenshain et al., 1990; Puchkov, 1997). The pre-mesozoic basement integrates various tectonic terranes accreted during the Late Paleozoic (Late Devonian–Permian) closing of oceanic basins and collision of the Siberian and Kazakh terranes with the eastward subducted eastern margin of the Russian platform and Baltica, the North European Craton (Echtler et al., 1996).

2.1 Geomorphology and Geology

The mesozoic evolution of the West Siberian Basin is dominated by significant subsidence and marine transgression after late and post-orogenic continental rifting. Marine basin evolution prevailed during Jurassic and Cretaceous times. During Aptian, Albian, and Cenomanian stages shallow-marine to paralic marine sedimentation dominate in the western part of the West Siberian basin (Ulmishek, 2003). These formations are the source of important hydrocarbon and gas fields.

During the Cenozoic period the major phases of alpidic orogeny e.g. the India-Eurasia collision along the south of the Eurasian continent, the northern West Siberian basin experienced uplift and erosion that continued until Middle Pliocene (Ulmishek, 2003; Volkova, 2014). Since Late Pliocene the geologic evolution and morphology was dominated by glacial dynamics with significant sea-level changes as well as ice extension. On the Yamal peninsula unconsolidated glacial marine and terrestrial sediments overlie older erosional surfaces (Chuvilin et al., 2000; Astakhov, 2004, 2011; Volkova, 2014). The Pleistocene deposits consist of mainly glacial deposits with marine, fluvio-glacial, and alluvial clastic sediments of up to 300 m thickness (**Figure 2**). Glacial and interglacial sedimentary processes e.g. erosion and deposition, the permafrost dynamics related to climate dynamics possibly moderate active tectonics (Forman et al., 2002) shape the Yamal peninsula since recent times and need to be considered in understanding the actual surface processes. The unconsolidated youngest sediments are subject to slide, creep, collapse, and talus formations and solifluction that are typical representatives of the cryogenic formations at surface.

Our study area is characterized by continuous permafrost. The thickness of the permafrost layer is up to 300 m in river valleys and about 250 m in hilly terrains. The mean annual temperature is between −2 to −7°C at 10 m depth (Chuvilin et al., 2000). The stratigraphic record on western Yamal peninsula shows active ice-wedge growth accompanied by active eolian and alluvial sedimentation during the Weichsel Glacial Stage (Forman et al., 2002).

The permafrost layer is enriched in organic matter in the region. The upper part is represented by layers of peat and plant remains (detritus). The lower part is represented by thin lignite beds and inclusions of organic matter.

Substantial summer warming (2–4°C) on the Yamal peninsula since the early Holocene resulted in permafrost degradation and increase of the layer above permafrost (active layer), enabling the establishment of trees (Forman et al., 2002). This degradation of permafrost is recognized across Eurasia and associated with substantially warmer summer temperatures, and enhanced since industrial times (Anisimov and Nelson, 1996; MacDonald et al., 2000, 2007).

Northward extension of treeline has been documented on Yamal peninsula and across Eurasia, reflecting a poleward shift of the boreal forest (MacDonald et al., 2007). The birch trees were subsumed by the start of peat growth and reflect a rising water table with permafrost aggradation. Peat accumulation occurred throughout the Holocene and continues today in one-to 2 m-deep depressions in eolian sand. Sources for eolian sand are denuded hilltops associated with reindeer overgrazing, erosion, and fluvial and wind-driven discharge (Forman et al., 2002).

3 DATA AND METHODS

3.1 Data

The SAR dataset used in this study was acquired by the Sentinel -1 A/B C-band (~5.7 cm wavelength) satellite sensor, covering the seasonal time period from June to October for 2017 and 2018. We used 18 Sentinel-1A/B IW SLC SAR images acquired in descending orbits with an incidence angle of 37–39 and a pixel spacing of 2.3 × 14.1 m (range × azimuth).

A Digital Elevation Model (DEM) from TanDEM-X mission is used for InSAR processing, with 90 m spatial resolution. TanDEM-X (TerraSAR-X add-on for Digital Elevation Measurements) is an Earth observation radar mission that consists of a SAR interferometer built by two almost identical satellites flying in close formation. With a typical separation between the satellites of 120–500 m a global DEM has been generated (Wessel et al., 2018). Along with TanDEM-X DEM from 2014 we used SRTM (Shuttle Radar Topographic Mission) DEM from 2000 (Jarvis et al., 2008), at 90 m spatial resolution data for morphology analysis.

3.2 InSAR Processing

SAR interferometry (InSAR) has proven to be a valuable geodetic tool, which scans the Earth surface regularly revisiting the same area. The InSAR technique exploits multiple SAR images and applies appropriate data processing and analysis procedures to separate the contribution of the phase caused by the deformation from the other phase components. The technique focuses on the identification of pixels in the SAR image characterized by small noise, related to properties of reflectors with radar response dominated by a strong reflecting object, and that remains constant over time (Persistent Scatterer, PS) (Ferretti et al., 2001). The PS technique is most accurate for mitigating atmospheric delay with high spatial resolution in SAR interferograms (Onn and Zebker, 2006; Perissin et al., 2011a).

We apply the persistent scatterer interferometry (PSI) method implemented in SARPROZ (Perissin, 2015). The SARPROZ can handle individual swaths of TOPSAR data and estimate the Atmospheric Phase Screen (APS) to improve the quality of the phase signal (Perissin et al., 2011b). Only PS points with a coherence value larger than 0.75 were used in further analyses.

PS candidates were chosen by applying threshold on the Amplitude Stability Index >0.75, following the standard PS InSAR processing (Ferretti et al., 2001). The topographic phase has been removed using TanDEM-X 90 m DEM (Wessel et al., 2018). For the selected points, height and displacement were estimated and deformation time-series were reconstructed. The PS time-series were estimated by assuming a linear displacement in time gaps and minimizing the offset between datasets.

3.3 Hot Spots and Cluster Analysis

InSAR time-series results comprise a large number of point data; to detect areas of locally enhanced changes we perform hot-spot and cluster analysis. Two statistical approaches are used for hot-spot and cluster analysis, the Getis-Ord Gi statistic (Getis and Ord, 2010) and kernel-density estimation (Silverman, 2018). The spatial clusters of similar values and significant spatial clustering of data are identified.

We apply hot-spot analyses on the mean velocity values. For each point feature in a dataset the Getis-Ord Gi* statistics are calculated. The spatial pattern is analyzed for each feature within the context of its neighbors. The Getis-Ord Gi* statistics requires neighbors to have elevated values. A point feature with a high value needs to be surrounded by similar values to be considered as a statistically significant hot spot. The local sum of a point feature

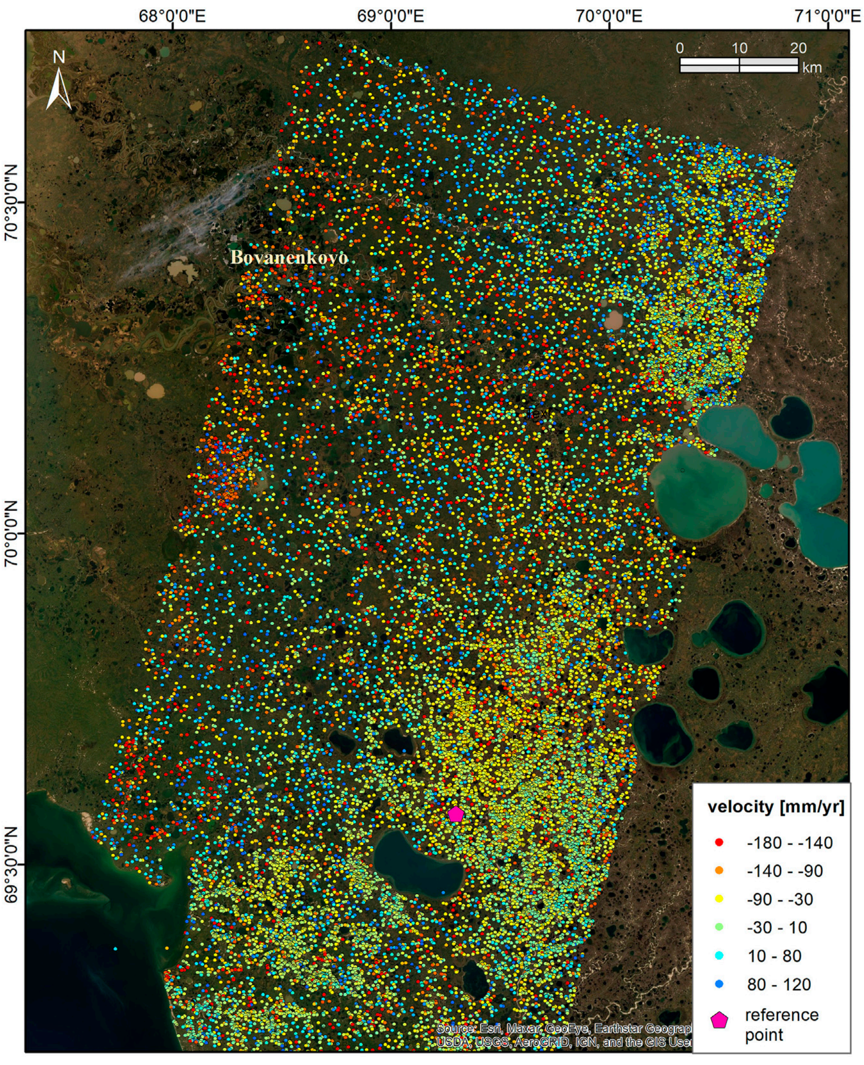

FIGURE 3 | Results of time-series InSAR analysis, colors show spatial pattern of seasonal subsidence velocity for June-October 2017–2018.

is compared proportionally to the sum of all point features. If the local sum is different, a statistically significant z-score is assigned to that point. The z-score values identify spatial clustering of point features with high or low values. The kernel-density estimator is performed on spatial clusters of point features with high and low values. The kernel-density estimator is used to convert a large number of point data into several hotspots. The result is a smooth kernel-density map.

3.4 Topography Openness—Digital Elevation Model (DEM) Image Processing

The parametric characterization of the relief and topography are essential to interpret surface dynamics. The parameter called openness is an expression degree of dominance or enclosure of localized irregular surface. Openness represents an angular measure of relation between surface relief and horizontal distance calculated from multiple zenith and nadir angles. Openness has two viewer perspectives: positive and negative. The positive openness is high for convex forms and represents values above the surrounding surface. The negative openness is high for concave forms and represents values below the surrounding surface (Yokoyama et al., 2002). We perform topography openness analysis on TanDEM-X and SRTM DEMs.

4 RESULTS

4.1 Geometry and Rates of Zones With Enhanced Subsidence

The results derived from Sentinel-1 InSAR time-series are the mean LOS (Line-of-Sight) seasonal velocities for 2017 and 2018 (**Figure 3**). The displacement rates were 60–120 mm/year and found mainly in the vicinity of Bovanenkovo settlement (**Figure 3**). We identified spatially clustered areas of high values of surface dynamics (hot spots), and their spatial

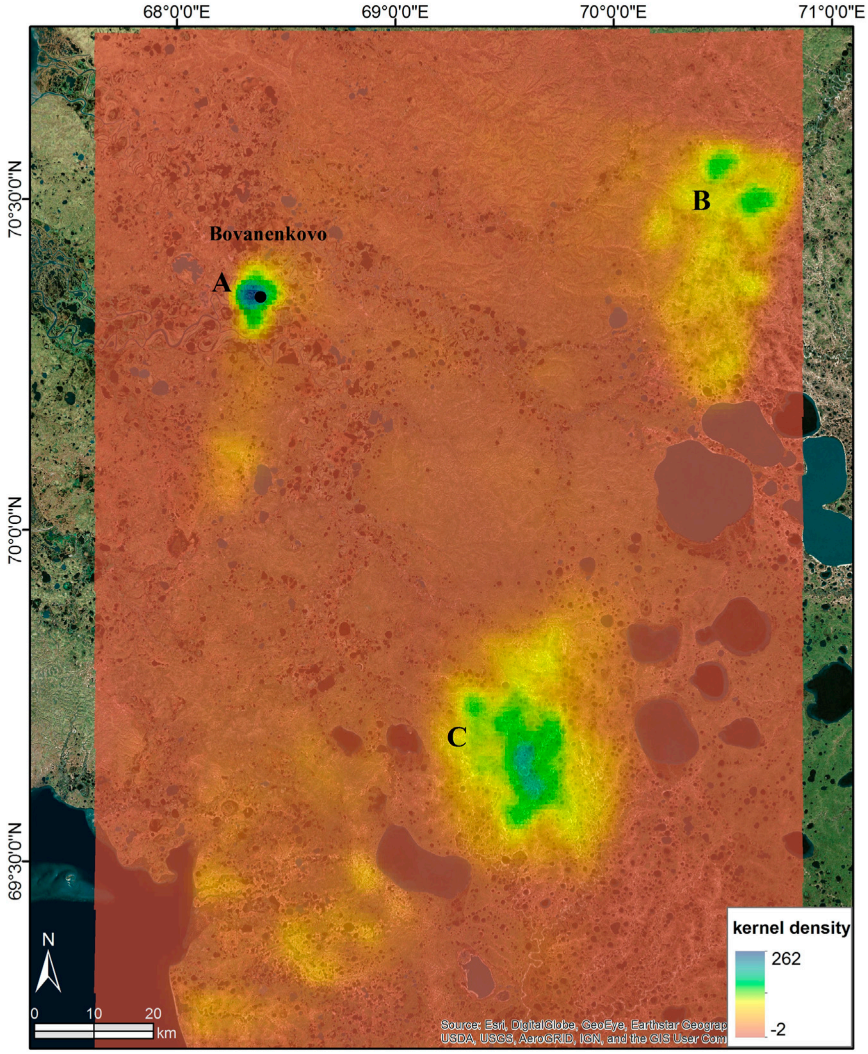

FIGURE 4 | Hotspot cluster kernel-density map showing smoothed spatial location of hotspot clusters in zones **(A,B)** and **(C)**. Analysis highlights areas of spatially correlative regions as high kernel-density values in blue. Hotspot analysis was performed on InSAR LOS velocities **(cf. Figure 3).**

evolution during the monitoring shows net subsidence in the three distinguished zones. They are located at the west and east part of our test area and were highlighted as A, B, and C zones (**Figure 4**). All three hotspots are characterized by their circular and centered geometry at the map scale (**Figure 4**). This geometry raises questions on the processes behind these outstanding features.

Zone A is located within area of Bovanenkovo settlement and gas field. It is subsiding with a mean velocity of approximately 120 mm/year. Zone A exhibits spatial dimensions of approximately 12 km length and 8 km width of enhanced subsidence (**Figures 4**, **5**). Zone B is located to the east with subsiding rates of approximately 60 mm/year (**Figure 3**). It has a spatial extension of approximately 41 km. Zone C is located south of the study area with a spatial dimension of 36 km (**Figures 3**, **4**). Zone C is subsiding with velocities of up to 70 mm/year. Both structures with anomalous subsidence rates are centered at topographic high in a smooth low-relief landscape (**Figure 5**). The subsiding rate of zone A is twice as high as that of B and C zones (**Figure 6**).

The time-series of the detected deformations between June-September 2017 and 2018 based on date-to-date LOS displacements is plotted in **Figure 6**. The deformation signal in all plots is a continuous LOS deformation with a gradual increase in signal from season to season. Plot A shows a seasonal displacement signal that gradually increases up to 160 mm, while plots B and C show differences up to 70 and 80 mm in the temporal evolution between the deformation signals. The signal indicates that the subsidence in these areas is associated with the seasonal thawing process and the evacuation of meltwater and associated sediment erosion.

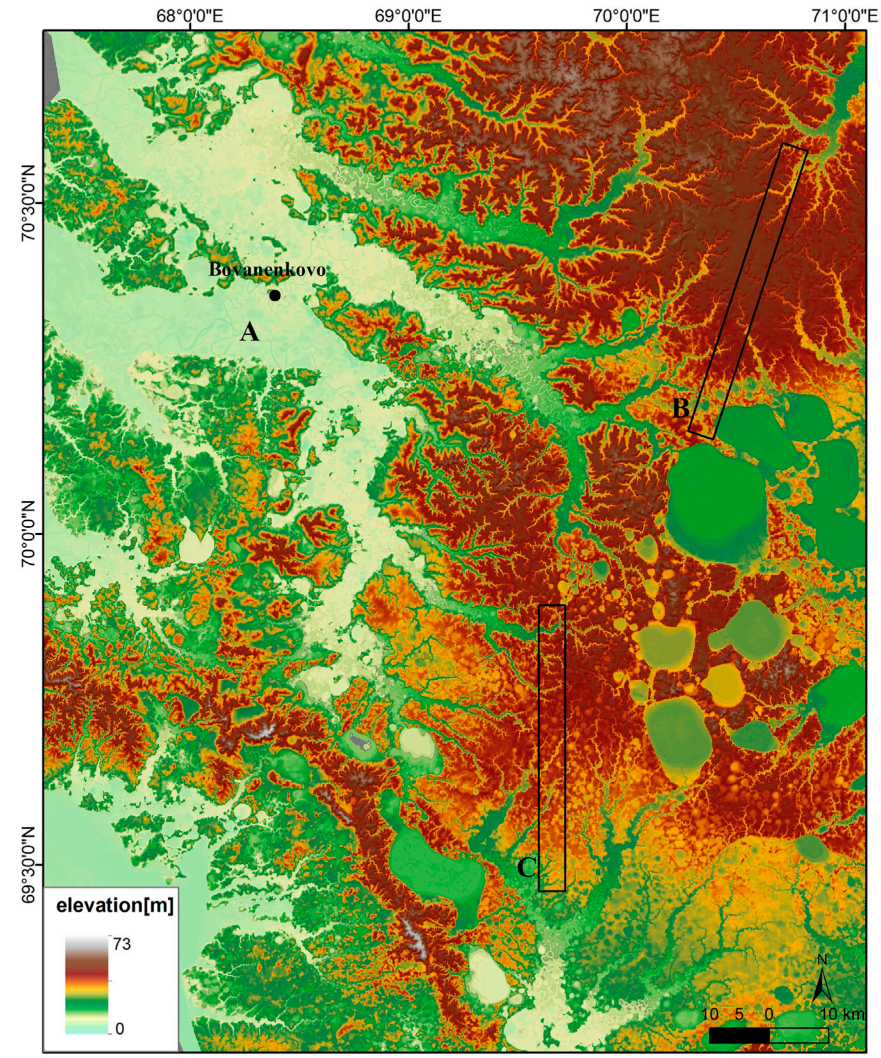

FIGURE 5 | TanDEM-X DEM elevation data 90 m resolution. The map shows the location of the subsiding zones **(A,B)** and **(C)** at different altitudes.

4.2 Surface Topography Dynamics

The geomorphic setting of zone A is low lands at elevations around 3 m a.s.l. Structures B and C represent topographic highs at 25–50 m a.s.l. (**Figures 5**, **7**, **8**). We analyzed two swath profiles across hotspot B and C zones (**Figures 7**, **8**) derived from SRTM and TanDEM-X DEMs. Based on these profiles, we examined the surface topography change along these profiles. Profiles B and C across the defined subsidence zones show mean 2 m surface topography elevation change for time period 2000–2014, indicating net elevation loss of approximately 2 m over 14 years (**Figures 7**, **8**). This suggests that InSAR defined subsiding B and C zones are an area with active surface dynamics with erosion likely related to permafrost degradation (Khomutov and Leibman, 2014).

The surface topography openness analyses from SRTM and TanDEM-X DEMs reveal a highly dynamic landscape. The analyses show change in permafrost surface within 14 years associated with denudation and degradation (**Figures 9**, **10**).

The hotspot zone B shows a clear extension of the drainage network of the rivers and gullies (**Figure 9**). The C zone shows very striking lakes that are extending in surface and number; all larger lakes in NE are increasing in size and many small lakes show migration toward the west (**Figure 10**). Hotspot B shows a number of little lakes only in its center (**Figure 9**).

In zone C all the lakes are becoming connected forming a larger basin, with sedimentation of fluvial and lacustrine deposits, with an interesting evolution of larger sediment influx from river hydrographic systems. Within 14 years the river deltas and valleys are getting deeper and broader, as also revealed from profiles (**Figures 7**, **8**).

Compared to zone B, in C zone old and newly formed lakes provide markers of ongoing surface processes. The rise of lake water level likely occurs as a consequence of enhanced thawing and degradation of permafrost along lake banks and/or runoff related to drainage basin water balance changes. The erosion of thin and instable soil (**Figure 12**), solifluction and development of gullies, ravines, and rivers is progressing

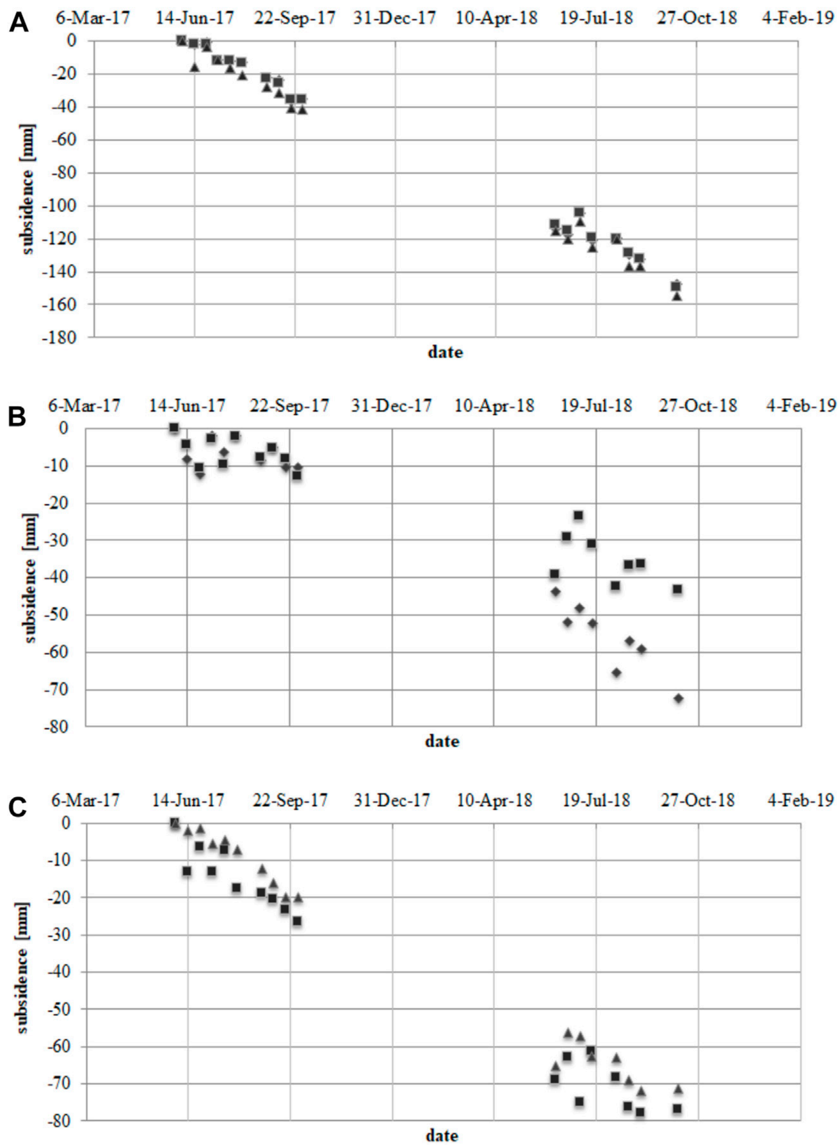

FIGURE 6 | InSAR time-series showing gradual seasonal subsidence for **(A,B)** and **(C)** zones **(Figures 3**, **4**, **6)**. This analysis reveals that zone **(A)** is subsiding with higher rates relative to **(B)** and **(C)** zones.

upward in the topography to where our subsidence hotspots are located.

5 DISCUSSION

5.1 Assessment of Permafrost Seasonal Subsidence

The PS-InSAR technique is a powerful tool to measure displacements of moving ground objects from time-series of SAR images to millimeter precision (Colesanti et al., 2003). It is not so straightforward to exactly identify individual objects acting as persistent scatterers in the SAR images over a remote permafrost region. With this technique, suited for remote permafrost areas with the absence of ground control, it can be assumed that the displacements of the objects reflecting the radar signal address the evolution of the surface.

To identify the interaction with the subsurface of remote permafrost displacement patterns can be challenging and different hypotheses should be tested. In the present study, we verified whether the observed slow subsidence in Yamal peninsula can be explained by specific geomorphic/geologic settings and/or result of anthropogenic impact.

The temporal evolution of the analyzed subsidence rates in zone A around the Bovanenkovo field shows significant higher rates compared to B and C zones (**Figures 3**, **6**). The higher rates of permafrost thaw around zone A are highly likely related to infrastructure and settlements (Teshebaeva et al., 2020). Studies have demonstrated

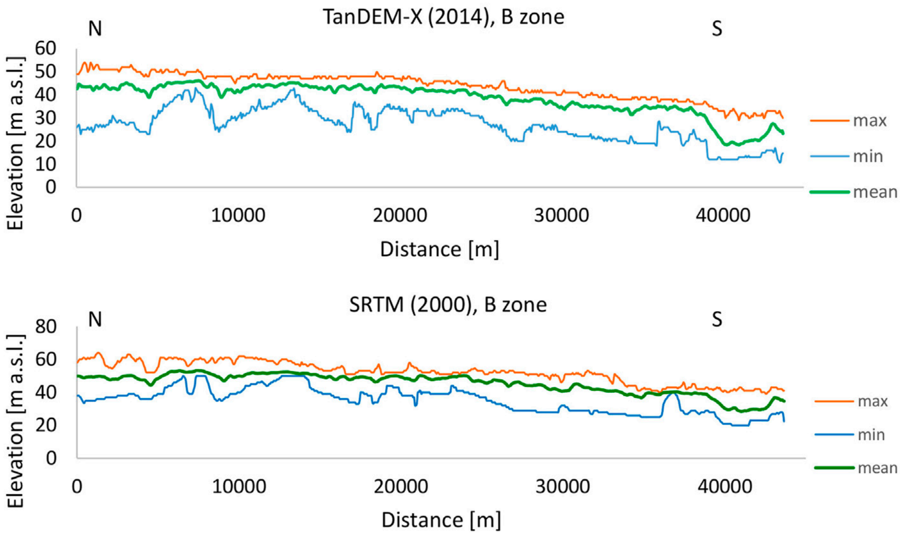

FIGURE 7 | North-South swath profiles across hot spot zone B. Elevation min, max, and mean values are derived from TanDEM-X and SRTM DEM data. The mean elevation values show up to 2 m net mass loss over 14 years.

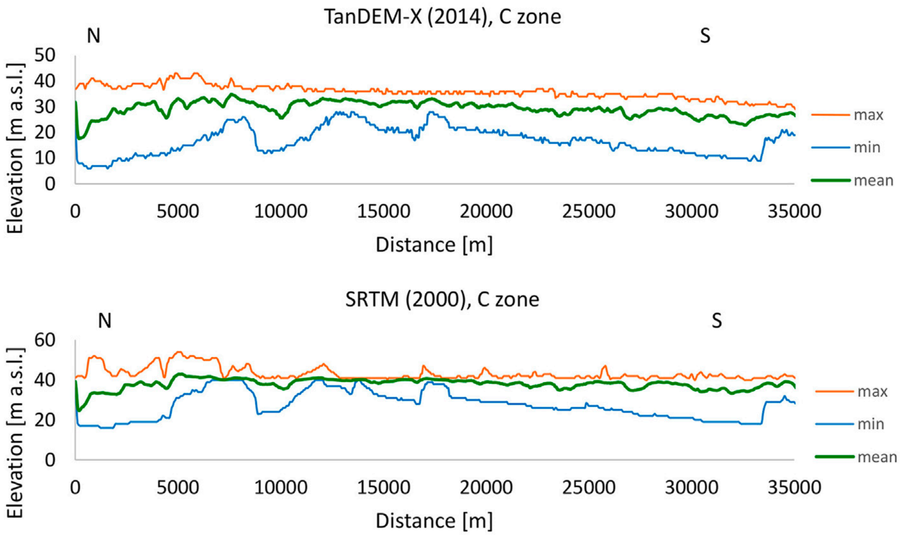

FIGURE 8 | North-South swath profiles across the hot spot zone C. Elevation min, max, and mean values are derived from TanDEM-X and SRTM DEM data. The mean elevation values up to 2 m net mass loss over 14 years.

that expansion of human activity as settlements and gas extraction have major impact on permafrost thaw and subsidence (Raynolds et al., 2014; Liu L. et al., 2015; Hjort et al., 2018). B and C zones show rates between 40 and 60 mm/yr of summer surface changes related to permafrost thaw. These rates are in accordance with the rates found by Bartsch et al. (2019) in central Yamal.

In addition, zone A is underlain by fine-grained marine deposits subsiding faster, probably because the silty-clay sediments are likely to have a higher ice content (**Figure 2**). The ground ice in the area has been detected by geophysical surveys (Olenchenko et al., 2015). The soils are also characterized by a high content of fine-grained clastics and in consequence a predominance of larger amounts of segregation ice in the transition zone at the top of the permafrost. The glacial marine sediments in the region are thin-tabular bedded, gray, and dark gray sand and clay (**Figure 11**) (Chuvilin et al., 2000; Astakhov, 2004; Volkova, 2014). The ice content is the main parameter in the dynamic permafrost environment and can be a challenge to interpret subsiding zones. According to Astakhov (2011) the glacial and inter-glacial sediments are mostly ice-bound unconsolidated alluvial sediments integrating moraines, fluvio-glacial or loess-like deposits (**Figures 2**, **11**, **14**).

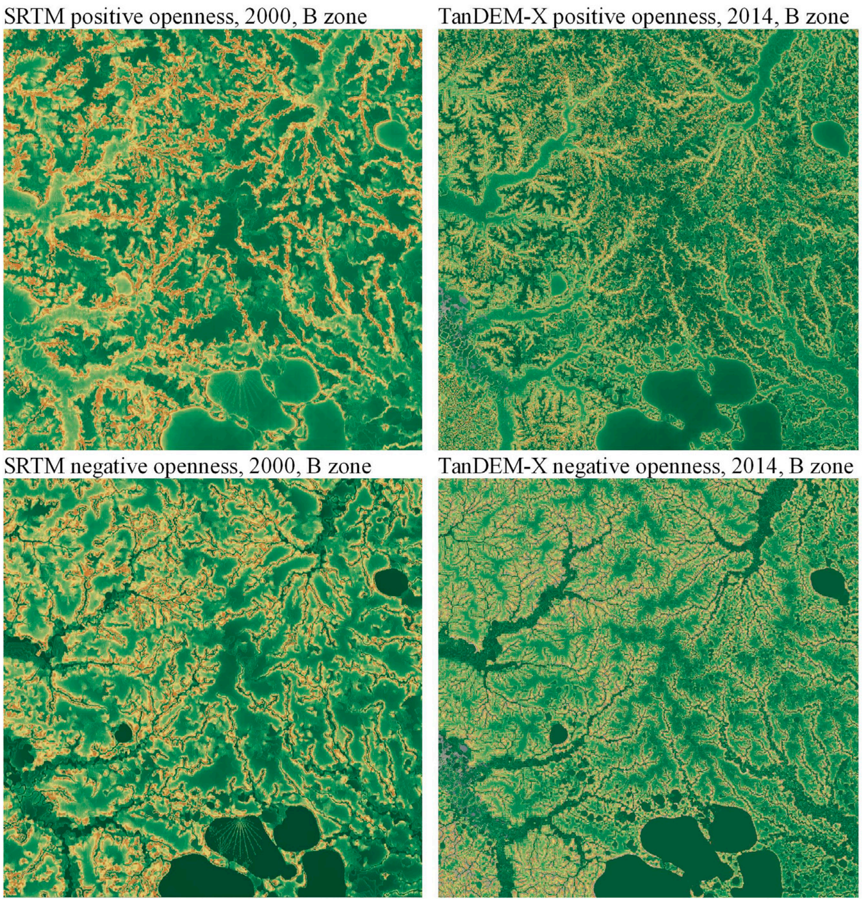

FIGURE 9 | SRTM and TanDEM-X DEMs openness metric showing surface relief changes over 14 years for B zone. Positive openness highlights the drainage network changes. Negative openness highlights the shape of lakes and formation of new lakes.

The subsidence rates in B and C zones are close to half of that of A zone. In B and C zones, predominantly glacial alluvial deposits with more homogenous and coarser grainsize and ice wedges with higher ice content (**Figures 2**, **11**). The alluvial and glacial deposits dominating in our B and C zones are distinguished by their type of ice distribution. Composition and structure of the glacial and glacio-fluvial deposits vary significantly. Thus, unsorted moraine clastics are typical of glacial landscapes consisting of blocs, boulders, and gravel with sandy, silty, and clay-rich materials, with different types of cryogenic ice structures and a high to variable ice content (30%), whereas smaller grainsize size formations of fluvial, lacustrine, or eolian sediments vary less in ice content and permafrost geometries.

5.2 Geomorphology and Geological Settings

To consider the geomorphic/geologic setting of the study areas is essential in our understanding of the analyzed active surface processes. The cryogenic structures of deposits of the internal floodplain of zone A are closely connected with the polygon-ridge aspect of its surface and the topography and hydrographic system of channels, levees, and flood basins (Anisimov et al., 2014; Leibman et al., 2014b; Kizyakov et al., 2017).

The subsidence zones are correlated with lithology of the area (**Figure 2**). Zone A is located in the area of marine deposits, B and C zones in the transition of alluvial above marine deposits. **Figure 11** shows soil profiles: the first two profiles are marine deposits and the third profile is alluvial deposits. The soils profiles show evidence of intense frost interaction (cryoturbation) and gleying processes in the region. The total carbon content in mineral horizons of soils varies from 0.1 to 1.6% and very low nitrogen content (Balykin et al., 2019). Soil profiles also revealed the active layer within study area that varies up to 40 cm in marine deposits and up to 150 cm in alluvial deposits from field work observations during early September 2017 (**Figure 11**).

The B and C subsiding hotspots are located at the apex of smooth cone-type topographic elevations and show a distinct morphologic pattern with regard to the hydrographic system. Zone B is characterized by water discharge in runoff oriented radial in all directions from top and the main subsidence center (**Figure 9**). The C shows a distinct N-S oriented water divide across the hotspot separating surface water runoff. The runoff system is oriented from East to West in the western segment and from North to South in the eastern segment (**Figures 10**, **14**). We relate these features to the specific geologic settings. Area C

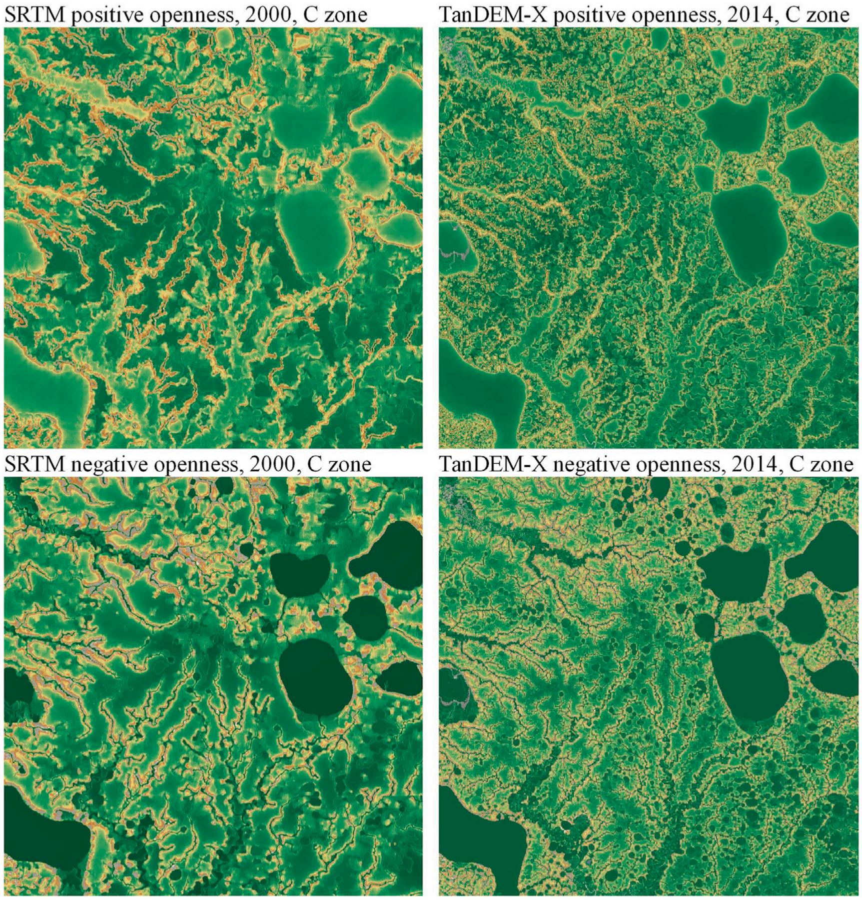

FIGURE 10 | SRTM and TanDEM-X DEMs openness metric showing surface relief changes over 14 years for C zone. Positive openness highlights the drainage network changes. Negative openness highlights the shape of lakes and formation of new lakes.

contains the transition of terrestrial alluvial to underlying glacial marine deposits (**Figure 13**). The alluvial terrestrial deposits are likely related with N-S propagation and retreat of glaciers, whereas the marine sequences are controlled by inherited E-W oriented sedimentary settings.

The geomorphologic analysis of the surface hydrographic system of area C for the period between 2000 and 2014 shows a very distinctive and net progressive evolution with a clear differentiation to higher order drainage channels and a striking increase of eroded and evacuated material (**Figure 12**). This observation infers continuous discharge of water from thawing of the subsurface ice and associated erosion and redeposition of the unconsolidated coarse sediments in adjacent lakes and rivers within the limits of available data (**Figure 12**). Along with slide, creep, collapse, and talus formations there are thaw slumps and solifluction that are typical representatives of cryogenic formations (**Figure 12**) (Leibman et al., 2003; Leibman et al., 2014b). This underlines active continuous denudation by erosion and sediment evacuation associated with meltwater runoff.

We propose two hypotheses on the origin of the denudation and subsidence processes that we analyzed.

Hypothesis I is classically based on heterogeneous ice distribution with higher ice content causing the higher thaw potential in such subsidence zones.

The B and C zones are located within higher topographically elevated areas (**Figure 5**). The common approach is, to assume that such morphological features are associated with varying permafrost extent and ice content. In addition, the dominant lithology in B and C are alluvial and glacial deposits. These deposits are first distinguished by the type of their freezing and ice accumulation in permafrost regions. The deposits have characteristic and distinctive cryogenic structures with development of ice wedges, which are varying in size and geometries. The subsurface consists of terrestrial moraine, the dominant alluvial sedimentary cover, and geomorphological features are characterized by linear geometry (**Figure 13**). Our interpretation is that the higher ice content in moraine type formations is associated with higher thawing rates and in turn erosion tends to be associated with typical moraine relief. Field observations would be necessary to further investigate these aspects of surface processes.

Thereon we bring forward another hypothesis II on the genesis of the presented hotspots of denudation. Here, we

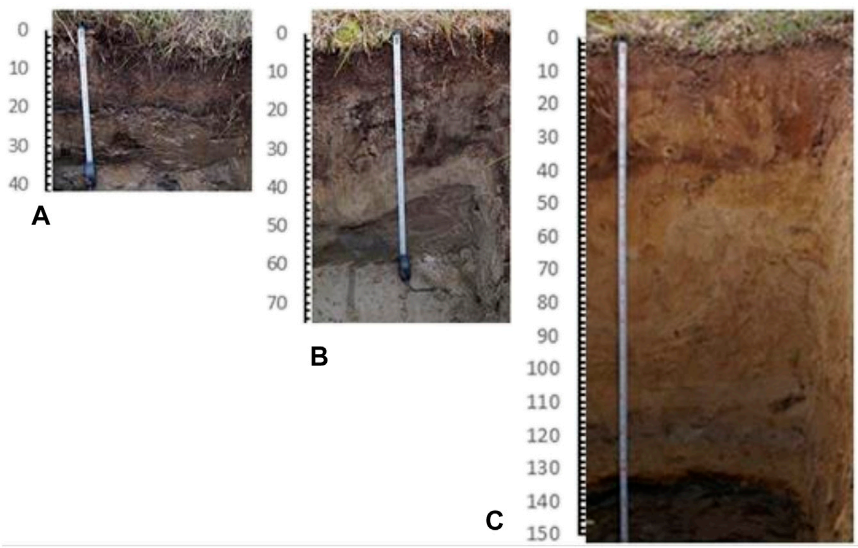

FIGURE 11 | Field campaign August 2017, soil profiles showing the depth of active layer 40–150 cm of the test site. **(A)** Histic Crysol with permafrost occurring at 40 cm consists of horizons: of decomposed organic matter and peat; and mineral gray to bluish soil with light loam texture, sand. **(B)** Histic Crysol with permafrost occurring at 70 cm consists of horizons: soil consist of peat; the mineral heterogeneous in color, gray with dark spots and light loam texture; unconsolidated Earth material with gray sandy loam texture. **(C)** Eutric Cryosols with permafrost occurring at 150 cm depth. The soil consists of horizons: mineral dark brown loam texture with fine-grained sand; yellow brown to dark brown sand; light brown sand (Photos: Balykin Dima).

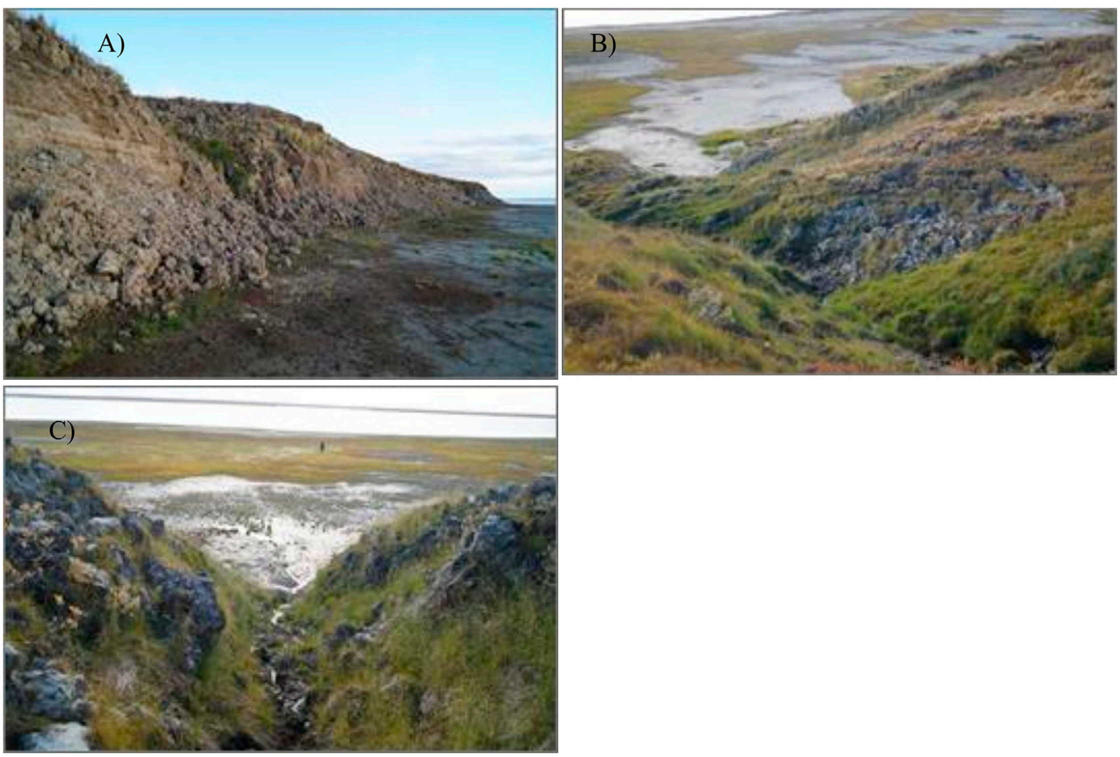

FIGURE 12 | Field campaign August 2018. **(A)** Sedimentation layer showing lake level in the past compared to present lake level. **(B)** Erosion, instability of the slopes, landslides within unconsolidated sediment layers. **(C)** Gullies showing seasonal incision due to permafrost melt in the study area (Photos: Anton Sinitskiy).

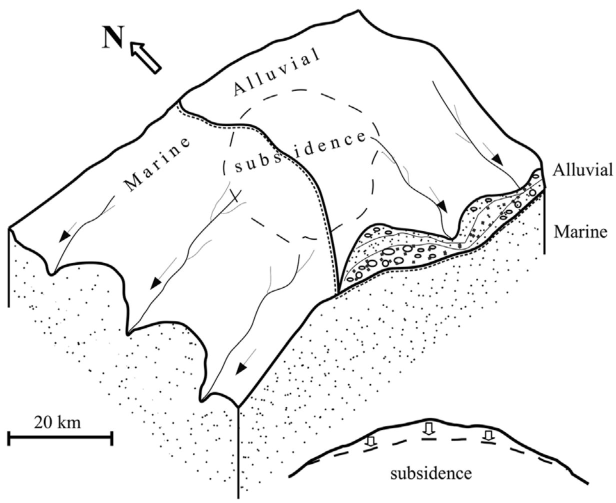

FIGURE 13 | 3D scheme of C zone with different lithology depending on the hydrographic system. The subsiding area at the topographic height. NS runoff in alluvial may be triggered sedimentary structures in marine segment. EW runoff controlled by inherited currents of the nearshore unconsolidated deposits.

discuss permafrost thaw at subsiding B and C zones due to the ascent of natural gas of deep origin stacked below an impermeable permafrost layer (**Figure 14**) (Skorobogatov et al., 1998). The continuously accumulating gas adds heat to the permafrost from below, resulting in a steeper geothermal gradient. This could result in a stronger impact of climate warming on ice-rich permafrost with more thawing and denudation. In this idea our presented B and C subsidence zones would represent hypothetic gas-accumulating structures causing surface thawing and denudation.

Our hypothesis II is supported by detailed geoelectric measurements of the shallow environment of the 2014 discovered outburst crater by Olenchenko et al. (2015). His analysis of water and ice distribution in the immediate subsurface vicinity show significant anomalies of degrading permafrost layer.

In this idea the natural gas seepage from deep origin results in additional subground heat and steep thermal gradients contributing to heating and shallowing of permafrost layer, making the permafrost locally warmer and more vulnerable to the impact of climate change. The Yamal gas fields are also characterized by a significant overpressure of its deep origin gas fields supporting the buoyancy in this pre-outburst scenario (**Figure 14**) (Matusevich et al., 1997; Skorobogatov et al., 1998; Semenov et al., 2019). Possibly, gas outbursts are more likely in subsidence hotspots like B and C zones. This should be corroborated by more detailed research on a deeper subsurface geological structure.

The observed surface changes represent important information on rates and spatial location of hotspots A, B, and C. In addition to spatial distribution of the subsiding B and C zones, a key question for future work in this context is: how high temperatures generated by both climate warming and subsurface heat transport affect this region with potential next gas outbursts? What is the potential to accelerate of subsidence rates or active layer thickening with catastrophic dimensions?

Our analyses and results reveal a potential relationship between the spatial distribution of subsiding zones and subsurface processes. Future studies of high-resolution precise DEM and decadal InSAR time-series may help to elucidate such potential relationships.

6 CONCLUSION

In this study, we underlined the potential of satellite radar imagery to detect and quantify permafrost surface changes. Surface relief dynamic analysis shows about 2 m net loss of surface topography over 14 years (2000–2014) associated with active discharge of water and sediments. In addition, InSAR time-series analysis shows active subsidence for the time period from 2017 to 2018 in three distinct spatial locations. The observed three locations show from 60 up to 120 mm/yr rates of seasonal surface permafrost changes. The

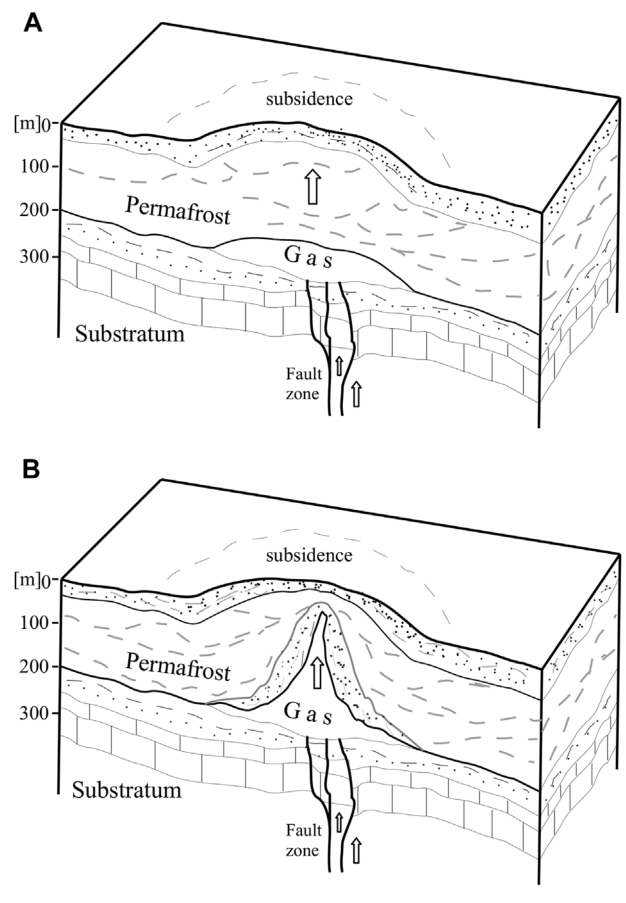

FIGURE 14 | 3D scheme representing pre-stages of possible outburst events due to ancient deep origin natural gas. Scheme **(A)** shows gas accumulation below the impermeable permafrost layer. The overpressure gas causes uplift at surface and triggers localized observed area of subsidence. Scheme **(B)** presents pre-outburst evolved stage, where deep gas causes further thermal and mechanical degradation of permafrost layer.

subsiding InSAR rates located within gas condensate field are double compared to other two locations. Further analyses of the subsidence show that their spatial occurrence is controlled by the lithology and human activity contributes to the continuous seasonal subsidence. The gas condensate field is located within marine sediments and is linked to anthropogenic impact on the permafrost thaw. Two other areas are located within alluvial sediments and are at top of topographic elevated zones.

We propose two hypotheses on possible relationship between the spatial location of subsiding zones and subsurface geologic environment. The classical hypothesis is based on heterogeneous ice distribution, with the higher ice content the higher thaw potential in subsidence zones. The second hypothesis is related to natural gas seepage from a deep origin that adds subsurface heat and steepens the thermal gradients contributing to heating and thinning of permafrost layer. We assume that such zones may be future gas outburst locations.

The study has shown the good potential of the recently released Tandem-X DEM and InSAR technique to improve an understanding of permafrost surface dynamics and long-term monitoring in the remote regions. The combination of InSAR with available geomorphological and geological data and on-site data may be used to develop conceptual and quantitative models to predict surface changes by permafrost thaw and CH_4 emission hotspots on a larger scale.

DATA AVAILABILITY STATEMENT

The original contributions presented in the study are included in the article/supplementary material further inquiries can be directed to the corresponding author.

AUTHOR CONTRIBUTIONS

KT performed the analyses and interpretation, she wrote the paper with contributions from HE, KH, AP, DB, AS, and NK helped with field work and analyses of soil profiles.

FUNDING

This research was funded by Netherlands Organization for Scientific Research NWO grant number ALW-GO/16-13 and Russian State Projects (121031200178-8, 1021032424138-9).

REFERENCES

Anisimov, O. A., Grebenets, V. I., and Streletskiy, D. A. (2014). “Chapter 6.4: Infrastructure Objects Located on Permafrost,“ in *Second Roshydromet Assessment Report on Climate Change and its Consequences in Russian Federation*. Editors S. M. Semenov and V. Kattcov (University of Oklahoma Press), 854–877.

Anisimov, O. A., and Nelson, F. E. (1996). Permafrost Distribution in the Northern Hemisphere under Scenarios of Climatic Change. *Glob. Planet. Change* 14, 59–72. doi:10.1016/0921-8181(96)00002-1

Astakhov, V. (2011). Ice Margins of Northern Russia Revisited. *Develop. Quaternary Sci*. Elsevier 15, 323–336. doi:10.1016/b978-0-444-53447-7.00025-8

Astakhov, V. (2004). Pleistocene Ice Limits in the Russian Northern Lowlands. *Quat. Glaciat. Chronol. Part.* 1, 309–319. doi:10.1016/s1571-0866(04)80081-2

Balykin, D. N., Kovalevskaya, N. M., Puzanov, A. V., Teshebaeva, K., and Huissteden, J. V. (2019). Results of a Reconnaissance Study of Soil and Surface Water of Bovanenkovo Gas-Condensate Field (Yamal Peninsula). *Probl. Reg. Ecol.* 4, 111–116. doi:10.24411/1728-323X-2019-11111

Bartsch, A., Leibman, M., Strozzi, T., Khomutov, A., Widhalm, B., Babkina, E., et al. (2019). Seasonal Progression of Ground Displacement Identified with Satellite Radar Interferometry and the Impact of Unusually Warm Conditions on Permafrost at the Yamal Peninsula in 2016. *Remote Sensing* 11, 1865. doi:10.3390/rs11161865

Chen, F., Lin, H., Zhou, W., Hong, T., and Wang, G. (2013). Surface Deformation Detected by ALOS PALSAR Small Baseline SAR Interferometry over Permafrost Environment of Beiluhe Section, Tibet Plateau, China. *Remote Sensing Environ.* 138, 10–18. doi:10.1016/j.rse.2013.07.006

Chuvilin, E. M., Yakushev, V. S., and Perlova, E. V. (2000). Gas and Possible Gas Hydrates in the Permafrost of Bovanenkovo Gas Field, Yamal Peninsula, West Siberia. *Polarforschung* 68, 215–219.

Colesanti, C., Ferretti, A., Locatelli, R., Novali, F., and Savio, G. (2003). “Permanent Scatterers: Precision Assessment and Multi-Platform Analysis,” in IGARSS 2003. 2003 IEEE International Geoscience and Remote Sensing Symposium. Proceedings (IEEE Cat. No. 03CH37477 IEEE), Toulouse, France, July 21–25, 2003, 1193–1195.

Duguay, C. R., Zhang, T., Leverington, D. W., and Romanovsky, V. E. (2005). *Satellite Remote Sensing of Permafrost and Seasonally Frozen Ground*. Geophys. Monogr. Geophys. UNION 163. Washington, D. C.: AGU American Geophysical Union, 91.

Echtler, H. P., Stiller, M., Steinhoff, F., Krawczyk, C., Suleimanov, A., Spiridonov, V., et al. (1996). Preserved Collisional Crustal Structure of the Southern Urals Revealed by Vibroseis Profiling. *Science* 274, 224–226. doi:10.1126/science.274.5285.224

Ferretti, A., Prati, C., and Rocca, F. (2001). Permanent Scatterers in SAR Interferometry. *IEEE Trans. Geosci. Remote Sensing* 39, 8–20. doi:10.1109/36.898661

Forman, S. L., Ingólfsson, Ó., Gataullin, V., Manley, W., and Lokrantz, H. (2002). Late Quaternary Stratigraphy, Glacial Limits, and Paleoenvironments of the Marresale Area, Western Yamal Peninsula, Russia. *Quat. Res.* 57, 355–370. doi:10.1006/qres.2002.2322

French, H. M. (2017). *The Periglacial Environment*. Hoboken, NJ: John Wiley & Sons.

Getis, A., and Ord, J. K. (2010). The Analysis of Spatial Association by Use of Distance Statistics. *Adv. Spat. Sci.* 24 (3), 127–145. doi:10.1007/978-3-642-01976-0_10

Hjort, J., Karjalainen, O., Aalto, J., Westermann, S., Romanovsky, V. E., Nelson, F. E., et al. (2018). Degrading Permafrost Puts Arctic Infrastructure at Risk by Mid-century. *Nat. Commun.* 9, 5147. doi:10.1038/s41467-018-07557-4

Jarvis, A., Reuter, H. I., Nelson, A., and Guevara, E. (2008). *Hole-Filled SRTM for the Globe Version 4*. Available From the CGIAR-CSI SRTM 90m Database (http://srtm.csi.cgiar.org) 15, 25–54.

Khomutov, A., and Leibman, M. (2014). *Assessment of Landslide Hazards in a Typical Tundra of Central Yamal, Russia. Landslides In Cold Regions in the Context of Climate Change*. Cham: Springer, 271–290. doi:10.1007/978-3-319-00867-7_20

Kizyakov, A., Zimin, M., Sonyushkin, A., Dvornikov, Y., Khomutov, A., and Leibman, M. (2017). Comparison of Gas Emission Crater Geomorphodynamics on Yamal and Gydan Peninsulas (Russia), Based on Repeat Very-High-Resolution Stereopairs. *Remote Sensing* 9, 1023. doi:10.3390/rs9101023

Leibman, M., Khomutov, A., and Kizyakov, A. (2014b). “Cryogenic Landslides in the West-Siberian Plain of Russia: Classification, Mechanisms, and Landforms,” in *In: Shan et al.: Landslides in Cold Regions in the Context of Climate Change* (London: Springer), 143–162.

Leibman, M. O., Kizakov, A. I, Sulerzhitsky, L. D., and Zaretskaia, N. E. (2003). “Dynamics of Landslide Slopes and Their Development on Yamal Peninsula,” in Permafrost. Proceedings of the 8th International Conference on Permafrost, Swets and Zeitlinger, Lisse, 651–656.

Leibman, M. O., Kizyakov, A. I., Plekhanov, A. V., and Streletskaya, I. D. (2014a). New Permafrost Feature - Deep Crater in Central Yamal (West Siberia, Rusia) as a Response to Local Climate Fluctuations. *Geogr. Environ. Sustain.* 7, 68–79. doi:10.24057/2071-9388-2014-7-4-68-79

Liu, J., Kang, S., Gong, T., and Lu, A. (2010). Growth of a High-Elevation Large Inland lake, Associated with Climate Change and Permafrost Degradation in Tibet. *Hydrol. Earth Syst. Sci.* 14, 481–489. doi:10.5194/hess-14-481-2010

Liu, L., Schaefer, K. M., Chen, A. C., Gusmeroli, A., Zebker, H. A., and Zhang, T. (2015a). Remote Sensing Measurements of Thermokarst Subsidence Using InSAR. *J. Geophys. Res. Earth Surf.* 120, 1935–1948. doi:10.1002/2015jf003599

Liu, X., Guo, Y., Hu, H., Sun, C., Zhao, X., and Wei, C. (2015b). Dynamics and Controls of CO 2 and CH 4 Emissions in the Wetland of a Montane Permafrost Region, Northeast China. *Atmos. Environ.* 122, 454–462. doi:10.1016/j.atmosenv.2015.10.007

MacDonald, G. M., Kremenetski, K. V., and Beilman, D. W. (2007). Climate Change and the Northern Russian Treeline Zone. *Phil. Trans. R. Soc. B* 363, 2283–2299. doi:10.1098/rstb.2007.2200

MacDonald, G. M., Velichko, A. A., Kremenetski, C. V., Borisova, O. K., Goleva, A. A., Andreev, A. A., et al. (2000). Holocene Treeline History and Climate Change across Northern Eurasia. *Quat. Res.* 53, 302–311. doi:10.1006/qres.1999.2123

Matusevich, V. M., Myasnikova, G. P., Maximov, E. M., Volkov, A. M., Chistiakova, N. F., Kanalin, V. G., et al. (1997). Abnormal Formation Pressures in the West Siberian Mega-basin, Russia. *Pet. Geosci.* 3 (3), 269–283.

Nauta, A. L., Heijmans, M. M. P. D., Blok, D., Limpens, J., Elberling, B., Gallagher, A., et al. (2015). Permafrost Collapse after Shrub Removal Shifts Tundra Ecosystem to a Methane Source. *Nat. Clim Change* 5, 67–70. doi:10.1038/nclimate2446

Olenchenko, V. V., Sinitsky, A. I., Antonov, E. Y., Eltsov, I. N., Kushnarenko, O. N., Plotnikov, A. E., et al. (2015). Results of Geophysical Surveys of the Area of "Yamal Crater". New Geological Structure. *Kriosf. Zemli* 19, 84–95. doi:10.1016/j.rgg.2015.05.014

Onn, F., and Zebker, H. A. (2006). Correction for Interferometric Synthetic Aperture Radar Atmospheric Phase Artifacts Using Time Series of Zenith Wet Delay Observations from a GPS Network. *J. Geophys. Res. Solid Earth* 111, 1–16. doi:10.1029/2005jb004012

Perissin, D., Rocca, F., Pierdicca, M., Pichelli, E., Cimini, D., Venuti, G., et al. (2011a). "Mitigation of Atmospheric Delay in InSAR: The ESA Metawave Project," in IEEE International Geoscience and Remote Sensing Symposium, Vancouver, BC, July 24–29, 2011 (IEEE), 2558–2561. doi:10.1109/igarss.2011.6049734

Perissin, D. (2015). *SARproZ Software*. Official Product Web Page (https://www.sarproz.com/).

Perissin, D., Wang, Z., and Wang, T. (2011b). The SARPROZ InSAR Tool for Urban Subsidence/manmade Structure Stability Monitoring in China. *Proc. Isrse, Sidney, Aust.* 1015, 271–280.

Puchkov, V. N. (1997). Structure and Geodynamics of the Uralian Orogen. *Geol. Soc. Lond. Spec. Publications* 121, 201–236. doi:10.1144/gsl.sp.1997.121.01.09

Raynolds, M. K., Walker, D. A., Ambrosius, K. J., Brown, J., Everett, K. R., Kanevskiy, M., et al. (2014). Cumulative Geoecological Effects of 62 Years of Infrastructure and Climate Change in Ice-Rich Permafrost Landscapes, Prudhoe Bay Oilfield, Alaska. *Glob. Change Biol.* 20, 1211–1224. doi:10.1111/gcb.12500

Schuur, E. A. G., McGuire, A. D., Schädel, C., Grosse, G., Harden, J. W., Hayes, D. J., et al. (2015). Climate Change and the Permafrost Carbon Feedback. *Nature* 520, 171–179. doi:10.1038/nature14338

Semenov, P., Malyshev, S. A., Nekrasov, D., Leibman, M. O., Kizyakov, A. I., Vanshtein, B. G., et al. (2019). "Gas Geochemistry of the Ground Ice Samples From the Exposure in Central Yamal," in *Solving the Puzzles From Cryosphere*, 31–33.

Short, N., LeBlanc, A.-M., Sladen, W., Oldenborger, G., Mathon-Dufour, V., and Brisco, B. (2014). RADARSAT-2 D-InSAR for Ground Displacement in Permafrost Terrain, Validation from Iqaluit Airport, Baffin Island, Canada. *Remote Sensing Environ.* 141, 40–51. doi:10.1016/j.rse.2013.10.016

Silverman, B. W. (2018). *Density Estimation for Statistics and Data Analysis*. Boca Raton: Routledge.

Teshebaeva, K., Van Huissteden, K. J., Puzanov, A. V., Balykin, D. N., Sinitsky, A. I., and Kovalevskaya, N. (2020). Permafrost Seasonal Surface Changes Revealed from Sentinel-1 InSAR Time-Series, Yamal peninsula. *Proc. IAHS* 382, 183–187. doi:10.5194/piahs-382-183-2020

Skorobogatov, V. A., Vladimir, S. Y., and Evgeny, M. C. (1998). "Sources of Natural Gas Within Permafrost North-West Siberia," in Permafrost Proceedings Seventh International Conference, Collection Nordicana 57.

Ulmishek, G. F. (2003). *Petroleum Geology and Resources of the West Siberian Basin, Russia*. Virginia: US Department of the Interior, US Geological Survey Reston.

Volkova, V. S. (2014). Geologic Stages of the Paleogene and Neogene Evolution of the Arctic Shelf in the Ob' Region (West Siberia). *Russ. Geol. Geophys.* 55, 483–494. doi:10.1016/j.rgg.2014.03.006

Wessel, B., Huber, M., Wohlfart, C., Marschalk, U., Kosmann, D., and Roth, A. (2018). Accuracy Assessment of the Global TanDEM-X Digital Elevation Model with GPS Data. *ISPRS J. Photogrammetry Remote Sensing* 139, 171–182. doi:10.1016/j.isprsjprs.2018.02.017

Yokoyama, R., Shirasawa, M., and Pike, R. J. (2002). Visualizing Topography by Openness: a New Application of Image Processing to Digital Elevation Models. *Photogramm. Eng. Remote Sensing* 68,257–266.

Zhang, T., Barry, R. G., and Armstrong, R. L. (2004). Application of Satellite Remote Sensing Techniques to Frozen Ground Studies. *Polar Geogr.* 28, 163–196. doi:10.1080/789610186

Zonenshain, L. P., Kuzmin, M. I., Natapov, L. M., and Page, B. M. (1990). *Geology of the USSR: A Plate-Tectonic Synthesis*, Geodyn. Ser. Washington, D.C.: American Geophysical Union, 242.

Conflict of Interest: The authors declare that the research was conducted in the absence of any commercial or financial relationships that could be construed as a potential conflict of interest.

Publisher's Note: All claims expressed in this article are solely those of the authors and do not necessarily represent those of their affiliated organizations, or those of the publisher, the editors and the reviewers. Any product that may be evaluated in this article, or claim that may be made by its manufacturer, is not guaranteed or endorsed by the publisher.

frontiers in Earth Science

ORIGINAL RESEARCH
published: 05 January 2022
doi: 10.3389/feart.2021.759085

Origin and Pathways of Dissolved Organic Carbon in a Small Catchment in the Lena River Delta

Lydia Stolpmann[1,2]*, *Gesine Mollenhauer*[3], *Anne Morgenstern*[1], *Jens S. Hammes*[4], *Julia Boike*[1,5], *Pier Paul Overduin*[1] and *Guido Grosse*[1,2]

[1]Permafrost Research Section, Alfred Wegener Institute Helmholtz Centre for Polar and Marine Research, Potsdam, Germany, [2]Institute of Geosciences, University of Potsdam, Potsdam, Germany, [3]Marine Geochemistry Section, Alfred Wegener Institute Helmholtz Centre for Polar and Marine Research, Bremerhaven, Germany, [4]Institute of Geosciences, University of Bonn, Bonn, Germany, [5]Geography Department, Humboldt-University Berlin, Berlin, Germany

OPEN ACCESS

Edited by:
Duane Froese,
University of Alberta, Canada

Reviewed by:
Jonathan Andrew O'Donnell,
National Park Service, United States
Suzanne Tank,
University of Alberta, Canada

****Correspondence:***
Lydia Stolpmann
lydia.stolpmann@awi.de

Specialty section:
This article was submitted to Biogeoscience, a section of the journal Frontiers in Earth Science

Received: *15 August 2021*
Accepted: *06 December 2021*
Published: *05 January 2022*

Citation:
Stolpmann L, Mollenhauer G, Morgenstern A, Hammes JS, Boike J, Overduin PP and Grosse G (2022) Origin and Pathways of Dissolved Organic Carbon in a Small Catchment in the Lena River Delta. Front. Earth Sci. 9:759085. doi: 10.3389/feart.2021.759085

The Arctic is rich in aquatic systems and experiences rapid warming due to climate change. The accelerated warming causes permafrost thaw and the mobilization of organic carbon. When dissolved organic carbon is mobilized, this DOC can be transported to aquatic systems and degraded in the water bodies and further downstream. Here, we analyze the influence of different landscape components on DOC concentrations and export in a small (6.45 km^2) stream catchment in the Lena River Delta. The catchment includes lakes and ponds, with the flow path from Pleistocene yedoma deposits across Holocene non-yedoma deposits to the river outlet. In addition to DOC concentrations, we use radiocarbon dating of DOC as well as stable oxygen and hydrogen isotopes ($\delta^{18}O$ and δD) to assess the origin of DOC. We find significantly higher DOC concentrations in the Pleistocene yedoma area of the catchment compared to the Holocene non-yedoma area with medians of 5 and 4.5 mg L^{-1} ($p < 0.05$), respectively. When yedoma thaw streams with high DOC concentration reach a large yedoma thermokarst lake, we observe an abrupt decrease in DOC concentration, which we attribute to dilution and lake processes such as mineralization. The DOC ages in the large thermokarst lake (between 3,428 and 3,637 ^{14}C y BP) can be attributed to a mixing of mobilized old yedoma and Holocene carbon. Further downstream after the large thermokarst lake, we find progressively younger DOC ages in the stream water to its mouth, paired with decreasing DOC concentrations. This process could result from dilution with leaching water from Holocene deposits and/or emission of ancient yedoma carbon to the atmosphere. Our study shows that thermokarst lakes and ponds may act as DOC filters, predominantly by diluting incoming waters of higher DOC concentrations or by re-mineralizing DOC to CO_2 and CH_4. Nevertheless, our results also confirm that the small catchment still contributes DOC on the order of 1.2 kg km^{-2} per day from a permafrost landscape with ice-rich yedoma deposits to the Lena River.

Keywords: Arctic lakes, ice complex, yedoma, thermokarst lakes, DOC, aquatic carbon cycle, permafrost, radiocarbon dating

INTRODUCTION

The Arctic experienced an increase of averaged near-surface air temperatures by 3.1°C since the 1970s (AMAP, 2021), which is accompanied by warming of Arctic permafrost (Biskaborn et al., 2019). The Arctic is rich in aquatic systems, which interact with the thawing permafrost, and Arctic warming has a strong influence on biogeochemical processes in these aquatic systems (Frey and McClelland, 2009; Wik et al., 2016). In particular, ice-rich permafrost, such as yedoma, is prone to rapid thaw causing ground-ice melt and associated volume loss. As a result, the land surface subsides and landforms like thermo-erosional valleys, thaw slumps, and thermokarst lakes develop. Thermokarst lakes and drained lake basins may regionally occupy three quarters of the yedoma landscape surface (Jones et al., 2011; Grosse et al., 2013). The presence of thermokarst lakes accelerates the thaw of permafrost (Langer et al., 2016), which delivers freshly thawed sediments and organic matter into water bodies (Turetsky et al., 2020). Here, soil carbon (C) can be mobilized and enters aquatic systems as dissolved organic C (DOC) and particulate organic C (POC), whereas DOC, once mobilized, can be degraded microbially or photo-chemically and emitted to the atmosphere as C dioxide (CO_2) and methane (CH_4) (Frey & Smith, 2005; Battin et al., 2008; Tranvik et al., 2009; Vonk et al., 2013a,b). Lakes and especially thermokarst lakes release a significant amount of CO_2 and CH_4 and are biogeochemical hotspots since they act as turnover of organic C (Abnizova et al., 2012; Walter Anthony et al., 2016; Evans et al., 2017; Hughes-Allen et al., 2021). Since these processes may amplify climate change (Schuur et al., 2015), investigations of DOC contributions to C cycling in Arctic freshwater systems on different scales are necessary to understand and predict climate change impacts and permafrost region C cycle feedbacks.

From non-yedoma permafrost landscapes in western Siberia, we know that DOC concentration decreases during the formation of thermokarst lakes from thermokarst depressions to ponds and thermokarst lakes, and increases after lake drainage due to autochthonous DOC production (Manasypov et al., 2014). The DOC concentrations in surface waters in thermokarst dominated permafrost landscapes vary with size (e.g. lake surface area), vegetation density, hydrological connectivity, and water residence time (Evans et al., 2017). Hydrological connectivity and water residence time influence the re-mineralization of DOC by lake processes, such as photo-degradation, microbial activity, and/or flocculation. Therefore, lakes with short water residence time typically have higher DOC concentrations (Manasypov et al., 2015). A recent pan-Arctic synthesis study for DOC in permafrost lakes suggests that there are differences between yedoma and non-yedoma lakes and that lake DOC concentrations can be highly variable, likely based on local environmental factors (Stolpmann et al., 2021a). For Arctic rivers and streams, thawing permafrost may lead to a shift of DOC fluxes. Previous studies found increasing DOC mobilization due to permafrost thaw (Frey and Smith, 2005; Guo et al., 2007; Drake et al., 2015; Mann et al., 2015; Spencer et al., 2015), and Littlefair et al. (2017) highlight the high variation of DOC mobilization in permafrost thaw-affected landscapes on a regional scale. (Kokelj et al., 2005). found that thermokarst, such as thaw slumping, regionally results in DOC mobilization decrease. Contrastingly, Spencer et al. (2015) found increasing DOC mobilization due to thermokarst processes, which suggests that the amount of mobilized DOC depends on the composition of the eroding material in different permafrost landscapes. In regions underlain by yedoma deposits, a rapid loss of ancient DOC was observed in connection with DOC age, bioavailability, and metabolism (Mann et al., 2015; Spencer et al., 2015). For the Siberian Kolyma River basin, incubation experiments showed microbial utilization of ancient organic C (OC) resulting in decreasing DOC concentrations and younger $\Delta^{14}C$ signatures downstream (Mann et al., 2015). The latter was confirmed by Rogers et al. (2021), highlighting the export of predominantly modern DOC to the Kolyma River. In contrast, Mann et al. (2015) found that small yedoma thaw streams featured higher DOC concentrations compared to larger main river channels. Kling et al. (2000) investigated the influence of lakes and rivers on a landscape mass balance and found that lake and river processes are critical for surface water chemistry. For delta systems, it was found that river deltas, especially with lake-rich floodplains, affect nutrient fluxes to the Arctic Ocean (Emmerton et al., 2008). Their model showed enhanced DOC in stream water flowing through the Mackenzie Delta. However, the contribution and influence of lakes and ponds, which are interposed in a stream catchment, on the DOC concentration and how the concentration changes due to these different landscape units are unexplored in yedoma permafrost regions.

Since we assume that DOC modification processes such as photo-oxidation are more prominent in standing waters, we hypothesize a measurable influence of lakes and ponds that are part of a runoff network on DOC processing within the stream catchment. Our goal in this study is to assess the influence of interposed lakes and ponds on DOC in a small stream catchment with and without the influence of yedoma deposits before the DOC reaches the main channels of the Lena River Delta. The specific objectives of this paper are to (1) characterize differences in DOC concentrations in different surface waters, (2) determine DOC ages, and (3) analyze changes in DOC concentrations and the DOC contribution along a flow path in a small yedoma influenced catchment. With this, our study provides insights on the origin of DOC in surface waters in yedoma landscapes and how DOC may be transformed on a flow path through different landscape units before reaching the river outlet.

STUDY SITE

Our study site on Kurungnakh Island (72° 23′N; 126° 03′E) is located in the central Lena River Delta in the continuous permafrost and subarctic tundra zone. The Lena Delta is divided into three main geomorphological units (Schwamborn et al., 2002). Our study site is situated partially on the 1st and on the 3rd Lena Delta unit. Whereas both units consist of ice-rich permafrost, they differ in depositional age, soil C stock characteristics, and watershed hydrology (**Figure 1C**). The 1st

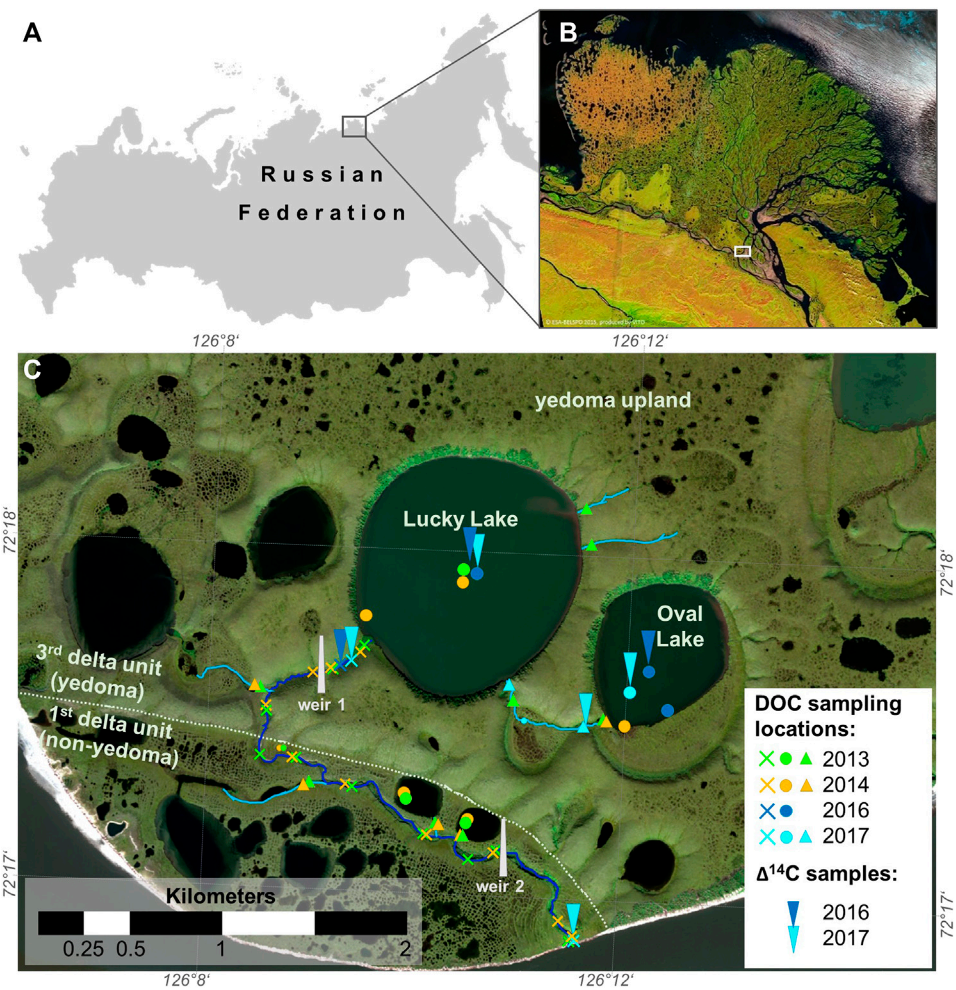

FIGURE 1 | Overview and sampling locations in the study site in **(A)** Northeastern Siberia (map: ESRI) in the **(B)** Lena River Delta (ESA Proba VITO Lena River Delta). The high resolution satellite image shows **(C)** DOC and ^{14}C sampling locations for lakes and ponds (circles), Lucky Lake stream (crosses), and inflows (triangles) in the south of Kurungnakh Island. Lucky Lake stream to the Olenyokskaya Channel is highlighted in dark blue and inflows are highlighted in light blue (WorldView2 image from 2015, copyright by DigitalGlobe).

is the youngest geomorphological unit representing the modern active delta. It was formed in the middle Holocene and is characterized by active floodplains and polygonal tundra with small and shallow lakes and ponds, and ice-wedges. The 3rd delta unit is the oldest unit of the Lena River Delta and was formed during the Late Pleistocene. It consists of remnants of yedoma deposits, which accumulated between 43 and 14 ka BP, overlies fluvial sands and is covered by Holocene deposits (Schwamborn et al., 2002). Kurungnakh Island belongs mainly to the 3rd Lena Delta unit (Grigoriev, 1993) and is characterized by typical yedoma landforms such as yedoma uplands with surface elevations of up to 55 m above river level (Morgenstern et al., 2011) and deeply incised thermo-erosional valleys, thermokarst depressions, and large thermokarst lakes, what formed since about 13 to 12 ka BP (Morgenstern et al., 2013). Kurungnakh Island is located close to Samoylov Island, which hosts the Research Station Samoylov Island that facilitated organization and logistics of our local field work.

Our study site is located in the south of Kurungnakh Island and comprises the catchment of Lucky Lake (unofficial name). On both units, supra-permafrost aquifers are restricted to the shallow active layer (Helbig et al., 2013). On the 3rd delta unit of Kurungnakh Island the active layer depth ranges from 38 to 82 cm (Ulrich et al., 2010). For active layer on the 1st delta unit we refer to data from Samoylov Island, where the mean depth ranges from 41 to 57 cm (Boike et al., 2019). The catchment includes several thermokarst lakes and ponds as well as inflowing and outflowing streams, both on the 3rd (yedoma) and on the 1st (non-yedoma) delta units. The outflowing stream and its associated valley are referred to as Lucky Lake stream and Lucky Lake valley, respectively. This study site offers the opportunity to analyze DOC released on the yedoma and non-yedoma delta units and how DOC is transformed along this flow path and reaches the Olenyokskaya Channel (the Lena River branch into which the Lucky Lake stream drains) (**Figure 1**). Lucky Lake and its neighbor Oval Lake (also unofficial name), which is located in

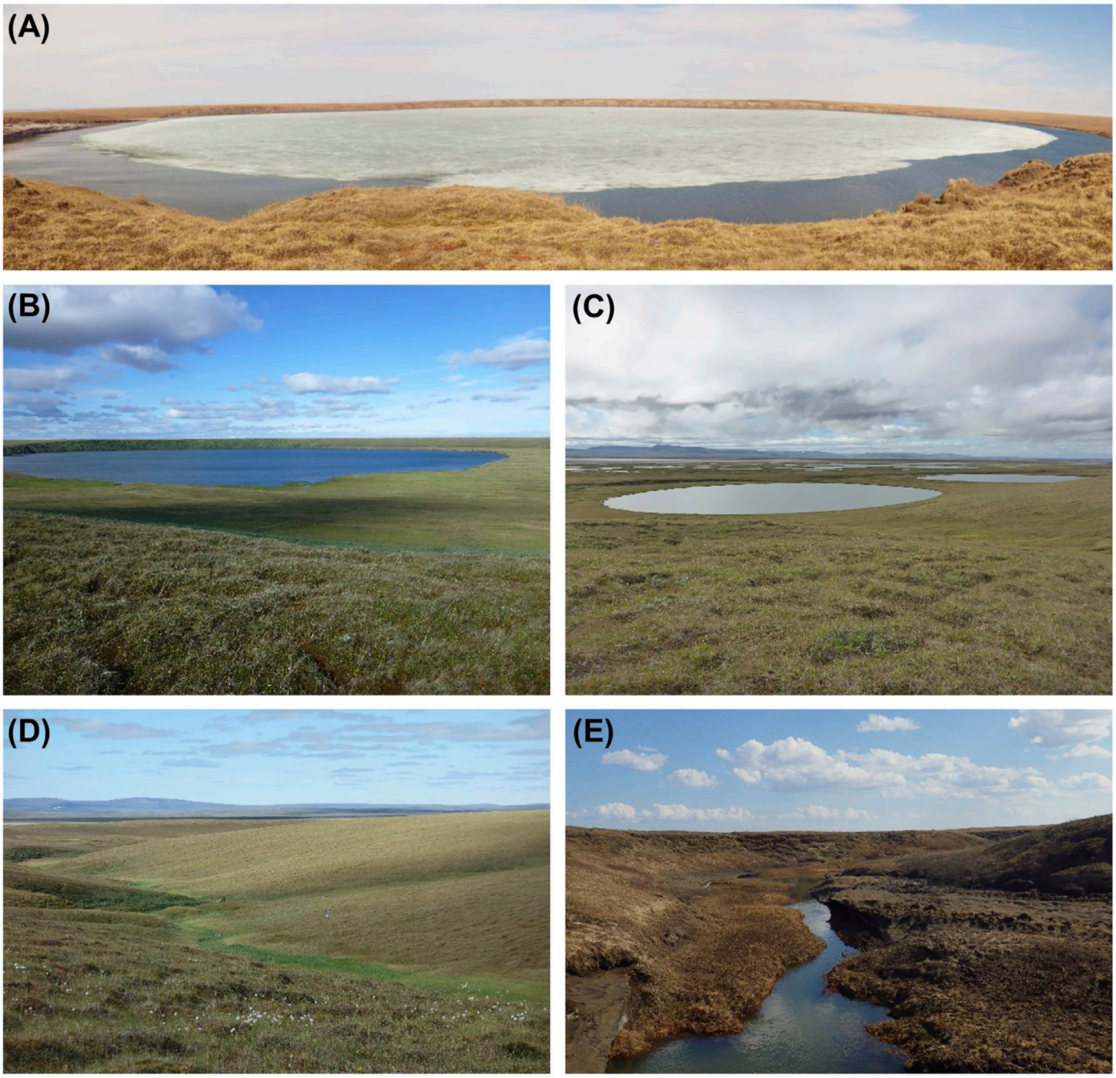

FIGURE 2 | Study site on Kurungnakh Island with **(A)** Lucky Lake (photo by Antje Eulenburg, June 2014), **(B)** Oval Lake in a drained lake basin (photo by Guido Grosse, July 2016), **(C)** two sampled thermokarst lakes on the 1st delta unit (photo by Justine Ramage, July 2016), **(D)** Lucky Lake valley incised into the yedoma upland on the 3rd delta unit (photo by Anne Morgenstern, July 2016), and **(E)** Lucky Lake valley incised in the 1st delta unit (photo by Antje Eulenburg, June 2014).

a partially drained lake basin, are both large thermokarst lakes that are deeply subsided into the local yedoma upland (**Figure 2**). Lucky Lake covers a surface area of 1.22 km^2, with a mean depth of 3.1 m and a maximum depth of 6.5 m, and is bordered by steep slopes with active erosion. Two inflows from the yedoma upland drain into Lucky Lake in the northeast. In the southwest, Lucky Lake drains into Lucky Lake stream via the yedoma upland and the 1st delta unit into the Olenyokskaya Channel. The Oval Lake has a surface area of 0.45 km^2 and a maximum depth of 9 m (Morgenstern et al., 2011).

Dry Arctic-continental climate with a mean annual air temperature of −13.6°C and a mean annual precipitation of about 140 mm characterize the climate in the Lena Delta (Boike et al., 2008). Due to these extreme climate conditions the vegetation period is limited to 3 months from mid-June to mid-September. According to the two different geomorphological delta units in our study site, vegetation differs between 3rd and 1st delta unit. Whereas the 1st delta unit is covered with wet, sedge and moss as well as moist grass dominated tundra vegetation, the 3rd is dominated by dry tussock and moist grass and moss tundra (Schneider et al., 2009).

MATERIALS AND METHODS

For our analysis, we collected 113 surface water samples in the Lucky Lake catchment on the 3rd delta unit with yedoma deposits (61 samples) and the 1st delta unit (52 samples). The samples were collected during summer expeditions in July and August 2013, June to September 2014, July and August 2016 and July 2017

(**Figure 1**). A total of 30 samples were from Lucky Lake and the surrounding lakes on both delta units, 27 samples of inflows, such as from neighboring ponds and yedoma uplands, and 56 samples from the Lucky Lake stream and crossing both delta units. We analyzed concentration and radiocarbon ages of DOC, stable isotopes of oxygen ($\delta^{18}O$) and hydrogen (δD), and obtained discharge measurements to examine the origin of DOC and to understand transformations of DOC on the flow path in our study site. We measured the DOC concentration of all samples, and $\delta^{18}O$ and δD of 99 samples. During the two sampling campaigns in 2016 and 2017, we were able to obtain 9 additional samples large enough to perform radiocarbon measurements of DOC.

Laboratory Analysis

DOC Measurements

For DOC measurements, we filtered the water samples in the field with a 0.7 µm pore size fiberglass (GF/F) syringe filter. Sampling bottles and filters were pre-rinsed with the sample. All samples were preserved with hydrochloric acid and kept cool and dark until analysis, which sometimes occurred months after sampling. In the lab, we used the non-purgeable OC method (NPOC) with the Shimadzu TOC-VCPH high-temperature catalytic combustion (Manual Shimadzu/TOC-V, 2008), recording DOC concentration in milligrams per liter (mg L^{-1}).

Radiocarbon Dating

We carried out Accelerator Mass Spectrometry (AMS) radiocarbon (^{14}C) dating with a Mini Carbon Dating System (MICADAS), which is described by Synal et al. (2007), and followed the methods outlined in Mollenhauer et al. (2021). In short, we dried our samples with a Heidolph LABORATA roto-evaporation apparatus to extract dissolved organic matter (DOM). Dried DOM samples were subsequently transferred into 50 µL liquid tin capsules using Milli-Q water, and radiocarbon analyses were conducted after combustion in an Elementar element analyzer using helium at 950°C. The gas mixture is transmitted to a gas interface system, described by Ruff et al. (2010), and further to the CO_2 accepting ion source of the AMS instruments. We report results as $\Delta^{14}C$ and as conventional radiocarbon ages (^{14}C years before present).

Stable Isotopes of $\delta^{18}O$ and δD

We measured stable isotopes of $\delta^{18}O$ and δD with a Finnigan MAT Delta-S mass spectrometer in the isotopic laboratory of Alfred Wegener Institute in Potsdam, applying the equilibration technique described by Meyer et al. (2000).

Discharge and DOC Flux

We conducted discharge measurements with two weirs with combined radar height sensors installed in the Lucky Lake stream on the 3rd and on the 1st delta unit during field work in 2013, when also DOC samples from the Lucky Lake stream were collected (**Figure 1**). The sill referenced water level in millimeter (mm) was measured in 10 min intervals and was subtracted from the sensor height. The discharge (Q) in liter per seconds (L s^{-1}) was calculated as follows:

$$Q = 0.0000004*(WL)^3 + 0.0011*(WL)^2 + 0.1358*WL - \sqrt{WL} + 3.488 \quad (1)$$

where WL is the sill referenced water level (Eijkelkamp, 2010). We converted the discharge into cubic meters per day (m^3 d^{-1}). The discharge data cover the time period from July 27, 2013 to August 26, 2013. Additionally, we estimated a watershed area of 6.45 km^2 for the entire study site above weir 2. Using the weir data, we calculated the DOC flux (kg km^{-2}) as a product of summed discharge and averaged concentration of DOC of Lucky Lake stream water samples at each weir for this time period, and calculated a DOC flux per day by dividing the DOC flux with 29, which is the number of discharge measurement days.

Statistical Analysis

For our statistical analysis we used RStudio (version 4.0.5). To test the distribution of values of our parameter (DOC concentration, $\delta^{18}O$, δD, and $\Delta^{14}C$) we used the Shapiro-Wilk normality test. Because our data do not follow a normal distribution we used the Spearman rank correlation coefficient (ρ) to measure the relationship between two parameters. We tested differences between mean values of a parameter by delta terrace or water source (lake water, stream water, and inflow water) using the Wilcoxon-Mann-Whitney test.

RESULTS

DOC Concentration

The DOC concentration in our study site ranged from 2.9 to 15.6 mg L^{-1}. The median was 5 mg L^{-1}. We found the highest DOC concentration of the entire catchment of 15.6 mg L^{-1} in a small polygonal pond on Holocene non-yedoma. Generally, we found significantly higher DOC concentrations in surface waters on Pleistocene yedoma (median DOC of 5 mg L^{-1}; exception see above) compared to surface waters on Holocene non-yedoma (median DOC of 4.5 mg L^{-1}) (**Figure 3A**; $\rho = 0.4$; $p < 0.05$). Regarding surface waters on Pleistocene yedoma unit, we found the highest DOC concentrations of 9–12.7 mg L^{-1} in inflows from the yedoma upland in the northeast of Lucky Lake. For inflows, we found significantly higher DOC concentrations and a larger range in DOC concentration on Pleistocene yedoma compared to Holocene non-yedoma, with median DOC concentrations of 4.1 and 3.3 mg L^{-1}, respectively ($p < 0.05$; **Figure 3D**; **Table 1**). For lakes, the median DOC concentration was higher on Pleistocene yedoma with 5.2 mg L^{-1} compared to Holocene non-yedoma with 3.6 mg L^{-1} (**Table 1**). However, this difference was not statistically significant. Additionally, we found a larger range of lake DOC concentration on Holocene non-yedoma (**Figure 3B**). For Lucky Lake stream, we found generally higher DOC concentrations on Pleistocene yedoma compared to Holocene non-yedoma, with median DOC concentrations of 5.2 mg L^{-1} and 4.8 mg L^{-1}, respectively (**Figure 3C**; **Table 1**). We analyzed changes in DOC concentration downstream in the catchment. Therefore, we defined Lucky Lake inflows, including yedoma thaw streams from the yedoma upland and Oval Lake, as the beginning of the flow path, draining into Lucky

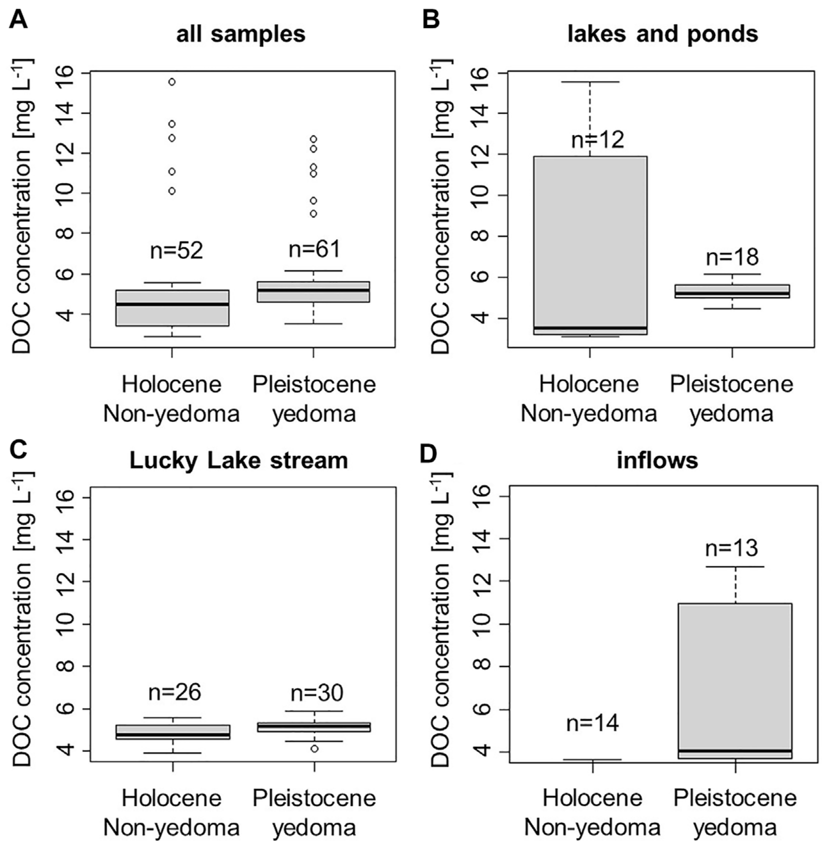

FIGURE 3 | Comparison of DOC concentrations of **(A)** all samples in the Lucky Lake catchment, **(B)** samples from lakes and ponds, **(C)** samples from Lucky Lake stream, and **(D)** from inflows; by Holocene non-yedoma and Pleistocene yedoma. The greyish shaded boxes represent the standard deviation from the mean (solid line).

TABLE 1 | Overview of DOC concentration and isotopic composition for lakes, Lucky Lake stream, and inflows on Pleistocene yedoma and Holocene non-yedoma from the years 2013, 2014, 2016, and 2017.

		Pleistocene yedoma			Holocene non-yedoma		
		Lakes	**Stream**	**Inflows**	**Lakes**	**Stream**	**Inflows**
DOC concentration [mg L^{-1}]	range	4.5–6.2	4.1–5.9	3.5–12.7	3.1–15.6	3.9–5.6	2.9–3.6
	median	5.2	5.2	4.1	3.5	4.8	3.3
$\delta^{18}O$ (‰) *vs*. SMOW	range	−17.8–7.1	−18.8–16.8	−19.6–16.2	−17.9–15.3	−20.7–16.9	−16.4–14.7
	median	−17.2	−17.4	−16.8	−16.1	−17.1	−15.6
δD (‰) *vs*. SMOW	range	−138.3–135.4	−146.4–133	−144.9–125.5	−138.9–123.2	−160.8–132.7	−131.1–119.4
	median	−137.3	−138.1	−131.5	−128.9	−135.3	−125.4

Lake, which then drains into the Lucky Lake stream, and subsequently discharges into the Olenyokskaya Channel (**Figure 4**). Along this flow path, we found decreasing DOC concentrations downstream to the Olenyokskaya Channel.

Radiocarbon Content of DOC

To define the origin of DOC in our study site, we conducted DOC radiocarbon analyses for a total of 9 samples. The $\Delta^{14}C$ values ranged from −373 ‰ (3,637 ^{14}C y BP) to -300 ‰ (2,782 ^{14}C y BP) (**Figure 4**). We found lowest $\Delta^{14}C$ values in the Lucky Lake samples and highest $\Delta^{14}C$ values in Oval Lake samples and in the Lucky Lake stream at the mouth to Olenyokskaya Channel (**Table 2**). We found decreasing $\Delta^{14}C$ values from Oval Lake to Lucky Lake and increasing $\Delta^{14}C$ values from Lucky Lake to the mouth at the Olenyokskaya Channel.

Stable Isotopes of $\delta^{18}O$ and δD

To discuss the origin of the sampled surface waters in our study site we used the stable isotopic composition of the water samples. We found a negative correlation between DOC concentration and water isotopic composition with significantly lower values in $\delta^{18}O$ and δD in samples of higher DOC concentration (ρ = −0.57 and −0.45,

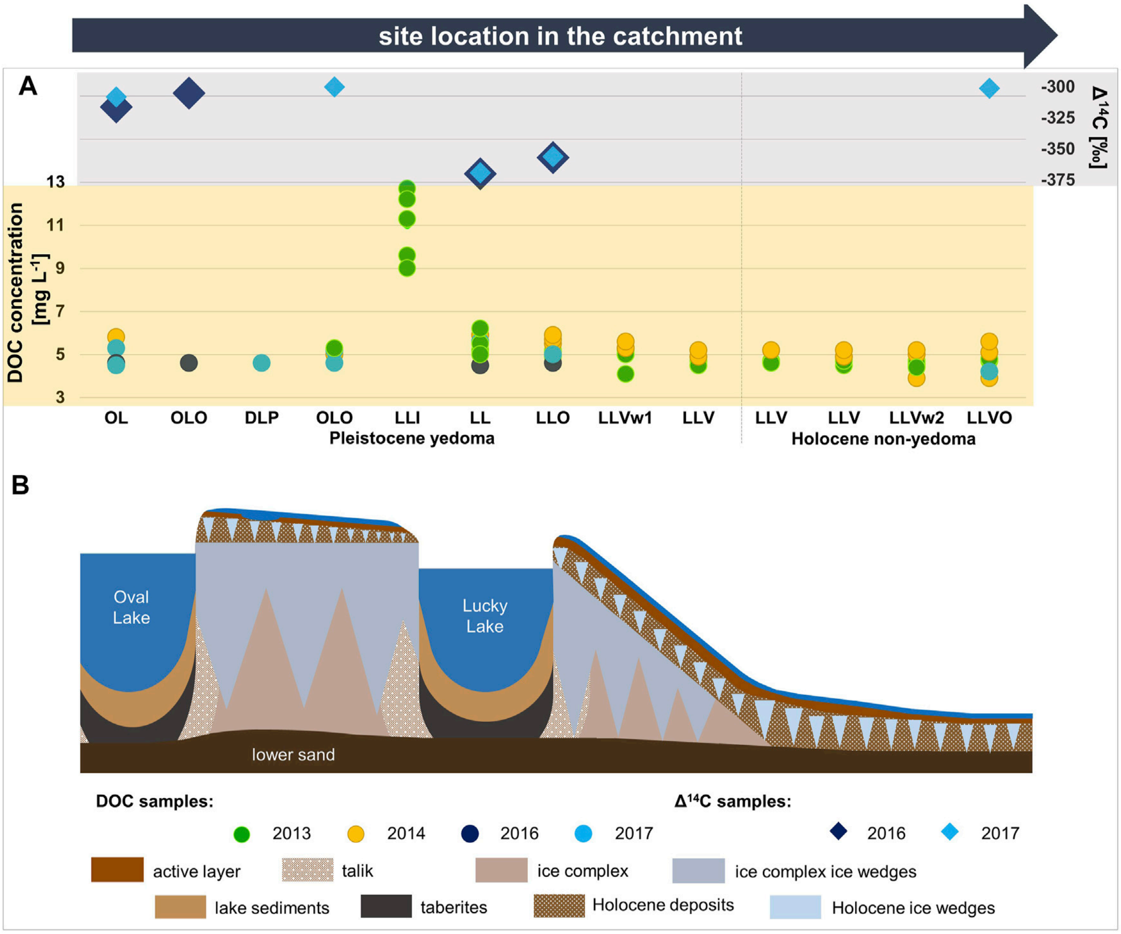

FIGURE 4 | Lucky Lake flow path with **(A)** DOC concentrations and $\Delta^{14}C$ along Pleistocene yedoma and Holocene non-yedoma with inflows from yedoma uplands (LLI), thermokarst lake Oval Lake (OL) and its outflow (OLO) draining a drained lake pond (DLP) and then draining into the Lucky Lake (LL), Lucky Lake outflow (LLO) and Lucky Lake stream (LLV) on Pleistocene yedoma with weir 1 (LLVw1), Lucky Lake stream on Holocene non-yedoma and weir 2 (LLVw2), and mouth of Lucky Lake stream (LLVO) to the Olenyokskaya Channel; and **(B)** schematic 2-dimensional cross section of the study site.

TABLE 2 | Results of the radiocarbon analyses of DOC samples collected in July and August 2016 and July 2017.

Sample location	2016		2017	
	$\Delta^{14}C$ [‰]	Age [^{14}C y BP]	$\Delta^{14}C$ [‰]	Age [^{14}C y BP]
OL - Oval Lake, lake center	−322	3,021	−308	2,871
OLO—Oval Lake, outflow	−305	2,840	−300	2,782
LL–Lucky Lake, lake center	−370	3,597	−371	3,613
LL–Lucky Lake, before outflow	−373	3,637	−356	3,428
LLO–Lucky Lake, outflow	−357	3,442		
LLVO–Lucky Lake stream, mouth to Olenyokskaya Channel			−301	2,783

respectively; $p < 0.05$). The stable isotopic composition ranged from −21.3 to −14.7 ‰ VSMOW in $\delta^{18}O$ and from −162.6 to −119.4 ‰ VSMOW in δD. Most of the samples fell below the Global Meteoric Water Line (GMWL) (**Figure 5**). For lakes and ponds, we found lower values for $\delta^{18}O$ and δD on Pleistocene yedoma compared to Holocene non-yedoma, and increasing values for $\delta^{18}O$ from Lucky Lake via the Lucky Lake stream from Pleistocene yedoma to Holocene non-yedoma. Additionally, two samples with lowest $\delta^{18}O$ and δD were outliers from the Lucky Lake stream on Holocene non-yedoma.

Water isotopic values of one sample lay close (within δD 10 ‰ and $\delta^{18}O$ 1 ‰) to the GMWL. This sample was collected in early September from a small polygonal pond on Holocene non-yedoma, draining into the Lucky Lake stream. Isotopic values

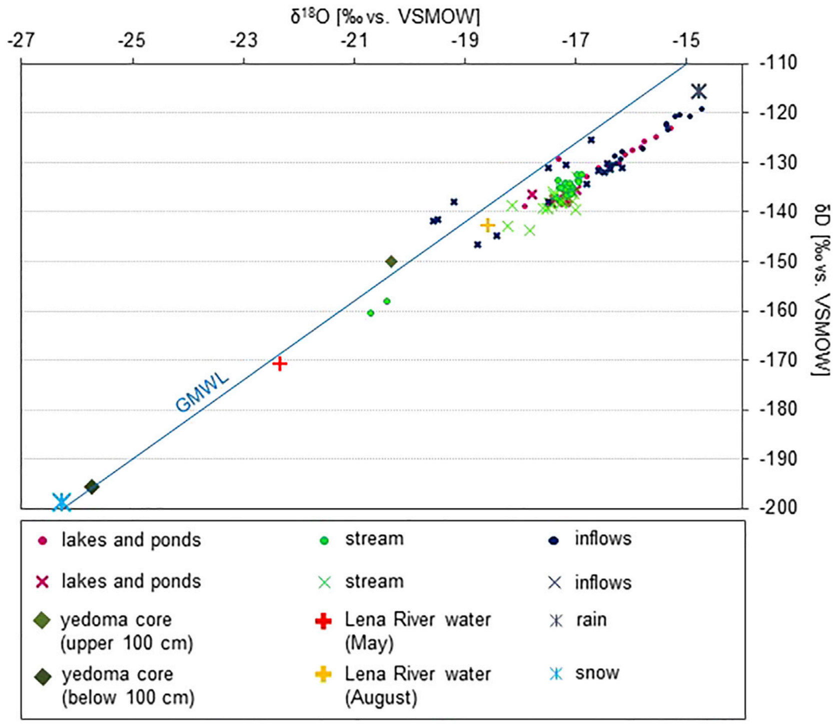

FIGURE 5 | δD and $\delta^{18}O$ values of lakes and ponds, Lucky Lake stream, and inflows in the Lucky Lake catchment by Holocene non-yedoma (dots) and Pleistocene yedoma (crosses). As references we added δD and $\delta^{18}O$ values of Lena River water samples from May and August 2014, rain and snow samples from Bykovsky Peninsula in the Lena River Delta (Meyer et al., 2002), a yedoma core collected north of the Lucky Lake catchment, and the GMWL.

of three samples of the yedoma upland inflows lay above the GMWL. We found the highest $\delta^{18}O$ and δD in samples of inflows and lakes on Holocene non-yedoma.

Discharge and DOC Flux

For the observation period from July 27, 2013 to August 26, 2013 we found decreasing discharge from 1,700 to 200 $m^3\,d^{-1}$ at weir 1, corresponding to decreasing DOC concentrations from 5 to 4.1 $mg\,L^{-1}$ at weir 1. For weir 2, the discharge decreased from 3,000–500 $m^3\,d^{-1}$, corresponding to decreasing DOC concentrations from 4.6 to 4.4 $mg\,L^{-1}$ at weir 2. Based on these values, we estimated a DOC flux of 92.5 kg at weir 1 and 220.5 kg at weir 2 for 29 days in 2013. With an estimated watershed area of 6.45 km^2, we calculated a DOC flux of 34.2 $kg\,km^{-2}$ for 29 days of discharge measurements and 1.2 $kg\,km^{-2}$ per day.

DISCUSSION

Differing DOC Concentrations in Inflows, Lakes, and Outflows on Holocene Non-yedoma and Pleistocene Yedoma

Yedoma deposits are especially prone to degradation processes (Strauss et al., 2013) such as erosion of thermokarst lake shores (Larsen et al., 2017), as for Lucky Lake and Oval Lake, and thermo-erosional gullies, as for yedoma thaw streams in our study area. During these processes organic-rich materials from degrading yedoma deposits are thawed and transported into lakes and streams, resulting in higher median DOC concentration in surface waters on Pleistocene yedoma. Whereas findings from Siberia and Alaska show that yedoma lakes have significantly higher DOC concentrations compared to non-yedoma lakes (Sepulveda-Jauregui et al., 2015), the differences in lake DOC concentration at our study site between Pleistocene yedoma and Holocene non-yedoma are statistically not significant (**Figure 3B**). We found high DOC concentration of 15.6 $mg\,L^{-1}$ in the smallest pond in the catchment on Holocene non-yedoma, which is characterized by low water depth and a high amount of submerged vegetation, whereas Lucky Lake and the neighboring Oval Lake on Pleistocene yedoma are lakes of lowest DOC concentrations and largest lake surface area. This negative correlation of lake DOC concentration and lake surface area was already shown for lakes in western Siberia with discontinuous and sporadic permafrost (Shirokova et al., 2013). As possible causes, they suggest low water depth and the fast release of DOC from vegetation in small ponds. Furthermore, small ponds are known to have a high input of allochthonous DOC due to a higher ratio of lake surface area and lake volume. Here, short water residence time results in reduced lake processes, such as mineralization or photo-degradation, causing higher DOC concentrations (Shirokova et al., 2013; Manasypov et al., 2014, 2015). In larger lakes an increasing consumption of dissolved organic matter by bacterio-plankton and photo-degradation takes place, resulting in decreasing DOC concentrations from small ponds to large thermokarst lakes. As a result of an increase in lake surface area due to thermokarst lake shore erosion, solar irradiance becomes increasingly important for stimulating photo-chemical processes such as photo-oxidation of DOC, causing a decrease in DOC concentrations in such larger lakes (Surdu et al., 2014; Williamson et al., 2014).

Coch et al. (2019) analyzed two catchments in the high and low Canadian Arctic, finding generally higher DOC concentrations in samples of standing waters compared to stream water samples. For our study site, we contrastingly found high DOC concentrations in samples of thaw streams from the yedoma uplands on Pleistocene yedoma, which are two to three times higher than in lakes of our study site. Additionally, DOC concentrations of Lucky Lake stream are partially higher than DOC concentrations of some of the lakes in our study site. This difference between their study and our results can be attributed to the presence of C-rich yedoma deposits on Pleistocene yedoma in our study site, whereas the study sites of Coch et al. (2019) are characterized by marine and glacial sediments underlain by bedrock deposits. A study in the Kolyma River basin also found the highest concentrations of highly labile DOC in small yedoma thaw streams compared to larger rivers and streams in the basin (Mann et al., 2015). Another study reports DOC concentrations from 155 to 196 $mg\,L^{-1}$ in actively eroding streams of a yedoma exposure on the Kolyma River bank (Vonk et al., 2013b), which is more than ten times higher than in thaw streams of our study site. In contrast, inflows on Holocene non-yedoma have DOC concentrations between 2.9 and 3.6 $mg\,L^{-1}$. By mixing with water from the yedoma upland these inflows might cause a dilution effect in the Lucky Lake stream, resulting in decreasing DOC concentrations along the flow path to the Olenyokskaya Channel.

DOC Flux From Pleistocene Yedoma to the Olenyokskaya Channel

When discussing fluxes in permafrost affected landscapes we need to clarify the role of groundwater. Walvoord and Kurylyk (2016) summarized supra-permafrost aquifers including unfrozen taliks below lakes and streams and the active layer on top of the permafrost table, intra-permafrost groundwater, and sub-permafrost aquifers as groundwater zones in discontinuous permafrost. In our study area in the continuous permafrost zone, groundwater exchange predominantly occurs in the supra-permafrost aquifer (Helbig et al., 2013). The amount of DOC released from permafrost to Arctic freshwaters changes in response to climate change (Wickland et al., 2018). These changes differ e.g. by permafrost composition and catchment characteristics, such as permafrost distribution. In regions of warmer discontinuous permafrost with connected intra- and supra-permafrost ground water aquifers, the DOC was shown to decline over the past 40 years (Striegl et al., 2005). In contrast, in regions of cold continuous permafrost with limited ground water flow, DOC mobilization increases (Wickland et al., 2018). Vonk et al. (2019) defined permafrost continuity, ice content, soil composition and morphology, as well as topography, as critical factors for C mobilization and transport in waters in thaw affected permafrost landscapes. In yedoma regions, DOC mobilization and transport is presumably accelerated by permafrost thaw and associated processes (Vonk et al., 2013a; Drake et al., 2015; Mann et al., 2015; Spencer et al., 2015). Moreover, it is important to mention climate change driven influencing processes such as abrupt thaw of permafrost, drainage of thaw lake basins, and active layer deepening (Opfergelt, 2020). Changes and especially increasing of active layer depth reveal subsurface fluxes (Helbig et al., 2013), which may affect the transport and flux of DOC. The stream from Lucky Lake to its mouth at the Lena River branch is dominated by rapid fluvial processes, transporting sediments and dissolved material. For our small lake catchment, we estimate a DOC flux of 1.2 $kg\,km^{-2}$ per day. Lewis et al. (2012) found comparable DOC flux of 350 $kg\,km^{-2}$ per year and a downscaled value of approximately 1 $kg\,km^{-2}$ per day for a small watershed of 8 km^2 in the high Canadian Arctic. For the entire Lena River a DOC flux of 6.79 Tg C per year was calculated (Juhls et al., 2020). This corresponds to a DOC flux of approximately 2,602 $kg\,km^{-2}$ and to 7 $kg\,km^{-2}$ per day, which is almost 6 times higher than DOC flux in our small catchment. With an estimation of approximately 3 $kg\,km^{-2}$ per day the Mackenzie River has a lower summer DOC flux (Coch et al., 2018). This lower flux might be caused by the absence of ice-rich yedoma deposits, the presence of large lakes, which might decrease DOC fluxes, and extensive wetlands in the Mackenzie Delta, as well as the glacial history (Raymond et al., 2007; Burn and Kokelj, 2009). Moreover, in contrast to previously mentioned catchments and watersheds the Mackenzie River catchment covers large areas with only sporadic permafrost distribution and also without permafrost deposits. On the other hand, peatlands, which occur in the Mackenzie Delta, are known to increase DOC mobilization (Frey and Smith, 2005; Olefeldt and Roulet, 2012).

Our estimates do not account for the impacts of rain or storm events, and DOC flux at our study site was calculated for only 29 days of a year. Furthermore, we do not account for seasonal variability in discharge, especially during spring snowmelt, since we are focusing on the summer season. In a recent study of Juhls et al. (2020) it was possible to calculate the seasonal variability of DOC flux for the Lena River. They found that approximately half of the annual DOC flux of 6.79 Tg C is transported in summer and 41% in spring, when spring snowmelt, the biggest hydrological event in this region, occurs. Furthermore, Ahmed et al. (2020) predicted a shift of seasonal discharge towards earlier spring floods resulting in decreasing summer discharge, which may lead to a decrease in summer DOC flux. Our estimations suggest that if we merge all catchments in the Lena River Delta or even in the Lena River watershed that are similar to the small catchment on Kurungnakh Island we present here, comparatively less DOC is released to the Lena River than further upstream in the catchment, and that this DOC is relatively young. Coch et al. (2018) compared their calculations of a 17 days summer DOC flux (mean flux: 82.7 ± 30.7 $kg\,km^{-2}$) of a small watershed on Herschel Island in the Canadian Arctic with different Arctic locations and found higher DOC fluxes in their low Arctic site compared to high Arctic locations. They also highlight the contribution of small watersheds and consider the snowmelt and related discharge to be a major influencing process of DOC flux. Based on expected changes in discharge due to climate change (Bintanja and Andry, 2017), such as shifting seasonal discharge, we assume changing DOC fluxes from small Arctic catchments as well as for major Arctic river catchments, and especially increasing DOC fluxes from yedoma catchments (Tank et al., 2020) like our Lucky Lake stream catchment in the coming decades.

DOC Sources in the Lucky Lake Catchment

Generally, lake DOC can be produced in the lake itself (autochthonous) and in the lake catchment (allochthonous), and previous studies identified several parameters influencing lake DOC concentration, such as lake perimeter and lake elevation (Xenopoulos et al., 2003), lake area (Tranvik et al., 2009; Shirokova et al., 2013; Zabelina et al., 2021), and hydrological connectivity of a lake (Bogard et al., 2019; Johnston et al., 2020). Lucky Lake is a thermokarst lake where lake shore erosion is active and causes transport of old organic material from the surrounding late Pleistocene permafrost deposits into the lake. For streams, erosion of stream banks leads to a higher amount of ^{14}C depleted DOC (Mann et al., 2015). Pleistocene yedoma is rich in fossil OC. But also Holocene deposits are rich in OC (Schirrmeister et al., 2011) and a Holocene surface layer overlies yedoma deposits on the 3rd delta unit. However, yedoma C is more bioavailable (Vonk et al., 2013a; Strauss et al., 2015) and decomposable than C in other thawed mineral soils (Walter Anthony et al., 2014). We found the lowest $\Delta^{14}C$ values in samples of Lucky Lake. Here, the DOC in our water samples is approximately 3,600 years old. $\Delta^{14}C$ values in an aquatic system such as Lucky Lake may result from fresh aquatic production in the water body, from leached material from the active layer, and/or from leached organic matter from eroded yedoma deposits.

Our results show DOC concentrations of 9–12.7 mg L^{-1} in inflows in the north-east of Lucky Lake, where yedoma upland is drained by thaw streams. After thaw stream water reaches Lucky Lake, DOC concentrations decrease to less than half, suggesting that yedoma-derived DOC likely is rapidly utilized or that low Lucky Lake DOC concentration causes a dilution. Regarding C input from the two delta units in our study area, we assume that C in the Lucky Lake also originates from both eroding Holocene materials and from the older yedoma deposits. With a DOC age of approximately 3,600 ^{14}C y BP we found the oldest DOC of the entire dataset in samples from the Lucky Lake with $\Delta^{14}C$ values between -370 and -373 ‰.

DOC in the Flow Path From Yedoma Uplands to the Olenyokskaya Channel

According to **Figure 6**, yedoma thaw streams, draining Pleistocene yedoma uplands, represent the hydrological start of the flow path in our study area. These inflows (**Figure 6A**) show DOC concentrations more than twice as high as the dataset's median. The inflows drain thaw-affected yedoma uplands and mobilize OC, as well as active layer and tundra vegetation. Unfortunately, we did not perform radiocarbon dating for samples of these inflows in our study site but for small yedoma thaw streams in the Kolyma River basin, Mann et al. (2015) found $\Delta^{14}C$ signatures of 883 ± 41 ‰, which corresponds to an age of more than 20,000 years. In contrast, DOC in large rivers and streams of the Kolyma River basin is modern (Neff et al., 2006; Vonk et al., 2013b; Mann et al., 2015; Spencer et al., 2015). The water isotopic composition ($\delta^{18}O$ and δD) of three yedoma inflow samples plot above the GMWL (**Figure 5**) caused by disequilibrium processes like thawing and freezing of the active layer in spring and fall.

After water from the yedoma thaw streams reached Lucky Lake (**Figure 6B**), we observed an abrupt decrease of DOC concentrations. The question of what happens to DOC in the lake arises. In contrast to yedoma thaw streams, which are small trickles with low discharge, Lucky Lake has a greater water volume of low DOC concentration and may dilute the inflowing yedoma thaw stream water of higher DOC concentrations. Moreover, the neighboring thermokarst lake Oval Lake, situated in a drained lake basin, drains into Lucky Lake via a small stream and a drained pond. Whereas DOC concentrations of Oval Lake are similar to those of Lucky Lake, $\Delta^{14}C$ signatures of Oval Lake (between −322 and −300 ‰) are much higher comparing to Lucky Lake $\Delta^{14}C$ signatures (between −373 and −370 ‰). These samples contain the oldest DOC in our entire dataset and might be a result of eroding yedoma lake shore and Holocene deposits. There are a number of lake processes that may lead to decreasing lake DOC concentration. Photo-oxidation or microbial activity lead to mineralization of DOC to CO_2 and CH_4, which can be emitted to the atmosphere (Tranvik et al., 2009; Vonk et al., 2013a, b). Studies of Mann et al. (2015) and Spencer et al. (2015) found that the lability of old yedoma DOC causes rapid mineralization and further lower DOC concentrations when yedoma thaw stream waters reach main stream water. Additionally, the process of flocculation may lead to deposition of DOC in lake sediments and hence to decreasing DOC concentration in the lake water (Tranvik et al., 2009). If we assume a yedoma age from the Pleistocene of approximately 30,000 years, DOC from this material should have a $\Delta^{14}C$ value of -980 ‰. Using isotope mass balance calculation and assuming that one part of this old DOC mixes with two parts of young DOC from surface leaching (Holocene, $\Delta^{14}C$ = -80 ‰) a theoretical lake DOC $\Delta^{14}C$ value of -373 ‰ is estimated. This suggests that dilution, rather than preferential utilization of DOC supplied to the lake by inflows, caused the decrease in DOC concentration from yedoma upland thaw streams to the Lucky Lake. We also assume a smaller amount of DOC released along the lake shore and from the talik than DOC that is mobilized at the surface and transported via inflows.

Directly after the Lucky Lake outflow, where Lucky Lake drained into the Lucky Lake valley and formed the Lucky Lake stream on Pleistocene yedoma (**Figure 6C**), we observed an increase in $\Delta^{14}C$ signature to -356 ‰. Samples from the Lucky Lake stream on Pleistocene yedoma show similar values of $\delta^{18}O$ and δD compared to those of Lucky Lake, and let us assume that the flowing water at this point is mostly influenced by

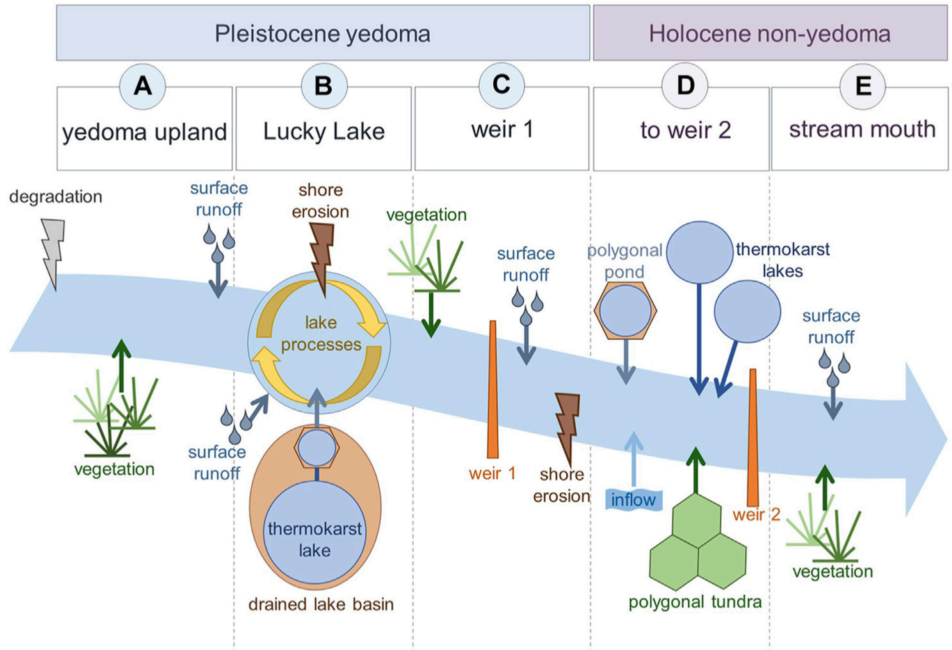

FIGURE 6 | Top view scheme of the flow path with **(A)** yedoma thaw stream as hydrological start of the flow path, draining into **(B)** the Lucky Lake, draining into **(C)** the Lucky Lake stream on Pleistocene yedoma to weir 1, and further on **(D)** Holocene non-yedoma to weir 2, and finally to **(E)** the stream mouth to the Olenyokskaya Channel. Arrows symbolize the input of OC from different sources. Whereas input from surface runoff and vegetation occurs at each sampling point, input from degradation of the yedoma upland, lake shore and stream bank erosion, inflows, thermokarst lakes, polygonal ponds, and polygonal tundra occur selectively.

Lucky Lake water. We found slightly decreasing DOC concentrations downstream to weir 1, where the concentration of DOC is mainly influenced by hydrological connectivity and erosion along river stream banks (Raymond et al., 2007; Mann et al., 2015). The main DOC sources here are Lucky Lake waters, as well as fresh DOC leached from vegetation, which also leads to younger DOC ages.

Where Lucky Lake stream reaches Holocene non-yedoma (**Figure 6D**), the setting changes rapidly to wetter polygonal tundra vegetation and the eroding Lucky Lake valley with its incised stream. Two small thermokarst lakes in the north of Lucky Lake stream and a stream from a neighboring side valley have low DOC concentrations between 3.1 and 3.6 mg L^{-1} and are connected with the Lucky Lake stream. Up to weir 2 we observed slightly decreasing DOC concentrations and similar $\delta^{18}O$ and δD values compared to $\delta^{18}O$ and δD values of thermokarst lakes of Pleistocene yedoma as well as Lucky Lake stream on Pleistocene yedoma.

After weir 2, the DOC concentration further decreases towards the mouth of Lucky Lake stream at the Olenyokskaya Channel (**Figure 6E**). In contrast, we observed increasing $\delta^{18}O$ values attributed to contributions from melted ice frozen during conditions of higher air temperatures during the Holocene. Two Lucky Lake stream samples close to the mouth at the Olenyokskaya Channel show especially low values for $\delta^{18}O$ and δD (**Figure 5**). These samples were collected in mid-June. Here, expedition members observed high flow on Olenyokskaya Channel during spring flood, causing tailback from river channel water into the Lucky Lake stream. At the mouth of Lucky Lake stream to the Olenyokskaya Channel we found an increased $\Delta^{14}C$ signature of -301 ‰, which corresponds to a DOC age of 2,783 ^{14}C y BP. For comparison, major streams and the main stream of the Kolyma River basin have $\Delta^{14}C$ signatures of 22–51 ‰ (Mann et al., 2015), and the averaged $\Delta^{14}C$ of DOC in the Lena River was determined to be 78 ‰ (Raymond et al., 2007). The younger DOC ages combined with decreasing DOC concentrations after the water of Lucky Lake exit the lake and drains into Lucky Lake stream and further to the mouth at the Olenyokskaya Channel could be caused by several processes: 1) Supply to the Lucky Lake stream fresh and young DOC leached from vegetation (e.g. Schuur et al., 2008; Coch et al., 2020). The downstream changes in $\Delta^{14}C$ along the flow path might thus result from mixing of water of different DOC concentrations and radiocarbon levels when the stream drains different geomorphological units. A mixing with younger DOC contributed from water of Holocene non-yedoma and deposits likely causes an overall dilution of older DOC signatures with younger DOC with increasing distance from the old DOC sources. 2) Old DOC might be re-mineralized. Old yedoma DOC has been shown to decompose and outgas faster than younger DOC because of higher bioavailability of the materials leached from yedoma permafrost (Vonk et al., 2013a; Drake et al., 2015). Drake et al. (2015) highlighted an especially rapid DOC turnover to CO_2 due to yedoma permafrost thaw and directly initiated DOC mineralization. Spencer et al. (2015) analyzed water samples of the Kolyma River basin and found the youngest C signature downstream at the river mouth. They suggest that a faster utilization of ancient C and thus outgassing is a possible cause for this observed downstream gradient. Our results show increasing $\Delta^{14}C$ from Pleistocene yedoma to the Holocene non-yedoma, which would be consistent with both scenarios, preferential re-mineralization of old DOC and a dilution by inflows. Because DOC radiocarbon values are higher (younger) at the mouth at the Olenyokskaya Channel, photochemical or microbial processes from Lucky Lake to the Olenyokskaya Channel might be rapidly degrading old DOC. Our observation of progressively younger signature of DOC downstream is consistent with trends also described for major Arctic rivers (Benner et al., 2004; Raymond et al., 2007; Striegl et al., 2007; Aiken et al., 2014). Changes in the isotopic composition with increasing values for $\delta^{18}O$ and δD from Pleistocene yedoma suggest the mixing of different waters.

In order to assess whether preferential re-mineralization of old DOC or mixing of waters with different DOC concentrations and higher $\Delta^{14}C$ values is the more likely process, we can again use isotope mass balance calculations. As radiocarbon measurements were only carried out for samples from a limited number of sites and no streams from Holocene non-yedoma were sampled for this purpose, we need to estimate which radiocarbon signature DOC in those streams would need to carry in order to explain the observed trend through mixing. We used as input parameters the DOC concentrations and the discharge measured at both weirs (minimum and maximum values to determine the possible range), and the $\Delta^{14}C$ values measured for DOC at the Lucky Lake outflow, and at the outflow of the small drainage system to the Olenyokskaya Channel. Based on this mass balance calculation, we estimate the DOC $\Delta^{14}C$ values of inflows between weir 1 and 2 to range between −292 and −287 ‰, respectively. Note that for this estimate, DOC concentrations and radiocarbon ages from different sampling years and months were used. We consider this an acceptable assumption, since we found no major inter-annual changes in DOC concentration and no major ranges in the sampled years. The $\Delta^{14}C$ signature of −292 to −287 ‰ (corresponding to ^{14}C ages of approximately 2,800 ^{14}C years) estimated for Holocene non-yedoma tributaries to the drainage system appears a plausible value considering the geological setting. While not excluded, preferential re-mineralization of old DOC likewise resulting in a progressive increase in $\Delta^{14}C$ and decrease in DOC concentration along the flow path is at least not the only plausible scenario for our study site.

CONCLUSION

In our study we analyze the influence of lakes and ponds, which are interposed in a stream catchment, on DOC concentrations and export; we discuss the origin of DOC in a small lake catchment on Kurungnakh Island in the central Lena River Delta, and how it may transform on its flow path to the river outlet. We show decreasing DOC concentrations from the beginning of the flow path at the yedoma upland thaw streams to the biggest lake in our study site, the Lucky Lake. Additionally, we found decreasing DOC concentration from Lucky Lake via the Lucky Lake stream to the Olenyokskaya Channel. Further, our data indicate that old yedoma and Holocene C might be mobilized into thermokarst lake systems. We found progressively younger DOC signatures in the downstream segments of the catchment. We discussed degrading yedoma and non-yedoma permafrost, active layer, and vegetation to be the major DOC sources in the catchment. Changes and especially the decrease of DOC concentration on the flow path might be ascribed to 1) dilution/mixing with water of lower concentrations and/or younger DOC; 2) lake processes such as photo-oxidation, microbial activity, and flocculation; and 3) a possible outgassing of DOC on the flow path downstream; or a combination of these processes. Finally, the input of DOC from our catchment to the Lena River is dominated by younger DOC compared to Lucky Lake DOC age. In our study, we discuss how OC from yedoma deposits enters aquatic systems as DOC and how DOC is transformed during transport in fluvial networks. Under future climate, degrading yedoma permafrost will cause changes in groundwater and subsurface flow in Arctic watersheds and may increase DOC export. We demonstrate that lakes and ponds may act as DOC filters by diluting incoming waters of higher DOC concentrations and modifying DOC to CO_2 and CH_4. Small thermokarst lake catchments may therefore critically determine C emissions of yedoma landscapes in a rapidly warming Arctic.

DATA AVAILABILITY STATEMENT

The ^{14}C, discharge, DOC and stable water isotopes data presented in this study are deposited in the PANGAEA repository (Hammes and Mollenhauer, 2020; Stolpmann et al., 2021b; Stolpmann et al., 2021c).

AUTHOR CONTRIBUTIONS

LS, GM, and AM developed the study design. JB designed the hydrological set up for lake level and discharge measurements in the field. Field work was conducted by AM in 2013, 2014. LS and JH ran laboratory analyses for DOC concentration and radiocarbon ages. LS performed statistical analyses, interpreted the data with input from JH, GM, AM, JB, PO, and GG and prepared the paper with contributions from all co-authors.

FUNDING

LS was funded by a PhD stipend of the Potsdam Graduate School, the Koordinationsbüro für Chancengleichheit of the University of Potsdam, and the ERC PETA-CARB project (338335). Field work was supported by the AWI base funds for the German-Russian LENA expedition and the BMBF project KoPf (# 03F0764).

ACKNOWLEDGMENTS

We thank all colleagues involved in the organization of field work and in the sample collection during the Russian-German LENA expeditions in 2013, 2014, 2016, and 2017 and the staff of the Research Station Samoylov Island for their great support. In particular, we thank Hanno Meyer, Mikaela Weiner, Niko Bornemann, Sascha Niemann, Vera Meyer and Thorsten Riedel, Hendrik Grotheer, Maria Winterfeld, Antje Eulenburg from the laboratory of AWI Potsdam, and the MICADAS staff at AWI Bremerhaven. Furthermore, we thank the editor Duane Froese, and the two reviewers Jonathan Andrew O'Donnell and Suzanne Tank, who helped to improve the paper.

REFERENCES

Abnizova, A., Siemens, J., Langer, M., and Boike, J. (2012). Small Ponds with Major Impact: The Relevance of Ponds and Lakes in Permafrost Landscapes to Carbon Dioxide Emissions. *Glob. Biogeochem. Cycles* 26, a–n. doi:10.1029/2011GB004237

Ahmed, R., Prowse, T., Dibike, Y., Bonsal, B., and O'Neil, H. (2020). Recent Trends in Freshwater Influx to the Arctic Ocean from Four Major Arctic-Draining Rivers. *Water* 12, 1189. doi:10.3390/w12041189

Aiken, G. R., Spencer, R. G. M., Striegl, R. G., Schuster, P. F., and Raymond, P. A. (2014). Influences of Glacier Melt and Permafrost Thaw on the Age of Dissolved Organic Carbon in the Yukon River basin. *Glob. Biogeochem. Cycles* 28, 525–537. doi:10.1002/2013GB004764

AMAP (2021). *Arctic Climate Change Update 2021: Key Trends and Impacts. Summary for Policy-Makers*. Tromsø, Norway: Arctic Monitoring and Assessment Programme, 16.

Battin, T. J., Kaplan, L. A., Findlay, S., Hopkinson, C. S., Marti, E., Packman, A. I., et al. (2008). Biophysical Controls on Organic Carbon Fluxes in Fluvial Networks. *Nat. Geosci.* 1, 95–100. doi:10.1038/ngeo101

Benner, R., Benitez-Nelson, B., Kaiser, K., and Amon, R. M. W. (2004). Export of Young Terrigenous Dissolved Organic Carbon from Rivers to the Arctic Ocean. *Geophys. Res. Lett.* 31, a–n. doi:10.1029/2003GL019251

Bintanja, R., and Andry, O. (2017). Towards a Rain-Dominated Arctic. *Nat. Clim. Change* 7, 263–267. doi:10.1038/nclimate3240

Biskaborn, B. K., Smith, S. L., Noetzli, J., Matthes, H., Vieira, G., Streletskiy, D. A., et al. (2019). Permafrost Is Warming at a Global Scale. *Nat. Commun.* 10, 264. doi:10.1038/s41467-018-08240-4

Bogard, M. J., Kuhn, C. D., Johnston, S. E., Striegl, R. G., Holtgrieve, G. W., Dornblaser, M. M., et al. (2019). Negligible Cycling of Terrestrial Carbon in many Lakes of the Arid Circumpolar Landscape. *Nat. Geosci.* 12, 180–185. doi:10.1038/s41561-019-0299-5

Boike, J., Nitzbon, J., Anders, K., Grigoriev, M., Bolshiyanov, D., Langer, M., et al. (2019). A 16-year Record (2002-2017) of Permafrost, Active-Layer, and Meteorological Conditions at the Samoylov Island Arctic Permafrost Research Site, Lena River delta, Northern Siberia: an Opportunity to Validate Remote-Sensing Data and Land Surface, Snow, and Permafrost Models. *Earth Syst. Sci. Data* 11, 261–299. doi:10.5194/essd-11-261-2019

Burn, C. R., and Kokelj, S. V. (2009). The Environment and Permafrost of the Mackenzie Delta Area. *Permafr. Periglac. Process* 20 2, 83–105. doi:10.1002/ppp.655

Coch, C., Juhls, B., Lamoureux, S. F., Lafrenière, M. J., Fritz, M., Heim, B., et al. (2019). Comparisons of Dissolved Organic Matter and its Optical Characteristics in Small Low and High Arctic Catchments. *Biogeosciences* 16, 4535–4553. doi:10.5194/bg-16-4535-2019

Coch, C., Lamoureux, S. F., Knoblauch, C., Eischeid, I., Fritz, M., Obu, J., et al. (2018). Summer Rainfall Dissolved Organic Carbon, Solute, and Sediment Fluxes in a Small Arctic Coastal Catchment on Herschel Island (Yukon Territory, Canada). *Arctic Sci.* 4, 750–780. doi:10.1139/as-2018-0010

Coch, C., Ramage, J. L., Lamoureux, S. F., Meyer, H., Knoblauch, C., and Lantuit, H. (2020). Spatial Variability of Dissolved Organic Carbon, Solutes, and Suspended Sediment in Disturbed Low Arctic Coastal Watersheds. *J. Geophys. Res. Biogeosci.* 125 (2). e2019JG005505. doi:10.1029/2019JG005505

Drake, T. W., Wickland, K. P., Spencer, R. G. M., McKnight, D. M., and Striegl, R. G. (2015). Ancient Low-Molecular-Weight Organic Acids in Permafrost Fuel Rapid Carbon Dioxide Production upon Thaw. *PNAS* 112 (45), 13946–13951. doi:10.1073/pnas.1511705112

Eijkelkamp (2010). *Operation Instructions of 13.17.08 RBC Flume*. Giesbeek, Netherlands: Eijkelkamp Agrisearch Equipment.

Emmerton, C. A., Lesack, L. F. W., and Vincent, W. F. (2008). Mackenzie River Nutrient Delivery to the Arctic Ocean and Effects of the Mackenzie Delta during Open Water Conditions. *Glob. Biogeochem. Cycles* 22, a–n. doi:10.1029/2006GB002856

Evans, C. D., Futter, M. N., Moldan, F., Valinia, S., Frogbrook, Z., and Kothawala, D. N. (2017). Variability in Organic Carbon Reactivity across lake Residence Time and Trophic Gradients. *Nat. Geosci.* 10, 832–835. doi:10.1038/NGEO3051

Frey, K. E., and McClelland, J. W. (2009). Impacts of Permafrost Degradation on Arctic River Biogeochemistry. *Hydrol. Process.* 23, 169–182. doi:10.1002/hyp.7196

Frey, K. E., and Smith, L. C. (2005). Amplified Carbon Release from Vast West Siberian Peatlands by 2100. *Geophys. Res. Lett.* 32, L09401. doi:10.1029/2004GL022025

Grigoriev, M. N. (1993). *Cryomorphogenesis of the Lena River Mouth Area, Siberian branch*. Yakutsk: USSR Academy of Sciences, 176. (in Russian).

Grosse, G., Jones, B., and Arp, C. (2013). "8.21 Thermokarst Lakes, Drainage, and Drained Basins," in *"Thermokarst Lakes, Drainage, and Drained Basins" in Treatise on Geomorphology Vol 8, Glacial and Periglacial Geomorphology*. Editors J. F. Shroder, R. Giardino, and J. Harbor (San Diego: Academic Press), 325–353. doi:10.1016/b978-0-12-374739-6.00216-5

Guo, L., Ping, C.-L., and Macdonald, R. W. (2007). Mobilization Pathways of Organic Carbon from Permafrost to Arctic Rivers in a Changing Climate. *Geophys. Res. Lett.* 34, a–n. doi:10.1029/2007GL030689

Hammes, J. S., and Mollenhauer, G. (2020). Radiocarbon content of dissolved and particulate organic matter in small water bodies of the Lena Delta. *PANGAEA* doi:10.1594/PANGAEA.913354

Helbig, M., Boike, J., Langer, M., Schreiber, P., Runkle, B. R. K., and Kutzbach, L. (2013). Spatial and Seasonal Variability of Polygonal Tundra Water Balance: Lena River Delta, Northern Siberia (Russia). *Hydrogeol. J.* 21, 133–147. doi:10.1007/s10040-012-0933-4

Hughes-Allen, L., Bouchard, F., Laurion, I., Séjourné, A., Marlin, C., Hatté, C., et al. (2021). Seasonal Patterns in Greenhouse Gas Emissions from Thermokarst Lakes in Central Yakutia (Eastern Siberia). *Limnol. Oceanogr.* 66, S98–S116. doi:10.1002/lno.11665

Johnston, S. E., Striegl, R. G., Bogard, M. J., Dornblaser, M. M., Butman, D. E., Kellerman, A. M., et al. (2020). Hydrologic Connectivity Determines Dissolved Organic Matter Biogeochemistry in Northern High-latitude Lakes. *Limnol. Oceanogr.* 65, 1764–1780. doi:10.1002/lno.11417

Jones, B. M., Grosse, G., Arp, C. D., Jones, M. C., Walter Anthony, K. M., and Romanovsky, V. E. (2011). Modern Thermokarst lake Dynamics in the Continuous Permafrost Zone, Northern Seward Peninsula, Alaska. *J. Geophys. Res.* 116, G00M03. doi:10.1029/2011JG001666

Juhls, B., Stedmon, C. A., Morgenstern, A., Meyer, H., Hölemann, J., Heim, B., et al. (2020). Identifying Drivers of Seasonality in Lena River Biogeochemistry and Dissolved Organic Matter Fluxes. *Front. Environ. Sci.* 8, 53. doi:10.3389/fenvs.2020.00053

Kling, G. W., Kipphut, G. W., Miller, M. M., and O'Brien, W. J. (2000). Integration of Lakes and Streams in a Landscape Perspective: the Importance of Material Processing on Spatial Patterns and Temporal Coherence. *Freshw. Biol.* 43, 477–497. doi:10.1046/j.1365-2427.2000.00515.x

Langer, M., Westermann, S., Boike, J., Kirillin, G., Grosse, G., Peng, S., et al. (2016). Rapid Degradation of Permafrost underneath Waterbodies in Tundra Landscapes-Toward a Representation of Thermokarst in Land Surface Models. *J. Geophys. Res. Earth Surf.* 121, 2446–2470. doi:10.1002/2016JF003956

Larsen, A. S., O'Donnell, J. A., Schmidt, J. H., Kristenson, H. J., and Swanson, D. K. (2017). Physical and Chemical Characteristics of Lakes across Heterogeneous Landscapes in Arctic and Subarctic Alaska. *J. Geophys. Res. Biogeosci.* 122, 989–1008. doi:10.1016/j.jhydrol.2004.03.02810.1002/2016jg003729

Lewis, T., Lafrenière, M. J., and Lamoureux, S. F. (2012). Hydrochemical and Sedimentary Responses of Paired High Arctic Watersheds to Unusual Climate and Permafrost Disturbance, Cape Bounty, Melville Island, Canada. *Hydrol. Process.* 26, 2003–2018. doi:10.1002/hyp.8335

Littlefair, C. A., Tank, S. E., and Kokelj, S. V. (20172017). Retrogressive Thaw Slumps Temper Dissolved Organic Carbon Delivery to Streams of the Peel Plateau, NWT, Canada. *Biogeosciences* 14, 5487–5505. doi:10.5194/bg-14-5487-2017

Manasypov, R. M., Pokrovsky, O. S., Kirpotin, S. N., and Shirokova, L. S. (2014). Thermokarst lake Waters across the Permafrost Zones of Western Siberia. *The Cryosphere* 8, 1177–1193. doi:10.5194/tc-8-1177-2014

Manasypov, R. M., Vorobyev, S. N., Loiko, S. V., Kritzkov, I. V., Shirokova, L. S., Shevchenko, V. P., et al. (2015). Seasonal Dynamics of Organic Carbon and Metals in Thermokarst Lakes from the Discontinuous Permafrost Zone of Western Siberia. *Biogeosciences* 12, 3009–3028. doi:10.5194/bg-12-3009-2015

Mann, P. J., Eglinton, T. I., McIntyre, C. P., Zimov, N., Davydova, A., Vonk, J. E., et al. (2015). Utilization of Ancient Permafrost Carbon in Headwaters of Arctic Fluvial Networks. *Nat. Commun.* 6, 7856. doi:10.1038/ncomms8856

Manual Shimadzu/Toc-V (2008). *Shimadzu TOC-V Series Total Organic Carbon Analysator. TOC-V CPH/CPN, TOC-Control V. Version 2.00*. Japan: Kyoto.

Meyer, H., Dereviagin, A. Y., Siegert, C., and Hubberten, H.-W. (2002). Paleoclimate Studies on Bykovsky Peninsula, North Siberia – Hydrogen and Oxygen Isotopes in Ground Ice. *Polarforschung* 70, 37–51.

Meyer, H., Schönicke, L., Wand, U., Hubberten, H. W., and Friedrichsen, H. (2000). Isotope Studies of Hydrogen and Oxygen in Ground Ice - Experiences with the Equilibration Technique. *Isotopes Environ. Health Stud.* 36 (2), 133–149. doi:10.1080/10256010008032939

Mollenhauer, G., Grotheer, H., Gentz, T., Bonk, E., and Hefter, J. (2021). Standard Operation Procedures and Performance of the MICADAS Radiocarbon Laboratory at Alfred Wegener Institute (AWI), Germany. *Nucl. Instr. Methods Phys. Res. Section B: Beam Interactions Mater. Atoms* 496, 45–51. doi:10.1016/j.nimb.2021.03.016

Morgenstern, A., Grosse, G., Günther, F., Fedorova, I., and Schirrmeister, L. (2011). Spatial Analyses of Thermokarst Lakes and Basins in Yedoma Landscapes of the Lena Delta. *The Cryosphere* 5, 849–867. doi:10.5194/tc-5-849-2011

Morgenstern, A., Ulrich, M., Günther, F., Roessler, S., Fedorova, I. V., Rudaya, N. A., et al. (2013). Evolution of Thermokarst in East Siberian Ice-Rich Permafrost: A Case Study. *Geomorphology* 201, 363–379. doi:10.1016/j.geomorph.2013.07.011

Neff, J. C., Finlay, J. C., Zimov, S. A., Davydov, S. P., Carrasco, J. J., Schuur, E. A. G., et al. (2006). Seasonal Changes in the Age and Structure of Dissolved Organic Carbon in Siberian Rivers and Streams. *Geophys. Res. Lett.* 33, L23401. doi:10.1029/2006gl028222

Olefeldt, D., and Roulet, N. T. (2012). Effects of Permafrost and Hydrology on the Composition and Transport of Dissolved Organic Carbon in a Subarctic Peatland Complex. *J. Geophys. Res.* 117, G01005. doi:10.1029/2011JG001819

Opfergelt, S. (2020). The Next Generation of Climate Model Should Account for the Evolution of mineral-organic Interactions with Permafrost Thaw. *Environ. Res. Lett.* 15 (9), 091003. doi:10.1088/1748-9326/ab9a6d

Raymond, P. A., McClelland, J. W., Holmes, R. M., Zhulidov, A. V., Mull, K., Peterson, B. J., et al. (2007). Flux and Age of Dissolved Organic Carbon Exported to the Arctic Ocean: A Carbon Isotopic Study of the Five Largest Arctic Rivers. *Glob. Biogeochem. Cycles* 21, a–n. doi:10.1029/2007GB002934

Rogers, J. A., Galy, V., Kellerman, A. M., Chanton, J. P., Zimov, N., and Spencer, R. G. M. (2021). Limited Presence of Permafrost Dissolved Organic Matter in the Kolyma River, Siberia Revealed by Ramped Oxidation. *J. Geophys. Res. Biogeosci.* 126, e2020JG005977. doi:10.1029/2020JG005977

Ruff, M., Szidat, S., Gäggeler, H. W., Suter, M., Synal, H. A., and Wacker, L. (2010). Gaseous Radiocarbon Measurements of Small Aamples. *Nucl. Instrum. Methods Phys. Res. B.* 268 (7–8), 790–794. doi:10.1016/j.nimb.2009.10.032

Schirrmeister, L., Grosse, G., Wetterich, S., Overduin, P. P., Strauss, J., Schuur, E. A. G., et al. (2011). Fossil Organic Matter Characteristics in Permafrost Deposits of the Northeast Siberian Arctic. *J. Geophys. Res.* 116, G00M02. doi:10.1029/2011JG001647

Schneider, J., Grosse, G., and Wagner, D. (2009). Land Cover Classification of Tundra Environments in the Arctic Lena Delta Based on Landsat 7 ETM+ Data and its Application for Upscaling of Methane Emissions. *Remote Sens. Environ.* 113 (2), 380–391. doi:10.1016/j.rse.2008.10.013

Schuur, E. A. G., Bockheim, J., Canadell, J. G., Euskirchen, E., Field, C. B., Goryachkin, S. V., et al. (2008). Vulnerability of Permafrost Carbon to Climate Change: Implications for the Global Carbon Cycle. *BioSci.* 58, 701–714. doi:10.1641/B580807

Schuur, E. A. G., McGuire, A. D., Schädel, C., Grosse, G., Harden, J. W., Hayes, D. J., et al. (2015). Climate Change and the Permafrost Carbon Feedback. *Nature* 520, 171–179. doi:10.1038/nature14338

Schwamborn, G., Rachold, V., and Grigoriev, M. N. (2002). Late Quaternary Sedimentation History of the Lena Delta. *Quat. Int.* 89 (1), 119–134. doi:10.1016/S1040-6182(01)00084-2

Sepulveda-Jauregui, A., Walter Anthony, K. M., Martinez-Cruz, K., Greene, S., and Thalasso, F. (2015). Methane and Carbon Dioxide Emissions from 40 Lakes along a north-south Latitudinal Transect in Alaska. *Biogeosciences* 12, 3197–3223. doi:10.5194/bg-12-3197-2015

Shirokova, L. S., Pokrovsky, O. S., Kirpotin, S. N., Desmukh, C., Pokrovsky, B. G., Audry, S., et al. (2013). Biogeochemistry of Organic Carbon, CO2, CH4, and Trace Elements in Thermokarst Water Bodies in Discontinuous Permafrost Zones of Western Siberia. *Biogeochemistry* 113, 573–593. doi:10.1007/s10533-012-9790-4

Spencer, R. G. M., Mann, P. J., Dittmar, T., Eglinton, T. I., McIntyre, C., Holmes, R. M., et al. (2015). Detecting the Signature of Permafrost Thaw in Arctic Rivers. *Geophys. Res. Lett.* 42, 2830–2835. doi:10.1002/2015GL063498

Stolpmann, L., Coch, C., Morgenstern, A., Boike, J., Fritz, M., Herzschuh, U., et al. (2021a). First Pan-Arctic Assessment of Dissolved Organic Carbon in Lakes of the Permafrost Region. *Biogeosciences* 18, 3917–3936. doi:10.5194/bg-18-3917-2021

Stolpmann, L., Boike, J., Morgenstern, A., Eulenburg, A., Bornemann, N., Niemann, S., et al. (2021b). Discharge Measurements in the Lucky Lake Catchment, Kurungnakh Island, Lena River Delta in 2013. *PANGAEA*. doi:10.1594/PANGAEA.939614

Stolpmann, L., Morgenstern, A., Boike, J., Eulenburg, A., Heim, B., Niemann, S., et al. (2021c). Measurements of Dissolved Organic Carbon and Stable Water Isotopes in the Lucky Lake Catchment, Kurungnakh Island, Lena River Delta (2013–2016). *PANGAEA*. doi:10.1594/PANGAEA.939591

Strauss, J., Schirrmeister, L., Grosse, G., Wetterich, S., Ulrich, M., Herzschuh, U., et al. (2013). The Deep Permafrost Carbon Pool of the Yedoma Region in Siberia and Alaska. *Geophys. Res. Lett.* 40, 6165–6170. doi:10.1002/2013GL058088

Strauss, J., Schirrmeister, L., Mangelsdorf, K., Eichhorn, L., Wetterich, S., and Herzschuh, U. (2015). Organic-matter Quality of Deep Permafrost Carbon - a Study from Arctic Siberia. *Biogeosciences* 12, 2227–2245. doi:10.5194/bg-12-2227-2015

Striegl, R. G., Aiken, G. R., Dornblaser, M. M., Raymond, P. A., and Wickland, K. P. (2005). A Decrease in Discharge-Normalized DOC export by the Yukon River during Summer through Autumn. *Geophys. Res. Lett.* 32, L21413. doi:10.1029/2005GL024413

Striegl, R. G., Dornblaser, M. M., Aiken, G. R., Wickland, K. P., and Raymond, P. A. (2007). Carbon export and Cycling by the Yukon, Tanana, and Porcupine Rivers, Alaska, 2001-2005. *Water Resour. Res.* 43, W02411. doi:10.1029/2006WR005201

Surdu, C. M., Duguay, C. R., Brown, L. C., and Fernández Prieto, D. (2014). Response of Ice Cover on Shallow Lakes of the North Slope of Alaska to Contemporary Climate Conditions (1950-2011): Radar Remote-Sensing and Numerical Modeling Data Analysis. *The Cryosphere* 8, 167–180. doi:10.5194/tc-8-167-2014

Synal, H.-A., Stocker, M., and Suter, M. (2007). MICADAS: a New Compact Radiocarbon AMS System. *Nucl. Instr. Methods Phys. Res. Section B: Beam Interactions Mater. Atoms* 259 (1), 7–13. doi:10.1016/j.nimb.2007.01.138

Tank, S. E., Vonk, J. E., Walvoord, M. A., McClelland, J. W., Laurion, I., and Abbott, B. W. (2020). Landscape Matters: Predicting the Biogeochemical Effects of Permafrost Thaw on Aquatic Networks with a State Factor Approach. *Permafrost and Periglac. Process.* 31 (3), 358–370. doi:10.1002/ppp.2057

Tranvik, L. J., Downing, J. A., Cotner, J. B., Loiselle, S. A., Striegl, R. G., Ballatore, T. J., et al. (2009). Lakes and Reservoirs as Regulators of Carbon Cycling and Climate. *Limnol. Oceanogr.* 54 (6/2), 2298–2314. doi:10.4319/lo.2009.54.6_part_2.2298

Turetsky, M. R., Abbott, B. W., Jones, M. C., Anthony, K. W., Olefeldt, D., Schuur, E. A. G., et al. (2020). Carbon Release through Abrupt Permafrost Thaw. *Nat. Geosci.* 13, 138–143. doi:10.1038/s41561-019-0526-0

Ulrich, M., Morgenstern, A., Günther, F., Reiss, D., Bauch, K. E., Hauber, E., et al. (2010). Thermokarst in Siberian Ice-Rich Permafrost: Comparison to Asymmetric Scalloped Depressions on Mars. *J. Geophys. Res.* 115, E10009. doi:10.1029/2010JE003640

Vonk, J. E., Mann, P. J., Davydov, S., Davydova, A., Spencer, R. G. M., Schade, J., et al. (2013a). High Biolability of Ancient Permafrost Carbon upon Thaw. *Geophys. Res. Lett.* 40, 2689–2693. doi:10.1002/grl.50348

Vonk, J. E., Mann, P. J., Dowdy, K. L., Davydova, A., Davydov, S. P., Zimov, N., et al. (2013b). Dissolved Organic Carbon Loss from Yedoma Permafrost Amplified by Ice Wedge Thaw. *Environ. Res. Lett.* 8, 035023. doi:10.1088/1748-9326/8/3/035023

Vonk, J. E., Tank, S. E., and Walvoord, M. A. (2019). Integrating Hydrology and Biogeochemistry across Frozen Landscapes. *Nat. Commun.* 10, 5377. doi:10.1038/s41467-019-13361-5

Walter Anthony, K. M., Zimov, S. A., Grosse, G., Jones, M. C., Anthony, P. M., Iii, F. S. C., III, et al. (2014). A Shift of Thermokarst Lakes from Carbon Sources to Sinks during the Holocene Epoch. *Nature* 511, 452–456. doi:10.1038/nature13560

Walter Anthony, K., Daanen, R., Anthony, P., Schneider von Deimling, T., Ping, C.-L., Chanton, J. P., et al. (2016). Methane Emissions Proportional to Permafrost Carbon Thawed in Arctic Lakes since the 1950s. *Nat. Geosci.* 9, 679–682. doi:10.1038/ngeo2795

Walvoord, M. A., and Kurylyk, B. L. (2016). Hydrologic Impacts of Thawing Permafrost-A Review. *Vadose Zone J.* 15 (6), vzj2016. doi:10.2136/vzj2016.01.0010

Wickland, K. P., Waldrop, M. P., Aiken, G. R., Koch, J. C., Jorgenson, M. T., and Striegl, R. G. (2018). Dissolved Organic Carbon and Nitrogen Release from Boreal Holocene Permafrost and Seasonally Frozen Soils of Alaska. *Environ. Res. Lett.* 13 (6), 065011. doi:10.1088/1748-9326/aac4ad

Wik, M., Thornton, B. F., Bastviken, D., Uhlbäck, J., and Crill, P. M. (2016). Biased Sampling of Methane Release from Northern Lakes: A Problem for Extrapolation. *Geophys. Res. Lett.* 43 (3), 1256–1262. doi:10.1002/2015GL066501

Williamson, C. E., Zepp, R. G., Lucas, R. M., Madronich, S., Austin, A. T., Ballaré, C. L., et al. (2014). Solar Ultraviolet Radiation in a Changing Climate. *Nat. Clim. Change* 4, 434–441. doi:10.1038/NCLIMATE2225

Xenopoulos, M. A., Lodge, D. M., Frentress, J., Kreps, T. A., Bridgham, S. D., Grossman, E., et al. (2003). Regional Comparisons of Watershed Determinants of Dissolved Organic Carbon in Temperate Lakes from the Upper Great Lakes Region and Selected Regions Globally. *Limnol. Oceanogr.* 48, 2321–2334. doi:10.4319/lo.2003.48.6.2321

Zabelina, S. A., Shirokova, L. S., Klimov, S. I., Chupakov, A. V., Lim, A. G., Polishchuk, Y. M., et al. (2021). Carbon Emission from Thermokarst Lakes in NE European Tundra. *Limnol. Oceanogr.* 66, S216–S230. doi:10.1002/lno.11560

Conflict of Interest: The authors declare that the research was conducted in the absence of any commercial or financial relationships that could be construed as a potential conflict of interest.

The reviewer JO declared a past co-authorship with one of the authors GG to the handling editor.

Publisher's Note: All claims expressed in this article are solely those of the authors and do not necessarily represent those of their affiliated organizations, or those of the publisher, the editors and the reviewers. Any product that may be evaluated in this article, or claim that may be made by its manufacturer, is not guaranteed or endorsed by the publisher.

frontiers in Earth Science

REVIEW
published: 12 January 2022
doi: 10.3389/feart.2021.757891

Yedoma Permafrost Genesis: Over 150 Years of Mystery and Controversy

Yuri Shur[1], Daniel Fortier[2], M. Torre Jorgenson[1,3], Mikhail Kanevskiy[1], Lutz Schirrmeister[4], Jens Strauss[4], Alexander Vasiliev[5] and Melissa Ward Jones[1]*

[1]Institute of Northern Engineering, University of Alaska Fairbanks, Fairbanks, AK, United States, [2]Geography Department, University of Montreal, Montreal, QC, Canada, [3]Alaska Ecoscience, Fairbanks, AK, United States, [4]Permafrost Research Section, Alfred Wegener Institute Helmholtz Centre for Polar and Marine Research, Potsdam, Germany, [5]Earth Cryosphere Institute of Tyumen Scientific Center SB RAS, Tyumen, Russia

Since the discovery of frozen megafauna carcasses in Northern Siberia and Alaska in the early 1800s, the Yedoma phenomenon has attracted many Arctic explorers and scientists. Exposed along coastal and riverbank bluffs, Yedoma often appears as large masses of ice with some inclusions of sediment. The ground ice particularly mystified geologists and geographers, and they considered sediment within Yedoma exposures to be a secondary and unimportant component. Numerous scientists around the world tried to explain the origin of Yedoma for decades, even though some of them had never seen Yedoma in the field. The origin of massive ice in Yedoma has been attributed to buried surface ice (glaciers, snow, lake ice, and icings), intrusive ice (open system pingo), and finally to ice wedges. Proponents of the last hypothesis found it difficult to explain a vertical extent of ice wedges, which in some cases exceeds 40 m. It took over 150 years of intense debates to understand the process of ice-wedge formation occurring simultaneously (syngenetically) with soil deposition and permafrost aggregation. This understanding was based on observations of the contemporary formation of syngenetic permafrost with ice wedges on the floodplains of Arctic rivers. It initially was concluded that Yedoma was a floodplain deposit, and it took several decades of debates to understand that Yedoma is of polygenetic origin. In this paper, we discuss the history of Yedoma studies from the early 19th century until the 1980s—the period when the main hypotheses of Yedoma origin were debated and developed.

Keywords: Yedoma, syngenetic permafrost, late Pleistocene, buried ice, ice wedges, mammoth, Northern Yakutia, Alaska

OPEN ACCESS

Edited by:
Duane Froese,
University of Alberta, Canada

Reviewed by:
Mary E. Edwards,
University of Southampton, United Kingdom
Frederick Nelson,
Michigan State University, United States
Vladimir Tumskoy,
Melnikov Permafrost Institute SB RAS, Russia

****Correspondence:***
Yuri Shur
yshur@alaska.edu

Specialty section:
This article was submitted to Cryospheric Sciences, a section of the journal Frontiers in Earth Science

Received: *13 August 2021*
Accepted: *26 November 2021*
Published: *12 January 2022*

Citation:
Shur Y, Fortier D, Jorgenson MT, Kanevskiy M, Schirrmeister L, Strauss J, Vasiliev A and Ward Jones M (2022) Yedoma Permafrost Genesis: Over 150 Years of Mystery and Controversy. Front. Earth Sci. 9:757891. doi: 10.3389/feart.2021.757891

INTRODUCTION

The term "Yedoma" (Russian "Едома") was historically a folk name for flat hills with gentle slopes or remnants of terraces several dozen meters high (Murzaev, 1984). For scientific descriptions, this term was probably used for the first time by Figurin (1823) and was later introduced into the scientific literature by Birkengof (1933). Originally it was used as a geomorphic term to describe the remnants of terrain with ice-rich permafrost that formed in east Siberia during the late Pleistocene. According to Sher (1997), at least three different meanings of the term "Yedoma" now exist in the Russian literature: 1) a "Yedoma surface" in the geomorphic sense, 2) a "Yedoma Suite" in the stratigraphic sense, or 3) a cryolithological feature implying a special kind of frozen

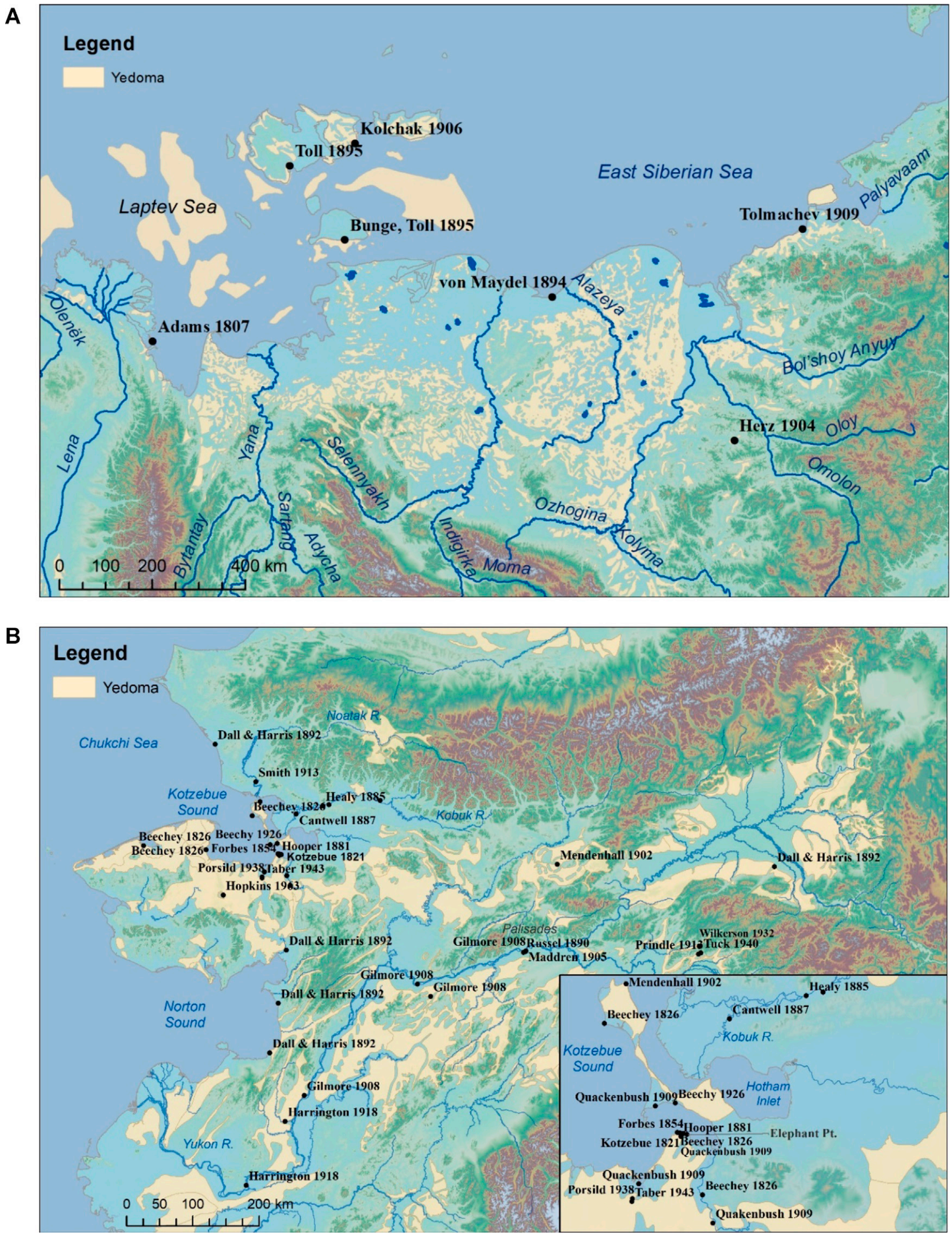

FIGURE 1 | Maps of locations of the first Yedoma sites in Siberia **(A)** and Alaska **(B)**, boundaries of Yedoma region are shown based on Strauss et al. (2021).

sediment, widely distributed in Beringia (area of land bounded by the Lena River in Russia to the west and the Mackenzie Delta in Canada to the east).

In this paper, we use the latter concept of Yedoma to characterize ice-rich silty deposits penetrated by large ice wedges, which resulted from sedimentation and syngenetic freezing in unglaciated areas amidst the last glaciation of the late Pleistocene (Schirrmeister et al., 2013 and references therein). We restrict the Yedoma formation to the late Pleistocene (post MIS five to the end of the last glaciation).

Accumulation of sediment in a former harsh cold climate created this unique and fascinating permafrost type, which has little to no analog in contemporary permafrost formations. Yedoma is also an essential stock of ancient carbon and a treasure of information on the natural history and paleoclimate of Arctic and Subarctic in the late Pleistocene. Yedoma attracted a special interest of native people, explorers, and scientists because of its preservation of remnants of enormous number of extinct animals including mammoths. Since the sensational presentation of the first intact mammoth corpse to the scientific community by Adams in 1807, the interest in Yedoma has continued to grow until the present day.

For over 150 years, supportable hypotheses on Yedoma formation eluded scientists, but recent advances in permafrost science may now have solved the problem. In this paper, we review the history and locations of early Yedoma observations, compare the various explanations that were proposed for its genesis and ice origins, and highlight some of the controversies among scientists defending their ideas.

FIRST YEDOMA FINDING IN SIBERIA

Yedoma, or late-Pleistocene Ice Complex has been known to native people of northeast Siberia and northwest Alaska for centuries. They associated Yedoma with the location of fossil remnants of "prehistoric" animals and looked for it as a source of mammoth tusks. Historically, the ivory market has been enormous, and numerous hunters and traders ("promyshlenniks" in Russia) have scoured the shores of Arctic seas and rivers to find mammoth tusks. Wrangel (1841) mentioned that in 1821 one fossil bone "hunter" brought 8,000 kg of tusks of perfect quality from the New Siberian Islands. He also noted that collectors found the biggest and best tusks on these islands, with smaller quantities located on the northern shore of the Laptev Sea and more seldom findings in southern parts of Siberia. von Toll (1959) mentioned that tusks hunters looked specifically for baydzherakhs (tall conical thermokarst mounds) to find the best quality ivory.

An interest in Yedoma within the scientific community was triggered in the beginning of the 19th century by two findings, one in Russia and the other in Alaska. In Russia, a young biologist named Michael Adams, employed as an adjunct in zoology at the Russian Academy of Sciences, was in Yakutsk in June 1806. A merchant told him that the Tungusian chief Shoumakhov had discovered a whole mammoth carcass on the shore of the Bykovskiy Peninsula (**Figure 1**). Adams was fascinated with the news (**Supplementary Quote S1** in the supplement); he immediately set off on his journey and in a few weeks reached the mammoth site, assisted by Shoumakhov and a crew of 14 people. Adams (1807, 1808) described in detail how Shoumakhov had found an unusually large chunk of ice that separated from the ice cliff in 1799. The following year, Shoumakhov saw two feet of a mammoth revealed from melting ice. It took almost 3 years for the mammoth body to melt free from the ice. In 1804, the Russian merchant Roman Boltunov drew the first sketch of the mammoth. Copies of his sketch made at the time (**Figure 2A**) were sent to Johann Friedrich Blumenbach in Göttingen and Georges Cuvier in Paris. Notes made on the sketch in Blumenbach's handwriting states: "Elephas primigenius in Russia, called mammoth, excavated with skin and hair 1806 in June at the outflow of the Lena into the Arctic Ocean. Roughly drawn as it was found mutilated and filthy." The other notes at the top right of the drawing are from Wilhelm Moritz Keferstein (1833–1870).

When Adams reached the mammoth site, the flesh and internal organs of the mammoth had been eaten by wild animals, but he gathered nearly the entire skeleton as well as some skin and fur. In Yakutsk, Adams bought two mammoth tusks (Shoumakhov earlier had sold the original tusks to Boltunov for 50 rubles) and brought his mammoth to Saint Petersburg where it was reassembled and is on display in the Museum of Zoology (**Figure 2B**). Adams' discovery of the first mammoth skeleton was a world sensation, and his publication was quickly translated into several languages.

Adams described the coastal exposure at the mammoth's location having a clear ice with a nauseating smell. He estimated that the exposure was 3 km long and 60–80 m high. von Baer (1842) thought that this description was an exaggeration. It is unclear how Adams could have evaluated the size of the bluff because at the time of his visit the exposed part of the bluff was 100 steps from the mammoth's position and 160 steps from the sea. The ice was covered by moss and a 50-cm-thick layer of soil that was partially frozen. Adams described mudflows slowly moving towards the sea; he also mentioned soil wedges among ice (**Supplementary Quote S2**).

From the permafrost science point of view, Adams' description of the site was rather disappointing; it is less than one page, and his explanations are difficult even for people familiar with Yedoma to understand. von Baer (1842) tried to make sense of Adams' short description but failed, blaming inaccuracies in Adams' paper (**Supplementary Quote S3**). von Middendorff (1860) noted that Adams' description of the site was unsatisfactory and not trustworthy. von Toll (1897) also found that the explanations in Adams' short description were unsatisfactory and unclear.

Adams' descriptions of the soil and ground ice are confusing. In some translations of his report, originally published in French in 1807, soil wedges were described as lumps or strips of eroded soil among ice floes. Some authors quoting Adams even omitted soil wedges in ice as unimportant detail. Nevertheless, there is a possibility that Adams wrote about soil wedges inside the ice of the exposure itself. Leffingwell (1919) in his short abstract of Adams' paper said: "The mammoth remains were found in the earth wedges between the ice masses." This interpretation is also consistent with the picture (**Figure 3**) drawn by von Toll (1897) who tried to reconstruct what Adams had potentially seen and used it as proof for his own ideas.

With our contemporary knowledge, we interpret Adams' description of the site as: 1) the cliff was not eroded by the sea at the time when Shoumakhov found the mammoth; 2) the cliff was affected by thermal denudation and therefore was not vertical; and 3) the mammoth slid downslope from the site where it thawed out. Overall, the main message gained from this site in the Russian Arctic was the existence of perennially frozen soil

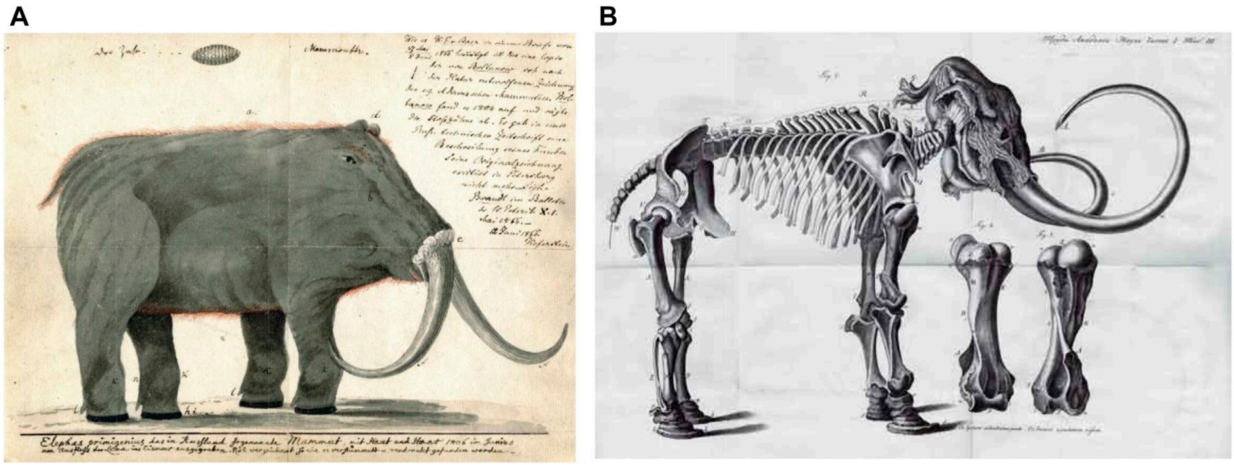

FIGURE 2 | (A)—The world's first reconstruction drawing of a mummified carcass of the so-called "Adams or Lena Mammoth" based on the original sketch by Roman Boltunov (in the Ethnological Collection of the University of Göttingen); **(B)**—Wilhelm Gottlieb Tilesius' etching of the Adams mammoth skeleton (now on display in the Museum of Zoology, Sankt-Peterburg).

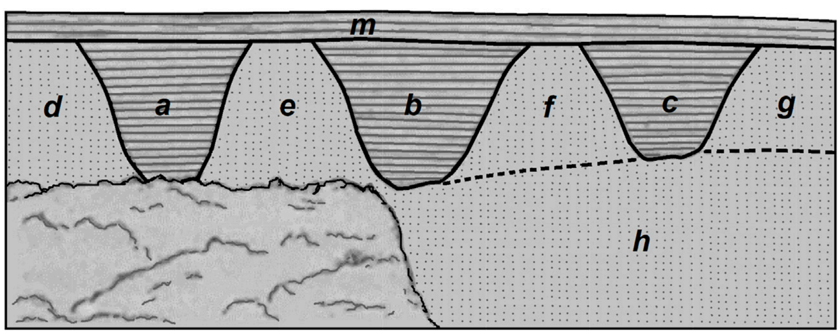

FIGURE 3 | von Toll (1897) perception of Adams (1808) description of a Yedoma cliff in Bykovskiy Peninsula; a, b, c—mineral soil; d, e, f, g, h—ice; m—surficial organic material.

containing large bodies of ground ice and the remnants of mammoths.

FIRST YEDOMA FINDING IN ALASKA

Ten years after Adams' discovery, the Russian ship "Rurik," commanded by Captain Otto von Kotzebue, sailed along the shores of northwest Alaska. On August 8, 1816, the crew found a high exposure of ground ice onshore (**Figure 1**). von Kotzebue (1821) described a remarkable finding made by Dr. Eschscholtz who discovered large masses of pure ice in the 30-m-high coastal bluff. To commemorate this remarkable discovery, von Kotzebue named the bay after Dr. Eschscholtz (**Supplementary Quote S4**). Von Kotzebue mentioned numerous mammoths' teeth and bones exposed at this place; he also provided the latitude (66° 15′ 36" N) that helped later explorers to find the site.

Adelbert von Chamisso (1821), a scientist of von Kotzebue's crew, provided additional descriptions of the exposure in Eschscholtz Bay and compared it to other locations in northern Asia and North America, including the site of Adams' mammoth discovery (**Supplementary Quote S5**). Ludwig Choris (1822), an artist in von Kotzebue's crew, created two paintings of the exposure (**Figure 4**). In **Figure 4A**, stripes of ice are seen that can be recognized as ice wedges, which in the middle of summer are commonly protruding outward relief relative to the columns of dark ice-rich soil that thaws faster than ice. **Figure 4B** shows the exposure at a larger scale, where bodies of ice that are several meters wide are divided by columns of soil.

EMERGING INTEREST AFTER THE FIRST YEDOMA FINDINGS BY ADAMS AND VON KOTZEBUE

For the scientific community, the first Yedoma findings were a sensation. For over 150 years since the works by von Kotzebue

A

B

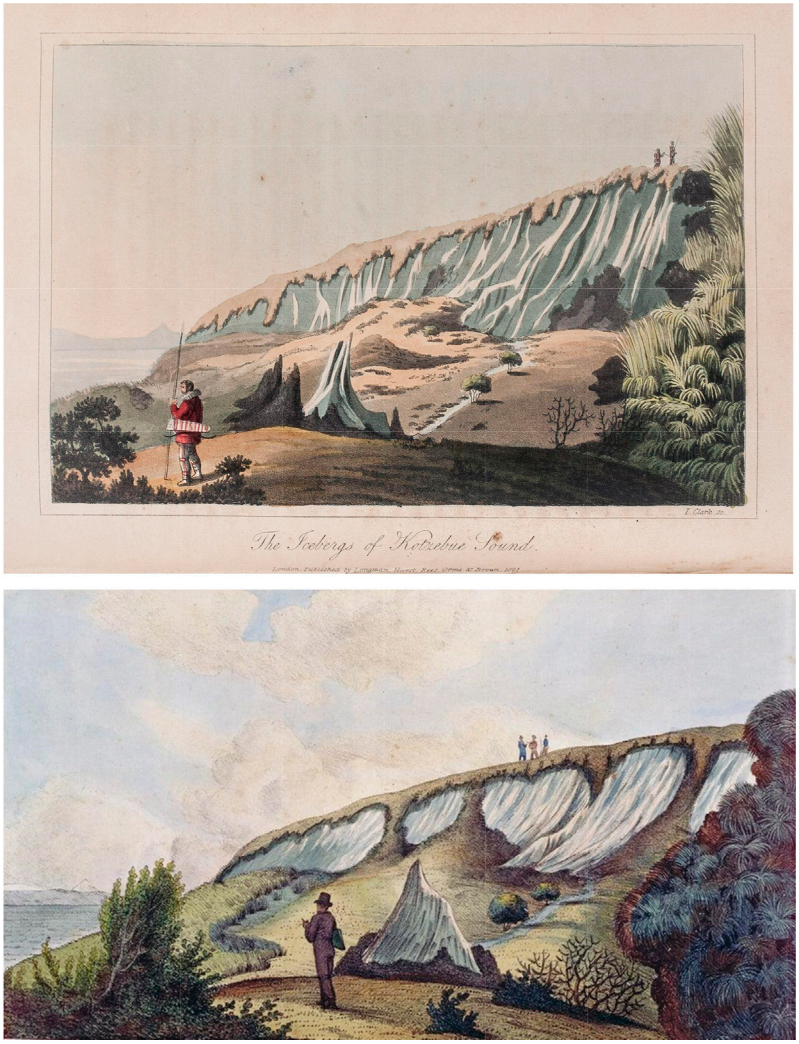

FIGURE 4 | Paintings "The icebergs of Kotzebue Sound" **(A)** and "Vue des Glaces dans le Golfe de Kotzebue (View of the Glaciers of the Gulf of Kotzebue)" **(B)** by Ludwig Choris (1822).

and Adams, attempts to determine the genesis of Yedoma have mainly been focused on the origin of the bodies of massive ice. Soil in Yedoma was often unnoticed or described as a secondary feature filling cavities made by erosion within the massive ice. Discussions focusing on the genesis of ice rather than the origin of the entire formation prevailed until the 1950s.

Alaska

In July 1826, 10 years after von Kotzebue's voyage, Captain Frederic W. Beechey and his crew revisited the site described by von Kotzebue (1821). After observation of the exposure from the boat and a brief inspection it by Mr. Collie, Beechey (1831) concluded that ice was just a coating on the bluff face and the ice was a product of snowdrift or freezing of water running over the surface of the cliff (**Supplementary Quote S6**). With such a perception, in September 1826, Captain Beechey looked at a similar exposure at Cape Blossom on the Baldwin Peninsula (**Figure 1**), which Beechey named after his ship (**Supplementary Quote S7**). The description by Beechey (1831) showed that in front of him was an exposure of ice wedges with intermittent soil columns. He explain ice as imbedded in the indentations in soil of the cliff. Most likely, he misinterpreted the origin of the ground ice in the exposure because he already had made up his mind before closely examining these features.

von Chamisso (1836), a crew member of von Kotzebue's expedition, rejected Beechey's conclusions, and insisted on the accuracy of von Kotzebue's report (von Chamisso, 1821) that described the occurrence of ice as a thick solid body (**Supplementary Quote S8**).

Beechey's crew members A. Collie and Lieutenant E. Belcher provided their opinions on the genesis of the ice (see **Table 1** for different hypotheses on the genesis of massive ground ice within Yedoma). Collie described three possible mechanisms of ground ice formation: 1) from snowdrifts converted into ice by successive thawing and freezing in spring and summer; 2) from water collected in deep fissures and cavities; and 3) from water

TABLE 1 | Hypotheses of the genesis of massive ground ice and respective authors.

Genesis of ice	Author
Ice coatings on the surface of exposure	Beechey (1831)
Glacier or ice sheet	Hooper (1884), Herz (1904), Muir (1917), Obruchev (1931), Saks (1947)
Infiltration ice	Belcher (Beechey, 1831)
Buried lake ice	Dall (1881), Russell (1890), Turner (1886), Mendenhall (1902), Maddren (1905), Grigoriev (1927)
Icing	Tyrrell (1917), Wilkerson (1932), Gusev (1958)
Open system pingo	Porsild (1938)
Firn and snow	Dawson (1894), Geikie (1894), von Toll (1897), Grigoriev (1927), Tolmachev (1903), Ermolaev (1932), Gorodkov (1948), Grave (1944), Gusev (1958)
Segregated ice	Taber (1943)
Wedge ice	Figurin (1823), von Bunge (1887), Leffingwell (1919), Popov (1952)

trickling from the slope above the frozen bluffs. Belcher proposed a hypothesis that water infiltrates every summer to the surface of the frozen soil, where it freezes, and accumulates into a thick horizontal sheet of pure transparent ice (Beechey, 1831).

Russia

In northern Yakutia, Dr. A. E. Figurin, a physician in Anzhu's expedition to the New Siberian Archipelago (1820–1824), observed numerous exposures of muddy ice along Siberian rivers, creeks and seashores of the mainland and islands. The ice mostly had the shape of wedges narrowing to their base. When describing the tundra terrain, he defined Yedoma as hills that appeared almost everywhere and at many places contained ice wedges. The Yedoma surface was covered by tussocks and bare, "mold-covered" spots (Figurin, 1823), which we interpret as frost boils. Figurin also described the formation of 'buyarakhs', which are known as baydzherakhs (conical thermokarst mounds typical of Yedoma) in the modern permafrost literature (van Everdingen, 1998). Figurin's major contribution to permafrost science was the first explanation of the formation of ice wedges caused by frost cracking (**Supplementary Quote S9**).

In his "Excerpts on Siberia," Mathias von Hedenström (1830) also described ice wedges and tried to explain the origin of alternating horizontal layers of ice and soils that he had observed in exposed bluffs of the Yana-Kolyma region of Northern Yakutia. He mentioned that ice wedges sometimes cross these horizontal layers (**Supplementary Quote S10**).

CONTINUING STUDIES IN ALASKA DURING THE 19TH CENTURY

In 1848, Eschscholtz Bay was visited by the ship "Herald" under the command of Captain Henry Kellett in search of the lost Franklin Expedition. The results of the expedition were reported in several volumes covering a general narrative of the cruise as well as the botany and zoology studied at the sites they visited (Seemann, 1853). Ice cliffs in Eschscholtz Bay were described in every volume, but in more detail in the volume on zoology written by the prominent British naturalist Sir John Richardson (1854). He was not part of the crew, however, and his extensive description is based on notes taken by members of the expedition, including H. Kellett, B. Seemann, and J. Goodridge. Richardson (1854) concluded that von Kotzebue (1821) was right about the ice originating as a "solid iceberg" and Beechey (1831) was wrong about the ice in bluff being a superficial coating of water freezing to the bluff face (**Supplementary Quote S11**). However, the issue of relating mammoth remains to a thin layer of soil covering ice remained a problem for Richardson (**Supplementary Quote S12**). Seemann (1853) also concluded that Captain Beechey was wrong in his explanation of the ice being just a coating on the face of the bluff and critically assessed the hypothesis of Belcher who assumed that surface water penetrated through peat and clay and that ice accumulated gradually (**Supplementary Quote S13**).

From the descriptions of several exposures based on notes by Goodridge, it is difficult for us to reconstruct the structure of the bluffs, Goodridge tended to interpret exposures as made of ice, describing one of exposures as "a few icy pillars and detached walls standing twenty feet above the surrounding level surface, and still covered with from seven to ten feet of soil." A description of the cliff is also illustrated by a painting (**Figure 5**), produced by artist W. Fitch from a sketch made by one of the members of the expedition. It would be especially interesting to see this original sketch. In the painting, the exposure is presented as a pure ice with a thin layer of clay and peat over ice.

Kellett and Richardson, who reviewed notes taken by Kellett and two of his companions, discussed several modes for the ice formation and did not come to a credible conclusion. It is interesting that they took literally von Kotzebue's definition "iceberg," while von Kotzebue and von Chamisso did not discuss the mode of ice formation. We think that von Kotzebue used the word "iceberg" just to describe an ice mountain (as "berg" means mountain in German) without any relation to real icebergs. In his memoir on the voyage, von Chamisso mentioned "so-called iceberg" (von Chamisso, 1836).

Dall (1881) visited Eschscholtz Bay in 1880 and compiled detailed descriptions of the exposed bluff. Among other interesting details, he mentioned that the solid ice was penetrated by deep vertical holes, in which organic-rich sediments had been deposited in layers, and appeared as soil cylinders on the exposed face of the bluff (**Supplementary Quote S14**).

In evaluating earlier hypotheses of ice genesis, Dall and Harris (1892) concluded that von Kotzebue and Eschscholtz (von Kotzebue, 1821) were right in their interpretation of the ice formation and that Beechey (1831), who thought that the ice

FIGURE 5 | Painting "The Ice Cliffs in Kotzebue Sound" by the artist W.W. Fitch painted from a sketch made by T. Woodward, one of the members of the expedition. Second half of the 19th century (Museum National d'Histoire Naturelle, Paris).

was a superficial deposit, was wrong (**Supplementary Quote S15**). Given the limitations of earlier explanations, Dall and Harris (1892) developed an elaborate regional scheme for relating an episode of ice formation to changing water levels in the Bering Sea and depositional processes in the surrounding area. They envisioned a land connection or enormous level plain covering much of the present area of the Bering Sea related to uplift of the area during the Miocene (**Supplementary Quote S16**), somewhat the reverse of the land connection caused by lowering of sea level associated with glaciation during the Pleistocene, as currently accepted. While the enormity of fluvial processes creating such widespread deposits is unimaginable given current knowledge, the hypothesis at least sought to address the widespread nature of the deposits, provided a link between ice accumulation and depositional process, and related ice accumulation to development of surface vegetation and soils.

Captain C. L. Hooper (1884) commanding the Revenue Cutter "Thomas Corwin" visited Eschscholtz Bay and Elephant Point near the mouth of the Buckland River in 1880 and 1881. He examined the ice and also found that the explanation given by Beechey was not correct. Hooper made several valuable observations and suggested wedge-ice origin of some of the massive ice bodies (**Supplementary Quote S17**).

John Muir (1917), a member of Hooper's expeditions, defined the massive ice at Elephant Point as buried glacier ice but he also noticed masses of dirty stratified ice of a different origin (**Supplementary Quote S18**).

John C. Cantwell (1887), Lieutenant on the U.S. Revenue Marine steamer "Corwin," described the occurrence of a chain of exposed ice cliffs up to 150 feet high along the Kobuk (Kowak) River starting about 130 km from the mouth (**Figure 6**) (**Supplementary Quote S19**). Cantwell (1896) speculated that maybe it was an old glacier buried beneath the deposits of a more recent inundation, but finally he admitted: "The formation of the remarkable ice cliffs in the lower country is, however, a geological nut which the writer admits his inability to crack."

Findings of Yedoma in Eschscholtz Bay, on the Baldwin Peninsula, and along the Kobuk and Buckland rivers showed vast areas surrounding Kotzebue Sound that were, and in some places still are, underlain by Yedoma, which for thousands of years has been eroded by the sea and rivers. This allows us to hypothesize that Eschscholtz Bay, Selawik Lake, and Hotham Inlet are results of thermokarst processes that have affected original Yedoma. Combined with lagoonal intermediate stages, erosion has formed the modern landscape leaving Yedoma remnants.

Turner (1886) studied the environment of Western Alaska from 1874 to 1881 and tried to explain the origin of the ice bluffs that had been observed at various parts of the coast, especially north of the Bering Strait. He described a hypothetical formation of a thick body of ice resulting from continuous covering of lakes with floating vegetation mats, whose thermal properties protect the ice underneath it from melting during the summer (**Supplementary Quote S20**). Another important factor supporting rapid freezing was a thin layer of snow. Turner evidently was the first to suggest a lacustrine origin for the massive ice exposed in the Yedoma bluffs.

Russell (1890), who made a reconnaissance of the Yukon River for the United States Geological Survey (USGS), visited the Palisades Bluff (**Figure 1B**) and came to the similar idea that the massive ice in these famous bluffs had a lacustrine origin (**Supplementary Quote S21**). Russell's work is of a special interest to permafrost science because it appears that he was the first to

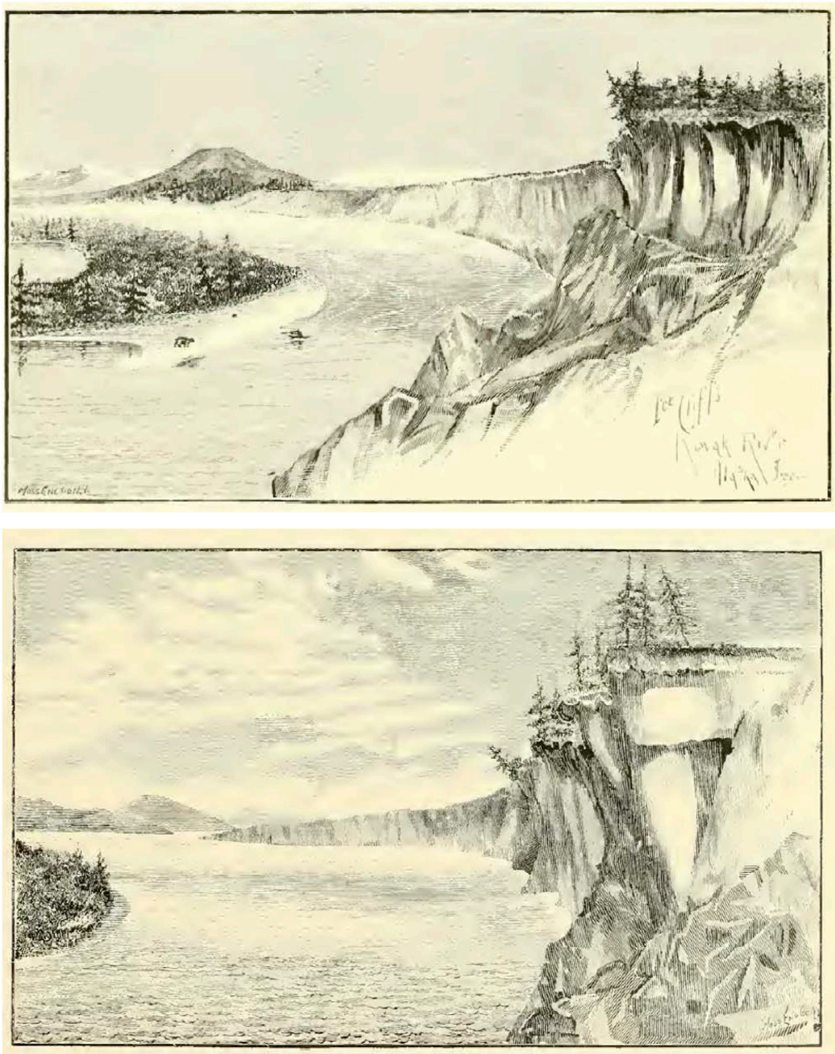

FIGURE 6 | Ice cliffs at the Kobuk River (Cantwell, 1887).

clearly define the process of syngenetic permafrost formation, presuming that under certain conditions deposition and freezing may occur at the same time, which explains the formation of alternating layers of clear ice and soil (**Supplementary Quote S22**).

While crediting Russell (1890) for a clear understanding of syngenetic permafrost formation, we also note that prior to Russel (1890), Lopatin (1876) had described the formation of interbedded ice and sand layers in the winter of 1868 on the Okhotsk Sea coast of the Sakhalin Island. In observing that the surface layers are frozen in winter and thaw during summer, Lopatin presumed that under colder climate these ice layers may be preserved for centuries (**Supplementary Quote S23**). He believed that the ice-rich soil he had described in the Yenisey River Delta could form in a similar way. Dall and Harris (1892) shared the opinions of Turner (1886) and Russell (1890) relating the origin of ice in the cliffs to frozen lakes buried by soil.

Dawson, the Director of the Geological Survey of Canada (1894) generally agreed with Dall and Harris (1892) on the timing of ice formation and the environmental conditions but thought that the ice was a result of snow accumulation. Soil, which was derived from adjacent highlands and deposited by rivers, covered ice and protected it from thawing.

Mendenhall (1902), who made a geological reconnaissance along the Yukon, Kanuti, and Kobuk rivers for the USGS, observed Yedoma exposures along the Kobuk (Kowak) River and Eschscholtz Bay and agreed with Russell (1890) that the ice originated from a frozen lake (**Supplementary Quote S24**).

THE SCIENTIFIC AND PERSONAL CONFRONTATION BETWEEN EDUARD VON TOLL AND ALEXANDER VON BUNGE

Although numerous hypotheses on the origin of Yedoma ice had been proposed since the initial discoveries by Adams (1808) and von Kotzebue (1821), the first serious discussion on the real origin of the massive ice within Yedoma took place between von Toll (1895, 1897) and von Bunge (1883, 1895) at the end of 19th century. These two prominent Arctic explorers were members of the same polar expeditions and talked about the same exposures on the northern shores of Yakutia, including the New Siberian Islands, but came to different conclusions on the origin of Yedoma ice. Their disagreement even took on a personal character. von Toll (1895) wrote an extensive paper, in which one of the main points was to prove that he was right, and von Bunge was wrong. According to von Bunge (1903), von Toll subjected von Bunge's hypothesis to "strict scientific criticism, calling it a "theory" without any reason."

Von Bunge's Theory

Von Bunge (1887) witnessed the formation of frost cracks accompanied by a loud noise "like shots under the surface remaining a distant cannonade," like earlier observations made by Figurin (1823). Von Bunge noted that the cracks penetrated to significant depth. The tundra he observed on the Lena Delta was divided into a myriad of irregular polygons, whose edges were higher than the center. Between the edges of neighboring polygons, there was a narrow trough, which often was used as a path by lemmings. This trough corresponded to a deep crack in the earth filled with ice. Von Bunge speculated that when the spring snowmelt water fills the cracks, it freezes, expands with tremendous pressure and pushes the walls of the crevices apart. By repeated cracking and freezing of snowmelt water, the ice volume around cracks becomes bigger over time.

From his observations of the formation, von Bunge (1895) concluded that huge masses of ice could be formed in this manner. He correctly described the morphology of Yedoma and the nature of ice but found it hard to comprehend how frost cracks could penetrate several dozens of meters in depth and develop the increased width of wedge ice at great depths. He found that an ice wedge, when exposed in coastal bluffs, could present an appearance of a continuous horizontal layer of ice. He also explained the impurities of ice (foliations) and the decrease in the size of ice crystals with depth. Given current knowledge, it is easy to find limitations in von Bunge's descriptions and conclusions, but at the time of his studies he made a significant contribution to our understanding of Yedoma ice formation.

Von Toll's Theory

In contrast, von Toll (1891, 1895) considered the masses of ice on Bol'shoy Lyakhovsky Island as the remnants of a mainland glacier assumed to have covered these islands, as well as the coasts of the continental Siberia from the Khara-Ulakh Ridge to the Chaun Bay (von Maydel, 1894) and extended 200 km south into the mainland. He stated: "No one geologist, looking at such an exposure, would have any reservation that the ice is older than the cracks filled with layers of ice and clay" (in Obruchev (1892) translation of von Toll (1891) paper). However, according to von Bunge (1903), von Toll had not seen Yedoma exposures during the summer when they were not covered with snow. He was relying instead on the outstanding photographs of Yedoma (e.g., **Figure 7**) given to him by von Bunge (von Toll, 1895) (**Supplementary Quotes S25, 26**). Von Toll's own photographs show only a slope covered by snow with just the tops of baydzherakhs visible on the surface. In his publications, von Toll described exposures of the southern shore of Bol'shoy Lyakhovsky Island near the mouth of the Vankina River (**Supplementary Quote S25**) based on the photograph by von Bunge (**Figure 7**, bottom). Von Toll studied crystals of ice taken from the upper part of an exposure. He concluded that "the structure of Quaternary ice layers on the New Siberian Islands speaks in favor of their origin from snow and strongly against the water origin." According to von Toll, the firn had remained at temperature below 0°C the entire time before it was covered with soil, and the growth of ice crystals was not possible (**Supplementary Quote S27**).

Von Toll—von Bunge Disagreement

According to von Toll, von Bunge described his idea for the first time in letters to Shrenk (von Bunge, 1887) and they were written in the winter of 1884 in Sagastyr during a few hours of rest in the midst of hard work, and in a difficult environment, therefore could not contribute to a strictly scientific treatment of the subject. In any case, he said that von Bunge was wrong in his explanation of the massive ice origin and did not solve the problem of the origin of ice that was presented to him. von Bunge (1903) answered von Toll's criticisms (**Supplementary Quotes S28, 29**), emphasizing that von Toll did not see the exposures in the summertime and arguing that by no means the ice could be older than the soil. Although von Bunge was certain of his hypothesis of the formation of ice, he admitted that the problem of the soil and ice origin was very complicated and that future researchers would solve it.

In 1903, while searching for the vanished group of von Toll, Kolchak (1906) visited Faddeevskiy Island where he described 70–80 feet (20–25 m) exposure of Yedoma as a glacier covered with soil and "typical cones of baydzherakhs." He was the first to describe remnants of Yedoma under water along the seafloor (**Supplementary Quote S30**).

CONSEQUENCES OF THE VON TOLL—VON BUNGE DISAGREEMENT ON YEDOMA STUDIES IN RUSSIA IN THE 20TH CENTURY

Summarizing the von Bunge—von Toll disagreement, we can conclude that von Bunge recognized that the focus of studies should have been the soil, while von Toll and others were preoccupied with the ice. Popov (1952) later said that both von Toll and von Bunge were not correct because soil and ice formed simultaneously (syngenetically). We agree with von Bunge that the soil is the primary substance, as the existence of soil sets conditions needed for ice formation.

Nevertheless, for the next 50 years, the majority of leading Russian scientists unequivocally supported von Toll in his dispute with von Bunge. In the introduction of the Russian translation of von Toll's diary (1959) from his voyage on the yacht "Zaria,"

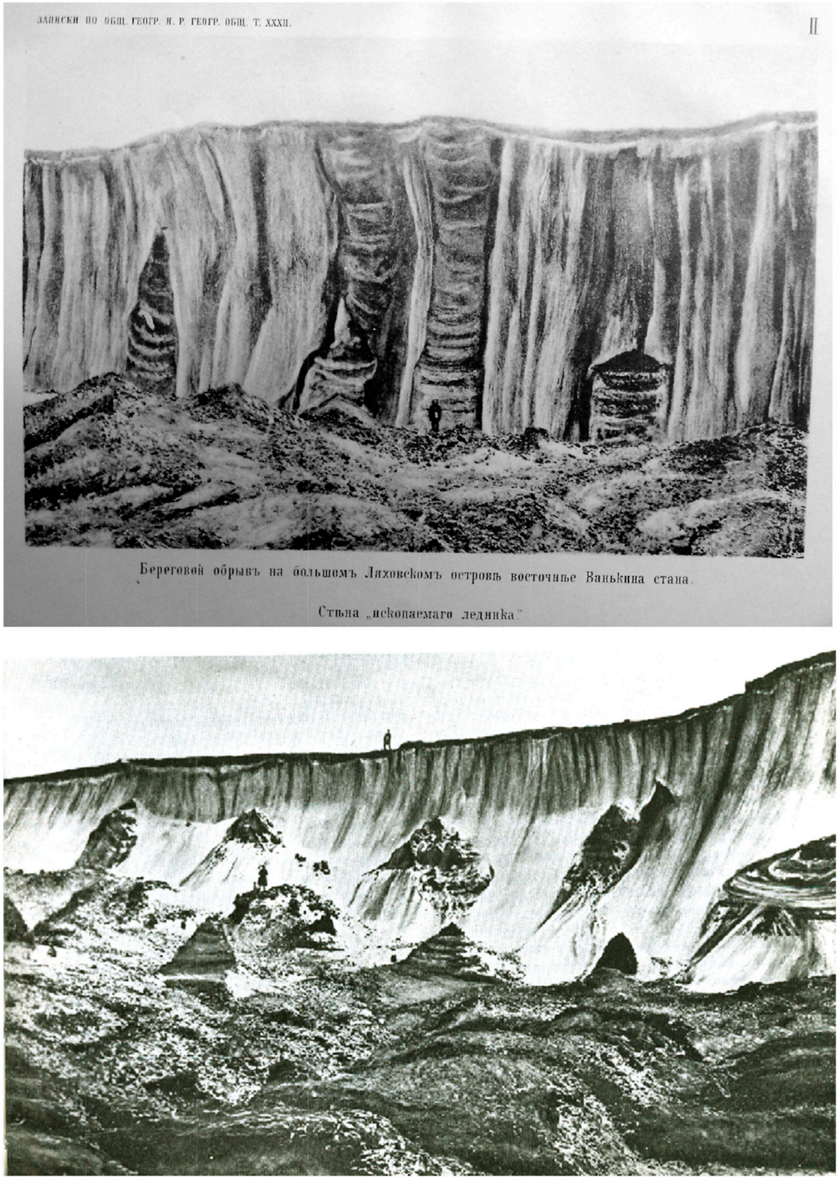

FIGURE 7 | Southern coast of Bol'shoy Lyakhovsky Island, Vankina River mouth, photographs by von Bunge (von Toll, 1897).

Wittenburg (1959), a prominent Arctic geologist, wrote: "von Toll's studies of fossil ice on Bol'shoy Lyakhovsky Island have not been outshined to date. They are included in every textbook on geology and physical geography and translated into many languages."

Many Russian scientists supported von Toll's concepts of buried glacial ice, or at least firn. In 1901, an expedition of the Russian Academy of Sciences recovered a mammoth on the bank of the Berezovka River, a tributary of the Kolyma River. A short description of the site was done by a zoologist, O.F. Herz (1904), as the geologist who was assigned to the trip did not participate. Herz took a photograph of the exposure (**Figure 8**), collected cores of ground ice from the site and ultimately supported a glacial origin of the ice (**Supplementary Quote S31**).

Tolmachev (1903) studied the samples of ice collected by Herz and evaluated their properties, such as unit weight, crystal size and shape, and air bubbles within the ice. Tolmachev stated that the origin of the ice could be easily recognized by its structure, and that ice formed by snow water, even extremely rich in dissolved air, cannot be as porous as snow ice. He concluded that the ice at the Berezovka site was firn. Tolmachev also noted that it would be extremely interesting to study the structure of ground ice and suggested that new observations were necessary to solve all remaining problems, referring to the discussion between von Toll and von Bunge (**Supplementary Quote S32**).

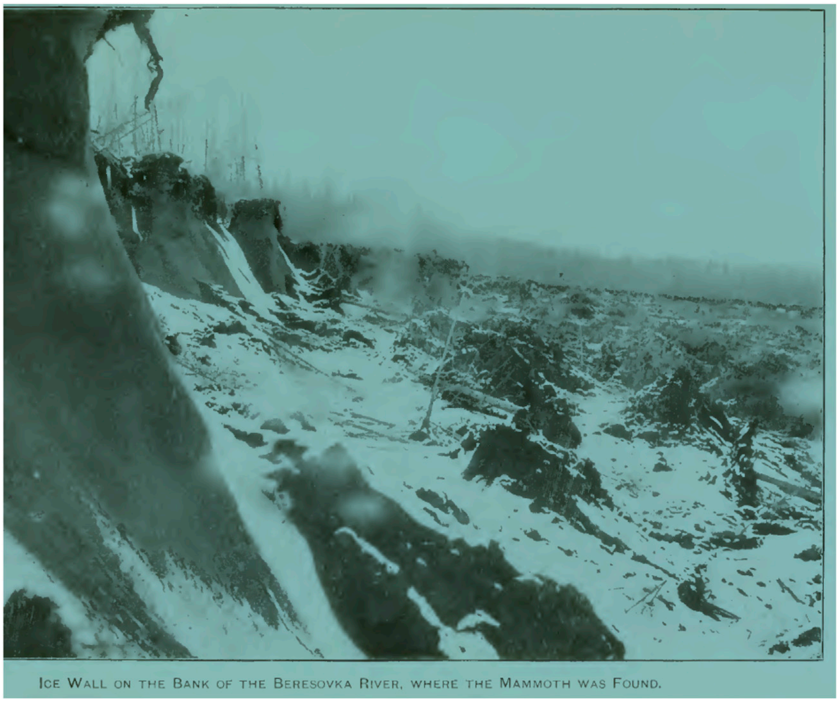

FIGURE 8 | Exposure of yedoma at the Berezovka River (Herz, 1904).

FIGURE 9 | Yedoma exposure at the mouth of the Bol'shaya (Rauchua) River (Tolmachev, 1911).

A few years later, Tolmachev (1906) visited the Yenisey-Khatanga region and admitted that the wedge ice was much more common than he had previously thought (**Supplementary Quote S33)** During his expedition along the shore of the East Siberian Sea, Tolmachev (1911) found that Yedoma occurred widely west of Chaun Bay (**Figure 9**). At that time, he avoided the discussion of Yedoma genesis and described it as tundra sand–clay soil with inclusion of huge bodies of underground ice. The question of the ice's origin had been of interest to Tolmachev for several decades; he identified it as one of the most important problems of Arctic geology (Tolmachev, 1928; Tolmachoff, 1929) (**Supplementary Quotes S34, 35**).

Vollosovich (1909, 1915), who participated in von Toll's expedition, shared von Toll's ideas on the origin of ice. At the Sanga-Yurakh mammoth site, Vollosovich (1909) described two ice horizons separated by a layer of soil and called this layer "the mammoth horizon." Later, Ermolaev (1932) did not find this horizon. In our interpretation, it seems that Vollosovich (1909) described soil accumulated on a thermal terrace as an original horizon. At Bol'shoy Lyakhovsky Island, Vollosovich (1915) also saw two layers of ice in the bluffs, separated by mudflow deposits and attributed them to two epochs of glaciation. In his opinion, the ice represented the remains of snowdrifts.

Sumgin (1927), the founder of the Russian (Soviet) Permafrost Institute, shared the opinion that ground ice of the New Siberian Islands, ice on the shore of the Arctic Ocean to the east of the mouth of the Lena River, and ice in the Lena-Aldan watershed was glacial ice. These ice masses, therefore, were interpreted as having been preserved in the ground from the glacial epochs to present. Sumgin was interested in Yedoma and mammoth fauna associated with it, which he considered as proof that permafrost was not a product of the contemporary climate but a very old formation.

Grigoriev (1927, 1930), a prominent Russian geographer and a founder of the Institute of Geography of the Russian Academy of Sciences, not only fully supported von Toll's opinion on ice formation, but also applied it to the formation of large bodies of massive ice with a thickness of up to 25–30 m in Central Yakutia (**Supplementary Quote S36**). According to Grigoriev (1927) descriptions, massive ice bodies in Central Yakutia consist of two types of ice—firn in the upper part and lake ice below it. Grigoriev (1927, 1930) described the formation of firn as followed: At the onset of a new period of glaciation and therefore a new climate, the rivers that had survived the new uplift of the country began to erode their channels intensively. This river erosion deepened, widened and created a new surface cut into previously deposited sediments. The rivers that had broken up and became separate lakes, underwent a different fate. In these lakes (due to the absence of flowing water), the freezing of water occurred deeper than in the active rivers. Thus, these lakes froze back to the bottom in most cases in winter (as is occurs in some undrained lakes of the area even today). Increased precipitation led to a greater accumulation of snow in the depressions. The snow covered the ice and prevented it from melting in the summer, as it was not able to melt completely under the climatic conditions of the time. Thus, the ice recrystallized into a granular structure, and lake basins were gradually filled with firn, which was deposited on top of lake ice. If at the beginning of this process there was still unfrozen water under the ice, it froze somewhat later, being exposed to the low temperature of the permafrost. In Grigoriev's opinion, the difference between these two types of ice was so obvious that they could not be missed in an exposure or a drilling core.

Ermolaev (1932) studied Yedoma on Bol'shoy Lyakhovsky Island and shared von Toll's opinion on ice genesis, but disagreed with Vollosovich on the existence of the two ice horizons. Ermolaev paid more attention than others to the deposits filling "cracks in ice." He found that soil was homogeneous with the size of most particles in the range 0.05–0.01 mm. This silty soil was interbedded with thin layers of ice, which were curved up at contacts with massive ice. During a summer, these cracks were a drainage pathway for meltwater. Water running from higher elevations, as well as winds, deposited silt over the ice layer. Such a cycle repeated every year and produced a series of silt-ice layers. The volume of ice within the sediment filling these cracks was about 70%. Peat that occurred in these cracks was also brought in by water. Ermolaev found that the structure of the ice was similar to ice from the Berezovka River exposure that was described earlier by Tolmachev (1903). Ermolaev (1932) described the soil wedges, or rather those spaces between the ice walls that were subsequently filled with soil, in relation to the genesis of the ice. Whatever their origin, he considered them a consequence of some coherent system of stresses existing within the whole mass of solid ice and that they could have been caused by a process that involved the entire ice mass. Ermolaev, a mechanical engineer by education, considered a few possible models of ice cracking and concluded that the ice was a glacier, and cracks in the ice were caused by ice folding. Based on his mechanical model, he estimated that the thickness of ice sufficient for such stresses should be 70–80 m. In light of modern knowledge of the origin of Yedoma, we can consider Ermolaev's evaluations as erroneous, and this example shows the importance of developing the correct conceptual models before quantitative modeling.

Vladimir A. Obruchev (1931), a patriarch of Siberian Geology, also supported von Toll's ideas. He believed that this fossil ice also had an extensive distribution along the coast of the Arctic Sea. He considered that most of it was formed during a glacial period and was represented by stagnant ice detached from glaciers during their retreat, with parts of it being remnants of stagnant firn fields (**Supplementary Quote S37**). The remnants of fauna and flora, found very often in wedge-shaped and pillar-like masses of layered sediment deposited among the ice bodies, supported his concept of ice that had formed during the last glaciation.

In 1940, the government of the Republic of Yakutia asked the Obruchev Permafrost Institute to investigate the distribution and properties of buried glacier ice in the vicinities of Abalakh Lake, Central Yakutia, for the purpose of extensive development of the area. Experienced permafrost scientists, such as N.A. Grave, A.I. Efimov, and P.A. Soloviev actively participated in this study and produced numerous reports and papers describing their investigations. According to Grave (1944), a buried firn field had occupied the vast area of the Lena-Aldan watershed; he identified specific locations of buried ice. He documented ice thicknesses of 25–30 m and estimated from the depth of alases (thermokarst basins) that it could reach up to 40 m. Grave presented a preliminary map of buried ice in the region. Based on an example of the exposure of buried ice (**Figure 10**), Grave found great similarity of the structure and shape of buried ice of the Lena-Aldan watershed with the fossil firn field of the North Cape of Bykovsky Peninsula, from which he concluded that they were formed simultaneously. He considered as proven that the fossil ice was formed from accumulations of snow and firn. The ice structure, the absence of moraines, and presence of meadow soil under ice without any traces of ice scouring were to Grave evidence of such a genesis. He noticed, but did not clearly explain, the homogeneous nature of the ice and absence of infiltration ice

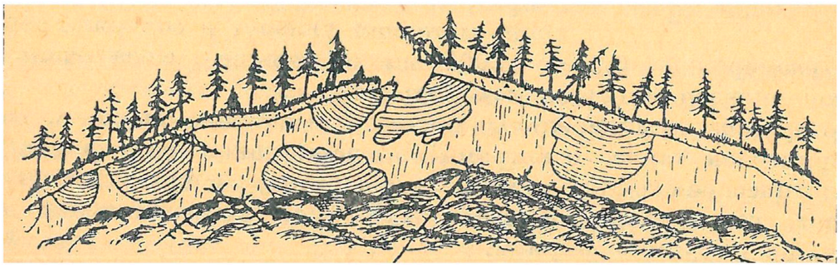

FIGURE 10 | Exposure of "fossil ice" with layered inclusions of soil at the left bank of the Aldan River (Grave, 1944).

in it. Studies driven by this approach regarding the genesis of ice were continued by the Permafrost Institute until 1950 (Shumskii, 1952).

Saks (1947) came to conclusion that the massive ice on the New Siberian Islands is not a thick continuous layer of firn but rather numerous separate snowfields. Gorodkov (1948), a leading Russian Arctic biologist, expressed his opinion on the nature of ice at Kotelny Island. He described the massive ice with inclusions of silt and small air bubbles, which was penetrated by thick wedges of a loess-like deposit and covered with a layer of loess-like silt about 40–60 cm thick. Gorodkov studied the properties of the ice and came to conclusion that it originated from firn. He also explained that soil wedges in ice formed as a result of silt accumulation in depressions that had developed from melting ice (**Supplementary Quote S38**).

Interesting, that Geikie (1894), the author of the monumental monograph on the Ice Age, compared ground ice formations of Northern Alaska with those of Siberia that had been previously described by von Toll and also came to conclusion that they are very similar and represent snowdrifts of a late glacial epoch (**Supplementary Quotes S39, 40**).

YEDOMA STUDIES IN NORTH AMERICA AT THE FIRST HALF OF THE 20TH CENTURY

In North America, ice- and organic-rich silt known to permafrost scientists as Yedoma was named 'muck' by gold miners in Canada and Alaska. Tyrrell (1904, 1917) studied "muck" deposits in the Klondike District, Yukon Territory, Canada. In some areas, he described muck strata up to 30 m thick that contained layers of clear ice. Tyrrell interpreted the ice as an underground icing formed by springs; the vertical veins or dikes of ice in his descriptions indicated positions of former water channels (**Supplementary Quote S41**).

Maddren (1905), who mapped known areas of Quaternary deposits with locations of Pleistocene mammals across Alaska, shared Russell's explanation of ice formation and was passionate about the idea of a lacustrine origin of ground ice (**Supplementary Quote S42**). Maddren was so confident with this idea of ice formation that he even modified Tolmachev's (1903) sketch of the bluff of the Berezovka River and added that the ice is underlined by silt of lacustrine genesis, which was not stated by Tolmachev. Tolmachev's statement was originally written as: "It can be ascertained, however, that the origin of such ice is easy to recognize by its structure. No matter how rich in air dissolved in snow water, it cannot make ice as porous as snow ice" (Tolmachev 1903, p. 133). However, Maddren's translation gave it the opposite meaning: "It may be remarked, the formation of the ice in such a way cannot be deduced from its structure." Maddren appears excessively critical of Tolmachev and overconfident in his own statements as for example, in one of his conclusions on Alaska he stated that there was no evidence that the climate of the Arctic had been colder in the Pleistocene than at present, and there were no ice-rich deposits of the Pleistocene age except glacial (**Supplementary Quote S43**).

A decade later, Leffingwell (1915, 1919) fully supported von Bunge's idea: "The writer leaves the origin of this ice an open question but holds the opinion that the most favorable line of inquiry will be along the lines suggested under the theory of ice wedges" (Leffingwell, 1919, p. 223). He even regretted that he did not know von Bunge's work when he began his studies of ice wedges in Alaska. Commenting on von Bunge's and von Toll's dispute, Leffingwell was surprised that von Bunge's theory did not get support in Russia. He saw some challenging questions in an application of the ice-wedge theory to Yedoma locations (during his work along the Beaufort Sea coast of Alaska, Leffingwell did not observe any Yedoma exposures). Nevertheless, Leffingwell presumed that symmetrically distributed inclusions of earth in Yedoma cliffs were closely related to symmetrically arranged frost cracks; he also figured out that the surface could grow upward because of the pressure that polygonal blocks had experienced from the growing ice wedges (**Supplementary Quote S44**). Earlier in his famous paper on the formation of wedge ice, Leffingwell (1915) was close to our understanding of syngenetic formation of ice wedges: "The usual covering for the ice is muck capped by turf, or peat capped by growing sphagnum (?) moss. As the thickness of this mantle increases by surface growth, the limit of the summer's thawing should rise, thus allowing a constant upward extension of the surface of the ice wedge at the locus of growth" (Leffingwell, 1915, p. 648). Thus, Leffingwell described two cases of "apparent upward growth of the surface." Leffingwell (1915) also commented on Yedoma in Alaska, suggesting that much of the ground ice at the famous bluffs at Eschscholtz Bay could be wedge ice (**Supplementary Quote S45**).

Between 1900 and 1920, ice-rich silt that we interpret as Yedoma was also observed in various parts of Alaska

(**Figure 1B**) by Gilmore (1908), Quackenbush (1909), Prindle et al. (1913), Smith (1993), and Harrington (1918).

Wilkerson (1932), a geology professor at the Alaska Agriculture College and School of Mines (now the University of Alaska Fairbanks), provided detailed descriptions of both the fine-grained, organic-rich silt (muck) and ground ice. He believed that the gold-bearing gravels and overburden soil were frozen soon after deposition, and that the upper portions were thawed each summer with the depth of thawing never quite equaling the depth of freezing. Thus, the thickness of the frozen materials was the result of numerous additions of materials that were frozen shortly after deposition. He argued that the 30–40 feet thickness of the deposits indicated that freezing could not have occurred after the whole thickness of the deposits had been formed. Wilkerson concluded that ice bodies were buried icings (called "glaciers" by the miners and some geologists) that had formed along hillsides by the groundwater seepages. He presumed that the ice was preserved by a protective mantle of muck, gravel, sand, and peat.

To Porsild (1938), the process of ice formation in Yedoma was identical to the formation of an open system pingo as we understand it now. Based on his studies of pingo formation in Canada and Alaska, he presumed that a similar process could lead to formation of sheets of solid ice in the Kotzebue Sound region and on the Seward Peninsula, as well as in other unglaciated parts of Alaska (**Supplementary Quote S46**).

Tuck (1940), a geologist with the USGS, observed Yedoma ("muck") exposures at gold mining sites near Fairbanks, Alaska. He described the fine-grained composition of mineral soil, the abundance of organic material, high water content, and vertebrate remains. He identified three types of ground ice that occurred in: 1) soil pore space and comprised 50% of the total mass; 2) sills from a few inches to 10 feet thick; and 3) dikes (wedges) formed in tension cracks filled with water. Figures in Tuck's paper show that sills and dikes were just different projections of ice wedges. He hypothesized that sills formed at the same time as the muck and, in his opinion, the muck was of aeolian origin and its freezing occurred almost simultaneously with deposition (**Supplementary Quote S47**).

REACHING MODERN TIMES: TABER'S "ORIGIN OF GROUND ICE"

Taber (1943), who spent the summer of 1935 studying permafrost in Alaska, published the first comprehensive monograph on permafrost in Alaska. The content of this important paper, the history of its writing and publication, acceptance by peers, and its legacy were discussed in the recent review by Nelson and French (2021). Here we discuss mainly one chapter of this monograph—"Origin of ground ice"—in which Taber explained his vision of the origin of Yedoma.

In the previous decades before his paradigm-changing monograph, Taber performed outstanding laboratory experiments and developed fundamentals of still valid views on the impact of soil freezing on properties of frozen ground and the associated frost heave (Taber, 1930). There is no doubt that Taber's contribution to permafrost science and engineering was enormous. Taber visited Alaska during the time of extensive active gold mining and observed Yedoma exposures in open pits in both the Fairbanks area and the Seward Peninsula. Taber understood the existence of epigenetic and syngenetic permafrost and indicated that, in an attempt to solve the problems of permafrost formation and the development of ground ice, one should consider four scenarios (Taber, 1943, p. 1504):

1) The deposits were formed during a warmer climate and subsequently frozen as a result of climatic conditions now prevailing;
2) deposition and freezing occurred simultaneously under climatic conditions now prevailing;
3) the deposits were formed during a warmer climate and subsequently froze as a result of a change to a colder Pleistocene climate; and
4) deposition and freezing took place simultaneously during a Pleistocene climate that is colder than what is now prevailing."

In terms of the origin of Yedoma, scenarios 1) and 2) contradict the presence of well-preserved remnants of mammoths and other prehistoric animals whose presence in the deposits is only possible in a frozen state and, therefore, only permafrost formation during the Pleistocene should be considered. Unfortunately, Taber did not discuss details of syngenetic permafrost formation (scenario 4). He applied his understanding of the formation of frozen soil from his laboratory experiments to natural processes and features that were completely new to him.

Taber's experiments reproduced epigenetic permafrost formation in both closed and open systems. The experiments did not include processes representative of simultaneous soil deposition and freezing, the existence of a periodically thawed soil at the surface, and they excluded the possibility of a surface water supply to a soil undergoing freezing. Taber concluded that the Yedoma sediment accumulated before its freezing that occurred downward from the surface, and the ice-rich soil and ice wedges were formed as a result of epigenetic freezing of soil in an open system with water migrating from underlying gravel where it was subjected to hydrostatic pressure.

During his field studies, Taber noticed extremely high water content of soil, yet he did not comment on it. We now know that it is impossible to achieve such high water contents from experiments with epigenetic soil freezing. Taber (1943, page 1526) dismissed all existing hypotheses of ice formation in Yedoma and found that "none of the older hypotheses is competent from the standpoint of physics." Building on his numerous laboratory experiments and interpretation of field observations, Taber outlined a new hypothesis of the origin of ground ice in Yedoma. Its main idea was that ice lenses formed a layered cryostructure and that ice lenses and ice wedges were developed in one process of ice segregation.

Taber separated the accumulation of silt and its freezing in time and stated that "freezing to a depth of several hundred feet, with the formation of great masses of ground ice, required a very long time" (Taber 1943, p. 1533–1534). This "very long time" is

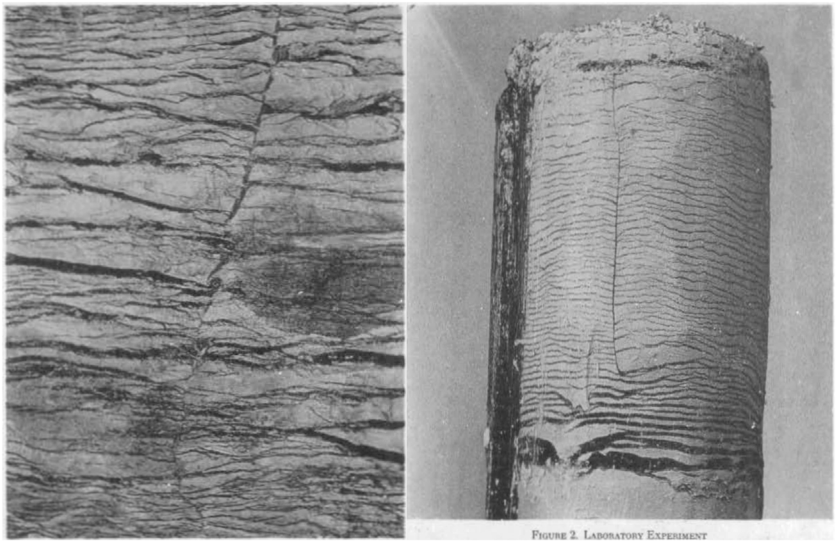

FIGURE 11 | Cryostructures of frozen soils (Taber, 1943). Left—from the exposure in an underground cold-storage excavation at Deering, Alaska; Right—from a laboratory experiment.

critical to Taber's new hypothesis. He believed that the small-scale polygonal structure formed in his experiments, continuing for days, could reach the size of ice-wedge polygons if freezing continued for thousands of years.

To prove his idea, Taber described an exposure in an underground cold-storage excavation at Deering (Alaska), which he found to be among the best and most remarkable exposures that he had ever examined. He compared a photograph of this exposure with a photograph taken from his experiments, and they show a perfect match (**Figure 11**). Unfortunately for Taber, the cryostructure of the exposed soil was not typical of Yedoma based on our present-day knowledge.

In the 1940–1960s, soils that we now identify as Yedoma, were described in various areas of Alaska including Seward Peninsula, the Yukon Flats, and the Yukon-Tanana uplands, and most researchers supported an aeolian genesis of soil (Black, 1951; Péwé, 1955, 1975; Williams, 1962; Hopkins, 1963; Sellmann, 1967).

STUDIES IN GERMANY AND THE FURTHER DEVELOPMENT OF THE ICE-WEDGE THEORY IN RUSSIA AND NORTH AMERICA

Sörgel (1936), studying ice-wedge casts in Thuringia, Germany, stated that "what diluvial ice wedges or wedge crevasses show in shape differences compared to Alaskan ice wedges is explained within the same genetic principle by the special conditions in the periglacial area at the time of diluvial ice wedge formation. These shape differences also confirm the ice wedge nature of the diluvial wedge crevasses." He came to an idea that the accumulation of sediment and formation of wedge ice can occur simultaneously. Earlier, Leffingwell (1915) mentioned such a process in relation to accumulation of peat. Sörgel's paper could have been a very important step in the explanation of Yedoma genesis, even if it had not directly dealt with Yedoma deposits. Unfortunately, this did not happen, and his paper was ignored. Scientists from the Obruchev Permafrost Institute, working in Central Yakutia, were mainly led by Grigoriev's ideas, Arctic geologists in Russia agreed with von Toll, and Taber worked hard to explain wedge ice as segregated.

Another important paper, which could have helped to explain the formation of massive ice in Yedoma, was written by Gallwitz (1949). Based on ice-wedge casts studies in Germany, he distinguished two types of ice wedges (epigenetic and syngenetic) and tried to derive information about permafrost conditions from the ice-wedge shapes. The importance of the Gallwitz' work for understanding of simultaneous formation of ice wedges and accumulation of sediment was stressed by Shumskii (1960).

Alexander I. Popov (1952), a scientist of the Obruchev Permafrost Institute, was the first to propose a hypothesis that led to the solution of the Yedoma formation problem. Working on the Taymyr Peninsula in 1949, Popov described ice wedges in a floodplain deposit and in the first terrace of the Mamontova River. He concluded that the formation of ice wedges takes place on a floodplain and the growth of ice occurs upwards and sideways accompanied by an increase in deposited floodplain sediments. Popov (1952, p. 17) concluded: "If ice growth is related to the mode of sediment accumulation, then we should also consider changes in this environment, i.e., epeirogeny dips and rises of alluvial plains. The correlation between the rate of sinking or uplift of an alluvial plain, the amount of water in the flood, the thickness of the annually accumulated sediment, and its composition determines the conditions of ice accumulation. Depending on the relation of these factors, either thick or thin ice is likely to accumulate, as well as the expansion of wedges sidewise."

FIGURE 12 | Photo of Yedoma by Vollosovich (1909), which was used as an illustration by Popov (1952).

Popov also observed foliations in the ice that were similar to the foliations on photographs taken by von Bunge and published by von Toll (1895). Before his first publication on the origin Yedoma, Popov had not personally seen Yedoma exposures and the photograph (**Figure 12**) in his publication was copied from a work by Vollosovich (1909). Popov extrapolated the processes of syngenetic permafrost formation involving the simultaneous growth of ice wedges that he had observed on a floodplain to the larger scale of Yedoma formation.

In this unifying connection, Popov was primary responsible for resolving the mystery of Yedoma genesis in spite of limiting Yedoma formation to floodplains of Arctic rivers. Popov's idea was proven a few years later by researchers of the Obruchev Permafrost Institute in Northern and Central Yakutia (Shumskii, 1952; Katasonov, 1954; Vtyurin, 1955; Korkina, 1959). (Shumskii (1952), p. 143) wrote about difficulties they encountered during these studies: "The mystery of the nature of the ice was due to its shape and the lack of anything resembling it among modern formations and the lack of direct observation of its formation. The relationship between fossil ice and soil is complicated and it requires hard work to clarify it. Exposures observed in natural environments allowed different interpretations."

Under the impact of Popov's work, Yedoma studies by the Obruchev Permafrost Institute in Central and Northern Yakutia were subsequently based on understanding the syngenetic nature of Yedoma involving sedimentation and ice-wedge formation occurring simultaneously. Among numerous results of these productive studies, there is a clarification of the Yedoma appearance in different projections by Shumskii (1959) which explains a puzzling and often confusing appearance of soil and massive ice in Yedoma exposures (**Figure 13**).

Russian Arctic geologists have had reservations about the explanation for Yedoma formation by permafrost scientists. Gusev (1954, 1958) still considered underground ice of Yedoma as buried firn or buried icings. Ermolaev visited Oyagossky Yar in 1968 and did not recognize ice wedges there (Ermolaev and Dibner, 2009).

Another important problem of Yedoma studies is the origin of sediments that host large syngenetic ice wedges. According to Popov (1967), the most favorable conditions for the syngenetic growth of ice wedges take place on floodplains, deltas, and in other similar depositional environments associated with tectonic lowering of the terrain, and in climate with low snow precipitation. He believed that Yedoma had been formed in such an environment. This was a guideline for numerous scientists in Russia for many decades even though some of them noticed the absence of the channel facies beneath a "floodplain deposit" (e.g., Romanovskii, 1958).

Shumskii et al. (1955) did not limit Yedoma formation to the floodplain environment. They stated (pp. 15–16): "If, simultaneously with the formation of ice wedges, new sediments accumulate on the soil surface—the growth of peatlands in swampy lowlands, alluvium deposits in river floodplains, slopewash at the foot of slopes, etc.—the upper boundary of continuous frozen strata gradually rises as the ground surface rises, and with it, ice wedges grow. Under such conditions, the ice wedges grow not only in width, but also upward, penetrating the accumulating strata of frozen deposits to their full thickness." This important insight had been unnoticed by permafrost researchers studying Yedoma, possibly because the publication addressed geological engineers specifically and not permafrost scientists, and as a result, the alluvial theory had prevailed for years.

An important deviation from the alluvial theory of Yedoma formation was work done by Gravis (1969). His detailed studies of frozen soil in numerous deep boreholes and pits in the foothills of the Kular Range in Northern Yakutia showed that an accumulation of Yedoma with tall ice wedges and typical cryostructures resulted from the accumulation of slope deposits.

Earlier (Schirrmeister et al., 2013) we distinguished between the dominant aeolian Yedoma genesis in Alaska/Canada and varying formation conditions in Siberia. In Russia, the aeolian theory was not popular. While Gravis' work was agreeably

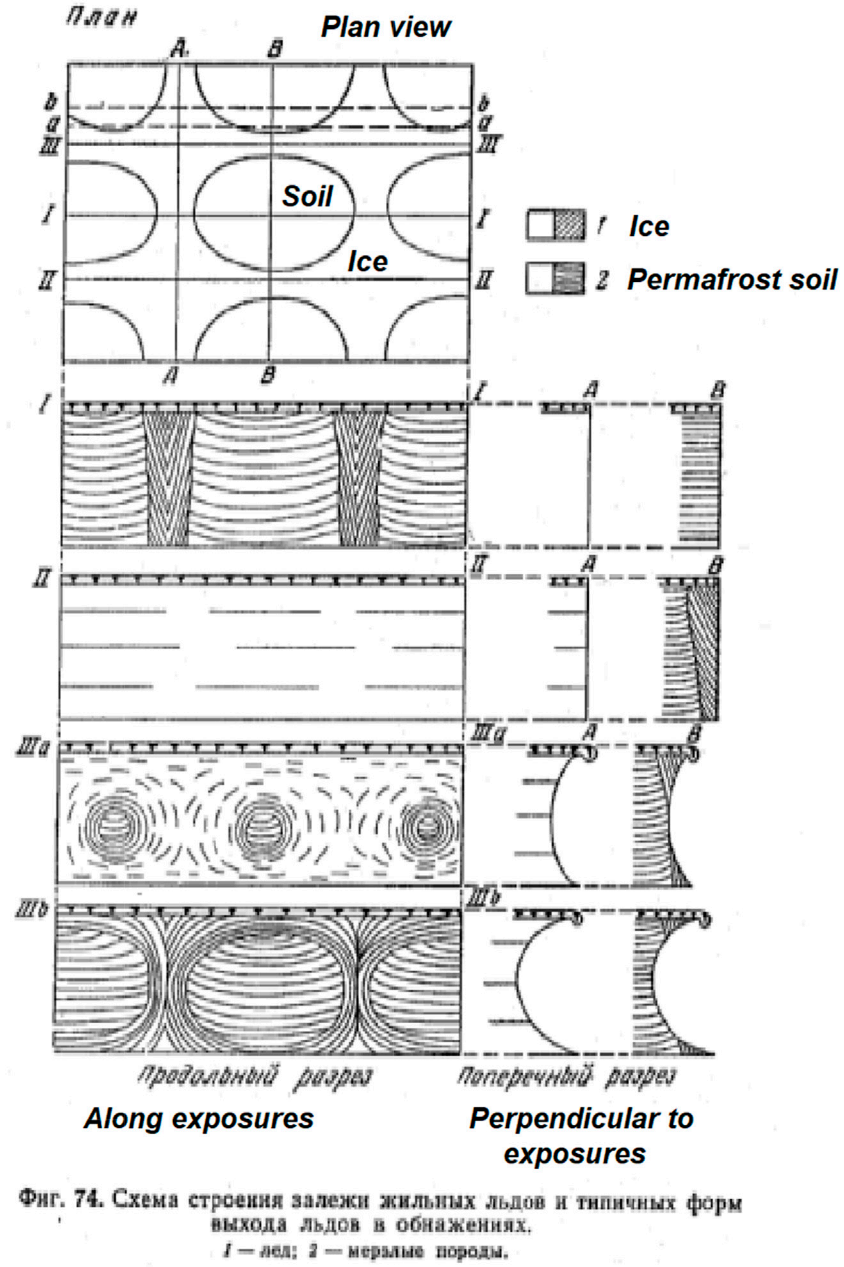

FIGURE 13 | Appearance of ice wedges and adjacent soil in exposures with different projections (Shumskii, 1959). Top image—plan view of the ice-wedge network; I, II, III a, III b—projections along exposures (visual appearance in the exposures); A, B—projections perpendicular to exposures (cross sections).

accepted by many permafrost scientists in Russia, the hypothesis of an aeolian genesis of Yedoma as proposed by Tomirdiaro (1978) met fierce opposition. His appeal to a similar opinion held by Péwé (1955) on the origin of Yedoma in Alaska did not help.

Konishchev (1981) supported the polygenetic origin of Yedoma and presumed that it could form in fluvial, slope, and lacustrine deposits. Zhestkova et al. (1982, 1986) agreed with the polygenetic origin too: they considered Yedoma as a climatic phenomenon because the mode of sediment accumulation did not restrict the formation of Yedoma. They also pointed out the importance of pedological processes and vegetation in the formation of properties of Yedoma and suggested considering Yedoma as a gigantic polypedon.

Extensive Yedoma studies during and after the 1950s had an enormous impact on the permafrost science. We agree with Konishchev (1981), who believed that cryolithology as part of permafrost science was triggered by the study of Yedoma genesis. He divided the study of massive ground ice into two stages. The first stage during the 19th and the first half of the 20th centuries involved the confrontation between supporters of a glacial origin and the proponents of an ice-wedge origin for the development of massive ground ice. A way out of this impasse was the concept of syngenetic growth of polygonal wedge ice and the simultaneous accumulation of host sediments as proposed by Popov, thus opening the door to the second (modern) stage of ground-ice studies.

After the long-held theory of a glacial origin of Yedoma there is tendency now to explain any large body of underground ice as wedge, segregated, or intrusive ice (Dubikov and Koreisha, 1964; Gasanov, 1969; Baulin and Dubikov, 1970; Mackay, 1971). Robust evidence of buried glacier ice has been found in Canada and Russia (e.g., Solomatin, 1986; Kokelj et al., 2017) but, ironically, it is currently difficult to convince the scientific community that buried glacier ice may exist in lowland areas (e.g., Sheinkman, 2017; Vasil'chuk, 2012). Recent findings (Anisimov et al., 2006; Basilyan et al., 2008) showed that buried glacier ice occurs in some parts of the New Siberian Islands, and sites of occurrence, properties and appearance of this ice are different from those that had been described in these areas by von Toll and von Bunge.

The origin of Yedoma is now considered a solved problem. Although discussions on the mode of sediment accumulation at specific Yedoma sites remain open, permafrost scientists agreed that Yedoma is late-Pleistocene syngenetic permafrost penetrated by ice wedges. This common understanding has helped to concentrate the attention of scientists on Yedoma as an outstanding and maybe the best source of information regarding the environment of the late Pleistocene. The number of Yedoma studies has been growing, and Yedoma has become one of the most intensive areas of permafrost research. The most recent synthesis article in English was published in the Encyclopedia of Quaternary Science (Schirrmeister et al., 2013).

CONCLUSION

In the beginning of the 19th century, the scientific world was introduced to an extraordinary geologic feature—Yedoma permafrost. It appeared as a strange combination of big masses of underground ice and deposits containing remnants of extinct Pleistocene animals, including mammoths. Since then, numerous geologists, geographers, and biologists proposed many hypotheses to explain the origin of this feature. They focused their attention predominantly on the ice and didn't consider the soil as an important component of Yedoma. Most of scientists at the time ignored soil completely, while others considered it as later inclusions within the ice. The two-dimensional appearance of Yedoma in exposures was often confusing. Explanations of ice genesis by geologists based on their previous knowledge have been unsuccessful. Features proposed in some hypotheses, like buried lake ice, have never been observed. The obsession with the origin of massive ice in Yedoma blocked scientific studies for many years.

The erroneous opinions of prominent and influential scientists prevailed over the currently accepted idea, proposed by Dr. Alexander von Bunge, and delayed attaining the solution of Yedoma origin for over 50 years. History shows that a mere hypothesis without ways for verification has a very low possibility to be fruitful. Chamberlin (1897) warned of the danger of premature theories: "The habit of precipitate explanation leads rapidly on to the development of tentative theories. The explanation offered for a given phenomenon is naturally, under the impulse of self-consistency, offered for like phenomena as they present themselves, and there is soon developed a general theory explanatory of a large class of phenomena similar to the original one. This general theory may not be supported by any further considerations than those which were involved in the first hasty inspection. For a time, it is likely to be held in a tentative way with a measure of candor. With this tentative spirit and measurable candor, the mind satisfies but the thoroughness, the completeness, the all-sidedness, the impartiality, of the investigation. It is in the tentative stage that the affectations enter with their blinding influence."

The search for the origin of Yedoma shows that when confronting new and extraordinary phenomena, both prominent scientists and young researchers have an equal chance to propose a valuable idea. It is interesting to note that in this controversy two medical doctors—Figurin and von Bunge—were much closer to deciphering the origin of Yedoma than many prominent geologists and geographers of their time. It seems that for a completely new problem, previous experience is not always an advantage but can be a burden that closes the mind to new ideas. As Kuhn (1970) noticed, "a new theory, however special its range of application, is seldom or never just an increment to what is already known. Its assimilation requires the reconstruction of prior theory and the re-evaluation of prior fact, an intrinsically revolutionary process that is seldom completed by a single man and never overnight."

After the mystery of Yedoma origin was generally solved as being syngenetic permafrost penetrated by ice wedges formed during the late Pleistocene, numerous international and interdisciplinary studies have been conducted in Russia, Alaska, and Canada. They have shown that during its formation Yedoma sequestered significant amounts of organic carbon and preserved a treasure of information on the environment of the late Pleistocene including its climate, vegetation, wildlife, and an extensive accumulation of syngenetic permafrost.

AUTHOR CONTRIBUTIONS

YS designed this study and drafted the first version of the manuscript. TJ compiled a map of Yedoma locations mentioned in the manuscript. YS, MK, and AV reviewed the Russian language references, LS and JS reviewed the German language references, and MWJ reviewed the French language references. YS, DF, MK, TJ, and MWJ reviewed the English language references. All co-authors contributed to the manuscript writing and editing process.

FUNDING

This study was supported by the National Science Foundation (NSF) grants OPP-1820883, OPP-1806213, and NNA-1928237. AV was supported by the Russian State Research Program No. 121041600043-4. This review was part of the Action Group "The Yedoma Region: A Synthesis of Circum-Arctic Distribution and Thickness," funded by the International Permafrost Association (IPA) to JS.

ACKNOWLEDGMENTS

We acknowledge the editor Duane Froese and reviewers Mary Edwards, Fritz Nelson, and Vladimir Tumskoy for their constructive critique and useful suggestions. We also greatly appreciate Joan Welc-LePain's help in editing the manuscript.

SUPPLEMENTARY MATERIAL

The Supplementary Material for this article can be found online at: https://www.frontiersin.org/articles/10.3389/feart.2021.757891/full#supplementary-material

REFERENCES

Adams, M. F. (1807). Relation d'un voyage à la mer glaciale et decouverte des restes d'un mamouth. St. Petersbourg. *Journal du Nord* XXXII, 633–650 (In French).

Adams, M. F. (1808). Some Accounts of a Journey to the Frozen Sea and the Discovery of the Remains of a mammoth. *Philadel. Med. Phys. J. Part 1* 3, 120–137.

Anisimov, M. A., Tumskoy, V. E., and Ivanova, V. V. (2006). Tabular Massive Ice of New Siberian Islands as a Relic of Ancient Glaciation. *Mater. glaciological Stud.* 101, 143–145. (in Russian).

Basilyan, A. E., Nikolskiy, P. A., and Anisimov, M. A. (2008). Pleistocene Glaciation of New Siberian Islands – No More Doubt. *News Int. Polar Year 2007/2008* #12, 7–9. (in Russian).

Baulin, V. V., and Dubikov, G. I. (1970). Tabular Bodies of Massive Ice. *Proc. PNIIIS* 2, 175–1993. (In Russian).

Beechey, F. W. (1831). *Narrative of a Voyage to the Pacific and Beering's Strait*, Vols. 1 and II. London: Henry Colburn and Richard Bentley.

Birkengof, A. L. (1933). "Observations on forest and Permafrost," in *Proceedings of Commission on Permafrost Studies*. Editor V. A. Obruchev (Leningrad: USSR Academy of Sciences), Vol. 3, 41–58. (In Russian).

Black, R. F. (1951). Eolian Deposits of Alaska. *Arctic* 4, 89–111. doi:10.14430/arctic3938

Cantwell, J. C. (1887). "A Narrative Account of the Exploration of the Kowak River, Alaska, under the Direction of Capt. Michael A. Healy, Commanding U.S. Revenue Steamer Corwin," in *Report of the Cruise of the Revenue Marine Steamer Corwin in the Arctic Ocean in the Year 1885*. Editor M. A. Healy (Washington, D.C: Government Printing Office), 21–52.

Cantwell, J. C. (1896). "Ice-cliffs on the Kowak River," in *The National Geographic Magazine* (Washington, D.C: The National Geographic Society), Vol. VII (10), 345–346.

Chamberlin, T. C. (1897). Studies for Students: The Method of Multiple Working Hypotheses. *J. Geology.* 5, 837–848. doi:10.1086/607980

Choris, L. (1822). *Voyage pittoresque autour du monde*. Paris: Impr. de Firmin Didot. (In French).

Dall, W. H. (1881). Notes on Alaska and the Vicinity of Bering Strait (Extract from a report to C.P. Patterson, Supt. Coast and Geodetic Survey). *Am. J. Sci.* XXI, 104–111. doi:10.2475/ajs.s3-21.122.104

Dall, W. H., and Harris, G. D. (1892). *Correlations Papers – Neocene. Bulletin of the United States Geological Survey*. Washington D.C.: Government Printing Office.

Dawson, G. M. (1894). Notes on the Occurrences of mammoth-remains in the Yukon District of Canada and in Alaska. *Q. J. Geol. Soc.* 50 (1), 1–9. doi:10.1144/gsl.jgs.1894.050.01-04.03

Dubikov, G. I., and Koreisha, M. M. (1964). Fossil Intrusive Ice on Yamal Peninsula. *Trans. USSR Acad. Sci. Geography* 5, 55–65. (In Russian).

Ermolaev, A. M., and Dibner, V. D. (2009). *Arctic Scientist, Gulag Survivor. The Biography of M.M. Ermolaev*. Calgary, Alberta: University of Calgary Press.

Ermolaev, M. M. (1932). Description of Geology and Geomorphology of Bol'shoy Lykhovsky Island. *Proc. SOPS USSR Acad. Sci.* 7, 147–226. (In Russian).

Figurin, A. E. (1823). "Notes by Medical Doctor Figurin on Natural History Observed in Ust-Yansk and its Vicinities," in *Siberian Proceedings*. Editor G. Spasskiy, 4, 185–248. (In Russian).

Gallwitz, H. (1949). Eiskeile und glaziale Sedimentation (Ice Wedges and Glacial Sedimentation). *Geologica* 2, 5–26. (in German).

Gasanov, Sh. Sh. (1969). *Structure and History of Formation of Permafrost of East Chukotka*. Moscow: Nauka. (In Russian).

Geikie, J. (1894). *The Great Ice Age and its Relation to the Antiquity of Man*. Third edition. London: Edward Stanford.

Gilmore, C. W. (1908). *Smithsonian Exploration in Alaska in 1907 in Search of Pleistocene Fossil Vertebrates*. Smithsonian Miscellaneous Collection. Part of volume LI, No 1807.

Gorodkov, B. N. (1948). Pleistocene Glacial Landscapes in Northern Asia. *Proc. Acad. Sci. USSR* LXI (3), 513–516. (In Russian).

Grave, N. A. (1944). Fossil Ice of the Watershed of the Lena and Aldan Rivers. *Proc. Obruchev Permafrost Inst.* 4, 10–32. (In Russian).

Gravis, G. F. (1969). *Slope Deposits in Yakutia*. Moscow: Nauka. (In Russian).

Grigoriev, A. A. (1927). "Geomorphology of Yakutia," in *Commission on Studies of Yakut Republic* (Leningrad: Academy of Sciences), Vol. 32, 39–89. (In Russian).

Grigoriev, A. A. (1930). Permafrost and Ancient Glaciation. *Proc. SOPS USSR Acad. Sci.* 80, 43–104. (In Russian).

Gusev, A. I. (1954). On a Genesis of Fossil Ice. *Proc. Inst. Arctic Geology.* 43 (Issue 3), 173–183. (In Russian).

Gusev, A. I. (1958). On Stratigraphy of Quaternary Deposits of Western Part of Coastal Plain. *Proc. Inst. Arctic Geology.* 80 (Issue 5), 79–86. (In Russian).

Harrington, G. L. (1918). *The Anvik-Andreafski Region Alaska*. United States Geol. Surv. Bull., 525.

Herz, O. F. (1904). *Frozen Mammoth in Siberia: Ann. Rep* (Washington: Smithsonian Institution), 611–625.

Hooper, C. L. (1884). *Report of the Cruise of the U.S. Revenue Steamer Thomas Corvin, in the Arctic Ocean*. Washington D.C.: Government Printing Office, 1881.

Hopkins, D. M. (1963). *Geology of the Imuruk Lake Area, Seward Peninsula, Alaska*. Washington, D.C.: U.S. Government Printing Office. U.S. Geological Survey Bulletin 1141-c.

Katasonov, E. M. (1954). *Lithology of Frozen Quaternary Deposits (Cryolithology) of Yana Coastal Plain* (Moscow: The Obruchev Permafrost Institute). Ph.D. Thesis. (In Russian).

Kokelj, S. V., Lantz, T. C., Tunnicliffe, J., Segal, R., and Lacelle, D. (2017). Climate-driven Thaw of Permafrost Preserved Glacial Landscapes, Northwestern Canada. *Geology* 45 (4), 371–374. doi:10.1130/G38626.1

Kolchak, A. V. (1906). *The Last Expedition to Bennett Island Sent by Academy of Sciences in Search for Baron Toll*. News of Russian Imperial Geographic Society. Vol. XLII issues II-III: 487–519. St. Petersburg (In Russian)

Konishchev, V. N. (1981). *Formation of Dispersed Rocks in Cryo-Lithosphere*. Novosibirsk: Nauka. (In Russian).

Korkina, R. I. (1959). On Genesis of Fossil Ice of Central Yakutia. Regional Permafrost-Geophysical Investigations. *Proc. Obruchev Permafrost Inst.* 15, 113–131. (in Russian).

Kuhn, T. S. (1970). "The Structure of Scientific Revolutions," in *International Encyclopedia of Unified Science* (Chicago: The University of Chicago Press), Vol. II.

Leffingwell, E. K. (1915). Ground-ice Wedges the Dominant Form of Ground-Ice on the north Coast of Alaska. *J. Geology.* 23 (No 7), 635–654. doi:10.1086/622281

Leffingwell, E. K. (1919). *The Canning River Region Northern Alaska*. Washington D.C: United States Geological Survey, Professional Paper 109.

Lopatin, I. A. (1876). Some Information on Ice Strata in Eastern Siberia. *Appendix 1 Proc. Acad. Sci.* XXIX, 3–32. (In Russian).

Mackay, J. R. (1971). The Origin of Massive Beds in Permafrost, Western Arctic Coast, Canada. *Can. J. Sci.* 8 (No 4), 397–4244. doi:10.1139/e71-043

Maddren, A. G. (1905). *Smithsonian Exploration in Alaska in 1904, in Search of Mammoth and Another Fossil Remains*. Smithsonian miscellaneous collections. Washington: The Smithsonian Institution, Vol. XLIX.

Mendenhall, W. C. (1902). *Reconnaissance from Fort Hamilton to Kotzebue Sound, Alaska*. Washington: Government Printing Office. United States Geological Survey Professional paper no. 10.

Muir, J. (1917). *The Cruise of the Corwin: Journal of the Arctic Expedition of 1881 in Search of De Long and the Jeannette*. Cambridge: The Riverside Press.

Murzaev, E. M. (1984). *Dictionary of Folk Geographical Terms*. Moscow: Mysl. (In Russian).

Nelson, F. E., and French, H. M. (2021). Stephen Taber and the Development of North American Cryostratigraphy and Periglacial Geomorphology. *Permafrost and Periglac Process* 32, 213–230. doi:10.1002/ppp.2096

Obruchev, V. A. (1892). Soil Ice and Conditions of Conservation of Post-Tertiary Carcasses in Northern Siberia of Baron Toll. *Izvestia Russkogo Geograficheskogo obshestva* 23 (2), 1–14. (In Russian).

Obruchev, V. A. (1931). Signs of the Ice Age in North and Central Asia. *Bull. Comm. Quat. Stud.* Issue 3, 43–120. USSR Academy of Sciences. (In Russian).

Péwé, T. L. (1955). Origin of the upland silt Near Fairbanks, Alaska. *Bull. Geol. Soc. Am.* 67, 699–724.

Péwé, T. L. (1975). *Quaternary Geology of Alaska*. U.S. Geological Survey professional paper 835. Washington D.C.: United States Government Printing Office.

Popov, A. I. (1952). Frost Cracking and Problems of Fossil Ice. Permafrost in Different Parts of the USSR. *Proc. Obruchev Permafrost Inst.* IX, 81–89. (In Russian).

Popov, A. I. (1967). *Cryogenic Phenomena in the Earth Crust (Cryolithology)*. Moscow: Moscow University Press. (in Russian).

Porsild, A. E. (1938). Earth Mounds in Unglaciated Arctic Northwestern America. *Geographical Rev.* 28 (No. 1), 46–58. doi:10.2307/210565

Prindle, L. M., Katz, F. J., and Smith, P. S. (1913). *A Geological Reconnaissance of the Fairbanks Quadrangle, Alaska*. United States Geol. Surv. Bull.. Washington: Government Printing Office, 525.

Quackenbush, L. S. (1909). Notes of Alaskan mammoth Expeditions of 1907 and 1908. *Bull. Am. Mus. Nat. Hist.* 26, 87–130.

Richardson, J. (1854). in *The Zoology of the Voyage of H.M.S. Herald, under the Command of Captain Henry Kellett, R.N., C.B., during the Years 1845-51*. London: Reeve and Co, Vol. III.

Romanovskii, N. N. (1958). Paleogeographic Conditions for the Formation of Quaternary Deposits on Bol'shoy Lyakhovsky Island (New Siberian Islands). *Issues Phys. Geogr. polar countries* 1, 68–81. (in Russian).

Russell, I. C. (1890). Notes on the Surface Geology of Alaska. *Bull. Geol. Soc. Am.* 1, 99–162. doi:10.1130/gsab-1-99

Saks, V. N. (1947). Quaternary Glaciation of Siberia. *Nature (Priroda)* 4, 16–25. (In Russian).

Schirrmeister, L., Froese, D., Tumskoy, V., Grosse, G., and Wetterich, S. (2013). "PERMAFROST and PERIGLACIAL FEATURES | Yedoma: Late Pleistocene Ice-Rich Syngenetic Permafrost of Beringia," in *Encyclopedia of Quaternary Sciences*. Editors S. A. Elias and C. J. Mock. Second edition (Amsterdam: Elsevier), 2, 542–552. doi:10.1016/b978-0-444-53643-3.00106-0

Seemann, B. (1853). *Narrative of the Voyage of H.M.S. Herald, under the Command of Captain Henry Kellett, R.N., C.B., during the Years 1845-51*. London: Reeve and Co, Vol. II.

Sellmann, P. V. (1967). *Geology of the USA CRREL Permafrost Tunnel, Fairbanks, Alaska*. Hanover, New Hampshire: US Army CRREL. Technical Report 199.

Sheinkman, V. S. (2017). Glaciation of Siberia and the Problem of Massive Ice Beddings. *Ice and Snow (Lyod i Sneg)* 57 (4), 527–542. (in Russian). doi:10.15356/2076-6734-2017-4-527-542

Sher, A. V. (1997). "Yedoma as a Store of Paleoenvironmental Records in Beringia," in Beringia Paleoenvironmental Workshop, Florissant, CO, September 20–23, 1997, Abstracts and Program. Editors S. Elias and J. Brigham-Grette, 92–94.

Shumskii, P. A. (1952). "Studies of Fossil Ice in Central Yakutia," in *Permafrost Research in Republic of Yakutia* (Moscow: USSR Academy of Sciences), 3, 142–161. (In Russian).

Shumskii, P. A. (1959). "Underground Ice," in *Fundamentals of Geocryology (Permafrost Science), Part 1 General Geocryology*. Editors P. F. Shvetsov and B. A. Dostovalov (Moscow: USSR Academy of Sciences), 274–327. (In Russian).

Shumskii, P. A. (1960). "On Genesis of Wedge Underground Ice," in *Collection of Articles on General Permafrost Studies. Proceedings of Obruchev Permafrost Institute*. Editor A. I. Efimov (Moscow: USSR Academy of Sciences), Vol. 16. (In Russian).

Shumskii, P. A., Shvetsov, P. F., and Dostovalov, B. N. (1955). *Peculiarities of Geotechnical Investigations in the Areas with Underground Wedge Ice*. Moscow: USSR Academy of Sciences. (In Russian).

Smith, P. S. (1993). *The Noatak-Kobuk Region Alaska*. Washington: United States Geological Survey, Bulletin, 536.

Solomatin, V. I. (1986). *Petrogenesis of Underground Ice*. Novosibirsk: Nauka. (In Russian).

Sörgel, W. (1936). Diluviale Eiskeile (Diluvial Ice Wedges). *Z. der Deutschen Geologischen Gesellschaft* 88, 223–247. (In German).

Strauss, J., Laboor, S., Schirrmeister, L., Fedorov, A. N., Fortier, D., FroeseFuchs, D. M., et al. (2021). Circum-Arctic Map of the Yedoma Permafrost Domain. *Front. Earth Sci.* 9. doi:10.3389/feart.2021.758360

Sumgin, M. I. (1927). *Permafrost in USSR*. Moscow-Leningrad: USSR Academy of Sciences. (In Russian).

Taber, S. (1930). The Mechanics of Frost Heaving. *J. Geology.* 38 (4), 303–317. doi:10.1086/623720

Taber, S. (1943). Perennially Frozen Ground in Alaska: its Origin and History. *Geol. Soc. America Bull.* 54 (10), 1433–1548. doi:10.1130/gsab-54-1433

Tolmachev, I. P. (1903). "Ground Ice from the Berezovka River (In Northeast Siberia)," in *Scientific Results of the Expedition Sent by Imperial Academy of Sciences to Excavate a mammoth Found at the Berezovka River in 1901* (Sankt-Peterburg: Imperial Academy of Sciences), Vol. 1, 125–139. (In Russian).

Tolmachev, I. P. (1906). News from Khatanga Expedition under Command of Tolmachev (From a Letter to Chernyshev). *Proc. Imperial Russ. Geographical Soc.* XLII, 785–796. (In Russian).

Tolmachev, I. P. (1911). *Along the Chukchi Coastline of the Arctic Ocean*. Sankt-Peterburg: Economic Typo-Lithography. (In Russian).

Tolmachev, I. P. (1928). "The Geology of Arctic Eurasia and its Unsolved Problems," in *Problems of Polar Research*. Editor W. L. G. Joerg (New York: American Geographical Society), 75–90.

Tolmachoff, I. P. (1929). "The Carcasses of the Mammoth and Rhinoceros Found in the Frozen Ground of Siberia," in *Transactions of the American Philosophical Society New Ser.* (Philadelphia: The American Philosophical Society), Vol. 23, 1.

Tomirdiaro, S. V. (1978). in *Permafrost Second International Conference July 13-28, 1973, USSR Contributions* (Washington, D.C: National Academy of Sciences), 817–819.*Cryogenic-Aeolian Genesis of Yedoma deposit*

Tuck, R. (1940). *Origin of the Muck-silt Deposits at Fairbanks, Alaska*, 51. Bulletin of the Geological Society of America, 1295–1310. Geological Society of America Bulletin. doi:10.1130/gsab-51-1295

Turner, L. M. (1886). *Contributions to the Natural History of Alaska*. Washington: U. S. Army No. II. Government printing office. Arctic series of publications issued in connection with the signal service.

Tyrrell, J. B. (1904). Crystosphenes or Buried Sheets of Ice in the Tundra of Northern America. *J. Geol.* 12 (3), 232–236.

Tyrrell, J. B. (1917). *Frozen Muck in the Klondike District*, Ser. 3, V. 11. Ottawa: Transactions of the Royal Society of Canada, 39–46.Section IV.

van Everdingen, R.O. (Editor) (1998). *Multi-Language Glossary of Permafrost and Related Ground-Ice Terms* (Calgary: University of Calgary).

Vasil'chuk, Yu. K. (2012). "Classification of Massive Ice," in *Proceedings of the Tenth International Conference on Permafrost, June 25-29, 2012, Salekhard, Russia*. Editors V. P. Melnikov, D. S. Drozdov, and V. E. Romanovsky (Salekhard, Russia: The Northern Publisher), Vol. 2, 493–497.

Vollosovich, K. A. (1909). Recovering of Sanga-Yuryakh mammoth. *Proc. Imperial Acad. Sci. Part* 633, 437–458. (In Russian).

Vollosovich, K. A. (1915). Mammoth of Bol'shoy Lyakhovsky Island. *Proc. Mineralogical Soc.* 50, 305–338. (In Russian).

von Baer, K. M. (1842). *Notes for a Study of Ground Ice in Siberia*. Russian translation of the manuscript. Sankt-Peterburg - Moscow - Yakutsk: Mel'nikov Permafrost Institute, 2000. (in Russian).

von Bunge, A. A. (1883). "Natural History News from the Polar Station at the Mouth of the Lena River. From a Letter to the Academician L.V. Schrenck," in *Bulletin of the Imperial Academy of Sciences* (St. Petersburg: Imperial Academy of Sciences), Vol. X1, 581–622. (In German).

von Bunge, A. A. (1887). "Bericht über den ferneren Gang der Expedition. Reise nach den Neusibirischen Inseln. Aufenthalt auf der Großen Ljachof-Insel," in *Expedition zu den Neusibirischen Inseln und dem Jana-Lande (1885)*. Editors L. V. Schrenk and C. J. Maximovicz (St. Petersburg: Commissionare der Kaiserlichen Akademie der Wissenschaften), Vol. III, 231–284. Beiträge zur Kenntnis des russischen Reiches und der angrenzenden Länder. (In German).

von Bunge, A. A. (1895). "The Lena Expedition 1881-1884," in *Observations of the Russian Polar Station at the Lena Mouth*. Editors A. Tillo and A. Tillo (St. Petersburg: Russian Geographical Society), 1–96. Beobachtungen der russischen Polarstation an der Lenamündung. Expedition der Kaiserlichen Russischen Geographischen Gesellschaft. (In German).

von Bunge, A. A. (1903). Einige Worte zur Bodeneisfrage. *Proc. Imperial St. Petersburg Mineralogic Soc. ser.* 40, 203–209. (In German).

von Chamisso, A. (1821). "Remarks and Opinions, of the Naturalist of the Expedition," in *A voyage of Discovery into the South Sea and Beering's straits, for the purpose of exploring a north-east passage, undertaken in the years 1815-1818, at the expense of His Highness the Chancellor of the Empire, Count Romanzoff, in the ship Rurick, under the command of the lieutenant in the Russian Imperial Navy, Otto von Kotzebue* (London: Longman, Hurst, Rees, Orme, and Brown), Vol. 3.

von Chamisso, A. (1836). *A Voyage Around the World with the Romanzov Exploring Expedition in the Years 1815-1818 in the Brig Rurik (English Translation)*. Honolulu: University of Hawaii Press.

von Hedenström, M. (1830). *Excerpts on Siberia*. Sankt-Peterburg: Medical Department of Ministry of Internal Affairs. (In Russian).

von Kotzebue, O. (1821). *A voyage of Discovery into the South Sea and Beering's straits, for the purpose of exploring a north-east passage, undertaken in the years 1815-1818, at the expense of His Highness the Chancellor of the Empire, Count Romanzoff, in the ship Rurick, under the command of the lieutenant in the Russian Imperial Navy, Otto von Kotzebue*, Vol. 1. London: Longman, Hurst, Rees, Orme, and Brown.

von Maydel, G. (1894). *Journey in north-west Yakutia in 1868-1870. Appendix to LXXIV Notes of Imperial Academy of Sciences*. St. Petersburg: Imperial Academy of Sciences.

von Middendorff, A. T. (1860). "Orographie und Geognosie," in *Dr. A. Th. v. Middendorff's Sibirische Reise. Übersicht der Natur Nord- und Ost-Sibiriens*. Editor A. T. von Middendorff (St. Petersburg: Kaiserliche Akademie der Wissenschaften), 201–332. Bd. 4, Th. 1, Lieferung 2. S. (In German).

von Toll, E. V. (1891). "Ueber die Wechselbeziehungen zwischen dem Steineise, der Eiszeit und dem Mammut Neusibiriens," in *Verhandlungen des neunten deutschen Geographentages zu Wien* (Berlin: Verlag von Dietrich Reimer), 53–64. (In German).

von Toll, E. V. (1895). *Wissenschaftliche Resultate der von der Kaiserlichen Akademie der Wissenschaften zur Erforschung des Janalandes und der Neusibirischen Inseln in den Jahren 1885 und 1886 ausgesandten Expedition. Abtheilung 3. Die fossilen Eislager und ihre Beziehungen zu den Mammuthleichen. Mémoires de L'Académie impérials des Sciences de St. Pétersbourg VII Série, Tome XLII, No. 13.* St. Petersbourg: Commissionnaires de I'Académie Impériale des Sciences, 1–86. (In German).

von Toll, E. V. (1897). *Fossil Glaciers on New Siberian Islands and Their Relation to Corps of Mammoths and to the Ice Age*. St. Petersburg: Imperial Academy of Sciences. (In Russian).

von Toll, E. V. (1959). *Sailing on the yacht "Zaria"*. Editor P. V. Wittenburg (Moscow: Geographical Literature). (In Russian).

Vtyurin, B. I. (1955). *Underground Ice. Structure, Genesis, and Areas of Occurrence of Big Masses of Underground Ice and its Geomorphic Significance*. Moscow: Ph.D. thesis. Moscow State University. (In Russian).

Wilkerson, A. S. (1932). *Some Frozen Deposits in the Goldfields of Interior Alaska a Study of the Pleistocene Deposits of Alaska*. New York: American Museum Novitates, No 525, American Museum of Natural History.

Williams, J. R. (1962). *Geologic Reconnaissance of the Yukon Flats District, Alaska*. Washington, DC: U.S. Geological Survey Bulletin 111-H, 290–311.

Wittenburg, P. V. (1959). *Introduction to von Toll's Diary (Sailing on the yacht "Zaria")*. Moscow: Geographical Literature, 3–6. (In Russian).

Wrangel, F. (1841). *Journey along Northern Shore of Siberia and Ice Sea*. Part 2. Sankt-Peterburg. (In Russian).

Zhestkova, T. N., Shvetsov, P. F., and Shur, Y. L. (1982). in *Yedoma, a Climatic Formation* (Moscow: XI Congress of International Union for Quaternary Research), Vol. II, 389. . Abstracts. (In Russian).

Zhestkova, T. N., Shvetsov, P. F., and Shur, Y. L. (1986). "On Genesis of Yedoma," in *Geocryology Studies*. Editor E. D. Ershov (Moscow: Moscow State University), 108–113. (In Russian).

Conflict of Interest: Author MJ owns company Alaska Ecoscience. The remaining authors declare that the research was conducted in the absence of any commercial or financial relationships that could be construed as a potential conflict of interest.

The handling editor is currently organizing a Research Topic with one of theauthors LS.

Publisher's Note: All claims expressed in this article are solely those of the authors and do not necessarily represent those of their affiliated organizations, or those of the publisher, the editors and the reviewers. Any product that may be evaluated in this article, or claim that may be made by its manufacturer, is not guaranteed or endorsed by the publisher.

frontiers in Earth Science

ORIGINAL RESEARCH
published: 19 January 2022
doi: 10.3389/feart.2021.737237

Sources of CO_2 Produced in Freshly Thawed Pleistocene-Age Yedoma Permafrost

*Jan Olaf Melchert[1], Philipp Wischhöfer[1], Christian Knoblauch[2,3], Tim Eckhardt[2,3], Susanne Liebner[4,5] and Janet Rethemeyer[1]**

[1]Institute for Geology and Mineralogy, University of Cologne, Cologne, Germany, [2]Institute for Soil Science, Universität Hamburg, Hamburg, Germany, [3]Center for Earth System Research and Sustainability, Universität Hamburg, Hamburg, Germany, [4]German Research Centre for Geosciences (GFZ), Helmholtz Centre Potsdam, Potsdam, Germany, [5]Institute of Biochemistry and Biology, University of Potsdam, Potsdam, Germany

The release of greenhouse gases from the large organic carbon stock in permafrost deposits in the circumarctic regions may accelerate global warming upon thaw. The extent of this positive climate feedback is thought to be largely controlled by the microbial degradability of the organic matter preserved in these sediments. In addition, weathering and oxidation processes may release inorganic carbon preserved in permafrost sediments as CO_2, which is generally not accounted for. We used ^{13}C and ^{14}C analysis and isotopic mass balances to differentiate and quantify organic and inorganic carbon released as CO_2 in the field from an active retrogressive thaw slump of Pleistocene-age Yedoma and during a 1.5-years incubation experiment. The results reveal that the dominant source of the CO_2 released from freshly thawed Yedoma exposed as thaw mound is Pleistocene-age organic matter (48–80%) and to a lesser extent modern organic substrate (3–34%). A significant portion of the CO_2 originated from inorganic carbon in the Yedoma (17–26%). The mixing of young, active layer material with Yedoma at a site on the slump floor led to the preferential mineralization of this young organic carbon source. Admixtures of younger organic substrates in the Yedoma thaw mound were small and thus rapidly consumed as shown by lower contributions to the CO_2 produced during few weeks of aerobic incubation at 4°C corresponding to approximately one thaw season. Future CO_2 fluxes from the freshly thawed Yedoma will contain higher proportions of ancient inorganic (22%) and organic carbon (61–78%) as suggested by the results at the end, after 1.5 years of incubation. The increasing contribution of inorganic carbon during the incubation is favored by the accumulation of organic acids from microbial organic matter degradation resulting in lower pH values and, in consequence, in inorganic carbon dissolution. Because part of the inorganic carbon pool is assumed to be of pedogenic origin, these emissions would ultimately not alter carbon budgets. The results of this study highlight the preferential degradation of younger organic substrates in freshly thawed Yedoma, if available, and a substantial release of CO_2 from inorganic sources.

Keywords: yedoma ice complex, permafost, carbon cycle, climat change, thermokarst, radiocarbon, greenhouse gas

OPEN ACCESS

Edited by:
Lutz Schirrmeister, Alfred Wegener Institute Helmholtz Centre for Polar and Marine Research (AWI), Germany

Reviewed by:
Ted Schuur, Northern Arizona University, United States
Elchin Jafarov, Los Alamos National Laboratory (DOE), United States

****Correspondence:***
Janet Rethemeyer
janet.rethemeyer@uni-koeln.de

Specialty section:
This article was submitted to Cryospheric Sciences, a section of the journal Frontiers in Earth Science

Received: *06 July 2021*
Accepted: *23 December 2021*
Published: *19 January 2022*

Citation:
Melchert JO, Wischhöfer P, Knoblauch C, Eckhardt T, Liebner S and Rethemeyer J (2022) Sources of CO_2 Produced in Freshly Thawed Pleistocene-Age Yedoma Permafrost. Front. Earth Sci. 9:737237. doi: 10.3389/feart.2021.737237

INTRODUCTION

Permafrost deposits in the northern circumpolar regions contain about 1,300 to 1,600 Gt of organic carbon (OC) that accumulated over thousands of years and was stored at sub-zero temperatures (Schuur et al., 2015). More than one quarter, about 327–466 Gt OC, is stored in the loess-like Yedoma sediments that were deposited during the late Pleistocene and early Holocene in unglaciated areas of the Arctic region (Schirrmeister, 2011; Strauss et al., 2017). These up to 50 m thick sediments include massive syngenetic ice wedges (Schirrmeister, 2011) resulting in very high ground ice contents of up to 80 vol.% (Strauss et al., 2017), thus making Yedoma deposits especially vulnerable to rapid thaw in a warming world. The melting of the ground ice due to rising ground temperatures (Biskaborn et al., 2019) causes surface subsidence and thereby may expose the sedimentary OC abruptly to microbial degradation (Czudek and Demek, 1970; Grosse et al., 2011; Strauss et al., 2017; Nitzbon et al., 2020; Turetsky et al., 2020). In consequence, the previously freeze-locked organic matter (OM) is decomposed and released to the atmosphere as carbon dioxide (CO_2), methane (CH_4), and other greenhouse gasses (GHGs) causing a positive climate feedback (Schuur et al., 2015).

The extent of the permafrost-carbon feedback is still under debate because it not only depends on OC quantity but also on OM quality, i.e., microbial degradability, which is still uncertain due to the limited analytical data. Most studies assessing OM quality and degradability, respectively rely on incubation experiments at different temperatures (Schädel et al., 2014, Schädel et al., 2016). The results of these laboratory studies may not necessarily apply to natural, more complex conditions. Additionally, chemical characterizations of the OM have been used to differentiate potentially labile and more recalcitrant OC pools based on OC/N ratios (e.g., Schädel et al., 2014; Kuhry et al., 2020) and characteristic organic compounds used as indicators for OM bioavailability and stage of degradation, respectively (e.g., Routh et al., 2014; Strauss et al., 2015; Stapel et al., 2016; Tanski et al., 2017; Jongejans et al., 2021).

Yedoma deposits were assumed to contain OM that accumulated and was freeze-locked quickly and thus has not undergone intense decomposition processes. Less transformed OM is supposed to be more reactive and thus more easily degradable upon thaw, which was reflected by high CO_2 fluxes measured in some incubation studies (Dutta et al., 2006; Zimov et al., 2006; Knoblauch et al., 2013) and the presence of easily biodegradable substrates (Stapel et al., 2016; Jongejans et al., 2018). In contrast, other studies measured a higher degree of OM decomposition (Kuhry et al., 2020), which, however, did not result in lower respiration rates during some incubation studies (Weiss et al., 2016). The contrasting results may be attributed to the large spatial and temporal variability of OC contents and OM composition in Yedoma deposited under different environmental and climatic conditions (Strauss et al., 2015; Weiss et al., 2016; Stapel et al., 2018; Walz et al., 2018; Windirsch et al., 2020). In addition, thermokarst may alter the degradability of the ancient Yedoma OM by introducing younger material from overlying sediments and changing thermal and hydrological conditions (Grosse et al., 2011; Strauss et al., 2015; Wild et al., 2016). The mixing of sediments is particularly pronounced on retrogressive thaw slumps, a dynamic form of thermokarst in ice-rich areas, expanding inland by melting of the ground ice in the headwall (Lantuit and Pollard, 2008; Costard et al., 2021).

TABLE 1 | Sampling locations on Kurugnakh Island and thaw depth (measured in August 2017).

	Site	North [°DEC]	East [°DEC]	Thaw depth [cm]
TM2	Thaw mound	72.33920	126.29199	70
SF3	Thaw slump floor	72.33900	126.29207	78
HT1	Holocene terrace	72.33914	126.28945	21

The release of GHGs deriving from the mineralization of modern and ancient OM can be differentiated by ^{14}C analyses, which has been applied in several field and incubation studies in high latitude regions (e.g., Schuur and Trumbore, 2006; Czimczik and Welker, 2010; Estop-Aragonés et al., 2018). In addition, organic and inorganic carbon sources can be identified and quantified by their $\delta^{13}C$ signature and by applying a dual isotopic mass balance calculation (Dorsett et al., 2011; Griffith et al., 2012; Pries et al., 2016). The contribution of inorganic carbon (IC) to CO_2 fluxes that may be released by abiotic processes (e.g., Biasi et al., 2008; Tamir et al., 2011; Ramnarine et al., 2012) has been neglected in most previous studies, which may thus have overestimated GHG fluxes from the mineralization of OC. Yedoma deposits contain substantial amounts of carbonates of about 0.2–18% in the north-east Siberian coastal lowlands (Schirrmeister, 2011) that may be released by dissolution processes (Zolkos et al., 2018, Zolkos et al., 2020).

The aim of this study is to quantify and differentiate between ancient and modern OC as well as IC contributions to the CO_2 emissions released from a retrogressive thaw slump in a Yedoma deposit in north-east Siberia by using a dual carbon isotopic approach. We selected two study sites on the thaw slump where freshly thawed Yedoma is 1) exposed as thaw mounds and 2) mixed with substrates from the overlaying Holocene terrace. To differentiate between Pleistocene and Holocene substrates, a third site on the Holocene terrace was sampled additionally. Beside field measurements, we incubated the sediments for 1.5 years and analyzed the isotopic compositions of the CO_2 after a few weeks and at the end of the long-term incubation. In addition, we analyzed the composition of the OM in the thaw layer at all sites to elucidate their potential effects on CO_2 production rates.

STUDY SITE

The retrogressive thaw slump is located on the island of Kurungnakh, which lies beside the Olenyeksky Channel, in the southern part of the Lena River Delta in north-eastern Siberia (**Table 1**). Kurungnakh Island is mainly composed of late Quaternary sediments, so-called Yedoma or Ice Complex (Schirrmeister, 2011), which are up to 40 m thick and contain

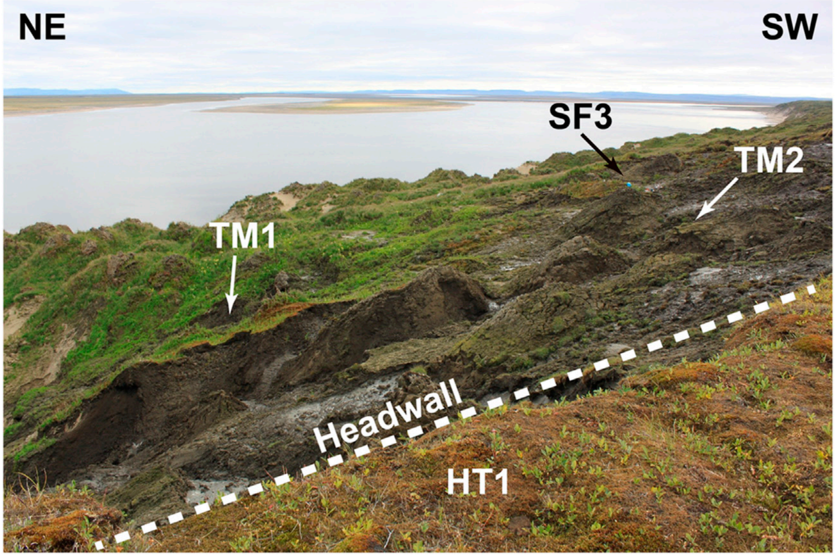

FIGURE 1 | Study sites on the retrogressive thaw slump on Kurungnakh Island including two thaw mounds (TM) in Pleistocene Yedoma, a site on the slump floor (SF) where sediments were mixed, and the Holocene terrace (HT).

large ice wedges resulting in ground-ice contents of up to 80 vol.% (Wetterich et al., 2008a; Schirrmeister, 2011). The Pleistocene-age Yedoma deposit is overlain by Holocene polygonal tundra (Grigoriev, 1993; Schwamborn et al., 2002). The surface layer of the Yedoma deposits thaws for about 4 months per year during summer (Boike et al., 2008) and may reach a depth of about 80 cm (**Table 1**). Recorded data for the years 1998–2011 document an annual mean air temperature of −12.5°C (measured on the nearby Samoylov Island), with maximum mean air temperatures of 10.1°C in July and 8.5°C in August (Boike et al., 2013). The mean annual precipitation (rainfall and snow water equivalent) is about 190 mm (Boike et al., 2013).

For this study, three different sites were selected on the retrogressive thaw slump about 15–35 m above river level including the overlying Holocene terrace (HT1), an intact thaw mound of Pleistocene Yedoma (TM2), and a site on the slump floor (SF3) where both types of sediments were mixed during erosion (**Figure 1**).

METHODS

Sediment Sampling

Samples were collected from the active layer of the soil in the Holocene terrace and the Yedoma sediment in August 2017. At each site, one soil pit of about 1 × 1 m was dug down to the to the frozen ground and four replicates were sampled from the pit wall using a hand shovel. Samples were collected in 10 cm intervals for bulk elemental analysis. The incubation experiment was conducted with replicates of up to four depth intervals per site. Therefore, some of the sampled depth intervals were combined and homogenized. All samples were stored in sealed plastic bags and kept frozen at −20°C until analysis.

Gas Sampling

Carbon dioxide was collected from three locations in about 0.5–1 m distance at each study site according to Wotte et al. (2017) using PVC collars that were placed on the sediment. At SF3 and TM2, sprouts were carefully removed from the mostly barren soil surface to prevent the contribution of autotrophic (plant) respiration. At HT1, aboveground vegetation was clipped with a knife and the uppermost 8 cm of the sediment were carefully removed from the ground to minimize contributions from autotrophic respiration.

The plastic collars (polyvinylchloride, 25 cm OD, 25 cm height) were placed 10 cm in the ground and left for 12 h prior to measurement. On the day of the measurement, an opaque chamber was placed on top of the collars and connected to an infrared gas analyzer (LI-840A, LI-COR Biosciences, Lincoln, United States). After closure of the chamber, the air was pumped in a closed loop for 5 min for CO_2 flux measurement. Moisture was removed using two traps filled with phosphorous pentoxide (Sicapent®, MERCK, Germany). Afterwards, atmospheric CO_2 was removed by pumping three chamber volumes through a soda lime trap (MERCK, Germany). Then, CO_2 emitted from the ground was trapped on a molecular sieve cartridge (MSC) filled with zeolite type 13X. The sampling time was about 30 min per site depending on CO_2 fluxes and volume of the emission chamber aiming to collect 2 mg of CO_2 on each MSC.

CO_2 fluxes were calculated from the recorded increase in CO_2 concentration inside the chamber during the first 5 minutes after closure. The first 30 s were discarded due to possible disturbances by closing the chamber. From the remaining data, the 2-min interval with the highest Pearson correlation coefficient (>0.9) was chosen for flux calculation.

Incubations

An aerobic long-term incubation experiment was conducted over a course of 1.5 years according to Knoblauch et al. (2013). Briefly, splits of the frozen sediment samples were thawed at 2°C and kept at 4°C for the duration of the incubation. The water content of each sample was determined prior to the start of the incubation. About 20 g of homogenized sediment was placed in 120 ml glass bottles, which were sealed by rubber stoppers and kept closed during the experiment to maintain constant moisture. The headspace of the bottles was flushed repeatedly with synthetic air prior to the start of the experiment to remove ambient CO_2 from each bottle. The CO_2 concentrations were recorded every week for the first 200 days and about every other month thereafter. If CO_2 concentrations exceeded 3%, the headspace was flushed repeatedly with synthetic air (20% O_2, 80% N_2). CO_2 samples were taken for isotope analysis at two times during the incubation: first, between 41 and 189 days after the samples had been flushed and again reached concentrations of about 3% CO_2. The second gas sampling was performed at the end of the experiment on day 537, regardless of the CO_2 concentration inside the bottles.

Sediment Analysis

Bulk sediment analysis was performed on freeze-dried samples that were ground and thereby homogenized using a porcelain mortar. Total carbon (C), total OC and total nitrogen (N) contents were quantified using an elemental analyzer (vario MICRO, Elementar, Germany). For OC analysis, aliquots of the sediment were decalcified by treatment with 40 ml of 1% hydrochloric acid (HCl) for 1 h at 60°C following 12 h at room temperature as described in Rethemeyer et al. (2019). After the acid treatment, the samples were washed to neutral pH by adding Mili-Q water and dried at 60°C. pH values were measured after DIN ISO 10390:2005-12 in a suspension of 5 g dry mineral soil and 25 ml Milli-Q water after shaking (1 h) and settling (1 h) using a pH meter (FE20, Mettler-Toledo, Ohio, United States).

Radiocarbon Analysis

^{14}C analysis of the bulk OC was performed by combustion and graphitization of the CO_2 as described in Rethemeyer et al. (2019). In short, an aliquot of the decalcified sediment was weighed into solvent-cleaned tin boats (4 × 4 × 11 mm, Elementar, Germany) for subsequent combustion in an elemental analyzer (VarioMicroCube, Elementar, Germany). The CO_2 produced was converted to elemental carbon ("graphite") in an automated graphitization system (AGE; Wacker et al., 2010) using hydrogen and iron powder as catalyst. The ^{14}C content of the IC was measured by hydrolyzing the sediment, with phosphoric acid (99%) for 6 h at 75°C. This was done without prior removal of OC from the sediment. Although experiences with this method were positive, we cannot exclude that small amounts of OC were dissolved along the IC and contributed to the ^{14}C analysis. The CO_2 evolved was then transferred into the AGE system with He and converted to graphite. The graphite was pressed into AMS target holders, which were analyzed with the 6 MV accelerator mass spectrometer (AMS) at CologneAMS (Dewald et al., 2013).

The CO_2 trapped on the MSCs was processed on a vacuum rig as described in Wotte et al. (2017). The MSC was heated to 500°C to release the CO_2 from the zeolite and flushed with He (grade 4.6) via a water trap immersed in dry ice-ethanol mixture (−80°C) to a CO_2 trap placed in liquid nitrogen. The amount of CO_2 was quantified in a calibrated volume with a pressure sensor and the glass tube containing the CO_2 was flame sealed.

The CO_2 from the aerobic incubation experiment was recovered from the glass bottles using sterile hypodermic needles. Similar to the MSC desorption procedure, the incubation-derived CO_2 was purified, quantified and flame sealed on the vacuum rig. ^{14}C analysis of the CO_2 was performed using the gas ion source of the AMS at the University of Cologne and the gas injection system described in (Stolz et al., 2017). ^{14}C results are reported in $F^{14}C$ (Reimer et al., 2013) and as uncalibrated years before present (BP; Stuiver and Polach, 1977).

Stable Carbon Isotope Analysis

Stable carbon isotopes of OC were measured in sediment samples, which were decalcified with phosphoric acid, using an elemental analyzer (Flash 2000; Thermo Scientific, Germany) coupled to a Delta V (Thermo Scientific, Germany) isotope ratio mass spectrometer (IRMS) (Knoblauch et al., 2013). For $\delta^{13}C$ analysis of IC, ground sediment aliquots were weighed into 50 ml glass bottles and closed with a rubber stopper. Ambient air was removed from the bottles using He and phosphoric acid (5%) was added to convert the IC into CO_2. Carbon dioxide stable isotope analyses from IC, the incubation experiments and field samples were conducted by injecting gas samples into a Trace GC 1310 gas chromatograph connected to a DeltaVPlus IRMS (Thermo Scientific, Germany) (two replicates per sample). The range of replicate measurements was equal to or less than ±0.3‰. The results of the stable carbon isotope measurements were calibrated with external standards and are reported in permille relative to the Vienna Pee Dee Belemnite (‰ VPDB).

Statistics and Calculations

CO_2 production rates were compared with the elemental and isotopic compositions and the pH of the sediments using the ANOVA add-in from Microsoft Excel. For better comparison, the CO_2 production rate after 175 days of the incubation and at the end of the experiment, after 537 days, were used. Additionally, the CO_2 production rates were normalized for the amount of C available in the sample to eliminate bias by different C quantities. Furthermore, Pearson correlation coefficients were calculated to evaluate possible correlations between the data sets. Variances of data were compared using a F-test. Mean values of data sets were then compared using a *t*-test assuming either same or different variances, based on the F-test run previously.

The CO_2 samples taken from respiration chambers might contain contributions from atmospheric CO_2 leaking into the system through small cracks in the soil next to the chamber. To account for this effect, ^{14}C ($F^{14}C_s$) and ^{13}C ($\delta^{13}C_s$) contents of the CO_2 samples were corrected for the fraction of atmospheric CO_2 (f_{atm}) contributing to the total CO_2 and reported as $F^{14}C_c$. The $\delta^{13}C$ value of the CO_2 released in the incubation experiment

TABLE 2 | $\delta^{13}C$ and $F^{14}C$ values of the sedimentary C sources used in the mass balance calculation.

Site	$\Delta^{13}C$			$F^{14}C$		
	IC	OCa	OCy	IC	OCa	OCy
TM2	−5.26	−26.8	−27.8	0.044	0.042	0.984
SF3	−7.46	−25.6	−27.8	0.047	0.038	0.984
HT1	-	−29.4	−27.3	-	0.597	1.021

($\delta^{13}C_{inc}$) is free of atmospheric contamination that may be introduced in the field. It thus was used to correct the $\delta^{13}C$ values of the CO_2 sampled in the field ($\delta^{13}C_c$). In addition, the ^{14}C ($F^{14}C_{atm}$) and ^{13}C contents ($\delta^{13}C_{atm}$) of an atmospheric air sample taken from HT1 were used to calculate the fraction of atmospheric CO_2 (f_{atm}) in the CO_2 samples and correct their ^{14}C content ($F^{14}C_c$) according to **Eq. 1** and **Eq. 2**.

$$F^{14}C_c = \frac{(F^{14}C_s - f_{atm} * F^{14}C_{atm})}{(1 - f_{atm})} \tag{1}$$

with

$$f_{atm} = \frac{(\delta^{13}C_s - \delta^{13}C_{inc})}{(\delta^{13}C_{atm} - \delta^{13}C_{inc})} \tag{2}$$

A mass balance approach was used to determine the fractions of ancient (fOCa) and young organic carbon (fOCy) as well as of inorganic carbon (fIC) in the CO_2 flux using the $F^{14}C$ and $\delta^{13}C$ values of the potential sources (**Table 2**) and of the CO_2 released in the field and during the incubation experiment (**Supplementary Tables S2, S3**) according to **Eq. 4** and **Eq. 5**:

$$\delta^{13}C_{CO2} = f_{IC} * \delta^{13}C_{IC} + f_{OCa} * \delta^{13}C_{OCa} + f_{OCy} * \delta^{13}C_{OCy} \tag{3}$$

and

$$F^{14}C_{CO2} = f_{IC} * F^{14}C_{IC} + f_{OCa} * F^{14}C_{OCa} + f_{OCy} * F^{14}C_{OCy} \tag{4}$$

$\delta^{13}C_{CO2}$ and $F^{14}C_{CO2}$ are the mean isotopic ratios of the CO_2 released from the thaw layer at each site. In the incubations, the mean isotopic values were weighted by the CO_2 production of each depth interval per site.

Average isotopic values of IC and OC in the whole thaw layer ($F^{14}C_{IC/OC}$, $\delta^{13}C_{IC/OC}$), were calculated by weighing the respective values from the different depth intervals with their IC or OC content (IC_i/OC_i), respectively, and considering the bulk density (ρ_i) and thickness of the depth interval (h_i) according to **Eq. 5** and **Eq. 6**.

$$\overline{F^{14}C_{IC/OC}} = \sum_{i=1}^{n} F^{14}C_i \times \left(\frac{\frac{IC/OC_i}{100} \times \rho_i \times h_i}{\sum_{i=1}^{n} \frac{IC/OC_i}{100} \times \rho_i \times h_i} \right) \tag{5}$$

$$\overline{\delta^{13}C_{IC/OC}} = \sum_{i=1}^{n} \delta^{13}C_i \times \left(\frac{\frac{IC/OC_i}{100} \times \rho_i \times h_i}{\sum_{i=1}^{n} \frac{IC/OC_i}{100} \times \rho_i \times h_i} \right) \tag{6}$$

For each site, different endmembers were used for defining young ($\delta^{13}C_{OCy}$ and $F^{14}C_{OCy}$) and ancient OC ($\delta^{13}C_{OCa}$ and $F^{14}C_{OCa}$) in the mass balance approach because the sediments are composed of different materials and the sites are situated at different heights above mean river level (a.m.r.l.) on the thaw slump (**Table 2**, **Supplementary Table S1**). The thaw mound (TM2) in the Pleistocene Yedoma is located at 30 m a.m.r.l., which is 8 m below the Holocene terrace (HT1). We defined the ancient OC and IC endmembers of TM2 as the average $\delta^{13}C$ and $F^{14}C$ content of the thaw layer weighted by its OC or IC content and bulk density. Contributions of young OC were assumed to derive mainly from the thaw layer at HT1, which had a close to modern ^{14}C content (0.984 $F^{14}C$). At the slump floor (SF3), different sediments have been mixed due to erosional processes. As for TM2, we assumed that young OC was delivered mainly from the eroded thaw layer at HT1. SF3 is located at 29 m a.m.r.l., which is lower than TM2. Thus, we chose a nearby thaw mound (TM1) that is on the same height as SF3 as ancient endmember and calculated the average $\delta^{13}C$ and $F^{14}C$ for the thaw layer as for TM2. Because the IC content of the TM1 sediment was very low, only two depth intervals could be analyzed for ^{14}C in IC and results were averaged. At HT1, IC was below the detection limit. We therefore used a two-pool mixing model considering only ancient and young OC sources contributing to respired CO_2. The $F^{14}C$ and $\delta^{13}C$ values of atmospheric CO_2 measured at this site (**Supplementary Table S2**) were used as young OC endmembers assuming that fresh plant OM contains the same isotopic ratios. The ancient OC endmember was defined by the lowest depth interval in the thaw layer at HT1.

Because of the differences in sediment ages at the three sites, the term "ancient" refers to OC and IC older than 4,000 years BP at SF3 and HT1 and Pleistocene-aged at TM1, respectively. The term "young" denotes OC younger than 4,000 years BP at TM1 and SF3, while it is near modern atmospheric ^{14}C concentrations at HT1 (**Table 2**).

To find feasible solutions for fIC, fOCa, and fOCy in **Eq. 4** and **Eq. 5**, the mass balance was solved using IsoSource (Phillips and Gregg, 2003). IsoSource iterates possible combinations of each source's contribution in pre-defined increments (1%) and within a defined tolerance (0.1‰). This underdetermined system (two equations with three variables) has no unique solution. Hence, a distribution of possible solutions is determined based on the isotopic ratios of three potential C sources (**Table 2**) that may contribute to the CO_2 emissions. By simplifying our model for HT1, fIC in **Eq. 5** and **Eq. 6** equals 0 and makes the equation system uniquely solvable.

The upper (maximum) and lower (minimum) limit of the calculated distributions of C sources were furthermore used to calculate the absolute amount of C released as CO_2 from the different C source at SF3 and TM2 after 175 and 537 days of the incubation experiment.

RESULTS

Bulk Sediment Analysis

The undisturbed Yedoma exposed as thaw mound (TM2) had the lowest ^{14}C contents in the range of 0.023–0.109 $F^{14}C_{OC}$ in the thaw layer (0–70 cm depth) corresponding to conventional ^{14}C ages of 17,830 to 29,790 years BP (**Supplementary Table S1**). The uppermost 10 cm had a higher ^{14}C content (0.109 $F^{14}C_{OC}$) than the underlying sediment at 10–70 cm depth (0.023–0.029 $F^{14}C_{OC}$). $F^{14}C_{OC}$ values in the thaw layer of the mixed sediment on the slump floor (SF3) ranged between 0.607 $F^{14}C_{OC}$ and 0.844 $F^{14}C_{OC}$ in 0–60 cm depth (1,370–4,010 years BP) and included two younger layers at 0–10 cm and 30–50 cm depth with 0.844 $F^{14}C_{OC}$ and 0.789–0.829 $F^{14}C_{OC}$ (1,370 and 1,500–1,900 years BP), respectively. The soil developed on the Holocene terrace (HT1) had the highest ^{14}C content between 0.597 and 0.946 $F^{14}C_{OC}$ in 0–17 cm depth. The organic layer on top of the mineral soil, which was removed prior to CO_2 analysis, had a^{14}C content slightly above atmospheric levels (1.149 $F^{14}C$) indicating the contribution of OM produced during times of higher atmospheric ^{14}C levels due to above ground nuclear weapon testing.

The $\delta^{13}C_{OC}$ results ranged from −25.3 to −32.3‰ with no clear differences between sites and no relation to sediment depth or to other parameters (**Supplementary Table S1**).

The OC and N contents did not change considerably with increasing sediment depth, except at HT1 (**Supplementary Table S1**). Here, the highest OC content was measured in the uppermost layer (9.2–9.7%) and the lowest OC content in the bottom layer (3.0%). At the mixed site (SF3), OC contents ranged from 3.9 to 5.5%, while they were considerably lower in the intact thaw mound (TM2) with values of 1.0–2.0%. Here, higher values were measured in 0–10 cm than in 10–70 cm (**Supplementary Table S1**). Similar to OC contents, the N content was highest in the uppermost layer at HT1 (0.70%) than in the lower layer (0.17%). Slightly lower N contents were determined SF3 (0.22–0.37%) and even lower values at TM2 (0.12–0.19%), which were higher in the upper 10 cm and lower below. The differences in OC and N content between the sites resulted in similar differences in OC/N ratios. HT1 had the highest values (14.0–37.6), SF3 slightly lower (13.9–17.4) and TM2 the lowest ratios (7.8–11.0).

No IC was measurable in the HT1 soil. At SF3, the IC content ranged from 1.1–2.8% in 0–50 cm, with considerably lower IC values of 0.2 and 0.7% in 20–30 cm and 50–60 cm depth, respectively. At TM2, IC contents were more consistent and ranged from 0.5–0.8%.

The ^{14}C and ^{13}C contents of the IC did not change with sediment depth. At SF3, $F^{14}C_{IC}$ values were in the range of 0.609–0.844 and thus were similar to the respective $F^{14}C_{OC,}$ while the $\delta^{13}C_{IC}$ values were much higher in the range of −9.1 to −12.8‰. At TM2, $F^{14}C_{IC}$ was between 0.019 and 0.056, which is higher than the respective $F^{14}C_{OC}$, except in the uppermost interval. Here, ^{14}C contents of the IC were lower compared to values of the OM. $\delta^{13}C_{IC}$ ranged from −4.5 to −7.0‰ in the thaw mound sediment.

The pH values at HT1 (4.3–5.8) and SF3 (4.9–6.1) were slightly acidic, while they were neutral to slightly alkaline (6.4–7.8) at TM2 (**Supplementary Table S1**).

CO_2 Fluxes and C Isotopic Signatures

The ^{14}C content of the CO_2 respired in the field differed distinctly between sites (**Supplementary Table S2**). The CO_2 respired from TM2 had the lowest ^{14}C contents between 0.230 and 0.329 $F^{14}C$ (8.9–11.8 kyrs BP) compared to the two other sites on the thaw slump (**Supplementary Table S2**). ^{14}C concentrations of the CO_2 released from SF3 ranged between 0.547 and 0.716 $F^{14}C$ (2.7–4.9 kyrs BP), while they were close to atmospheric contents (1.022 $F^{14}C$) at HT1 with 0.975–0.985 $F^{14}C$ matching values of bulk OC in the uppermost (0–11 cm) layer (0.946 $F^{14}C$) (**Supplementary Table S1**).

The CO_2 fluxes measured prior to CO_2 sampling for isotopic analysis varied considerable between the different sites and between the three replicates taken at each site (**Supplementary Table S2**). CO_2 fluxes were highest at TM2 (2.7–12.3 g CO_2 m^{-2} d^{-1}) and SF3 (6.1–11.6 g CO_2 m^{-2} d^{-1}) with a considerable scatter, while they were much lower at HT1 (0.8–2.0 g CO_2 m^{-2} d^{-1}). However, the results were affected by weather conditions at the day of measurements and thus difficult to compare.

The stable carbon isotopic composition of CO_2 released in the incubation experiment differed between sites and duration of the incubation (**Figure 2**, **Supplementary Table S3**). At TM2, $\delta^{13}C$ values of the CO_2 released from the different depth intervals after the first incubation period ranged between −22.0 and −23.4‰ (**Figure 2B**), which is consistently heavier than values of OC from the corresponding bulk sediment (−25.3 to −30.8‰). Even higher values were determined for the CO_2 emitted from the mixed site, SF3, in the range of −19.5 to −24.6‰ (**Figure 2C**), while OC values of the corresponding bulk sediment ranged between −27.5 and −32.3‰. In contrast, CO_2 produced from the active layer of HT1 had the lowest isotopic ratios of −27.0 and −26.3‰ in 0–11 cm and 11–17 cm depth, respectively (**Figure 2A**). No depth trend of stable isotope signatures of the CO_2 produced in the incubations could be determined at all sites.

At TM2 and SF3 $\delta^{13}C$ values decreased at the end of the incubation by 0.9–2.0‰, except for the 20–40 cm interval and ranged between −21.1 and −22.9‰ at TM2 (**Figure 2B**) and −24.2 and −25.6‰ at SF3 (**Figure 2C**). The $\delta^{13}C$ of CO_2 released from HT1 remained close to values measured after the first incubation period at −27.3 to −28.5‰ with slightly lighter values for the 11–17 cm depth interval.

The overall lowest ^{14}C contents of the CO_2 released after the first incubation period were measured at TM2 and ranged from 0.147–0.188 $F^{14}C$ (**Figure 2E**; **Supplementary Table S3**), which is higher than values of the bulk sediment (0.023–0.109 $F^{14}C$). At the mixed site, SF3, the released CO_2 had higher ^{14}C contents ranging from 0.585 to 0.718 $F^{14}C$ (**Figure 2F**) with higher values in the upper intervals 0–40 cm (0.702–0.718 $F^{14}C$) and lower values in 40–60 cm (0.585 $F^{14}C$), the latter being lower than the $F^{14}C$ of the bulk sediment. At HT1, CO_2 from the first incubation period had an overall higher ^{14}C content (**Figure 2D**) than the respective bulk sediment with 1.011 $F^{14}C$ in 0–11 cm, which is just below the atmospheric ^{14}C content measured at this site (1.021 $F^{14}C$; **Supplementary Table S2**), while 0.859 $F^{14}C$ was measured for CO_2 of the incubations from 11–17 cm depth.

The ^{14}C contents of the CO_2 changed slightly at the end of the long-term incubation (**Supplementary Table S3**). At TM2, consistently lower values were measured in all depth intervals (0.077–0.138 $F^{14}C$) after 1.5 years than after few weeks of incubation (**Figure 2E**). In contrast, ^{14}C contents increased

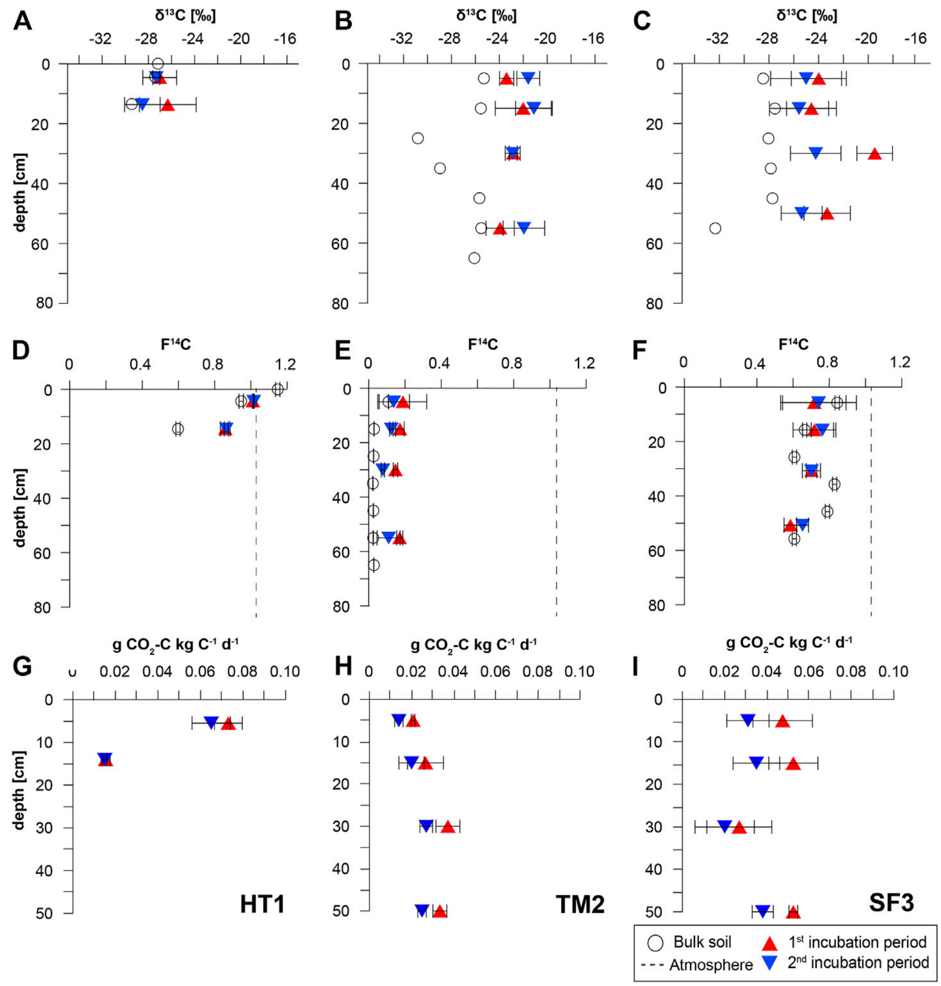

FIGURE 2 | $\delta^{13}C$ **(A–C)** and ^{14}C contents **(D–F)** of bulk soil OC of the different sampling sites as well as CO_2 released from the incubation experiment **(G–I)** during the first (red triangles) and the second incubation period (blue triangles) normalized to the amount of soil carbon.

during the incubation of SF3 sediment (0.652–0.762 $F^{14}C$), except for the CO_2 released from 20–40 cm (0.701 $F^{14}C$) (**Figure 2F**). The CO_2 produced from HT1 soil had similar values (0.864–1.016 $F^{14}C$) within the measurement uncertainty after few weeks and 1.5 years of incubation (**Figure 2D**).

The daily CO_2 production during the aerobic incubation differed considerably between sites and duration of the incubation (**Supplementary Table S3**). The lowest cumulative CO_2 production was measured at TM2 in the range of 0.41 and 0.76 µg CO_2-C gdw^{-1} d^{-1} after 175 days. Higher CO_2 production rates were measured for the mixed sediments from SF3 of 1.18–2.85 µg CO_2-C gdw^{-1} d^{-1}. At HT1, most CO_2 was released from the uppermost depth interval after 175 days with 7.54 µg CO_2-C gdw^{-1} d^{-1}, while much less CO_2 was produced from 11–17 cm with 0.55 µg CO_2-C gdw^{-1} d^{-1}, which is comparable to the rates measured in TM2 sediment. When normalized to the amount of available thawed C, the daily release of C as CO_2 corresponds to 0.021–0.037 g CO_2-C kgC^{-1} d^{-1} at TM2 (**Figure 2H**), 0.027–0.052 g CO_2-C kgC^{-1} d^{-1} at SF3 (**Figure 2I**), and between 0.015 and 0.093 g CO_2-C kgC^{-1} d^{-1} at HT1 (**Figure 2G**, **Supplementary Table S3**). The CO_2 production decreased towards the end of the incubation, after 1.5 years, by about 30% both, at TM2 (0.28–0.55 µg CO_2-C gdw^{-1} d^{-1}) and at SF3 (0.89–1.90 µg CO_2-C gdw^{-1} d^{-1}), and much less, by about 8%, at HT1 (0.51–6.68 µg CO_2-C gdw^{-1} d^{-1}). Accordingly, the normalized C release at the end of the incubation experiment decreased to 0.014–0.027 g CO_2-C kgC^{-1} d^{-1} at TM2, to 0.020–0.038 g CO_2-C kgC^{-1} d^{-1} at SF3, and to 0.015–0.065 g CO_2-C kgC^{-1} d^{-1} at HT1.

Contributions of Organic and Inorganic Sources to CO_2 Release

A three C pool, two isotope (^{13}C, ^{14}C) mass balance approach was used to calculate the contribution of different C sources to CO_2 emissions in the field and during the incubation experiment for sites TM2 and SF3 (**Figure 3**). Since HT1 contained no IC, a two-pool model excluding IC was applied.

The range of possible contribution of the three different carbon sources to the CO_2 efflux is shown in **Table 3** and the

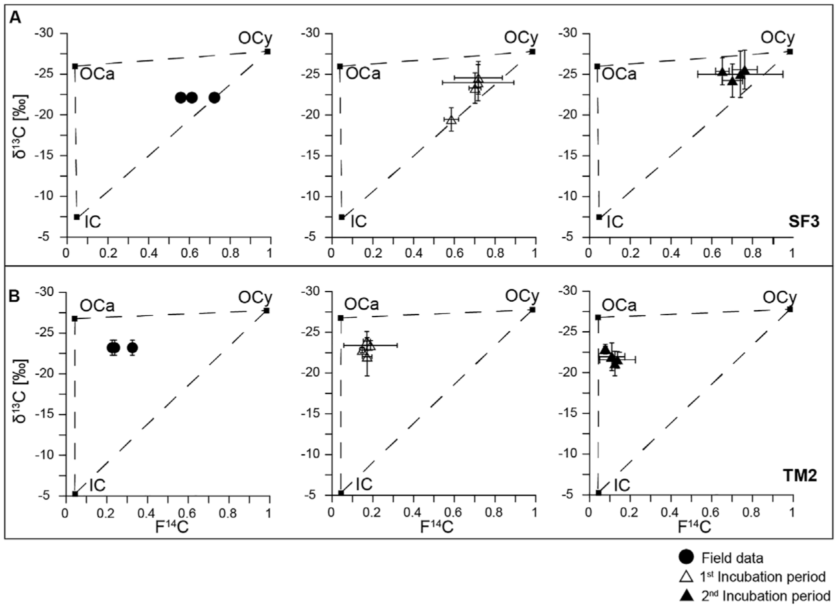

FIGURE 3 | Carbon isotope biplots for **(A)** SF3 and **(B)** TM2 indicating endmembers (squares) on which the three-pool mass balance approach is based and including field and incubation data (mean values of depth intervals and standard deviation).

TABLE 3 | Distributions of C pools contributing to the CO_2 released in the field and in the incubations.

Site	Minimum feasible fraction CO_2			Maximum feasible fraction CO_2		
	OCy	OCa	IC	OCy	OCa	IC
FIELD MEASUREMENTS						
TM2	0.15	0.48	0.18	0.34	0.67	0.18
SF3	0.51	0.02	0.24	0.72	0.25	0.26
HT1	0.87	0.09	-	0.91	0.13	-
1ST INCUBATION PERIOD						
TM2	0.03	0.59	0.17	0.23	0.80	0.18
SF3	0.56	0	0.24	0.74	0.20	0.26
HT1	0.94	0.04	-	0.96	0.06	-
2ND INCUBATION PERIOD						
TM2	0	0.61	0.22	0.17	0.78	0.22
SF3	0.61	0.06	0.10	0.81	0.29	0.13
HT1	0.95	0.03	-	0.97	0.05	-

corresponding absolute amount of CO_2 released as C in **Supplementary Table S4**. During the field measurements, most of the CO_2 (82%) released from the Yedoma thaw mound TM2 derived from OC sources including 15–34% of young OC and 48–67% of ancient OC. However, a significant amount of the CO_2 emissions of about 18% was of inorganic origin. At the mixed site SF3, a similar large amount of 74–76% of the CO_2 was released from organic sources. However, the majority of CO_2 at this site originated from young OC (51–72%) and less from ancient OC (2–25%). An even larger amount of 24–26% of the CO_2 derived from IC. At HT1, the two-pool model revealed that here mainly modern OM was mineralized and released as CO_2 (87–91%), while older substrates from greater depth made up only 9–13% of the CO_2 flux.

During the first 159–189 days of the aerobic incubation, until CO_2 was sampled, about 82% of the CO_2 produced from TM2 sediment was released from OC sources including 3–12% or 15–23% young (13–14% exceeds the 0.1‰ model tolerance) and 71–80% or 59–67% ancient OC. A significant amount of 17–18% of the CO_2 originated from IC. At SF3, slightly less CO_2 of about 74–76% was released from OC during the first 41–99 days until CO_2 sampling. Most of this CO_2, between 56–74%, was of young origin, while only 0–20% derived of ancient organic sources. The remaining 24–26% of the CO_2 originated from IC. At HT1, modern OC was the major

CO_2 source (94–96%), while only 4–6% originated from older OM.

The largest change in C sources at the end of the incubation experiment (after 537 days) was measured at TM2. Here, the contribution of IC in the CO_2 produced increased to 22%, while the fraction of young OC decreased to 0–17% and the ancient OC contribution to 61–78%. At SF3, slightly more CO_2 was released from young (61–81%) and ancient OC (6–29%), respectively, while IC contributions decreased from 24–26% to 10–13%. No significant change in C sources during the incubation period was determined at HT1 (3–5% fOCa; 95–97% fOCy).

DISCUSSION

Carbon Sources of *in situ* CO_2 Fluxes

The analyses of CO_2 collected in the field revealed that the largest proportion of the emissions (48–67%) released from freshly thawed Yedoma (TM2) derived from the degradation of ancient OM, while a much smaller amount is mineralized from young OM (15–34%). This result agrees well with high respiration rates of Pleistocene-age Yedoma measured in previous incubation experiments (Dutta et al., 2006; Zimov et al., 2006; Lee et al., 2012) that were related to higher amounts of labile OM than in Holocene deposits (Walz et al., 2018). The young OM at TM2 most likely was deposited on top of the thaw mound by melt water and erosion. The $\delta^{13}C$ signatures of the CO_2 released in the laboratory incubations indicate that about 18% of the CO_2 released at the field sites originated from IC sources. However, we cannot rule out that the CO_2 release from carbonates during the incubations was biased by the incubation conditions. Measurements of the stable C isotope signatures of CO_2 released from the thaw slump and flux measurements would be required to construct Keeling plots (Keeling, 1958; Kohler et al., 2006) giving direct evidence for IC dissolution under *in situ* conditions. Although the IC content of the sediment was relatively low (0.5–0.8%) and the pH neutral to slightly alkaline (7.3–7.8 in 0–60 cm and 6.4 in 60–70 cm) it is possible that in this pH range, the soil or sediment pH is buffered by carbonate dissolution to bicarbonate (HCO_3^-), which is dissolved in ground water (Guo et al., 2015; Raza et al., 2020). However, for net CO_2 emissions to be produced from IC, it has been speculated that the chemical equilibrium of chemical weathering must have been shifted by organic acids towards carbonate dissolution (Zolkos et al., 2018). As suggested by Zolkos et al. (2018), thermokarst activity in retrogressive thaw slumps can increase HCO_3^- concentrations in the pore water of the sediments thus changing the chemical equilibrium to favor dissolution of carbonate and degassing of CO_2 (Fritz et al., 2015).

At the slump floor (SF3), where thermokarst processes caused the mixing of Pleistocene Yedoma with younger sediments eroded from the Holocene terrace, mostly young OM (51–72%) was released as CO_2 and much less derived from Pleistocene-age OM (2–25%). This indicates the preferential mineralization of the admixed Holocene-age OM. At SF3, thermokarst-related sediment mixing resulted in higher IC contents (0.2–2.8%) and lower pH values (4.9–6.1) promoting IC-derived CO_2 emissions. Here, the amount of IC in the CO_2 emissions (24–26%) was even larger than in the Yedoma thaw mound (TM2) supporting observations by (Zolkos et al., 2018, 2020) that thermokarst amplifies IC cycling. The lower pH of the mixed sediment may result from higher OC and N contents that possibly supported the formation of organic acids causing the dissolution of $CaCO_3$ (Ramnarine et al., 2012; Tamir et al., 2012; Zolkos et al., 2018).

The sedimentary IC most probably is not derived from lithogenic sources because it exhibited lower $\delta^{13}C$ values (**Supplementary Table S1**) than average values for lithogenic IC in exchange with fresh water of about 2–4‰ PDB (Weber and Bergenback, 1965). Besides, the IC had similar ^{14}C concentrations like the sedimentary OC indicating coeval formation. Ca^{2+} may have been leached from silicate minerals to form pedogenic carbonate coatings on clay and silt-sized particles without lithogenic carbonates being present in the sediment (Schlesinger, 1985; Cailleau et al., 2005; Rovira and Vallejo, 2008; Ramnarine et al., 2012). Pedogenic carbonate may also have formed from HCO_3^- derived from CO_2 emitted by microbial degradation of the OM. The $\delta^{13}C$ of the pedogenic carbonate thus is lighter, in the range of −10 to 0‰ PDB, compared to lithogenic carbonate (Cerling, 1984). A further source of IC may be ostracods that lived in polygon centers during the Pleistocene and became part of the present Yedoma sediment. The $\delta^{13}C$ values of the sedimentary IC at SF3 (−9.1 to −12.8‰ PDB; **Supplementary Table S1**) agree well with reported $\delta^{13}C$ values of subfossil ostracod valves found in thermokarst lakes at Kurungnakh Island (−6.9 to −7.1‰ PDB) and subfossil intrapolygonal ostracod valves (−10.8 to −11.1‰ PDB; Wetterich et al., 2008b). Thus, a fraction of the sedimentary IC may also have derived from dissolution of these fossil remains. Further investigations are needed to disentangle potential IC sources more precisely, because the dissolution of pedogenic carbonates would release CO_2 that originally formed from microbial degradation of OM and would therefore not alter the net CO_2 emissions of the sediment from where it is released (Zolkos et al., 2018).

The Holocene terrace (HT1) was investigated because it was used as modern endmember in the isotopic mass balance calculation. At HT1 mainly modern OM with atmospheric ^{14}C content was degraded and released as CO_2 (87–91%), while the remaining fraction of the CO_2 originated from the OM stored in the deeper mineral soil intervals, as indicated by the abrupt decrease in $F^{14}C$ of the bulk soil below 17 cm depth (**Supplementary Table S1**). The soil did not contain any measurable IC. Although the vegetation was removed from HT1, small contributions of modern CO_2 derived from autotrophic respiration of roots cannot be fully excluded. However, these may be negligible, because the ^{14}C results of the CO_2, which were close to the atmospheric values, were corrected for atmospheric CO_2 contributions (**Eq. 1** and **Eq. 2**). However, if any root remains released bomb-spiked enriched $^{14}CO_2$, it would have slightly skewed our results towards modern OM.

The CO_2 produced after few weeks of the aerobic incubation represent the emissions of approximately one thaw season, i.e., about 120 days (Boike et al., 2013). The results of the mass balance approach were similar to the field data at SF3 but slightly different at TM2 and HT1. No positive priming promoting the decomposition of the old OM as demonstrated in previous incubations (Wild et al., 2016; Walz et al., 2018; Pegoraro et al., 2019) took place at the slump floor SF3, where Holocene-age sediments were mixed with Pleistocene-age Yedoma (**Supplementary Table S4**). Most CO_2 was released from young OM (2.6–6.8 g CO_2-C kgC^{-1}) and much less from ancient OM (0–1.8 g CO_2-C kgC^{-1}) indicating the preferential mineralization of young sources. In contrast to the field data, less CO_2 was produced from young OM (3–23%; 0.1–1.5 g CO_2-C kgC^{-1}) from the Yedoma thaw mound TM2 during the first few weeks of the incubation. This suggests that less young organic substrates were present and thus were rapidly consumed, i.e., within roughly one thawing season. This result agrees well with high CO_2 production rates measured in previous aerobic incubation studies of Yedoma that were attributed to the presence of labile OM, which can be readily mineralized after thawing (Dutta et al., 2006; Lee et al., 2012; Knoblauch et al., 2013; Walz et al., 2018). At SF3 and TM2, the contribution of IC to the total CO_2 flux was similar to the field data (17–18%). The CO_2 produced during 41–159 days of incubation of soil from the Holocene terrace (HT1) contained slightly, but statistically not significant higher amounts of young OC compared to the field data. This may be related to the CO_2 collection with respiration chambers giving a mixed signal that may also include CO_2 from deeper parts of the thawed layer (21 cm) containing older OC while the CO_2 in the incubation experiment was only released from the uppermost 17 cm.

The CO_2 production from the Yedoma thaw mound at TM2 during the first 175 days of (0.41–0.76 µg CO_2-C gdw^{-1} d^{-1}) was very low compared to previous results in which Pleistocene-age Yedoma from the Kolyma region was incubated for a shorter period (41–99 days) resulting in about five times larger CO_2 production rates compared to TM2 (Dutta et al., 2006), or, up to one order of magnitude larger CO_2 production rates in an incubation at higher temperatures (15°C, Lee et al., 2012). These differences may be related to different OM composition, stage of degradation and bioavailability, i.e., interaction with mineral particles in the heterogeneous Yedoma deposits and of cause to the different incubation temperatures.

The highest CO_2 production was measured in the uppermost, youngest layer at HT1 and much less in the lower depth interval (10–17 cm; 0.55 µg CO_2-C gdw^{-1} d^{-1}). This difference is related to the larger amounts of young (close to atmospheric ^{14}C levels), little degraded substrates in the surface layer having high OC content (9.7%) and OC/N ratio (14). Likewise, more than three times higher production rates were measured for the mixed sediment at the slump floor containing more OC compared to the Yedoma thaw mound (**Supplementary Table S1**). These data underline the strong relation of CO_2 production to OC content (R^2 = 0.9; $p < 0.005$) persistent for all sites and both, field and incubation data, and, to a lesser extent, to OM quality represented by the OC/N ratio. The latter may have promoted the mineralization of OM, which has a lower stage of degradation at SF3 and HT1, suggested by higher OC/N ratios compared to TM2.

The CO_2 production rates normalized to the available C differed in a smaller range between the sites (**Supplementary Table S3**). Most CO_2 was still produced from the carbon-rich surface soil at HT1, while about 40–70% less was generated from the mixed sediment SF3 (except from 20–40 cm depth) and about 25% less from the Yedoma thaw mound at SF3. The varying CO_2 production rates can be explained by the higher amount of younger OM that is preferentially degraded in HT1 soil and SF3 sediments. In addition, physical stabilization processes may reduce the bioavailability of the OM differently in the different sediments (Höfle et al., 2013; Gentsch et al., 2015).

The results measured after 1.5 years of incubations can give information on the future development of OM degradation and CO_2 production as shown in previous long-term incubation studies (Dutta et al., 2006; Knoblauch et al., 2013; Faucherre et al., 2018). The trend of young OM depletion in the thaw mound TM2, which was observed during the initial period of the incubation, continued resulting in a further decline of this OM pool by about 3–6% at the end of the incubation. Carbon dioxide emissions from ancient sources thus increased of which about 2% originate from the mineralization of Yedoma-derived OM and a larger proportion of 4–5% from the abiotic degradation of IC. Given the length of the long-term incubation, it is possible that the degradation of OM led to the oxidation of NH_4^+, which releases H^+ ions in aerated TM2 sediments during the incubation that decreased the pH and thus increased the dissolution of IC and consequently the contribution of IC to total CO_2 release (Tamir et al., 2012). The amino acids that are required for the microbial oxidation, if not present initially, may have been released into the sediment dissolved in water from melted ice wedges (Drake et al., 2015), leading to acidification of the sediment, which was experimentally shown to occur rapidly within few weeks (Tamir et al., 2011, Tamir et al., 2012).

At the mixed site SF3, slightly more CO_2 was released from both, young and old OM, while IC contribution declined at the end of the incubation. The lower contribution of IC may be caused by the overall decreasing heterotrophic respiration during the long-term incubation (**Supplementary Table S3**). The 50% lower proportion of IC may be related to the reduction of microbial respiration and CO_2 production from OM. A decreased CO_2 concentration could slow down carbonate dissolution and reduce IC emissions. In contrast to TM2, the soil of SF3 had a lower pH that indicates a lower concentration of inorganic carbon. These could have dissolved the carbonates in the sediment, which may occur as rapidly as within 1 year (Biasi et al., 2008).

The CO_2 production from the thaw layer of the sediments at TM2 and SF3 decreased at the end of the incubation by about the same amount of approximately 24–34%, while it decreased much less, by 6–11%, at HT1. This decline in CO_2 production at all sites is smaller compared to previous long-term incubations, which attributed the reduction in production rates to a decline of labile OM (Dutta et al., 2006; Knoblauch et al., 2013; Walz et al., 2018). Thus, the lower decrease in CO_2 production in this study, may indicate that less labile OM was present here.

Overall, our source assessment indicates that relative proportions of CO_2 derived from young OM in Pleistocene-age Yedoma decline during the incubation (of TM2). However, when young OM is available in sufficient amounts, like in the mixed sediment SF3 and the soil in the Holocene terrace HT1, most of the CO_2 is produced from this young OM pool during the entire duration of the incubation. The reduction in CO_2 production thus may be related to other effects, e.g., changes in the microbial community as a result of the length of the experiment, the lack of nutrients that may have led to a decreased microbial diversity and favored conditions for slower metabolizing oligotrophic bacteria, which has been proposed but not yet experimentally verified (Schädel et al., 2020).

CONCLUSION

The dual carbon isotopic source assessment revealed that large proportions of up to 80% ancient organic and about 18% inorganic carbon, despite not being shown directly in the field, were likely released from freshly thawed, Pleistocene-age Yedoma exposed as thaw mound in a retrogressive thaw slump. A young OM pool, which derived from overlaying sediments or was transported by meltwater to the thaw mound, was preferentially respired. The contribution of ancient C sources, both organic and inorganic, to the CO_2 produced from thawed Yedoma may further increase (by about 6–7%) upon longer thaw as indicated at the end of the aerobic incubation at 4°C after 1.5 years. The mixing of Pleistocene-age Yedoma with Holocene material at the slump floor by erosional processes did not cause a positive priming, i.e., increasing the release of ancient OC. Most of the CO_2 (51–72%) produced from the mixed sediments originated from young OM, which was available in sufficient quantities even at the end of the incubation. CO_2 production rates were positively correlated with sedimentary OC content and decreased over the course of the incubation. Considerable amounts of IC were abiotically released as CO_2 from the freshly thawed Yedoma and from the mixed sediments, which is supposed to be related to thermokarst activities and transport of HCO_3^- by meltwater from the ice wedges into the Yedoma causing dissolution of IC. Besides, pH values may be lower by the production of organic acids during microbial OM decomposition. The substantial IC contribution to CO_2 emissions from thawing Yedoma may overestimate CO_2 fluxes from organic sources. IC-related emissions may be even larger because significantly larger amounts of sedimentary IC were found in the circumarctic region compared to this study suggesting the possibility of a yet overseen source of CO_2 emissions. The dissolution of pedogenic carbonates that formed after Yedoma thaw, from bicarbonate of organic origin, would ultimately not alter the CO_2 budget, in contrast to lithogenic sources. However, the CO_2 budget might be altered if those pedogenic carbonates formed from OC over a longer time scale and were destabilized recently. Thus, further investigations are of interest and are required to determine precisely the potential sources of the sedimentary IC.

DATA AVAILABILITY STATEMENT

The datasets of this study are available in the Zenodo online repository https://doi.org/10.5281/zenodo.5644763.

AUTHOR CONTRIBUTIONS

JR and CK contributed to conception and design of the study. JM and PW performed data evaluation, calculations and statistical analysis. TE and CK performed incubation experiments and evaluation of these data. JM and JR wrote the manuscript. All authors contributed to manuscript revision, read, and approved the submitted version.

FUNDING

This work was financially supported by the German Ministry of Science and Education (BMBF) within the project “KoPf” (grant no. 03F0764A/E) and “KoPf” Synthesis project (grant no. 03F0834A/D). CK received additional funds from the Clusters of Excellence CLICCS (EXC2037/1) at the Universität Hamburg funded by the German Research Foundation (DFG).

ACKNOWLEDGMENTS

We are grateful for logistical support by AWI and station personnel during the Russian-German expedition Lena 2017. We thank Stefan Heinze, Svetlana John, Elisabeth Krewer, Ulrike Patt, Alexander Stolz and Anja Wotte (Cologne) for helping collecting and processing samples and performing AMS ^{14}C analysis, Ralf Lendt (Hamburg) for stable carbon isotope analysis, and Jelena Gerloff (Hamburg) for helping with the incubation experiment.

SUPPLEMENTARY MATERIAL

The Supplementary Material for this article can be found online at: https://www.frontiersin.org/articles/10.3389/feart.2021.737237/full#supplementary-material

REFERENCES

Biasi, C., Lind, S. E., Pekkarinen, N. M., Huttunen, J. T., Shurpali, N. J., Hyvönen, N. P., et al. (2008). Direct Experimental Evidence for the Contribution of Lime to CO2 Release from Managed Peat Soil. *Soil Biol. Biochem.* 40, 2660–2669. doi:10.1016/j.soilbio.2008.07.011

Biskaborn, B. K., Smith, S. L., Noetzli, J., Matthes, H., Vieira, G., Streletskiy, D. A., et al. (2019). Permafrost Is Warming at a Global Scale. *Nat. Commun.* 10, 1–11. doi:10.1038/s41467-018-08240-4

Boike, J., Kattenstroth, B., Abramova, K., Bornemann, N., Chetverova, A., Fedorova, I., et al. (2013). Baseline Characteristics of Climate, Permafrost and Land Cover from a New Permafrost Observatory in the Lena River Delta, Siberia (1998-2011). *Biogeosciences* 10, 2105–2128. doi:10.5194/bg-10-2105-2013

Boike, J., Wille, C., and Abnizova, A. (2008). Climatology and Summer Energy and Water Balance of Polygonal Tundra in the Lena River Delta, Siberia. *J. Geophys. Res.* 113. doi:10.1029/2007JG000540

Cailleau, G., Braissant, O., Dupraz, C., Aragno, M., and Verrecchia, E. P. (2005). Biologically Induced Accumulations of CaCO3 in Orthox Soils of Biga, Ivory Coast. *CATENA* 59, 1–17. doi:10.1016/j.catena.2004.06.002

Cerling (1984). The Stable Isotopic Composition of Modern Soil Carbonate and its Relationship to Climate. *Earth Planet. Sci. Lett.* 71, 229–240. doi:10.1016/0012-821X(84)90089-X

Costard, F., Dupeyrat, L., Séjourné, A., Bouchard, F., Fedorov, A., and Saint-Bézar, B. (2021). Retrogressive Thaw Slumps on Ice-Rich Permafrost under Degradation: Results from a Large-Scale Laboratory Simulation. *Geophys. Res. Lett.* 48. doi:10.1029/2020GL091070

Czimczik, C. I., and Welker, J. M. (2010). Radiocarbon Content of CO2 Respired from High Arctic Tundra in Northwest Greenland. *Arctic, Antarctic, Alpine Res.* 42, 342–350. doi:10.1657/1938-4246-42.3.342

Czudek, T., and Demek, J. (1970). Thermokarst in Siberia and its Influence on the Development of Lowland Relief. *Quat. Res.* 1, 103–120. doi:10.1016/0033-5894(70)90013-X

Dewald, A., Heinze, S., Jolie, J., Zilges, A., Dunai, T., Rethemeyer, J., et al. (2013). CologneAMS, a Dedicated center for Accelerator Mass Spectrometry in Germany. *Nucl. Instr. Methods Phys. Res. Section B: Beam Interactions Mater. Atoms* 294, 18–23. doi:10.1016/j.nimb.2012.04.030

Dorsett, A., Cherrier, J., Martin, J. B., and Cable, J. E. (2011). Assessing Hydrologic and Biogeochemical Controls on Pore-Water Dissolved Inorganic Carbon Cycling in a Subterranean Estuary: A 14C and 13C Mass Balance Approach. *Mar. Chem.* 127, 76–89. doi:10.1016/j.marchem.2011.07.007

Drake, T. W., Wickland, K. P., Spencer, R. G. M., McKnight, D. M., and Striegl, R. G. (2015). Ancient Low-Molecular-Weight Organic Acids in Permafrost Fuel Rapid Carbon Dioxide Production upon Thaw. *Proc. Natl. Acad. Sci. USA* 112, 13946–13951. doi:10.1073/pnas.1511705112

Dutta, K., Schuur, E. A. G., Neff, J. C., and Zimov, S. A. (2006). Potential Carbon Release from Permafrost Soils of Northeastern Siberia. *Glob. Change Biol.* 12, 2336–2351. doi:10.1111/j.1365-2486.2006.01259.x

Estop-Aragonés, C., Cooper, M. D. A., Fisher, J. P., Thierry, A., Garnett, M. H., Charman, D. J., et al. (2018). Limited Release of Previously-Frozen C and Increased New Peat Formation after Thaw in Permafrost Peatlands. *Soil Biol. Biochem.* 118, 115–129. doi:10.1016/j.soilbio.2017.12.010

Faucherre, S., Jørgensen, C. J., Blok, D., Weiss, N., Siewert, M. B., Bang-Andreasen, T., et al. (2018). Short and Long-Term Controls on Active Layer and Permafrost Carbon Turnover across the Arctic. *J. Geophys. Res. Biogeosci.* 123, 372–390. doi:10.1002/2017JG004069

Fritz, M., Opel, T., Tanski, G., Herzschuh, U., Meyer, H., Eulenburg, A., et al. (2015). Dissolved Organic Carbon (DOC) in Arctic Ground Ice. *The Cryosphere* 9, 737–752. doi:10.5194/tc-9-737-2015

Gentsch, N., Mikutta, R., Shibistova, O., Wild, B., Schnecker, J., Richter, A., et al. (2015). Properties and Bioavailability of Particulate and mineral-associated Organic Matter in Arctic Permafrost Soils, Lower Kolyma Region, Russia. *Eur. J. Soil Sci.* 66, 722–734. doi:10.1111/ejss.12269

Griffith, D. R., McNichol, A. P., Xu, L., McLaughlin, F. A., Macdonald, R. W., Brown, K. A., et al. (2012). Carbon Dynamics in the Western Arctic Ocean: Insights from Full-Depth Carbon Isotope Profiles of DIC, DOC, and POC. *Biogeosciences* 9, 1217–1224. doi:10.5194/bg-9-1217-2012

Grigoriev, M. N. (1993). Cryomorphogenesis of the Lena River Mouth Area. *Siberian Branch, USSR Academy of Sciences, Yakutsk*, 176, 1993 (in Russian).

Grosse, G., Harden, J., Turetsky, M., McGuire, A. D., Camill, P., Tarnocai, C., et al. (2011). Vulnerability of High-Latitude Soil Organic Carbon in North America to Disturbance. *J. Geophys. Res.* 116. doi:10.1029/2010JG001507

Guo, J., Wang, F., Vogt, R. D., Zhang, Y., and Liu, C.-Q. (2015). Anthropogenically Enhanced Chemical Weathering and Carbon Evasion in the Yangtze Basin. *Sci. Rep.* 5, 1–8. doi:10.1038/srep11941

Hicks Pries, C. E., Schuur, E. A. G., Natali, S. M., and Crummer, K. G. (2016). Old Soil Carbon Losses Increase with Ecosystem Respiration in Experimentally Thawed Tundra. *Nat. Clim Change* 6, 214–218. doi:10.1038/nclimate2830

Höfle, S., Rethemeyer, J., Mueller, C. W., and John, S. (2013). Organic Matter Composition and Stabilization in a Polygonal Tundra Soil of the Lena Delta. *Biogeosciences* 10, 3145–3158. doi:10.5194/bg-10-3145-2013

Jongejans, L. L., Liebner, S., Knoblauch, C., Mangelsdorf, K., Ulrich, M., Grosse, G., et al. (2021). Greenhouse Gas Production and Lipid Biomarker Distribution in Yedoma and Alas Thermokarst lake Sediments in Eastern Siberia. *Glob. Change Biol.* 27, 2822–2839. doi:10.1111/gcb.15566

Jongejans, L. L., Strauss, J., Lenz, J., Peterse, F., Mangelsdorf, K., Fuchs, M., et al. (2018). Organic Matter Characteristics in Yedoma and Thermokarst Deposits on Baldwin Peninsula, West Alaska. *Biogeosciences* 15, 6033–6048. doi:10.5194/bg-15-6033-2018

Keeling, C. D. (1958). The Concentration and Isotopic Abundances of Atmospheric Carbon Dioxide in Rural Areas. *Geochimica et Cosmochimica Acta* 13, 322–334. doi:10.1016/0016-7037(58)90033-4

Knoblauch, C., Beer, C., Sosnin, A., Wagner, D., and Pfeiffer, E.-M. (2013). Predicting Long-Term Carbon Mineralization and Trace Gas Production from Thawing Permafrost of Northeast Siberia. *Glob. Change Biol.* 19, 1160–1172. doi:10.1111/gcb.12116

Kohler, P., Fischer, H., Schmitt, J., and Munhoven, G. (2006). On the Application and Interpretation of Keeling Plots in Paleo Climate Research – Deciphering $\delta^{13}C$ of Atmospheric CO_2 Measured in Ice Cores. 18.

Kuhry, P., Bárta, J., Blok, D., Elberling, B., Faucherre, S., Hugelius, G., et al. (2020). Lability Classification of Soil Organic Matter in the Northern Permafrost Region. *Biogeosciences* 17, 361–379. doi:10.5194/bg-17-361-2020

Lantuit, H., and Pollard, W. H. (2008). Fifty Years of Coastal Erosion and Retrogressive Thaw Slump Activity on Herschel Island, Southern Beaufort Sea, Yukon Territory, Canada. *Geomorphology* 95, 84–102. doi:10.1016/j.geomorph.2006.07.040

Lee, H., Schuur, E. A. G., Inglett, K. S., Lavoie, M., and Chanton, J. P. (2012). The Rate of Permafrost Carbon Release under Aerobic and Anaerobic Conditions and its Potential Effects on Climate. *Glob. Change Biol.* 18, 515–527. doi:10.1111/j.1365-2486.2011.02519.x

Nitzbon, J., Westermann, S., Langer, M., Martin, L. C. P., Strauss, J., Laboor, S., et al. (2020). Fast Response of Cold Ice-Rich Permafrost in Northeast Siberia to a Warming Climate. *Nat. Commun.* 11, 1–11. doi:10.1038/s41467-020-15725-8

Pegoraro, E., Mauritz, M., Bracho, R., Ebert, C., Dijkstra, P., Hungate, B. A., et al. (2019). Glucose Addition Increases the Magnitude and Decreases the Age of Soil Respired Carbon in a Long-Term Permafrost Incubation Study. *Soil Biol. Biochem.* 129, 201–211. doi:10.1016/j.soilbio.2018.10.009

Phillips, D. L., and Gregg, J. W. (2003). Source Partitioning Using Stable Isotopes: Coping with Too many Sources. *Oecologia* 136, 261–269. doi:10.1007/s00442-003-1218-3

Ramnarine, R., Wagner-Riddle, C., Dunfield, K. E., and Voroney, R. P. (2012). Contributions of Carbonates to Soil CO2 Emissions. *Can. J. Soil Sci.* 92, 599–607. doi:10.4141/cjss2011-025

Raza, S., Miao, N., Wang, P., Ju, X., Chen, Z., Zhou, J., et al. (2020). Dramatic Loss of Inorganic Carbon by Nitrogen-induced Soil Acidification in Chinese Croplands. *Glob. Change Biol.* 26, 3738–3751. doi:10.1111/gcb.15101

Reimer, P. J., Bard, E., Bayliss, A., Beck, J. W., Blackwell, P. G., Ramsey, C. B., et al. (2013). IntCal13 and Marine13 Radiocarbon Age Calibration Curves 0-50,000 Years Cal BP. *Radiocarbon* 55, 1869–1887. doi:10.2458/azu_js_rc.55.16947

Rethemeyer, J., Gierga, M., Heinze, S., Stolz, A., Wotte, A., Wischhöfer, P., et al. (2019). Current Sample Preparation and Analytical Capabilities of the Radiocarbon Laboratory at CologneAMS. *Radiocarbon* 61, 1449–1460. doi:10.1017/rdc.2019.16

Routh, J., Hugelius, G., Kuhry, P., Filley, T., Tillman, P. K., Becher, M., et al. (2014). Multi-proxy Study of Soil Organic Matter Dynamics in Permafrost Peat Deposits Reveal Vulnerability to Climate Change in the European Russian Arctic. *Chem. Geology.* 368, 104–117. doi:10.1016/j.chemgeo.2013.12.022

Rovira, P., and Vallejo, V. R. (2008). Changes in δ13C Composition of Soil Carbonates Driven by Organic Matter Decomposition in a Mediterranean Climate: A Field Incubation experiment. *Geoderma* 144, 517–534. doi:10.1016/j.geoderma.2008.01.006

Schädel, C., Bader, M. K.-F., Schuur, E. A. G., Biasi, C., Bracho, R., Čapek, P., et al. (2016). Potential Carbon Emissions Dominated by Carbon Dioxide from Thawed Permafrost Soils. *Nat. Clim Change* 6, 950–953. doi:10.1038/nclimate3054

Schädel, C., Beem-Miller, J., Aziz Rad, M., Crow, S. E., and Hicks Pries, C. E., (2020). Decomposability of Soil Organic Matter over Time: the Soil Incubation Database (SIDb, Version 1.0) and Guidance for Incubation Procedures. *Earth Syst. Sci. Data* 12, 1511–1524. doi:10.5194/essd-12-1511-2020

Schädel, C., Schuur, E. A. G., Bracho, R., Elberling, B., Knoblauch, C., Lee, H., et al. (2014). Circumpolar Assessment of Permafrost C Quality and its Vulnerability over Time Using Long-Term Incubation Data. *Glob. Change Biol.* 20, 641–652. doi:10.1111/gcb.12417

Schirrmeister, L., Kunitsky, V., Grosse, G., Wetterich, S., Meyer, H., Schwamborn, G., et al. (2011). Sedimentary Characteristics and Origin of the Late Pleistocene Ice Complex on north-east Siberian Arctic Coastal Lowlands and Islands - A Review. *Quat. Int.* 241, 3–25. doi:10.1016/j.quaint.2010.04.004

Schlesinger, W. H. (1985). The Formation of Caliche in Soils of the Mojave Desert, California. *Geochimica et Cosmochimica Acta* 49, 57–66. doi:10.1016/0016-7037(85)90191-7

Schuur, E. a. G., McGuire, A. D., Schädel, C., Grosse, G., Harden, J. W., Hayes, D. J., et al. (2015). Climate Change and the Permafrost Carbon Feedback. *Nature* 520, 171–179. doi:10.1038/nature14338

Schuur, E. A. G., and Trumbore, S. E. (2006). Partitioning Sources of Soil Respiration in Boreal Black spruce forest Using Radiocarbon. *Glob. Change Biol.* 12, 165–176. doi:10.1111/j.1365-2486.2005.01066.x

Schwamborn, G., Rachold, V., and Grigoriev, M. N. (2002). Late Quaternary Sedimentation History of the Lena Delta. *Quat. Int.* 89, 119–134. doi:10.1016/S1040-6182(01)00084-2

Stapel, J. G., Schirrmeister, L., Overduin, P. P., Wetterich, S., Strauss, J., Horsfield, B., et al. (2016). Microbial Lipid Signatures and Substrate Potential of Organic Matter in Permafrost Deposits: Implications for Future Greenhouse Gas Production. *J. Geophys. Res. Biogeosci.* 121, 2652–2666. doi:10.1002/2016JG003483

Stapel, J. G., Schwamborn, G., Schirrmeister, L., Horsfield, B., and Mangelsdorf, K. (2018). Substrate Potential of Last Interglacial to Holocene Permafrost Organic Matter for Future Microbial Greenhouse Gas Production. *Biogeosciences* 15, 1969–1985. doi:10.5194/bg-15-1969-2018

Stolz, A., Dewald, A., Altenkirch, R., Herb, S., Heinze, S., Schiffer, M., et al. (2017). Radiocarbon Measurements of Small Gaseous Samples at CologneAMS. *Nucl. Instr. Methods Phys. Res. Section B: Beam Interactions Mater. Atoms* 406, 283–286. doi:10.1016/j.nimb.2017.03.031

Strauss, J., Schirrmeister, L., Grosse, G., Fortier, D., Hugelius, G., Knoblauch, C., et al. (2017). Deep Yedoma Permafrost: A Synthesis of Depositional Characteristics and Carbon Vulnerability. *Earth-Science Rev.* 172, 75–86. doi:10.1016/j.earscirev.2017.07.007

Strauss, J., Schirrmeister, L., Mangelsdorf, K., Eichhorn, L., Wetterich, S., and Herzschuh, U. (2015). Organic-matter Quality of Deep Permafrost Carbon - a Study from Arctic Siberia. *Biogeosciences* 12, 2227–2245. doi:10.5194/bg-12-2227-2015

Stuiver, M., and Polach, H. A. (1977). Discussion Reporting of 14C Data. *Radiocarbon* 19, 355–363. doi:10.1017/s0033822200003672

Tamir, G., Shenker, M., Heller, H., Bloom, P. R., Fine, P., and Bar-Tal, A. (2011). Can Soil Carbonate Dissolution Lead to Overestimation of Soil Respiration? *Soil Sci. Soc. America J.* 75, 1414–1422. doi:10.2136/sssaj2010.0396

Tamir, G., Shenker, M., Heller, H., Bloom, P. R., Fine, P., and Bar-Tal, A. (2012). Dissolution and Re-crystallization Processes of Active Calcium Carbonate in Soil Developed on Tufa. *Soil Sci. Soc. America J.* 76, 1606–1613. doi:10.2136/sssaj2012.0041

Tanski, G., Lantuit, H., Ruttor, S., Knoblauch, C., Radosavljevic, B., Strauss, J., et al. (2017). Transformation of Terrestrial Organic Matter along Thermokarst-Affected Permafrost Coasts in the Arctic. *Sci. Total Environ.* 581-582, 434–447. doi:10.1016/j.scitotenv.2016.12.152

Turetsky, M. R., Abbott, B. W., Jones, M. C., Anthony, K. W., Olefeldt, D., Schuur, E. A. G., et al. (2020). Carbon Release through Abrupt Permafrost Thaw. *Nat. Geosci.* 13, 138–143. doi:10.1038/s41561-019-0526-0

Wacker, L., Němec, M., and Bourquin, J. (2010). A Revolutionary Graphitisation System: Fully Automated, Compact and Simple. *Nucl. Instr. Methods Phys. Res. Section B: Beam Interactions Mater. Atoms* 268, 931–934. doi:10.1016/j.nimb.2009.10.067

Walz, J., Knoblauch, C., Tigges, R., Opel, T., Schirrmeister, L., and Pfeiffer, E.-M. (2018). Greenhouse Gas Production in Degrading Ice-Rich Permafrost Deposits in Northeastern Siberia. *Biogeosciences* 15, 5423–5436. doi:10.5194/bg-15-5423-2018

Weber, J. N., and Bergenback, R. E. (1965). Reconstruction of Depositional Environments in the Pennsylvanian Vanport basin by Carbon Isotope Ratios. *Sepm Jsr* Vol. 35, 36–48. doi:10.1306/74D711EA-2B21-11D7-8648000102C1865D

Weiss, N., Blok, D., Elberling, B., Hugelius, G., Jørgensen, C. J., Siewert, M. B., et al. (2016). Thermokarst Dynamics and Soil Organic Matter Characteristics Controlling Initial Carbon Release from Permafrost Soils in the Siberian Yedoma Region. *Sediment. Geology.* 340, 38–48. doi:10.1016/j.sedgeo.2015.12.004

Wetterich, S., Kuzmina, S., Andreev, A. A., Kienast, F., Meyer, H., Schirrmeister, L., et al. (2008a). Palaeoenvironmental Dynamics Inferred from Late Quaternary Permafrost Deposits on Kurungnakh Island, Lena Delta, Northeast Siberia, Russia. *Quat. Sci. Rev.* 27, 1523–1540. doi:10.1016/j.quascirev.2008.04.007

Wetterich, S., Schirrmeister, L., Meyer, H., Viehberg, F. A., and Mackensen, A. (2008b). Arctic Freshwater Ostracods from Modern Periglacial Environments in the Lena River Delta (Siberian Arctic, Russia): Geochemical Applications for Palaeoenvironmental Reconstructions. *J. Paleolimnol.* 39, 427–449. doi:10.1007/s10933-007-9122-1

Wild, B., Gentsch, N., Čapek, P., Diáková, K., Alves, R. J. E., Bárta, J., et al. (2016). Plant-derived Compounds Stimulate the Decomposition of Organic Matter in Arctic Permafrost Soils. *Sci. Rep.* 6, 25607. doi:10.1038/srep25607

Windirsch, T., Grosse, G., Ulrich, M., Schirrmeister, L., Fedorov, A. N., Konstantinov, P. Y., et al. (2020). Organic Carbon Characteristics in Ice-Rich Permafrost in Alas and Yedoma Deposits, central Yakutia, Siberia. *Biogeosciences* 17, 3797–3814. doi:10.5194/bg-17-3797-2020

Wotte, A., Wischhöfer, P., Wacker, L., and Rethemeyer, J. (2017). 14 CO 2 Analysis of Soil Gas: Evaluation of Sample Size Limits and Sampling Devices. *Nucl. Instr. Methods Phys. Res. Section B: Beam Interactions Mater. Atoms* 413, 51–56. doi:10.1016/j.nimb.2017.10.009

Zimov, S. A., Davydov, S. P., Zimova, G. M., Davydova, A. I., Schuur, E. A. G., Dutta, K., et al. (2006). Permafrost Carbon: Stock and Decomposability of a Globally Significant Carbon Pool. *Geophys. Res. Lett.* 33, L20502. doi:10.1029/2006GL027484

Zolkos, S., Tank, S. E., and Kokelj, S. V. (2018). Mineral Weathering and the Permafrost Carbon-Climate Feedback. *Geophys. Res. Lett.* 45, 9623–9632. doi:10.1029/2018GL078748

Zolkos, S., Tank, S. E., Striegl, R. G., Kokelj, S. V., Kokoszka, J., Estop-Aragonés, C., et al. (2020). Thermokarst Amplifies Fluvial Inorganic Carbon Cycling and export across Watershed Scales on the Peel Plateau, Canada. *Biogeosciences* 17, 5163–5182. doi:10.5194/bg-17-5163-2020

Conflict of Interest: The authors declare that the research was conducted in the absence of any commercial or financial relationships that could be construed as a potential conflict of interest.

frontiers in Earth Science

ORIGINAL RESEARCH
published: 10 February 2022
doi: 10.3389/feart.2021.744775

Check for updates

Structural Properties of Syngenetic Ice-Rich Permafrost, as Revealed by Archaeological Investigation of the Yana Site Complex (Arctic East Siberia, Russia): Implications for Quaternary Science

Vladimir V. Pitulko[1]* *and Elena Y. Pavlova*[2]

[1]*Institute for the History of Material Culture, Russian Academy of Sciences, St. Petersburg, Russia,* [2]*Arctic & Antarctic Research Institute, St. Petersburg, Russia*

Edited by:
Lutz Schirrmeister,
Alfred Wegener Institute Helmholtz Centre for Polar and Marine Research (AWI), Germany

Reviewed by:
Julie Brigham-Grette,
University of Massachusetts Amherst, United States
Frank Kienast,
Senckenberg Research Institute and Natural History Museum Frankfurt, Germany

***Correspondence:**
Vladimir V. Pitulko
pitulkov@gmail.com

Specialty section:
This article was submitted to Cryospheric Sciences, a section of the journal Frontiers in Earth Science

Received: *20 July 2021*
Accepted: *08 December 2021*
Published: *10 February 2022*

Citation:
Pitulko VV and Pavlova EY (2022) Structural Properties of Syngenetic Ice-Rich Permafrost, as Revealed by Archaeological Investigation of the Yana Site Complex (Arctic East Siberia, Russia): Implications for Quaternary Science . Front. Earth Sci. 9:744775. doi: 10.3389/feart.2021.744775

Ice-rich syncryogenic (termed "Ice Complex") deposits are common in northern East Siberia and constitute the most important feature of the Quaternary geology of the region. The Ice Complex formed throughout the Late Pleistocene and not only contains an archive of paleoenvironmental proxies such as Pleistocene faunal remains, but also comprises a record of human habitation spanning ~50,000 years, beginning with early MIS3. The development of syngenetic permafrost is an important variable in the formation of archaeological contexts in this depositional setting. Excavations of the Yana site complex in the lower Yana River area provide a unique opportunity to study archaeological finds preserved in Ice Complex deposits. Based on long-term field observations and dating results, we present important conclusions concerning the geology of the Yana sites. Taphonomic biases with potential to obscure the archaeological record are discussed. The thawing of frozen primary deposits has distorted depositional sequences, leading to the formation of secondary features and contexts, e.g., ice-wedge casts. Collapsed blocks of frozen sediment with undisturbed fragments of frozen layers containing artifacts and/or paleobiotic remains may become incorporated and refrozen into another depositional sequence and a source of misinterpretation and chronometric error. Furthermore, severe cryoturbation within the polygonal mounds warps the sediment in contact with the ice wedges; as a result, the contents of the sediment is uplifted with important consequences: 1) the hypsometric provenience of datable material is altered, creating chronometry problems; 2) in archaeology, there is an increased potential for misinterpretations with respect to dating, cultural classification, and human behavior; 3) transported material may form secondary concentrations at different hypsometric levels and thus bring further complications for its understanding; 4) in geology, the transportation of geochemical signatures may lead to erroneous interpretation of the geological potential of the area; 5) uplifted deposits contribute to increased Ice Complex thickness, which is thus not a direct function of sedimentation, but a combined result of sedimentation and redistribution of the deposits within an existing polygon deposit. Thus, the analysis of Ice Complex deposits during archaeological excavations at the Yana site complex has wider implications for Quaternary science.

Keywords: Arctic East Siberia, ice complex, syngenetic permafrost development, cryoturbation, permafrost polygon pattern, Yana site complex, geoarchaeology, cultural layer

INTRODUCTION

In the Northern hemisphere, permafrost underlies approximately 22.79 × 106 km^2, or 23.9% of the exposed land surface. Permafrost is a trans-zonal natural phenomenon found in the Arctic and the cold temperate (boreal) climatic belt, spanning several landscape zones. The largest permafrost areas are the Asian (~13 × 106 km^2) and North American (~7.2 × 106 km^2) (Zhang et al., 2008); they extend from the shores of the Arctic Ocean southward, deep into the continents. In Northern Eurasia, the permafrost zone reached its greatest extent during the Late Pleistocene. During the Last Glacial Maximum (LGM), it was almost twice as extensive as at present (Velichko, 1973; Vandenberghe et al., 2014). In this enormous territory, frozen ground has various properties related to its formation and evolution that have been investigated for more than a century.

Siberia contains a variety of frozen deposits. Ice-rich permafrost, or "Ice Complex deposits," are the most widely known phenomenon of the Siberian permafrost, first characterized by Solovyov (1959). Ice complex deposits, also known as the Yedoma Suite, are common in the arctic coastal lowlands of East Siberia (Murton et al., 2015; Opel et al., 2019; Romanovskii, 1993; Schirrmeister et al., 2011; 2013; 2017, Wetterich et al., 2014; 2020), and in northwestern North America (Froese et al., 2009; Kanevskiy et al., 2011), but also occur in the continental regions of East Siberia (Solovyov, 1959; Ashastina et al., 2017). These deposits accumulated across the Beringian landmass at its greatest extent during MIS3 and MIS2, including the exposed shelf areas, and thus they are present also on the arctic islands (Makeyev et al., 2003; Romanovskii et al., 2004; Schirrmeister et al., 2011; Pavlova and Pitulko, 2020). Stratigraphic profiles studied to date are primarily of MIS3 age (Schirrmeister et al., 2011; Wetterich et al., 2014), among which the Bykovsky Peninsula exposure spanning MIS4 – MIS2 is believed to be the most comprehensive.

Ice Complex deposits are represented by ice-rich silty sandy loams, clayey loams, and sands penetrated by syngenetic wedge ice. Deposits forming the Ice Complex include alluvial, lacustrine, slope, and aeolian sediments accumulated under an extremely cold and arid continental climate. The total ice content is very high, up to 80–95% in the arctic Yana-Indighirka Lowland and on the New Siberian Islands. Observed in profiles, Ice Complex deposits are dozens of meters thick and contain organic-rich deposits, such as inclusions and layers of peat, plant macro-fossils, and paleosol horizons.

The East Siberian Ice Complex deposits represent a unique late Pleistocene paleoenvironmental record comprising pollen, paleobotanical, and insect proxies (e.g., Kienast et al., 2005; Sher et al., 2005; Andreev et al., 2011; Wetterich et al., 2011; Jørgensen et al., 2012; Zimmermann et al., 2017; Pavlova and Pitulko, 2020), bones of Pleistocene animals (Sher et al., 2005; Nikolskiy et al., 2011; Pitulko et al., 2014), human remains (Lee et al., 2018; Sikora et al., 2019), and archaeological materials (Pitul'ko, 1993; Pitulko et al., 2016; 2017; Pitulko, 2019a). Information on past environments and landscape evolution, human behavior, and the development of the faunal communities are based on the taphonomy and chronometry of the deposits containing these remains. Partial or complete thawing of frozen deposits beginning ~15,000 years ago and continuing throughout the Holocene generated multiple taphonomic biases obscuring the archaeological and environmental record (Katasonov, 1979; Kaplina, 1981, 2009; Shur, 1988; Makeyev et al., 2003; Gavrilov et al., 2006; Morgenstern et al., 2013; Pitulko and Pavlova, 2016).

In the archaeological record of arctic East Siberia, there are some gaps that may be attributed to permafrost degradation (Pitulko et al., 2016; 2017). Sites dating to the Pleistocene-Holocene boundary are most common, but cultural deposits of all the known sites have been significantly transformed due to permafrost degradation of the area, marked by the development of the alas complex 13,000–8,000 years ago. Many sites of that age may have been lost due to massive thermokarst processes and landscape restructuring during the Pleistocene-Holocene transition (Pitul'ko, 2001; Pavlova and Pitulko, 2020). Breaks observed in the archaeological record and/or the small number of known sites dating to specific intervals can be accounted for by a taphonomic bias due to permafrost degradation.

Owing to their nature, ice-rich deposits have significant potential for the formation of such biases. However, breaks in the archaeological record and small numbers of sites for a given period also are observed in continuously frozen and undisturbed geological contexts, as is shown in the study presented here of Ice Complex deposits in the Yana River area, arctic East Siberia.

Here, we present an account of geological observations made in the course of long-term archaeological excavation and geological investigation at the Yana site complex, and provide conclusions and interpretation of the findings with wider implications for Quaternary science, including its geological, cryological, and archaeological branches.

THE YANA SITE COMPLEX: LOCATION AND SPATIAL ORGANIZATION

The Yana RHS site, discovered in 2001 (Pitulko et al., 2004), is situated at the lower Yana River at 70°43′N and 135°25′E (**Figure 1A**) in the westernmost portion of the extensive coastal lowlands between the Yana River in the west to the

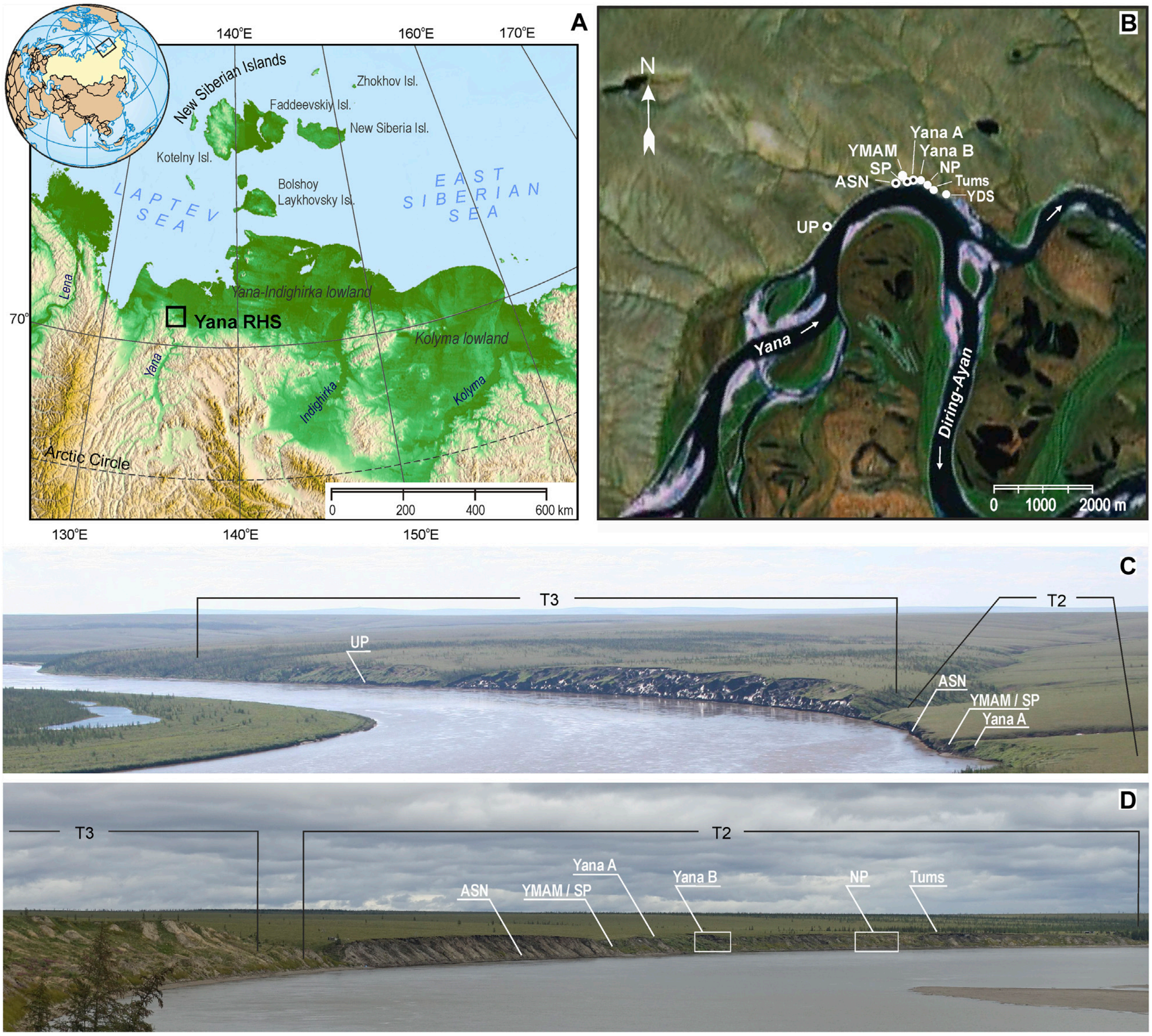

FIGURE 1 | The Yana RHS site location and relationship between its structural elements: **(A)** – westernmost part of the late Pleistocene arctic Western Beringia (a fragment of ETOPO1 Global Relief Model image is used); **(B)** – schematic map of the area (a fragment of Google Earth satellite image is used. White circles mark localities that retain cultural material *in situ* – Yana B, Northern Point (NP), Tums 1, Yana Downstream Point (YDS), and Yana mass accumulation of mammoth (YMAM); circles with black center mark localities that yielded surface finds: Upstream Point (UP), ASN, Yana A, and Southern Point (SP); **(C)** – extent of the second (T2) and the third (T3) terrace, and location of archaeological objects on the left riverbank of the Yana river viewed from the East and **(D)** – archaeological objects of the left riverbank viewed from southwest respectively.

Kolyma River in the east, within present-day Arctic East Siberia. This area is also known as the westernmost part of late Pleistocene Arctic Western Beringia.

Although “Yana RHS” is labeled an archaeological site, it is actually a complex of geoarchaeological sites. The individual localities apparently represent separate but roughly synchronic traces of human occupation (Pituko et al., 2013). The Yana site complex comprises at least seven known separate localities discovered within terrace 2 (T2), and at the Upstream Point locality (UP), which is confined to terrace 3 (T3) deposits (**Figures 1B–D**). The Southern Point (SP) area and Yana A area are spatially associated with the Yana mass accumulation of mammoth, or YMAM (Basilyan et al., 2011), while ASN locality represents a small concentration of lithic artifacts found roughly 150 m upstream from YMAM. The Yana B area is located approximately 200 hundred meters downstream from this group of sites and occupies a portion of the riverbank that recently has been subject to massive thermodenudation, which led to the formation of a thermoterrace. The Northern Point area (NP) of the Yana site complex is located few hundred meters downstream from the Yana B area (**Figures 1B–D**). Well described in

FIGURE 2 | The Northern Point area (NP) of the Yana site complex: **(A)** panoramic view on the exposure of the Ice Complex deposits with the area excavated in 2008; **(B)** – the Northern Point excavation area viewed from the North-West in 2007 with clearly visible permafrost polygonal patterns including areas covered by culture-bearing deposits isolated inside the polygons walled by the ice-wedge network; **(C)** – excavations of the cultural layer in neighboring polygons in 2009; **(D)** – recording of the excavated material during 2012 excavation campaign; **(E)** – example of the excavated area of the cultural layer bearing dense accumulation of archaeological finds – lithic and bone artifacts, and Pleistocene animal bones.

Pitulko et al. (2004), the Tums1 exposure locates next to the NP area in some 200 m downstream from it. Finally, the Yana Downstream Point (YDP) is situated more than in 1,000 m downstream from the NP area. This locale so far has yielded only a single piece of human-modified mammoth tusk (Pitulko et al., 2017).

The state of preservation of these localities varies considerably. Some of them, including ASN, the Southern Point (SP area), and Tums1, are completely washed out (Pitulko et al., 2013), whereas others comprise extensive portions of extremely rich culture-bearing deposits. The latter are primarily represented by 1) YMAM, although this locality was heavily looted by local residents due to mammoth ivory mining (Pitulko et al., 2015a); 2) the dwelling site uncovered at the NP locality, which was the main excavation area in 2003–2015 (**Figures 2A–E**) and until it had been fully excavated; and 3) the Yana B area (**Figures 3A–E**). Yana "B" was first studied in 2003 and 2004. Test excavations continued in 2008 and 2009; since 2014, excavations at the Yana site complex have largely focused on this portion of the site. These two localities at the Yana site complex have yielded the most important archaeological, geological, and paleoenvironmental information (see, e.g.,

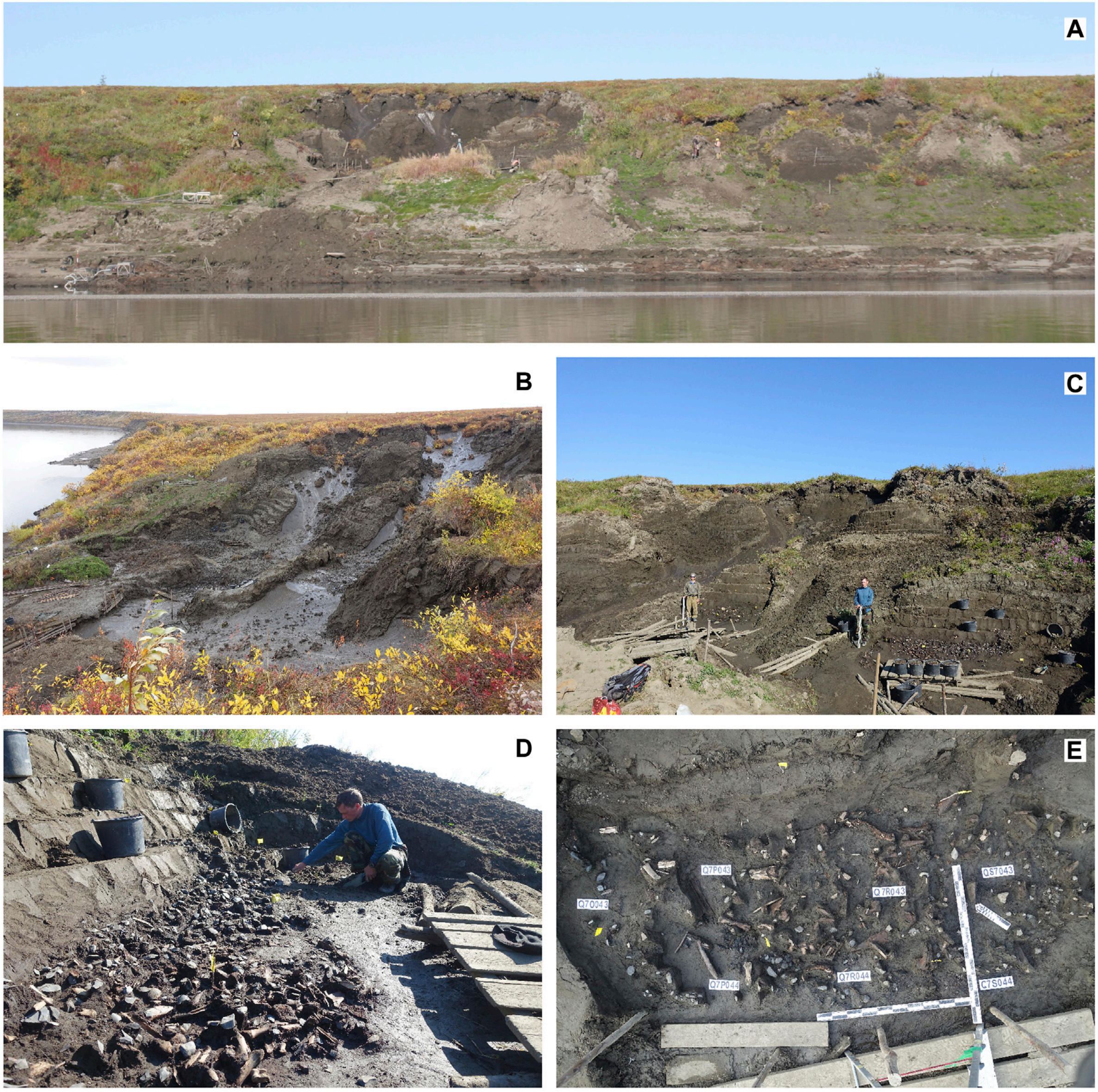

FIGURE 3 | The Yana B area of the Yana site complex: **(A)** left riverbank in the location of the Yana B area of the Yana complex of sites viewed in 2017; **(B)** excavations in the Ice Complex environment viewed from an Eastern elevation in 2019; **(C)** excavated areas of the cultural horizon in two polygons located nearby, in 2019; **(D)** excavation process on one of such polygons performed in 2018; **(E)** ancient habitation surface displaying numerous finds of lithic artifacts and Pleistocene animal bones and their fragments.

Basilyan et al., 2011; Nikolskiy and Pitulko, 2013; Pavlova and Pitulko, 2020; Pitulko and Pavlova, 2016; 2019; Pitulko et al., 2007; 2013; 2015a; 2017).

Study Area

The complex of Yana sites is located within the permafrost zone. Vegetation of this area is typical for the transition from southern hypoarctic tundra to open northern woodland (Atlas of the Arctic, 1985; Yurtsev, 1994; CAVM Team, 2003). These tundra landscapes are composed of tussock-sedge, dwarf-shrub, and moss tundra associations. Moist tundra is dominated by tussock cotton grass (*Eriophorum vaginatum*) and dwarf-shrubs with some *Betula exilis* shrub vegetation, which coexists with grassy moss bog vegetation and occasional larch (*Larix gmelinii*) with dwarf shrubs (*Vaccinium vitis-idaea, Arctous alpina, Empetrum nigrum, and Ledum palustre*), lichen, and mosses in open floodplain woodlands.

The study area is located in the eastern part of a region characterized by a transitional climate: the coastal climate of the Arctic Siberian zone (Gakkel and Korotkevich, 1960; Atlas of the Arctic, 1985). The annual average temperature varies within −13.9 – (−)14.2°C, the mean January temperature is −37.4 – (−)

38°C, and the mean July temperature reaches +11 – (+)11.5°C (Izyumenko, 1966; 1968). This is a harsh, cold, and dry environment with a short frostless period (57 days per a year). Average precipitation varies from 200 to 240 mm per year.

Within the study area, the Yana River alters course sharply (almost 90°), flowing roughly from West to East, and then turns again to the North (**Figure 1**). Along this portion of the river, the terraces are preserved only as fragments. At the present time the 3rd terrace level (T3) is 40–45 m, the 2nd terrace (T2) is 16–18 m, and the 1st terrace (T1) is 10–11 m above the water level (a.w.l.). All geomorphological surfaces lower than 9–10 m a.w.l. are within the modern floodplain.

Ice-rich permafrost deposits with polygonal syngenetic and epigenetic ice wedges are present in all three of the terraces. The ice wedges represent several generations (Pitulko et al., 2007; Basilyan et al., 2011). The ice content of the deposits varies from 30 to 70%. Such ice-rich deposits are termed Ice Complex deposits (Romanovskii, 1993; Romanovskii et al., 2004; Schirrmeister et al., 2011). Archaeological finds such as lithic and bone artifacts and artifact production waste, and Pleistocene animal bone remains, are abundant in the formerly occupied areas and form well-defined culture-bearing layers. Such layers occur in the middle part of T2 at 7–7.5 m a.w.l., and are an important stratigraphic marker for T2 deposits, providing chronological control.

The thickness of the seasonally thawed layer (STL) varies depending on exposure, lithology, and vegetation, but does not exceed 70–80 cm. All deposits at greater depth remain perennially frozen. At the level of the culture-bearing layer, the temperature of the deposits is presumed to be roughly −9°C, based on borehole measurements near Spirka Lake, 8 km northeast of the Yana site complex. As reported by Nekrasov and Devyatkin (1974), temperature values of −9–10°C have been recorded at a depth of 7–8 m below surface; observed temperature next to the village of Kazachie some 30 km downstream from the Yana site complex area was −8.5°C at the same depth. The frozen sediment has ensured excellent artifact preservation required a special excavation strategy (Pitulko 2008). At the same time, these deposits are highly susceptible to natural agents such as running water, summer insolation, and atmospheric heat that cause erosion.

To study them, an annual topographic survey has been conducted on the left bank where T3 and T2 are well expressed. The study area covers 2.5 km of the riverbank, where retreat of the latter comprising Ice Complex deposits is closely associated with erosion caused by the Yana River, as well as thermal denudation and thermokarst processes, and the impact of solar radiation, both direct and indirect (i.e., water-reflected). The rate of riverbank erosion also depends on water discharge. There is a direct connection between mean summer temperatures and riverbank retreat. The latter is accompanied by the development of erosional landforms such as thermoerosional pits, thermokarst, erosion channels, and niches. The combination of all these factors causes rapid destruction of the riverbank.

High water stands in the Yana River reach 7–8 m above the average water level. The ice-rich deposits of the site are subject to lateral river erosion. Retreat of the T3, observed for 17 years (2003 through 2020), averaged 12–13 m/year during 2003–2009, but then slowed to 3–4 m/year. A maximum rate of 22 m/year was observed in 2006. The mean rate of erosion for T2 for the same period was 6–7 m/year, whereas the maximum was 30 m/year, observed in 2014–2016. Within the excavated area of Yana RHS, the mean value for riverbank retreat was 7 m/year with a range between 1.8 m/year and 9.8 m/year (Pitulko et al., 2012).

In 2019, it was discovered that the Northern Point excavation area of the Yana site complex had been almost entirely washed out (**Figure 4**). Based on a long-term observation, active erosion correlates with gradual migration of the upstream portion of the gravel bar opposite the middle part of T3, which redirects the stream into a westerly direction. This process affected a portion of the bank located further downstream, undercutting the previously stable T2 riverbank slope and eroding culture-bearing deposits of the Yana site complex. Overall, based on both measurements and information provided by local residents, we conclude that in 2005–2006, the Yana River entered new hydrological cycle, following an interval of low activity that began in the early 1990s. The length of such short-term cycles may be roughly 15 years.

Geology and Age of the Yana Site Complex

In the T2 section that contains the cultural layer of the Yana RHS, four geological members can be distinguished (**Figure 5A**). These members are separated by stratigraphic unconformities and erosion surfaces that correspond to extensive sedimentation breaks. The basal erosional part of the T2 (**Figure 5A**: Members 1–2) occurs only in the upstream area of the exposure. Member 1 is represented by alluvium-lacustrine and thaw-lake deposits with ice-wedge casts; these deposits were formed during the upper Lower Pleistocene and Middle Pleistocene. Although it is well expressed locally within a portion of T2 near its junction with T3 (**Figure 5A**), only heavily eroded patches of Member 1 deposits appear sporadically at the base of T2 within the Yana site area. Member 2 consists of alluvium-lacustrine and aeolian deposits of early Late Pleistocene age, which are found only in the area adjacent to the T2/T3 junction. The age of the basal unit of T2 probably lies between the end of the Early Pleistocene and the beginning of the Late Pleistocene (Basilyan et al., 2009; Basilyan et al., 2011). This ancient alluvium is a remnant of the T3 fill that has been laterally eroded and down-cut by the river during the formation of T2.

Member 3 (**Figures 5A,B**: Bed 1–4) and Member 4 represent the fill of T2. Alluvial deposits of T2 started to accumulate shortly after 40,000 years ago. Alluvial deposition ceased around 13,000 ^{14}C years ago (when T1 deposits began to accumulate) with the beginning of aeolian sedimentation. Geologically young erosional cuts filled with terminal Pleistocene and Holocene deposits (Member 4) were observed at the top of the T2 sequence. Geological age estimates are based on multiple radiocarbon age determinations, which are consistent throughout the study area (**Figures 5A,B**). The culture-bearing horizon reflects several human habitation episodes taking place in the late MIS3 (Pitulko et al., 2013; Pitulko et al., 2015a). Although their number and length are not clear, we conclude that humans occupied the Yana site complex for several thousand years at the

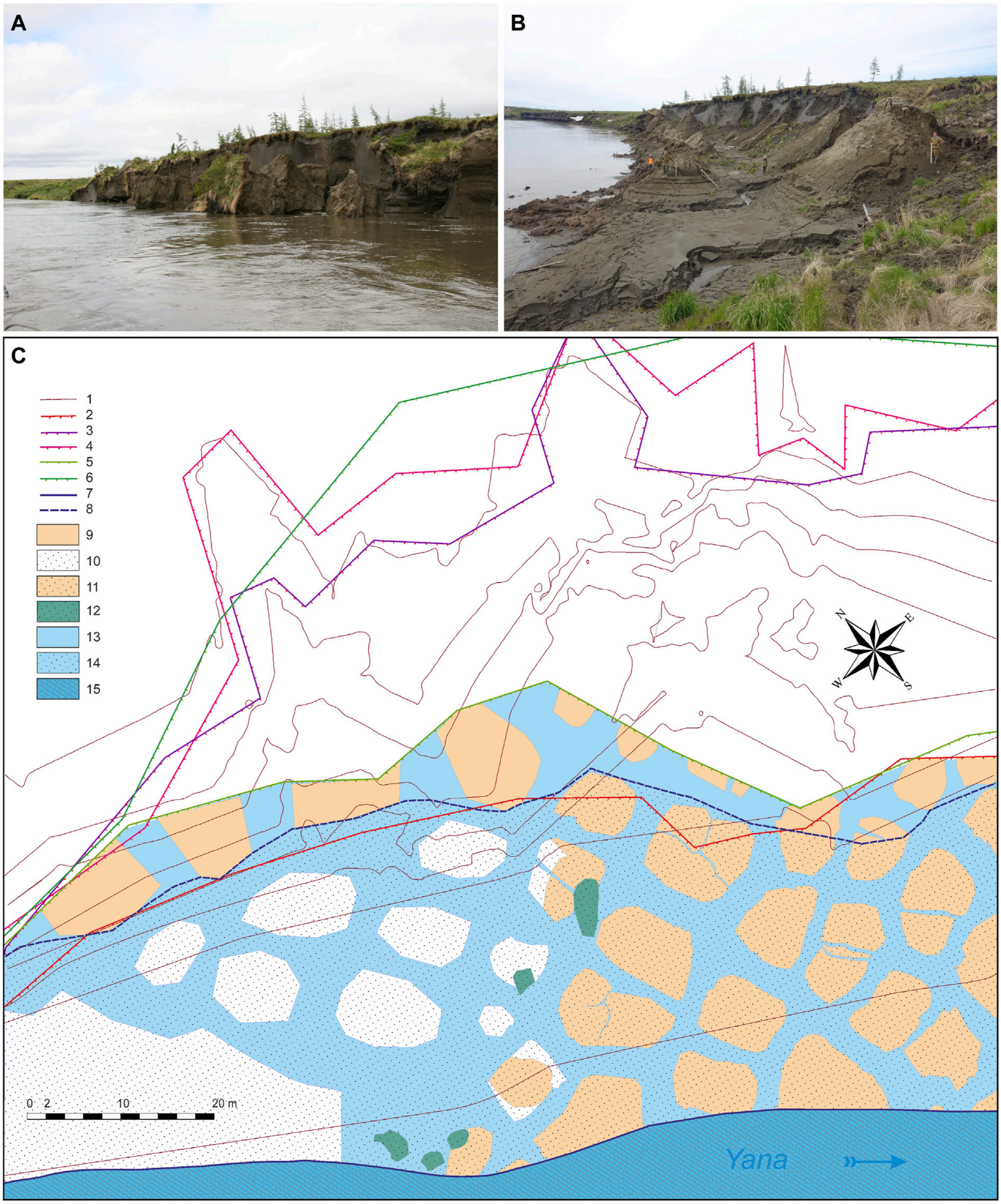

FIGURE 4 | Destruction of the left river bank in the area of the Northern Point area of the Yana complex of sites by the thermal erosion: **(A)** – the catastrophic collapse of large blocks of the bank deposits between Northern Point and Yana B zone in 2016; **(B)** view of the same area in 2017 during low water stand; **(C)** – development of the lateral erosion observed on the river bank in the western portion of the excavation at the Northern Point area based on topographic survey. Illustration key: 1—contour lines are given in 2 m increments; 2–6—location of the second terrace brow recorded in different observation years (2—2007; 3—2013; 4—2014; 5—June 2016; 6—September 2016); 7—the lowest water level in 2016; 8—the highest water level of 2016; 9—permafrost polygons holding *in situ* cultural layer; 10—modern alluvium covering thawed permafrost polygons; 11—modern alluvium covering permafrost polygons, in which the cultural layer was studied during excavations in 2003–2015; 12—collapsed frozen blocks, which contained a cultural layer, studied in a sub-"*in situ*" position in 2016; 13—polygonal ice wedges in frozen cliffs; 14—thawed polygonal ice wedge covered with modern alluvium; 15— channel alluvium. Compiled by S.G. Kritsuk and E.Y. Pavlova.

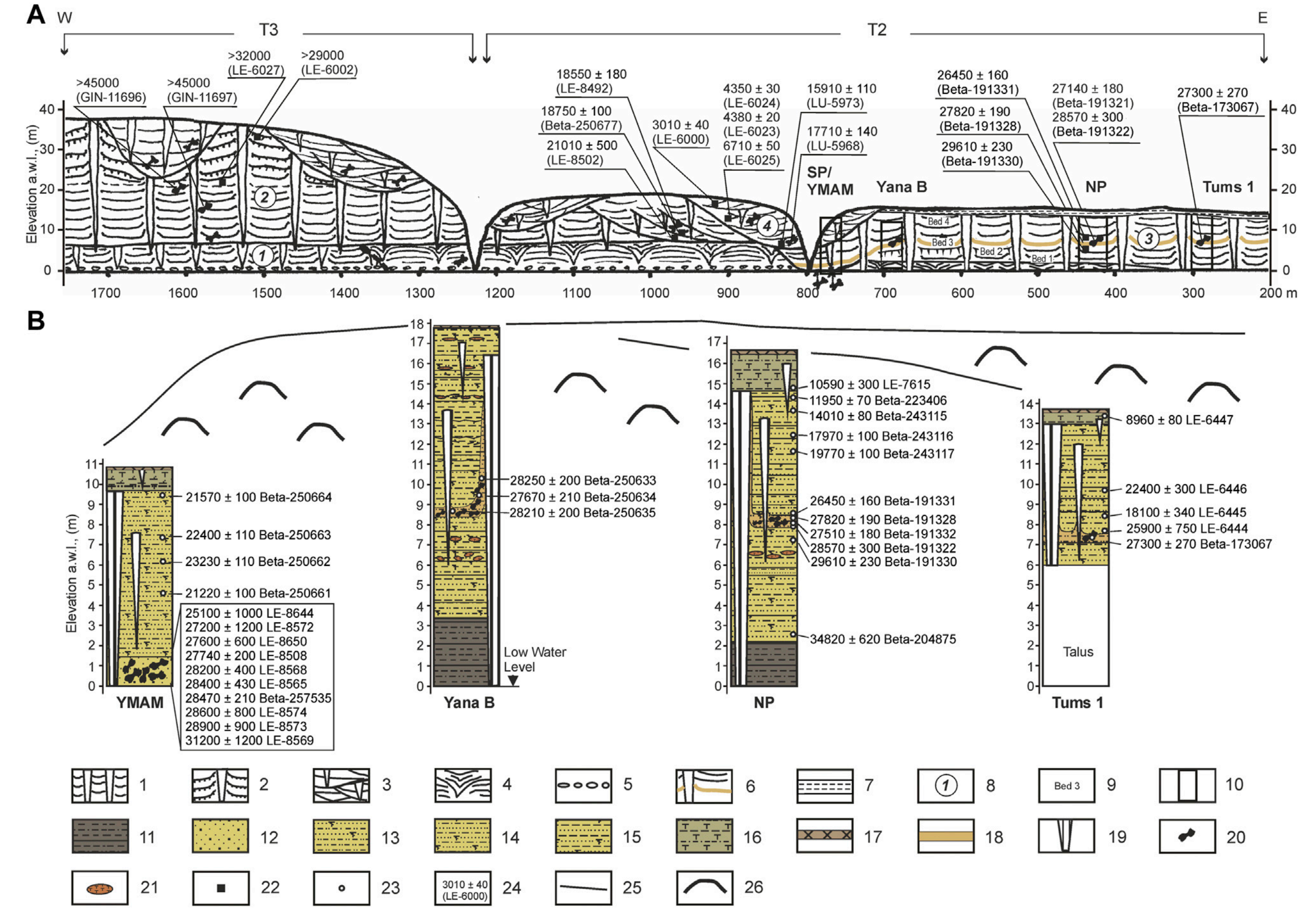

FIGURE 5 | Overview of the geology of the Yana complex of sites. Soplivaya Gora (Yana-195) reference profile of Quaternary deposits **(A)** and cryolithology for different localities within the Yana RHS – YMAM, Yana B, Northern Point, TUMS 1 **(B)**. Illustration key: 1—Ice Complex deposits of different geological age, with syncryogenic ice wedges in alluvial and proluvial deposits; 2—aeolian deposits; 3—cross bedding; 4—ice-wedge cast; 5—conglomerates; 6—position of the Upper Paleolithic Yana RHS cultural layer; 7—deposits of the Holocene cover complex; 8—number for geological Member; 9—bed number within the Member 3; 10—location of cryolithological profiles; 11—interbedding of clays, silts, and clayey silts; 12—sand with small pebbles; 13—sandy silt; 14—clayey-sandy silt; 15—sandy-clayey silt; 16—interbedding of clayey silt bands and sandy-clayey silt with beds and lenses of peat; 17—active layer; 18—cultural layer *in situ*; 19—polygonal ice wedges; 20—position of Pleistocene animal bones within the deposits; 21—peat lens; 22—position of ^{14}C samples on the geological profile **(A)** (plant remains dated); 23—position ^{14}C samples within local cryolithological profiles **(B)**; 24—radiocarbon date and lab code; 25—terrace edge (schematic); 26—permafrost mound (baidzharakh) —cone-shaped land forms resulted from partial thawing of polygonal ice-wedge network.

very end of MIS3 and briefly visited the area during the LGM (Pitulko et al., 2017).

Member 4 (**Figure 5**) caps the T2 sequence. It is composed of alluvial and proluvial deposits of varying terminal Pleistocene and Holocene age. Deposits of this member consist of fine-grained sand with gray silt – cross-bedded, shoestring/lenticular sands that fill erosion channels. These deposits exhibit numerous unconformities with Member 3. These unconformities represent backfilling of erosional channels and depressions that largely formed in Member 3 deposits during the terminal Pleistocene and middle Holocene, whereas some of them may be relatively recent. These sediments contain a large number of plant remains, such as allochthonous peat concentrations and grass hummocks, roots and twigs of woody plants, and fragments of driftwood. The Member 4 sequence is capped with Holocene surface deposits (after Kaplina, 1981), represented by ice-rich silts with peat inclusions, peat-bog deposits, locally distributed on the surface of the terrace, and proluvial deposits backfilling recent stream channels incised into its surface. The base of the Holocene cover layer truncates the uppermost portion of the ice wedges that belong to the Ice Complex deposits. Member 4 is characterized by epigenetic freezing represented by alternating layers with ataxitic and reticulated cryotextures, and short and wide epigenetic ice wedges, the width of which in the upper part reaches 1.5 m. Member 4 deposits vary 1.0–2.5 m in thickness.

The structure and geocryology of Member 3 are highly germane to the present study, and below we present a detailed description based on the observations of the profiles in the NP area of the Yana site complex (**Figures 6A,B**). The sequence is uniform along the riverbank. Similar geology is observed for T2 also at the Tums1 locality (Pitulko et al., 2004) and at Yana B as well (Pitulko, 2019a) (**Figure 6C**).

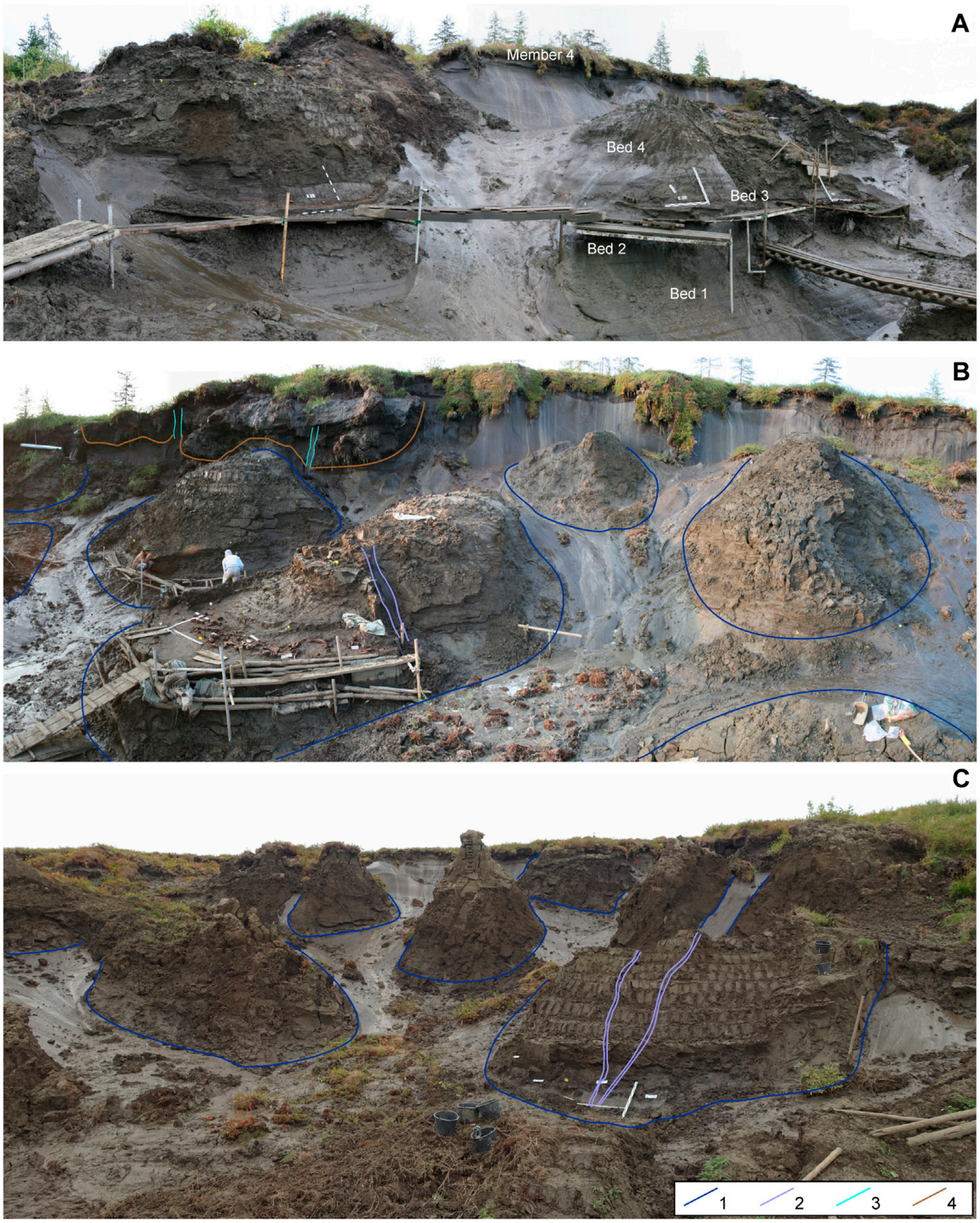

FIGURE 6 | Cryology of Member 3 deposits: **(A,B)** – Northern Point area; **(C)** – Yana B area of the Yana complex of sites. Illustration key: 1—outlines of the first generation of the late Pleistocene (MIS3) ice wedges; 2—outlines of the second generation of the late Pleistocene (MIS2) ice wedges initiated at the LGM; 3—Holocene ice veins; 4—base of the peaty deposits of Member 4 of Holocene age.

The syngenetically frozen deposits of Member 3 (**Figures 5, 6**) are composed of several stratigraphic units of varying appearance and thickness. Additionally, it contains the characteristic cultural horizon of the Yana sites, which occurs 7.5 m above the average summer water level (**Figures 5A,B**). The four clearly distinguishable beds include the following:

Bed 1, represented by a near-channel alluvium facies, occurs in the lower part of Member 3. Bed 1 deposits are composed of fine-grained sands interbedded with sandy silts and layers of gray and dark gray plant detritus. Bed 1 is up to 5–6 m in thickness. The contact with overlying Bed 2 sediments is gradual reflecting the shift to floodplain conditions.

Bed 2 consists of a floodplain alluvium facies, represented by clayey-sandy and sandy-clayey silts with washed plant detritus. The thickness of Bed 2 is 0.5–0.6 m.

Bed 3 is represented by a floodplain alluvial facies of sandy and clayey-sandy silts of gray-brownish and reddish-brownish color, with thin layers of fine-grained sand. The sediments are rich in

FIGURE 7 | Hearth structures opened in the culture-bearing deposits of the Yana site complex: **(A)** – 20 cm thick cultural layer in the frozen front within the excavation area, depression related to the hearth structure is clearly seen at the crossing of F16 excavation unit of the Northern Point area, excavations of 2004; **(B)** – excavated habitation surface with stone knapping workshop area near the hearth discovered in 2J25 excavation unit, excavations of the NP area in 2009; **(C)** – hearth structure in 3Z37 excavation unit at NP area in 2008; **(D)** – hearth structure in Q7R043 unit, excavations at the Yana B area of the Yana site complex in 2018; **(E)** – cryogenic deformation of the hearth structure observed in the frozen wall next to the polygon deposit contact with the ice vein observed in B22 unit, Northern Point, in 2005; **(F)** – cryogenic deformation observed in the frozen wall next to the contact between the ice vein and the polygon deposit in J29 unit, NP area in 2007.

plant detritus and contain a large number of thin plant roots *in situ* (i.e., in primary context). Bed 3 contains lithic artifacts (stone tools and lithic debitage pieces), bone and mammoth ivory artifacts, and abundant Pleistocene animal bones and bone fragments (**Figures 2D,E**, **3D,E**). Additionally, there are multiple hearth structures, typically circular, about 1 m wide and 20–25 cm deep (**Figures 7A–F**). Bed 3 represents the culture-bearing horizon of the Yana site complex, or the ancient habitation surface. The thickness of Bed 3 varies between 0.3 and 0.6 m. The presence of *in situ* cultural material marking the living surface briefly occupied by late Pleistocene humans also indicates a break in the fluvial sedimentation and a shift to aeolian deposition.

Bed 4 deposits represent a high floodplain facies, with two strata of horizontally layered sandy, clayey-sandy, and sandy-clayey silt containing two paleosol horizons, characterized by a high saturation of *in situ* plant roots (Bakina et al., 2017). Bed 4 deposits are 5–5.5 m thick.

Generally, Member 3 is composed of sandy-silt and silty sediments. The sand content changes within the profile (Pitulko et al., 2013; Pitulko and Pavlova, 2016), decreasing from bottom to top. Beds 1 and 2, which form the base of the T2 profile, have a higher sand and ice content than Beds 3 and 4, which are composed mostly of fine-grained silt. The sequence reflects a pattern typical of Ice Complex deposits of alluvial origin, exhibiting no visible breaks except for the period of human habitation. It reflects the accumulation of deposits on a floodplain that gradually changed to a high floodplain before the cultural remains were deposited, and then remained a high floodplain until the alluvial sedimentation stopped at around 13,000 years BP. Thus, the accumulation of Member 3 deposits of terrace T2 spans a period between late MIS3 and MIS2, which also is confirmed by the paleoenvironmental proxy record, reflecting relevant temperature and humidity trends (see, e.g., Pitulko et al., 2007; 2017; Pavlova and Pitulko, 2020).

The geocryological properties of Member 3 reveal the freezing of the deposits under varying environmental conditions. The cryotextures of Member 3 deposits represent layered parallel-concave striations, typical for high floodplain topography with low-centered permafrost polygons (Danilov, 1983). Well-expressed ice belts are characteristic of the lower part of the stratigraphic sequence, below the culture-bearing horizon (**Figure 6A**: Bed 1). Along with these ice belts, the lithological boundaries and the cultural layer exhibit a pronounced warping at the marginal parts of the polygon body. Generally, Beds 1, 2, and 3 are characterized by syngenetic freezing, indicated by the formation of thin micro streaks, and also by massive cryotextures and three generations of ice wedges.

Wide syngenetic ice wedges of the main/oldest generation penetrate Beds 1, 2, and 3 extending below the average water level (**Figures 2A**, **5A,B**). Their vertical length varies 16–18 m. In the lower part of Member 3, their width is 1.5 m, but gradually increases upward to 4 m at the top of the profile, where they are truncated and covered by Holocene deposits. These ice wedges form a regular polygonal pattern (**Figure 6**); the sides of the polygon vary between 4 and 9 m in length and, thus, the area of the polygon may reach 25–50 sq.m. The width of the ice wedges may be 6–8 m at the junction of two ice wedges. Remarkably, at the elevation of 11–12 m a.w.l., the width of ice wedges of the oldest generation decreases to 1.5 m. This indicates significant environmental change during their development, i.e., reduction in moisture and decline in winter temperatures.

The second generation of ice veins wedges displays an irregular pattern superimposed on the polygonal network formed by the older ice wedges (**Figures 6B,C**). The ice wedges are 0.2–0.3 m wide. Their upper surfaces are found at an elevation of 11–13 m a.w.l.; from this elevation, they penetrate downward into deposits of Member 3 for roughly 5–7 m and terminate at ~6–6.5 m a.w.l., extending into Bed 3 (the culture-bearing horizon) and the upper portion of Bed 2. Accordingly, the second generation of ice wedges is epigenetic to Beds 2 and 3, but syngenetic to Bed 4 deposits. As indicated by their spatial distribution, they are often superimposed on the previously formed polygons of the first generation.

The third and youngest generation of the ice wedges is common in the upper part of Member 3 deposits. These ice wedges penetrate T2 deposits to a depth of 3–4 m and do not extend to the culture-bearing deposits.

The above-mentioned geocryological features of the Member 3 deposits were observed during investigations of the Northern Point area (Pitulko et al., 2013). They are typical for the study area within the portion of T2 to which the culture-bearing deposits are confined, as demonstrated by the study of the Tums1 exposure (Pitulko et al., 2004) and the Yana B area (Pitulko, 2019a). The Tums1 sequence shows patterns resembling the NP area; however, the Yana B polygonal ice wedge network is slightly different from that at NP. The difference is manifested by increasing ice wedge width and reduced intra-polygonal area at the Yana B locality compared to Northern Point, where areas within the polygons are larger.

Most likely, this difference is due to differences in available moisture at the time of ice wedge development in various locations on the floodplain; the Yana B area seems to have been saturated, whereas the NP area was dryer. Additionally, second-generation ice wedges are more common at Yana B, whereas almost absent in the central part of the Northern Point locality, but better represented near the margin, where deposits indicate waterlogging.

Because the chronometry of T2 is well established, the development of the syncryogenic deposits of Member 3 can be linked to the paleoclimatic record. Hence, the formation of the oldest generation of ice wedges follows the start of Bed 1 accumulation roughly 40,000 years ago. Generally, this time corresponds to middle MIS3, or middle Karginian in the widely known Siberian geological terminology. Although no significant cooling during this interval was found in Western Beringian paleoenvironmental records (e.g., Wetterich et al., 2014: Figure 11; Pavlova and Pitulko, 2020), the formation of the main generation of ice wedges of T2 probably correlates with the H4/GS 9 stadial of the Greenland ice core climatic record, that is, ~39,900–38,200 years ago (Svensson et al., 2008; Rasmussen et al., 2014). At that time, near-channel deposits of Bed 1 formed under alternating alluvial and aeolian deposition during warmer months, and clearly remained subaerially exposed over the winter, which is a precondition for initial frost cracking and ice wedge development. It should be stressed that the present-day high floodplain deposits in the study area are perennially frozen and contain ice wedges of recent age, being formed within the past two thousand years and demonstrating that the environmental conditions necessary for ice wedge growth were present in the recent past.

For the next 10–12 thousand years, the accumulation of Bed 1 continued and its surface eventually reached an elevation where it remained above the water level for most of the year including the summer months, as indicated by the seasonality of the occupation at Northern Point, deduced from the composition of faunal remains and reconstruction of human activity (Pitulko et al., 2013; Pitulko and Pavlova, 2019). The Yana B area was wetter and hence could be used during the winter, which is supported by multiple lines of archaeological evidence (Pitulko, 2019a); the

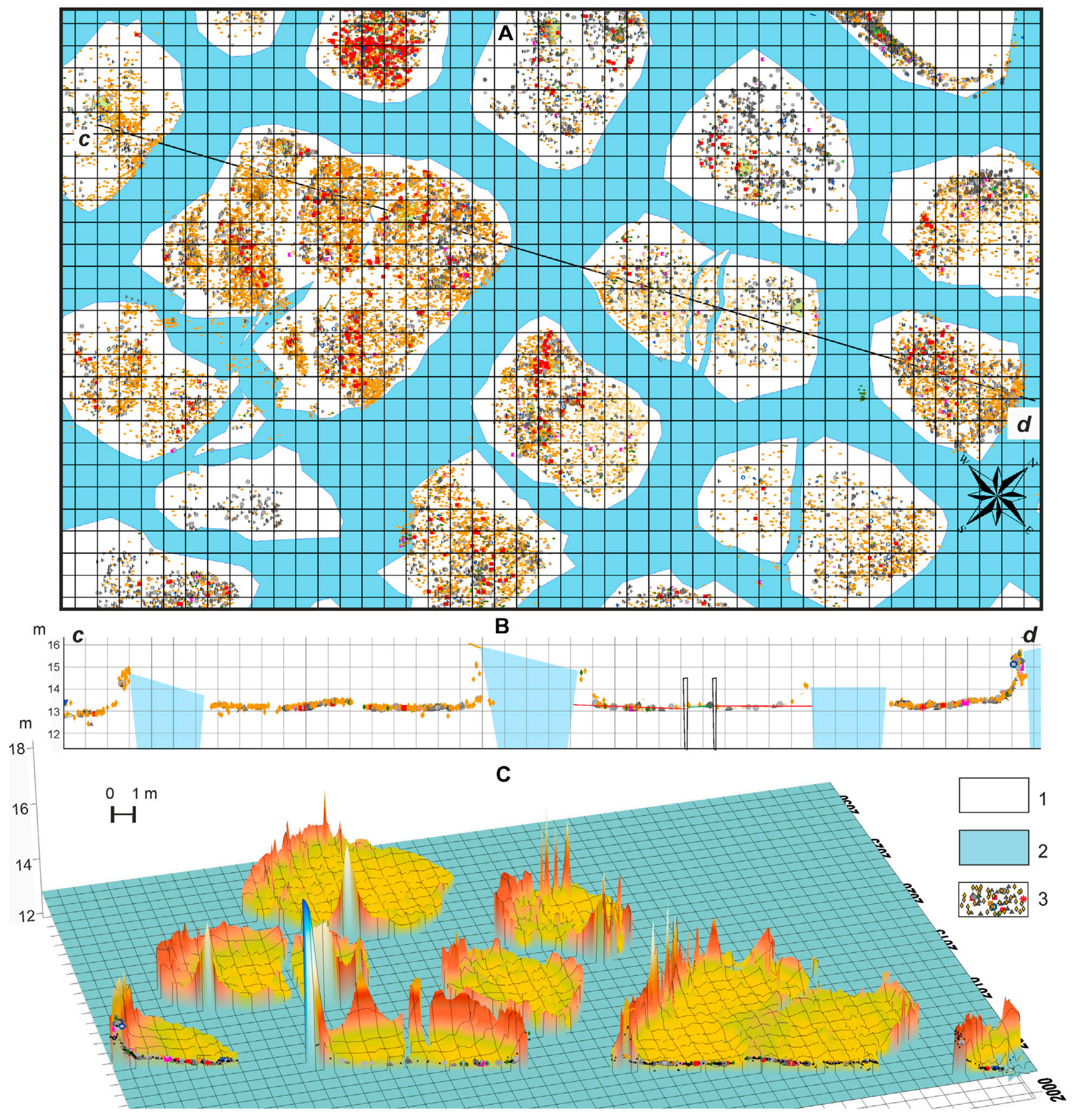

FIGURE 8 | Spatial distribution of *in situ* mapped cultural material of the Northern Point locality: **(A)** – excavation map; **(B)** - hypsometric profile along line along line ***c–d*** shown in part **(A)** within 13–16 m elevation in absolute marks viewed from South; **(C)** - spatial distribution chart for archaeological material along line ***c–d*** shown in part **(A)** viewed from North. Illustration key: 1—polygon ground body deposits; 2—ice wedge; 3—cultural material. After Pitulko and Pavlova (2016).

preference for winter occupation in this area likely reflects human decision-making based on several factors, including variation in snow cover depth, for sanitary reasons, and/or proximity to mammoth bones concentrated at YMAM and used for fuel at Yana B in large quantities (Pitulko, 2019a). Moreover, summer temperatures at the time of occupation of the Yana sites were warmer than at present (Pitulko et al., 2007), and thus the depth of the STL base should have been greater than at present.

The second generation of ice wedges formed shortly after occupation of the Yana site area ended about 26,000 years ago, most probably due to climate change corresponding to the beginning of the LGM. Frost fissures penetrated through compact deposits of the living surface (Bed 3) and the upper part of Bed 2, and the second generation of ice wedges began forming. Then, both generations of ice wedges continued to grow but the older ice wedges exhibit some reduction in width during

FIGURE 9 | The culture-bearing horizon of the Yana complex of sites: **(A)** excavations of the Northern point area in 2009: in the front of the central part of the polygon, the cultural layer is opened in subhorizontal position while in the rear part of the polygon next to the ice-wedge contact the cultural layer is found 2 m higher due to vertical deformation caused by the ice-wedge growth; **(B)** excavations of 2020 at the Yana B area: the cultural layer stretches horizontally in the middle part of the polygon deposit but becomes smashed in its marginal zone gradually taking a vertical position seen in bending and archaeological finds that moved upward by ~1.5 m; **(C)** the same polygon viewed from the North, with a narrow (1 m wide) strip of cultural material taking a position higher than the source level; **(D)** excavations of 2019, Yana B area, vertical frozen wall at the polygon boundary near the contact zone between the polygon body and the ice wedge, vertical and nearly vertical distribution of archaeological material in the bended part of the layer occurred due to cryogenic deformation of the cultural layer because of the ice-wedge growth after the formation of perennially frozen deposit which included the cultural horizon.

the LGM. These events are reflected in the spatial patterns of the archaeological remains at the Yana site.

Excavations of the Northern Point area of the Yana site complex performed in 2003 through 2015 opened more than 3,500 sq.m of the ancient living surface and revealed a dense concentration of occupation debris. The original permafrost polygonal pattern is clearly visible among the mapped cultural features and distribution of artifacts (**Figure 8A**). Cultural materials and structures are confined to the area within the perimeter of the polygonal bodies, which are separated from each other by the ice wedges. Combined with the latter, which are devoid of cultural materials, the total excavated area equals roughly 8,000 sq.m.

The excavations yielded an enormous quantity of material, including more than 150,000 artifacts, bones, and bone fragments (Pitulko et al., 2013; Pitulko, 2019a) with a complex spatial distribution, further complicated by the polygonal pattern of the permafrost disturbing the occupation surface (**Figures 9A–D**, **10A–D**) and distorting the spatial arrangement of the cultural remains (**Figures 8B,C**). Separate pieces of that puzzle, however, may be conjoined by matching portions of the living floor that have been divided by ice wedge formation with their counterparts across the adjacent ice wedge. Remarkably, the former hearths found within many of the polygons appear to be unrelated to the margins of the permafrost polygons (**Figures 7B–D**); some are located adjacent to an ice wedge margin and have been significantly disturbed by its growth (**Figures 7A,E,F**).

The pattern described above suggests that the occupation surface was not subdivided into separate polygon-related areas at the time of human occupation. Instead, the paleo-surface was relatively dry, well drained, level and intact, and unaffected by either a low- or a high-centered polygonal pattern, which would have been avoided by humans as a habitation area. The ice wedge network was in the process of formation, but the uppermost portion of the developing ice wedges remained at least 1 m below the surface, as indicated by analysis of the geology and geomorphology of similar contexts at the Yana site complex, i.e., on the former low and high floodplain surfaces, where observed depth of the permafrost table equals 1 m. Thus, the spatial pattern observable at the culture-bearing horizon is a function of ice wedge development, which continued after the

FIGURE 10 | Spatial and hypsometric distribution of the cultural layer observed in different parts of the same permafrost polygon revealed by the excavations at the Yana B area in 2017: **(A)** polygon with cultural horizon viewed from the West, arrows indicate locations of b, c, and d photographs documenting different parts of polygonal mound; **(B)** – subhorizontal position of the cultural layer in the middle part of the polygon deposit viewed from the East; **(C)** portion of the cultural layer near the ice-wedge border in the rear part of the polygon lays 3 m higher relative to the source level shown in a, view from the North-East; **(D)** narrow strip of the cultural layer bended up near the polygon margin, view from the North-West.

period of human occupation, until the end of the Pleistocene. Portions of the culture-bearing horizon were subdivided by the constant and intense pressure of the growing ice wedges on their sedimentary matrix.

Based on the measurement of individual finds (artifacts, animal bones, and their fragments) in a 3-D coordinate system, performed with a TOPCON GTS-229 total station and a SOKKIA CX-106 instrument, we can estimate the degree of cryogenic deformations of the culture-bearing horizon resulting from ice wedge development (**Figures 8B,C**, **11A,B**). Recorded changes in the hypsometric position of the artifacts adjacent to the margins of the polygons show displacement of 3–5 m relative to the undisturbed portion of the cultural horizon in the center of the polygon. Thus, in polygons containing a portion of the cultural layer, a sterile zone without artifacts can be observed along the perimeter of the polygon at the level of the cultural horizon (**Figures 8A,B**, **11C**). Typically, the artifact-free zone is approximately 1 m wide; here, the cultural deposits are replaced by a yellow-greenish ice-rich sandy silt derived from beneath the cultural horizon (i.e., uplifted from its original stratigraphic provenience).

Additionally, there is a pronounced warping of the cultural horizon beginning approximately 1 m from the polygon margin, and significantly uplifted cultural material near the contact of the polygon deposits and the ice wedge (**Figures 8B**, **11C**). The horizontal orientation of the cultural layer is transformed to a nearly vertical one (**Figures 11D,E**); in some cases, former hearths were found heavily disturbed along the contact zone. The upwarped portions of the cultural layer have been transformed into bands of isolated artifacts and bones which have been uplifted with the increasing thickness of the deposits. The vertical provenience of artifacts found within these cryogenic deformations adjacent to the margins of the polygon is 3–4 m above the cultural layer in the central part of the polygon; isolated bones derived from the ice-wedge contact zone are uplifted even higher. Such displaced finds were recorded whenever possible, but many of them were lost before they could be recorded due to the constraints of excavating as a controlled retrogressive thaw slump (Pitulko, 2008; Pitulko, 2015; Pitulko, 2019b).

The 3-D provenience data allow visualization of spatial patterns as shown in **Figure 8** (see also Pitulko, 2008; Basilyan et al., 2011; Pitulko et al., 2013). Each polygon in the profile is surrounded by peaks in the distribution of artifacts indicating the distance of vertical transport of archaeological finds from their original position relative to the concentrations inside the polygon perimeter. In theory, some artifacts and animal bones may have been transported to the upper surface of the ice wedge, or practically

FIGURE 11 | Vertical deformations of the cultural layer related to the growth of the ice wedges belonging to the oldest (MIS3) generation dissecting Member 3 deposits: **(A)** position of frozen *in situ* cultural layer bended up following the ice-wedge contact (in the right part of the picture) and hypsometric position of bones traveled up from the cultural layer and found 1.5 m below the second terrace (T2) brow (central upper on the picture), viewed from the South, NP area, excavations of 2005; **(B)** position of the cultural layer with deformations and a bone moved up alongside the ice wedge almost to T2 brow, the bone is found at 1.2 m depth below the present surface, view from the South, Yana B excavation area, excavations of 2016; **(C)** cultural layer observed in the frozen vertical wall: subhorizontal strip of the cultural layer sharply bends up in 1 m distance from MIS3 ice-wedge margin, view from South-Southwest, NP area, 2004; **(D)** vertical deformation of the cultural layer alongside the contact of the ice wedge and polygon deposit, viewed from the North, Northern point, 2007; **(E)** portion of the cultural layer in vertical position near the boundary between MIS3 ice wedge and the polygon deposit, viewed from the West, NP, 2006.

to the STL base (**Figures 11A,B**). Hence, they might end up in a hypsometric position that has no relation to their true geological age. Such cryoturbation occurs due to the continuous pressure of the growing ice wedges on a once intact surface, which is subdivided into separate polygons exposed by the excavations at Yana NP and Yana B. The same pattern of upward movement of material also is noted for the second generation of ice wedges, although the vertical distance of transport is comparatively modest (and proportional to the reduced dimensions of the ice wedges).

The Yana B locality exhibits a similar pattern of cryoturbation, but also illustrates its further development caused by thawing of the deposits. At present, this area of the Yana site complex is associated with a riverbank slope that has been subject to massive thermoerosion. Hence, the slope is largely transformed by a retrogressive thaw slump leading to the formation of thermokarst mounds (baydzharakhs) outlined by a polygon trough network (**Figure 3A**). After the ice wedges melted, the troughs were filled with younger sediment.

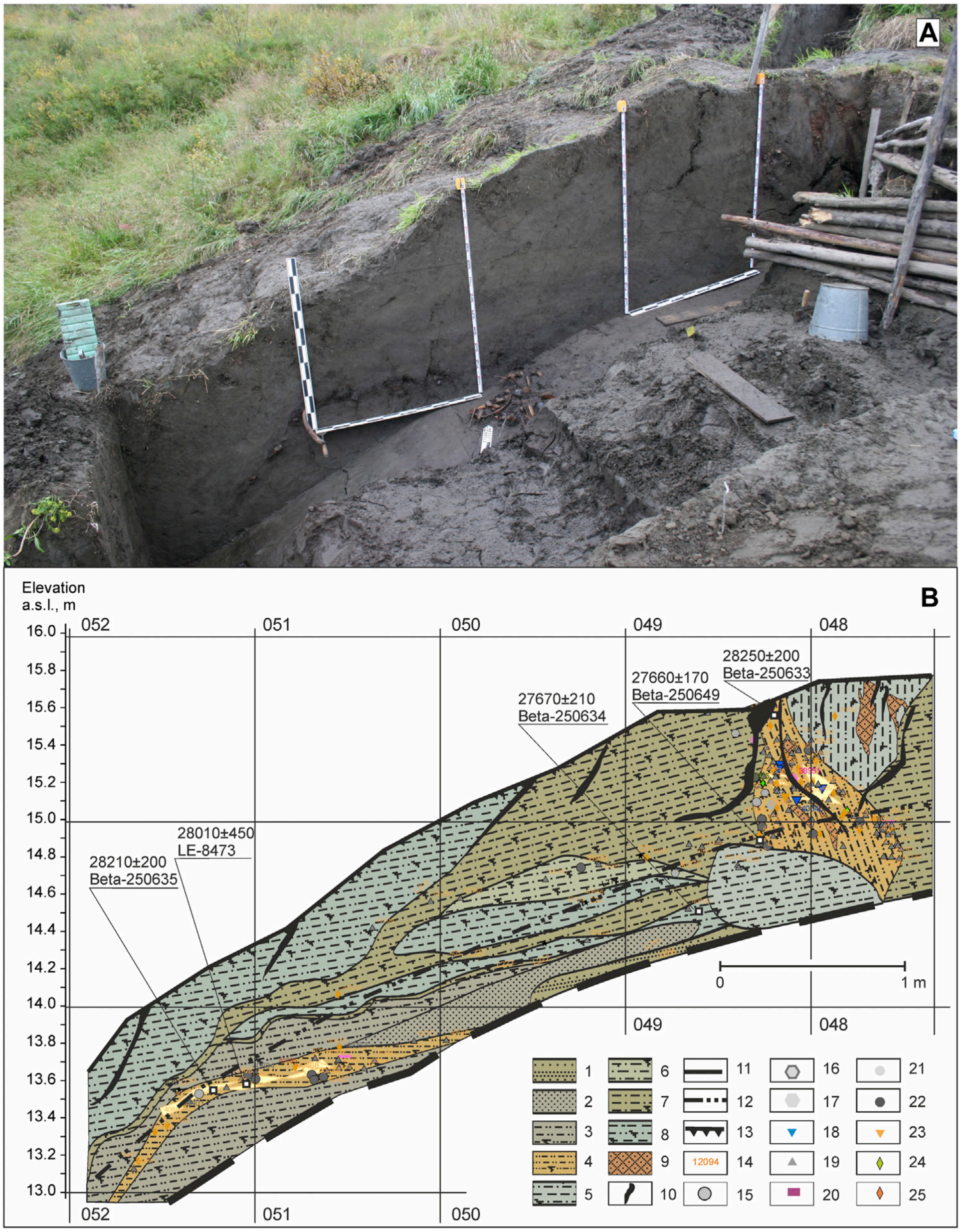

FIGURE 12 | Yana site complex, Yana B area, testing trench on the river bank slope at the Dvoinoy polygon unit **(A)** and lithology sequence observed in the NE excavation wall at grid line Q6F052 - Q6F049 **(B)**. Profile key: 1—unsorted sand of brownish-gray color; 2—fine-grained sand of gray color; 3—sandy silt of gray color; 4—sandy silt of brown color; 5—silt of gray color; 6—sandy-clayey silt of brownish-gray color; 8—clayey silt of light-gray color; 9—peat lenses; 10—drying fissure; 11—profile bottom; 12—STL boundary; 13—profile edge; 14—artifact number; 15—lithic side scraper; 16—core; 17—blank; 18—lithic tool; 19—flake; 20—blade; 21—pebble; 22—burnt rock; 23—bone tool; 24—mammoth ivory fragment; 25—fauna remains. After (Pitulko, 2019a).

Archaeological material (artifacts and animal bones) was displaced upward by as much as 6–7 m, due to the development of ice wedges, and redeposited in a secondary context by the infilling of thawed ice-wedge troughs (**Figures 12A,B**). There is no alternative source for these secondary concentrations than the primary culture-bearing horizon in the central portion of T2, 7–8 m below the modern surface. Such concentrations are related to ice wedge casts during their initial formation; further development of these features may lead to full transformation of the primary *in situ* context to a secondary concentration of archaeological material similar to that investigated at the Zhokhov site in the New Siberian islands (see, e.g., Pitul'ko, 1993; Pitulko et al., 2015b).

DISCUSSION

Within the larger context of Quaternary science, the properties of ice-rich permafrost, or Ice Complex deposits, have important

FIGURE 13 | Thermal erosion of the area in the Northern Point area of the Yana site complex: **(A)** - block collapse at the left bank of the Yana River due to continuously high water stand (collapse zone in between Northern Point and Area B of the Yana site; yellow flags seen in the lower right corner mark the western border of the excavation area); **(B)** - a cultural layer incorporated in the collapsed blocks, its position is indicated by I.G. Kovaltsov (excavations of 2016). Photo: E.Y. Pavlova.

implications for geology, geoarchaeology, and archaeology. Although the cryogenic processes described here are well known, their study is enhanced by insights derived from archaeological excavations in ice-rich permafrost, and geological observations made during the excavations, as concentrations of *in situ* cultural material serve as an excellent stratigraphic marker. The observations presented above were made over the course of many years of geoarchaeological investigation at the Yana site complex and they may be applied to Quaternary geology. By region, these observations should be applied to East Siberia/Western Beringia first of all; however, they can be extrapolated to any territory of the Northern Hemisphere where syngenetic permafrost deposits are present today or where there is evidence of their presence in the past, that is, mostly Northern Eurasia (see, e.g., Velichko, 1973; Velichko et al., 1997; Vandenberghe et al., 2014).

The most obvious cases are associated with the well-known, generally low resistance of thaw-sensitive Ice Complex deposits to changes in heating and moisture regimes that result in permafrost thawing, which includes thermal erosion and denudation, subsidence of the ground, and a variety of thermokarst processes. In stratigraphic record, they are represented by thaw unconformities and ice-wedge casts. Permafrost melting also entails thaw consolidation of the deposits, resulting in reduced ice component.

It is widely known that thermal erosion generates high rates of riverbank erosion (Kanevskiy et al., 2016; Fuchs et al., 2020; Wetterich et al., 2020; Morgenstern et al., 2021) and the erosion of marine shorelines (Are, 1980; Romanovskii et al., 2004; Günther et al., 2013; Overduin et al., 2016). The process often leads to an enormous loss of ice-rich deposits, followed by accelerated

FIGURE 14 | Yana site complex, excavations at the Northern Point area. Excavations of frozen deposits from a collapsed block containing a portion of the cultural layer **(A)** and a hearth structure discovered in this block remnant **(B)**. Photo: Elena Pavlova.

erosion, which involves collapse of frozen blocks undercut by running water, forming erosional niches due to combined thermal and mechanical action. Thus, the riverbank retreats several dozen meters per year. For example, Kanevskiy et al. (2016) calculated an average shoreline retreat of 45.4 m/yr on the Itkilik River, Alaska, with a maximum of 81.1 m/yr recorded at one bank/frozen cliff segment.

Such processes may be observed in the vicinity of the Yana site complex as well (see above) (**Figures 4**, **13A**). Although the erosional rate is slower than that on the Itkilik River, it may reach 20–30 m/yr. Relatively large collapsed blocks may be fully eroded. However, under certain conditions they can be rapidly buried in riverine sediment and incorporated into a new stratigraphic sequence. This phenomenon also may have taken place in the past. It should be stressed that such blocks (**Figure 13B**) may be buried in a frozen state and contain much information including archaeological finds and even fully datable features containing artifacts and faunal remains. Only the sediment block as a whole may be out of context in its new location (**Figures 14A,B**). If this is not recognized, the hypsometric position and age of the context may lead to erroneous assumptions, conclusions, and interpretations, which often have occurred in East Siberian Stone Age archaeology (see Pitulko and Pavlova (2016) for details).

Some cryogenic processes, such as solifluction and landslides, provide an analog to the previously described case. However, the contribution of slope processes to the transformation of culture-bearing deposits can be significantly greater. An impressive example is found at Afontova Gora in Krasnoyarsk, southern Siberia. Despite a hundred years of research, the geology of the site has remained controversial for decades (see review in Astakhov (1999)), inhibiting interpretation of the archaeology. Based on a detailed study of the deposits uncovered in the sections of Afontova, Zolnikov et al. (2017) demonstrated that site formation was a result of a viscoplastic flow of thawed, waterlogged loamy silt deposits containing cultural remains, including massive sediment blocks. It may be regarded as thaw slumping, combining a variety of slope processes, both water-derived and gravitational, that can occur anywhere in ice-rich permafrost regions.

The most noticeable impact on the landscape of thawing frozen deposits is slope (defluction, cryogenic creep) and solifluction processes. Although similar, these processes differ in the degree of water saturation, slope angle, and the rate of sediment transport. Solifluctional and other slope processes can contribute to the formation of a secondary archaeologic context at the base of the slope, as well as in secondary transformations of the cultural horizon *in situ*. An example is known from the Paleo-Eskimo Tayara Site on Qikirtaq Island, Canadian Arctic. When the site formed, cultural remains became buried in deposits resulting from the solifluction of reworked glacial-marine deposits. This process buried the northern part of the site. The rate of movement of the soliflucted deposit is estimated at roughly 1.68–2.86 cm/yr for approximately 350 years. As a result, three successive "cultural horizons" were formed (Todisco and Bhiry, 2008). Remarkably, this postdepositional process did not alter the spatial distribution of the material associated with human activities, as confirmed by statistical analysis of stone artifact concentrations. At the same time, researchers found that the orientation of bone was modified in part due to the impact of low-energy surface runoff (Todisco et al., 2009). Any natural concentration of fossils (e.g., animal bones, insect and plant fossils, pollen grains) may be reworked in the same way.

In arctic Western Beringia, many sites have been affected by cryogenic processes. The Urez-22 site in the western Yana-Indighirka lowland north-east of the Yana River provides a good example of sequential redepositing due to thermal denudation and slope processes (Pitulko et al., 2016). This small site has been subject to several stages of disturbance since it was originally formed approximately 11,000 years ago. At present, most of the cultural material is found adjacent to the steep slope of a gorge-like depression containing a small stream. Its original setting, however, was on the surface of the watershed. Shortly thereafter, it was redeposited into a thermokarst lake and then gradually transported down slope. As a result, "tertiary" concentrations formed. The same process was attributed by Nikolskiy et al. (2010) for the mass concentration of mammoth remains at Achchaghyi-Allaikha; most probably, the concentration also was human-induced, as it was at Urez-22, Nikita Lake, and other sites (Pitulko et al., 2016; Pitulko et al., 2017; Pitulko V., 2019).

The impact of slope processes on culture-bearing deposits can be significant even without evidence for redeposition, as is evident at such Palaeolithic sites of the Russian Plain as Kostenki (Holliday et al., 2007), Khotylevo (Gavrilov, 2015), and Zaraysk (Amirkhanov et al., 2009), where the culture-bearing deposits were probably disturbed by cryogenic processes. Today there is no permafrost at or near these sites, but it was present during the LGM. For instance, Zaraisk lacks a permafrost polygonal pattern, but there are other, local postdepositional processes contributed to disturbance of the culture-bearing deposits.

Despite a slow rate of transport, measuring only mm/yr, frost creep may have significant effects on cultural horizons, specifically with respect to the vertical distribution of the material. The apparent stratigraphic position of the material may be altered, as the deposit is transported without loss of structural integrity. If locally developed cracks open slowly and are gradually filled with the sedimentary matrix of the cultural horizon, they may form what appear to be cultural features in the form of pits, similar to those found at Zaraysk (Amirkhanov et al., 2009). The fill would contain concentrations of occupation debris, such as ash, charcoal, artifacts, and bones, redeposited in the cracks at a roughly 90° angle to the cultural horizon (indicating the natural origin of the feature as a result of frost creep).

Ice-wedge casts formed due to permafrost thawing are the most spectacular features in cryostratigraphy; this is one of the widely accepted criteria for identifying past permafrost development (Washburn, 1979; 1980). The sediment fill in the trough formed by the thawing of an ice wedge may contain a variety of paleobiotic materials redeposited in the ice-wedge cast. In archaeology, this may result in the formation of a secondary context, sometimes impressive because of the presence of mammoth bones and tusks. Ancient humans are often thought to be tireless builders of mammoth bone dwelling structures. Under certain circumstances, especially in the former permafrost areas, similar concentrations of mammoth bones and tusks may be mis-interpreted by researchers as *in situ* materials and evidence for human-made constructions, with other conclusions on related human activity and behavior.

A misunderstanding of the processes that underlie the formation of secondary concentrations in ice wedge casts may lead to misconceptions and erroneous interpretations of the cultural material. A good example is the subrectangular "blindage-like" features interpreted as semi-subterranean dwelling structures at the Upper Palaeolithic Timonovka sites on the Russian Plain (Gorodtsov, 1935; Krainov, 1956). As demonstarted by Velichko et al. (1977), the blindage-like structures are in fact large ice-wedge casts mistakenly attributed by Gorodtsov to human activity. In the ice-wedge cast fill, there was archaeological material from the overlying culture-bearing horizon which remained *in situ*, except for minor changes related to the thaw consolidation of the deposits. Cryogenic deformations of the culture-bearing deposits related to the formation of ice-wedge casts after the LGM are noted also at Eliseevichi and at other archaeological sites of the Russian Plain

(Velichko et al., 1997) within the limits of the former permafrost zone (Vandenberghe et al., 2014). In theory, they should be common within the area.

At the Yana site complex, an example of secondary concentrations of archaeological material in ice-wedge casts is found at the Yana B locality. Such concentrations, or secondary contexts, which formed when artifacts and bones were uplifted up by the pressure resulting from ice-wedge growth, may be seen in the geological profiles (**Figure 12**). If refrozen, such concentrations might be mistakenly regarded as in the primary context, leading to erroneous interpretations. In the case of Yana B, for instance, the cultural layer could be interpreted as three separate horizons at different hypsometric levels, subdivided by thick artifact-free deposits.

As the ice wedges in the study area remain frozen, none of the studied locations at the Yana sites provides evidence for fully formed ice-wedge casts containing redeposited cultural material. By contrast, the Zhokhov site provides evidence for the formation of such features in the East Siberian record. At this site, thick refrozen artifact-bearing deposits filled in troughs formed due to massive degradation of MIS3 ice-rich permafrost during the Terminal Pleistocene and Holocene in a series of formation cycles (Pitulko et al., 2015b; Pitulko, 2019b).

Finally, we turn to the cryogenic disturbance of fossils or, in the case of the Yana sites, the cryogenic disturbance of archaeological material, as a consequence of the pressure of growing ice wedges on frozen deposits within the polygons (Pitulko et al., 2011). During this process, the uppermost portion of the ice wedge grows upward in concert with the increasing thickness of the sediment. It should be emphasized that the width of the ice wedge is also increasing. As shown above (**Figures 8–11**), as the ice thickness increases, the archaeological material is driven up along the ice-wedge contact zone to a significant degree, in some cases, up to the base of the STL (**Figures 11A,B**). As a result, radiocarbon-datable materials (Pitulko and Pavlova, 2015), as well as dispersed sediment containing pollen, other microfossils, and geochemical signatures of the source horizon, are uplifted, forming a train of fossils within roughly 1 m from the ice-wedge contact. In their new hypsometric position within the profile, the fossils and artifacts are asynchronic to their sedimentary context. The same mechanism accounts for the transmission of geochemical signatures indicating goldfield deposits near the surface, detected by Victor (Pitulko, 1977) in the 1970s, and adopted as a tool for prospecting deeply buried metal-bearing deposits in the Kular goldfields of the Yana area (Pitulko et al., 1985). It was demonstrated that these characteristic geochemical signatures are transported upward by as much as 40–50 m along the ice-wedge contact zones due to ice-wedge growth.

The uplifted materials preserve *in situ* characteristics, despite being redeposited from the ice-wedge boundary and from the surface, and they remain frozen. Such material, if used for 14C dating, may lead to erroneous conclusions about the age of the deposits, for example, indicating 28,000 years BP for a level that may be only half that age (**Figures 5B**, **9A,B**, **10**, **11**). A series of dates obtained on such material at different levels along the ice wedge contact zone will yield ages similar to those obtained on the sediments overlying the source horizon. Such age estimates would be correct for the source horizon, but not for the overlying sediments, as the dated material is asynchronous to sedimentation.

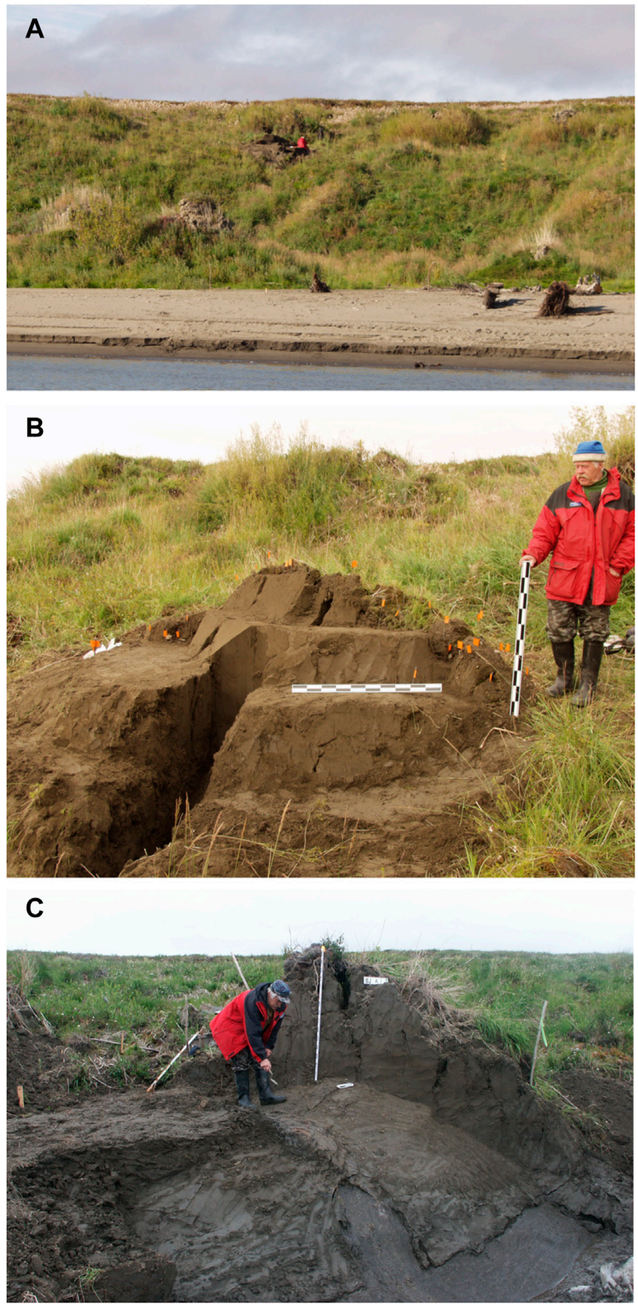

FIGURE 15 | Testing excavations in the Yana B area in 2003 and 2004: **(A)** left bank of the Yana River near the Yana B area of the Yana site complex in 2004 viewed from the South; **(B)** – excavated upper part of the thermokarst mound with faunistic and lithic finds marked by the flags making a circle, view from the South; **(C)** excavated part of the thermokarst mound after finds taken away, view from the South-West; it appears to be artifact-free deposit while in fact there is a cultural layer in 7 m depth.

In the Yana site profiles, due to the high density of observable archaeological material in the source horizon, it is relatively easy to avoid such sampling errors. However, it should be kept in mind that the cryogenic disturbance processes described above are common in permafrost areas with polygonal ice wedges. The observations made here may be applied to isolated fossils found in ice-wedge permafrost. In Quaternary geology, this is a common source of dating errors in thawed permafrost deposits, specifically in the former permafrost zone.

Cryogenic disturbance processes may underlie another source of errors in the interpretation of geology and age of the cultural remains and mistakes in the interpretation of past human behavior. This also is illustrated by the excavations at the Yana sites. We observed rich concentrations of cultural material confined to the upper portions of thermokarst mounds studied during test excavations at Yana B in 2003 and 2004 (**Figures 15A,B**). The concentrations of material exhibited a peculiar spatial pattern: the archaeological materials displayed a ring-like structure parallel to the margins of the thermokarst mound. Cultural material was absent in the center of the mounds but common within an approximately 1 m-wide zone adjoining the margins of the mound.

Although the source of the spatial pattern initially was unclear, it became apparent when it was observed that in the upper part of the Yana site geological sequence, the layer containing artifacts often displays a reverse dip. When the uppermost deposits of the polygon containing uplifted faunal remains and artifacts slumped in the course of thawing, a ring-like spatial pattern in the distribution of the material formed (**Figures 15B,C**). The archaeological material is represented primarily by bone fragments with a mean size class of 10–15 cm. Such spatial patterns appear when frozen deposits begin to thaw from the surface down to subhorizontal features. Although entirely a result of cryogenic processes, the spatial patterns acquire a characteristic signature in a cultural deposit. However, in our case, it is 5–5.5 m above the original cultural context from which the artifacts and bones are derived, as is shown by the age of 28,000 years BP obtained from the source horizon. The patterns reflect a complex interplay of cryogenic processes and archaeological site formation, and it would be a mistake to interpret them as entirely the product of human occupation.

Another feature observed in the Yana Ice Complex relates to bedded and warped pattern of the ice-wedge polygon deposits, which contain peat inclusions, concentrations of plant remains, and the cultural horizons. Alternating ice streaks and sediment layers are warped near the ice-wedges bordering the polygons. The pattern is found at many places bearing MIS3 Ice Complex deposits across arctic East Siberia, including the Yana River (see, e.g., Tomirdiaro and Chernenkiy, 1987; Schirrmeister et al., 2011; 2013; Wetterich et al., 2014; Murton et al., 2015). In the past, it was assumed that the pattern arose from the former microtopography of the polygons, including polygon ponds, in which layered peat/plant remains were deposited, creating the low central depression of the polygons (Romanovskii, 1977; see also Schirrmeister et al., 2013; Wetterich et al., 2014 for overview).

The development of the polygons is thought to be a stepwise transformation of the deposits from seasonally unfrozen to perennially frozen, taking place under climate conditions that also effect changes in the sedimentation regime between aeolian and shallow stream settings (see Vasil'chuk, 2006; 2013; Wetterich et al., 2014). This approach, which is based on actualistic observations, is tied to a hypothesis of a uniform origin of Ice Complex deposits, but there exist various alternative hypotheses [for an overview, see Schirrmeister et al. (2011; 2013)].

Although a general discussion of Ice Complex origins is outside our scope, we note that the polygenetic genesis of the Ice Complex deposits proposed by Sher (1997) is the most compelling one from our perspective, based on our research at the Yana site complex. The concept of polygenetic genesis suggests an accumulation of Ice Complex deposits under various sedimentation regimes, controlled by similar landscape and topography, climate conditions, and periglacial processes. In the Yana area, the Ice Complex deposits of T2 are clearly linked to alluvial deposition, with a succession of changes in the sedimentation environment beginning with alluvial sedimentation gradually changing to subaerial, followed by a return to subaquatic accumulation, which is superseded by a final shift to aeolian deposition before 13,000 years ago. Additionally, in the Yana site complex we have an ideal chrono-stratigraphic marker: an intensively occupied human habitation surface with hundreds of thousands of artifacts and bones, and former hearths.

This culture-bearing horizon, as well as other ice-rich sediments and ice layers present in the profiles, demonstrate the hallmark pattern of the Ice Complex deposits; all of them are warped in contact with the ice wedges, with artifacts, animal bones, and traces of hearths incorporated into the warped layer. The layers exhibit varying angles of warping: the deeper the layer, the larger the angle of warping. The pattern is a consistent one and can be observed throughout the Yana site complex. The culture-bearing horizon displays a pronounced warp at an angle of almost 90° within ~1 m distance to the ice wedge that may be traced with cultural materials, former hearths, and sedimentary matrix. This suggests that polygonal patterns were not present at the time of occupation, including either low- or high-centered permafrost polygons. A polygonal topography would be incompatible with human habitation. The surface was level at that time, well drained and dry year-round, probably except for occasional flooding events. The warping of the cultural layer took place after abandonment of the site, which is evident in the uplifted margins of the former hearths. The cultural horizon subsequently was buried by river sediments and later became incorporated into the sequence of permafrost deposits of T2, which remain frozen today.

Ice wedges of the oldest generation, formed about 40,000 years ago, continued to grow, resulting in compression of the sediment and causing warping and uplifting. At the time of human habitation, the ice wedges were relatively thin. When the initial frost fissures occurred 40,000 years ago, they were approximately 12 m apart from each other with a diameter of approximately 10–12 m. At present, they are only 5–6 m at the hypsometric position of the culture-bearing horizon. The deposits did not disappear but were displaced by growing ice wedges and partially consolidated, but also partially uplifted and warped. The latter was a function of time in the upper part of the MIS3 sequence of T2.

The continuous growth of ice wedges resulted in the compression of the deposits within the polygons, warping and uplifting of some of the deposits with implications for the rate of accumulation of the Ice Complex. Because uplifted deposits do not disappear but remain in place, they contribute to the increased thickness of the deposits, in conjunction with the continued accumulation of surficial sediment. The increased thickness of Ice Complex deposits within the depositional cycle, thus, is not a function of sedimentation alone, but a combined result of sedimentation and redistribution of existing polygonal deposits. Also, there is positive feedback between ice-wedge growth and increased polygonal sediment thickness: the uplifted deposits result in increased thickness, which promotes further ice-wedge growth. Finally, the frost-related pressure forming the warped pattern of the deposits may account for the formation of a low-centered polygonal pattern on the surface. This explanatory model may be incorporated into the classic theory of Ice Complex development.

It is difficult to determine, whether or not, and to what degree, these observations can be extrapolated to other areas, but they should be taken into account and further explored in other regions of arctic East Siberia. Thus, it is unclear whether peat inclusions can be included in this discussion because they likely reflect the "thaw-lake cycle" hypothesized by Ellis et al. (2008) to explain the formation of arctic wetlands, or the formation of the thermokarst terrain in a broader sense. However, paleosol horizons known in Ice Complex deposits (Gubin, 1994; Lupachev and Gubin, 2008; Zanina et al., 2011) most probably can be regarded as indications of a formerly level surface based on the study of paleosol horizons in the Yana area (Bakina et al., 2017). The current theory of Ice Complex formation may be revised by postulating 1) initial sediment accumulation on level terrain under various depositional regimes, 2) later modified by ice-wedge growth, 3) resulting in warping and uplifting of deposits in contact with ice wedges, as inferred from archaeological investigations at the Yana site complex.

CONCLUSION

The properties of ice-rich deposits generate a variety of potential taphonomic biases. Most of them have implications for dating the deposits. Generally, such biases are related to the thawing of frozen deposits, which results in the formation of secondary contexts at various scales, which include ice-wedge casts containing thawed material. Such secondary depositional contexts as result of thermokarst processes are found in a lower-lying position than the original hypsometric position. Collapsed blocks of frozen deposits may contain intact fragments of frozen layers with artifacts and/or other fossils and may be incorporated into a new stratigraphic context and subsequently refrozen. If not recognized as such, this can result in erroneous age estimates and overall interpretation of the sequence.

Severe cryoturbation occurs in Ice Complex deposits within the polygons, resulting in warping of the layers in contact with the ice wedge. This process is primarily responsible for the distorted pattern of Ice Complex deposits. The warping of layers is due to the pressure generated by growth of the ice wedges on the polygon structure. As a result, the materials contained in the warped layer are displaced upward, sometimes to a significant degree.

The consequences include the following: 1) chronometry problems, because datable material can be transposed to a different hypsometric position; 2) problems of interpretation in archaeology with respect to dating, culture, and human behavior; 3) material redeposited this way may form secondary concentrations at different hypsometric levels and thus become a basis for multiple misinterpretations (see above); 4) in geology, the transportation of geochemical signatures may lead to erroneous interpretation of the geological potential of the area; 5) uplifted deposits contribute to increased Ice Complex thickness, which is not a direct function of sediment accumulation, but a combined result of sedimentation and redistribution of accumulated matter within an existing polygon deposit.

It should be stressed that these observations can be made only in conjunction with archaeological investigations, which provide an excellent stratigraphic context and a detailed reconstruction of the ancient living surface. We suggest that outstanding questions about Ice Complex deposits can be addressed with the findings presented here. In any case, the results demonstrate the potential of a "geoarchaeological" approach, which therefore deserves further study.

DATA AVAILABILITY STATEMENT

The raw data supporting the conclusions of this article will be made available by the authors, without undue reservation.

ETHICS STATEMENT

Written informed consent was obtained from the relevant individual(s) for the publication of any potentially identifiable images or data included in this article.

AUTHOR CONTRIBUTIONS

Authors have contributed equally to the project both in the fieldwork by data collecting and in the preparation of the manuscript. VP leads the Yana excavation project and designed the present study. Field observations are recorded by

EP who also participated in writing of the text and designed all illustrations.

FUNDING

Authors are more than grateful to the Rock Foundation of New York, U.S., for unlimited support given to Zhokhov/Yana project since 2000 and to the present study. Since 2014, the Yana excavations remain a part of research funded by the Russian Science Foundation (project nos. 16-18-10265P RNF and 21-18-00457 RNF). Unlimited thanks due to all participants of the fieldwork in Yana for their endless patience, labour, and intellectual investment into investigations of Yana's ice-rich permafrost. Written informed consent was obtained from the Yana project participants S. O. Remizov, I. A. Spiridonov, S. G. Kritsuk, P. I. Pulmanen, VP, S. N. Astakhov, N. O. Chetverikov, E. A. Pushkov, I. G. Kovaltsov, I. V. Chasnyk, M. D. Kupriyanova, A. P. Shubenkin, and A. O. Mashezerskaya for the publication of any potentially identifiable images or data included in this article.

DEDICATION

We dedicate this article to the memory of Victor M. Pitulko, Vladimir's father — outstanding scholar, geologist, and explorer of East Siberia.

ACKNOWLEDGMENTS

Author's special thanks due to John F. Hoffecker for kindly provided assistance with the editing of the final version of the article. Finally, we want to thank LS for encouraging us to produce this article, and two reviewers whose valuable comments helped to improve its quality.

REFERENCES

Amirkhanov, K. A., Akhmetgaleeva, N. B., Buzhilova, A. P., Burova, N. D., Lev, S. I., and Mashchenko, E. N. (2009). *Investigation of the Paleolithic in Zaraisk. 1999–2005*. Moscow: Paleograf, 466.

Andreev, A. A., Schirrmeister, L., Tarasov, P. E., Ganopolski, A., Brovkin, V., Siegert, C., et al. (2011). Vegetation and Climate History in the Laptev Sea Region (Arctic Siberia) during Late Quaternary Inferred from Pollen Records. *Quat. Sci. Rev.* 30, 2182–2199. doi:10.1016/j.quascirev.2010.12.026

Are, F. E. (1980). *Thermal Abrasion of Sea Coasts*. Moscow: Nauka, 160.

Ashastina, K., Schirrmeister, L., Fuchs, M., and Kienast, F. (2017). Palaeoclimate Characteristics in interior Siberia of MIS 6-2: First Insights from the Batagay Permafrost Mega-Thaw Slump in the Yana Highlands. *Clim. Past* 13, 795–818. doi:10.5194/cp-13-795-2017

Astakhov, S. N. (1999). *Paleolithic of the Yenisei. The Paleolithic Sites at Afontova Gora at the City of Krasnoyarsk*. St. Petersburg: Izdatel'stvo "Evropeiskii Dom", 207.

Atlas of the Arctic (1985). *Atlas of the Arctic*. Moscow: GUGK.

Bakina, L. G., Pavlova, E. Y., Kritsuk, S. G., and Pitulko, V. V. (2017). "Humus Content and Fraction-Group Composition of the Ice Complex Deposits of the Yana RHS Site (Western Part of Yana-Indighirka lowland)," in Fundamental problems of the Quaternary: results and perspectives of the research. Proceeding of the X All-Russian Quaternary Conference, Moscow, September 25-29, 2017 (Moscow: GEOS), 33–34.

Basilyan, A. E., Anisimov, M. A., Nikolskiy, P. A., and Pitulko, V. V. (2011). Wooly mammoth Mass Accumulation Next to the Paleolithic Yana RHS Site, Arctic Siberia: its Geology, Age, and Relation to Past Human Activity. *J. Archaeological Sci.* 38 (9), 2461–2474. doi:10.1016/j.jas.2011.05.017

Basilyan, A. E., Anisimov, M. A., Pavlova, E. Y., Pitulko, V. V., and Nikolskiy, P. A. (2009). "Base Reference Section of Quaternary Deposits for Yana-Indighirka lowland in the Yana River Downstream Area," in Fundamental Problems of Quaternary: Results and Trends of Further Research. Proceedings of the VI All-Russian Quaternary Conference, Novosibirsk, October 19–23, 2009 (Novosibirsk: SB RAS), 63–65.

CAVM Team (2003). *Circumpolar Arctic Vegetation Map. Scale 1: 7,500,000Conservation of Arctic Flora and Fauna (CAFF) Map No. 1*. Anchorage, Alaska: U.S. Fish and Wildlife Service.

Danilov, I. D. (1983). *Methods of Cryological Studies*. Moscow: Nedra, 238.

Ellis, C. J., Rochefort, L., Gauthier, G., and Pienitz, R. (2008). Paleoecological Evidence for Transitions between Contrasting Landforms in a Polygon-Patterned High Arctic Wetland. *Arctic, Antarctic, Alpine Res.* 40 (4), 624–637. doi:10.1657/1523-0430(07-059)[ellis]2.0.co;2

Froese, D. G., Zazula, G. D., Westgate, J. A., Preece, S. J., Sanborn, P. T., Reyes, A. V., et al. (2009). The Klondike Goldfields and Pleistocene Environments of Beringia. *GSA Today* 19 (8), 4–10. doi:10.1130/gsatg54a.1

Fuchs, M., Nitze, I., Strauss, J., Günther, F., Wetterich, S., Kizyakov, A., et al. (2020). Rapid Fluvio-Thermal Erosion of a Yedoma Permafrost Cliff in the Lena River Delta. *Front. Earth Sci.* 8, 336. doi:10.3389/feart.2020.00336

Gakkel, Y. Y., and Korotkevich, E. S. (1960). *Severnaya Yakutiya (Fiziko-geograficheskaya Kharakteristika [Northern Yakutia (Phisycal Geography)]*. Leningrad: Morskoy transport, 280. (In Russian).

Gavrilov, A. V., Romanovskii, N. N., and Hubberten, H.-W. (2006). Paleogeographic Scenario of the Postglacial Transgression on the Laptev Sea Shelf. *Earth Cryosphere* 10, 39–50.

Gavrilov, K. N. (2015). "The Archaeological Context of the New Radio-Carbon Datings of the Khotylevo 2 - point B (V) Site," in *Ancient Cultures of the Eastern Europe: Important Sites and Reference Complexes in the Context of Modern Archaeological Research*. Editor G. A. Khlopachev (St. Petersburg: Peter the Great Museum), 103–112.

Gorodtsov, V. A. (1935). *Timonovskaya Palaeolithic Site. Results of Archaeological Excavations of 1933*. Moscow and Leningrad: Izdatelstvo AN SSSR Publ., 35. (in Russian).

Gubin, S. V. (1994). Pozdnepleistotsenovoe Pochvoobrazovanie Na Primorskikh Nizmenostyakh Severa Yakutii (Late Pleistocene Pedogenesis in Coastal Lowlands of Northern Yakutia). *Pochvovedenie (Soil Sci.)* 8, 5–14. (in Russian).

Günther, F., Overduin, P. P., Sandakov, A. V., Grosse, G., and Grigoriev, M. N. (2013). Short- and Long-Term Thermo-Erosion of Ice-Rich Permafrost Coasts in the Laptev Sea Region. *Biogeosciences* 10, 4297–4318. doi:10.5194/bg-10-4297-2013

Holliday, V. T., Hoffecker, J. F., Goldberg, P., Macphail, R. I., Forman, S. L., Anikovich, M., et al. (2007). Geoarchaeology of the Kostenki-Borshchevo Sites, Don River valley, Russia. *Geoarchaeology* 22, 181–228. doi:10.1002/gea.20163

Izyumenko, S. A. (1966). *Spravochnik Po Klimatu SSSR. Vypusk 24. Yakutskaya ASSR. Chast II. Temperatura Vozdukha I Pochvy [Handbook on the Climate of the USSR. Issue 24. Yakut ASSR. Part II. Air and Soil Temperatures]*. Leningrad: Gidrometeoizdat. (In Russian).

Izyumenko, S. A. (1968). Spravochnik Po Klimatu SSSR. Vypusk 24. Yakutskaya ASSR. Chast IV. Vlaznost Vozdukha, Atmosfernye Osadki I Snezhnyi Pokrov *[Handbook on the Climate of the USSR. Issue 24. Yakut ASSR. Part IV. Atmospheric Moisture, Precipitation and Snow Cover]*. Leningrad: Gidrometeoizdat. (In Russian).

Jørgensen, T., Haile, J., Möller, P., Andreev, A., Boessenkool, S., Rasmussen, M., et al. (2012). A Comparative Study of Ancient Sedimentary DNA, Pollen and Macrofossils from Permafrost Sediments of Northern Siberia Reveals Long-Term Vegetational Stability. *Mol. Ecol.* 21, 1989–2003. doi:10.1111/j.1365-294X.2011.05287.x

Kanevskiy, M., Shur, Y., Fortier, D., Jorgenson, M. T., and Stephani, E. (2011). Cryostratigraphy of Late Pleistocene Syngenetic Permafrost (Yedoma) in Northern Alaska, Itkillik River Exposure. *Quat. Res.* 75, 584–596. doi:10.1016/j.yqres.2010.12.003

Kanevskiy, M., Shur, Y., Strauss, J., Jorgenson, T., Fortier, D., Stephani, E., et al. (2016). Patterns and Rates of riverbank Erosion Involving Ice-Rich Permafrost (Yedoma) in Northern Alaska. *Geomorphology* 253, 370–384. doi:10.1016/j.geomorph.2015.10.023

Kaplina, T. N. (2009). Alas Complex of North Yakutia. *Earth Cryosphere* 12, 3–17.

Kaplina, T. N. (1981). "Late Cenozoic Development of Frozen Deposits in Northern Yakutia," in *Permafrost Development in Eurasia (Based on Examples of Specific Regions)*. Editors G. D. Dubikov and V. V. Baulin (Moscow: Nauka), 153–181.

Katasonov, E. M. (1979). *Stroenie I Absolyutnaya Geokhronologiya Alasnykh Otlozhenii Tsentral'noi Yakutii [Structure and Absolute Geochronology of Alassy Deposits of Central Yakutia]*. Novosibirsk: Nauka. (In Russian).

Kienast, F., Schirrmeister, L., Siegert, C., and Tarasov, P. (2005). Palaeobotanical Evidence for Warm Summers in the East Siberian Arctic during the Last Cold Stage. *Quat. Res.* 63, 283–300. doi:10.1016/j.yqres.2005.01.003

Krainov, D. A. (1956). Dwellings of Timonovskaya Palaeolithic Site (Based on the Excavations of V.A. Gorodtsov). *Soviet Archaeology XXV* 1, 13–34. (in Russian).

Lee, E. J., Merriwether, D. A., Kasparov, A. K., Khartanovich, V. I., Nikolskiy, P. A., Shidlovskiy, F. K., et al. (2018). A Genetic Perspective of Prehistoric hunter-gatherers in the Siberian Arctic: Mitochondrial DNA Analysis of Human Remains from 8000 Years Ago. *J. Archaeological Sci. Rep.* 17, 943–949. doi:10.1016/j.jasrep.2016.06.001

Lupachev, A., and Gubin, S. V. (2008). Role of Pedogenesis in the Formation of Permafrost Transition Layer Structure (In Russian). *Earth' Cryosphere* 12, 75–83.

Makeyev, V. M., Ponomareva, D. P., Pitulko, V. V., Chernova, G. M., and Solovyeva, D. V. (2003). Vegetation and Climate of New Siberian Islands for the Past 15 000 Years. *Arctic, Antarctic, Alpine Res.* 35, 28–35. doi:10.1657/1523-0430(2003)035[0056:vacotn]2.0.co;2

Morgenstern, A., Overduin, P. P., Günther, F., Stettner, S., Ramage, J., Schirrmeister, L., et al. (2021). Thermo-erosional Valleys in Siberian Ice-Rich Permafrost. *Permafrost and Periglac Process* 32, 59–75. doi:10.1002/ppp.2087

Morgenstern, A., Ulrich, M., Günther, F., Roessler, S., Fedorova, I. V., Rudaya, N. A., et al. (2013). Evolution of Thermokarst in East Siberian Ice-Rich Permafrost: A Case Study. *Geomorphology* 201, 363–379. doi:10.1016/j.geomorph.2013.07.011

Murton, J. B., Goslar, T., Edwards, M. E., Bateman, M. D., Danilov, P. P., Savvinov, G. N., et al. (2015). Palaeoenvironmental Interpretation of Yedoma Silt (Ice Complex) Deposition as Cold-Climate Loess, Duvanny Yar, Northeast Siberia. *Permafrost Periglac. Process.* 26, 208–288. doi:10.1002/ppp.1843

Nekrasov, I. A., and Devyatkin, V. N. (1974). *Morphology of the Criolithozone of the Yana River basin and Adjacent Regions*. Novosibirsk: Nauka, 73.

Nikolskiy, P. A., Basilyan, A. E., Sulerzhitsky, L. D., and Pitulko, V. V. (2010). Prelude to the Extinction: Revision of the Achchagyi-Allaikha and Berelyokh Mass Accumulations of mammoth. *Quat. Int.* 219, 16–25. doi:10.1016/j.quaint.2009.10.028

Nikolskiy, P. A., Sulerzhitsky, L. D., and Pitulko, V. V. (2011). Last Straw versus Blitzkrieg Overkill: Climate-Driven Changes in the Arctic Siberian mammoth Population and the Late Pleistocene Extinction Problem. *Quat. Sci. Rev.* 30, 2309–2328. doi:10.1016/j.quascirev.2010.10.017

Nikolskiy, P., and Pitulko, V. (2013). Evidence from the Yana Palaeolithic Site, Arctic Siberia, Yields Clues to the riddle of mammoth Hunting. *J. Archaeological Sci.* 40, 4189–4197. doi:10.1016/j.jas.2013.05.020

Opel, T., Murton, J. B., Wetterich, S., Meyer, H., Ashastina, K., Günther, F., et al. (2019). Past Climate and Continentality Inferred from Ice Wedges at Batagay Megaslump in the Northern Hemisphere's Most continental Region, Yana Highlands, interior Yakutia. *Clim. Past* 15, 1443–1461. doi:10.1594/PANGAEA.90410510.5194/cp-15-1443-2019

Overduin, P. P., Wetterich, S., Günther, F., Grigoriev, M. N., Grosse, G., Schirrmeister, L., et al. (2016). Coastal Dynamics and Submarine Permafrost in Shallow Water of the central Laptev Sea, East Siberia. *The Cryosphere* 10, 1449–1462. doi:10.5194/tc-10-1449-2016

Pavlova, E. Y., and Pitulko, V. V. (2020). Late Pleistocene and Early Holocene Climate Changes and Human Habitation in the Arctic Western Beringia Based on Revision of Palaeobotanical Data. *Quat. Int.* 549, 5–25. doi:10.1016/j.quaint.2020.04.015

Pitulko, V. (2015). "Digging through Permafrost in Siberia," in *Field Archaeology from Around the World. Ideas and Approaches*. Editors M. Carver, B. Gaydarska, and S. Monton-Subias (Springer International Publishing Switzerland), 111–113. doi:10.1007/978-3-319-09819-7_16

Pitulko, V. (2019c). "In Pursuit of the Time: Searching for the Initial Human Settlement of the Siberian Arctic," in *The Past of Humankind as Seen by the Petersburg Archaeologists at the Dawn of the Millenium (To the Centennial of the Russian Academic Archaeology)*. Editors Y. A. Vinogradov, S. A. Vasiliev, and K. N. Stepanova (St. Petersburg: St. Petersburg: Centre for Oriental Studies Publishers), 103–136. doi:10.31600/978-5-85803-525-1-103-136

Pitulko, V. M., Reznikov, I. N., and Ulyanov, N. K. (1985). *Lithochemical Prospecting Methods in Geology*. Leningrad: Nedra, 199.

Pitulko, V. M. (1977). *Secondary Scattering in the Cryolithozone*. Leningrad: Nedra, 197.

Pitulko, V., Nikolskiy, P., Basilyan, A., and Pavlova, E. (2013). "Human Habitation in the Arctic Western Beringia Prior the LGM," in *Paleoamerican Odyssey*. Editors K. Graf, C. V. Ketron, and M. R. Waters (College Station, TX: Center for the Study of the First Americans, Texas A&M University Press), 13–44.

Pitulko, V., Pavlova, E., and Nikolskiy, P. (2017). Revising the Archaeological Record of the Upper Pleistocene Arctic Siberia: Human Dispersal and Adaptations in MIS 3 and 2. *Quat. Sci. Rev.* 165, 127–148. doi:10.1016/j.quascirev.2017.04.004

Pitul'ko, V. (2001). Terminal Pleistocene—Early Holocene Occupation in Northeast Asia and the Zhokhov Assemblage. *Quat. Sci. Rev.* 20, 267–275. doi:10.1016/S0277-3791(00)00117-7

Pitul'ko, V. V. (1993). An Early Holocene Site in the Siberian High Arctic. *Arctic Anthropol.* 30 (1), 13–21. Available at: http://www.jstor.org/stable/40316326.

Pitulko, V. V., Basilyan, A. E., and Pavlova, E. Y. (2014). The Berelekh Mammoth "Graveyard": New Chronological and Stratigraphical Data from the 2009 Field Season. *Geoarchaeology* 29, 277–299. doi:10.1002/gea.21483

Pitulko, V. V., Ivanova, V. V., Kasparov, A. K., and Pavlova, E. Y. (2015b). Reconstructing Prey Selection, Hunting Strategy and Seasonality of the Early Holocene Frozen Site in the Siberian High Arctic: a Case Study on the Zhokhov Site Faunal Remains, De Long Islands. *Environ. Archaeology* 20, 120–157. doi:10.1179/1749631414Y.0000000040

Pitulko, V. V., Nikolsky, P. A., Girya, E. Y., Basilyan, A. E., Tumskoy, V. E., Koulakov, S. A., et al. (2004). The Yana RHS Site: Humans in the Arctic before the Last Glacial Maximum. *Science* 303, 52–56. doi:10.1126/science.1085219

Pitulko, V. V., Pavlova, E. Y., Basilyan, A. E., and Kritsuk, S. G. (2011). "Features of Vertical Distribution of the Materials within the Marginal Zones of Permafrost Polygonal Structures and its Importance for Dating of Quaternary Deposits in Cryolitozone," in Proceeding of the VII All-Russian Quaternary Conference. The Quaternary in all of its variety. Basic issues, results, and major trends of further research. Apatity, Russia, September 12-17, 2011. Editors O. P. Korsakova and V. V. Kolka (Apatity and Saint Petersburg: Kola Research Center Geological Institute, RAS), 149–153.

Pitulko, V. V., Pavlova, E. Y., and Basilyan, A. E. (2016). Mass Accumulations of mammoth (mammoth 'graveyards') with Indications of Past Human Activity in the Northern Yana-Indighirka lowland, Arctic Siberia. *Quat. Int.* 406, 202–217. doi:10.1016/j.quaint.2015.12.039

Pitulko, V. V., and Pavlova, E. Y. (2015). Experience of Mass Radiocarbon Dating of Culture-Bearing Deposits of the Zhokhov Site. *Trans. Inst. Hist. Mater. Cult.* 12, 27–55.

Pitulko, V. V., and Pavlova, E. Y. (2016). *Geoarchaeology and Radiocarbon Chronology of Stone Age Northeast Asia*. College Station, TX: Center for the Study of the First Americans, Texas A&M University Press, 334.

Pitulko, V. V., Pavlova, E. Y., and Kritsuk, S. G. (2012). "Alluvial Complex Structure and Development Dynamics in Low-Stream Yana River valley in the Vicinity of Paleolithic Yana RHS Site," in Proceedings of the Joint Conference "Geomorphology and Quaternary Palaeogeography of Polar Regions", Symposium "Leopoldina" and the INQUA Peribaltic working group Workshop, Saint Petersburg, 9-17 September 2012. Editors A. Zhirov, V. Kuznetsov, D. Subetto, and J. Thiede (Saint Petersburg: Saint Petersburg State University), 313–316. (In Russian).

Pitulko, V. V., Pavlova, E. Y., Kuzmina, S. A., Nikolsky, P. A., Basilyan, A. E., Tumskoy, V. E., et al. (2007). Natural–Climatic Changes in the Yana–Indigirka Lowland during the Terminal Kargino Time and Habitat of Late Paleolithic Man in Northern Part of East Siberia. *Doklady Earth Sci.* 417, 1256–1260.

Pitulko, V. V., Pavlova, E. Y., and Nikolskiy, P. A. (2015a). Mammoth Ivory Technologies in the Upper Palaeolithic: a Case Study Based on the Materials from Yana RHS, Northern Yana-Indighirka lowland, Arctic Siberia. *World Archaeology* 47 (3), 333–389. doi:10.1080/00438243.2015.1030508

Pitulko, V. V., and Pavlova, E. Y. (2019). Upper Palaeolithic Sewing Kit from the Yana Site, Arctic Siberia. *Stratum plus* 1, 157–224.

Pitulko, V. V. (2019b). "Permafrost Digging," in *Encyclopedia of Global Archaeology*. Editor C. Smith. 2nd edition (Cham: Springer). doi:10.1007/978-3-319-51726-110.1007/978-3-319-51726-1_1513-2

Pitulko, V. V. (2008). Principal Excavation Techniques under Permafrost Conditions (Based on Zhokhov and Yana Sites, Northern Yakutia). *Archaeology, Ethnology Anthropol. Eurasia* 34, 26–33. doi:10.1016/j.aeae.2008.07.003

Pitulko, V. V. (2019a). Yana B Area of the Yana Site: Some Observations Done during the Excavations of 2015 through 2018. *PAJIS* 1, 64–91. doi:10.31600/2658-3925-2019-1-64-91

Rasmussen, S. O., Bigler, M., Blockley, S. P., Blunier, T., Buchardt, S. L., Clausen, H. B., et al. (2014). A Stratigraphic Framework for Abrupt Climatic Changes during the Last Glacial Period Based on Three Synchronized Greenland Ice-Core Records: Refining and Extending the INTIMATE Event Stratigraphy. *Quat. Sci. Rev.* 106, 14–28. doi:10.1016/j.quascirev.2014.09.007

Romanovskii, N., Hubberten, H.-W., Gavrilov, A. V., Tumskoy, V. E., and Kholodov, A. L. (2004). Permafrost of the East Siberian Arctic Shelf and Coastal Lowlands. *Quat. Sci. Rev.* 23, 1359–1369. doi:10.1016/j.quascirev.2003.12.014

Romanovskii, N. N. (1977). *Formirovanie Poligonal'no-Zhil'nykh Struktur (Formation of Polygonal-Wedge Systems)*. Novosibirsk: Nauka, 215. (in Russian).

Romanovskii, N. N. (1993). *Fundamentals of Cryogenesis of Lithosphere*. Moscow: Moscow University Press, 336. (in Russian).

Schirrmeister, L., Froese, D., Tumskoy, V., Grosse, G., and Wetterich, S. (2013). "Permafrost and Periglacial Features | Yedoma: Late Pleistocene Ice-Rich Syngenetic Permafrost of Beringia," in *The Encyclopedia of Quaternary Science*. Editor S. A. Elias. second ed. (Amsterdam: Elsevier), 3, 542–552. doi:10.1016/b978-0-444-53643-3.00106-0

Schirrmeister, L., Kunitsky, V., Grosse, G., Wetterich, S., Meyer, H., Schwamborn, G., et al. (2011). Sedimentary Characteristics and Origin of the Late Pleistocene Ice Complex on north-east Siberian Arctic Coastal Lowlands and Islands - A Review. *Quat. Int.* 241, 3–25. doi:10.1016/j.quaint.2010.04.004

Schirrmeister, L., Schwamborn, G., Overduin, P. P., Strauss, J., Fuchs, M. C., Grigoriev, M., et al. (2017). Yedoma Ice Complex of the Buor Khaya Peninsula (Southern Laptev Sea). *Biogeosciences* 14, 1261–1283. doi:10.5194/bg-14-1261-2017

Sher, A. V., Kuzmina, S. A., Kuznetsova, T. V., and Sulerzhitsky, L. D. (2005). New Insights into the Weichselian Environment and Climate of the East Siberian Arctic, Derived from Fossil Insects, Plants, and Mammals. *Quat. Sci. Rev.* 24, 533–569. doi:10.1016/j.quascirev.2004.09.007

Sher, A. V. (1997). "Yedoma as a Store of Paleoenvironmental Records in Beringida," in Abstracts and Program of the Beringia Paleoenvironmental Workshop, Colorado, September 20-23, 1997. Editors S. Elias and J. Brigham-Grette (Florissant, CO), 92–94.

Shur, Y. A. (1988). *Upper Stratigraphic Horizon of the Permafrost Amd Thermokarst*. Novosiborsk: Nauka, 211.

Sikora, M., Pitulko, V. V., Sousa, V. C., Allentoft, M. E., Vinner, L., Rasmussen, S., et al. (2019). The Population History of Northeastern Siberia since the Pleistocene. *Nature* 570, 182–188. doi:10.1038/s41586-019-1279-z

Solovyov, P. A. (1959). *Cryolithic Zone of the Northern Lena-Amga Interfluve*. Moscow: AN SSSR, 159.

Svensson, A., Andersen, K. K., Bigler, M., Clausen, H. B., Dahl-Jensen, D., Davies, S. M., et al. (2008). A 60 000 Year Greenland Stratigraphic Ice Core Chronology. *Clim. Past* 4, 47–57. doi:10.5194/cp-4-47-2008

Todisco, D., Bhiry, N., and Desrosiers, P. M. (2009). Paleoeskimo Site Taphonomy: An Assessment of the Integrity of the Tayara Site, Qikirtaq Island, Nunavik, Canada. *Geoarchaeology* 24, 743–791. doi:10.1002/gea.20285

Todisco, D., and Bhiry, N. (2008). Palaeoeskimo Site Burial by Solifluction: Periglacial Geoarchaeology of the Tayara Site (KbFk-7), Qikirtaq Island, Nunavik (Canada). *Geoarchaeology* 23, 177–211. doi:10.1002/gea.20217

Tomirdiaro, S. V., and Chernenkiy, B. I. (1987). Kriogenno-eolovye Otlozheniya VostochnoiArktiki I Subarktiki *[Cryogenic-Aeolian Deposits of the Eastern Arctic and Subarctic]*. Moscow: Nauka.

Vandenberghe, J., French, H. M., Gorbunov, A., Marchenko, S., Velichko, A. A., Jin, H., et al. (2014). The Last Permafrost Maximum (LPM) Map of the Northern Hemisphere: Permafrost Extent and Mean Annual Air Temperatures, 25-17 Ka BP. *Boreas* 43, 652–666. doi:10.1111/bor.12070

Vasil'chuk, Y. K. (2013). "Syngenetic Ice Wedges: Cyclical Formation, Radiocarbon Age and Stable Isotope Records by Yurij K. Vasil 'chuk, Moscow University Press, Moscow, 2006. 404 Pp. ISBN 5-211-05212 -9. *Permafrost Periglac. Process.*, 24, 82–93. doi:10.1002/ppp.1764

Vasil'chuk, Y. K. (2006). *Povtorno-zhilnye L'dy: Geterotsiklichnost', Geterokhronost', Geterogennost' (Syngenetic Ice Wedges: Cyclical Formation, Radiocarbon Age and Stable Isotope Records)*. Moscow: Moscow University Press, 404. (in Russian).

Velichko, A. A., Grekhova, L. V., Gribchenko, Y. N., and Kurenkova, E. I. (1997). *Early Man in the Extreme Environmental Conditions. Eliseevich Site*. Moscow: Institute of Geography RAS, 192. (in Russian).

Velichko, A. A., Grekhova, L. V., and Gubonina, Z. P. (1977). *Environments of the Ancient Man of the Timonovka Sites*. Moscow: Nauka, 142. (in Russian).

Velichko, A. A. (1973). *Natural Process in the Pleistocene*. Moscow: Nauka, 256. (in Russian).

Washburn, A. L. (1979). *Geocryology*. London: Edward Arnold, 406.

Washburn, A. L. (1980). Permafrost Features as Evidence of Climatic Change. *Earth-Science Rev.* 15, 327–402. doi:10.1016/0012-8252(80)90114-2

Wetterich, S., Meyer, H., Fritz, M., Opel, T., and Schirrmeister, L. (2020). Cryolithology of the Sobo-Sise Yedoma Cliff (Eastern Lena Delta). *PANGAEA* 1, 1. doi:10.1594/PANGAEA.919470

Wetterich, S., Rudaya, N., Tumskoy, V., Andreev, A. A., Opel, T., Schirrmeister, L., et al. (2011). Last Glacial Maximum Records in Permafrost of the East Siberian Arctic. *Quat. Sci. Rev.* 30, 3139–3151. doi:10.1016/j.quascirev.2011.07.020

Wetterich, S., Tumskoy, V., Rudaya, N., Andreev, A. A., Opel, T., Meyer, H., et al. (2014). Ice Complex Formation in Arctic East Siberia during the MIS3 Interstadial. *Quat. Sci. Rev.* 84, 39–55. doi:10.1016/j.quascirev.2013.11.009

Yurtsev, B. A. (1994). Floristic Division of the Arctic. *J. Vegetation Sci.* 5, 765–776. doi:10.2307/3236191

Zanina, O. G., Gubin, S. V., Kuzmina, S. A., Maximovich, S. V., and Lopatina, D. A. (2011). Late-Pleistocene (MIS 3-2) Palaeoenvironments as Recorded by Sediments, Palaeosols, and Ground-Squirrel Nests at Duvanny Yar, Kolyma lowland, Northeast Siberia. *Quat. Sci. Rev.* 30, 2107–2123. doi:10.1016/j.quascirev.2011.01.021

Zhang, T., Heginbottom, J. A., Barry, R. G., and Brown, J. (2000). Further Statistics on the Distribution of Permafrost and Ground Ice in the Northern Hemisphere1. *Polar Geogr.* 24 (2), 126–131. doi:10.1080/10889370009377692

Zimmermann, H., Raschke, E., Epp, L., Stoof-Leichsenring, K., Schirrmeister, L., Schwamborn, G., et al. (2017). The History of Tree and Shrub Taxa on Bol'shoy Lyakhovsky Island (New Siberian Archipelago) since the Last Interglacial Uncovered by Sedimentary Ancient DNA and Pollen Data. *Genes* 8, 273. doi:10.3390/genes8100273

Zolnikov, I. D., Deev, E. V., Slavinskiy, V. S., Tsybankov, A. A., Rybin, E. P., Lysenko, D. N., et al. (2017). Afontova Gora II Archaeological Site: Geology and Postdepositional Deformation (Krasnoyarsk, Siberia). *Russ. Geology. Geophys.* 58 (2), 190–198. doi:10.1016/j.rgg.2016.04.016

Conflict of Interest: The authors declare that the research was conducted in the absence of any commercial or financial relationships that could be construed as a potential conflict of interest.

frontiers in Earth Science

ORIGINAL RESEARCH
published: 03 March 2022
doi: 10.3389/feart.2021.758800

Yedoma Cryostratigraphy of Recently Excavated Sections of the CRREL Permafrost Tunnel Near Fairbanks, Alaska

Mikhail Kanevskiy[1], Yuri Shur[1], Nancy H. Bigelow[2], Kevin L. Bjella[3], Thomas A. Douglas[3], Daniel Fortier[4], Benjamin M. Jones[1] and M. Torre Jorgenson[5]*

[1]Institute of Northern Engineering, University of Alaska Fairbanks, Fairbanks, AK, United States, [2]Alaska Quaternary Center, University of Alaska Fairbanks, Fairbanks, AK, United States, [3]Cold Regions Research and Engineering Laboratory (CRREL), Fairbanks, AK, United States, [4]Geography Department, University of Montreal, Montreal, Canada, [5]Alaska Ecoscience, Fairbanks, AK, United States

OPEN ACCESS

Edited by:
Duane Froese, University of Alberta, Canada

Reviewed by:
Matthew Lachniet, University of Nevada, Las Vegas, United States
Alberto Reyes, University of Alberta, Canada

***Correspondence:**
Mikhail Kanevskiy
mkanevskiy@alaska.edu

Specialty section:
This article was submitted to Cryospheric Sciences, a section of the journal Frontiers in Earth Science

Received: 15 August 2021
Accepted: 07 December 2021
Published: 03 March 2022

Citation:
Kanevskiy M, Shur Y, Bigelow NH, Bjella KL, Douglas TA, Fortier D, Jones BM and Jorgenson MT (2022) Yedoma Cryostratigraphy of Recently Excavated Sections of the CRREL Permafrost Tunnel Near Fairbanks, Alaska. Front. Earth Sci. 9:758800. doi: 10.3389/feart.2021.758800

Recent excavation in the new CRREL Permafrost Tunnel in Fox, Alaska provides a unique opportunity to study properties of Yedoma — late Pleistocene ice- and organic-rich syngenetic permafrost. Yedoma has been described at numerous sites across Interior Alaska, mainly within the Yukon-Tanana upland. The most comprehensive data on the structure and properties of Yedoma in this area have been obtained in the CRREL Permafrost Tunnel near Fairbanks — one of the most accessible large-scale exposures of Yedoma permafrost on Earth, which became available to researchers in the mid-1960s. Expansion of the new ~4-m-high and ~4-m-wide linear excavations, started in 2011 and ongoing, exposes an additional 300 m of well-preserved Yedoma and provides access to sediments deposited over the past 40,000 years, which will allow us to quantify rates and patterns of formation of syngenetic permafrost, depositional history and biogeochemical characteristics of Yedoma, and its response to a warmer climate. In this paper, we present results of detailed cryostratigraphic studies in the Tunnel and adjacent area. Data from our study include ground-ice content, the stable water isotope composition of the variety of ground-ice bodies, and radiocarbon age dates. Based on cryostratigraphic mapping of the Tunnel and results of drilling above and inside the Tunnel, six main cryostratigraphic units have been distinguished: 1) active layer; 2) modern intermediate layer (ice-rich silt); 3) relatively ice-poor Yedoma silt reworked by thermal erosion and thermokarst during the Holocene; 4) ice-rich late Pleistocene Yedoma silt with large ice wedges; 5) relatively ice-poor fluvial gravel; and 6) ice-poor bedrock. Our studies reveal significant differences in cryostratigraphy of the new and old CRREL Permafrost Tunnel facilities. Original syngenetic permafrost in the new Tunnel has been better preserved and less affected by erosional events during the period of Yedoma formation, although numerous features (e.g., bodies of thermokarst-cave ice, thaw unconformities, buried gullies) indicate the original Yedoma silt in the recently excavated sections was also reworked to some extent by thermokarst and thermal erosion during the late Pleistocene and Holocene.

Keywords: ice wedge, thermokarst-cave ice, intermediate layer, cryostructures, thermokarst, thermal erosion, late Pleistocene

1 INTRODUCTION

Yedoma is the ice- and organic-rich syngenetic permafrost, which accumulated in unglaciated regions during the late Pleistocene in various regions of Eurasia and North America (Schirrmeister et al., 2013). Yedoma deposits contain large ice wedges that can reach up to 10 m in width and more than 40 m in vertical extent (Tomirdiaro 1980; Zhestkova et al., 1982; Sher, 1997; Romanovskii et al., 2004; Kanevskiy et al., 2011; Murton, 2013; Schirrmeister et al., 2013; Schirrmeister et al., 2020). Yedoma remnants are abundant in various parts of Siberia, Canada, and Alaska (Kanevskiy et al., 2011; Schirrmeister et al., 2013; Strauss et al., 2017; Strauss et al., 2021; and citations therein).

Yedoma in Siberia and North America occurs in an area of ~450,000 km^2, including ~90,000 km^2 in Alaska (Strauss et al., 2021), and contains up to 130 gigatons of organic carbon (Strauss et al., 2017). Yedoma is vulnerable to climate change and disturbance because of its high ice content and silty composition. Thermokarst and thermal erosion of these ice-rich sediments create serious hazards for the environment and socioeconomic systems, which in some cases may require a costly relocation of a variety of infrastructure. Growing interest in Yedoma studies during recent decades has been related to the high content of frozen organic matter whose release upon thaw leads to changes in biogeochemical processes and greenhouse gas emission (Grosse et al., 2011; Schuur et al., 2015; Strauss et al., 2017).

Yedoma deposits contain large amounts of ground ice. The volumetric moisture content of Yedoma silt due to pore and segregated ice usually varies from 60% to more than 80%. Lenses of segregated ice in silt form a specific set of cryostructures named “micro-cryostructures” (Kanevskiy et al., 2011). Large syngenetic ice wedges penetrate the entire section of Yedoma, and their volume may exceed 50%. At some locations, the thickness of syngenetic permafrost with large ice wedges can reach 30–40 m. The most impressive section of Yedoma in Alaska was previously studied in the 35-m-high exposure along the Itkillik River (Kanevskiy et al., 2011; Kanevskiy et al., 2016; Shur et al., 2021a).

Formation of Yedoma took place in the extremely cold, dry, grassy environment called “tundra-steppe” or “mammoth steppe” (Kaplina, 1981; Yurtsev, 1981; Guthrie, 1990; Sher, 1997). Such terrain occupied vast areas of Eurasia and North America in the late Pleistocene. Yedoma does not have direct analogs to permafrost formed during the Holocene. The most similar to Yedoma deposits is syngenetic permafrost of modern floodplains of Arctic rivers in Siberia and Alaska that is not more than several meters thick (Popov, 1953; Katasonov, 1954; Zaikanov, 1991; Shur and Jorgenson, 1998), as well as the Holocene eolian silt with large ice wedges in the Canadian Arctic (Fortier and Allard, 2004).

Since the 1800s, numerous hypotheses for Yedoma origin have been developed, and for a long time massive ice in Yedoma was considered to be buried snow, lake, or glacier ice (Shur et al., 2021b). Popov (1953) proposed a hypothesis of alluvial sedimentation accompanied by formation of large syngenetic ice wedges, and most Russian investigators have agreed. Other hypotheses for Yedoma genesis include eolian (Péwé, 1954, 1955, 1975a; Williams, 1962; Hopkins, 1963; Tomirdiaro, 1980; Hopkins, 1982; Carter, 1988), colluvial (Gravis, 1969), and nival (Kunitskiy, 1989; Schirrmeister et al., 2008; Schirrmeister et al., 2010) modes of sedimentation. Zhestkova et al., (1982, 1986) proposed a polygenetic origin of Yedoma that considers Yedoma as a climatic phenomenon and applied the idea of “equifinality,” which suggests that similar results may be achieved by various processes and under different initial conditions. They concluded that the leading factors of Yedoma formation are a cold climate and continuous long-term sedimentation. They also emphasized that Yedoma is a gigantic polypedon and that soil forming processes (from a pedological point of view) played an important role in Yedoma formation Sher (1997) and Sher et al. (2005) supported this explanation of the Yedoma genesis.

Our preliminary maps of Yedoma occurrence in Alaska (Kanevskiy et al., 2011; Kanevskiy et al., 2016; Shur et al., 2021a) show that Yedoma is widespread across both arctic and boreal regions (**Supplementary Figure S1**). Yedoma is abundant along the lower portion of the Arctic Foothills, in the northern part of the Seward Peninsula, and in numerous areas in Interior Alaska. In Canada, Yedoma sites were identified in south-western Yukon by Fraser and Burn (1997), Kotler and Burn (2000), Froese et al. (2009), and Fortier et al. (2018).

In Interior Alaska, ice-rich silt, which can be identified as Yedoma, has been observed at numerous sites mainly within the Yukon-Tanana uplands (Péwé, 1975a; Péwé, 1975b; Black, 1978; Kreig and Reger, 1982; Brown and Kreig, 1983; Meyer et al., 2008; Kanevskiy et al., 2012; Jorgenson et al., 2013; Nossov et al., 2013; Schirrmeister et al., 2016). Yedoma studies were also performed at the Palisades riverbank exposure in the central Yukon River valley (Matheus et al., 2003; Reyes et al., 2010a; Reyes et al., 2010b; Reyes et al., 2011; Jensen et al., 2013). Most of these studies consider Yedoma deposits to be of eolian and reworked eolian origin.

The most comprehensive data on the structure and properties of Yedoma in Interior Alaska have been obtained from the CRREL Permafrost Tunnel near Fairbanks, which became available to researchers in the mid-1960s. Many papers have been published on the geology and geomorphology of the Tunnel (e.g., Sellmann, 1967; Sellmann, 1972; Hamilton et al., 1988; Shur et al., 2004; Douglas et al., 2011) and engineering properties of sediments (Chester and Frank, 1969; Thompson and Sayles, 1972; Pettibone, 1973; Johansen, et al., 1980; Johansen and Ryer, 1982; Weerdenburg and Morgenstern, 1983; Arcone and Delaney, 1984; Delaney and Arcone, 1984; Huang et al., 1986; Delaney, 1987; Bray, 2008; Douglas and Mellon, 2019). The methods of Tunnel construction have also been described (Chester and Frank, 1969; Dick, 1970; Swinzow, 1970; Linell and Lobacz, 1978; Cysewski et al., 2012; Bjella and Sturm, 2012).

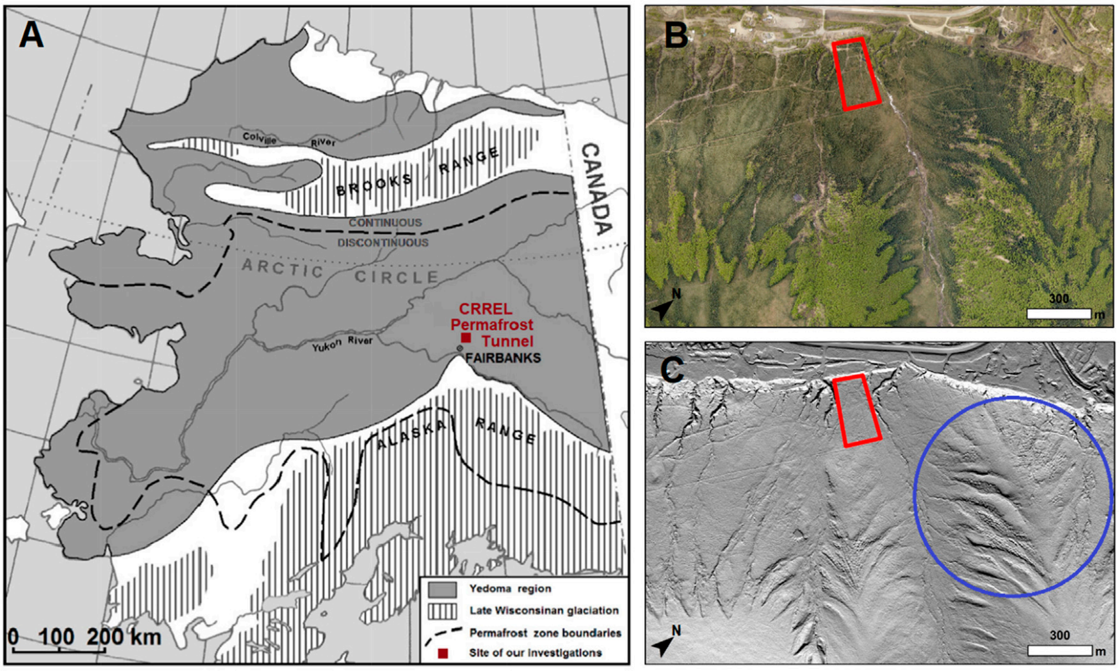

FIGURE 1 | (A) Location of the CRREL Permafrost Tunnel. Boundaries of Yedoma region in Alaska (defined as area of potential Yedoma occurrence) are shown after Kanevskiy et al. (2011); limits of late Wisconsinan glaciation are shown after Péwé (1975a) and Hamilton (1994); and boundaries of permafrost zones are shown after Jorgenson et al. (2008). **(B)** Aerial photo of the Tunnel area, 2020 (the Tunnel is located within the red rectangular). **(C)** LiDAR image of the Tunnel area, 2017. Note the occurrence of numerous thermo-erosional gullies and baydzherakhs (conical thermokarst mounds) that indicate areas of thawing Yedoma permafrost (blue circle).

Excavation of the new sections of the CRREL Permafrost Tunnel, which started in 2011 (Bjella and Sturm, 2012), has significantly increased the Tunnel footprint, and now the total length of the Tunnel network is approximately 600 m. The newly exposed surfaces provide unique opportunities for scientists interested in paleoecology and studies of the structure, biogeochemical characteristics, and depositional history of the ice-rich syngenetic permafrost. Studies in the new Tunnel allow us to make more detailed descriptions and cryostratigraphic maps because the freshly cut walls and ceiling have even surfaces that are not covered with thick layers of dry sublimated soil, unlike the old Tunnel.

In this study, we describe cryostratigraphy of the recently excavated sections of the CRREL Permafrost Tunnel based on mapping of the walls and ceiling of a 110-m-long section of the main Tunnel and a 50-m-long crosscut connecting the new and old Tunnels. We also present the data obtained from several boreholes drilled around the Tunnel from the soil surface and inside the Tunnel from its floor. The major goals of this paper are to: 1) describe cryostratigraphy of the new Tunnel and present the data on radiocarbon dating of sediments and stable isotope composition of various types of ground ice, 2) compare subsurface conditions in the old and new sections of the Permafrost Tunnel, and 3) provide a basic cryostratigraphic map of the new Tunnel facilities, which can be used for the future research.

2 EXCAVATION OF THE COLD REGIONS RESEARCH AND ENGINEERING LABORATORY TUNNEL

The CRREL Permafrost Tunnel was initially constructed in the early 1960s in Fox, Alaska (**Figure 1**) by the U.S. Army Cold Regions Research and Engineering Laboratory (CRREL) to test mining, tunneling, and construction techniques in permafrost (Sellmann, 1967; Cysewski et al., 2010; Cysewski et al., 2012; Bjella and Sturm, 2012). The Tunnel portal is located on the eastern margin of the Goldstream Creek valley at the base of a steep 10-m-high escarpment created by placer gold mining activities in the early to mid-1900s. The surface of the valley that lies immediately above the long axis of the Tunnel rises gently from the top of the escarpment in which the entrance is located toward the east side of the Goldstream Creek valley. The active layer of the terrain that overlies the Tunnel varies from 0.5 to 1 m thick; this range is typical of the Fairbanks area, but it has been expanding downward over the past decade (Douglas et al., 2021).

The old Tunnel, which was constructed in the 1960s, comprises two portions (**Figure 2**). The adit (a nearly horizontal Tunnel from the base of the slope into the hillside, T1 in **Figure 2**) was excavated by the U.S. Army Corps of Engineers using continuous mining methods in the winters of 1963–64, 1964–65, and 1965–66 (Sellmann, 1967). The winze (an inclined Tunnel, W in **Figure 2**) was driven by the U.S. Bureau of Mines (USBM) from 1968 to 1969 using drill and blast, thermal

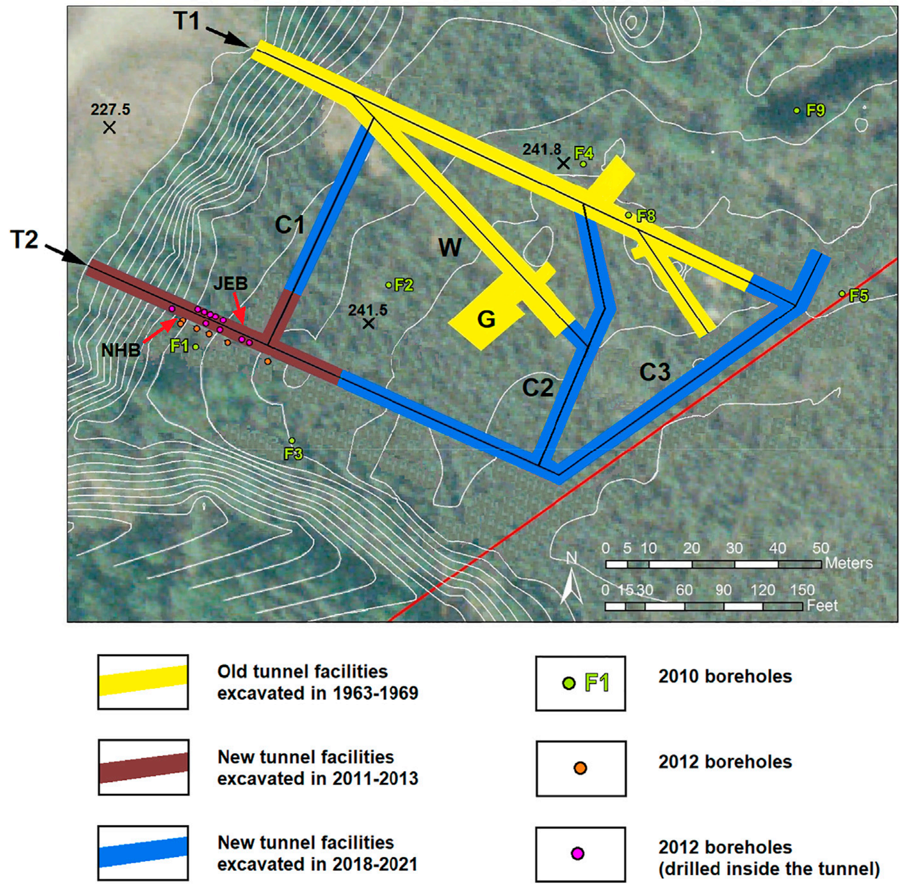

FIGURE 2 | Plan view of the CRREL Permafrost Tunnel facilities, including old (northern adit, T1) and new (southern adit, T2) Tunnels, inclined winze (W), gravel room (G), crosscuts that connect old and new Tunnels (C1, C2, and C3), and boreholes. Locations of NHB and JEB sections are marked with red arrows. Contour lines have 1 m intervals. Modified from Bjella and Sturm (2012).

relaxation, and hydraulic relaxation methods (Chester and Frank, 1969). The adit was excavated mainly in frozen silt and extended approximately 110 m in length. The winze begins approximately 30 m into the adit and drops at an incline of 14 percent for 45 m, passing into the frozen gravel unit and ultimately into weathered bedrock, where the Gravel Room (G in **Figure 2**) was excavated (Pettibone, 1973). The Tunnel is chilled by natural ventilation in winter and by artificial refrigeration in summer, supporting permafrost stability.

Recent excavation of the Permafrost Tunnel was performed by CRREL in five phases: 2011 (Bjella and Sturm, 2012; Cysewski et al., 2012), 2013, 2018, 2020, and 2021. For this expansion, an excavator equipped with a 62-cm-wide drum-style rotary cutter (Eco-Cutter EC-25) was used. The cutter was outfitted with the two types of picks: chisel type for frozen silt and massive ice, and conical type for frozen gravel. For removal of excavated material, a John Deere 333D rubber-tired skid loader was used (Bjella and Sturm, 2012).

The current length of the main adit of the new Tunnel (T2 in **Figure 2**) is approximately 110 m from the portal, and its average width and height are approximately 4.25 m. Crosscuts (C1, C2, and C3 in **Figure 2**) connect old (T1) and new (T2) Tunnels. In this paper, we present the results of cryostratigraphic studies performed in T2 and C1.

3 PREVIOUS CRYOSTRATIGRAPHIC STUDIES IN THE COLD REGIONS RESEARCH AND ENGINEERING LABORATORY PERMAFROST TUNNEL

Geology, paleoecology, and cryostratigraphy of the sediments exposed in the old CRREL permafrost Tunnel have been described in numerous papers (Sellmann, 1967; Sellmann, 1972; Watanabe, 1969; Hamilton et al., 1988; Long and Péwé 1996; Shur et al., 2004; Bray et al., 2006; Wooller et al., 2007; Wooller et al., 2011; Fortier et al., 2008; Kanevskiy et al., 2008a; Kanevskiy et al., 2008b; Douglas et al., 2011; Lachniet et al., 2012). Sediments exposed in the Tunnel consist mainly of ice- and organic-rich frozen silt (loess) of eolian origin that was partly reworked and retransported by hillslope and fluvial processes (Péwé, 1975a; Péwé, 1975b; Hamilton et al., 1988). The silt, which is 14–18 m thick, formed between 30,000 and 43,000 years BP

(Hamilton et al., 1988). The silt overlies the Fox Gravel of early to middle Pleistocene age, which was derived from the surrounding hills of the Yukon–Tanana Uplands; the thickness of the Fox Gravel near the village of Fox was up to 15 m (Péwé, 1975a). Hamilton et al. (1988) estimated the thickness of gravel in the Tunnel to be 3–4 m and suggested that the gravel deposit beneath the silt could form shortly before 43,000 years BP. The Fox Gravel overlies Pre-Cambrian Fairbanks Schist bedrock (Newberry et al., 1996). Near the Tunnel portal, fanlike deposits of poorly sorted debris unconformably overlie the silt; these deposits accumulated between 12,500 and 11,000 years BP during deep erosion of the Goldstream Creek valley slopes (Hamilton et al., 1988).

Sellmann (1967, 1972) was the first to provide information on geology and permafrost of the Tunnel. He described segregation ice, foliated wedge ice, and large clear masses of ice (identified as buried "aufeis"). Hamilton et al. (1988) identified four major types of ground ice: pore ice, segregated ice, foliated wedge ice, and buried surface ice (frozen thaw ponds formed in ice-wedge troughs). They described two independent systems of ice wedges with a thaw unconformity between them. Further studies interpreted the clear ice bodies in the CRREL Tunnel to be thermokarst-cave ice (Shur et al., 2004; Bray et al., 2006; Kanevskiy et al., 2008a; Fortier et al., 2008; Douglas et al., 2011). Cryostratigraphic mapping of the main adit of the old Tunnel was performed by Bray et al. (2006) (**Supplementary Figures S2, S3**). Cryostratigraphic mapping of the 38-m-long winze section was performed by Kanevskiy et al. (2008b) at various scales (**Supplementary Figures S4–S7**).

Recent cryostratigraphic studies in the old CRREL Tunnel (Shur et al., 2004; Bray et al., 2006; Fortier et al., 2008; Kanevskiy et al., 2008a) described typical ground-ice features related to syngenetic permafrost formation. The dominant cryostructure that was observed in the CRREL Tunnel is micro-lenticular (Shur et al., 2004), which is typical of syngenetic permafrost. The term "micro-lenticular" refers to the presence of very small, sub-horizontal (sometimes wavy), relatively short ice lenses. Usually, the thickness of uniformly distributed ice lenses (and the spacing between them) does not exceed 0.5 mm. In the Tunnel, gravimetric moisture contents of the sediments with micro-lenticular cryostructure varied from 80 to 240% (Bray et al., 2006; Fortier et al., 2008; Kanevskiy et al., 2008a; Kanevskiy et al., 2008b). The great variability in gravimetric moisture contents of silt is associated with existence of several varieties of micro-lenticular cryostructure (e.g., latent micro-lenticular, micro-braided, micro-ataxitic); we suggested a term "micro-cryostructures" as a general term that covers all these varieties (Kanevskiy et al., 2011).

Ice-rich silt contains numerous peat layers and inclusions of poorly decomposed organic matter, including abundant rootlets, which is very common in syngenetic permafrost. For example, seven thin organic horizons were observed in the upper part of the winze at a depth of approximately 12–14 m below the ground surface (**Supplementary Figure S5**). The radiocarbon dates for bulk samples obtained from these organic layers varied from 31,000 to 35,000 ^{14}C yr BP (Kanevskiy et al., 2008a). Below each peat horizon, at a depth of approximately 0.4–0.6 m, were distinct icy layers (called "belts" in the Russian literature). These layers were interpreted to be temporary positions of the former permafrost table (base of the active layer) during the time of peat accumulation. The approximate positions of the active layer during these periods are indicated by arrows in **Supplementary Figure S5**. Numerous small cracks partially filled with ice (ice veins) extend downward from the peat horizons to depths of up to 0.5 m. These cracks form polygons up to 0.5 m across.

Numerous bodies of massive ice are exposed in the walls and ceiling of the CRREL Tunnel. Wedge ice is the main type of massive ice in the Tunnel; it can be recognized by distinctive vertical foliation. The size of the ice wedges is difficult to quantify: although the wedges appear to range in width from 1 to 7 m, their true width varies mainly between 0.5 and 3.0 m. The apexes of ice wedges terminate at the stratigraphic contact between the overlying silt and the underlying alluvial gravel.

Ice-rich syngenetic permafrost with large ice wedges is highly susceptible to thermal erosion that promotes the formation of gullies and subterranean channels (Fortier et al., 2007). When such channels are finally filled with sediment, water that is ponded behind the blockage begins to freeze. This process results in the formation of lenticular-shaped bodies of thermokarst-cave ("pool") ice. The term "thermokarst-cave ice" was suggested by Shumskii (1959) for massive ice formed by the freezing of water trapped in underground cavities that were cut through permafrost by running water. In Canada, this type of ice was described as "pool ice" by (Mackay, 1997; Mackay, 2000). The largest apparent horizontal extent of thermokarst-cave ice that can be viewed in the Tunnel was approximately 7 m (Shur et al., 2004; Bray et al., 2006).

Numerous sites of former gullies and underground channels were observed in the silty sediments at various depths. In the winze, a gully filled with sediments was observed at interval 29–35 m (**Supplementary Figures S4, S5**). Beneath the gully was a truncated ice wedge affected by thermal erosion. The sediment filling the gully was mostly ice-poor stratified silt with lenses of sand and numerous inclusions of reworked organic matter (Kanevskiy et al., 2008a).

Underground channels were cut by running water and later filled with thermokarst-cave ice and sediments whose structure and properties differ from the original syngenetic permafrost (Shur et al., 2004; Bray et al., 2006; Fortier et al., 2008; Kanevskiy et al., 2008a; Kanevskiy et al., 2008b; Douglas et al., 2011). Examination of the main adit of the old Tunnel revealed that, of 20 ice wedges identified, 19 had been subject to thermal erosion, either surficial or underground. Approximately 60% of the channels cutting through the ice wedges and the enclosing syngenetic permafrost were partially or entirely filled by thermokarst-cave ice (Fortier et al., 2008).

Lenses of thermokarst-cave ice were usually underlain by layers of silt with a reticulate-chaotic cryostructure (Shur et al., 2004; Fortier et al., 2008), which can be easily recognized by relatively thick multi-directional ice veins (**Supplementary Figure S8**). These ice veins were formed by inward freezing of saturated sediments trapped in underground channels incised in the permafrost by thermal erosion. Formation of the reticulate-chaotic cryostructure was reproduced in laboratory experiments (Fortier et al., 2008).

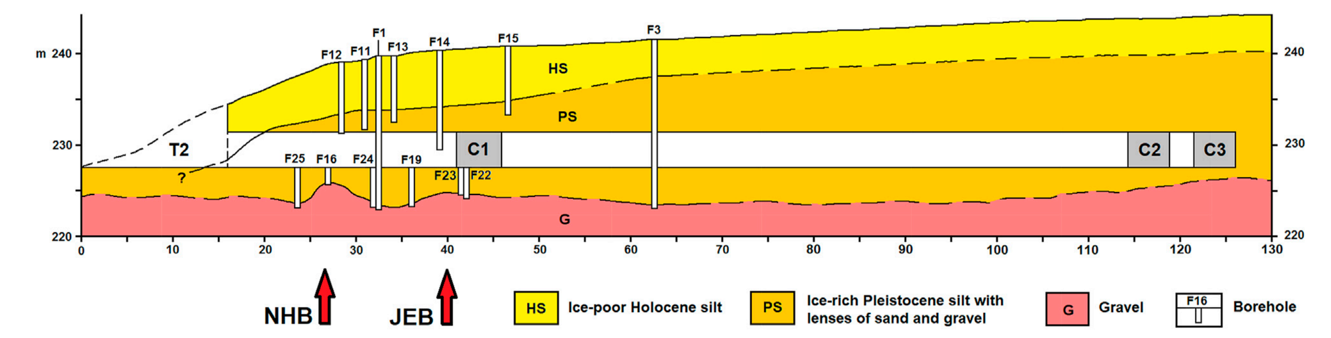

FIGURE 3 | General geological profile along the main adit of the new CRREL Permafrost Tunnel (T2), positions of the boreholes drilled from the surface and from the Tunnel floor in 2010 and 2012, and locations of crosscuts C1, C2, and C3 that connect the new Tunnel (T2) with the old Tunnel (T1). Locations of NHB and JEB sections are marked with red arrows. For location of boreholes and Tunnel facilities on the map, see **Figure 2**.

4 METHODS

4.1 Cryostratigraphy and Ground-Ice Content

We characterized permafrost in the new CRREL Tunnel by mapping massive-ice bodies and other permafrost features exposed in the Tunnel and studying frozen sediment cores from 24 boreholes drilled around and above the Tunnel and from its floor (**Figures 2**, **3**). For mapping purposes, the datum for locations started from the toe of the escarpment at the new Tunnel entrance (**Figure 3**), with left and right directions given as if walking into the Tunnel.

In April 2010, prior to excavation of the new Tunnel, eight boreholes were drilled in the adjacent area by GeoTek Alaska. The drill rig was a Geoprobe model 8040DT with DT45 tooling for direct push sampling. In March 2012, CRREL drilled six boreholes from the surface and 10 boreholes inside the Tunnel to the gravel. The drill rig was a Geoprobe 7822DT with DT45 (3-inch diameter) and MC5 (2.25-inch diameter) tooling for direct push sampling. Frozen cores were described and sub-sampled in 2010–2013 in the Institute of Northern Engineering (INE) UAF Frozen Ground Laboratory in Fairbanks, Alaska; remaining frozen cores are stored inside the CRREL Permafrost Tunnel. Cryostratigraphic studies in the new Tunnel facilities were performed in 2011–2014 and 2020 (before excavation of Crosscut #3).

Cryostratigraphic descriptions were based on classifications of massive ground ice and cryostructures (patterns formed by ice inclusions in the frozen soil) adapted from Russian and North American literature (French and Shur, 2010; Kanevskiy et al., 2011; Kanevskiy et al., 2013 and references therein). To estimate ground-ice content, frozen samples were weighed, oven-dried (90 C, 72 h) and reweighed. Gravimetric moisture content of frozen sediments was calculated as the ratio of the mass of the ice in a sample to the mass of the dried sample. To estimate volumes of massive ground ice, we transformed cryostratigraphic maps into binary (black and white) images showing distribution of massive-ice bodies; the areas occupied by wedge ice and thermokarst-cave ice on the walls and ceiling of the Tunnel were measured using ImageJ software (Ferreira and Rasband, 2012).

4.2 Water Stable Isotope Composition

The stable oxygen and hydrogen isotopic composition of ground ice is useful for assessing the conditions during the formation of different types of ground ice and helps to differentiate ground-ice bodies of various origins (Lacelle and Vasil'chuk, 2013; Vasil'chuk and Murton, 2016; Porter and Opel, 2020). For oxygen and hydrogen isotopic composition ($\delta^{18}O$ and $\delta^{2}H$), samples of different types of ground ice were collected from the new CRREL Permafrost Tunnel and adjacent boreholes and analyzed at the Alaska Stable Isotope Facility at the University of Alaska Fairbanks (UAF) and the CRREL Alaska geochemistry laboratory using standard mass spectrometry (UAF) and cavity ringdown (CRREL) methods.

Samples for stable isotope analyses at the Alaska Stable Isotope Facility at the University of Alaska Fairbanks were processed using continuous-flow isotope ratio mass spectrometry (CFIRMS). $\delta^{2}H$ and $\delta^{18}O$ values are measured using pyrolysis-EA-IRMS. This method utilizes a ThermoScientific high temperature elemental analyzer (TC/EA) and Conflo IV interface with a DeltaVPlus Mass Spectrometer. The pyrolysis reactor consists of a reaction tube packed with glassy carbon/graphite. Water samples are injected into the TC/EA with a CTC Analytics A200SE liquid autosampler. The sample is pyrolyzed into H_2 and CO gases then separated chromatigraphically. These gases are then transferred to the IRMS, where the isotopes are measured. Typical Quality Control scheme involves analyzing laboratory working standards every twenty-five replicate samples. Stable isotope ratios are reported in δ notation as parts per thousand (%) deviation from the international standards, V-SMOW (Standard Mean Ocean Water). Typically, instrument precision is < 3.0% for hydrogen and <0.5% for oxygen.

Samples for stable isotope analyses at the CRREL Alaska geochemistry laboratory were filtered through acid-washed 0.45-μm polypropylene filters. Stable isotopes of oxygen and hydrogen were measured using Wavelength-Scanned Cavity Ringdown Spectroscopy on a Picarro L2120i (Sunnyvale, California) on Fort Wainwright, Alaska. Samples were injected into the analyzer for seven separate analyses. Results from the first

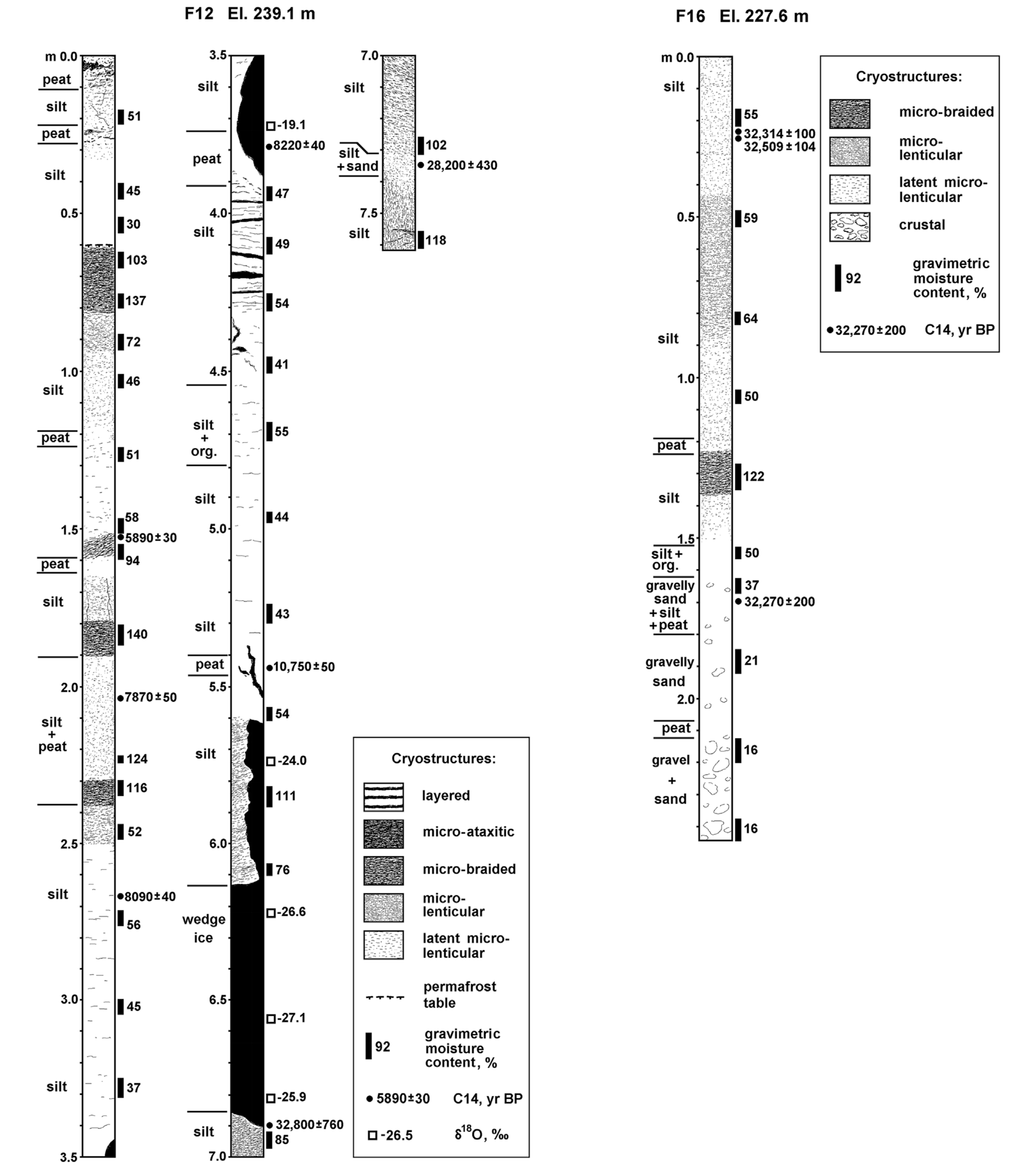

FIGURE 4 | Cryostratigraphy (ice is black) and ice contents of frozen sediments, boreholes F12 (Left) and F16 (Right).

four injections were not used to calculate the stable isotope values to reduce potential internal system memory. The mean value from the final three sample injections was used to calculate the mean and standard deviation value for each sample. Values are reported in standard per mil notation. Repeated analyses of five internal laboratory standards representing a range of values spanning the samples analyzed and analyses of SMOW, GISP, and SLAP standards (International Atomic Energy Agency) were

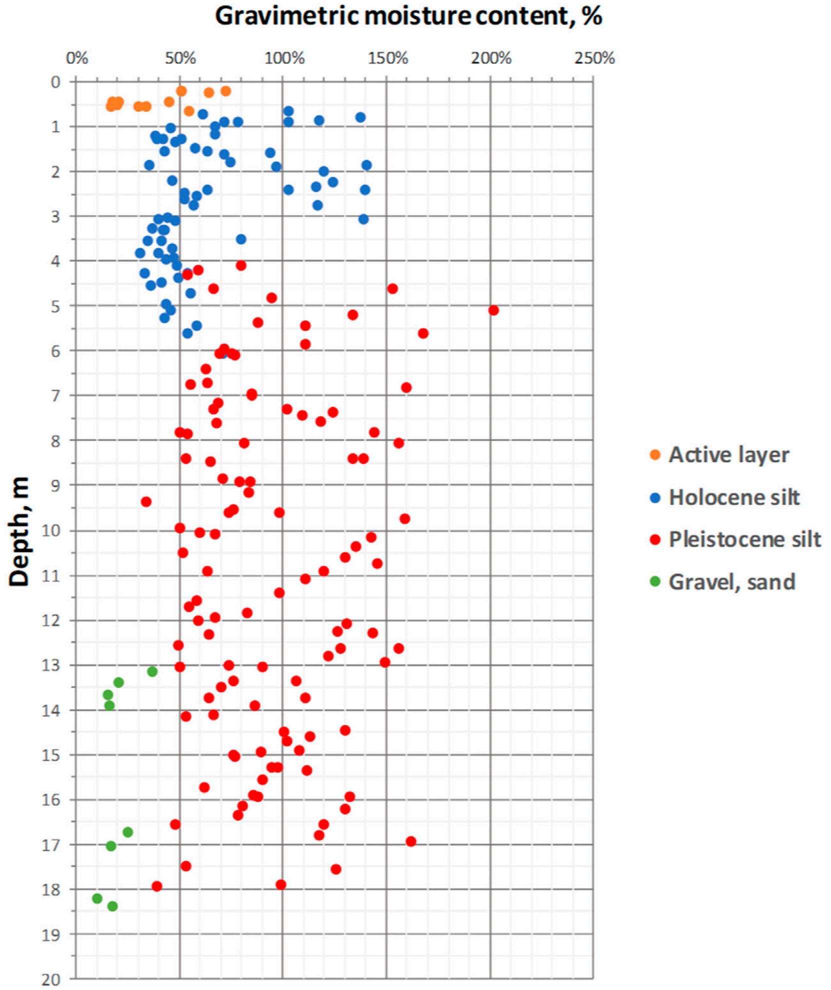

FIGURE 5 | Gravimetric moisture contents of sediments with depth, based on the drilling data (Boreholes F1, F2, F3, F4, F12, and F16). Average values: Active layer–39.7 ± 19.3% (*n* = 12); Holocene silt (including the intermediate layer)–65.4 ± 31.0% (*n* = 64); Pleistocene silt–94.0 ± 34.4% (*n* = 111); Gravel and gravelly sand–19.9 ± 8.0% (*n* = 8).

used to calibrate the analytical results. Based on thousands of these standards analyses and of sample duplicate analyses we estimate the precision is ± 0.2% for $\delta^{18}O$ and ± 0.5% for $\delta^{2}H$. Stable hydrogen and oxygen isotopic compositions from both analytical methods are expressed as delta values in per mil (%) relative to Vienna Standard Mean Ocean Water (VSMOW).

4.3 Radiocarbon Dating

Radiocarbon samples were collected from three localities in the new CRREL Permafrost Tunnel. The NHB section was located on the right wall at ~27 m from the base of the slope at the Tunnel entrance, while JEB section was located on the left wall at ~40 m (**Figures 2**, **3**). Lastly, the thermokarst-cave ice site was located on the right wall at 39–42 m. Radiocarbon samples were also collected from the cores of three boreholes (F3, F12, and F16); F3 and F12 was drilled from the surface and F16 was drilled from the Tunnel floor; both F12 and F16 are located very close to the NHB section.

Radiocarbon samples for AMS analysis were washed in distilled reverse osmosis water, photographed, and oven-dried prior to shipment to the radiocarbon lab (Beta analytic [Beta–*], University of Georgia [UGAMS–*] or Woods Hole [OS–*]). Only terrestrial plant remains, such as wood or herbaceous items (generally graminoid stems, leaves, root crowns, or roots) were dated. The resulting dates were calibrated with Calib ver 8.0.1, which uses the IntCal20 calibration dataset (Reimer et al., 2020).

5 RESULTS

5.1 Structure and Properties of the Upper Permafrost in the Tunnel Area Based on the Drilling Data

In 2010, prior to excavation of the new Tunnel sections, eight boreholes penetrating the Yedoma were drilled in the adjacent area. In 2012, six boreholes were drilled from the surface, and 10 boreholes were drilled

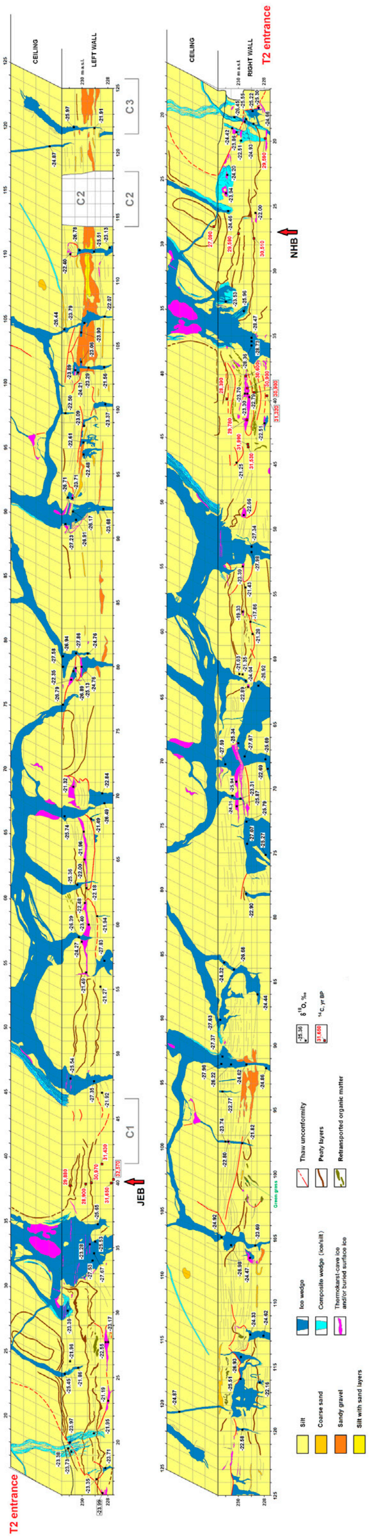

FIGURE 6 | General cryostratigraphic maps of the walls and the ceiling of the main adit of the new Tunnel (T2). Locations of NHB and JEB sections are marked with red arrows.

inside the Tunnel to the gravel horizon. Borehole locations are shown in **Figures 2**, **3**. Two 2012 boreholes–F12 and F16 (**Figure 4**)–were especially important for our study because F12 was drilled in a close proximity to the new Tunnel and F16 was drilled approximately at the same location from the Tunnel floor; numerous samples for radiocarbon dating were collected from these cores to complement the dates obtained from the samples collected inside the Tunnel. Cryostratigraphy and ice contents of frozen sediments of 2010 boreholes F1, F2, F3, and F4 are shown in **Supplementary Figures S9–S12**.

Study of cryostructures of frozen cores showed the thickness of the frozen active layer varied from 0.55 to 0.8 m (0.65 m average). The active layer comprised 10–15 cm of peat underlain by organic-rich silt. Below the active layer we could detect the modern ice-rich intermediate layer [quasi-syngenetically frozen layer typical of the upper permafrost, see Shur (1988), French and Shur (2010), Shur et al. (2011)] composed of silt with mainly micro-braided and micro-ataxitic cryostructures; the thickness of this layer varied from 0.15 to 0.6 m (0.4 m average). The intermediate layer was underlain by a 3- to 6-m-thick layer of relatively ice-poor silt with peat layers and organic matter inclusions. This layer contained thin ice wedges and random 0.1- to 1.0-m-thick layers with micro-cryostructures (presumably syngenetically frozen soils or buried intermediate layers). According to radiocarbon dates obtained from Borehole F12, this layer formed during the Holocene (**Figure 4**); it comprised mainly Yedoma deposits reworked by thermal erosion and slope processes. The Holocene silt was underlain by ice-rich late Pleistocene Yedoma silt, 10–14 m thick, with prevailing micro-cryostructures and large ice wedges. In Borehole F2, vertical extent of the ice wedge exceeded 9 m (**Supplementary Figure S10**), which confirms the syngenetic nature of the ice wedges at the study site. Ice-bonded fluvial gravel and gravelly sand with predominantly crustal cryostructure were encountered at depths from 13 to 18 m below the surface.

Ground-ice content of frozen sediments due to pore and segregated ice (gravimetric and volumetric moisture contents) was determined from the samples obtained from six boreholes: F1, F2, F3, F4, F12, and F16 (**Figures 4**, **Supplementary Figures S9–S12**). Gravimetric moisture contents for different cryostratigraphic units are shown in **Supplementary Table S1** and **Figure 5**.

The highest ice content was detected for the intermediate layer and Yedoma silt. An average gravimetric moisture content of the modern intermediate layer was 91.8 ± 27.6%. The underlying Holocene silt was relatively ice-poor (in comparison with Yedoma deposits) and contained relatively small amount of visible ground ice. Gravimetric moisture contents for most of the samples obtained from this unit ranged between 30 and 50% (**Figure 5**), but the average value (61.6 ± 29.7%) is significantly higher, which can be explained by the occurrence of several ice-rich layers (probably buried intermediate layers) within generally ice-poor deposits (**Figures 4**, **Supplementary Figures S9–S12**). In general, ice contents of the Holocene silt decreased with depth (**Figure 5**). Gravimetric moisture contents in Yedoma varied from <50 to >150% with the average value of 94.0 ± 34.4%, which was similar to that of the modern intermediate layer. Unlike the Holocene silt, there was no significant change in ground-ice

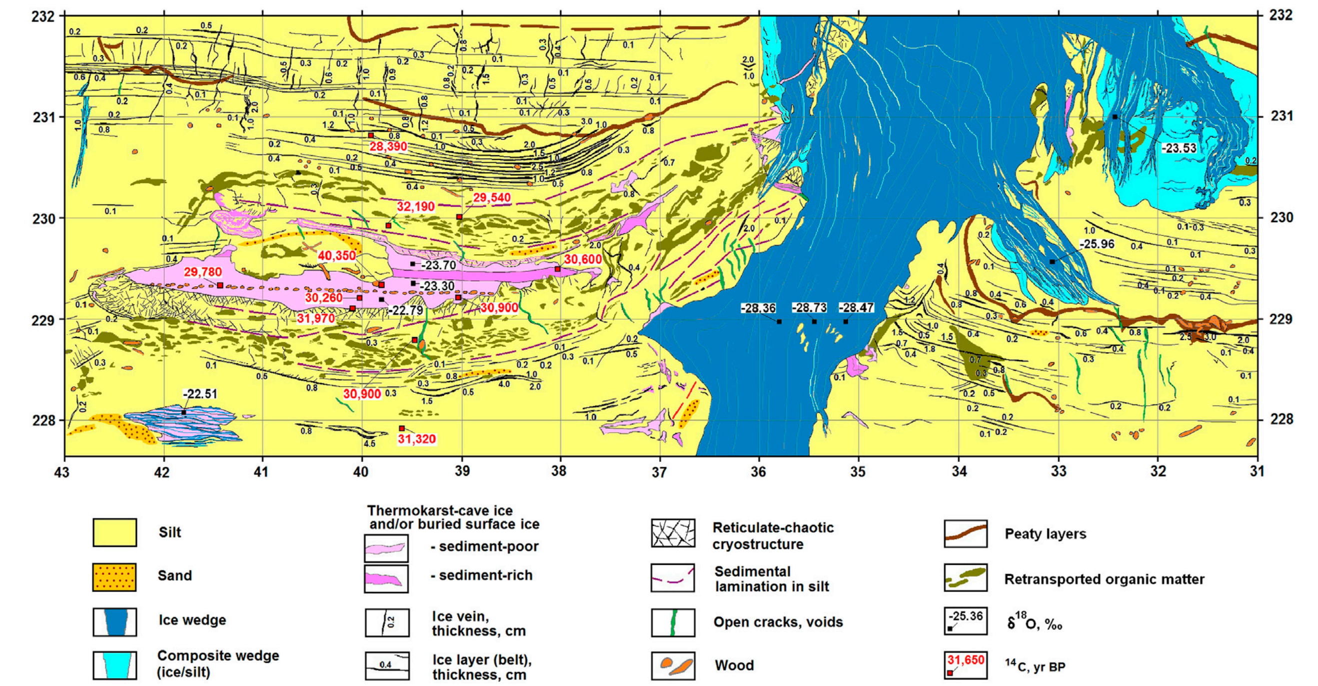

FIGURE 7 | Cryostratigraphic map of the right wall of the main adit of the new Tunnel (T2), distance 31–43 m.

distribution with depth (**Figure 5**); such a wide range in ice content is typical of syngenetic permafrost. Gravel and gravelly sand were relatively ice poor with an average gravimetric moisture content of 19.9 ± 8.0%.

5.2 Cryostratigraphy of the Main Adit of the New Tunnel (T2)

Cryostratigraphic mapping of the main adit of the new Tunnel (T2) resulted in compiling a general map of the two walls and ceiling (**Figure 6**). Additionally, some parts of the adit were mapped at a larger scale (e.g., **Figure 7**). Photographs of massive ground-ice bodies and other permafrost features exposed in the walls of the adit are shown in **Supplementary Figures S13–S30**; more photographs are available through the Arctic Data Center dataset (Shur and Kanevskiy, 2015).

The Tunnel presents features typical of ice-rich syngenetic permafrost (Yedoma): large foliated syngenetic ice wedges (**Figure 8A**), prevalence of micro-cryostructures (**Figure 9A**), distinctive ice belts (**Figure 9B**), and occurrence of large amounts of almost undecomposed organic matter, including small rootlets, through the entire thickness of Yedoma silt. Occurrence of numerous bodies of thermokarst-cave ice (**Figures 8C,D**), thaw unconformities, buried gullies, and other erosional features suggests that the original Yedoma silt at many places was reworked by thermokarst and thermal erosion during Yedoma formation.

A major inclined thaw unconformity was observed in the Tunnel at distances from 16 to 22 m. We presume this unconformity, which truncated original soil layers and massive-ice bodies (**Figure 6**), was created by a thermokarst or thermo-erosional event that occurred during the Pleistocene/Holocene transition, based on radiocarbon dates from the adjacent Borehole F12 (**Figures 3**, **4**).

Ice wedges exposed in the Tunnel had distinctive vertical foliation due to particles of mineral soils and organic matter and contained numerous air bubbles. Some ice wedges were surrounded by individual ice veins forming composite (ice/silt) wedges (**Figure 8B**). Large ice wedges were mainly syngenetic, based on their shape and dimensions; smaller buried epigenetic ice wedges and veins were also observed in various parts of the Tunnel. Small ice and composite wedges of presumably Holocene age were visible on the walls and ceiling near the entrance at distances from 16 to 22 m; apexes of the Holocene ice wedges were also visible on the ceiling and upper walls at distances from 25 to 50 m (**Figure 6**). More likely, the upper parts of the larger Pleistocene ice wedges exposed in the Tunnel also contained ice veins of the Holocene age that could penetrate in deeper layers. Such veins were sediment rich and often had a different color (**Supplementary Figure S14**). The true width of the Pleistocene ice wedges usually did not exceed 1.5–2 m, and distance between them varied from 5 to 12 m (measured across polygons visible on the ceiling of the Tunnel, see **Figure 6**).

Thermokarst-cave ice bodies were encountered at various elevations in many places along the Tunnel. Some of these bodies could form in underground channels cut by running water, mainly along ice wedges but also partly in the enclosing sediments, others may have a different origin. For example, one such body was observed on the right wall of the Tunnel at distances from 37 to 43 m (**Figures**

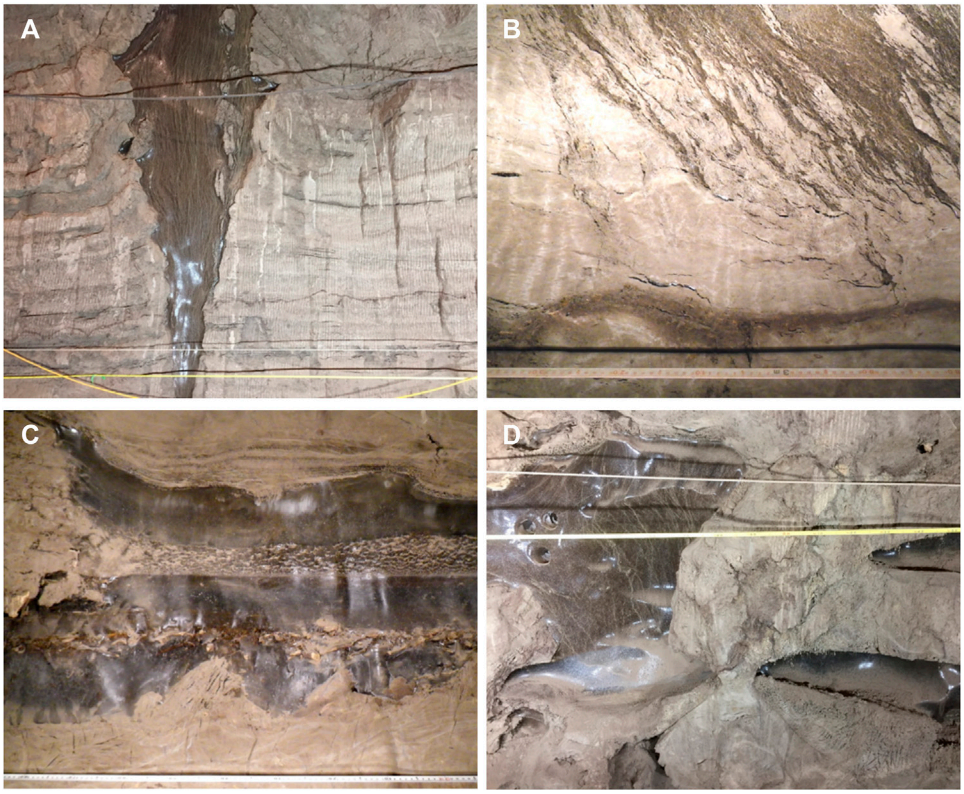

FIGURE 8 | Massive-ice bodies exposed in the new Permafrost Tunnel. For locations, see **Figures 6**, **7**, **10**. **(A)** Syngenetic ice wedge. Left wall of Crosscut #1 of the new Tunnel (C1), distance 9.4–13.9 m, elevation 228.8–231.6 m. **(B)** Ice wedge surrounded by individual ice veins forming composite (ice/silt) wedge; note a dark-brown layer of buried peat. Right wall of the main adit of the new Tunnel (T2), distance 32.8–33.4 m, elevation 229.0–229.5 m. **(C)** Thermokarst-cave ice. Horizontal stratification and suspended wood fragments indicate several stages of water accumulation and thermokarst-cave ice aggradation in the underground cavity. Right wall of the main adit of the new Tunnel (T2), distance 38.9–39.9 m, elevation 229.0–229.9 m. **(D)** Underground erosional channels filled with thermokarst-cave ice underlain by silt with reticulate-chaotic cryostructure. The channels started developing along ice wedges but eventually expanded and affected enclosing sediments. Left wall of Crosscut #1 of the new Tunnel (C1), distance 27.0–28.6 m, elevation 228.2–229.4 m.

6, **7**). It consisted of several horizontal layers of clean and sediment-rich ice, including a layer with wood fragments suspended in the ice, and was underlain by a silt layer with reticulate-chaotic cryostructure and numerous randomly oriented inclusions of reworked peat (**Supplementary Figures S16–S18**). Such a complex ice body could form at the bottom of a shallow thermo-erosional gully whose bank was undercut by water and subsequently collapsed. This process could result in the formation of an irregularly shaped cavity, which probably stayed partially open for several years and experienced several cycles of flooding and freezing, until it became completely filled with ice and buried by fresh deposits.

Active thermal erosion at the time of Yedoma formation resulted in the fast burial of gullies. Such events can be illustrated by the presence of overturned sod with green grass visible at 100.5 m along the right wall of the Tunnel (**Figure 6** and **Supplementary Figure S28**). Numerous disrupted peat layers, visible mainly from 16 to 77 m along the Tunnel walls (**Figure 6**), formed during periods of temporary surface stabilization that existed between periods of fast silt accumulation or erosion events. Some of the most distinctive peat layers contained roots and twigs, which belonged to shrubs buried in the growing position (e.g., at 31–33 m along the right wall of the Tunnel, see **Figure 7**, and at 23–25 m along the left wall, see **Supplementary Figure S13**).

Layers of gravel and gravelly sand were observed on the left (80–125 m) and right (90–110 m) walls of the main adit of the Tunnel. These layers were penetrated by 0.2- to 0.5-m-wide ice wedges; some of them (e.g., at 102–108 m along the left wall of the Tunnel, see **Figure 6**) had well-developed horizontal parts parallel to the gravel layers (**Supplementary Figures S25, S26**). Wedge-ice content was significantly lower from approximately 100 m; this is probably related to occurrence of layers of gravelly layers.

We estimated areas occupied by wedge ice and thermokarst-cave ice on the walls and ceiling of the main adit of the new Tunnel (T2) at distances from 24 to 100 m (**Table 1**), the areas with the Holocene ice wedges (16–24 m) and with low wedge-ice content (100–125 m) were excluded. Average values for wedge ice and thermokarst-cave ice were 17.4 and 1.8%, respectively.

5.3 Cryostratigraphy of Crosscut #1

Cryostratigraphic mapping of Crosscut #1 (**Figure 10**), which connects the old and new Tunnels, revealed sediment and

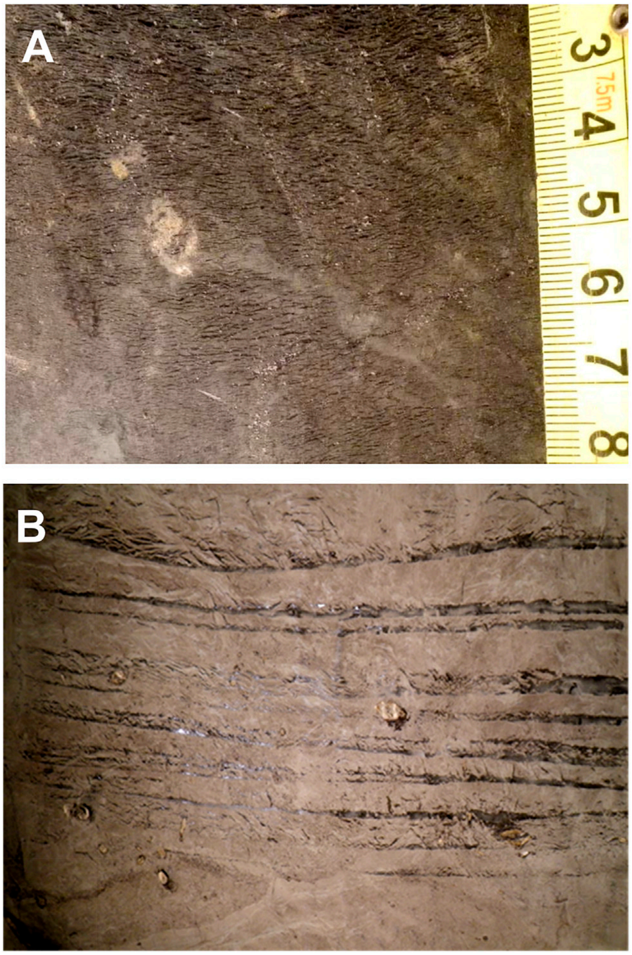

FIGURE 9 | Typical cryostructures of syngenetically frozen silt (ice is dark colored). **(A)** micro-braided cryostructure; left wall of the main adit of the new Tunnel (T2), distance 24.1 m, elevation 229.5 m. **(B)** ice belts (thick layers of segregated ice); right wall of the main adit of the new Tunnel (T2), distance 38.2–39.1 m, elevation 230.2–230.8 m. For locations, see **Figures 6**, **7**.

TABLE 1 | Areas occupied by massive ground ice of the new CRREL Permafrost Tunnel, % (relative to the total areas of the walls and ceiling of the Tunnel), measured based on cryostratigraphic maps (**Figures 6**, **10**) using ImageJ software.

Parts of the Tunnel	Wedge ice	Thermokarst-cave ice
T2, left wall, distance 24–100 m	11.2	1.8
T2, right wall, distance 24–100 m	15.7	1.6
T2, ceiling, distance 24–100 m	25.2	2.0
Average for T2	17.4	1.8
C1, left wall, distance 0–36 m	18.6	2.9
C1, right wall, distance 0–36 m	19.1	2.2
C1, ceiling, distance 0–36 m	23.7	0.7
Average for C1	20.4	1.9
Average for T2 and C1	**18.9**	**1.9**

ground-ice patterns very similar to those of the main adit of the new Tunnel. Photographs of massive ground-ice bodies and other permafrost features exposed in the walls of the crosscut are shown in **Supplementary Figures S31–S44**. Sediment in Crosscut #1 was mainly ice- and organic-rich silt that contained *in-situ* peat layers and numerous inclusions of organic matter reworked by erosion. Micro-cryostructures and distinctive ice belts were typical of undisturbed Yedoma exposed in the crosscut (**Supplementary Figures S33, S36, S37**).

Pleistocene ice wedges were 0.2–1.5 m wide, and distance between them varied from 3 to 10 m (**Figure 10**). Some of the syngenetic ice wedges were truncated by thermokarst and/or thermal erosion, while others extended from the ceiling to the floor (**Supplementary Figure S31**). Composite wedges up to 0.5 m wide were also observed at some places. Multiple erosional features, including thermokarst-cave ice bodies, which formed mainly in the underground channels, were observed in various parts of Crosscut #1 (**Supplementary Figures S34, S38, S40, S41, S42, S44**).

A distinctive thaw unconformity, which separated the ice-rich Late Pleistocene Yedoma unit from the ice-poor Holocene deposits (silt with layers and lenses of gravel and gravelly sand) was observed from ~35 to 50 m, in the part of the crosscut adjacent to the old Tunnel (**Supplementary Figure S43**). The main feature of this part of the crosscut is a large ice-wedge pseudomorph filled with poorly sorted gravelly soil, which was clearly visible on the walls and ceiling (**Supplementary Figure S39**).

We estimated areas occupied by wedge ice and thermokarst-cave ice on the walls and ceiling of Crosscut #1 at distances from 0 to 36 m (**Table 1**), the area of thaw unconformity adjacent to the old Tunnel (36–50 m), which did not contain ice wedges, was excluded. Average values for wedge ice and thermokarst-cave ice were 20.4 and 1.9%, respectively.

5.4 Water Stable Isotope Composition

A total of 267 samples were collected and analyzed for the stable isotope composition of ground ice, 17 of them from boreholes F2, F4, and F12 (**Supplementary Table S2**), 147 from the main adit of the new Tunnel (T2) (**Supplementary Tables S3, S4**), 78 from Crosscut #1 of the new Tunnel (C1) (**Supplementary Tables S5, S6**), and 25 from Crosscut #2 of the new Tunnel (C2) (**Supplementary Tables S7, S8**). Most of the samples were obtained from ice wedges (n = 184) and bodies of thermokarst-cave ice and underlying silt with reticulate-chaotic cryostructure (n = 68); several samples were obtained from layers of segregated ice (ice belts) (n = 12) and thin ice veins (n = 2), and for one sample the origin of ice was not identified.

Average $\delta^{18}O$, δ^2H, and deuterium excess values of various types of ground ice in new CRREL Permafrost Tunnel and adjacent boreholes are presented in **Table 2**, and $\delta^{18}O$–δ^2H diagram for different types of ground ice is presented in **Figure 11**. Since stable isotopes of hydrogen and oxygen in meteoric water have a consistent relationship ($\delta^2H = 8{*}\delta^{18}O$) the difference between expected δ^2H to $\delta^{18}O$ relationships in a given sample is calculated by deuterium excess (d); d = $\delta^2H–8{*}\delta^{18}O$ (Dansgaard, 1964). The global meteoric water line (GMWL) has a d-excess value of 10% so departures from this value yield insights into potential enrichment or depletion in ^{18}O

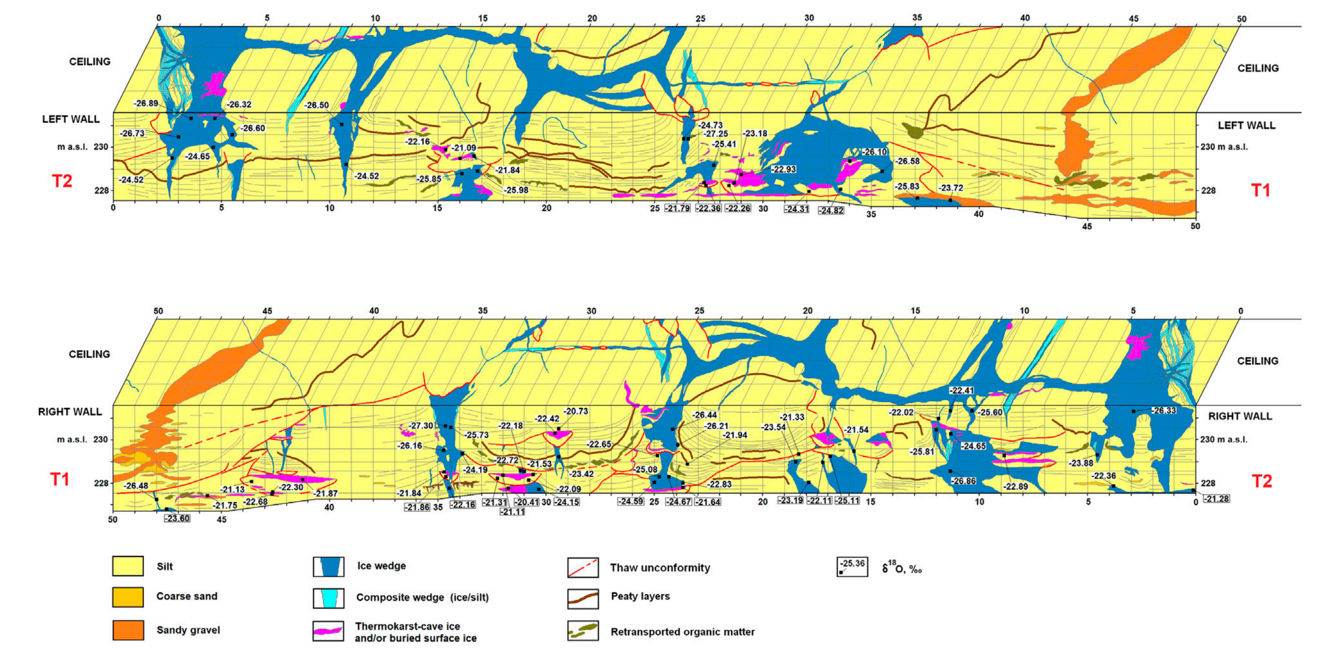

FIGURE 10 | General cryostratigraphic maps of the walls and the ceiling of Crosscut C1.

over ^{16}O (Craig, 1961). Rain and snow tend to fall on the GMWL, so d-excess values close to 10% usually identify precipitation that has not undergone significant fractionation. Negative d-excess values are considered evaporatively enriched surface waters and thus the water source (for the ice formation) experienced evaporation at some point. Greater δ^{18}O values and increasingly negative d-excess values in a given sample type indicate a period of warming.

The isotope composition of ice wedges ranged between −28.7% and −20.4% for δ^{18}O (average value −24.9 ± 1.9%, n = 184). We detected 16 samples, mainly from the main adit (T2), which could be identified as the Holocene ice wedges (**Table 2**; for raw data see **Supplementary Tables S2, S3, and S4**; for locations see **Figure 6**), and the average δ^{18}O value for them (−24.0 ± 1.3%, n = 16) was slightly higher than the average value for all other ice wedges (−25.0 ± 1.9%, n = 168). Greater δ^{18}O values for Holocene ice wedges signify winter temperatures warmer than the other ice wedges, and the high d-excess values signify that frost cracks during the ice-wedge formation were filled mainly with snowmelt water.

The isotope composition of thermokarst-cave ice and underlying silt with reticulate-chaotic cryostructure ranged between −26.1% and −19.1% for δ^{18}O (average value -22.7 ± 1.5%, n = 68). Comparison of values obtained from the thermokarst-cave ice bodies and from segregated ice that formed in underlying silt with reticulate-chaotic cryostructure showed a very small difference (**Table 2**), which suggests that the source of water was the same. Relatively high δ^{18}O values and the negative d-excess values, which were found for many samples obtained from these types of ground ice, indicate evaporative processes that occurred in the surface or shallow subsurface waterbodies from which the ice formed. More likely, these types of ice formed in the summer from a mixture of snowmelt water, rainwater, and water from melting ice wedges that accumulated in thermo-erosional gullies and underground cavities.

The isotope composition of layers of segregated ice (ice belts) ranged between −23.4 and −21.0% for δ^{18}O (average value −21.7 ± 0.7%, n = 12). These relatively high values (in comparison with the ice wedges) can be explained by a different source of water: while for ice wedges it is mostly snowmelt water, ice belts form from the ground water of the active layer, which is mainly a mixture of snowmelt water and rainwater.

Distribution of δ^{18}O values for various types of ground ice with depth and, correspondingly, age of sediments (**Figure 12**) does not show any significant trends, probably because only several samples were obtained from the Holocene silt unit.

5.5 Radiocarbon Dating

A total 54 ^{14}C dates provide age control in the new CRREL Permafrost Tunnel and boreholes F3 and F12 (drilled from the surface) and F16 (drilled from the floor of the Tunnel) (**Table 3**). According to these dates, the NHB and JEB sections date between about 31,000 and 38,500 years BP (all ages are in calibrated years). A number of dates were measured from wood suspended in the ice (presumably thermokarst-cave ice). Those dates range between about 32,500 and 35,000 years, although one sample yielded an age of nearly 43,500 years.

Dates obtained from borehole F16, which was drilled from the floor of the Tunnel near the NHB section, showed the range between 36,300 and 36,800 years ago. The oldest date (42,300 years) was obtained from borehole F3 at 18.2 m below the surface near the boundary between silt and gravel.

TABLE 2 | Radiocarbon dates, new CRREL Permafrost Tunnel and adjacent boreholes.

Section	Lab Code	Material	Elevation, m a.s.l	Radiocarbon age, years BP	1 SD error	Cal. age (median), years BP	Younger cal limit BP (2 SD)	Older cal limit BP (2 SD)
Entrance	Beta-312256	Wood[a] (*Salix*)	227.9	29,590	170	34,161	33,782	34,463
JEB	OS-110810	Herb[b]	231.6	27,300	700	31,464	30,106	33,114
JEB	OS-111150	Herb[b]	231.3	27,700	410	31,719	31,096	32,899
JEB	Beta-326662	Herb[b]	231.1	29,880	190	34,374	34,043	34,671
JEB	**UGAMS-18339**	Wood[c]	231.0	29,933	85	34,409	34,212	34,592
JEB	**UGAMS-18340**	Herb[b]	231.0	30,638	88	34,996	34,682	35,298
JEB	OS-110809	Herb[b]	230.4	28,700	840	32,953	31,217	34,514
JEB	**UGAMS-18342**	Herb[b]	230.1	31,611	138	35,979	35,560	36,275
JEB	**OS-111254**	Wood[d]	230.1	33,700	1600	38,414	35,250	41,485
JEB	**OS-113379**	Wood[d]	230.1	31,300	610	35,663	34,523	36,824
JEB	**OS-110808**	Herb[b]	229.9	29,300	920	33,557	31,528	35,384
JEB	**OS-110807**	Wood[c]	229.9	31,100	1140	35,550	33,091	38,569
JEB	Beta-326663	Wood[a] (Betula)	229.7	28,900	210	33,378	32,289	34,051
JEB	Beta-310925	Wood[a] (*Salix*)	229.3	30,970	200	36,311	36,094	36,581
JEB	UGAMS-18341	Herb[b]	229.3	31,998	96	35,336	34,751	35,870
JEB	Beta-326660	Wood[a] (Betula)	228.5	31,430	240	35,794	35,323	36,235
JEB	UGAMS-18343	Herb[b]	228.5	32,393	98	36,689	36,373	36,985
JEB	Beta-326664	Wood[a] (*Salix*)	227.8	31,650	230	35,984	35,439	36,400
JEB	Beta-326665	Wood[a] (Salicaceae)	227.7	32,570	250	36,896	36,322	37,526
NHB	Beta-312255	Wood[c]	232.1	27,090	140	31,162	31,003	31,410
NHB	OS-111607	Herb[b]	231.9	28,200	320	32,341	31,491	33,277
NHB	OS-111151	Herb[b]	231.9	28,100	420	32,244	31,214	33,331
NHB	**Beta-373717**	Wood[c]	230.5	31,670	240	36,002	35,433	36,442
NHB	**UGAMS-18345**	Herb, *Carex* and Empetrum seeds, dicot leaf frags, bud scales[b]	230.5	32,382	104	36,677	36,359	36,982
NHB	Beta-310924	Wood[a] (Betula)	230.0	29,590	200	34,150	33,717	34,497
NHB	Beta-373716	Wood[c]	229.6	32,890	260	37,333	36,536	38,465
NHB	UGAMS-18346	Herb[b]	229.6	32,063	99	36,364	36,135	36,679
NHB	UGAMS-18347	Herb/rootlets[b]	228.8	32,281	100	36,574	36,288	36,900
NHB	Beta-310923	Wood[a] (Betula)	228.8	30,510	180	34,901	34,524	35,297
NHB	UGAMS-18344	Herb/rootlets[b]	228.1	32,380	98	36,675	36,364	36,975
Cave Ice	Beta-326667	Wood[a]	227.9	31,320	220	35,710	35,278	36,162
Cave Ice	Beta-326668	Wood[a]	228.8	30,900	220	35,250	34,671	35,789
Cave Ice	Beta-326669	Wood[a] (*Salix*)	229.1	31,970	210	36,313	35,882	36,852
Cave Ice	Beta-326670	Wood[a]	229.2	30,260	180	34,653	34,345	35,166
Cave Ice	Beta-326671	Wood[a]	229.3	31,990	200	36,330	35,951	36,850
Cave Ice	Beta-326672	Wood[a] (Betula)	229.3	31,530	190	35,879	35,435	36,251
Cave Ice	Beta-326666	Wood[a] (Betula)	229.4	40,350	570	43,545	42,776	44,389
Cave Ice	Beta-326673	Wood[a]	229.9	32,190	250	36,529	36,075	37,055
Cave Ice	Beta-326675	Wood[a] (*Salix*)	230.1	29,540	170	34,118	33,730	34,436
Cave Ice	Beta-326674	Wood[a] (*Salix*)	230.8	28,390	160	32,528	31,944	33,116
Cave Ice	OS-95371	Wood[a] (*Salix*)	229.2	30,900	200	35,251	34,689	35,728
Cave Ice	Beta-317443	Wood[a] (Betula)	229.3	29,780	190	34,305	33,944	34,603
Cave Ice	OS-95370	Rootlets[b]	229.5	30,600	210	34,966	34,545	35,379
Borehole F12	Beta-326676	Herb and small wood[b,c]	237.6	5,890	30	6,709	6,653	6,786
Borehole F12	Beta-326678	Wood[a]	237.1	7,870	50	8,683	8,544	8,980
Borehole F12	Beta-326677	Wood[a]	236.4	8,090	40	9,018	8,779	9,250
Borehole F12	Beta-326679	Wood[a]	235.3	8,220	40	9,185	9,024	9,398
Borehole F12	Beta-326680	Herb[b]	233.7	10,750	50	12,731	12,677	12,764
Borehole F12	OS-111153	Wood[b]	232.2	32,800	760	37,470	35,776	39,362
Borehole F12	OS-111152	Herb[b]	231.7	28,200	430	32,382	31,286	33,533
Borehole F16	**UGAMS-18348**	Herb[b]	227.4	32,314	100	36,608	36,313	36,927
Borehole F16	**UGAMS-18349**	Wood[c]	227.4	32,509	104	36,811	36,445	37,104
Borehole F16	Beta-326681	Wood[a]	225.9	32,270	200	36,587	36,196	37,012
Borehole F3	Beta-310926	Wood	223.4	38,220	260	42,343	42,130	42,553

Notes: Dates marked in bold are splits from the same bulk sample.
[a]*Single wood fragment dated.*
[b]*Samples containing multiple herbaceous fragments.*
[c]*Samples containing multiple wood fragments.*
[d]*Sub-sample of the original submission of multiple wood fragments.*

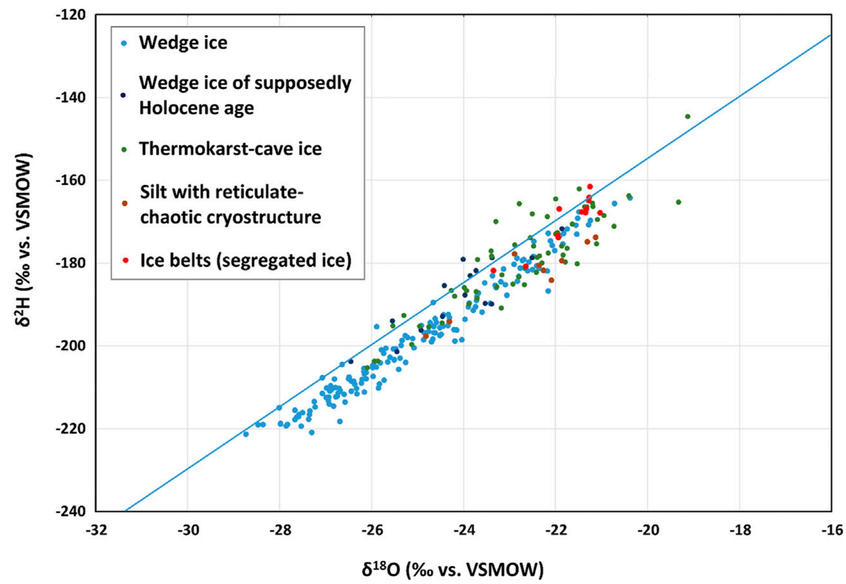

FIGURE 11 | $\delta^{18}O$–$\delta^{2}H$ diagram for different types of ground ice in the CRREL Permafrost Tunnel. Blue line represents the Global Meteoric Water Line (GMWL).

Radiocarbon samples obtained from borehole F12, which was drilled from the surface near the NHB section, showed the wide range of dates–from 6,700 to 37,500 years, with a significant hiatus between 37,500 years BP at 7 m and 12,600 years BP at 5.5 m below the surface; the samples collected from the upper 4 m all showed the Holocene age (6,700 to 9,200 years) (**Table 3**).

To assess whether there were systematic differences between dates on wood versus herbaceous plant debris, we submitted both woody and non-woody material from the same bulk sample (samples marked in bold in **Table 2**). The results indicated no systematic bias associated with woody versus non-woody material. In some cases, the wood was older, while in other cases the herbaceous material was older. The age difference between these materials ranged between nearly 2000 and 300 years.

A number of the radiocarbon dates also have very large standard errors (>800 years). In at least one case, this was a problem at the radiocarbon facility. We were able to re-date one of the samples (OS-111254), yielding both a younger age and a smaller standard error (OS-113379), which was more similar to the non-woody material from the same bulk sample (**Table 3**).

6 DISCUSSION

6.1 Cryostratigraphy and Ground-Ice Content

6.1.1 Cryostratigraphic Units

Based on our ground-ice studies of the new CRREL Tunnel facilities and the cores, and the data from the old Tunnel and adjacent areas (Sellmann, 1967; Sellmann, 1972; Péwé, 1975a; Péwé et al., 1976; Hamilton et al., 1988; Shur et al., 2004; Bray et al., 2006; Fortier et al., 2008; Kanevskiy et al., 2008a; Kanevskiy et al., 2008b), we distinguish six main cryostratigraphic units (described from the top):

(1) Active layer, 0.55–0.8-m thick; peat underlain by organic-rich silt; average gravimetric moisture content 39.7% (this study);
(2) Modern intermediate layer of the upper permafrost; ice-rich silt, up to 0.6 m thick; average gravimetric moisture content 91.8% (this study);
(3) Holocene silt—Ready Bullion Formation (Péwé, 1975a; Péwé et al., 1976), Yedoma deposits reworked by thermokarst and thermal erosion during the Holocene, 3–6 m thick, organic-rich silt, relatively ice poor, with thin ice wedges and several buried ice-rich intermediate layers; average gravimetric moisture content 61.6% (this study);
(4) Late Pleistocene Yedoma silt—Goldstream Formation (Péwé, 1975a; Péwé et al., 1976), 10–14 m thick, ice- and organic rich, with large ice wedges; with lenses and layers of gravel and gravelly sand in the lower part of this unit; average gravimetric moisture content of silt 94.0% (this study);
(5) Pleistocene alluvial gravel and gravelly sand–Fox Gravel (Péwé, 1975a; Péwé et al., 1976), 3–4 m thick, generally ice poor; average gravimetric moisture content 19.9% (this study);
(6) Bedrock—weathered Pre-Cambrian muscovite-quartz Fairbanks Schist (Newberry et al., 1996), generally ice poor, exposed near the floor of the Gravel Room; average gravimetric moisture content 11.7% (Hamilton et al., 1988).

According to Péwé, both the Ready Bullion Formation and Goldstream Formation originated from the upland Fairbanks Loess of Illinoian through Holocene age reworked and retransported from upper slopes to lower slopes and valley bottoms. The Ready Bullion Formation, which is 1–10 m

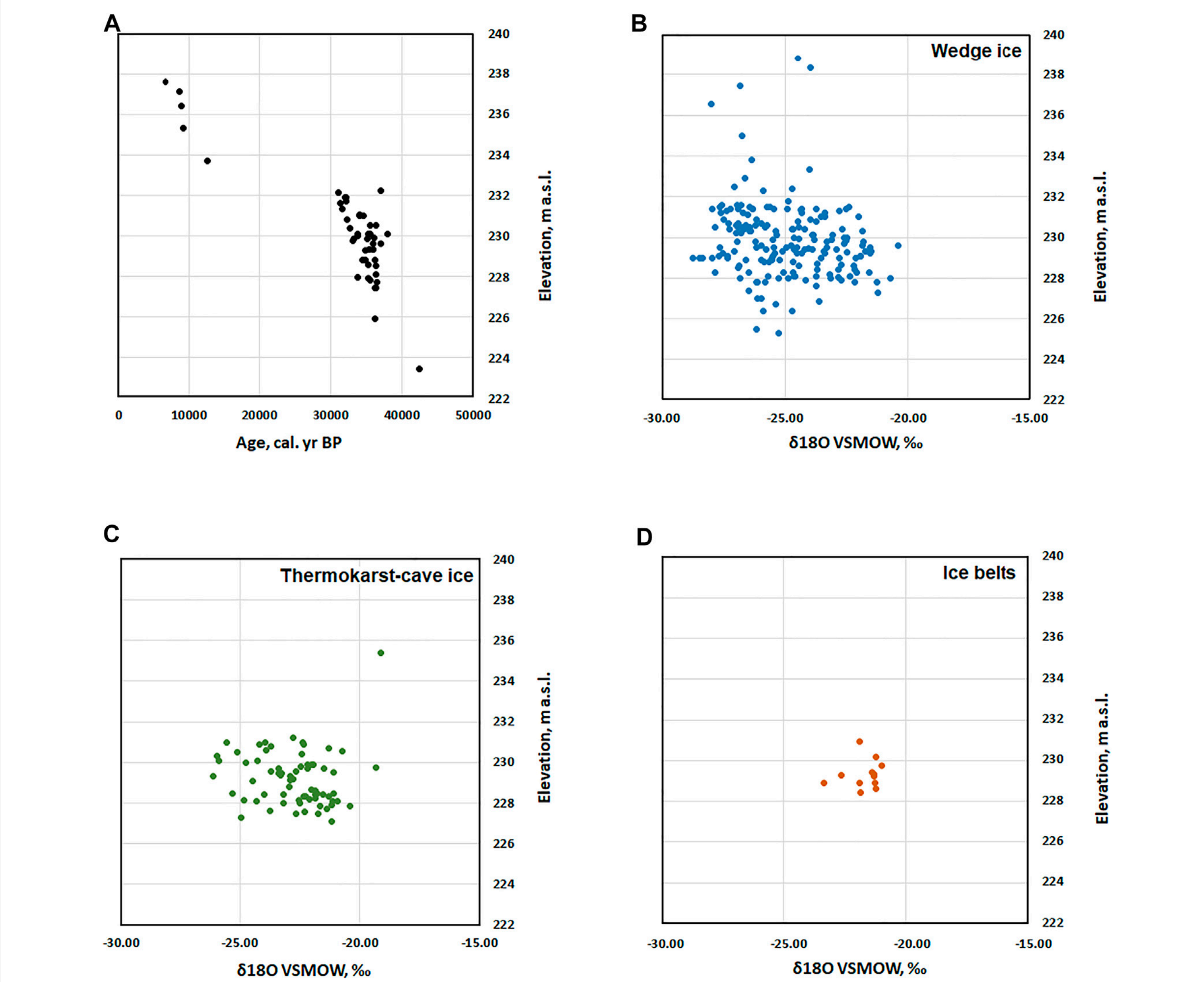

FIGURE 12 | Age of sediments **(A)** and stable oxygen isotopic composition ($\delta^{18}O$) of various types of ground ice **(B,C,D)** obtained from the samples collected in the new CRREL Permafrost Tunnel and surrounding area at various elevations. **(A)** Radiocarbon dates (cal. years BP); **(B)** stable oxygen isotopic composition of wedge ice (average value −24.9 ± 1.9%, n = 184); **(C)** stable oxygen isotopic composition of thermokarst-cave ice and underlying silt with reticulate-chaotic cryostructure (average value −22.7 ± 1.5%, n = 68); **(D)** stable oxygen isotopic composition of layers of segregated ice (ice belts) (average value -21.7 ± 0.7%, n = 12).

TABLE 3 | Stable-isotope composition (average $\delta^{18}O$, $\delta^{2}H$, and Deuterium Excess values) of various types of ground ice, new CRREL Permafrost Tunnel and adjacent boreholes. For raw data, see Supplementary Tables S2 to S8.

Type of ground ice	Number of samples	δ^2H Average (%)	δ^2H Std Dev (%)	δ^{18}O Average (%)	δ^{18}O Std Dev (%)	d-Excess Average (%)	d-Excess Std Dev (%)
Wedge ice	168	−198.34	14.33	−25.01	1.92	1.76	3.02
Wedge ice of supposedly Holocene age	16	−186.68	9.49	−23.97	1.26	5.04	4.44
Thermokarst-cave ice	59	−179.24	11.83	−22.76	1.55	2.86	5.65
Silt with reticulate-chaotic cryostructure	9	−182.67	8.21	−22.56	1.26	−2.20	3.86
Ice belts (segregated ice)	12	−169.78	6.36	−21.73	0.68	4.06	2.70

thick, unconformably overlies the Goldstream Formation (Péwé, 1975a; Péwé et al., 1976). Péwé did not find any evidence of ice-wedge occurrence in the Ready Bullion Formation, he only mentioned ice lenses <1 cm thick (Péwé, 1975a). However, small ice wedges were observed in the Holocene deposits of vertical ventilation shaft of the CRREL permafrost Tunnel

(Sellmann, 1967; Hamilton et al., 1988). We also observed presumably Holocene ice wedges in Borehole F12 and near the entrance of the new CRREL Tunnel. Occurrence of small buried ice wedges and relatively thin ice-rich layers with micro-cryostructures in generally ice-poor silt indicates that the Holocene silt froze partly epigenetically and partly syngenetically and quasi-syngenetically, with possible formation of the intermediate layers during the periods of surface stabilization and subsequent growth of vegetation.

Large areas in the discontinuous permafrost zone of Alaska have been affected by deep thawing and thermal erosion during the Holocene, as indicated by a layer of ice-poor reworked sediments on top of many Yedoma sections (Péwé, 1975a; Péwé, 1975b; Kanevskiy et al., 2012; Kanevskiy et al., 2014). Péwé (1975b) mentioned that a significant lowering of the permafrost table had occurred during the Pleistocene/Holocene transition, and we also conclude that the ice-poor Holocene silt could form as a result of *in situ* thawing and refreezing of the ice-rich Yedoma silt in some areas of the Yukon-Tanana Upland (Kanevskiy et al., 2012) and the Koyukuk Flats (Kanevskiy et al., 2014). However, numerous Holocene dates obtained from the Ready Bullion Formation (Péwé, 1975a; Hamilton et al., 1988; and this study) suggest that in the CRREL Tunnel and adjacent area these deposits were largely retransported during the period of high erosional activity that was caused by a significant increase in precipitation and strongly affected the poorly vegetated Yedoma surface.

Occurrence of the ice-poor sediments in the upper permafrost protects ice-rich Yedoma deposits from thermokarst development. Thickness of this layer may be a key to understanding the susceptibility of Yedoma to degradation. Péwé (1954) reported that thermokarst mounds and pits started developing since the numerous agricultural fields were cleared for cultivation around Fairbanks in the areas with large masses of ground ice (i.e., ice wedges). While some fields were strongly affected by thermokarst, others could stay relatively stable for many years, until deep thawing reached undisturbed Yedoma that had been protected from above by ice-poor deposits. Occurrence of the ice-poor layer on top of Yedoma may explain the resilience of Yedoma to climatic impacts and local disturbances even in the areas of warm discontinuous permafrost.

6.1.2 Ground-Ice Content of Yedoma

Numerous studies in Siberia and North America showed that Yedoma contains large amounts of ground ice, including wedge ice and segregated ice. Based on our measurements of wedge ice areas in the new CRREL Tunnel facilities (**Table 1**), we estimated the volumetric content of wedge ice to be 15–20%. Probably this value is greater at higher elevations because ice wedges exposed near the ceiling are significantly wider than those exposed near the floor of the new Tunnel facilities (**Figures 6**, **10**). This observation corresponds to our measurements of wedge-ice areas that are higher at the ceiling (24–25%) than on the walls (11–19%) of T2 and C1 (**Table 1**).

In general, wedge-ice in the Tunnel area is significantly less than that in other Alaskan sites underlain by Yedoma. For example, wedge-ice content has been estimated to be 61% at the Itkillik River exposure, northern Alaska (Kanevskiy et al., 2011; Kanevskiy et al., 2016), up to 61% in the Devil Mountains area, Seward Peninsula (Shur et al., 2012), and up to 47% in the Livengood area (9-Mile Hill site) in Interior Alaska (Kanevskiy et al., 2012), although sections of Yedoma with high content of segregated ice and low wedge-ice content also have been described in this area (Kanevskiy et al., 2012).

Average area occupied by thermokarst-cave ice on the walls and ceiling of the main adit (T2) and Crosscut #1 (C1) of the new Tunnel was 1.9% (**Table 1**). Previously we did a similar estimation at the 600-m-long and 7- to 10-m-high coastal exposure near the village of Kaktovik at Barter Island (Alaskan Beaufort Sea coast), which showed that the thermokarst-cave ice occupied practically the same area—approximately 2.0% of the face of the bluff (Kanevskiy et al., 2013).

Based on the results of drilling in the Tunnel area, gravimetric ice contents of Yedoma silt varied from <50 to >150% with an average value of 94.0%. These numbers are similar to the values measured in the old Tunnel by Hamilton et al. (1988), who reported that gravimetric moisture content of the Pleistocene silt varied from 39 to 139%.

The ice content of the Pleistocene silt strongly depends on cryostructures. For sediments with micro-cryostructures (original Yedoma), gravimetric moisture content in the main adit of the old Tunnel varied from 80 to 180%, averaging 130% (Bray et al., 2006). A similar range (100–240%) was found in the winze (**Supplementary Figure S6A**) (Kanevskiy et al., 2008a). For reworked sediments (modified Yedoma), which filled gullies and underground channels, gravimetric moisture content in the main adit of the old Tunnel varied from 50 to 95%, averaging 69% (Bray et al., 2006). For the same sediments in the winze, gravimetric moisture content was 70–100% (Kanevskiy et al., 2008a). Such values are very high for ice-poor sediments that do not contain any significant amount of excess ice. This unusually high moisture content may be explained by occurrence of reworked organic material in these sediments (**Supplementary Figure S6B**). For the cross-stratified sand filling underground channels, the average gravimetric moisture content was 44.6%, whereas it was 107.7% in the surrounding undisturbed Yedoma with micro-lenticular cryostructure (Fortier et al., 2008). For sediments with reticulate-chaotic cryostructure, gravimetric moisture content in the main adit of the old Tunnel varied from 60 to 115%, averaging 85% (Bray et al., 2006).

We found similar values of gravimetric moisture content in Yedoma silt in the 9-Mile Hill study area located ~90 km NW of the CRREL Tunnel. Sediments between ice wedges were characterized by a wide range (from ~40% to >200%) and high values (85.5% average) of gravimetric moisture content that did not change significantly with depth; such distribution is typical of syngenetic permafrost. Thaw strain values of Yedoma silt in this area varied from 20 to 60%. With typical wedge-ice content of 30–50%, complete thawing of 30-m-thick Yedoma in this area can result in thaw settlement of more than 20 m (Kanevskiy et al., 2012).

6.1.3 Comparison of Cryostratigraphy of the Old and New Cold Regions Research and Engineering Laboratory Tunnel Facilities

There is a significant difference in cryostratigraphy of the old and new sections of the Tunnel. Yedoma in the old Tunnel was greatly modified by erosional and thermokarst events that occurred following initial deposition. Almost all ice wedges identified in the old Tunnel were truncated by thermal erosion, and thermokarst-cave ice bodies are very common (Kanevskiy et al., 2008b; Fortier et al., 2008). In the new Tunnel (T2 and C1), we could also observe erosional features and thermokarst-cave ice bodies, but original Yedoma here was preserved much better.

Early studies of the old Tunnel (Sellmann, 1967; Sellmann, 1972; Hamilton et al., 1988) described upper and lower silt units with independent systems of ice wedges separated by a continuous thaw unconformity presumably caused by regional or widespread thermokarst. In our previous studies, we emphasized the syngenetic nature of permafrost in the old Tunnel and presented evidence that processes of Yedoma formation and thermal erosion were occurring simultaneously. Results of our studies in the old Tunnel did not confirm the existence of two silt units divided by a continuous thaw unconformity, as described previously. We attributed thaw unconformities to local thermokarst and thermo-erosional events (Shur et al., 2004; Kanevskiy et al., 2008b), and our studies in the recently excavated sections of the Tunnel gave us new evidence to confirm these ideas. First, there are numerous ice wedges extending from the ceiling to the floor (unlike the old Tunnel), although some exposed ice wedges were truncated by thermokarst and/or thermal erosion. Second, the vertical extent of the ice wedge in Borehole F2 exceeded 9 m (**Supplementary Figure S10**), which confirms the syngenetic nature of ice wedges in this study area. Third, all thaw unconformities in the new Tunnel were discontinuous and randomly distributed. Continuous unconformities were observed only near the portal of the new Tunnel and in the part of Crosscut #1 adjacent to the old Tunnel (**Figures 6**, **10**, respectively). We attribute both of them to the Pleistocene/Holocene transition and consider them to be major stratigraphic boundaries separating the Pleistocene and Holocene deposits.

Another significant difference in cryostratigraphy of the new CRREL Tunnel compared to the old one was the absence of gravelly Holocene deposits, which were described near the portal of the old Tunnel. According to Hamilton et al. (1988), these fanlike deposits of poorly sorted debris, which unconformably overlie the Pleistocene silt, accumulated between 12,500 and 11,000 years BP during deep erosion of the Goldstream Creek valley slopes. We presume that accumulation of the Holocene gravel, which contains numerous logs and bones of Pleistocene mammals, occurred in a large gully that was filled relatively fast as a result of stream and mudflow activity during the Pleistocene/Holocene transition. Similar deposits filled the ice-wedge pseudomorph, which is visible on the walls and the ceiling of Crosscut #2 at 43–50 m, in the area adjacent to the old Tunnel (**Supplementary Figure S39**).

6.2 Water Stable Isotope Composition

In general, our data on the stable isotope composition of ground ice (**Tables 1**, **Supplementary Tables S2–S8**; **Figures 11**, **12**) are in agreement with the available isotope data (Meyer et al., 2008; Douglas et al., 2011; Lachniet et al., 2012; Sloat, 2014; Jorgenson et al., 2015a, Jorgenson et al., 2015b; Porter et al., 2016; Schirrmeister et al., 2016) for different sites of Interior Alaska and adjacent regions of Canada (**Table 4**). In the old CRREL Permafrost Tunnel, the stable oxygen isotope values for the Pleistocene ice wedges ranged between −29.3 and −24.1%, and thermokarst-cave ice between −27.0 and −24.4% (Douglas et al., 2011). Sloat (2014) reported that average δ^{18}O values for eight ice wedges ranged between −28.9 and −20.4% (average value -26.0%), while average values for seven “ice pools” (thermokarst-cave ice bodies) ranged between −26.6 and −21.8% (average value −23.4%). These values are slightly lower than the average δ^{18}O values obtained during our study in the new CRREL Tunnel: −25.0% (n = 168) for the Pleistocene ice wedges and −22.7% (n = 68) for thermokarst-cave ice.

In the Vault Creek permafrost tunnel located ~10 km N of the CRREL Tunnel, the stable oxygen isotope values for 25 ice wedges (145 individual samples) ranged between ~ −29.2 and −20.5%; values for segregated ice (23 samples) ranged between ~ −26.6 and −12.9% (Meyer et al., 2008; Schirrmeister et al., 2016). In the Horseshoe Lake study area located ~35 km SE of the CRREL Tunnel, we sampled two late Pleistocene ice wedges covered by ~3-m-thick layer of ice-poor Holocene silt. In the first one, sampled at depths from 3.1 to 10.0 m, the stable oxygen isotope values ranged between −29.5 and −24.3% (n = 10, average value −28.0%). In the second one, sampled at depths from 3.6 to 3.8 m, the stable oxygen isotope values ranged between −26.2 and −25.3% (n = 3, average value −25.8%) (Jorgenson et al., 2015a). In the 9-Mile Hill study area located ~90 km NW of the CRREL Tunnel (Kanevskiy et al., 2012), late Pleistocene ice wedges enclosed in Yedoma silt were sampled at depths from 2.7 to 16.0 m; the stable oxygen isotope values ranged between −29.3 and −27.8% (n = 5, average value −28.4%) (unpublished data).

For Holocene ice wedges in Interior Alaska, stable isotope data are limited. In the Vault Creek permafrost tunnel, the average stable oxygen isotope value for the presumably Holocene ice wedge was −21.9% (Meyer et al., 2008; Schirrmeister et al., 2016). In the Creamer’s Field study area located ~10 km SW of the CRREL Tunnel, we sampled nine Holocene wedges (three of them were active) at depths from 0.7 to 3.3 m; the stable oxygen isotope values ranged between −23.9 and −21.2% (n = 22, average value −22.7%) (Jorgenson et al., 2015b). These values are slightly higher than the average δ^{18}O value for the Holocene ice wedges obtained during our study in the new CRREL Tunnel (n = 16, average value −24.0%).

Thus, stable oxygen isotope values for Holocene ice wedges in various study areas of Interior Alaska and Canada are usually 2–5% higher than those of Pleistocene wedges (**Table 4**), which is related to lower winter temperatures during the late Pleistocene. Stable oxygen isotope values for the late Pleistocene thermokarst-cave ice are higher and have a wider range in comparison with the late Pleistocene ice wedges. This can be explained by different sources of water: while for ice wedges it is mostly snowmelt water, for thermokarst-cave ice it is a mixture of snowmelt water, rainwater, and water from melting ice wedges that accumulated in thermo-erosional gullies and underground cavities.

TABLE 4 | $\delta^{18}O$ values for various types of ground ice in Interior Alaska and adjacent regions of Canada.

Study area	$\delta^{18}O$ values, %			References
	Min	Max	Average	
Ice wedges, Pleistocene				
New CRREL Tunnel	−28.7	−20.4	−25.0	This study
Old CRREL Tunnel	−29.3	−24.1	—	Douglas et al. (2011)
Old CRREL Tunnel	−28.9	−20.4	−26.0	Sloat (2014)
Vault Creek tunnel	−29.2	−20.5		Schirrmeister et al. (2016)
Horseshoe Lake-1	−29.5	−24.3	−28.0	Jorgenson et al. (2015a)
Horseshoe Lake-2	−26.2	−25.3	−25.8	Jorgenson et al. (2015a)
9-Mile Hill	−29.3	−27.8	−28.4	Unpublished data
Quartz Creek (Klondike)	—	—	−29.3	Porter et al. (2016)
Ice wedges, Holocene				
New CRREL Tunnel	−26.5	−21.8	−24.0	This study
Vault Creek tunnel	—	—	−21.9	Schirrmeister et al. (2016)
Creamer's Field	−23.9	−21.2	−22.7	Jorgenson et al. (2015b)
Klondike	—	—	−23.4	Porter et al. (2016)
Thermokarst-cave ice, Pleistocene				
New CRREL Tunnel	−26.1	−19.1	−22.7	This study
Old CRREL Tunnel	−27.0	−24.4	—	Douglas et al. (2011)
Old CRREL Tunnel	−26.6	−21.8	−23.4	Sloat (2014)
Segregated ice, Pleistocene				
New CRREL Tunnel	−23.4	−21.0	−21.7	This study
Vault Creek tunnel	−26.6	−12.9	—	Schirrmeister et al. (2016)

6.3 Radiocarbon Dating

The assemblage of ^{14}C dates from the new CRREL Tunnel are generally stratigraphically consistent (**Table 2**; **Figure 12A**). The basal ages are usually older than the uppermost ages, but there are several reversals, and ages on subsamples of the same bulk sample can be as much as 2000 years different in age. In addition, there is no systematic bias in the dated material, sometimes the wood is older, other times non-woody material is older.

The stratigraphy of the Tunnel does not suggest wholesale mixing of the sediments (i.e., "the Quaternary in a blender") as the radiocarbon dates show some stratigraphic integrity and the buried soils extend for 10 s of meters, albeit highly deformed adjacent to ice wedges and with abrupt elevation changes in other areas. The radiocarbon dates suggest either smaller-scale reworking during burial and afterwards or the deposition of material of different ages. In an active depositional environment, in a region of slow organic matter decomposition (such as the permafrost region), older material is frequently re-deposited, which complicates interpretation of depositional patterns (Lenz et al., 2016). Various problems of radiocarbon dating in the permafrost region were discussed by Kennedy et al. (2010) and (Reyes et al., 2010a; Reyes et al., 2010b; Reyes et al., 2011) and highlighted the need to date multiple material types (wood vs. non-woody), especially when reworking is a possibility.

Numerous age inversions have been reported for the old CRREL Tunnel (Hamilton et al., 1988; Lachniet et al., 2012). Shur et al. (2004) suggested that inconsistency in radiocarbon dates obtained from the old Tunnel by Hamilton et al. (1988) may be related to the dating of material from thermokarst-cave ice bodies and soil pseudomorphs. Lachniet et al. (2012) stated that multiple age inversions in stratigraphic sections of the old CRREL Tunnel occurred through the incorporation of older organic matter by various processes of sediment redistribution.

Based on above-mentioned studies and our observations, we see several possible explanations for age inversions typical of Yedoma deposits: 1) deposition of different-aged material on the ground surface, 2) reworking of sediments during burial, 3) slump and collapse of sediments after burial as a result of surficial and underground erosion, which was common at the time of Yedoma formation, and 4) deposition of same-aged material at various elevations simultaneously (e.g., not only on the main surface, but inside the gullies or underground cavities).

In general, radiocarbon dates obtained from the new Tunnel are in agreement with those previously obtained from the old Tunnel (Sellmann, 1967; Hamilton et al., 1988; Long and Péwé, 1996; Kanevskiy et al., 2008a; Kanevskiy et al., 2008b; Lachniet et al., 2012). Radiocarbon dating at other sites in Interior Alaska showed a similar age of Yedoma silt. In the Vault Creek permafrost tunnel area, silt accumulation and ice-wedge growth occurred from 40,000–50,000 years BP to at least 25,000 years BP, forming ~15-m-thick Yedoma unit; Holocene dates were reported for the uppermost 2-m-thick silty sand unit (Schirrmeister et al., 2016). In the 9-Mile Hill study area, radiocarbon dates for ~25–30-m-thick Yedoma silt were 22,600 to 43,100 ^{14}C years BP (8 samples, depths from 1.7 to 17.8 m), and no Holocene dates were reported for this area (Kanevskiy et al., 2012). For the Klondike area, Fraser and Burn (1997) and Zazula et al. (2007) reported dates from 24,000 to 31,000 and from 24,000 to 29,500 ^{14}C years BP, respectively.

During our study, we weren't looking specifically for tephra deposits and didn't see any obvious ones. This does not rule out that they are present, especially cryptotephras (Payne et al., 2008; Pyne-O'Donnell et al., 2012). A pair of tephras at Halfway House site in Interior Alaska (Dawson and possibly the Chatanika tephras) date to ~30,000 cal yr BP (Jensen et al., 2016). Based on radiocarbon dates obtained from our study, if they are present in T2, they would be right at the ceiling. The next older identified tephra at Halfway House is ~77,000 cal yr BP (Dominion Creek tephra), which would be below the floor of T2. However, a number of thin tephra layers have been observed between these tephras at Halfway House site, which could also be present in the walls of T2.

6.4 Age and Nature of Ice Wedges in Yedoma

The absence of dates between ~31,000 and 12,600 years BP, which we found in the new Tunnel and adjacent boreholes (**Table 2**; **Figures 12A** is also typical of the old Tunnel, where Hamilton et al. (1988) reported a similar hiatus. However, radiocarbon dating of the carbon dioxide in air bubbles and the organic carbon dissolved within the wedge ice showed much younger age than host sediments, and some Pleistocene ice wedges in the old Tunnel formed between 28,000 and 22,000 years BP while the age of host sediments exceeded 35,000 years BP (Lachniet et al., 2012). Similar studies in other regions (Opel et al., 2019; Holland et al., 2020; Wetterich et al., 2021) also found that ice wedges may be several thousand years younger than enclosing sediments. We hope a similar approach will be used during the future studies in the new Tunnel.

These studies, which revealed a large difference in age between ice wedges and host sediments, suggest our understanding of Yedoma as a sediment with large syngenetic ice wedges is probably oversimplified. Based on classification by Mackay, ice wedges can be classified as being either epigenetic, syngenetic, or anti-syngenetic in nature (Mackay, 2000; Murton, 2013; French, 2018). However, it is almost impossible to find “pure” epigenetic or syngenetic ice wedges. For example, the uppermost portions of many epigenetic ice wedges have some features typical of syngenetic ice wedges like ragged lateral margins and so-called “shoulders” (Romanovskii, 1977). Formation of such features may be caused by fluctuations in thaw depths. Lewkowicz (1994) described growth stages of modern ice wedges in relation to short-term climatic variability, which included alternating truncation and rejuvenation processes.

Very often the vertical extent of epigenetic ice wedges exceeds the local depth of frost cracking. The best example of such ice wedges are epigenetic wedges that develop within the intermediate layer after termination of sedimentation. Their formation occurs along with a gradual decrease in the active-layer thickness, mostly because of accumulation of organic matter; such a decrease leads to formation of the intermediate layer whose thickness under certain conditions may reach 1.5–2 m and even more (Shur, 1988; French and Shur, 2010; Shur et al., 2011). As a result, vertical extent of ice wedges may significantly exceed a depth of frost cracking. Romanovskii (1977) named such ice wedges “false syngenetic” because they had features typical of syngenetic ones, despite their epigenetic nature in relation to host sediments. We suggest to name these ice wedges “quasi-syngenetic” after Shur who used this term to describe a specific type of permafrost, which aggrades upward, like syngenetic permafrost, but without accumulation of a new sediment on the soil surface, and forms the ice-rich intermediate layer (Shur, 1988; Shur et al., 2011). Such ice wedges are very common in the continuous permafrost zone, where they form in the modern intermediate layer that has developed on top of Yedoma (Kanevskiy et al., 2011; Shur et al., 2021a).

Similarly, it is difficult to find “pure” syngenetic ice wedges because some portions of these wedges are always epigenetic, at least their lowermost parts (Shumskii, 1959; Shur et al., 2004). Technically, any syngenetic ice wedge can be defined as an assemblage of epigenetic ice veins because host sediments are always older than individual ice veins. That means that we should either determine what time gap between sedimentation and ice-wedge formation is sufficient to consider a wedge epigenetic, or use a different approach based on ice-wedge morphology and, first of all, comparison of vertical extent of ice wedges with a depth of frost cracking. In the new Tunnel, we observed numerous small buried epigenetic ice wedges and veins (**Figures 6**, **10**) but the shape and dimensions of larger ice wedges indicate that these wedges are either syngenetic or consist of several generations of epigenetic ice wedges, which probably better explains a significant difference in age between ice wedges and host sediments reported by Lachniet et al. (2012).

6.5 Cryostratigraphy of the CRREL Permafrost Tunnel and its Importance for Quaternary Studies of Eastern Beringia

In this study, we focus mainly on permafrost features and do not discuss paleoenvironmental issues. However, it is important to note that the new CRREL Permafrost Tunnel is a unique place to study the late-Pleistocene paleoenvironment in conjunction with general studies of eastern Beringia that have been performed in Alaska and Canada (Hopkins, 1982; Anderson and Lozhkin, 2001; Begét, 2001; Muhs et al., 2003; Bigelow, 2007; Elias and Brigham-Grette, 2007; Wooller et al., 2007; Froese et al., 2009; Porter et al., 2016). While many Quaternary studies around Fairbanks, including detailed studies of the Gold Hill, Birch Hill, and Halfway House sites (e.g., Muhs et al., 2003; Jensen et al., 2016), were performed in the areas where Yedoma and underlying loess deposits had already thawed, in the CRREL Permafrost Tunnel we can describe and sample frozen sediments perfectly preserved since the late Pleistocene.

Permafrost Tunnel facilities are especially important for researchers because exposed surfaces remain stable for decades (rates of sublimation are relatively small), while natural exposures of ice-rich permafrost retreat very fast and often become covered by reworked sediments in several years, which makes impossible revisiting them to continue studies of exposed bluffs. The newly exposed surfaces also provide unique opportunities to expand previous Quaternary studies performed in the old CRREL Tunnel (Sellmann, 1967; Sellmann, 1972; Hamilton et al., 1988; Long and Péwé, 1996; Wooller et al., 2007; Douglas et al., 2011; Wooller et al., 2011; Lachniet et al., 2012). We hope that the results of cryostratigraphic mapping presented in this study will serve as a foundation for the future Quaternary research in the new CRREL Permafrost Tunnel.

7 CONCLUSION

Excavation of the new sections of the CRREL Permafrost Tunnel, which started in 2011, provides a new and unique opportunity to study structure, properties, biogeochemical characteristics, and deposition history of Yedoma—ice-rich syngenetically frozen silt with large ice wedges.

In Interior Alaska, Yedoma has been observed at numerous sites within the Yukon-Tanana uplands. The most comprehensive data on the structure and properties of Yedoma in this area have been obtained in the CRREL Permafrost Tunnel near Fairbanks, which became available to researchers in the mid-1960s. In this paper, we introduce a new and unique research facility for yedoma studies and present the results of cryostratigraphic mapping of the walls and ceiling of a 110-m-long section of the main adit of the new Tunnel and a 50-m-long crosscut connecting the new and old Tunnels.

General cryostratigraphic maps and detailed maps of some parts of the new Tunnel show various characteristics typical of Yedoma: foliated ice wedges with a vertical extent of more than 10 m, the prevalence of micro-cryostructures, distinctive ice belts, and the occurrence of large amounts of weakly decomposed organic matter throughout the entire thickness of Yedoma.

Based on the studies in the Tunnel and results of drilling, six main cryostratigraphic units were distinguished (described from the top): 1) active layer; 2) modern intermediate layer (ice-rich silt); 3) 3- to 6-m-thick layer of the Holocene silt, mainly ice poor, with small ice wedges; 4) 10- to 14-m thick layer of the ice-rich late Pleistocene Yedoma silt with large ice wedges; 5) relatively ice-poor fluvial gravel; and 6) ice-poor bedrock.

Modern ice-rich intermediate layer and ice-poor silt layer protect ice-rich Yedoma deposits with large ice wedges from thermokarst development. Occurrence of these layers explains resilience of Yedoma to recent climatic impacts and local disturbances even in the areas of warm discontinuous permafrost.

Comparison of cryostratigraphy of the old and new parts of the CRREL Permafrost Tunnel shows significant differences. Yedoma in the old Tunnel was greatly destroyed or modified by erosional and thermokarst events, and almost all ice wedges in the main adit of the old Tunnel were truncated by thermal erosion. In the recently excavated sections of the Tunnel, erosional features and thermokarst-cave ice bodies also occur, but original Yedoma is much better preserved. Another significant difference in cryostratigraphy of the new sections of the CRREL Tunnel compared to the old ones is the absence of gravelly Holocene deposits, which were described near the portal of the old Tunnel.

Our studies in the CRREL Permafrost Tunnel do not confirm the existence of two Pleistocene silt units divided by a continuous thaw unconformity, as described previously. The processes of Yedoma formation and thermal erosion were going simultaneously, and we attribute thaw unconformities to local thermokarst and thermo-erosional events.

We are planning to continue our cryostratigraphic studies in the CRREL Permafrost Tunnel and perform mapping of two other crosscuts in the future.

DATA AVAILABILITY STATEMENT

Data are available through the NSF-funded Arctic Data Center (Shur et al., 2015 https://arcticdata.io/catalog/view/doi%3A10.18739%2FA2SP6G).

AUTHOR CONTRIBUTIONS

MK designed this study, performed cryostratigraphic mapping, and drafted a first version of the manuscript. YS developed a general concept of Yedoma cryostratigraphy in the study area. MK, NHB, KLB, and TAD collected samples in the new CRREL Permafrost Tunnel. TAD processed water stable isotope samples and analyzed the results. NHB collected radiocarbon samples and analyzed the results. All co-authors performed Yedoma studies at other Alaskan sites, including the old CRREL Permafrost Tunnel. All co-authors contributed to the manuscript writing and editing process.

FUNDING

This study was supported by the Department of Defense grant (AKRO-CRREL Soil and Water Sample Analyses) and National Science Foundation grants OPP-1820883, ARC-1107571, OPP-1806213, NNA-1928237, and NNA-2022590. TD acknowledges funding from the U.S. Army Corps of Engineers Engineer Research and Development Center Basic Research Program under PE 0601102/AB2 (Protection, Maneuver, Geospatial, Natural Sciences) and the Department of Defense's Strategic Environmental Research and Development Program project RC18-1170.

ACKNOWLEDGMENTS

We thank James Begét, Margaret Cysewski, Matthew Sturm, and Daniel Vandevort for their participation in the study. Isotope analyses of ground ice were performed at the Alaska Stable Isotope Facility (UAF) by Tim Howe and Norma Haubenstock and the CRREL Alaska geochemistry laboratory. Drilling in the study area was performed by GeoTek Alaska (2010) and Arthur Gelvin and Stephanie Saari, CRREL (2012). We thank Associate Editor Duane Froese and reviewers Matthew Lachniet and Alberto Reyes for their valuable comments and suggestions.

SUPPLEMENTARY MATERIAL

The Supplementary Material for this article can be found online at: https://www.frontiersin.org/articles/10.3389/feart.2021.758800/full#supplementary-material

REFERENCES

Anderson, P. M., and V. Lozhkin, A. (2001). The Stage 3 Interstadial Complex (Karginskii/middle Wisconsinan Interval) of Beringia: Variations in Paleoenvironments and Implications for Paleoclimatic Interpretations. *Quat. Sci. Rev.* 20, 93–125. doi:10.1016/s0277-3791(00)00129-3

Arcone, S. A., and Delaney, A. J. (1984). Field Dielectric Measurements of Frozen silt Using VHF Pulses. *Cold Regions Sci. Technology* 9, 29–37. doi:10.1016/0165-232X(84)90045-4

Begét, J. E. (2001). Continuous Late Quaternary Proxy Climate Records from Loess in Beringia. *Quat. Sci. Rev.* 20, 499–507. doi:10.1016/s0277-3791(00)00102-5

Bigelow, N. H. (2007). "POLLEN RECORDS, LATE PLEISTOCENE | Northern North America," in *Encylopedia of Quaternary Science*. Editor S. A. Elias (Amsterdam: Elsevier), 2633–2648. doi:10.1016/b0-44-452747-8/00193-9

Bjella, K., and Sturm, M. (2012). "A New Permafrost Research Tunnel: Methodology, Design, and Excavation," in Proceedings of the Tenth International Conference on Permafrost, Salekhard, Yamal-Nenets Autonomous District, Russia, June 25–29. Editor K. M. Hinkel (Salekhard: The Northern Publisher), 39–44.

Black, R. F. (1978). "Fabrics of Ice Wedges in central Alaska," in Proceedings of the Third International Conference on Permafrost, Edmonton, July 10–13, 1978 (Ottawa: National Research Council of Canada), 248–253.

Bray, M. T. (2008). "Effects of Soil Cryostructure on the Long-Term Strength of Ice-Rich Permafrost Near Melting Temperatures," in Proceedings of the Ninth International Conference on Permafrost, Fairbanks, Alaska, June 29 – July 3, 2008. Editors D. L. Kane and K. M. Hinkel (Fairbanks: Institute of Northern Engineering; University of Alaska Fairbanks) Vol. 1, 183–188.

Bray, M. T., French, H. M., and Shur, Y. (2006). Further Cryostratigraphic Observations in the CRREL Permafrost Tunnel, Fox, Alaska. *Permafrost Periglac. Process.* 17 (3), 233–243. doi:10.1002/ppp.558

Brown, J., and Kreig, R. A. (Editors) (1983). Guidebook to permafrost and related features along the Elliott and Dalton Highways, Fox to Prudhoe Bay, Alaska. Fairbanks: University of Alaska Fairbanks.

Carter, L. D. (1988). "Loess and Deep Thermokarst Basins in Arctic Alaska," in Proceedings of the Fifth International Conference on Permafrost, Trondheim, Norway (Trondheim: Tapir publishers), 706–711.

Chester, J. W., and Frank, J. N. (1969). *Fairbanks Placers Fragmentation Research Final Report. Minneapolis: Twin Cities Mining Research Center*. Minneapolis: U.S. Bureau of Mines, Heavy Metals Program. Auth. No. 9-1115-33.

Craig, H. (1961). Isotopic Variations in Meteoric Waters. *Science* 133 (3465), 1702–1703. doi:10.1126/science.133.3465.1702

Cysewski, M., Bjella, K., and Sturm, M. (2010). "The History and Future of the Permafrost Tunnel Near Fox, Alaska," in Proceedings of the 6th Canadian Conference on Permafrost, Calgary, Alberta, Canada, September 12-16, 1222–1227.

Cysewski, M., Sturm, M., and Bjella, K. (2012). "The Significance of the Permafrost Tunnel (Fox, Alaska)," in Proceedings of the Tenth International Conference on Permafrost, Salekhard, Yamal-Nenets Autonomous District, Russia, June 25–29. Editor K. M. Hinkel (Salekhard: The Northern Publisher), 73–78.

Dansgaard, W. (1964). Stable Isotopes in Precipitation. *Tellus* 16 (4), 436–468. doi:10.3402/tellusa.v16i4.8993

Delaney, A. J. (1987). *Preparation and Description of a Research Geophysical Borehole Site Containing Massive Ground Ice Near Fairbanks, Alaska. CRREL Special Report*. Hanover, NH: Cold Regions Research and Engineering Laboratory, 87–7.

Delaney, A. J., and Arcone, S. A. (1984). Field Dielectric Measurements of Frozen silt Using VHF Pulses. *Cold Regions Sci. Technology* 9, 29–37. doi:10.1016/0165-232X(84)90045-410.1016/0165-232x(84)90046-6

Dick, R. A. (1970). *Effects of Type of Cut, Delay and Explosive on Underground Blasting in Frozen Ground. U.S. Bureau of Mines Report of Investigations 7356.* Washington, DC: U.S. Department of Interior, Bureau of Mines.

Douglas, T. A., and Mellon, M. T. (2019). Sublimation of Terrestrial Permafrost and the Implications for Ice-Loss Processes on Mars. *Nat. Commun.* 10 (1), 1716–1719. doi:10.1038/s41467-019-09410-8

Douglas, T. A., Fortier, D., Shur, Y. L., Kanevskiy, M. Z., Guo, L., Cai, Y., et al. (2011). Biogeochemical and Geocryological Characteristics of Wedge and Thermokarst-Cave Ice in the CRREL Permafrost Tunnel, Alaska. *Permafrost Periglac. Process.* 22, 120–128. doi:10.1002/ppp.709

Douglas, T. A., Hiemstra, C. A., Anderson, J. E., Barbato, R. A., Bjella, K. L., Deeb, E. J., et al. (2021). Recent Degradation of Interior Alaska Permafrost Mapped with Ground Surveys, Geophysics, Deep Drilling, and Repeat Airborne LiDAR. *Cryosphere Discuss.* doi:10.5194/tc-2021-47

Elias, S. A., and Brigham-Grette, J. (2007). *GLACIATIONS | Late Pleistocene Events in Beringia*. Amsterdam, Netherlands; Boston Mass: Elsevier, 1057–1066. doi:10.1016/b0-44-452747-8/00132-0

Ferreira, T., and Rasband, W. S. (2012). *ImageJ User Guide — IJ 1.46*. Available at: http://rsbweb.nih.gov/ij/docs/guide/user-guide.pdf. (Accessed August 12, 2021).

Fortier, D., and Allard, M. (2004). Late Holocene Syngenetic Ice-Wedge Polygons Development, Bylot Island, Canadian Arctic Archipelago. *Can. J. Earth Sci.* 41 (8), 997–1012. doi:10.1139/e04-031

Fortier, D., Allard, M., and Shur, Y. (2007). Observation of Rapid Drainage System Development by thermal Erosion of Ice Wedges on Bylot Island, Canadian Arctic Archipelago. *Permafrost Periglac. Process.* 18 (3), 229–243. doi:10.1002/ppp.595

Fortier, D., Kanevskiy, M., and Shur, Y. (2008). "Genesis of Reticulate-Chaotic Cryostructure in Permafrost," in Proceedings of the Ninth International Conference on Permafrost, June 29 – July 3, 2008 Fairbanks, Alaska. Editors D. L. Kane and K. M. Hinkel (Fairbanks: Institute of Northern Engineering; University of Alaska Fairbanks) Vol. 1, 451–456.

Fortier, D., Strauss, J., Sliger, M., Calmels, F., Froese, D., and Shur, Y. (2018). "Pleistocene Yedoma in South-Western Yukon (Canada): a Remnant of Eastern Beringia?" in 5th European Conference on Permafrost – Book of Abstracts, Chamonix, France, 23 June – 1 July 2018, 637–638.

Fraser, T. A., and Burn, C. R. (1997). On the Nature and Origin of "Muck" Deposits in the Klondike Area, Yukon Territory. *Can. J. Earth Sci.* 34, 1333–1344. doi:10.1139/e17-106

French, H. M. (2018). *The Periglacial Environment*. 4th ed. Chichester, UK: John Wiley & Sons.

French, H., and Shur, Y. (2010). The Principles of Cryostratigraphy. *Earth-Science Rev.* 101, 190–206. doi:10.1016/j.earscirev.2010.04.002

Froese, D. G., Zazula, G. D., Westgate, J. A., Preece, S. J., Sanborn, P. T., Reyes, A. V., et al. (2009). The Klondike Goldfields and Pleistocene Environments of Beringia. *GSA Today* 19 (8), 4–10. doi:10.1130/gsatg54a.1

Gravis, G. F. (1969). *Slope Deposits in Yakutia*. Moscow: Nauka, 128 (in Russian).

Grosse, G., Harden, J., Turetsky, M., McGuire, A. D., Camill, P., Tarnocai, C., et al. (2011). Vulnerability of High-Latitude Soil Organic Carbon in North America to Disturbance. *J. Geophys. Res.* 116, G00K06. doi:10.1029/2010JG001507

Guthrie, R. D. (1990). *Frozen Fauna of the Mammoth Steppe: The story of Blue Babe*. Chicago: Univ. Chicago Press.

Hamilton, T. D. (1994). "Late Cenozoic Glaciation of Alaska," in *The Geology of Alaska. The Geology of North America*. Editors G. Plafker and H. C. Berg (Boulder, Colorado: Geological Society of America), G-1, 813–844.

Hamilton, T. D., Craig, J. L., and Sellmann, P. V. (1988). The Fox Permafrost Tunnel: A Late Quaternary Geologic Record in central Alaska. *Geol. Soc. America Bull.* 100, 948–969. doi:10.1130/0016-7606(1988)100<0948:tfptal>2.3.co;2

Holland, K. M., Porter, T. J., Froese, D. G., Kokelj, S. V., and Buchanan, C. A. (2020). Ice-Wedge Evidence of Holocene Winter Warming in the Canadian Arctic. *Geophys. Res. Lett.* 47, e2020GL087942. doi:10.1029/2020GL0879424712

Hopkins, D. M. (1963). Geology of the Imuruk Lake Area, Seward Peninsula, Alaska. *U.S. Geol. Surv. Bull.* 1141-c, 101.

Hopkins, D. M. (1982). "Aspects of the Paleogeography of Beringia during the Late Pleistocene," in *Paleoecology of Beringia*. Editors D. M. Hopkins, J. V. Mathews, C. E. Schweger, and S. B. Young (New York: Academic Press), 3–28. doi:10.1016/b978-0-12-355860-2.50008-9

Huang, S. L., Aughenbaugh, N. B., and Wu, M. C. (1986). Stability Study of CRREL Permafrost Tunnel. *J. Geotechnical Eng.* 112 (8), 777–790. doi:10.1061/(asce)0733-9410(1986)112:8(777)

Jensen, B. J. L., Reyes, A. V., Froese, D. G., and Stone, D. B. (2013). The Palisades Is a Key Reference Site for the Middle Pleistocene of Eastern Beringia: New Evidence from Paleomagnetics and Regional Tephrostratigraphy. *Quat. Sci. Rev.* 63, 91–108. doi:10.1016/j.quascirev.2012.11.035

Jensen, B. J. L., Evans, M. E., Froese, D. G., and Kravchinsky, V. A. (2016). 150,000 Years of Loess Accumulation in central Alaska. *Quat. Sci. Rev.* 135, 1–23. doi:10.1016/j.quascirev.2016.01.001

Johansen, N. I., Chalich, P. C., and Wellen, E. W. (1980). "Sublimation and Sublimation Control in the CRREL Tunnel," in Proceedings of the Second International Symposium on Ground Freezing, Trondheim, Norway, June 24-26 (Rotterdam; Boston: A.A. Balkema), 952–968.

Johansen, N. I., and Ryer, J. W. (1982). "Permafrost Creep Measurements in the CRREL Tunnel," in Proceedings of the Third International Symposium on Ground Freezing, Hanover, New Hampshire (Hanover, New Hampshire: U.S. Army CRREL), 61–63.

Jorgenson, T., Yoshikawa, K., Kanevskiy, M., Shur, Y., Romanovsky, V., Marchenko, S., et al. (2008). "Permafrost Characteristics of Alaska," in Proceedings of the 9th International Conference on Permafrost, Extended Abstracts, Fairbanks, June 29–July 3, 2008. Editors A. K. Kane, D. L. Kane, and K M. Hinkel (Fairbanks: Institute of Northern Engineering, University of Alaska Fairbanks), 121–122.

Jorgenson, M. T., Harden, J., Kanevskiy, M., O'Donnell, J., Wickland, K., Ewing, S., et al. (2013). Reorganization of Vegetation, Hydrology and Soil Carbon after Permafrost Degradation across Heterogeneous Boreal Landscapes. *Environ. Res. Lett.* 8 (3), 035017. doi:10.1088/1748-9326/8/3/035017

Jorgenson, M. T., Kanevskiy, M., and Shur, Y. (Dataset 2015a). *Horseshoe Lake Data*. Arctic data center. doi:10.18739/A2SK86

Jorgenson, M. T., Kanevskiy, M., and Shur, Y. (Dataset 2015b). *Creamer's Field Data*. Arctic data center. doi:10.18739/A22W61

Kanevskiy, M., Fortier, D., Shur, Y., Bray, M., and Jorgenson, T. (2008a). "Detailed Cryostratigraphic Studies of Syngenetic Permafrost in the Winze of the CRREL Permafrost Tunnel, Fox, Alaska," in Proceedings of the Ninth International Conference on Permafrost, Fairbanks, Alaska, June 29 – July 3, 2008. Editors D. L. Kane and K. M. Hinkel (Fairbanks: Institute of Northern Engineering, University of Alaska Fairbanks) Vol. 1, 889–894.

Kanevskiy, M., French, H., Shur, Y., Bjella, K. L., Bray, M. T., Collins, C. M., et al. (2008b). "Late-Pleistocene Syngenetic Permafrost in the CRREL Permafrost Tunnel, Fox, Alaska," in A Guidebook Prepared for Ninth International Conference on Permafrost, Fairbanks, Alaska, June 29-July 3, 2008, 22 pp.

Kanevskiy, M., Shur, Y., Fortier, D., Jorgenson, M. T., and Stephani, E. (2011). Cryostratigraphy of Late Pleistocene Syngenetic Permafrost (Yedoma) in Northern Alaska, Itkillik River Exposure. *Quat. Res.* 75, 584–596. doi:10.1016/j.yqres.2010.12.003

Kanevskiy, M., Shur, Y., Connor, B., Dillon, M., Stephani, E., and O'Donnell, J. (2012). "Study of the Ice-Rich Syngenetic Permafrost for Road Design (Interior Alaska)," in Proceedings of the Tenth International Conference on Permafrost, Salekhard, Russia. The Northern Publisher, Salekhard, Russia, June 25-29, 2012. International Contributions. Editor K. M. Hinkel, 191–196.

Kaplina, T. N. (1981). History of Permafrost Development in Late Cenozoic. In: G. I. Dubikov and V. V Baulin(eds) *History of Development of Permafrost in Eurasia*. Moscow, Nauka, 153–180. (in Russian).

Katasonov, E. M. (1954). Lithology of Frozen Quaternary Deposits (Cryolithology) of the Yana Coastal Plain. PhD Thesis: Obruchev Permafrost Institute: Moscow, PNIIIS, 176. (in Russian).

Kennedy, K. E., Froese, D. G., Zazula, G. D., and Lauriol, B. (2010). Last Glacial Maximum Age for the Northwest Laurentide Maximum from the Eagle River Spillway and delta Complex, Northern Yukon. *Quat. Sci. Rev.* 29 (9), 1288–1300. doi:10.1016/j.quascirev.2010.02.015

Kotler, E., and Burn, C. R. (2000). Cryostratigraphy of the Klondike "muck" Deposits, West-central Yukon Territory. *Can. J. Earth Sci.* 37, 849–861. doi:10.1139/e00-013

Kreig, R. A., and Reger, R. D. (1982). Air-photo Analysis and Summary of Landform Soil Properties along the Route of the Trans-Alaska Pipeline System. *DGGS, College, Alaska Geologic Rep.* 66. doi:10.14509/426

Kunitskiy, V. V. (1989). *Cryolithology of the Low Lena River*. Yakutsk: Permafrost institute, Academy of Sciences of the USSR. (in Russian).

Lacelle, D., and Vasil'chuk, Y. K. (2013). Recent Progress (2007-2012) in Permafrost Isotope Geochemistry. *Permafrost Periglac. Process.* 24 (2), 138–145. doi:10.1002/ppp.1768

Lachniet, M. S., Lawson, D. E., and Sloat, A. R. (2012). Revised 14C Dating of Ice Wedge Growth in interior Alaska (USA) to MIS 2 Reveals Cold Paleoclimate and Carbon Recycling in Ancient Permafrost Terrain. *Quat. Res.* 78, 217–225. doi:10.1016/j.yqres.2012.05.007

Lenz, J., Jones, B. M., Wetterich, S., Tjallingii, R., Fritz, M., Arp, C. D., et al. (2016). Impacts of Shore Expansion and Catchment Characteristics on Lacustrine Thermokarst Records in Permafrost Lowlands, Alaska Arctic Coastal Plain. *Arktos* 2, 25. doi:10.1007/s41063-016-0025-0

Lewkowicz, A. G. (1994). Ice-wedge Rejuvenation, Fosheim peninsula, Ellesmere Island, Canada. *Permafrost Periglac. Process.* 5, 251–268. doi:10.1002/ppp.3430050405

Linell, K. A., and Lobacz, E. F. (1978). "Some Experiences with Tunnel Entrances in Permafrost," in Proceedings of the Third International Permafrost Conference, Edmonton, Alberta, Canada, July 10-13, 1978 (Ottawa, Canada: National Research Council of Canada), 813–819.

Long, A., and Péwé, T. L. (1996). Radiocarbon Dating by High-Sensitivity Liquid Scintillation Counting of wood from the Fox Permafrost Tunnel Near Fairbanks, Alaska. *Permafrost Periglac. Process.* 7 (3), 281–285. doi:10.1002/(sici)1099-1530(199609)7:3<281:aid-ppp222>3.0.co;2-y

Mackay, J. R. (1997). A Full-Scale Field experiment (1978-1995) on the Growth of Permafrost by Means of lake Drainage, Western Arctic Coast: a Discussion of the Method and Some Results. *Can. J. Earth Sci.* 34, 17–33. doi:10.1139/e17-002

Mackay, J. R. (2000). Thermally Induced Movements in Ice-Wedge Polygons, Western Arctic Coast: A Long-Term Study. *Geographie Physique et Quaternaire* 54 (1), 41–68.

Matheus, P., Begét, J., Mason, O., and Gelvin-Reymiller, C. (2003). Late Pliocene to Late Pleistocene Environments Preserved at the Palisades Site, central Yukon River, Alaska. *Quat. Res.* 60, 33–43. doi:10.1016/s0033-5894(03)00091-7

Meyer, H., Yoshikawa, K., Schirrmeister, L., and Andreev, A. (2008). "The Vault Creek Tunnel (Fairbanks Region, Alaska) – A Late Quaternary Palaeoenvironmental Permafrost Record," in Proceedings of the Ninth International Conference on Permafrost, Fairbanks, Alaska, June 29 – July 3, 2008. Editors D. L. Kane and K. M. Hinkel (Fairbanks: Institute of Northern Engineering; University of Alaska Fairbanks) Vol. 2, 1191–1196.

Muhs, D., Ager, T. A., Bettis, E. A., III, McGeehin, J., Been, J. M., Begét, J. E., et al. (2003). Stratigraphy and Palaeoclimatic Significance of Late Quaternary Loess-Palaeosol Sequences of the Last Interglacial-Glacial Cycle in central Alaska. *Quat. Sci. Rev.* 22, 1947–1986. doi:10.1016/s0277-3791(03)00167-7

Murton, J. B. (2013). "8.14 Ground Ice and Cryostratigraphy," in *Treatise on Geomorphology Glacial and Periglacial Geomorphology, Schoder, J. F. (editor-in-Chief*. Editors R. Giardino and J. Harboor (San Diego: Academic Press), 8, 173–201.

Newberry, R. J., Bundtzen, T. K., Clautice, K. H., Combellick, R. A., Douglas, T., Laird, G. M., et al. (1996). *Preliminary Geologic Map of the Fairbanks Mining District*. Alaska: Alaska Division of Geological & Geophysical Surveys Public Data File, 96–16. doi:10.14509/1740

Nossov, D. R., Torre Jorgenson, M., Kielland, K., and Kanevskiy, M. Z. (2013). Edaphic and Microclimatic Controls over Permafrost Response to Fire in interior Alaska. *Environ. Res. Lett.* 8 (3), 035013. doi:10.1088/1748-9326/8/3/035013

Opel, T., Murton, J. B., Wetterich, S., Meyer, H., Ashastina, K., Günther, F., et al. (2019). Past Climate and Continentality Inferred from Ice Wedges at Batagay Megaslump in the Northern Hemisphere's Most continental Region, Yana Highlands, interior Yakutia. *Clim. Past* 15 (4), 1443–1461. doi:10.5194/cp-15-1443-2019

Payne, R., Blackford, J., and van der Plicht, J. (2008). Using Cryptotephras to Extend Regional Tephrochronologies: An Example from Southeast Alaska and Implications for Hazard Assessment. *Quat. Res.* 69, 42–55. doi:10.1016/j.yqres.2007.10.007

Pettibone, H. C. (1973). "Stability of an Underground Room in Frozen Gravel," in North American Contribution to Permafrost: Second International Conference, Yakutsk, U.S.S.R, 13-28 July 1973 (Washington DC: National Academy of Sciences), 699–706.

Péwé, T. L. (1954). *Effect of Permafrost on Cultivated fields, Fairbanks Area, Alaska*. Washington DC: US Government Printing Office.

Péwé, T. L. (1955). Origin of the upland silt Near Fairbanks, Alaska. *Geol. Soc. America Bull.* 66, 699–724. doi:10.1130/0016-7606(1955)66[699:ootusn]2.0.co;2

Péwé, T. L. (1975a). *Quaternary Geology of Alaska*. U.S. Geological Survey Professional Paper 835. Washington DC: Washington, United States Government Printing Office.

Péwé, T. L. (1975b). *Quaternary Stratigraphic Nomenclature in Unglaciated Central Alaska*. Geological Survey Professional Paper 862. Washington DC: United States Government Printing Office.

Péwé, T. L., Bell, J. W., Forbes, R. B., and Weber, F. R. (1976). Geologic Map of the Fairbanks D-2 SW Quadrangle, Alaska: U.S. Geological Survey Miscellaneous Investigations Series Map 829-A, 1 Sheet. *scale* 1, 24000.

Popov, A. I. (1953). Lithogenesis of Alluvial Lowlands in the Cold Climatic Conditions. *Izvestiya (Transactions) USSR Acad. Sci. Geogr.* 2 (in Russian).

Porter, T. J., Froese, D. G., Feakins, S. J., Bindeman, I. N., Mahony, M. E., Pautler, B. G., et al. (2016). Multiple Water Isotope Proxy Reconstruction of Extremely Low Last Glacial Temperatures in Eastern Beringia (Western Arctic). *Quat. Sci. Rev.* 137, 113–125. doi:10.1016/j.quascirev.2016.02.006

Porter, T. J., and Opel, T. (2020). Recent Advances in Paleoclimatological Studies of Arctic Wedge- and Pore-ice Stable-water Isotope Records. *Permafrost and Periglac Process* 31 (3), 429–441. doi:10.1002/ppp.2052

Pyne-O'Donnell, S. D. F., Hughes, P. D. M., Froese, D. G., Jensen, B. J. L., Kuehn, S. C., Mallon, G., et al. (2012). High-precision Ultra-distal Holocene Tephrochronology in North America. *Quat. Sci. Rev.* 52, 6–11. doi:10.1016/j.quascirev.2012.07.024

Reimer, P. J., Austin, W. E. N., Bard, E., Bayliss, A., Blackwell, P. G., Bronk Ramsey, C., et al. (2020). The IntCal20 Northern Hemisphere Radiocarbon Age Calibration Curve (0-55 Cal kBP). *Radiocarbon* 62, 725–757. doi:10.1017/rdc.2020.41

Reyes, A. V., Jensen, B. J. L., Zazula, G. D., Ager, T. A., Kuzmina, S., La Farge, C., et al. (2010a). A Late-Middle Pleistocene (Marine Isotope Stage 6) Vegetated Surface Buried by Old Crow Tephra at the Palisades, interior Alaska. *Quat. Sci. Rev.* 29, 801–811. doi:10.1016/j.quascirev.2009.12.003

Reyes, A. V., Froese, D. G., and Jensen, B. J. L. (2010b). Permafrost Response to Last Interglacial Warming: Field Evidence from Non-glaciated Yukon and Alaska. *Quat. Sci. Rev.* 29, 3256–3274. doi:10.1016/j.quascirev.2010.07.013

Reyes, A. V., Zazula, G. D., Kuzmina, S., Ager, T. A., and Froese, D. G. (2011). Identification of Last Interglacial Deposits in Eastern Beringia: a Cautionary Note from the Palisades, interior Alaska. *J. Quat. Sci.* 26 (3), 345–352. doi:10.1002/jqs.1464

Romanovskii, N. N. (1977). in *Formirovanie Poligonal'no-Zhil'nykh Struktur [Formation of Polygonal-Wedge Structures]*. Editor K. A. Kondratieva (Novosibirsk: Nauka), 215. (in Russian).

Romanovskii, N., Hubberten, H.-W., Gavrilov, A. V., Tumskoy, V. E., and Kholodov, A. L. (2004). Permafrost of the East Siberian Arctic Shelf and Coastal Lowlands. *Quat. Sci. Rev.* 23, 1359–1369. doi:10.1016/j.quascirev.2003.12.014

Schirrmeister, L., Meyer, H., Wetterich, S., Siegert, C., Kunitsky, V. V., Grosse, G., et al. (2008). "The Yedoma Suite of the Northeastern Siberian Shelf Region: Characteristics and Concept of Formation,". Proceedings of the Ninth International Conference on Permafrost. June 29 – July 3, 2008. Fairbanks, Alaska. Editors D. L. Kane and K. M. Hinkel (Fairbanks: Institute of Northern Engineering; University of Alaska Fairbanks), 2, 1595–1600.

Schirrmeister, L., Kunitsky, V., Grosse, G., Wetterich, S., Meyer, H., Schwamborn, G., et al. (2011). Sedimentary Characteristics and Origin of the Late Pleistocene Ice Complex on North-East Siberian Arctic Coastal Lowlands and Islands - a Review. *Quat. Int.* 241, 3–25. doi:10.1016/j.quaint.2010.04.004

Schirrmeister, L., Froese, D., Tumskoy, V., Grosse, G., and Wetterich, S. (2013). "PERMAFROST and PERIGLACIAL FEATURES | Yedoma: Late Pleistocene Ice-Rich Syngenetic Permafrost of Beringia," in *Encyclopedia of Quaternary Science*. Second Edition, 542–552. doi:10.1016/b978-0-444-53643-3.00106-0

Schirrmeister, L., Meyer, H., Andreev, A., Wetterich, S., Kienast, F., Bobrov, A., et al. (2016). Late Quaternary Paleoenvironmental Records from the Chatanika River valley Near Fairbanks (Alaska). *Quat. Sci. Rev.* 147, 259–278. doi:10.1016/j.quascirev.2016.02.009

Schirrmeister, L., Dietze, E., Matthes, H., Grosse, G., Strauss, J., Laboor, S., et al. (2020). The Genesis of Yedoma Ice Complex Permafrost - Grain-Size Endmember Modeling Analysis from Siberia and Alaska. *E&G Quat. Sci. J.* 69, 33–53. doi:10.5194/egqsj-69-33-2020

Schuur, E. A. G., Mcguire, A. D., Schädel, C., Grosse, G., Harden, J. W., Hayes, D. J., et al. (2015). Climate Change and the Permafrost Carbon Feedback. *Nature* 520, 171–179. doi:10.1038/nature14338

Sellmann, P. V. (1967). *Geology of the USA CRREL Permafrost Tunnel, Fairbanks, Alaska*. Technical Report 199. Hanover, New Hampshire: U.S. Army Cold Regions Research & Engineering Laboratory.

Sellmann, P. V. (1972). *Geology and Properties of Materials Exposed in the USA CRREL Permafrost Tunnel, Fairbanks, Alaska*. Hanover, New Hampshire: U.S. Army Cold Regions Research & Engineering Laboratory, Special Report 177, 16.

Sher, A. V. (1997). "A Brief Overview of the Late Cenozoic History of the Western Beringian Lowlands," in Proceedings of a joint Russian-American Workshop, Fairbanks, Alaska, June 1991. *Terrestrial Paleoenvironmental Studies in Beringia*. Editors M. E. Edwards, A. V. Sher, and R. D. Guthrie (Fairbanks: Alaska Quaternary Center), 3–7.

Sher, A. V., Kuzmina, S. A., Kuznetsova, T. V., and Sulerzhitsky, L. D. (2005). New Insights into the Weichselian Environment and Climate of the East Siberian Arctic, Derived from Fossil Insects, Plants, and Mammals. *Quat. Sci. Rev.* 24, 533–569. doi:10.1016/j.quascirev.2004.09.007

Shumskii, P. A. (1959). "Ground (Subsurface) Ice." in *Principles of Geocryology, Part I, General Geocryology* (Moscow: Academy of Sciences of the USSR), 274–327. Chapter IX (in Russian) (English translation: C. de Leuchtenberg, 1964, National Research Council of Canada, Ottawa, Technical Translation 1130, 118 pp.).

Shur, Y. L. (1988). "The Upper Horizon of Permafrost Soils," in Proceedings of the Fifth International Conference on Permafrost, Norway (Trondheim: Tapir Publishers), 867–871.

Shur, Y., and Jorgenson, M. T. (1998). "Cryostructure Development on the Floodplain of Colville River Delta, Northern Alaska," in Proceedings of 7th International Conference on, Permafrost, Yellowknife, Canada, 993–999.

Shur, Y., French, H. M., Bray, M. T., and Anderson, D. A. (2004). Syngenetic Permafrost Growth: Cryostratigraphic Observations from the CRREL Tunnel Near Fairbanks, Alaska. *Permafrost Periglac. Process.* 15 (4), 339–347. doi:10.1002/ppp.486

Shur, Y., Jorgenson, M. T., and Kanevskiy, M. Z. (2011). "Permafrost," in *Encyclopedia of Earth Sciences Series, Encyclopedia of Snow, Ice and Glaciers*. Editors V. P. Singh, P. Singh, and U. K. Haritashya, 841–848. doi:10.1007/978-90-481-2642-2

Shur, Y., Kanevskiy, M., Jorgenson, T., Dillon, M., Stephani, E., and Bray, M. (2012). "Permafrost Degradation and Thaw Settlement under Lakes in Yedoma Environment," in Proceedings of the 10th International Conference on Permafrost, Salekhard, Russia, June 25–29, 2012. International Contributions. Editor K. M. Hinkel (Salekhard, Russia: The Northern Publisher), 383–388.

Shur, Y., and Kanevskiy, M. (Dataset: 2015). *Mapping, New CRREL Tunnel.* Arctic Data Center. doi:10.18739/A2J61K

Shur, Y., Kanevskiy, M., Bigelow, N. H., and Beget, J. (2015). Dataset: Forty-Thousand Years of Yedoma: An Investigation into the Spatial Heterogeneity and Paleo-History of Organic-Rich Permafrost in Alaska. *urn:node:ARCTIC*. doi:10.18739/A2SP6G

Shur, Y., Jones, B. M., Kanevskiy, M., Jorgenson, T., Jones, M. K. W., Fortier, D., et al. (2021a). Fluvio-thermal Erosion and Thermal Denudation in the Yedoma Region of Northern Alaska: Revisiting the Itkillik River Exposure. *Permafrost and Periglac Process* 32, 277–298. doi:10.1002/ppp.2105

Shur, Y., Fortier, D., Jorgenson, T., Kanevskiy, M., Schirrmeister, L., Strauss, J., et al. (2021b). Yedoma Permafrost Genesis: Over 150 Years of Mystery and Controversy. *Front. Earth Sci.*

Kanevskiy, M., Shur, Y., Jorgenson, M. T., Ping, C.-L., Michaelson, G. J., Fortier, D., et al. (2013). Ground Ice in the Upper Permafrost of the Beaufort Sea Coast of Alaska. *Cold Regions Sci. Technology* 85, 56–70. doi:10.1016/j.coldregions.2012.08.002

Kanevskiy, M., Jorgenson, T., Shur, Y., O'Donnell, J. A., Harden, J. W., Zhuang, Q., et al. (2014). Cryostratigraphy and Permafrost Evolution in the Lacustrine Lowlands of West-Central Alaska. *Permafrost Periglac. Process.* 25 (1), 14–34. doi:10.1002/ppp.1800

Kanevskiy, M., Shur, Y., Strauss, J., Jorgenson, T., Fortier, D., Stephani, E., et al. (2016). Patterns and Rates of Riverbank Erosion Involving Ice-Rich Permafrost (Yedoma) in Northern Alaska. *Geomorphology* 253, 370–384. doi:10.1016/j.geomorph.2015.10.023

Sloat, A. (2014). Modern to Late Pleistocene Stable Isotope Climatology of Alaska. PhD thesis. UNLV Theses/Dissertations Las Vegas: University of Nevada.

Strauss, J., Schirrmeister, L., Grosse, G., Fortier, D., Hugelius, G., Knoblauch, C., et al. (2017). Deep Yedoma Permafrost: A Synthesis of Depositional

Characteristics and Carbon Vulnerability. *Earth-Science Rev.* 172, 75–86. doi:10.1016/j.earscirev.2017.07.007
Strauss, J., Laboor, S., Schirrmeister, L., Fedorov, A. N., Fortier, D., Froese, D., et al. (2021). Circum-Arctic Map of the Yedoma Permafrost Domain. *Front. Earth Sci.* 9, 758360. doi:10.3389/feart.2021.758360
Swinzow, G. K. (1970). *Permafrost Tunneling by a Continuous Mechanical Method*. CRREL Technical Report 221. Hanover, NH: Cold Regions Research and Engineering Laboratory.
Thompson, E. G., and Sayles, F. H. (1972). *In Situ* creep Analysis of Room in Frozen Soil. *J. Soil Mech. Found. Div.* 9202 (SM9), 899–915. doi:10.1061/jsfeaq.0001780
Tomirdiaro, S. V. (1980). *Loess-ice Formation of Eastern Siberia in the Late Pleistocene and Holocene*. Moscow: Nauka. (in Russian).
Vasil'chuk, Y. K., and Murton, J. B. (2016). Stable Isotope Geochemistry of Massive Ice. *Geogr. Environ. Sustainability* 03 (09), 4–23.
Watanabe, O. (1969). On the Structure of Ground Ice in the USA CREEL Permafrost Tunnel, Fairbanks, Alaska. *J. Jpn. Soc. Snow Ice* 31 (3), 53–62. doi:10.5331/seppyo.31.53
Weerdenburg, P. C., and Morgenstern, N. R. (1983). "Underground Cavities in Ice-Rich Frozen Ground," in Permafrost: Fourth International Conference Proceedings, Fairbanks, Alaska, July 17–22, 1983 (Washington DC: National Academy Press), 1384–1389.
Wetterich, S., Meyer, H., Fritz, M., Mollenhauer, G., Rethemeyer, J., Kizyakov, A., et al. (2021). Northeast Siberian Permafrost Ice-Wedge Stable Isotopes Depict Pronounced Last Glacial Maximum Winter Cooling. *Geophys. Res. Lett.* 48, e2020GL092087. doi:10.1029/2020GL092087
Williams, J. R. (1962). *Geologic Reconnaissance of the Yukon Flats District, Alaska*. Washington, DC: U.S. Geological Survey Bulletin 111-H, 290–311.
Wooller, M. J., Zazula, G. D., Edwards, M., Froese, D. G., Boone, R. D., Parker, C., et al. (2007). Stable Carbon Isotope Compositions of Eastern Beringian Grasses and Sedges: Investigating Their Potential as Paleoenvironmental Indicators. *Arctic, Antarctic, Alpine Res.* 39 (2), 318–331. doi:10.1657/1523-0430(2007)39[318:scicoe]2.0.co;2
Wooller, M. J., Zazula, G. D., Blinnikov, M., Gaglioti, B. V., Bigelow, N. H., Sanborn, P., et al. (2011). The Detailed Palaeoecology of a Mid-wisconsinan Interstadial (Ca. 32 000 14 C a BP) Vegetation Surface from interior Alaska. *J. Quat. Sci.* 26, 746–756. doi:10.1002/jqs.1497
Yurtsev, B. A. (1981). *Relic Steppe Complexes of North-East Asia*. Novosibirsk: Nauka. (in Russian).
Zaikanov, V. G. (1991). "Formation of Structure and Properties of Floodplain Deposits of Large Rivers of Northern Yakutia," in *The Upper Horizon of Permafrost*. Editors P. Melnikov and Y. Shur (Moscow: Nauka), 31–47. (in Russian).
Zazula, G. D., Froese, D. G., Elias, S. A., Kuzmina, S., and Mathewes, R. W. (2007). Arctic Ground Squirrels of the mammoth-steppe: Paleoecology of Late Pleistocene Middens (~24000-29450 14C Yr BP), Yukon Territory, Canada. *Quat. Sci. Rev.* 26, 979–1003. doi:10.1016/j.quascirev.2006.12.006
Zhestkova, T. N., Shvetsov, P. F., and Shur, Y. L. (1982). "Yedoma, Climatic Formation," in *XI Congress of International Union for Quaternary Research*. Moscow: Abstracts, Vol. II, 389.
Zhestkova, T. N., Shvetsov, P. F., and Shur, Y. L. (1986). "On Genesis of Yedoma," in *Geocryology Studies*. Editor E. D. Ershov (Moscow: Moscow State University), 108–113. (in Russian).

Conflict of Interest: The authors declare that the research was conducted in the absence of any commercial or financial relationships that could be construed as a potential conflict of interest.

Publisher's Note: All claims expressed in this article are solely those of the authors and do not necessarily represent those of their affiliated organizations, or those of the publisher, the editors and the reviewers. Any product that may be evaluated in this article, or claim that may be made by its manufacturer, is not guaranteed or endorsed by the publisher.

frontiers in Earth Science

ORIGINAL RESEARCH
published: 09 March 2022
doi: 10.3389/feart.2022.741932

Heavy and Light Mineral Association of Late Quaternary Permafrost Deposits in Northeastern Siberia

L. Schirrmeister[1], S. Wetterich[1], G. Schwamborn[2], H. Matthes[3], G. Grosse[1], I. Klimova[4], V. V. Kunitsky[4] and C. Siegert[1]*

[1]*Alfred Wegener Institute, Permafrost Research, Helmholtz Centre for Polar and Marine Research, Potsdam, Germany,* [2]*Eurasia Institute of Earth Sciences, Istanbul Technical University, Istanbul, Turkey,* [3]*Alfred Wegener Institute, Atmospheric Physics, Helmholtz Centre for Polar and Marine Research, Potsdam, Germany,* [4]*Melnikov Permafrost Institute, Yakutsk, Russia*

We studied heavy and light mineral associations from two grain-size fractions (63–125 µm, 125–250 µm) from 18 permafrost sites in the northern Siberian Arctic in order to differentiate local versus regional source areas of permafrost aggradation on the late Quaternary time scale. The stratigraphic context of the studied profiles spans about 200 ka covering the Marine Isotope Stage (MIS) 7 to MIS 1. Heavy and light mineral grains are mostly angular, subangular or slightly rounded in the studied permafrost sediments. Only grains from sediments with significantly longer transport distances show higher degrees of rounding. Differences in the varying heavy and light mineral associations represent varying sediment sources, frost weathering processes, transport mechanisms, and post-sedimentary soil formation processes of the deposits of distinct cryostratigraphic units. We summarized the results of 1141 microscopic mineral analyses of 486 samples in mean values for the respective cryostratigraphic units. We compared the mineral associations of all 18 sites along the Laptev Sea coast, in the Lena Delta, and on the New Siberian Archipelago to each other and used analysis of variance and cluster analysis to characterize the differences and similarities among mineral associations. The mineral associations of distinct cryostratigraphic units within several studied profiles differ significantly, while others do not. Significant differences between sites as well as between single cryostratigraphic units at an individual site exist in mineral associations, heavy mineral contents, and mineral coefficients. Thus, each study site shows individual, location-specific mineral association. The mineral records originate from multiple locations covering a large spatial range and show that ratios of heavy and light mineral loads remained rather stable over time, including glacial and interglacial periods. This suggests mostly local sediment sources and highlights the importance of sediment reworking under periglacial regimes through time, including for example the formation of MIS 1 thermokarst and thermo-erosional deposits based on remobilized MIS 3 and 2 Yedoma Ice Complex deposits. Based on the diverse mineralogical results our study supports the viewpoint that Yedoma Ice Complex deposits are mainly results of local and polygenetic formations (including local aeolian relocation) superimposed by cryogenic weathering and varying climate conditions rather than exclusive long distance aeolian transport of loess, which would have highly homogenized the deposits across large regions.

Keywords: mineral content, permafrost deposits, Quaternary, Yedoma, northeastern Siberia, terrestrial Arctic

OPEN ACCESS

Edited by:
Alexandra Veremeeva, Institute of Physical-Chemical and Biological Problems in Soil Science (RAS), Russia

Reviewed by:
Barbara Woronko, University of Warsaw, Poland
Denis Shmelev, Lomonosov Moscow State University, Russia

****Correspondence:***
L. Schirrmeister
lutz.schirrmeister@awi.de

Specialty section:
This article was submitted to Cryospheric Sciences, a section of the journal Frontiers in Earth Science

Received: *15 July 2021*
Accepted: *14 February 2022*
Published: *09 March 2022*

Citation:
Schirrmeister L, Wetterich S, Schwamborn G, Matthes H, Grosse G, Klimova I, Kunitsky VV and Siegert C (2022) Heavy and Light Mineral Association of Late Quaternary Permafrost Deposits in Northeastern Siberia. Front. Earth Sci. 10:741932. doi: 10.3389/feart.2022.741932

INTRODUCTION

Periglacial landscapes are widespread in northern high latitudes and are affected by specific cold-region physical weathering, sediment production, transport and deposition (Murton, 2021). Understanding periglacial deposition and associated landscape and permafrost dynamics on long and short time-scales is important for the interpretation of currently ongoing rapid changes in permafrost regions. In particular, changes in air temperatures and precipitation regimes (Box et al., 2019), warming and thawing of permafrost (Biskaborn et al., 2019), and rapid hydrological and geomorphological change (Nitzbon et al., 2020) do all affect cryogenic weathering, sediment transport, and deposition processes. While the cryostratigraphy of permafrost deposits (French & Shur, 2010), and cryolithology (Popov, 1953; Katasonov, 1955; Popov, 1967) have been used for decades to decipher indicators of past and modern periglacial landscape changes, the analysis of mineral associations is still rarely applied for the investigation of sedimentary dynamics of periglacial landscapes and the role of cryogenic weathering (Konishchev and Rogov, 1993).

However, heavy and light mineral associations of sediments are widely used in present-day non-permafrost environments to reconstruct source (provenance) areas and their changes and to identify modifications of sediments after their deposition (e.g., Morton and Hallsworth, 1999; Woronko et al., 2013; Pisarska-Jamroży et al., 2015). Therefore, identifying linkages of mineral associations in sediments to local bedrock, fluvial sources, or far-ranging sources for, e.g., the potential aeolian transport are useful to shed light on permafrost formation and landscape changes in the late Quaternary past.

The origin and genesis of periglacial deposits such as late Pleistocene Yedoma Ice Complex that has been formed during Marine Isotope Stage (MIS) 3 to MIS 2 have been under discussion for decades (for overview see Astakhov, 2013; Murton et al., 2015; Schirrmeister et al., 2013). To foster the understanding of permafrost aggradation and degradation on late Quaternary timescale, we conducted comprehensive paleo-environmental and paleo-landscape reconstructions using the permafrost deposits as archives for a total of 20 study sites in the framework of joint Russian-German research projects in the northeast Siberian Arctic since 1998. The main research foci for the fieldwork were paleoecology, sedimentology, stable water and carbon isotope geochemistry, geophysics, biogeochemistry, and geochronology. Site-specific information and resulting publications are summarized in **Supplementary Table S1**. In the present paper, we report on the heavy and light mineral associations from 18 study sites and discuss their use for reconstructing the sources of permafrost deposits. Grain-size data from most of these sites are available in Schirrmeister et al. (2002b); Schirrmeister et al. (2003a); Schirrmeister et al. (2008); Schirrmeister et al. (2010); Schirrmeister et al. (2011a); Schirrmeister et al. (2011b); Schirrmeister et al. (2013); Schirrmeister et al. (2020).

Our approach is based on the mineralogical composition of periglacial deposits that is affected by the respective source material (bed rocks or older sediments), the local periglacial settings during deposition in, e.g., floodplains, polygonal ponds, thermokarst lakes and at the foot of slopes, and the influence of frost weathering and soil formation after deposition.

Beyond Yedoma Ice Complex, we investigated its stratigraphic context below and above as well as deposits in thermokarst basins and thermo-erosional valleys and further regionally exposed deposits. Therefore, a wide spectrum of middle and late Quaternary periglacial deposition in Northeast Siberia has been comprehensively captured. To disentangle different source rocks and areas, transport pathways, final deposition and freezing, and post-sedimentary processes, we used the associations of heavy and light minerals in fine (63–125 μm) and coarse (125–250 μm) grain-size fractions as indicators. Fine sand heavy mineral associations of the Laptev Sea margin have been studied already elsewhere and can be used for comparison (Peregovich et al., 1999; Schwamborn et al., 2002; Siegert et al., 2002). With the present study we aim 1) to differentiate mineralogical properties of permafrost deposits from various sites, 2) to characterize the mineralogical variability of different cryostratigraphic units at distinct sites over time, and 3) to detect post-sedimentary changes in mineral compositions. Our study sheds light on late Quaternary periglacial depositional processes and their variations over time and contributes to the understanding of permafrost formation in Northeast Siberia.

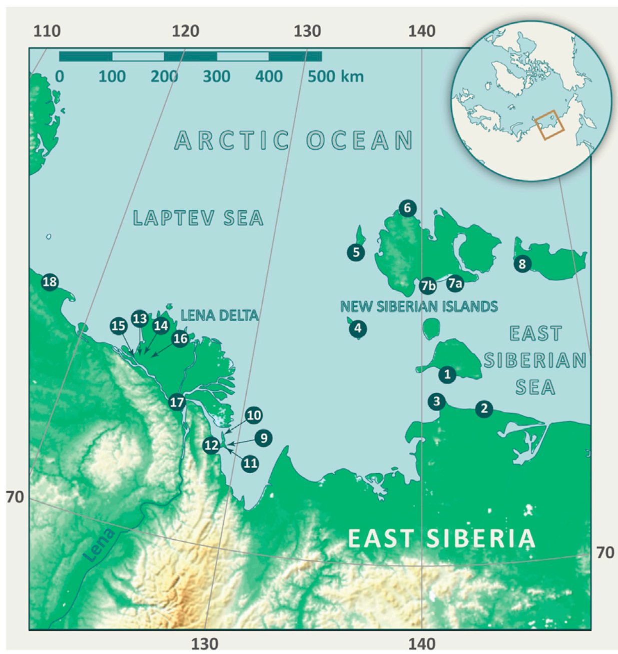

FIGURE 1 | Position of the study region in the Laptev Sea area and the positions of the study sites. 1—Bol'shoy Lyakhovsky Island; 2—Oyogos Yar coast; 3—Cape Syatoy Nos; 4—Stolbovoy Island; 5—Bel'kovsky Island; 6—Cape Anisii, Kotel'ny Island; 7—Bunge Land (a—higher terrace, b—lower terrace); 8—Novaya Sibir' Island. Bykhovsky Peninsula: 9—Mamontovy Khayata; 10—Bykovsky North; 11—Ivashkina Lagoon; 12—Khorogor Valley. Lena Delta: 13—eastern Ebe Basyn Island; 14—Turakh Island; 15—Nagym, southern Ebe Basyn Island; 16—Khardang Island; 17—Kurungnakh Island; 18—Cape Mamontov Klyk (maps compiled by S. Laboor, AWI Potsdam).

TABLE 1 | The regional Quaternary stratigraphic schemes and the corresponding Marine Isotope Stage (MIS; Lisiecki and Raymo, 2005) used in this work according to Andreev et al. (2004, 2009), Wetterich et al. (2019, 2021) and Zimmermann et al. (2017) and references cited therein.

MIS ages (and periods) [kyr]	Dated age ranges [kyr]	Dating method	Siberian nomenclature
0 to 11.7 (MIS 1)	c. 0 to 10.1	^{14}C	Holocene (thermokarst, thermo-erosional, lagoon, and modern cover deposits)
11.7 to 29 (MIS 2)	c. 22.4 to 29.4	^{14}C	Sartan Yedoma Ice Complex
29 to 57 (MIS 3)	c. 29.0 to 62.8	^{14}C	Molotkov (Kargin) Yedoma Ice Complex
57 to 71 (MIS 4)	c. 57 ± 10 to 77 ± 14	IRSL	Zyryan (Ermakovo)
71 to 115 (MIS 5a-d)	c. 89 ± 5 to 126 ± 16	Th/U	Buchchagy Ice Complex
71 to 115 (MIS 5a-d)	c. 99 ± 15 to 112.5 ± 9.6	IRSL	Kuchchugui stratum
115 to 130 (MIS 5e)	c. 99 ± 15 to 102 ± 9.7	IRSL	Krest Yuryakh (Kazantsevo)
	c. 96 ± 26 to 114 ± 28	TL	
130 to 191 (MIS 6)	c. 134 ± 22	IRSL	Zimov'e stratum
191 to 243 (MIS 7)	c. 178 ± 14 to 221 ± 24	Th/U	Yukagir (Tazov) Ice Complex

Radiocarbon ages (^{14}C) are shown as uncalibrated ages. IRSL—Infrared-stimulated luminescence dating, Th/U—Thorium/Uranium radiometric disequilibria dating, TL—thermo-luminescence dating.

STUDY REGION

The study region covers the coastal lowlands of the western and the eastern Laptev Sea, the Lena Delta, the coasts of the Dmitry Laptev Strait connecting the Laptev and the East Siberian seas, and several coastal sites of the New Siberian Archipelago (**Figure 1**; **Supplementary Figure S1**). Small mountain ridges of 200–500 m height such as the Pronchishchev Ridge, the Chekanovky Ridge and the Kharaulakh Range frame the coastal lowlands in the western part of the study region (study sites 9–18; **Figure 1**). In the eastern part of the study region (study sites 1–8; **Figure 1**), only isolated basement elevations of granite domes exist such as those on Bol'shoy Lyakhovsky Island and in the hinterland of the Oyogos Yar coast, while on Stolbovoy, Belkovsky, and Kotel'ny islands denudated fold ranges are present. The small mountains and heights are often surrounded by multilevel cryopalanation terraces reaching altitudes between 20 and 150 m above sea level (asl). Many of the sites are located at the distal lowland ends of hillslope foreland plains such as in Bykovsky Peninsula.

The stratigraphic classification of the middle Pleistocene to the Holocene in the East Siberian Arctic lowlands is based mostly on palynological (e.g., Gitermann et al., 1982; Kaplina and Lozhkin, 1984), palaeozoological (e.g., Sher, 1971; Vangenheim, 1977), and cryolithological (e.g., Kaplina, 1981; Kaplina, 1989; Tumskoy, 2012) and geochronological data (e.g., Schirrmeister et al., 2002a; Schirrmeister et al., 2003a; Schirrmeister et al., 2008; Schirrmeister et al., 2011b; Andreev et al., 2004; Andreev et al., 2009; Wetterich et al., 2009; Wetterich et al., 2011; Wetterich et al., 2014; Wetterich et al., 2016; Wetterich et al., 2019; Wetterich et al., 2020; Wetterich et al., 2021; Zimmermann et al., 2017). The study of local profiles resulted in numerous separate stratigraphic schemes, often with individual terms for single suites, layers, or horizons, which were correlated for further chronostratigraphic classification. However, for some periods, the stratotype, the palaeoenvironmental interpretation, and the absolute age, such as of the Kargin stratum, are still under discussion (Astakhov and Mangerud, 2005; Astakhov, 2013). Because of the inconsistent regional Quaternary stratigraphy of northern East Siberia, we present the Russian classification of the studied period in correlation with the Marine Isotope Stage (MIS) (**Table 1**).

MATERIALS AND METHODS

Field Work

Our research is based on detailed field work during spring and summer seasons between 1998 and 2007 (see **Supplementary Table S1**). Permafrost coastal cliffs and riverbank exposures up to 40 m asl were studied. In places, drilling up to 10 m depth below land or ice surface (bs) was carried out. At permafrost outcrops, it often was necessary to study accessible subsections and extrapolate their characteristics across the entire section. Steep bluffs and extensive mudflows from melting ground ice limited the accessibility at some sites. Subsections consisted of sediment sequences deposited in fossil ice-wedge polygon centers exposed between melting ice wedges on steep bluffs or in still-frozen, undisturbed thermokarst mounds (baidzherakhs) on thermo-terraces in front of bluffs. The geometry and thickness of such exposures were surveyed using a laser tachymeter and measuring tapes, accompanied by an initial stratigraphic assessment. We described the frozen sediments in the field by color, organic remains, sediment type, and cryostructures according to own experiences and based on commonly acknowledged terminology (for overview see French and Shur, 2010). General exposure profiles were created by combining and stacking sub-sections up to 5 m thick. Depending on exposure conditions and the accessibility of steep cliffs such sequences were studied in overlapping subsections or in full vertical profiles. We cleaned outcrop walls and drill core segments with shovels, scrapers, and knifes and described the visible cryolithology. Each subsection was sampled at 0.2–1.0 m intervals with hammer and axe. Collected single frozen sediment samples weighed from 0.5 to 1.0 kg and were sealed in plastic bags for transport to the lab.

Analytical Studies

In total, 486 samples were studied for heavy mineral associations of the fine fraction (63–125 μm) and in 282 of these samples the coarse fraction (125–250 μm) was additionally analyzed.

TABLE 2 | Number of analyzed samples per site and fractions (heavy and light minerals and grain-size fractions).

No	Site (short name), year of sampling	Heavy mineral	Light mineral	Heavy mineral	Light mineral
		Fine fraction (63–125 µm)		Coarse fraction (125–250 µm)	
1	Bol'shoy Lyakhovsky Island (R, L, L7), 1999, 2007	91	46	37	23
2	Oyogos Yar coast (Oy7), 2007	21	—	6	—
3	Cape Svyatoy Nos (X-99), 1999	14	13	12	10
4	Stolbovoy Island (Sto), 2002	16	—	10	—
5	Belkovsky Island (Bel), 2002	5	—	—	—
6	Cape Anisii, Kotelny Island (Mya), 2002	3	—	1	—
7	Bunge Land (Bun), 2002	21	—	17	—
8	Novaya Sibir Island (NSI), 2002	6	4	4	5
9	Bykovsky Peninsula, Mamontovy Khayata (Mkh), 1998, 1999	59	62	61	62
10	Bykovsky Peninsula, Bykovsky North (B-S), 1998	6	6	6	5
11	Bykovsky Peninsula, Ivashkina Lagoon (iv-2), 1999	5	4	4	3
12	Khorogor Valley (Khg), 2002	22	24	14	23
13	Lena Delta, eastern Ebe Basyn Island (Ebe), 2005	13	13	12	—
14	Lena Delta, Turakh Island (Tur), 2005	41	40	36	—
15	Lena Delta, Nagym, southern Ebe Basyn Island (Nag), 2000	10	—	10	—
16	Lena Delta, Khardang Island (Kha), 2005	12	7	11	—
17	Lena Delta, Kurungnakh Island (Bkh), 2002	10	—	—	—
18	Cape Mamontov Klyk (Mak), 2003	131	23	41	—
	Sum of samples	486	242	282	131

Furthermore, light mineral associations were studied in 242 samples of the fine fraction and 131 samples of the coarse fraction (**Table 2**).

To remove organic matter samples were treated three times a week over several weeks with 100 ml of 3% H_2O_2 in a horizontal shaker. Approximately 3 g of an organic-free sample was separated into the two fractions (63–125 µm and 125–250 µm) by wet sieving on the sieve tower. According to Zadkova (1973), and Boenigk (1983), the 63–125 µm fraction contains the richest heavy mineral association, less affected by transport processes. Therefore, this fraction is the most suitable for subdividing sediment sequences by mineralogical composition. The 125–250 µm fraction is used complementarily. The mineral preparation was performed according to standard procedures (Boenigk, 1983; Mange and Maurer, 1992) using sodium metatungstate solution ($Na_6(H_2W_{12}O_{40}) \times H_2O$; density 2.89 g/cm^3). After 20 min centrifugation, the heavy fraction was frozen in liquid nitrogen (Fessenden, 1959; Scull, 1960) and the heavy and light fractions were separated.

The mineralogical composition was analyzed by O. Babiy and I. Klimova at the Melnikov Permafrost Institute in Yakutsk (Russia) under the stereo microscope TECHNIVAL 2 including mineral determination, grain rounding, shape, weathering degree, intergrowths. Additionally, a polarization microscope (POLAM L-213M) was used for quantitative analysis on slides applying immersion liquids with n = 1.53 and n = 1.63 for the light and heavy fraction, respectively. For each fraction mostly 300 to 400 grains per sample were counted in the coarser fraction. Sometimes fewer grains could be counted while the numbers of counted grains are always indicated in the analysis data. The mineralogical composition was calculated in grain percentages. In addition, rock fragments were counted. For the main minerals specific color appearance, grain shape, and signs of weathering on grain surfaces were noted. Grain shapes were observed visually during microscopic analysis. The terminology follows Moorhouse (1959).

The heavy mineral association includes ilmenite, epidote, clinopyroxene (monocline), orthopyroxene (rhombic), amphibole, garnet, zircon, apatite, tourmaline, sphene, rutile, anatase, leucoxene, disthene, staurolite, andalusite, chloritoide, spodumene, corundite, orthite, sillimanite, chromite, spinelle, pyrite, biotite, chlorite, muscovite, and weathered mica. The light mineral association includes quartz, feldspar, zeolithe, carbonate, muscovite, biotite, chlorite, broken mica, and rock debris and aggregates.

Since the micas can occur in heavy and light mineral fractions according to their marginal density, they were listed in both fractions and used for comparisons within these fractions. They are shown graphically as biotite, muscovite and weathered mica individually. Thereby also weathered muscovite (Fe accumulations) can be found in the heavy mineral fraction, and vice versa biotite can be present the light mineral fraction after removal of Fe during chemical weathering. The heavy mineral content was calculated for each sample and average values were determined for the respective stratigraphic units.

To characterize the separate profiles, different mineral coefficients were used. The zircon + tourmaline + rutile (ZTR) index indicates the chemical and mechanical alteration of a sediment composition (Hubert, 1962). The zircon + tourmaline + rutile/pyroxenes + amphibole (ZTR/Py + Am) coefficient estimates the weathering intensity following soil formation (modified from Marcinkowski and Mycielska-Dowgiałło, 2013). For example, a ZTR/Py + Am value of 0.003 indicates low weathering; the unstable minerals (pyroxene, amphibole) dominate the stable minerals (zircon, tourmaline, rutile). In contrast, a ZTR/Py + Am value of 0.46 indicates more intense weathering, as the stable minerals dominate over the unstable minerals. The noticeable differences between the pyroxenes/amphiboles (Py/Am) coefficient and the quartz/feldspar (Q/Fs) coefficient point to changes in the source areas (Nesbitt et al., 1996). The role of quartz during frost weathering (Konishchev, 1982) gives another indication of the intensity of this process.

Statistics

In a first step of statistical analysis, we performed an analysis of variance (ANOVA), using a Tukey Honest Significant Differences Test (Tukey, 1949) for multiple comparison of mineral content means averaged according to site and statistical units of sample mineral associations. The test was performed using R's inbuilt TukeyHSD functionality (R core team, 2021), with the default 95% family-wise confidence level. This test allows minerals to be identified that contribute significantly to a distinction related to the statistical unit of a sample at a specific sample site. We consider separation between stratigraphic units to be prominent when at least five minerals show statistically significant separation.

In order to further explore differences and commonalities between mineral associations from different ages and different sites, we performed an agglomerative hierarchical cluster analysis on means of mineral associations according to age and sample site. Since the mineral associations are determined as grain counts, we used chi-squared distances in the analysis, and the clustering method was average. We assessed the statistical significance of determined clusters using a bootstrapping approach following Suzuki and Shimodaira (2006). The analysis was performed using R's pvclust package (Suzuki et al., 2019).

RESULTS

The Coasts of the Dmitry Laptev Strait

The study sites on Bol'shoy Lyakhovsky Island are located on the northern shore of the Dmitry Laptev Strait (**Figure 1**; study site 1). The heavy mineral content of the fine fraction was highest in the MIS 5d (MIS 5a-d) (0.9%) and MIS 1 (1.5%) sediments. The heavy mineral content of the coarse fraction was highest in MIS 5e (3.6%) and MIS 1 (2.1%). In the other units the heavy mineral content was between 0.2 and 0.7 in both fractions. Grains of both fractions from this sample set (91 samples) are mostly subangular and angular. Detailed grain descriptions for each stratigraphic unit are summarized in **Supplementary Table S2**. In the heavy mineral fractions, ilmenite, sphene, and anatase are partly leucoxenized. Epidote shows irregular greenish fragments. Zoisite occurs in small amounts. Rhombic pyroxenes are represented by hypersthene and enstatite. Enstatite occurs as fragments of prismatic crystals with distinct cleavage cracks, slightly greenish and colorless. Amphiboles are mostly dark green, rarely brown or colorless. Pyroxenes and amphiboles are sometimes chloritized. Tourmalines are columnar, blue, pink, brown, and green with strong pleochroism. Zircons and anatase are prismatic bipyramidal. Garnet (almandine) is pink, sometimes corroded, with numerous ore inclusions. The light mineral fractions consist of organo-mineral aggregates. Quartz and feldspar are contaminated with iron-humus stains and often occur in intergrowths. Feldspars are partly chloritized. Calcite is colorless or brown (ferruginous) and micro-oolitic.

Regarding the heavy mineral composition (**Figure 2A**) of the fine fraction, more ilmenite and garnet are present in the MIS 7 and 6 sediments, while epidote is increased in MIS 2 deposits. Amphibole dominates the spectrum and is most abundant in MIS 3 and 1 deposits. Leucoxene content is higher in MIS 7, 6, and 2 deposits. Mica and chlorite contents are significantly increased in deposits of MIS 5e, 5a–d, and 4 ages (36, 54, and 40% respectively). The coarse fraction shows comparable heavy mineral associations. The light mineral fractions contain little quartz (especially in MIS 5e, 5a–d, 4, and 3) and are dominated by feldspar (34–62%, **Figure 2A**). The second most dominant components are rock fragments (debris) and aggregates. Mica occurs at elevated levels in MIS 5e, 5a–d, and 2 (in the fine fraction: 16, 20, and 13% respectively).

With respect to the studied mineral coefficients of the fine fraction, the MIS 7, 6, and 2 sediments indicate stronger weathering, as can be seen from the ZTR (9.6, 11.3, and 8.0 respectively) and ZTR/Py + AM (0.46, 0.10, and 0.07 respectively) values. The Py/Am and Q/Fs quotients show no clear distinction within the stratigraphic profile. This implies that the source area of the sediments did not change significantly over time. For the coarse fraction, the ZTR/Py + Am coefficients for MIS 7, 6, and 5e are increased (0.15, 0.14, and 0.10 respectively). The ZTR values are increased for MIS 7, 6, 4, and 1 units. The Py/AM ratios vary between 0.63 (MIS 7) and 0.14 (MIS 1). The Q/Fs quotients are similar in MIS 7, 6, and 5a–d sediments (0.29) and highest in the MIS 3 deposits (0.59).

The study area of the Oyogos Yar coast is located on the mainland shore of the Dmitry Laptev Strait (**Figure 1**; study site 2), about 100 km southeast of the Bol'shoy Lyakhovsky Island site. From this sample set (21 samples) only the fine heavy mineral fractions from MIS 5e, 5a–d, 4, and 3 were analyzed. The heavy mineral content was quite low (0.3, 0.3, 0.2, and 0.02% respectively). Most of the grains are subangular and angular. Epidote is of variable preservation, with small amounts of zoisite. Monoclinic pyroxene is represented mainly by diopside. Rhombic pyroxene (hypersthene) is rare. Amphiboles are mostly dark green, more rarely brown and light green. Garnet, epidote, and ilmenite are often intergrown with feldspars. Titaniferous minerals are partially leucoxenized. In general, the associations in the four sedimentary units studied here are quite similar (**Figure 2B**). There is little ilmenite (2–3%), relatively high epidote (10–20%), monoclinic pyroxene (15–23%), and amphibole (30–40%). Rhombic pyroxene, garnet, zircon, apatite, and tourmalines are few (1–5%). Leucoxene also occurs (4–6%). Micas and chlorite are completely absent. The ZTR/Py + Am (0.01–0.03) and ZTR (0.70–1.28) coefficients are quite low and similar for the four sedimentary units. The Py/Am quotient (0.44–1.02) is much higher than on the opposite Bol'shoy Lyakhov Island site.

Cape Svyatoy Nos is also located on the mainland side of the Dmitry Laptev Strait about 100 km west of the Oyogos Yar site

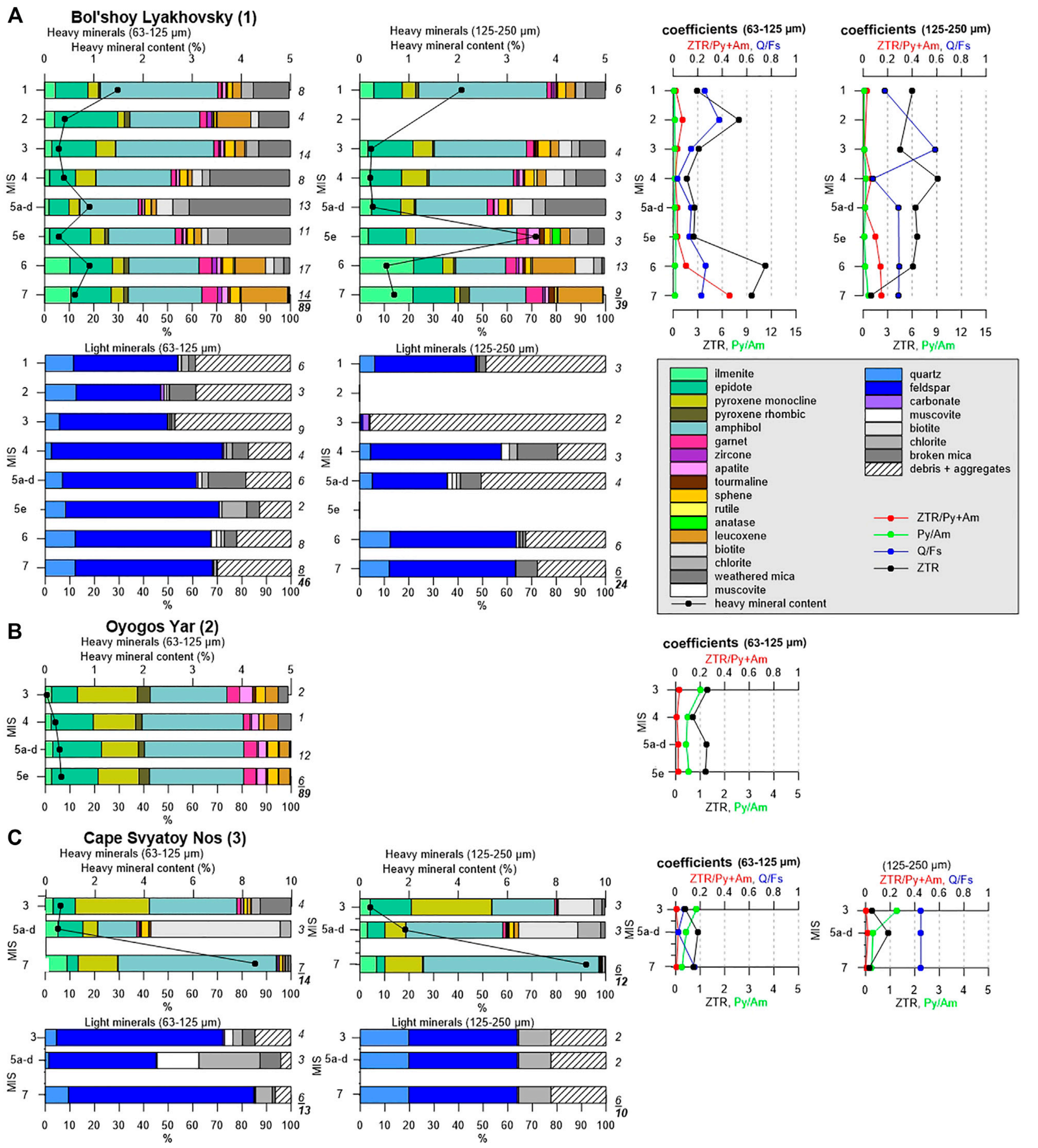

FIGURE 2 | Heavy and light mineral associations of the fine and coarse fractions, the heavy mineral contents, and the corresponding mineral coefficients from **(A)** Bol'shoy Lyakhovsky Island (1), **(B)** the Oyogos Yar coast (2), and **(C)** Cape Svyatoy Nos (3). The number of samples is in italics to the left of each diagram (Note the different scales for heavy mineral contents and the mineral coefficients).

and about 50 km south of the Bol'shoy Lyakhovsky Island site (**Figure 1**, site 3). The upper profile section between 9–25 m asl was dated as MIS 3 (Schirrmeister et al., 2011b). The middle and the lower parts of the exposure were assigned to MIS 5a–d and MIS 7 (**Table 1**), respectively (Gilichinsky et al., 2007; Blinov et al., 2009). The heavy mineral content of these three units clearly differs. The MIS 7 deposits have a very high heavy mineral load in the fine and coarse fractions (8.2 and 9.2% respectively). The

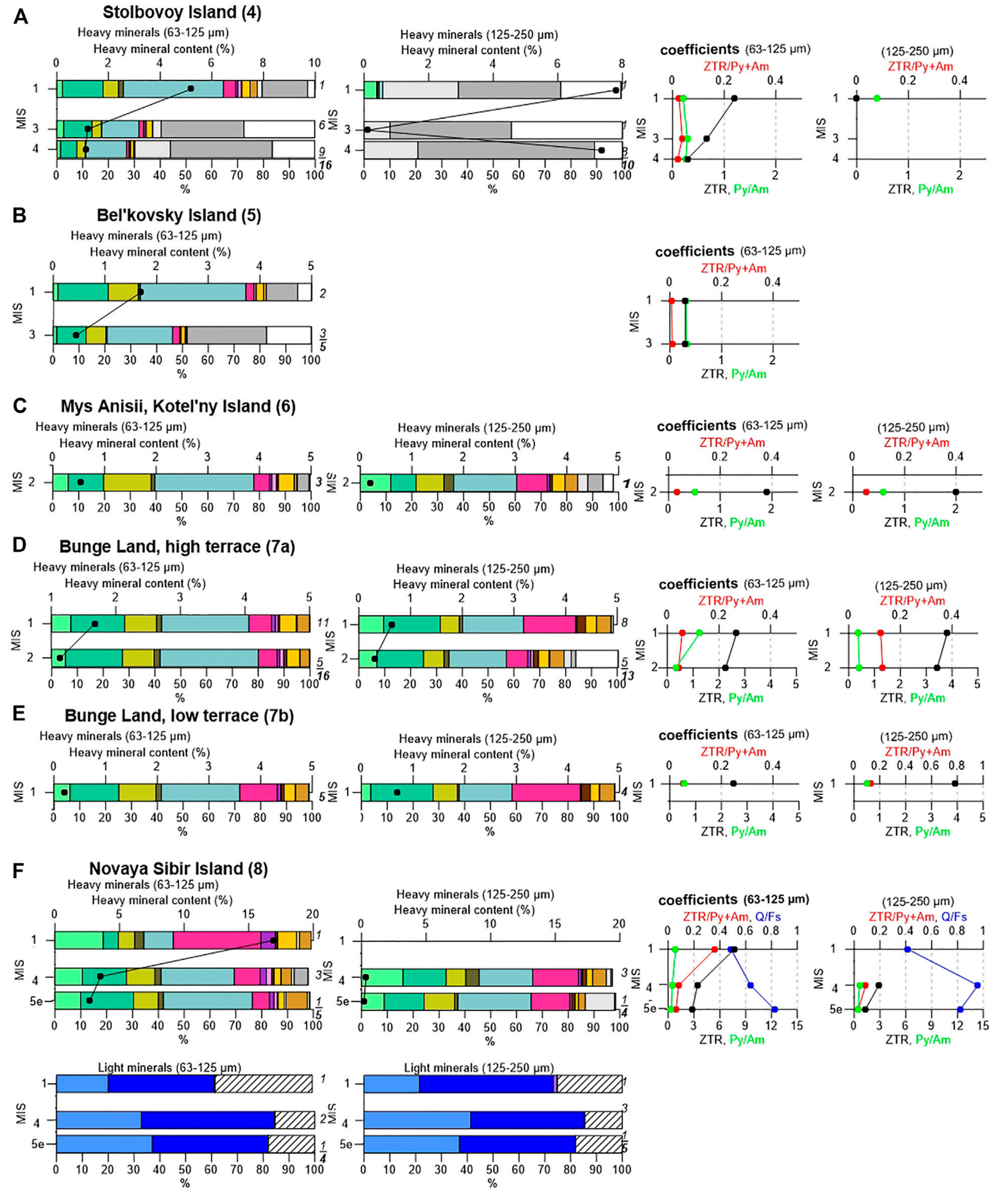

FIGURE 3 | Heavy and light mineral associations of the fine and coarse fractions, the heavy mineral contents, and the corresponding mineral coefficients from the northern New Siberian Islands: **(A)** Stolbovoy Island (4), **(B)** Bel'kovsky Island (5), **(C)** Mys Anisii, Kotel'ny Island (6), **(D)** Bunge Land, high terrace (7a), **(E)** Bunge Land, low terrace (7b), and **(F)** Novaya Sibir Island (8). The number of samples is in italics to the left of each diagram (note the different scales for the heavy mineral contents and mineral coefficients). For the legend, see **Figure 2**.

other samples at Cape Svyatoy Nos range between 1.8 and 0.4%. The grains of this sample set (14 samples) are angular and often consist of mineral aggregates. Pyroxene and amphibole are partially chloritized and iron-bearing (**Supplementary Table S2**). Monocline pyroxene is diopside. Amphibole mostly predominates the heavy mineral associations. In the MIS 5a–d unit mica and chlorite are enriched. In light mineral fractions angular and fresh plagioclase predominates. Carbonate occurs as micro-oolith. The mineral compositions show clear differences between the three stratigraphic units studied here, in both heavy mineral fractions and the fine light mineral fraction. The coarse fraction of the light mineral association shows a similar composition for all three units. The heavy mineral associations are similar for each unit in both fractions (**Figure 2C**). Epidote, pyroxene, and amphibole dominate the MIS 3 and MIS 7 sediments, whereas amphibole in the MIS 7 deposits makes up more than half of the composition. The MIS 5a–d sediments are characterized by a high concentration of mica and chlorite in both the heavy and the fine light mineral fraction. This corresponds to similar observations on Bol'shoy Lyakhov Island (**Figure 2A**). The ZTR, Q/Fs, and ZTR/Py + AM mineral coefficients differ only slightly between the fine and coarse fractions. Only Py/Am shows a significant increase from MIS 7 to MIS 3 (from 0.2 to 1.28).

Northern New Siberian Islands

We studied coastal outcrops of Stolbovoy, Bel'kovky, and Novaya Sibir islands and on Bunge Land as well as a thermokarst mound near Cape Anisii on northern Kotel'ny Island (**Figure 1**; study sites 4–8) during a ship expedition in 2002 (**Supplementary Table S1**). No descriptions of grain shapes and mineral properties (except for Bunge Land) are available for most of these sites.

From Stolbovoy Island there are heavy mineral analyses of fine and coarse fractions (16 samples). Heavy mineral contents are high for both fractions and almost all units (1.1–7.8%). The composition is characterized by a predominance of mica and chlorite in the MIS 4 and 3 units of the fine fraction and even greater enrichment in all three units of the coarse fraction (**Figure 3A**). In particular, we did not find muscovite in any of the heavy mineral compositions. A single Holocene (MIS 1) sample is dominated by ilmenite, epidote, pyroxene, and amphibole. The mineral coefficients are relatively low and do not show strong differences between the three studied units.

From Bel'kovsky Island, we analyzed the fine heavy mineral fraction of five samples from a 1.5 m profile. The heavy mineral contents average between 0.4 and 1.7%. In the MIS 3 unit ilmenite, epidote, pyroxenes, and amphibole are approximately equally represented compared to biotite and muscovite, while they dominate the composition in the MIS 1 unit (**Figure 3B**). The ZTR, ZTR/Py + Am, and Py/Am coefficient are small and do not differ between the two units.

From Cape (Mys) Anisii in the north of Kotel'ny Island, we studied three samples from a 1.5 m profile (MIS 2). The heavy mineral content is low (0.2–0.5%) but from the deepest sample both heavy mineral fractions could be analyzed. The mineral association in both fractions is similar (**Figure 3C**). Ilmenite, epidote, pyroxene, and amphibole dominate the spectra. Relatively high garnet contents in these two fractions of 6 and 12% are remarkable. The ZTR, ZTR/Py + AM, and Py/Am mineral coefficients are 1.9–2.0, 0.03–0.05, 0.5–0.6 respectively.

From Bunge Land, a 70 × 70 km wide sandy plain between the Kotel'ny and Faddeyevsky islands (**Figure 1**), two sites (with 21 samples) have been studied (Schirrmeister et al., 2010). One is the remnant of a Lateglacial (upper MIS 2) to Holocene (MIS 1) higher terrace (ca. 15 m asl). The other site, the lower terrace, is located near the shore on a 2–5 m high wide sandy area. The sediment is of late Holocene age (MIS 1). Heavy mineral contents are high in the fine fractions (1.1–4.1%) and small in the coarse fractions (0.3–0.7%). The grains of both heavy fractions are well rounded and well preserved (without clear marks of weathering). Ilmenite is often leucoxenized and intergrown with feldspars (**Supplementary Table S2**). Epidotes are fragments of irregular shape, transparent to cloudy. Monocline pyroxenes consist of colorless and light green diopside, more rarely of augite. The amphibole belongs to ordinary hornblende and is mostly a dark green, almost black color; brown and colorless varieties rarely occur. Mineral compositions in the fine fraction of the higher terrace are similar for both units (**Figures 3D,E**). Mica and chlorite occur only in the coarse fraction of the MIS 2 unit. The high garnet content in all samples (8–26%) is remarkable. The relatively low heavy mineral coefficients (ZTR/Py + Am 0.05–0.13, ZTR 2.4–3.9; Py/Am 0.4–0.5) confirm the microscope observations of fresh, unaltered mineral grains.

On Novaya Sibir Island, a profile was investigated that was assigned to the MIS 4 (four samples). In addition, one sample was defined as marine MIS 5e and one surface sample belongs to the MIS 1. The heavy mineral contents are high (0.9–3.5%). The surface sample is very rich in heavy minerals with 16.9%. The MIS 5e and 4 deposits have comparable heavy and light mineral compositions (**Figure 3F**). Remarkable are the relatively high garnet contents, which increase up to 34% in the fine fraction of the MIS 1 surface sample. The mineral coefficients are relatively similar for the MIS 5e and MIS 4 deposits (ZTR/Py + Am 0.03–0.09, ZTR 1.3–3.4, Py/Am 0.3–0.6, Q/Fs 0.4–1.0). The MIS 1 surface sediment is characterized by increased ZTR/Py + Am (0.36), ZTR (7.7), and Py/Am (0.9) values, and similar Q/Fs value (0.5).

Bykovsky Peninsula and the Adjacent Khorogor Valley

The main study site on Bykovsky Peninsula (**Figure 1**; study sites 9–12) was the Yedoma cliff of Mamontovy Khayata and the adjacent thermokarst basin (61 samples). In addition, we included the Bykovsky North site (six samples) about 10 km to the north and the Ivashkina Lagoon (five samples) about 4 km to the south. Most mineral grains from the Bykovsky Peninsula are slightly rounded, but angular. Quartz grains occur predominantly as fresh quartz in the light mineral fraction. The heavy mineral composition is dominated by pyroxene and amphibole. Pyroxene consists mainly of greyish brown augite with rare occurrence of diopsite and hypersthene (**Supplementary Table S2**). Amphibole is dominated by ordinary green colored hornblende. Ilmenite,

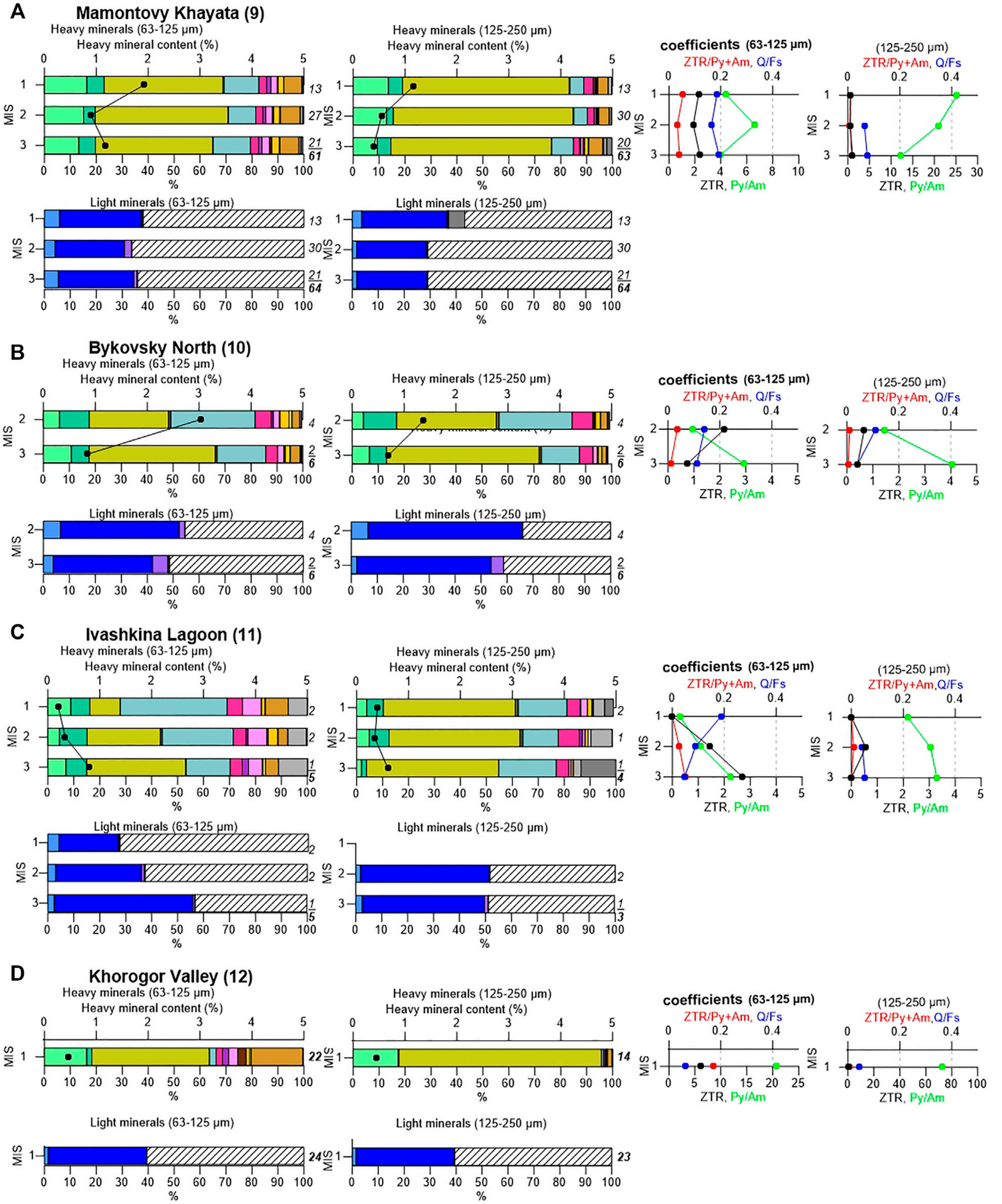

FIGURE 4 | Heavy and light mineral associations of the fine and coarse fractions, the heavy mineral contents, and the corresponding mineral coefficients from Bykovsky Peninsula at study sites **(A)** Mamontovy Khayata (9), **(B)** Bykovsky North (10), **(C)** Ivashkina Lagoon (11), and **(D)** the Khorogor Valley (12). The number of samples is in italics to the left of each diagram (Note the partly different scales for the mineral coefficients). For the legend, see **Figure 2**.

leucoxene, and epidote are present, and garnet, apatite, and sphene occur in smaller amounts. Zircon and tourmaline are observed in minor amounts. Chlorite occurs in most samples. Weathered mica occurs less frequently. Small amounts of rutile, disthen, chloritoid, staurolith, and andalusite were counted. Angular intergrowths of pyroxene, amphibole, and opaque minerals occur. Aggregations with feldspars were also observed. Augite and hornblende are mainly unchanged. Only some grains show signs of weathering. Feldspars, predominantly potassium feldspar, are often cloudy.

The profiles of the Mamontovy Khayata outcrop include sediments from MIS 3 to MIS 1. The heavy mineral content is relatively high in the fine fraction (0.9–1.9%) and lower in the coarse fraction (0.4–1.2%). The heavy and light mineral associations in both fractions are similar in the three stratigraphic units (**Figure 4A**). This is also reflected in the similar values of the ZTR (1.9–2.4), ZTR/Py + Am (0.03–0.05), and Q/Fs (0.16–0.19) mineral coefficients of the fine fraction. Only the Py/Am ratio changes more between the units. The coarse fraction also has coefficients quite close to each other, but they are higher for ZTR and Py/Am and lower for the other two coefficients. The light mineral association is dominated by mineral debris and aggregates.

The profile of Bykovky North covers six samples from MIS 3 and 2. The heavy mineral contents for both fractions are relatively high (0.7–3.1%). The mineral associations are slightly different from the Mamontovy Khayata outcrop (**Figure 4B**). First, there is significantly more amphibole (15–33%), which is also reflected in a lower Py/Am ratio. Second, there are stronger differences between the two MIS 2 and 3 investigated units in ilmenite, epidote, monocline pyroxene, and amphibole contents. Carbonate (2–6%) is present in both units as well as in both fractions.

All five samples from a drill core from the Ivashkina Lagoon are characterized by a quite low heavy mineral content (0.2–0.8%), subangular grains, insignificant ore mineral content or lack thereof, and uniform mineralogical composition. Monoclinic pyroxenes are represented by gray-brown augite; a minor amount of light green diopside is present. Amphiboles are represented by dark green hornblende. Pyroxene and amphibole are partially fractured and ferruginous. The light fraction is represented by feldspars, clasts of chlorite schists, sedimentary rock fragments, and aggregate grains. Reddish brown ferruginous carbonate grains occur in dense aggregation (probably micro concretions). The mineral associations from Ivashkina Lagoon show clear differentiations between the units in the fine fraction. From MIS 3 to MIS 1 the pyroxene content decreases and the amphibole content increases (**Figure 4C**). For the light minerals, the feldspar content decreases. In contrast, mineral associations and coefficients are quite similar in the coarse fraction.

The Kharaulakh Range including the Khorogor Valley is considered the source area for the late Pleistocene deposits of Bykovsky Peninsula (Schirrmeister et al., 2002a; Siegert et al., 2002; Slagoda, 2004; Grosse et al., 2007). Modern (MIS 1) samples (24) from different surface sites, like frost boils or river sediments, were taken during field work around Tiksi in 2002 (Grosse et al., 2003). The samples have mostly the same mineralogical composition of terrigenous material, but they differ in quantity. The average heavy mineral content is about 0.5%. They contain rock fragments - predominantly fragments of chloritic shales, which occur as outcrops in the valley slopes. In addition, there are small amounts of sedimentary and metamorphic rock fragments. All mineral grains are angular, but in fluvial sediments some grains are rounded to subrounded. Very often they occur as clusters of several minerals (ilmenite and augite, leucoxene and sphene, feldspars with minerals of the heavy fraction, etc.). This is typical for a close source area. Predominant heavy minerals are pyroxene (19–72%) and titaniferous minerals like ilmenite, leucoxene, sphene, and rutile (15–53%). Feldspar, which predominates in the light fractions, is mostly altered and turbid. Samples rich in humus and iron hydroxide show brownish colored grains with stained surfaces and fillings in cleavage cracks. The studies of the modern sediments from the Khorogor Valley show a strong dominance of pyroxene and underrepresented amphibole in both fractions (**Figure 4D**). Therefore, the Py/Am coefficients of 21 and 73 in these two fractions are significantly higher than in many other results shown here.

The Lena Delta

We collected samples from riverbank outcrops from Kurungnakh, Khardang, and Ebe Basyn islands in the western Lena Delta, and two bank outcrops and a 11.4 m deep adjacent borehole from Turakh Island also in the western Lena Delta (**Figure 1**, study sites 13–17). Further details on fieldwork and results can be found in references of **Supplementary Table S1**.

For the eastern part of Ebe Basyn Island, we analyzed seven samples from three 1–2 m deep trenches and five samples from a 4 m deep shore profile. These were fluvial sediments deposited during MIS 2 and MIS 1 periods. The average heavy mineral contents are high, with 9–12% for fine and about 2.5% for the coarse fractions. Grains are mostly angular or subangular. Most epidote grains are dark and occur as fresh mineral fragments (**Supplementary Table S2**). Some epidote grains are intergrown with hornblende. Zoisite is rare. Ilmenite is partially leucoxenized. Rhombic pyroxenes are represented by hypersthene. Enstatite is rare. Monoclinic pyroxenes are represented by diopside and augite. Zircons have an oval-elongated pomegranate shape and are bipyramidal. The heavy mineral association of the fine fraction is similar for both units (**Figure 5A**). The coarse fraction is characterized by higher epidote, pyroxene, and garnet contents and lower amphibole contents than the finer fraction. There is more pyroxene (14–27%) and less amphibole (30–43%) compared to the Nagym site. The garnet content (6–12%) is quite similar. The light mineral fraction is dominated by feldspars (approx. 60%). At 13–17%, quartz is represented as frequently as on Khardang Island. The mineral coefficients have ranges similar to those of the previous sites.

Turakh Island belongs to the Arga Complex, a large sandy plain with many oriented lakes, which forms the second terrace of the Lena Delta (Schwamborn et al., 2002). We analyzed a total of 41 samples from two outcrops (6 and 2 m high) and one 11.4 m

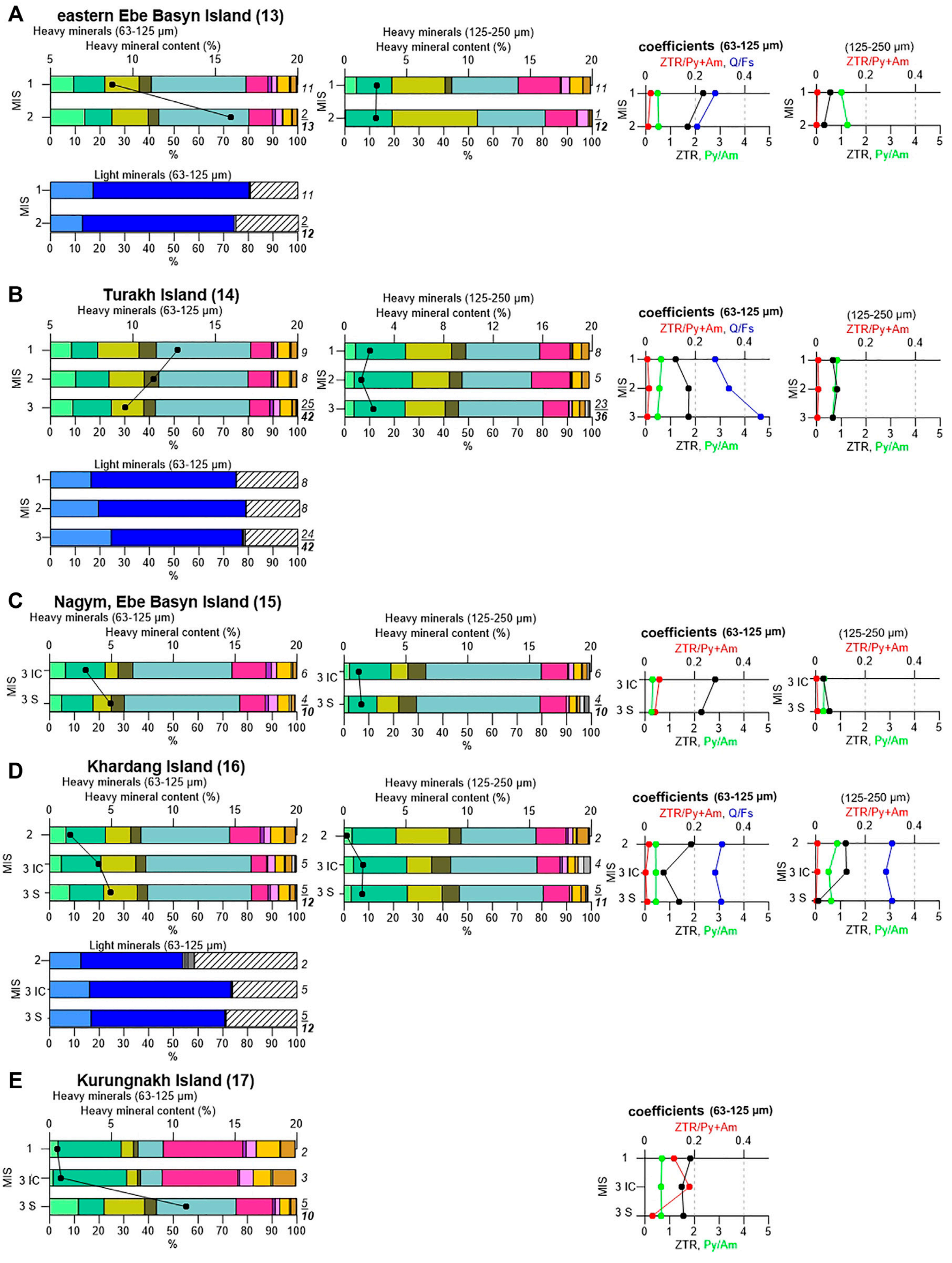

FIGURE 5 | Heavy and light mineral associations of the fine and coarse fractions, the heavy mineral contents, and the corresponding mineral coefficients from the Lena Delta sites on **(A)** eastern Ebe Basyn Island (13), **(B)** Turakh Island (14), **(C)** Nagym, southern Ebe Basyn Island (15), **(D)** Khardang Island (16), and **(E)** Kurungnakh Island (17). The number of samples is in italics to the left of each diagram (Note the mineral coefficients have smaller scales than in previous figures). For the legend, see **Figure 2**.

long drill core. This approximately 17 m long sand profile was formed between MIS 3 and 1. The average heavy mineral contents are very high for the fine fraction (10–13%) and also high for the coarse fraction (1.3–2.3%). Most grains are angular or subangular. Titanium minerals (ilmenite, sphene) are often leucoxenitized (**Supplementary Table S2**). Epidote is more often opaque with secondary alteration products. Aggregations of several minerals often occur: e.g., of pyroxene with feldspars, zircon with garnet, epidote with chlorite, garnet with epidote, sphene with rutile, ilmenite with feldspars, and others. Rhombic pyroxenes consist of hypersthene. Monoclinic diopsites have colors of different intensity; augite occurs rarely. Garnet is completely angular. Iron bearing carbonates are considered as new formations (probably siderite). Colorless calcite crystals are rare. Fe hydroxides occur in the form of rounded relocation products. All three units (MIS 3 to 1) show similar heavy and light mineral associations. In comparison, the coarse fraction contains more epidote (20–24%) and garnet (10–16%), but less ilmenite (about 4%), while the pyroxene (18–24%) and amphibole (28–38%) contents are relatively similar. (**Figure 5B**). The mineral coefficients are quite similar for both fractions.

The set of 10 samples from the Nagym site in the southern part of Ebe Basyn Island includes the lower fluvial sands (MIS 3S) and the overlying Yedoma Ice Complex (MIS 3 IC). The average heavy mineral contents are quite high in both units and fractions (1.2–4.9%). Mineral grains have different roundness. Some minerals are fissured with black and brown parts. Ilmenite is often leucoxenized. Epidote is clear and dark; zoisite and intergrowths with hornblende and feldspar occur (**Supplementary Table S2**). Pyroxenes (diopside and augite) are colorless or brown and are present in aggregates with feldspar, sometimes ferruginous. Enstatite is present among the rhombic pyroxenes. Amphibole is clear and dark with a fractured surface and is sometimes contaminated with clayey material. Garnets are colorless, pink, and brown; grains are angular and occur in aggregates with hornblende and epidote. Zircon is colorless and brownish. Staurolite occurs with carbonaceous inclusions and chlorite is intergrown with ilmenite interspersed with rutile needles. The heavy mineral associations are not significantly different between the lower fluvial sand and the Yedoma Ice Complex deposits and between the fine and coarse fractions (**Figure 5C**). Amphibole (40–50%) dominates, epidote (11–17%) and pyroxenes (13–16%) are not very frequent, while garnet (10–14%) is quite strongly represented. The ZTR coefficients of the fine fractions of the sands and the Yedoma Ice Complex are 2.3 and 2.8 respectively, which are much higher than in the coarse fraction (0.3 and 0.5 respectively).

The Yedoma Ice Complex sediments from Khardang Island were formed during MIS 3 (10 samples) and MIS 2 (2 samples). In addition, the MIS 3 sequence is divided into lower fluvial sands (MIS 3 S) and the overlying Yedoma Ice Complex (MIS 3 IC). However, there are no clear differentiations between these two units regarding heavy mineral contents and mineral associations. Ilmenite grains are leucoxenized (**Supplementary Table S2**). The light fraction is calcified and weakly rounded. Quartz grains are intergrown with rutile. Feldspars are contaminated and have black spotty inclusions. Carbonate microaggregates exist as parts of organo-mineral aggregates. The mineral contents in the sand and the Yedoma units and in both fractions are quite similar (**Figure 5D**). Garnet also occurs frequently (6.5–12%) but not as frequently as on Kurungnakh Island. Traces of carbonate minerals (0.2%) are present, but low. This, however, differs from all other Lena Delta sites, where carbonate minerals are lacking. The mineral coefficients are quite similar (ZTR/PY + Am 0.002–0.015, ZTR 0.1–1.9, Py/Am 0.4–0.9, Q/Fs 0.3) and do not reflect either changes in the source areas or strong weathering and soil formation processes.

On Kurungnakh Island, we analyzed the lower fluvial sands (MIS 3S, 4 samples), the overlying Yedoma Ice Complex (MIS 3 IC, 3 samples), and the Holocene cover (MIS 1, 2 samples). From these studies, no mineral grain descriptions are available. The average heavy mineral content of the fine fraction differs clearly between the MIS 3 sand (11%) and the MIS 3 Yedoma Ice Complex (0.9%) units. The MIS 1 unit is similar to the Yedoma Ice Complex unit (0.6%). Pyroxene and amphibole contents are significantly higher (21% and 32% respectively) in the MIS 3 sand (**Figure 5E**). The MIS 3 Yedoma Ice Complex and MIS 1 sediments have higher epidote (27–30%) and garnet (31–32%) contents. Mineral coefficients reflect low weathering intensities for the MIS 3 sands (ZTR/Py + Am = 0.02) relative to the other two units (0.10–0.12). The Py/Am coefficient shows no significant differences (0.62–0.95) and thus no significant changes in the source area.

Cape Mamontov Klyk, Western Laptev Sea

The outcrops of Cape Mamontov Klyk are located on the coast of the western Laptev Sea, about 200 km west of the Lena Delta (**Figure 1**; study site 18). These are fluvial sands (MIS 3 S, 10 samples) overlain by Yedoma Ice Complex deposits (MIS 3 IC, 33 samples; MIS 2, 65 samples) and Holocene (MIS 1, 22 samples) cover sediments and deposits from a thermokarst basin and a thermoerosional valley. The heavy mineral contents are high for the fine fraction (2.3–5.5%) and quite small (0.4–0.8%) for the coarse fractions (**Figure 5**). The mineral grains are mainly weakly rounded and are well preserved, except for epidote and micas. The predominant minerals of the heavy fraction are epidote, pyroxene, and amphibole. Ilmenite is rounded and weakly rounded, occurs in assemblages with sphene, and is sometimes leucoxenized (**Supplementary Table S2**). Epidote occurs in the form of irregularly shaped fragments and is clouded by secondary alteration products. Less common are well preserved prismatic crystals. Sometimes epidote grains are found in aggregates with other minerals (e.g., zoisite). Monoclinic pyroxenes are represented by colorless and light green diopside grains. Augites are present as a minor admixture; sometimes the ratio of augites and diopside changes. Rhombic pyroxenes are represented by hypersthene. Amphiboles are represented by mostly dark green, rarely brown hornblende. Garnets are irregularly shaped, weakly rounded, colorless to pink (almandine). Brown, orange, and bright yellow varieties are rare. Zircon is found as prismatic-bipyramidal minerals and their fragments. Tourmaline occurs as prismatic crystals and their fragments. Their coloration is brown (magnesian variety)

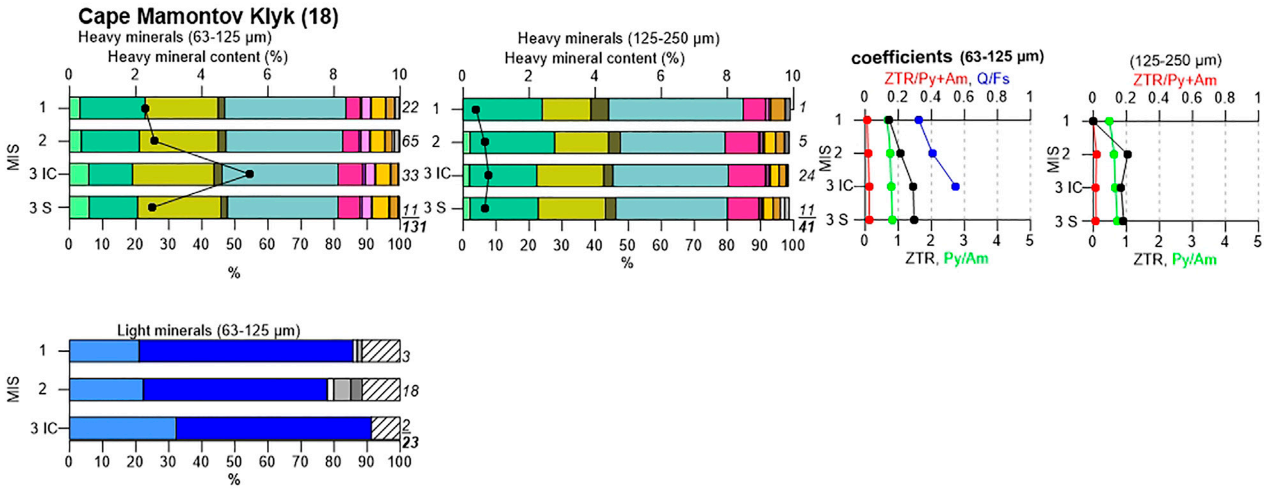

FIGURE 6 | Heavy and light mineral associations of the 63–125 µm and 125–250 µm fraction, the heavy mineral contents, and the corresponding mineral coefficients from Cape Mamontov Klyk (18). The number of samples is in italics to the left of each diagram (Note the larger scales for heavy mineral contents and some mineral coefficients than in previous figures). For the legend, see **Figure 2**.

or more rarely blue (ferruginous variety). Sphene occurs in the form of prisms and envelope-like flattened crystals, but more often as irregular fragments and aggregate grains, often leucoxenized. The coloration of the grains varies from light brown to intense brown, reddish, with strong pleochroism. Rutile is partially leucoxenized. Mica is ferruginous and is fissured. Hydrous iron oxides are often found as spherical formations. They are probably ferruginous marcasite. Carbonates (calcite) are colorless, irregularly shaped fragments; more rarely prismatic crystals, micro-oolites, and rosettes are found.

Although the general distribution of mineral associations in the fine and coarse fractions is similar, there are minor differences between MIS 1 + 2 and MIS 3 IC + S sediments. This concerns especially the mean contents of epidote, monoclinic pyroxene, garnet, and quartz (**Figure 6**). The predominant minerals of both heavy fractions are epidote, pyroxene, and amphibole (about 80%). Mica and chlorite rarely occur in the heavy mineral fractions, but they are present in the light mineral fraction of the MIS 2 and MIS 1 samples. The similarities of the main components are supported by the quite similar mineral coefficients of ZTR = 0.7–1.5, ZTR/Py + Am = 0.01–0.02, Py/Am = 0.5–0.8, and Q/Fs = 0.3–0.5.

DISCUSSION

Differences and Similarities—Site Specific and Between Different Sites

The profiles from Bol'shoy Lyakhovsky Island cover the stratigraphically longest period of all sites presented here. High mica and chlorite contents in the heavy (10–54%) and the light mineral association (3–20%) indicates that eolian activities could not have played the major role in the formation of these sediments. According to Reineck and Singh (1980) wind activities would result in destruction of unstable minerals, especially of micas. Only the lowermost exposed unit (MIS 7) has relatively low mica and chlorite contents (1–9%) that might indicate a higher share of aeolian transport in the formation of the unit. Throughout the stratigraphic profile, the MIS 5e interglacial deposits as well as the MIS 5a–d floodplain deposits and the MIS 4 Ice Complex sediments are characterized by high mica and chlorite contents (**Figure 2A**). The heavy mineral compositions of the MIS 3 and 2 Yedoma Ice Complex deposits and the MIS 1 Holocene sediments are very similar in both fractions. This indicates that the mineral sources and transport pathways did not change significantly during the MIS 3 interstadial and MIS 2 stadial periods and that the mineral content of Holocene sediments mainly derived from thawed and re-deposited late Pleistocene Yedoma Ice Complex deposits. The relatively stable Py/Am (0.14–0.36) and Q/Fs (0.04–0.6) mineral coefficients indicate that the sediment supply area did not change significantly over the studied period. Increased ZTR values of the MIS 7, 6, 4, and 1 units reflect more intense weathering during these periods. Comparing the light and coarse heavy mineral fractions, there are similar trends in mineral contents and associations. Anatase occurs only in the coarse fraction in MIS 5a–d and 5e. The light mineral coarse fraction is dominated by rock debris and aggregates, while the fine fraction is dominated by feldspars. The organo-mineral aggregates in the light fraction are typical of intense soil formation or post-sedimentary alteration under subaquatic conditions. The most probable mineral source area for Bol'shoy Lakhovsky Island are Permian sandstones and phyllitic slates of the nearby Khaptagai-Tas hill and rocks of Permian quartzitic sandstone, slates, basalt, granites, quartz-pebbles, and porphyry found as debris or as solid rocks on the beach (Volnov et al., 1998; Schirrmeister et al., 2000; Kunitsky et al., 2002).

On the Oyogos Yar coast the stratigraphic units of MIS 5e, 5a–d, 4, and 3 ages show very similar heavy mineral associations in the fine fraction. This is also reflected in the similar mineral coefficients within the profile. In contrast to Bol'shoy Lyakhovsky Island, mica and chlorite play only a minor role. The pyroxene content of 17–30% is significantly higher than that found on Bol'shoy Lyakhovsky Island (5–8%). The low ZTR and ZTR/Py + Am coefficients indicate a uniform and relatively low degree of weathering. This means that although Bol'shoy Lyakhovsky Island is close and certainly formed an accumulation area with the Oyogos Yar site in the past, the latter had a different mineral source area that might be Tertiary sediments in the bedrock of the hinterland, according to the regional geological map (Volnov et al., 1998).

The deposits of Cape Svatoy Nos have significantly high heavy mineral content in the fine and coarse fractionsof the MIS 7 unit. In the stratigraphic profile, each unit has a different heavy mineral composition in both fractions. Low ZTR and ZTR/Py + Am coefficients indicate an relatively low weathering degree. Although the associations are quite different in some cases, the mineral coefficients are close to each other, which indicate an relatively low weathering degree for ZTR and ZTR/Py + Am. We assumed the chain of Cretaceous granite domes (Volnov et al., 1998) that dominates the landscape of Cape Svyatoy Nos as source rock.

The MIS 4 and 3 samples from Stolbovoy Island show the highest mica and chlorite contents (fine fraction 22–70%) of all the studied sites. The pyroxene content is lower than 10%. The fine and coarse fractions have distinctly different compositions. The coarse fraction consists almost entirely of mica and chlorite. The low and similar ZTR and ZTR/PY + Am coefficients indicates a low weathering degree and uniform source rocks of Jurassic and Cretaceous sedimentary rocks, exposed at the coast and in higher hill positions (Volnov et al., 1998; Schirrmeister et al., 2003b).

The heavy mineral association of Bel'kovsky Island, located about 140 km to the north, differs by slightly higher pyroxene and amphibole contents (8–13% and 25–40% respectively), and lower but still high mica and chlorite contents (18–48%). The coarse fraction of the heavy minerals contains more ilmenite, garnet, leucoxene, and mica than the fine fraction but less epidote, pyroxene, and amphibole. The small mineral coefficients reflect low weathering degrees and no changes in source rocks. Bedrock consisting of strongly folded Paleozoic sediments (Volnov et al., 1998) and outcrops at the study site (Schirrmeister et al., 2003b) are considered as source rocks.

The composition of the small sample set from Cape Anisii is again different from the two previous sample sets from the northern New Siberian Islands. Mica and chlorite play a minor role (5–14%), while pyroxene is much more represented (15–20%). Mineral coefficients are slightly higher than at the other two sites on the northern New Siberian Islands. Palaeozoic basement of Ordovician and Silurian limestone (Volnov et al., 1998), which is exposed at the beach, is assumed as source rock.

The sediments origin on the higher and lower terraces of Bunge Land differs from the other sites studied on the New Siberian Archipelago. The good rounding of the grains indicates longer transport processes According to Schirrmeister et al. (2010) the higher terrace was accumulated under periglacial flood plain conditions during the Lateglacial to Holocene and the lower terrace has been affected by frequent modern marine inundation. However, the compositions are not much different from those of the neighboring Cape Anisi site, located about 150 km to the north, and the Novaya Sibir Island site located about 150 km to the east; this might point to the same mineral source area, although these sediments are from different time periods and have a different genesis. The northwestern area of strongly folded Kotel'ny Island Paleozoic rocks is considered as source area. The lower terrace is furthermore characterized by high garnet contents. This can be explained by marine relocations in the beach area.

The MIS 1 sample of fine heavy mineral fraction from Novaya Sibir Island is characterized by very high garnet, low amphibole, and very high heavy mineral content. Preliminary, this might be explained with locally scaled aeolian or hydrodynamic sorting in a surface sample. The heavy mineral contents of the other samples are also high. The light mineral data of both fractions are quite similar. The mineral coefficients show significantly different values only for the Holocene cover sediment. This supports a greater amount of alteration of grains and different source rocks for the Holocene cover sediment if compared to any older deposits here. According to the geological map (Volnov et al., 1998), the bedrock consists of Paleogene and Oligocene sandy sediments. These may have originated from the folded ridges on Kotel'ny Island. Therefore, similar heavy mineral associations are found at sites that are 100–200 km away from each other.

The goals for the mineralogical studies on the Bykovsky Peninsula and the adjacent Khorogor Valley was to determine how Yedoma Ice Complex sediments were transported from the Kharaulakh Range to the foreland. Most of the heavy mineral fractions studied here (except for MIS 3 and MIS 2 fine fractions from Ivashkina Lagoon) are characterized by high clinopyroxene contents (31–78%) and quite low amphibole contents (5–13%). Also remarkable are the comparatively low quartz contents of 2–7%. This distinguishes these sediments from most of the other sites studied in the New Siberian Archipelago and at the coasts of the Dmitry Laptev Strait. The high pyroxene and higher titaniferous mineral contents in the Khorogor Valley and in the two Yedoma Ice Complex sites (Mamontovy Khayata and Bykovsky North) indicate that the sediment source for the late Pleistocene sediments were permo-carboniferous sandstones and slates from the Kharaulakh Range (Siegert et al., 2002; Slagoda, 2004). However, there are higher amphibole contents in the Yedoma Ice Complex sediments than in the Khorogor Valley deposits, which may indicate input from an additional sediment source. In the Ivashkina Lagoon prove different mineral associations and coefficients of the fine fraction different sources of the parent material and distinct changes during the different stages of formation (Yedoma deposition, thermokarst formation, lagoon formation).

In the Lena Delta, the MIS 3 Sand-Yedoma Ice Complex profile from Kurungnakh Island differs significantly within the profile as well as from the other two more western sites (Khardang, Nagym) regarding ilmenite, pyroxene, amphibole, and garnet contents (**Figure 5**). On the other hand, the sites in the west of the delta differ little within their profiles or from each other despite their different genesis. Except for the MIS 3 Yedoma

Ice Complex and the Holocene thermokarst deposits from Kurungnakh Island, all other sites show mineral associations strongly reminiscent of Lena River deposits (Schwamborn et al., 2002; Schirrmeister et al., 2003a). However, the composition of the MIS 3 Yedoma Ice Complex and the Holocene thermokarst deposits from Kurungnakh Island are similar to the sediments originating from the southern Chekanovsky Ridge, mainly because of the high garnet content (Schirrmeister et al., 2003a). The Chekanovsky Ridge consists of Mesozoic sandstones and slates in a sequence of overthrusted imbricate synclines (Mikulenko, 1996).

At the Mamontovy Klyk site in the west of the study region, the mineral associations and coefficients are dominated by epidote, pyroxene, and amphibole and are relatively uniform within the profile as well as in the fine and the coarse fractions (**Figure 6**). However, there are minor differences between the MIS 3, the MIS 2 and the MIS 1 sediments. The weathering and soil formation processes and the source areas did not change significantly during the deposition of the different units. The source area, the Pronchshishev Ridge, is located to the south and is composed of Mesozoic sandstones and siltstones. We assume that the source area has not changed significantly over time, but it is possible that transport processes and pathways changed somewhat. In addition, the Holocene units resemble mainly MIS 2 Yedoma Ice Complex deposits from which thawed and re-located built the Holocene sequences.

Many of the sections do not differ clearly in their mineral coefficients; values remain in a narrow range. Small scale variations might be explained by hydrodynamic sorting rather than indicating source rock change. The Bol'shoy Lyakhovsky section is the site with the largest number of samples and the longest record; stretching over two glacial-interglacial cycles, exemplarily demonstrating the coefficient range in the study area. Even though the coefficient span, e.g., in the ZTR, is greatest here among all sites, the mineral spectrum does not change over time and sediments in the area have likely been remobilized in varying depositional environments (i.e., floodplain, aggrading polygonal tundra soils, thermokarst lakes). We assume that this is also the case with other sites around the Laptev Sea margin.

In general, Q/Fs coefficients are <1 for all studied sites. This agrees with experimental studies of Konishchev and Rogov (1993) showing a quartz enrichment in silt when compared with feldspar and which is interpreted to be typical for permafrost terrain with frequent freeze/thaw cycling.

Our results show that local heavy and light mineral spectra are relatively constant over time in the region, although the mineral proportions individually vary from site to site. This finding strongly suggest that local bedrock properties drive the composition of deposits as opposed to long-range transported contributions.

General Overview From the Statistics

We performed an ANOVA on the association of heavy minerals in the sediment samples to allow quantification of the differences in sample sets with regard to the stratigraphic units. If the stratigraphy can be clearly distinguished at a site, we assume that sedimentary conditions were different or that sediments were altered after sedimentation by different processes.

Tukey Honest Significant Differences Test (Tukey, 1949) was used for multiple comparisons of mineral content means averaged according to site and stratigraphy of sample mineral associations. **Figure 7** summarizes the comparison of stratigraphic-wise means of the mineral associations of the fine fraction, where each block table refers to one sample site. Minerals with significantly different means among the compared stratigraphic units are shown with different background coloring in the table.

For the Oyogos Yar coast, Bunge Land high terrace, the Novaya Siber Island, Mamontovy Khayata, Ivashkina Lagoon, Eastern Ebe Basyn Island, Nagym (southern Ebe Basyn Island), and Khardang Island, the ANOVA analysis shows that no clear separation of the stratigraphy by heavy mineral content is possible. This implies that sedimentary conditions during the different ages and source material were somewhat similar is at these sites.

For Bol'shoy Lyakhovsky Island, the ANOVA analysis demonstrates that both MIS 6 and MIS 7 are significantly different from all other stratigraphic units, but cannot be distinguished from each other. The other stratigraphic units also do not show strong distinctions from each other. In contrast, at Cape Svyatoy Nos, all studied stratigraphic units (MIS 3, MIS 5a, MIS 7) are distinguishable from each other. At Stolbovoy Island, the MIS 1 mineral composition is clearly different from those of MIS 3 and MIS 4, while MIS 3 and MIS 4 are similar to each other. For Bel'kovsky Island and Bykovsky North, MIS 2 and MIS 3 mineral associations can be differentiated. For Turakh Island, MIS 1 has no clear distinction from MIS 2, and MIS 2 in turn has no clear distinction from MIS 3. MIS 1 and MIS 3, however, are clearly distinguished from each other. The Kurungakh Island sediments from MIS 3 S can be distinguished from MIS 3 IC and MIS 1 sediments through their fine heavy mineral content, while there is no apparent difference between MIS 1 and MIS 3 IC indicating that MIS 1 deposits here formed from re-deposited MIS 3 deposits. For Cape Mamontov Klyk, MIS 1 and MIS 2 are indistinguishable, similar to MIS 3 IC and MIS 3S. However, both MIS 1and MIS 2 are clearly different from MIS 3 IC and MIS 3S.

In general, ANOVA shows that the heavy mineral contents contributing to a statistically significant separation of stratigraphic units are mainly epidote, garnet, ilmenite, zircon, and weathered mica. Weathered mica content seems to gain importance with increasing age of the samples.

In order to assess the implications of differences between stratigraphic units and sites, a cluster analysis was performed on age means of mineral associations for the heavy and light minerals in the fine fraction. Clusters containing one sample site each would indicate that the geographical location dominates the similarities between mineral associations. Clusters containing one stratigraphic unit each would indicate that the stratigraphic unit of the sediments dominated the mineral association and in turn the sedimentary conditions. Eight clusters were extracted from the dendrogram in **Supplementary Figure S3** for the fine fraction heavy mineral associations, using a combination of cluster significance and height.

FIGURE 7 | Comparison of stratigraphic-wise mean values of mineral associations of the fine fraction from sites (site numbers according to **Figure 2**) with sufficient number of samples. using the Tukey Honest Significant Differences Test (Tukey, 1949). The background coloring shows minerals with significantly different means among the compared stratigraphic units. (Ep—epidote, Cpx—clinopyroxene, Opx—orthopyroxene, Amp—amphibole, Grt—garnet, Zrn—zircon, Ap—apatite, Tur—tourmaline, Ilm—ilmenite, Rt—rutile, Leuc—leucoxene, Spn—sphene, Bt—biotite, Chl—chlorite, Ms—muscovite, WM—weathered mica).

The clusters do not show a clear differentiation by stratigraphic units for the fine heavy mineral associations, but they highlight site-specific relationships and differences.

The three stratigraphic units from Cape Svyatoy Nos (MIS 3, MIS 5a-d, MIS 7) could not be assigned to any cluster.

The Stolbovoy Island MIS 3 and MIS 4 deposits form cluster 1, along with Bel'kovsky Island MIS 3. Cluster 4 contains MIS 1 from both Bel'kovsky Island and Stolbovoy Island.

Cluster 2 consists of all stratigraphic units from Bunge Land (Bunge Land, low terrace MIS 1, Bunge Land, high terrace MIS 1 and MIS 2), Turakh Island (MIS 1, MIS 2, and MIS 3), eastern Ebe Basyn Island (MIS 1, MIS 2) and Nagym, Ebe Basyn Island (MIS 3S, MIS 3 IC). Additionally, this cluster contains Novaya Sibir Island (MIS 5e), Khardang Island (MIS 2 and MIS 3 S), and Kurungnakh Island (MIS 3 S). Both other stratigraphic units of Kurungnakh Island (MIS 1, MIS 3 IC) form cluster 8, while two other units from Novaya Sibir Island (MIS 4, MIS 1) cannot be assigned to any cluster. The third stratigraphic unit from Khardang Island (MIS 3 IC) is assigned to cluster 3.

In addition, cluster 3 contains all stratigraphic units from Cape Mamontov Klyk (MIS 1, MIS 2, MIS 3 IC, MIS 3 S), Mys Anisii, Kotel'ny Island (MIS 2), Oyogos Yar (MIS 5a–d and MIS 5e) and Bykovsky North (MIS 2). Oyogos Yar MIS 3 and MIS 4 cannot be assigned to a cluster. Bykovsky North MIS 3 is contained in cluster 6.

Cluster 5 contains Ivashkina Lagoon MIS 2 and MIS 3 deposits, while MIS 1 could not be assigned to any cluster. Cluster 6 contains all stratigraphic units from Mamontovy Khayata (MIS 1, MIS 2, and MIS 3) together with Bykovsky North (MIS 3).

Cluster 7 contains five stratigraphic units from Bol'shoy Lyakhovsky (MIS 1, MIS 3, MIS 4, MIS 5a–d, MIS 5e). The other three stratigraphic units from Bol'shoy Lyakhovsky (MIS 2, MIS 6, MIS 7) could not be assigned.

Aside from Mamontov Klyk, where ANOVA suggests a separation between MIS 1 + MIS 2 and MIS 3 IC + MIS 3 S that is not reflected in the cluster analysis, all separations shown in the ANOVA are also present in the cluster analysis, sorting the different units into different clusters. Additionally, units from Novaya Sibir Island and Ivashkina Lagoon are sorted into different clusters, reflecting the differences apparent from the means shown in **Supplementary Figures S3 and S4** that ANOVA cannot detect due to too few samples.

The fine light mineral associations can be separated into four clusters (**Supplementary Figure S4**). Ten stratigraphic units from different sites could not be assigned. Cluster 1 contains Cape Svyatoy Nos MIS 3 and Bol'shoy Lyakhovsky MIS 4 associations. Bol'shoy Lyakhovsky MIS 5a–d, MIS 5e, and MIS 6 associations could not be assigned to a cluster, while MIS 1, MIS 2, and MIS 3 associations are contained in cluster 4. Cape Svyatoy Nos MIS 5a–d and MIS 7 associations could not be assigned to any cluster. Novaya Sibir Island MIS 4 and MIS 5a–d associations form cluster 2 along with Turakh Island MIS 3. Turakh Island MIS 1 and MIS 2 associations are contained in cluster 3 along with eastern Ebe Basyn Island MIS 1 and MIS 2, Khardang Island MIS 3c and MIS 3 IC, and Bol'shoy Lyakhovsky MIS 7 associations. In addition to the stratigraphic units from Bol'shoy Lyakhovsky listed above, cluster 4 contains all stratigraphic units from Ivshkina Lagoon (MIS 1, MIS 2, and MIS 3), Khorogor Valley MIS 1, both Bykovsky North MIS 2 and MIS 3, all stratigraphic units from Mamontovy Khayata (MIS 1, MIS 2, and MIS 3), and Khardang Island MIS 2. All three stratigraphic units from Cape Mamontov Klyk with light mineral records (MIS 1, MIS 2, and MIS 3 IC) are outside of all clusters. Novaya Sibir Island MIS 1 could also not be assigned to a cluster.

Cluster associations from the fine light minerals fraction are distinctly different from those of the fine heavy minerals fraction. However, they also indicate that there is no clear differentiation by stratigraphic units at certain sites or by geographic location of the study sites.

The cluster analyses of the fine heavy and light mineral associations contain clusters that explain a local genetic association with the same source rocks (Bykovsky Peninsula, Lena Delta). There are also clusters where the site units are several hundred kilometers distant from each other. Furthermore, close correlations between the MIS 3 Yedoma units and the MIS 1 thermokarst units were often evident. This supports the hypothesis that the mineral composition of Holocene deposits in most cases derives from thawed and redeposited Yedoma Ice Complex deposits.

Generally, the mineral compositions are results of several process factors. These include the source rock, the sedimentation conditions, the duration of frost weathering after deposition in the active layer, and the impact of post-sedimentary soil formation processes.

Regional and Methodical Context

Finally, we have compared the best studied heavy mineral fraction (63–125 μm) in the most widespread stratigraphic units (MIS 3, 2 and 1) (**Figure 8**). In general, this regional comparison demonstrates that heavy mineral contents are specific to the sample sites within similar sedimentary context, which indicates that local processes determine the heavy mineral content. The heavy mineral associations of some neighboring sites are similar within limits for certain stratigraphic units.

For MIS 3, the Laptev Strait sites (**Figure 8**, study sites 1–3), the Stolbovoy and Belkovsky islands (study sites 4 and 5), Bykovsky Island (study sites 9–11); and the Kurungnakh sands and all other sites in the Lena Delta and Mamontov Klyk (study sites 17S, 13–18) are relatively similar.

Not as many data sets are available for MIS 2. Here the sites of Cape Anissi on Kotel'ny Island and from the higher terrace of Bunge Land (study sites 6 and 7a), on the Bykovsky Peninsula the sites Bykovsky North and Ivashkina Laguna (study sites 10 and 11) and in the Lena Delta the sites eastern Ebe Basyn Island, Tuarakh Island and Khardang Island as well as further west Cape Mamontov Klyk are similar.

For MIS 1, there are relative similarities at Stolbovoy and Belkovsky Islands (study sites 4, 5), at the two sites on Bunge Land (study sites 7a, 7b), at Tuarakh Island and eastern Ebe Sise Island in the Lena Delta. The sites at Novaya Sibir' Island and Kurungnakh Island (MIS 1 and MIS 3 Ice Complex) stand out primarily because of their high garnet contents. In the Lena Delta, the MIS 3 sand and Yedoma Ice Complex deposits of study sites 13–16 have a similar heavy mineralogical signature (**Figure 8**). It is similar to the sediments of the Lena River (Schwamborn et al., 2002; Schirrmeister et al., 2011a). While the MIS 3 Ice Complex deposits from Kurungnakh Island (study site 17) were formed by proluvial sediments from Chekanovsky Ridge which accumulated on a flat foreland plain in front of the mountain range (Schirrmeister et al., 2011a). The MIS 1 deposits from this site are similar to the MIS 3 sediments as they were formed from the redeposited Yedoma Ice Complex sediments.

Stolbovoy and Belkovsky islands (**Figure 8**, study sites 4 and 5) are characterized by high mica content compared to all other sites. This could be caused by changes in heavy mineral content dominated by mica weathering which leads to higher percentage of all other heavy minerals in MIS1 compared to MIS3. On Bykovsky Peninsula the development of Mamontovy Khayata (study site 9) from MIS3 to MIS1 show very small changes, while for the Ivashkina Lagoon (study site 11), MIS3 and MIS2 are similar, but MIS1 looks very differently. This is due the Holocene lagoon impact.

Over many decades there has been a debate on how to interpret the origin of the Yedoma deposits. Transport via aeolian drift over long distances has been proposed to explain the silty to sandy sediment load that has built up the several meters to tens of meters high Yedoma uplands in the otherwise flat Northern Siberian lowland (e.g., Tomirdiaro, 1996; Murton et al., 2015). In contrast, other studies favored local sediment sources and dynamics delivering the detritus (e.g., Kunitsky et al., 2002; Schirrmeister et al., 2020). While a number of studies have described heavy mineral associations of Arctic sediments both from the Laptev Sea region (Siegert et al., 2002; Siegert et al., 2009; Schwamborn et al., 2002; Schirrmeister et al., 2003a; Schirrmeister et al., 2008; Schirrmeister et al., 2010; Schirrmeister et al., 2011b) and the neighboring shelf sea areas (Behrends et al., 1999; Peregovich et al., 1999; Kaparulina et al., 2018), our study presents the first comprehensive analysis of heavy mineral associations as a proxy for provenance. This analysis is restricted methodically to sand fractions, due to weathering processes that alter the silt fractions and the fact

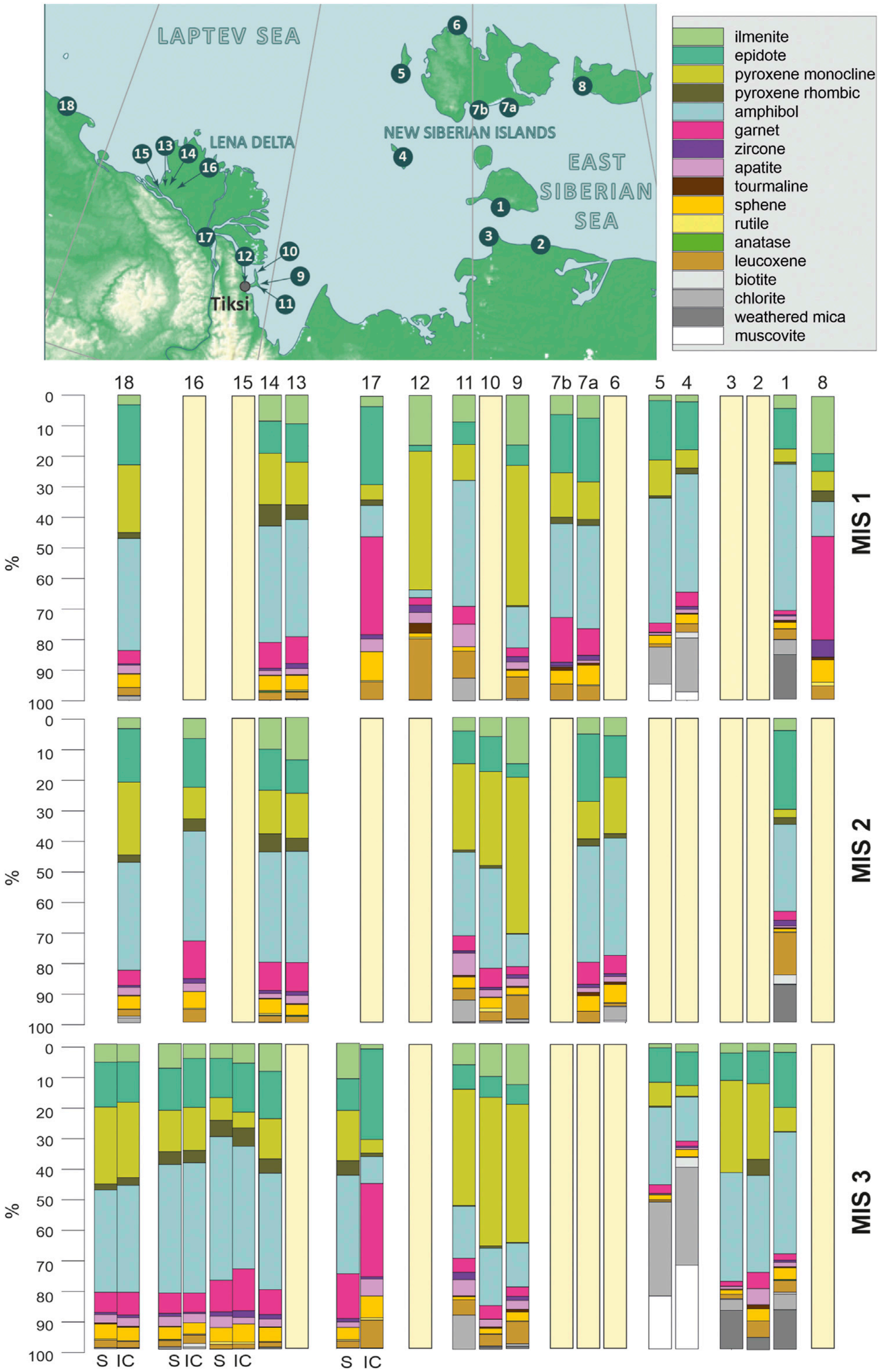

FIGURE 8 | Regional comparison of the best studied heavy minerals association (63–125 µm) in the most widespread stratigraphic units (MIS 3, 2 and 1). For the light-yellow boxes are no data available. The map is a cutout from the map of **Figure 1**. (1—Bol'shoy Lyakhovsky Island; 2—Oyogos Yar coast; 3—Cape Syatoy Nos; 4—Stolbovoy Island; 5—Bel'kovsky Island; 6—Cape Anisii, Kotel'ny Island; 7—Bunge Land (a—higher terrace, b—lower terrace); 8—Novaya Sibir' Island. Bykhovsky Peninsula: 9—Mamontovy Khayata; 10—Bykovsky North; 11—Ivashkina Lagoon; 12—Khorogor Valley. Lena Delta: 13—eastern Ebe Basyn Island; 14—Turakh Island; 15—Nagym, southern Ebe Basyn Island; 16—Khardang Island; 17—Kurungnakh Island; 18—Cape Mamontov Klyk).

that in the silt fractions, the minerals cannot be identified anymore. Therefore, this analysis allows no direct conclusions on the origins of the Yedoma sediment silt fraction, where a homogeneous heavy mineral association would fit the long-range aeolian transport hypothesis, while heterogeneous associations would be consistent with local and polygenetic origin of the sediments. In accordance with the grain size distribution analysis presented in Schirrmeister et al., 2020, our results demonstrate a polygenetic origin of coarse grain Yedoma sediments, which make up 5–50% of the Yedoma deposits.

Perhaps in the future, mineralogical studies of the finer fractions of the Yedoma deposits could help to further clarify the genesis of this Arctic phenomenon.

CONCLUSION

At most of our 18 study sites in Northeast Siberia (except on Bunge Land) the studied heavy and light mineral grains of more than 450 samples from a wide range of Late Quaternary permafrost deposits are weakly rounded, rounded to subangular, and angular. For the fine sand fraction this finding indicates that the sediments did not experience long transport distances.

Within single outcrop profiles we found clear differences, but also relatively similar mineral associations in stratigraphic units of different ages. We suggest two possible scenarios resulting in this:

(1) the mineral source areas and/or transport mechanisms and distances changed over time for a distinct site, resulting in clear differences in the mineral composition of stratigraphic units of different ages (such as on Bol'shoy Lyakhovsky Island); and
(2) the mineral source area did not change over time and the main transport mechanism and distance remained the same resulting in rather similar mineral associations at distinct sites (such as on Bykovsky Peninsula). In addition, there are distinct regional differences in the heavy mineral associations that mainly reflect differences in provenance.

Mineral associations of the same age differ significantly between different sites, not in their spectra but in their mineral proportions. This means that different sites had different source rocks. However, there are also some sites with similar mineral associations that are sometimes dozens or hundreds of kilometers away from each other, but that had clearly different formation periods and conditions. In these cases, the source rocks, like sandstones or slates, were somewhat similar in composition.

Cluster associations of the fine light mineral fraction are distinctly different from those of the fine heavy mineral fraction. The light minerals are much more subject to frost weathering and are therefore more likely to indicate the intensity of these processes. The heavy minerals, on the other hand, provide information on the provenance areas.

Our study of heavy and light mineral associations from permafrost deposits helps disentangling periglacial sediment dynamics in Northeast Siberia. In particular for the late Pleistocene Yedoma Ice Complex deposits, our findings suggest a strong local sediment source for individual sites, in agreement with dominance of periglacial weathering and local transport processes (including local aeolian relocation) instead of solely far-ranging transport and mixing during aeolian loess deposition.

DATA AVAILABILITY STATEMENT

Several datasets presented in this study can be found in online repositories. The names of the repository/repositories and accession number(s) can be found below: https://doi.pangaea.de/10.1594/PANGAEA.879589 and https://doi.org/10.1594/PANGAEA.879592. Further inquiries can be directed to the corresponding author.

AUTHOR CONTRIBUTIONS

LS and CS have designed the long-term studies. LS, CS, GG, SW, and VK participated in the field work and performed the cryolithological and stratigraphical investigations. IK has done large parts of microscopic analysis. HM conducted the statistical analyses. All authors contributed in writing and editing the manuscript.

FUNDING

This work has been supported by the Deutsche Forschungsgemeinschaft (DFG grants No. WE4390/7-1 to SW).

ACKNOWLEDGMENTS

First and foremost, we thank Olga Babiy of the Melnikov Permafrost Institute for conducting the analyses in the very early years. We thank our colleagues from the Hydrobase Tiksi for help with fieldwork from 1998 to 2007, which was supported by the joint Russian-German System Laptev Sea projects. Sample preparations were done in the AWI Potsdam Sediment Laboratory. We thank Ute Bastian/Kuschel and Dyke Scheidemann for their support. The manuscript benefited from English language corrections by Candace O'Connor (Fairbanks, Alaska).

SUPPLEMENTARY MATERIAL

The Supplementary Material for this article can be found online at: https://www.frontiersin.org/articles/10.3389/feart.2022.741932/full#supplementary-material

REFERENCES

Andreev, A. A., Grosse, G., Schirrmeister, L., Kuznetsova, T. V., Kuzmina, S. A., Bobrov, A. A., et al. (2009). Weichselian and Holocene Palaeoenvironmental History of the Bol'shoy Lyakhovsky Island, New Siberian Archipelago, Arctic Siberia. *Boreas* 38 (1), 72–110. doi:10.1111/j.1502-3885.2008.00039.x

Andreev, A., Grosse, G., Schirrmeister, L., Kuzmina, S., Novenko, E., Bobrov, A., et al. (2004). Late Saalian and Eemian Palaeoenvironmental History of the Bol'shoy Lyakhovsky Island (Laptev Sea Region, Arctic Siberia). *Boreas* 33 (4), 319–348. doi:10.1080/03009480410001974

Astakhov, V. I. (2013). Pleistocene Glaciations of Northern Russia - a Modern View. *Boreas* 42, 1–24. doi:10.1111/j.1502-3885.2012.00269.x

Astakhov, V., and Mangerud, J. (2005). The Age of the Karginsky Interglacial Strata on the Lower Yenisei. *Doklady Earth Sci.* 403, 673–676.

Behrends, M., Hoops, E., and Peregovich, B. (1999). "Distribution Patterns of Heavy Minerals in Siberian Rivers, the Laptev Sea and the Eastern Arctic Ocean: An Approach to Identify Sources, Transport and Pathways of Terrigenous Matter," in *Land-Ocean Systems in the Siberian Arctic*. Editor H. H. Kassens (Berlin, Heidelberg: Springer), 265–286. doi:10.1007/978-3-642-60134-7_24

Biskaborn, B. K., Smith, S. L., Noetzli, J., Matthes, H., Vieira, G., Streletskiy, D. A., et al. (2019). Permafrost Is Warming at a Global Scale. *Nat. Commun.* 10, 264. doi:10.1038/s41467-018-08240-4

Blinov, A., Alfimov, V., Beer, J., Gilichinsky, D., Schirrmeister, L., Kholodov, A., et al. (2009). Ratio of36Cl/Cl in Ground Ice of East Siberia and its Application for Chronometry. *Geochem. Geophys. Geosyst.* 10 (1), a–n. doi:10.1029/2009GC002548

Boenigk, W. (1983). *Schwermineralanalyse*. Stuttgart, Germany: Ferdinand Enke Publishers, 158. in German.

Box, J. E., Colgan, W. T., Christensen, T. R., Schmidt, N. M., Lund, M., Parmentier, F.-J. W., et al. (2019). Key Indicators of Arctic Climate Change: 1971-2017. *Environ. Res. Lett.* 14 (4), 045010. doi:10.1088/1748-9326/aafc1b

Fessenden, F. W. (1959). Removal of Heavy Liquid Separates from Glass Centrifuge Tubes. *J. Sed. Petrol.* 29, 269–280. doi:10.2110/jsr.28.621

French, H., and Shur, Y. (2010). The Principles of Cryostratigraphy. *Earth-Science Rev.* 101, 190–206. doi:10.1016/j.earscirev.2010.04.002

Gilichinsky, D. A., Nolte, E., Basilyan, A. E., Beer, J., Blinov, A. V., Lazarev, V. E., et al. (2007). Dating of Syngenetic Ice Wedges in Permafrost with 36Cl. *Quat. Sci. Rev.* 26, 1547–1556. doi:10.1016/j.quascirev.2007.04.004

Giterman, R. E., Sher, A. V., and Matthews, J. V. (1982). "Comparison of the Development of Tundra-Steppe Environments in West and East Beringia: Pollen and Macrofossil Evidence from Key Sections," in *Paleoecology of Beringia*. Editors D. M. Hopkins, J. V. Matthews, C. E. Schwerger, and S. B. Young (NY, London: Academy Press), 43–73. doi:10.1016/b978-0-12-355860-2.50011-9

Grosse, G., Schirrmeister, L., Kunitsky, V., and Dereviagyn, A. (2003). "Periglacial Features Around Tiksi," in *Russian-German Cooperation System Laptev Sea - the Expedition Lena 2002*. Editors M. N. Grigoriev, V. Rachold, D. Bolshiyanov, E. M. Pfeiffer, L. Schirrmeister, D. Wagner, et al. (Bremerhaven: Reports on Polar and Marine Research), 137–191. doi:10.2312/BzPM_0466_2003

Grosse, G., Schirrmeister, L., Siegert, C., Kunitsky, V. V., Slagoda, E. A., Andreev, A. A., et al. (2007). Geological and Geomorphological Evolution of a Sedimentary Periglacial Landscape in Northeast Siberia during the Late Quaternary. *Geomorphology* 86 (1/2), 25–51. doi:10.1016/j.geomorph.2006.08.005

John F. Hubert, J. F. (1962). A Zircon-Tourmaline-Rutile Maturity index and the Interdependence of the Composition of Heavy mineral Assemblages with the Gross Composition and Texture of Sandstones. *Sepm Jsr* 32 (3), 440–450. doi:10.1306/74D70CE5-2B21-11D7-8648000102C1865D

Kaparulina, E., Junttila, J., Strand, K., and Lunkka, J. P. (2018). Provenance Signatures and Changes of the Southwestern Sector of the Barents Ice Sheet during the Last Deglaciation. *Boreas* 47, 522–543. doi:10.1111/bor.12293

Kaplina, T. N. (1981). "History of Frozen Ground in Northern Yakutia during the Late Cenozoic," in *History of Permafrost Development in Eurasia*. Editors V. V. Baulin and I. Dubikov (Moscow: Nauka Press), 153–181. in Russian.

Kaplina, T. N. (1989). "Stages of Formation of Geocryological Conditions," in *Geocryology of the USSR, East Siberia and the Far East*. Editor E. D. Yershov (Moscow: Nedra), 20–25. in Russian.

Kaplina, T. N., and Lozhkin, A. V. (1984). "Age and History of Accumulation of the "Ice Complex" of the Maritime Lowlands of Yakutiya," in *Late Quaternary Environments of the Soviet Union*. Editors A. A. Velichko, H. E. Wright, and C. W. Barnosky (University of Minnesota Press, MN), 147–151.

Katasonov, E. M. (1955). *Lithology of Frozen Quaternary Sediments (Cryolithology) of the Yana Coastal lowland*. Moscow: Author's abstract of the Candidate's thesis, 25.

Konishchev, V. N. (1982). Characteristics of Cryogenic Weathering in the Permafrost Zone of the European USSR. *Arctic Alpine Res.* 14 (3), 261–265. doi:10.2307/1551158

Konishchev, V. N., and Rogov, V. V. (1993). Investigations of Cryogenic Weathering in Europe and Northern Asia. *Permafrost Periglac. Process.* 4, 49–64. doi:10.1002/ppp.3430040105

Kunitsky, V., Schirrmeister, L., Grosse, G., and Kienast, F. (2002). Snow Patches in Nival Landscapes and Their Role for the Ice Complex Formation in the Laptev Sea Coastal Lowlands. *Polarforschung* 70, 53–67. doi:10.2312/polarforschung.70.53

Lisiecki, L. E., and Raymo, M. E. (2005). A Pliocene-Pleistocene Stack of 57 Globally Distributed Benthic δ18O Records. *Paleoceanography* 20, a–n. doi:10.1029/2004PA001071

Mange, M. A., and Maurer, H. F. W. (1992). *Heavy Minerals in Colour*. London: Chapman & Hall, 147. doi:10.1007/978-94-011-2308-2

Marcinkowski, B., and Mycielska-Dowgiałło, E. (2013). Heavy-mineral Analysis in Polish Investigations of Quaternary Deposits: a Review. *Geologos* 19 (1–2), 5–23. doi:10.2478/logos-2013-0002

Mikulenko, K. I. (1996). "Questions of the Geology of the Arctic Region of West Yakutia," in *Geology, Seismicity and Permafrost Processes of the Arctic Region of West Yakutia* (Yakutsk, Russia: Scientific Center SD RAS). in Russian.

Moorhouse, W. W. (1959). *The Study of Rocks in Thin Section*. New York: Harper & Brothers, 514.

Morton, A. C., and Hallsworth, C. R. (1999). Processes Controlling the Composition of Heavy mineral Assemblages in Sandstones. *Sediment. Geology.* 124, 3–29. doi:10.1016/S0037-0738(98)00118-3

Murton, J. B., Goslar, T., Edwards, M. E., Bateman, M. D., Danilov, P. P., Savvinov, G. N., et al. (2015). Palaeoenvironmental Interpretation of Yedoma silt (Ice Complex) Deposition as Cold-Climate Loess, Duvanny Yar, Northeast Siberia. *Permafrost Periglac. Process.* 26, 208–288. doi:10.1002/ppp.1843

Murton, J. B. (2021). What and where Are Periglacial Landscapes? *Permafrost and Periglac Process* 32, 186–212. doi:10.1002/ppp.2102

Nesbitt, H. W., Young, G. M., McLennan, S. M., and Keays, R. R. (1996). Effects of Chemical Weathering and Sorting on the Petrogenesis of Siliciclastic Sediments, with Implications for Provenance Studies. *J. Geology.* 104 (5), 525–542. doi:10.1086/629850

Nitzbon, J., Westermann, S., Langer, M., Martin, L. C. P., Strauss, J., Laboor, S., et al. (2020). Fast Response of Cold Ice-Rich Permafrost in Northeast Siberia to a Warming Climate. *Nat. Commun.* 11, 2201. doi:10.1038/s41467-020-15725-8

Peregovich, B., Hoops, E., and Rachold, V. (1999). Sediment Transport to the Laptev Sea (Siberian Arctic) during the Holocene - Evidence from the Heavy mineral Composition of Fluvial and marine Sediments. *Boreas* 28, 205–214. doi:10.1111/j.1502-3885.1999.tb00215.x

Pisarska-Jamroży, M., van Loon, A. J., and Woronko, B. (2015). Sorting of Heavy Minerals in Sediments Deposited at a High Accumulation Rate, with Examples from Sandurs and an Ice-Marginal valley in NW Poland. *GFF* 137 (2), 126–140. doi:10.1080/11035897.2015.1009158

Popov, A. I. (1967). *Cryolithogenesis as a Process of Lithogenesis. Underground Ice, Issue 3*. Moscow: Moscow State University, Geographical Faculty, Department of Polar Lands and Glaciology, 7–25.

Popov, A. I. (1953). Peculiarities of Lithogenesis of Alluvial plains under Harsh Climate Conditions. Bulletin of the Academy of Sciences of the USSR Geographic Series. *No* 2, 29–41. doi:10.1007/bf01188237

R Core Team (2021). "R: A Language and Environment for Statistical Computing," in *R Foundation for Statistical Computing* (Vienna: Springer).

Reineck, H.-E., and Singh, I. B. (1980). *Depositional Sedimentary Environments: With Reference to Terrigenous Clastics*. Berlin, Heidelberg, New York: Springer, 551.

Schirrmeister, L., Dietze, E., Matthes, H., Grosse, G., Strauss, J., Laboor, S., et al. (2020). The Genesis of Yedoma Ice Complex Permafrost - Grain-Size Endmember Modeling Analysis from Siberia and Alaska. *E&g Quat. Sci. J.* 69, 33–53. doi:10.5194/egqsj-69-33-2020

Schirrmeister, L., Froese, D., Tumskoy, V., Grosse, G., and Wetterich, S. (2013). "Permafrost and Periglacial Features | Yedoma: Late Pleistocene Ice-Rich Syngenetic Permafrost of Beringia," in *The Encyclopedia of Quaternary Science*. Editor S. A. Elias (Amsterdam: Elsevier), 542–552. doi:10.1016/B978-0-444-53643-3.00106-0

Schirrmeister, L., Grosse, G., Kunitsky, V., Magens, D., Meyer, H., Dereviagin, A., et al. (2008). Periglacial Landscape Evolution and Environmental Changes of Arctic lowland Areas for the Last 60 000 Years (Western Laptev Sea Coast, Cape Mamontov Klyk). *Polar Res.* 27 (2), 249–272. doi:10.1111/j.1751-8369.2008.00067.x

Schirrmeister, L., Grosse, G., Kunitsky, V., Meyer, H., Derivyagin, A., and Kuznetsova, T. (2003b). "Permafrost, Periglacial and Paleo-Environmental Studies on New Siberian Islands," in *Russian-German Cooperation System Laptev Sea - the Expedition Lena 2002* (Bremerhaven: Reports on Polar and Marine Research), 195–265. doi:10.2312/BzPM_0466_2003

Schirrmeister, L., Grosse, G., Kunitsky, V. V., Fuchs, M. C., Krbetschek, M., Andreev, A. A., et al. (2010). The Mystery of Bunge Land (New Siberian Archipelago): Implications for its Formation Based on Palaeoenvironmental Records, Geomorphology, and Remote Sensing. *Quat. Sci. Rev.* 29, 3598–3614. doi:10.1016/j.quascirev.2009.11.017

Schirrmeister, L., Grosse, G., Schnelle, M., Fuchs, M., Krbetschek, M., Ulrich, M., et al. (2011a). Late Quaternary Paleoenvironmental Records from the Western Lena Delta, Arctic Siberia. *Palaeogeogr. Palaeoclimatol. Palaeoecol.* 299, 175–196. doi:10.1016/j.quascirev.2009.11.01710.1016/j.palaeo.2010.10.045

Schirrmeister, L., Grosse, G., Schwamborn, G., Andreev, A. A., Meyer, H., Kunitsky, V. V., et al. (2003a). Late Quaternary History of the Accumulation Plain North of the Chekanovsky Ridge (Lena Delta, Russia): A Multidisciplinary Approach. *Polar Geogr.* 27 (4), 277–319. doi:10.1080/789610225

Schirrmeister, L., Kunitsky, V., Grosse, G., Wetterich, S., Meyer, H., Schwamborn, G., et al. (2011b). Sedimentary Characteristics and Origin of the Late Pleistocene Ice Complex on North-East Siberian Arctic Coastal Lowlands and Islands - a Review. *Quat. Int.* 241, 3–25. doi:10.1016/j.quaint.2010.04.004

Schirrmeister, L., Kunitsky, V., Grosse, V., Meyer, H., Kuznetsova, T., Kuzmina, S., et al. (2000). Quaternary Deposits of Bol'shoy Lyakhovsky Island. *Rep. Polar Res.* 354, 113–168. doi:10.2312/BzP_0354_1_2000

Schirrmeister, L., Siegert, C., Kunitzky, V. V., Grootes, P. M., and Erlenkeuser, H. (2002a). Late Quaternary Ice-Rich Permafrost Sequences as a Paleoenvironmental Archive for the Laptev Sea Region in Northern Siberia. *Int. J. Earth Sci.* 91, 154–167. doi:10.1007/s005310100205

Schirrmeister, L., Siegert, C., Kuznetsova, T., Kuzmina, S., Andreev, A., Kienast, F., et al. (2002b). Paleoenvironmental and Paleoclimatic Records from Permafrost Deposits in the Arctic Region of Northern Siberia. *Quat. Int.* 89, 97–118. doi:10.1016/S1040-6182(01)00083-0

Schwamborn, G., Rachold, V., and Grigoriev, M. N. (2002). Late Quaternary Sedimentation History of the Lena Delta. *Quat. Int.* 89, 119–134. doi:10.1016/s1040-6182(01)00084-2

Scull, B. J. (1960). Removal of Heavy Liquid Separates from Glass Centrifuge Tubes--Alternative Method. *J. Sediment. Res.* 30, 626. doi:10.1306/74d70ad8-2b21-11d7-8648000102c1865d

Sher, A. V. (1971). *Mammals and Pleistocene Stratigraphy of the Extreme Northeast of the USSR and North America*. Moscow: Nauka Press, 344.

Siegert, C., Kunitsky, V. V., and Schirrmeister, L. (2009). "Ice Complex Deposits - A Data Archive for the Reconstruction of Climate and Ecology at the Laptev Sea Coast during the Late Pleistocene," in *System of the Laptev Sea and the Adjacent Arctic Seas - Modern and Past Environments* (Moscow: Moscow University Press), 320–331.

Siegert, C., Schirrmeister, L., and Babiy, O. (2002). The Sedimentological, Mineralogical and Geochemical Composition of Late Pleistocene Deposits from the Ice Complex on the Bykovsky peninsula, Northern Siberia. *Polarforschung* 70 (2000), 3–11. doi:10.2312/polarforschung.70.3

Slagoda, E. A. (2004). *Cryolithogenic Deposits of the Laptev Sea Coastal plain: Lithology and Micromorphology*. Tyumen, Publishing and Printing Centre Express, 119.

Suzuki, R., and Shimodaira, H. (2006). Pvclust: an R Package for Assessing the Uncertainty in Hierarchical Clustering. *Bioinformatics* 22 (12), 1540–1542. doi:10.1093/bioinformatics/btl117

Suzuki, R., Terada, Y., and Shimodaira, H. (2019). *Pvclust: Hierarchical Clustering with P-Values via Multiscale Bootstrap Resampling*. Kyoto: R package version 2.2-0. http://stat.sys.i.kyoto-u.ac.jp/prog/pvclust/

Tomirdiaro, S. V. (1996). "Palaeogeography of Beringia and Arctida," in *American Beginnings* (Chicago: University of Chicago), 58–69.

Tukey, J. W. (1949). Comparing Individual Means in the Analysis of Variance. *Biometrics* 5 (2), 99–114. doi:10.2307/3001913

Tumskoy, V. E. (2012). Peculiarities of Cryolithogenesis in Northern Yakutia from the Middle Neopleistocene to the Holocene [Особенности КриолитоҐенеза Отложений Северной Якутии В Нреднем КеоШлейстоцене – Голоцене]. *Earth' Cryosphere [*Криосфера Земли*]* 16 (1), 12–21.

Vangenheim, E. A. (1977). *Paleontological Substantiation of the Anthropogene Stratigraphy of Northern Asia*. Moscow: Nauka Press, 170.

Volnov, D. A., Ivanenko, G. V., Kosko, M. K., and Lopatin, B. G. (1998). *Map of Pre Quaternary Formations, S-53-55 (New Siberian Islands) State Geological Map of the Russian Federation, Scale 1: 1 000 000, Ministry of Natural Resources of the Russian Federation*. Springer.

Wetterich, S., Kizyakov, A., Fritz, M., Wolter, J., Mollenhauer, G., Meyer, H., et al. (2020). The Cryostratigraphy of the Yedoma Cliff of Sobo-Sise Island (Lena delta) Reveals Permafrost Dynamics in the central Laptev Sea Coastal Region during the Last 52 Kyr. *The Cryosphere* 14, 4525–4551. doi:10.5194/tc-14-4525-2020

Wetterich, S., Meyer, H., Fritz, M., Mollenhauer, G., Rethemeyer, J., Kizyakov, A., et al. (2021). Northeast Siberian Permafrost Ice-Wedge Stable Isotopes Depict Pronounced Last Glacial Maximum Winter Cooling. *Geophys. Res. Lett.* 48, e2020GL092087. doi:10.1029/2020GL092087

Wetterich, S., Rudaya, N., Kuznetsov, V., Maksimov, F., Opel, T., Meyer, H., et al. (2019). Ice Complex Formation on Bol'shoy Lyakhovsky Island (New Siberian Archipelago, East Siberian Arctic) since about 200 Ka. *Quat. Res.* 92 (2), 530–548. doi:10.1017/qua.2019.6

Wetterich, S., Rudaya, N., Tumskoy, V., Andreev, A. A., Opel, T., Schirrmeister, L., et al. (2011). Last Glacial Maximum Records in Permafrost of the East Siberian Arctic. *Quat. Sci. Rev.* 30, 3139–3151. doi:10.1016/j.quascirev.2011.07.020

Wetterich, S., Schirrmeister, L., Andreev, A. A., Pudenz, M., Plessen, B., Meyer, H., et al. (2009). Eemian and Late Glacial/Holocene Palaeoenvironmental Records from Permafrost Sequences at the Dmitry Laptev Strait (NE Siberia, Russia). *Palaeogeogr. Palaeoclimatol. Palaeoecol.* 279, 73–95. doi:10.1016/j.palaeo.2009.05.002

Wetterich, S., Tumskoy, V., Rudaya, N., Andreev, A. A., Opel, T., Meyer, H., et al. (2014). Ice Complex Formation in Arctic East Siberia during the MIS3 Interstadial. *Quat. Sci. Rev.* 84, 39–55. doi:10.1016/j.quascirev.2013.11.009

Wetterich, S., Tumskoy, V., Rudaya, N., Kuznetsov, V., Maksimov, F., Opel, T., et al. (2016). Ice Complex Permafrost of MIS5 Age in the Dmitry Laptev Strait Coastal Region (East Siberian Arctic). *Quat. Sci. Rev.* 147, 298–311. doi:10.1016/j.quascirev.2015.11.016

Woronko, B., Rychel, J., Karasiewicz, M. T., Ber, A., Krzywicki, T., Marks, L., et al. (2013). Heavy and Light Minerals as a Tool for Reconstructing Depositional Environments: an Example from the Jałówka Site (Northern Podlasie Region, NE Poland). *Geologos* 19 (1-2), 47–66. doi:10.2478/logos-2013-0004

Zadkova, I. I. (1973). *Composition and Lithological Structure of Deposits. In.: Main Features of the Lithology of Quaternary Sediments in the Interfluve basin of the Lower Irtysh River*. Novosibirsk: Nauka, 23–72.

Zimmermann, H., Raschke, E., Epp, L., Stoof-Leichsenring, K., Schirrmeister, L., Schwamborn, G., et al. (2017). The History of Tree and Shrub Taxa on Bol'shoy Lyakhovsky Island (New Siberian Archipelago) since the Last Interglacial Uncovered by Sedimentary Ancient DNA and Pollen Data. *Genes* 8 (10), 273. doi:10.3390/genes8100273

Conflict of Interest: The authors declare that the research was conducted in the absence of any commercial or financial relationships that could be construed as a potential conflict of interest.

The handling editor is currently organizing a Research Topic with one of the authors LS.

Publisher's Note: All claims expressed in this article are solely those of the authors and do not necessarily represent those of their affiliated organizations, or those of the publisher, the editors and the reviewers. Any product that may be evaluated in this article, or claim that may be made by its manufacturer, is not guaranteed or endorsed by the publisher.

frontiers | Frontiers in Earth Science

ORIGINAL RESEARCH
published: 19 April 2022
doi: 10.3389/feart.2022.741524

Check for updates

Seasonal Impact on 3D GPR Performance for Surveying Yedoma Ice Complex Deposits

Stephan Schennen[1†], Sebastian Wetterich[2†], Lutz Schirrmeister[2], Georg Schwamborn[2†] and Jens Tronicke[1]*

[1]Institute of Geosciences, University of Potsdam, Potsdam, Germany, [2]Alfred Wegener Institute Helmholtz Center for Polar and Marine Research, Department of Permafrost Research, Potsdam, Germany

Edited by:
*Go Iwahana,
University of Alaska Fairbanks,
United States*

Reviewed by:
*Tatsuya Watanabe,
Kitami Institute of Technology, Japan
Alexandra Veremeeva,
Institute of Physical-Chemical and Biological Problems in Soil Science (RAS), Russia*

***Correspondence:**
*Stephan Schennen
stephan.schennen@leibniz-liag.de*

[†]Present Address:
*Stephan Schennen,
Leibniz Institute for Applied Geophysics, Hanover, Germany
Sebastian Wetterich,
Heisenberg Chair of Physical Geography with Focus on Paleoenvironmental Research, Institute of Geography, Dresden, Technische Universität Dresden, Germany
Georg Schwamborn,
Eurasian Institute of Earth Sciences, Istanbul Technical University, Istanbul, Turkey*

Specialty section:
This article was submitted to Cryospheric Sciences, a section of the journal Frontiers in Earth Science

Received: *14 July 2021*
Accepted: *07 March 2022*
Published: *19 April 2022*

Citation:
Schennen S, Wetterich S, Schirrmeister L, Schwamborn G and Tronicke J (2022) Seasonal Impact on 3D GPR Performance for Surveying Yedoma Ice Complex Deposits. Front. Earth Sci. 10:741524. doi: 10.3389/feart.2022.741524

Ground-penetrating radar (GPR) is a popular geophysical method for imaging subsurface structures with a resolution at decimeter scale, which is based on the emission, propagation, and reflection of electromagnetic waves. GPR surveys for imaging the cryosphere benefit from the typically highly resistive conditions in frozen ground, resulting in low electromagnetic attenuation and, thus, an increased penetration depth. In permafrost environments, seasonal changes might affect not only GPR performance in terms of vertical resolution, attenuation, and penetration depth, but also regarding the general complexity of data (e.g., due to multiple reflections at thaw boundaries). The experimental setup of our study comparing seasonal differences of summertime thawed and winter- and springtime frozen active layer conditions above ice-rich permafrost allows for estimating advantages and disadvantages of both scenarios. Our results demonstrate major differences in the data and the final GPR image and, thus, will help in future studies to decide about particular survey seasons based on the GPR potential for non-invasive and high-resolution investigations of permafrost properties.

Keywords: GPR, seasonal effects, resolution, yedoma, permafrost

INTRODUCTION

The mean surface air temperature in the Arctic has increased from 1960 to 2019 by nearly 4°C (GISTEMP Team, 2021) and from 2006 to 2017, the average ground temperature increase across all polar and mountain permafrost regions was 0.29 ± 0.12°C (Biskaborn et al., 2019). In addition, an increase of high temperature events has been observed, while cold temperature events have declined (AMAP, 2021). In the following decades, Arctic temperatures are expected to continue rising (Meredith et al., 2019). As a consequence, frozen ground is or will be exposed to widespread thawing conditions in near future. The resulting subsidence and wetting poses a risk to infrastructure founded on yet frozen ground. Furthermore, thawing of permafrost bears the risk of greenhouse gas release, resulting in a positive feedback mechanism for climate change (e.g., Koven et al., 2015). This is particularly true for Yedoma Ice Complex (IC) deposits being a major carbon pool in the Arctic (Strauss et al., 2013, 2017).

The expected dynamics of permafrost landscape change show a demand for subsurface investigations to extrapolate permafrost sampling results from coring and exposure sites or to monitor vulnerable infrastructure bound to climate-sensitive ground. Given the vulnerability of the environment and the scale of interest, a noninvasive method with resolution capabilities at a decimeter scale is needed for subsurface permafrost investigations. A suitable geophysical tool for

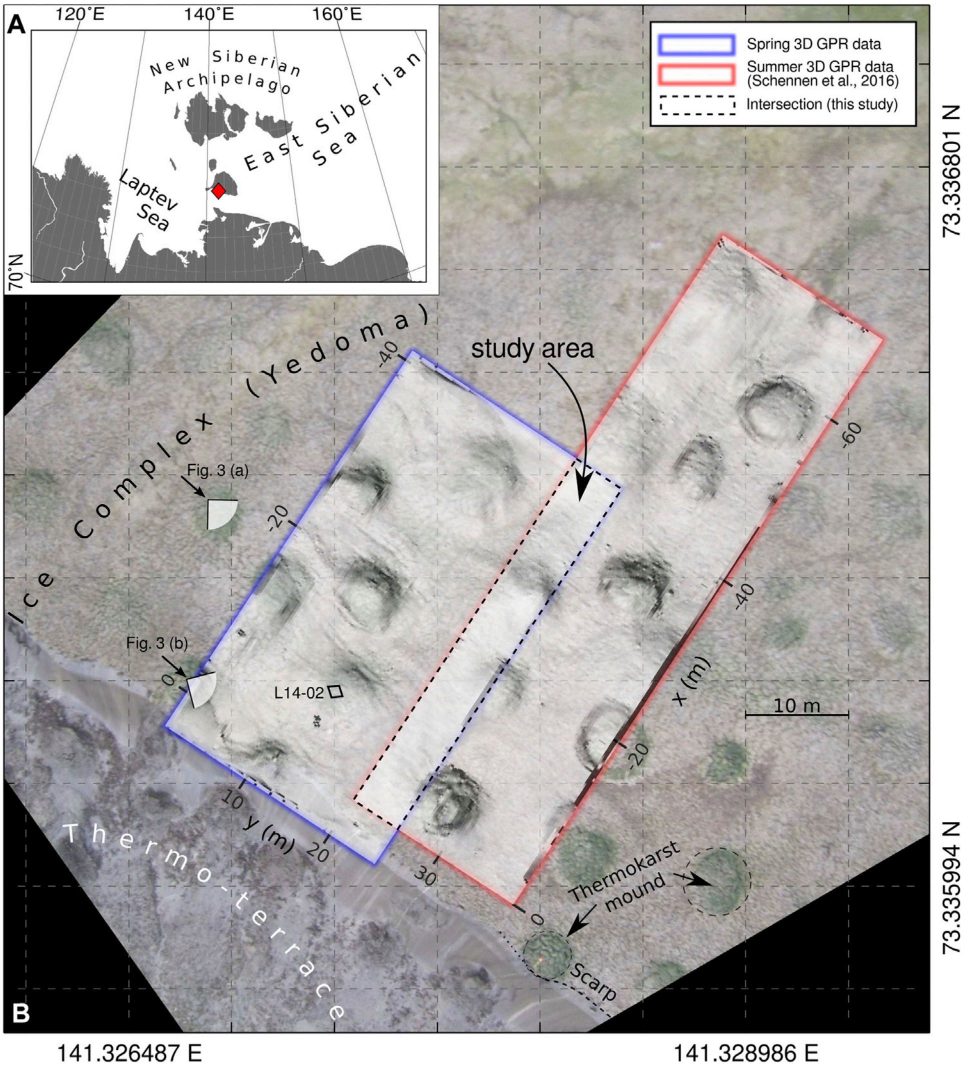

FIGURE 1 | GPR survey site showing **(A)** the location of the study area on Bol'shoy Lyakhovsky Island and **(B)** an aerial orthophoto of the field site with an overlain transparent hillshade-like visualization of the digital terrain model. The dashed rectangle denotes the study area; i.e., the area where GPR data have been recorded in spring and summer 2014. The coring site L14-02 (**Supplementary Table S1**) is located inside the area covered by our spring GPR survey. The general elevation slope from SW to NE is −10%.

non-invasive imaging of subsurface structures in these regions is ground-penetrating radar (GPR). GPR is based on the emission of electromagnetic (EM) waves, and the recording of the electromagnetic energy reflected at interfaces defined by a contrast of electrical permittivity. Allowing subsurface imaging with a decimeter resolution in a non-invasive manner, GPR has found a wide field of applications addressing different problems from civil engineering, hydrology, geology, or archeology.

In periglacial regions, GPR reflection surveying has been used to investigate geomorphological features such as pingos (Yoshikawa et al., 2006), thermokarst lakes (Schwamborn et al., 2002), deposits in glacier forelands (Schwamborn et al., 2008a), and the seasonally unfrozen uppermost active layer (Schwamborn et al., 2008b; Brosten et al., 2009). Furthermore, GPR has been used to analyze infrastructure risk at polar research stations (Campbell et al., 2018; Grigoreva et al., 2020) or to monitor snowpack accumulation (Schmid et al., 2014). Dominant interfaces in the subsurface are, for example, the permafrost table below a thawed active layer, and interfaces of adjacent sedimentary units, which exhibit different ice content and, thus, resulting in different electrical material properties.

In such GPR surveys, EM energy is transmitted and recorded typically using surface-launched antennas. The radiation characteristics are strongly focused towards the subsurface half-space depending on the permittivity of the subsurface. Thus, an antenna placed on a thawed active layer will radiate more EM energy into the subsurface than an antenna on a frozen active layer. However, the increased electromagnetic attenuation within a thawed active layer and the strong reflectivity contrast at the permafrost table may hinder EM energy to propagate into

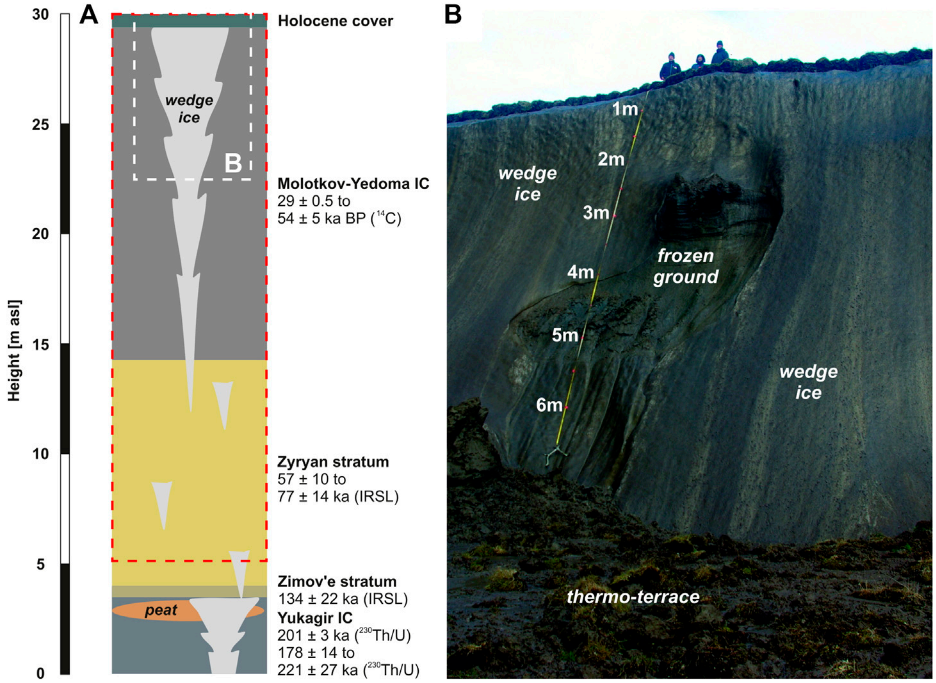

FIGURE 2 | (A) Major stratigraphic sequences at our survey site as also summarized in **Supplementary Table S1**. The red box denotes the depth range as covered by our GPR data and the white box indicates **(B)** the exposed uppermost 7 m of the Holocene cover and the Yedoma Ice Complex above a thermo-terrace.

deeper permafrost layers below. In contrast, a frozen active layer is characterized by less attenuation, i.e., higher electrical resistivity, and a decreased contrast in reflectivity at the bottom of the active layer. Furthermore, the EM wavefield in a thawed active layer is expected to be more complex, because a strong increase of velocity (up to a factor of five and more) at the upper and lower interface of the active layer results in wave-guide phenomena related to such a thawed layer.

In this study, we compare two 3D GPR data sets recorded across the same field site (characterized by Yedoma Ice Complex deposits) within five months under 1) frozen and 2) thawed active layer conditions in spring (April) and summer (August) 2014, respectively. We aim to point out advantages of both scenarios to guide decisions about choosing a particular survey season for specific applications of future GPR surveying in such environments.

SURVEY SITE AND GEOLOGICAL BACKGROUND

Our survey site is a late Pleistocene Yedoma Ice Complex on Bol'shoy Lyakhovsky Island, the southern island of the New Siberian Archipelago. **Figure 1** shows an aerial orthophoto of our survey site next to a scarp, representing the sharp transition to a thermo-terrace roughly 7 up to 15 m below. The individual areas surveyed in spring (April) and summer (August) 2014 are visualized as hillshade-like representations of digital terrain models (DTM). In detail, the visualization is obtained from the vertical component of the surface normals. We chose this representation 1) to apply a uniform detrending on our tilted DTM surface and 2) to point out morphological features, namely several decimeter elevated thermokarst mounds (baidzherakhs) and depressions in between. Here, bright areas represent horizontal (flat) regions, while black areas are tilted with angles ≥11.5°. Both survey areas overlap on an area of approximately 40 × 5 m (dashed rectangle in **Figure 1B**), that represents our study area.

Investigations of permafrost deposits on Bol'shoy Lyakhovsky Island have been carried out since the end of the 19th century (Bunge, 1887; von Toll, 1897). Quaternary permafrost deposits were studied in the 20th century by Russian (Romanovskii, 1958a; Romanovskii, 1958b; Romanovskii, 1958c; Arkhangelov et al., 1996; Kunitsky, 1998) and by Russian-Japanese projects (Nagaoka, 1994; Nagaoka et al., 1995). Since 1999 Bol'shoy Lyakhovsky Island has been the object of several expeditions within the frame of a German-Russian science cooperation (e.g., Andreev et al., 2004, 2009, 2011; Wetterich et al., 2009, 2011, 2014, 2019, 2021; Zimmermann et al., 2017). In 2014, geophysical research of Quaternary sediments on Bol'shoy Lyakhovsky Island was carried out for the first time (Schennen et al., 2015, 2016).

The stratigraphy exposed at the southern coast of Bol'shoy Lyakhovsky Island spans discontinuously the last about 200 ka, and differentiates into ten main units. The presence of four generations of stadial and interstadial Ice Complex deposits

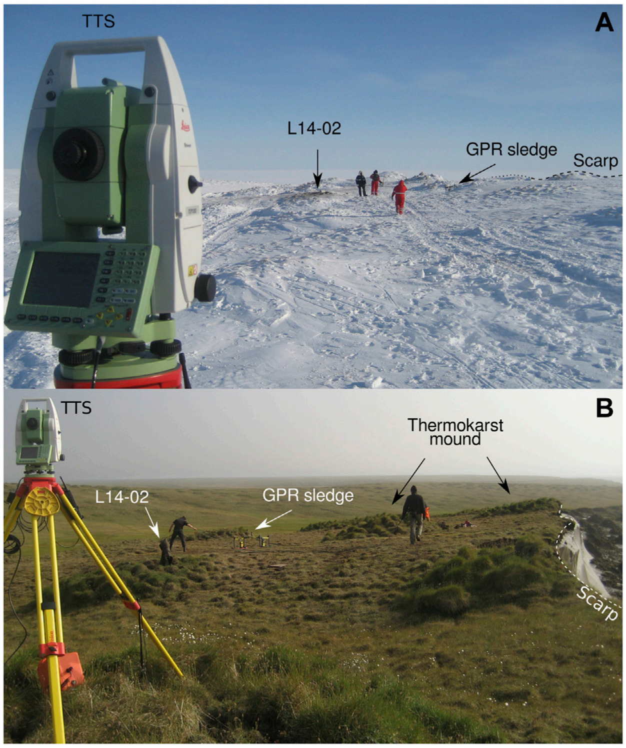

FIGURE 3 | Impression of survey conditions in **(A)** spring and **(B)** summer 2014. The scarp at the southern end of our survey area represents a sharp transition to a thermo-terrace ~7–15 m below. The coring site L14-02 (see also **Supplementary Table S1**) was covered by our GPR survey in spring. The viewpoints of both photos are annotated in **Figure 1**.

(Tumskoy, 2012; Wetterich et al., 2019) is striking. Those are divided by thermokarst and floodplain deposits of different ages, and topped by a Holocene cover. The vertical and lateral stratigraphic contacts of the exposed units differ along the coastline depending on past climate, permafrost, and geomorphologic dynamics that defined accumulation and preservation conditions for the individual units. The stratigraphic sequence of our survey site is shown in **Figure 2**. In chronological order the stratigraphic units are summarised in **Supplementary Table S1**.

The study site chosen for the 3D GPR measurements refers to **Figure 2**, where the Yedoma Ice Complex of Marine Isotope Stage (MIS) 3 below the Holocene cover (MIS 1) constitutes most of the exposed permafrost. Deeper lying deposits belong to the Zyryan floodplain stratum of MIS 5–4 age, the Zimov'e stratum of MIS 6 age and the Yukagir Ice Complex of MIS 7 age (**Supplementary Table S1**).

MATERIAL AND METHODS

We acquired our 3D GPR data using a PulseEkko system from Sensors & Software equipped with a pair of unshielded 100 MHz antennas (nominal mid-frequency). To perform our survey in a kinematic manner, we mounted our antennas on a sledge and used a total tracking station (TTS, Leica TPS 1200) to track the sledge positions continuously during data acquisition (**Figure 3**). More details regarding this setup can be found in Böniger and Tronicke (2010). We used the same survey setup in spring (**Figure 3A**) and summer (**Figure 3B**). We recorded our data

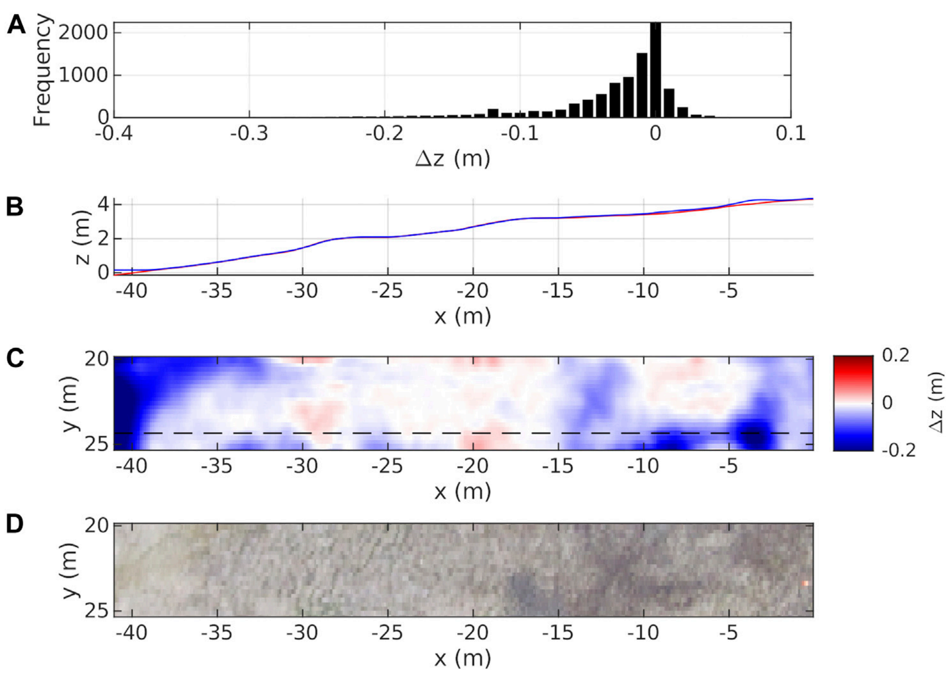

FIGURE 4 | DTM elevation change from spring to summer in our study area as seen in **(A)** the histogram of height differences across all DTM grid cells, **(B)** extracted profile [dashed line in **(C)**] from summer DTM (red) and spring DTM (blue), **(C)** a map of elevation change from spring to summer 2014, **(D)** detail of orthophoto extracted from **Figure 1**.

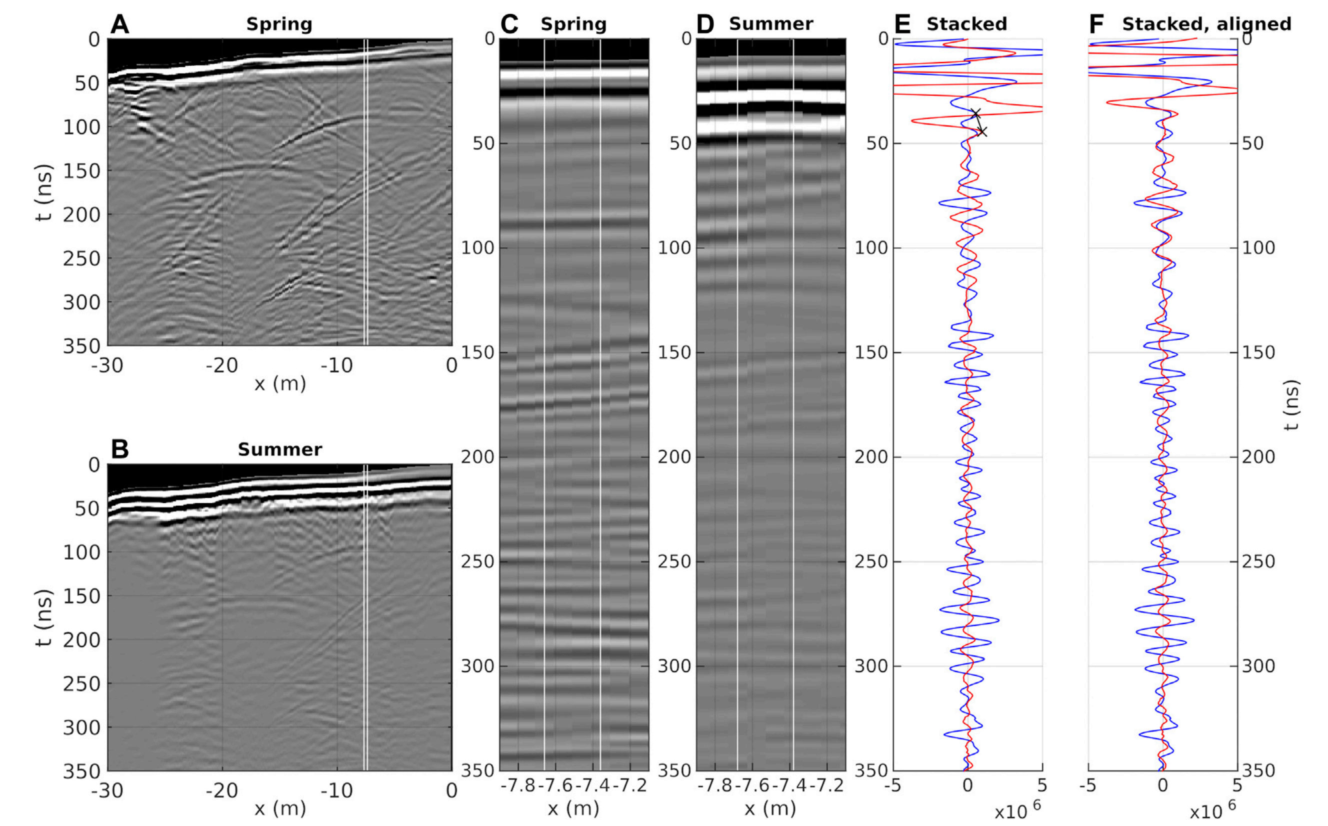

FIGURE 5 | Comparison of stacked traces extracted from gridded profile data after amplitude scaling using a t^2-scaling function. From left to right: 2D profile recorded **(A)** in spring and **(B)** in summer. Zoom-ins to illustrate the data used for stacking (indicated by the white box) of **(C)** the spring data and **(D)** the summer data. **(E)** Stacked trace of spring (blue) and summer data (red). **(F)** Trace-to-trace comparison after alignment at the 50 ns reflection event (see black crosses in e) resulting in a time shift of −9 ns. The shown time window of 350 ns corresponds to a depth interval of ~30 m depth for v = 0.17 m/ns.

in free run mode with a line spacing of ~25 cm and an inline trace spacing of ~5 cm. Our data processing flow follows a standard processing sequence including zero-time-correction, bandpass filtering, gridding to a regular grid (25 cm crossline and 10 cm inline grid-point spacing), 3D topographic migration including the same amplitude scaling (Allroggen et al., 2015), and topographic correction. We used two different velocity models for migration to consider a thawed and a frozen active layer, respectively, in the data sets recorded in different seasons. For migrating our spring data, we used a uniform velocity model of v = 0.17 m/ns. For the summer data, our velocity model consists of two layers: a 40 cm thick top layer with v = 0.06 m/ns (representing the thawed active layer) and an underlying layer with v = 0.17 m/ns representing frozen ground. We extracted our velocity models from a) common-midpoint data (i.e., consequently increasing the distance between transmitting and receiving antenna, centered on a constant midpoint) and b) diffraction analysis (calculating traveltime hyperbolas and fitting these to hyperbolic diffraction patterns in the survey data). More details can be found in Schennen et al. (2016). Our TTS data processing comprised gridding on the same regular grid we used for our GPR data. We did not correct our spring TTS data for snow cover depth.

RESULTS

With our kinematic surveying strategy tracking the GPR antenna sledge with a TTS (Böniger and Tronicke, 2010), we acquired two Digital Terrain Models (DTMs) with a spatial resolution in the order of cm. As visible in **Figure 1**, surface morphology of our winter DTM appears smoother compared to our summer DTM. This observation can partly be attributed to a snow cover with a thickness of up to 10 cm (see also **Figure 3A**) and a more slippery ground, resulting in a smoother movement of our GPR sledge. In the following, we focus on the intersecting area of both DTM and elaborate surface differences from spring to summer. Afterwards, we proceed with differences in subsurface imaging based on exemplary zoom-ins extracted from our migrated 3D GPR data sets.

Differences in Digital Terrain Model

When creating a DTM for our GPR processing flow (as needed for topographic migration and topographic correction), relative elevations within our survey area are generally sufficient. For relating our DTMs to each other, we smooth both DTMs using a 2D Gaussian kernel (standard deviation: 0.2 m, radius: 1 m) and calculate the difference height $\Delta z = z_{summer}—z_{spring}$. Finally, we

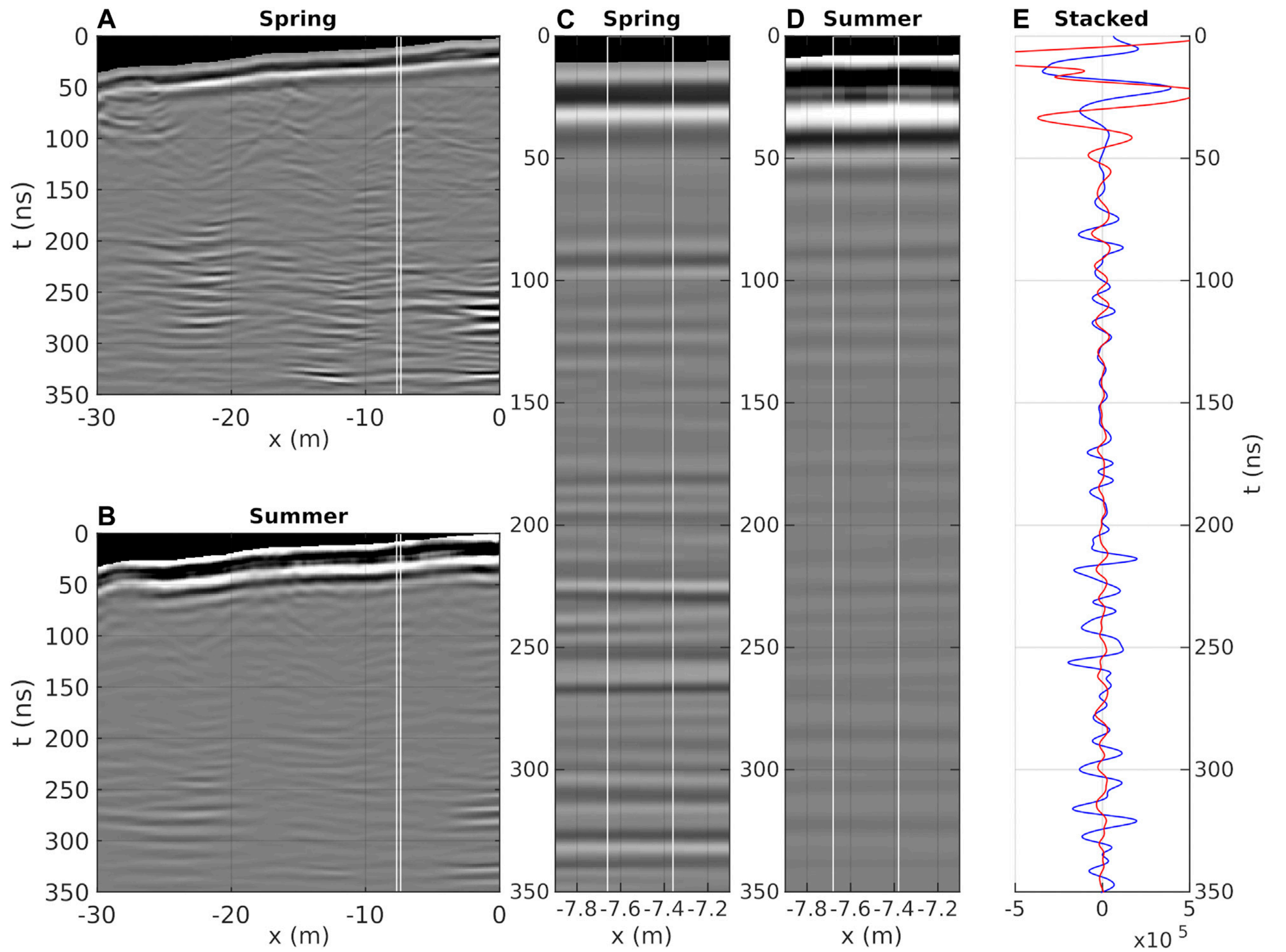

FIGURE 6 | Comparison of stacked traces extracted from gridded profile data after 3D topographic migration. From left to right: 2D profile recorded **(A)** in spring and **(B)** in summer. Zoom-ins to illustrate the data used for stacking (indicated by the white box) of **(C)** the spring data and **(D)** the summer data. **(E)** Stacked trace of spring (blue) and summer data (red). In contrast to **Figure 5E**, there was no manual time shift applied, because both traces appear aligned after topographic migration. The shown time window of 350 ns corresponds to a depth interval of ~30 m depth for v = 0.17 m/ns.

shift our Δz model to a mode of $\Delta z = 0$ to remove any global trend and focus on small scale topographic variations.

Figure 4A shows all grid cells of our resulting Δz model as a histogram. Because we shifted our differential DTM to quasi-equilibrium, the dominant loss of elevation is 0 cm. Some grid cells exhibit a relative elevation loss of more than 0.2 cm. **Figure 4B** shows a height profile that was extracted from the differential DTM illustrated in **Figure 4C**. The height profiles indicate an eroded thermokarst mound at the upper part of our survey area ($x > -5$ m) as the major region of elevation loss, as both height profiles diverge. The differential DTM below confirms that this elevation loss extends also laterally and is associated with a formerly elevated thermokarst mound at $x = -3$ m and $y = 25$ m. Grid cells that exhibit the dominant value of less than 3 cm elevation change are not bound to any particular region, but widely spread across our survey area and, thus, are interpreted to reflect the resolution capabilities of our DTM.

Differences in Ground-Penetrating Radar Data

We compare our GPR data using two approaches. In the first approach (signal loss at the active-layer base), we use stacked traces before and after topographic migration for the same location to point out differences in 1D with a focus on reflectivity and absorption. In the second approach (imaging of interfaces, resolution and interpretability within 3D data), we extract exemplary 2D patches from our data sets and analyze those in time and frequency domain to investigate differences of 2D structural imaging such as those related to variations in vertical resolution and lateral continuity of reflectors. We relate our observed reflections, both between major stratigraphic units and within, to differences in ice content. According to Schwamborn et al. (2008b), these reflections can already result from a change of 30% in gravimetric ice content. Please note that all coordinates are referring to the survey grid as introduced in **Figure 1**.

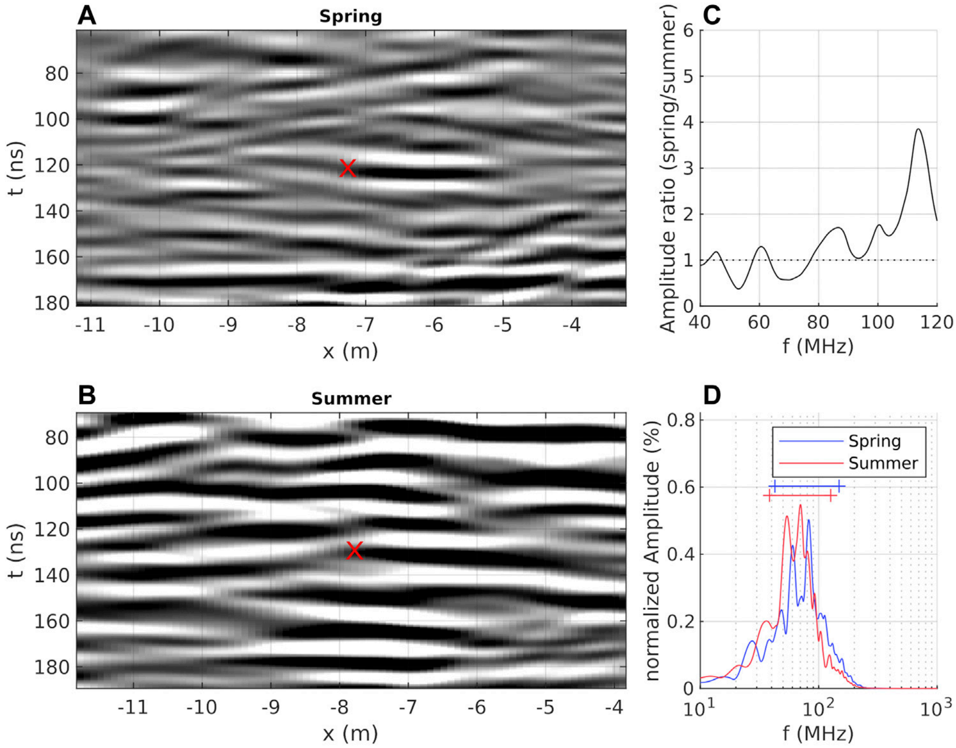

FIGURE 7 | Exemplary 2D detail in time **(A,B)** and frequency domain **(C,D)**. 2D data were extracted from our migrated **(A)** spring and **(B)** summer data cube (between x = −11 and −4 m, at y = 21 m), and manually aligned based on image details (red marker at center). Note, a gain factor of two has been applied to the summer data for visualization. Right column: **(C)** ratio of unnormalized amplitude spectra around our nominal antenna frequency and **(D)** normalized amplitude spectra for spring (blue) and summer (red) data. In **(D)**, horizontal lines denote frequency range between 10th percentile A_{10} and 90th percentile A_{90} (comprising 80% of the recorded amplitudes).

Signal Loss at the Active-Layer Base

Figure 5 illustrates our processed GPR data including a topographic correction but without applying topographic migration. We show the same 2D line extracted from our spring data (**Figure 5A**) and our summer data (**Figure 5B**). As major differences, the summer 2D profile shows a more complex waveform pattern at traveltimes t < 60 ns (resulting from interference phenomena of antenna crosstalk and energy reflected at the active layer base) and the frozen ground below elevated areas (thermokarst mounds, see **Figure 4**) appears rather blind (i.e., only minor reflected energy is visible in these areas). In contrast, our spring data show a simpler early time wavefield at t < 60 ns (without dominating interference patterns) and the data provide further insights into subsurface structures within and below the thermokarst mounds. However, the spring data exhibit a more complex waveform pattern towards later traveltimes (e.g., x = −25 m, t > 210 ns) due to a higher amount of diffracted energy.

Based on the profiles shown in **Figures 5A,B**, we select a location dominated by horizontal reflections (**Figures 5C,D**) and calculate a median trace using five traces between x = −7.5 m ± 0.2 m as indicated by the white boxes in **Figures 5A–D**. **Figures 5E,F** shows trace-to-trace comparisons between our calculated median traces of unmigrated spring and summer data, respectively. Despite the mentioned differences at early times (t < 60 ns), the median trace of the summer data exhibits a reflection pattern similar to that of the spring data, although shifted by a lag of 9 ns as applied in **Figure 5F**. Exemplary ratios (summer/spring) of maximal reflection amplitudes extracted from our stacked and aligned median trace data in **Figure 5F** are, e.g., 0.77 (at t = 83 ns), 0.70 (at t = 107 ns), and 0.24 (at t = 234 ns), indicating an up to four times higher signal loss in summer compared to spring.

Figure 6 shows a similar illustration of the GPR data after applying the full processing flow, i.e., including 3D topographic migration before applying the topographic correction. In contrast to the unmigrated 2D profiles (**Figure 5**), all diffraction hyperbolas are successfully collapsed and the reflections appear smoother (**Figures 6A–D**). Furthermore, the trace-to-trace comparison (**Figure 6E**), demonstrates that the stacked traces from both data sets show already high coherency in reflection patterns below the active layer bottom (t > 60 ns) without applying an additional time shift. This observation can be interpreted as a validation of our velocity models used for the topographic migration. Here, former differences in traveltime within the unmigrated data have been corrected: i.e., diffracted energy was properly propagated back using our data set-specific rms-velocity models. Exemplary ratios (summer/spring) of maximal reflection amplitudes extracted from our migrated and stacked median trace data in **Figure 5F** are, for

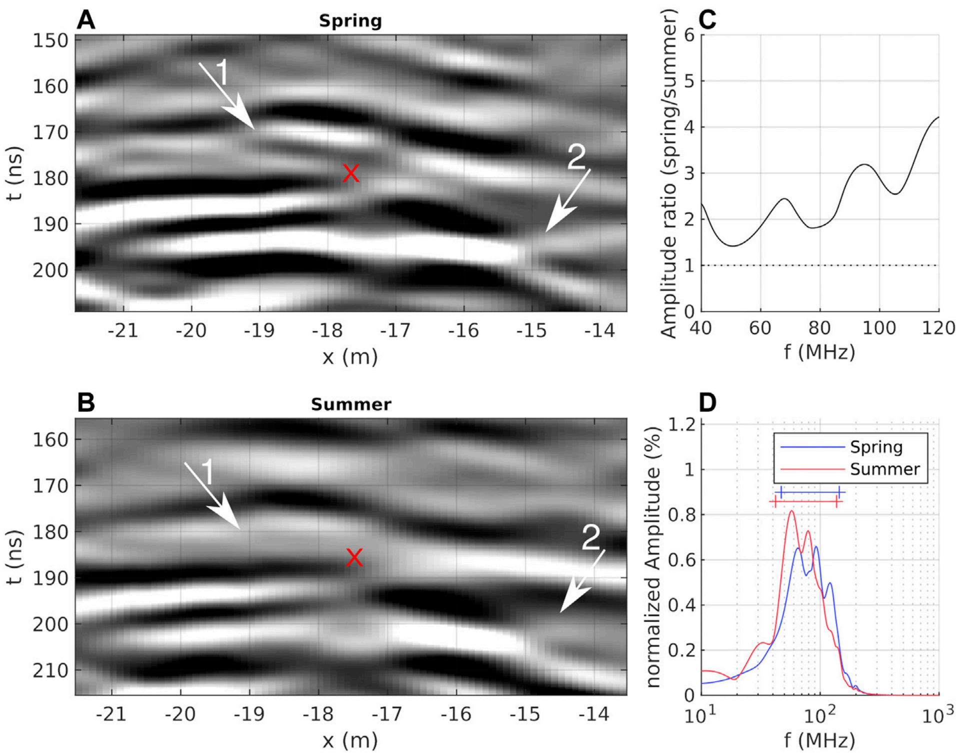

FIGURE 8 | Exemplary 2D detail in time **(A,B)** and frequency domain **(C,D)**. 2D data were extracted from our migrated **(A)** spring and **(B)** summer data cube (between x = −22 and −14 m, at y = 21 m), and manually aligned based on image details (red marker at center). Note, a gain factor of two has been applied to the summer data for visualization. Right column: **(C)** ratio of unnormalized amplitude spectra around our nominal antenna frequency and **(D)** normalized amplitude spectra for spring (blue) and summer (red) data. In **(D)**, horizontal lines denote frequency range between 10th percentile A_{10} and 90th percentile A_{90} (comprising 80% of the recorded amplitudes). Arrows identify features that are further discussed in the text.

example, 0.36 (at t = 87 ns), 0.51 (at t = 110 ns), and 0.18 (at t = 234 ns), implying an up to five times higher signal loss in summer compared to spring. In comparison to the ratios delineated from unmigrated stacked traces at the same travel times, we observe typically lower ratios. We relate this observation to a more effective migration of our spring data compared to summer, where a) diffraction patterns do not occur as widespread (due to higher attenuation), and our estimated velocity model will more often deviate from reality, for example, due to small-scale contrasts in wetness, resulting in a more heterogeneous near-surface velocity field.

Imaging of Interfaces, Resolution and Interpretability Within 3D Data

Figure 7 compares the surroundings of an internal cryolithological reflection recorded at 120 ns (~10.2 m depth for v = 0.17 m/ns, extracted at x = −7.5 m) from our spring data (**Figure 7A**) to the corresponding area extracted from our summer data (**Figure 7B**). Compared to the summer data, the spring data exhibit both a higher dynamic range in amplitudes and a higher vertical resolution resulting in a generally sharper image of subsurface structures. Thus, the denoted reflector appears more distinct in the spring data, while the summer data provide a smoother but less detailed image of subsurface structures which could ease reflector tracing. The corresponding amplitude spectra (**Figures 7C,D**) confirm these observations. Although the total amount of energy is comparable, the amplitude spectra of the summer data appear shifted towards lower frequencies and exhibit a sharper focus of energy (i.e., narrower bandwidth) compared to the spring data. This can be seen particularly in the normalized amplitude spectra shown in **Figure 7D**, where the summer spectrum (red) exhibits a sharp descent from ~80 to ~105 MHz compared to the spring spectrum (blue). As a consequence, the spring spectrum exhibits up to four times higher amplitudes around ~110 MHz as demonstrated by the spectral ratios in **Figure 7C**.

Figure 8 compares the surroundings of an internal cryolithological reflection recorded at 180 ns (~15.3 m depth for v = 0.17 m/ns, extracted at x = −17.5 m) from our spring data to the corresponding region extracted from our summer data. Both images show roughly the same dynamics in amplitude, whereas the spring data provide a slightly sharper image due to a higher vertical resolution. The summer data look smoother and miss some information from the spring data (see arrow 1 and 2 in **Figure 8**). In contrast to the previous example discussed in **Figure 7**, the seasonal difference between total recorded energy is much more distinct between spring and summer data. Again, the summer mode is shifted towards lower frequencies (~70 MHz compared to ~95 MHz in the spring data) and exhibits a much

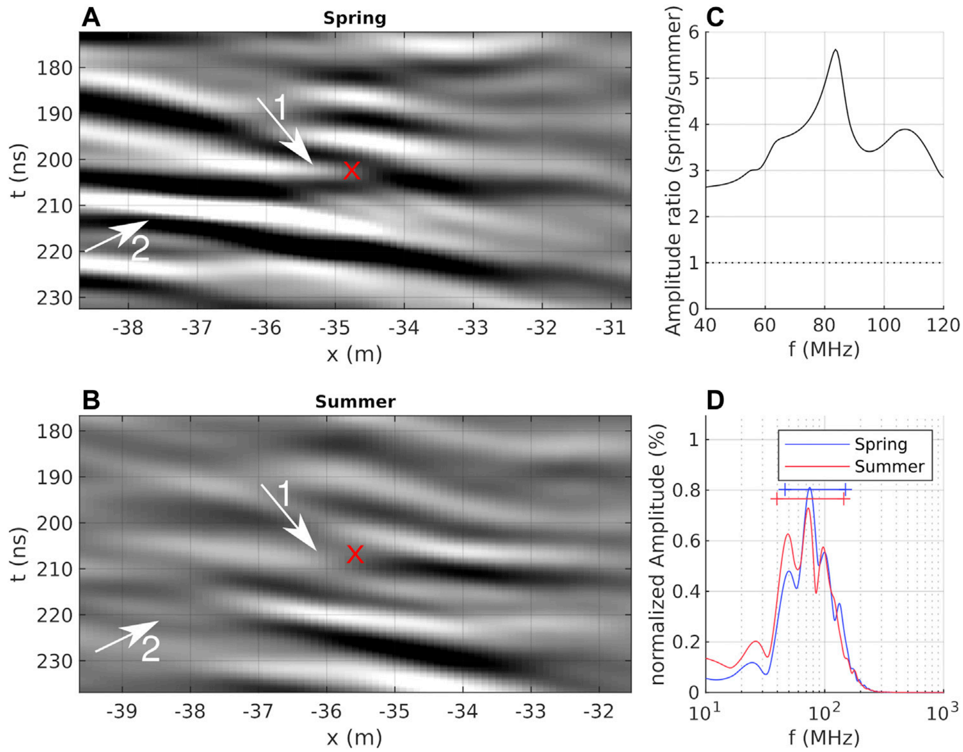

FIGURE 9 | Exemplary 2D detail in time **(A,B)** and frequency domain **(C,D)**. 2D data were extracted from our migrated **(A)** spring and **(B)** summer data cube (between x = –39 and –31 m, at y = 21 m), and manually aligned based on image details (red marker at center). Note, a gain factor of two has been applied to the summer data for visualization. Right column: **(C)** ratio of unnormalized amplitude spectra around our nominal antenna frequency and **(D)** normalized amplitude spectra for spring (blue) and summer (red) data. In **(D)**, horizontal lines denote frequency range between 10th percentile A_{10} and 90th percentile A_{90} (comprising 80% of the recorded amplitudes). Arrows identify features that are further discussed in the text.

TABLE 1 | Evaluation of amplitude spectra: amplitude ratio of spring to summer data and bandwidth (defined by 10th percentile A_{10} and 90th percentile A_{90}). Depth interval is estimated for the time window of spring data and assuming v = 0.17 m/ns.

Data example	Depth Interval	Spectral amplitude Ratio Spring/Summer	Bandwidth Spring (MHz)		Bandwidth Summer (MHz)	
			f (A_{10})	f (A_{90})	f (A_{10})	f (A_{90})
1 (**Figure 7**)	5–15 m	1.2	43	149	39	127
2 (**Figure 8**)	13–18 m	2.5	47	145	42	137
3 (**Figure 9**)	15–20 m	3.6	46	150	40	143
4	21–27 m	3.3	60	158	41	153
5	16–21 m	2.5	42	161	42	146
6	12–17 m	2.9	46	147	42	140
7	12–16 m	2.5	46	155	38	148
8	16–20 m	2.5	50	168	45	149

stronger decrease at frequencies f > 80 MHz. Normalizing both spectra to their total amplitude provides a consistent picture; i.e., the summer data exhibit a narrower shape with increased amplitude at lower frequencies (e.g., ~0.8 at ~70 MHz compared to 0.65 at ~ 95 MHz).

Figure 9 compares the surroundings of an internal cryolithological reflection recorded at 205 ns (~17.4 m depth for v = 0.17 m/ns, extracted at x = −34.5 m) from our spring data to the corresponding region extracted from our summer data. Similar to **Figures 7**, **8**, the summer image (**Figure 9B**) shows smoother reflection patterns than the spring image (**Figure 9A**). Thus, the interference around the analysis point (red marker) is not resolved and we are not able to continuously follow the black (positive) phase of the tilted reflector in the summer data (similar features are observed for other reflectors). In the

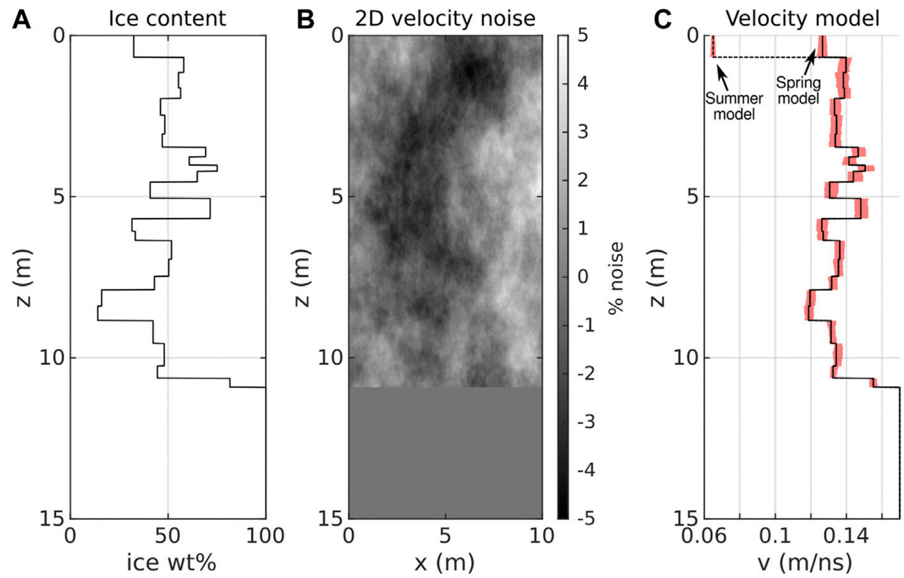

FIGURE 10 | Construction of a heterogeneous 2D GPR velocity field for FDTD modeling. **(A)** gravimetric ice content of L14-02 (Schwamborn and Wetterich, 2016), **(B)** 2D stochastic noise field, **(C)** black: corresponding 1D GPR velocity model (black line) following a 2-phase CRIM model (Birchak et al., 1974) and the velocity range (red area) resulting from superposition with our 2D noise field.

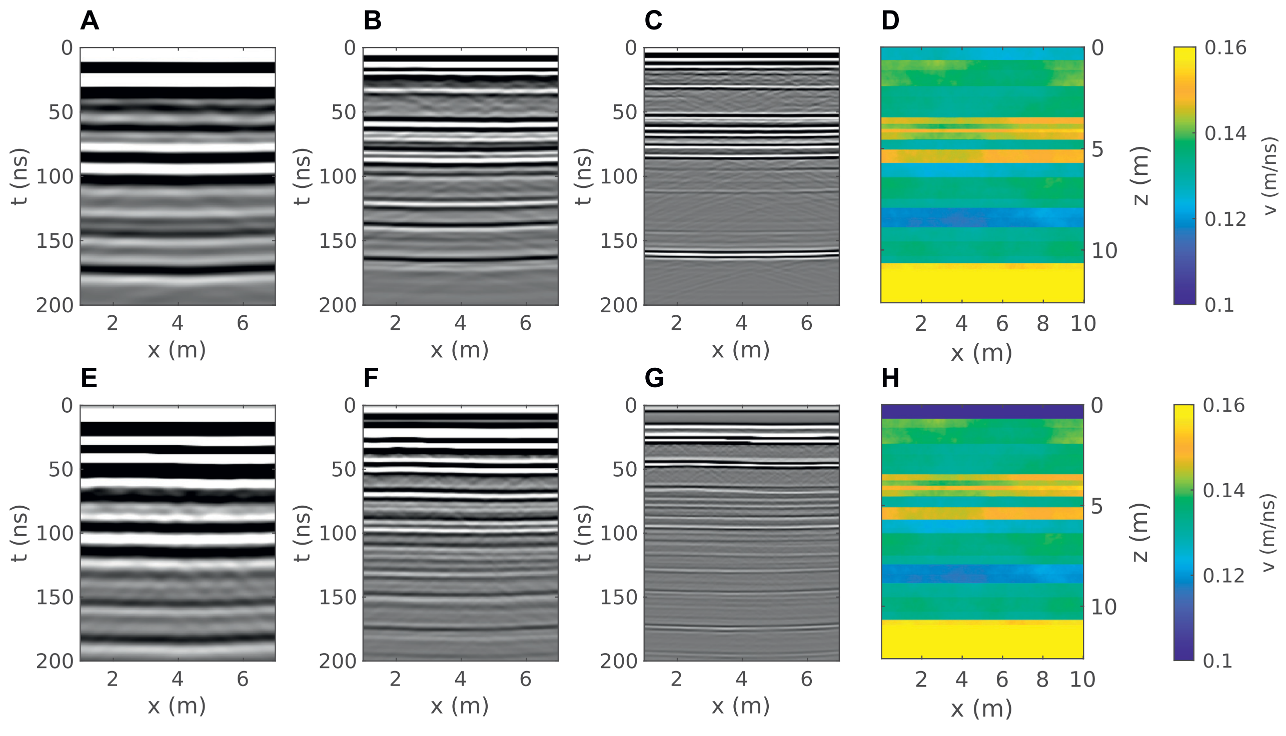

FIGURE 11 | Finite-difference time-domain modeling results for our 2D velocity model for 50 MHz **(A,E)**, 100 MHz **(B,F)**, and 200 MHz **(C,G)** for spring and summer scenarios, respectively. The corresponding velocity models are shown in **(D)** and **(H)**. Both models differ only in the uppermost 60 cm (active layer).

spectral domain, the normalized spectra of both data sets differ less compared to the previous examples (**Figure 9D**). However, the spectrum of the summer data contains, across all frequencies, approximately 25% compared to the spring as demonstrated by the amplitude ratios in **Figure 9C**.

DISCUSSION

Our three presented detailed examples show a loss of resolution from spring to summer and an increased complexity, especially, at the early travel times. In the following, we intend 1) to relate these observations to a wider assessment of the entire data cube, 2) to quantify the differences in the spectral domain, 3) to relate our observations to modeling and physics, and 4) to translate our observations into practical recommendations for future surveys.

Evaluation of Amplitude Spectra

Table 1 summarizes spectral differences between our spring and summer data for eight selected data segments. Segments 1–3 are shown in **Figures 7–9**, respectively. Similar to those, all segments were manually selected and cover the surrounding of distinct reflections in our 3D data. The lateral and vertical position was aligned by visual inspection. Our previous observations of an increased amplitude and resolution in the spring data is confirmed throughout all segments; i.e., the energy ratio (spectral energy in spring related to summer) varies between 1.2 and 3.6. Furthermore, we observe a frequency downshift of our spectral energy, which is quantified by defining a bandwidth criterion based on the percentile 10 and 90 as lower and upper boundary. We notice that the lower bound is generally lower in summer compared to spring. Furthermore, our upper bandwidth bound exhibits generally smaller frequencies in summer. Thus, our earlier described subjective interpretation of smoother images in summer can be expressed as a mean frequency downshift of 9 MHz in and a mean bandwidth narrowing of 5 MHz.

However, our observations may be partly related to our assumptions during data processing. For a more fair approach in terms of data interpretation, we calculate our spectral attributes on migrated data, incorporating a velocity model of the subsurface. For summer data our assumptions are likely to diverge stronger from the *in situ* GPR velocities (e.g., due to small-scale wetness heterogeneities in the active layer), leading to a weaker focusing of diffracted energy and a smoother appearance of reflections.

Several loss mechanisms affect an electromagnetic wave during propagation. These comprise spherical spreading, geometrical loss due to refraction, and intrinsic attenuation.

The loss due to spherical divergence results from the enlarging spherical surface of the electromagnetic pulse as the electromagnetic wave propagates concentrically away from the transmitter. Once emitted, the electromagnetic energy per surface element decreases with $1/t^2$ assuming a constant wavelength (i.e., constant propagation velocity).

Focusing effects at refraction interfaces result in geometrical loss (Bogorodsky et al., 1985). Here, due to the transition in another medium, the electromagnetic wavelength is altered resulting in an abrupt increase in electromagnetic energy per surface element (focusing effect for $v_2 < v_1$, i.e., if the velocity of the underlying layer is smaller) or an energy decrease (defocusing for $v_2 > v_1$). We calculate the radius of the first Fresnel Zone along an exemplary ray path and estimate a geometrical loss of −7 dB in summer with respect to spring at the lower boundary of the active layer.

Another signal loss mechanism we expect to differ in spring and summer is the intrinsic attenuation due to relaxation mechanism and electrical conduction. The intrinsic attenuation $\alpha[\frac{dB}{m}]$ is calculated in the wave regime ($\sigma \ll \omega\varepsilon$) as

$$\alpha = 8.68 \cdot \frac{\sigma}{2}\sqrt{\mu/\varepsilon}$$

with the electrical conductivity $\sigma = \frac{1}{\rho}$, angular frequency $\omega = 2\pi f$, dielectric permittivity $\varepsilon = \varepsilon_r \cdot \varepsilon_0$, vacuum permittivity $\varepsilon_0 \approx 8.854 \cdot 10^{-12}\frac{F}{m}$, magnetic permeability $\mu = \mu_r\mu_0$, vacuum permeability $\mu_0 = 4\pi 10^{-7}\frac{H}{m}$ and the electrical resistivity ρ.

We estimate the intrinsic attenuation for a thawed active layer using an electrical resistivity of $\rho = 200\Omega m$ and a relative permittivity of $\varepsilon_r = 25$. We observed both values in summer 2014 by electrical resistivity tomography and common midpoint GPR data, respectively. We choose a electrical resistivity of $\rho = 5000\Omega m$ and a relative permittivity of $\varepsilon_r = 5$ to estimate the intrinsic attenuation for a frozen layer. In both cases, we consider a relative permeability of $\mu_r = 1$. In total, we estimate a loss due to intrinsic attenuation of −2 dB/m in summer with respect to spring.

Thus, we relate our observed increase in energy loss from spring to summer dominantly to the strong electric contrast in summer and only to a minor part to the increase in electrical conductivity.

2D Finite-Difference Time-Domain Modelling

In the following, we use finite-difference time-domain (FDTD) modelling (Warren et al., 2016) to verify our observations in terms of synthetic 2D GPR data for our two scenarios. We rely our model on the borehole-based L14-02 ice content data (Schwamborn and Wetterich, 2016) shown in **Figure 10A**; i.e., a sediment core that was drilled during the spring survey in 2014 (for borehole location see **Figures 1**, **3**). Taking into account typical bulk density values for Yedoma Ice Complex deposits (Strauss et al., 2013) and a two-phase CRIM model (Birchak et al., 1974), we calculate volumetric ice contents and the corresponding 1D GPR velocity function. We duplicate our 1D velocity function laterally and multiply the resulting 2D velocity field with a 2D noise model exhibiting small-scale heterogeneities (**Figure 10B**) to obtain our final 2D GPR velocity function. **Figure 10C** shows a vertical profile through our resulting velocity model, with the calculated velocity profile in black and the resulting velocity range for each depth in red.

Figure 11 shows our 2D FDTD modeling results for both the spring and the summer scenarios using source wavelets with center frequencies of 50, 100, and 200 MHz, respectively. All data are calculated for an antenna offset of 1 m. We applied an t^2 amplitude scaling to correct for spherical divergence. For our synthetic spring scenario, the active layer is only resolved in the 200 MHz data. In 50 MHz and 100 MHz data the reflection of the lower active layer base is not visible due to the larger wavelength and antenna crosstalk. In contrast, the active layer bottom is detected at 100 MHz in the summer scenario due to the lower active layer GPR velocity. At ~4.5–5.25 m depth, our velocity model exhibits a sequence of high velocity layers with thicknesses below 0.25 m. The sequence is resolved in the spring and the summer scenario at 100 and 200 MHz (with a different degree of detail), and integrated to a single reflector in our 50 MHz data due to the larger wavelength. A layer with lower GPR velocity at a depth of ~8.5 m is resolved in both spring and summer data at 100 and 200 MHz in terms of two-sided reflections. For the 50 MHz data, this layer is only resolved as a single reflector. The transition to a massive ground ice body at a depth of z ~ 11 m is resolved with all frequencies.

Although the number of resolved layers remains equal for each frequency, all layers resolved in our synthetic spring data are also resolved in our summer data. However, the spring data generally exhibit a higher contrast below the active layer, resulting in an easier interpretation and tracing of particular interfaces. For active layer imaging, an effective antenna mid-frequency of at least 100 MHz is recommended in summer and at least 200 MHz in spring.

SUMMARY

For the first time, comparative 3D GPR observations have been undertaken at the same study area to point out advantages and disadvantages for deducing subsurface permafrost properties under completely frozen (springtime) and superficially thawed (summertime) conditions. Both datasets were collected using a nominal center frequency of 100 MHz. Summer GPR data differ from those obtained during spring due to the presence of an uppermost seasonally thawed active layer. This is seen in more complex waveform patterns at early times (i.e., $t < 60$ ns) in the summer data and results from interference between antenna crosstalk and reflected energy from the active layer base, while the spring data exhibit dominantly antenna crosstalk and less interference with reflected energy resulting in a less complex early time wavefield.

When comparing the surroundings of selected reflections recorded in summer and spring at different depths, the spring data show a higher dynamic range in amplitudes and a higher vertical resolution, resulting in a generally sharper image of subsurface structures, and the denoted reflectors appear more distinct. In contrast, the summer images provide a lower dynamic range and lower vertical resolution resulting in a smoother image of subsurface structures. This might ease reflector tracing and picking, but hinders a detailed imaging and interpretation as using the spring data.

Spectra of both data sets normalized to their respective total energy provide a consistent picture and differ much less than those of specific spring and summer reflection details. However, the spectra of our migrated summer data only contain around 40% of the energy compared to the spring data and also show a mean frequency downshift and bandwidth narrowing. We relate our observations dominantly to the strong increase in permittivity contrast at the active layer base in summer, but also to the increased superficial heterogeneity, causing our velocity model to deviate more likely from the actual *in situ* velocities. Although we show dominantly 2D data, a 3D survey setup is very important to ensure a successful migration by taking off-profile diffracted energy into account.

Due to topographic dynamics from season to season, we point out that combining datasets of different years will be challenging. Furthermore, a joint processing of data acquired at different seasons is not recommended. When interested in a larger picture of general reflectors of distinct (cryostratigraphic) units, which shall be traced in 3D, we recommend to perform the survey in summer to benefit from the smoother data. If active layer imaging is of major interest, we suggest an effective antenna mid-frequency of at least 100 MHz in summer and at least 200 MHz in spring, based on our modeling result. If detailed structural information is relevant and the object of interest is at the edge of resolution capabilities, we recommend performing the survey in spring. Thus, it is ensured to get the best performance with the drawback of more complex interpretation and higher surveying effort (e.g., related to lower battery performance and harsher conditions for field work).

DATA AVAILABILITY STATEMENT

The datasets presented in this study can be found in online repositories. The names of the repository/repositories and accession number(s) can be found below: The datasets analyzed for this study can be found in the PANGAEA data repository (https://doi.org/10.1594/PANGAEA.868978, https://doi.org/10.1594/PANGAEA.859798).

AUTHOR CONTRIBUTIONS

SS and JT contributed to conception of the study and acquired the survey data. SW, GS, and LS conducted sediment sampling and analysis. SS wrote the first draft of the manuscript. SW wrote the section survey site. All authors contributed to manuscript revision, read, and approved the submitted manuscript.

FUNDING

We gratefully acknowledge the German Federal Ministry of Education and Research (BMBF) for funding this study as part of the CARBOPERM project (03G0836B, 03G0836J).

ACKNOWLEDGMENTS

We thank M. Dubnitzki, W. Schneider, and V. Zykov for technical and logistical support. Furthermore, we thank N. Allroggen for his support in acquiring the spring data set and two reviewers for their valuable comments on the manuscript.

SUPPLEMENTARY MATERIAL

The Supplementary Material for this article can be found online at: https://www.frontiersin.org/articles/10.3389/feart.2022.741524/full#supplementary-material

REFERENCES

Allroggen, N., Tronicke, J., Delock, M., and Böniger, U. (2015). Topographic Migration of 2D and 3D Ground-penetrating Radar Data Considering Variable Velocities. *Near Surf. Geophys.* 13, 253–259. doi:10.3997/1873-0604.2014037

AMAP (2021). *Arctic Climate Change Update 2021: Key Trends and Impacts. Summary for Policy-makersArctic Monitoring and Assessment Programme (AMAP)*. Tromsø, Norway, 16.

Andreev, A. A., Grosse, G., Schirrmeister, L., Kuznetsova, T. V., Kuzmina, S. A., Bobrov, A. A., et al. (2009). Weichselian and Holocene Palaeoenvironmental History of the Bol'shoy Lyakhovsky Island, New Siberian Archipelago, Arctic Siberia. *Boreas* 38, 72–110. doi:10.1111/j.1502-3885.2008.00039.x

Andreev, A. A., Schirrmeister, L., Tarasov, P. E., Ganopolski, A., Brovkin, V., Siegert, C., et al. (2011). Vegetation and Climate History in the Laptev Sea Region (Arctic Siberia) during Late Quaternary Inferred from Pollen Records. *Quat. Sci. Rev.* 30, 2182–2199. doi:10.1016/j.quascirev.2010.12.026

Andreev, A., Grosse, G., Schirrmeister, L., Kuzmina, S., Novenko, E., Bobrov, A., et al. (2004). Late Saalian and Eemian Palaeoenvironmental History of the Bol'shoy Lyakhovsky Island (Laptev Sea Region, Arctic Siberia). *Boreas* 33, 319–348. doi:10.1111/j.1502-3885.2004.tb01244.x

Arkhangelov, A. A., Mikhalev, D. V., and Nikolaev, V. I. (1996). "About Early Epochs of Permafrost Formation in Northern Yakutia and Age of Ancient Relicts of Underground Glaciation," in *Razvitie Oblasti Mnnogoletnei Merzloty I Periglyatsial'noi Zony Severnoi Evrazii I Usloviya Rasseleniya Drev- Nego Cheloveka*. Editors A. A. Velichko, A. A. Arkhangelov, O. K. Borisova, Y. N. Gribchenko, A. N. Drenova, E. M. Zelikson, et al. (Moscow: Institute of Geography), 102–109. (in Russian).

Birchak, J. R., Gardner, C. G., Hipp, J. E., and Victor, J. M. (1974). High Dielectric Constant Microwave Probes for Sensing Soil Moisture. *Proc. IEEE* 62, 93–98. doi:10.1109/PROC.1974.9388

Biskaborn, B. K., Smith, S. L., Noetzli, J., Matthes, H., Vieira, G., Streletskiy, D. A., et al. (2019). Permafrost Is Warming at a Global Scale. *Nat. Commun.* 10, 1–264. doi:10.1038/s41467-018-08240-4

Bogorodsky, V. V., Bentley, C. R., and Gudmansen, P. E. (1985). *Radioglaciology, Glaciology and Quaternary Geology*. Dodrecht, Holland: D. Reidel Publishing Company.

Boniger, U., and Tronicke, J. (2010). On the Potential of Kinematic GPR Surveying Using a Self-Tracking Total Station: Evaluating System Crosstalk and Latency. *IEEE Trans. Geosci. Remote Sensing* 48, 3792–3798. doi:10.1109/TGRS.2010.2048332

Brosten, T. R., Bradford, J. H., McNamara, J. P., Gooseff, M. N., Zarnetske, J. P., Bowden, W. B., et al. (2009). Estimating 3D Variation in Active-Layer Thickness beneath Arctic Streams Using Ground-Penetrating Radar. *J. Hydrol.* 373, 479–486. doi:10.1016/j.jhydrol.2009.05.011

Bunge, A. A. (1887). "Bericht ueber den ferneren Gang der Expedition. Reise nach den Neusibirischen Inseln. Aufenthalt auf der Grossen Ljachof-Insel," in *Expedition zu den Neusibirischen Inseln und dem Jana-Lande (1885). Beitraege zur Kenntnis des russischen Reiches und der angrenzenden Laender*. Editors L. V. Schrenk and C. J. Maximovicz, III, 231–284. (in German).

Campbell, S., Affleck, R. T., and Sinclair, S. (2018). Ground-penetrating Radar Studies of Permafrost, Periglacial, and Near-Surface Geology at McMurdo Station, Antarctica. *Cold Regions Sci. Tech.* 148, 38–49. doi:10.1016/j.coldregions.2017.12.008

GISTEMP Team (2021). GISS Surface Temperature Analysis (GISTEMP), Version 4. NASA Goddard Institute for Space Studies. Dataset. Available at: data.giss.nasa.gov/gistemp/(accessed 05 01, 2021).

Grigoreva, S. D., Kiniabaeva, E. R., Kuznetsova, M. R., Popov, S. V., and Kashkevich, M. P. (2020). Examples of Application of GPR for Ensuring Safety of Infrastructure Objects at the Area of the Russian Antarctic Station Progress (East Antarctica). *Proc. EAGE Eng. Mining Geophys.* 2020, 1–11. doi:10.3997/2214-4609.202051010

Koven, C. D., Schuur, E. A. G., Schädel, C., Bohn, T. J., Burke, E. J., Chen, G., et al. (2015). A Simplified, Data-Constrained Approach to Estimate the Permafrost Carbon-Climate Feedback. *Phil. Trans. R. Soc. A.* 373, 205420140423. doi:10.1098/rsta.2014.0423

Kunitsky, V. V. (1998). "Ice Complex and Cryoplanation Terraces of Bol'shoy Lyakhovsky Island," in *Problems of Geocryology. Collected Papers*. Editors R. M. Kamensky, V. V. Kunitsky, B. A. Olovin, and V. V. Shepelev (Yakutsk: RAS, Permafrost Institute), 60–72. (in Russian).

Meredith, M., Sommerkorn, M., Cassotta, S., Derksen, C., Ekaykin, A., Hollowed, A., et al. (2019). "Polar Regions," in *IPCC Special Report on the Ocean and Cryosphere in a Changing Climate*. Editors H. O. Pörtner, D. C. Roberts, V. Masson-Delmotte, P. Zhai, M. Tignor, E. Poloczanska, et al. In press. accessed on 2021-05-22. https://www.ipcc.ch/srocc/chapter/chapter-3-2/.

Nagaoka, D. (1994). "Properties of Ice Complex Deposits in Eastern Siberia," in Proceedings of the 2nd Symposium on the Joint Siberian Permafrost Studies between Japan and Russia in 1993, Tsukuba, Japan, 14–18.

Nagaoka, D., Saijo, K., and Fukuda, M. (1995). "Sedimental Environment of the Edoma in High Arctic Eastern Siberia," in Proceedings of the 3rd Symposium on the Joint Siberian Permafrost Studies between Japan and Russia, Tsukuba, Japan. Editors K. Takahashi, A. Osawa, and Y. Kanazawa (Hokkaido University), 8–13.

Oezen, L. D., and Geyh, M. A. (2002). 230Th/U Dating of Frozen Peat, Bol'shoy Lyakhovsky Island (Northern Siberia). *Quat. Res.* 57, 253–258. doi:10.1006/qres.2001.2306

Romanovskii, N. N. (1958a). New Data about Quaternary Deposits Structure on the Bol'shoy Lyakhovsky Island (Novosibirskie Islands). *Nauchnye Doklady Vysshei Shkoly. Seriya Geologo-geograficheskaya* 2, 243–248. (in Russian).

Romanovskii, N. N. (1958b). "Paleogeographic Conditions of Formation of the Quaternary Deposits on Bol'shoy Lyakhovsky Island (Novosibirskie Islands)," in *Voprosy Fizicheskoi Geografii Polyarnykh Stran. Vypysk I*. Editor V. G. Bogorov (Moscow: Moscow State University), 80–88. (in Russian).

Romanovskii, N. N. (1958c). Permafrost Structures in Quaternary Deposits. *Nauchnye Doklady Vysshei Shkoly. Seriya Geologo-geograficheskaya* 3, 185–189. (in Russian).

Schennen, S., Allroggen, N., and Tronicke, J. (2015). "Near Surface Geophysics," *Russian-German Cooperation CARBOPERM: Field Campaigns to Bol'shoy Lyakhovsky Island in 2014*. Editors G. Schwamborn and S. Wetterich Reports on Polar and marine Research 686, 48–63. doi:10.2312/BzPM_0686_2015

Schennen, S., Tronicke, J., Wetterich, S., Allroggen, N., Schwamborn, G., and Schirrmeister, L. (2016). 3D Ground-Penetrating Radar Imaging of Ice Complex Deposits in Northern East Siberia. *Geophysics* 81 (1), WA195–WA202. doi:10.1190/geo2015-0129.1

Schirrmeister, L., Oezen, D., and Geyh, M. A. (2002). 230Th/U Dating of Frozen Peat, Bol'shoy Lyakhovsky Island (Northern Siberia). *Quaternary Research* 57, 253–258. doi:10.1006/qres.2001.2306

Schmid, L., Heilig, A., Mitterer, C., Schweizer, J., Maurer, H., Okorn, R., et al. (2014). Continuous Snowpack Monitoring Using Upward-Looking Ground-Penetrating Radar Technology. *J. Glaciol.* 60, 509–525. doi:10.3189/2014JoG13J084

Schwamborn, G. J., Dix, J. K., Bull, J. M., and Rachold, V. (2002). High-resolution Seismic and Ground Penetrating Radar-Geophysical Profiling of a Thermokarst lake in the Western Lena Delta, Northern Siberia. *Permafrost Periglac. Process.* 13 (4), 259–269. doi:10.1002/ppp.430

Schwamborn, G., Heinzel, J., and Schirrmeister, L. (2008a). Internal Characteristics of Ice-Marginal Sediments Deduced from Georadar Profiling and Sediment Properties (Brøgger Peninsula, Svalbard). *Geomorphology* 95, 74–83. doi:10.1016/j.geomorph.2006.07.032

Schwamborn, G., Wagner, D., and Hubberten, H.-W. (2008b). The Use of GPR to Detect Active Layers in Young Periglacial Terrain of Livingston Island, Maritime Antarctica. *Near Surf. Geophys.* 6, 331–336. doi:10.3997/1873-0604.2008008

Schwamborn, G., and Wetterich, S. (2016). *Geochemistry and Physical Properties of Permafrost Core L14-02*. PANGAEA. doi:10.1594/PANGAEA.868978

Strauss, J., Schirrmeister, L., Grosse, G., Fortier, D., Hugelius, G., Knoblauch, C., et al. (2017). Deep Yedoma Permafrost: A Synthesis of Depositional Characteristics and Carbon Vulnerability. *Earth-Science Rev.* 172, 75–86. doi:10.1016/j.earscirev.2017.07.007

Strauss, J., Schirrmeister, L., Grosse, G., Wetterich, S., Ulrich, M., Herzschuh, U., et al. (2013). The Deep Permafrost Carbon Pool of the Yedoma Region in Siberia and Alaska. *Geophys. Res. Lett.* 40, 6165–6170. doi:10.1002/2013gl058088

Tumskoy, V. E. (2012). Osobennosti Kriolitogeneza Otlozhenii Severnoi Yakutii V Srednem Neopleistotsene-Golotsene (Peculiarities of Cryolithogenesis in

Northern Yakutia from the Middle Neopleistocene to the Holocene). *Kriosfera Zemli* 16, 12–21. (in Russian).
von Toll, E. V. (1897). Iskopaemye Ledniki Novo-Sibirskikh Ostrovov, Ikh Otnoshenie K Trupam Mamontov I K Lednikovomu Periodu (Ancient Glaciers of New Siberian Islands, Their Relation to mammoth Corpses and the Glacial Period). *Zapiski Imperatorskogo Russkogo Geograficheskogo Obshestvapo Obshei Geografii (Notes of the Russian Imperial Geographical Society)* 32, 1–137.
Warren, C., Giannopoulos, A., and Giannakis, I. (2016). gprMax: Open Source Software to Simulate Electromagnetic Wave Propagation for Ground Penetrating Radar. *Comp. Phys. Commun.* 209, 163–170. doi:10.1016/j.cpc.2016.08.020
Wetterich, S., Meyer, H., Fritz, M., Mollenhauer, G., Rethemeyer, J., Kizyakov, A., et al. (2021). Northeast Siberian Permafrost Ice-Wedge Stable Isotopes Depict Pronounced Last Glacial Maximum Winter Cooling. *Geophys. Res. Lett.* 48, e2020GL092087. doi:10.1029/2020GL092087
Wetterich, S., Rudaya, N., Kuznetsov, V., Maksimov, F., Opel, T., Meyer, H., et al. (2019). Ice Complex Formation on Bol'shoy Lyakhovsky Island (New Siberian Archipelago, East Siberian Arctic) since about 200 ka. *Quat. Res.* 92 (2), 530–548. doi:10.1017/qua.2019.6
Wetterich, S., Rudaya, N., Tumskoy, V., Andreev, A. A., Opel, T., Schirrmeister, L., et al. (2011). Last Glacial Maximum Records in Permafrost of the East Siberian Arctic. *Quat. Sci. Rev.* 30, 3139–3151. doi:10.1016/j.quascirev.2011.07.020
Wetterich, S., Schirrmeister, L., Andreev, A. A., Pudenz, M., Plessen, B., Meyer, H., et al. (2009). Eemian and Late Glacial/Holocene Palaeoenvironmental Records from Permafrost Sequences at the Dmitry Laptev Strait (NE Siberia, Russia). *Palaeogeogr. Palaeoclimatol. Palaeoecol.* 279, 73–95. doi:10.1016/j.palaeo.2009.05.002
Wetterich, S., Tumskoy, V., Rudaya, N., Andreev, A. A., Opel, T., Meyer, H., et al. (2014). Ice Complex Formation in Arctic East Siberia during the MIS3 Interstadial. *Quat. Sci. Rev.* 84, 39–55. doi:10.1016/j.quascirev.2013.11.009
Wetterich, S., Tumskoy, V., Rudaya, N., Kuznetsov, V., Maksimov, F., Opel, T., et al. (2016). Ice Complex Permafrost of MIS5 Age in the Dmitry Laptev Strait Coastal Region (East Siberian Arctic). *Quat. Sci. Rev.* 147, 298–311. doi:10.1016/j.quascirev.2015.11.016
Yoshikawa, K., Leuschen, C., Ikeda, A., Harada, K., Gogineni, P., Hoekstra, P., et al. (2006). Comparison of Geophysical Investigations for Detection of Massive Ground Ice (Pingo Ice). *J. Geophys. Res.* 111, E06S19. doi:10.1029/2005JE002573
Zimmermann, H., Raschke, E., Epp, L., Stoof-Leichsenring, K., Schirrmeister, L., Schwamborn, G., et al. (2017). The History of Tree and Shrub Taxa on Bol'shoy Lyakhovsky Island (New Siberian Archipelago) since the Last Interglacial Uncovered by Sedimentary Ancient DNA and Pollen Data. *Genes* 8, 273E273. doi:10.3390/genes8100273

Conflict of Interest: The authors declare that the research was conducted in the absence of any commercial or financial relationships that could be construed as a potential conflict of interest.

The handling editor and the reviewer AV are currently organizing a Research Topic with the author LS.

Publisher's Note: All claims expressed in this article are solely those of the authors and do not necessarily represent those of their affiliated organizations, or those of the publisher, the editors, and the reviewers. Any product that may be evaluated in this article, or claim that may be made by its manufacturer, is not guaranteed or endorsed by the publisher.

frontiers | Frontiers in Earth Science

ORIGINAL RESEARCH
published: 04 May 2022
doi: 10.3389/feart.2022.789421

Cryolithostratigraphy of the Middle Pleistocene to Holocene Deposits in the Dmitry Laptev Strait, Northern Yakutia

Vladimir Tumskoy[1,2] and Tatiana Kuznetsova[3]**

[1]Laboratory of General Geocryology, Melnikov Permafrost Institute SB RAS, Yakutsk, Russia, [2]Pacific Oceanological Institute, Russian Academy of Sciences, Vladivostok, Russia, [3]Department of Paleontology, Faculty of Geology, Lomonosov Moscow State University, Moscow, Russia

OPEN ACCESS

Edited by:
Alexandra Veremeeva, Institute of Physical-Chemical and Biological Problems in Soil Science (RAS), Russia

Reviewed by:
Thomas Opel, Alfred Wegener Institute Helmholtz Centre for Polar and Marine Research (AWI), Germany
J. Murton, University of Sussex, United Kingdom

***Correspondence:**
Vladimir E. Tumskoy
vtumskoy@gmail.com
Tatiana V. Kuznetsova
tatkuz2012@mail.ru

Specialty section:
This article was submitted to Cryospheric Sciences, a section of the journal Frontiers in Earth Science

Received: *04 October 2021*
Accepted: *05 April 2022*
Published: *04 May 2022*

Citation:
Tumskoy V and Kuznetsova T (2022) Cryolithostratigraphy of the Middle Pleistocene to Holocene Deposits in the Dmitry Laptev Strait, Northern Yakutia. Front. Earth Sci. 10:789421. doi: 10.3389/feart.2022.789421

The northernmost part of continental Yakutia in the Dmitry Laptev Strait region developed under non-glacial conditions during the Quaternary period. During cooling periods, ice-rich deposits with syngenetic ice wedges, called the Ice Complex, formed here. During periods of warming, they partially thawed under thermokarst lakes and a peculiar complex of lacustrine-boggy deposits (the Alas Complex) was formed. The article presents a description of ice-rich deposit sequences in several Ice Complex horizons and their transformation in lake taliks from the Middle Pleistocene to the Holocene (MIS 7—MIS 1). The Oyogos Yar section structure is considered as an example using additional geological data from the southern coast of Bol'shoy Lyakhovsky Island. Specific examples show the results of changes in the structure of sections via cryogenic processes—ice wedge formation and thawing. We confirm that cryogenic processes are important factors, along with accumulation and erosion processes, which change the geological and cryolithological structure of the sections. It is shown that to clearly understand the stratigraphic subdivision of Quarternary deposits in areas of Ice Complex development, geological and analytical studies of the sections are insufficient; an elucidation of the sequence of sediment freezing and thawing and the resulting cryolithogical phenomena is necessary.

Keywords: cryostratigraphy, Late Pleistocene, Yedoma ice complex, Oyogos Yar, Dmitry Laptev Strait

INTRODUCTION

The Arctic coast of Yakutia has long been known for findings of the remains of mammoth fauna mammals. The existence of low-temperature permafrost during almost the entire Quaternary Period contributed to quick burying of dead animals and their good preservation for thousands of years. The overwhelming majority of findings of large mammal remains were made in ice-rich Yedoma deposits with thick ice wedges (Kuznetsova and Starodubtseva, 2009). In the middle of the 20th century, these remains were recognized as constituting their own layer, named the "Mammoth Horizon" (Gusev, 1958). A few years later, this horizon was renamed the Yedoma Suite (Vas'kovsky, 1963), after which "Yedoma" became a generic term for such deposits (Schirrmeister et al., 2013). Unique findings of representative mammoth fauna remains from yedoma deposits take place almost every year, including at Oyogos Yar. For example, in 2009, the well-preserved body of a mammoth named Yuka was found here (Boeskorov et al., 2012, 2013).

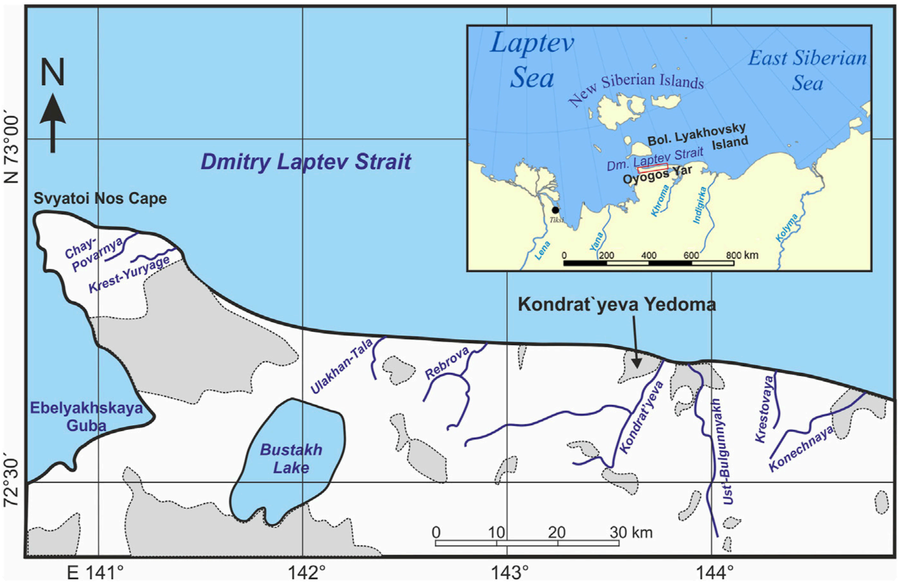

FIGURE 1 | Location map of the study region. The gray areas with dotted outlines are Yedoma highlands.

Oyogos Yar refers to the southern coast of the Dmitry Laptev Strait, which connects the Laptev and East Siberian seas and is 50–60 km wide (**Figure 1**). In the west, it begins at Cape Svyatoy Nos and stretches for 106 km eastward to the mouth of the Kondrat`yeva River. In the east, Oyogos Yar ended 6 km to east from the mouth of Konechnaya River. Several rivers fall into the sea over the entire stretch of Oyogos Yar. The longest of them—the Kondrat`yeva River—is only about 50 km long.

The steep coastal cliffs near Cape Svyatoy Nos are several dozen meters high. They are composed of Cretaceous volcanogenic-depositional formations (Prokhorova and Ivanov, 1973). From the cape east to the mouth of the Chay-Povarnya River, the cliffs become less steep and lose height. To the east of the Krest-Yuryage River, the surface level near the coast gradually drops; only frozen loose Quaternary deposits are present in this section. The coastal zone at this site resembles large bottoms of drained thermokarst lakes, which have merged to form alases. Individual uplands called "yedoma" (gray areas on **Figure 1**) rise among them. On sites where the coastline intersects the alases, the height of the coastal cliff is 10–15 m. The yedoma uplands reach a height of 30–40 m, forming higher and often terraced cliffs, but there are only a few such places along the coast. In the western part of Oyogos Yar, the yedoma meets the seacoast to the east of the Krest-Yuryage River mouth for a stretch of about 6 km. A small yedoma upland is located 5 km east of the Rebrova River mouth; here, the mammoth named Yuka was found in the upland's lower cliff (Boeskorov et al., 2012, 2013). The largest yedoma upland, located west of the Kondrat`yeva River, stretches along the coast for about 5 km. We will henceforth call it the Kondrat`yeva Yedoma (**Figure 1**). Its maximum height is 41 m above sea level (a.s.l). There are two more yedomas to the east, near the mouths of the Ust-Bulgunnyakh and Konechnaya rivers.

Despite the long history of research at Oyogos Yar, there is still no agreement on the age, origin, and even sedimentation conditions of the deposits exposed in its outcrops. This is explained by the location of the cliff's deposits within a zone of continuous syncryogenic permafrost with a high volumetric ice content, reaching 80%–90% in places. The history of the geological development of these deposits in the Pleistocene and Holocene includes not only stages of deposition and erosion but also periods of cryogenic transformation (freezing and thawing), which significantly changed not only the composition and structure of the deposits but also their deposition conditions. Currently, continuous permafrost 500–700 m deep with a mean ground temperature of −11 to −10°C at a depth of 15–20 m is distributed in the Oyogos Yar area (Geocryology of USSR, 1989).

The goal of the present article is to discuss contemporary understandings of the cryolithological structure and stratigraphy (cryolithostratigraphy) of the Oyogos Yar coast Quarternary deposits.

PREVIOUS RESEARCH HISTORY

Oyogos Yar has been known since the times when the Cossacks developed the Siberian north (the first half of the 17th century), but geological research in this area began in the first half of the 19th century with studies of the southern coast of Bol'shoy Lyakhovsky Island and more northern islands. From the beginning of the 19th century to the middle of the 20th century, this region has seen the geographical and geological expeditions of M.I. Gedenshtrom (1830), P.F. Anzhu (1849), A.A. Bunge (1887), E.V. Toll (1897), K.A. Vollosovich (1930), and M.M. Ermolaev (1932). Their research revealed a wide

TABLE 1 | Local stratigraphic chart of the Dmitry Laptev Strait region Middle Pleistocene–Holocene deposits and the correlation of these deposits with general and regional stratigraphic scales.

General stratigraphic chart			Marine isotopic stages (MIS) (Pillans, Gibbard, 2012)	Age, ka	Regional stratigraphic chart of the north-east of Siberia (Resheniya, 1987)		Local stratigraphic chart of the dmitry Laptev Strait area	Cryostratigraphic type of deposits	
Period	Epoch	Stage	1		Modern		Holocene (Hal)	alas complex and other deposits	
Quaternary	Holocene			11,7	Yedoma superhorizon	Sartan	Yana suite (Van)	Ice Complex	
	Pleistocene	Upper	2	29		Molotkov	Oyogos suite (01^{1}9)	Ice Complex	
			3	57		Oyogos			
			4	71	Kazantsev		Krest-Yurukh suite (KrY)	alas complex	
			5	126					
							Bychchagy suite (Bch)	Ice Complex	
		Middle	6	191	Keremesit superhorizon		Kuchchugui suite (Kch)	Syncryogenic cryofacies (Kch-S)	tabler cycofaciess (Kch-T)
			7	243			Zimov'e layer (Zim)	alas complex and relic active layer	
			8	301			Yukagir suite (Yuk)	Ice Complex	

distribution of thick ground ice in this area and the presence of a great number of mammoth fauna mammal bones in the permafrost.

Astronomer E. F. Skvortsov and topographer N. A. Iyudin completed the first detailed description and topographic survey of Oyogos Yar in 1909 (Skvortsov, 1914, 1930). After this, over the course of many years, researchers who visited Northern Yakutia did not work at the cliff itself. Until the end of the 1950's, understanding of the stratigraphy and structure of Quaternary deposits in the Dmitry Laptev Strait area was based on data obtained on the New Siberian Islands and was described in a series of general works (Grigoriev, 1932; Spizharskiy, 1940; Saks, 1948; Lobanov, 1957; Zagorskaya, 1959).

The upper ice-rich horizon of Dmitry Laptev Strait area deposits was considered to be a result of the existence of a specific type of slow-moving glaciation, termed the Novosibirsk type, in the Pleistocene (Toll, 1897), which was transformed during the Holocene. According to Ermolaev (1932), its remains were called "ice facies", which formed low watersheds, and the local depressions dividing them were called "aly facies". Presently, such watersheds are called yedoma, while the depressions between them are called alas basins (drained thermokarst depression). In 1958, Gusev proposed a stratigraphic coastal lowland column (Yana-Indigirka and Kolyma lowlands together), which identified for the first time a "mammoth horizon" occupying a particular stratigraphic position and connecting the bone-bearing layers with the main masses of ground ice, which Gusev considered fossil aufeis (Gusev, 1958).

Geological data on the age and structure of Oyogos Yar Quaternary deposits, which have not lost their value to this day, were obtained during the work of a thematic expedition of the Permafrost Institute of the Academy of Sciences of the Soviet Union in 1952–53. The work was conducted in the valley of the Yana and Indigirka rivers under the leadership of P.A. Shumskiy, N.F. Grigoriev, and P.F. Shvetsov. In the spring of 1953, a group formed by N. F. Grigoriev and T. P. Kuznetsova inspected Oyogos Yar and the southern coast of Bol'shoy Lyakhovsky Island (Kuznetsova, 1965). As a result of this reconnaissance work, deposits occurring under ice-bearing layers of the yedoma "mammoth horizon", represented by loams with faint wavy horizontal layering, were described for the first time. It was proven for the first time that the main mass of ground ice in the Yana-Indigirka Lowland of Yakutia is represented by ice wedges, rather than by glacial ice. As a result, a working chart of Quaternary deposit stratigraphy was proposed (Vtyurin et al., 1957), which matched M.M. Ermolaev's chart.

N. N. Romanovskii worked on the Complex Physical-Geographical Expedition of the Arctic Research Institute in 1956 and on the expedition of the Geological Research Institute (NIIGA) in 1957. He was the first to describe in detail the frozen deposits and ground ice outcrops of the southern Bol'shoy Lyakhovsky Island coast and the western part of Oyogos Yar (Romanovskii, 1958; 1961a,b). N. N. Romanovskii was the first to consider the Quaternary deposits of this region from the perspective of their cryostratigraphy. He described in detail the low ice-content

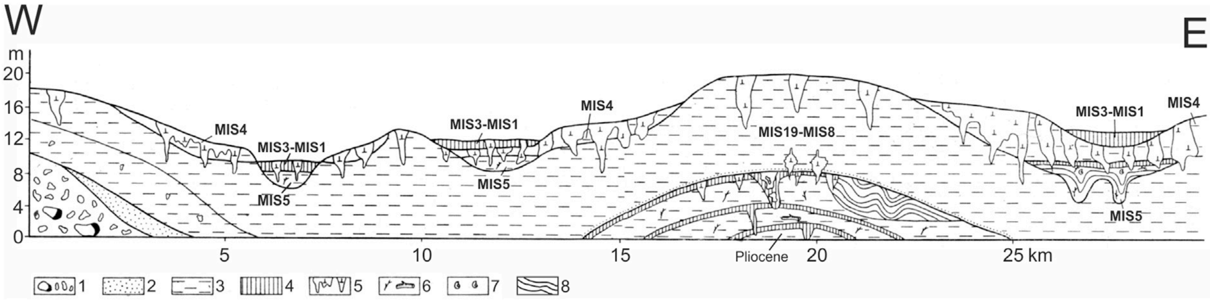

FIGURE 2 | Schematic section of deposits in the Oyogos Yar outcrop (Konishchev and Kolesnikov, 1981). Legend: 1—coarse clastic material; 2—sand; 3—silty loam; 4—peat; 5—ice wedges; 6—plant remains; 7—freshwater mollusk remains; 8—silty loams with lenticular layering. MIS—marine isotope stage.

loam horizon with poorly defined wavy layering, which he attributed to Middle Pleistocene lagoon deposits. Later, V. I. Kayalainen and Yu. N. Kulakov named this horizon the Khromskaya Suite, which, they concluded, has a littoral marine genesis and a mid-Late Quaternary age (Kayalainen and Kulakov, 1965).

N.N. Romanovskii gave particular attention to the contact between lagoon loams and overlying deposits, which was complicated by numerous concave structures that he called "draping permafrost structures" (Romanovskii, 1958) and identified as ice wedge casts. N.N. Romanovskii attributed overlying ice-rich deposits with ice wedges to various facies of floodplain alluvium, while Kayalainen and Kulakov (1965) related them to shoreline marine and lacustrine-boggy deposits connected by a facies transition. The latter authors named these deposits the Oyogos Suite. Its age, based on the findings of *Mammuthus Primigenius,* was determined to be Late Pleistocene.

A significant accomplishment of N. N. Romanovskii is his consideration of the question of thermokarst depression formation and the accumulation of deposits in these basins. He recognized within them taberal, lacustrine, and alas-specific (polygonal-boggy) deposit facies (Romanovskii, 1961a). These facies and related deposits were named the "alas complex" (Kaplina, 2009).

In 1965, around the Svyatoi Nos Cape and to the south, work to estimate the presence of tin was performed by NIIGA researchers S. M. Prokhorova, O. A. Ivanov, S. I. Andreev, and others. As a result, a local stratigraphic column was created (Prokhorova and Ivanov, 1973). According to this column, the remains of mammoth fauna representatives characterize several suites of Middle and Late Pleistocene age at this point. Low ice content loams with wavy layering described earlier were named the Kuchchugui horizon, which combined the Kuchchugui Suite itself in the Dmitry Laptev Strait area, the Khromskaya Suite in the Khroma River basin, and the Allaikhovskaya Suite in the Indigirka River basin. Genesis was viewed as lacustrine-lagoon for the Kuchchugui and Khromskaya suites and alluvial for the Allaikhovskaya Suite, following Lavrushin (1963). Later, by the decision of the Interdepartmental Stratigraphic Committee (Resheniya, 1987), the Kuchchugui horizon was abolished, and the three aforementioned suites were joined into the Keremesit superhorizon (**Table 1**).

For the first time, in this stratigraphic chart, deposits composing draping permafrost structures (as cited in Romanovskii, 1958) were named as an individual subdivision: the Krest-Yuryakh Suite. These deposits were recognized as lacustrine and attributed to the beginning of the Late Pleistocene. All suites represented by morphogenetic ice-rich deposits (Ice Complex) were joined into the Oyogos horizon: Oyogos, Vorontsov, Muskhain, and other suites. They compose the top part of yedomas and contribute to the formation of the third floodplain terrace of the Yana and Indigirka river valleys. Most researchers consider the genesis of these suites' deposits to be alluvial and lacustrine-alluvial, while some have viewed it as eolian (Tomirdiaro, 1980).

In 1977, researchers of the Department of Cryolithology and Glaciology of the Faculty of Geography of Moscow State University, V.N. Konishchev and S. F. Kolesnikov, worked at the Oyogos Yar outcrop, studying its structure and composition (Konishchev and Kolesnikov, 1981). They compiled the first published Oyogos Yar deposits' section (**Figure 2**) and confirmed the exact structure of the section, which had been described earlier by Ivanov (1972).

During the Permafrost Institute's expedition fieldwork at Oyogos Yar, G.F. Gravis obtained the first radiocarbon dates from Oyogos Suite deposits (Gravis, 1978), to which D.K. Bashlavin's dates were later added (Kaplina and Lozhkin, 1982). Six dates from *in situ* peat lenses showed an age from >41,000 (MAG-545) at the base of the suite to 34,200 ± 2,300 (MAG-544) at a height of 30 m above sea level.

In 1993–1994, a joint expedition of the Permafrost Institute of the Siberian Branch of the Russian Academy of Sciences (SB RAS) and the Institute of Low Temperature Science (Sapporo, Japan) worked on the outcrops at the southern coasts of Bol'shoy Lyakhovsky Island and Oyogos Yar. During the work, new radiocarbon dates for peat interlayers in the Oyogos Yar section were obtained. An accelerator mass spectrometry (AMS) date of 22,940 ± 390 (NUTA-3521) was obtained at a depth of 1 m below the surface, and two infinite dates were obtained lower (Nagaoka et al., 1995).

In the mid-1990s, A. A. Arkhangelov found deposits with ice wedges on the southern coast of Bol'shoy Lakhovsky Island, and in the western part of Oyogos Yar, the age of which was estimated to be one million years based on paleomagnetic data and the results of

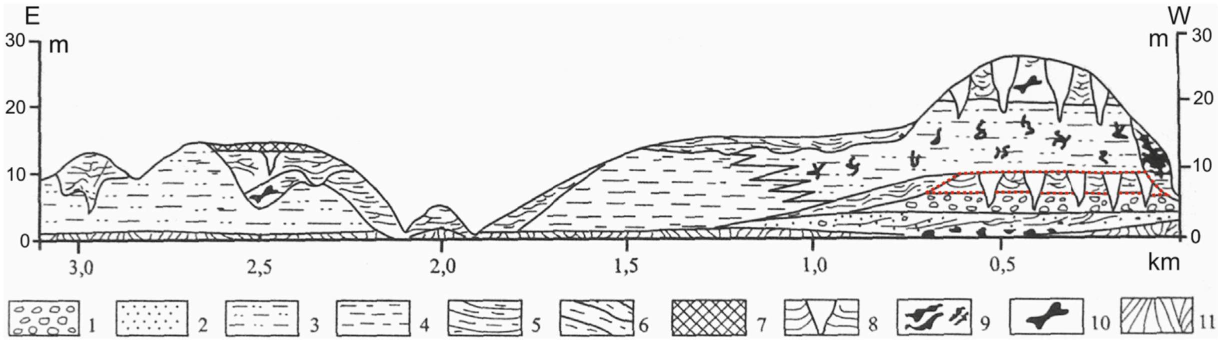

FIGURE 3 | Structure of the Quaternary deposits section 7.5 km east of Cape Svyatoy Nos (as cited in Nikolsky and Basilyan, 2004). The Yukagir Suite is indicated by the red dotted outline. Legend: 1–gravel with sand and loam layers; 2—oblique sands with casts; 3—thin layered loamy sands with grass rootlets; 4–more aleuritic thin layered loamy sands; 5—aleurites with ice wedges; 6—Pleistocene and Holocene alas complexes; 7—peat; 8—ice wedges; 9—woody remains; 10—remains of large mammals; 11—talus.

thermoluminescence dating (Arkhangelov, 1996). A.A. Arkhangelov correlated these deposits with the Olyor (Sher, 1971) and Serkinskaya (Ivanov, 1972; Prokhorova and Ivanov, 1973) suites of Pliocene-early Pleistocene age. However, further research showed that Arkhangelov's understanding was in error (Nikolskiy et al., 1999; Schirrmeister et al., 2002; Nikolskiy and Basilyan, 2004).

The briefly discussed history of cryolithological and stratigraphic research in the Dmitry Laptev Strait area, including at Oyogos Yar itself, shows that only toward the end of the 20th century were the main geological bodies identified and the local stratigraphic column compiled (**Table 1**); the description of the local stratigraphic column, however, was not widely accepted (Resheniya, 1987). The permafrost evolution, the relationship between the identified bodies, and the age and genesis of the deposits remained poorly studied, and the results were often contradictory until the end of the 20th century.

In 1996, 1999, and 2001, researchers of the Geological Institute RAS, P. A. Nikolskiy and A. E. Basilyan, worked in the Svyatoy Nos Cape area and in the western part of Oyogos Yar. They studied the section at the northern coast of the Svyatoy Nos Peninsula, where they designated the aforementioned deposits with ice wedges, described by A. A. Arkhangelov, as the Yukagir Suite (Nikolskiy et al., 1999; Nikolskiy and Basilyan, 2004). In 1999, 2002, and 2007, a joint Russian-German expedition worked on the Dmitry Laptev Strait outcrops within the “Laptev Sea System” program, and in 2004, a group within the Russian-American archeological project “The High-Latitude Arctic and Humans” worked here as well. The authors of the article conducted cryolithological and paleontological research into the structure and stratigraphy of the frozen Quaternary deposits on these expeditions (Kunitsky et al., 2000, Schirrmeister et al., 2003, 2008; Tumskoy and Basilyan, 2006, 2009; Tumskoy, 2012). The results of their fieldwork are the main content of this article.

Prior to describing the section construction, it is essential to call attention to one important term, the Ice Complex. We will not discuss in detail the meaning of “Ice Complex” because that is a separate, complex subject, but in the present article, Ice Complex refers to syncryogenic frozen deposits, which have been accumulated during cool climate periods of different durations and contain syngenetic ice wedges that form a closed polygon network. Using this definition, it is possible to distinguish Ice Complexes of different ages, which are divided by either interstadial deposit horizons or strongly pronounced thaw unconformity contacts of a regional or local scale. Three such Ice Complexes of different ages were identified in the Dmitry Laptev Strait area (Tumskoy, 2012). Later studies made it possible to identify four Ice Complexes (Wetterich et al., 2019). The MIS 4–MIS 3 aged Ice Complex deposits, which form the yedoma uplands, are called the Yedoma Ice Complex (Schirrmeister et al., 2013).

CRYOLITHOLOGICAL STRUCTURE OF THE OYOGOS YAR SECTION

The Quaternary deposits exposed in the Oyogos Yar outcrop largely match the deposits studied in the section at the Bol'shoy Lyakhovsky Island southern coast (Andreev et al., 2004; Schirrmeister et al., 2002, 2008, 2011; Tumskoy, 2012; Wetterich et al., 2011, 2014, 2016, 2019, 2021). Owing to this, the stratigraphy and deposition conditions of the deposits on Bol'shoy Lyakhovsky Island and in the Oyogos Yar area can be taken into consideration together. However, there are also certain differences that reflect the different tectonic positions of the strait's coasts.

The Oyogos Yar section can be divided into two parts. On the northern coast of Svyatoy Nos Peninsula, from its cape to approximately the Chay-Povarnya River mouth, Quaternary deposits occur on bedrock represented mainly by Early Cretaceous basaltic andesites and their tuffs, broken by granodiorites. To the east of the Krest-Yuryage River mouth, the coast for more than 120 km is composed entirely of frozen unconsolidated deposits.

Unlithified deposits, more ancient than those described in the Bol'shoy Lyakhovsky Island section, are exposed within Oyogos Yar at two areas. The first is located on the northern coast of the Svyatoy Nos Peninsula in the coastal outcrop near the mouth of

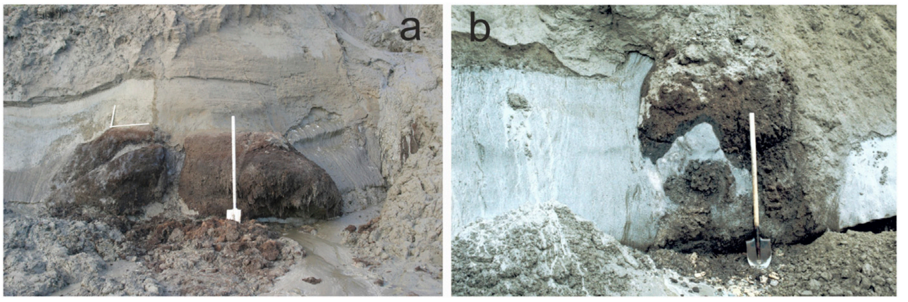

FIGURE 4 | Polygonal autochthonous peat lenses with ice wedge generation **(A)** and with partially thawed Yukagir ice wedges **(B)** on Bol'shoy Lyakhovsky Island.

the Chay-Povarnya River. The section structure (**Figure 3**) and formation history of this location are discussed in detail in the articles of P. A. Nikolskiy and A. E. Basilyan (Nikolskiy et al., 1999; Nikolskiy and Basilyan, 2004). The second outcrop of the ancient deposits is located between the mouths of the Ulakhan-Tala and Rebrova rivers. It was apparently first described at the end of the 1970's (Konishchev and Kolesnikov, 1981). The deposits and structure of these two sites differ significantly from each other, which complicates their direct comparison.

At the base of the coastal cliff on the northern coast of Cape Svyatoy Nos, grayish-yellow sands with lenses containing gravel and small rock debris are exposed, as well as lens-like loam interlayers with remains of carbonized vegetation detritus. The total thickness of this deposit is approximately 3 m. Ice wedge casts up to 1.5 m in height and composed of ice rich loams are situated at the top of the gravel-debris lenses. The top of the layer contains another ice wedge casts composed of overlain and enclosing deposits (both horizons of the casts are not shown on the general section in **Figure 3**). The height of the wedge casts reaches 2 m. Higher up, poorly sorted rock debris beds occur in an enclosing sandy loam layer with lens-like interlayers of ice-rich loams. The cryogenic texture of the rock debris beds is massive; that of the loams is inclined-reticular.

Yukagir Suite and Zimov`e Layer

A sandy layer with gravel and rock debris is overlain by ice rich light bluish-gray loams (**Figure 3**) described by P. A. Nikolskiy and A. E. Basilyan (Nikolskiy et al., 1999) on the Svyatoi Nos Cape and named the Yukagir Suite (**Table 1**). The same deposits were also identified in 1999 on Bol'shoy Lyakhovsky Island (Tumskoy and Basilyan, 2006, 2009), and described and dated (Schirrmeister et al., 2002; Meyer et al., 2002; Andreev et al., 2004; Blinov et al., 2009; Tumskoy, 2012; Wetterich et al., 2014, 2019). The Yukagir Suite deposits are 3 m thick at Oyogos Yar and reach 4.5 m on Bol'shoy Lyakhovsky Island. The deposits are characterized by a high ice content; ice belt cryogenic structures with a belt thickness of up to 2 cm are typical for them. Two generations of ice wedges are developed in this suite. The first generation is represented by syngenetic ice wedges up to 1.5 m wide with no less than 5 m between them (**Figure 3**); the second is represented by syngenetic wedges up to 0.5 m wide that fracture the polygons of the first generation (the second generation is described only on Bol`shoy Lyakhovsky Island). The first generation's ice wedges penetrate approximately 2 m into the underlying deposits. The genesis of these deposits is supposedly slope (Nikolskiy and Basilyan, 2004; Tumskoy, 2012). Nikolskiy and Basilyan (2004) estimate the Yukagir Suite deposits to be of Middle Pleistocene age (390–220 ka), while Tumskoy (2012) estimates the age to be 250–200 ka as determined by U-Th datings of overlying peats (Schirrmeister et al., 2002) on Bol`shoy Lyakhovsky Island. The latest U-Th data from Yukagir Suite peat are about 200 ka (the average between 178 ± 14 and 221 ± 27 according to different models of U-Th age determination) (Wetterich et al., 2019). The Yukagir Suite deposits resemble an Ice Complex in their cryolithological characteristics.

To the east, the Yukagir Ice Complex on Svyatoy Nos Peninsula is overlain by inclining and gradually lateral disappear sandy loams with lenses of shingle beds and sand with gravel and a massive cryogenic texture (**Figure 3**) (Nikolskiy and Basilyan, 2004). In terms of contact type, they resemble a lens that is included in or leaning against the Yukagir Ice Complex deposits. In Bol'shoy Lyakhovsky Island sections, polygonal autochthonous peat lenses 1.0–1.2 m thick occur on partially thawed ice wedges and ice rich deposits of the Yukagir Ice Complex (**Figure 4**). The author's point of view differs from that of our colleagues (Schirrmeister et al., 2002; Wetterich et al., 2019), who believe that these peat lenses are a part of the Yukagir Ice Complex.

A 0.3–0.6 m thick layer that is represented by yellowish-gray cryoturbated loams containing rock debris (**Figure 5**) overlies the deposits of the Yukagir Ice Complex, the sandy loam lenses, and the peat lenses enclosed within it. The concentration of debris near the top of the horizon indicates that it underwent cryogenic heaving. Overall, this layer covers the top of the underlying deposits and was viewed as a relic active layer (Tumskoy, 2012). In a later publication, this relic active layer is named the Zimov`e stratum (Wetterich et al., 2019).

All described deposits on the Svyatoi Nos Cape and Bol'shoy Lyakhovsky Island, which are enclosed within the Yukagir Ice Complex or overlay it, are identified by V. E. Tumskoy as the Zimov`e Layer ("Zimov inskaya Thickness" in the initial thesis, Tumskoy and Basilyan, 2006; Tumskoy, 2012). These deposits are envisaged to be the result of thermokarst and thermodenudation development of ice-rich Yukagir Ice Complex deposits and can be

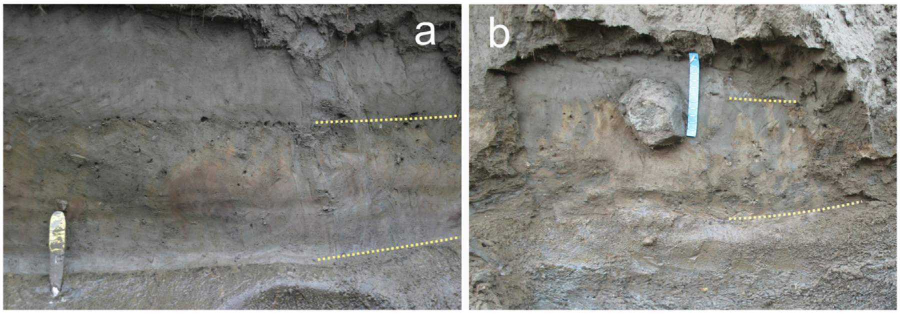

FIGURE 5 | Zimov`e stratum is a relic active layer over Yukagir Ice Complex deposits on the Svyatoi Nos Cape **(A)** and Bol`shoy Lyakhovsky Island **(B)**. The yellow dotted lines show the top and bottom of this stratum.

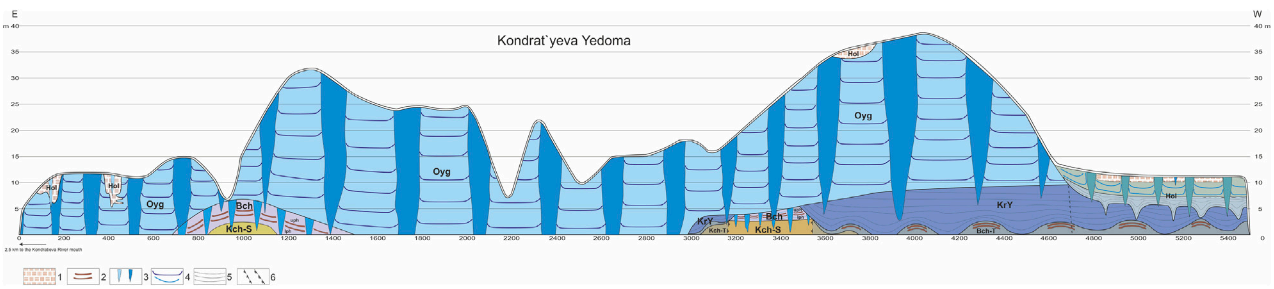

FIGURE 6 | Cryolithostratigraphic structure of the Kondrat`yeva yedoma section on the Oyogos Yar at a site 2.5–8 km west of the Kondrat`yeva River mouth. Legend: 1—peat, 2—lenses of polygonal autochthonous peats and peaty aleurites, 3—ice wedges of different generations, 4—ice belt cryogenic structures in syncryogenic deposits, 5—stratification of sediments in deposits, and 6—boundaries between taberal and non-thawed deposits. The unit`s symbols explained in **Table 1** (in addition: Bch-T stands for Bychchagy Ice Complex taberal deposits).

described as fragments of an alas complex formed as the result of partial thawing of the Yukagir Ice Complex. The age of the Zimov`e Layer peat lenses was determined to be about 200 ka using U-Th dating (Schirrmeister et al., 2002; Wetterich et al., 2019).

Ancient unconsolidated deposits occur as an extended arched uplift at the second Oyogos Yar site (between the mouths of the Ulakhan-Tala and Rebrova rivers at a distance of 15–25 km from West in **Figure 2**). Their top reaches a height of 8–10 m a.s.l. and gently slopes down both westward and eastward. In the section, two types of these deposits are seen. The first type is present as relatively homogenous gray and light bluish-gray loams with autochthonous peat lenses up to 0.3 m thick. The second type is present as alternating layers of aleurites, loams, and peaty loams, where casts of the wrapping structure with a polygon network 8–12 m between casts occur. These deposits have been described (Konishchev and Kolesnikov, 1981) but, despite a visible thickness of approximately 10 m, have not been studied in detail yet. Their age has not been determined.

Yukagir Suite and Zimov`e Layer deposits are not exposed within the studied Kondrat`yeva Yedoma section. The most ancient deposits that are exposed here at the base of the coastal cliff are Kuchchugui Suite deposits of the Keremesit superhorizon (**Figure 6**).

Kuchchugui Suite

A peculiarity of Kuchchugui Suite deposits on both coasts of the Dmitry Laptev Strait is that they are represented by deposits of two types. They were not differentiated in the works of the first researchers (N. N. Romanovsky, V. I. Kayalaynen, Yu.N. Kulakov, O. A. Ivanov, V. N. Konishchev et al.). Later, they were viewed as two varieties that had formed under different conditions–subaerial and subaqueous (Kunitskiy, 1996; Andreev et al., 2004). Tumskoy (2012) argued for their single sedimentational origin but demonstrated that these layers differ in the cryogenic history of development. He marked two Kuchchugui Suite deposit cryofacies—syncryogenic (Kch-S in **Figure 6**) and taberated (Kch-T in **Figure 6**). The geological age of these cryofacies sediments is the same because the contact between them is a thaw unconformity, not a sedimentological type (Tumskoy, 2012, 2021). Based on their position in the section, micropaleontological study results, and an infinite radiocarbon dating age (Nikolskiy and Basilyan, 2004), most researchers estimate these layers to have a Middle Pleistocene age. A single infrared stimulated luminescence (IRSL) date of 112.5 ± 9.6 ka obtained from the top part of the Kuchchugui Suite deposit section at Oyogos Yar (Opel et al., 2017) indicates that the formation of these deposits was possible until the beginning of the MIS 5.

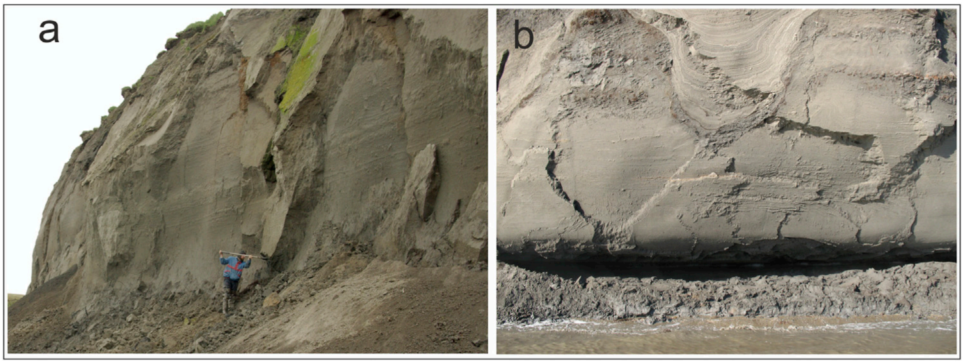

FIGURE 7 | Kuchchugui deposits: **(A)** syncryogenic cryofacies on Oyogos Yar (yellow-greenish color mark modern lichens on the outcrope`s wall) and **(B)** taberated cryofacies (under Krest-Yuryakh`s casts) on Bol`shoy Lyakhovsky Island.

Deposits of the **syncryogenic cryofacies** within the Kondrat`yeva Yedoma are exposed at two sites approximately 1 and 3.4 km west of the Kondrat`yeva River mouth (**Figure 6**).

These deposits were exposed at the base of the visible part of the section for distances of approximately 200 and 400 m, respectively. The lowest of the suite's deposits is positioned below sea level, and the top of the suite's deposits is positioned at a height of approximately 3 m a.s.l. The deposits consist of brown, grayish-brown, and yellowish-gray loams and dusty loamy sands with a high plant detritus content (**Figure 7A**). Faint horizontal and fine wave horizontal layering is typical for them owing to changing layer color and the distribution of plant detritus. The layers are 1–5 mm thick. In addition to detritus, the deposits are enriched in places by thread-like rootlets 10–15 cm long. Rounded subhorizontal peat inclusions up to 10 cm diameter are seen. In places, the layering is disrupted by a series of small wedge-like deformations. They occur in individual layers, with vertical lengths from 1 to 2–3 cm and widths of no more than 1 cm. Visually, they resemble traces of small desiccation cracks. Syncryogenic cryofacies deposits have a low gravimetric ice content usually not exceeding 30%–40%. The cryostratigraphy is relatively homogenous and is characterized by prevailing massive and microlens textures. Ice wedges within syncryogenic cryofacies of the Kuchchugui Suite were described in the Kondrat`yeva Yedoma (Opel et al., 2017) and in other places. Very narrow, up to 10–15 cm wide, epigenetic ice wedges permeating Kuchchugui Suite deposits are noted in outcrops near Cape Svyatoy Nos (Nikolskiy and Basilyan, 2004) and Bol'shoy Lyakhovsky Island (Tumskoy, 2012). Syngenetic ice wedges up to 0.5 m wide in the bottom part of Kuchchugui Suite are described west of the Kondrat`yeva Yedoma in outcrops closer to the Ulakhan-Tala River (Konishchev and Kolesnikov, 1981, **Figure 2**) and on Bol'shoy Lyakhovsky Island (Tumskoy, 2012). In both places, the structure of the syngenetic ice wedge upper parts has specific feature—higher than level with maximal wide, they make narrow upward and disappear through 0.5–1 m. Ground-ice wedges (sand-ice wedges) up to 0.75 m wide were described within Kondrat`yeva Yedoma by Th. Opel (Opel et al., 2017) and in Bol`shoy Lyakhovsky Island by first author. Larger syngenetic wedges up to 1.5–2 m wide are noted only in the middle part of the described cryofacies on Bol'shoy Lyakhovsky Island (Tumskoy, 2012).

Taberated cryofacies of Kuchchugui Suite deposits are distributed in Oyogos Yar outcrops much more widely than are syncryogenic cryofacies. The term "taberated" is used in the Russian scientific literature (Romanovskii, 1961a, 1993) to refer to deposits with low ice content, which thawed within taliks. Taberated deposits preserve the main peculiarities of structure (lamination and so on) after they have thawed, unlike taberal deposits, which form as a result of thawing of very ice-rich deposits and which completely lose their initial sediment structure. The bottom of the taberated deposits of this cryofacies is exposed only near the arched uplift by the Ulakhan-Tala River, and the nature of the contact with underlying deposits has not been studied yet. In Kondrat`yeva Yedoma sections, 2–3 m thick taberated cryofacies deposits are described at the base of the western part of the yedoma massif.

The taberated cryofacies are represented by dense bluish-gray and light bluish-gray loams, often dusty, with numerous dark gray and black spots 1–1.5 cm in size (**Figure 7B**). The loams have a well-defined thin, uneven horizontal, and fine wavy layering; the layers are 2–10 mm thick. The ice content is insignificant (the gravimetric ice content is not more than 30%–40%), and the cryogenic textures are massive. Except for the bottom ends of ice wedges that protrude into this layer from overlying deposits, massive ice is entirely absent in the deposits.

The lateral transition between the two described cryofacies is usually subvertical or gently inclined. The width of the contact zone does not exceed 5–10 m. Taberated cryofacies deposits always occur on syncryogenic cryofacies deposits in the case of inclined contact.

Kuchchugui Suite deposits were initially viewed as lagoon (Romanovsky, 1961b), lacustrine-lagoon (Ivanov, 1972), or lacustrine (Nikolskiy and Basilyan, 2004) in origin. During the course of the work on Bol'shoy Lyakhovsky Island and Oyogos Yar traces of erosional scours within syncryogenic cryofacies deposits, syngenetic ice wedges, interlayers of sod cover in the original bedding, and other indications of a subaerial origin of the deposits were found (Tumskoy and Basilyan, 2006, 2009). German researchers adhere to an alluvial origin of the

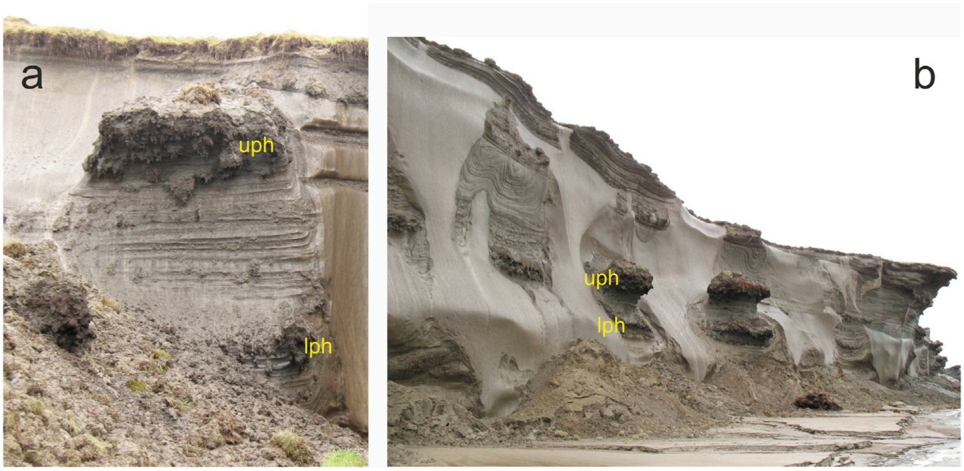

FIGURE 8 | Bychchagy Ice Complex deposits with two horizons of polygonal autochthonous peat lenses: **(A)** Oyogos Yar (height of outcrop is 3 m) and **(B)** Bol`shoy Lyakhovsky Island (uph–upper peat horizon, lph—lower peat horizon; height of outcrope is 12–15 m).

Kuchchugui Suite deposits, attributing them to floodplain deposits (Opel et al., 2017). Earlier, V. E. Tumskoy suggested that these deposits represent a complex of syncryogenic fluvioglacial deposits with ice wedges related to the degradation of the glacial cover in the northeast of the New Siberian Islands (Tumskoy, 2012). Afterwards, they were subjected in places to thawing within lake taliks. At sites where the deposit kept its initial sedimentation structure and cryostratigraphy, it is represented by syncryogenic cryofacies deposits, and at sites where the deposits thawed and were transformed into taliks, these deposits are represented by taberated cryofacies. The formation of taberated cryofacies is linked by the authors of the present study to the formation of Krest-Yuryakh Suite deposits; this formation is described below and took place during the first warm interglacial of Late Pleistocene (MIS 5).

Bychchagy Suite

The deposits of Kuchchugui Suite syncryogenic cryofacies are overlain by deposits that were first noted in 2004 (Tumskoy and Basilyan, 2006, 2009) on the southern coast of Bol'shoy Lyakhovsky Island. Based on their cryolithological features, these deposits are attributed to the Ice Complex and identified as their own stratigraphic subdivision, the Bychchagy Suite, which was identified by V. E. Tumskoy on the southern coast of the Dmitry Laptev Strait in 2007 in the Kondrat`yeva Yedoma section. Bychchagy Suite deposits have not yet been found in other places at Oyogos Yar. The Bychchagy Suite always occurs directly atop the deposits of the Kuchchugui Suite syncryogenic cryofacies; it is 3–4 m thick at the site located closer to the mouth of the Kondrat`yeva River and about 2–2.5 m thick 3.5 km away from the river mouth (**Figure 6**). The thickness of the Bychchagy Suite reaches 6–8 m on Bol'shoy Lyakhovsky Island (Tumskoy, 2012). Contact with Kuchchugui Suite deposits is gradual, but well-defined. In sections, the Bychchagy Suite transitions up the section into the Yedoma Ice Complex, but stratigraphically Krest-Yuryakh Suite deposits are positioned between them.

Bychchagy Suite deposits (**Figure 8**) are represented by ice-rich gray or brown-gray sandy loams and loams with individual rounded peat inclusions up to 10 cm in diameter. The cryostratigraphy depends on ice belt structures; the ice belt thickness ranged from 1–2 cm to 3–5 cm, and belts were positioned from 5 to 15 cm apart from each other. Between ice belts, microlens-like and sometimes reticular structures with ice lens thickness of up to 1 mm prevail. Large syngenetic ice wedges up to 3 m wide are developed in the deposits. They form a closed polygon network with a distance of approximately 12–15 m between the axes of the ice wedges. The total volumetric ice content of these Ice Complex deposits reaches 80%–90%.

A distinguishing peculiarity of Bychchagy Suite deposits is two horizons of very peaty dusty sandy loams or peat bogs. Each horizon is represented by individual peat lenses occurring at approximately the same level between ice wedges (**Figure 8**).

These deposits are divided vertically by a layer of icy loams or sandy loams as described above. The thickness of the peaty lenses on the southern coast of Bol'shoy Lyakhovsky Island is 1–1.5 m, and the vertical distance between lenses reaches 3–4 m. The thickness of the lenses in Kondrat`yeva Yedoma sections is reduced to 0.8–1 m, and the distance between them is 1–2 m. At the base of the lenses, the remains of mossy and grassy vegetation are present as rounded or wedge-like inclusions 10–20 cm in diameter, enclosed in icy deposits. Upward, toward the top of the lenses, the quantity of the inclusions increases, and near the top, the inclusions merge into a single peat body. The lenses are traced as the upper and lower peat horizons (**uph** and **lph** in **Figures 6, 8**) for hundreds of meters along the outcrop, disrupted by later erosional scours. Ice wedges of a second generation up to 1 m wide that divide the ground blocks in the middle often begin between the top and bottom

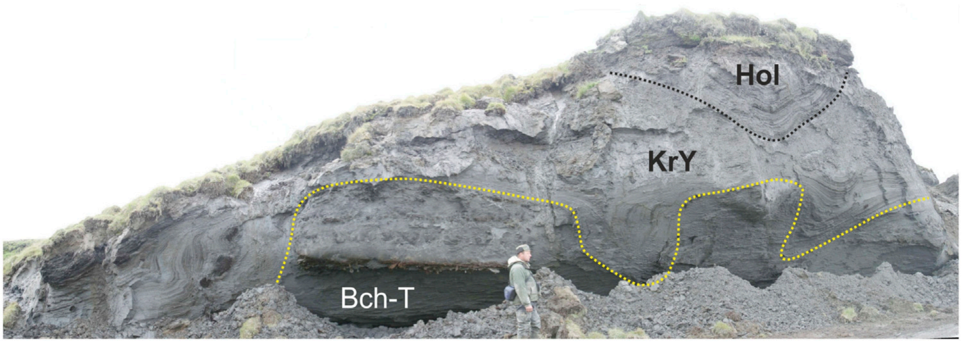

FIGURE 9 | Krest-Yuryakh Suite deposits (KrY) form ice-wedge casts as the result of Bychchagy Ice Complex thawing. In this section (Oyogos Yar), there are taberal Bychchagy Ice Complex (Bch-T) deposits with a thawed peat lens and the Holocene ice-wedge cast (Hol) as a result of yedoma Ice Complex thawing.

peaty lenses. They are 3–5 m in vertical length and sometimes penetrate into underlying deposits.

Bychchagy Suite deposits are viewed by the authors as lacustrine and bog in origin and in places, possibly, as lacustrine-alluvial deposits. They formed under cold, but more humid conditions compared to Kuchchugui Suite deposits, which is evidenced by their isotopic composition and significantly higher ice content (Meyer et al., 2002; Wetterich et al., 2016). The age of the deposits is determined by the authors, according to their stratigraphic position and specific composition, to be the early beginning of the Late Pleistocene (the beginning of the Eemian warming, MIS 5). Infinite radiocarbon dates and the results of U-Th dating of the polygonal peaty lenses confirm this: 126 + 16/−13 and 117 + 19/−14 kyr for the bottom, 93 ± 5 and 89 ± 5 kyr for the top horizons means that the accumulation period of the Bychchagy Suite is MIS 5e-5b (Wetterich et al., 2016).

Krest-Yuryakh Suite

Krest-Yuryakh Suite deposits are positioned stratigraphically higher than the Bychchagy Suite (Ivanov, 1972). They are widely distributed in sections on both coasts of the Dmitry Laptev Strait, occurring as individual lenses from 1-2 to 10 m thick and stretching from several dozen meters to several kilometers in length. Within Oyogos Yar, Krest-Yuryakh deposits were studied in the bottom part of Kondrat'yeva Yedoma (**Figure 6**) and in sections to the west of Cape Svyatoy Nos (Nikolskiy and Basilyan, 2004). These deposits may also occur at other sites, but those occurrences would be below sea level.

Krest-Yuryakh deposits are represented by gray and blue-gray loams, with plant detritus including fragments of shrub twigs and roots up to 5–8 cm in diameter. Entire valves of genus *Pisidium* shells (Pfeiffer, 1821) and their fragments are often present. The deposits are layered, and the thickness of the individual layers varies from a few millimeters to 1–2 cm. Small current ripple structures composed of diagonal layers less than 1 mm thick are present within many layers. The primary lamination has been destroyed by a series of subvertical fractures with amplitude 1–3 cm. Ferruginization of deposits along the fractures yields an ochre coloration 1–2 cm wide. Cryogenic textures in the loams are massive; ice lenses less than 1 mm thick, which are oriented parallel to the layering, are rarely seen. Overall, the deposits are very dense and dry, and the gravimetric ice content of the deposits does not exceed 15%–20%.

Krest-Yuryakh deposits were first viewed as lacustrine (Ivanov, 1972). It was long thought that they formed as a result of the thawing of Kuchchugui Suite deposits, but given the insignificant ice content, this appears to be almost impossible. In the beginning of the 21st century, it was suggested that these lacustrine deposits are the result of lake thermokarst development in icy Bychchagy Suite deposits (Tumskoy and Basilyan, 2006, 2009); moreover, sites of the section were found in which the geological contact between deposits is exposed (Tumskoy, 2012). Krest-Yuryakh lacustrine deposits form relatively thin lenses enclosed in the Bychchagy Suite. The bottom of the lenses forms a well-defined network of rounded ice wedge casts (previously described as draping permafrost structures (Romanovskii, 1958), which were formed as the result of Bychchagy Suite Ice Complex thawing (**Figures 7B**, **9**). The distance between casts is about 10–15 m, and the vertical size is 3–5 m. The layering of the lacustrine deposits in the casts has a well-defined draping form. The layering above the lacustrine deposits gradually changes to horizontal and the vegetation detritus content in the deposits decreases. Highly condensed and partially deformed lenses of peaty material occur everywhere in brownish loams between the pseudomorphs. Overall, two horizons of peaty lenses have been formed, which, together with the loams which contain them, the authors view as taberal formations (thawed remains) of the Bychchagy Suite peat lens.

Almost everywhere, the top horizons of the Krest-Yuryakh Suite deposits are scoured and exhibit a distinct erosional boundary with overlying deposits. A horizon of polygonal peats up to 2 m thick containing a network of ice wedges up to 2–2.5 m thick and covering the section of lacustrine loams was found only on Bol'shoy Lyakhovsky Island near the Vankina River (Tumskoy, 2012). Thus, the complete section of Krest-Yuryakh deposits consists of taberal formations which formed after the thawed Bychchagy Ice Complex, and lacustrine and

FIGURE 10 | Yedoma Ice Complex deposits on the Kondrat`yeva yedoma coastal bluff. The height of the bluff is 15 m.

lacustrine-boggy (specifically alas) deposits of peat bogs with ice wedges that cover the section. Such a structure is completely identical to the structure of Holocene Alas Complex deposits, which has been studied extensively on the Yana-Indigirka lowland of northern Yakutia (Romanovskii, 1961a), so we can discuss a Krest-Yuryakh Alas Complex. Taliks formed beneath Krest-Yuryakh lakes, within which underlying deposits thawed and froze again. The transformation of part of the Kuchchugui syncryogenic cryofacies into a taberated cryofacies and its partial diagenesis is attributed specifically to Krest-Yuryakh Alas Complex development.

The formation of Krest-Yuryakh Suite deposits was previously attributed to the beginning of the Late Pleistocene and linked to the first Pleistocene warming period (Ivanov, 1972; Prokhorova and Ivanov, 1973). Environmental conditions of sedimentation, composition of the deposits, pollen spectra, and findings of woody remains attest to this. A single IRSL dating of Krest-Yuryakh deposits is 102.4 ± 9.7 ka (Opel et al., 2017); this date contradicts dating from Bychchagy peat lenses. The direct geological contact between the Bychchagy Ice Complex and the Krest-Yuryakh deposits is observed near the Van`kina River on Bol'shoy Lyakhovsky Island (Tumskoy, 2012) where Krest-Yuryakh deposits lie over or are embedded within the Bychchagy Ice Complex. The same contact on Oyogos Yar has not been described until now. This indicates that the Krest-Yuryakh thermokarst lacustrine deposits are younger than the Bychchagy Suite.

Yedoma Superhorizon

Krest-Yuryakh Suite deposits are overlain by Yedoma Ice Complex deposits (**Figure 10**), which are marked stratigraphically as the Oyogos Suite of the Yedoma superhorizon (**Table 1**) in the Dmitry Laptev Strait area (Prokhorova and Ivanov, 1973; Resheniya, 1987). These deposits reach 30–35 m thickness in the Oyogos Yar area (**Figure 6**).

The composition of the Yedoma Ice Complex deposits in Northern Yakutia changes horizontally and vertically, contrary to the widespread opinion about its homogeneity (Tomirdiaro, 1980). It varies from dusty sandy loams to dusty loams and is represented in places by almost pure aleurites (Schirrmeister et al., 2011). The color of the deposits changes from yellowish-brown to gray and brownish-gray, depending on peatiness. A typical feature of the Ice Complex deposits is the presence of numerous peat inclusions of rounded and wedge-like shape, which gravitate to the central parts of the ground column between the ice wedges. The diameter of the peat inclusions usually does not exceed 10–15 cm. Wedge-shaped inclusions have a height of approximately 20–30 cm and are oriented radially downward from the middle of the polygonal blocks.

A peculiarity of the structure of all Yedoma Ice Complex sections is the cyclic repetition of the cryostratigraphical structure of the polygonal blocks (Popov, 1953; Vasil'chuk, 2017). Ice belts, thick lenticular cryogenic structures, have developed at the base of each cryogenic cycle. The belts in this part of the cryogenic cycle usually have a subhorizontal orientation and where they contact ice wedges either meet them perpendicularly or bend upward insignificantly. Within one cryogenic cycle, the belt thickness increases up the section, and the distance between belts decreases. The degree of ice belt bending increases upward near the ice wedges within each cryogenic cycle. From approximately the middle of the cryogenic cycle in the central part of the ground column between ice wedges, there is an increase in the content and size of peaty inclusions. In the top part of the section, they can form lenses of almost pure peat. The total ice volume barely changes at different levels of the cryogenic cycle, constituting 40%–50%; only the cryostratigraphy changes. Syngenetic ice wedges reach a vertical length of 30 m and more, and their width is 3–4 m on average, increasing to 6–8 m in places. There are second generation ice wedges in places.

The Yedoma Ice Complex is underlain by Bychchagy or Krest-Yuryakh Suite deposits. The contact with Bychchagy Suite deposits manifests in different ways. In some places, partially thawed ice wedges, or erosional downcuts, or changes in deposit composition are seen, while in other places visible contact is missing. In the latter case, possibly deposition was not disrupted or, for some reason, disruption may have occurred but is not manifested in the section. The contact with Krest-Yuryakh Suite deposits is clearly visible. Such a contact usually has an erosional nature and is marked by an interlayer of peaty material 0.1–0.2 m thick. Most likely, this interlayer formed as a result of erosion and redeposition of Bychchagy peaty horizons and of peat bogs covering the Krest-Yuryakh deposit section. Krest-Yuryakh Suite deposit layers, which are oriented subhorizontally at the level of contact, are often cut by this interlayer with insignificant angular unconformity.

The contact of the Yedoma Ice Complex with underlying deposits is a horizon that can be used to reconstruct the relief of the surface which existed in the beginning of MIS 4. Currently, the level of the lower thermoterrace in many yedoma uplands forms because the less icy deposits below this contact are more resistant to thermoabrasion, thermal denudation, and erosion than the more ice-rich Yedoma Ice Complex deposits above. However, Oyogos Yar thermoterraces may have formed throughout the thickness of Yedoma Ice Complex deposits (**Figure 6**).

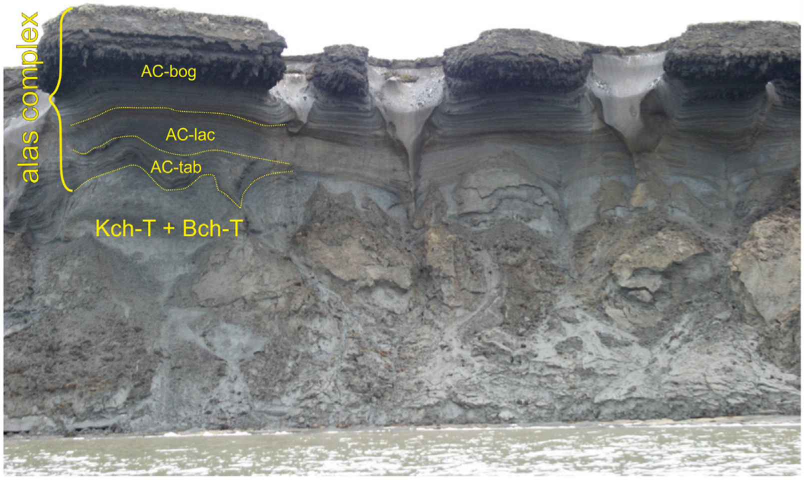

FIGURE 11 | Typical structure of the Holocene Alas Complex with taberal (AC-tab), lacustrine (AC-lac), and lacustrine-boggy (AC-bog) facies. The coastal section of the alas depression is located on Bol`shoy Lyakhovsky Island. Kch-T + Bch-T—taberated deposits of Kuchchugui and Bychchagy Suites. The height of the outcrope is 12 m.

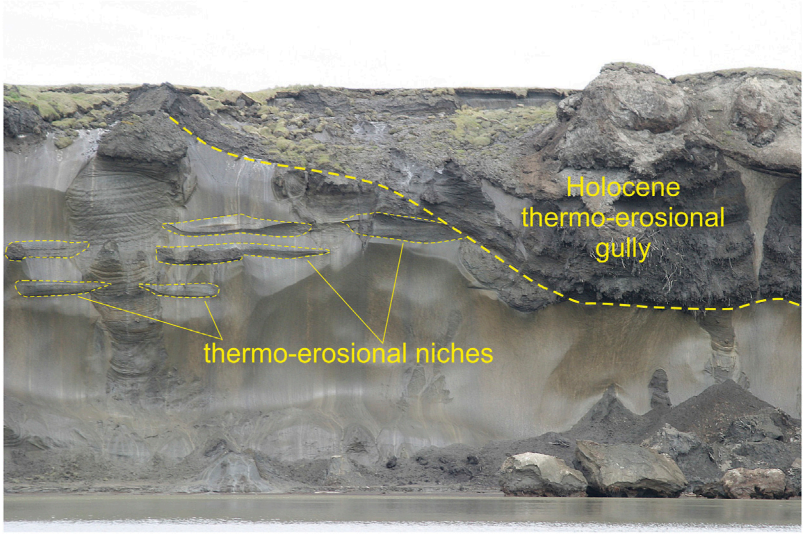

FIGURE 12 | Holocene thermo-erosional gully and niches in the yedoma Ice Complex.

On the northern coast of Svyatoy Nos Peninsula, the bottom of the Yedoma Ice Complex occurs at heights up to 19–20 m a.s.l. (Nikolskiy and Basilyan, 2004). To the east, the Ice Complex bottom drops to 5–8 m a.s.l. and then rises to 12–15 m a.s.l. again in the vicinity of the arched uplift near the Ulkhan-Tala and Rebrova rivers. To the east of the arched uplift, the elevation of the bottom gradually decreases to approximately 10 m a.s.l. in the western part of the Kondrat`yeva Yedoma. In the eastern part of this yedoma, for more than 2 km, the bottom of the Yedoma Ice Complex is positioned below sea level, rising insignificantly higher than sea level further east. To the east of the mouth of the Krestovaya River, the bottom declines below sea level again. The overall tendency of the bottom of the Ice Complex to decline in elevation is apparently tectonic in nature, while local slumps are related to erosional scours.

The genesis of Yedoma Ice Complex deposits in the Oyogos Yar area remains under discussion. Different researchers have suggested it to be lacustrine-allulvial (Romanovskii, 1961b; Konishchev and Kolesnikov, 1981), eolian (Tomirdiaro, 1980), and alluvial-proluvial (Gravis, 1996). In our opinion, the genesis of these deposits may differ in different parts of the coast, although lacustrine-alluvial genesis apparently dominates.

The age of the deposits was determined by a series of final radiocarbon dates obtained for the top part of the Oyogos Suite section (from 49 to 32 ka.; Gravis, 1978; Kaplina and Lozhkin, 1982; Tomirdiaro et al., 1982; Opel et al., 2017) and by infinite dates for lower horizons. Overall, Yedoma Ice Complex deposit accumulation began during the first climatic cooling of the Late Pleistocene (MIS 4) and continued until the middle of the Molotkov Epoch (the relatively warm interstadial MIS 3).

In the second half of the Late Pleistocene, in the period from 32 ka to the beginning of the Holocene, an accumulation of deposits analogous in structure, which are cryolithologically the same as an Ice Complex but were developed more locally, took place within river valleys, in erosional downcuts, and under some slopes. Such deposits were found on Bol'shoy Lyakhovsky Island (Wetterich et al., 2011, 2014; Tumskoy, 2012). It may be that they also exist within Oyogos Yar since they have peat dates of 22.940 ± 390 ka BP (NUTA-3521) in the top part of the section (Nagaoka et al., 1995), but they have not yet been clearly defined geologically. Overall, they were identified as a separate stratigraphic unit (Sartan Ice Complex) called the Yana Suite (Tumskoy, 2012), but this matter requires further study.

Holocene Alas Complex

Widespread deposits of the Holocene Alas Complex on the territory of northern Yakutia are positioned stratigraphically higher than the Yedoma Ice Complex. The same stratigraphic position has a Holocene cover layer also. Like Yedoma Ice Complex deposits, the Holocene Alas Complex deposits are morphogenetic, forming the bottoms of alas basins which divide yedoma hills. Alas Complex deposits are genetically linked to the formation, evolution, and degradation of thermokarst lakes and their basins. They resemble a complex of paragenetically interrelated deposits among which taberal formations and lacustrine and alas-specific (lacustrine-boggy) deposits (**Figure 11**) are usually emphasized (Romanovskii, 1961a). The thickness of the Alas Complex deposits within Oyogos Yar does not usually exceed 10 m and depends mainly on the thickness of lacustrine and alas-specific deposits. The structure of the Alas Complex deposits is quite well studied (Katasonov, 1960, 1982; Romanovskii, 1961a; Ospennikov and Trush, 1974; Kaplina, 1981, 2009; Wetterich et al., 2009).

Alas Complex taberal formations resemble Yedoma Ice Complex deposits, which thawed beneath a lake and were partially reworked within the thermokarst basin. In the Dmitry Laptev Strait area, on both Bol'shoy Lyakhovsky Island and at Oyogos Yar, deposits from the Bychchagy Ice Complex, which thawed together with the Yedoma Ice Complex, are included in the composition of both Bol'shoy Lyakhovsky Island and Oyogos Yar in many cases (**Figure 7**). Furthermore, Yana Suite Ice Complex deposits can participate in Alas Complex formation too. In cases when taberal formations of the Alas Complex are identified in sections, they are represented by dusty gray, brownish-gray, or light bluish-gray loams, which are not layered and often have randomly distributed vegetation remains or peaty inclusions within deposits. The thickness of the taberal deposits can reach 2–3 m. In overall composition, including paleontological content, they correspond to Ice Complex deposits which did not thaw.

Taberal deposits are overlain by lacustrine deposits; the thickness of these lacustrine deposits does not exceed several meters. Taberal deposits are usually represented by gray and brownish-gray loams with inclusions of vegetation detritus including pieces of peat and wood and shrub vegetation. Freshwater shells of the genus *Pisidium* no more than 1–1.5 cm length can sometimes be found. A distinguishing difference between lacustrine deposits and taberal formations is the extent of lamination. Layers are a few millimeters to 1–2 cm thick. Bedding is parallel, horizontal, or wavy, and sometimes structures of underwater landslides 1–2 m in size can be seen.

Lacustrine-boggy (alas-specific) deposits cover the Alas Complex section. They are represented by polygonal peat bogs from 1 to 2.5 m thick, which are penetrated by a system of syngenetic ice wedges up to 2–4 m wide and 5–6 m high.

At the base of the Alas Complex developed, ice-wedge casts can usually be found, which are an integral part of the Alas Complex structure. Such casts can be seen in the base of almost all Oyogos Yar alas deposits. They are completely identical in origin to Krest-Yuryakh Suite casts but often have a wedge-like shape. They are filled with taberal material and lacustrine deposits with strongly deformed layering.

The formation of thermokarst lakes and taliks beneath them began about 13–12 kyr BP (Kaplina and Lozhkin, 1979; Kaplina, 2009). The thickness of the taliks, as calculations show (Tumskoy et al., 2001), did not exceed 100–150 m even in favorable conditions. If a talik took over an area on which not only a Yedoma but also a Bychchagy Ice Complex was developed, the latter thawed in the talik and formed pseudomorphs and taberated underlying Kuchchugui Suite deposits. If the talik under a Holocene lake formed in an area of Krest-Yuryakh deposit distribution where casts after Bychchagy ice wedges had formed earlier, the underlying Kuchchgui Suite deposits were taberated (thawed and refrozen) twice: initially during the period of Krest-Yuryakh thermokarst lake development, and later in the Holocene.

Alas Complex deposits occur as lenses which stretch along the coast for a distance of several hundred meters to 4–5 or more kilometers. These lenses are enclosed in Yedoma Ice Complex deposits. Their lateral contacts with the latter are clearly seen in places. These are erosional-cryogenic contacts from 50 to 200 m long horizontally, which have a gentle slope toward the center of the alas basins. The cryolithological relationship of the Alas Complex and Yedoma Ice Complex deposits unequivocally shows that the former deposits are younger, positioned higher stratigraphically, and formed at the very end of the Late Pleistocene and in the Holocene. Numerous radiocarbon dates also indicate this: The beginning of lacustrine deposit deposition is dated to 14–11 k.a., while the end of alas peat bog formation is dated to 1,000 years ago or earlier (Kaplina, 2009; Opel et al., 2017).

Thermodenudation occurred, and small lakes that did not develop into full-sized large thermokarst lakes formed in places on the yedoma hills' surface in parallel to the formation of the Alas Complex in thermokarst basins. Increasing thawing depth beneath such lakes led to the emergence at the top of the Yedoma Ice Complex of small depressions in the form of subsidence troughs, which are currently composed of very ice-rich peaty dusty loams up to 2–3 m thick with ice belt cryogenic structures and small ice wedges. Schematically, they are shown in the top part of the section at the 3,700 m mark (**Figure 6**). Very thin taberal deposits over the Yedoma Ice Complex and boggy deposits can be identified by their composition. Paleontologically such subsidence depressions will contain fauna that matches the temporal interval of the thawed Yedoma Ice Complex, but can also include younger Holocene flora and fauna remains.

Deposits of the first floodplain terrace and floodplains of all river valleys (from Chay-Povarnya to Konechnaya), including coastal-marine deposits, also belong to the Holocene at Oyogos Yar, but they are not discussed here.

It is important to pay attention to proluvial-deluvial deposits of the thermal erosion system. These deposits are widely distributed on the coasts of the Dmitry Laptev Strait, including at Oyogos Yar. The thermal erosion developed with particular intensity at the beginning of the Holocene and at the Holocene optimum; some gullies also continue to grow intensely today. Ice-rich deposits and ground ice contribute to the formation of thermo-erosional gullies. These gullies differ from other types due to their formation in frozen ground; frozen ground can retain steep vertical sides during erosion. Thermal pits and numerous horizontal thermo-erosional niches with an extent of up to 10–15 m long can form inside them at different levels (**Figure 12**). Subsequently, thermo-erosional gullies can fill with thawed and relocated material from the slopes of the gully and freeze again.

CONCLUSION

We managed to answer some questions about the structure of frozen Quaternary sediments on the coast of the Dmitry Laptev Strait after field work including detailed geological and cryolithostratigraphic investigations. The boundaries of the main geological bodies exposed in the coastal sections of the Dmitry Laptev Strait were clearly established. An identical structure was revealed within both the Oyogos Yar and the southern coast of Bol'shoy Lyakhovsky Island. The Middle Pleistocene deposits found in Yukagir Ice Complex deposits (MIS 8 or 7) and the Kuchchugui Suite (MIS 6) included relatively ice-poor strata with rare syngenetic ice wedges. The complex Zimov`e layer deposits (MIS 7?) included the ancient alas complex deposits and a relic active layer. The Kuchchugui deposits accumulated in subaerial conditions as fluvial-glacial (?) deposits. The Bychchagy Suite Ice Complex (MIS 5e-5b) with two specific polygonal peat horizons covered the Kuchchugui Suite. The thermokarst lake deposits of the Krest-Yuryakh Alas Complex suite formed as a result of thawing during MIS 5a climatic warming. According to the conditions of occurrence, composition, and structure, the Krest-Yuryakh Alas Complex cannot be considered as part of the Kuchchugui Suite.

The sediments of the Bychchagy Suite served as a very ice-rich substrate for the development of massive lacustrine thermokarst at the beginning of the Late Pleistocene (MIS 5), which is now represented by the sediments of the Krest-Yuryakh Suite. Despite the insufficient number of available Bychchagy and Krest-Yuryakh suite datings (Wetterich et al., 2016), the geological relationship between these suites and their sequence of formation are beyond doubt. Convincing evidence has been obtained, based on direct geological observations, of the existence of two cryofacies of the Kuchchugui Formation—syncryogenic and taberated.

On the whole, the cryolithostratigraphic subdivisions identified on both sides of the Dmitry Laptev Strait turned out to be identical and well diagnosed. This made it possible to reconstruct the history of the geological development of this territory starting from the end of the Middle Pleistocene to the present. However, for chronological accuracy of geological reconstruction, we need tens of new datings of pre-Yedoma superhorizon deposits (from MIS 8 to MIS 5). We hope that collecting these essential data will be possible in the future.

DATA AVAILABILITY STATEMENT

The original contributions presented in the study are included in the article/Supplementary Material, further inquiries can be directed to the corresponding authors.

AUTHOR CONTRIBUTIONS

VT and TK designed the study and wrote the manuscript.

FUNDING

The Russian-German "Laptev Sea System" program supported this work. The work of VT was also supported by Russian-American scientific project "Zhokhov-2000" led by V. V. Pitulko and sponsored by the private scientific Rock Foundation (New York, United States). The Russian Science Foundation (the grant #21-77-30001) also supported this study.

ACKNOWLEDGMENTS

We thank all German and Russian participants of the expeditions for their help. We thank Thomas Opel and Julian Murton for valuable comments that greatly helped to improve the paper. The authors are especially grateful to Lutz Schirrmeister for their help at all stages of preparing the article.

REFERENCES

Andreev, A., Grosse, G., Schirrmeister, L., Kuzmina, S., Novenko, E., Bobrov, A., et al. (2004). Late Saalian and Eemian Palaeoenvironmental History of the Bol'shoy Lyakhovsky Island (Laptev Sea Region, Arctic Siberia). *Boreas* 33, 319–348. doi:10.1080/03009480410001974

Anzhu, P. F. (1849). "Opis` Beregov Ledovitogo Morya, Mezhdu Rek Olenek I Indigirka, I Severnykh Ostrovov Leytenanta Anzhu. 1821, 22 I 23 Godov (Description of the Arctic Ocean Coasts between Olenek and Indigirka Rivers and Northern Islands after Lieutenant Anzhu)," in *Reviews of the Hydrography Department of Marine Ministry* (Sankt-Petersburg: Marine typography Publ.), 147. Iss. VII. (in Russian).

Arkhangelov, A. A. (1996). "O Rannikh Etapakh Formirovaniya Mnogoletney Merzloty Na Severe Yakutii I Vozrast Drevnikh Reliktov Podzemnogo Oledeneniya (Initial Periods of Permafrost Formation at the Yakutian north and Age of Old Relic of Ground Glaciation)," in *Razvitie Oblasti Mnogoletney Merzloty I Periglatsialnoy Zony Severnoy Evrazii I Usloviya Rasseleniya Drevnego Cheloveka (Evolution of the Permafrost Area and Periglacial Zone of the Northern Eurasia and Residential Conditions of Old Humans)* (Moscow: Publ. in Institute of Geography AN SSSR), 102–109. (in Russian).

Boeskorov, G. G., Protopopov, A. V., Mashchenko, E. N., Potapova, O. R., Kuznetsova, T. V., Plotnikov, V. V., et al. (2013). Novye Nakhodki Iskopaemykh Mlekopitayushchikh Unikal'noi Sokhrannosti V Mnogoletney Merzlote Yakutii (New Findings of Fossil Mammals of the Unique Preservation in Yakutian Permafrost). *Doklady Earth Sci.* 452 (4), 461–465. (in Russian). doi:10.1134/s0012496613050116

Boeskorov, G. G., Protopopov, A. V., Mashchenko, E. N., Potapova, O. R., Tikhonov, A. N., Kuznetsova, T. V., et al. (2012). Predvaritel'nye Dannye Ob Unikal'nykh Nakhodkakh Mlekopitayushchikh Lednikovogo Perioda Na Yano-Indigirskoy Nizmennosti (Preliminary Data of the Unique Findings of the Ice Age Mammals on the Yana-Indigirka Lowland). *Bull. North-East Fed. Univ.* 9 (4), 10–16. (in Russian).

Bunge, A. A. (1887). Predvaritel'nyi Otchet Ob Ekspeditsii Na Novosibirskie Ostrova (Preliminary Report of the Expedition on New Siberian Islands). *Bull. Imperator's Russ. Geogr. Soc.* XXIII (1-6), 573–591. (in Russian).

Geocryology of USSR (1989). in *Eastern Siberia and Far East.* Editor E. D. Ershov (Moscow: Nedra Publ), 515.

Ermolaev, M. M. (1932). "Geologicheskii I Geomorfologicheskii Ocherk Ostrova Bol'shogo Lyakhovskogo (Geological and Geomorphological Review of the Bol'shoy Lyakhovsky Island)," in *Polyarnaya Geophizicheskaya Stantsia Na Ostrove Bol'shom Lyakhovskom (Polar Geophysical Station on the Bol'shoy Lyakhovsky Island)* (Leningrad: Proceedings of SOPS, Yakutian series), 7, 147–223. (in Russian).

Gedenshtrom, M. M. (1830). "O Ledovitom More (About of Polar Sea)," in *Otryvki O Sibiri (Essay about Siberia)* (Sankt-Petersburg: Typography of medical Department Publ.), 105–132. (in Russian).

Gravis, G. (1978). "Cyclic Nature of Thermokarst on the Maritime plain in the Upper Pleistocene and Holocene," in Third International Conf. on Permafrost. English translation of twenty-six of the Soviet papers. Part I, Edmonton, Canada, 245–257.

Gravis, G. F. (1996). "Allyuvialno-prolyuvialnaya Model' Formirovaniya Mnogoletnemerzlykh Tolshch Na Flyuvial'nykh Ravninakh Kriolitozony (Alluvial-Proluvial Model of Frozen Deposits Formation on the Fluvial Lowlands of Cryolithozone)," in *Abstracts of the First Conference of Russian Geocryologists* (Moscow, Russia: Lomonosov Moscow State University), Vol. 1, 186–192. (in Russian).

Grigoriev, A. A. (1932). "Ob Oledenenii Territorii Yakutii V Chetvertichnyi Period (To the Glaciation of Yakutia at the Quaternary)," in *Proceedings of the Committee for Quaternary Investigation* (Leningrad: Academia of Science Publ.), 31–42. (in Russian).

Gusev, A. I. (1958). K Stratigrafii Chetvertichnykh Otlozhenii Zapadnoi Chasti Primorskoi Ravniny (To the Stratigraphy of Quaternary Deposits of the Western Part of Coastal lowland). *A. Collection Papers Geology. Arctic* 80 (5), 79–86. (in Russian).

Ivanov, O. A. (1972). "Stratigrafiya I Korrelyatsiya Neogenovykh I Chetvertichnykh Otlozhenii Subarkticheskikh Ravnin Vostochnoi Yakutii (Stratigraphy and Correlation of Neogene and Quaternary Deposits on the Subarctic Lowlands of the Eastern Yakutia)," in *Problemy Izucheniya Chetvertichnogo Perioda (Problems of Investigation of the Quaternary)* (Moscow: Nauka Publ.), 202–211. (in Russian).

Kaplina, T. N. (2009). Alasnye Kompleksy Severnoi Yakutii (Alas Complexes of the Northern Yakutia). *Earth's Cryosphere* XIII (4), 3–17. (in Russian).

Kaplina, T. N. (1981). "Istoriya Merzlykh Tolshch Severnoi Yakutii V Pozdnem Kainozoe (History of Frozen Grounds in the Northern Yakutia at the Late Cenozoic)," in *Istoriya Razvitiya Mnogoletnemerzlykh Porod Severnoi Evrazii (History of Permafrost Evolution at the Northern Eurasia)* (Moscow: Nauka Publ.), 153–181. (in Russian).

Kaplina, T. N., and Lozhkin, A. V. (1979). Vozrast Alasnykh Otlozheniy Primorskoy Nizmennosti Yakutii (Radiouglerodnoe Obosnovanie) (Age of an Alas Complex Deposits of Yakutian Coastal lowland (14C Evidence)). *Izvestiya SSSR (Proceedings Sssr), Ser. Geol.* 1979 (2), 69–76.

Kaplina, T. N., and Lozhkin, A. V. (1982). Vozrast "Ledovogo Kompleksa" Primorskikh Nizmennostei Yakutii (Age of an Ice Complex on the Coastal lowland of Yakutia). *Izvestiya SSSR (Proceedings Sssr), Ser. Geogr.* 2, 84–95. (in Russian).

Katasonov, E. M. (1982). "Alasnye Otlozheniya I Taberal'nye Obrazovaniya Yakutii (Alas Deposits and Taberal Formations of the Yakutia)," in *Geologiya Kainozoya Yakutii (Cenozoic Geology of the Yakutia)* (Yakutsk: Yakutian branch of SO AN SSSR Publ.), 110–121. (in Russian).

Katasonov, E. M. (1960). Ob Alasnykh Otlozheniyakh Yanskoi Primorskoi Nizmennosti (About Alas Deposits of the Yana Coastal lowland). *Geologiya i geofizika (Geology geophysics)* 2, 103–112. (in Russian).

Kayalaynen, V. I., and Kulakov, Yu. N. (1965). "Osnovnye Cherty Istorii Geologicheskogo Razvitiya Yano-Indigirskoy (Primorskoy) Nizmennosti V Neogen-Chetvertichnoe Vremya (Main Peculiarities of the Geological History of the Yana-Indigirka (Primorskaya) lowland at the Neogene and Quaternary," in *Antropogenovyi Period V Arktike I Subarktike (Quaternary Period in the Arctic and Subarctic)* (Moscow: Nedra Publ.), 56–64. (in Russian).

Konishchev, V. N., and Kolesnikov, S. F. (1981). Osobennosti Stroeniya I Sostava Pozdnekaynozoiskikh Otlozhenii V Obnazhenii Oyogosskii Yar (Peculiarities of the Structure and Composition of Late Cenozoic Deposits in the Outcrop Oyogos Yar). *Probl. cryolithology* IX, 107–117. (in Russian).

Kunitskiy, V. V. (1996). "Khimicheskiy Sostav Skvoznykh Ledyanykh Zhil Ledovogo Kompleksa (Chemical Composition of through Ice Wedges of Ice Complex)," in *Kriolitozona I Podzemnye Vody Sibiri. Chast' 1. Morfologiya Kriolitozony (Cryolithozone and Ground Water of the Siberia. Part 1. Morphology of Cryolithozone)* (Yakutsk: Permafrost Institute publ.), 93–117. (in Russian).

Kunitsky, V., Schirrmeister, L., Grosse, G., et al. (2000). "Paleoclimate Signals of Ice-Rich Permafrost Deposits," in *Berichte zur Polarforschung. Reports on Polar Research. Russian-German Cooperation System Laptev Sea 2000. The expedition Lena 1999*, 354, 187–263.

Kuznetsova, T. P. (1965). "O Chetvertichnykh Otlozheniyakh S Podzemnym L'dom Na Yano-Indigirskoy Nizmennosti I O-Ve Bol'shom Lyakhovskom (About Quaternary Deposits with Ground Ice on the Yana-Indigirka lowland and Bol'shoy Lyakhovsky Island)," in *Podzemnyi Led (Underground Ice)* (Moscow: Moscow University Publ.), 120–132. (in Russian).

Kuznetsova, T. V., and Starodubtseva, I. A. (2009). "Mamonty I Istoriya Geologicheskogo Izucheniya Poberezh'ya Morya Laptevykh I Novosibirskikh Ostrovov (Mammoths and History of Geological Investigations of the Laptev Sea Coasts and New Siberian Islands)," in *Sistema Morya Laptevykh I Prilegayushchikh Morey Arktiki: Sovremennoe Sostoyanie I Istoriya Razvitiya (System of the Laptev Sea and the Adjacent Arctic Seas: Modern and Past Environments)* (Moscow: MSU Publ.), 481–500. (in Russian).

Lavrushin, Yu. A. (1963). "Allyuviy Ravninnykh Rek Subarkticheskogo Poyasa I Periglyatsial'nykh Oblastei Materikovykh Oledenenii (Alluvium of plain Rivers in Subarctic Zone and Periglacial Zones of Cover Glaciations)," in *Trudy Geologicheskogo Instituta an SSSR (Proceedings of the Geological Research institute of Academia of Science USSR)*, 87, 253. (in Russian).

Lobanov, M. F. (1957). "Geologicheskoe Stroenie Novosibirskikh Ostrovov (Geological Structure of the New Siberian Islands)," in *Geologiya Sovetskoy Arktiki (Geology of the Soviet Arctic). Proceedings of the Research institute of Arctic Geology*, 81, 484–503. (in Russian).

Meyer, H., Dereviagin, A., Siegert, C., Schirrmeister, L., and Hubberten, H.-W. (2002). Palaeoclimate Reconstruction on Big Lyakhovsky Island, north Siberia?

hydrogen and Oxygen Isotopes in Ice Wedges. *Permafrost Periglac. Process.* 13, 91–105. doi:10.1002/ppp.416

Nagaoka, D., Saljo, K., and Fukuda, M. (1995). "Sedimental Environment of the Yedoma in High Arctic Eastern Siberia," in Proc. of the Third Symposium on the Joint Siberian Permafrost Studies between Japan and Russia in 1994, Tsukuba, Hokkaido, Japan, 8–13.

Nikol'skiy, P. A., and Basilyan, A. E. (2004). "Mys Svytoi Nos – Opornyi Razrez Chetvertichnykh Otlozhenii Severa Yano-Indigirskoy Nizmennosti (Svyatoi Nos Cape – the Main Section of Quaternary Deposits at the north of Yana-Indigirka lowland)," in *Estestvennaya Istoriya Rossiyskoi Vostochnoi Arktiki V Pleistotsene I Golotsene (Natural History of the Russian East Arctic in Pleistocene and Holocene)* (Moscow: GEOS publ.), 5–13. (in Russian).

Nikol'skiy, P. A., Basilyan, A. E., and Simakova, A. N. (1999). "Novye Dannye Po Stratigrafii Verkhnekaynozoiskikh Otlozheniy V Rayone Mysa Svyatoi Nos (New Data on Stratigraphy of Upper Cenozoic Deposits Around the Svyatoi Nos Cape," in *Landshaftno-klimaticheskie Izmeneniya, Zhivotnyi Mir I Chelovek V Pozdnem Pleistotsene I Golotsene (Landscape and Climate Changes, Fauna and Human at the Late Pleistocene and Holocene)* (Moscow: Institute of Geography publ.), 51–60. (in Russian).

Opel, T., Wetterich, S., Meyer, H., Dereviagin, A. Y., Fuchs, M. C., and Schirrmeister, L. (2017). Ground-ice Stable Isotopes and Cryostratigraphy Reflect Late Quaternary Palaeoclimate in the Northeast Siberian Arctic (Oyogos Yar Coast, Dmitry Laptev Strait). *Clim. Past* 13, 587–611. doi:10.5194/cp-13-587-2017

Ospennikov, E. N., and Trush, N. I. (1974). L'distost' Alasnykh I Ozerno-Allyuvial'nykh Otlozheniy Yano-Omoloiskogo Mezhdurech'ya I Metodika Ee Polevogo Opredeleniya. *Merzlotnye issledovaniya (Geocryological investigation)* XIV, 35–42. (in Russian). doi:10.5194/cp-13-587-2017

Popov, A. I. (1953). Peculiarities of Lithogenesis on Alluvial plains under Severe Climate, *Izvestiya an SSSR [Bulletin of Academia of Science, USSR]. Series Geography*, 1953 (2), 29–43. (in Russian).

Prokhorova, S. M., and Ivanov, O. A. (1973). *Olovonosnye Granitoidy Yano-Indigirskoi Nizmennosti I Svyazannye S Nimi Rossypi (Tin-Bearing Granitoids of the Yana-Indigirka lowland and Associated with Them Placers)*. Leningrad: Nedra Publ., 229. (in Russian).

Resheniya (1987). "Resheniya Mezhvedomstvennogo Stratigraficheskogo Soveshchaniya Po Chetvertichnoi Sisteme Vostoka SSSR (Decisions of the Interdepartmental Stratigraphic Meeting on the Quaternary System of the East of USSR)," in *Explanation Reports to the Regional Stratigraphic Charts of Quaternary Deposits of East of USSR* (Magadan: SVKNII DVO AN SSSR Publ.), 241. p. (in Russian).

Romanovskii, N. N. (1961a). Erozionno-termokarstovye Kotloviny Na Severe Primorskikh Nizmennostey Yakutii I Novosibirskikh Ostrovakh (Thrermokarst-Erosional Depressions on the north of Coastal Lowlands and New Siberian Islands). *Merzlotnye issledovaniya (Geocryological investigation)* I, 124–144. (in Russian).

Romanovskii, N. N. (1958). Merzlotnye Struktury Oblekaniya V Chetvertichnykh Otlozheniyakh (Draping Permafrost Structures in Quaternary Deposits). *Nauchnye doklady Vysshey shkoly (Scientific Rep. High School), Geol. geographical Sci.* 3, 185–188. (in Russian).

Romanovskii, N. N. (1961b). O Stroenii Yano-Indigirskoi Primorskoi Allyuvialnoi Ravniny I Usloviyakh Ee Formirovaniya (About Structure of the Yana-Indigirka Coastal Alluvial plain and Conditions of it Formation). *Merzlotnye issledovaniya (Geocryological investigation)* II, 129–138. (in Russian).

Romanovskii, N. N. (1993). *Osnovy Kriogeneza Litosphery (Fundamentals of Lithosphere's Cryogenesis)*. Moscow: Moscow State University Publ., 336. (in Russian).

Saks, V. N. (1948). Chetvertichnyi Period V Sovetskoi Arktike (Quaternary Period in the Soviet Arctic). *Trudy Arkticheskogo NII (Proceedings Arctic Res. institute)* 201, 131. (in Russian).

Schirrmeister, L., Froese, D., Tumskoy, V., Grosse, G., and Wetterich, S. (2013). "Permafrost and Periglacial Features | Yedoma: Late Pleistocene Ice-Rich Syngenetic Permafrost of Beringia," in *The Encyclopedia of Quaternary Science*. Editor S. A. Elias (Amsterdam: Elsevier), 542–552. doi:10.1016/b978-0-444-53643-3.00106-0

Schirrmeister, L., Grosse, G., Kunitsky, V., Meyer, Y., Derevyagin, A., Kuznetsova, T., et al. (2003). "Permafrost, Periglacial and Paleoenvironmental Studies on New Siberian Islands," in *Berichte zur Polarforschung. Reports on Polar and Marine Research. Russian-German Cooperation System Laptev Sea. The Expeditions Lena 2002*, 466, 195–314.

Schirrmeister, L., Kunitsky, V., Grosse, G., Wetterich, S., Meyer, H., Schwamborn, G., et al. (2011). Sedimentary Characteristics and Origin of the Late Pleistocene Ice Complex on north-east Siberian Arctic Coastal Lowlands and Islands – A Review. *Quat. Int.* 241 (1-2), 3–25. doi:10.1016/j.quaint.2010.04.004

Schirrmeister, L., Oezen, D., and Geyh, M. A. (2002). 230Th/U Dating of Frozen Peat, Bol'shoy Lyakhovsky Island (Northern Siberia). *Quat. Res.* 57, 253–258. doi:10.1006/qres.2001.2306

Schirrmeister, L., Wetterich, S., Kunitsky, V., Tumskoy, V., Dobrynin, D., Derevyagin, A., et al. (2008). "Palaeoenviromental Studies on the Oyogos Yar Coast," in *Berichte zur Polarforschung. Reports on Polar and Marine Research. The Expedition Lena – New Siberian Islands 2007*, 584, 85–265.

Sher, A. V. (1971). *Mlekopitayushchie I Stratigrafiya Pleistotsena Krainego Severo-Vostoka SSSR I Severnoi Ameriki (Mammals and Pleistocene Stratigraphy of the North-East of USSR and Northern America)*. Moscow: North-East of USSR and Northern America.

Skvortsov, E. F. (1914). Lensko-Kolymskaya Ekspeditsiya 1909 G. (Lena-Kolyma Expedition, 1909). *Izvestiya Imperatorskogo Russkogo Geograficheskogo Obshchestva (Bulletin of the Imperator's Russian Geographic Society*, 50 (7), 401–428. (in Russian).

Skvortsov, E. F. (1930). "V Pribrezhnykh Tundrakh Yakutii (Dnevnik Astronoma Lensko-Kolymskoy Ekspeditsii 1909 G. (On the Coastal Tundra of the Yakutia. Diary of the Leno-Kolyma Expedition's Astronomer in 1909)," in *Izvestiya Komiteta Po Izucheniyu Yakutskoy SSR (Proceedings of the Committee for Yakutian SSR Investigation)* (Leningrad: Academia of Science Publ.), XV, 1–244. (in Russian).

Spizharskiy, T. N. (1940). Chetvertichnoe Oledenenie Leno-Indigirskoy Oblasti (Quaternary Glaciation of the Lena-Indigirka Region). *Problemy Arktiki (Problems of the Arctic)* 11, 70–81. (in Russian).

Toll', E. V. (1897). "Iskopaemye Ledniki Novosibirskikh Ostrovov, Ikh Otnoshenie K Trupam Mamontov I K Lednikovomu Periodu (Fossil Glaciers of New Siberian Islands, that Relationship with mammoth Cadavrs and)," in *Sankt-Petersburg* (Moscow: Imperator's Academia of Science Publ), XXXII, 139. (in Russian).

Tomirdiaro, S. V., Chernen'kiy, B. I., and Bashlavin, D. K. (1982). "Lessovo-ledovaya Formatsiya Shel'fovogo Tipa I Obnazhenie Oyagosskii Yar (Loess-Ice Formation of Shelf Type and Oyogos Yar Outcrop)," in *Merzlotno-geologicheskie Protsessy I Paleogeografiya Nizmennostey Severo-Vostoka Azii (Cryogenic Processes and Palaeogeography of the Lowlands of North-East of Asia)* (Magadan: SVKNII DVNC AN SSSR publ), 30–53. (in Russian).

Tomirdiaro, S. V. (1980). *Lessovo-ledovaya Formatsiya Vostochnoi Sibiri V Pozdnem Pleistotsene I Golotsene (Loess-Ice Formation of East Siberia in Late Pleistocene and Holocene)*. Moscow: Nauka Publ., 184. (in Russian).

Tumskoy, V. E., and Basilyan, A. E. (2006). "Opornyi Razrez Chetvertichnykh Otlozheniy Ostrova Bol'shoy Lyakhovskii (Novosibirskie Ostrova) (The Main Section of Quaternary Deposits on the Bol'shoy Lyakhovskii Island (New Siberian Islands)," in Abstracts of the international conference "Problems of correlation of Pleistocene events on the Russian North", Sankt-Petersburg, 106–107. (in Russian).

Tumskoy, V. E., and Basilyan, A. E. (2009). "Stratigrafiya Chetvertichnykh Otlozheniy Beregov Proliva Dmitriya Lapteva (Stratigraphy of Quaternary Deposits on the Coasts of Dmitry Laptev Strait)," in Abstracts of the VI Russian conference on the Quaternary "Fundamental problems of Quaternary: results and main directions of future investigations", Novosibirsk, 592–593. (in Russian).

Tumskoy, V. E. (2021). Cryolithostratigraphy and Cryofacies Analysis. *Earth's Cryosphere* 25 (4), 3–16. (in Russian). doi:10.15372/kz20210401

Tumskoy, V. E. (2012). Osobennosti Kriolitogeneza Otlozheniy Severnoi Yakutii V Srednem Pleistotsene – Golotsene (Peculiarities of Cryolithogenesis of Deposits in Northern Yakutia in the Middle Neopleistocene-Holocene). *Earth's Cryosphere* XVI (1), 12–21. (in Russian).

Tumskoy, V. E., Romanovskii, N. N., and Tipenko, G. S. (2001). "Formirovanie Talikov Pod Termokarstovymi Ozerami Na Severo-Vostoke Yakutii: Rezul'taty Modelirovaniya (Talik Formation under Thermokarst Lakes on the north-east

of Yakutia)," in *Abstracts of the Second Conference of the Russian Geocryologists, Moscow*, 2, 292–300. (in Russian).
Vasil'chuk, Yu. K. (2017). "Cycles in Stratigraphy of Yedoma Deposits. Part 1," in *Arktika I Antarktika [Arctic and Antarctica]*, 2017, 62–83. (in Russian).
Vas'kovsky, A. P. (1963). "Ocherk Stratigrafii Antropogenovykh (Chetvertichnykh) Otlozhenii Krainego Severo-Vostoka Asii (Stratigraphy Review of the Anthropohen (Quaternary) Deposits of the Far North-East of Asia)," in *Geologiya Koryakskogo Nagorya (Geology of the Koryak Upland)* (Moscow: Geology of the Koryak Upland), 143–168. (in Russian).
Vollosovich, K. A. (1930). Geologicheskie Nablyudeniya V Tundre Mezhdu Nizhnimi Techeniyami Rek Leny I Kolymy (Geological Observations in the Tundra between the Lower Parts of Lena and Kolyma Rivers). *Proc. Committee Invest. Yakutian ASSR* 15, 299–357. (in Russian).
Vtyurin, B. I., Grigoriev, N. F., Katasonov, E. M., Kuznetsova, T. P., Shvetsov, P. F., and Shumskii, P. A. (1957). "Mestnaya Stratigraficheskaya Shema Chetvertichnykh Otlozhenii Poberezh'ya Morya Laptevykh (Local Stratigraphic Scheme of Quaternary on the Coast of the Laptev Sea)," in *Proceedings of Interdepartmental Meeting for Preparation of Uniform Stratigraphic Charts of Siberia, 1956* (Leningrad: Publ. in Gosud. nauch. -tech. izd-vo neftyanoi i gorno-toplivnoi lit-ry), 564–572. (in Russian).
Wetterich, S., Meyer, H., Fritz, M., Mollenhauer, G., Rethemeyer, J., Kizyakov, A., et al. (2021). Northeast Siberian Permafrost Ice-Wedge Stable Isotopes Depict Pronounced Last Glacial Maximum Winter Cooling. *Geophys. Res. Lett.* 48, e2020GL092087. doi:10.1029/2020GL092087
Wetterich, S., Rudaya, N., Kuznetsov, V., Maksimov, F., Opel, T., Meyer, H., et al. (2019). Ice Complex Formation on Bol'shoy Lyakhovsky Island (New Siberian Archipelago, East Siberian Arctic) since about 200 Ka. *Quat. Res.* 92 (2), 530–548. doi:10.1017/qua.2019.6
Wetterich, S., Rudaya, N., Tumskoy, V., Andreev, A. A., Opel, T., Schirrmeister, L., et al. (2011). Last Glacial Maximum Records in Permafrost of the East Siberian Arctic. *Quat. Sci. Rev.* 30, 3139–3151. doi:10.1016/j.quascirev.2011.07.020
Wetterich, S., Schirrmeister, L., Andreev, A. A., Pudenz, M., Plessen, B., Meyer, H., et al. (2009). Eemian and Late Glacial/Holocene Palaeoenvironmental Records from Permafrost Sequences at the Dmitry Laptev Strait (NE Siberia, Russia). *Palaeogeogr. Palaeoclimatol. Palaeoecol.* 279, 73–95. doi:10.1016/j.palaeo.2009.05.002
Wetterich, S., Tumskoy, V., Rudaya, N., Andreev, A. A., Opel, T., Meyer, H., et al. (2014). Ice Complex Formation in Arctic East Siberia during the MIS3 Interstadial. *Quat. Sci. Rev.* 84, 39–55. doi:10.1016/j.quascirev.2013.11.009
Wetterich, S., Tumskoy, V., Rudaya, N., Kuznetsov, V., Maksimov, F., Opel, T., et al. (2016). Ice Complex Permafrost of MIS5 Age in the Dmitry Laptev Strait Coastal Region (East Siberian Arctic). *Quat. Sci. Rev.* 147, 298–311. doi:10.1016/j.quascirev.2015.11.016
Zagorskaya, N. G. (1959). "Novosibirskie Ostrova (New Siberian Islands)," in *Chetvertichnye Otlozheniya Sovetskoy Arktiki (Quaternary Deposits of the Russian Arctic).* Editors V. N. Saks and S. A. Strelkov (Moscow, Publ. Gosud. nauch.-tech. izd-vo lit-ry po geologii i okhrane nedr SSSR), 200–211. (in Russian).

Conflict of Interest: The authors declare that the research was conducted in the absence of any commercial or financial relationships that could be construed as a potential conflict of interest.

frontiers | Frontiers in Earth Science

ORIGINAL RESEARCH
published: 08 June 2022
doi: 10.3389/feart.2022.757629

Mammoth Fauna Remains From Late Pleistocene Deposits of the Dmitry Laptev Strait South Coast (Northern Yakutia, Russia)

Tatiana V. Kuznetsova[1,2], Sebastian Wetterich[3,4], Heidrun Matthes[5], Vladimir E. Tumskoy[6,7] and Lutz Schirrmeister[3]**

[1]Department of Paleontology, Faculty of Geology, Lomonosov Moscow State University, Moscow, Russia, [2]Institute of Geology and Oil and Gas Technologies, Kazan Federal University, Kazan, Russia, [3]Permafrost Research, Alfred Wegener Institute Helmholtz Center for Polar and Marine Research, Potsdam, Germany, [4]Current Address, Heisenberg Chair of Physical Geography with Focus on Paleoenvironmental Research, Institute of Geography, Technische Universität Dresden, Potsdam, Germany, [5]Atmospheric Physics, Alfred Wegener Institute Helmholtz Center for Polar and Marine Research, Potsdam, Germany, [6]Laboratory of General Geocryology, Melnikov Permafrost Institute SB RAS, Yakutsk, Russia, [7]Pacific Oceanological Institute, Russian Academy of Sciences, Vladivostok, Russia

OPEN ACCESS

Edited by:
Bruce S. Lieberman, University of Kansas, United States

Reviewed by:
Ryan T. Tucker, Stellenbosch University, South Africa
Terry A. Gates, North Carolina State University, United States
Bruce S. Lieberman, University of Kansas, United States

***Correspondence:**
Tatiana V. Kuznetsova
tatkuz2012@mail.ru
Lutz Schirrmeister
lutz.schirrmeister@awi.de

Specialty section:
This article was submitted to Paleontology, a section of the journal Frontiers in Earth Science

Received: *12 August 2021*
Accepted: *21 April 2022*
Published: *08 June 2022*

Citation:
Kuznetsova TV, Wetterich S, Matthes H, Tumskoy VE and Schirrmeister L (2022) Mammoth Fauna Remains From Late Pleistocene Deposits of the Dmitry Laptev Strait South Coast (Northern Yakutia, Russia). Front. Earth Sci. 10:757629. doi: 10.3389/feart.2022.757629

The Yedoma Ice Complex in northern Yakutia provides perfect preservation conditions for frozen remains of vertebrate animals. Even complete mummified specimens of the late Pleistocene Beringian Mammoth fauna such as woolly mammoth, woolly rhinoceros, horse, and bison are occasionally found in permafrost deposits across eastern Siberia, i.e., in West Beringia, although bones are much more commonly found. The present study characterizes mammal bones from late Pleistocene and Holocene permafrost deposits exposed on the Oyogos Yar coast, part of the southern shore of the Dmitry Laptev Strait that connects the Laptev and East Siberian seas. The study applies a method to characterize fossil bone samples by the location of their discovery and by the accuracy of their relation to a depositional horizon. We analyzed a total of 38 finite radiocarbon ages of bone material from mammoth, horse, and musk ox, spanning from about 48.8 to 4.5 ka BP and including both our own data and data from the literature, in addition to previous publications that reported numerous bones with infinite ages from the Oyogos Yar coast. The distribution of bones and tooth along the coastal permafrost exposure is not uniform; it depends upon whether the material was found *in situ*, on thermo-terraces, or on the shore. The overall bone collection consists of 13 species of which *Mammuthus primigenius* (woolly mammoth, 41%), *Bison priscus* (bison, 19%), *Equus* ex gr., *caballus* (horse, 19%), and *Rangifer tarandus* (reindeer, 16%) predominate. The fossil bone species distribution is similar to those of other prominent Yedoma outcrops in the region, i.e., on Bykovsky Peninsula and on Bol'shoy Lyakhovsky Island. Correlation analysis shows that the Oyogos Yar bone sampling sites of different geomorphological settings are similar to each other but not to all sampling sites within the other two locations on Bykovsky Peninsula and on Bol'shoy Lykahovsky Island. High similarities in terms of correlation coefficients between specific sampling sites are often not represented in the cluster analysis.

Keywords: paleozoology, Mammoth fauna, permafrost, Yedoma Ice Complex, late Pleistocene, west Beringia, Oyogos Yar coast

INTRODUCTION

Numerous finds of bones and soft tissues of large mammals have been made on the southern shore of the Dmitry Laptev Strait on the Oyogos Yar coast (**Figure 1**) since the 19th century. The first detailed description and topographic survey of the Oyogos Yar coast was carried out in 1909 by two members of an expedition of the Ministry of Trade and Industry of Russia, E.F. Skvortsov and N.A. Iyudin (Skvortsov, 1914; Skvortsov, 1930). They noted abundant bone fossils on the beach, especially those of woolly mammoths. Here, bones and tooth accumulate occasionally due to thermo-denudation and thermo-erosion of the permafrost coast and subsequent slumping. The Yana-Indigirka Lowland, including the Oyogos Yar coast, has been actively studied since the end of the 1920's. Mammal bones from this area were sent to the zoological, geological, and paleontological institutes in Moscow, where they have been stored until now (Kuznetsova et al., 2004; Kuznetsova and Starodubtseva, 2009).

In the 20th century, Grigoriev (1932), Spizharskii (1940), Gusev (1958), Romanovskii (1958), Romanovskii (1961a), Romanovskii (1961b), and Kuznetsova (1965) actively studied the geological structure of this region and developed stratigraphic schemes for the late Quaternary deposits exposed here. The stratigraphic scheme for the Yana-Indigirka coastal plain by Gusev (1958) defined for the first time a "Mammoth horizon" occupying a distinct stratigraphic position. Later stratigraphic schemes for the region by Ivanov (1972) and Prokhorova and Ivanov (1973) characterized several formations of the middle and late Pleistocene by the presence of Mammoth fauna remains. Active exploration for fossil mammoth tusks resumed at the end of the 20th century, even in previously inaccessible regions. Consequently, the number of harvested tusks sharply increased. Furthermore, carcasses and soft tissue material of large Mammoth fauna animals became available for paleontological research (e.g., Boeskorov et al., 2013; Boeskorov et al., 2014).

According to Sher et al. (2005) the taxonomic composition of mammal bone assemblages can be affected by external factors, especially local geological processes and taphonomic conditions. Therefore, such collections may provide a modified picture of the relative abundances of species in the past. Furthermore, the typical patterns of taphonomy (Efremov, 1950) suggest that fossil bones represent only a small fraction of previously existing animals.

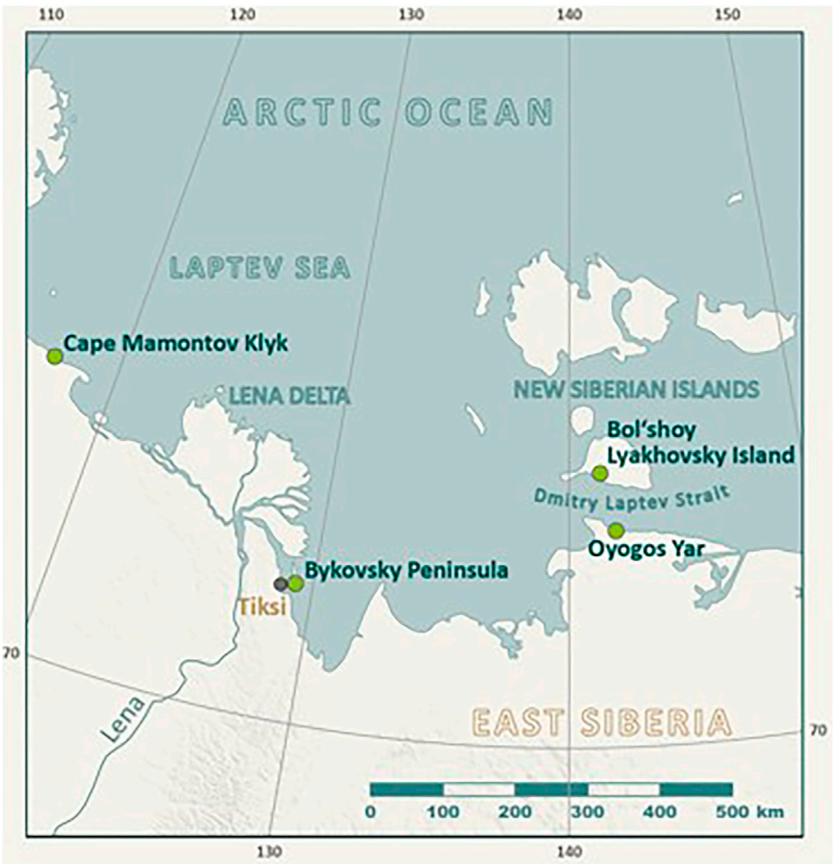

FIGURE 1 | Study region in the East Siberian Arctic showing the Oyogos Yar study site and other relevant study sites on the New Siberian Archipelago (Bol'shoy Lyakhovsky Island) and at the shore of the Laptev Sea (Cape Mamontov Klyk, Bykovsky Peninsula, and Lena Delta) mentioned in the paper.

The Beringia Land Bridge connected Eurasia and North America during the sea-level low stand of the last glacial period. Therefore, vast shelf and lowland areas between the Scandinavian-Kara ice sheets and the Laurentide ice sheet remained unglaciated and provided space for extensive permafrost formation in polygonal tundra landscapes. Here, abundant tundra-steppe vegetation sustained the Mammoth fauna, which was characterized by large grazers such as woolly mammoth, bison, musk ox, horse, reindeer, saiga, and woolly rhinoceros. Fossil evidence of this unique ecosystem of the last ice age still attracts public interest, while paleo-environmental research that employs floral and faunal fossils enables insights into ecosystem functioning as well as mechanisms of adaptation to changing climatic conditions (Sher et al., 2005; Andreev et al., 2011; Nikolskiy et al., 2011; Pitulko et al., 2017; Pavlova and Pitulko, 2020). In this context, the present study contributes to paleo-environmental research in West Beringia and aims 1) to describe and document the paleozoological characteristics of the late Pleistocene and Holocene deposits of the Oyogos Yar coast, 2) to assign whenever possible the mammal bone findings to cryostratigraphic units either by dating or by detailed documentation of the sites of finds in a systematic manner, and 3) to deduce the local distribution pattern of mammal bones onthe Oyogos Yar coast and to compare the composition of the West Beringian Mammoth fauna to that of mammal bone collections from neighboring prominent localities on the New Siberian Islands and on the Bykovsky Peninsula.

STUDY SITE AND PREVIOUS RESEARCH

Oyogos Yar is a stretch of the Arctic Ocean coastline located in the southwesternmost part of the East Siberian Sea, and forming part of the southern coast of the Dmitry Laptev Strait (**Figure 1**). Our study was performed at the Kondrat'eva Yedoma and the surrounding thermokarst basins (alases in Russian) in the eastern part of the Oyogos Yar coast. The Kondrat'eva Yedoma is the largest permafrost outcrop along this part of the coastline and stretches for about 5 km, from the mouth of the Kondrat'eva River to the west (between about 72.683°N, 143.475°E and 72.672°N, 143.635°E). The height of the Kondrat'eva Yedoma reaches 41 m above sea level (asl). The paleontological material discussed in this study was collected in 2002 and 2007 over 10 km of coastline, on the exposures as well as on the beach (Kuznetsova, 2003; Kuznetsova, 2008).

The modern periglacial landscape of the Oyogos Yar hinterland is characterized by Yedoma uplands intersected by alases and thermo-erosional gullies and valleys. Based on the cryostratigraphy exposed on the coast and its geocryological properties, such as ice content, the interplay of thermo-dedunation and thermo-abrasion erosional processes has shaped the coastal topography into steep bluffs and thaw slumps (thermo-cirques in Russian), with thermo-terraces topped by thermokarst mounds (baidzherakhs in Russian) that represent sedimentary centers of ice-wedge polygons that remained after the wedge ice melted (**Figure 2**). The Oyogos Yar coast erodes at an overall long-term rate of up to −6.5 ±

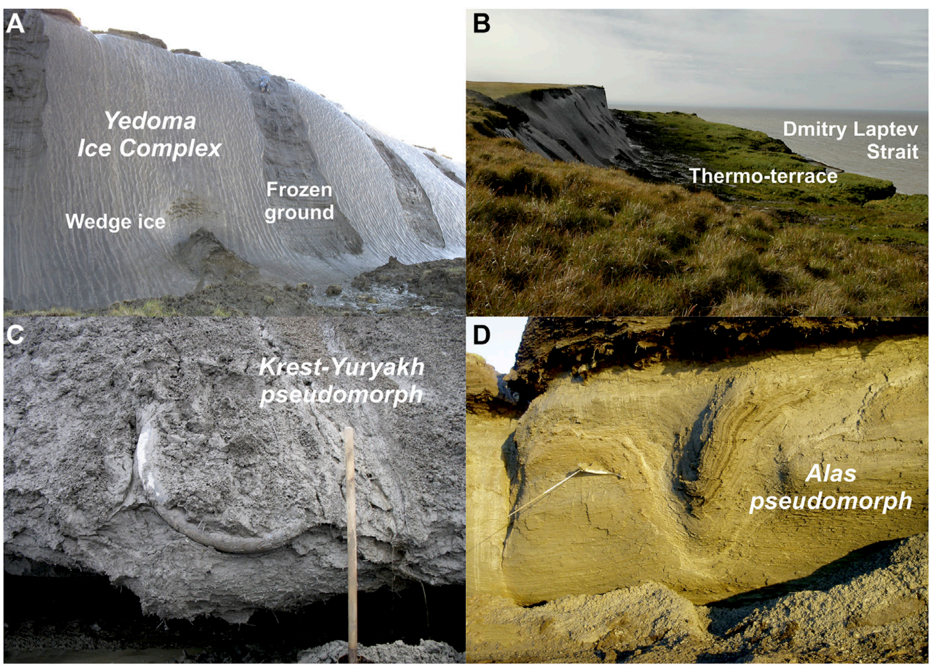

FIGURE 2 | Coastal exposures at the Kondrat'eva Yedoma (Dmitry Laptev Strait) showing **(A)** the Yedoma Ice Complex headwall (note climber dressed in blue at the top of the frozen ground deposit for scale), **(B)** the thermo-terrace below the headwall, **(C)** an ice wedge pseudomorph in Krest Yuryakh deposits, and **(D)** an ice wedge pseudomorph in lateglacial to Holocene alas deposits. Note *in situ* tusk findings in **(C)** and **(D)**. Photographs in August 2007 by T. Opel, AWI **(A)**, F. Kienast, Senckenberg Weimar **(B)**, L. Schirrmeister, AWI **(C)**, and V.V. Kunitsky, MPI Yakutsk **(D)**.

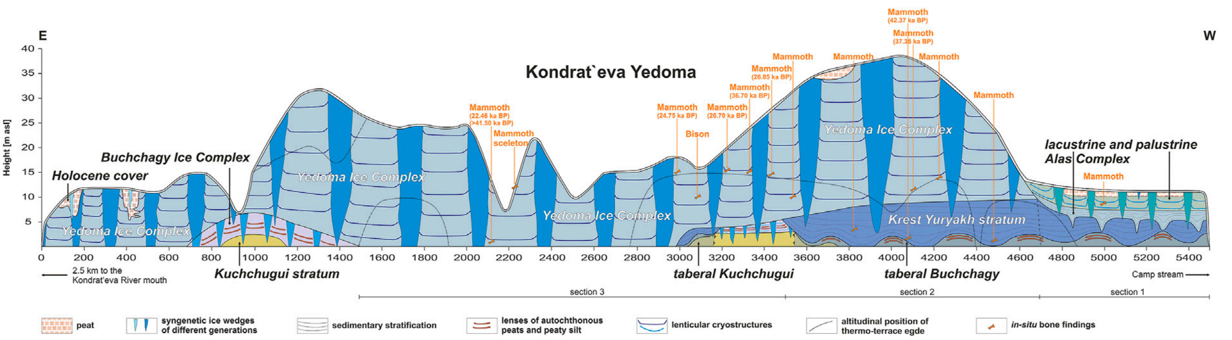

FIGURE 3 | Schematic structure of the Kondrat'eva Yedoma exposure on the Oyogos Yar coast from 2.5 to 8 km west of the Kondrat'eva River mouth [redrawn with changes from Tumskoy and Kuznetsova (2022).

$0.2\ ma^{-1}$ (Günther et al., 2013). Such rapid permafrost erosion provides annually renewed access to formerly frozen material, including the fossil mammal bones which are the focus of our study.

In recent years, geocryological investigations of the Oyogos Yar coastal exposures have been undertaken during Russian, Russian-Japanese, and Russian-German efforts that provided a general understanding of the local cryostratigraphic horizons (**Figure 3**) and their formation (Konishchev and Kolesnikov, 1981; Tomidiaro et al., 1982; Nagaoka et al., 1995; Tumskoy, 2012), as well as insights into paleo-ecology and paleo-climate (Wetterich et al., 2009; Andreev et al., 2011; Kienast et al., 2011; Opel et al., 2011; Boeskorov et al., 2013; Rudaya et al., 2015; Wetterich et al., 2016; Opel et al., 2017a; Opel et al., 2017b; Neretina et al., 2020). Based on the stratigraphic chart proposed by Tumskoy and Kuznetsova (2022) for northern Yakutia, and follow-up permafrost studies that included dating results (Schirrmeister et al., 2002a; Wetterich et al., 2014; Wetterich et al., 2016; Wetterich et al., 2019; Opel et al., 2017a; Zimmermann et al., 2017; Wetterich et al., 2021a), the permafrost deposits exposed on both coasts of the Dmitry Laptev Strait discontinuously cover the last about 200,000 years before present and span from Marine Isotope Stage (MIS) 7 to MIS 1. At the study site, a Yedoma Ice Complex of MIS 3 age is preserved in the Yedoma upland, while adjacent thermokarst basins of lateglacial as in **Figure 2** and MIS 1 age are composed of lacustrine and palustrine deposits and reach up to 15 m asl (**Figure 3**). Deposits underlying these two main sequences belong to the lacustrine Krest-Yuryakh stratum of MIS 5 age, which is commonly considered to represent the last Interglacial (e.g., Andreev et al., 2009; Wetterich et al., 2009; Kienast et al., 2011). Further MIS 5 deposits belong to the Buchchagy Ice Complex, while the chronostratigraphic position of the Kuchchugui stratum is still in question due to scarcity of geochronologic data (MIS 5 vs. MIS 6; Andreev et al., 2004; Tumskoy, 2012). After their formation, ice-rich permafrost deposits such as the Buchchagy Ice Complex or the Yedoma Ice Complex might have been subjected to thaw during successive warm periods such as the Last Interglacial or the Holocene. If thawing occurred, the remaining and refrozen mineral and organic depositional components are defined as taberal deposits (Kaplina, 2009). Taberal deposits are present in the cryostratigraphic record of the Oyogos Yar coast and are therefore considered in the study (**Figure 3**).

It is well known that well-preserved Mammoth fauna fossils can be found on the Oyogos Yar coast and at the Kondrat'eva Yedoma in particular (Smirnov, 2003). However, only two skeletal elements from the eastern part of the Oyogos Yar coast are stored in the Zoological Institute of the Russian Academy of Sciences (St. Petersburg, Russia); the upper left tooth of a woolly mammoth, transferred to the institute in 1972, and a horse skull without a lower jaw, found at the mouth of the Rebrova River and transferred to the collection in 1991 by M.V. Sablin and O.R. Potapova. Single finds of the remains of fossil mammals from the area of the Kondrat'eva Yedoma are stored in the Diamond and Precious Metals Geology Institute, Siberian Branch, RAS and the Mammoth Museum of the North-eastern Federal University (NEFU, Yakutsk, Russia).

In 2009 and 2010, two outstanding discoveries were made on the Oyogos Yar coast. In 2009, 30 km west of the mouth of the Kondrat'eva River, a part of the carcass of a woolly mammoth was found; this specimen is known as mammoth Yuka and was radiocarbon-dated to 34,300 +260/−240 a BP (GrA 53289; Boeskorov et al., 2013). The remains of the Yuka woolly mammoth include by the skull with cheek teeth and tusks, the lower jaw with cheek teeth, the lower parts of the legs with soft tissues, the skin, some soft tissues of the body, and part of the axial skeleton. The left ear, trunk, and lips are preserved on the head. There are three finger-like processes at the end of the trunk. The hair is gray-brown and dark brown on the body and red on the legs. The maximum length of the hair on the hips is 40–42 cm (Boeskorov et al., 2013). A fragment of a horse carcass was found in the same area in 2010, and radiocarbon-dated to 4,630 ± 30 a BP (GrA 54209; Boeskorov et al., 2013). Today, this partial horse carcass is named the Yukagir horse, of which the head and neck, part of the torso containing some internal organs, the hind legs, and the tail have been preserved. The dark brown mummified skin was preserved in fragments. Short hair, 4.5–7 cm long and so dark brown as to be almost black, is preserved on the distal parts of the legs only (Boeskorov et al., 2013).

A total of 43 radiocarbon dates for mammoth bones and tooth, of which 20 are finite dates for specimens from the mainland shore of the Dmitry Laptev Strait, was first presented by Nikolskiy and Basilyan (2004) and Nikolskiy et al. (2011). These age determinations were obtained for bones from three locations, namely Svyatoy Nos, Ulakhan-Taala, and Kondrat'eva Yedoma, and are discussed in the context of the present study.

MATERIALS AND METHODS

Although scientific sampling of large mammal bone remains on the Oyogos Yar coast (**Figure 1**) has been taking place for more than 100 years, the paleontological collection of the Russian-German SYSTEM LAPTEV SEA collaboration (since 1998) is the most complete and representative for this coastal region. Mammal bones and bone fragments were collected on the Oyogos Yar coast during fieldwork in 2002 and 2007, and identified afterwards (Kuznetsova, 2003; Kuznetsova, 2008). For a comprehensive and complete study of the paleozoological material, all mammalian remains regardless of their state of preservation, including small bone fragments, were collected and identified. This allowed the most accurate possible estimation of the relative abundances of primary large mammal species of the late Pleistocene Mammoth fauna that inhabited this area. The overwhelming majority of the finds were identified down to species level using the collection of the Department of Osteology of the Zoological Museum of Lomonosov Moscow State University (Russia) as comparative material. Thus, we determined the paleozoological characteristics of the late Pleistocene and Holocene deposits of the eastern part of the Oyogos Yar coast. In 2002 and 2007, we collected 1977 samples of fossil bones and tooth (**Table 1**).

Statistical analyses were conducted in order to evaluate the degree of similarity among the species distributions for the Mammoth fauna at the different sampling sites associated with the three areas discussed: the Oyogos Yar coast at the Kondrat'eva Yedoma west of the mouth of the Kondrat'eva River, the southern coast of Bol'shoy Lyakhovsky Island near the mouth of the Zimov'e River, and on the Bykovsky Peninsula at the Mamontova Khayata Yedoma (**Figure 1**). First, Pearson correlation coefficients were calculated between the species distributions of all sampling sites to assess whether the level of uniformity among sites within one location characterized by different geomorphological settings is comparable to the level of uniformity among sites in different locations. Second, to further explore those differences and similarities, agglomerative hierarchical cluster analysis was then performed on the species counts for each sample site Given that the numbers are actual counts of Mammoth fauna bones, chi-squared distances were used in the analysis; clustering method was "average." The statistical significance of the clusters recovered by the analysis was assessed using a bootstrapping approach following Suzuki and Shimodeira (2006). The analysis was performed using R's Pvclust Package (Suzuki et al., 2019; R Core Team, 2021).

While collecting bones, each sample was marked immediately upon discovery and the location of the find was mapped (Kuznetsova, 2008). Group A bones were obtained *in situ*, i.e., within the frozen sediment, so that the location and vertical position in the section are known. Group A contains the smallest number of bone specimens due to the specifics of collecting paleontological material from ice-rich permafrost deposits that thaw intensively during the summer season, and in which freshly exposed boness are rather quickly relocated and buried in slump debris. Group B bones were obtained from thermo-terraces of thaw slumps, having been previously thawed and relocated, but were found in positions that indicated roughly which part of the bluff above they had come from. Therefore, the upper and lower boundaries of their possible occurrence in the section could be determined, and aligned to a specific cryostratigraphic unit. Group C bones also occurred within the thawed debris at the base of the exposure, but in locations that provided no indication of their original positions. Group D bones, which were found on the beach, represent the most abundant category. This group is further divided into three subgroups: those from the west part of the coast, those from the east part of the coast, and those from the mouth of the stream. Group E bones were found on the surface of the tundra in the hinterland. specimens of the A and B groups have direct stratigraphic importance for the interpretation of the permafrost sequences. For *in situ* group A specimens, the stratigraphic position is known, or the minimum height in section can at least be estimated. For group B specimens, approximate upper and lower bounds can be placed on their original stratigraphic positions.

To document the sites of finds on the beach with greater precision, the coast at Kondrat'eva Yedoma west was divided during field work into three parts (**Figure 3**). **Section 1** was the beach under the Alas basin lying between 7.2 and 8.0 km from the mouth of the Kondrat'eva River (4,700–5,500 m of the Kondrat'eva Yedoma profile); **Section 2** spanned the beach below the cliff of the high Yedoma upland, between 6 and 7.2 km from the river mouth (3,500–4,700 m of the Kondrat'eva Yedoma profile); and **Section 3** spanned the beach between 4 and 6 km from the river mouth (1,500—3,500 m of the Kondrat'eva Yedoma profile), which is the coast of a less elevated part of the Yedoma upland. However, when the sea is rough, bones can be transported along the beach for considerable distances, as we observed during fieldwork. Therefore, the division into **Sections 1–3** was not strict, and was used only with reference to the numerous bones found on the east part of the coast. All bones from the western shore (west from the Camp stream, area is not shown in **Figure 3**) are considered to belong to one group.

In total, 21 bone fragments representing mammoth, horse, bison, and musk oxen were selected for radiocarbon dating, which was done either by acceleration mass spectrometry (AMS) or conventional ^{14}C age determination. The latter required sample weights of about 1 kg. Dating was performed at the Laboratory of Isotope Geochemistry and Geochronology of the Geological Institute of the Russian Academy of Sciences Moscow, Russia (GIN), at the Leibniz Laboratory for Radiometric Dating and Stable Isotope Research, University of Kiel, Germany (KIA), and at the Center of Isotope Research, University of Groningen, the Netherlands (GrA). Dating was

TABLE 1 | Collection of mammalian remains sampled at Oyogos Yar in 2002 and 2007.

					Collection 2007						**Collection 2002**			
			Total 2002 2007	**Total 2007**	**Exposure**	**Shore**				**Tundra surface and other places**	**Total 2002**	**Exposure**	**Shore**	**Tundra surface**
Location group					**Group A, B, C**	**Group D**				**Group E, remote areas**		**Group A, B, C**	**Group D**	**Group E**
Order	**Family**	**Taxon**				**Total shore**	**Eastern shore**	**Western shore**	**Other shore**					
Proboscidea	Elephan-tidae	*Mammuthus primigenius* (Blumenbach, 1799)	779	632	39	561	306	225	30	35	147	12	131	4
Artiodactyla	Bovidae	*Bison priscus* (Bojanus, 1827)	366	286	14	272	135	127	10		80	13	67	
		Ovibos moschatus (Zimmermann, 1780)	87	75	1	71	35	36		3	12	1	11	
		Saiga tatarica L., 1758	1	1		1	1							
	Cervidae	*Rangifer tarandus* L., 1758	305	262	21	241	136	98	7		43	10	33	
		Alces alces (L., 1758)	3	3		3	2	1						
		Alces americanus Clinton, 1822	2	2		2	1	1						
Perissodac-tyla	Equidae	*Equus* ex gr. *caballus* L., 1758	361	303	8	295	144	138	13		58	8	50	
	Rhinocero-tidae	*Coelodonta antiquitatis* Blumenbach, 1790	2	1		1		1			1		1	
Carnivora	Felidae	*Panthera spelaea* (Goldfuss, 1810)	3	2		2		2			1	1		
	Canidae	*Canis* sp.	6	6		6	2	4						
Lagomorpha	Leporidae	*Lepus* sp.	7	6		6	3	3			1		1	
Rodentia	Myomorpha		3	3		3	1	2						
		Other	5	5		5	4	1						
		Undefined	47	21	3	18	10	7	1		26	3	23	
		Total	1977	1608	86	1487	780	646	61	38	369	48	317	4

TABLE 2 | List of radiocarbon dates derived from collagen of Mammoth fauna bones collected at Oyogos Yar shown in order of increasing age. GIN - Geological Institute of the Russian Academy of Sciences, Moscow (Russia); GrA—Center of Isotope Research University of Groningen (Netherlands); KIA—Leibniz Laboratory for Radiometric Dating and Stable Isotope Research University of Kiel (Germany). Samples 2 and 19 were taken from the same costa of *Mammuthus primigenius*.

No.	Sample no.	Lab. No.	^{14}C date [a BP]	Taxon	Skeleton element	Preservation	Locality	First publication
1	Oyg-07-O63	GIN-14091	12,550 ± 80	*Equus* ex gr. *caballus*	femur	distal fragment	thermo-terrace of the largest thaw slump, at 38.5 to 8 m asl (group B)	This study
2	NS-OgK-O286	GrA-47134	22,460 ± 100	*Mammuthus primigenius*	costa	fragment	*In situ* in Yedoma Ice Complex, shore, 100 m east of the stream mouth (near 2,200 m of the Kondrat'eva Yedoma profile), at 1 m asl (group A)	This study
3	NS-OgK-O175	GIN -13221	24,750 ± 210	*Mammuthus primigenius*	tibia, right	fragment	thermo-terrace (group B)	This study
4	Oyg-07-O352	GIN-14094	25,260 ± 310	*Equus* ex gr. *caballus*	radius	fragment, juv.	western coast, shore near the mouth of Rebrova River (group D)	This study
5	Oyg-07-O336	GIN-14093	25,620 ± 1,100	*Equus* ex gr. *caballus*	tibia	distal fragment	western coast, shore near the mouth of Rebrova River (group D)	This study
6	NS-OgK-O151	GIN-13236	26,700 ± 1,400	*Equus* ex gr. *caballus*	femur, right	distal fragment	thermo-terrace (group B)	This study
7	NS-OgK-O151	GIN-13245	26,850 ± 150	*Equus* ex gr. *caballus*	femur, right	distal fragment	thermo-terrace (group B)	This study
8	NS-OgK-O386	GIN-13267	30,000 ± 650	*Equus* ex gr. *caballus*	tibia, right	distal fragment	eastern shore (group D)	This study
9	Oyg-07-O985	GIN-14092	32,330 ± 700	*Equus* ex gr. *caballus*	femur	fragment	eastern coast, shore (group D)	This study
10	NS-OgK-O208	GIN-13252	34,800 ± 700	*Equus* ex gr. *caballus*	scapula, right	fragment	eastern shore, near stream mouth (near 2,200 m of the Kondrat'eva Yedoma profile) (group D)	This study
11	NS-OgK-O267-a	GIN-14057	35,250 ± 330	*Equus* ex gr. *caballus*	pelvis, left part	sample cut out	eastern shore (group D)	This study
12	NS-OgK-O270	GIN-13899	36,700 ± 400	*Mammuthus primigenius*	ulnae, left	fragment, cut out	thermo-terrace (group B)	This study
13	Oyg-07-O61	GIN-14059	37,350 ± 320	*Equus* ex gr. *caballus*	pelvis	fragment	thermo-terrace of the largest thaw slump, at 38.5 to 8 m asl (group B)	This study
14	NS-OgK-O271	KIA 27803	40,700 + 2,110/-1,670	*Mammuthus primigenius*	ulnae, left	fragment, with marrow	eastern shore (group D)	Rompler et al. (2006)
15	NS-OgK-O461	GrA-44920	42,140 + 480/-410	*Ovibos moschatus*	vertebra	fragment	eastern shore (group D)	This study
16	Oyg-07-O855	KIA 42888	42,370 + 860/-780	*Mammuthus primigenius*	tusk	fragment	*In situ* in Krest-Yuryakh; eastern coast; bluff below the second small thaw slump; height 2.2 m asl (group A)	This study
17	NS-OgK-O360	GIN-13260	>30,000	*Equus* ex gr. *caballus*	tibia, right	distal fragment	eastern shore (group D)	This study
18	NS-OgK-O343	GIN-13263	>35,000	*Ovibos moschatus*	Cervical vertebra	damaged	eastern shore, near stream mouth (group D)	This study
19	NS-OgK-O286	GIN-13223	>41,500	*Mammuthus primigenius*	costa	fragment	*In situ* in Yedoma Ice Complex, eastern coast, 100 m east of the stream mouth (near 2,200 m of the Kondrat'eva Yedoma profile), altitude 1 m asl (group A)	This study

initially possible only using the conventional radiocarbon method, in the laboratory of the Geological Institute RAS in Moscow. Large, well-preserved samples were selected for this. After fieldwork in 2002 a single *in situ* sample from the outcrop was dated, as were four large mammoth and horse samples from the thermo-terrace and six samples from the shore. The largest musk ox bone collected on the coast was also dated, because this species is rare. After fieldwork in 2007, five horse bones were given to the same laboratory, two from the thermo-terrace and three from the shore. Four samples (three mammoth and one musk ox) were dated by the AMS radiocarbon method due to the small size of the bone fragment (**Table 2**). Ages are reported as uncalibrated years before present (a BP).

RESULTS

From the entire mammal bone collection sampled in 2002 and 2007 (1977 samples in total), 1925 bones were identified and analyzed (**Figure 4**). Most of the collection was systematically

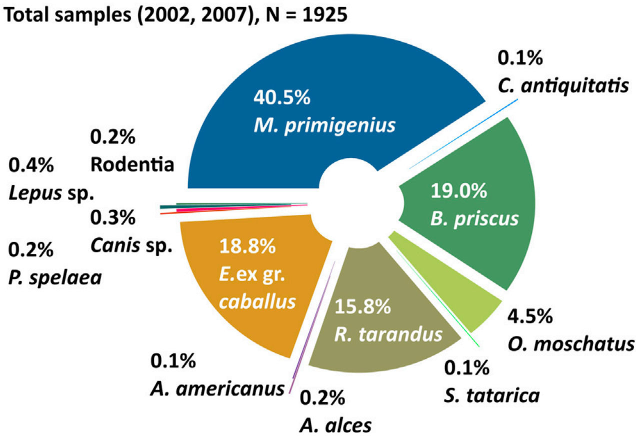

FIGURE 4 | Composition of the mammal bone collections from Oyogos Yar showing the total collection from 2002 to 2007 (N = 1925). The percentages are calculated from the total number of identified samples (**Table 1**).

obtained in August 2007 near the Kondrat'eva Yedoma and adjacent alases. Over 4 weeks of fieldwork it was possible to study the host deposits, and to carefully differentiate the sites where bones were found. In contrast, the samples from 2002 derived from a limited 1 day reconnaissance; consequently, the 2002 and 2007 collections are considered separately. The 2007 samples include more *in situ* finds and more small bones and small fragments of large bones, which commonly require more time and effort to locate (**Figure 5**). The 2002 samples, by contrast, include more large bones and more finds from the beach (**Figure 6**).

Mammal Bone Collection From 2007

In total, the collection from 2007 comprises 1,608 bones and fragments, of which 21 could not be identified and five belong to birds or to arctic ringed seals. Only the 1582 identified terrestrial mammal bones (**Figure 5A**) are considered further. Among this total, woolly mammoth [*Mammuthus primigenius* (Blumenbach, 1799)] bones and fragments prevail (39.9%), while horse [*Equus* ex gr. *caballus* L., 1758] (19.2%), Pleistocene bison [*Bison priscus* (Bojanus, 1827)] (18.1%), reindeer [*Rangifer tarandus* L., 1758] (16.6%), and musk ox [*Ovibos moschatus* (Zimmermann, 1780)] (4.7%) make up lesser shares of the collection. Bones of other mammals such as woolly rhinoceros [*Coeleodonta antiquitatis* (Blumenbach, 1790)], elk [*Alces alces* L., 1758], moose [*A. americanus* (Clinton, 1822)], saiga antelope [*Saiga tatarica* L., 1758], rodents [Rodentia], lagomorphs [*Lepus* sp.], and predators such as wolves [*Canis* sp.] and cave lions [*Panthera spelaea* (Goldfuss, 1810)], are rare and each represent far less than 1% of the collection (**Figure 5A**; **Table 1**).

The 2007 bone collection is differentiated into exposure samples, including groups A, B, and C (**Figure 5B**) and shore samples corresponding to group D (**Figures 5C–E**). A few samples were collected on the surface of the tundra (group E), and at other outcrops far west of Kondrat'eva Yedoma. Samples collected from the outcrops (exposure samples defined as groups A, B, and C) sum up to 83 identified fossil bones, representing only about 5.2% of the entire collection. Such a proportion is typical for Yedoma Ice Complex localities. From the Kondrat'eva exposures, remains of woolly mammoth predominate (47.0%), followed by reindeer (25.3%), bison (16.9%), and horse (9.6%) (**Figure 5B**).

Only six bones were found *in situ* in the exposure (group A, **Figure 3**). In total, 78 samples were collected from the thermo-terraces (group B) of Kondrat'eva Yedoma, and 2 samples (bison and reindeer) were found within the thawed debris at the base of the exposure (group C). The Group A specimens include one damaged radius of a bison, and five fragments of woolly mammoth tusks. The *in situ* findings were confined to the sediments of the Yedoma Ice Complex and to taberal Kuchchugui, Krest-Yuryakh, and Alas deposits (**Figure 3**).

The samples collected directly from the thermo-terrace (group B), were found mainly at altitudes from 8 to 16 m asl. Of the 78 fossil bones or fragments, 75 have been identified, while three remain unidentified. Remains of *M. primigenius* (45.3%) predominate, followed by *R. tarandus* (26.7%), *B. priscus* (16.0%), and *E.* ex gr. *caballus* (10.7%), related to the identified 75 bones.

The majority of the bone material considered in this study, totaling 1464 identified samples, was obtained from the shore and constitutes group D. There are 1404 samples from the eastern and western shores (**Figure 5C**), and 60 bones collected from the shore in remote areas ("other shore" in **Table 1**; not shown in **Figure 5**).

From the beach at the Kondrat'eva Yedoma cliff and the eastern part of the alas (eastern shore, **Table 1**), 766 samples were collected and identified (**Figure 5D**). Woolly mammoth predominates (39.9%), followed by horse (18.8%), reindeer (17.8%), bison (17.6%), and musk ox (4.6%) (**Figure 5D**). Among rare species, saiga antelope were represented by a distal fragment of a humerus, elk by thoracic and lumbar vertebrae and a second phalanx, wolves by a pelvic fragment and second upper molar (identified by M.V. Sotnikova, Geological Institute RAS Moscow, Russia), hares by skull, pelvic, and femoral fragments, and lemmings by a skull (*Dicrostonyx* sp., determined by A.S. Tesakov, Geological Institute RAS Moscow, Russia).

West of the Camp stream at the beach below the alas outcrop (western shore, **Table 1**; not shown in **Figure 3**), 646 samples were collected, of which 638 were identified (**Figure 5E**). Here, woolly mammoth (35.3%), horse (21.6%), bison (19.9%), reindeer (15.4%), and musk ox (5.6%) were the most common species. Woolly rhinoceros were represented by the proximal fragment of the third metacarpal bone (Mc III), cave lions by a tooth and epistrophy of, *Canis lupus* by three teeth and a femur fragment (identified by M.V. Sotnikova), hares by three limb bones, lemmings by a pelvis and a right mandibular ramus containing two teeth (*Dicrostonyx* cf. *torquatus*, identified by A.S. Tesakov), and *Alces* sp. by a distal femur fragment, a damaged lumbar vertebra, and a fragment of a thoracic vertebra. Moose were represented by a right lower third molar (M_3) and a second phalanx, identified as *A. americanus* (identified by P.A. Nikolskiy, Geological Institute RAS Moscow, Russia).

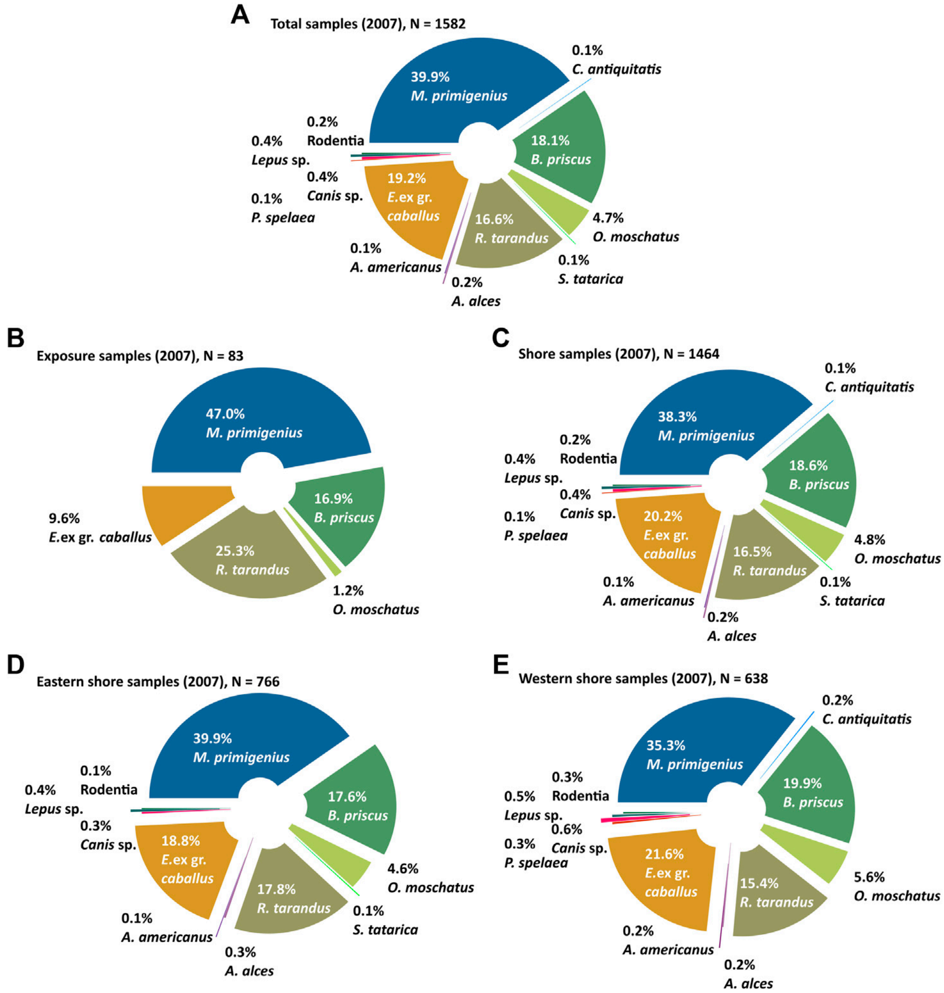

FIGURE 5 | Composition of the mammal bone collections from Oyogos Yar showing **(A)** the total collection from 2007 (N = 1582) differentiated into **(B)** the exposure collection (N = 83) and **(C)** the shore collection (N = 1464), which is further differentiated into **(D)** the eastern shore collection (N = 766) and **(E)** the western shore collection (N = 638). The percentages are calculated from the total number of identified samples (**Table 1**). Note, that 35 bones found at other places and 61 bones found at other shore locations than **(D)** or **(E)** are summarized in **(A)**, but not differentiated in this figure. The full record is given in **Table 1**.

With respect to species that were part of the Mammoth fauna and still inhabit the territory, it is difficult to distinguish between fossil and modern material collected on the shore, which are often in a similar state of preservation. Therefore, it is impossible to say for sure whether fossil or modern remains of reindeer, wolf, and hare were found. The last of these, at least, is present in the fossil bone collection from Bykovsky Peninsula, where fossil hare remains were collected *in situ* (Kuznetsova et al., 2019).

In terms of bone fragmentation and quality of bone preservation, specimens from the western shore (**Figure 5E**) differ from those from the eastern part (**Figure 5D**). On the western shore, there were fewer unbroken large limb bones, but many small limb bones, small fragments of various bones, and small fragments of mammoth tusks. This indicates that the bones were repeatedly redeposited from older to younger deposits and sorted by waves on the beach. This hypothesis is also confirmed by the collection of samples from a small part of the western coast, which we identified as “coast with small bones” (2.6–3.1 km west of the Camp stream). This area was almost completely covered with small tusk and bone fragments, and small bones. On this small part of the beach, 8.4% of the total western coast samples were collected; about 80% of the samples from this area are small fragments of mammoth tusks.

Interesting paleontological material includes a slightly damaged skull of a male musk ox with the lower jaw, and a fragment of a humerus with soft tissues and the ulna (Tumskoy and Dobrynin, 2008). Both were found at the mouth of a stream located 2.3 km southeast of the mouth of the Krest-Yuryakh River, in slumping debris at an altitude of 6–7 m asl. This fragment of the musk ox skeleton probably thawed out of Bychchagy Ice Complex sediments. We can assume that these are fragments of the skeleton of one individual, because they were found close to one another and in an identical state of preservation.

A fragmentary woolly mammoth skeleton was found on the surface of the tundra near a stream at a distance of 4.7 km from the mouth of the Kondrat'eva River (at 2,200 m along the Kondrat'eva Yedoma profile) (**Figure 3**), at an altitude of 12 m asl. This skeleton thawed in a thermokarst mound of the Yedoma Ice Complex and was first found in 1994 by local people (personal communication). The skull was broken into many small pieces, probably when tusks and teeth were knocked out of it. We collected 32 pieces of this skeleton: a tooth fragment, six fragments of the cervical vertebrae, four fragments of the thoracic vertebrae, five fragments of the lumbar vertebrae, some ribs, a scapula, a fragment of the pelvis, a metapodium, and an os carpale.

Mammal Bone Collection From 2002

We conducted a reconnaissance trip to the Kondrat'eva Yedoma on 30 August 2002 (Schirrmeister et al., 2003a) and collected 369 bones and fragments, of which 343 were identified (**Table 1**; **Figure 6A**). We consider the 2002 collection separately as it was collected in 1 day, which is reflected in an even greater predominance of bones collected on the shore over material collected at the outcrop. The 2002 collection contains many large limb bones and few small bone fragments and small mammal bones and teeth. The 2002 landing site was located at the mouth of a creek situated 4.7 km west of the Kondrat'eva River mouth, at a horizontal distance of 2,200 m on the Kondrat'eva Yedoma profile shown in **Figure 3**. As in the 2007 collection, mammoth (42.9%), bison (23.3%), horse (16.9%), and reindeer (12.5%) bones predominate, while musk ox remains (3.5%) make up a smaller share (**Figure 6A**).

A total of 48 specimens (45 identified) representing groups A and B were collected from the exposure and the thermo-terrace (**Figure 6B**), but only one bone (a large fragment of a mammoth rib) was found *in situ*. Next to this rib in the coastal outcrop, at a height of 1 m asl, several more ribs were observed, but they could not be collected due to inaccessibility. The ribs protruded from the roof of a wave-cut notch right above the beach. Most likely a part of this skeleton, or the complete mammoth skeleton, which had been buried in the exposed Yedoma Ice Complex was destroyed. It is possible that the bones found directly next to the described site of the possible burial of this mammoth skeleton, including a pelvis (right and left halves), a damaged left femur, and a fragment of the left humerus, were part of the destroyed skeleton. The bones belong to a young individual and bone marrow is preserved in the limb bones. The rib, sampled *in situ*, was dated twice (**Table 2**) to >41,500 a BP (GIN-13223) and 22,460 ± 100 a BP (GrA-47134). It is not clear how such considerable age differences between samples from one bone can be explained. A fragment of the left half of the pelvis was also dated, to 35,250 ± 330 a BP (GIN-14057).

Forty-seven specimens were collected from the thermo-terrace, including three indeterminate bone fragments. Among the 44 identified specimens found on the thermo-terrace (**Figure 6B**), bison bones (28.9%) predominate slightly over

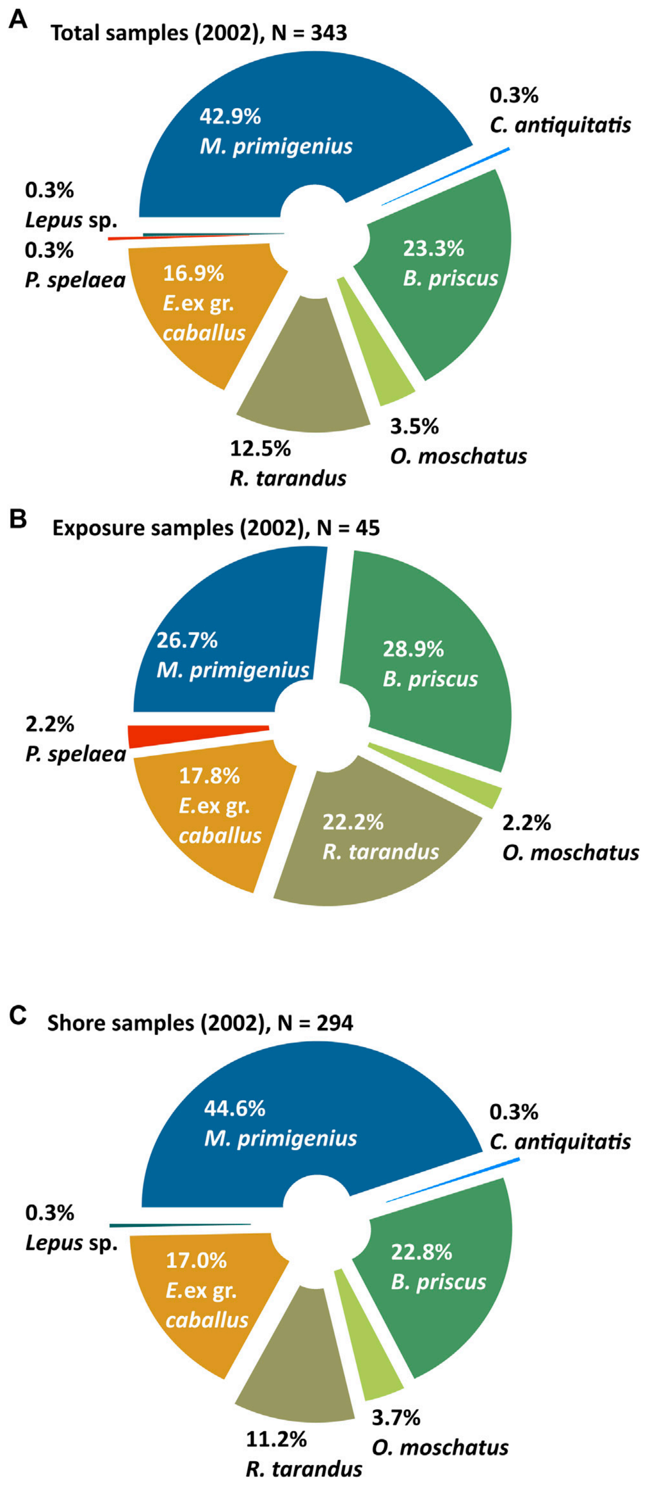

FIGURE 6 | Composition of the mammal bone collections from Oyogos Yar showing **(A)** the total collection from 2002 (N = 343) differentiated into **(B)** the exposure collection (N = 45) and **(C)** the shore collection (N = 294). The percentages are calculated from the total number of identified samples (**Table 1**).

mammoth bones (26.7%), whereas reindeer bones make up 22.2% of the total, and horses 17.8%. The 44 specimens also include a single musk ox horn sheath, and a single fragment of a cave lion femur.

Some 317 specimens collected from the shore represent 86% of the entire 2002 collection, but 23 could not be identified due to poor preservation. The species present among the 294 identified bone remains include woolly mammoth (44.6%), bison (22.8%), horse (17.0%), reindeer (11.2%), and musk ox (3.7%) (**Figure 6C**). In addition to bones of these five most common Mammoth fauna species, a damaged cervical vertebra of woolly rhinoceros and a tibial fragment of hare were found. The entire 2002 collection differentiates into 245 samples from the shore below the highest outcrop of the Kondrat'eva Yedoma (between 2,200 m and 5,500 m on the Kondrat'eva Yedoma profile shown in **Figure 3**) and 68 samples from the shore at the mouth of the creek at the landing site (at 2,200 m on the Kondrat'eva Yedoma profile shown in **Figure 3**). The last group of samples includes four bones, which probably belong to the mammoth skeleton described above and were collected at a distance of 150 m east of the landing site. No specimens were collected to the east of the landing site due to lack of time. Two mammoth partial limb bones (ulnare and radius fragments), and two tusk fragments, were found on the tundra surface (group E) near the landing site.

Preservation of the Paleontological Specimens

Permafrost is very favorable for the preservation of bone material, but the bodies of dead animals in permafrost pass through different taphonomic filters, e.g., animal feeding, frost weathering, chemical alteration, and abrasion by running water (Sher et al., 2005). A single bone indicates the prior existence of not only hundreds of missing bones of the same animal, but perhaps thousands of non-preserved bones of other animals. A further argument for high abundance of animals in the Mammoth fauna is that mammoth, horse, bison, and reindeer are all herd species; they never live alone. Therefore, the large quantities of bones clearly indicate that a relatively large number of these grazing animals existed in the past, and suggest the existence of appropriate pastures and a tolerable climate.

The total collection of paleontological material can be divided into two unequal parts according to quality of preservation. The smaller part consists of the few samples that provide a basis for partially reconstructing the conditions of their burial, which in turn must have influenced the process of fossilization (taphonomy). The larger part consists of bones, in varying states of preservation, that provide no evidence from which the conditions of their burial might be reconstructed. In some cases, mode of preservation makes it possible to partly reconstruct the depositional or redepositional processes to which a given sample was subjected. Furthermore, some bones show signs of having been gnawed by predators. Large limb bones retain bone marrow preserved inside.

The first way bones can be preserved in permafrost is by being covered in concretions of hydrated iron phosphate (vivianite), indicating diagenetic mineralization and waterlogged storage conditions. The presence of vivianite on bones indicates the conditions under which they were buried, or potentially redeposited. Bones covered in vivianite were buried either in swampy conditions or in deposits with high ice content, which melted and re-froze to form taberal deposits. In either case, the bones were preserved under relatively anoxic conditions and the decomposition of organic matter led to the formation of authigenic aggregates of phosphates, present assoil forms of vivianite (Rothe et al., 2016). Most of the bones in the collection that are covered in vivianite belong to mammoths (16 samples). Far fewer represent other animals: bison (five), horse (two), musk ox (one), and reindeer (one). Three out of five mammoth tusk fragments found *in situ* exhibit vivianite concretions. These tusks were obtained from taberal Kuchchugui deposits, from Krest-Yuryakh deposits in the eastern part of the section (**Figure 3**), and from taberal Yedoma Ice Complex deposits in the western part of the section. Most of the bones and bone fragments covered in vivianite were collected from the western and eastern parts of the coast. The preservation of vivianite, however, indicates that the bone material was not transported over a large distance, as such transport would have destroyed the crystal concretions.

The second way bones can be preserved is by being covered with iron oxides. A total of ten specimens covered with amorphous iron oxides were collected: three mammoth samples (tusk, tooth, and rib fragments), four bison samples (femur and humerus fragments, astragalus, tooth), and three reindeer bones (damaged femur and os centrotarsale, distal fragment of metatarsale). Three of these samples were found on the outcrop, and the other seven on the east shore. The three skeletal elements found on the outcrop include the tusk fragment, which was discovered *in situ*, as well as the mammoth rib fragment and damaged reindeer femur. The rib fragment is from the first rib, and was found on a thermo-terrace beneath the Yedoma Ice Complex at a height of 10 m in the eastern part of the section, whereas the damaged femur was collected on a 6–8 m high thermo-terrace which was also located beneath the Yedoma Ice Complex. The presence of amorphous iron oxides on the bones indicates a long residence time in well-aerated low-moisture sediments, or on the surface of the ground, and limited relocation.

Three samples are coated with both vivianite and iron oxides. These are fragments of the tusk (*in situ*) from the taberal Kuchchugui deposits, and fragments of mammoth tooth and bison femur from the beach. The presence of both vivianite and iron oxides indicates that a given bone was alternately under conditions conducive to the formation of vivianite and conditions conducive to the formation of iron oxides. For example, a mammoth tusk fragment was syncryogenetically buried in Kuchchugui deposits and covered in oxides. Subsequently, the syncryogenic Kuchuguy sediments were thawed, so that the tusk fragment was then subjected to conditions of excess water and lack of oxygen, and became overgrown with vivianite.

The third state in which bones can be found is showing evidence of having been gnawed by predators; samples showing evidence of such damage include fragments of large limb bones, a pelvic fragment, heel bones, and astragali. In our opinion, the bones were gnawed before they were buried, but unequivocal confirmation of this interpretation will require examination of the tooth marks left by the predators. Bones in this condition include four mammoth bones, three horse bones, and one bone each from musk ox and bison. The gnawed mammoth and horse bones were collected from both the western and eastern parts of the shore; the single musk ox and bison bones were collected from one part of the shore only. As mentioned earlier, the musk ox specimen, a distal fragment of the humerus with associated soft tissue, was found in slumped debris on the outcrop located 2.3 km southeast of the mouth of the Krest-Yuryakh River.

Eight fragments of large limb bones are probably the best preserved because they contain bone marrow; these represent the fourth preservation type. The presence of bone marrow is an indicator of rapid bone burial. Four mammoth bone fragments, two musk ox bone fragments, and one each from bison and reindeer, all containing marrow, were found. All were found on the shore. It is possible that a much greater number of bones contain bone marrow; many of the whole large limb bones of horses, bison, reindeer, and musk ox probably contain bone marrow inside, but we did not carry out any special research in this direction.

There are also two interesting samples in the collection. One is a fragment of horse humerus which is gnawed by predators and covered with vivianite. This combination suggests that the bone most likely lay on the surface for some time, and then was redeposited in marshy conditions or it was buried in Ice Complex deposits which melted and re-froze to form taberal deposits. Another single specimen is a fragment of a bison femur with bone marrow that is covered with vivianite. This combination indicates that the bone was probably quickly buried in swampy conditions, The largest number of bones and their fragments were well preserved but show different stages of alteration. In this group we noted bones with varying degrees of roundness indicating transportation. A total of 135 rounded bones and fragments were identified, which is 7.0% of the entire collection (7.9% of the 2007 collection) They are visually differentiated into weakly-rounded, medium-rounded, and strongly-rounded bones, and bones worn by sea-ice. Weakly-rounded bones include carpal and tarsal bones and fragments of the second phalanges of horses, bison, and reindeer totaling 13 samples collected on the beach west of the Camp stream. The medium-rounded bones comprise 107 samples and consist of bones and fragments from 39 horse specimens, 33 bison specimens, 23 reindeer specimens, six mammoth bone fragments, five musk ox bone fragments, and one wolf bone fragment. The small number of rounded mammoth bones, which otherwise dominate the shore collection, indicates a significant resistance of mammoth bones to mechanical abrasion and rounding. Among the rounded bones, tarsal and carpal bones predominate, due to their shape. Sesamoid bones, phalanges, and fragments of large limb bones are present significantly less frequently. Bones of medium roundness were collected both on the eastern and the western parts of the shore. The strongly-rounded bones include nine samples. Five bone fragments belong to bison limb bones and two to horse limb bones; one bone each belongs to mammoth and reindeer. The rounded bones also include bones worn by sea-ice. There are only six such bones: three horse bones (two astrogalus and a tibia fragment), a bison carpal bone, a musk ox astrogalus, and a reindeer astrogalus. This form of preservation is characterized by a completely flat surface on one side of the bones; all morphological structures of the bone (outgrowths, depressions, grooves, broadness, etc.) have been erased. This level surface could have been formed by ice rubbing against the bone while the bone was frozen in beach sediments. A strong degree of such wear is very clearly visible on the bones. Such bones are found on both sides of the coast. The small number of samples preserved in this state does not mean that the other bones, especially the rounded and strongly-rounded ones, did not experience ice friction, but ice rubbing against bones frozen into the sediments of the beach can be clearly established for a few bones only.

Dating of the Paleontological Material From Oyogos Yar

Unfortunately, radiocarbon dates of bones from the Oyogos Yar coast, in contrast to bone dates from the Bykovsky Peninsula, the New Siberian Islands, and the Lena River Delta, are scarce. We submitted 21 samples from our collection for dating; 19 dates have been received (**Table 2**). In a fragment of a left mammoth humerus and in a fragment of a left mammoth ulna, collected on the shore at a relative distance of 2,350 m and between 2,200 and 5,500 m (**Figure 3**), collagen was absent. The humerus fragment was collected on the shore under the outcrop at a relative distance of 2,350 m (**Figure 3**), and the ulna fragment was collected on the shore (**Figure 3**). Of the 19 radiocarbon dates obtained, three are infinite. Two dates were determined from one sample, a *Mammuthus primigenius* rib. The youngest date is 12,550 ± 80 a BP; the oldest is 42,370 + 860/-780 a BP. Of the 18 bones examined, ten specimens are from horses, six specimens are from mammoths with two dates from one bone, and two specimens are from musk ox (**Table 2**). If we consider where samples chosen for dating were collected, two bones (which yielded three dates), a fragment of a rib and a fragment of a mammoth tusk, were collected *in situ*. Six samples from thermo-terraces were dated: two fragments of mammoth bones (ulnare, tibia) and four fragments of horse bones (three femur fragments and a pelvis fragment). Ten specimens were dated from the shore, including six horse bone fragments, two specimens belonging to mammoths, and two specimens from musk ox (**Table 2**). Specimens from the shore were collected near the mouth of the Rebrova River (horse radius and ulna fragments), from the shore below the Kondrat'eva Yedoma and an alas at a relative distance of 5,000 m shown in **Figure 3** (fragments of two tibia and a femur fragment from a horse, a fragment of a mammoth pelvis, and a musk ox vertebra fragment), at the mouth of the stream at 2,200 m relative distance shown in **Figure 3**

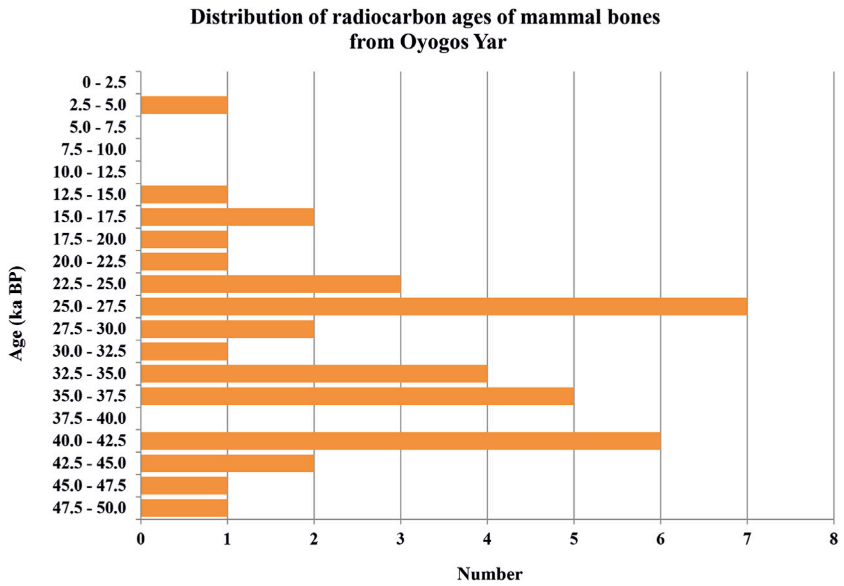

FIGURE 7 | Distribution of radiocarbon ages of mammal bones (38) from the Oyogos Yar coast including data from Nikolskiy et al., 2011 (N = 20), Boeskorov et al., 2013 (N = 2), Rompler et al., 2006 (N = 1), and this study (N = 15). Only finite dates are given as uncalibrated ages.

(horse shovel fragment and damaged musk ox vertebra), and 150 m from the 2002 drop-off site (mammoth pelvis).

The fragment of a mammoth rib collected *in situ* has been dated twice. The time scatter turned out to be significant: >41,500 a BP (GIN-13223) and 22,460 ± 100 a BP (GrA-47134). We cannot explain this significant time discrepancy, because the samples given for dating were both from one bone. The left branch of pelvis that probably belongs to the same mammoth individual as the fragment of rib was dated to 35,250 ± 330 a BP (GIN-14057). The AMS date of 42,370 + 860/-780 a BP (KIA-42888) obtained from the tusk which was found *in situ* is also unexpected. It does not correspond to the stratigraphic position of the host sediments as it is too young. We attribute this discrepancy to the contamination of the sample with modern organic matter.

We cannot clearly confirm the regularity of the distribution of new radiocarbon dates and radiocarbon dates from the Oyogos Yar published earlier (Rompler et al., 2006; Nikolskiy et al., 2011; Boeskorov et al., 2013). The total of 38 radiocarbon final dates is a small database. Most of the dates fall in the time interval from 42.5 to 22.5 ka BP, of which seven dates in the period from 27.5 to 25 ka BP. In the period from 40 to 37.5 ka BP dates are absent (**Figure 7**).

DISCUSSION

Mammal Bone Distribution and Dating at Oyogos Yar

In general, the ratio of bone remains from the main large grazer species of the Mammoth fauna that we found is close to the known percentage of animals in the past fauna. However, the predominance of woolly mammoth remains in the collection can be explained not only by a significant mammoth predominance in the fauna, but also due to the better preservation of large and thick mammoth bones. The large percentage of reindeer bones may be due to bones of modern reindeer being included in the collection. Reindeer is the only large mammalian species of Mammoth fauna that still inhabits the described territory at the present time.

The bones of small adult mammoths (vertebral, carpal, and tarsal bones and others) were collected from both the eastern and western parts of the Oyogos Yar coast. These bones are much smaller in size than similar bones of other mammoths of the same age. Single finds of bones of small adult mammoths were previously described from Bol'shoy Lyakhovsky Island, Bykovsky Peninsula, and the interfluve of the Olenek and Anabar rivers (Kuzmina et al., 1999; Kuznetsova and Kuzmina, 2000; Sher et al., 2000; Kuznetsova et al., 2004). These findings make it possible to put forward a hypothesis about the co-existence of larger and smaller woolly mammoths during some time intervals (Nikolaev et al., 2011) which was further confirmed by Boeskorov et al. (2017) and the present study.

Age information from mammoth bones of group A and group B was obtained from nine samples (**Table 2**; **Figure 3**), which range from >41.5 to 12.5 ka BP. This aligns the MIS 3 to 2 period of Yedoma Ice Complex formation with the presence of Mammoth fauna, although *in situ* findings in deposits predating the Yedoma Ice Complex complicate the picture. For example, the age of a mammoth tusk dated to 42.37 ka BP (**Figure 3**; KIA 42888) and the age of wood fragments dated to 47.7 ka BP (KIA 25730; Opel et al., 2017a), both found in ice-wedge casts attributed to the MIS 5 Krest-Yuryakh stratum, call into question the *in situ* preservation of the organic material or, in turn, the age of the Krest-Yuryakh stratum that has previously been IRSL-dated to 102.4 ± 9.7 kyr ka (Opel et al., 2017a). Here, permafrost degradation, material mobilization, and re-freezing might explain the discordance of older host deposits and the clearly younger bone ages. If this explanation is correct, the present Krest-Yuryakh host deposits must have thawed to incorporate re-located bone material from stratigraphically younger strata, and subsequently have re-frozen *in situ*. This would further imply a warm period sometime between MIS 5 (Krest-Yuryakh) and MIS 3 (Yedoma) or during MIS 3. The regional MIS climate optimum as recorded on Bol'shoy Lyakhovsky Island took place between 48 and 38 ka BP (Andreev et al., 2009; Wetterich et al., 2014) while, in the broader regional context, warmer-than-today summers have been reconstructed on Bykovsky Peninsula at about 48 and 35 ka BP based on pollen, plant macrofossils, and insects (Schirrmeister et al., 2002b; Kienast et al., 2005) and in the Lena Delta at about 48 ka BP, 43.5 to 41 ka BP, and 36 ka BP based on chironomids (Wetterich et al., 2021b). If such a warming episode was able to melt surface wedge ice and create initial thermokarst with a high-center polygonal surface in places, the finding of bones and other organic material post-dating the Krest-Yuryakh host deposits could make sense. However, the intact, thus undisturbed, sedimentary structures of lacustrine laminated Krest-Yuryakh ice-wedge casts call this interpretation into question. The fact that some bones, including this tusk, were for a long time in thawed sediments without access to oxygen under the water of a lake is also indicated by the vivianite covering them.

The 28 radiocarbon dates are known from the Kondrat'eva Yedoma outcrop and the coast below it. Seventeen dates were obtained from bones from this collection (**Table 2**) and 11 dates were published earlier (Nikolskiy et al., 2011). The date range is from >50.0 to 12.5 ka BP. Of these, eight (28.6%) are infinite dates, which may indicate a significant amount of bone remains from deposits older than 47.4 thousand years and a wide distribution of these deposits. Many infinite dates (more than 42%) were also obtained from the bones from the Zimov'e outcrop of the Bolshoy Lyakhovsky Island (the northern coast of the Dmitry Laptev Strait). This also seems to be due to the good exposure of ancient Ice Complexes (Tumskoy, 2012).

The range of finite mammal bone ages at the Kondrat'eva Yedoma exposure covers the MIS 3 to 2 period of Yedoma Ice Complex formation almost completely (**Figure 8**), while host deposits are radiocarbon-dated from 48.5 to 32.2 ka BP (Schirrmeister et al., 2011). The 12 radiocarbon dates belong to the period of Kondrat'eva Yedoma Ice Complex deposition. A fragment of a mammoth ulna with bone marrow dated to 40.7 + 2.1/−1.7 ka BP indicates very rapid sedimentation of some layers of the Ice Complex (**Table 2**). It should be noted that eight dates are younger than 32.2 ka BP, which is the upper age limit obtained from Yedoma Ice Complex deposits (**Figure 8**). The MIS 2 Yedoma Ice Complex, including the sedimentary legacy of the Last Glacial Maximum, has not yet been identified on the Oyogos Yar coast. We noted a similar situation when studying the southern coast of B.L. Island and explained it by fragmentation of the MIS 2 aged deposits (Andreev et al., 2009). Further research on the Zimov'e section on Bol'shoy Lyakhovsky Island indicated

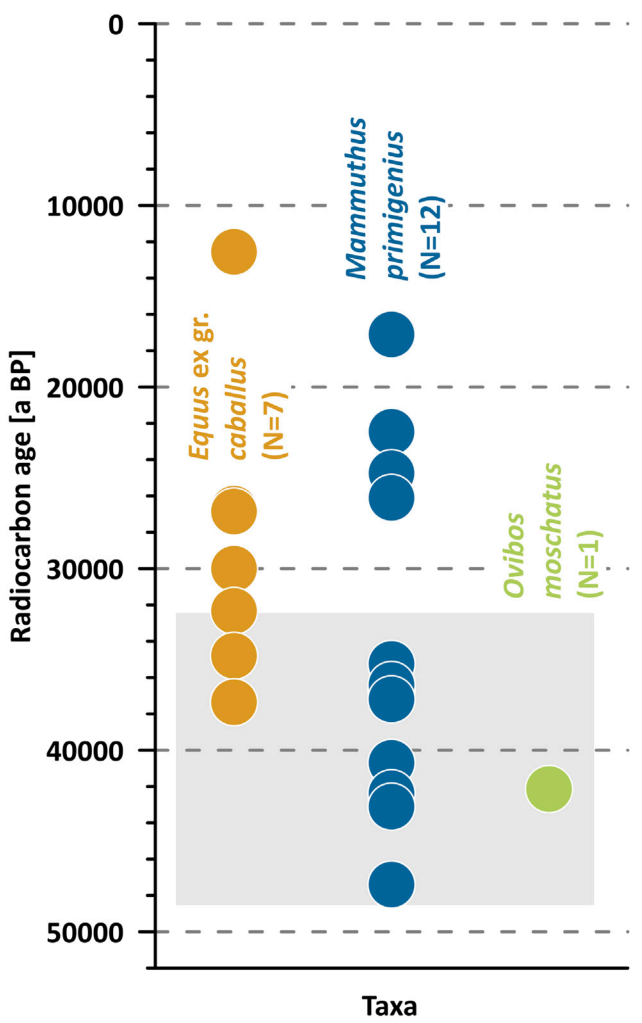

FIGURE 8 | Distribution of radiocarbon ages of mammal bones differentiated by taxa from the Kondrat'eva Yedoma exposure including data from Nikolskiy et al., 2011 (N = 6), Rompler et al., 2006 (N = 1), and this study (N = 13). Only finite dates are given as uncalibrated ages. The gray rectangle highlighted the age range of Kondrat'eva Yedoma Ice Complex host deposits, which was radiocarbon-dated from 48.5 to 32.2 ka a BP (Schirrmeister et al., 2011)

MIS 2 deposits dated from 29.3 to 21.7 ka BP (Wetterich et al., 2011; Wetterich et al., 2021a). Apparently on the Kondrat'eva Yedoma outcrop deposits younger than 32.2 ka BP were fragmented and melted.

One bone was found on the thermo-terrace; it was a distal fragment of horse femur, dated 12.55 ± 0.08 ka BP. It was buried in deposits younger than the Yedoma Ice Complex, but older than the Holocene deposits. Such deposits have not been found either on the Kondrat'eva Yedoma or on the Zimov'e outcrop, although there are bones of this age from both outcrops (Andreev et al., 2009). Thus, dating of bone material often gives dates different from those of the sediments indicating that sediments that were deposited on these outcrops are currently eroded, extending the geological history of the area.

	Oyogos Yar Eastern Shore 2007	Oyogos Yar Western Shore 2007	Oyogos Yar Exposure 2007	Oyogos Yar Exposure 2002	Oyogos Yar Shore 2002	Oyogos Yar Tundra 2002	Bykovsky Exposure Mamontovy Khayata	Bykovsky Shore Mamontovy Khayata	Bykovsky Mamontovaya Terrasa	Bykovsky Cape Mamont	Lyakhovsky Western Exposure	Lyakhovsky Eastern Exposure	Lyakhovsky Western Shore	Lyakhovsky Eastern Shore Exposure	Lyakhovsky Eastern Shore	Lyakhovsky Zimov'e mouth	Lyakhovsky Zimov'e river
Oyogos Yar Eastern Shore 2007		0.99	0.96	0.91	0.98	0.78	0.86	0.95	0.94	0.86	0.92	0.68	0.85	0.94	0.95	0.67	0.97
Oyogos Yar Western Shore 2007	0.99		0.92	0.93	0.97	0.72	0.82	0.95	0.97	0.90	0.96	0.76	0.86	0.96	0.98	0.69	0.96
Oyogos Yar Exposure 2007	0.96	0.92		0.86	0.94	0.83	0.87	0.87	0.85	0.80	0.81	0.50	0.81	0.84	0.85	0.63	0.90
Oyogos Yar Exposure 2002	0.91	0.93	0.86		0.88	0.49	0.68	0.80	0.95	0.94	0.94	0.76	0.91	0.87	0.93	0.85	0.79
Oyogos Yar Shore 2002	0.98	0.97	0.94	0.88		0.82	0.82	0.93	0.90	0.91	0.90	0.60	0.75	0.88	0.95	0.55	0.95
Oyogos Yar Tundra 2002	0.78	0.72	0.83	0.49	0.82		0.79	0.77	0.56	0.55	0.53	0.14	0.39	0.60	0.62	0.10	0.83
Bykovsky Exposure Mamontovy Khayata	0.86	0.82	0.87	0.68	0.82	0.79		0.90	0.77	0.61	0.74	0.47	0.76	0.79	0.72	0.53	0.88
Bykovsky Shore Mamontovy Khayata	0.95	0.95	0.87	0.80	0.93	0.77	0.90		0.92	0.76	0.91	0.71	0.79	0.94	0.89	0.58	0.99
Bykovsky Mamontovaya Terrasa	0.94	0.97	0.85	0.95	0.90	0.56	0.77	0.92		0.88	0.99	0.85	0.90	0.96	0.95	0.79	0.90
Bykovsky Cape Mamont	0.86	0.90	0.80	0.94	0.91	0.55	0.61	0.76	0.88		0.91	0.64	0.74	0.78	0.93	0.64	0.76
Lyakhovsky Western Exposure	0.92	0.96	0.81	0.94	0.90	0.53	0.74	0.91	0.99	0.91		0.86	0.88	0.95	0.97	0.77	0.88
Lyakhovsky Eastern Exposure	0.68	0.76	0.50	0.76	0.60	0.14	0.47	0.71	0.85	0.64	0.86		0.82	0.87	0.79	0.81	0.65
Lyakhovsky Western Shore	0.85	0.86	0.81	0.91	0.75	0.39	0.76	0.79	0.90	0.74	0.88	0.82		0.89	0.84	0.95	0.75
Lyakhovsky Eastern Shore Exposure	0.94	0.96	0.84	0.87	0.88	0.60	0.79	0.94	0.96	0.78	0.95	0.87	0.89		0.94	0.75	0.93
Lyakhovsky Eastern Shore	0.95	0.98	0.85	0.93	0.95	0.62	0.72	0.89	0.95	0.93	0.97	0.79	0.84	0.94		0.70	0.89
Lyakhovsky Zimov'e mouth	0.67	0.69	0.63	0.85	0.55	0.10	0.53	0.58	0.79	0.64	0.77	0.81	0.95	0.75	0.70		0.53
Lyakhovsky Zimov'e river	0.97	0.96	0.90	0.79	0.95	0.83	0.88	0.99	0.90	0.76	0.88	0.65	0.75	0.93	0.89	0.53	

FIGURE 9 | The Pearson correlation coefficients for the different sampling sites of the collections from Oyogos Yar 2007 + 2002, Bykovsky Peninsula 1998, and Bol'shoy Lyakhovsky Island 1999.

The distribution of the radiocarbon dates of the present study and of studies published earlier (Rompler et al., 2006; Nikolskiy et al., 2011; Boeskorov et al., 2013) from Oyogos Yar coast, a total 64 dates from >51.0 to 4.63 ka BP, is available. The 38 finite dates from 48.8 to 12.55 ka BP and the Holocene date (4.63 ka BP) have been analyzed (**Figure 7**). The largest number of dates refers to the time interval from 45 to 22.5 ka BP (MIS 3-2 Yedoma Ice Complex) with three time-peaks: 45–40, 37.5–32.5, and 30–22.5 ka BP. The age of the most famous find from Oyogos Yar, the Yuka mammoth (34.3 ka BP; Boeskorov et al., 2013; Lopatin, 2021), also fits well into the upper part of the MIS 3 Yedoma Ice Complex of Oyogos Yar. The ages of E. ex gr. *caballus* bones in the present study are restricted to the MIS 3-2 period and range from 37.4 to 12.55 ka BP. The discovery of the Yukagir horse (*Equus* sp.) dated to 4.63 ka BP (Boeskorov et al., 2013) confirms a horse presence in the Holocene on Arctic coasts from the Taimyr Peninsula to Oyogos Yar and maybe even further east, as well as on the New Siberian Islands (Lazarev, 1980; Kuznetsova et al., 2001; Kuznetsova and van der Plicht, 2009).

The observed pattern, covering the vast area of Beringia during the late Pleistocene with different local geologies and collection histories, cannot be explained by a random interaction of different local factors. We believe that it is related to a general influence of environmental changes that affected northeastern Siberia during this period.

Regional Comparisons

Bone collections of a similar size as collections from the Oyogos Yar coast are known from Bol'shoy Lyakhovsky Island (Kuznetsova et al., 2015; Wetterich et al., 2011; Wetterich et al., 2021a) and the Bykovsky Peninsula (Sher et al., 2005; Kuznetsova et al., 2019). Other collections from Cape Mamontov Klyk (western Laptev Sea shore, Schirrmeister et al., 2008), from different locations in the Lena Delta (Schirrmeister et al., 2003a; Wetterich et al., 2008; Wetterich et al., 2020; Wetterich et al., 2021b), from the Yana Lowland (Yana RHS site, e.g., Basilyan et al., 2011), the Indigirka Lowland (site, e.g., Pitulko, 2011; Pitulko et al., 2014), the Kolyma Lowland (e.g., Sher, 1971), and Wrangel Island (e.g., Vartanyan et al., 1993) complement the regional picture of the West Beringian mammoth fauna.

In detail, the bone collection from the southern coast of Bol'shoy Lyakhovsky Island comprises 1,026 bones, including one bird bone and 14 unidentified bones (Kuznetsova and

Kuzmina, 2000; Kuznetsova, 2007). The resulting 1011 bones of the Mammoth fauna almost equally represent mammoth (257) and horse bones (253), as well as bison (200) and reindeer (185). Hare (24), cave lion (4), and woolly rhinoceros (6) are more abundant in this collection than in collections from Oyogos Yar and Bykovsky.

The bone collection obtained at different locations on Bykovsky Peninsula, but mainly at the Mamontova Khayata, comprises a total of 1,192 bones, including five bird bones and 71 unidentified bones (Kuznetsova et al., 2019). The resulting total of 1,116 identified mammal bones lacks findings of rare species found in the Oyogos Yar record such as woolly rhinoceros and saiga antelope.

Regional statistical analyses (**Figure 9**) were done for the Oyogos Yar collection in comparison to the Bol'shoy Lyakhovsky Island collection from 1999 (Kuznetsova and Kuzmina, 2000; Kuznetsova, 2007) and the Bykovsky Peninsula from 1998 (Kuznetsova et al., 2019). Consideration of the three collections shows similar proportions for mammoth at Oyogos Yar (39.1%) and Bykovsky Peninsula (38.0%), while Lyakhovsky has fewer mammoth bones (26.5%). The proportion of bison bones in the Oyogos Yar collection (19.5%) is similar to that at Bykovsky (20.8%). Reindeer bones are similar in abundance in all three collections (Oyogos Yar 16.3%, Bykovsky 14.4%, Lyakhovsky 18.5%). Horse bones are least frequent from Oyogos Yar (19.0%) while they are similar for Bykovsky (24.5%) and Lyakhovsky (23.3%). Musk ox finds differ by a few percent (Oyogos Yar 4.6%, Bykovsky 1.9%, Lyakhovsky 7.3%).

The two Oyogos Yar Shore 2007 sampling sites and the Oyogos Yar Exposure 2007 sample site have high correlation coefficients among each other, with highest correlation coefficients between the shore sites, where Oyogos Yar Western and Eastern Shore 2007 have a correlation coefficient of 0.99 (**Figure 9**). Similarly, high correlation is found between those two sampling sites and Oyogos Yar Shore 2002 (0.98 and 0.97).

The Bykovsky Peninsula sampling sites show weaker correlations among each other. The Bykovsky Exposure Mamontovy Khayata site and the Bykovsky Shore Mamontovy Khayata site show a correlation coefficient of 0.9; the Bykovsky Shore Mamontovy Khayata and the Bykovsky Mamontovaya Terrasa (alas) site show a correlation coefficient of 0.92 (**Figure 8**).

The samples from Bol'shoy Lyakhovsky Island show high similarity between the Eastern Exposure, the Eastern Shore Exposure, and the Eastern Shore sites (**Figure 9**). In addition, the Eastern Shore Exposure is similar to the Western Exposure site with a correlation coefficient of 0.95. The Western Shore site is similar to the Zimov'e mouth site, with a correlation coefficient of 0.95.

The Lyakhovsky Zimov'e mouth sample site is not highly correlated to any other site at any location. The Lyakhovsky Eastern Exposure also does not exhibit much similarity to any other sample site, like the Oyogos Yar Tundra 2002 sample, which is the most weakly correlated to all other samples, with correlation coefficients between 0.49 and 0.83. The Bykovsky Mamontovy Khayata Exposure is somewhat similar to the Bykovsky Mamontovy Khayata Shore site (correlation coefficient 0.90), but different from all other sampling sites. Bykovsky Cape Mamont is also somewhat different than all other sites; its highest similarity is to the Oyogos Yar Exposure site with a correlation coefficient of 0.94.

The Oyogos Yar Exposure 2002 sample site shows high correlation with Bykovsky Mamontovaya Terrasa and Bykovsky Cape Mamont (0.95 and 0.94, respectively). The samples from the Bykovsky Mamontovy Khayata Shore site also show high correlation coefficients with the Oyogos Yar Western and Eastern Shore 2007 sites (both 0.95) and the Oyogos Yar Shore 2002 site (0.93). The Lyakhovsky Eastern Shore site also shows high correlation coefficients with the Oyogos Yar Shore 2002 site and the Oyogos Yar Eastern and Western Shore 2007 sites, while the correlation of the Lyakhovsky Eastern Shore site with the Bykovsky Mamontovy Khayata Shore site is only 0.89 (**Figure 9**).

Contrary to the correlation analysis, similarity analysis *via* agglomerative hierarchical cluster analysis (**Figure 10**) groups the Lyakhovsky Western Shore together with the Lyakhovsky Zimov'e Mouth (high similarity, height 0.078) and the Lyakhovsky Eastern Exposure (lower similarity, cluster height 0.190) sites. Furthermore, high similarity is found between the Oyogos Yar Shore 2002, Oyogos Yar Eastern Shore 2007, and Oyogos Yar Western Shore 2007 sites. Those three sampling sites are grouped together with the Lyakhovsky Eastern Shore Exposure and the Lykhovsky Eastern Shore sites (high similarity, cluster height 0.096). The similarity of the Oygos Yar Western and Eastern Shore 2007 sites to the Bykovsky Mamontovy Khayata Shore and the Lyakhovsky Zimov'e River sites shown from the correlation analysis is not reflected in the clustering. Furthermore, the Oyogos Yar Exposure 2002, Bykovsky Mamontovaya Terrasa, and Lyakhovsky Western Exposure sites are grouped together (high similarity, cluster height 0.079), forming a cluster of exposure-like sites from all three locations. The Bykovsky Cape Mamont, Bykovsky Mamontovy Khayata Exposure, and Oyogos Yar Exposure 2007 sites cannot be associated directly with any cluster. The Lyakhovsky Zimov'e River and Bykovsky Mamontovy Khayata Shore sites form a fourth cluster (high similarity, cluster height 0.076). Again, the similarity of those sites to the Oyogos Yar Western and Eastern Shore 2007 sites demonstrated in the correlation analysis is not reflected in the clustering. The Oyogos Yar Tundra 2002 site is distinctly different from all other sampling sites.

In summary, the correlation analysis shows that the Oyogos Yar sampling sites are rather similar to each other, with the exception of the Tundra sample site. Cluster analysis, however, indicates that the Oyogos Yar Shore sites are more similar to shore sites from Bol'shoy Lyakhovsky Island and less similar to the other Oyogos Yar sites. Correlation analysis does not show overall similarities of all sampling sites within the other two locations. High similarities in terms of correlation coefficients between specific sampling sites are often not represented in the cluster analysis. In addition to the "shore cluster," there is one cluster containing exposure-like sites from all locations

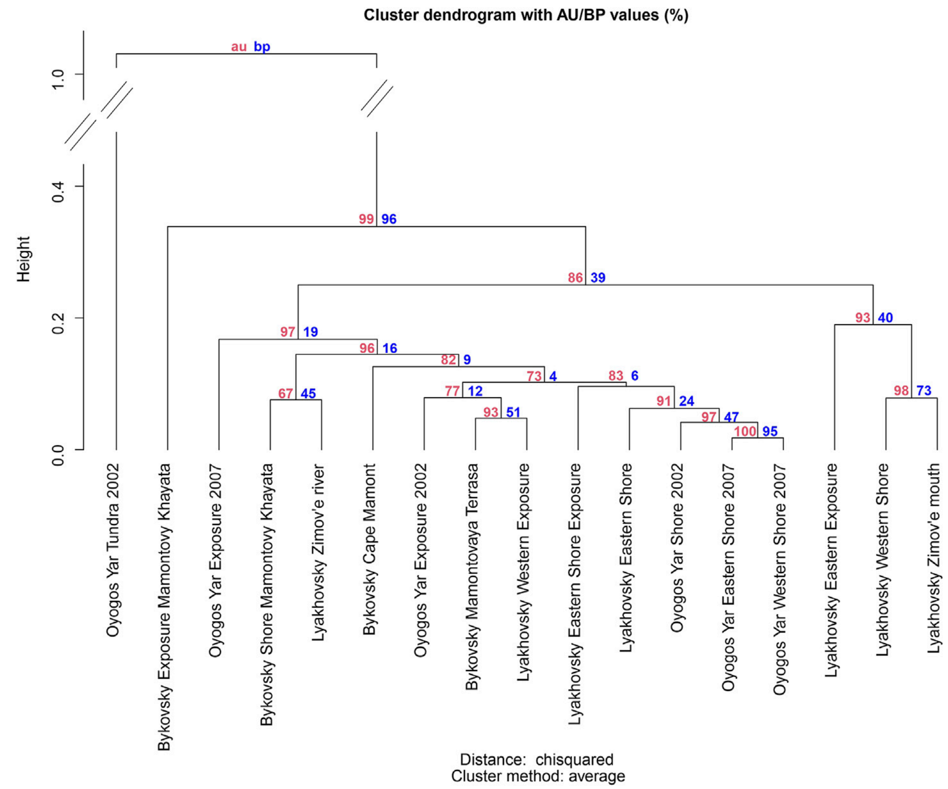

FIGURE 10 | Cluster dendrogram for the hierarchical clustering of mammoth fauna species bone counts for all sampling sites. Distances are assessed using the chi-squared method. Clustering method is "average." Numbers at the dendrogram edges are for basic bootstrapping probability significance values (red) and corrected approximately unbiased significance values (green), statistical significances according to the bootstrapping approach used in pvclust.

(Oyogos Yar Exposure 2002, Bykovsky Mamontovy Terrasa, and Lyakhovsky Western Exposure), where cluster analysis favors the similarities between those samples over similarities to other sites shown in the correlation analysis, e.g., between the Oyogos Yar Exposure 2002 and the Bykovsky Cape Mamont sites and between the Bykovsky Mamontovy Terrasa and the Oyogos Yar Shore sites. Both cluster analysis and correlation analysis show a high similarity between the Bykovsky Mamontovy Khayata Shore and Lyakhovsky Zimov'e River sites. While the correlation analysis clearly indicates low similarities for the Lyakhovsky Eastern Exposure site, cluster analysis places this sample site together with the Lyakhovsky Western Shore and the Lyakhovsky Zimov'e River sites with a statistical significance of 0.93. However, cluster analysis also suggests that this cluster is distinctly different from the other clusters.

CONCLUSIONS

The Oyogos Yar coast is known for finds of late Pleistocene Mammoth fauna remains. Exceptional recent findings of frozen mammoth and horse carcasses in permafrost deposits exposed on the Oyogos Yar coast have drawn attention to this paleo-environmental archive. However, to date the paleontological characteristics of the deposits in this area have not been described in detail. There are also few mammal bone remains from this region kept in museums. Our studies in 2002 and 2007 allow us to give a paleozoological description of the Kondrat'eva Yedoma outcrop, which is one of the Oyogos Yar locations that is richest in paleontological remains. The newly presented collection of mammal bones from the Oyogos Yar coast, sampled in 2002 and 2007, provides well-based insights into species composition and prevalence of the regional Mammoth fauna due to its large total size of 1925 bone specimens. The approach of collecting 100% of bone remains both at the outcrop and on the shore allowed for the most complete restoration to date of the percentage of large mammal late Pleistocene Mammoth fauna that inhabited this area.

The collection from Oyogos Yar consists of 13 mammal species, of which woolly mammoth (40.5%), bison (19%), horse (18.8%), and reindeer (15.8%) predominate. Rare findings of woolly rhinoceros, saiga antelope, elk, and moose as well as of cave lion and wolf are each below 1% of the entire collection. This is fairly comparable to findings from other prominent Yedoma outcrops in the Laptev Sea region on Bykovsky Peninsula and on Bol'shoy Lyakhovsky Island.

The identification of various forms of bone material preservation made it possible to identify different groups of bones, indicating their burial conditions. Limb bones containing bone marrow can serve as indicators of rapid burial in permafrost sediments, without subsequent thawing or redeposition. Bones covered with vivianite indicate that the decomposition of organic matter took place under anoxic conditions, which led to the formation of vivianite crusts on the bone surface. This could happen either when fragments of the skeleton were deposited under bog conditions and were subsequently rapidly buried, or as a result of thawing of ancient ice complexes and the formation of taberal deposits.

Parallel radiocarbon dating of Yedoma Ice Complex sediments and mammal bones has produced interesting results. About half of the finite radiocarbon bone dates are younger than the dates of the sediments in which they were found. This indicates that the Yedoma formation occurred later than 32.3 ka BP, and these deposits were subsequently eroded. The formation of the Oyogos Yar Yedoma Ice Complex ceased at about 32 ka BP. Younger deposits are only small local bodies containing a large amount of mammalian bone remains; we were unable to identify these remains during our work on the section. The discovery of a Holocene horse mummy once again confirms our assumptions about the distribution of horses from Taimyr Peninsula to the Kolyma River during the Holocene.

Considering the locations where the bones were found within the modern coastal morphology enhances estimates of the cryostratigraphic and paleontological implications of the bone findings.

Correlation analysis of three bone collections shows that the Oyogos Yar sampling sites are rather similar to each other but not to all sampling sites at two other locations on Bykovsky Peninsula and on Bol'shoy Lykahovsky Island sampled in 1998 and 1999, respectively. The cluster analysis does not reflect the high similarities in terms of correlation coefficients between specific sampling sites.

DATA AVAILABILITY STATEMENT

Publcly available datasets were analyzed in this study. This data can be found here: The datasets analyzed for this study can be found in the PANGAEA database (https://www.pangaea.de/) as Kuzmina (2007; https://doi.org/10.1594/PANGAEA.615803), Kuznetsova (2007; https://doi.org/10.1594/PANGAEA.615995), Kuznetsova (2007; https://doi.org/10.1594/PANGAEA.619071), and Kuznetsova (2009; https://doi.org/10.1594/PANGAEA.728108).

AUTHOR CONTRIBUTIONS

TK designed the study, collected and identified the bone samples. VT, LS, and SW took part in the fieldwork and contributed cryostratigraphic data and interpretations. HM provided statistical analyses. TK, VT, LS, HM, and SW wrote the manuscript and contributed to the final submitted version.

FUNDING

This work was supported by the Laptev Sea System program and the RFBR grant No. 16-05-01116. For financial support of the research TK is grateful to the scholarship program of the Otto Schmidt Laboratory St. Petersburg (OSL Fellowship 2002–2009, 2015 programs). The research VT was supported by the RSF grant No. 21-77-30001.

ACKNOWLEDGMENTS

The authors gratefully cordially thank their expedition team members in 2002 and 2007, Alexander Derevyagin and Dmitry Dobrynin (both MSU), Viktor Kunitsky (Mel'nikov Permafrost Institute Yakutsk SB RAS), Thomas Opel (AWI), Frank Kienast (Senckenberg Weimar), Lyubov Kudrevataya (Lena Delta Reserve Tiksi), and Andrey Gorodinsky (AARI St. Petersburg). Logistical support was provided by the LENA expeditions 2002 and 2007. Waldemar Schneider (AWI) as well as Dmitry Mel'nichenko and colleagues (Hydrobase Tiksi) are acknowledged. We are grateful to Sebastian Laboor (AWI) who assembled **Figure 1** and to Candace O'Connor who helped with native English corrections and editing. N.E. Zaretskaya (Laboratory of Paleogeography, Institute of Geography RAS Moscow, Russia) and J. van der Plicht (Center for Isotope Research, University of Groningen, The Netherlands) are acknowledged for the radiocarbon dating. We are grateful to our colleagues A.S. Tesakov, M.V. Sotnikova and P.A. Nikolskyi (Quaternary Stratigraphy Laboratory, Institute of Geology RAS Moscow, Russia), and A.N. Kalyakin (MSU) for support identifying material from rodents and lagomorphs, predatory mammals, elk, moose, and birds.

REFERENCES

Andreev, A. A., Grosse, G., Schirrmeister, L., Kuznetsova, T. V., Kuzmina, S. A., and Bobrov, A. A. (2009). Weichselian and Holocene Palaeoenvironmental History of the Bol'shoy Lyakhovsky Island, New Siberian, Arctic Siberia. *Boreas* 38, 72–110. doi:10.1111/j.1502-3885.2008.00039.x

Andreev, A. A., Schirrmeister, L., Tarasov, P. E., Ganopolski, A., Brovkin, V., Siegert, C., et al. (2011). Vegetation and Climate History in the Laptev Sea Region (Arctic Siberia) during Late Quaternary Inferred from Pollen Records. *Quat. Sci. Rev.* 30, 2182–2199. doi:10.1016/j.quascirev.2010.12.026

Andreev, A., Grosse, G., Schirrmeister, L., Kuzmina, S., Novenko, E., Bobrov, A., et al. (2004). Late Saalian and Eemian Palaeoenvironmental History of the Bol'shoy Lyakhovsky Island (Laptev Sea Region, Arctic Siberia). *Boreas* 33, 319–348. doi:10.1080/03009480410001974

Basilyan, A. E., Anisimov, M. A., Nikolskiy, P. A., and Pitulko, V. V. (2011). Wooly Mammoth Mass Accumulation Next to the Paleolithic Yana RHS Site, Arctic Siberia: its Geology, Age, and Relation to Past Human Activity. *J. Archaeol. Sci.* 38 (9), 2461–2474. doi:10.1016/j.jas.2011.05.017

Boeskorov, G. G., Potapova, O. R., Mashchenko, E. N., Protopopov, A. V., Kuznetsova, T. V., Agenbroad, L., et al. (2014). Preliminary Analyses of the Frozen Mummies of Mammoth (*Mammuthus primigenius*), Bison (*Bison priscus*) and Horse (*Equus* sp.) from the Yana-Indigirka Lowland, Yakutia, Russia. *Integr. Zool.* 9, 471–480. doi:10.1111/1749-4877.12079

Boeskorov, G. G., Protopopov, A. V., Mashchenko, E. N., Potapova, O. R., Kuznetsova, T. V., Plotnikov, V. V., et al. (2013). New Findings of Unique Preserved Fossil Mammals in the Permafrost of Yakutia. *Dokl. Biol. Sci.* 452, 291–295. doi:10.1134/s0012496613050116

Boeskorov, G., Zhegallo, V., Kuznetsova, T., and Tikhonov, A. (2017). "The Possible Cases of "dwarfism" in Woolly Mammoths from Eastern Siberia," in Abstracts of the VII International Conference Mammoths and their relatives-ICMR-2017 (Taiwan: Taichung), P-02.

Efremov, I. A. (1950). Taphonomy i Geologicheskaya letopis' (Taphonomy and Geological Record). *Trudy Paleontologicheskogo Instituta SSSR* 24, 1–178. (in Russian).

Grigoriev, A. A. (1932). "Ob Oledenenii Territorii Yakutii v Chetvertichnyi Period (To the Glaciation of Yakutia at the Quaternary),," in Proceedings of the Quaternary Research Commission (Leningrad: Soviet Academy of Sciences Publishers), 31–42. (in Russian).

Günther, F., Overduin, P. P., Sandakov, A. V., Grosse, G., and Grigoriev, M. N. (2013). Short- and Long-Term Thermo-Erosion of Ice-Rich Permafrost Coasts in the Laptev Sea Region. *Biogeosciences* 10, 4297–4318. doi:10.5194/bg-10-4297-2013

Gusev, A. I. (1958). K Stratigrafii Chetvertichnykh Otlozhenii Zapadnoi Chasti Primorskoi Ravniny (Towards Stratigraphy of Quaternary Deposits of the Western Part of the Coastal Lowland). *Arct. Geol.* 80 (5), 79–86. *Article Collection on* (in Russian).

Ivanov, O. A. (1972). "Stratigrafiya i Korrelyatsiya Neogenovykh i Chetvertichnykh Otlozhenii Subarkticheskikh Ravnin Vostochnoi Yakutii (Stratigraphy and Correlation of Neogene and Quaternary Deposits on the Subarctic Lowlands of the Eastern Yakutia)," in *Problemy Izucheniya Chetvertichnogo Perioda (Problems of Investigation of the Quaternary)* (Moscow: Nauka), 202–211. (in Russian).

Kaplina, T. N. (2009). Alasnye Kompleksy Severnoi Yakutii (Alas Complexes of Northern Yakutia). *Earth's Cryosphere* XIII (4), 3–17. (in Russian).

Kienast, F., Schirrmeister, L., Siegert, C., and Tarasov, P. (2005). Palaeobotanical Evidence for Warm Summers in the East Siberian Arctic during the Last Cold Stage. *Quat. Res.* 63 (3), 283–300. doi:10.1016/j.yqres.2005.01.003

Kienast, F., Wetterich, S., Kuzmina, S., Schirrmeister, L., Andreev, A. A., Tarasov, P., et al. (2011). Paleontological Records Indicate the Occurrence of Open Woodlands in a Dry Inland Climate at the Present-Day Arctic Coast in Western Beringia during the Last Interglacial. *Quat. Sci. Rev.* 30 (17-18), 2134–2159. doi:10.1016/j.quascirev.2010.11.024

Konishchev, V. N., and Kolesnikov, S. F. (1981). "Osobennosti Stroeniya i Sostava Pozdnekaynozoiskikh Otlozhenii v Obnazhenii Oyogosskii Yar (Peculiarities of the Structure and Composition of Late Cenozoic Deposits at the Oyogos Yar Exposure)". *Problems Cryolithology* IX, 107–117. (in Russian).

Kuzmina, S., Kuznetsova, T., and Sher, A. (1999). Paleontological Research on the Bykovsky Peninsula. *Rep. Polar Res.* 315, 179227–187257. doi:10.2312/BzP_0315_1_1999

Kuznetsova, T. (2008). Fossils of the Mammoth Fauna. *Rep. Polar Mar. Res.* 584 (139–140), 215–248. doi:10.2312/BzPM_0584_2008

Kuznetsova, T., and Kuzmina, S. (2000). Paleontological Research at the Southern Coast of Bol'shoy Lyakhovsky Lsland. *Rep. Polar Mar. Res.* 354 (151–161), 223–253. doi:10.2312/BzP_0354_1_2000

Kuznetsova, T. P. (1965). "Chetvertichnykh Otlozheniyakh s Podzemnym L'dom na Yano-Indigirskoy Nizmennosti i o-ve Bol'shom Lyakhovskom (About Quaternary Deposits with Ground Ice on the Yana-Indigirka lowland and Bol'shoy Lyakhovsky Island)" in *Podzemnyi Led (Underground Ice)* (Moscow: MSU Publishers), 120–132. (in Russian).

Kuznetsova, T. V. (2007). Paleontological Collection of the "Mammoth" Fauna From the Museum of the Lena Delta Reserve. *Rep. Polar Mar. Res.* 550 (135–138), 173–195.

Kuznetsova, T. V. (2009). *Bones Collection on New Siberian Islands from the Expedition LENA 2007, Appendix 4.2.* PANGAEA. doi:10.1594/PANGAEA.728108

Kuznetsova, T. (2003). List of Bone Samples of the New Siberian Islands. *Rep. Polar Mar. Res.* 466, 289–313. doi:10.1594/PANGAEA.619071

Kuznetsova, T. V., Schirrmeister, L., and Noskova, N. G. (2004). "Kollektsii "Mammontovoy fauny" iz raiona morya Laptevykh v muzeyakh i institutakh Rossiyskoy Arfdemii nauk (Colldection of "Mammoth Fauna" from the Laptev Sea Region in Museums and Institutes of the Russian Academy of Sciences)," in Abstracts, of the conference "Regional Geology Problems, Museum Perspective" (Moscow, 45–50. (in Russian).

Kuznetsova, T. V., Schirrmeister, L., and Tumskoy, V. E. (2015). "Pleistocene - Holocene Terrestrial Palaeoenvironmental Changes at the New Siberian Islands and Adjacent Areas (Arctic Siberia)," in Abstracts of the Third International Conference and Workshop Past Gateways-2015, May 18–22, 2015 (Potsdam, Germany: Terra Nostra), 51.

Kuznetsova, T. V., and Starodubtseva, I. A. (2009). "Mamonty i istoriya geologicheskogo izucheniy poberezhiya morya Laptevikh i Novosibirskikh ostrovov (Mammoths and the History of Geological Research of the Laptev Sea Region and the New Siberian Islands)" in *System Laptev Sea and Adjacent Arctic Seas: State of the Art and History of Development*. Editors H. Kassens, A. P. Lisitsyn, J. Thiede, E. I. Polyakova, L. A. Timokhov, and I. E. Frolov (Moscow: MSU Publishers), 481–500. (in Russian).

Kuznetsova, T. V., Sulerzhitsky, L. D., and Siegert, C. (2001). "New Data on the "Mammoth" Fauna of the Laptev Shelf Land (Arctic Siberia)", in Proceedings of First International Congress – The World of Elephants (Rome), 289–292.

Kuznetsova, T. V., Tumskoy, V. E., Schirrmeister, L., and Wetterich, S. (2019). Paleozoologitcheskaya kharakteristika pozdneneopleistotsen - golotsenovykh otlozheniy Bikovskogo poluostrova (Severnaya Yakutiya) (Paleozoological Characteristics of Late Neopleistocene–Holocene Deposits of the Bykovsky Peninsula, Northern Yakutia). *Zoological J.* 98 (11), 1268–1290. (in Russian). doi:10.1134/S0044513419110102

Kuznetsova, T. V., and van der Plicht, H. (2009). "Pozdnepleistocenovie i golocenovie loshadi Severnoy Yakutii (Late Pleistocene and Holocene Horses of Northern Yakutia)" in Proceedings of the All-Russian Conference "200th Anniversary of Patriotic Paleotology" (Moscow, Russia, 65–66. (in Russian).

Lazarev, P. A. (1980). *Antropogenovie loshadi Yakutii. (Anthropogenic Horses in Yakutia)*. Moscow: Nauka, 1–190. (in Russian).

Lopatin, A. V. (2021). Yuka the Mammoth, a Frozen Mummy of a Young Female Woolly Mammoth from Oyogos. *Paleontol. J.* 55 (11), 1270–1274. doi:10.1134/S0031030121110046

Nagaoka, D., Saijo, K., and Fukuda, M. (1995). Sedimental Environment of the Edoma in High Arctic Eastern Siberia. Proceedings of the Third Symposium on the joint Siberian permafrost Studies between Japan and Russia in 1994 (Tsukuba, Japan), 8–13.

Neretina, A. N., Gololobova, M. A., Neplyukhina, A. A., Zharov, A. A., Rogers, C. D., Horne, D. J., et al. (2020). Crustacean Remains from the Yuka Mammoth Raise Questions about Non-analogue Freshwater Communities in the Beringian Region during the Pleistocene. *Sci. Rep.* 10, 859. doi:10.1038/s41598-020-57604-8

Nikolaev, V. I., Kuznetsova, T. V., and Alekseev, O. A. (2011). "Predvaritel'nie rezultati izotopnikh i geokhimicheskikh issledovaniy pozdnepleistotsenovikh mamontov Severnoi Yakutii (Preliminary Results of Isotopic and Geochemical Studies of Late Pleistocene Mammoths of Northern Yakutia)" *Izv. Ross. Akad. Nauk. Seriya Geogr.* 2, 78–88. (in Russian).

Nikolskiy, P. A., and Basilyan, A. E. (2004). "Mys Svytoi Nos – opornyi razrez chetvertichnykh otlozhenii severa Yano-Indigirskoy nizmennosti (Svyatoi Nos Cape – the Main Section of Quaternary Deposits at the North of Yana-Indigirka Lowland)," in *Estestvennaya Istoriya Rossiyskoi Vostochnoi Arktiki v Pleistotsene i Golotsene (The Natural History of the Russian Eastern Arctic in Pleistocene and Holocene)* (Moscow: GEOS), 5–13. (in Russian).

Nikolskiy, P. A., Sulerzhitsky, L. D., and Pitulko, V. V. (2011). Last Straw versus Blitzkrieg Overkill: Climate-Driven Changes in the Arctic Siberian Mammoth Population and the Late Pleistocene Extinction Problem. *Quat. Sci. Rev.* 30, 2309–2328. doi:10.1016/j.quascirev.2010.10.017

Opel, T., Dereviagin, A. Y., Meyer, H., Schirrmeister, L., and Wetterich, S. (2011). Palaeoclimatic Information from Stable Water Isotopes of Holocene Ice Wedges on the Dmitrii Laptev Strait, Northeast Siberia, Russia. *Permafr. Periglac. Process.* 22, 84–100. doi:10.1002/ppp.667

Opel, T., Wetterich, S., Meyer, H., Dereviagin, A. Y., Fuchs, M. C., and Schirrmeister, L. (2017a). Ground-ice Stable Isotopes and Cryostratigraphy Reflect Late Quaternary Palaeoclimate in the Northeast Siberian Arctic (Oyogos Yar Coast, Dmitry Laptev Strait). *Clim. Past.* 13, 587–611. doi:10.5194/cp-13-587-2017

Opel, T., Laepple, T., Meyer, H., Dereviagin, A. Y., and Wetterich, S. (2017b). Northeast Siberian Ice Wedges Confirm Arctic Winter Warming over the Past Two Millennia. *Holocene* 27, 1789–1796. doi:10.1177/0959683617702229

Pavlova, E. Y., and Pitulko, V. V. (2020). Late Pleistocene and Early Holocene Climate Changes and Human Habitation in the Arctic Western Beringia Based on Revision of Palaeobotanical Data. *Quat. Int.* 549, 5–25. doi:10.1016/j.quaint.2020.04.015

Pitulko, V., Pavlova, E., and Nikolskiy, P. (2017). Revising the Archaeological Record of the Upper Pleistocene Arctic Siberia: Human Dispersal and

Adaptations in MIS 3 and 2. *Quat. Sci. Rev.* 165, 127–148. doi:10.1016/j.quascirev.2017.04.004

Pitulko, V. V., Basilyan, A. E., and Pavlova, E. Y. (2014). The Berelekh Mammoth "Graveyard": New Chronological and Stratigraphical Data from the 2009 Field Season. *Geoarchaeology* 29, 277–299. doi:10.1002/gea.21483

Pitulko, V. V. (2011). The Berelekh Quest: A Review of Forty Years of Research in the Mammoth Graveyard in Northeast Siberia. *Geoarchaeology* 26, 5–32. doi:10.1002/gea.20342

Prokhorova, S. M., and Ivanov, O. A. (1973). *Olovonosnye Granitoidy Yano-Indigirskoi Nizmennosti i Svyazannye s Nimi Rossypi (Tin-Bearing Granitoids of the Yana-Indigirka Lowland and Associated with Them Placers)*. Leningrad: Nedra, 229. (in Russian).

R Core Team (2021). *R: A Language and Environment for Statistical Computing*. Vienna, Austria: R Foundation for Statistical Computing.

Romanovskii, N. N. (1961a). Erozionno-termokarstovye Kotloviny na Severe Primorskikh Nizmennostey Yakutii i Novosibirskikh Ostrovakh (Thrermokarst-Erosional Depressions in the Northern Coastal Lowlands of Yakutia and the New Siberian Islands). *Merzlotnye issledovaniya (Permafrost Res.) I*, 124–144. (in Russian).

Romanovskii, N. N. (1961b). O Stroenii Yano-Indigirskoi Primorskoi Allyuvialnoi Ravniny i Usloviyakh ee Formirovaniya (About the Structure of the Yana-Indigirka Coastal Alluvial plain and Conditions of its Formation). *Merzlotnye issledovaniya (Permafrost Res.) II*, 129–138. (in Russian).

Romanovskii, N. N. (1958). Permafrost Envelopment Structures in Quaternary Sediments. *Sci. Rep. High. Sch. Geol. Geogr. Sci.* 3, 185–188. (in Russian).

Römpler, H., Rohland, N., Lalueza-Fox, C., Willerslev, E., Kuznetsova, T., Rabeder, G., et al. (2006). Nuclear Gene Indicates Coat-Color Polymorphism in Mammoths. *Science* 313 (5783), 62. doi:10.1126/science.1128994

Rothe, M., Kleeberg, A., and Hupfer, M. (2016). The Occurrence, Identification and Environmental Relevance of Vivianite in Waterlogged Soils and Aquatic Sediments. *Earth-Science Rev.* 158, 51–64. doi:10.1016/j.earscirev.2016.04.008

Rudaya, N., Protopopov, A., Trofimova, S., Plotnikov, V., and Zhilich, S. (2015). Landscapes of the 'Yuka' Mammoth Habitat: A Palaeobotanical Approach. *Rev. Palaeobot. Palynology* 214, 1–8. doi:10.1016/j.revpalbo.2014.12.003

Schirrmeister, L., Grosse, G., Kunitsky, V., Magens, D., Meyer, H., Dereviagin, A., et al. (2008). Periglacial Landscape Evolution and Environmental Changes of Arctic Lowland Areas for the Last 60 000 Years (Western Laptev Sea Coast, Cape Mamontov Klyk). *Polar Res.* 27, 249–272. doi:10.1111/j.1751-8369.2008.00067.x

Schirrmeister, L., Grosse, G., KunitskyMayer, V. H., Derevyagin, A., and Kuznetsova, T. (2003a). Permafrost, periglacial and paleo-environmental studies on New Siberian Islands. *Reports on Polar and Marine Research. Russian-German Cooperation System Laptev Sea. The Expeditions Lena* 466, 195–314.

Schirrmeister, L., Grosse, G., Schwamborn, G., Andreev, A. A., Meyer, H., Kunitsky, V. V., et al. (2003b). Late Quaternary History of the Accumulation Plain North of the Chekanovsky Ridge (Lena Delta, Russia): A Multidisciplinary Approach. *Polar Geogr.* 27 (4), 277–319. doi:10.1080/789610225

Schirrmeister, L., Kunitsky, V., Grosse, G., Wetterich, S., Meyer, H., Schwamborn, G., et al. (2011). Sedimentary Characteristics and Origin of the Late Pleistocene Ice Complex on North-East Siberian Arctic Coastal Lowlands and Islands - A Review. *Quat. Int.* 241, 3–25. doi:10.1016/j.quaint.2010.04.004

Schirrmeister, L., Oezen, D., and Geyh, M. A. (2002a). ^{230}Th/U Dating of Frozen Peat, Bol'shoy Lyakhovsky Island (Northern Siberia). *Quat. Res.* 57, 253–258. doi:10.1006/qres.2001.2306

Schirrmeister, L., Siegert, C., Siegert, C., Kuznetsova, T., Kuzmina, S., Andreev, A., et al. (2002b). Paleoenvironmental and Paleoclimatic Records from Permafrost Deposits in the Arctic Region of Northern Siberia. *Quat. Int.* 89, 97–118. doi:10.1016/s1040-6182(01)00083-0

Sher, A., Parmuzin, I., and Bortsov, A. (2000). Mamma1 Bone Collecting. *Rep. Polar Res.* 354, 181268–182269. doi:10.2312/BzP_0354_1_2000

Sher, A. V., Kuzmina, S. A., Kuznetsova, T. V., and Sulerzhitsky, L. D. (2005). New Insights into the Weichselian Environment and Climate of the East Siberian Arctic, Derived from Fossil Insects, Plants, and Mammals. *Quat. Sci. Rev.* 24, 533–569. doi:10.1016/j.quascirev.2004.09.007

Sher, A. V. (1971). Säugetierfunde und Pleistozänstratigraphie in der Kolyma Niederung. *Berichte Dtsch. Ges. für Geol. Wiss. A* 16 (2), 113–125. (in German).

Skvortsov, E. F. (1914). Lensko-Kolymskaya Ekspeditsiya 1909 g. (Lena-Kolyma Expedition, 1909). *Izvestiya Imperatorskogo Russkogo Geograficheskogo Obshchestva (Trans. Imperial Russ. Geogr. Soc.)* 50 (7), 401–428. (in Russian).

Skvortsov, E. F. (1930). ℌV Pribrezhnykh Tundrakh Yakutii (Dnevnik Astronoma Lensko-Kolymskoy Ekspeditsii 1909 g. (On the Coastal Tundra of Yakutia. (Diary of the Astronomer of the Leno-Kolyma Expedition 1909))," in Izvestiya Komiteta po Izucheniyu Yakutskoy SSR (Proceedings of the Committee for Yakutian SSR Investigation), XV. Leningrad: Academy of Sciences Publishers, 1–244. (in Russian).

Smirnov, A. N. (2003). Iscopaemaya mamontovaya kost' (Fossil Mammoth Bone). Proc. NIIGA-VNIIOkeangeologia. Saint-Petersburg. 172. (in Russian).

Spizharskii, T. N. (1940). Quaternary Glaciation of the Lena-Indigirka Region. *Problems Arct.* 11, 70–81. (in Russian).

Suzuki, R., and Shimodaira, H. (2006). Pvclust: an R Package for Assessing the Uncertainty in Hierarchical Clustering. *Bioinformatics* 22 (12), 1540–1542. doi:10.1093/bioinformatics/btl117

Suzuki, R., Terada, Y., and Shimodaira, H. (2019). Pvclust: Hierarchical Clustering with P-Values via Multiscale Bootstrap Resampling. R Package Version 2.2-0. Available at: https://CRAN.R-project.org/package=pvclust.

Tomidiaro, S. V., Chernen'kiy, B. I., and Bashlavin, D. K. (1982). "Loess-ice Formation of the Shelf Type and the Outcrop Oyogos Yar," in *Permafrost and Geological Processes and the Palaeogeography of the Northeast Asian Lowlands*. Editor Yu. V. Shumilov (Magadan: Soviet Academy of Sciences Publishers, Far-east Scientific Center), 30–53. (in Russian).

Tumskoy, V. E., and Dobrynin, D. (2008). Stratigraphical and Geomorphological Studies along the South Coast of Bol'shoy Lyakhovsky Island and along the Oyogos Yar Coast. *Rep. Polar Mar. Res.* 584, 41–50. doi:10.2312/BzPM_0584_2008

Tumskoy, V. E., and Kuznetsova, T. V. (2022). Geological Structure and Cryostratigraphy of the Quaternary Deposits of Oyogos Yar (South Coast of the Dmitry Laptev Strait, Northern Yakutia). *Front. Earth Sci.* 10, 789421 doi:10.3389/feart.2022.789421

Tumskoy, V. E. (2012). Osobennosti Kriolitogeneza Otlozheniy Severnoi Yakutii v Srednem Pleistotsene – Golotsene (Peculiarities of Cryolithogenesis of Deposits in Northern Yakutia in the Middle Neopleistocene-Holocene). *Earth's Cryosphere* XVI (1), 12–21. (in Russian).

Vartanyan, S. L., Garutt, V. E., and Sher, A. V. (1993). Holocene Dwarf Mammoths from Wrangel Island in the Siberian Arctic. *Nature* 362 (6418), 337–340. doi:10.1038/362337a0

Wetterich, S., Kizyakov, A., Fritz, M., Wolter, J., Mollenhauer, G., Meyer, H., et al. (2020). The Cryostratigraphy of the Yedoma Cliff of Sobo-Sise Island (Lena Delta) Reveals Permafrost Dynamics in the Central Laptev Sea Coastal Region during the Last 52 Kyr. *Cryosphere* 14, 4525–4551. doi:10.5194/tc-14-4525-2020

Wetterich, S., Kuzmina, S., Andreev, A. A., Kienast, F., Meyer, H., Schirrmeister, L., et al. (2008). Palaeoenvironmental Dynamics Inferred from Late Quaternary Permafrost Deposits on Kurungnakh Island, Lena Delta, Northeast Siberia, Russia. *Quat. Sci. Rev.* 27 (15), 1523–1540. doi:10.1016/j.quascirev.2008.04.007

Wetterich, S., Meyer, H., Fritz, M., Mollenhauer, G., Rethemeyer, J., Kizyakov, A., et al. (2021a). Northeast Siberian Permafrost Ice-Wedge Stable Isotopes Depict Pronounced Last Glacial Maximum Winter Cooling. *Geophys. Res. Lett.* 48, e2020GL092087. doi:10.1029/2020gl092087

Wetterich, S., Rudaya, N., Nazarova, L., Syrykh, L., Pavlova, M., Palagushkina, O., et al. (2021b). Paleo-Ecology of the Yedoma Ice Complex on Sobo-Sise Island (EasternLena Delta, Siberian Arctic). *Front. Earth Sci.* 9, 681511. doi:10.3389/feart.2021.681511

Wetterich, S., Rudaya, N., Kuznetsov, V., Maksimov, F., Opel, T., Meyer, H., et al. (2019). Ice Complex Formation on Bol'shoy Lyakhovsky Island (New Siberian Archipelago, East Siberian Arctic) Since about 200 Ka. *Quat. Res.* 92 (2), 530–548. doi:10.1017/qua.2019.6

Wetterich, S., Rudaya, N., Tumskoy, V., Andreev, A. A., Opel, T., Schirrmeister, L., et al. (2011). Last Glacial Maximum Records in Permafrost of the East Siberian Arctic. *Quat. Sci. Rev.* 30, 3139–3151. doi:10.1016/j.quascirev.2011.07.020

Wetterich, S., Schirrmeister, L., Andreev, A. A., Pudenz, M., Plessen, B., Meyer, H., et al. (2009). Eemian and Late Glacial/Holocene Palaeoenvironmental Records from Permafrost Sequences at the Dmitry Laptev Strait (NE Siberia, Russia). *Palaeogeogr. Palaeoclimatol. Palaeoecol.* 279, 73–95. doi:10.1016/j.palaeo.2009.05.002

Wetterich, S., Tumskoy, V., Rudaya, N., Andreev, A. A., Opel, T., Meyer, H., et al. (2014). Ice Complex Formation in Arctic East Siberia during the MIS3 Interstadial. *Quat. Sci. Rev.* 84, 39–55. doi:10.1016/j.quascirev.2013.11.009

Wetterich, S., Tumskoy, V., Rudaya, N., Kuznetsov, V., Maksimov, F., Opel, T., et al. (2016). Ice Complex Permafrost of MIS5 Age in the Dmitry Laptev Strait Coastal Region (East Siberian Arctic). *Quat. Sci. Rev.* 147, 298–311. doi:10.1016/j.quascirev.2015.11.016

Zimmermann, H., Raschke, E., Epp, L., Stoof-Leichsenring, K., Schirrmeister, L., Schwamborn, G., et al. (2017). The History of Tree and Shrub Taxa on Bol'shoy Lyakhovsky Island (New Siberian Archipelago) since the Last Interglacial Uncovered by Sedimentary Ancient DNA and Pollen Data. *Genes* 8, 273. doi:10.3390/genes8100273

Conflict of Interest: The authors declare that the research was conducted in the absence of any commercial or financial relationships that could be construed as a potential conflict of interest.

Publisher's Note: All claims expressed in this article are solely those of the authors and do not necessarily represent those of their affiliated organizations, or those of the publisher, the editors and the reviewers. Any product that may be evaluated in this article, or claim that may be made by its manufacturer, is not guaranteed or endorsed by the publisher.

Advantages of publishing in Frontiers

OPEN ACCESS
Articles are free to read for greatest visibility and readership

FAST PUBLICATION
Around 90 days from submission to decision

HIGH QUALITY PEER-REVIEW
Rigorous, collaborative, and constructive peer-review

TRANSPARENT PEER-REVIEW
Editors and reviewers acknowledged by name on published articles

Frontiers
Avenue du Tribunal-Fédéral 34
1005 Lausanne | Switzerland

Visit us: www.frontiersin.org
Contact us: frontiersin.org/about/contact

REPRODUCIBILITY OF RESEARCH
Support open data and methods to enhance research reproducibility

DIGITAL PUBLISHING
Articles designed for optimal readership across devices

FOLLOW US
@frontiersin

IMPACT METRICS
Advanced article metrics track visibility across digital media

EXTENSIVE PROMOTION
Marketing and promotion of impactful research

LOOP RESEARCH NETWORK
Our network increases your article's readership